V INTERNATIONAL CONFERENCE ON
INFORMATION TECHNOLOGY AND NANOTECHNOLOGY

PROCEEDINGS OF ITNT - 2019

CEUR Workshop Proceedings

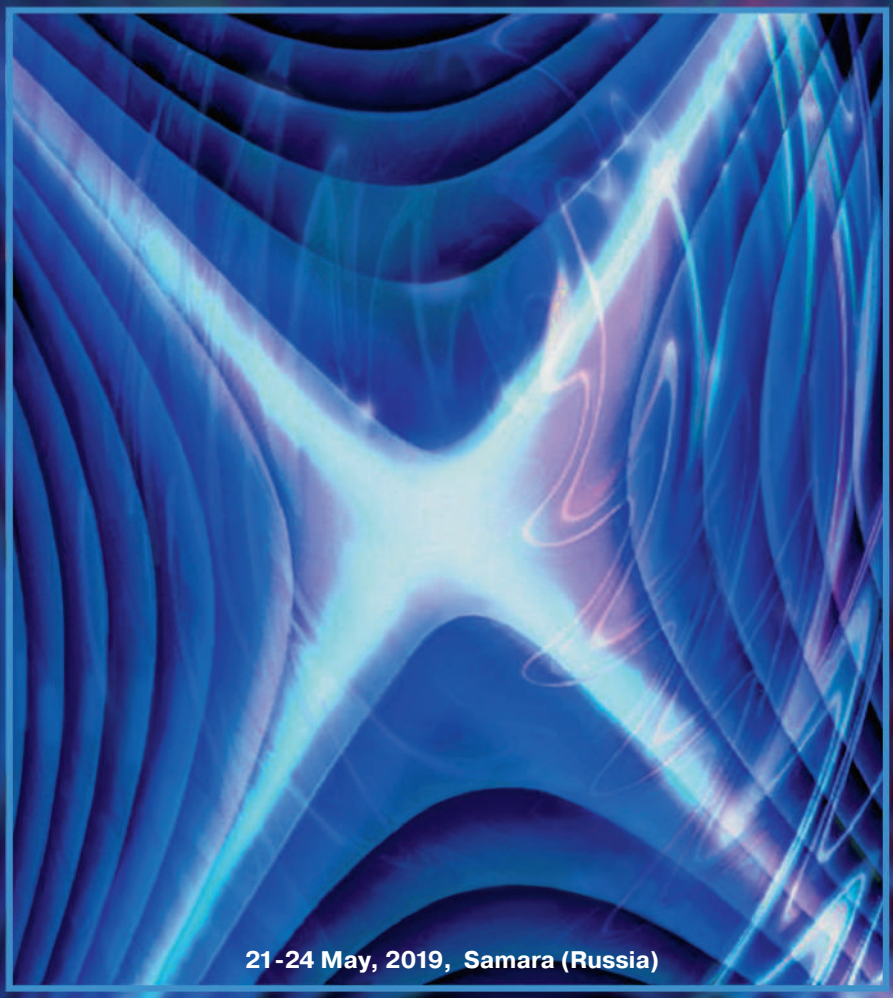

21-24 May, 2019, Samara (Russia)

Samara National Research University
Image Processing Systems Institute of the RAS - branch of the Federal Scientific Research Centre “Crystallography and Photonics” of Russian Academy of Sciences

INFORMATION TECHNOLOGY AND NANOTECHNOLOGY (ITNT-2019)

Section: Image Processing and Earth Remote Sensing
Section: Data Science

Collection of selected papers of the IV International Conference on Information Technology and Nanotechnology
(Samara, 2019, 21-27 May)

978-5-6047396-0-0
Publisher: IP Zaitsev V.D.

Samara
2019

Collection of selected papers of the V International Conference on Information Technology and Nanotechnology (ITNT-2019). Section. Image Processing and Earth Remote Sensing. Section. Data Science. Samara, Individual Proprietor Zaitsev V.D. 2019, 21-27 May. ISBN 978-5-6047396-0-0.

Compilers of the volume: Vladislav Myasnikov, Vladislav Sergeyev, Vladimir Fursov
Issuing editor: Denis Kudryashov
Publisher: Individual Proprietor Zaitsev V.D.

The conference is a forum for leading researchers from all over the world aimed to discuss the latest advances in the basic and applied research in the field of Information Technology and Nanotechnology. It is also aimed to attract young people to advanced scientific research and share the latest trends in training and research programs for future ITNT specialists.

CONTENTS
Image Processing and Earth Remote Sensing

CONTENTS
Data Science

Preface

D V Kudryashov[1,2], E S Kozlova[1,2], V V Myasnikov[1,2] and V A Fedoseev[1,2]

[1]Samara National Research University, Moskovskoe Shosse 34, Samara, Russia, 443086
[2]Image Processing Systems Institute of the RAS - Branch of the Federal Scientific Research Centre “Crystallography and Photonics” of Russian Academy of Sciences, Molodogvardeyskaya str. 151, Samara, Russia, 443001

This volume contains the papers presented at the session "Image Processing and Earth Remote Sensing" within the V International Conference on Information Technology and Nanotechnology (ITNT-2019).

The conference was held in Samara, Russia, during May 21-24, 2019 (itnt-conf.org). The conference is a forum for leading researchers from all over the world aimed to discuss the latest advances in the basic and applied research in the field of Information Technology and Nanotechnology. It is also aimed to attract young people to advanced scientific research and share the latest trends in training and research programs for future ITNT specialists [1].

In addition to the session "Image Processing and Earth Remote Sensing", ITNT-2019 also included three other sessions: "Computer Optics and Nanophotonics", "Mathematical Modeling of Physico-Technical Processes and Systems", and "Data Science". The whole forum brought together more than 450 scientists from United Kindom, Japan, Switzerland, Iran, Poland, Bulgaria, Finland, China, Kazakhstan and Russia, as well as representatives of global high-tech corporations, developers of modern electronics – Huawei, Nvidia, Intel, and Azimuth Photonics, and more than 60 cities in the world. 436 talks enabled discussion on a wide range of topics.

The topics of the session "Image Processing and Earth Remote Sensing" were grouped into the following key directions:

- Digital Image Processing (Filtering, Enhancement, Color Mapping, Compression, Spectral Transformations and Invariants);
- Visual Recognition and Retrieval (Segmentation, Clusterization, Classification, Retrieval, Feature Extraction and Selection, Descriptors, Dimensionality Reduction);
- Motion Analysis (Object Detection and Tracking, Face, Gesture and Action Recognition);
- Scene Reconstruction (3D Vision, Shape or Relief Reconstruction, Registration, Geometry Transformation);
- Remote Sensing Image Processing and Analysis (Geometric and Radiometric Correction, Mosaic, Classification, Dimensionality Reduction, Spectral Unmixing, Change Detection, Anomaly Detection, Data Fusion);
- Multimedia Protection and Information Hiding (Watermarking, Authentication, Forgery Detection, Steganography, Steganalysis);
- Geoinformatics (Vectorization, Tracing, Geospatial Analysis and Modeling).

This year we have received 120 submissions addressed to "Image Processing and Earth Remote Sensing". Each submission was carefully reviewed by the Program Committee members and the reviewers. Based on the reviews, we accepted 88 papers for the presentation at the conference (30 oral and 58 poster reports) and selected 51 papers out of 88 for publication in this volume.

We thank all the participants of ITNT-2019 for excellent presentations and discussions, and we wish to see all of them at our future events.

Conference Organizers

- Samara National Research University, Samara, Russia
- Image Processing Systems Institute of the RAS - Branch of the Federal Scientific Research Centre “Crystallography and Photonics” of Russian Academy of Sciences, Samara, Russia

Program Committee Chair

- Viktor Soifer, Samara National Research University

Organizing Committee Chair

- Vladimir Bogatyrev, Samara National Research University

Vice-chairs

- Nikolay Kazanskiy, Image Processing Systems Institute of the RAS
- Vladislav Sergeyev, Samara National Research University
- Alexander Kupriyanov, Samara National Research University

Compilers of the volume

- Vladislav Myasnikov, Image Processing Systems Institute of the RAS
- Vladislav Sergeyev, Samara National Research University
- Victor Fedoseev, Samara National Research University
- Valeriy Labunets, Ural State Forest Engineering University, Yekaterinburg, Russia
- Vitaliy Kober, Chelyabinsk State University, Chelyabinsk, Russia
- Dmitry Murashov, Federal Research Center “Computer Science and Control” of RAS, Moscow, Russia

Issuing editor

- Denis Kudryashov, Samara National Research University

The conference was financially supported by the Ministry of Science and Higher Education of the Russian Federation.

Reference

[1] Savelyev D A 2017 *Computer Optics* **41(5)** 775-785 DOI: 10.18287/2412-6179-2017-41-5-775-785

Preface

D V Kudryashov[1,2], E S Kozlova[1,2], Ye V Goshin[1]

[1]Samara National Research University, Moskovskoe Shosse 34, Samara, Russia, 443086
[2]Image Processing Systems Institute of the RAS - Branch of the Federal Scientific Research Centre "Crystallography and Photonics" of Russian Academy of Sciences, Molodogvardeyskaya str. 151, Samara, Russia, 443001

This volume contains the papers presented at the session "Data Science" within the V International Conference on Information Technology and Nanotechnology (ITNT-2019).

The conference was held in Samara, Russia, during May 21-24, 2019 (itnt-conf.org). The conference is a forum for leading researchers from all over the world aimed to discuss the latest advances in the basic and applied research in the field of Information Technology and Nanotechnology. It is also aimed to attract young people to advanced scientific research and share the latest trends in training and research programs for future ITNT specialists [1].

In addition to the session "Data Science", ITNT-2019 also included three other sessions: "Computer Optics and Nanophotonics", "Image Processing and Earth Remote Sensing" and "Mathematical Modeling of Physico-Technical Processes and Systems". The whole forum brought together more than 450 scientists from United Kindom, Japan, Switzerland, Iran, Poland, Bulgaria, Finland, China, Kazakhstan and Russia, as well as representatives of global high-tech corporations, developers of modern electronics – Huawei, Nvidia, Intel, and Azimuth Photonics, and more than 60 cities in the world. 436 talks enabled discussion on a wide range of topics.

The topics of the session "Data Science" were grouped into the following key directions:

- Data Mining (Big data, Systems and platforms, Methods);
- Machine Learning (Neural networks, Statistical methods, Feature-based classification, Applications);
- Security, Cryptography (Cryptosystems design and analysis, Mathematical and algorithmic aspects, Efficient implementations of algorithms, Network security);
- High Performance Computing (Parallel programming models and languages, High-performance implementations, Complex systems simulation).

This year we have received 188 submissions addressed to "Data Science". Each submission was carefully reviewed by the Program Committee members and the reviewers. Based on the reviews, we accepted 140 papers for the presentation at the conference (60 oral and 80 poster reports) and selected 69 papers for publication in this volume.

We thank all the participants of ITNT-2019 for excellent presentations and discussions, and we wish to see all of them at our future events.

Conference Organizers

- Samara National Research University, Samara, Russia
- Image Processing Systems Institute of the RAS - Branch of the Federal Scientific Research Centre "Crystallography and Photonics" of Russian Academy of Sciences, Samara, Russia

Program Committee Chair

- Viktor Soifer, Samara National Research University

Organizing Committee Chair

- Vladimir Bogatyrev, Samara National Research University

Vice-chairs

- Nikolay Kazanskiy, Image Processing Systems Institute of the RAS
- Vladislav Sergeyev, Samara National Research University
- Alexander Kupriyanov, Samara National Research University

Compilers of the volume

- Vladimir Fursov, Samara National Research University
- Yegor Goshin, Samara National Research University

Issuing editor

- Denis Kudryashov, Samara National Research University

The conference was financially supported by the Ministry of Science and Higher Education of the Russian Federation.

Reference

[1] Savelyev D A 2017 *Computer Optics* **41(5)** 775-785 DOI: 10.18287/2412-6179-2017-41-5-775-785

Identification of thawed and frozen soil state in some Siberia regions by multi-temporal Sentinel 1 radar data in 2017-2018

N V Rodionova[1]

[1]Institute of Radioengineering and Electronics, Russian Academy of Sciences, Vvedenskiy sq. 1, Fryazino, Russia, 141190

e-mail: rnv1948123@yandex.ru

Abstract. The paper deals with the identification of thawed/frozen soils in the topsoil layer for three stations in Siberia: Salekhard, Tiksi and Norilsk by using Sentinel 1B C-band radar data for the period of 2017-2018. Determination of the frozen/thawed soil state is carried out in three ways: 1) by multi-temporal radar data on the basis of a significant in 3-5 dB difference in the backscatter coefficient σ^0 in the transition of freezing/thawing soil state, 2) by finding the threshold value of σ^0 at which the temperature in the topsoil layer falls below 0^0C, 3) by texture features. The first method allows determining the period of time during which the process of freezing/thawing of the soil occurs. The second and third methods allow making local maps of frozen/thawed soils. It is shown that for the studied areas the Spearman correlation coefficient between σ^0 and air temperature for cross - polarization exceeds the correlation coefficient for co-polarization. The graphs of the AFI (air freezing index) for the period of 2012-2018 are constructed based on the archive data of air temperature for the study areas.

1. Introduction

More than 65% of Russia territory is occupied by permafrost. The study of permafrost is more related to ground-based measurements of the freezing/thawing soil depth. The history of permafrost ground research in Russia from the 17th century to the middle of the 20th century is quite fully described in [1].

Frozen soil parameters are difficult to measure directly by remote sensing (RS) because these parameters are related to subsurface phenomena. The potential of remote sensing using optical and microwave methods is limited to the study of the near-surface layer of permafrost, its spatial distribution, the study of the parameters of the active soil layer [2]. So the waves of RS sensors penetrate to a depth of several mm (visible and IR waves) or several cm (microwaves). A fairly detailed review of the work using RS for the study of frozen soils (FS) is given in [2].

It should be noted that the use of RS tools for the study of FS is less expensive than the provision of ground services because of their expensive logistics, short field season, time constraints, but it can not replace ground services, and only provides additional information [2].

Remote sensing offers promising methods for monitoring the near-surface state of frozen/thawed soils on a wide geographical scale [3], [4]. The use of radiometers is limited due to their low spatial

resolution. In contrast to IR and microwave radiometers, synthetic aperture radar (SAR) systems potentially provide information concerning soil freezing dynamics under snow cover at high resolution regardless of cloud cover and time of day and night.

Studies of the thawed/frozen soil state by SAR have been carried out since the early 90-s last century by ERS-1 C-band data [5], [6]. Research continued with the missions ENVISAT ASAR [7], ALOS PALSAR L–band [8], RADARSAT-2 C-band [9] and others.

The radar signal from the surface mainly depends on the dielectric constant (DC) of soil which is directly related to the water and ice content, also radar signal depends on surface roughness and vegetation cover.

Active sensors discern frozen soil by detecting variations in liquid water soil content. These variations are related to soil DC values [10]. The average DC value of dry soil is about 2-3, while that of liquid water is 80. DC soil increases proportionally with volumetric liquid water content. Under critical winter conditions, a greater proportion of soil water freezes which leads to a significant decrease of the average value of soil DC; frozen water has DC of ice (3.2), which is similar to that of dry soil [11]. The opposite process occurs in spring when the ice within soil melts, which results in an increase in radar backscatter by several dB [12].

Soil properties (i.e., structure, texture, drainage) affect the soil water content and consequently its freezing dynamics. Mineralized soils freeze more quickly and more deeply than organic soils because of their lesser capacity to store water [13]. The same relation exists between sandy and clay soils.

The aim of this work is to identify the thawed/frozen soil state in topsoil layer and to construct local maps of frozen/thawed soils in the study areas of some Siberia regions: Salekhard, Tiksi and Norilsk, by using Sentinel 1B radar data.

2. Study area and SAR data

2.1 Salekhard

Salekhard is the only city in the country located on the Arctic circle. It is located on the territory of the Yamal-Nenets Autonomous district. The coordinates of the Salekhard meteorological station (WMO 23330) $66^0$31.86'N, 66^0 40.08' E. The area of the city of Salekhard is a flat undulating plain on the right Bank of the Poluy river, a major right-Bank feeder to the Ob river (figure 1(a)). It is the area of intermittent permafrost. The depth of seasonal soil thawing/freezing varies from 0.9 m to 3 m and depends on soil lithological composition, moisture and vegetation cover character. The forest covers 8% of the area. The grass cover is poor, the area is mostly covered with mosses and lichens. The territory soil texture is dominated by sandy loam, loam, sand-gravel mixture, but no sand.

Mean annual temperature is -6.4°C, the absolute minimum is -54°C, the absolute maximum is + 31°C, the maximum depth of the snow cover is 62 cm.

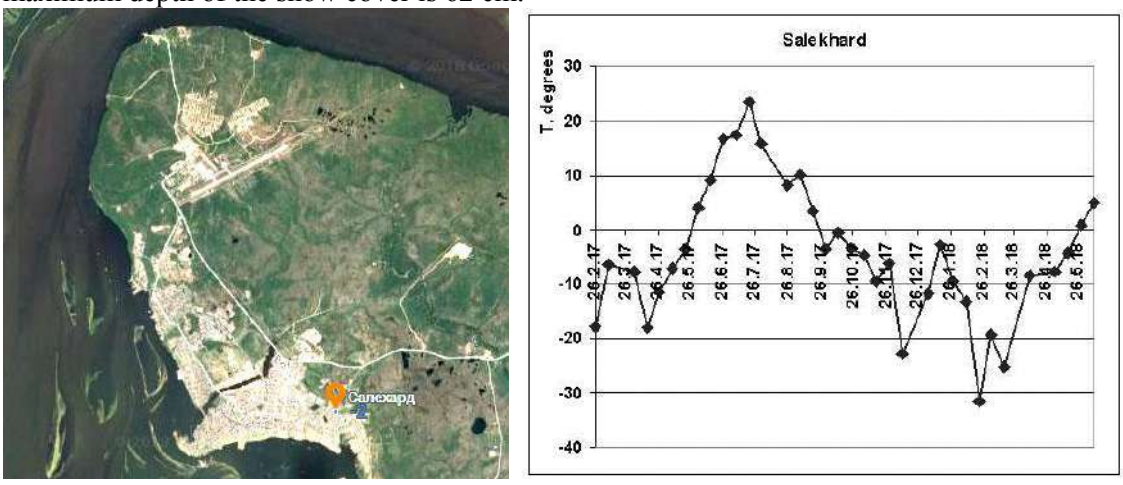

(a) (b)

Figure 1. (a) Salekhard satellite image, (b) air temperature in degrees Celsius for Salekhard.

Figure 1 shows the satellite image of Salekhard and air temperature plot for the period 26.2.2017 – 9.6.2018 by the rp5.ru data.

2.2. Tiksi

Tiksi is an urban-type village, the center of Bulun district of the Republic of Sakha-Yakutia. It is located above the Arctic circle, to the East of the Lena mouth on the shore of Tiksi Bay in the Laptev Sea. Coordinates of Tiksi airport weather station (WMO 21824) $71^0$41.85' N., 128^0 54.18 E (figure 2(b)).

Tiksi Bay is surrounded by low gravelly treeless hills. The sea slightly softens the frosts, the mean January temperature is -37.3^{0}C, July and August—+7.6^{0}C and +7.7^{0}C, respectively. The absolute minimum temperature in Tiksi is -50.5^{0}C. The highest possible snow depth is 99 cm. April in Tiksi has the lowest average monthly temperature in Russia, which was in 2006 -27.6^{0}C. Figure 3 displays a photograph of the village and air temperature plot for the period 7.2.2017–14.6.2018 by the rp5.ru data. Temperatures were taken at time of site survey of the radar S1.

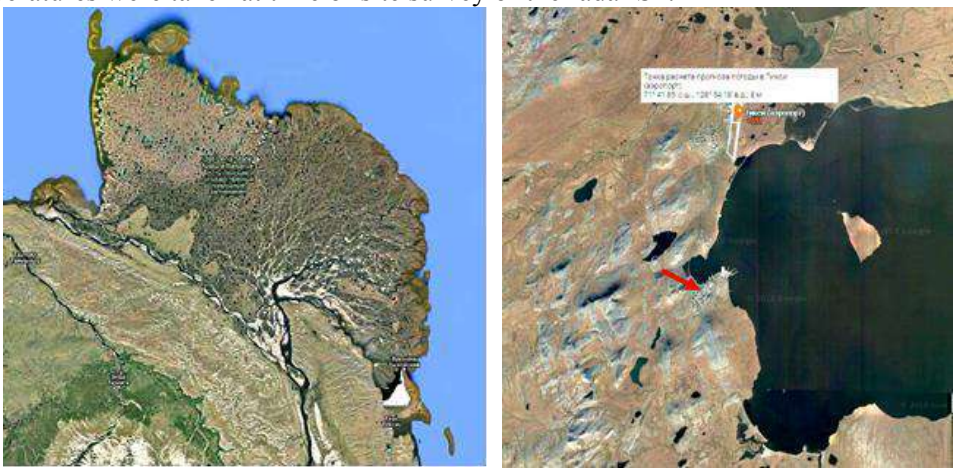

(a) (b)

Figure 2. (a) the mouth of the Lena river and Ust Lena state nature reserve, (b) Tiksi Bay with the village of Tiksi.

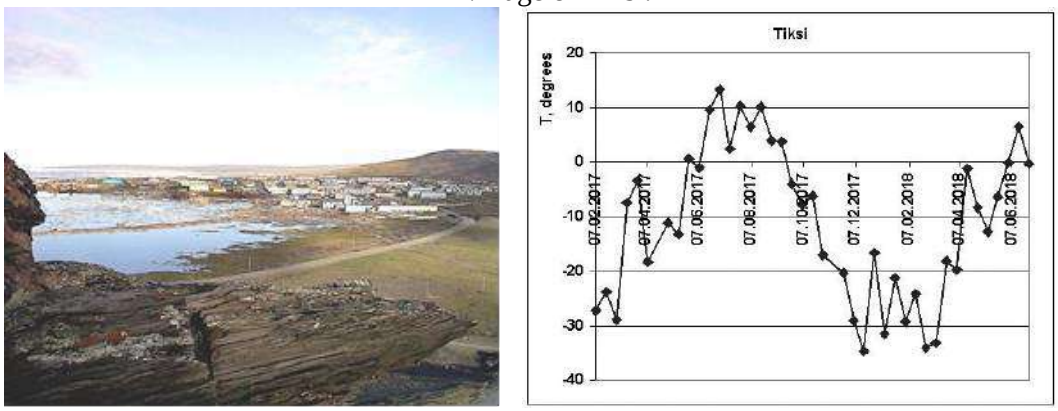

Figure 3. Tiksi village and air temperature in Tiksi.

2.3. Norilsk-Talnakh

Norilsk is located in the North of Krasnoyarsk region, in the South of the Taimyr Peninsula (WMO ID=23078). Talnakh - district of Norilsk, is 25 kilometers North-East of the center of Norilsk. Talnakh is located on the right Bank of the Norilsk river; (Norilsk-on the left Bank) at the spurs of the Putoran plateau. Talnakh mines are the main raw material base of Norilsk Nickel. At a distance of 2.5 km on Southeast from the Talnakh is R32 CALM ground station with coordinates 69^{o}26'01" N, 88^{0}28'03" E. The climate is with negative mean annual temperature -9,80^{0}C, long (8 months, from November to May) winter with severe frosts and blizzards, short rainy, cold summer.

Figure 4 shows a satellite image of Norilsk and Talnakh (indicated by arrows), and a plot of changes in air temperature for the period 3.3.17-13.8.18 according to rp5.ru.

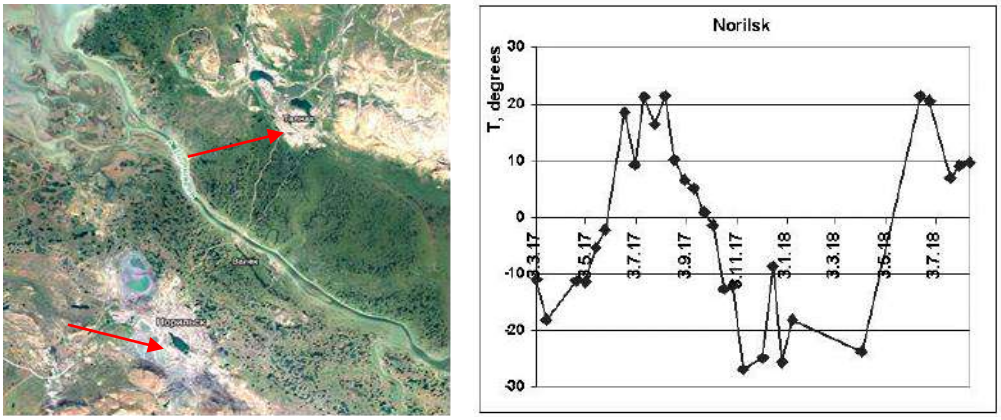

(a) (b)

Figure 4. (a) satellite image of Norilsk (lower arrow) and Talnakh (upper arrow), (b) air temperature in degrees Celsius for Norilsk-Talnakh.

2.4. Sentinel 1B radar data

The study used free open Sentinel 1B (S1) C –band radar data IW (interferometric wide swath) mode, VV and VH polarizations with spatial resolution 10 m. S1 images have been processed by program S1Toolbox and later SNAP [14]. Data pre-processing includes study area fragment selection and radiometric calibration.

Table 1 describes S1 data used: 1) number of processed images, 2) view angle, 3) radar survey time, 4) number of profile pixels for radar backscatter average.

Table 1. Sentinel 1B radar data used.

Place name	Number of processed S1 images	View angle	S1 survey time	Number of profile pixels
Salekhard	35	34^0	26.2.2017–09.6.2018	~20
Tiksi	39	40.5^0	19.2.2017–14.6.2018	~20
Norilsk	29	40^0	03.3.2017-13.8.2018	~10

Figure 5 illustrates the changes of the mean value of the backscatter coefficient for VV and VH polarizations near the airport of Salekhard (coordinates of profile midpoint $66{,}592^0$ N, $66{,}647^0$ E) for the period 26.2.2017–9.6.2018 and Tiksi (midpoint profile coordinates 71.7015^0 N and 128.9205^0 E) for the period 19.2.2017–14.6.2018. For Norilsk-Talnakh plots of changes of radar backscatter coefficient are shown in figure 6: the first profile near Valek airport in Norilsk (coordinates 69.3917^0 N, 88.3147^0 E), second profile in the area of Talnakh near the site CALM R32 (coordinates 69.4343^0 N, 88.4674^0 E) for the period 3.3.2017-13.8.2018. The profile positions are marked in radar images by red lines (figure 7).

Spearman's correlation coefficient between air temperature and the backscatter coefficient for Salekhard is ρ_S=0.58 ($p=10^{-4}$, N=35, where N is the number of processed images) for VV polarization and slightly more for VH polarization ρ_S=0.7 ($p=10^{-6}$). For Tiksi ρ_S=0.21 (p=0.1, N=39) for VV polarization (weak correlation) and ρ_S=0.69 ($p=10^{-6}$) for VH polarization. For Norilsk ρ_S=0.57 ($p=6*10^{-4}$, N=29) for VV polarization and for VH polarization ρ_S=0.82 (p=0). For Talnakh ρ_S=0.58 ($p=4*10^{-4}$) for VV polarization and for VH polarization ρ_S=0.74 ($p=10^{-6}$). For all profiles the correlation in cross - polarization exceeds the correlation coefficient in co- polarization.

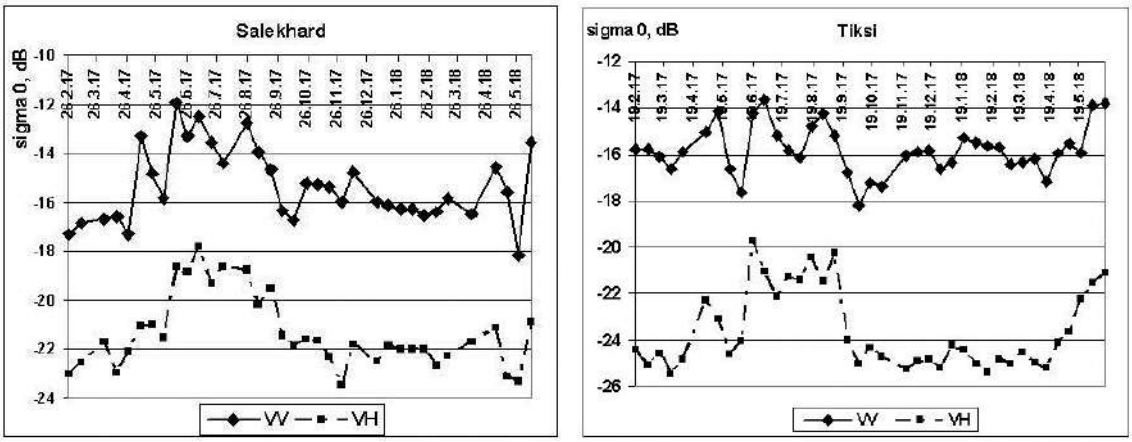

Figure 5. The mean value of the backscatter coefficient near Salekhard and Tiksi.

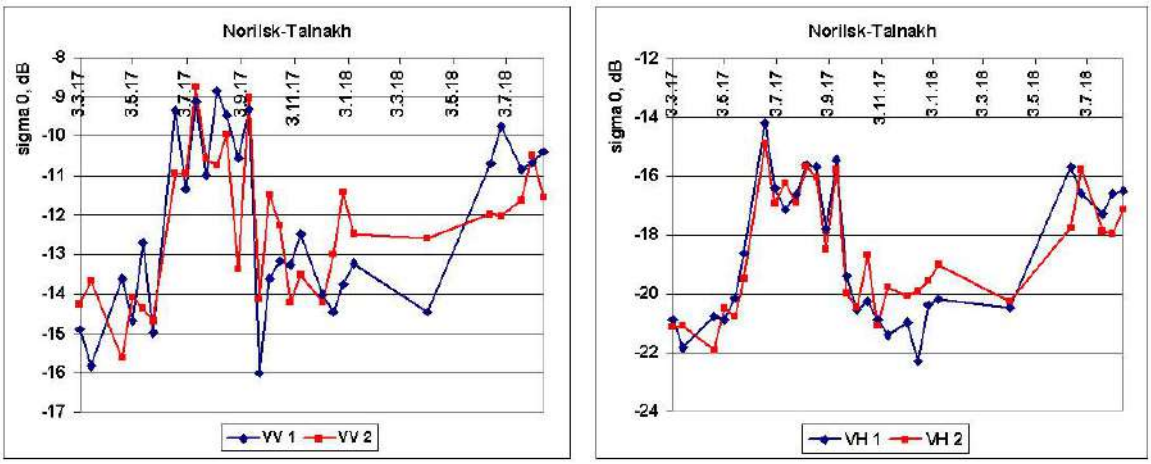

Figure 6. The mean value of the backscatter coefficient for Norilsk-Talnakh.

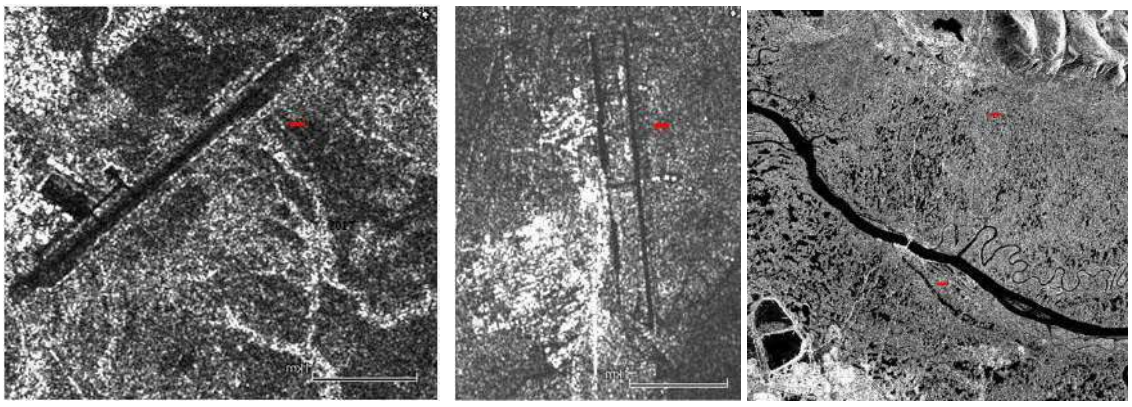

(a) (b) (c)

Figure 7. The position of the profiles in radar images (highlighted by red line) near the airports of Salekhard (a), Tiksi (b) and Norilsk-Talnakh (c).

3. Methods and results of determining frozen/thawed soil state by radar data

3.1. The determination of FS state by multi-temporal radar data

The depth penetration e/m wave into the soil is determined by the equation $\delta p = \frac{\lambda \cdot (\varepsilon')^{1/2}}{2 \cdot \pi \cdot \varepsilon''}$, where λ - the length of the wave, $\varepsilon = \varepsilon' - i\varepsilon''$ -soil dielectric permeability. For Sentinel 1 the wavelength is 5.4

cm. In the case of frozen soil with $\varepsilon' \approx 5.5$ and $0.1 \le \varepsilon'' \le 0.5$ a penetration depth equals $4 \le \delta p \le 20$ cm.

Identification of thawed/frozen soil state involves knowledge of changes in soil moisture and DC when the temperature decreases. To understand what changes occur with the soil DC, models of phase transitions (freezing/thawing) of water from the liquid to the frozen state (and vice versa) were created. The best known is the semi-empirical dielectric mixed model Dobson et al. [15], generalized to negative temperatures Zhang et al. [16]. The paper [17] shows the relative DC values for three soil types (silty clay, silt loam, sandy loam) obtained from this model depending on the soil temperature from - 30^0C to 30^0C for frequencies from C to Ku-band. It is shown that when the soil temperature drops below 0^0C, there is a sharp decrease in the values of soil DC for all types of soils and all frequencies. Thus, for the C-band, the jump in the soil DC value is about 20 units for silty clay, 15 for silt loam and about 10 for sandy loam. And as shown by [3], [4], the jump in backscatter coefficient is 3-5 dB, what is the basis for identification of thawed/frozen soils by radar data.

Using the time series S1, we can determine the start dates of freezing/thawing of FS by significant changes in backscatter coefficient and then stably low/high σ^0 values. Figure 8 shows graphs of the difference $|\sigma^0|$ in the absolute value in dB for the adjacent date radar imagery for Salekhard (a), Tiksi (b) and Norilsk (c) where the maxima differences $|\sigma^0|$ (shown in the figures by arrows) determine the start date of soil freeze/thaw.

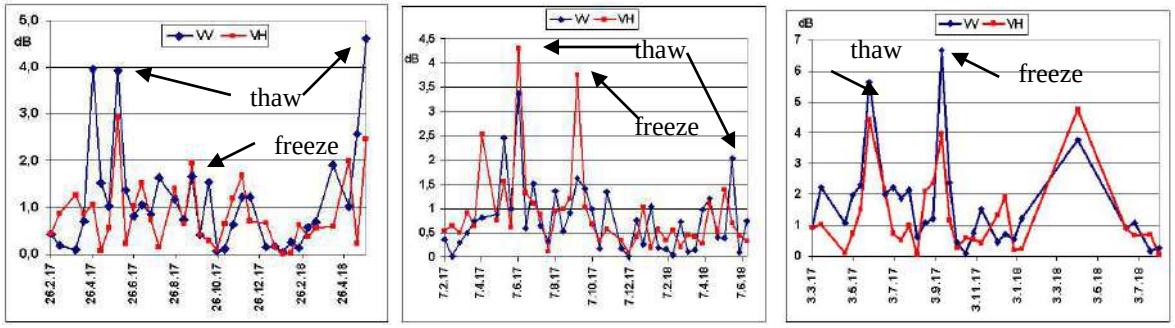

(a) (b) (c)

Figure 8. The difference between the values $|\sigma^0|$ in dB for the adjacent radar imagery date.

Based on Dubois et al. [18] equation that defines the relationship between co-polarization σ^0 with soil parameters (the real part of the soil DC and the surface roughness), it is possible to determine the jump of the DC during soil thaw/freeze. The differences of the real part of the soil DC are for Salekhard up to 14 units during thawing and up to 5 units during freezing, for Tiksi up to 8 units during thawing and up to 4 units during soil freezing, for Norilsk up to 14 units during thawing and up to 17 units during soil freezing.

3.2. Determining of the FS by surface state factor and σ^0 threshold value

Another way to determine the state of FS only by radar data, without using ground measurements, is given in [19].

The authors [19] characterize the state of the soil surface through the surface state factor (SSF):

$$\text{SSF} = \frac{1}{2} + \frac{\sigma^0(t) - \sigma^0_{Summer}}{\sigma^0_{Summer} - \sigma^0_{Winter}} \quad (1)$$

where σ^0_{Summer} and σ^0_{Winter} - the average σ^0 values in dB in summer and winter, $\sigma^0(t)$ -the current value of σ^0, t–time.

The authors [19] argue that the seasonal variation of SSF are highly correlated with seasonal variations in soil temperatures, taking negative values when the soil temperature is below 0^0C. Then, 5-cm topsoil layer can be classified as frozen if the SSF value measured by the radar becomes negative. Figure 9 shows the SSF graphs for Salekhard and Tiksi.

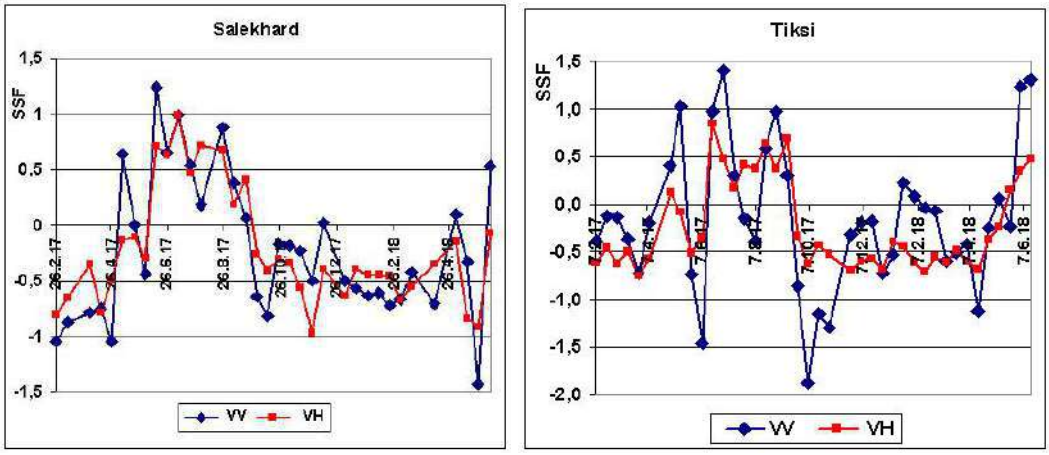

Figure 9. SSF change for Salekhard (a) and Tiksi (b).

According to the equation (1) it turns out that the intersection of the value of SSF=0 occurs for the same value $\sigma^0(t)$, but for different times t , i.e. the value σ^0 is the same for both the freezing point and the thawing point in the 5-cm upper layer. And this value can be determined for each place by knowing the mean σ^0_{Summer} and $\sigma^0_{W\,inter}$. Let's call this σ^0 value by $\sigma^0_{Threshold}$.

For Salekhard, the value σ^0_{Summer} was determined for the period 2.6.2017÷18.9.2017, and for VV polarization the value σ^0_{Summer}=-13.6 dB, and for VH polarization σ^0_{Summer}=-19.2 dB. The value $\sigma^0_{W\,inter}$ was determined for the period 30.9.2017÷28.5.2018. For VV polarization $\sigma^0_{W\,inter}$=-16 dB, for VH polarization $\sigma^0_{W\,inter}$=-22.1 dB. Then, by equation (1) we obtain for $\sigma^0_{Threshold}$=-14.8 for VV polarization and $\sigma^0_{Threshold}$=-20.6 for VH polarization.

For Tiksi, the value σ^0_{Summer} was determined for the period 19.6.2017÷11.9.2017, and for VV polarization σ^0_{Summer}=-14.9 dB, and for VH polarization σ^0_{Summer}=-20.95 dB. The value $\sigma^0_{W\,inter}$ was determined for the period 23.9.2017÷21.5.2018. For VV polarization $\sigma^0_{W\,inter}$=-16.3 dB, for VH polarization $\sigma^0_{W\,inter}$=-24.6 dB. Then, by equation (1) we obtain for $\sigma^0_{Threshold}$=-15.6 dB for VV polarization and $\sigma^0_{Threshold}$=-22.8 dB for VH polarization.

Using the threshold value $\sigma^0_{Threshold}$, let us construct local maps of thawed/frozen soils, for example, in the area of Salekhard airport for the dates 9.5.2017 and 14.6.2017–thawing, and 18.9.2017 and 12.10.2017–freezing. The resulting images, 2.8*3 km in size, are shown in figure 10. Blue color-values $\sigma^0 < \sigma^0_{Threshold}$ (frozen soil), yellow color–values $\sigma^0 \geq \sigma^0_{Threshold}$ (thawed soil). Note the significant decrease in the area of frozen soil on the image for 14/06/2017 during thawing and, consequently, increasing the area of frozen soil on the image for 12.10.2017 during freezing.

3.3. Determining the status of the FS by textural features

The paper [20] shows the possibility of distinguishing different types of surface in radar images by the use of Haralick texture features [21]: ‘contrast’, ‘entropy’ and ‘inverse moment’. ‘Contrast' is a weighted square of brightness levels and serves as a natural measure of the spread of brightness. The

‘inverse moment’ is a measure of local similarity. ‘Entropy’ is a measure of disorder in an image. The area with the highest value of ‘contrast’ distinguishes places with height differences (urban areas and so on), areas with a high value of inverse moment-smooth surfaces. Having built a texture image, it can be used the texture feature 'inverse moment’ as an indicator of frozen/thawed soil, because its value is greater for frozen soils. Figure 11 demonstrates texture images after speckle filtering for test site in Salekhard for dates, as in figure 10 (down), in RGB coding: red-'contrast', green-'entropy', blue-'inverse moment’.

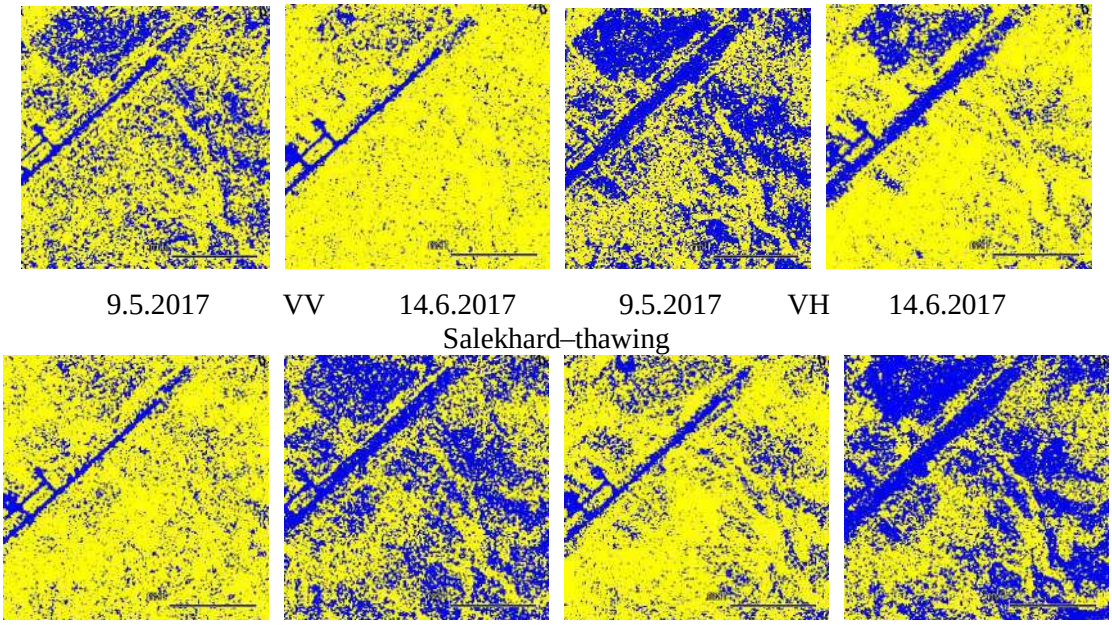

Figure 10. Local maps of thawed/frozen soils in Salekhard during soil thawing (up) and soil freezing (down).

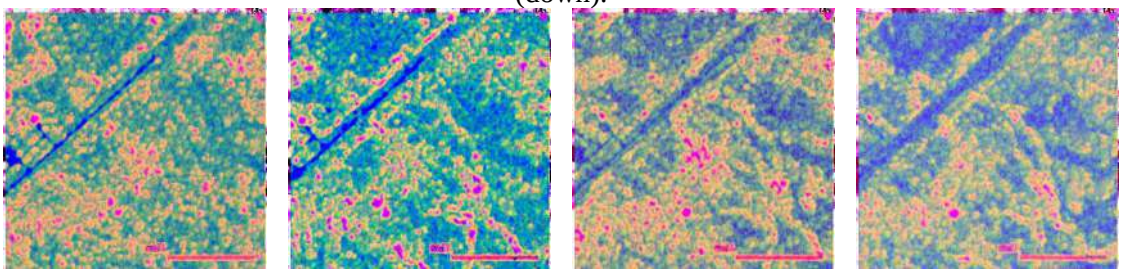

Figure 11. Textural images of place under study in Salekhard.

One of the segmentation methods on the basis of paired metrics for extracting homogeneous objects in multi-temporal radar images is given in [22].

4. Soil freezing/thawing index

Air temperature correlates with soil temperature and soil freezing depth [23]. Accurate prediction of soil freezing depth is an important aspect of various engineering projects. The real depth of soil freezing is influenced by its mechanical composition, thermal properties, soil moisture, climatic conditions (air temperature, wind speed, precipitation, solar radiation). The freezing depth can be estimated using numerical or analytical methods, but the inputs required in the models are not always available or expensive to obtain. If the input data are available, the results of such models could be quite accurate. In the absence of some input data, it is necessary to estimate how much it affected the accuracy of the result. Of the existing models for predicting the depth of soil freezing, the most well-known is the Stefan model used today, the Berggren model and the Chisholm and Phang model. The

paper [24] considers the accuracy of prediction of soil freezing depth for these three analytical and semi-empirical models. Since none of the models gives accurate results, the authors [24] proposed a modified empirical model for different types of soils that requires only daily maximum and minimum air temperatures as input. This model is based on the measured values of the depths of frost penetration in 2010-2011 in the state of Michigan and the calculated values of the cumulative freezing index (CFI):

for clay soils $$h = 4.0388 \times (CFI)^{0.4896}$$

with a coefficient of determination of 0.94 (the number of measured data points 29),

for sandy soils $$h = 3.3787 \times (CFI)^{0.5423}$$

with determination coefficient of 0.91 (the number of measurements 129),

where h is the depth of soil freezing in cm, $CFI = \sum_{i=1}^{n} \left(T_{\min}^{air} + T_{\max}^{air}\right)/2$, $T_{\min}^{air}$ and T_{max}^{air} is daily minimum and maximum air temperature.

The authors [24] obtained a generalized empirical equation for all soil types, taking into account the measurement of the average thermal conductivity of soil samples in Michigan, noting that the use of their empirical equations for other areas requires calibration.

The maximum depth of soil freezing/thawing for every year is determined by the difference between the maximum and minimum values of CFI. The maximum CFI corresponds to the transition from positive to negative temperatures, the minimum CFI corresponds to the transition from negative to positive temperatures. In the first case, the difference between the extremes corresponds to the assessment of the maximum depth of soil thawing, in the second–the maximum depth of soil freezing. This value is called AFI (air freezing index). Figure 12 shows the AFI values characterizing the maximum depth of soil freeze/thaw for Salekhard, Tiksi and Norilsk for 2012-2018. It is incorrect to talk about the trend in linear approximation here since the coefficient of determination R^2 has very small values-from 0.001 to 0.2.

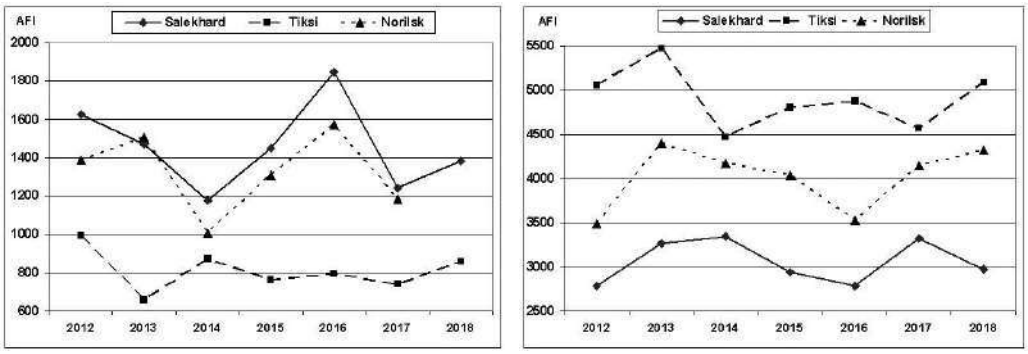

(a) (b)

Figure 12. AFI values characterizing the maximum depth of soil thawing (a) and freezing (b) for Salekhard, Tiksi and Norilsk.

5. Conclusion

The paper deals with the identification of thawed/frozen topsoil layer state near Salekhard, Tiksi and Norilsk by radar Sentinel 1B C-band data VV/VH polarizations for the period 2017-2018. Determination of frozen/thawed soil state is carried out by three ways: 1) by multi-temporal radar data on the basis of a significant 3-5 dB difference in the values of the backscattering coefficient during the transition to freezing/thawing soil state. The numerical values of the σ^0 differences are 4.6, 3.4, 5.6 dB for soil thawing for VV polarization and 2.9, 3.3, 4.4 dB for VH polarization, respectively, for Salekhard, Tiksi and Norilsk; 2) by calculating the threshold $\sigma^0_{threshold}$ at which the temperature in the upper soil layer falls below 0^0C. The values $\sigma^0_{threshold}$ allowed creating local maps of frozen and thawed soil in the area of test sites; 3) by the Haralick texture features. It is shown that textural feature 'inverse moment' identifies areas with frozen soil.

It is shown that for the test areas of Salekhard, Tiksi and Norilsk the Spearman correlation coefficient between σ^0 and the air temperature for cross-polarization exceeds the correlation coefficient for the co-polarization.

The obtained AFI values characterizing the maximum depth of soil freezing/thawing did not reveal a significant trend for the period 2012-2018 according to the air temperature archive data for the studied areas.

6. References

[1] Shiklomanov N I 2005 *Physical Geography* **4** 249-263
[2] Duguay C R, Zhang T, Leverington D W and Romanovsky V E 2005 *Remote sensing of Northern hydrology, geophysical monograph series* **163** 91-117
[3] Khaldoune J, Van Bochove E, Bernie M and Nolin M C 2008 *Proc. IGARSS'2008* (Boston. Mass.) **III** 382-385
[4] Khaldoune J, Van Bochove E, Bernie M and Nolin M C 2011 *Appl. Environment. Soil Sci*. Article ID 193237 1-16 DOI: 10.1155/2011/193237
[5] Wegműller U 1990 *Remote Sens. Environ*. **33** 123-135
[6] Rignot E, Way J B, McDonald K, Viereck L, Willia C, Adams P, Payne C, Wood W and Shi J 1994 *Remote Sens. Environ*. **49** 145-154
[7] Park S-E, Bart A, Sabel D, Wagner W, Naeimi V and Yamaguchi Y 2011 *Remote Sens. Environ*. **115** 3457-3467
[8] Mironov V L, Muzalevskij K V, Boike Dj, Shveleva A A, Evtiushkin A V and Filatov A V 2013 *Izvestiya vuzov. Fizika* **1** 1-3
[9] Rousseau L P, Magagi R, Leconte R, Berg A and Toth B 2009 *Proc. IGARSS'2009* (Cape Town, South Africa) 598-601
[10] Hallikainen M T, Ulaby F T, Dobson M C, El-Rayes M A and Wu L K 1985 *IEEE Trans. GRS* **23** 25-34
[11] URL: www.iki.rssi.ru/books/2003boyarsky.pdf
[12] Ulaby F T, Moore R K and Fung A K 1982 *Fundamentals and Radiometry* (Dedham, Mass, USA: Artech House)
[13] Nyberg L, St¨ahli M, Mellander P E and Bishop K H 2002 *Hydrol. Process.* **15** 909-926
[14] URL: https://sentinel.esa.int/web/sentinel/toolboxes/sentinel-1.
[15] Dobson M C, Ulaby F T, Hallikaine M T and El-Rayes M A 1985 *IEEE Trans. GRS* **23** 35-46
[16] Zhang L, Shi J, Zhan Z and Zhao K 2003 *Proc. IGARSS'2003* (Toulouse, France) 608-611
[17] Jagdhuber Th, Stockamp J, Hajnsek I and Ludwig R 2014 *Remote Sens*. **6** 2008-2023
[18] Dubois P C, van Zyl J J and Engman T 1995 *IEEE Trans. GRS* **33** 916-926
[19] Mironov V L and Muzalevsky K V 2013 *Russian Physics Journal* **55** 899-902
[20] Rodionova N V 2007 *Issledovanie Zemli iz kosmosa* **34** 8-14
[21] Haralick R M 1979 *Proc. IEEE* **67** 786-804
[22] Plotnikov D E, Kolbudaev P A and Bartalev S A 2018 *Computer Optics* **42(3)** 447-456 DOI: 10.18287/2412-6179-2018-42-3-447-456
[23] Brown W G 1964 *Canadian geotechnical J*. **1** 215-226
[24] Rajaei P and Baladi G Y 2015 *94st Transportation Research Board Annual Meeting* (Washington D.C.) 1-15

Vegetation Drought Dynamic Analysis in European Russia

M S Boori[1,2,3], R Paringer[1,4], K Choudhary[1,2,5] and A Kupriyanov[1,4]

[1]Samara National Research University, Moskovskoe Shosse 34A, Samara, Russia, 443086
[2]University of Rennes 2, Rennes, France
[3]American Sentinel University, Colorado, USA
[4]Image Processing Systems Institute of RAS - Branch of the FSRC "Crystallography and Photonics" RAS, Molodogvardejskaya street 151, Samara, Russia, 443001
[5]The Hong Kong Polytechnic University, Hong Kong

e-mail: msboori@gmail.com

Abstract. This research work deals with the spatial-temporal characteristics of the relationship between drought events (Standardized Precipitation Index [SPI]), land surface temperature (LSI) and vegetation indexes (VIs) in the spring-summer (May-August) over the European Russia (ER) from 2000 to 2018. We use Terra- MODIS - NDVI and LST product and TRMM for rainfall data. Statistical results indicate that year 2004, 2009 and 2015 were the most significant changing-point in mean annual rainfall values and VIs. Results indicate that vegetation area and VIs variate according to SPI values. Analysis results also indicate that low NDVI values (0.2-0.4) shift in high NDVI values (0.5-0.8) with high SPI values and vice-versa, also high LST values associated with low VIs values and vice-versa, with correlation coefficients 0.90, means high-temperature show low vegetation. Correlation analysis of VIs, SPI and LST deficit shows that vegetation is closely related to rainfall and temperature, especially under the dry and wet conditions and indicates that this correlation can use for near-real-time monitoring of vegetation drought dynamics. All predictions and monitoring using satellite-derived VIs is a low cost and effective means of identifying longer-term changes as opposed to natural inter-annual variability in vegetation growth.

1. Introduction

This is a global phenomenon that rainfall and temperature are the key parameters for vegetation condition, health, growth and responsible for a wide range of forest ecosystem. Globally, maximum forest areas are under mortality situation due to increasing temperature and reducing soil moisture [1, 2]. Simultaneously, we have a lot of evidence, that under future climate scenario, maximum world forest area will suffer increasing forest mortality rate due to severe and frequent drought events [3], especially in dry parts of the world [4]. Among the various factors, climate change is influencing serious negative trends in forest ecosystem structure and function by expected increase drought intensity and frequency [5]. Coping with these consequences of climate change represents in many forest regions, such as changes in rainfall patterns, increase average temperature, increase in drought frequency, intensity and can impede tree vulnerability [6], increase mortality rate [7] and seem to have a significant impact on the growth and development of forest in all over the world [8, 9, 10]. As vegetation condition, rainfall and temperature have a close relationship so any change in rainfall pattern and temperature will have a significant impact on the growth and potentially triggering large-

scale changes in the forest distribution, structure, function, and composition [11] and threatening terrestrial net primary production [12]. Still, the relationship between vegetation, rainfall, and the temperature is of fundamental importance [13]. Specifically, reducing rainfall and increasing temperature are reducing soil moisture and the increasing possibility of severe drought events, which increase evaporation rate and salinity, that directly effect on net production, growth and survival, ultimately loss of biodiversity, ecosystem and increase forest vulnerability to other human natural stress [14, 15, 16]. So to predict future forest ecosystem with climate change is a basic requirement to understand the ecological mechanisms with governing vegetation droughts dynamics [17]. The Russian climate is influenced by severing factors [18] such as southern mountains, a plain area in the west, Indian Ocean warm-air and the Arctic and Atlantic influences in the north. Russia has extreme dry winter or precipitation as a high snowfall in winter and hot summer with rains [19] with a semi-arid climate. Around 65% Russian territory comes under permafrost with 65–75 cm (24–30in) Annual precipitation but in the south part, its only 4-5 cm (1-2 in) annual precipitation [18] so extreme weather condition have been badly effecting on vegetation in ER [20].

Human society and the global economy are closely linked with forest in terms of their livelihood, providing food, water, wood products, medicines and in last supporting biodiversity [21]. ER forest spread for 2000 km from 66°N to 53°N with 1/4 of the world's reserves wood [22]. The Russian timber industry is one of the oldest industries which provide around 20 billion dollars per year in the Russian economy. The main species of coniferous tree are pine, spruce, larch, cedar. Despite this Russian forest ecosystem is endangered by harvest, fuel, grazing, farming, industrial development, construction, mining, pollutions, forest fire, unmanaged tourism, and non-native wildlife animals destroy seeds, trunks, and branches and put further stress on the ecosystem [23]. Tree vulnerability to drought estimation based on the surveys, visual interpretation of canopy conditions and expert knowledge is expensive, time-consuming, less accurate, require more manpower, difficult to extrapolate over large, inaccessible areas and tough in regular monitoring [20]. Satellite remote sensing, on the other hand, has several advantages due to its repetitive, synoptic coverage of large, inaccessible areas in a quick and economical fashion [24]. Remotely sensed data has been used to monitor the impacts of drought on canopy water loss, ecosystem carbon dynamics and water use efficiency [25]. Other hand many regions especially inaccessible area, where the density of meteorological stations are not sufficient or frequency of data collection are low and field work is impossible than drought monitoring is not possible accurately based on rainfall data. But satellite-based rainfall data is continuously available for the large, inaccessible area and quickly on low cost or free of cost with the availability of historical data. That`s why remote sensing is proved a powerful tool for measuring and monitoring of drought conditions with temporal and spatial aspects [26]. There is a lot of ways to monitor and mapping forest disturbance by insect and burning using satellite remote sensing [27]. Same-date high resolution multispectral and hyperspectral imagery such as IKONOS and Hyperion and multi-date imagery from medium resolution can easily detect insect outbreaks [28]. The Ecosystem Disturbance and Recovery Tracker (eDaRT) system, for example, is being developed by many countries for forest disturbance mapping and monitoring with medium resolution satellite data [29]. These methods can detect high- and moderate-magnitude disturbances at a relatively high spatial resolution, such as fire burns, clear-cuts or severe mortality [30]. But still, regular monitoring of tree vulnerability on a large area is a chilling task [31].

The main cause of drought is the shortage of rainfall in terms of low water availability from the average annual condition and it's related to increasing temperature and evaporation, which effect on local vegetation condition. In ER long term drought occurrence and significant changes in rainfall patterns are the most imperative factor, which affects the vegetation. The effects of drought occurrence on vegetation in the ER have not been computed yet. Currently, various drought indicators have been used for drought events effect on vegetation including meteorological [32], remotely sensed, hydrological and other indicators to measure drought impacts. Other than this traditional method of drought assessment and monitoring based on rainfall data are palmer drought severity index (PDSI) [33], SPI [34] and Palmer hydrological drought index (PHDI) [35]. The easy-to-use SPI has been widely employed to determine the occurrence of drought episodes and enables investigations of water deficiencies at different spatial and temporal scales [36, 37, 38]. The main objective of this research

work is to identify a relationship between spatial-temporal change in drought events [rainfall (SPI)] and temperature (LST) for vegetation condition. This research work enumerates the relationship in between vegetation with droughts intensities and trends to protection and restoration of ER vegetation on timely and effectively. For that, we used satellite and long term rainfall data from 2000 to 2018 for ER and figured out SPI to identify changes in rainfall patterns, which show changing-point year, that indicate drought dynamics in last two decades. Then we correlate SPI and drought occurrence to identify changes in the vegetation area and condition in the ER. We also quantify the changes in vegetation condition and area separately for the intervals before and after of the changing-point years.

2. Study area

The study area of this research work is the entire European Russia (figure 1). Russia is the world`s largest and a transcontinental country. European Russia is the western part of Russia that is a part of Eastern Europe, with a population of 110 million people, European Russia has about 77% of Russia's population, but covers 23% of Russia's territory; and occupies almost 40% of Europe's total area.

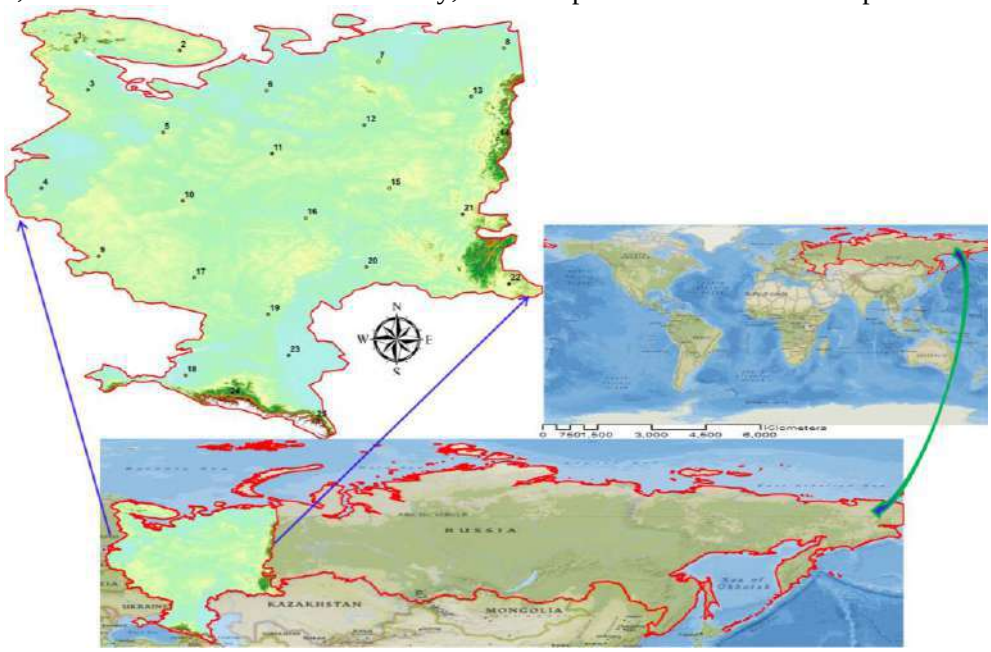

Figure 1. The geographic location of European Russia with 25 rainfall sampling location and DEM.

3. Materials and methods

3.1. Datasets

To obtain a sufficient spatial and temporal coverage of the study area on a yearly basis and at low costs, multispectral data were download from united states geological survey (USGS) website such as advance very high-resolution radiometer (ASTER), MODIS and global land data assimilation system (GLDAS) Noah land surface model [39]. We used MODIS product MOD11A2 for LST, MOD13Q1 for VIs and MOD09Q1 for surface reflectance information. For elevation and slope information we used ASTER-GDEM with 30m spatial resolution and for rainfall measurements or SPI, national aeronautics and space administration (NASA) global land data assimilation system (GLDAS) and other meteorological data were used. During fieldwork, we used high-quality handheld global positioning system (GPS) for ground truth and to georeference satellite images. In secondary data, we used other ancillary data and ground data from meteorology, climatology, agriculture, forest and survey departments such as geology and geography (topographic sheets). For geographical information system (GIS) analysis and image processing work, we used ArcGIS, ER-Mapper and ERDAS software's and prepare thematic maps with the help of satellite data, topographic maps, field, and ancillary data: such as vegetation, digital elevation model (DEM), rainfall, NDVI, LST. So to take

the dual advantage in this research work, we used both primary (satellite data) and secondary data (field and socio-economic data). Mainly we use MODIS instrument, which is operating on both the Terra and Aqua spacecraft. It has a viewing swath width of 2,330 km and views the entire surface of the Earth every one to two days. Its detectors measure 36 spectral bands between 0.405 and 14.385 μm and it acquires data at three spatial resolutions -- 250m, 500m and 1,000m. MODIS products are available from several sources such as LAADS web, DAAC at the U. S. geological survey.

3.2 Pre-processing

This research work was benefited from ground-based information collected during fieldwork. Then complete image pre-processing steps such as remove all radiometric, geometric distortions and projected all datasets in world geodetic system – 1984 universal transverse Mercator coordinate system (WGS-1984 UTM) projection with the help of ground control points (GCP) so that all noise or sensors related errors such as droplines was removed and each pixel was geocoded as its exact location on the globe and then used best band combination and enhancement techniques to identify specific features in false color composite images. After it, all field data were vectorized and interpolated as grid datasets so that it was combined with satellite data and later on easy to use in GIS format analysis, which was a great help to derive meteorological information, phonological information and vegetation based indices for vegetation drought dynamics.

3.3 NDVI & LST

Following the streamlines in methodology, after image processing, all satellite data was processed for the mapping of vegetation indices - VIs (NDVI & EVI) and LST. For vegetation indices (NDVI & EVI) a 16-day time series L3 global 250m resolution MODIS product MOD13Q1 and an 8 day L3 Global 1km average value of the composite LST MODIS product MOD11A2 were used in the study area from 2000 to 2018. NDVI is a proxy for photosynthetic activity and primary production from vegetation biomass and is a common index for monitoring vegetation health. Enhanced vegetation index *(*EVI) is similar to NDVI but less sensitive to noise from background soil and atmospheric conditions and less saturated in high-biomass areas. Here VIs was calculated from visible and infrared bands combinations in ArcGIS software, whereas LST was calculated by thermal bands (ground emissivity) combinations. VIs was helping to identify forest canopy cover mapping and vegetation condition index (VCI), while LST can measure temperature condition index (TCI). The important thing is that NDVI generated VCI and LST generated TCI was useful to make vegetation health index (VHI), which show the actual vegetation health condition.

These continuous VIs and LST time series values were helpful to calculate the baseline and change metrics of forest health for tree vulnerability detection to drought. MODIS MOD11A2 product consists of 16-bit unsigned integer values from 7500 to 65500 and to derive actually ground temperature in Kelvin, need to multiply it with scaling factor 0.02 [40]. In NDVI some values are zero or less than zero, which represent water body or the cloud in the image so need filters and finally generate maps of the study area from 2000 to 2018.

3.4 NASA Global Land Data Assimilation System (GLDAS Noah Surface Model)

This data product is a replacement for GLDAS-1 0.25-degree monthly data product. Global land data assimilation system version 2 (hereafter, GLDAS-2) has two components: one forced entirely with the Princeton meteorological forcing data (hereafter, GLDAS-2.0), and the other forces with a combination of model and observation based forcing data sets (hereafter, GLDAS-2.1). This research work used this data for calculating the meteorological drought index (SPI). GLDAS Noah land surface model combines remotely sensed precipitation estimation with land surface gauge analysis and was help precipitation rates and vegetation response to rainfall over the accumulation period for each pixel as the amount of rainfall associated with vegetation condition.

3.5 Standardized precipitation index (SPI)

Generally, rainfall directly effects on temperature and soil moisture and later on vegetation. Normally in high rainfall regions, vegetation is very healthy and dense. A short time period of SPI values (1 to 3

months) is related to soil moisture changes that have a greater effect on agriculture. A longer time period (6 to 12 months) SPI values show longer time period change on precipitation, available water, land use/cover and ecosystem. This research work used almost two-decade summer rainfall data (May to Aug months.) from 2000 to 2018 to access the change in drought and to determine changing-point in rainfall pattern in ER (fig. 2). Figure 1 shows the location of all 25 rainfall stations from where we collect rainfall data and derive a relationship between drought and vegetation indices.

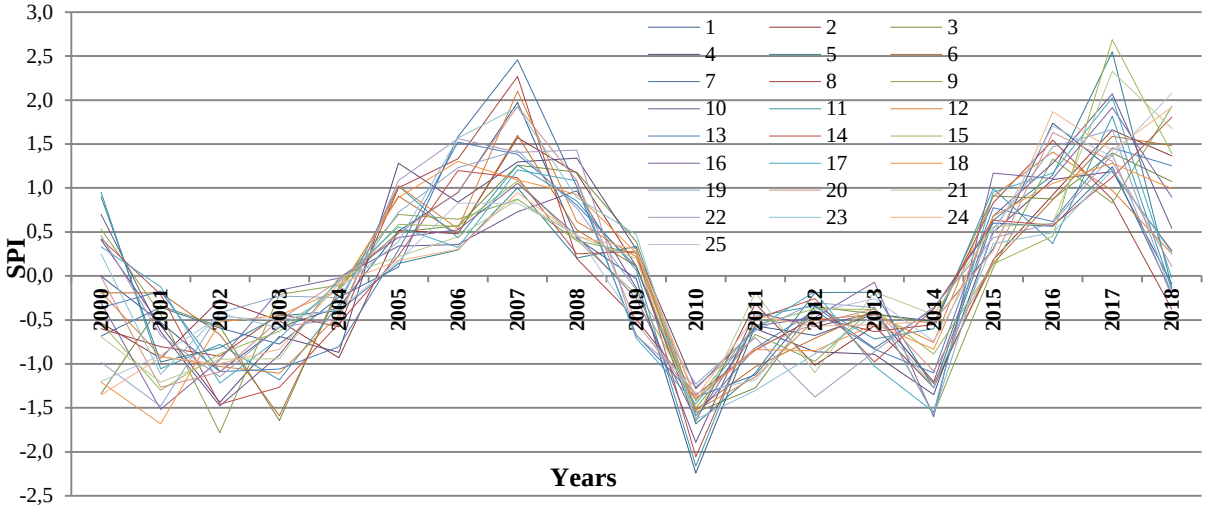

Figure 2. SPI based drought identification from 25 rainfall stations in ER from 2000 to 2018. SPI values above 2 indicate extreme wetness, between 2 and 1 severe to moderate wetness, between 1 and -1 normal condition, between -1 and -2 moderate to severe droughts and below -2 extreme droughts.

3.6 Change point detection

To detect changes in vegetation with drought, change point or breakpoint identification in rainfall pattern is a compulsory thing which helps to understand the whole ecosystem process. A changing point is defining a point where frequency and distribution of variables change their direction for a time (figure. 2). There are many methods to identify change point such as [42, 43, 44, 45] tests that enable detection of changes in a data series. This research work defines change point in a time series of rainfall by using Pettitt-Mann-Whitney-Test and cumulative sum method (CUSUM) in the Change Point Analyzer (CPA) software [42]. The CUSUM method is a very simple and flexible method and originally developed for controlling industrial process and can use in trained data in place of natural data. Many times it used in environmental monitoring programs to identify change point in time series of environmental and climatic variables. After identifying change point in rainfall data series, we confirm it with t-test by comparing the mean value of rainfall data before and after the change years.

3.7 Mapping VIs area

Vegetation health or condition and total vegetation cover area are highly correlated with NDVI values [46]. To identify changes in vegetation health over a period of time, we used [47] method that change in NDVI values are proxy of change in vegetation condition. According to this, we classify NDVI values in terms of very healthy to no vegetation class as in table 1. Finally, first we calculate total vegetation and non-vegetation area and then subclass level vegetation area according to NDVI values as table 1for over the last two decades from 2000 to 2018 for European Russia. As atmospheric condition were different for the different years during the image capturing so field work was an important task to increase accuracy in subclass level vegetation area calculations. For accuracy assessment of the all yearly NDVI maps from 2000 to 2018, 250 sampling plots with 30*30m were established in the entire study area. Other than this we also take help from Arial photos, high-resolution satellite data, and ancillary data related to vegetation for accuracy assessment and derive user accuracy, producer accuracy, and overall accuracy. Finally, calculate total area change in vegetation as well as area change in different NDVI values for the period before and after the

change/breakpoint year in the time series of rainfall data. Here we also did a key interview with old peoples who live in the study area for a long time (more than 25 years).

Table 1. Vegetation classes according to NDVI values.

Class name	NDVI range	Class level I	Class level II	Class level III	NDVI range	Subclass name
1	0.9 to 1	Vegetation	Dense vegetation	Very healthy vegetation	0.85 <	A
2	0.5 to 0.8		Open vegetation	Temperate and tropical rainforests	0.79 – 0.84	B
					0.66 – 0.78	C
					0.51 – 0.65	D
3	0.2 to 0.4		Degraded vegetation	Shrub and grassland	0.41 – 0.50	E
					0.31 – 0.40	F
					0.20 – 0.30	G
4	-0.1 to 0.1	No-Vegetation		Barren areas of rock, sand, or snow	0.00 – 0.19	H
5	-0.1 to -1			Water	0.00 – -0.50	I
					-0.51 >	J

4. Results

4.1. SPI patterns

Figure 2 shows the spatial and temporal pattern of SPI from 2000 to 2018 in the summer month from 25 rainfall stations in the ER. As above or positive values of normal rainfall distribution show wetness and negative or below values of normal rainfall indicate dryness. SPI values above 2 indicate extreme wetness, between 2 and 1 severe to moderate wetness, between 1 and -1 normal condition, between -1 and -1 moderate to severe droughts, and below -2 extreme droughts.

We find that from 2001 to 2004 all SPI values falls 0 to -1.5, which show moderate to the severe dry situation and from the year of 2004 all values move to the positive direction so the year 2004 was a changing point year. From 2005 to 2009 all SPI values were in a positive direction, means its show wet weather condition. The Year of 2007 has 2.5 SPI values means it was the extreme wet condition year. The year 2009 was again a changing point year as all values go in a negative direction till 2014, with the extremely dry year of 2010. From 2015 SPI values again move in the above direction with the extreme wet year 2017. In short, we find 3 changing point years as 2004, 2009 and 2015. We also find that year 2007 and 2017 have the extreme wet condition and year 2010 had an extremely dry condition (figure 2) so based on SPI values from 2000 to 2018, the wet and dry years patterns can be divided into four parts.

Maximum parts of the study area were the tendency of decreasing SPI values special from 2001 to 2004 and then 2009 to 2014, which show the increasing dryness in the different parts of the study area. The southern and southeast part of the ER was maximum affected area due to dryness and severe droughts.

4.2 Rainfall analysis

With the help of Pettit-Mann-Whitney method, we find the maximum probability of change year was 2004, 2009 and 2015 from the period of 2000 to 2018 from all 25 rainfall stations (figure 3). In particular these years, there was a significant change in mean summer rainfall. This was also confirmed by the CUSUM method. Figure 3 represent maximum, minimum, mean and standard deviation values of rainfall for spring-summer (May-August) season from 2000 to 2018 in European Russia. Figure 3 also shows that the year 2007 and 2017 have the highest rainfall and year 2010 had the lowest rainfall in the study area.

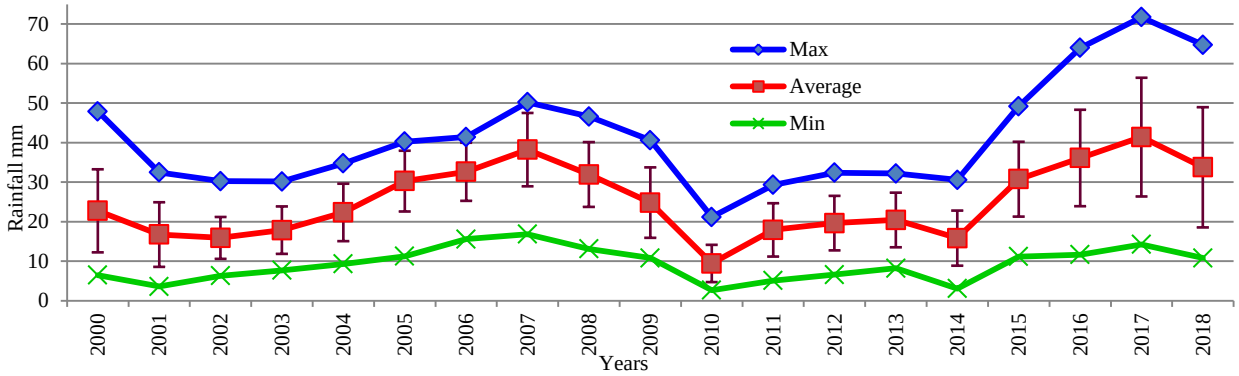

Figure 3. Maximum, minimum, average and standard deviation values of rainfall (mm) for spring-summer (May-August) season from 2000 to 2018.

4.3 Analyses of vegetation cover change

The satellite image analysis of vegetation cover in European Russia from 2000 to 2018 showed a significant change in the area between vegetation and non-vegetation (figure 4). Total vegetation area (A to G NDVI classes) was continuously increased from 2001 to 2007 and reach 3582036km^2 in 2007 and it was highest as 3681070km^2 in 2017. The non-vegetation area was highest as 982348 and 895479km^2 in 2000 and 2010 respectively (figure 4).

4.4 Analysis of SPI and VIs relationship

Analysis results show that VIs area was increased with increased SPI values and decreased with decreasing SPI values (reducing rainfall or more drought condition). The correlation and coefficients of SPI and VIs have linear regression (R^2) exceeded 0.90. According to SPI values, as the year 2010 was the driest year from 2000 to 2018 period and it's also represented by non-vegetation area as it was highest in 2010 (figure 4). When compare the highest values of SPI as it was in the year 2007 and 2017, we find that total vegetation cover area was also highest in both years (figure 4). So this research work confirms that SPI values are also associated with vegetation indices (VIs). As high SPI values represent high VIs values and vice-versa.

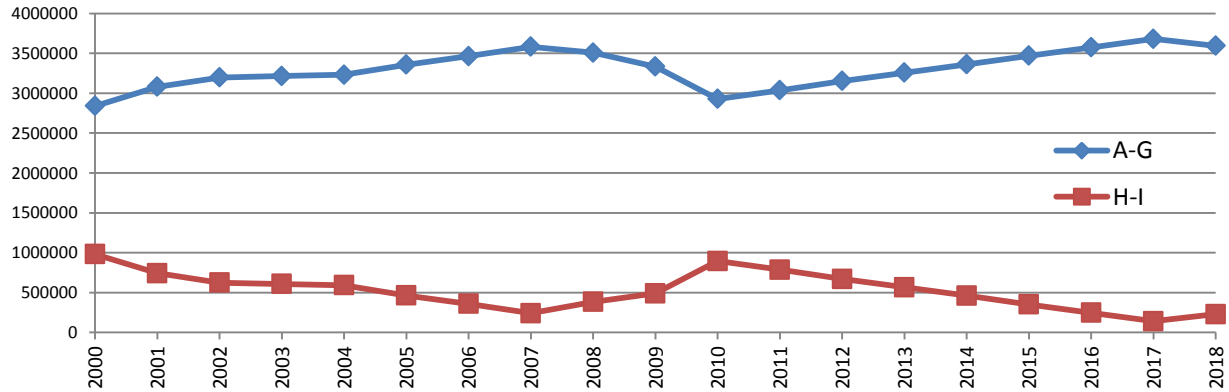

Figure 4. Vegetation and non-vegetation area in ER from 2000 to 2018.

4.5 LST and VIs

To get a relationship between LST and VIs, we used Pearson correlation coefficient during two decades study period (figure 5) and find a clear negative correlation. The correlation coefficient of determination of each linear regression (r^2) exceeded more than 0.90 in all years [48, 49]. Extreme temperature shows low vegetation and reducing temperature represent increasing high and healthy vegetation condition. Here EVI has high correlation than NDIV as it's not affected by background features effects (figure 5).

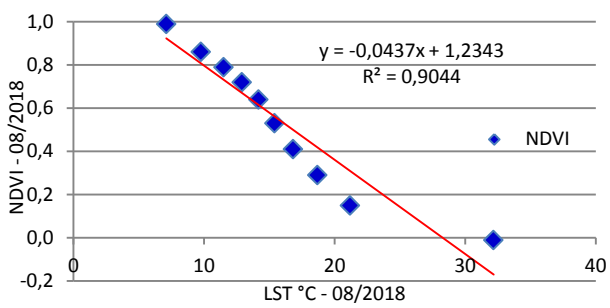
y = -0,0437x + 1,2343
R² = 0,9044
NDVI
NDVI - 08/2018
LST °C - 08/2018

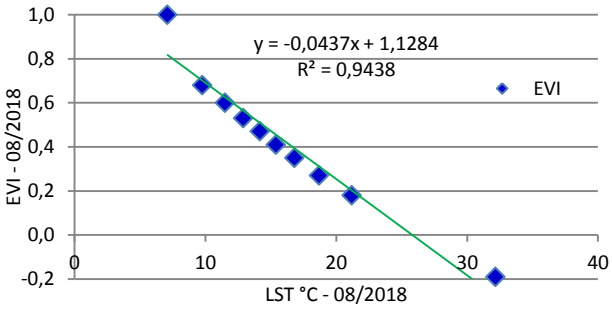
y = -0,0437x + 1,1284
R² = 0,9438
EVI
EVI - 08/2018
LST °C - 08/2018

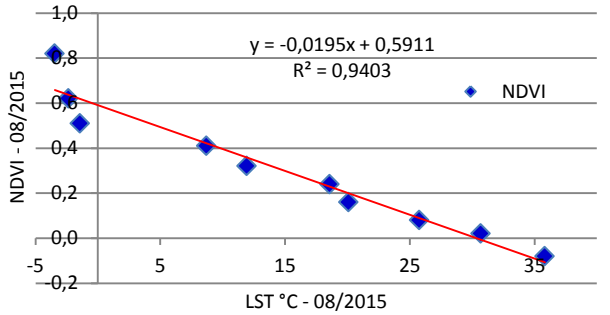
y = -0,0195x + 0,5911
R² = 0,9403
NDVI
NDVI - 08/2015
LST °C - 08/2015

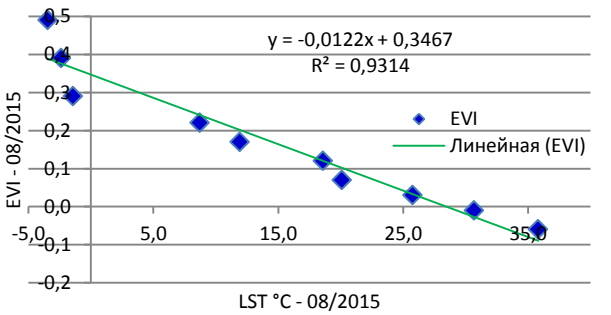
y = -0,0122x + 0,3467
R² = 0,9314
EVI
Линейная (EVI)
EVI - 08/2015
LST °C - 08/2015

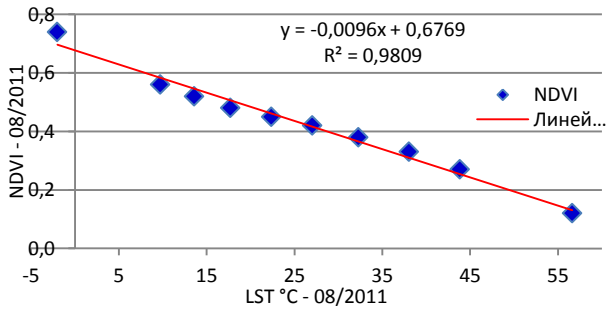
y = -0,0096x + 0,6769
R² = 0,9809
NDVI
Линей...
NDVI - 08/2011
LST °C - 08/2011

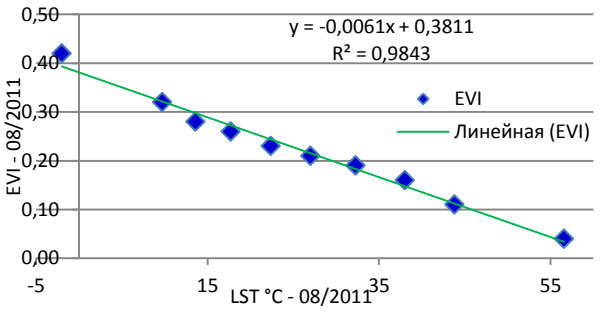
y = -0,0061x + 0,3811
R² = 0,9843
EVI
Линейная (EVI)
EVI - 08/2011
LST °C - 08/2011

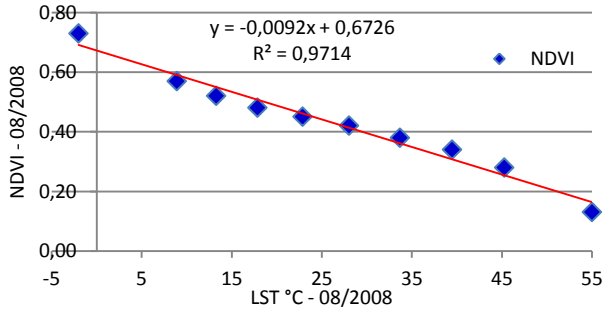
y = -0,0092x + 0,6726
R² = 0,9714
NDVI
NDVI - 08/2008
LST °C - 08/2008

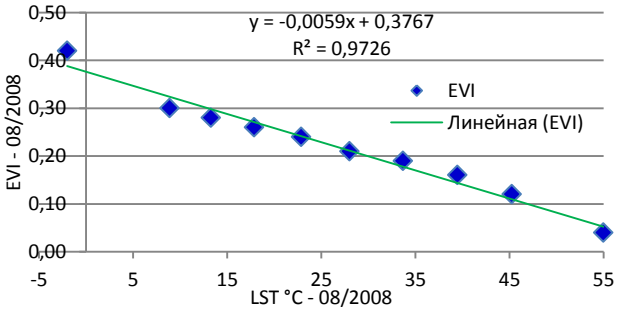
y = -0,0059x + 0,3767
R² = 0,9726
EVI
Линейная (EVI)
EVI - 08/2008
LST °C - 08/2008

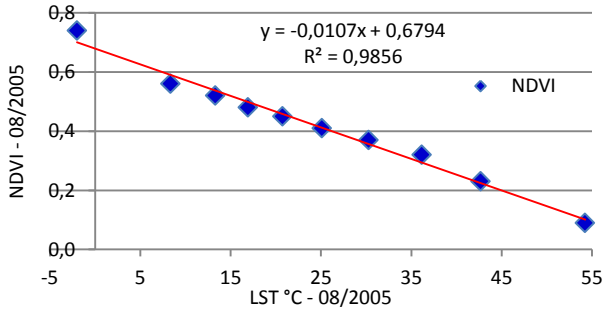
y = -0,0107x + 0,6794
R² = 0,9856
NDVI
NDVI - 08/2005
LST °C - 08/2005

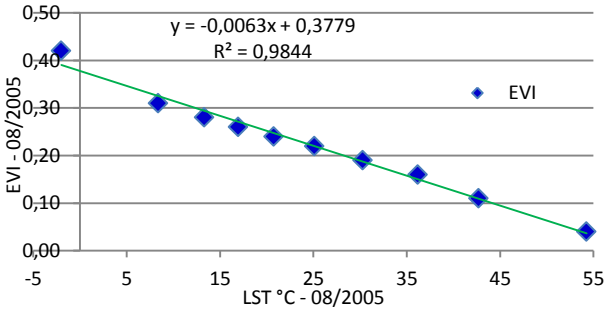
y = -0,0063x + 0,3779
R² = 0,9844
EVI
EVI - 08/2005
LST °C - 08/2005

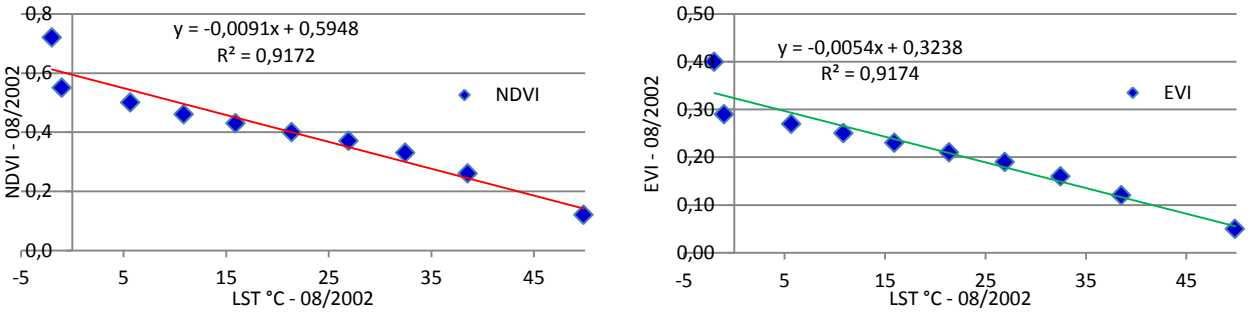

Figure 5. LST and VIs relationship during spring-summer (May-August) season from 2000 to 2018.

Normally VIs represents the land use feature and LST symbolizes thermal condition of land surface features [50]. Figure 4 illustrates the relationships between VIs (NDVI & EVI) for the different years' time period in European Russia from 2000 to 2018. In general, the NDVI value increases with enhanced vegetation coverage. It is easy to understand that higher vegetation coverage would lead to lower LST; however, when the NDVI is below a certain value, the LST appears to increase with the VIs [51].

5. Conclusion

This research work analysis three primary data (Rainfall, LST and VIs) and identify a relationship between climate condition and its direct effect on vegetation. A reduction in rainfall and high LST are increasing drought occurrence, which also indirectly influenced by human interference. The main work was using SPI time series values from rainfall and detects changes in drought and later on its effect on vegetation covers area and vegetation condition with LST. Especially identification of changing point (2004, 2009, 2015) and extreme wet (2007, 2017) and extreme dry years (2002, 2010) and effects on vegetation with LST relationship in between different time periods. The southern part of the study area was maximum affected by severe drought with high LST and low VIs. Understanding these relationships and the characteristics of droughts is crucial for improving our knowledge of vegetation vulnerability to climate fluctuations and climate change for vegetation drought dynamics.

6. References

[1] Anderegg W R L 2012 The roles of hydraulic and carbon stress in a widespread climate-induced forest die-off *Proc Natl Acad Sci USA* **109(1)** 233-237
[2] Adams H D, Zeppel M J B, Anderegg W R L, Hartmann H, Landhäusser S M, Tissue D T, Huxman T E, Hudson P J, Franz T E and Allen C D 2017 A multispecies synthesis of physiological mechanisms in drought induced tree mortality *Nature Ecology and Evolution* **1** 1285-1291
[3] Dai A 2013 Increasing drought under global warming in observations and models *Nature Climate Change* **3** 52-58 DOI: 10.1038/nclimate1633
[4] Steinkamp J and Hickler T 2015 Is drought-induced forest dieback globally increasing? *Journal of Ecology* **103** 31-43
[5] Rigling A, Bigler C and Eilmann B 2013 Driving factors of a vegetation shift from Scots pine to pubescent oak in dry Alpine forests *Global Change Biology* **19** 229-240
[6] van Mantgem P J, Stephenson N L and Byrne J C 2009 Widespread increase of tree mortality rates in the Western United States *Science* **323** 521-524
[7] Urrego L E, Correa-Metrio A, Gonzalez C, Castano A R and Yokoyama Y 2013 Contrasting responses of two Caribbean mangroves to sea-level rise in the Guajira Peninsula (Colombian Caribbean) *Palaeogeogr. Palaeoclimatol. Palaeoecol* **370** 92-102
[8] Alongi D M 2015 The impact of climate change on mangrove forests *Curr. Clim. Change Rep.* **1(1)** 30-39

[9] Galeano A, Urrego L E, Botero V and Bernal G 2017 Mangrove resilience to climate extreme events in a Colombian Caribbean Island *Wetl. Ecol. Manag* **25(6)** 743-760 DOI: 10.1007/s11273-017-9548-9
[10] McIntyre P J, Thorne J H, Dolanc C R, Flint A L, Flint L E, Kelly M and Ackerly D D 2015 Twentieth-century shifts in forest structure in California: denser forests, smaller trees, and increased dominance of oaks *Proceedings of the National Academy of Sciences of the USA* **112** 1458-1463
[11] Zhou X, Yamaguchi Y and Arjasakusuma S 2018 Distinguishing the vegetation dynamics induced by anthropogenic factors using vegetation optical depth and AVHRR NDVI: A cross-border study on the Mongolian Plateau *Science of The Total Environment* **616-617** 730-743
[12] Asbridge E, Lucas R, Ticehurst C and Bunting P 2016 Mangrove response to environmental change in Australia's Gulf of Carpentaria *Ecol. Evol.* **6(11)** 3523-3539
[13] Djebou D C S, Singh V P and Frauenfeld O W 2015 Vegetation response to precipitation across the aridity gradient of the southwestern United States *J. Arid Environ* **115** 35-43
[14] Brandt M, Tappan G, Diouf A A, Beye G, Mbow C and Fensholt R 2017 Woody vegetation die off and regeneration in response to rainfall variability in the west African Sahel *Remote Sens* **9(1)** p 39
[15] Williams A P, Allen C D and Macalady A K 2013 Temperature as a potent driver of regional forest drought stress and tree mortality *Nature Climate Change* **3** 292-297
[16] Bruno A 2018 Climate history of Russia and the Soviet Union *WIREs Climate Change* **9(5)** e534
[17] Marengo J A, Alves L M, Alvala R C S, Cunha A P, Brito S and Moraes O L L 2018 Climatic characteristics of the 2010-2016 drought in the semiarid Northeast Brazil region *Anais da Academia Brasileira de Ciências* **90(2)** 1973-1985
[18] Goodarzi M, Pourhashemi M and Azizi Z 2019 Investigation of Zagros forests cover changes under recent droughts using satellite imagery *J. For. Sci* **65** 9-17
[19] Asner G P, Brodrick P G, Anderson C B, Vaughn N, Knapp D E and Martin R E 2016 Progressive forest canopy water loss during the 2012–2015 California drought *Proc. Natl. Acad. Sci. The USA* **113** E249-E255
[20] Klein T, Cahanovitc R, Sprintsin M, Herr N and Schiller G 2019 A nation-wide analysis of tree mortality under climate change: Forest loss and its causes in Israel 1948-2017 *Forest Ecology and Management* **432** 840-849
[21] USDA 2016 New Aerial Survey Identifies More Than 100 Million Dead Trees in California (*USDA: Vallejo, CA, USA*)
[22] Liang L 2015 Remote Sensing Monitoring and Ecological Modeling of Insect Outbreak Dynamics in the Southern Rocky Mountains Ecoregion *Ph.D. thesis: University of California, Berkeley*
[23] Slaton M, Koltunov A and Ramirez C 2016 Application of the Ecosystem Disturbance and Recovery Tracker in Detection of Forest Health Departure from Desired Conditions in Sierra Nevada National Forests
[24] Wulder M A, White J C, Coops N C and Buston C R 2008 Multi-temporal analysis of high spatial resolution imagery for disturbance monitoring *Remote Sens. Environ* **112** 2729-2740
[25] Cohen W B, Yang Z, Stehman S V, Schroeder T A, Bell D M, Masek J G, Huang C and Meigs GW 2016 Forest disturbance across the conterminous United States from 1985-2012: The emerging dominance of forest decline *For. Ecol. Manag* **360** 242-252
[26] Wilhite D A, Svoboda M D and Hayes M J 2007 Understanding the complex impacts of drought: a key to enhancing drought mitigation and preparedness *Water Resour. Manage* **21** 763-774
[27] Labe dzki L 2017 Categorical forecast of precipitation Anomaly using the standardized precipitation index SPI *Water* **9(1)** p 8
[28] Kamali B, Houshmand Kouchi D, Yang H and Abbaspour K C 2017 Multilevel drought hazard assessment under climate change scenarios in semi-arid regions- a case study of the Karkheh river basin in Iran *Water* **9(4)** p 241

[29] Wan Z, Hook S and Hulley G 2015 MOD11A2 MODIS/Terra Land Surface Temperature / Emissivity 8-Day L3 Global 1km SIN Grid V006 [Data set] *NASA EOSDIS LP DAAC*
[30] Lee A F and Heghinian S M 1977 A shift of the mean level in a sequence of independent normal random variables-a bayesian approach *Technometrics* **19(4)** 503-506
[31] Hubert P, Carbonnel J P and Chaouche A 1989 Segmentation des series hydro-meteorological application des series de precipitations et de debits de l'Afrique de l'ouest *J. Hydrol* **110(3)** 349-367
[32] Berdanier A B and Clark J S 2016 Multiyear drought-induced morbidity preceding tree death in southeastern US forests *Ecol. Appl* **26** 17-23
[33] Schabenberger and Gotway 2005 Statistical methods for spatial data Analysis *Chapman & Hall* (Taylor & Francis)
[34] Filipchuk A, Moiseev B, Malysheva N and Strakhov V 2018 Russian forests: A new approach to the assessment of carbon stocks and sequestration capacity *Environmental Development* **26** 68-75
[35] Zhu Q, Liu Y, Jia R, Hua S, Shao T and Wang B *2018* A numerical simulation study on the impact of smoke aerosols from Russian forest fires on the air pollution over Asia *Atmospheric Environment* **182** 263-274
[36] Marengo J A, Alves L M, Alvala R C S, Cunha A P, Brito S and Moraes O L L 2018 Climatic characteristics of the 2010-2016 drought in the semiarid Northeast Brazil region *Anais da Academia Brasileira de Ciências* **90(2)** 1973-1985
[37] Boori M S, Paringer R, Choudhary K and Kupriyanov A 2018 Supervised and unsupervised classification for obtaining land use/cover classes from hyperspectral and multi-spectral imagery *Proc. SPIE 10773, 6th International Conference on Remote Sensing and Geoinformatics of the environment (RSCy 2018)* **107730L** 1-11
[38] Palmer W C 1965 Meteorological Drought *US Department of Commerce, Weather Bureau, Washington, DC, USA* **30**
[39] McKee T B, Doesken N J and Kleist J 1993 The relationship of drought frequency and duration to time scales *Proceedings of the 8th Conference on Applied Climatology* **17(22)** 179-183
[40] Karl T and Knight RW 1985 Atlas of monthly Palmer hydrological drought indices (1931-1983) for the contiguous United States *Natl. Clim. Data Cent*
[41] Khadr M 2017 Temporal and spatial analysis of meteorological drought characteristics in the upper Blue Nile River region *Hydrol. Res* **48(1)** 265-276
[42] Beaudoing H and Rodell M 2016 NASA/GSFC/HSL, GLDAS Noah Land Surface Model L4 monthly 0.25 x 0.25 degree V2.1, Greenbelt, Maryland, USA, Goddard Earth Sciences Data and Information Services Center (GES DISC) URL: https://disc.gsfc.nasa.gov/ datasets/GLDAS_NOAH025_M_V2.1/summary?keywords=GLDAS
[43] Pettitt A N 1979 A non-parametric approach to the change-point problem *Appl. Stat* 126-135
[44] Buishard T 1984 Tests for detecting a shift in the mean of hydrological time series *J. Hydrol* **58** 51-69
[45] Boori M S, Paringer R, Choudhary K, Kupriyanov A and Banda R 2018 Land cover classification and build spectral library from hyperspectral and multi-spectral satellite data: A data comparison study in Samara, Russia *CEUR Workshop Proceedings* **2210** 390-401
[46] Boori M S, Choudhary K, Evers M and Kupriyanov A 2017 Environmental dynamics for Central Dry Zone area of Myanmar *International Journal of Geoinformatics* **13(3)** 1-12
[47] Giri C, Pengra B, Zhu Z, Singh A and Tieszen L L 2007 Monitoring mangrove forest dynamics of the Sundarbans in Bangladesh and India using multi-temporal satellite data from 1973 to 2000 *Estuar. Coast. Shelf Sci* **73(1)** 91-100
[48] Pavelyeva E A 2018 Image processing and analysis based on the use of phase information *Computer Optics* **42(6)** 1022-1034 DOI: 10.18287/2412-6179-2018-42-6-1022-1034
[49] Boori M S, Paringer R, Choudhary K and Kupriyanov A 2018 Comparison of hyperspectral and multi-spectral imagery to build a spectral library and land cover classification performances *Computer Optics* **42(6)** 1035-1045 DOI: 10.18287/2412-6179-2018-42-6-1035-1045

[50] Bibikov S A, Kazanskiy N L and Fursov V A 2018 Vegetation type recognition in hyperspectral images using a conjugacy indicator *Computer Optics* **42(5)** 846-854 DOI: 10.18287/2412-6179-2018-42-5-846-854
[51] Belov A M and Denisova A Y 2018 Spectral and spatial super-resolution method for earth remote sensing image fusion *Computer Optics* **42(5)** 855-863 DOI: 10.18287/2412-6179-2018-42-5-855-863

Acknowledgment
This work was partially supported by the Ministry of education and science of the Russian Federation in the framework of the implementation of the Program of increasing the competitiveness of Samara University among the world's leading scientific and educational centers for 2013-2020 years; by the Russian Foundation for Basic Research grants (# 15-29-03823, # 16-41-630761, # 17-01-00972, # 18-37-00418), in the framework of the state task #0026-2018-0102 "Optoinformation technologies for obtaining and processing hyperspectral data".

Parameter space dimension reduction of an adaptive interpolator during multidimensional signal differential compression

A I Maksimov[1], M V Gashnikov[1,2]

[1]Samara National Research University, Moskovskoe Shosse 34A, Samara, Russia, 443086
[2]Image Processing Systems Institute of RAS - Branch of the FSRC "Crystallography and Photonics" RAS, Molodogvardejskaya street 151, Samara, Russia, 443001

e-mail: aleksei.maksimov.ssau@gmail.com

Abstract. We propose a new adaptive multidimensional signal interpolator for differential compression tasks. To increase the efficiency of interpolation, we optimize its parameters space by the minimum absolute interpolation error criterion. To reduce the complexity of interpolation optimization, we reduce the dimension of its parameter range. The correspondence between signal samples in a local neighbourhood is parameterized. Besides, we compare several methods for such parameterization. The developed adaptive interpolator is embedded in the differential compression method. Computational experiments on real multidimensional signals confirm that the use of the proposed interpolator can increase the compression ratio

1. Introduction

There are many interpolation [1, 2] methods have been already developed, and they continue to evolve. It is worth mentioning techniques based on context modeling [3], least mean squares [4], Kronecker bases [5], matrix pencil method [6], compressed sensing [7], etc. However, these methods are recourse consuming and computationally complex, therefore are not suitable for differential compression algorithms.

Differential compression of multidimensional signals, also called DPCM (differential pulse-code modulation [8 - 11]), is based on interpolation (prediction) of signal samples based on already processed samples and further interpolation error encoding (post-interpolation residues encoding). A high correlation usually characterizes real digital signals, so a transition to a differential representation entails a significant non-uniformity of the probability distribution of post-interpolation residues, which, in turn, leads to a decrease [12 - 14] of compressed data entropy, and a compression ratio increase.

In his paper, we propose a new adaptive DPCM interpolator of multidimensional signals [2, 15 – 16], for which three different ways of parameterization of already processed samples correspondence are proposed. The complexity of optimizing the parameters of the proposed interpolator is decreased by reducing the dimension of its parameters space. An experimental study of the proposed adaptive interpolator on a test set of multidimensional signals of the SpecTIR spectrometer was made; its results demonstrate that the proposed interpolation method outperforms the most common one.

The article is structured as follows: first, a general method of DPCM is given. After which the proposed interpolator is described: the general scheme for constructing adaptive interpolators, the procedure for reducing the parameter space and the interpolation procedure. After that, the results of an experimental study are presented.

2. Multidimensional signals differential compression

During differential compression of a multidimensional signal, the samples are processed in the order of some scan, which generalizes the line-by-line scan of the two-dimensional case. Let $\mathrm{C}(\vec{x})$ be the multidimensional signal and $\vec{x}$ be the vector of its arguments. Every sample of $\mathrm{C}(\vec{x})$ id processed in the following way:

1. Interpolation.

The interpolated value $P(\vec{x})$ of the current sample is calculated using the already processed (compressed and decompressed) samples $\{C_k(\vec{x})\}$:

$$P(\vec{x}) = \mathbf{P}\left(\left\{\hat{C}_k(\vec{x})\right\}\right), \tag{1}$$

via interpolation function **P.**

2. Calculation of the differential signal f (the difference between the interpolated and the real value):

$$f(\vec{x}) = \mathrm{C}(\vec{x}) - P(\vec{x}). \tag{2}$$

where $f(\vec{x})$ - is the differential signal.

3. Quantization of differential signal:

$$f_q(\vec{x}) = Q\left(f(\vec{x})\right), \tag{3}$$

where $f_q(\vec{x})$ - quantized difference, Q - quantization function.

In this work, we used a uniform quantization scale:

$$f_q(\vec{x}) = sign\left(f(\vec{x})\right)\left[\frac{|f(\vec{x})|\varepsilon_{\max}}{2\varepsilon_{\max}+1}\right], \tag{4}$$

where $\varepsilon_{\max}$ – preset maximum error (compression algorithm parameter), [..] means an integral part of the number. This quantization scale controls the maximum error between the initial $C(\vec{x})$ and decompressed $\hat{C}(\vec{x})$ signals:

$$\varepsilon_{\max} = \max_{\vec{x}}\left|C(\vec{x}) - \hat{C}(\vec{x})\right|. \tag{5}$$

4. Reconstruction of current value:

$$\hat{C}(\vec{x}) = P(\vec{x}) + f_q(\vec{x})(2\varepsilon_{\max}+1). \tag{6}$$

i.e. calculation of decompressed value $\hat{C}(\vec{x})$. This value will be used in the compression stage during the interpolation (3) of the next samples. This feedback is necessary to ensure that the interpolators work identically during compression and decompression.

5. Encoding of the quantized differential signal. In this work, Huffman encoder was used [8 - 10].

3. Multidimensional signals adaptive interpolation

3.1. Approach to adaptive interpolator construction

We have developed proposed interpolator according to the following general structure of adaptive interpolation of multidimensional signals. It generalizes two-dimensional interpolation algorithms described in [2, 8].

Let us consider a current sample $C(\vec{x})$ which is to be interpolated on the basis of neighbor ones $\{C_k(\vec{x})\}$. Let $\{\mathbf{P}_i(\{C_k(\vec{x})\})\}$ – be the set of simple and fast interpolation functions. Therefore, for every sample a set of interpolated values can be calculated:

$$P_i(\vec{x}) = \mathbf{P}_i(\{C_k(\vec{x})\}). \quad (7)$$

Resulting interpolated value is chosen via the parameterized decision rule R:

$$P(\vec{x}) = C_i(\vec{x}), \quad i = R(\eta(\vec{x}), \eta^{\lim}), \quad (8)$$

which uses the vector of local features $\eta(\vec{x})$ calculated on the basis of neighbor samples $\{C_k(\vec{x})\}$. The decision rule is also dependent on the parameter $\eta^{\lim}$, which is calculated during the optimization of some criterion (for example, interpolation error). The certain form of the criterion is determined by the method application area.

Averaging over the nearest processed samples interpolators are usually used [2] to reduce the computational complexity in differential compression:

$$P(\vec{x}) = \frac{1}{N}\sum_{i=1}^{N}\hat{C}_k(\vec{x}), \quad (9)$$

where $\hat{C}_k(\vec{x})$ – are the neighbor samples, N – is the number of neighbor samples.

The interpolator of this type work quite accurately on relatively smooth signal parts due to averaging over noised samples, but it has a large error on the contours (extended brightness differences). When interpolating contour readings, interpolators based on interpolation “along” the contour work more accurately. An example of these interpolators for the two-dimensional case is, for example, Graham interpolator [2, 8].

During Graham interpolation, the interpolated value is equal to the neighbor sample value which lies in the direction of the contour. However, this interpolation is less accurate on smooth parts of the signal.

In this paper, we propose an adaptive interpolator that combines the advantages of both described approaches. Proposed interpolator automatically switches between averaging interpolation and interpolation “along the contour” depending on the presence and intensity of the contour in the local neighborhood of each signal sample.

Let us describe in more detail interpolation function (7) and decision rule (8). Let L be the number of possible contour directions (usually, it is greater than or equal to signal dimension). Let $\{\lambda_i(\vec{x}): 0 \le i < L\}$ be the set of averaged difference moduli $|\hat{C}_t(\vec{x}) - \hat{C}_\tau(\vec{x})|$ between already processed samples $\hat{C}_k(\vec{x})$ in every direction possible (this set is computed in every signal sample). Difference values $\lambda_i(\vec{x})$ determine the presence and intensity of the contour in the current signal sample local neighbourhood. The least of these differences might be used to determine the direction of the contour if one passes through the processed sample. To decide whether there is a contour in a signal and what direction it goes in, several threshold values $\eta_i^{\lim}$ are used. Thresholds are compared with local features values $\eta(\vec{x})$. If there are no contours detected, averaging interpolation (9) is used:

$$P(\vec{x}) = P^{(1)}(\vec{x}) = \frac{1}{N}\sum_{k=1}^{N}\hat{C}_k(\vec{x}), \quad if\ i = \arg\min_{\lambda}\{\lambda_i(\vec{x})\}\ \&\ \eta(\vec{x}) \le \eta_i^{\lim}, i \in [0, N_c). \quad (10)$$

Otherwise, the neighbouring sample, located in the differences minimum direction is used as an interpolating value (interpolation “along the contour” is performed):

$$P(\vec{x}) = P^{(2)}(\vec{x}) = \hat{C}_j(\vec{x}), \quad if\ i = \arg\min_{\lambda}\{\lambda_i(\vec{x})\}\ \&\ \eta(\vec{x}) > \eta_i^{\lim}, i \in [0, N_c). \quad (11)$$

Therefore, to calculate the best $\eta_i^{\lim}$ values, we have to perform the optimization in N_c-dimensional parameter space.

The application task determines the number of dimensions N_c of parameter space $\lambda_i^{\lim}$. For differential compression, the complexity of the task is determined not only by the signal dimension but also by the number of contour directions taken into account. For example, for differential compression of two-dimensional signals (images), $N_c = 2$ if we consider horizontal and vertical contours $N_c = 4$ if we consider horizontal, vertical and diagonal contours. Given the limitations on computational complexity, even for $N_c = 2$ searching the $\eta_i^{\lim}$ parameters can be an overly time-consuming task.

3.2. Interpolator parameter space dimension reduction

In this paper, we propose to reduce the parameter space dimension to lower the computational complexity of finding these parameters. To do that we propose to use decision rules based on the relationships between $\lambda_i\left(\vec{x}\right)$ instead of their absolute values. If there are no contours in a sample's neighborhood, differences λ_i will have close values. If there is a distinct contour, the desired λ_j will be not only the least but also distant from the other ones. Figure 1 shows described situations pictorially.

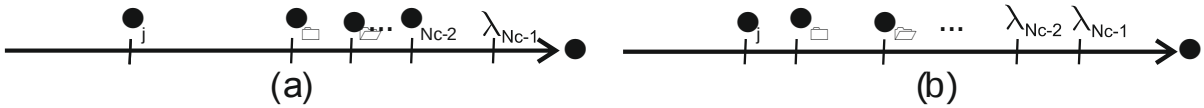

Figure 1. Differences distribution during the interpolation: (a) – a contour passes through the processed sample, (b) – there are no contours in the sample's neigbourhood.

We propose three new contour features based on described statements:

$$\eta_{\mathrm{I}}\left(\vec{x}\right) = \lambda_r\left(\vec{x}\right) - \lambda_j\left(\vec{x}\right),\ j\left(\vec{x}\right) = \arg\min_i\left\{\lambda_i\left(\vec{x}\right)\right\},\ r\left(\vec{x}\right) = \arg\min_{i:\, i\neq j}\left\{\lambda_i\left(\vec{x}\right)\right\}, \tag{12}$$

$$\eta_{\mathrm{II}}\left(\vec{x}\right) = \frac{\lambda_j\left(\vec{x}\right)}{\bar{\lambda}\left(\vec{x}\right)},\ \bar{\lambda}\left(\vec{x}\right) = \frac{1}{N_C}\sum_{k=0}^{N_C-1}\lambda_k\left(\vec{x}\right), \tag{13}$$

$$\eta_{\mathrm{III}}\left(\vec{x}\right) = \frac{\lambda_1^V\left(\vec{x}\right) - \lambda_0^V\left(\vec{x}\right)}{\frac{1}{N_C-1}\sum_{i=0}^{N_C-2}\lambda_{i+1}^V\left(\vec{x}\right) - \lambda_i^V\left(\vec{x}\right)}, \tag{14}$$

where $\lambda_i^V\left(\vec{x}\right)$ – is the element of the difference ordered series.

During the interpolation procedure, proposed contour features are compared with a single threshold value $\eta^{\lim}$. Thus, by reducing the parameter space dimension, it is possible to reduce the multi-parameter optimization problem to a single-parameter one, where the only parameter is $\eta^{\lim}$. To calculate this parameter, an automatic optimization procedure is used, similar to one described in [16].

3.3. Adaptive interpolation algorithm for differential compression

We considered a three-dimensional signal during experimental research $C\left(\vec{x}\right) = C\left(x, y, z\right)$, which is processed "layer-wise" with line-by-line scan in each layer. We have considered the following set of differences, each difference in accordance with a contour direction:

$$\lambda_1 = \lambda_- = \Big(\big|\hat{C}(x,y-1,z) - \hat{C}(x-1,y-1,z)\big| + \big|\hat{C}(x-1,y-1,z) - \hat{C}(x-2,y-1,z)\big| + \\ + \big|\hat{C}(x-1,y+1,z) - \hat{C}(x-2,y+1,z)\big| \Big) \Big/ 3 \tag{20}$$

$$\lambda_2 = \lambda_| = \Big(\big|\hat{C}(x-1,y-1,z) - \hat{C}(x-1,y-2,z)\big| + \big|\hat{C}(x-1,y,z) - \hat{C}(x-1,y-1,z)\big| + \\ + \big|\hat{C}(x-1,y+1,z) - \hat{C}(x-1,y,z)\big| \Big) \Big/ 3 \tag{21}$$

$$\lambda_3 = \lambda_/ = \Big(\big|\hat{C}(x,y-1,z) - \hat{C}(x-1,y,z)\big| + \big|\hat{C}(x-1,y,z) - \hat{C}(x-2,y-1,z)\big| + \big|\hat{C}(x-1,y-1,z) - \hat{C}(x-2,y,z)\big| \Big) \Big/ 3, \tag{22}$$

$$\lambda_4 = \lambda_\backslash = \Big(\big|\hat{C}(x,y-1,z) - \hat{C}(x-1,y-2,z)\big| + \big|\hat{C}(x-1,y,z) - \hat{C}(x-2,y-1,z)\big| + \big|\hat{C}(x+1,y-1,z) - \hat{C}(x,y-2,z)\big| \Big) \Big/ 3, \tag{23}$$

$$\lambda_5 = \lambda_\bullet = \Big(\big|\hat{C}(x-1,y,z) - \hat{C}(x-1,y,z-1)\big| + \big|\hat{C}(x,y-1,z) - \hat{C}(x,y-1,z-1)\big| + \\ + \big|\hat{C}(x-1,y-1,z) - \hat{C}(x-1,y-1,z-1)\big| + \big|\hat{C}(x+1,y-1,z) - \hat{C}(x+1,y-1,z-1)\big| \Big) \Big/ 4 \tag{24}$$

Figure 2 demonstrates the discussed differences.

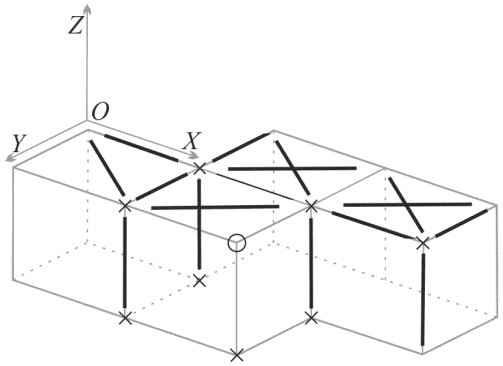

Figure 2. Discrete differences for five contour directions (bold lines) during sample «○» interpolation with the use of «×» samples as reference.

As one may notice $\lambda_-, \lambda_|, \lambda_/, \lambda_\backslash$ are the averaged differences of vertical, horizontal and diagonal directions inside the current layer $C(x,y,z)$, and $\lambda_\bullet$ is the "cross-layer" averaged difference, i.e., the difference between samples from layer $C(x,y,z)$ and layer $C(x-1,y,z)$.

In this case, contour features (12- 14) can be described in the following way:

$$\eta_{\mathrm{I}}(x,y,z) = \lambda_r(x,y,z) - \lambda_j(x,y,z), \\ j(x,y,z) = \arg\min_i \{\lambda_i(x,y,z)\},\ r(x,y,z) = \arg\min_{i:\, i\neq j} \{\lambda_i(x,y,z)\},\ i,j \in [1,5] \tag{25}$$

$$\eta_{\mathrm{II}}(x,y,z) = \frac{\lambda_j(x,y,z)}{\bar{\lambda}(x,y,z)},\ \bar{\lambda}(x,y,z) = \frac{1}{5}\sum_{k=1}^{5}\lambda_k(x,y,z), \tag{26}$$

$$\eta_{\mathrm{III}}(x,y,z) = \frac{\lambda_1^V(x,y,z) - \lambda_0^V(x,y,z)}{\frac{1}{4}\sum_{i=1}^{4}\lambda_{i+1}^V(x,y,z) - \lambda_i^V(x,y,z)}, \tag{27}$$

In this work, we have compared the adaptive interpolator with proposed contour features (25 - 27) with an averaging one (9). The averaging interpolator for this case can be described in the following way:

$$P(x,y,z) = \frac{1}{8}\sum_{i=1}^{8}\hat{C}_k(x,y,z). \tag{28}$$

4. Experimental study of the proposed adaptive interpolator

A set of 6 hyper-spectral Earth remote sensing signals were used during the experimental research. The set was obtained via SpecTIR hyper-spectrometer. Signals are 160×200×356 with 16-bit color depth. Figure 3 demonstrates several channels of test signals.

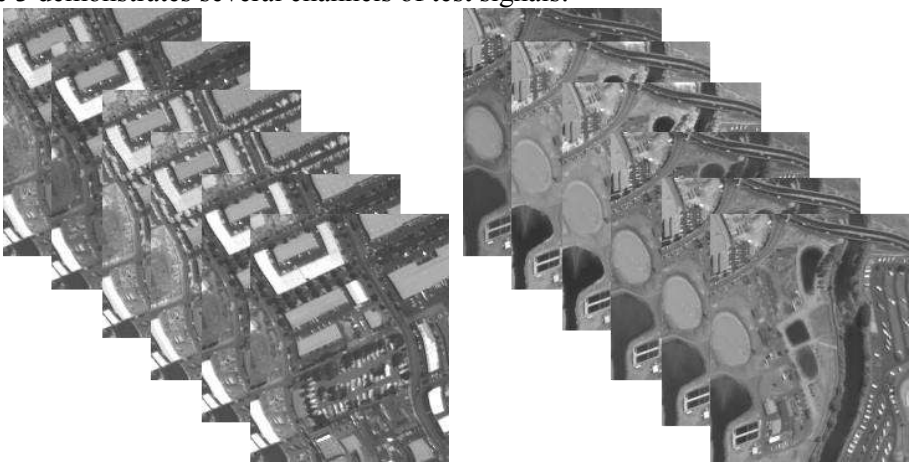

Figure 3. Several contrasted signal channels of the test set.

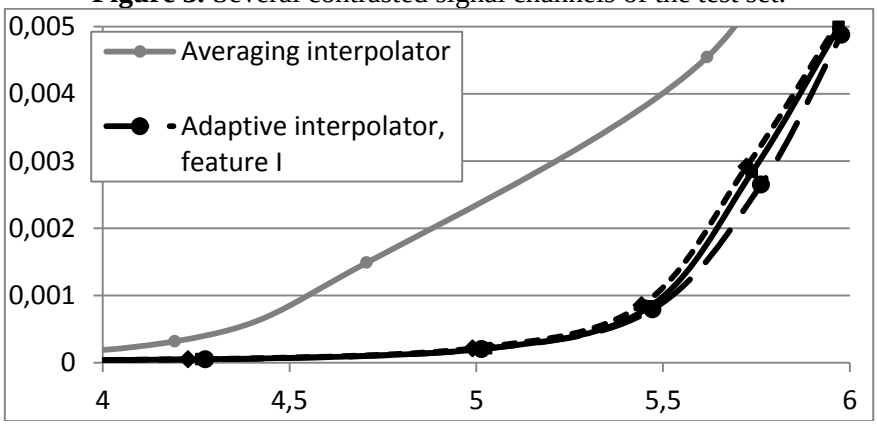

Figure 4. Dependence of decompressed signal RMS on compression coefficient with the use of the adaptive (with different contour features) and averaging interpolators.

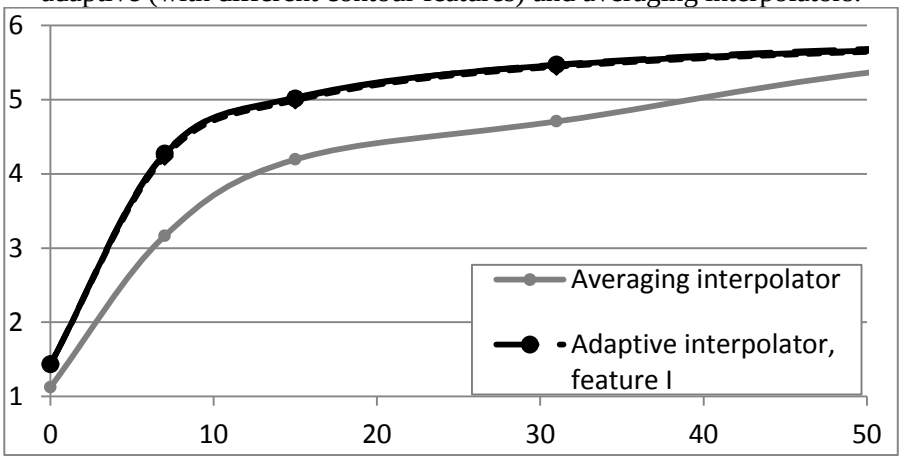

Figure 5. Dependence of the averaged over the test set compression ratio on the absolute error.

Experimental research was held in the following way - each test signal was compressed and then decompressed with a different maximum error value after that root mean square error (RMS) was

calculated for the decompressed signal. Results were averaged over all test set. Figure 4-7 demonstrates the results of the experimental study.

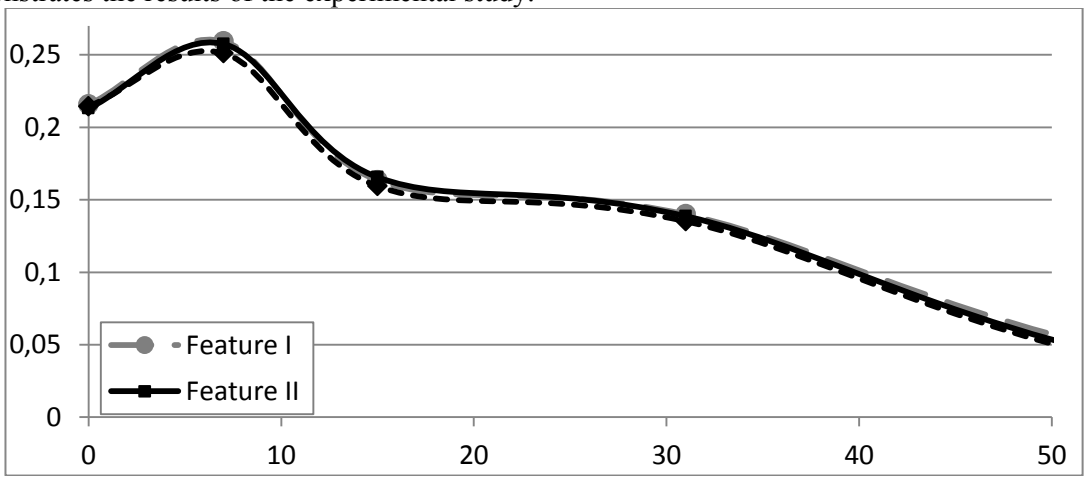

Figure 6. Dependence of the relative gain in archive size from the averaging interpolator on the absolute error.

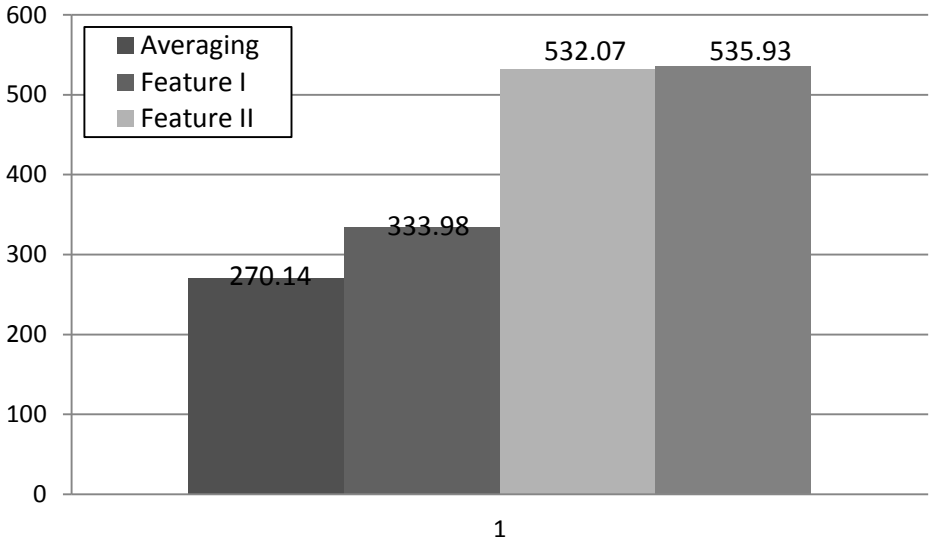

Figure 7. Averaged over the test set time of processing of one test image.

As one may notice, proposed adaptive interpolator significantly reduces decompressed signal RMS. for example, it gives 11 times less RMS then averaging interpolator for compression coefficient 5. The least RMS is obtained with the use of the contour feature that uses the difference between two minimum values (see 25 and its general form 12). One may notice, that the use of feature I (12, 25) results in faster image processing with the same performance (in terms of RMS and compression ratio) as features II (13, 26) and III (14, 27).

5. Conclusions

In this paper, new adaptive interpolator for differential compression tasks was proposed. It uses the contour features to switch between interpolation methods in every processed signal sample. The parameter space dimension reduction procedure was performed to lower the computational complexity of the proposed interpolator. Three methods for the contour feature calculation were proposed.

During the experimental research, every setup of the proposed interpolator outperformed the averaging one. The least RMS is obtained with the use of contour feature that uses the difference between two minimum values.

5. References

[1] Sergeyev V V and Chicheva M A 2013 *Digital processing of signals and images theory* (Samara: Samara University Press)
[2] Gashnikov M V 2016 Parameterization of the nonlinear Graham predictor for digital image compression *Computer Optics* **40(2)** 225-231 DOI: 10.18287/2412-6179-2016-40-2-225-231
[3] Gashnikov M V 2018 Interpolation based on context modeling for hierarchical compression of multidimensional signals *Computer Optics* **42(3)** 468-475 DOI: 10.18287/2412-6179-2018-42-3-468-475
[4] Cohen A, Davenport M A and Leviatan D 2013 On the stability and accuracy of least squares approximations *Computational mathematics* **13** 819-834
[5] Caiafa C F and Cichocki A 2016 Computing Sparse Representations of Multidimensional Signals Using Kronecker Bases *Neural Computation* **25** 186-220
[6] Verstakov E V and Zakharchenko V D 2015 The comparative analysis of approximation algorithms of two-dimensional signals by Proni method and matrix bunches method *Radio engineering and telecommunication systems* **1** 26-31
[7] Bigot J, Boyer C and Weiss P 2016 An analysis of block sampling strategies in compressed sensing *IEEE Transactions on Information Theory* **62** 2125-2139
[8] Soifer V A et al. 2009 *Computer Image Processing, Part II: Methods and algorithms* (Saarbrücken: VDM Verlag)
[9] Salomon D 2007 *Data Compression. The Complete Reference* (Berlin: Springer-Verlag)
[10] Sayood K 2012 *Introduction to Data Compression*. (Burlington: The Morgan Kaufmann Series in Multimedia Information and Systems)
[11] Vaseghi S V 2000 *Advanced Digital Signal Processing and Noise Reduction* (Hoboken: John Wiley & Sons)
[12] Fursov V A 2011 *Information theory* (Samara: Samara University Press)
[13] Gashnikov M V 2017 Minimizing the entropy of post-interpolation residuals for image compression based on hierarchical grid interpolation *Computer Optics* **41(2)** 266-275 DOI: 10.18287/2412-6179-2017-41-2-266-275
[14] Woods J 2011 *Multidimensional Signal, Image, and Video Processing and Coding* (Cambridge: Academic Press)
[15] Donoho D L 2006 Compressed sensing *IEEE Trans. Inform. Theory* **52** 1289-12306
[16] Maksimov A I and Gashnikov M V 2018 Adaptive interpolation of multidimensional signals for differential compression *Computer Optics* **42(4)** 679-687 DOI: 10.18287/2412-6179-2018-42-4-679-687

Acknowledgments
The reported study was funded by:
- RFBR according to the research projects 18-01-00667, 18-07-01312;
- the RF Ministry of Science and Higher Education within the state project of FSRC “Crystallography and Photonics” RAS under agreement 007-GZ/Ch3363/26.

Interpolation of multidimensional signals using the reduction of the dimension of parametric spaces of decision rules

M V Gashnikov[1,2]

[1]Samara National Research University, Moskovskoe Shosse 34A, Samara, Russia, 443086
[2]Image Processing Systems Institute of RAS - Branch of the FSRC "Crystallography and Photonics" RAS, Molodogvardejskaya street 151, Samara, Russia, 443001

e-mail: mgash@smr.ru

Abstract. In this paper, we consider the interpolation of multidimensional signals problem. We develop adaptive interpolators that select the most appropriate interpolating function at each signal point. Parameterized decision rule selects the interpolating function based on local features at each signal point. We optimize the adaptive interpolator in the parameter space of this decision rule. For solving this optimization problem, we reduce the dimension of the parametric space of the decision rule. Dimension reduction is based on the parameterization of the ratio between local differences at each signal point. Then we optimize the adaptive interpolator in parametric space of reduced dimension. Computational experiments to investigate the effectiveness of an adaptive interpolator are conducted using real-world multidimensional signals. The proposed adaptive interpolator used as a part of the hierarchical compression method showed a gain of up to 51% in the size of the archive file compared to the smoothing interpolator.

1. Introduction

Currently, the need to use multidimensional digital signals is becoming more acute [1]. It is primarily about such areas as remote sensing [2-3], processing of multispectral and hyperspectral signals [4], as well as video processing.

Now we know a large number of interpolation and approximation algorithms for such signals [1-16], and the high-performance requirements often do not allow us to use trivial linear, bilinear or bicubic interpolators [1]. In other words, there is a tendency to the more and more widespread use of more complex interpolation methods, such as the support vector method [5], locally optimal well-adapted basis functions [6], approximation by multidimensional orthogonal polynomials [7], multidimensional approximation and interpolation [8] etc.

However, the presence of a large number of well-developed solutions did not stop research in the development and modification of interpolation and approximation algorithms for multidimensional signals. The approximation based on Kronecker bases [9], splines [10], and tensors [11] continues to be improved. Artificial neural networks [7,12] are also increasingly used for interpolating signals. Even the well-known least squares method (OLS) continues to be modified [13] in recent years. In the foreign literature, special attention is paid to the sparse approximation method [14], which is the basis for the “compressed sensing” approach [15–16].

All the above algorithms have a sufficiently high accuracy in solving the corresponding applied problems. However, these algorithms have high computational complexity. In this paper, we propose fast interpolation algorithms for multidimensional signals that are adaptive due to automatic switching between interpolating functions at each point of the signal. This adaptability makes it possible to ensure high interpolation accuracy with low computational complexity, due to the simplicity of the interpolating functions used.

The proposed interpolators are parameterized. Therefore, we can optimize them according to various criteria, the choice of which is determined by the specifics of the applied problem being solved. Optimization of adaptive interpolators is carried out in the space of their parameters. The complexity of this optimization is substantial if resources are limited. In this paper, we propose an algorithm for reducing the complexity of optimization due to the dimension reduction of the interpolator parametric space.

2. Adaptive interpolation of multidimensional signals

Let $C(\vec{x})$ be a multidimensional digital signal, and $\vec{x}$ be the vector of arguments. Let an arbitrary count $C(\vec{x})$ be necessary to interpolate using the nearest reference samples $\left\{\hat{C}_k(\vec{x})\right\}$. Let $\left\{\mathbf{P}^{(i)}\left(\left\{\hat{C}_k(\vec{x})\right\}\right)\right\}$ be the set of interpolation functions used. Thus, for the current sample $C(\vec{x})$ several interpolating values can be calculated:

$$P_i(\vec{x}) = \mathbf{P}^{(i)}\left(\left\{\hat{C}_k(\vec{x})\right\}\right). \quad (1)$$

The parameterized decision rule *R* performs the choice of the interpolating value for each signal sample:

$$P(\vec{x}) = P^{(i)}(\vec{x}), \quad i = R\left(\eta(\vec{x}), \eta^{\lim}\right), \quad (2)$$

Rule *R* uses a local feature vector $\eta(\vec{x})$, which is calculated based on the nearest reference samples $\left\{C_k(\vec{x})\right\}$. Let the decision rule be parameterized, i.e. depends on the parameter $\eta^{\lim}$. The value of this parameter is determined by optimizing a specific criterion, which depends on the applied task. This criterion can be, for example, the criterion for minimizing the energy of post-interpolation residues:

$$\delta\left(\eta^{\lim}\right) = \sum_{\vec{x}} \left| f(\vec{x}) \right| \to \min_{\eta^{\lim}}, \quad f(\vec{x}) = C(\vec{x}) - P(\vec{x}), \quad (3)$$

where $f(\vec{x})$ are post-interpolation residues.

The criterion for minimizing the energy of post-interpolation residues can be used, in particular, when solving the problem of matching [17-18] of heterogeneous signals that differ in resolution, number of components, etc.

In this paper, we propose to use the criterion for minimizing the entropy [19] of post-interpolation residues. This criterion is more suitable for the problem of signal compression than the criterion considered above. When using the criterion for minimizing entropy, one should take into account that post-interpolation residues are quantized before statistical coding in many compression methods, for example, in differential [20-21] and hierarchical [22-23] compression methods. In this paper, the quantizer with a uniform [19] scale is used to calculate quantized post-interpolation residues $q(\vec{x})$:

$$q(\vec{x}) = \left[\left(f(\vec{x}) + \varepsilon_{\max}\right) / \left(2\varepsilon_{\max} + 1\right)\right] sign\left(f(\vec{x})\right), \quad (4)$$

where $[..]$ means the selection of the integer part of the number, $\varepsilon_{\max}$ is the maximum error [20] when quantizing.

Thus, when using the specified "entropy" optimization criterion for the interpolator, it is necessary to minimize the entropy *H* of the quantized post-interpolation residues $q(\vec{x})$:

$$H\left(\eta^{\lim}\right) = -\sum_{q=-M+1}^{M-1} N_q\left(\eta^{\lim}\right)\ln N_q\left(\eta^{\lim}\right) \to \min_{\eta^{\lim}}, \quad M = \max_{\dot{x}}\left(C\left(\vec{x}\right)\right), \tag{5}$$

where $N_q\left(\eta^{\lim}\right)$ is the number of quantized post-interpolation residues equal to q, and M is the maximum value of the original signal.

3. Reduction of the parametric space dimension

With significant constraints on computational complexity, interpolation algorithms are often used [1,4], which use "smoothing" (averaging) over some a set of nearest reference samples:

$$P\left(\vec{x}\right) = \frac{1}{N}\sum_{k=1}^{N}\hat{C}_k\left(\vec{x}\right), \tag{6}$$

where $\hat{C}_k\left(\dot{x}\right)$ are the nearest reference samples, N is the number of these samples.

The specific of the interpolator application determines the arrangement of these reference samples. This arrangement can be quite non-trivial (see below) for some tasks related, for example, to the use of some image compression methods.

As mentioned above, the use of such simple interpolation algorithms is typical in situations where it is necessary to minimize the computational complexity. In particular, interpolators of this type are used in differential [20-21] and hierarchical [22-23] compression methods for multidimensional signals.

The "smoothing" interpolation algorithm is sufficiently accurate on smoothly varying signal regions since averaging reduces noise. However, the "smoothing" interpolator is always characterized by an increase in the interpolation error at the boundaries of the indicated smoothly varying regions (i.e., at the boundaries). To interpolate such boundaries, we can use algorithms that use the so-called interpolation "along the border". For a two-dimensional signal, in particular, Graham's nonlinear interpolation algorithm [20] works in this way.

When using this algorithm, the Interpolated value is equal to the reference signal sample to which the local boundary is directed. However, this algorithm, for obvious reasons, has less accuracy on smoothly varying parts of the signal.

In this article, we propose an adaptive parameterized interpolation algorithm that combines the advantages of both the described approaches: "smoothing" approach and "boundary" approach. The proposed interpolation algorithm is based on the approach described in Section 2. The proposed algorithm automatically switches between "smoothing" and "boundary" interpolators, depending on how sharp the boundary is in the local neighborhood of the processed sample.

Next, we describe the proposed adaptive interpolator. We also specify the interpolating functions (1) and decision rule (2). Denote by N_c the number of boundary directions taken into account. Let $\left\{\lambda_i\left(\vec{x}\right): 0 \le i < N_c\right\}$ be the set of averaged absolute values of differences between the reference samples $\hat{C}_k\left(\dot{x}\right)$ in each of the directions under consideration:

$$\lambda_i\left(\vec{x}\right) = \left|\hat{C}_t\left(\vec{x}\right) - \hat{C}_\tau\left(\vec{x}\right)\right| \tag{7}$$

where t and τ are the indices of the reference samples.

The differences $\lambda_i\left(\dot{x}\right)$ determine the presence and intensity of the boundary in the local neighborhood of the current signal sample. We can use several thresholds $\lambda_i^{\lim}$ to decide on the presence and direction of the boundary. We compare the described differences λ_i with these threshold values $\lambda_i^{\lim}$. If there is no boundary in the neighborhood of the current signal sample, then we use a "smoothing" interpolating function of the form (6):

$$P(\vec{x}) = P^{(1)}(\vec{x}) = \frac{1}{N}\sum_{k=1}^{N}\hat{C}_k(\vec{x}), \ \ if \ \ \lambda_i \le \lambda_i^{\lim}, i \in [0, N_c) \quad (8)$$

If there is a boundary in the local neighborhood, then for interpolation we use the average value $\hat{C}_j(\vec{x})$ of the two nearest reference samples located in the direction of the local boundary:

$$P(\vec{x}) = P^{(2)}(\vec{x}) = \tilde{C}_j(\vec{x}), \ \ if \ \ \lambda_i > \lambda_i^{\lim}, i \in [0, N_c) \quad (9)$$

Thus, we need to solve an optimization problem in a N_c-dimensional parametric space to find the best thresholds $\lambda_i^{\lim}$.

The application determines the dimension N_c of the parameter space $\lambda_i^{\lim}$. As we show below, in the problem of hierarchical compression [22-23] $N_c = 2$ for a two-dimensional signal, $N_c = 4$ for a three-dimensional signal (in the simplest case), and then N_c grows rapidly with increasing signal dimension. However, the search for parameters can be an overly time-consuming task during compression even when $N_c = 2$.

In this paper, we propose to reduce the dimension of the parameter space $\lambda_i^{\lim}$ to reduce the computational complexity of finding these parameters. For this, we propose to use not the absolute values of the differences λ_i, but their ratio during interpolation. If there is no boundary (or the boundary is weak) in the neighborhood of the current sample, all differences have close values. If there is a clear boundary in this neighborhood, then the smallest difference λ_j corresponds to the direction of this boundary:

$$j(\vec{x}) = \arg\min_i \{\lambda_i(\vec{x})\}.$$

Moreover, if there is a boundary in the neighborhood, this difference is significantly different from all other differences, including the nearest difference λ_r:

$$r(\vec{x}) = \arg\min_{i:\, i \ne j} \{\lambda_i(\vec{x})\}.$$

Based on this reasoning, in this article the feature of the boundary direction is defined as the difference between the two smallest differences λ_i:

$$\eta(\dot{x}) = \lambda_r(\dot{x}) - \lambda_j(\dot{x}). \quad (10)$$

When interpolating each sample, the feature $\eta(\dot{x})$ is compared with a threshold $\eta^{\lim}$. If the feature $\eta(\dot{x})$ is small enough (less than the threshold $\eta^{\lim}$), then it is considered that there is no boundary in the neighborhood of the current sample. Therefore, a "smoothing" interpolation of the form (8) is used:

$$P(\vec{x}) = P^{(1)}(\vec{x}) = \frac{1}{N}\sum_{k=1}^{N}\hat{C}(\vec{x}_k), \ \ if \ \ \eta(\vec{x}) \le \eta^{\lim} \quad (11)$$

The difference from (8) is that now this interpolation is one-parameter. If the feature $\eta(\vec{x})$ is larger than the threshold $\eta^{\lim}$, then interpolation of the form (9) "along the boundary" is performed:

$$P(\vec{x}) = P^{(2)}(\vec{x}) = \hat{C}_j(\vec{x}), \ j = \arg\min_i \{\lambda_i\}, \ if \ \eta(\vec{x}) > \eta^{\lim}. \quad (12)$$

Thus, by reducing the dimension of the parameter space, we reduce the multiparameter optimization problem to a one-parameter one, in which the only parameter is $\eta^{\lim}$. An automatic optimization procedure similar to [23] is used to calculate this parameter.

4. Multidimensional adaptive interpolator in the problem of hierarchical compression

The proposed multidimensional adaptive interpolator can be used in various signal processing tasks. In particular, in this paper, we consider the use of this interpolator in the problem of compression. As an example of the compression method, we consider the hierarchical compression method [22-23].

This method uses a unique hierarchical non-redundant representation (see Figures 1-2) of the original multidimensional signal $\mathbf{C}=\{C(\vec{x})\}$ as a set of L scale levels $\mathbf{C}_l$:

$$\mathbf{C}=\bigcup_{l=0}^{L-1}\mathbf{C}_l \quad , \quad \mathbf{C}_l=\{C_l(\vec{x})\}=\{C(\vec{x}):\vec{x}\in I_l\}, \tag{17}$$

where I_l is the set of sample indices of the corresponding scale level $\mathbf{X}_l$:

$$I_{L-1}=\{2^{L-1}\dot{x}\} \quad , \quad I_l=\{2^l\dot{x}\}\setminus\{2^{l+1}\dot{x}\},\ 0\le l<L \quad . \tag{18}$$

Thus, the most resampled scale level $\mathbf{C}_{L-1}$ is a "grid" of signal samples with step of $2^{(L-1)}$, and all other scale levels with the numbers $l = (L\text{-}1),(L\text{-}2),..,1,0$ are grids of signal samples with the step of 2^l, of which samples are removed with the step of 2^{l+1}.

With hierarchical compression, the scale levels of the signal are compressed sequentially, from the most resampled level $\mathbf{C}_{L-1}$ to the least resampled level $\mathbf{C}_0$. In this case, samples of more resampled levels are used for interpolation of samples of less resampled levels.

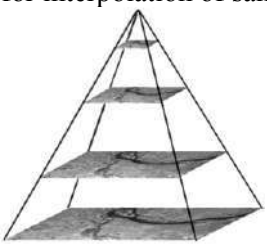

Figure 1. Hierarchical representation of a two-dimensional signal by four scale levels.

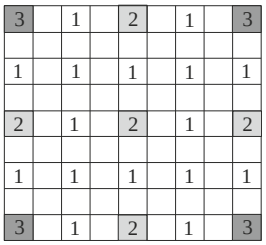

Figure 2. Level numbers in the hierarchical representation of the signal (the level number is zero in the empty cells).

Most often, to reduce computational complexity with hierarchical compression, a smoothing interpolator of the form (6) is used. In the three-dimensional case, this interpolator can be written as:

$$P_l^{(1)}(2m+1,2n+1,2k+1)=\frac{1}{8}\sum_{m'=0}^{1}\sum_{n'=0}^{1}\sum_{k'=0}^{1}C_{l+1}(m+m',n+n',k+k') \quad . \tag{19}$$

Differences λ_i (7) in this case take the form:

$$\lambda_l^{(0)}(2m+1,2n+1,2k+1)=\left|C_{l+1}(m+1,n+1,k+1)-C_{l+1}(m,n,k)\right| \quad , \tag{20}$$

$$\lambda_l^{(1)}(2m+1,2n+1,2k+1)=\left|C_{l+1}(m,n+1,k+1)-C_{l+1}(m+1,n,k)\right| \quad , \tag{21}$$

$$\lambda_l^{(2)}(2m+1,2n+1,2k+1)=\left|C_{l+1}(m,n,k+1)-C_{l+1}(m+1,n+1,k)\right| \quad , \tag{22}$$

$$\lambda_l^{(3)}(2m+1,2n+1,2k+1)=\left|C_{l+1}(m+1,n,k+1)-C_{l+1}(m,n+1,k)\right| \quad . \tag{23}$$

Thus, the adaptive three-dimensional interpolator allows us to automatically switch between smoothing interpolation (19) and interpolation along the boundary of one of the four directions shown in Fig. 3. In other words, at each point of the signal we can use the interpolating value (19) or one of the following four interpolating values:

$$V_l^{(0)}(2m+1,2n+1,2k+1)=\frac{1}{2}\left(C_{l+1}(m+1,n+1,k+1)+C_{l+1}(m,n,k)\right) \quad , \tag{24}$$

$$V_l^{(1)}\left(2m+1,2n+1,2k+1\right)=\frac{1}{2}\left(C_{l+1}\left(m,n+1,k+1\right)+C_{l+1}\left(m+1,n,k\right)\right), \quad (25)$$

$$V_l^{(2)}\left(2m+1,2n+1,2k+1\right)=\frac{1}{2}\left(C_{l+1}\left(m,n,k+1\right)+C_{l+1}\left(m+1,n+1,k\right)\right), \quad (26)$$

$$V_l^{(3)}\left(2m+1,2n+1,2k+1\right)=\frac{1}{2}\left(C_{l+1}\left(m+1,n,k+1\right)+C_{l+1}\left(m,n+1,k\right)\right). \quad (27)$$

The "boundary" interpolating function (12) in this situation takes the form:

$$P_l^{(2)}\left(2m+1,2n+1,2k+1\right)=V_l^{(j)}\left(2m+1,2n+1,2k+1\right),\ j=\arg\min_i\left\{\lambda_i\left(2m+1,2n+1,2k+1\right)\right\}. \quad (28)$$

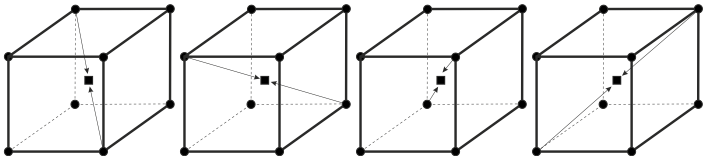

Figure 3. Three-dimensional interpolating functions (24-27) of the adaptive interpolator.

Thus, in the introduced notation, the three-dimensional adaptive interpolator is described by the expression:

$$P_l\left(2m+1,2n+1,2k+1\right)=\begin{cases}P_l^{(1)}\left(2m+1,2n+1,2k+1\right), if\ \eta_l\left(2m+1,2n+1,2k+1\right)\le\eta_l^{\lim}\\ P_l^{(2)}\left(2m+1,2n+1,2k+1\right), if\ \eta_l\left(2m+1,2n+1,2k+1\right)>\eta_l^{\lim}\end{cases} \quad (29)$$

where, for each scale level, the feature $\eta_l\left(2m+1,2n+1,2k+1\right)$ is calculated according to expressions (8-10), and compared with threshold $\eta^{\lim}$ for each level.

In the two-dimensional case, the smoothing interpolator (6) can be written in the form:

$$P_l^{(1)}\left(2m+1,2n+1\right)=\frac{1}{4}\left(C_{l+1}\left(m,n\right)+C_{l+1}\left(m+1,n\right)+C_{l+1}\left(m,n+1\right)+C_{l+1}\left(m+1,n+1\right)\right) \quad (30)$$

Differences λ_i (7) in this case take the form:

$$\lambda_l^{(0)}\left(2m+1,2n+1\right)=\left|C_{l+1}\left(m,n\right)-C_{l+1}\left(m+1,n+1\right)\right|, \quad (31)$$

$$\lambda_l^{(1)}\left(2m+1,2n+1\right)=\left|C_{l+1}\left(m,n+1\right)-C_{l+1}\left(m+1,n\right)\right|. \quad (32)$$

The corresponding interpolating values are written as follows:

$$V_l^{(0)}\left(2m+1,2n+1\right)=\frac{1}{2}\left(C_{l+1}\left(m+1,n+1\right)+C_{l+1}\left(m,n\right)\right), \quad (33)$$

$$V_l^{(1)}\left(2m+1,2n+1\right)=\frac{1}{2}\left(C_{l+1}\left(m,n+1\right)+C_{l+1}\left(m+1,n\right)\right). \quad (34)$$

For the interpolation itself in the two-dimensional case, it is more appropriate to use a two-parameter adaptive interpolation function:

$$P_l\left(2m+1,2n+1\right)=\begin{cases}V_l^{(0)}\left(2m+1,2n+1\right),\ if\ \ \eta_l\left(2m+1,2n+1\right)<\eta_l^{\lim(-)}\\ P_l^{(1)}\left(2m+1,2n+1\right),\ if\ \ \eta_l^{\lim(-)}\le\eta_l\left(2m+1,2n+1\right)\le\eta_l^{\lim(+)}\\ V_l^{(1)}\left(2m+1,2n+1\right),\ if\ \ \eta_l\left(2m+1,2n+1\right)>\eta_l^{\lim(+)}\end{cases} \quad (35)$$

where $\eta_l\left(m,n\right)$ is the feature of boundary direction.

$$\eta_l\left(m,n\right)=\lambda_l^{(0)}\left(m,n\right)-\lambda_l^{(1)}\left(m,n\right) \quad (36)$$

At each signal point, the feature $\eta_l\left(m,n\right)$ is compared with two thresholds $\eta_l^{\lim(-)}$, $\eta_l^{\lim(+)}$, because optimization by these parameters can be done separately.

5. Experimental study of the adaptive interpolator for real-world multidimensional signals

The proposed adaptive interpolator (30-36) was implemented programmatically in C++ and built into the hierarchical compression method. This software implementation was used in this article to study the effectiveness of the proposed interpolator. To this end, computational experiments were performed in real-world multidimensional signals (see Figure 4-5) of two signal sets:

set no. 1 - TokyoTech hyperspectral dataset [24] (signal sizes 500x500x31 samples, 13 bits)

set no. 2 - AVIRIS hyper-spectrometer [25] (signal sizes 1086x614x224 samples, 16 bits).

A measure of the effectiveness of the proposed interpolator was the relative gain in the archive size, which was achieved by replacing the smoothing interpolator with an adaptive interpolator in the frame of hierarchical compression method:

$$\Delta = \left(K_{adapt} / K_{smooth} - 1 \right) \cdot 100\% , \quad (37)$$

where K_{smooth}, K_{adapt} are the compression ratios of the hierarchical compression method when using a smoothing and adaptive interpolator, respectively. Typical results of computational experiments are shown in Fig. 6-7 and Table 1. The adaptive interpolator has a gain of up to 51% in the size of the archive file compared to the smoothing interpolator.

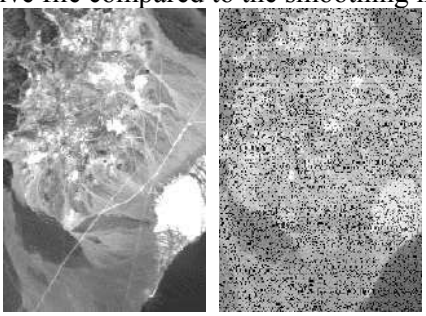

Figure 4. Fragments of bands 10, 86 of test multidimensional signal «Cuprite-2».

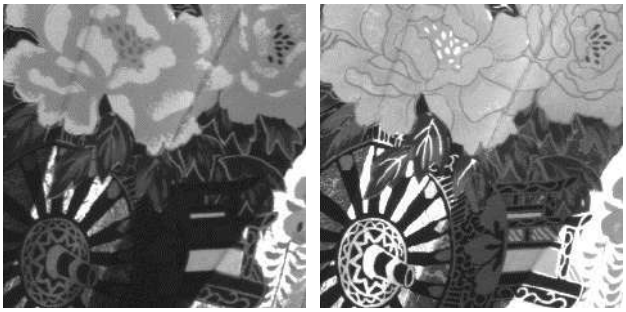

Figure 5. Bands 0, 30 of test multidimensional signal «Fan2».

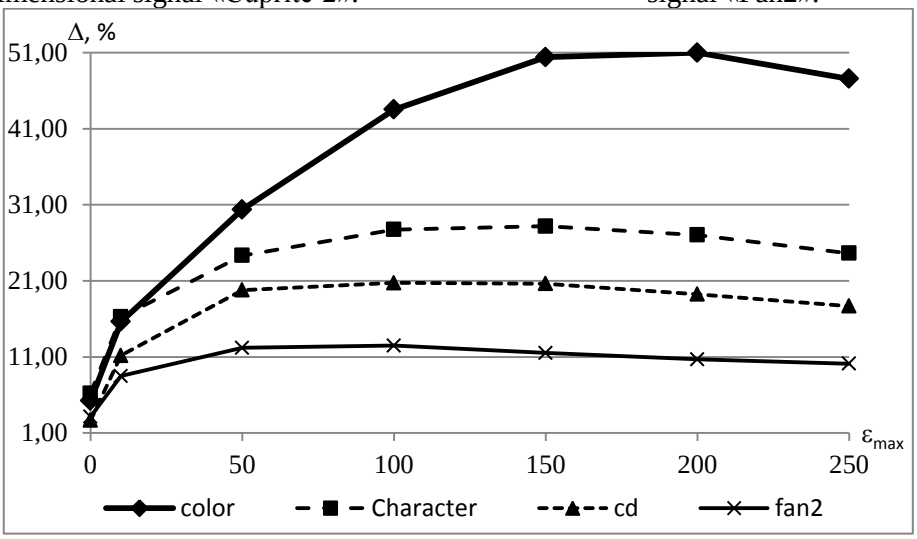

Figure 6. Gain Δ (in %) the adaptive interpolator for the averaging interpolator in test signals «Color», «Character», «CD», «Fan2».

6. Conclusion

We proposed interpolation algorithms for multidimensional signals based on automatic switching between simple interpolating functions at each point of the signal. We described the parameterized decision rules that perform this switch. We optimized the parameters of these decision rules on the criteria for the minimum energy of post-interpolation residues and criteria of the minimum entropy of quantized post-interpolation residues. We proposed a method for reducing the dimension of the parametric space of decision rules. We performed computational experiments to study the proposed

interpolators on real-world multidimensional signals. We experimentally proved that using the adaptive interpolator instead of a smoothing one can significantly improve the efficiency of hierarchical signal compression.

Table 1. The gain Δ (in %) of the adaptive interpolator for the averaging interpolator depending on maximum error ε_{max} in test signals «Butterfly2», « Butterfly3», ... ,«Low Altitude», «Moffett Field».

ε_{max}	Signal set	0	10	50	100	150	200	250	max(Δ)
Butterfly2	set no.1	1.17	4.84	8.00	9.17	9.57	9.19	8.62	9.57
Butterfly3	set no.1	1.87	7.24	13.81	17.07	17.74	16.74	14.98	17.74
Butterfly4	set no.1	1.87	6.37	11.45	13.17	13.81	13.51	12.98	13.81
Butterfly5	set no.1	1.30	6.36	11.35	12.63	12.47	11.00	9.41	12.63
Butterfly6	set no.1	1.23	5.20	9.01	10.90	11.58	11.28	11.10	11.58
Butterfly7	set no.1	1.48	5.24	9.81	11.55	12.16	11.55	10.39	12.16
Butterfly	set no.1	1.68	5.49	9.02	9.89	9.49	8.64	7.64	9.89
Butterfly8	set no.1	1.88	7.03	11.46	12.37	12.36	12.14	10.72	12.37
cd	set no.1	2.66	11.18	19.79	20.74	20.64	19.25	17.69	20.74
Character	set no.1	6.21	16.26	24.34	27.73	28.19	27.02	24.64	28.19
Chart24	set no.1	5.57	18.18	36.27	40.18	36.60	30.42	25.57	40.18
ChartRes	set no.1	7.80	18.76	28.57	36.31	39.30	39.49	38.91	39.49
Cloth2	set no.1	0.64	1.62	2.28	2.13	1.92	1.48	1.14	2.28
Cloth3	set no.1	1.16	2.88	4.11	4.28	4.18	2.98	1.88	4.28
Cloth4	set no.1	0.58	1.32	2.11	2.18	1.51	0.66	0.06	2.18
Cloth5	set no.1	2.10	4.60	6.42	5.91	5.66	5.11	4.07	6.42
Cloth	set no.1	0.84	1.94	2.92	2.74	2.40	1.81	1.27	2.92
colorchart	set no.1	4.10	15.40	37.31	44.07	39.92	34.67	30.61	44.07
color	set no.1	5.24	15.63	30.38	43.53	50.40	51.00	47.56	51.00
doll	set no.1	0.44	1.34	1.72	1.82	1.83	1.87	1.78	1.87
fan2	set no.1	3.15	8.50	12.19	12.49	11.51	10.68	10.11	12.49
fan3	set no.1	2.50	6.54	9.77	9.92	9.41	8.82	8.23	9.92
fan	set no.1	1.76	4.12	6.29	6.25	5.51	4.70	3.99	6.29
flower2	set no.1	1.60	4.35	5.63	4.59	2.75	1.24	-0.71	5.63
flower3	set no.1	2.28	6.74	9.43	8.57	6.85	4.97	3.07	9.43
flower	set no.1	2.79	8.42	11.50	9.18	6.54	4.00	2.34	11.50
party	set no.1	3.18	9.51	15.22	16.70	17.03	16.46	16.45	17.03
tape2	set no.1	4.60	9.87	14.46	14.54	13.07	11.37	9.95	14.54
tape	set no.1	1.61	3.99	5.63	5.61	5.22	4.64	4.11	5.63
Tshirts2	set no.1	0.76	2.32	3.96	4.77	4.65	4.48	4.52	4.77
Tshirts	set no.1	0.75	2.26	3.82	4.59	4.88	5.11	5.28	5.28
Cuprite-1	set no.2	0.73	1.89	2.96	3.40	3.44	3.41	2.47	3.44
Cuprite-2	set no.2	1.26	3.45	5.63	6.84	7.11	6.92	5.95	7.11
Low Altitude	set no.2	1.15	2.91	3.47	2.29	0.79	-0.69	-2.16	3.47
Moffett Field	set no.2	0.71	1.74	1.87	1.64	1.34	1.06	0.76	1.64

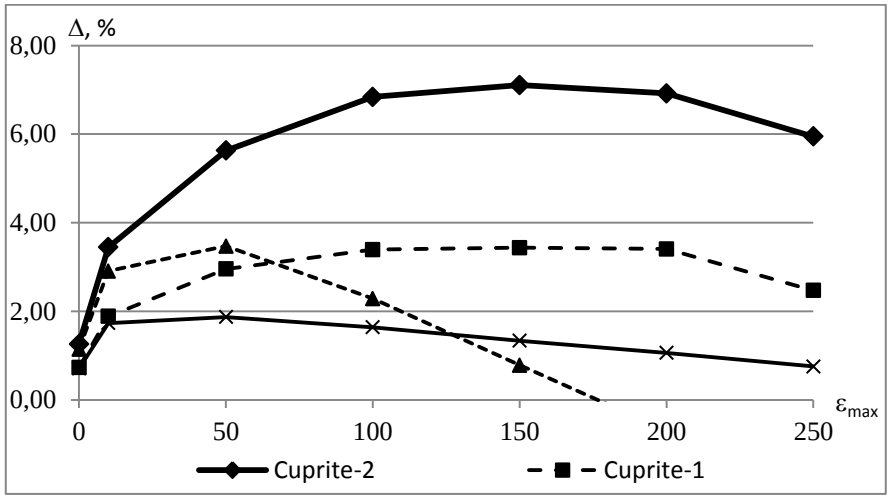

Figure 7. Gain Δ (in %) the adaptive interpolator for the averaging interpolator in test signals «Cuprite-1», «Cuprite-2», «Low Altitude», «Moffett Field».

7. References

[1] Woods J 2011 *Multidimensional Signal, Image, and Video Processing and Coding* (Academic Press) p 211
[2] Jensen J 2007 *Remote sensing of the environment: an Earth resource perspective* (Prentice Hall) p 619
[3] Campbell J 2002 *Introduction to remote sensing* (Guilford Press) p 667
[4] Borengasser M, Hungate W and Watkins R 2007 *Hyperspectral remote sensing: Principles and applications* (CRC Press) p 128
[5] Vapnik V 1998 *Statistical Learning Theory* (John Wiley & Sons)
[6] Vasin Y and Neymark Y 1978 Adaptive compression recurrent algorithms using well-adapted local restoring functions *Mathematical software for CAD: Interuniversity collection* **13**
[7] Gulakov K 2013 The choice of neural network architecture for solving the problems of approximation and regression analysis of experimental data *Bulletin of Bryansk State Technical University* **2** 95-105
[8] Bakhvalov Y 2007 *The method of multidimensional interpolation and approximation and its applications* (M: Sputnik+) p 108
[9] Caiafa C 2016 Computing Sparse Representations of Multidimensional Signals Using Kronecker Bases *Neural Computation Volume* **25** 186-220
[10] Butyrsky E, Kuvaldin I and Chalkin V 2010 Approximation of multidimensional functions *Scientific instrument-making* **20** 82-92
[11] Cobanu M and Makarov D 2014 Compression of images by tensor approximation *Problems of development of promising micro- and nanoelectronic systems* 109-112
[12] Gulakov K 2016 Modeling multidimensional objects on the basis of cognitive maps with neural network identification of parameters *Thesis for Ph.D*
[13] Cohen A, Davenport M and Leviatan D 2013 On the stability and accuracy of least squares approximations *Comput. Math.* **13** 819-834
[14] Sahnoun S, Djermoun E, Brie D and Comon P 2017 A simultaneous sparse approximation method for multidimensional harmonic retrieval *Signal Processing* **131** 36-48
[15] Donoho D 2006 Compressed sensing *IEEE Trans. Inform. Theory* **52** 1289-1306
[16] Bigot J, Boyer C and Weiss P 2016 An analysis of block sampling strategies in compressed sensing *IEEE Trans. Inform. Theory* **62** 2125-2139
[17] German E 2014 Algorithms for combining heterogeneous images in on-board visualization systems *PhD Thesis*
[18] Muratov E and Nikiforov M 2014 Methods to reduce the computational complexity of algorithms for combining heterogeneous images *Cloud of Science* **1**

[19] Sayood K 2012 *Introduction to Data Compression* (The Morgan Kaufmann Series in Multimedia Information and Systems) p 743
[20] Gonzalez R and Woods E 2007 *Digital Image Processing* (Prentice Hall) p 976
[21] Maksimov A I and Gashnikov M V 2018 Adaptive interpolation of multidimensional signals for differential compression *Computer Optics* **42** 679-687 DOI: 10.18287/2412-6179-2018-42-4-679-687
[22] Sergeev V, Gashnikov M and Glumov N 1999 The Informational Technique of Image Compression in Operative Remote Sensing Systems *RAS Samara Research Center Bulletin* **1** 99-107
[23] Gashnikov M V 2018 Interpolation based on context modeling for hierarchical compression of multidimensional signals *Computer Optics* **42(3)** 468-475 DOI: 10.18287/2412-6179-2018-42-3-468-475
[24] TokyoTech 31-band Hyperspectral Dataset URL: http://www.ok.sc.e.titech.ac.jp/res/MSI/MSIdata31.html (03.11.2018)
[25] AVIRIS Data – Ordering Free AVIRIS Standard Data Products *Jet Propulsion Laboratory* URL: http://aviris.jpl.nasa.gov/data/free_data.html (03.11.2018)

Acknowledgments
The work was partly funded by RFBR according to the research project 18-01-00667 in parts of «2 Adaptive interpolation of multidimensional signals» – «5 Experimental study of the adaptive interpolator for real-world multidimensional signals» and by the Russian Federation Ministry of Science and Higher Education within a state contract with the "Crystallography and Photonics" Research Center of the RAS under agreement 007-ГЗ/Ч3363/26 in part of «1 Introduction».

Double stochastic wave models of multidimensional random fields

V R Krasheninnikov[1], A U Subbotin[1]

[1]Department of Applied Mathematics and Informatics, Ulyanovsk State Technical University, Ulyanovsk, Russia

e-mail: kvrulstu@mail.ru

Abstract. The paper deals with the development of mathematical models of random fields to describe and simulate images. In the wave model, a random field is the result of the influence of perturbations (waves) that occur at random times in random places and have random shapes. This model allows representing and simulate isotropic and anisotropic images (and their temporal sequences) defined on arbitrary areas of multidimensional space, as well as on any surfaces. The problems of correlation analysis and synthesis can be relatively easily solved. However, this model allows representing only homogeneous fields. In this paper, we consider «double stochastic» wave models, when the first wave random field (control field) sets the parameters of the second (controlled field). As a result, the controlled field becomes non-uniform, since its parameters vary randomly. We also consider options when two fields mutually influence each other. These models allow us to represent and simulate multidimensional inhomogeneous images (and their temporal sequences), as well as systems of such images with mutual correlations.

1. Introduction

A rigorous mathematical formulation of image processing tasks is required for their effective solution. This formulation primarily includes the model of the image as an object of study. The representation of images by random fields (RF) is generally accepted. To date, there is an extensive literature on image models (or RF models), for example, [1-6]. Much attention is paid to the modeling and processing of medical images for example, [7-11]. However, the vast majority of works consider two-dimensional flat RF, less often their sequence. Therefore, it is rather difficult to solve the problems of image imitation, descriptions of inhomogeneous images, correlation analysis and synthesis. A wave model of a random field was proposed in [12-14], which makes it possible to describe homogeneous images and their sequences defined on regions and surfaces of any dimension with small computational costs for simulation. In this model, the RF is the result of the influence of perturbations (waves) that occur at random times in random places and have random shapes. The generated fields are isotropic if waves are spherical. Anisotropic RF can be obtained, for example, with ellipsoidal waves. The main influence on the form of the correlation function of RF is exerted by only one parameter, namely the probability distribution of the wave scale factor, therefore, the problems of correlation analysis and synthesis are relatively easy to solve.

However, this model describes only homogeneous RF. In [15, 16], a double stochastic autoregressive model of RF was proposed for describing inhomogeneous images. In this model, the first wave RF (control field) sets the parameters of the second RF (controlled field), which turns out to be non-uniform, since its parameters randomly vary in space. So the structure of the resulting image is significantly different in different places. This idea is used in the present paper to the wave model, which made it possible to obtain models of a wide class of inhomogeneous images defined on regions and surfaces of any dimensions.

2. Basic wave model of a random field

Let us consider the RF wave model [12] that generalizes a number of other models and helps to solve the tasks of analysis and synthesis effectively. This model is simple enough and can serve as a basis for simulating images and their sequences with given covariance function (CF) without increasing the number of model parameters.

In the wave model, the RF is determined by the stochastic equation

$$x_{\bar{j}}^{t} = \sum_{\{k:\tau_k \le t\}} f\left[(\bar{j},t),(\bar{u}_k,\tau_k),\bar{\omega}_k\right] \tag{1}$$

where an (n+1)-dimensional domain $\{(\bar{j},t)\}$ may be discrete or continuous, $\{(\bar{u}_k,\tau_k)\}$ is a discrete field of random points (FRP) in an (n+1)-dimensional continuous space, t and τ_k are interpreted as time, $\bar{\omega}_k$ is a random vector of function f parameters. This field can be represented as the effect of random disturbances or waves $f\left[(\bar{j},t),(\bar{u}_k,\tau_k),\bar{\omega}_k\right]$ appearing in random places $\bar{u}_k$ at random time τ_k and changing according to a given law in time and space. Selection of function f, the FRP parameters and $\bar{\omega}$ allow us to obtain a vast class of fields.

Let us consider a particular case of a wave model, for which correlation tasks of analysis and synthesis can easily be solved:

$$f\left[(\bar{j},t),(\bar{u}_k,\tau_k),\bar{\omega}_k\right] = g(\rho_k / R_k)\exp(-\mu/|t-\tau_k|)\xi_k \tag{2}$$

where the FRP is a Poisson one with constant density λ, $\rho_k = |\bar{j} - \bar{u}_k|$ is a distance between $\bar{j}$ and $\bar{u}_k$, $\{R_k\}$ is a set of independent non-negative equally distributed random variables density $w(\alpha)$, $\{\xi_k\}$ is a system of independent equally distributed random variables with zero mean. Waves are motionless, independent, have spherical sections in space and exponentially attenuate over time. System $\{\xi_k\}$ determines a wave intensity and $\{R_k\}$ is their spatial scale. If $g(y) = c\exp(-2y^2)$ then the generated field X is stationary, homogeneous, has zero mean and its CF

$$V(\rho,t) = \frac{c^2\pi^{n/2}\lambda}{2^{n+1}}\exp(-\mu t)\int_0^\infty \alpha^n \exp\left(-\rho^2/\alpha^2\right)w(\alpha)\mathrm{d}\alpha \tag{3}$$

is spatially isotropic with variance

$$\sigma_n^2 = \frac{c^2\pi^{n/2}\lambda}{2^{n+1}\mu}M[R^n]. \tag{4}$$

Simulation of a discrete field on an n-dimensional grid $S = \{\bar{j}\}$ with time quantization Δt can be implemented by the following algorithm. At the initial time $t_0 = 0$, the field values in all nodes are equal to zero. At each subsequent moment $t_m = m\Delta t$, a Poisson FRP with density $\lambda\Delta t$ is formed over continuous space or grid, which somehow overlaps S. At each generated point $\bar{u}_k$, random values ξ_k and R_k are formed. After that the following transformation of all field values on grid $\{\bar{j}\}$ is carried out:

$$x_{\bar{j}}^{t_m} = x_{\bar{j}}^{t_{m-1}}\exp(-\mu\Delta t) + c\sum_k \exp(\rho_k / R_k)\xi_k, \tag{5}$$

which forms a sequence of frames that are n-dimensional images defined on S.

Note that the field values are calculated independently of each other. This makes it possible to simulate images on the desired area *S*, for example, on a certain surface.

An example of image simulation with the described wave model is represented in figure 1. It is necessary to underline that (5) actually implements time-varying images. Therefore, this figure shows only one frame of this process.

Each field value in (5) is a sum of random numbers of the random variables. Thus, generally speaking, the field will not be Gaussian even with Gaussian $\{\xi_k\}$. However, when the model parameter $h = \lambda M[R^n]/\mu$ grows, then the number of summands (5) with similar distributions increase and the field is normalized.

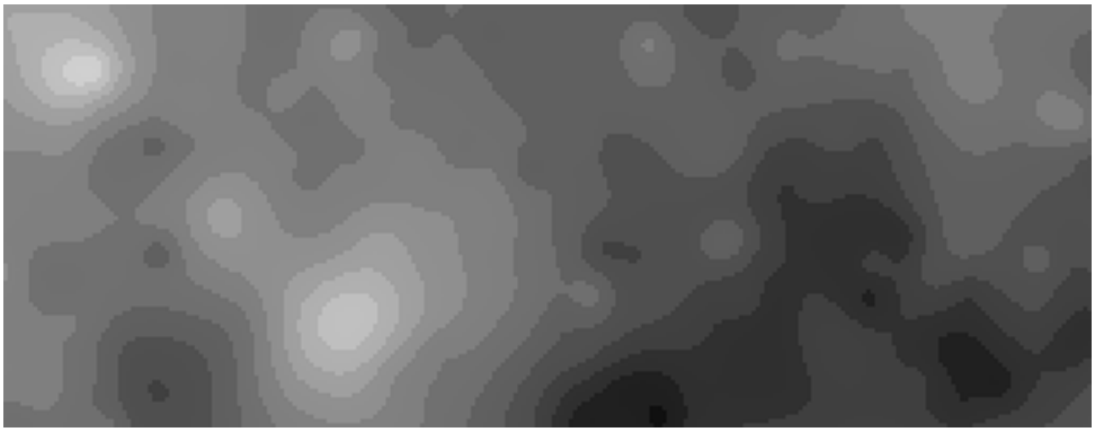

Figure 1. Example of image simulation using a wave model.

Now consider the solution of correlation analysis and synthesis task. It follows (4) that the formed field has an exponential time normalised CF (NCF) $e^{-\mu t}$ and space NCF.

$$r(\rho) = \frac{1}{M[R^n]} \int_0^\infty \alpha^n \exp\left(-\rho^2/\alpha^2\right) \omega(\alpha) \mathrm{d}\alpha \tag{6}$$

Thus, solving analysis tasks, when the density $\omega(\alpha)$ is given, the required NCF can be found analytically or by numerical integration. Solving synthesis tasks, when the NCF $r(\rho)$ is given, it is necessary to solve integral equation (6) with respect to unknown $\omega(\alpha)$. As it is not always possible to find an analytical solution of (6), we consider a method of its approximate solution. It follows from (2) that in the case of degenerate distribution ($R=\alpha$=const) we obtain the NCF equal to $\exp(-\rho^2/\alpha^2)$. Let now an arbitrary non-increasing NCF $r(\rho)$ be given. Let us approximate it with adequate accuracy by a sum of Gaussoids with positive coefficients $r(\rho) \approx h(\rho) = \sum_i q_i \exp\left(-\rho^2/\alpha_i^2\right)$, where $\sum_i q_i = 1$, when $r(0) = 1$. Then, for discrete distribution $P(R = \alpha_i) = k^{-1} q_i/\alpha_i^n$, where $k = \sum_i q_i/\alpha_i^n$, the generated field will have NCF equal to $h(\rho)$. Thus, the generated model allows us approximately to solve a synthesis task by changing only the density of scale *R*.

3. Double stochastic wave models

The wave model described above only defines homogeneous images. For the formation of inhomogeneous images, it is necessary that the model parameters vary in the domain of *S*. This can be achieved by breaking *S* into parts, in each of which the wave model has its own set of parameters. But, taking into account the possible uncertainty of real images, "double stochastic" models are considered in [6, 7], in which one or several autoregressive (control) RF set the parameters of the final (controlled) autoregressive RF. We use this idea for wave models.

Let the control field *X* be given by model (2) with some values of its parameters. We use for the controlled field *Y* a model of the same type but with a modified density $\omega(\alpha)$ depending on *X*. For example,

$$R_k^Y = r_m + \left(x^t(\bar{u}_k) - \min X^t\right)R_k, \tag{7}$$

where X^t is the field *X* at the time t, $\bar{u}_k$ is formed the point of FRP for Y^t, $x^t(\bar{u}_k)$ is field value at this point, r_m is the minimum allowable scale value R_k^Y for *Y*, R_k^Y is random scale value (when it is distributed for the field *X*). Transformation (7) leads to the corresponding conversion $w_X(\alpha) \to w_Y(\alpha)$ of the *Y* field scale, which should be used in (6) when calculating the CF of field *Y*. Note that other doubly stochastic models are possible when other parameters of the resulting image are also possible (c value, FRP density, and so on) are determined by one or several control images.

Figure 2 (b) shows the image *Y*, controlled by the top image *X* in figure 2 (a). It is noticeable that the smoother areas of the image *Y* correspond to the brighter areas of the image *X*, that is, its larger values and larger values of the wave stretch factor R_k^Y. The sample value of the interval of absolute correlation in a smoother region of this image is 87, and at the less smooth region is only 12.

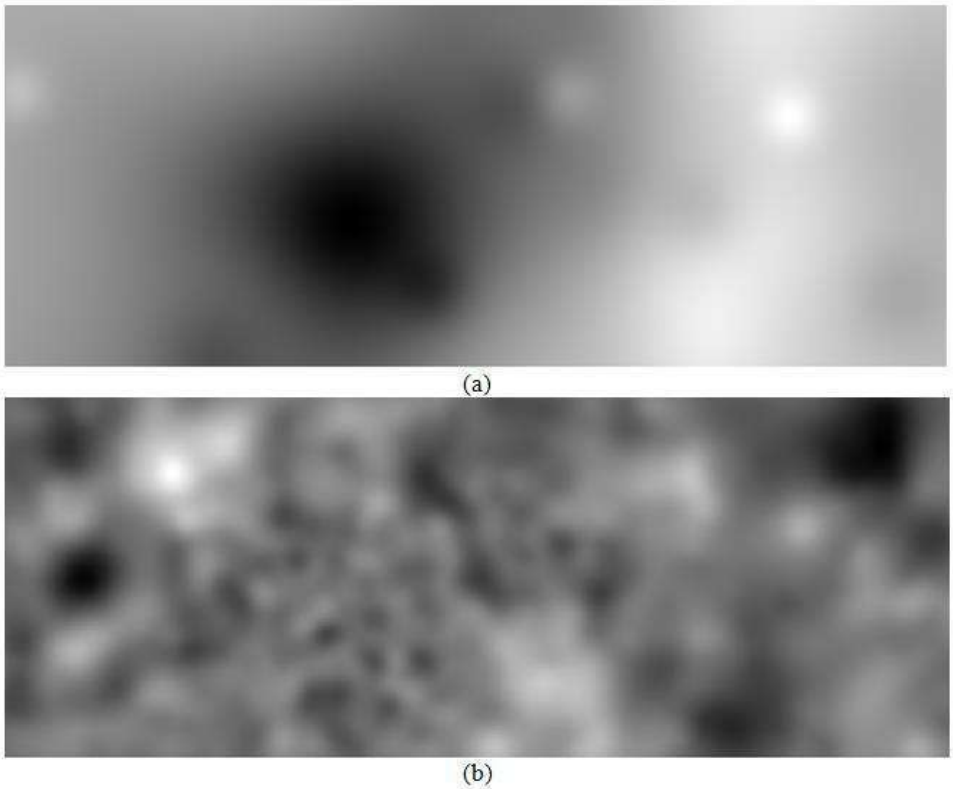

Figure 2. An example of simulating double stochastic images: (a) is a control image, (b) is a controlled image.

However, the boundaries between more and less smooth areas on *Y* are blurred, since the waves have a considerable length and the brightness *X* varies smoothly. In [6], to obtain clearer boundaries on double-stochastic autoregressive images, the quantization of the control image is applied, which provides a stepwise change in the parameters of the controlled one. This method can also be applied to wave models. Figure 3 (a) shows a 3-level quantized image in figure 2 (a). The image controlled by this quantized image is shown in figure 3 (b). Here, the boundaries between areas of different smoothness are clearer than in figure 2(b). The sample values of the correlation interval are approximately the same as in figure 2 (b).

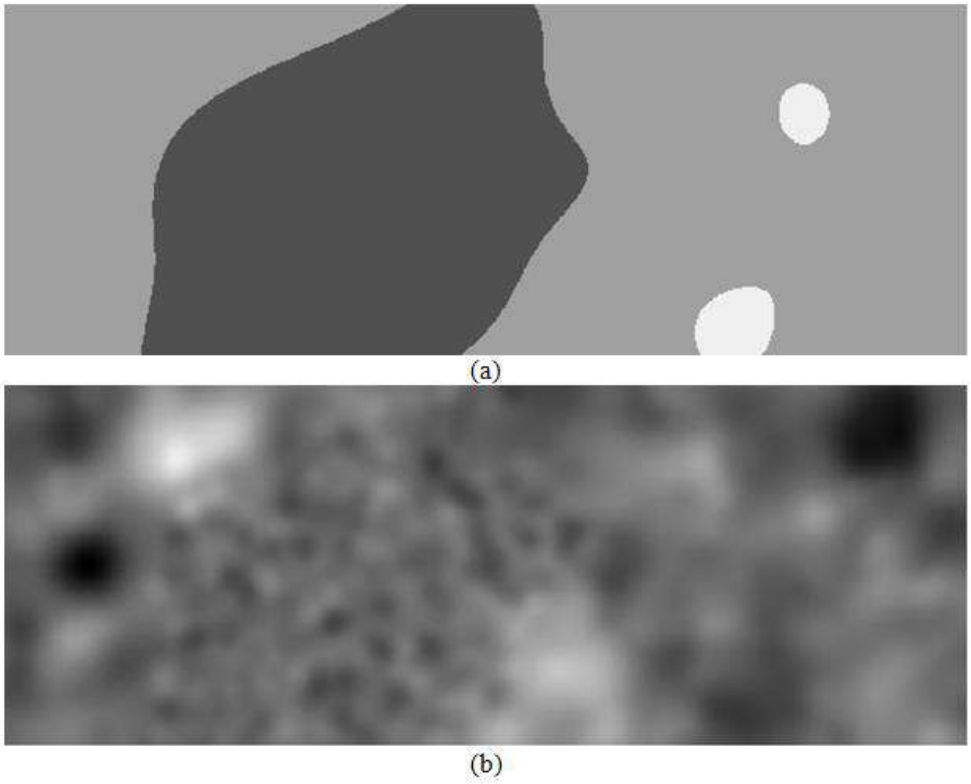

Figure 3. An example of simulating double-stochastic images with quantization: (a) is a control image, (b) is a controlled image.

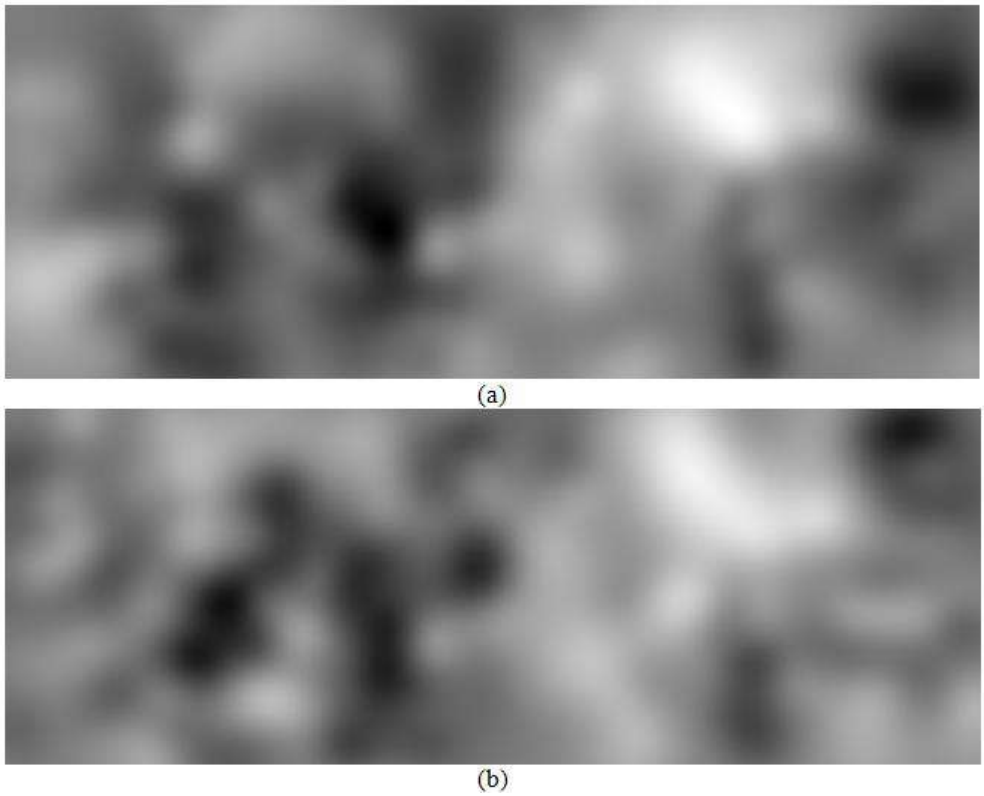

Figure 4. An example of simulating double stochastic images with mutual influence.

Two images are unequal in the described model: one controls the parameters of the other. In [8], a model of autoregressive images defined on a cylinder was proposed, jointly controlling the parameters of each other. We apply this approach to the considered wave models. Consider the sequence $X_1, X_2, X_3, \ldots$ of images. Images X_1 and Y_1 are formed in the same way as *X* and *Y* in the model described above. Image $X_2 = aX_1 + bY_1$ controls the formation of the image Y_2, and so on. Here should be $|a| < 1$. This process is similar to autoregression. As a result, in the steady state, the frames of the formed sequence mutually control the parameters of each other. The correlation weakens with an increase in the time interval between frames. Figure 4 shows two consecutive images formed in the manner described. Their correlation is visually noticeable (the sample correlation coefficient is 0.769). This is significantly different from simple control (figure 2), where the correlation between the images is almost zero.

4. Conclusions

This paper presents double stochastic wave models of random fields (images). In these models, the control wave random field sets the parameters of the controlled random field. As a result, the structure of the controlled image turns out to be significantly different in different places, which makes it possible to describe inhomogeneous images with random inhomogeneities. Options are also considered when two or more fields mutually influence each other. These models allow to represent and simulate multidimensional inhomogeneous images (and their temporal sequences), as well as systems of such images with mutual influences.

5. References

[1] Soifer V A, Popov S B, Mysnikov V V and Sergeev V V 2009 *Computer image processing. Part I: Basic concepts and theory* (VDM Verlag Dr.. Muller) p 300
[2] Vizilter Y V, Pyt'ev Y P, Chulichkov A I and Mestetskiy L M 2015 Morphological image analysis for computer vision applications *Computer Vision in Control Systems-1, ISRL* **73** (Springer International Publishing Switzerland) 9-58
[3] Shalygin A S and Palagin Y I 1986 *Applied methods of statistical modeling* (Mechanical engineering, American society of mechanical engineers) p 320
[4] Gonzalez R C and Woods R E 2002 *Digital image processing* (Prentice Hall, Upper Saddle River) p 976
[5] Myasnikov V V 2018 Description of images using a configuration equivalence relation *Computer Optics* **42(6)** 998-1007 DOI: 10.18287/2412-6179-2018-42-6-998-1007
[6] Labunets V G, Koch E V and Ostkhaymer E 2018 Algebraic models and methods of computer image processing. Part 1. Multiplet models of multichannel images *Computer Optics* **42(1)** 84-95 DOI: 10.18287/2412-6179-2018-42-1-84-95
[7] Bourne R 2010 *Fundamentals of Digital Imaging in Medicine* (London: Springer) p 200
[8] Ammari H (ed) 2012 *Mathematical Modeling in Biomedical Imaging II: Optical, Ultrasound, and Opto-Acoustic Tomographies* (Springer) p 173
[9] Shirokanev A S, Kirsh D V, Ilyasova N Yu and Kupriyanov A V 2018 Investigation of algorithms for coagulate arrangement in fundus images *Computer Optics* **42(4)** 712-21 DOI: 10.18287/2412-6179-2018-42-4-712-721
[10] Khorin P A, Ilyasova N Yu and Paringer R A 2018 Informative feature selection based on the Zernike polynomial coefficients for various pathologies of the human eye cornea *Computer Optics* **42(1)** 159-166 DOI: 10.18287/2412-6179-2018-42-1-159-166
[11] Krasheninnikov V R and Kopylova A S 2012 Algorithms for automated processing images of blood serum facies *Pat Rec Im An* **22** 583-592
[12] Krasheninnikov V R and Vasil'ev K K 2018 Multidimensional image models and processing *Computer Vision in Control Systems-3, ISRL* **135** (Springer International Publishing Switzerland) 11-64

[13] Krasheninnikov V R 2012 Models of random fields on surfaces *Proceedings of the Samara Scientific Center of the Russian Academy of Sciences* **4** 812-816
[14] Krasheninnikov V R and Subbotin A Yu 2018 Doubly stochastic model of a quasi-periodic process as an image on a cylinder *Proceedings of the International Scientific and Technical Conference "Advanced Information Technologies" (PIT-2018)* (Samara: Samara Scientific Center of the Russian Academy of Sciences) 1017-1021
[15] Vasilyev K K and Dement'iev V E 2017 *Presentation and processing of satellite multi-zone images* (Ulyanovsk: Ulyanovsk State Technical University) p 251
[16] Vasil'ev K K, Dement'ev V E and Andriyanov N A 2015 Doubly stochastic models of images *Pat Rec Im An* **25** 105-110

Human action recognition using dimensionality reduction and support vector machine

L V Shiripova[1], E V Myasnikov[1,2]

[1]Samara National Research University, Moskovskoe Shosse 34A, Samara, Russia, 443086
[2]Image Processing Systems Institute of RAS - Branch of the FSRC "Crystallography and Photonics" RAS, Molodogvardejskaya street 151, Samara, Russia, 443001

e-mail: shiripova.lubov@yandex.ru

Abstract. The paper is devoted to the problem of recognizing human actions in videos recorded in the optical range of wavelengths. An approach proposed in this paper consists in the detection of a moving person on a video sequence with the subsequent size normalization, generation of subsequences and dimensionality reduction using the principal component analysis technique. The classification of human actions is carried out using a support vector machine classifier. Experimental studies performed on the Weizmann dataset allowed us to determine the best values of the method parameters. The results showed that with a small number of action classes, high classification accuracy can be achieved.

1. Introduction

Human action recognition is actively used in various fields: in creating human-machine interfaces, in entertainment, in ensuring public safety, etc.

Human actions recognition involves solving two problems [1]:

1. The extraction of some feature information, i.e., converting a video stream or image sequence into a form suitable for subsequent classification.

2. Actually classification of the feature information obtained at the first stage.

To solve these problems, many approaches have been proposed, described in detail in [1]. Let us consider some of them.

To obtain the feature information, the authors of the paper [6] proposed to extract a silhouette from each frame, calculate images of the difference between adjacent frames and build the final image, superimposing the obtained images on each other. The resulting image was called Motion Energy Image (MEI). In addition, the authors introduce the concept of Motion History Image (MHI), i.e., the image, in which the intensity of each pixel depends on the time of action occurrence at a given point. The proposed approach has shown good results, but it has drawbacks when the angle of observation changes [6].

To eliminate this problem, a generalizing approach related to the use of 3D motion history volume (MHV) was proposed in [7]. MHV is based on 3D voxels obtained for various viewing angles. Further, the Fourier transform is used to acquire features that are invariant to position and rotation.

Another approach to obtaining features is associated with the extraction of space-time interest points (STIPs). Thus, the authors of [2,8] extended the Harris angle detector to the space-time domain.

The Gaussian function is then used to determine changes in movement in the spatial and temporal domains. In papers [9, 10, 11], a histogram of oriented gradients (HOG) and a histogram of optical flow (HOF) are used to obtain features. However, points of interest help to get information only for a short period of time. The authors of paper [12] proposed to use the Kanade – Lucas – Tomasi (KLT) feature tracker to track changes in points of interest.

In [13], simple parameters of convex figures are used as features.

For classification of the obtained features, various approaches are used, namely, the support vector machine (SVM) [14, 15, 9], k-nearest neighbors algorithm (k-NN) [16, 17, 18], as well as Hidden Markov Models (HMM) [19, 20, 21], etc.

In this paper, an approach based on the dimensionality reduction using the principal component analysis and subsequent classification using the support vector machine is used to solve the problem of human action recognition. A similar approach was successfully used by us earlier [22, 23] in solving the problem of person recognition by gait.

The paper has the following structure. Section 2 describes the developed method for human action recognition. Section 3 describes the results of experimental studies performed on the Weizmann dataset. The conclusions and the list of literature is given at the end of the paper.

2. Methods

The method proposed previously [22, 23] consists of the following steps:

- detection of a moving person in the video sequence,
- normalization of the frame size of the selected video sequence fragment,
- generation of subsequences,
- dimensionality reduction of the generated subsequences,
- classification of video sequences.

2.1. Detection of a moving person on a video sequence

At the first stage of the developed method, the moving person is detected in the video sequence. When the video sequence source is a video surveillance camera, background subtraction methods are used most frequently. The main idea of the methods of this class is to use a certain background model and to decide whether the particular pixel belongs to the background or a moving object, based on its correspondence to the background model. The background model is gradually refined over time. Although the time-averaged observation image can be used as a background model in the simplest applications, better results to this problem are given by more complex models, for example, [24-26].

In this paper, we use the background subtraction algorithm based on the mixture of Gaussian distributions (Gaussian mixture model, GMM) [25] to extract a moving person in a video sequence. According to this method, each background pixel is modeled by a weighted sum (mixture) of Gaussians. The weights of Gaussians correspond to the periods of time during which the corresponding Gaussian color is present on the video sequence.

We note that when choosing a method based on a mixture of Gaussian distributions, both our preliminary experiments and the experience by other researchers in solving the problem under consideration, were taken into account [27, 28].

As a result of the first stage, the set of masks corresponding to individual frames of the video sequence is formed. Each mask reflects the result of the segmentation of a frame into the foreground area corresponding to a moving person and the background.

2.2. Normalization of the size of detected fragments

At the second stage of the method, obtained masks are processed as follows. First, the center of mass for each foreground region is calculated, then the linear sizes of the region are determined, and a framing (a truncation of the mask image) is performed. After that, the cropped image is resized (compressed) to the specified size.

Taking into account the time coordinate, the dimensionality of the sequence of masks, which describes the movement of a person, remains high even after the size normalization (framing and

compression). In this regard, the fourth stage reduces the dimensionality of data describing the movement of a person.

2.3. Generation of subsequences

For each sequence of frames containing motion, a set of subsequences of a given length is allocated. Generation of subsequences is carried out with some specified step, starting from the beginning of the original sequence. A detailed description of the allocation of subsequences is given in previous papers [22, 23].

For each selected subsequence, the vector of features is formed as follows: each normalized frame of the subsequence is expanded into a row, and the rows obtained for individual frames are concatenated to each other.

The feature vectors of the subsequences of all sequences form the input matrix for the dimensionality reduction stage.

2.4. Dimensionality reduction using the principal component analysis technique

Both linear and nonlinear methods are used to reduce the dimensionality of multidimensional data. Linear methods such as principal component analysis (PCA) [29] and independent component analysis (ICA) are most commonly used. Nonlinear dimensionality reduction methods (for example, nonlinear mapping, ISOMAP, LLE) are used less often due to the high computational complexity of such methods. It should be noted that recent attempts have been made to accelerate such methods [30].

In this paper, we use the principal component analysis technique, as the most often used in similar cases and in other tasks (for example, see our previous papers [22, 23, 31]). This technique searches for a linear projection into the subspace of a smaller dimension that maximizes the variance of data. The PCA is often considered as a linear dimensionality reduction technique, minimizing the loss of information.

When principal components are found, the projection of feature vectors onto the first N principal components is taken as a feature description.

2.5. Classification of video sequences

The features obtained as a result of the principal component analysis are used to train the classifier Support Vector Machine (SVM) [33]. In the considered case, the classes correspond to individual actions, and feature vectors obtained for all subsequences correspond to individual observations (examples).

Note that the description given above is valid for the training mode in which the parameters of the dimensionality reduction and classifier are configured. In the testing mode, the data is processed in the same way, except that the parameters of the linear transformation are fixed to the values obtained in the training mode, and the trained SVM classifier performs the classification.

3. Experiments

The proposed method was implemented in C ++ using the OpenCV library. A PC based on the Intel Core i5-3470 CPU 3.2 GHz was used to perform experimental studies.

For the experimental study of the proposed method, the video sequences from the open Weizmann dataset (Figure 1) were used. This dataset contains sequences of binary images corresponding to individual frames of the video sequence, on which moving objects have already been extracted (foreground and background segmentation). The dataset contains video sequences for 9 people performing 10 different actions. The total dataset contains 90 sequences. Thus, there were 9 sequences in each class. The minimum sequence length was 28 frames.

The sequences were divided into the training and test sets containing four and five sequences correspondingly for each class. The sequences were pre-processed using the algorithm described in Section 2.2. Further, subsequences were generated according to Section 2.3. Then, the dimensionality reduction using the method described in Section 2.4 and classification using the algorithm described in section 2.5 were performed. To estimate the quality of the method, we used the classification accuracy, defined as the proportion of correctly classified objects.

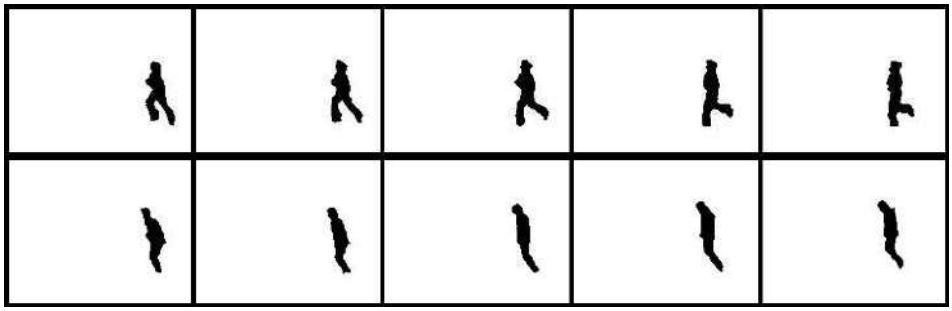

Figure 1. Examples of sequences from the Weizmann database: running and long jumps.

In the first experiment, we studied the dependence of the classification accuracy on the step size used in the generation of subsequences. The length of the subsequence was 28 frames. The output dimension of the feature vectors formed in step 2.4 of the considered method was equal to 8.

The experimental results are shown in figure 2. It was experimentally determined that the best classification accuracy is achieved with small step values. In further experiments, a step equal to 2 was used.

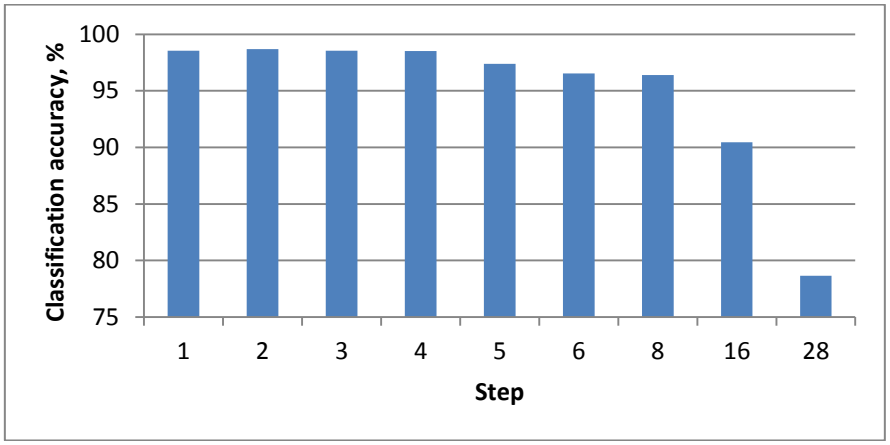

Figure 2. Dependence of the classification accuracy on step size.

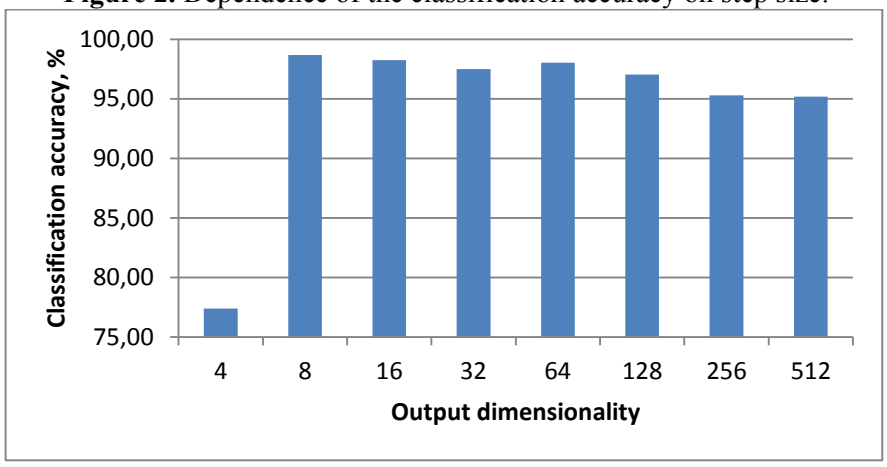

Figure 3. Dependence of the classification accuracy on the dimensionality.

In the second experiment, we investigated the dependence of the classification accuracy on the output dimensionality of the feature vectors, formed in step 2.4 of the proposed method. The output dimensionality varied from 4 to 512, while other parameters remained fixed. In particular, the step used in the allocation of subsequences was 2 frames.

The results of the experiment are shown in figure 3. As can be seen from the above results, the best values of the classification accuracy are achieved for dimensionality 8, 16 and 64.

In the third experiment, we investigated the dependence of classification accuracy on the length of subsequences. The length of the subsequence varied from 4 to 28 frames, while other parameters remained fixed. Thus, the step used in the allocation of subsequences was 2 frames; the output dimension was 64. The results of the experiment are shown in figure 4. As it can be seen from the results, the best values of the classification accuracy are achieved with a subsequence of 28 frames.

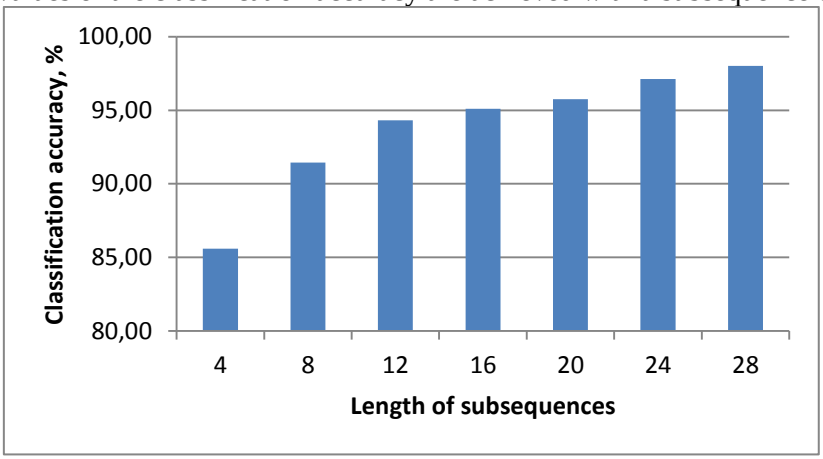

Figure 4. Dependence of classification accuracy on the length of subsequences.

As can be seen from the results of these experiments, with a relatively small number of classes (10 classes), a high (not less than 95%) classification accuracy can be achieved.

4. Conclusion

The proposed method for human actions recognition consists in the detection of a moving person in a video sequence, normalization of the size, generation of subsequences, dimensionality reduction using the principal component analysis and classification using the support vector machine.

The experiments performed on the Weizmann dataset allowed us to determine the best values of the parameters of the developed method. It was shown that with a small number of classes (10 classes), the proposed method provides on this dataset a high (with a wide range of parameters - at least 95%, and using the best values - up to 98%) accuracy of classification.

In the future, it is planned to expand the list of algorithms used to form a feature description and the list of classification methods. Another possible direction of further research is the detection of abnormal behavior (see, for example, [32]).

5. References

[1] Kong Y and Fu Y 2018 Human action recognition and prediction: a survey *J. of Latex class files* **19**
[2] Laptev I 2005 On space-time interest points *IJCV* **64** 107-123
[3] Raptis M and Sigal L 2013 Poselet key-framing: a model for human activity recognition *CVPR* 2650-2657
[4] Ji S, Xu W, Yang M and Yu K 2013 3d convolutional neural networks for human action recognition *IEEE Trans. Pattern Analysis and Machine Intelligence* **35** 221-231
[5] Carreira J and Zisserman A 2017 Quo vadis, action recognition? a new model and the kinetics dataset *CVPR* 6299-6308
[6] Bobick A F and Davis J W 2001 The recognition of human movement using temporal templates *IEEE Trans Pattern Analysis and Machine Intelligence* **23** 257-267
[7] Weinland D, Ronfard R and Boyer E 2006 Free viewpoint action recognition using motion history volumes *Computer Vision and Image Understanding* **104** 249-257
[8] Laptev I and Lindeberg T 2003 Space-time interest points *ICCV* 432-439

[9] Laptev I, Marszalek M, Schmid C and Rozenfeld B 2008 Learning realistic human actions from movies *CVPR*
[10] Klaser A, Marszalek M and Schmid C 2008 A spatio-temporal descriptor based on 3d-gradients *BMVC*
[11] Dalal N and Triggs B 2005 Histograms of oriented gradients for human detection *CVPR*
[12] Messing R, Pal C and Kautz H 2009 Activity recognition using the velocity histories of tracked keypoints *ICCV*
[13] Gosciewska K and Frejlichowski D 2018 Sillhouette-based action recognition using simple shape descriptors *Springer*
[14] Laptev I, Schuldt C and Caputo B Recognizing human actions: a local SVM approach *Proc. ICPR'04* (Cambridge, UK)
[15] Marszalek M, Laptev I and Schmid C 2009 Actions in context *CVPR*
[16] Blank M, Gorelick L, Shechtman E, Irani M and Basri R 2005 Actions as space-time shapes *Proc. ICCV*
[17] Laptev I and Perez P 2007 Retrieving actions in movies *ICCV*
[18] Tran D and Sorokin A 2008 Human activity recognition with metric learning *ECCV*
[19] Duong T V, Bui H H, Phung D Q and Venkatesh S 2005 Activity recognition and abnormality detection with the switching hidden semi-markov model *CVPR*
[20] Rajko S, Qian G, Ingalls T and James J 2007 Real-time gesture recognition with minimal training requirements and on-line learning *CVPR*
[21] Ikizler N and Forsyth D 2007 Searching video for complex activities with finite state models *CVPR*
[22] Shiripova L, Strukova O and Myasnikov E 2018 Gait analysis for person recognition using principal component analysis and support vector machines *CEUR Workshop Proceedings* **2210** 170-176
[23] Shiripova L and Myasnikov E 2018 Comparative analysis of classification methods for human identification by gait *CEUR Workshop Proceedings* **2268** 118-128
[24] KadewTraKuPong P and Bowden R 2001 An improved adaptive background mixture model for real-time tracking with shadow detection
[25] Zivkovic Z 2004 Improved adaptive Gausian mixture model for background subtraction
[26] Andrew B, Matsukawa A and Goldberg K 2012 Visual tracking of human visitors under variable-lighting conditions for a responsive audio art installation
[27] Murukesh C, Thanushkodi K, Padmanabhan P and Mohamed D 2014 Secured authentication through integration of gait and footprint for human identification *Journal of Electrical Engineering and Technology*
[28] Wang L, Tan T, Hu W and Ning H 2003 Automatic gait recognition based on statistical shape analysis *Transactions on image processing* **12**
[29] Fukunaga K 2003 *Introduction to statistical pattern recognition* (London: Academic Press)
[30] Myasnikov E V 2017 Fast techniques for nonlinear mapping of hyperspectral data *Proc. SPIE* **10341** 103411D.
[31] Myasnikov E V 2017 Hyperspectral image segmentation using dimensionality reduction and classical segmentation approaches *Computer Optics* **41(4)** 564-572 DOI: 10.18287/2412-6179-2017-41-4-564-572
[32] Shatalin R A, Fidelman V R and Ovchinnikov P E 2017 Abnormal behavior detection method for video surveillance applications *Computer Optics* **41(1)** 37-45 DOI: 10.18287/2412-6179-2017-41-1-37-45
[33] Cortes C and Vapnik V 1995 Support-vector networks *Machine Learning* **20(3)** 273-297

Acknowledgments
The work was partly funded by RFBR according to the research project 17-29-03190 in parts of «1. Introduction» – «2. Methods» and by the Russian Federation Ministry of Science and Higher Education within a state contract with the "Crystallography and Photonics" Research Center of the RAS under agreement 007-ГЗ/Ч3363/26 in part of «3. Experiments».

Applying doubly stochastic filters to evaluate the dynamics of object sizes on satellite image sequences

V E Dementyev[1], D S Kondratyev[1]

[1]Ulyanovsk State Technical University, ul. Severny Venets, 32, Ulyanovsk, Russia, 432027

e-mail: dve@ulntc.ru

Abstract. One of the important tasks facing the regional authorities is to monitor the condition of roads and power lines. In the Ulyanovsk region more than 8 thousand km of power lines and more than 9 thousand km of roads (including rural). A significant part of these facilities is located outside the settlements in places with medium and low availability. In many such places there is a problem of uncontrolled forest overgrowth. This work is devoted to solving the problem of automated satellite monitoring of such areas. For this purpose, it is proposed to use a modified convolutional neural network that processes time sequences of multispectral satellite images and allows to allocate territories occupied by forest and undergrowth with high accuracy. This approach allows us to assess the dynamics of overgrowth of the territory and perform the appropriate forecast with sufficient accuracy for practice.

1. Introduction

One of the important tasks of the satellite image processing is its thematic mapping, i.e. division of image into identifiable areas containing the similar visual, correlation or texture characteristics of pixels. The use of standard segmentation algorithms [1-3] for thematic mapping of satellite images usually leads to significant errors caused by two reasons. Firstly, these algorithms are largely incapable of taking into account the multi-zonal nature of remote sensing (RS), so each satellite image contains the results of the Earth's surface registration in different spectral ranges. Some works [4-6] suggest the possibility of processing hyperspectral images. Thus, the authors based their theory on criterion of uniformity for reception of connected areas of such hyperspectral image [4], modification and generalization of algorithm K-means [5] and use of physical properties of a satellite data [6]. Secondly, the existing approaches unable to use data on the observed territory received at previous points of time for image segmentation. But using such data can significantly improve the quality of processing at the expense of a fundamentally larger amount of information, but it is fraught with difficulties of aggregation.

It is possible to overcome the mentioned disadvantages by using neural network procedures of segmentation and classification of multidimensional data. In work [9] the variant of the U-NET neural network with full-connected layers (FCN) modification is presented. Herewith the input layer of the network consisting from spectral layers of the multizonal image has been extended by three auxiliary 2d halftone images obtained from the original using NDVI, EVI, SAVI transformations and two 2d arrays , representing the segmentation results at the previous point of time and one year ago. The use of two such reference markings allows one's to reduce the error of classification in case of rapid changes of the terrain due to the change of year time and in case of marking array absence at the

previous point of time in connection, for example, with cloudiness. The quality analysis of such an algorithm shows the processing comparable accuracy to the qualified operator results.

It should be noted that the results of the satellite images thematic processing provides information related to the peculiarities of the Earth's surface in the previous and current moments of time. However, the necessary element of the RS processing system is the tool that allow to forecast the state of certain objects and form recommendations for responsible persons. For example, let's consider the task related to the forecasting about the dangerous convergence possibility of various natural and technogenic objects. An example of such convergence may be the gradual growth of the forest area along roads or power lines or landslide processes leading to the destruction of various infrastructures.

2. Satellite Image Processing

Let us formulate the given problem as follows. Let there be an aggregate of segments describing a certain extended object $\mathbf{T_o}$ (a road, an electric power transmission line etc.). The given aggregate is usually described by a vector object having geographical reference in absolute coordinates. Let us separate on this extended object a set of points $\mathbf{T_{oi}} = (\mathbf{x_{0i}}, \mathbf{y_{oi}})$ having the distance between them equal to $\Delta_\mathbf{o}$. Let us assume that at a certain time instant $\mathbf{t}$ next to the object there lies a certain extended domain $\mathbf{G_R}^\mathbf{t}$ defined by a set of points each corresponding to a pixel in the original halftone image. For each point $\mathbf{T_{oi}}$ let us construct a perpendicular to the segment $[\mathbf{T_{oi}}, \mathbf{T_{oi+1}}]$. Let us find the point $\mathbf{T_{Ei}}^\mathbf{t} = \left(\mathbf{z^t_{Exi}}, \mathbf{z^t_{Eyi}}\right)$ of intersection of this perpendicular and the domain $\mathbf{G_R}^\mathbf{t}$. Obviously the set of points $\{\mathbf{T_{Ei}}^\mathbf{t}, \mathbf{i} = \mathbf{1}, .., \mathbf{N_o}\}$ describe a conditional boundary of the domain $\mathbf{G_R}^\mathbf{t}$ as viewed from the extended object. It enables to use estimates of the points coordinates $\{\mathbf{T_{Ei}}^\mathbf{t}, \mathbf{i} = \mathbf{1}, .., \mathbf{N_o}\}$ obtained at different times $\mathbf{t} = \mathbf{1}, .., \mathbf{T}$ as a source of information on the domain $\mathbf{G_R}^\mathbf{t}$ dynamics for the purpose of forming a prediction about its boundaries at future times $\mathbf{t} > \boldsymbol{T}$ as well. (Figure 1).

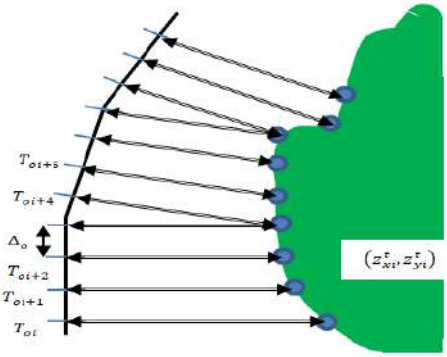

Figure 1. Geometric interpretation of the distance estimate between the stationary object and the movable area.

In view of errors arising at satellite images recording and processing we get the following relations (Eq. 1), in which $\boldsymbol{n^t_{Exi}}$ and $\boldsymbol{n^t_{Eyi}}$ – white noise samples with zero mean and variance $\boldsymbol{\sigma^2_n}$.

$$z^t_{Exi} = x^t_{Ei} + n^t_{Exi}, z^t_{Eyi} = y^t_{Ei} + n^t_{Eyi}, i = 1, .., N_o, t = 1, .., T, \quad (1)$$

where $\boldsymbol{n^t_{Exi}}$ and $\boldsymbol{n^t_{Eyi}}$ – white noise samples with zero mean and variance $\boldsymbol{\sigma^2_n}$.

Direct measurements based on the results of satellite material image-type related mapping show that MSE $\sqrt{\boldsymbol{\sigma^2_n}}$ is approximately equal to $\mathbf{1.5D_{xy}}$, where $\mathbf{D_{xy}}$ – resolution of the original images.

Let us suppose that the boundary of the domain $\boldsymbol{G_R}^\boldsymbol{t}$ can move non-uniformly. Thus, for example, the area of a precipice or a ravine can increase by tens of centimeters per each year and at a certain moment its rate might increase exponentially. Then we will use doubly stochastic (DS) model [3,10] to describe unknown coordinates in the following form (Eq. 2). In this case $\mathbf{r_{ax}}, \mathbf{r_{ay}}$ – scalar parameters determining change potential for the accelerations $\mathbf{a^t_{Exi}}$and $\mathbf{a^t_{Eyi}}$; $\boldsymbol{\xi}^\mathbf{t}_\mathbf{axi}$, $\boldsymbol{\xi}^\mathbf{t}_\mathbf{ayi}$ – independent normal random variables with zero mean and variance $\boldsymbol{\sigma^2_\xi}$:

$$x^t_{Ei} = 2x^{t-1}_{Ei} - x^{t-2}_{Ei} + a^t_{Exi}\left(x^{t-1}_{Ei} - x^{t-2}_{Ei}\right),$$

$$y_{Ei}^{t} = 2y_{Ei}^{t-1} - y_{Ei}^{t-2} + a_{Eyi}^{t}\left(y_{Ei}^{t-1} - y_{Ei}^{t-2}\right), \quad (2)$$
$$a_{Exi}^{t} = r_{ax}a_{Exi}^{t-1} + \xi_{axi}^{t},\ a_{Eyi}^{t} = r_{ay}a_{Eyi}^{t-1} + \xi_{ayi}^{t},$$

The model (2) can be rewritten in the form:

$$\bar{X}_{Ei}^{t} = \varphi_{Exi}^{t}(\bar{X}_{Ei}^{t-1}) + \bar{\xi}_{xi}^{t},\ \bar{Y}_{Ei}^{t} = \varphi_{Eyi}^{t}(\bar{X}_{Ei}^{t-1}) + \bar{\xi}_{yi}^{t},$$

where

$$\varphi_{Exi}^{t}\left(\bar{X}_{Ei}^{t-1}\right) = \begin{pmatrix} x_{Ei}^{t-1} & v_{Exi}^{t} & 0 \\ 0 & v_{Exi}^{t-1}(1 + a_{Exi}^{t}) & 0 \\ 0 & 0 & a_{Exi}^{t-1}r_{ax} \end{pmatrix},$$
$$\varphi_{Eyi}^{t}\left(\bar{Y}_{Ei}^{t-1}\right) = \begin{pmatrix} y_{Ei}^{t-1} & v_{Eyi}^{t} & 0 \\ 0 & v_{Eyi}^{t-1}(1 + a_{Eyi}^{t}) & 0 \\ 0 & 0 & a_{Eyi}^{t-1}r_{ay} \end{pmatrix},$$
$$\bar{\xi}_{xi}^{t} = \begin{pmatrix} 0 \\ 0 \\ \xi_{axi}^{t} \end{pmatrix},\ \bar{\xi}_{xi}^{t} = \begin{pmatrix} 0 \\ 0 \\ \xi_{ayi}^{t} \end{pmatrix}.$$

The assigned notations enable to apply DS nonlinear filtering to observations and for construction of predictions of behaviour of the region $\boldsymbol{R_0}$ in reference to the object$\boldsymbol{T_o}$. In doing so let us introduce $\bar{\boldsymbol{X}}_{\boldsymbol{Эxi}}^{\boldsymbol{t}} = \boldsymbol{\varphi}_{\boldsymbol{Exi}}^{\boldsymbol{t}}(\bar{\boldsymbol{X}}_{\boldsymbol{Ei}}^{\boldsymbol{t-1}})$ and $\bar{\boldsymbol{Y}}_{\boldsymbol{Ei}}^{\boldsymbol{t}} = \boldsymbol{\varphi}_{\boldsymbol{Eyi}}^{\boldsymbol{t}}(\bar{\boldsymbol{X}}_{\boldsymbol{Ei}}^{\boldsymbol{t-1}})$– extrapolated predictions for the point $\mathbf{T_{Ei}}$ coordinates at the time point $\mathbf{t}$ based on the preceding observations $\mathbf{z}_{\mathbf{Exi}}^{\mathbf{t-1}}$and $\mathbf{z}_{\mathbf{Eyi}}^{\mathbf{t-1}}$. Denote by $\mathbf{P_{xi}}^{\mathbf{t-1}}$, $\mathbf{P_{yi}}^{\mathbf{t-1}}$ – filtering error covariance matrices at the time point $(\mathbf{t-1})$, $\mathbf{V_{x_\xi i}}^{\mathbf{t}} = \mathbf{M}\{\bar{\boldsymbol{\xi}}_{\mathbf{xi}}^{\mathbf{t}}\bar{\boldsymbol{\xi}}_{\mathbf{xi}}^{\mathbf{t}\ T}\}$, $\mathbf{V_{y_\xi i}}^{\mathbf{t}} = \mathbf{M}\{\bar{\boldsymbol{\xi}}_{\mathbf{yi}}^{\mathbf{t}}\bar{\boldsymbol{\xi}}_{\mathbf{yi}}^{\mathbf{t}\ T}\}$ – diagonal covariance matrices for random increments$\bar{\boldsymbol{\xi}}_{\boldsymbol{xi}}^{\boldsymbol{t}}$. Then error covariance matrices for such extrapolation have the following form:

$$P_{Эxi}{}^{t} = M\left\{\left(\hat{\bar{X}}_{Эi}^{t} - \bar{X}_{Эi}^{t}\right)\left(\hat{\bar{X}}_{Эi}^{t} - \bar{X}_{Эi}^{t}\right)^{T}\right\} = \varphi_{Exi}^{t}{}'(\bar{X}_{Ei}^{t-1})P_{x}{}^{t-1}\varphi_{Exi}^{t}{}'(\bar{X}_{Ei}^{t-1})^{T} + V_{x_\xi i}{}^{t},$$
$$P_{Эyi}{}^{t} = M\left\{\left(\hat{\bar{Y}}_{Эi}^{t} - \bar{Y}_{Эi}^{t}\right)\left(\hat{\bar{Y}}_{Эi}^{t} - \bar{Y}_{Эi}^{t}\right)^{T}\right\} = \varphi_{Eyi}^{t}{}'(\bar{Y}_{Ei}^{t-1})P_{yi}{}^{t-1}\varphi_{Eyi}^{t}{}'(\bar{Y}_{Ei}^{t-1})^{T} + V_{y_\xi i}{}^{t},$$

If we denote by $\hat{\boldsymbol{x}}_{\boldsymbol{Эi}}^{\boldsymbol{t}}$,$\hat{\boldsymbol{y}}_{\boldsymbol{Эi}}^{\boldsymbol{t}}$ - the first elements of the vectors $\hat{\bar{\boldsymbol{X}}}_{\boldsymbol{Эi}}^{\boldsymbol{t}}$ and $\hat{\bar{\boldsymbol{Y}}}_{\boldsymbol{Эi}}^{\boldsymbol{t}}$; $\boldsymbol{B_{xi}}^{\boldsymbol{t}} = \boldsymbol{P_{Эxi}}^{\boldsymbol{t}}\boldsymbol{C_x}^{\boldsymbol{T}}\boldsymbol{D_{xi}^{t}}^{\boldsymbol{-1}}$; $\boldsymbol{B_{yi}}^{\boldsymbol{t}} = \boldsymbol{P_{Эyi}}^{\boldsymbol{t}}\boldsymbol{C_y}^{\boldsymbol{T}}\boldsymbol{D_{yi}^{t}}^{\boldsymbol{-1}}$; $\boldsymbol{D_{xi}^{t}} = \boldsymbol{C_x}\boldsymbol{P_{Эxi}}^{\boldsymbol{t}}\boldsymbol{C_x}^{\boldsymbol{T}} + \boldsymbol{\sigma_n^2}$; $\boldsymbol{D_{yi}^{t}} = \boldsymbol{C_y}\boldsymbol{P_{Эyi}}^{\boldsymbol{t}}\boldsymbol{C_y}^{\boldsymbol{T}} + \boldsymbol{\sigma_n^2}$; $\mathbf{C_x} = \mathbf{C_y} = (\mathbf{1}\quad \mathbf{0}\quad \mathbf{0})$, then we can write the following relations (Eq. 27) for DS coordinate filters:

$$\hat{\bar{X}}_{Ei}^{t} = \hat{\bar{X}}_{Эi}^{t} + B_{xi}{}^{t}\left(z_{Exi}^{t} - \hat{x}_{Эi}^{t}\right),\hat{\bar{Y}}_{Ei}^{t} = \hat{\bar{Y}}_{Эi}^{t} + B_{yi}{}^{t}\left(z_{Eyi}^{t} - \hat{y}_{Эi}^{t}\right). \quad (3)$$

The filtering error variance at each step is determined by the matrices $\boldsymbol{P_{xi}}^{\boldsymbol{t}} = (\boldsymbol{E} - \boldsymbol{B_{xi}}^{\boldsymbol{t}})\boldsymbol{P_{Эxi}}^{\boldsymbol{t}}$, $\boldsymbol{P_{yi}}^{\boldsymbol{t}} = (\boldsymbol{E} - \boldsymbol{B_{yi}}^{\boldsymbol{t}})\boldsymbol{P_{Эyi}}^{\boldsymbol{t}}$.

Special attention must be given to the fact that due to the necessity for the distance from the extended object $\boldsymbol{T_o}$ to the domain $\boldsymbol{R_0}$ to be surveyed, it is possible to simplify the boundaries coordinates filtering process $\mathbf{R_0}$ by processing only one coordinate, namely, the distance $\mathbf{x}_{\mathbf{ri}}^{\mathbf{t}}$ from the point $\mathbf{T_{oi}}$ belonging to $\mathbf{T_o}$ up to the boundary $\mathbf{R_0}$ at the time point $\mathbf{t}$. An aggregate of similar observations $\mathbf{z}_{\mathbf{Ex_ri}}^{\mathbf{t}}$ can be processed by a technique identical to the above-described one.

As an illustration of such a technique in figures below series satellite images fragments for the forest tract in Cherdakly district of the Ulyanovsk region for the period 2001-2017 years (figure 2) and Milanovsky opencast colliery on riverbank of the Volga in the northern part of the city of Ulyanovsk for the period 2013-2017 years (figure 3) are presented. Here for convenience of color image perception and its recovery overlapping of visible spectral bands and superposition of the segmented image fragment and normals to the object to be monitored is carried out. In the first case the number of multispectral images to be processed amounted to 42 snapshots, in the second case - 32 snapshots. The minimal time interval for satellite information production amounts to 14 days.

July 2003 June 2011 July 2017

Figure 2. Forest tract satellite images fragments and the results of these images processing.

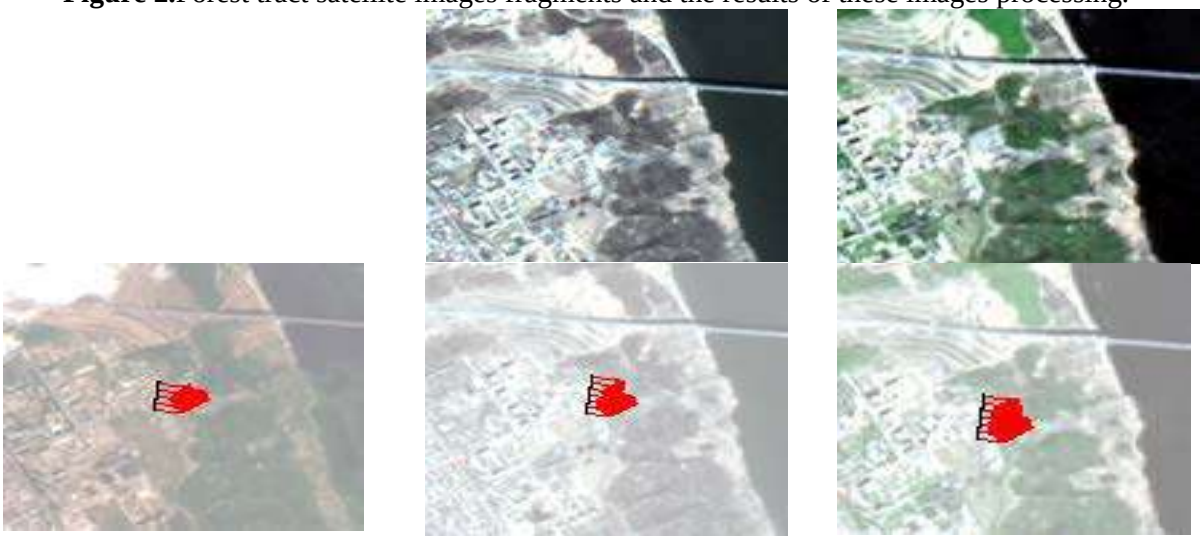

August 2015 April 2016 May 2016

Figure 3. Milanovsky opencast colliery satellite images fragments and the results of these images processing.

The above-mentioned groups of multispectral images were separated into a training and an operating samples. The training samples were used to specify the filtering parameters, in particular, to estimate the parameters $\mathbf{r_{ax}}$and $\boldsymbol{\sigma_{\xi}^{2}}$. The operating part of the sample was processed by three algorithms enabling to carry out the distance prediction $\mathbf{x_{ri}^{t+1}}$ basing on the preceding observations. The first algorithm (I) involves constructing a simple prediction $\hat{\mathbf{x}}_{\mathbf{ri}}^{\mathbf{t+1}} = \mathbf{2z_{ri}^{t}} - \mathbf{z_{ri}^{t}}$ wherein only the variable $\hat{\mathbf{x}}_{\mathbf{ri}}$ change speed is taken into account for the time interval $(\mathbf{t-1}, \mathbf{t})$. The second algorithm (II) assumes linear Kalman filtering of the observations $\mathbf{z_{ri}^{t}}$ and construction of the extrapolated prediction $\hat{\mathbf{x}}_{\mathbf{Эri}}^{\mathbf{t+1}}$ based on the results of the processing. The third algorithm (III) is in the above-described doubly stochastic filtering of an aggregate of the observations $\mathbf{z_{ri}^{t}}$ and construction of the vector $\widehat{\widehat{\mathbf{X}}}_{\mathbf{ЭEi}}^{\mathbf{t+1}}$. In the table 1 below the values of prediction average errors depending on the object kind are presented.

On average the DS filter provides prediction accuracy 6% higher than in case of using Kalman filter and 58% higher than in case of simple linear predictions. It enables to estimate coordinates and rate change dynamics for boundaries of the domain to be monitored by using the DS filter. It is

essential that the DS filter enables to quicker respond to abrupt rate change of the processes determining the object behaviour. As an illustration we provide the estimates behaviour for the distance from opencast colliery to one of the points to be monitored (figure 4a) and the parameter $\hat{a}_i^t$ estimate (figure 4b).

Table 1. Prediction average errors.

	Average error for the algorithm I	Average error for the algorithm II	Average error for the algorithm III
The forest tract snapshot. October 2014	6.7 m	2.7 m	2.6 m
The forest tract snapshot. May 2015	10.7 m	3.9 m	3.7 m
The forest tract snapshot. June 2016	6.2 m	3.6 m	3.3 m
Milanovsky opencast colliery snapshot. May 2014	7.1 m	3.8 m	3.6 m
Milanovsky opencast colliery snapshot. May 2015	7.3 m	3.9 m	3.8 m
Milanovsky opencast colliery snapshot. May 2016	6.9 m	3.9 m	3.7 m
Milanovsky opencast colliery snapshot. April 2016. Beginning of the avalanche processes.	12.4 m	8.9 m	7.8 m
Milanovsky opencast colliery snapshot. April 2016. Continuation of the avalanche processes.	30.7 m	32.8 m	12.6 m
Milanovsky opencast colliery snapshot. May 2016. Cessation of the avalanche processes.	20.3 m	18.1 m	17.3 m

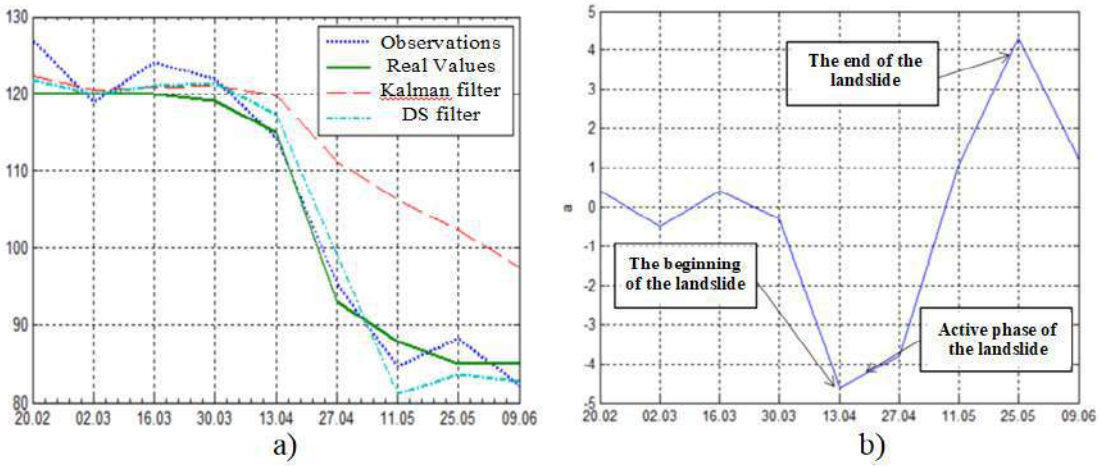

Figure 4. Dependence of the filtering results versus survey time.

3. Conclusion

Direct analysis of the given results in comparison with the data of objective monitoring (solid line) indicates superiority of the DS filter over conventional linear Kalman filter in filtering accuracy. As it takes place, this superiority makes itself evident in the most distinct manner in case of abrupt change of the rock collapsing process (and the corresponding reduction of the distance between the opencast

colliery and the point to be monitored). This change corresponds to a significant change of the parameter $\boldsymbol{a_i^t}$ estimate which enables to register considerable changes in the opencast colliery domain state basing only on this estimate dependence nature versus survey time.

4. References

[1] Vasiliev K K 2016 *Optimum processing of signals in discrete time* (Moscow: Radiotehnika)
[2] Krasheninnikov V R and Vasil'ev K K 2018 Multidimensional image models and processing *Intelligent Systems Reference Library* **135** 11-64
[3] Vasiliev K K and Dementyev V E 2017 *Presentation and processing of satellite multi-zone images* (Ulyanovsk)
[4] Fursov V A, Bibikov S A and Baida O A 2014 Thematic classification of hyperspectral images by conjugacy index *Computer Optics* **38(1)** 154-158
[5] Zimichev E A, Kazansky N L and Serafimovich P G 2014 Spatial classification of hyperspectral images using the k-means ++ clustering method *Computer Optics* **38(2)** 281-286
[6] Blokhinov Yu B, Gorbachev V A, Rakutin Yu O and Nikitin A D 2018 Development of an algorithm for semantic segmentation of real-time aerial photographs *Computer Optics* **42(1)** 141-148 DOI: 10.18287/2412-6179-2018-42-1-141-148
[7] Belim S V and Larionov S V 2016 Image segmentation algorithm based on searching communities on graphs *Computer Optics* **40(6)** 904-910 DOI: 10.18287/2412-6179-2016-40-6-904-910
[8] Dementyev V E, Kondratyev D S and Frenkel A G 2018 *Application of convolutional neural networks for thematic mapping of sequences of satellite multispectral images* (Moscow: Radiotehnika)
[9] Dementyev V E 2017 *The use of double-stochastic autoregressive models for processing satellite images* (Moscow: Radiotehnika)
[10] Andriyanov N A and Dement'ev V E 2018 Application of mixed models of random fields for the segmentation of satellite images *CEUR Workshop Proceedings* **2210** 219-226

Groundwater Potential Zones in Relation to Catchment Condition in Orenburg, Russia

K Choudhary[1,2,3], M S Boori[1,3,4] and A Kupriyanov[1,5]

[1]Samara National Research University, Moskovskoe Shosse 34A, Samara, Russia, 443086
[2]The Hong Kong Polytechnic University, Hong Kong
[3]University of Rennes 2, Rennes, France
[4]American Sentinel University, Colorado, USA
[5]Image Processing Systems Institute of RAS - Branch of the FSRC "Crystallography and Photonics" RAS, Molodogvardejskaya street 151, Samara, Russia, 443001

e-mail: komal.kc06@gmail.com

Abstract. The main objective of this study was to detect groundwater availability for agriculture in the Orenburg, Russia. Remote sensing data (RS) and geographic information system (GIS) were used to locate potential zones for groundwater in Orenburg. Diverse maps such as a base map, geomorphological, geological structural, lithology, drainage, slope, land use/cover and groundwater potential zone were prepared using the satellite remote sensing data, ground truth data, and secondary data. ArcGIS software was utilized to manipulate these data sets. The groundwater availability of the study was classified into different classes such as very high, high, moderate, low and very low based on its hydro-geomorphological conditions. The land use/cover map was prepared using a digital classification technique with the limited ground truth for mapping irrigated areas in the Orenburg, Russia.

1. Introduction

Groundwater is a form of water occupying all the voids within geological layers. The occurrence of groundwater in a geological formation and the scope for its absorption primarily depend on the formation porosity. The conventional methods used to prepare groundwater potential zones are mainly based on ground surveys. The groundwater conditions are significantly depending upon the slope, surface water body, depth of weathering, canals and irrigated fields, etc. These factors can be interpreted in remote sensing data. Minor et al. [1] developed an integrated interpretation strategic to characterize groundwater resources for identification of well location in Orenburg using GIS. Gustafson [2] used GIS for the analysis of lineament data received from SPOT imagery for groundwater potential mapping. Krishnamurthy et al. [3] developed a GIS-based model to describe groundwater potential zones. The field verification of this model established the efficacy of GIS in demarcating the potential groundwater reserves.

A GIS framework was developed and analyzed by Das et al. [4] with rational conditions to groundwater zones using thematic layers like geomorphology, geology, drainage, slope and land use/cover generated by ArcGIS software. Based on the status of groundwater irrigated areas through remote sensing artificial recharge structures such as tanks, dams can be recommended upstream of groundwater irrigated areas to recharge wells in the downstream areas to increase groundwater resources [5].

Previous studies show a wide range of using remote sensing (RS) and geographical information system (GIS) technology for groundwater potential zone (GWPZ) assessment. In that, they use different thematic layers, give specific weight to all classes and each thematic layer based on their sensitivity or specific importance on groundwater potentiality. In this paper, we use RS and GIS technology, create different thematic layers, which are responsible for groundwater possibility and then give specific weight. This research work confirms conservation of sustainable aquifer development judicious extraction of dynamic groundwater resource available in the Orenburg of Russia [6].

2. Study area

We choose the east part of Orenburg Oblast, Russia (figure 1) as a study area. It's situated on the boundary of Europe and Asia on Ural rives with Kazakhstan border. The study area latitude is 51°77′ and longitude 55°10′ with 107 meters above sea level elevation. Orenburg has a relatively dry humid continental climate with long hot summers and long cold winters. The average January temperature is -15.6 °C (3.9 °F) and the average July temperature is 29.0 °C (84.2 °F). The most important river of the Oblast is the Ural River.

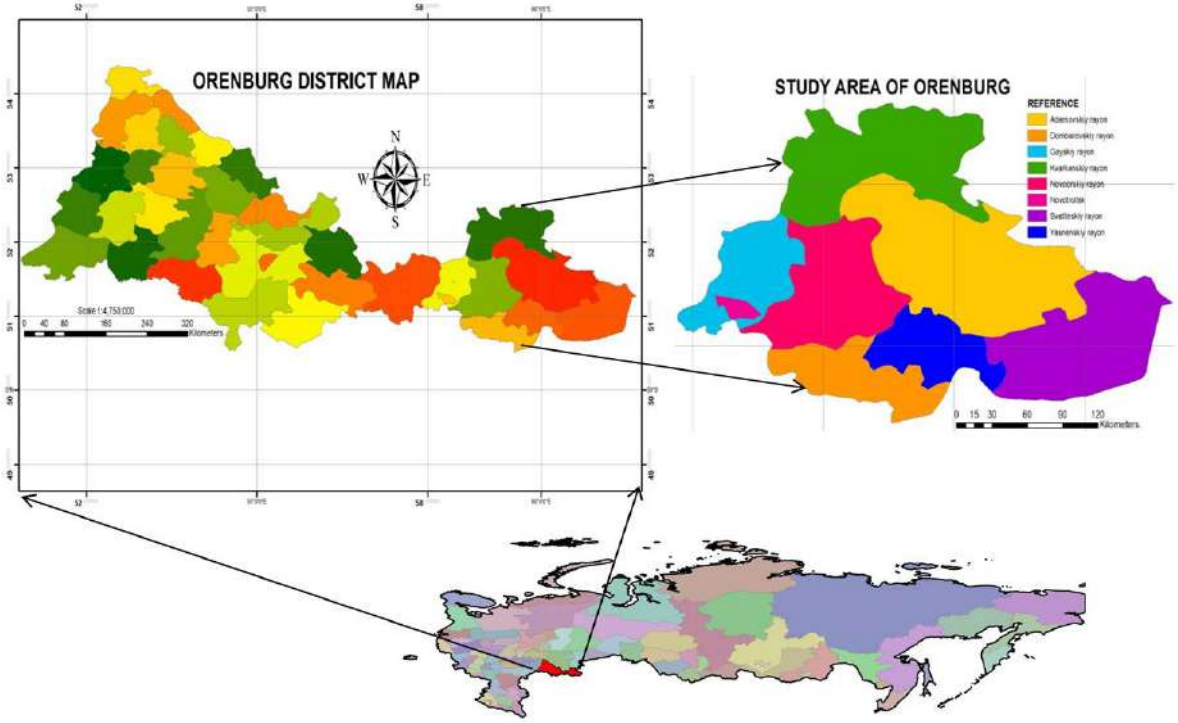

Figure 1. Location map of the Orenburg, Russia.

3. Materials and methods

This research work used Landsat-8/OLI (Operational land imager) images to make different thematic layers such as agriculture, forest, geomorphology, land use, lithology, soil, land use/cover, surface water, drainage density, flow accumulation, flow direction, and base map. Also, use Digital Elevation Model (DEM) from ASTER satellite (ASTER-GDEM) with the 30m spatial resolution to create a slope map for height information. We use ArcGIS and ERDAS software for all types of image processing and GIS analysis work. For accuracy assessment and verify our results we used ancillary data, topographic maps, field data and specific government departmental information's.

In methodological steps after georeferenced the imagery in UTM/WGS84 projection, we remove radiometric and geometric errors [7]. Then identify best band combination for image interpretation and create following thematic layers (figure 2).

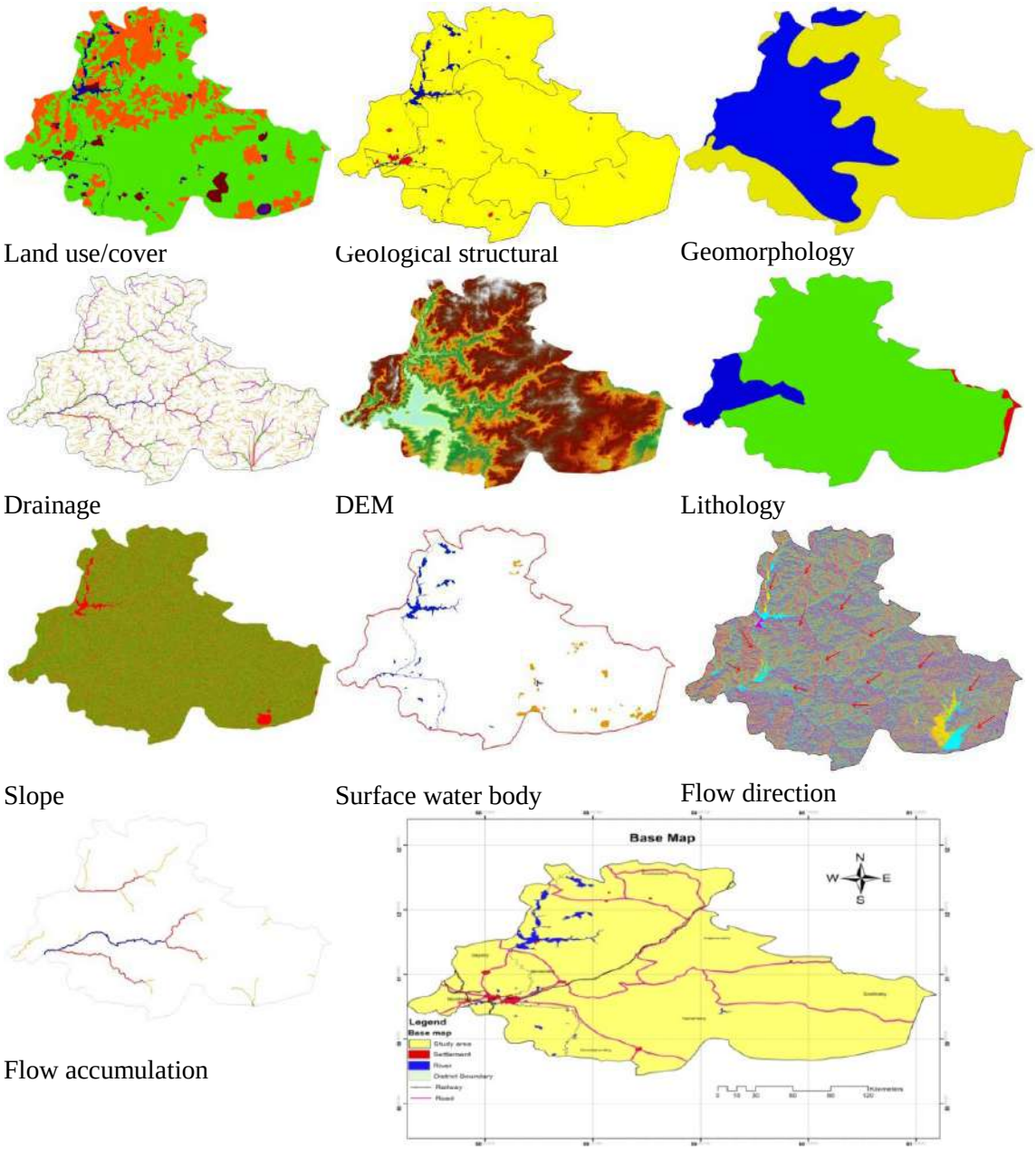

Figure 2. Thematic layers which used for groundwater potential zone mapping.

After creating above thematic layers, we combined all layers in ArcGIS software by using the raster calculator module to generate the final groundwater potential zone map of Orenburg, Russia. Than all factors in each thematic layer were given a specific weight (arithmetic value in between 1 to 9) based on its sensitivity or strength of influence to the groundwater possibility [8, 9, 10]. In last further, classify final groundwater potentiality map into five classes from very high to very low classes.

After giving specific weight to all factors, then calculate a normalized weight (Wn) by geometric mean (GM) and in finally get groundwater potential zone map ($GWPZ$) using the following equations:

$$Wn = \left(GMn / \sum_{n=1}^{nf} GMn \right)$$

Where the geometric mean of the i[th] row of the judgment matrices is calculated as:

$$GMn = \sqrt[n]{\text{p1np2n} \ldots \ldots \text{pnNf}}$$

The groundwater potential zone map was mathematically calculated using ArcGIS raster analysis as follows:

$$GWPZ = \sum Wi * Ri,$$
$$Ef = Wi * Ri$$
$$\text{GWPZ} = \sum(Ef\ of\ all\ thematic\ layers)$$

Where the meaning of equations words as follows:

- E_f = effectiveness of a factor for groundwater potentiality in the study area.
- W_i = map weight for factor i,
- R_i = rating value for i factor.

Table 1. Calculation of factors weight.

	1	2	3	4	5	6	7	8	9	10	11	GM	Wn
1	1.00	0.93	1.17	0.78	1.75	1.07	1.55	2.33	0.88	1.75	1.75	1.23	0.062
2	1.07	1.00	1.25	0.83	1.87	1.15	1.66	2.50	0.93	1.87	1.87	1.31	0.067
3	0.86	0.80	1.00	0.67	1.50	0.92	1.33	2.00	0.75	1.50	1.50	1.05	0.053
4	1.29	1.20	1.50	1.00	2.25	1.38	2.00	3.00	1.13	2.25	2.25	1.58	0.080
5	0.57	0.53	0.67	0.44	1.00	0.61	0.88	1.33	0.50	1.00	1.00	0.70	0.036
6	0.92	0.86	1.08	0.72	1.62	1.00	1.44	2.16	0.81	1.62	1.62	1.14	0.058
7	0.64	0.60	0.75	0.50	1.12	0.69	1.00	1.50	0.56	1.12	1.12	0.79	0.040
8	0.43	0.40	0.50	0.33	0.75	0.46	0.66	1.00	0.38	0.75	0.75	0.53	0.027
9	1.14	1.06	1.33	0.89	2.00	1.23	1.77	2.67	1.00	2.00	2.00	1.40	0.071
10	0.57	0.53	0.67	0.44	1.00	0.61	0.88	1.33	0.50	1.00	1.00	0.70	0.036
11	0.57	0.53	0.67	0.44	1.00	0.61	0.88	1.33	0.50	1.00	1.00	0.70	0.036

4. Results

The eleven factors for groundwater potentiality mapping (land use/cove, geomorphology, geology, geological structure, elevation, slope, drainage density, surface water body, base map, flow accumulation, flow direction) were examined separately and describe in the following paragraphs.

4.1 Land use/cover: Land use/cover is one of the most important human-induced activity affecting the occurrence and development of groundwater. Inland use/cove, groundwater used for irrigation, industry and daily uses, etc. LULC map was classified in the water body, settlements, vegetation, and bare land. We assigned 0.062 weights to LULC map. As water body and vegetation have a high possibility of water, so assigned the highest rating. While bare and dry land area consider less significant so given lowest rating (table 1 & figure 2).

4.2 Geomorphology: To prepare a geomorphology map, we used ancillary data, satellite imagery, lithology map, land use map, and field data. For satellite image interpretation, we used interpretation key such as tone, texture, color, shape, and size, etc. In the final geomorphology map, we assigned 0.053 weights and reclassify the whole map in 5 classes based on groundwater possibility (table 1 & figure 2).

4.3 Geology: Geology layer assigned 0.067 weights. Geological structure map was derived from ancillary data and available geological maps. The whole map was divided into 5 classes according to their possibility of storage groundwater capacity (table 1 & figure 2).

4.4 Geological structure: Geology layer assigned 0.080 weights. In lithology fractures, joins, dikes and porosity are influencing features to increase groundwater storage capacity. The sedimentary aquifers with primary porosity have higher groundwater storage capacity. The lithology map was derived from ancillary data and available geological maps. The whole map was divided into 5 classes according to their possibility of storage groundwater capacity (table 1 & figure 2).

4.5 Elevation: We prepared an elevation map from ASTER-GDEM, the elevation is directly related to the ruggedness of the terrain, which has a major role in the identification of groundwater. A planning area or lower elevation with steep slope has smaller runoff, less drainage, higher infiltration rate so higher possibility of groundwater. In the study area, high elevation area has high groundwater possibility due to a higher amount of rainfall. Kalmykia has -103m lowest and

285m highest elevation point. The study area can be divided into 5 major classes as (1) higher then >120, (2) 120 to 70, (3) 70 to 25, (4) 25 to -6, and less then < - 6. Elevation layer assigned 0.036 weights (table 1 & figure 2).

4.6 Slope: Slope is directly related to groundwater because, in high slope, water velocity is high so infiltration rate is low so overall groundwater recharge possibility is low. In the other hand in lower slop, the infiltration rate is high due to low water velocity so greater chance of groundwater recharge. Slope map was prepared by ASTER-GDEM data in ArcGIS software and assigned 0.058 weights (table 1 & figure 2).

4.7 Drainage density: We used ASTER-GDEM data to prepare drainage map and later on create drainage density map via "line density" commend in ArcGIS software and in last reclassify it into 5 classes from very low to very high (table 1 & figure 2). Drainage network produces a dendritic pattern, resulting in water flow in a homogenous soil surface with the same geological conditions. The denser the drainage has the less capacity of groundwater recharge and vice versa. We assigned 0.40 weights to drainage density layer.

4.8 Base map: Base map also directly relevant to the possibility of groundwater as in study area where is a higher possibility of vegetation such as agriculture, forest and plantation show green areas. In another side, less vegetation cover area shows desert or drought areas (east-south) have less possibility of groundwater (figure 2).

4.9 Surface water: Surface waterbody is directly related to groundwater possibility. If an area has a higher number of surface water bodies then it might be a higher possibility of groundwater. Surface water assigned 0.71 weights (table 1 & figure 2).

4.10 Flow accumulation: We used ASTER-GDEM data to prepare a flow accumulation map in ArcGIS software and reclassify it into 5 classes from very low to very high (figure 2). Low accumulation values represent ridge tops so less possibility of groundwater due to low infiltration, steep slow, and higher water flow. Whereas higher accumulation values represent valleys and stream channels so a higher possibility of groundwater due to high infiltration. Flow accumulation assigned 0.036 weights (table 1 & figure 2).

4.11 Flow direction: Flow direction map gives us the flow across a surface which will always be in the steepest down-slope direction and is used to determine the stream network. Flow direction map created from ASTER-GDEM grid shows the direction of river flow from northeast to southwest and finally reached in Caspian sea. We assigned 0.036 weights to flow direction map (table 1 & figure 2).

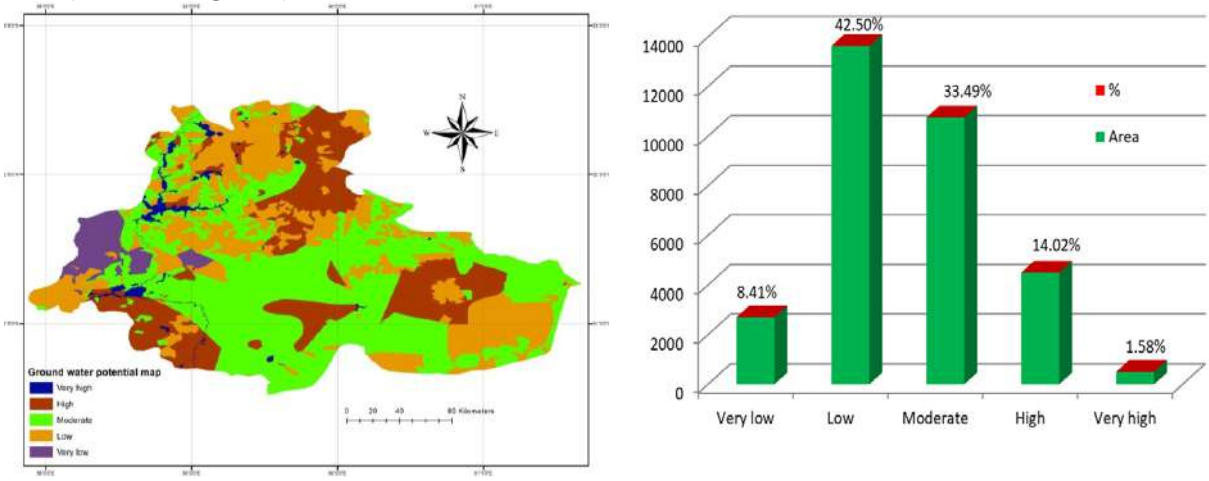

Figure 3. Groundwater potential map of Orenburg, Russia.

Finally after combined all thematic layers, we get groundwater potential zone map of Orenburg (figure 3) with five classes from very high to very low possibility of groundwater. Approximately 16% of the study area in the northwest part comes under high and a very high class, means they have the maximum possibility of groundwater. Generally, low elevations, less slop, low drainage density have high soil porosity which increases high infiltration rate of water so its increase the groundwater

possibility [11, 12]. Around 33% study area show the moderate possibility of groundwater. The north part of the study area comes under low water possibility due to its higher slop, unfavorable geological and geomorphological conditions and covers 42.50% area of the study site (figure 3).

5. Conclusion

This research work generates groundwater potential zone map of Orenburg, Russia by combined different thematic layers, which relevant to groundwater possibility by giving them specific weight in RS and GIS technology. Recent year's groundwater resources mapping has been increasing due to increased demand for water for different purposes.

6. References

[1] Minor T, Carter J 1994 The use of GIS and remote sensing in groundwater exploration for developing countries *Proceedings of the tenth thematic conference on geologic remote sensing* (San Antonio, Texas, USA, Environmental Research Institute of Michigan, Ann Arbor) MI

[2] Gustafsson P 1993 High resolution satellite data and GIS as a tool for assessment of groundwater potential of semiarid area *IXth thematic conference on geologic remote sensing* **1** 609-619

[3] Krishnamurthy J, Venkatesesa K N 1996 An approach to demarcate groundwater potential maps through remote sensing and GIS *Int J Remote Sens* **7** 1867-1884

[4] Das P, Bahara S C 1997 Hydrogeomorphological mapping in ground water exploration using remotely sensed data – a case study in Keunjhar District, Orissa *J Ind Soc Remote Sens* **25(4)** 247-260

[5] Laishram K S, Madan K Jha and Chowdary V M 2018 Assessing the accuracy of GIS-based Multi-Criteria Decision Analysis approaches for mapping groundwater potential *Ecological Indicators* **91** 24-37

[6] Choudhary K, Boori M S and Kupriyanov A 2017 Spatio-temporal analysis through remote sensing and GIS in Moscow region, Russia *CEUR Workshop Proceedings* **1901** 42-46

[7] Agarwal R, Garg P K 2016 Remote sensing and GIS based groundwater potential & recharge zones mapping using multi-criteria decision making technique *Water Resource Management* **30(1)** 243-260

[8] Choudhary K, Boori M S and Kupriyanov A 2017 Mapping and evaluating urban density patterns in Moscow, Russia *Computer Optics* **41(4)** 528-534 DOI: 10.18287/2412-6179-2017-41-4-528-534

[9] Pavelyeva E A 2018 Image processing and analysis based on the use of phase information *Computer Optics* **42(6)** 1022-1034 DOI: 10.18287/2412-6179-2018-42-6-1022-1034

[10] Choudhary K, Boori M S and Kupriyanov A 2017 mapping and evaluating urban density patterns in Moscow, Russia *Computer Optics* **41(4)** 528-534 DOI: 10.18287/2412-6179-2017-41-4-528-534

[11] Bibikov S A, Kazanskiy N L and Fursov V A 2018 Vegetation type recognition in hyperspectral images using a conjugacy indicator *Computer Optics* **42(5)** 846-854 DOI: 10.18287/2412-6179-2018-42-5-846-854

[12] Belov A M, Denisova A Y 2018 Spectral and spatial super-resolution method for earth remote sensing image fusion *Computer Optics* **42(5)** 855-863 DOI: 10.18287/2412-6179-2018-42-5-855-863

Acknowledgments

This work was partially supported by the Ministry of education and science of the Russian Federation in the framework of the implementation of the Program of increasing the competitiveness of Samara University among the world's leading scientific and educational centers for 2013-2020 years; by the Russian Foundation for Basic Research grants (# 15-29-03823, # 16-41-630761, # 17-01-00972, # 18-37-00418), in the framework of the state task #0026-2018-0102 "Optoinformation technologies for obtaining and processing hyperspectral data".

Public transport route planning in the stochastic network based on the user individual preferences

A A Borodinov[1], A S Yumaganov[1] and A A Agafonov[1]

[1]Samara National Research University, Moskovskoe Shosse 34A, Samara, Russia, 443086

e-mail: ant.agafonov@gmail.com

Abstract. Nowadays transport systems becomes more and more complex. Therefore, passengers have difficulty with route planning due to the variety of possible ways to get from the starting point to the destination one. Since the travel time often not considered as single and main criteria by passengers, it is important to take into account their own preferences which may be very different. In this paper, we proposed a stochastic route planning algorithm, which considers the user individual preferences. This method is based on the modified Dijkstra's algorithm. The proposed algorithm is tested using real public transport dataset obtained from the transportation network of Samara, Russia.

1. Introduction

Congestion of transport networks is growing everywhere. It is caused both by an increase in the number of the vehicle in large metropolitan areas and by the a prior unpreparedness of the road infrastructure created in the past to modern flows. This makes it increasingly important to solve navigation problems associated with the problems of choosing the optimal route on personal and public transport. There are many systems and applications for navigation (Yandex.Navigator and others). However, they work with a simplified static transport network graph (instead of a stochastic time-dependent graph), do not take into account predictive information about the public transport movement when building traffic routes, and do not consider user preferences for solving navigation problems. All this leads to the fact that decision-making by the user (especially on the usual traffic routes) is carried out according to subjective criteria and, often, differs from the optimal one. The solution of these problems will reduce the total time of transport correspondence in the network, increase user satisfaction and the transport infrastructure efficiency as a whole.

The article is structured as follows. The first section briefly provides a literature overview on finding the optimal route for public transport in time-dependent deterministic and stochastic transport networks. The second section describes the transport network model. The third section provides the proposed algorithm for calculating the optimal way for public transport in the stochastic network, taking into account the predictive information about the vehicles arrival time and using the individual participant preferences. The fourth section presents the formulation and results of experimental studies. In conclusion, presents the conclusion and possible directions for further research.

2. Literature review

Existing navigation systems mainly work with static transport networks, i.e. suggest that the travel time of the road segments is constant and does not depend on the time of day, weather conditions and other factors. Because the road situation is not static, to improve the movement time estimation accuracy, it is necessary to take into account the dynamic and stochastic traffic flows characteristics.

A routing methods overview in time-dependent transport networks is provided in [1]. Hierarchical routing [2] and bidirectional algorithm A* [3] were used to speed up routing algorithms.

The multicriterial algorithm for finding the shortest path in the stochastic network A* was presented in [4]. It was assumed in the paper that the transit time values of adjacent road segments are correlated.

Modern methods for solving the navigation problem in stochastic time-dependent transport networks simulate the road segments transit time as a random variable with a time-dependent distribution function [5, 6, 7].

A separate task is to combine the routeing reliability and the expected time of movement. Most works use the average risk model [8, 9], which takes into account the average and variance of the road segments travel time within a linear objective function that needs to be optimized. The objective function coefficients are often chosen heuristically based on experimental studies.

The main problem in multimodal transport systems is a uniform information combination about the various movement modes [10]. The most common approach is to build a transport network graph, in which various traffic routes are connected by edges, meaning transplants at stopping points.

Moreover, it is necessary to take into account the importance of user individual preferences, when routing in multimodal transport systems. Often travel time is not the only criterion for choosing a route. The transfers number, fare, vehicles waiting time, etc. should be taken into account. [11]. Therefore, multi-criteria optimization algorithms should be used to improve accuracy.

A research separate area is finding the optimal navigation strategy, which is a hierarchical rule for deciding the further route choice based on actual passenger transport movement data. The spatial and temporal stochastic transit time dependencies of road segments are investigated in [12]. In the article [13] the authors included actual information on the movement of the vehicle in the navigation strategy.

In the article [14] presented an algorithm for finding the shortest path on public transport, taking into account dynamic and stochastic information about the movement of the vehicle. Emphasis is placed on the practical implementation of the algorithm. The article [15] presents a routing algorithm that simultaneously takes into account the stochastic transit time of the road segments and the vehicles waiting time and optimizes both the routes speed and reliability.

This paper presents an algorithm for calculating the optimal way for public transport in a stochastic network. In contrast to [14, 15], the arrival time is used to take into account waiting times based on current and predicted information on the movement of the vehicle, instead of the vehicles movement frequency. In addition, the algorithm takes into account user preferences when choosing the parameters of the target optimization function.

3. Transport Network Model

The transport network will be considered as a directed graph $G = (N, E)$, vertices $n_i \in N$ of which correspond to stops, edges $e_ij \in E, i \in V, j \in V$ - to segments of the transport network with length $|e_{ij}|$, each stop being represented by at least three vertices of the graph.

We introduce the following notation: S_k - stop from set S; R_i - passenger transport route from the set R.

The part of the graph representing the two routes R_1 and R_2, containing the common stop S_k, is shown in figure 1.

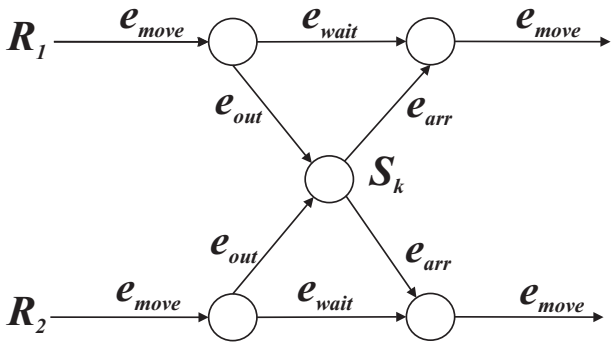

Figure 1. The route network graph structure.

The graph contains edges of several types:

- e_{move} - represents the segment of the route between stops, characterized by the average time μ_{ij} and the dispersion σ_{ij};
- e_{wait} - waiting for passengers boarding/alighting at the bus stop, in the work, constant waiting time is used as the edge weight;
- e_{out} - alighting edge, in the work as the edge weight is used constant alighting time;
- e_{arr} - boarding edge (vehicle waiting) is determined by the vehicle arrival time of the corresponding route to stop;
- e_{walk} (not shown in the figure) - walk from stops to the points of departure/arrival, the edge weight depends on the transition distance;

The route finding task is reduced to the task of finding the shortest path in the graph. The algorithm for solving the problem in a time-dependent stochastic transport network, taking into account the road users individual preferences, is presented in the next section.

4. Algorithm for finding the shortest path

Dijkstra's modified algorithm is used to find the shortest path in a time-dependent stochastic transport network [14] (algorithm 1).

The algorithm uses the pair $(n_i, cost_i)$ as the vertex label l_i, containing the vertex n_i and the multidimensional route price $cost_i$, which must be spent to reach the vertex n_i from the departure vertex n_s. The route price is represented as a pair $cost_i = (c_i, t_i)$, where c_i - the generalized price, t_i - the trip time.

The queue with priority pq determines the next vertex to be viewed based on the generalized price c_i. Associative arrays $predMap$ and $costsMap$ respectively are used to store the previous vertex for the given and the trip price to the specified vertex.

In the algorithm, the getCost() and getTime() functions - getting the generalized price c_i and time t_i from the price of reaching the vertex $cost_i$.

The main interest is the estimation obtaining function of the passing the graph edge price $calculateCost()$. The proposed method for determining the cost of an edge depending on its type is described in Algorithm 2. In algorithm 2, the following notation is used:

- $t_{wait} = 30$ (seconds) - alighting/boarding time;
- $t_{out} = 10$ (seconds) - alighting time;

Algorithm 1: Algorithm for finding the shortest path

Input data: departure vertex n_s, arrival vertex n_d,
departure time t
Output data: shortest path
`// Initialization`
PriorityQueue $pq = \emptyset$
Map $predMap = \emptyset$
Map $costsMap = \emptyset$
Label $l_s = Label(n_s, cost_s)$
pq.insert(l_s)
while $!pq = \emptyset$ **do**
  Label $l_i = pq$.pop()
  $n_i = l_i$.getNode()
  foreach $e_{ij} \in E$ **do**
    $cost_j = calculateCost(e_{ij}, t + l_i$.getCost().getTime())
    if $cost_j$.getCost() $> costsMap$.get(n_i).getCost() **then**
      continue;
    end
    $costsMap$.put($n_j, cost_j$)
    $predMap.put(n_j, n_i)$
    Label $l_j = Label(n_j, cost_j)$
    pq.insert(l_j)
  end
end

- t_{arr} - the vehicle arrival estimated time at the stop;
- $s_{walk} = 1$ (m/s) - walking speed;
- $\alpha_0, \alpha_1, \alpha_2$ -individual preferences parameters that affect the reliable path choice, the transfers number and walking distance.

5. Experiment

Experimental studies of the developed method were carried out for the Samara street-road network. The road network consists of 48139 segments. The data on the passenger transport bus routes movement were used to predict the time of arrival.

Six pairs of different departure and arrival vertices on the transport network graph were chosen to study the algorithm quality, after which for each pair they solved the problem of finding a way on public transport, varying the departure time.

Two standard metrics were used to compare the prediction quality: Mean Absolute Percentage Error (MAPE) and Mean Absolute Error (MAE).

$$\text{MAPE} = \frac{1}{N}\sum_{i=1}^{N}\frac{|t_i - \hat{t}_i|}{t_i} \times 100\%$$

$$\text{MAE} = \frac{1}{N}\sum_{i=1}^{N}|t_i - \hat{t}_i|$$

where t_i - is the actual route time value, $\hat{t}_i$ - the predicted value, N - number of experiments.

Algorithm 2: *calculateCost*

Input data: graph edge e_ij, arrival time t to the vertex i
Output data: cost $cost_j = (c_j, t_j)$
if e_{ij} *is* e_{move} **then**
  `// route segment between stops`
  return $(\mu_{ij} + \alpha_0\sqrt{\sigma_{ij}},\ \mu_{ij})$;
end
else if e_{ij} *is* e_{wait} **then**
  `// alighting/boarding`
  return $(t_{wait},\ t_{wait})$;
end
else if e_{ij} *is* e_{out} **then**
  `// alighting`
  return $(t_{out},\ t_{out})$;
end
else if e_{ij} *is* e_{arr} **then**
  `// waiting for transport`
  return $(\alpha_1(t_{arr} - t),\ t_{arr} - t)$;
end
else if e_{ij} *is* e_{walk} **then**
  `// foot transition`
  return $(\alpha_2|e_{ij}|/s_{walk},\ |e_{ij}|/s_{walk})$;
end

The average trip time was $t_{avg} = 2645$ seconds. The following values were obtained from the experimental analysis results: $MAPE = 6.62\%$, $MAE = 179.8$ seconds. The obtained values allow us to conclude about the good quality of the proposed algorithm..

6. Conclusion

The paper presents an algorithm for calculating the shortest path on public transport in a stochastic time-dependent transport network that takes into account the average time and variance of the road segment travel time when building a route. The proposed algorithm uses real-time data and forecast data on the movement of vehicles to estimate the waiting time for public transport at bus stops. Algorithm parameters are selected according to individual user preferences.

Experimental analysis of the proposed algorithm showed high accuracy in estimating the time of movement, which is close to real time along the selected route.

A further work direction includes comparing the proposed algorithm with other algorithms for solving the navigation problem, as well as modifying the edge weight estimating function to increase the found route reliability of motion.

7. References

[1] Delling D and Wagner D 2009 Time-dependent route planning *Lecture Notes in Computer Science (including subseries Lecture Notes in Artificial Intelligence and Lecture Notes in Bioinformatics)* **5868** 207-230
[2] Delling D and Nannicini G 2012 Core routing on dynamic time-dependent road networks *INFORMS Journal on Computing* **24** 187-201

[3] Nannicini G, Delling D, Schultes D and Liberti L 2012 Bidirectional A* search on time-dependent road networks *Networks* **59** 240-251
[4] Chen B Y, Lam W H K, Sumalee A and Li Z -l. 2012 Reliable shortest path finding in stochastic networks with spatial correlated link travel times *International Journal of Geographical Information Science* **26** 365-386
[5] Miller-Hooks E D and Mahmassani H S 2000 Least expected time paths in stochastic, time-varying transportation networks *Transportation Science* **34** 198-215
[6] Sun S, Duan Z, Sun S and Yang D 2014 How to find the optimal paths in stochastic time-dependent transportation networks? *17th IEEE International Conference on Intelligent Transportation Systems, ITSC* 2348-2353
[7] Agafonov A A and Myasnikov V V 2016 Method for the reliable shortest path search in time-dependent stochastic networks and its application to GIS-based traffic control *Computer Optics* **40(2)** 275-283 DOI: 10.18287/2412-6179-2016-40-2-275-283
[8] Lim S, Sommer C, Nikolova E and Rus D 2013 Practical route planning under delay uncertainty: Stochastic shortest path queries *Robotics: Science and Systems* **8** 249-256
[9] Nikolova E 2010 Approximation algorithms for reliable stochastic combinatorial optimization *Lecture Notes in Computer Science (including subseries Lecture Notes in Artificial Intelligence and Lecture Notes in Bioinformatics)* **6302** 338-351
[10] Grasman S E 2006 Dynamic approach to strategic and operational multimodal routing decisions *International Journal of Logistics Systems and Management* **2** 96-106
[11] Grbener T, Berro A and Duthen Y 2010 Time dependent multiobjective best path for multimodal urban routing *Electronic Notes in Discrete Mathematics* **36** 487-494
[12] Gao S, Frejinger E and Ben-Akiva M 2010 Adaptive route choices in risky traffic networks: A prospect theory approach *Transportation Research Part C: Emerging Technologies* **18** 727-740
[13] Wu C, Zhang X and Dong Y 2014 Adaptive route guidance based on real-time information in stochastic time-dependent transportation networks *17th IEEE International Conference on Intelligent Transportation Systems, ITSC* 2392-2397
[14] Demeyer S, Audenaert P, Pickavet M and Demeester P 2014 Dynamic and stochastic routing for multimodal transportation systems *IET Intelligent Transport Systems* **8** 11223
[15] Ni P, Vo H T, Dahlmeier D, Cai W, Ivanchev J and Aydt H 2015 DEPART: Dynamic Route Planning in Stochastic Time-Dependent Public Transit Networks *IEEE Conference on Intelligent Transportation Systems, Proceedings, ITSC* 16727

Acknowledgments
The reported study was funded by the Ministry of Science and Higher Education of the Russian Federation (unique project identifier RFMEFI57518X0177).

Optimal filtering of multidimensional random fields generated by autoregressions with multiple roots of characteristic equations

N A Andriyanov[1,2], K K Vasiliev[1]

[1]Ulyanovsk State Technical University, Severny Venets, 32, Ulyanovsk, Russia, 432027
[2]Ulyanovsk Civil Aviation Institute, Mozhaiskogo, 8/8, Ulyanovsk, Russia, 432071

e-mail: nikita-and-nov@mail.ru

Abstract. The use of mathematical models allows to compare the theoretical expressions and simulation results. Autoregressive random fields can be used for description of the images, however, such models have pronounced anisotropy, and the simulated images are too sharp. The elimination of this drawback is possible through the use of models with multiple roots of characteristic equations. The analysis shows that using models with multiple roots in filtering images with smoothly varying brightness provides smaller errors than the use of autoregressive random fields. However, studies of the dependences of filtering efficiency on various model parameters and signal-to-noise ratios for multidimensional autoregressive random fields were almost not carried out. The article discusses the solution of the problem of optimal filtering of images based on models with multiple roots of characteristic equations. Theoretical dependences of the relative variance of the filtering error on the dimension of random fields are obtained. Furthermore, it was presented some results of filtering real images by such model in comparison with autoregressive model.

1. Introduction

Currently there are many different mathematical models of random fields (RF) using for describing images [1-5]. The popularity of this approach is due to a number of advantages that mathematical models provide. First of all, it is the generation of sufficiently large volumes of material for research, and also mathematical models act as a tool for developing and testing various algorithms. The simplest autoregressive models generate RF with pronounced anisotropy and such models are suitable for describing only a narrow class of real multidimensional images. Doubly stochastic models [6,7] provide a change in the probabilistic properties of the generated RF at each point, but on average the properties of such a model depend on the model chosen for the main RF simulation. Therefore, to obtain RFs that are close to isotropic fragments of multispectral images, it is necessary to use autoregression with multiple roots of characteristic equations [8–10].

However, one of the main tasks of signal processing is the noise reducing or filtering. It is often considered that the observed signal is an additive mixture of the information (useful) signal and white noise. In this paper we analyze the efficiency of spatial Wiener filtering of multidimensional autoregressive RFs with multiple roots of characteristic equations against additive white Gaussian noise background. At the same time the investigation is aimed at such models of different multiplicities, which provide equivalent correlation properties. The developed filtering algorithms can become very useful tool in solving various applied problems of image processing, among which an

important place is occupied by the detection and localization of various objects in the image [11,12]. Furthermore filtering and segmentation tasks are of interesting [13,14].

2. Model of a multidimensional random field and its linear filter

The following equations are commonly used to describe a multidimensional autoregressive Gaussian RF

$$x_{\bar{i}} = \sum_{\bar{j}\in D} \alpha_{\bar{j}} x_{\bar{i}-\bar{j}} + \sigma_x \beta_0 \xi_{\bar{i}}, \bar{i} \in \Omega, \quad (1)$$

where $X = \{x_{\bar{i}}, \bar{i} \in \Omega\}$ is simulated RF defined on *N*-dimensional grid $\Omega = \{\bar{i} = (i_1, i_2, \ldots i_N) : i_k = 1 \ldots M_k,\ k = 1 \ldots N\}$; $\{\beta_0, \alpha_{\bar{j}}, \bar{j} \in D\}$ are coefficients of the model; $\{\xi_{\bar{i}}, \bar{i} \in \Omega\}$ is RF of random values with Gaussian distribution having zero mathematical expectation, and its variance is equal to one; σ_x^2 is variance of RF $x_{\bar{i}}$; $D \subset \Omega$ is causal region of local states.

For such a model it is easy to find the transfer function of a linear filter. Using Z-transformation for model (1) it is possible to get a spatial linear filter, which is described by the transfer function of the following form

$$H(\bar{z}) = \frac{\sigma_x \beta_0}{1 - \sum_{\bar{j}\in D} \alpha_{\bar{j}} \bar{z}^{-\bar{j}}}, \quad (2)$$

where $\bar{z}^{-\bar{j}} = z_1^{-j_1} z_2^{-j_2} \ldots z_N^{-j_N}$.

It should be noted that the transfer function (2) also depends on the parameters of the signal model, as does the energy spectrum of such a RF. The relationship of the transfer function (2) and the energy spectrum of the RF *X* is determined by the expression

$$S_x(\bar{z}) = H(\bar{z}) H(\bar{z}^{-1}). \quad (3)$$

The analysis of probabilistic properties of the RF is simplified if the transfer function of a multidimensional filter can be factorized: $H(\bar{z}) = \prod_{k=1}^{N} H_k(z_k)$. Then the energy spectrum $S_x(\bar{z}) = \prod_{k=1}^{N} S_k(z_k)$ and correlation function (CF) $B(\bar{r}) = \prod_{k=1}^{N} B_k(r_k)$ are also can be factorized. Simple and very useful for applications multidimensional splittable RF $x_{\bar{i}}$ can be represented using spatial autoregression

$$\prod_{k=1}^{N} (1 - \rho_k z_k^{-1})^{m_k} x_{\bar{i}} = \sigma_x \beta_0 \xi_{\bar{i}}, \bar{i} \in \Omega, \quad (4)$$

with multiple roots ρ_k of characteristic equations having multiplicities m_k, $k = 1, 2, \ldots, N$.

The transfer function of such a RF will be factorizable and will be written as

$$H(\bar{z}) = \sigma_x \beta_0 \Big/ \prod_{k=1}^{N} (1 - \rho_k z_k^{-1})^{m_k}, \quad (5)$$

where $\beta_0 = \prod_{k=1}^{N} \beta_k$; $\beta_k(m_k) = (1 - \rho_k^2)^{2m_k - 1} / \sum_{l=0}^{m_k - 1} (C_{m_k-1}^{l} \rho_k^l)^2$, $C_j^i = j! / (i!(j-i)!)$.

3. Filtering efficiency of multidimensional random fields with multiple roots of characteristic equations

One of the difficult tasks of filtering image sequences on multidimensional grids is the analysis of the effectiveness of such filtering. In this case, the necessary criterion for analysis is the dependence of the variance of the filtering error on various model parameters and noise. Formally, spatial covariance

matrices of estimation errors can be calculated using the recurrence relations for the Kalman filter [6,7]. However, if it is necessary to compare the algorithms for different values of the parameters of the stochastic equations and noise levels, the determination of even steady-state values of the elements of the covariance matrices becomes a very laborious task.

Consider a relatively simple way to determine the effectiveness of estimating homogeneous fields on infinite grids based on the basic principles of Wiener's filter theory [8]. Using the observations $z_{\bar{j}} = x_{\bar{j}} + n_{\bar{j}}$, $\bar{j} = (j_1\ j_2 \ldots j_N)^T \in \Omega$, which are the sum of informational (useful) RF and additive white Gausian noise with a variance $\sigma^2 = M\left\{n_{\bar{j}}^2\right\}$ it is necessary to make the best (in the sense of the minimum error variance) linear estimate $\hat{x}_{\bar{0}} = \sum_{\bar{j}\in\Omega} h_{\bar{j}} z_{\bar{j}}$ of element $x_{\bar{0}}$ in informational RF. This estimation will use coefficients $h_{\bar{j}}$ which will determine the optimal filtering. The search of minimum error variance $\sigma_\varepsilon^2 = M\left\{\left(\hat{x}_{\bar{0}} - x_{\bar{0}}\right)^2\right\} = M\left\{\left(\sum_{\bar{j}\in\Omega} h_{\bar{j}} z_{\bar{j}} - x_{\bar{0}}\right)^2\right\}$ can be written as a system of linear equations

$$h_{\bar{q}}\sigma^2 + \sum_{\bar{j}\in\Omega} h_{\bar{j}} B(\bar{r} - \bar{j}) = B(\bar{r}), \quad \bar{r} \in \Omega, \tag{6}$$

which can be considered as a spatial analogue of the Wiener-Hopf equations.

Using multidimensional $z-$transformation it is possible to find equations system solution and expression for the relative error variance [8]:

$$\frac{\sigma_\varepsilon^2}{\sigma_ч^2} = \frac{1}{(2\pi)^N} \int_{-\pi}^{\pi} \ldots \int_{-\pi}^{\pi} \frac{\beta_0^2}{\prod_{k=1}^{N} \left(1 + \rho_k^2 - 2\rho_k \cos\lambda_k\right)^{m_k} + q\beta_0^2} d\bar{\lambda}. \tag{7}$$

where $q = \sigma_x^2 / \sigma^2$ is signal-to-noise ratio, N is the dimension of RF, m_k is the model's multiplicity for *k-th* dimension, ρ_k is correlation parameter in *k-th* dimension.

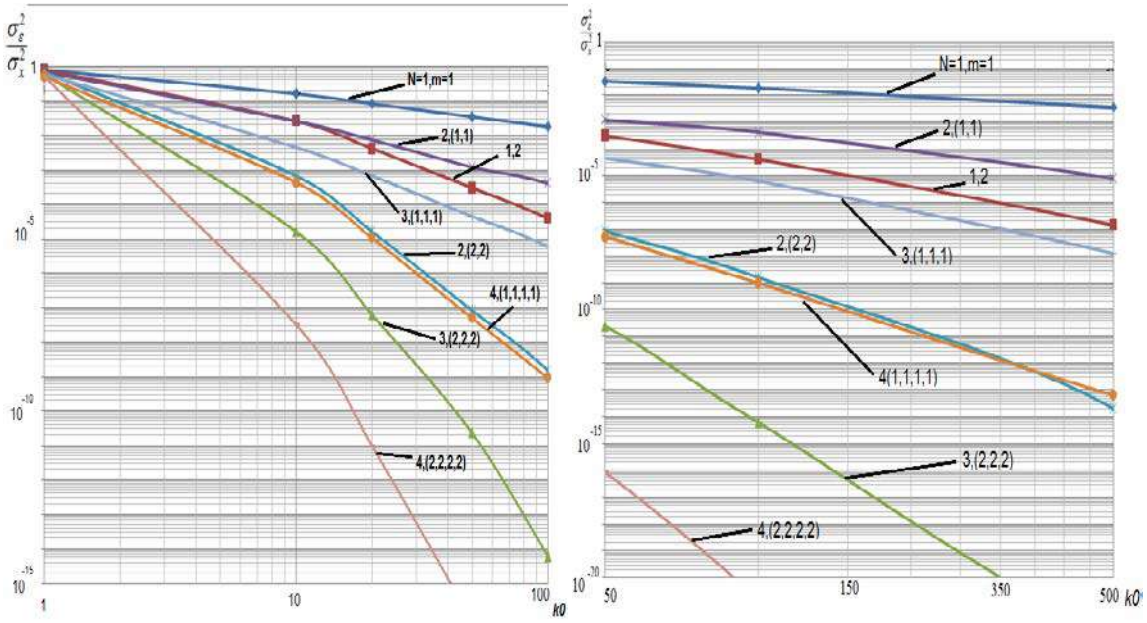

a) b)

Figure 1. Relative variances of errors of multidimensional RF.

Figure 1 shows the dependence of the relative error of the filter variance on the correlation interval k_0 for models of different dimensions and orders with *q=0.1*. Correlation interval is less than 100 in figure 1a and less than 500 in figure 1b. This interval determines the equivalence of models of different multiplicities. On the graphs, the dimension is indicated as *N*, the multiplicity as *m*.

The analysis of the obtained dependences shows that with sufficiently small correlation intervals $(k_0 < 10)$ the variances of filtering errors of autoregressive RF of the 1st and 2nd orders are rather close. An increase in the dimensions and a further increase in the correlation interval leads to the distancing of the curves. At the same time the smallest values of relative variances of filtering errors are obtained for the cases *N=3, m=(2,2,2), N=4, m=(2,2,2,2)*. This is because when *m=1* autoregression along the axes are quite prickly and their filtering is a more difficult task.

Using expression (7), one can obtain the following equations for models of various dimensions, presented in Table 1.

Table 1. Filtering efficiency of RFs of different dimensions.

N	$\sigma_\varepsilon^2 / \sigma_x^2$
1	$\frac{1}{2\pi}\int_{-\pi}^{\pi}\frac{\beta_0^2}{(1+\rho_1^2-2\rho_1\cos\lambda_1)^{m_1}+q\beta_0^2}d\lambda_1$
2	$\frac{1}{(2\pi)^2}\int_{-\pi}^{\pi}\int_{-\pi}^{\pi}\frac{\beta_0^2}{(1+\rho_1^2-2\rho_1\cos\lambda_1)^{m_1}(1+\rho_2^2-2\rho_2\cos\lambda_2)^{m_2}+q\beta_0^2}d\lambda_1 d\lambda_2$
3	$\frac{1}{(2\pi)^3}\int_{-\pi}^{\pi}\int_{-\pi}^{\pi}\int_{-\pi}^{\pi}\frac{\beta_0^2}{(1+\rho_1^2-2\rho_1\cos\lambda_1)^{m_1}(1+\rho_2^2-2\rho_2\cos\lambda_2)^{m_2}(1+\rho_3^2-2\rho_3\cos\lambda_3)^{m_3}+q\beta_0^2}d\lambda_1 d\lambda_2 d\lambda_3$
4	$\frac{1}{(2\pi)^4}\int_{-\pi}^{\pi}\int_{-\pi}^{\pi}\int_{-\pi}^{\pi}\int_{-\pi}^{\pi}\frac{\beta_0^2}{(1+\rho_1^2-2\rho_1\cos\lambda_1)^{m_1}(1+\rho_2^2-2\rho_2\cos\lambda_2)^{m_2}(1+\rho_3^2-2\rho_3\cos\lambda_3)^{m_3}(1+\rho_4^2-2\rho_4\cos\lambda_4)^{m_4}+q\beta_0^2}d\lambda_1 d\lambda_2 d\lambda_3 d\lambda_4$

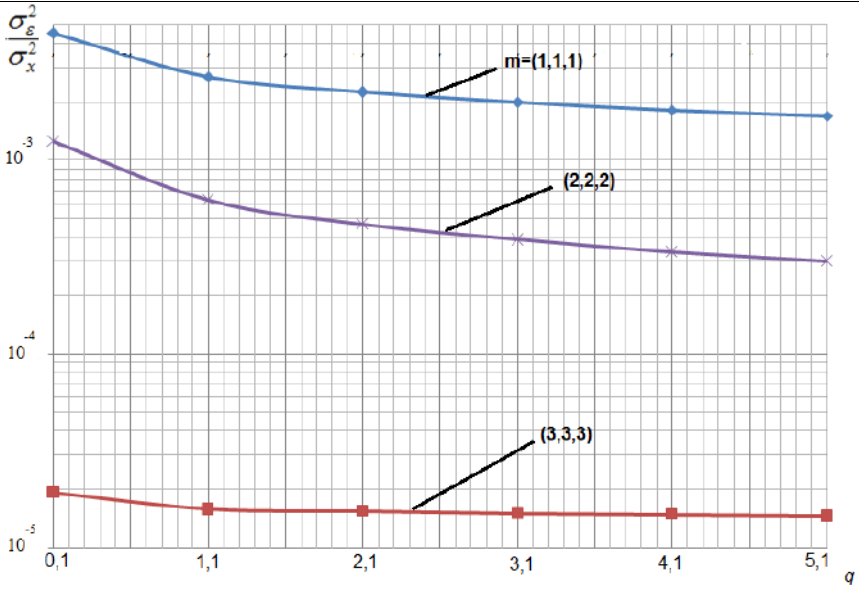

Figure 2. Relative variances of filtering errors for three-dimensional RF.

Figure 2 shows the dependences of the relative error of filtering variance on the signal-to-noise ratio q for models of three-dimensional RF of different orders with k_0 *=50*.

An analysis of the curves in the graph shows that in the case of a large dimension of the RF, for example N = 3, the variance of the filtration error is rather small. In this connection, effective filtering is obtained both for small signal-to-noise ratios and for large ones. At the same time, an increase in the multiplicity of models leads to a decrease in the relative dispersion of the filtering error.

Figure 3 shows the dependences of the relative variance of filtering errors on the dimension of the AR for the cases *k0*=100, *q*=0.01 with multiplicities *m=1* and *m=2*.

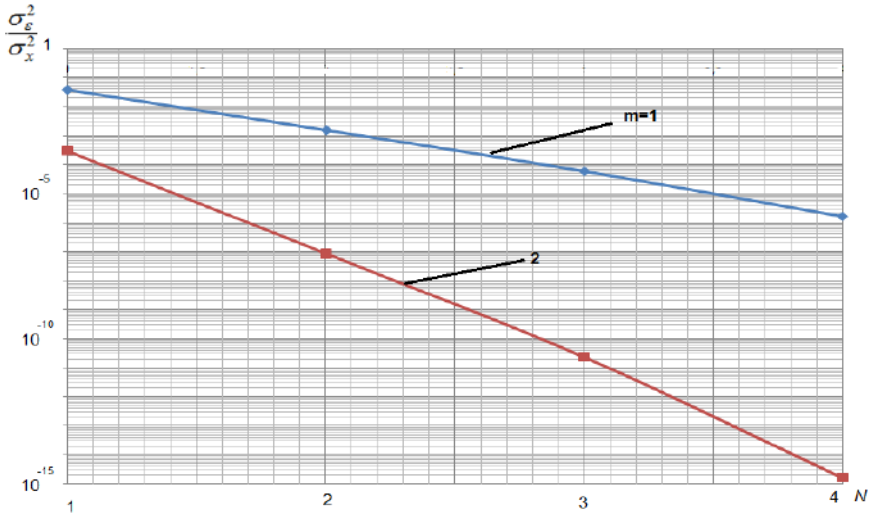

Figure 3. Dependence of the relative error variance on the dimension.

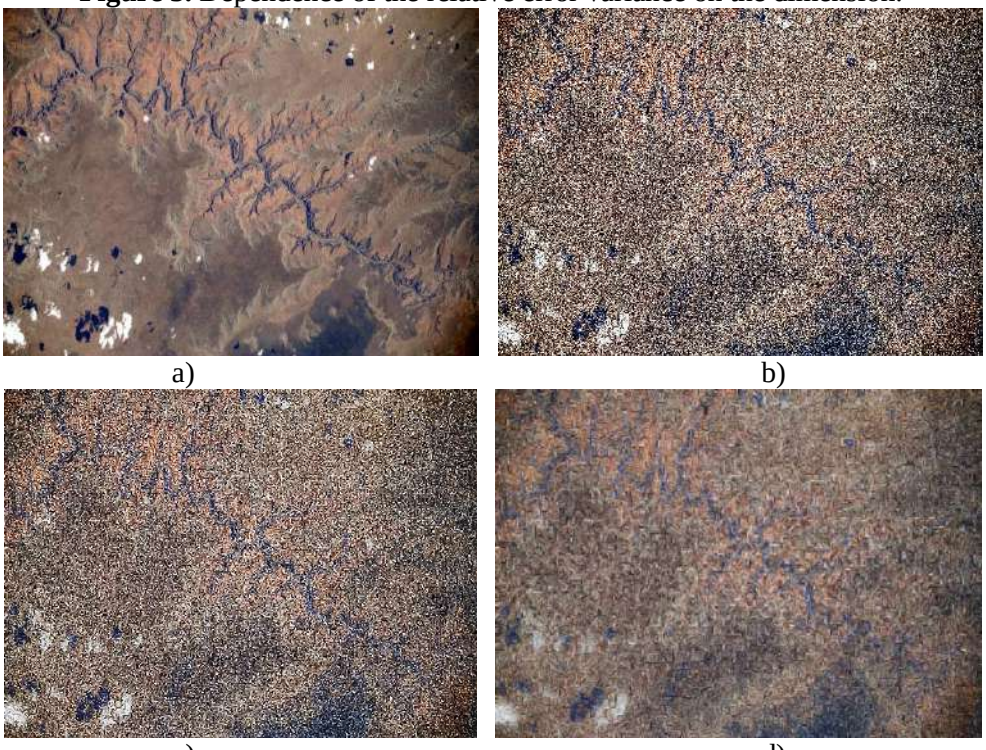

a) b)

c) d)

Figure 4. Filtering of satellite images.

The analysis of the curves presented in Figure 3 shows that increasing the dimension of the RF leads to a significant increase in filtration efficiency, which is associated with a large number of correlations in the multidimensional model. At the same time large dimensions provide variance of filtering errors tending to 0 (~10^{-15}) already with multiplicities *m=2* along each axis. At the same time if *m=1* then the variance of the filtering error is several orders of magnitude greater.

4. Real image processing

The filtering algorithm based on a multiple-root model was tested on a multidimensional satellite image compared to an algorithm based on autoregressive models. Figure 4 shows the filtering results

for one of the images. Figure 4a shows the source image, figure 4b shows the noisy image, figure 4c shows the filtering results using autoregressive model of the first order and figure 4d shows the filtering results using autoregressions with multiple roots model.

The analysis of the presented pictures shows the model with multiple roots provides better results in variance of filtering error, for example, the results for image on figure 4 is following: relative error variance for figure 4c is 0.782, error variance for figure 4d is 0.358. The signal-to-noise ratio is 0.5.

5. Conclusion

Thus, in this paper, the filtration efficiency of multidimensional RF with multiple roots of characteristic equations is investigated. At the same time, an increase in the dimensions and orders of the models leads to a significant decrease in the relative dispersion of filtering error. Therefore, it is advisable to use less computationally sophisticated mathematical models of RFs that provide fairly small errors. For example, already for the dimension $N=3$ it is possible to achieve relative error equal 10^{-5} for q=0.01 and multiplicities m=(3,3,3). In addition, studies have been conducted on the effectiveness of filtration depending on the dimension of the RF. It should be noted that in the logarithmic axes, these dependencies are close to linear for the dimensions $N=1,...,4$. Such models are also useful in processing real images having strong correlation properties.

6. References

[1] Ohtsu K, Peng H and Kitagawa G 2015 Time Series Analysis Through AR Modeling *Time Series Modeling for Analysis and Control* (Springer Briefs in Statistics. Springer, Tokyo) 7-56

[2] Aue A, Horvath L 2011 Quasi-Likelihood Estimation In Stationary And Nonstationary Autoregressive Models With Random Coefficients *Statistica Sinica* **21** 973-999

[3] Praline E Yu 2017 Trends in the processing of random fields in modeling *Collection of scientific works based on proceedings of conference New paradigm of science and education: on the way to the convergence of knowledge, technology* 72-73

[4] Vasil'ev K K, Dement'ev V E and Andriyanov N A 2015 Doubly stochastic models of images *Pattern Recognition and Image Analysis. Advances in Mathematical Theory and Applications* **25(1)** 105-110

[5] Bolin, D 2012 *Models and Methods for Random Fields in Spatial Statistics with Computational Efficiency from Markov Properties* (Centre for Mathematical Sciences, Mathematical Statistics, Lund University) 118-126

[6] Vasiliev K, Dementiev V and Andriyanov N 2018 Representation and processing of multispectral satellite images and sequences *Procedia Computer Science* **126** 49-58 DOI: 10.1016/j.procs.2018.07.208

[7] Andriyanov N A 2018 Software Complex for Representation and Processing of Images with Complex Structure *CEUR Workshop Proceedings* **2274** 10-22

[8] Andriyanov N A, Vasiliev K K 2018 Use autoregressions with multiple roots of the characteristic equations to image representation and filtering *CEUR Workshop Proceedings* **2210** 273-281

[9] Vasiliev K K, Andriyanov N A 2017 Analysis of autoregression with multiple roots of characteristic equations *Radiotekhnika* **6** 13-17

[10] Vasiliev K K, Andriyanov N A and Abdulkadim Kh A 2018 Filtration efficiency of random fields with multiple roots of characteristic equations *Radiotekhnika* **6** 20-23

[11] Ilyasova N A, Paringer R, Shirokanev A, Kupriyanov A and Ushakova N 2017 Smart feature selection technique for object localization in ocular fundus images with the aid of color subspaces *Procedia Engineering* **201** 736-745

[12] Andriyanov N A, Vasiliev K K and Dementiev V E 2017 Anomalies detection on spatially inhomogeneous polyzonal images *CEUR Workshop Proceedings* **1901** 10-15 DOI: 10.18287/1613-0073-2017-1901-10-15

[13] Filimonov P A, Belov M L, Fedotov Yu V, Ivanov S E and Gorodnichev V A 2018 Aerosol

inhomogeneity segmentation algorithm *Computer Optics* **42(6)** 1062-1067 DOI: 10.18287/2412-6179-2018-42-6-1062-1067

[14] Chervyakov N I, Lyakhov P A and Orazaev A R 2018 Two methods of adaptive median impulse noise filtering on images *Computer Optics* **42(4)** 667-678 DOI: 10.18287/2412-6179-2018-42-4-667-678

Acknowledgement
The study was supported by RFBR, Project №17-01-00179.

Solution for the problem of the parameters identification for autoregressions with multiple roots of characteristic equations

N A Andriyanov[1,2], M N Sluzhivyi[1]

[1]Ulyanovsk State Technical University, Severny Venets, 32, Ulyanovsk, Russia, 432027
[2]Ulyanovsk Civil Aviation Institute, Mozhaiskogo, 8/8, Ulyanovsk, Russia, 432071

e-mail: nikita-and-nov@mail.ru

Abstract. When describing a real image using a mathematical model, the problem of model parameters identification is of importance. In this case the identification itself is easier to perform when a particular type of model is known. In other words, if there is a number of models characterized by different properties, then if there is a correspondence with the type of suitable images, then the model to be used can be determined in advance. Therefore, in this paper, we do not consider the criteria for model selection, but perform the identification of parameters for autoregressive models, including those with multiple roots of characteristic equations. This is due to the fact that the effectiveness of identification is verified by the images generated by this model. However, even using this approach where the model is known, one must first determine the order of the model. In this regard, on the basis of Yule-Walker equations, an algorithm for determining the order of the model is investigated, and the optimal parameters of the model are also found. In this case the proposed algorithm can be used when processing real images.

1. Introduction

Mathematical modeling is used in many areas of science and technology, including image processing. In particular, methods focused on the description of images using models of random fields (RF), allow the development of algorithms for parameter estimation, filtering, detection of anomalies in the background of images and analyze them for a large number of simulated images.

There exist many images that are characterized by a smooth change in brightness [1,2]. Usually such images have a slowly decreasing correlation function (CF) in a certain given neighborhood. The first-order autoregressive (AR) image models [3,4] do not provide a strong correlation between pixels, since its CF decreases exponentially. Meanwhile, separable RFs that can be generated by one-dimensional autoregression with multiple roots of characteristic equations [5-6] are known. An important feature of ARs with multiple roots is their considerable simplicity compared to arbitrary high-order ARs. Also doubly stochastic models are used to describe real images [7-10]. However, if the structure of the described image is not so complicated, then it is better to use simpler models. This is due to the fact that the computational complexity of a double-stochastic model is much higher than, for example, a model with multiple roots, for which the AR of any order can be described using a single parameter.

At the same time, when describing images, for example, satellite images using mathematical models, it is necessary to identify parameters of the model. At the same time, the model should be selected in such a way that a compromise is found between its complexity and the similarity of the

simulated image with the real one. The paper discusses the solution of the problem of the parameters identification for AR models with multiple roots of characteristic equations, which, owing to the separability of the CF, can significantly simplify this task. It should be noted that the application of the parameter identification approach based on Yule-Walker equations to determining the order and correlation parameters of AR models with multiple roots has a scientific novelty.

2. Brief overview of the parameters identification methods for a random processes

At present, the identification task for AR processes, the moving average (MA) and autoregression with moving average model (ARMA) by single-channel observations without noise is the most well-studied. Especially many methods have been developed for estimating the parameters of such processes. The estimation methods are based either on the direct use of observations, or on the initial calculation of the sample statistical characteristics (autocorrelations, spectral densities) from these observations, and then using them to determine parameter estimates. The first group of methods includes the least squares method (LSM) for the AR process [10,11], the maximum likelihood method (ML) for the AR, MA, and ARMA processes, and various types and modifications of these methods [12-14]. The second group is the Yule-Walker method for the AR process [13], the Box and Jenkins correlation methods for the ARMA, MA [13] processes, the Lindberger method for the AR, MA, and ARMA processes [15], the Durbin method for the MA process [16] , the Cleveland inverse autocorrelation method for the ARMA process [17] and other methods [18]. In both groups, there are methods in which parameter estimates are calculated by linear algorithms by solving a certain system of linear equations for example, LSM and Yule-Walker method for the AR process, as well as methods that use nonlinear methods for calculating estimates, which are reduced to numerical minimization algorithms for a certain function of the parameters, for example, the ML method and the Lindberger method for the APMA processes. The methods for determining the class of processes that can be AR, MA, and ARMA are much less developed [19]. In the work of Kitler and Whitehead [20], the problem of class determination is reduced to the problem of determining the order of the ARMA process. Therefore, the solution of the determination order and class of the model task is of interest. In the simplest case, such a task is reduced to a problem when it is necessary to determine its order using the selected model of AR. So optimal identification is very important for satellite image processing [21,22].

3. Autoregressions with multiple roots of characteristic equations

Using AR models with multiple roots of characteristic equations, it is possible to obtain realizations of RFs that will be close in their properties to real images. In this case an important property of the generated RF will be its quasi-isotropy. The general formula for models of different multiplicities can be written as follows

$$x_{i,j} = \beta\xi_{i,j} - \sum_{i_1=0}^{N_1}\sum_{j_1=0}^{N_2}\alpha_{i_1,j_1}x_{i-i_1,j-j_1}, \quad (1)$$

where N_1 and N_2 characterize the multiplicity of the model; coefficients $\alpha_{i_1,j_1}(\alpha_{0,0}=0)$ are the products of the corresponding coefficients of one-dimensional AR along the axes x and y

$$\alpha_{i_1,j_1} = \alpha_{xi_1}\alpha_{yj_1}. \quad (2)$$

The coefficients of one-dimensional AR (2) can be obtained using expressions

$$\alpha_{xi_1}(\rho_x, N_1) = (-1)^{i_1+1}C_{N_1}^{i_1}\rho_x^{i_1}, \alpha_{yj_1}(\rho_y, N_2) = (-1)^{j_1+1}C_{N_2}^{j_1}\rho_y^{j_1}, \quad (3)$$

where $C_n^m = \frac{n!}{m!(n-m)!}$. Two-dimensional model's coefficient β is the normalized product of the corresponding coefficients of one-dimensional AR along the axes x and y

$$\beta = \frac{\sigma_x}{\sigma_\xi}\beta_x\beta_y, \quad (4)$$

where $\beta_x = \left((1-\rho_x^2)^{2N_1-1} \Big/ \sum_{l=0}^{N_1-1} (C_{N_1-l}^l \rho_x^l)^2 \right)^{-\frac{1}{2}}$, $\beta_y = \left((1-\rho_y^2)^{2N_2-1} \Big/ \sum_{l=0}^{N_2-1} (C_{N_2-l}^l \rho_y^l)^2 \right)^{-\frac{1}{2}}$.

When identifying parameters, let's approximate the CF of the initial data by the most appropriate model. In order to obtain the CF models of arbitrary orders, it is necessary to use expressions for one-dimensional CF of AR with multiple roots of characteristic equations [22]

$$B_x(k) = \sigma_x^2 \sum_{l=0}^{m-1} g(m,l,k) \frac{\rho^{2(m-l-1)}}{(1-\rho^2)^{2k-l-1}}, \quad (5)$$

where $g(m,l,k) = \frac{(m+k-1)!(2m-l-2)!}{l!(m-1)!(m-l-1)!(m+k-l-1)!}$. The variance of independent random values ξ_i, $i = 1,2,...,n$, can be found for a given variance of simulated RF $B_x(0) = \sigma_x^2$

$$\sigma_\xi^2 = \frac{\sigma_x^2 (1-\rho^2)^{2m-1}}{\sum_{l=0}^{m-1} \left(C_{m-1}^l \rho^l \right)^2}. \quad (6)$$

Thus, for spatial AR equation with characteristic roots of multiplicities (m_1,m_2) the expression for CF can be written as

$$B_{xy}(k_1,k_2) = \sigma_x^2 \sum_{l=0}^{m_1-1} g(m_1,l,k_1) \frac{\rho_x{}^{2(m_1-l-1)}}{(1-\rho_x{}^2)^{2k_1-l-1}} \sum_{l=0}^{m_2-1} g(m_2,l,k_2) \frac{\rho_y{}^{2(m_2-l-1)}}{(1-\rho_y{}^2)^{2k_2-l-1}}. \quad (7)$$

However, in the case of a model with multiple roots it is possible to separately carry out the identification of parameters by row and column, using formula (5).

4. Identification of parameters based on theoretical values of correlation functions

To solve the problem of identification, we will use AR models of arbitrary order

$$x_i = \rho_1 x_{i-1} + \rho_2 x_{i-2} + ... + \rho_m x_{i-m} + \xi_i, \quad i = 1,2,...,M, \quad (8)$$

where m is order of AR model.

Choosing parameters $\rho_1, \rho_2, ..., \rho_m$ it is possible to get a Gaussian RF $\{x_i\}$, $i = 1,2,...,M$ with a variety of correlation properties. In this case to write values of CF you can use the following expression

$$R_x(k) = \rho_1 R_x(k-1) + \rho_2 R_x(k-2) + ... + \rho_m R_x(k-m), \quad k > 0. \quad (9)$$

CF of models with multiple roots for different roots z_ν, $\nu = 1,2,...,m$, of characteristic equations described by expression

$$z^m - \rho_1 z^{m-1} - \rho_2 z^{m-2} - ... - \rho_m = 0, \quad (10)$$

under the condition of stability $|z_\nu| < 1$, $\nu = 1,2,...,m$, are represented by the following sum

$$R_x(k) = A_1 z_1^{|k|} + A_2 z_2^{|k|} + ... + A_m z_m^{|k|}. \quad (11)$$

Substitution in (9) values k = 1, 2, … , m leads to the well-known Yule-Walker system of equations, which, for example, for second-order systems takes the form

$$\begin{aligned} \rho_1 + \rho_2 R(1) &= R(1), \\ \rho_1 R(1) + \rho_2 &= R(2). \end{aligned} \quad (12)$$

The solution of this system allows you to find the coefficients $\rho_1, \rho_2, ..., \rho_m$ of equation (8) based on predetermined or estimated values of CF $R_x(1)$, $R_x(2)$, …, $R_x(m)$.

We will perform parameter identification for models with multiple roots of characteristic equations of *1-4th* orders. In this case the order can be identified if we take into account only the coefficients that make some contribution to the model. Table 1 presents the results of identification of the correlation

parameters for the values of CF of AR with multiple roots. By rows, the actual multiplicity is presented, by columns — estimated parameters are presented. We assume $\rho = 0.8$ for models of all orders. In the left column – the values found, in the right column - the real values.

Table 1. Identification of parameters based on the theoretical values of CF

	m*=1		m*=2		m*=3		m*=4	
m=1	$\rho_1 = 0.8,$ $\rho_2 = 0,$ $\rho_3 = 0,$ $\rho_4 = 0$	$\rho_1 = 0.8,$ $\rho_2 = 0,$ $\rho_3 = 0,$ $\rho_4 = 0$	$\rho_1 = 0.8,$ $\rho_2 = 0,$ $\rho_3 = 0,$ $\rho_4 = 0$	$\rho_1 = 0.8,$ $\rho_2 = 0,$ $\rho_3 = 0,$ $\rho_4 = 0$	$\rho_1 = 0.8,$ $\rho_2 = 0,$ $\rho_3 = 0,$ $\rho_4 = 0$	$\rho_1 = 0.8,$ $\rho_2 = 0,$ $\rho_3 = 0,$ $\rho_4 = 0$	$\rho_1 = 0.8,$ $\rho_2 = 0,$ $\rho_3 = 0,$ $\rho_4 = 0$	$\rho_1 = 0.8,$ $\rho_2 = 0,$ $\rho_3 = 0,$ $\rho_4 = 0$
m=2	$\rho_1 = 0.976,$ $\rho_2 = 0,$ $\rho_3 = 0,$ $\rho_4 = 0$	$\rho_1 = 1.6,$ $\rho_2 = -0.64,$ $\rho_3 = 0,$ $\rho_4 = 0$	$\rho_1 = 1.6,$ $\rho_2 = -0.64,$ $\rho_3 = 0,$ $\rho_4 = 0$	$\rho_1 = 1.6,$ $\rho_2 = -0.64,$ $\rho_3 = 0,$ $\rho_4 = 0$	$\rho_1 = 1.6,$ $\rho_2 = -0.64,$ $\rho_3 = 3\times10^{-14},$ $\rho_4 = 0$	$\rho_1 = 1.6,$ $\rho_2 = -0.64,$ $\rho_3 = 0,$ $\rho_4 = 0$	$\rho_1 = 1.6,$ $\rho_2 = -0.64,$ $\rho_3 = 3\times10^{-14},$ $\rho_4 = 0$	$\rho_1 = 1.6,$ $\rho_2 = -0.64,$ $\rho_3 = 0,$ $\rho_4 = 0$
m=3	$\rho_1 = 0.992,$ $\rho_2 = 0,$ $\rho_3 = 0,$ $\rho_4 = 0$	$\rho_1 = 2.4,$ $\rho_2 = -1.92,$ $\rho_3 = 0.512,$ $\rho_4 = 0$	$\rho_1 = 1.92,$ $\rho_2 = -0.937,$ $\rho_3 = 0,$ $\rho_4 = 0$	$\rho_1 = 2.4,$ $\rho_2 = -1.92,$ $\rho_3 = 0.512,$ $\rho_4 = 0$	$\rho_1 = 2.4,$ $\rho_2 = -1.92,$ $\rho_3 = 0.512,$ $\rho_4 = 0$	$\rho_1 = 2.4,$ $\rho_2 = -1.92,$ $\rho_3 = 0.512,$ $\rho_4 = 0$	$\rho_1 = 2.4,$ $\rho_2 = -1.92,$ $\rho_3 = 0.512,$ $\rho_4 = -1\times10^{-13}$	$\rho_1 = 2.4,$ $\rho_2 = -1.92,$ $\rho_3 = 0.512,$ $\rho_4 = 0$
m=4	$\rho_1 = 0.995,$ $\rho_2 = 0,$ $\rho_3 = 0,$ $\rho_4 = 0$	$\rho_1 = 3.2,$ $\rho_2 = -3.84,$ $\rho_3 = 2.048,$ $\rho_4 = -0.41$	$\rho_1 = 1.969,$ $\rho_2 = -0.979,$ $\rho_3 = 0,$ $\rho_4 = 0$	$\rho_1 = 3.2,$ $\rho_2 = -3.84,$ $\rho_3 = 2.048,$ $\rho_4 = -0.41$	$\rho_1 = 2.837,$ $\rho_2 = -2.724,$ $\rho_3 = 0.886,$ $\rho_4 = 0$	$\rho_1 = 3.2,$ $\rho_2 = -3.84,$ $\rho_3 = 2.048,$ $\rho_4 = -0.41$	$\rho_1 = 3.2,$ $\rho_2 = -3.84,$ $\rho_3 = 2.048,$ $\rho_4 = -0.41$	$\rho_1 = 3.2,$ $\rho_2 = -3.84,$ $\rho_3 = 2.048,$ $\rho_4 = -0.41$

Analysis of table 1 shows that the values of the correlation coefficients are estimated the more accurately, the higher the multiplicity is. If the estimated multiplicity exceeds the real value, then the additional coefficients are either 0 or very close to it. Thus, the process of the model order identification can be carried out first for some large multiplicity. If the resulting coefficients do not have zero coefficients, then the calculation should be carried out at a higher multiplicity until we get zero coefficients. If there are zero coefficients, the order corresponds to the number of the last significant coefficient.

A similar relationship between correlation coefficients and CF values can also be obtained for the two-dimensional case, i.e. images. The relation for CF values corresponding to expression (9) for the three-point model, is written as

$$R(k_1, k_2) = \rho_{10} R(k_1 - 1, k_2) + \rho_{01} R(k_1, k_2 - 1) + \rho_{11} R(k_1 - 1, k_2 - 1), k_1 > 0, k_2 > 0. \quad (13)$$

It is easy to verify that solving the two-dimensional Yule-Walker system of equations (13) for the Habibi model CF will give correlation coefficients identical to the coefficients of the first-order two-dimensional AR model. To increase the order of the AR, as in the one-dimensional case it is necessary to increase the number of correlation coefficients. In this case, the RF model can be written as follows

$$x_{i,j} = \sum_{l=0}^{m_j} \sum_{k=0}^{m_i} \rho_{kl} x_{i-k,j-l} - \rho_{00} x_{i,j} + \xi_{i,j}, \; i = \overline{1, M_1}, \; j = \overline{1, M_2}, \quad (14)$$

where $\{x_{i,j}\}$ is RF implementation or simulated image; ρ_{kl} are correlation coefficients for elements lagging behind each other along the axes i and j by k and l pixels respectively; $\{\xi_{i,j}\}$ is two-dimensional RF of independent Gaussian random variables with zero mean $M\{\xi_{i,j}\} = 0$ and variance $M\{\xi_{i,j}^2\} = \sigma_\xi^2 = [1 - \sum_{l=0}^{mj} \sum_{k=0}^{mi} \rho_{kl} R(k,l) + \rho_{00} R(0,0)]\sigma_x^2$; m_i and m_j are orders of the model; M_1 and M_2 are the image size.

The number of components of the model, taking into account the random increment will be equal to $(m_i+1)\times(m_j+1)$. Using formulas (9) and (13), we can write the relation for calculating the CF values

$$R(k_1,k_2)=\sum_{l=0}^{m_j}\sum_{k=0}^{m_i}\rho_{kl}R(k_1-k,k_2-l)-\rho_{00}R(k_1,k_2),\ k_1>0,k_2>0. \quad (15)$$

The expression (15) can also be used for the case of non-separable CFs if the parameters of an arbitrary AR RF are identified and the order is a priori unknown.

5. Parameter identification on the basis of real images CF

Let us identify the parameters of the model based on the proximity of the CF model and the given data. In the first case, we will consider the AR with a separable CF and separately calculate the coefficients for the row and column. In the second case, we use equations based on the expression (15).

Let there be a real image represented as $I(i,j), i\in 1,...,M_1, j\in 1,...,M_2$. Then its CF can be expressed as follows

$$R_I(k_1,k_2)=\frac{1}{\sigma_I^2}\sum_{i=k_1+1}^{M_1}\sum_{j=k_2+1}^{M_2}(I(i,j)-m_I)(I(i-k_1,j-k_2)-m_I), \quad (16)$$

where m_I is average brightness over the entire image; σ_I^2 is brightness variance calculated over the entire image.

Figure 1a and Figure 1b show the image to be investigated and its CF, respectively. Identification is performed for the 4th order AR model.

- for RF having separable CF the results are as follows: $\rho_{10}=1.098;\rho_{20}=-0.39;\rho_{30}=0.364;\rho_{40}=-0.082;\quad \rho_{01}=0.828;\rho_{02}=0.0047;\rho_{03}=0.111;\rho_{04}=0.038$; $\varepsilon=(\hat{R}-R)^2=0.387$.
- for RF having non-separable CF the results are as follows: $\rho_{10}=0.998;\rho_{20}=-0.514;\rho_{30}=0.43;\rho_{40}=-0.133;\quad \rho_{01}=0.185;\rho_{11}=0.152;\rho_{21}=-0.194,\rho_{31}=0.142;\rho_{41}=-0.092;$ $\rho_{02}=-0.174;\rho_{12}=0.309;\rho_{22}=-0.265;\rho_{32}=0.217;\rho_{42}=-0.097;\rho_{03}=-0.048;\rho_{13}=0.186;\rho_{23}=-0.205;$ $\rho_{33}=0.153,\rho_{43}=-0.079;\rho_{04}=-0.122;\rho_{14}=0.267;\rho_{24}=-0.242;\rho_{34}=0.22;\rho_{44}=-0.102;\ \varepsilon=(\hat{R}-R)^2=0.014$.

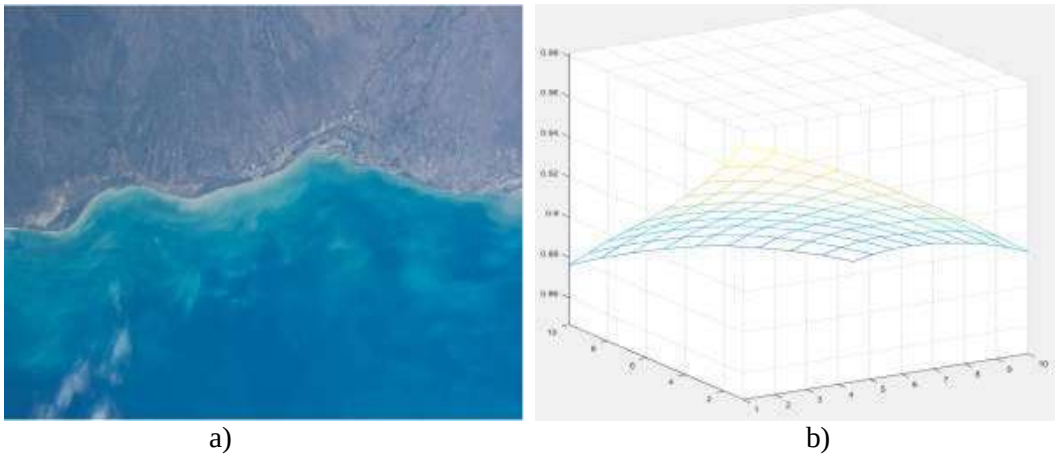

a) b)

Figure 1. The image (a) for which the adjustment of the parameters is carried out and its CF (b).

Analysis of the obtained values of the error variances shows that the use of the model with an non-separable CF provides a greater proximity between the modeled and the real CF. This is explained by the fact that for this model 24 correlation parameters were calculated, while for a model with a separable CF only 8 parameters. At the same time, a sufficient proximity of the CF is provided, especially in the neighborhood of zero. Therefore, it is advisable to use such models to reduce

computational costs. Figure 2 shows the CF cross sections for the original image (presented by solid line), as well as for the RF with separable CF (presented by dash-dotted line) and the RF with non-separable CF (presented by dashed line).

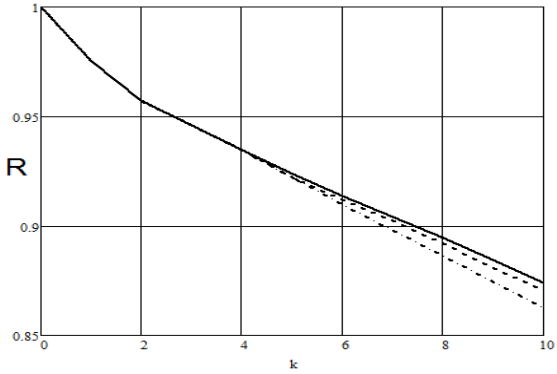

Figure 2. CF cross sections of the original image and identifiable models.

Analysis of the presented curves shows that as *k* increases the discrepancy between the real and simulated CF also increases. It is possible to achieve greater proximity by increasing the order of the AR, but this leads to higher computational costs. Similar research was conducted with a sample of 100 images. Analysis of the results shows that the use of non-separable CF models provides the proximity of CF to 10-15 times more than the use of separable CF models in 85% of cases. However, in 15% of cases separable models were successfully used to describe the real image, which made it possible to significantly reduce computational costs of image processing.

6. One dimensional example of calculating parameters

However, if a model with multiple roots is used, it is sufficient to calculate only the first correlation coefficient, then calculate the correlation parameter using the first correlation coefficient and use correlation parameter to find the remaining correlation coefficients according to the expression (3).

For example, if $\rho_1 = 3.6$ and N=4 then it is easy to calculate parameter of the AR with multiple roots of characteristic equations from the following equation

$$3.6 = (-1)^{1+1} C_4^1 \rho^1, \rightarrow \rho = 0.9. \tag{17}$$

After that we find the second, third and fourth correlation coefficients

$$\begin{aligned} \rho_2 &= (-1)^{1+2} C_4^2 \rho^2 = -4.86, \\ \rho_3 &= (-1)^{1+3} C_4^3 \rho^3 = 2.916, \\ \rho_4 &= (-1)^{1+4} C_4^4 \rho^4 = -0.6561. \end{aligned} \tag{18}$$

So it is quite a simple task to perform identification of parameters in this case.

7. Conclusion

In this paper a brief overview of the methods used to identify the parameters of the AR processes is presented. Models with multiple roots and a method for determining the order of the model based on the Yule-Walker equations are considered. It is shown that the proposed method enables to determine the order of the model for simulated images with sufficient accuracy. A comparative analysis of the identification of the parameters of models with a separable and non-separable CF of the real image is performed. The analysis shows that models with a non-separable CF require more computational costs at the same order of a model, however, they provide greater proximity of the CF in comparison with separable CF models. The identification results may be used to describe real satellite images and for the processing of such images.

8. References

[1] Soifer V A 2001 *Methods of computer image processing* (Fizmatlit) 784 p
[2] Gonzalez R, Woods R 2005 *Digital image processing* (Moscow: Technosphere) 1072 p

[3] Vasiliev K K, Omelchenko V A 1995 *Applied theory of random processes and fields* (Ulyanovsk: UlSTU) 256 p
[4] Glazov G N, Kostevich A G 2002 Modeling discrete Gaussian random fields *Intellectual systems in management, design and education* **2** 19-27
[5] Vasiliev K K, Andriyanov N A 2017 Analysis of autoregression with multiple roots of characteristic equations *Radiotekhnika* **6** 13-17
[6] Andriyanov N A, Vasiliev K K 2018 Application of autoregression with multiple roots of characteristic equations for image representation and filtering *Information technologies and nanotechnologies Proceedings of ITNT-2018* (Samara National Research University) 1023-1031
[7] Andriyanov N A, Vasiliev K K and Dement'ev V E 2018 Analysis of the efficiency of satellite image sequences filtering *Journal of Physics: Conference Series* **1096** 012036 DOI: 10.1088/1742-6596/1096/1/012036
[8] Danilov A N, Andriyanov N A and Azanov P T 2018 Ensuring the effectiveness of the taxi order service by mathematical modeling and machine learning *Journal of Physics: Conference Series* **1096** 012188 DOI: 10.1088/1742-6596/1096/1/012188
[9] Vasiliev K K, Andriyanov N A 2017 Synthesis and analysis of doubly stochastic models of images *CEUR Workshop Proceedings* **2005** 145-154
[10] Bolshakov A A, Karimov R N 2006 *Methods for processing multidimensional data and time series: a manual for universities* (Moscow: Hotline - Telecom) 522 p
[11] Zhdanov A I, Katsyuba O A 1982 Identification by the method of least squares of the parameters of the autoregression equations with additive measurement errors *Automatics* **43(2)** 29-38
[12] Anderson T 1976 *Statistical analysis of time series* (Moscow: Mir) 755 p
[13] Box G, Jenkins G 1974 *Analysis of time series. Forecast and management* (Moscow: Mir) 406 p
[14] Koreisha S, Yoshimoto G 1991 A Comparison among Identification Procedures for Autoregressive Moving Average Models *International Statistical Review/ Revue Internationale de Statistique* **59(1)** 37-57
[15] Lindberger N A 1974 Computer identification of linear random process *Intern. J. Control* **19(6)** 1021-1045
[16] Durbin J 1959 Efficient estimation of parameters in moving average models *Biometrika* **46(3-4)** 306-316
[17] Cleveland W S 1972 The inverse autocorrelations of a time series and their applications *Technometrics* **14(2)** 277-293
[18] Lukashin Yu P 2003 *Adaptive methods for short-term forecasting of time series: a textbook for universities.* (Moscow: Finance and Statistics) 416 p
[19] Andrianov N A, Gavrilina Yu N 2017 The problem of identifying the parameters of auto-regressions with multiple roots *Modern problems of design, production and operation of radio systems* **1-2(10)** 95-98
[20] Kittler J, Whitehead P G 1976 Determination of the model structure using pattern recognition techniques *Proc. of 4th IFAC Symp. Ident. Syst. Parameter Estimation* **3** 22-30
[21] Plotnikov D E, Kolbudaev P A and Bartalyov S A 2018 Selection of seasonally homogeneous areas based on the analysis of time series of satellite images *Computer Optics* **42(3)** 447-456 DOI: 10.18287/2412-6179-2018-42-3-447-456
[22] Varlamova A A, Denisova A Yu and Sergeev V V 2018 Information technology for processing remote sensing data for assessing plant ranges *Computer Optics* **42(5)** 864-876 DOI: 10.18287/2412-6179-2018-42-5-864-876
[23] Vasiliev K K, Krasheninnikov V R 2015 *Statistical image analysis* (Ulyanovsk, UlSTU) 214 p

Acknowledgement
The work was supported by RFBR, Projects №17-01-00179, №18-31-00056.

A new real-time method for finding temporary and permanent road marking and its applications

R V Dosaev[1], K I Kiy[1]

[1]Keldysh Institute of Applied Mathematics of RAS, Miusskaya square 4, Moscow, Russia, 145047

e-mail: konst.i.kiy@gmail.com

Abstract. In this paper, a new real-time method for finding temporary and permanent road marking is proposed. The method is based on the geometrized histograms method for segmenting and describing color images. This method is able to deal with both rectilinear and curvilinear marking, as well as with color temporary and permanent road marking. It also makes it possible to distinguish temporary road marking from white permanent road marking. The developed method is stable under illumination and is able to work even for partially disappearing road marking, typical for late winter and early spring. In contrast to many other methods, this method does not require any information about camera parameters and calibration and is able to find road marking in images taken under unknown conditions. The proposed method has been implemented by a program written in C++, operating under Windows and Linux. The program operation has been tested on video records shot on typical Russian roads during different seasons and under diverse whether and illumination conditions. The processing speed is about 20 fps for a standard modern computer. Using parallel computing, this speed is reduced considerably. The results of program operation are presented and discussed. The developed program is a part of the computer vision component of the control system of the AvtoNiva pilotless vehicle.

1. Introduction

The problem of finding road markings is very important due to applications in advanced driver assistance systems (ADAS) and vision systems of autonomous vehicles. Efficient algorithms for finding road marking implemented in ADAS can prevent many road accidents and save many lives. The first efficient methods for real-time lane (road marking) detection were proposed and implemented by E.D. Dickmanns and his colleagues [1, 2]. These methods were dated back to the late 1980s and employed the so-called 4D approach proposed by E.D. Dickmanns [1]. Many methods based on Hough transform, RANSAC algorithm, and learning approaches, including deep learning of convolutional networks, have been proposed (see [3–7] and the references in these papers) since then. The most recent review of the results obtained in this area can be found in [6]. In spite of the serious progress in investigations on this topic, vital problems connected with lane marking, disappearing in early spring and late winter, wet places and occlusion still take place. It deserves special mentioning that temporary lane markings may have extremely high curvature, which may pose additional problems to the existing methods. Despite of the impressing results reached by application of convolutional networks, there are certain problems that arise in using them, such as overfitting, a large

amount of training data required, the high computational cost leading to using expensive SIMD architectures. In addition, as it has been stressed in recent publications [6], there are problems in finding a colored temporary lane marking in real time and distinguishing it from a permanent white lane marking. In [7], the histograms of two components of the color coordinate system (Y, C_b, C_r) were used for finding white and yellow road markings in real time. It was mentioned that the previous attempts of applying color suffered from high computational complexity [8, 9]. However, the approach proposed [7] is sensitive to color blobs caused by dirty places and other objects in the frame. It becomes especially clear when the road marking starts rather far from the bottom of the frame on its left or right boundary (this may occur in sharp turns). In this connection, it seems to be reasonable to apply the real-time geometrized histograms method for segmentation and description of color images [10–13] for finding and distinguishing road markings. This method makes it possible to find both white road marking of arbitrary shape and colored road making (for example, temporary one) and provides the technique for distinguishing them even under difficult illumination condition. The geometrized histograms method is based on a method for approximate description of the value distribution of a scalar (intensity) or vector function (color) giving the image. This description is called a geometrized histogram. Geometrized histograms make it possible to find even very small connected objects in the image plane (with diameter up to three pixels) and to construct from them continuous objects like lane markings. Geometrized histograms can distinguish objects with very small local contrasts and automatically adapt themselves to very small local differences in intensity and color of connected objects.

In this paper, we propose an image understanding system that can find road markings based on the real-time geometrized histograms method for complete image segmentation. This method allows us to use only standard computational facilities and provides adequate results even for images taken by cheap cameras like those employed in camcorders. In section 2, we remind briefly the main points of the geometrized histograms method and explain the main ideas in order to apply them to finding road markings. In section 3, we present the algorithms for finding road markings. Section 4 is devoted to the comparison of the proposed method with methods proposed earlier. Several examples of finding road markings, demonstrating the ability of the method, are presented in section 5 and discussed.

2. A brief description of the geometrized histograms method

A detailed description of the geometrized histograms method can be found in [10—13]. To construct the geometrized histogram for a color or grayscale image, this image is divided into strips St_i, $i = 1, \ldots, n$, of the same small width W with sides parallel to the horizontal (or vertical) axis Os of the image plane. Suppose that we deal with horizontal strips. The case of vertical strips is considered in a similar way. To describe approximately the image in a chosen narrow image strip St_i, it is necessary to describe approximately the distribution of values of the vector function specifying it. The vector functions (R, G, B), (H, S, I), or ($G/(G+B)$, $G/(G+R)$, I), introduced by the author, can be examples of this vector function. This approximate description will be called the geometrized histogram of the image in St_i. Let us explain first how to construct the geometrized histogram for a scalar function $f(x, y)$, giving a grayscale image. The geometrized histogram describes approximately the level sets L_z of $f(x, y)$, i.e., the sets of points (x, y) of the strip St_i, where $f(x, y) = z$. Since we deal with a discrete representation of the image, the projection of L_z onto Os is a union of intervals (segments) I_{kz} in this axis $Pr(L_z) = \cup_k I_{kz}$. For each segment I_{kz}, its cardinality is the number of the points of the level set L_z in the strip St_i that are projected onto this interval. It is clear that the set of cardinalities of the intervals I_{kz} for all possible z determines the classical histogram of $f(x, y)$ in the strip St_i. The collection of intervals I_{kz} approximately describes L_z, since the set of level z belongs to the preimage of $\cup_k I_{kz}$, $L_z \subset Pr^{-1}(\cup_k I_{kz})$, and the strip is narrow. The union of I_{kz} for all z determines the space of intervals on Os with the scalar function of cardinality on them. Note that intervals I_{kz} for different z may have a nonempty intersection on Os. This occurs when the intervals correspond to different objects in the strip and one object lies over another in it. The space of intervals $\cup_k^z I_{kz}$ is called the local geometrized histogram ($\mathbf{HG}_n$) of $f(x, y)$ in St_i.

An example of the geometrized histogram of the grayscale component of a strip in a color image of a road scene can be found in Fig. 1. The ***ox*** axis in the figure presents the value of the grayscale function, which varies from 0 to 63. The ***oy*** axis presents the coordinates of pixels *Os*. The coordinate on this axis varies from 0 to ***DimX*** – 1, where ***DimX*** is the horizontal dimension of the image (we consider a horizontal strip). The geometrized histogram of this strip in the grayscale version describes the geometry of intensity distribution in the strip. In the place of intersection of a strip with the lane marking, one can see a local burst of intensity. This burst is selected by a red circle. This means that the geometrized histogram of the grayscale component can be employed as a road marking detector.
However, not only white road marking is important for automatic driving vehicles. Yellow and orange road markings are also of great interest. To detect yellow (orange) road marking, it is necessary to segment and describe color images in real-time. For this purpose, the construction of the geometrized histogram is generalized for vector functions representing color images. We deal with the representation of the color image by the function (*G/(G+B), G/(G+R), I*) [10]. Note that the component *I* means here the grayscale intensity (it is equal to *Y* in the (Y, C_b, C_r) coordinates [6]). Let us introduce a characteristic function *CF*. If the hue of the point belongs to the yellow part of the color triangle, then *CF* coincides with *G/(G+B)*. When passing to the next range (green, blue, red), the value of *G/(G+B)* is shifted by *M*, where *M* is the number of grades of the function *G/(G+B)*. The geometrized histogram of *CF*, supplemented for each interval I_{kz} by the classical histogram of the other color component *G/(G+R)*, is called the geometrized histogram of the color image in St_i.

Figure 1. A road scene and the geometrized histogram of the grayscale component of the i-th horizontal strip.

Using this data for each of its members I_{kz}, we determine the localization interval $\mathbf{Int}_{kz} = [beg_{kz}, end_{kz}]$ on *Os*, the range and the mean value of hue $\Delta_H^{kz} = [H_{min}^{kz}, H_{max}^{kz}]$ and H_{mean}^{kz}, the range and the mean value of saturation $\Delta_S^{kz} = [S_{min}^{kz}, S_{max}^{kz}]$ and S_{mean}^{kz}, and the range and the mean value of grayscale intensity $\Delta_I^{kz} = [I_{min}^{kz}, I_{max}^{kz}]$ and I_{mean}^{kz} [7]. In addition, each interval of the geometrized histogram has the cardinality $Card^{kz}$. Figure 2 presents the geometrized histogram of a strip of a color image of a road scene. The ***ox*** axis in the figure presents the value of the characteristic function *CF*, which varies within its range of values. As in Fig. 1, the ***oy*** axis presents the coordinates of pixels along *Os*. The coordinate on this axis varies from 0 to ***DimX*** – 1, where ***DimX*** is the horizontal dimension of the image (we consider a horizontal strip). The geometrized histogram in the colored version of this strip describes the geometry of color distribution in the strip.

The red closed curve in the right part of the figure demonstrates the intervals of the geometrized histogram corresponding to the part of the yellow marking in the chosen strip. Two yellow squares in the upper left-hand corner of the right part of the figure show the color of this group of intervals. Usually, there are too many intervals of the geometrized histogram of a grayscale or color image I_{kz} to solve complex real problems. To reduce the number of them, a clustering procedure is introduced [10, 12], which joins intervals $\mathbf{Int}_{kz}$ that are close as intervals on *Os* and have close intensity (for the geometrized histogram of the grayscale image) and intensity-color characteristics (for the geometrized histogram of a color image). The joined intervals are called grayscale or color bunches. Each strip St_i is described by the set of grayscale or color bunches B_i. Each grayscale bunch $b \in B_i$ is characterized by the following parameters:

1. the localization interval $int_b = [beg_b, end_b]$, belonging to *Os*;
2. $\Delta_I^b = [I_{min}^b, I_{max}^b]$ and I_{mean}^b – the range and the mean value of the grayscale intensity;
3. the cardinality $Card^b$ (approximately, the number of points in the strip St_i whose coordinate x belongs to the localization interval $[beg_b, end_b]$ that have grayscale characteristics belonging to the range Δ_I^b of the grayscale bunch).

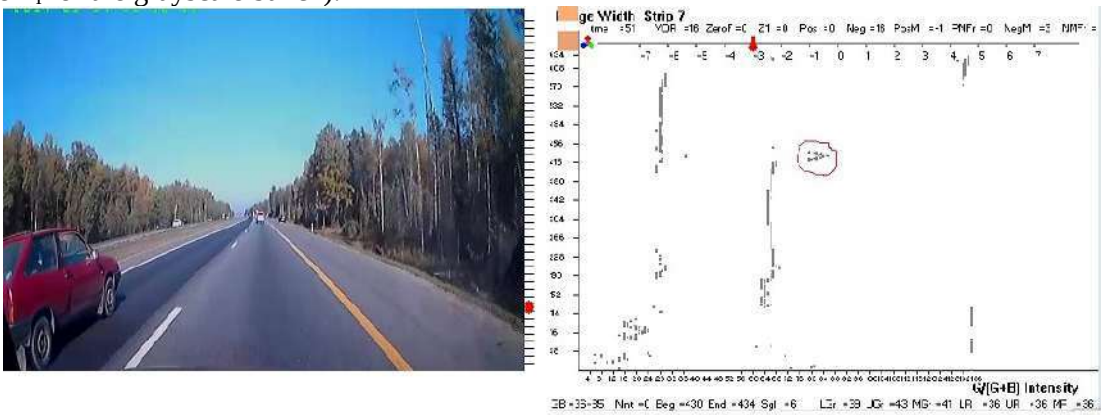

Figure 2. A road scene and the geometrized histogram of the color image of the 7-th horizontal strip.

Each color bunch $b \in B_i$ is characterized by the following parameters:
1. the localization interval $int_b = [beg_b, end_b]$, belonging to *Os*;
2. $\Delta_H^b = [H_{min}^b, H_{max}^b]$ and H_{mean}^b – the range and the mean value of the hue of b;
3. $\Delta_S^b = [S_{min}^b, S_{max}^b]$ and S_{mean}^b – the range and mean value of saturation;
4. $\Delta_I^b = [I_{min}^b, I_{max}^b]$ and I_{mean}^b – the range and the mean value of the grayscale intensity;
5. the cardinality $Card^b$ (approximately, the number of points in the strip St_i whose coordinate x belongs to the localization interval $[beg_b, end_b]$ that have color characteristics belonging to the ranges Δ_H^b, Δ_S^b, and Δ_I^b of the color bunch).

Here, the I component is equal to Y in (Y, C_b, C_r). Using the methods developed in [10—13], we can attach to each color image the graph of color bunches *STG* (STructural Graph). Suppose that we deal with horizontal strips. Each strip St_i is described by the set of color bunches B_i. $B = \cup B_i$ is the set of nodes of *STG*. Two color (grayscale) bunches $b_1 \in B_i$ and $b_2 \in B_{i+1}$ in the adjacent strips are connected by an edge if their localization intervals have a nonempty intersection. A similar construction can be produced for grayscale bunches. Color bunches b_1 and b_2 lying in the same strip are called adjacent if their localization intervals int_{b1} and int_{b2} are adjacent. Color bunches lying in the adjacent strips are called adjacent if their localization intervals have a nonempty intersection. Edges of *STG* join all adjacent color bunches. Informally, each bunch describes a certain part of a real object in the strip, its projection on *Os* and the description of the numerical characteristics of this part of the object. The graph *STG* can be interpreted geometrically by overlaying localization intervals of its bunches ($[beg_b, end_b]$) in the vicinity of the middle lines of the corresponding strips. Figure 3 demonstrates the representation of an image by the *STG* graph. Color bunches of each strip are superimposed on or near (slightly below) the middle lines of the corresponding strips. There are two types of color or grayscale bunches. Color or grayscale bunches of the first type are called dominating. Dominating bunches are the bunches that in some places of their localization interval int_b have the maximum density $dens_b = Card^b/l(int_b)$, where $l(int_b)$ is the length of the interval int_b. The second type of non-dominating bunches is generated by color or grayscale bunches that do not have maximum density at any point of their localization interval int_b. Non-dominating bunches are also important in image understanding. For example, as a rule, braking signal zones of distant vehicles in front on the road are non-dominating because of their small size (parts of the vehicle body are dominating in this case). To understand clearly the future behavior of the vehicle in front, we have to know the state of its signal zones to determine precisely the moment when it starts to brake.

Figure 3. A road scene and the corresponding image of color bunches of the *STG* graph.

Figure 3 demonstrates a set of color bunches for a road image taken by a usual cheap camcorder on a Russian road. Color bunches corresponding to parts of the road almost always give dominating color bunches. Color bunches corresponding to the road marking provide dominating bunches only in the nearest strips. The same is valid for grayscale bunches corresponding to road parts and parts of the road marking. Figure 3 clearly shows that the parts of road marking in the sequence of strips going to the upper part of the image generate in a sense a continuous sequence of dominating and non-dominating color (grayscale) bunches. As a rule, the bunches corresponding to parts of road marking have locally a maximum intensity and are small relative to adjacent dominating color bunches. In the visualization, the localization intervals of dominating bunches are put on the entire middle line, while non-dominating bunches locate slightly below middle lines. The construction and numerous experiments with images have shown that color bunches represent any connected color or grayscale object in the real image with the size greater than three pixels. The description of a color or grayscale image by color bunches compresses the information on images from millions of pixels to several hundreds of bunches. However, this image description contains all important features of the image, including a description of the geometry of objects belonging to it. It is important to note that the main operations of the construction of *STG* are the same for all strips. This means that the computation of *STG* can be parallelized using particular processors in multiprocessor computers. Computational experiments on modern personal computers have shown that *STG* can be constructed in real time for HD video frames.

2.1. Problem statement and facilities for its solution

The problem of finding road marking in the images of video sequences of images of road scenes is investigated in this paper. Both temporary and permanent road markings are of interest. The aim of this investigation is to introduce a new technique for solving this problem in real time. Moreover, the technique will provide tools for distinguishing temporary and permanent road markings when they are both present on the road. Since any connected real object in the image generates a corresponding formal object in *STG* [10—13], we will investigate images of real road makings in this graph. For this purpose, the geometrized histogram of the color image and the geometrized histogram of its grayscale component will be employed.

At the first step of the algorithms, in each strip, objects that can represent a part of a road marking in this strip are described and found. We do not employ here any information about the camera position and calibration in order to take into account complex situations on sharp turns and to improve the portability of the software. In this case, it can be installed even in rather cheap ADAS systems not requiring the camera calibration. At the second stage, continuous sequences of the found local objects located in different adjacent strips are constructed. The construction of continuous sequences of local objects is based on a modification of the concept of left and right contrast curves (germs of left and right global objects) introduced in [11, 12]. The main specific feature of the method is that we construct the image of road markings in the graph *STG*. This makes it possible to avoid laborious operations on the image array and to provide real-time mode of the method. In the next subsection, the procedure for finding local objects in the strip that can represent different types of road markings is presented. In section 3, the algorithms for constructing the continuous sequences of local objects will be proposed.

2.2 Local constructions

The procedure for constructing local grayscale or color bunches in a narrow strip is described in detail in [12]. Let us recall its main steps. To start the construction, we select among intervals of the geometrized histogram the following ones: 1. dominating intervals that have a maximum density in some places; 2. intervals with maximum grayscale in some places (for grayscale and color geometrized histograms); 3. intervals with maximum saturation (for the color geometrized histogram). It is supposed that the density of the selected intervals is greater than some constant. We take these intervals as seeds in a clustering procedure. We add to the cluster determined by a selected seed the intervals of HG_i that have a rather big intersection with the corresponding seed interval [12] and close intensity or intensity-color characteristics to those of the seed. However, intervals with small densities may be not included in this clustering procedure. This situation is typical for intervals corresponding to the road marking in distant strips. Small groups of intervals of the geometrized histogram of the grayscale component of the image, similar to those presented in Fig. 1, are called burst bunches or simply bursts. Informally, bursts are generated by groups of rather small intervals that have close intensities and are mutually close as intervals and have an essential difference in intensity with the basic dominating bunches in a certain neighbourhood of their union on *Os*.

Let us present an algorithm for finding bursts. We label all intervals of the geometrized histogram as free or occupied. At the initial stage of the algorithm all intervals are free. A free interval becomes occupied (belonging to a burst), if it is chosen as a *seed* or belongs to the cluster of some seed. We choose intervals I_{kz} with a highest local intensity z in $\mathbf{HG}_i$ as seeds for burst bunches. For each seed, we define on the axis *Os* a neighborhood [a, b] □ I_{kz}. Let [$I_{\min}$, $I_{\max}$] be the interval limiting the intensities of the dominating intervals intersecting the neighborhood [a, b]. We require that the distance of the intensity z from the intensity interval [$I_{\min}$, $I_{\max}$] be more than a constant I_{not} making z noticeable against the basic dominating bunches whose intervals intersect [a, b]. Starting from each seed interval Int_{kz} = [beg_{kz}, end_{kz}], we grow the burst b by adding intervals I_{ly}, y < z, [a, b] □ I_{ly}, and $Int_{kz} \cap Int_{ly}$ is nonempty. For each new step, we obtain a new boundary intensity interval [$i_{\min}$, $i_{\max}$] for the constructed burst b. The condition [$I_{\min}$, $I_{\max}$] ∩ [$i_{\min}$, $i_{\max}$] is empty is a necessary condition for continuing the process. Moreover, it is required that the gap between these intervals has to be more a certain constant. In addition, by establishing the maximum gap between intensities of the added interval of the geometrized histogram and the boundary of the interval [$I_{\min}$, $I_{\max}$], we introduce a stop condition: if the ratio of the length of the maximum gap d_1 to the length of the gap to the closest dominating bunch d_2 (Fig. 4) in $\mathbf{HG}_i$ is greater than some value (e.g. 2), we stop the growing algorithm.

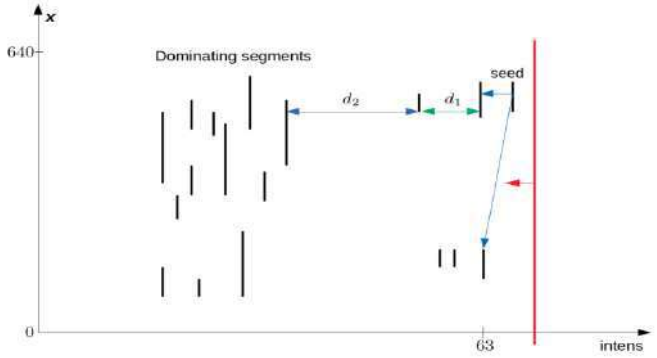

Figure 4. Burst bunches growing algorithm.

Due to relative thresholding, the stop condition is independent of the average intensity of the marking and its vicinity. Thus, it makes it possible to adapt the construction to different types of illumination and to efficiently find burst bunches**.** For a color geometrized histogram, the procedure for finding local objects for constructing a lane marking starts from detecting rather small color bunches whose color varies in a certain range about the yellow one. This is explained by the fact that in real images, due to dust, wet places, illumination, the color of permanent or temporary yellow road markings may vary from orange to slightly green. The localization intervals of the bunches

corresponding to a yellow road marking, as well as localization intervals of bursts, have a limitation on their lengths. In both cases (grayscale bursts and color bunches) the limitation on the length of localization intervals are not very strong. They are selected so that we can construct candidates for parts of road marking in strips without any information on the camera position and calibration. Because of this, the algorithms can operate successfully with a wide range of photos. Similar to the previous case, there are conditions on the intensity ranges of color bunches corresponding to road markings, discriminating them from the intensity ranges of the adjacent dominating color bunches.

To formulate these conditions, we need to recall the concept of search lattice on *STG* [13]. As it was proved in [13], it is possible to construct in each strip a linearly ordered sequence of adjacent dominating bunches whose localization intervals cover the middle line of the strip. In this sense, these bunches generate a basis in the strip. All linear ordered basic subsets of bunches, joined for all strips, generate on the image a "search lattice" SearchLat (*STG*) [13]. In the constructed SearchLat (*STG*) bunches are numbered with preservation of the adjacency relation. The search lattice allows one to formulate the relations of a chosen bunch with its main neighbors. Consider a bunch *b* that has suitable color characteristics. There are two possible cases: 1. *b* is included in SearchLat (*STG*); 2. *b* is a non-dominating bunch. In the first case, we formulate a system of rules that connect the color, density, and geometry characteristics of the bunch with those of the adjacent bunches. The rules describe the differences and ratios of the characteristics of the bunch and its adjacent members of SearchLat (*STG*), keeping in mind that one of or both adjacent bunches belong to parts of the road. In a way, they give a system of axiomatic description of the adjacency of a road marking bunch and the adjacent road bunches. In the second case, we find a subsequence of bunches of SearchLat (*STG*) covering the localization interval $int_{\mathbf{b}}$ and formulate a similar system of rules. All these conditions detect in each strip color bunches that can represent yellow lane markings. All color bunches of such a type are labelled by a special array for each of the strips. It is necessary to note that in close strips color bunches corresponding to road marking may be dominating, while distant bunches are not dominating as a rule. This can be clearly seen from Fig. 3. Figure 5 demonstrates color bunches that are candidates for the yellow lane markings chosen by the outlined systems of rules. Yellow color bunches that may be parts of road markings selected based on local reasoning described above are superimposed on the grayscale components of the corresponding color images. Since the program does not have any information about the camera calibration and position, there are some false candidates in different parts of images. For example, false candidates are located on vehicle bodies, roadsides, and in other places. However, real candidates generate continuous chains with decreasing sizes of candidate's localization intervals.

Figure 5. Candidates for parts of yellow road markings in strips.

3. Construction of continuous systems of bursts and color bunches

The problem of finding lane markings is reduced to construction of continuous systems of local objects (bursts or color bunches) in *STG*. The method for constructing continuous objects in *STG* (the so-called left or right germs of global objects) was developed in [11, 12]. This method was implemented as a program operating in real-time. However, this method was aimed at constructing global objects, such as a road**,** the sky [15], etc. and deals with rather big dominating bunches. This imposed certain limitations in the systems of rules for finding the next object in the sequence. As a rule, local objects for finding road marking are usually not dominating and rather small. The concept and the structure of the program have to be seriously modified to produce a new system for

constructing road marking. The following subsections are devoted to describing the main points of these modifications.

3.1 Finding road markings based of grayscale bursts

Now we can construct chains of bursts going over strips of the image. Any chain is a sequence of adjacent bunches b_k, b_{k+1}, …, b_n, located on adjacent strips St_k, St_{k+1}, …, St_n respectively. The chain can represent a real road marking line or its part, so it is worthwhile to find it.

We construct chain in the upward direction, beginning from its lowest strip, finding a corresponding adjacent burst on the next strip for the burst in the previous one. To find the corresponding next burst, the following two expected properties are employed: 1. a limited size and density of next bursts, and 2. the smoothness criterion for the left and right boundary curves of the chain. According to the first rule, we filter out long horizontal bursts, which cannot be a part of the road marking for obvious reasons. For this purpose, approximate thresholds for the length and density are established. For the closest strips, they are chosen to be suitable for a wide range of camera characteristics. For the next strips, as a rule, the lengths of candidates for extension cannot increase (in the ideal case, they depend only on the inclination of the line of the lane marking) and their densities should decrease. The smoothness criterion means that the absolute values of the differences of $\mathrm{abs}(end_{b(k+1)} - end_{bk})$ (the right curves) or $\mathrm{abs}(beg_{b(k+1)} - beg_{bk})$ (the left curves) for the adjacent bursts are bounded by a constant connected with the width of the strip. Introducing these constraints, we eliminate the effect of a sharp change in the shape of the boundary curve.

If there are no adjacent bursts in the strip to extend the chains, we terminate the process of chains construction. At the next stages, using the geometric characteristics of the chains, we can join some of them in order to obtain an intermittent lane marking. It is worth noting that the consideration of only burst bunches for chains construction makes our algorithm resistant to shadows and allows us to take into account possible jumps of intensity near the border of illuminated and shadowed places. All these rules make our algorithm rather robust for changing situations in the road scene and significantly improve the quality of lane marking detection.

3.2 Finding road markings based on color bunches

Temporary road markings convey very important information, and it is difficult to drive a car in the road without clear recognition of them. It is also necessary to distinguish permanent and temporary road markings in the case when they both present on the road. This makes it necessary to use color in detecting and recognizing road marking. To detect a colored lane marking, we employ the technique for constructing left and right germs of contrast global objects developed in [11, 12]. This technique is adapted to dealing with non-dominating color bunches and with color bunches satisfying additional conditions on their size, density, and color, similar to those formulated in the previous subsection. To avoid false extensions and to be able to deal with curvilinear lane markings, we use conditions imposed on the relations between the directions of the segments joining the previous bunch and a possible next bunch D_1, the first bunch of the chain and bunch constructed at the previous step D_2, and the first bunch of the chain and the possible next bunch D_3 of the chain. Since the curvature of the road marking is bounded, reasonable relations between D_1, D_2, and D_3 allow us to avoid false extensions. This means that we do not suppose that the line of road marking investigated is just a straight line. In this way, we can find a lane marking of a curvilinear shape as well.

3.3 Using global image analysis for system improvement

The global image analysis developed in [13] makes it possible to solve in real-time such tasks as detection of the boundary of the vegetational and ground roadsides, finding the road and its parts in the case of occlusion caused by other participants of the traffic, and sky region detection. These tasks are solved based on the analysis of *STG* without operations at the pixel level. All such operations are performed in constructing *STG*. It was stressed in the previous papers on the subject of road marking detection that finding road boundaries and the vanishing point is highly desirable ([7, 14]). Since in our method the problem of finding road marking is solved together with the problems listed above and does not practically affect the total computation time, we use the opportunity to reduce the region of

interest, decreasing the computational effort and eliminating a lot of noisy objects (like lights on a wet road). For example, we employ the information about the lower bound of the sky region.

4. Comparison with other methods for finding road markings

As was mentioned above, the most recent review of methods for finding road markings can be found in [6]. In that paper, all known methods are described. The areas where they can give appropriate results are also determined. We will also use the very useful discussion of related methods found in [7]. In that paper, three types of methods were separated and discussed. The main drawbacks of the methods of the selected groups were described in detail. We will not reply these arguments and refer to [7] for necessary details. We resume only that methods of the first two classes (the first one is based on edges and gradients, and the second one leans on the use of geometric information about the camera and lane) suffer from different illumination conditions, from difficulties in precise definition of geometric parameters (descends and ascends in the road), and occlusion and edges that arise due to the presence of other vehicles. In one or another way, methods of the third class apply color information of the image. It is clear that our method belongs to the third class, and it is reasonable to compare it with the other methods of this class. Typical methods that use color information are described in [7-9]. It was mentioned in [7] that the existing methods that use complete color information (e.g. complete HSI information) suffer from high computational complexity and cannot be implemented in real time (e.g. methods of [8, 9]).

In [7] to overcome the problems connected with high computational complexity, particular components (Y-component and C_b-component) of (Y, C_b, C_r) coordinates [6] are applied, and ordinary histograms of them in a certain neighborhoods of road marking locations are employed. It was stressed in [6] that Y-component is the most used component for finding white lane markings. Actually, we use it for finding bursts. Since colored points of the yellow road marking determine a small peak of the histogram, the decision on the color of the road marking is made if this peak exists. Note that this decision is very sensitive to blobs of dirt that are always present on and near the road marking in winter and early spring in northern countries (like Russia). Moreover, at this time, the color of the road marking is seriously deteriorated by the climatic conditions. Even white lane markings may have yellow color characteristics. To discriminate the white and yellow road marking, we need a detailed analysis of color-intensity characteristics of the road marking and the adjacent parts of the road, including the analysis of the color of the precise parts of the road marking. The geometrized histograms method applied in our approach makes it possible to take into account all specific features of the posed problem. It allows us to perform the joint analysis of complete color-intensity characteristics of the road marking and those of the adjacent parts of the road using complete HSY information. The necessity of this analysis is stressed by the fact that we have images (taken under winter and early spring conditions) in which the yellow marking cannot be distinguished in grayscale components, while in the color image it can be clearly seen. In this case, our technique is very useful. The possibility of the local-global joint analysis of the road marking and its vicinity is provided by the global image analysis [13], using SearchLat (*STG*). This allows us to design reasoning systems to judge whether this marking is considered by human vision as a yellow one. In addition, temporary road marking may have a very high curvature, which it makes difficult to find it, using the binary image and the Hough transform, as in [7]. Our approach makes it possible to deal with road markings with any curvature. We also do not use any information about the camera calibration and position, which makes it possible to the road marking to start at any row of the image array. This is very useful in sharp turns, crossings, on ascends, and descends of the road. This also improves the portability of the software, not imposing requirements on the camera calibration.

5. Software implementation, demonstration of the results and discussion

The algorithms for finding lane markings have been implemented by programs written in C++ and operating under Windows and Linux environments. These programs process video sequences in real time on standard computers with processors I3-I7 and records the results for each frame of the video sequence tested. For color frames of resolution 640x480, the programs solve the complex of tasks, such as finding the sky, the road, the vegetation surrounding, the road body, and road markings with

operation speed about 20 fps when all operations of the code are performed sequentially. The first experiments with the use of parallel computations of the mentioned processors with four cores and hyper-threading technology have shown that the operation speed in computing *STG* can be reduced a factor of eight. This means that the program can work in real time for high resolution video. At present we are working on simultaneous calculations of *STG* for divisions of the image in both horizontal and vertical strips. This is important for finding in the image all types of road marking, as well as other vehicles in the road, moving in the same direction, entering the road, and moving on crossings in perpendicular directions.

Figure 6. An example of finding a road marking.

The programs have been tested on many real images taken from cars on different Russian roads under different seasons, times of the day, under different illumination conditions. Figures 6, 7 present two examples from records of the results.

Figure 7. An example of finding a road marking in an image from a video sequence.

In these figures, the road marking bunches are superimposed on the image and are painted red. These results were obtained for a division of the image into horizontal strips. However, to find stop lines and pedestrian crossings, it is necessary to divide images into vertical strips. It is clear that for full frame analysis, we need to divide the image into both vertical and horizontal strips. It is also clear that these processes can be used in a parallel manner, using several cores and threads for computing. The results of the joint analysis of two types of *STG* (obtained for divisions of the image into vertical and horizontal strips) in order to find different types of road marking will be the subject of our next publication. We are also applying the developed methods to traffic sign detection. In this connection, getting acquainted with the results of [16] motivated us to start this research.

6. References

[1] Dickmanns E D 2007 *Dynamic vision for perception and control and control of motion* (Berlin: Springer-Verlag Ltd.)
[2] Dickmanns E D 2002 Vision for ground vehicles: history and prospects *Int. J. of Vehicle Autonomous Systems* **6(3)** 1-44
[3] Wu P Ch, Chang Ch U and Lin Ch H 2014 Lane-mark extraction for automobiles under

complex conditions *Pattern Recognition* **47(8)** 2756-2767
[4] Tian Y, Gelernter J and Wang X 2018 Lane marking detection via deep convolutional neural network *Neurocomputing* **280** 46-55
[5] Mathibela B, Newman P and Posner I 2015 Reading the road: road marking classification and interpretation *IEEE Transactions on Intelligent Transportation Systems* **16(4)** 2072-2081
[6] Norote S P, Bhujbal P N, Norote A S and Dhane D M 2018 A review of recent advances in lane detection and departuture warning system *Pattern Recognition* **73** 216-234
[7] Son J, Yoo H, Kim S and Sohn K 2015 Real-time invariant lane detection for lane departure warning system *Expert Systems with Applications* **42** 1816-1824
[8] Chiu K-Y and Lin S-F 2005 Lane detection using color-based segmentation *Proc. IEEE Intelligent Vehicles Sym.* 706-711
[9] Sun T-Y, Tsai S-J and Chan V 2006 HIS color model based lane-marking detection *Proc. IEEE Intelligent Transportation Conf.* 1168
[10] Kiy K I 2010 A new real-time method for description and generalized segmentation of color images *Pattern Recognit. Image Anal.* **20(2)** 169-178
[11] Kiy K I 2015 Segmentation and detection of contrast objects and their application in robot navigation *Pattern Recognit. Image Anal.* **25(2)** 338-346
[12] Kiy K I 2015 A new real-time method of contextual image description and its application in robot navigation and intelligent control *Computer Vision in Control Systems-2 Innovations in Practice Intelligent Systems Reference Library 75* (Berlin: Springer) 109-133
[13] Kiy K I 2018 A new method of global image analysis and its application in understanding road scenes *Pattern Recognit. Image Anal.* **28(3)** 483-494
[14] Liu W, Li Sh and Huang X 2014 Extraction of lane markings using orientation and vanishing point constraints in structured road scenes *International Journal of Computer Mathematics* **91(11)** 2359-2373
[15] Demonstration site URL: https://www.facebook.com/100004887018729/videos
[16] Yakimov P Y 2015 Tracking traffic signs in video sequences based on a vehicle velocity *Computer Optics* **39(5)** 795-800 DOI: 10.18287/0134-2452-2015-39-5-795-800

Acknowledgments
This work was partially supported by the Russian Foundation for Basic Research, projects 18-07-00127 and 19-08-01159.
The authors thank Professor E.D. Dickmanns for his interest to the work, careful reading of the preliminary materials, and useful remarks and recommendations.

Adaptive interpolation of multidimensional signals for compression on board an aircraft

N I Glumov[1,2], M V Gashnikov[1,2]

[1]Samara National Research University, Moskovskoe Shosse 34A, Samara, Russia, 443086
[2]Image Processing Systems Institute of RAS - Branch of the FSRC "Crystallography and Photonics" RAS, Molodogvardejskaya street 151, Samara, Russia, 443001

e-mail: mgash@smr.ru

Abstract. We consider the compression of multidimensional signals on the aircraft board. We describe the data of such signals as a hypercube, which is "rotated" in a special way. To compress this hypercube, we use a hierarchical compression method. As one of the stages of this method, we use an adaptive interpolation algorithm. The adaptive algorithm automatically switches between different interpolating functions at each signal point. We perform computational experiments in real-world multidimensional signals. Computational experiments confirm that the use of proposed adaptive interpolator allows increasing (up to 31%) the compression ratio of the “rotated” hypercube corresponding to multidimensional hyperspectral signals.

1. Introduction

The growing interest in applied problems in the field of processing multidimensional signals [1-4] determines the relevance of research in this area. One of the main issues is the data size corresponding to the multi-dimensional signals. For example, data of hyperspectral remote sensing [1, 3], as one of the types of multidimensional signal, contain up to several hundred large-sized components of high bit depth. With airborne compression, this information needs to be transmitted through a limited communication channel. In this situation, the use of compression [5-8] is the only possible solution.
Currently, there are many methods of compression: wavelet [9], spectral [10], fractal [11], etc. However, all of them are very limited in airborne compression due to the high computational complexity and complexity of error control in the spatial domain. Besides, when a hyper-spectral data is received, a hypercube of a multidimensional signal is often “rotated” (see Figure 1-2) in a specific way: the first component (band) contains the first lines of the source bands; the second band includes the second lines, etc. We can see that this leads to the appearance of anisotropic correlation peculiarities in the signal cross-sections.

In the described conditions, the method of multidimensional signal compression based on hierarchical grid interpolation [12–13] has proven itself well. The most difficult stage of this compression method, which largely determines the efficiency of the method as a whole, is an interpolator of a multidimensional signal. In this paper, an adaptive interpolator based on hybrid technology is proposed for interpolation of specifically “rotated” multidimensional signals corresponding to hyperspectral remote sensing data. This technology combines the autoregressive

prediction of the signal cross-sections and adaptive parameterized interpolation within the cross-sections, which makes it possible to use the above-described correlation anisotropy of the multidimensional signal effectively.

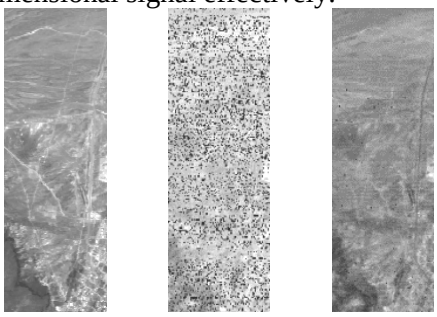

Figure 1. Cross-sections No. 10, 100, 120 of an "un-rotated" hyperspectral cube corresponding to the "natural" state of a multidimensional signal that can be processed and visualized in the data repository.

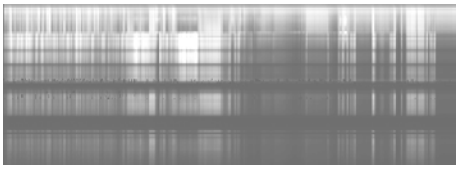

Figure 2. An example of a "rotated" cross-section of hyperspectral cube corresponding to a multidimensional signal compressed on board.

To study the proposed multidimensional interpolator, computational experiments are performed on natural multidimensional signals.

2. Autoregressive prediction of cross-sections of multidimensional signal

Consider a multidimensional (D-dimensional) signal

$$X = \left\{ x\left(d_0, d_1, .., d_{D-1}\right) \right\} . \quad (1)$$

This signal can also be considered as a set of (D–1) dimensional cross-sections:

$$X^t = \left\{ x^t\left(d_1, .., d_{D-1}\right) \right\} = \left\{ x\left(t, d_1, .., d_{D-1}\right) \right\}, \; 0 \le t < T \; . \quad (2)$$

Often these cross-sections are highly correlated (see Figures 1-2), for example, when processing hyperspectral data of remote sensing (for a hyperspectral signal of this type $D = 3$, and T coincides with the number of spectral bands). To account for the interdependency of the components, we use the linear autoregressive model:

$$P^t = k_1 X^{t-1} + k_2 X^{t-2} + ... + k_N X^{t-N} , \quad (3)$$

where P is the predicted cross-section of the multidimensional signal X, k_i are regression coefficients, N is the number of reference cross-sections used for the prediction. These coefficients are found from the condition of minimizing the quadratic error between the original and predicted components:

$$\varepsilon_t^2 = E\left\{ \left(X^t - \sum_{i=1}^{N} k_i X^{t-i} \right)^2 \right\} \to \min_{\{k_i\}} . \quad (3)$$

Consider also the differential cross-section of the signal

$$R^t\left(d_1, .., d_{D-1}\right) = X^t\left(d_1, .., d_{D-1}\right) - P^t\left(d_1, .., d_{D-1}\right), \; 1 \le t < T \; . \quad (4)$$

The variance of differential cross-section R^t is usually much smaller than the variance of the original cross-section X^t, and the probability distribution is much less uniform. Therefore, the differential cross-sections (4) are much more preferable for some types of processing, for example for compression.

3. Hierarchical compression of multidimensional signals

The difference cross-sections (4) are decorrelated, so that they can be processed independently. In this paper, these difference components are compressed using a hierarchical compression method [12–13], which uses a non-redundant hierarchical representation of a multidimensional signal $\mathbf{X} = \left\{ x\left(\vec{d}\right) \right\}$ as a set of L scale levels $\mathbf{X}_l$:

$$\mathbf{X} = \bigcup_{l=0}^{L-1} \mathbf{X}_l \ , \ \mathbf{X}_l = \left\{ x\left(\vec{d}\right) : \vec{d} \in I_l \right\}, \tag{5}$$

where I_l is the set of sample indices for scale level $\mathbf{X}_l$:

$$I_{L-1} = \left\{ 2^{L-1}\vec{d} \right\}, \ I_l = \left\{ 2^l \vec{d} \right\} \setminus \left\{ 2^{l+1}\vec{d} \right\}, \ 0 \le l < L \, . \tag{6}$$

The scale level number $(L-1)$ is the resampled "grid" of signal samples with the step of $2^{(L-1)}$ along each of the coordinates, and any other level (number l) is the grid of samples with the step of 2^l, from which all samples with doubled step are excluded.

During compression, the scale levels are compressed sequentially in order of decreasing their numbers. At the same time, more resampled levels are interpolated based on samples of less resampled levels. Since peculiarities of post-interpolation residues are similar to peculiarities of differences (4), their coding is much more efficient than coding sources samples.

4. Adaptive interpolation of multidimensional signals during compression

The most critical step of hierarchical compression is the interpolator. In this work, differential cross-sections (4) are compressed. The dimension of these differential cross-sections is one less than the dimension of the original signal. Thus, for three-dimensional remote sensing, the interpolator will work with two-dimensional data. Therefore, further, to simplify the presentation, we describe a two-dimensional version of the adaptive interpolator.

To ensure low computational complexity of hierarchical compression, we often use trivial interpolation procedures, based on averaging over the nearest samples of more resampled scale levels. Here is an example of an interpolation procedure:

$$\hat{x}_l^{(1)}\left(2m+1,2n+1\right) = \frac{1}{4}\left(\overline{x}_{l+1}\left(m,n\right) + \overline{x}_{l+1}\left(m+1,n\right) + \overline{x}_{l+1}\left(m,n+1\right) + \overline{x}_{l+1}\left(m+1,n+1\right) \right), \tag{7}$$

where $\overline{x}_{l+1}\left(m,n\right)$ are samples of a more resampled scale level, which have already passed compression and decompression.

This scheme is straightforward, but does not take into account local signal characteristics, for example, the oblong structures of onboard remote sensing data [14-16] (see Figure 2). Therefore, in this work, an adaptive interpolator is used to compress such remote sensing data. Besides function (7) this adaptive interpolator, uses two more interpolating functions that increase interpolation accuracy of oblong structures by averaging "along" them

$$\hat{x}_l^{(0)}\left(2m+1,2n+1\right) = \frac{1}{2}\left(\overline{x}_{l+1}\left(m,n\right) + \overline{x}_{l+1}\left(m+1,n+1\right) \right) \tag{8}$$

$$\hat{x}_l^{(2)}\left(2m+1,2n+1\right) = \frac{1}{2}\left(\overline{x}_{l+1}\left(m+1,n\right) + \overline{x}_{l+1}\left(m,n+1\right) \right) \tag{9}$$

The choice of the interpolating function for each signal sample is carried out by the parameterized decision rule:

$$\hat{x}_l\left(m,n\right) = \hat{x}_l^{(j)}\left(m,n\right), \ j = \begin{cases} 0, & \mu_l\left(m,n\right) < \alpha; \\ 1, & \alpha \le \mu_l\left(m,n\right) \le \beta; \\ 2, & \mu_l\left(m,n\right) > \beta; \end{cases}$$

where α, β are parameters of the decision rule (thresholds for switching between interpolating functions). These parameters are calculated automatically based on minimization of interpolation error or entropy of quantized post-interpolation residues; $\mu_l\left(m,n\right)$ is a feature describing the magnitude and direction of the elongated structure in the local neighborhood of the current signal sample:

$$\mu_l\left(2m+1,2n+1\right) = \left| \overline{x}_{l+1}\left(m,n\right) - \overline{x}_{l+1}\left(m+1,n+1\right) \right| - \left| \overline{x}_{l+1}\left(m,n+1\right) - \overline{x}_{l+1}\left(m+1,n\right) \right|. \tag{10}$$

The large absolute values $\left|\mu_l\left(2m+1,2n+1\right)\right|$ of the feature (10) describe to the samples corresponding the stable oblong structures. In these situations, interpolation (8-9) "along" these

structures is preferred. Small values of the attribute (10) correspond to the signal samples located in relatively uniform signal areas. In these areas, the "averaging" interpolation (7) works more precisely by averaging a noise.

The optimization of the adaptive interpolator according to the parameters α, β is performed separately [17] for each signal realization (more precisely, separately for each hierarchical signal level).

5. Experimental study of the adaptive interpolator

The proposed hybrid interpolator, including an intercomponent approximator and an intracomponent adaptive interpolator, was implemented by software and built into the hierarchical compression method. Based on this software, we performed an experimental study of the proposed interpolator effectiveness in nature multidimensional signal sets, "rotated" in a specific way to airborne compression (see the example in Figure 2). We used the following signal sets:

- signals [14] of hyper-spectrometer AVIRIS (224 bands);
- signals [15] of «TokyoTech» hyperspectral dataset (31 bands);
- signals [16] of hyper-spectrometer SpecTIR (360 bands, see Figure 1).

As a measure of the proposed interpolator efficiency, we used the gain G in the archive size (in %), which was provided by replacing the averaging interpolator (7) with the proposed hybrid interpolator in the frame of hierarchical compression method:

$$G = 100\% \cdot \left(S_{new} - S_{base} \right) / S_{base} \ , \qquad (11)$$

where S_{base}, S_{new} are the archive sizes when using averaging and proposed interpolators, respectively. We estimated the dependence of gain (11) on the quadratic error ε^2 introduced during compression. Typical results are shown in Tables 1-9. We can see that the proposed hybrid interpolator provides a noticeable gain (up to 31%) for the averaging interpolator.

Table 1. The gain of the adaptive interpolator for the averaging interpolator in the test signal "Agriculture & Vegetation" of SpecTIR hyper-spectrometer.

ε^2	0.00	0.67	2.00	9.80	33.74	118.02	249.83
G,%	5.74	7.57	8.45	9.69	11.44	10.36	9.07

Table 2. The gain of the adaptive interpolator for the averaging interpolator in the test signal "Cuprite" of AVIRIS hyper-spectrometer.

ε^2	0.00	0.66	1.99	9.81	34.82	126.82	271.50
G,%	13.09	17.95	20.98	24.95	25.05	22.72	19.67

Table 3. The gain of the adaptive interpolator for the averaging interpolator in the test signal "Cloth-2" of "TokyoTech" hyperspectral dataset.

ε^2	0.00	36.23	813.24	3068.88	6470.68	10730.59	15513.49
G,%	5.22	9.94	13.96	3.43	-3.16	-6.81	-9.16

Table 4. The gain of the adaptive interpolator for the averaging interpolator in the test signal "Gulf of Mexico Wetland" of SpecTIR hyper-spectrometer.

ε^2	0.00	0.67	1.99	9.52	31.98	111.70	232.48
G,%	5.22	6.84	7.67	8.84	8.67	5.76	2.83

Table 5. The gain of the adaptive interpolator for the averaging interpolator in the test signal "Doll" of "TokyoTech" hyperspectral dataset.

ε^2	0.00	36.20	780.62	2874.67	6064.38	10200.76	15172.86
G,%	8.87	13.93	5.22	0.19	-2.49	-4.21	-5.49

Table 6. The gain of the adaptive interpolator for the averaging interpolator in the test signal "Low Altitude" of AVIRIS hyper-spectrometer.

ε^2	0.00	0.67	2.00	9.99	36.25	132.80	282.44
G,%	5.95	8.02	9.27	11.25	11.10	8.24	5.23

Table 7. The gain of the adaptive interpolator for the averaging interpolator in the test signal "T-shirts" of "TokyoTech' hyperspectral dataset.

ε^2	0.00	36.21	818.07	3152.23	6664.50	11060.42	16190.09
G,%	9.49	14.41	7.23	1.70	-1.31	-3.27	-4.87

Table 8. The gain of the adaptive interpolator for the averaging interpolator in the test signal "Moffett Field" of AVIRIS hyper-spectrometer.

ε2	0.00	0.66	1.99	9.74	34.55	125.98	270.11
G,%	14.49	19.26	21.87	27.52	30.81	28.98	27.40

Table 9. The gain of the adaptive interpolator for the averaging interpolator in the test signal "Urban and Mixed Environment" of SpecTIR hyper-spectrometer.

ε^2	0.00	0.67	2.00	9.94	35.77	131.16	280.30
G,%	7.24	9.44	10.40	11.38	11.90	13.01	12.25

6. Conclusion

We considered the compression of multidimensional signals, which are described by the hypercube, «rotated» in a manner specific for onboard processing. To compress this hypercube, we used the hierarchical compression method. As one of the stages of this method, we used the adaptive interpolation algorithm based on automatic switching between different interpolating functions at each point of the signal. We confirmed computational experiments in natural multidimensional signals, which confirmed that the use of proposed adaptive interpolator allows increasing (up to 31%) the compression ratio of the «rotated» hypercube corresponding to multidimensional hyperspectral signals.

7. References

[1] Chang C 2013 *Hyperspectral data processing: Algorithm design and analysis* (Wiley & Sons)
[2] Dajion D and Mercero R 1988 *Digital processing of multidimensional signals* (M: Mir)
[3] Schowengerdt R 2007 *Remote sensing: models and methods for image processing* (Academic Press)
[4] Woods J 2011 *Multidimensional Signal, Image, and Video Processing and Coding* (Academic Press)
[5] Rehman M, Sharif M and Raza M 2014 Image compression: A survey *Research Journal of Applied Sciences, Engineering and Technology* **7** 656-672
[6] Bookstein A and Klein S 1990 Compression, information theory and grammars: a unified approach *ACM Trans. Inf. Systems* **8** 27-49
[7] Soifer V 2009 *Computer Image Processing, Part II: Methods and algorithms* (VDM Verlag)
[8] Woods E and Gonzalez R 2007 *Digital Image Processing* (Prentice Hall)
[9] Fouad M 2015 A Lossless Image Compression Using Integer Wavelet Transform with a Simplified Median-edge Detector Algorithm *International Journal of Engineering & Technology* **15** 68-73
[10] Plonka G and Tasche M 2005 Fast and numerically stable algorithms for discrete cosine transforms *Linear Algebra and its Applications* **394** 309-345
[11] Muruganandham A and Banu R 2010 Adaptive fractal image compression using PSO *Procedia Computer Science* **2** 338-344

[12] Sergeev V, Gashnikov M and Glumov N 1999 The Informational Technique of Image Compression in Operative Remote Sensing Systems *RAS Samara Research Center Bulletin* **1** 99-107
[13] Maksimov A I and Gashnikov M V 2018 Adaptive interpolation of multidimensional signals for differential compression *Computer Optics* **42(4)** 679-687 DOI: 10.18287/2412-6179-2018-42-4-679-687
[14] URL: http://aviris.jpl.nasa.gov/data/free_data.html
[15] URL: http://www.ok.sc.e.titech.ac.jp/res/MSI/ MSIdata31.html
[16] URL: http://www.spectir.com/free-data-samples
[17] Gashnikov M V 2017 Minimizing the entropy of post-interpolation residuals for image compression based on hierarchical grid interpolation *Computer Optics* **41(2)** 266-275 DOI: 10.18287/2412-6179-2017-41-2-266-275

Acknowledgments
The reported study was funded by: RFBR according to the research projects 18-01-00667, 18-07-01312; the RF Ministry of Science and Higher Education within the state project of FSRC “Crystallography and Photonics” RAS under agreement 007-GZ/Ch3363/26.

Adaptation of the mathematical apparatus of the Markov chain theory for the probabilistic analysis of recurrent estimation of image inter-frame geometric deformations

G L Safina[1], A G Tashlinskii[2] and M G Tsaryov[2]

[1]National Research Moscow State University of Civil Engineering, Yaroslavskoe Shosse, 26, Moscow, Russia, 129337
[2]Ulyanovsk State Technical University, Severnii Venetz, 32, Ulyanovsk, Russia, 432027

e-mail: tag54@mail.ru

Abstract. The paper is devoted to the analysis of the possibilities of using Markov chains for analyzing the accuracy of stochastic gradient relay estimation of image geometric deformations. One of the ways to reduce computational costs is to discretize the domain of studied parameters. This approach allows to choose the dimension of transition probabilities matrix a priori. However, such a matrix has a rather complicated structure. It does not significantly reduce the number of computations. A modification of the transition probabilities matrix is proposed, it's dimension does not depend on the dimension of estimated parameters vector. In this case, the obtained relations determine a recurrent algorithm for calculating the matrix at the estimation iterations. For the one-step transitions matrix, the calculated expressions for the probabilities of image deformation parameters estimates drift are given.

1. Introduction

At estimation of the parameters of image inter-frame geometric deformations (IID) under conditions of a priori uncertainty the non-identification stochastic gradient procedures (SGP) [1-2] are widely used [3-6]:

$$\hat{\boldsymbol{\alpha}}_t = \hat{\boldsymbol{\alpha}}_{t-1} - \boldsymbol{\Lambda}_t \boldsymbol{\beta}_t \left(Q\left(\mathbf{Z}^{(1)}, \mathbf{Z}^{(2)}, \hat{\boldsymbol{\alpha}}_{t-1} \right) \right), \quad (1)$$

where $\mathbf{Z}^{(1)}$ and $\mathbf{Z}^{(2)}$ are images; $\boldsymbol{\alpha} = (\alpha_1, \ldots, \alpha_m)^T$ is a vector of estimated parameters of geometric deformations; $\boldsymbol{\Lambda}_t$ is gain matrix; $\hat{\boldsymbol{\alpha}}_0$ is an initial of the parameter vector; $\boldsymbol{\beta}_t$ is a stochastic gradient of the cost function (CF) $Q(\cdot)$, characterizing the estimation quality.

The most practical application have relay procedures [8], when in (1) $\boldsymbol{\beta}_t = \left(\operatorname{sign}\left(\partial Q(\cdot) / \partial \alpha_1 \right), \operatorname{sign}\left(\left(\partial Q(\cdot) / \partial \alpha_2 \right) \right), \ldots, \operatorname{sign}\left(\left(\partial Q(\cdot) / \partial \alpha_m \right) \right) \right)^T$. At a good accuracy of the estimates, they have high velocity and better impulse noise resistance compared to gradient procedures [9]. The next parameter estimate α_i is determined as:

$$\hat{\alpha}_{i,t} = \hat{\alpha}_{i,t} - \lambda_{i,t-1} \operatorname{sign}\left(\partial \hat{Q}_i \left(\mathbf{Z}_1, \mathbf{Z}_2, \hat{\boldsymbol{\alpha}}_{t-1} \right) / \partial \alpha_i \right), \ \hat{\alpha}_{i0} \in \Omega(\boldsymbol{\alpha}), \quad (2)$$

where $\Omega(\boldsymbol{\alpha})$ is the domain of $\boldsymbol{\alpha}$. The estimates sequence

$$\hat{\boldsymbol{\alpha}}_0, \hat{\boldsymbol{\alpha}}_1, \ ..., \hat{\boldsymbol{\alpha}}_t, ..., \hat{\boldsymbol{\alpha}}_T \,, \tag{3}$$

obtained with SGP in the form of (1), is m-dimensional sequence without aftereffect and is a vector Markov process. At the same time, the joint probability density (PD) of IID parameters at any iteration can be expressed through the PD $w(\hat{\boldsymbol{\alpha}}_0)$ of the initial approximation $\hat{\boldsymbol{\alpha}}_0$ and one-step conditional PD $\pi_t(\hat{\boldsymbol{\alpha}}_t \,|\, \hat{\boldsymbol{\alpha}}_{t-1})$ of the Markov sequence transitions from $(t-1)$-th iteration to the t-th iteration, $t = \overline{1,T}$ [9]:

$$w(\hat{\boldsymbol{\alpha}}_0, \hat{\boldsymbol{\alpha}}_1, ..., \hat{\boldsymbol{\alpha}}_T) = w(\hat{\boldsymbol{\alpha}}_0) \prod_{t=1}^{T} \pi_t(\hat{\boldsymbol{\alpha}}_t \,|\, \hat{\boldsymbol{\alpha}}_{t-1}) \,.$$

The apparatus for analysis of Markov sequences makes it possible to take into account the finiteness of the domain $\Omega_{\hat{\boldsymbol{\alpha}}}$ of possible values of IID parameter estimates for different rules of PD behavior at the boundaries of parameter domain.

If the domain $\Omega_{\hat{\boldsymbol{\alpha}}}$ of $\hat{\boldsymbol{\alpha}}_t$ is continuous, then the sequence (3) is a simple Markov sequence; if it is discrete, then (3) is a Markov chain [10]. The latter is true, in particular, in the relay procedure (2). Attracting a well-developed mathematical apparatus of Markov sequences [10, 11] and chains [10, 12] for analyzing the effectiveness of PD with a finite number of iterations allows to obtain a number of useful results.

Let us consider the possibility of using the apparatus of the Markov chain theory for modeling the process of stochastic gradient estimation of IID parameters.

2. The relationship of the matrix of transition probabilities with the probabilities of drift estimates

If in (1) the gain matrix $\boldsymbol{\Lambda}_t$ is diagonal, then the matrix of conditional probabilities $\boldsymbol{\Pi}_i(l,t) = \left\| P\left\{\hat{\alpha}_{it} = a_{ik} \,|\, \hat{\alpha}_{il} = a_{ij}\right\}\right\|$ can be expressed in terms of estimates drift probabilities (EDP) of the IID parameters [13, 14]. The EDP of the parameter is the probability of the estimate improvement after the SGP iteration (taking into account possible changes in the estimates of other parameters). Then, with a variable step λ_t of the increment in (2), the elements $\pi_{jk}(l,t)$ of matrix $\boldsymbol{\Pi}(l,t)$:

$$\pi_{jk}(l,t) = \begin{cases} \rho_\alpha^+(\varepsilon_j), & \text{if} \quad l = t-1, k = j + \Delta_t \operatorname{sign} \varepsilon_j, \\ \rho_\alpha^o(\varepsilon_j), & \text{if} \quad l = t, k = j;, \\ \rho_\alpha^-(\varepsilon_j), & \text{if} \quad l = t-1, k = j - \Delta_t \operatorname{sign} \varepsilon_j, \\ 0, & \text{other case}, \end{cases}$$

where $\pi_{jk}(l,t)$ is the probability that the estimate $\hat{\alpha}_i$ will be equal to value a_{ik}, if at an earlier iteration $l < t$ the estimate had a value a_{ij}; $\rho_\alpha^+(\varepsilon_j)$ is the probability of changing the parameter to α_{ir}; $\rho_\alpha^-(\varepsilon_j)$ is probability of estimate change from α_{ir}; $\rho_\alpha^0(\varepsilon_j)$- probability of no change of the estimate; $\varepsilon_{ij} = (\alpha_{\text{ir}} - a_{ij})$; α_{ir} is the exact value of the parameter α_{i}; Δ_t is the number of possible states of parameter α in the interval from a_j to a_k, including the state a_k. In the future, to simplify the recording, the index «*i*» will be omitted when considering one parameter.

At a constant step λ_t the elements $\pi_{jk}(l,t)$ are also directly expressed through the EDP:

$$\pi_{jk}(l,t) = \begin{cases} \rho_{\alpha i}^+(\varepsilon_j), & \text{if} \quad l = t-1, k = j + sign\, \varepsilon_j; \\ \rho_{\alpha i}^o(\varepsilon_j), & \text{if} \quad l = t, k = j; \\ \rho_{\alpha i}^-(\varepsilon_j), & \text{if} \quad l = t-1, k = t - sign\, \varepsilon_j; \\ 0, & \text{other case}. \end{cases} \tag{4}$$

Under these conditions, we obtain a homogeneous Markov chain (3), for which

$$\boldsymbol{\Pi}(t) = \boldsymbol{\Pi}^t \,, \tag{5}$$

where $\boldsymbol{\Pi}$ is the matrix of one-step transition probabilities. At $t \to \infty$ such a chain becomes stationary.

However, with an increasing the number of estimated parameters, the application of the classical mathematical apparatus of Markov chains becomes problematic due to the sharp increase in the size of the transition probability matrix.

One of the main parameters determining computing costs, when using the Makovsky chain apparatus, is the number of possible values of IID parameter estimates. A priori, choose the size of the matrix **Π** allows the discretization of the estimated parameters domain. However, the use of the classical apparatus of the Markov chain theory remains reasonable only when estimating one parameter, since an increase in the number m of estimated parameters by one leads to an increase in computational costs at least by K^2, where K is the number of possible discrete values of estimates of the $(m+1)$-th parameter. In problems of measuring the IID parameters, the value K reaches several orders of magnitude. In this case, the determination of PD of parameter estimates, based on the use of a matrix of one-step transitions, becomes an obstacle for probabilistic modeling of the stochastic gradient process of measuring the parameters of inter-frame deformations.

3. Adaptation of the Markov chains apparatus to the solved problem

To reduce computational costs, we use the fact that at the t-th iteration, regardless of the state of the estimates of other parameters, transitions from the j-th state of parameter α_i estimate are possible only to the known k-th state, where $k \in \{j+\nu_{it}+1, j+\nu_{it}, j, j-\nu_{it}, j-\nu_{it}-1,\}$, $\nu_{it} = \text{int}\,(\lambda_{it}/\Delta_{\alpha i})$. In this case, the transition probabilities are determined by the state of other parameter estimates. The integral probability of the transition of estimate $\hat{\alpha}_i$ from the j-th state $(\hat{\alpha} = a_{ij})$ to the k-th state $(\hat{\alpha} = a_{ik})$ is determined by the sum of the transition probabilities from the subdomains $\omega_{\bar{i}k}$ of the parameter space, $i = \overline{1,m}$, $k = \overline{1,K_i}$. For example, to use relay-type procedures when evaluating three parameters α_1, α_2 and α_3 the overall probability $\tilde{\rho}_{ij}$ of deterioration of the estimate $\hat{\alpha}_1 = a_{1j}$ at the t-th iteration can be written as [15]:

$$\tilde{\rho}^{-}_{1j} = \sum_{k=1}^{K_1}\left(p_{2k}(t-1)\sum_{l=1}^{K_3} p_{3l}(t-1)\rho^{-}\left(\varepsilon_{1j},\varepsilon_{2k},\varepsilon_{3l}\right)\right),$$

where $p_{lk}(t-1) = P(\hat{\alpha}_l = a_{lk} \mid \hat{\alpha}_1 = a_{ij})$ is the probability that at the $(t-1)$-th iteration for $\hat{\alpha}_l = a_{lk}$, $k = \overline{1,K_l}$ the value $\hat{\alpha}_1$ is equal to a_{1j}; $\varepsilon_{lk} = a_{lk} - \alpha_{l\text{т}}$ is deviation of the estimate $\hat{\alpha}_l$ from the exact value $\alpha_{l\text{т}}$, $l = 1, 2, 3$. For m parameters we have:

$$\tilde{\rho}^{-}_{1j} = \sum_{k=1}^{K_2}\left(p_{2k}(t-1)\sum_{l=1}^{K_3}\left(p_{3l}(t-1)...\sum_{n=1}^{K_m}\left(p_{mn}(t-1)\rho^{-}\left(\varepsilon_{1j},\varepsilon_{2k},...,\varepsilon_{mn}\right)\right)...\right)\right). \quad (6)$$

Similarly, the expressions for probabilities $\tilde{\rho}^{o}_{1j}$ and $\tilde{\rho}^{+}_{1j}$ can be written.

With this approach, the matrices of one-step transitions are also change, which for this case we denote $\tilde{\tilde{\mathbf{\Pi}}}_i(t) = \left\| \pi^{(t)}_{jk}\left(i, \tilde{\rho}^{*}_{i_j}\right)\right\|$, where i is the number of parameter; $\pi^{(t)}_{jk}\left(i, \tilde{\rho}^{*}_{ij}\right)$ is probability of transition of i-th estimate from the state a_j at the $(t-1)$-th iteration to the state a_k to the t-th iteration:

$$\tilde{\rho}^{*}_{ij} = \sum_{\nu=1}^{K_2}\left(p_{1\nu}(t-1)...\sum_{l=1}^{K_m}\left(p_{ml}(t-1)\rho^{*}_i\left(\varepsilon_{1\nu},...,\varepsilon_{ij},...,\varepsilon_{ml}\right)\right)\right), \quad (7)$$

where $\rho^{*}_i(\cdot)$ are values of probabilities $\rho^{+}_i(\cdot)$, $\rho^{o}_i(\cdot)$ and $\rho^{-}_i(\cdot)$ at a vector of estimates mismatch $\bar{\varepsilon}_i = \left(\varepsilon_{1\nu},...,\varepsilon_{ij},...,\varepsilon_{ml}\right)^T$, $\varepsilon_{ik} = a_{ik} - \alpha_{i\text{т}}$. At the same time, the size of the matrix with m parameters compared with the traditional approach is reduced from $\sum_{i=1}^{m} K_i \times \sum_{i=1}^{m} K_i$ to $K_i \times K_i$. Computational costs are about as much reduced. This reduction occurs due to the loss of information about the probability of belonging to the estimation of the parameter vector of each of the subdomains of the parameter space. Only information about the projections of the distribution in this space is saved. In this case,

this information is sufficient for calculating the PD of IID estimates for a finite number of iterations. To calculate the PD of the estimate of the i-th parameter at the t-th iteration of the SGP, you need to know the PD of the estimates of all parameters on the $(t-1)$-th iteration:

$$\mathbf{p}_i^{\,T}(t) = \mathbf{p}_i^{\,T}(0)\prod_{s=1}^{t}\widetilde{\mathbf{\Pi}}_i(s)\cdot \tag{8}$$

Thus, determining the matrix $\widetilde{\mathbf{\Pi}}_i(t)$ allows only a recurrent method of calculation. Note also that, when $\widetilde{\mathbf{\Pi}}_i(t)$ is used even at $\lambda_i = const$ the Markov chain of estimates formed by the SGP, it can no longer be considered homogeneous. Accordingly, the expression (5) for this case is not true. To calculate the discrete probability distribution $\mathbf{p}_i^T(t)$ of estimates of the i-th parameter using the matrix $\widetilde{\mathbf{\Pi}}_i(t)$, we obtain the recurrent procedure:

$$\mathbf{p}_i^T(t) = \mathbf{p}_i^T(t-1)\widetilde{\mathbf{\Pi}}_i(t),\ i=\overline{1,m}\,. \tag{9}$$

For a variable step λ_{it} with adopted simplifications, the matrix $\widetilde{\mathbf{\Pi}}_i(t)$ for the parameter α_i can be determined as:

$$\widetilde{\mathbf{\Pi}}_i(t) = \begin{Vmatrix} \widetilde{\rho}^{-}_{i_1}+\widetilde{\rho}^{o}_{i_1} & 0 & \ldots & \widetilde{\rho}^{+}_{i_{1-1}} & \widetilde{\rho}^{+}_{i_{1-2}} & \ldots & 0 & 0 \\ \widetilde{\rho}^{-}_{i_2} & \widetilde{\rho}^{o}_{i_2} & \ldots & 0 & \widetilde{\rho}^{+}_{i_{2-1}} & \ldots & 0 & 0 \\ \widetilde{\rho}^{-}_{i_{3-2}} & \widetilde{\rho}^{-}_{i_{3-1}} & \ldots & 0 & 0 & \ldots & 0 & 0 \\ 0 & \widetilde{\rho}^{-}_{i_{4-2}} & \ldots & 0 & 0 & \ldots & 0 & 0 \\ \ldots & \ldots & \ldots & \ldots & \ldots & \ldots & \ldots & \ldots \\ 0 & 0 & \ldots & 0 & 0 & \ldots & \widetilde{\rho}^{o}_{i_{Ki-1}} & \widetilde{\rho}^{+}_{i_{Ki-1}} \\ 0 & 0 & \ldots & 0 & 0 & \ldots & 0 & \widetilde{\rho}^{o}_{i_{Ki}}+\widetilde{\rho}^{+}_{i_{Ki}} \end{Vmatrix}. \tag{10}$$

For constant λ_i the expression, determining the matrix element is significantly simplified:

$$\pi_{jk}^{(i)}\left(t,\widetilde{\rho}^{*}_{i_j}\right) = \begin{cases} \widetilde{\rho}^{-}_{i_j}+\widetilde{\rho}^{o}_{i_j}, & \text{if} \quad j=k=1, \\ \widetilde{\rho}^{-}_{i_j}, & \text{if} \quad j=k-1, 1<j<K_i, \\ \widetilde{\rho}^{o}_{i_j}, & \text{if} \quad j=k, 1<j<K_i, \\ \widetilde{\rho}^{+}_{i_j}, & \text{if} \quad j=k+1, 1<j<K_i, \\ \widetilde{\rho}^{o}_{i_j}+\widetilde{\rho}^{+}_{i_j}, & \text{if} \quad j=k=K_i, \\ 0, & \text{another case.} \end{cases} \tag{11}$$

Relations (7)-(11) determine the recurrent algorithms for calculating the matrix $\widetilde{\mathbf{\Pi}}_i(t)$ and the PD of the parameter estimation errors for the required iteration of estimation, starting from the initial approximation. The size of $\widetilde{\mathbf{\Pi}}_i(t)$ does not depend on the dimension of the vector $\overline{\alpha}$ and is determined only by the discretization parameters of the domain of definition of a specific parameter α_i. Computational costs with an increase in the dimension of the vector of parameters grow in proportion to $\sum_{i=1}^{m} K_i$, which allows to find a compromise between the accuracy of the calculation of PD and the requirements for computational resources. Further reduction of computational costs is possible due to the imposition of restrictions on the range of allowable values of the estimated parameters and the introduction of rules for taking into account probabilities beyond the boundaries of this area.

4. Conclusion

It is shown that the sequence of estimates of the parameters of IID, obtained using GSP, is a sequence without aftereffect and is a vector Markov process. With one estimated parameter for probabilistic modeling of the stochastic gradient estimation process, it is advisable to use the mathematical apparatus of the Markov chain theory. The study of expressions that allow calculating the transition probabilities of the matrix of one-step transitions through the probabilities of parameter estimation

drift showed that for relay algorithms with one estimated parameter, the single-step transition matrix has a five-diagonal structure and does not depend on the iteration number, determining the Markov chain uniformity. However, for the vector of parameters, the use of the classical apparatus of the Markov chain theory becomes problematic due to a sharp increase in the size of the transition probability matrix. A priori, the matrix size can be chosen to discretize the domain of the parameters to be estimated, but even with this approach, the use of the classical apparatus makes sense only when evaluating one parameter.

In order to reduce computational costs, one-step transition matrices are proposed, the dimension of which is determined only by discretization of the domain of the corresponding parameters and does not depend on their number. The resulting matrix allows only a recurrent method of its calculation from the initial approximation of the parameters to the required iteration. Moreover, the Markov chain of estimates loses the property of homogeneity. Also, accurate information about the probability distribution in the parameter space is lost. Only the projections of this spatial distribution are saved. However, this is enough to solve the problem of finding the PD of parameter estimates for inter-frame deformations with a finite number of iterations.

5. References

[1] Tashlinskii A G 2003 Computational expenditure reduction in pseudo-gradient image parameter estimation *Lecture Notes in Computer Science* **2658** 456-462
[2] Tashlinskii A G 2007 Pseudogradient estimation of digital images interframe geometrical deformations *Vision Systems: Segmentation and Pattern Recognition* (Vienna: I Tech Education and Publishing) **25** 465-494
[3] Shalev-Shwartz S and Zhang T 2016 Accelerated proximal stochastic dual coordinate ascent for regularized loss minimization *Mathematical Programming* **155(1)** 105-145
[4] Borisova I V, Legkiy V N and Kravets S A 2017 Application of the gradient orientation for systems of automatic target detection *Computer Optics* **41(6)** 931-937 DOI: 10.18287/2412-6179-2017-41-6-931-937
[5] Tashlinskii A G, Smirnov P V and Tsaryov M G 2017 Pixel-by-pixel estimation of scene motion in video *International Archives of the Photogrammetry Remote Sensing and Spatial Information* **XLII-2/W4** 61-65
[6] Fursov V A, Gavrilov A V, Goshin Ye V and Pugachev K G 2017 Conforming identification of the fundamental matrix in the image matching problem *Computer Optics* **41(4)** 559-563 DOI: 10.18287/2412-6179-2017-41-4-559-563
[7] Maksimov A I and Gashnikov M V 2018 Adaptive interpolation of multidimensional signals for differential compression *Computer Optics* **42(4)** 679-687 DOI: 10.18287/2412-6179-2018-42-4-679-687
[8] Tsypkin Ya Z 1995 *Information theory of identification* (Moscow: Fizmatlit) p 336
[9] Tashlinskii A G 2008 Optimization of goal function pseudogradient in the problem of interframe geometrical deformations estimation *Pattern Recognition Techniques, Technology and Applications* (Vienna: I Tech Education and Publishing) **10** 249-280
[10] Tichonov V I and Mironov M A 1977 *Markov processes* (Moscow: Sovetskoe Radio) p 488
[11] Neveu J 1964 *Mathematical foundations of probability theory* (Paris: Masson et cie) p 309
[12] Dynkin E B 1959 *Foundations of the Markov processes theory* (Moscow: Fizmatlit) p 227
[13] Tashlinskii A G and Tichonov V O 2001 Methods for analyzing the error of pseudogradient measurement of the parameters of multidimensional processes *Izvestiya vuzov: Radioelectronika* **44** 75-80
[14] Tashlinskii A G and Voronov I V 2014 The probability of the demolition of estimates of the parameters of image interframe geometric deformations with a pseudogradient measurement *Izvestiya Samarskogo nauchnogo tsentra Rossiiskoi akademii nauk* **6(2)** 612-615
[15] Tashlinskii A G, Gorin A A, Muratkhanov D S and Tikhonov V O Priority approach to the estimation of the parameters of the spatial image distortions 2001 *Pattern Recognition and Image Analysis* **11(1)** 251-253

Acknowledgments
The reported study was supported by RFBR and Government of Ulyanovsk region, project 18-41-730006.

Algorithm for detecting spherulite marker in human blood serum facies

O E Malenova[1], L I Trubnikova[2], A S Yashina[3] and M L Albutova[2]

[1]Ulyanovsk State Technical University, Severny Venetz Street, 32, Ulyanovsk, Russia, 432027
[2]Ulyanovsk State University, Lev Tolstoy Street, 42, Ulyanovsk, Russia, 432017
[3]Research-and-Production Association Mars, Solnechnaya Street, 20, Ulyanovsk, Russia, 432022

e-mail: nika-lilu@yandex.ru

Abstract. One of the effective methods of early medical diagnosis is the method of wedge dehydration. It is based on the analysis of facies images. Facia is a thin film of dried human biological fluids. The presence of special structures (markers) indicates various pathologies of the organism at their earliest stages. In this article, the algorithm for detecting spherulite marker on microscopic images of human serum facies is presented. The presence of spherulites on facies is the norm. However, the atypical form of spherulite is a marker of precancerous diseases: uterine fibroids, endometrial hyperplastic processes and the mammary gland. Due to the visual analysis of the marker, its characteristic features were identified. Then algorithmic detection methods for these features were developed. The decision on the probable presence of a marker was made if there was a combination of features of this marker. As a result of the application of the developed algorithm, most images of atypical spherulites were identified.

1. Introduction

Currently, early medical diagnostic methods are actively developing. Of particular interest are methods based on the analysis of human biological fluids (BF). One such method is the wedge dehydration method. It consists of applying a drop of BF on a specially prepared and degreased slide. This drop is dried at room temperature in a closed cabinet and the film is formed and called the facies (from the Lat. Faciens - appearance, shape). The scheme of interaction of the elements of BF is recorded on the facies. After dehydration, information from the liquid phase is represented as various structures on the film. These structures are viewable under a microscope.

D.K. Maxwell compiled the first theoretical description of the process of evaporation of a fixed large droplet flowing in the diffusion mode. In 1877 he considered the case of evaporation of a spherical drop in the article "Diffusion" [1]. L. Bohlen was the first to investigate dehydration in the field of medicine in 1942. He examined the capillary blood facies with a simple optical microscope and revealed a connection between the structures in these images and gastrointestinal tumors [2]. V.N. Shabalin and S.N. Shatokhin gave a justification for the possibility of using this method in medical research [3]. The development of algorithms for automated image analysis of the BF facies is of interest. This will allow the use of non-invasive diagnostic methods for mass screening of the

population with low costs and time. The detection algorithms for a number of markers are described in [5-11].

In the present work, the algorithm for the detection of spherulite markers is presented. The presence of spherulites on facies is considered normal. However, the atypical form of spherulite is a marker of serious diseases. Among them are such as uterine fibroids, hyperplastic endometrial processes and the mammary gland, which are among the precancerous.

2. Spherulite detection algorithm

For the development of a detection algorithm the main features of the spherulite marker were highlighted. These features distinguish it from the basic structure of facies and other markers.

2.1. Marker description

Spherulite is a complex rounded mineral aggregate. It consists of thin needle-like crystals and found in nature in the form of balls of radial-radiant structure [4]. The spherulite looks like a rounded crystalline formation on the facies in normal conditions. However, it can significantly change its shape in the presence of pathologies. Spherulites on facies of a healthy person are shown in figure 1. Spherulites on facies with pathology are shown in figure 2. It is noticeable that spherulites have a darker background, low variation, and a rounded shape in normal conditions. In pathology, the shape of a spherulite is different from an ellipse.

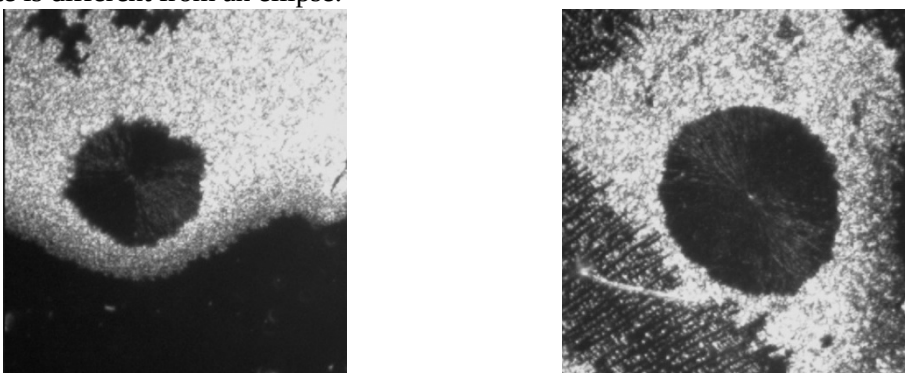

Figure 1. Typical spherulites.

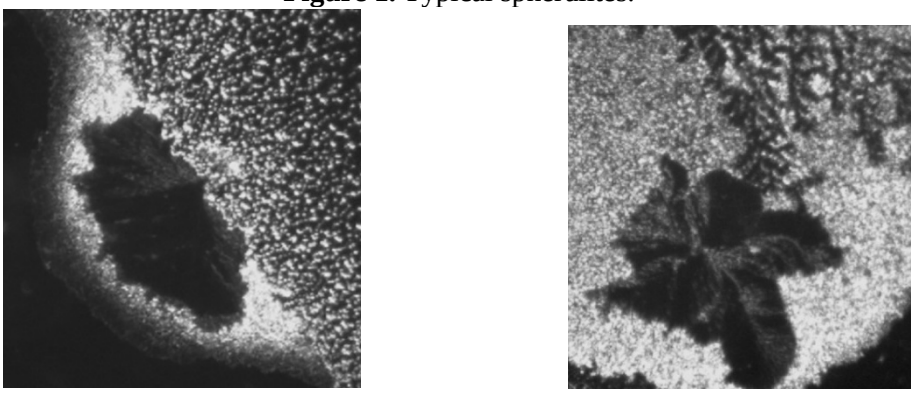

Figure 2. Atypical spherulites.

2.2. Marker detection algorithm

The algorithm was developed based on the features described above. It consists in the sequential application of the following operations to the original image.

- Image segmentation by brightness. Spherulites are darker than the main color of the facies. The average brightness of the image is calculated and all areas are darker than they stand out.
- Search the contours of areas with low brightness.
- Search for closed contours.
- Approximation by ellipse of the found closed contours.
- Decision-making.

3. Description of the algorithm

This paragraph displays the results of the analysis using this algorithm using the example of the image of the facies shown in figure 2 on the left.

3.1. Image preparation for processing

The color image is loaded into memory when you start the program. The entire image is converted to grayscale because the marker colors do not carry important information (figure 3). A median filter is carried out to get rid of random noise [12]. This reduces the number of false loops in the following steps.

3.2. Image segmentation by brightness

Sections of the image with brightnesses above the average are removed. The result of the threshold section is shown in figure 3a.

3.3. Search the contours

Outlining is implemented by the Canny algorithm [13] with thresholds T_1=100 и T_2=180. Where T_1 and T_2 are the thresholds of the minimum and maximum of the algorithm. Remove short borders with a length of less than 50 pixels using a pixel-by-pixel loop traversal. This is necessary to exclude random short contours. The bypass is implemented using the “Beetle” algorithm [14]. The remaining contours form the set *C*. The result is shown in figure 3b.

3.4. Search for closed contours

The set of closed contours C_z is selected among the set *C* of the remaining contours. The definition of closed loop is implemented using pixel bypass. The criterion of closure is the return of the bypass to the starting point.

3.5. Approximation by ellipse

Approximating ellipse *E* is found for each contour from C_z. It approximates the set of its boundary points $O = \{P(i) = (x(i), y(i)),\ \ i = 1,..., N\}$. Consider a second-order curve equation

$$x^2 + Bxy + Cy^2 + Dx + Ey + F = 0, \quad (1)$$

and choose the coefficients of this equation so that the sum of squared residuals of points of the set *O* is minimal: $\sum_{i=1}^{N} [x^2(i) + Bx(i)y(i) + Cy^2(i) + Dx.(i) + Ey(i) + F]^2 = \min$. An example of approximation of the system of points *O* by an ellipse is shown in figure 3c.

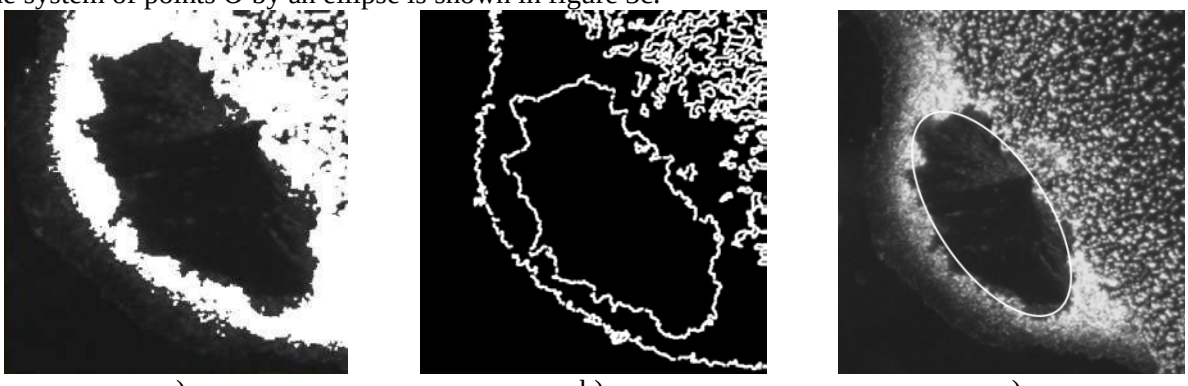

a) b) c)

Figure 3. Processing steps: threshold section (a), selection of contours (b), approximation with an ellipse (c).

3.6. Decision-making

The atypical spherulite marker has large deviations of the boundaries from the approximating ellipse. In addition, the major and minor axes of the ellipse should be almost equal to the norm.

Therefore, the evaluation form takes place in two stages.

- The axes of the approximating ellipse are compared. The value $r=a/b$ is considered, where a and b are the major and minor semiaxes of the ellipse. When $r \in [1; 1,3)$ spherulite is considered normal, with $r \in [1,3; 3)$ - with pathology, and for $r \in [3; \infty)$ - the contour is removed from consideration.
- The maximum and minimum distance of the boundary points from the center of the ellipse is estimated. Spherulite is considered pathological. If one of the thresholds is exceeded, a message on the presence of a marker is displayed. The threshold is calculated adaptively based on the size of the approximating ellipse. The minimum distance is defined as 0.8 from the minor axis and the maximum as 1.2 from the main axis.

4. Results of experiments

The algorithm was tested on 200 images of facies of blood serum with x400 optical magnification. As a result of the test, 86% of the atypical spherulites images were correctly identified. The algorithm made false detections and chose several structures similar to the desired marker in 11% of the images. This suggests that in the future it is advisable to expand the set of features of this marker for more accurate identification. It should be noted that there were other markers among the images from the list of false alarms. Search for other markers is also included in the tasks of the developed marker detection software complex.

5. Conclusions

In the course of this work, an algorithm and software for the automated detection of facies with suspicion of finding an atypical spherulite marker was created. Algorithm tests on real facies images showed acceptable results.

6. References

[1] Kraevoy S A and Koltovoy N A 2016 *Diagnosis using a single drop of blood, biofluid crystallization* (Moscow - Smolensk)
[2] Bolen H L 1942 The Blood Pattern as a Clue to the Diagnosis of Malignant Disease *J Lab Clin Med* **27** 1522-1536
[3] Shatokhina S N and Shabalin V N 2001 *Morphology of human biological fluids* (Moscow: Chrysostom) p 304
[4] Godovikov A A, Ripinen O I and Stepanov V I 1989 Spherulites, Spherocrystals, Spheroidites, Nucleospherolites *Tr. Mineral. Museum of the USSR Academy of Sciences* **36**
[5] Krasheninnikov V R and Kopylova A S 2011 Identification of Pectinate Structures in Images of Blood Serum Facia *Pattern Recognition and Image Analysis* **21(3)** 508-510
[6] Krasheninnikov V R and Kopylova A S 2012 Algorithms for automated processing images blood serum facies *Pattern Recognition and Image Analysis* **22(4)** 583-592
[7] Krasheninnikov V R, Trubnikova L I, Albutova M L, Kopylova A S and Tarasova A V 2013 Algorithm for detecting tongue structures on images of blood serum *Ulyanovsk medico-biological journal* **4** 70-73
[8] Krasheninnikov V R, Trubnikova L I, Albutova M L, Kopylova A S and Tarasova A V 2013 Detection of sickle-shaped cracks in images of facies of cervical mucus of a woman *Ulyanovsk medico-biological journal* **4** 81-85
[9] Krasheninnikov V R, Trubnikova L I, Albutova M L and Yashina A S 2015 Algorithm for detecting a marker of gallbladder disease on images of blood serum *Ulyanovsk Medical and Biological Journal* **4** 104-110
[10] Krasheninnikov V R, Yashina A S and Malenova O E 2017 Markers detection on facies of human biological fluids *Procedia Engineering* **201** 312-321
[11] Krasheninnikov V R, Yashina A S and Malenova O E 2017 Algorithms for detection of markers onthe facies of human biological fluids *Proceedings of the III International Conference ITNT-2017* (Samara: New technology) 655-662

[12] Chervyakov N I, Lyakhov P A and Orazaev A R 2018 Two methods of adaptive median filtering of pulse noise in images *Computer Optics* **42(4)** 667-678 DOI: 10.18287/2412-6179-2018-42-4-667-678
[13] Canny J A 1986 Computational Approach to Edge Detection *IEEE Transactions on Pattern Analysis and Machine Intelligence* **6** 679-698
[14] Potapov N N and Tupikov P A 2007 Methods for selecting contours in images *8th international conference Image recognition and image analysis: new information technologies* 105-108
[15] Khorin P A, Ilyasova N Yu and Paringer R A 2018 The selection of informative features based on the coefficients of Zernike polynomials in various pathologies of the cornea of the human eye *Computer Optics* **42(1)** 159-166 DOI: 10.18287/2412-6179-2018-42-1-159-166

Convergence characteristics at stochastic estimation of image inter-frame deformations

A G Tashlinskii[1], A V Zhukova[1] and D G Kraus[1]

[1]Ulyanovsk State Technical University, Severnii Venetz, 32, Ulyanovsk, Russia, 432027

e-mail: kraus_bak@mail.ru

Abstract. Several approaches to the numerical description of image inter-frame geometric deformations parameters estimates behavior at iterations of non-identification relay stochastic gradient estimation are considered. The probability density of the Euclidean mismatch distance of estimates vector is chosen as an argument of the characteristics forming the numerical values. It made it possible to ensure invariance of research to the set of parameters of the used inter-frame geometric deformations model. The mathematical expectation, the probability of exceeding a given threshold value of the convergence rate and the confidence interval of the Euclidean mismatch distance were investigated as characteristics. Probabilistic mathematical modeling is applied to calculate the probability density of the Euclidean mismatch distance.

1. Introduction

The systems of information extraction with spatial apertures of signal sensors are widely spread. These systems form dynamic arrays of spatially correlated data represented by image sequence. This representation has the clarity, compactness, and information capacity. In this case, one of the important tasks is to estimate the geometric deformations parameters of the image sequence [1-5]. To solve this problem, non-identification stochastic estimation proved to be good [6], wherein the formation of vector estimate $\overline{\boldsymbol{\alpha}}$ of deformation parameters of reference $\{z_{\mathbf{j}}^{(1)}\}$ and deformed $\{z_{\mathbf{j}}^{(2)}\}$ images (where $\{\mathbf{j}=(j_x,j_y)^T\}$ - pixel coordinates of $z_{\mathbf{j}}^{(1)}$ and $z_{\mathbf{j}}^{(2)}$), can be described by the procedure [7, 8]:

$$\hat{\boldsymbol{\alpha}}_t = \hat{\boldsymbol{\alpha}}_{t-1} - \boldsymbol{\Lambda}_t \boldsymbol{\beta}_t(Z_t, \hat{\boldsymbol{\alpha}}_{t-1}), \quad (1)$$

where $\boldsymbol{\beta}(\cdot)$ – stochastic gradient of an objective function, which characterizes the quality of evaluation (the mean square of the difference between the brightness of the reference and deformed images was used as the objective function to calculate examples); $\boldsymbol{\Lambda}_t$ – gain matrix, determining a value of the estimates change at the t-th iteration; Z_t – two-dimensional local sample of the reference and deformed images used to determine the stochastic gradient at the t-th iteration [9, 10].

The local sample size (LSS) largely determines the nature of estimates deformation convergence and the computational cost. The research direction is due to the fact that the problems of LSS optimization are not investigated enough. The paper discusses the possibilities of numerical description of vector estimates of geometric deformations parameters estimates behavior at iterations of non-identification relay stochastic gradient estimation.

As initial information for the numerical description of vector estimates behavior, the probability distributions of the estimates deformation parameters are chosen. The paper investigated the mathematical expectation, the probability of exceeding a given threshold value of convergence rate and the confidence interval as characteristics that form numerical values. When estimating one deformation parameter, these characteristics are directly applicable to its evaluation. If the set of parameters is estimated, then at the same iteration for each parameter different values of the optimal LSS can be obtained. Since one local sample is formed at each iteration, its value will be chosen corresponding to the maximum of the optimal volumes, which will lead to unreasonable computational costs. Therefore, in the paper, the probability distribution of the Euclidean mismatch distance (EMD) for the vector of deformation parameter estimates is chosen as the argument of the studied characteristics. This made possible to ensure the invariance of the study to the set of parameters of the deformation model used.

2. Choice of argument characteristics

For definiteness, we assume that geometric deformations of the images are estimated and described by the model of similarity, which include parameters of parallel shift $\mathbf{h} = (h_x, h_y)^T$, rotation angle φ, scale factor κ. In this case, we note that limitation of the parameter vector does not limit the following consideration.

Let, after the $(t-1)$-th iteration the vector of deformation parameters estimates has values $\boldsymbol{\alpha}_{t-1} = (\hat{h}_{x(t-1)}, \hat{h}_{y(t-1)}, \hat{\varphi}_{t-1}, \hat{\kappa}_{t-1})^T$. In addition, each estimate $\hat{h}_{x(t-1)}$, $\hat{h}_{y(t-1)}$, $\hat{\varphi}_{t-1}$ and $\hat{\kappa}_{t-1}$ has its own probability distribution: $w_{t-1}(\hat{h}_x)$, $w_{t-1}(\hat{h}_y)$, $w_{t-1}(\hat{\varphi})$ and $w_{t-1}(\hat{\kappa})$. Then, on the t-th iteration in the local sample the sample from resampled reference image with coordinates (x_a, y_b) will be taken for a couple with sample from deformed image with coordinates (a,b):

$$\begin{aligned} x_a &= x_0 + \hat{\kappa}_{t-1}((a-x_0)\cos\hat{\varphi}_{t-1} - (b-y_0)\sin\hat{\varphi}_{t-1}) + \hat{h}_{x(t-1)}, \\ y_b &= y_0 + \hat{\kappa}_{t-1}((a-x_0)\sin\hat{\varphi}_{t-1} + (b-y_0)\cos\hat{\varphi}_{t-1}) + \hat{h}_{y(t-1)}, \end{aligned} \tag{2}$$

where (x_0, y_0) – the coordinates of the rotation center.

The method for calculating the probability distribution of estimates of the image geometric deformations parameters was proposed in [11] and involves the sampling of the domain of parameter definition. Using the method it is possible to obtain discrete probability distributions (DPD) of the parameters for the selected deformation model:

$$w(h_x) = \{p_{l_x} = P(\hat{h}_x = h_{l_x})\},\ l_x = \overline{1, L_x},\ w(h_y) = \{p_{l_y} = P(\hat{h}_y = h_{l_y})\},\ l_y = \overline{1, L_y},$$
$$w(\varphi) = \{p_{l_\varphi} = P(\hat{\varphi} = \varphi_{l_\varphi})\},\ l_\varphi = \overline{1, L_\varphi},\ w(\kappa) = p_{l_\kappa} = P(\hat{\kappa} = \kappa_{l_\kappa}),\ l_\kappa = \overline{1, L_\kappa},$$

where $P(z)$ - the probability of z; L_x, L_y, L_φ и L_κ – the number of intervals for splitting the parameter space h_x, h_y, φ and κ. Then the coordinates (2) with the probability $P_{l_x l_y l_\varphi l_\kappa} = p_{l_x} p_{l_y} p_{l_\varphi} p_{l_\kappa}$ take the values:

$$\begin{aligned} x_{l_x l_y l_\varphi l_\kappa} &= x_0 + \kappa_{l_\kappa}((a-y_0)\cos\varphi_{l_\varphi} - (b-x_0)\sin\varphi_{l_\varphi}) + h_{l_x}, \\ y_{l_x l_{y_1} l_\varphi l_\kappa} &= y_0 + \kappa_{l_\kappa}((a-y_0)\sin\varphi_{l_\varphi} + (b-x_0)\cos\varphi_{l_\varphi}) + h_{l_y}. \end{aligned}$$

Thus, it is possible to calculate a probability distribution of distances between a point with coordinates (a,b) on the deformed image and possible positions of the conjugate point on the reference image for current estimates of the deformation parameters, i.e. get DPD of the euclidean mismatch distance (EMD) $w_t(r)$ at the t-th iteration.

Let consider a few examples of the results for the calculation DPD of EMD. Let the images have a Gaussian autocorrelation function and a signal-to-noise ratio (ratio of the variances of image and

noise) equal to 14. For parameters estimation the stochastic procedure (1) of relay type with diagonal gain matrix

$$\mathbf{\Lambda} = \begin{Vmatrix} \lambda_{hx} & 0 & 0 & 0 \\ 0 & \lambda_{hy} & 0 & 0 \\ 0 & 0 & \lambda_{\varphi} & 0 \\ 0 & 0 & 0 & \lambda_{\kappa} \end{Vmatrix}$$

and constant elements: $\lambda_{hx} = \lambda_{hy} = 0{,}05$, $\lambda_{\varphi} = 0{,}4$ and $\lambda_{\kappa} = 0{,}005$ is used. The value of the gain matrix coefficients is selected based on the autocorrelation function of the image (the value of the correlation radius of this function). The same experimental conditions are used for the examples given below.

Figure 1a and 1b show an example of the calculated DPD of estimates $\hat{\varphi}$ and $\hat{\kappa}$ with μ=1 and the parameter mismatch $h_x = h_y = 4$, $\varphi = 15^o$ and $\kappa = 1{,}2$, after 60 iterations. Note that the probability distribution of estimates of all parameters are close to the Gaussian. Figure 1c shows DPD $w_{60}(r)$ of absolute value EMD after 60 iterations:

$$r_{l_x l_{y_l} l_\varphi l_\kappa} = \sqrt{(a - x_{l_x l_{y_l} l_\varphi l_\kappa})^2 + (b - y_{l_x l_{y_l} l_\varphi l_\kappa})^2}$$

In this case, the expectation value of the EMD is 1.9, and the variance is 4.0.

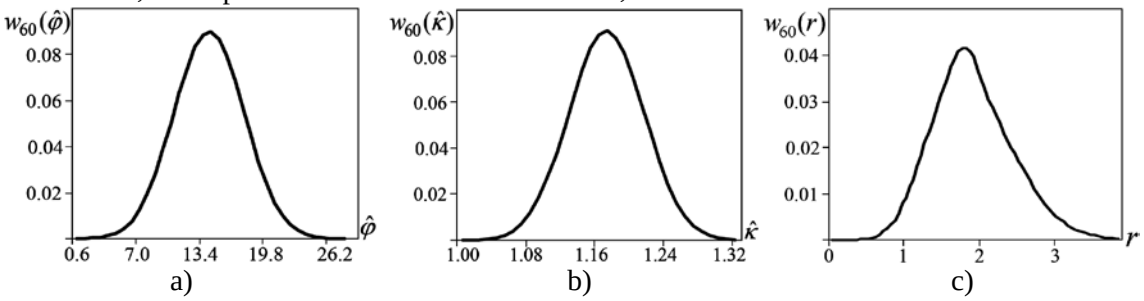

a) b) c)

Figure 1. Examples of DPD of deformation parameter estimates and EMD.

Figure 2a shows an example calculation for sample size $\mu = 3$.

In the general case, different points of the local sample plan correspond to different distribution of EMD. Totality of all local sample points corresponds to the total distribution. Examples of such distributions are shown in Figure 2. The local sample plan was formed as follows. At the t-th iteration of estimating the coordinate $(j_{x1},\ j_{y1})$ of the first count on the deformed image were chosen randomly within a certain domain, and the other two according to the rule:

$$(j_{xi},\ j_{yi}) = (\text{int}\,[R_i \sin\phi_i], \text{int}[R_i \sin\phi_i]),$$

where $i = 2, 3$; $\text{int}\,[z]$ - integer part of z; $\phi_2 = arctg\big((j_{y1} - y_0)/(j_{x1} - x_0)\big) - 120^o$, $\phi_3 = arctg\big((j_{y1} - y_0)/(j_{x1} - x_0)\big) + 120^o$; (x_0, y_0) - image center coordinates; R_i - random number.

Another example of DPD of EMD after 65 iteration that estimates mismatch parameters $h_x = 4$, $h_y = 4$, $\varphi = 15^0$ and $\kappa = 1$ with the volume of the local sample $\mu = 2$ is shown in the figure 2b.

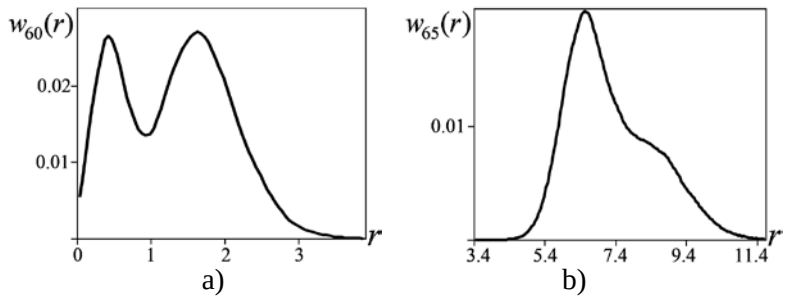

a) b)

Figure 2. Examples DPD of EMD with $\mu > 1$.

The result shows that with increasing LSS the distribution of EMD is not normalized. This is due to that EDM has non-linear dependence on deformation parameters, with the result that different points of the local sample plan give statistically significantly different mathematical expectations and variances of EDM.

3. Characteristics of changes in the vector estimations

Using the probability distribution of EMD we find the expression for the numerical description of image geometric deformations parameters estimates behavior at iterations of non-identification relay stochastic gradient estimation. As the characteristics that form the numerical values, we consider mathematical expectation, the probability of exceeding a given threshold value of the convergence rate and the confidence interval EMD.

3.1 Mathematical expectation of change EMD

The mathematical expectation of EMD determines the average rate of convergence of the estimated parameters at the t-th iteration. At LSS $\mu = m$, this characteristic can be found through a change in the distribution of EMD on adjacent iterations:

$$\mathrm{M}[\Delta r]\big|_{\mu=m} = \int_0^{\infty} r\left(w_{t-1}(r) - w_t(r)\right)dr\,. \tag{3}$$

A positive value (3) corresponds to the improvement of the parameter estimates vector $\hat{\boldsymbol{\alpha}}$, a negative value corresponds to the deterioration.

When using DPD the value $\mathrm{M}[\Delta r]$ is determined by the ratio:

$$\mathrm{M}[\Delta r]\big|_{\mu=m} = \sum_{i=1}^{L_r} r_i\left(p_{i,t-1} - p_{i,t}\right),$$

where L_r is the number of intervals splitting the domain of definition EMD. Clearly, that the expectation value $\mathrm{M}[\Delta r(+k)]$ of improving the vector of parameter estimates with increasing LSS by k can be found as:

$$\mathrm{M}[\Delta r(+k)] = \sum_{i=1}^{L_r} r_i\left(p_{i,t}\big|_{\mu=m} - p_{i,t}\big|_{\mu=m+k}\right).$$

For example, Figure 3a shows the dependence $w_{60}(r) - w_{61}(r)$ on EMD, which calculated at $\mu = 1$ for 61 iterations. This dependence describes parameter estimation vector changing for one iteration. In the given example for 61 iteration. Obviously, that with small EMD the probability differences are negative, for large ones they are positive. At the same time, the average value describes the integral change of the vector of estimates is positive (which indicates an improvement in the estimates) and equal to 0.017. The dependence numerically describe the improvement of the convergence estimates with increasing sample size is shown in Figure 3b. It shows the change of DPD of EMD after 60 iterations of the estimate when $\mu = 2$ compared to the case $\mu = 1$. As in Figure 3a, for small EMD, the probability differences are negative, for large ones, they are positive.

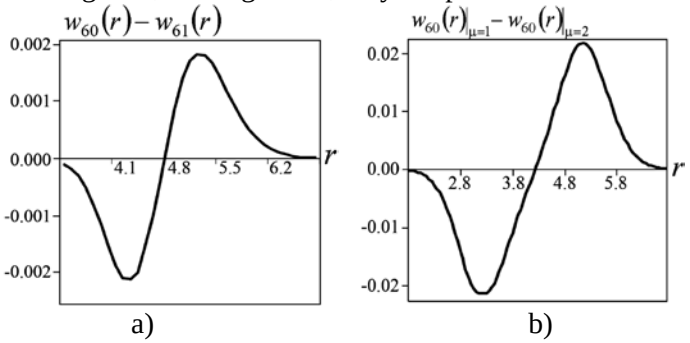

a) b)

Figure 3. Examples of differences in the DPD of EMD on adjacent iterations (a) and different LSS (b).

However, the average value was 0.02, which indicates a significantly higher rate of convergence of estimates.

3.2. Probability of exceeding a given threshold value of EMD convergence rate

Let us consider the possibility of using the probability of exceeding the given threshold value by the rate of convergence of the EMD to zero as a numerical characteristic of the convergence rate.

It is necessary to determine the distribution $w_t(\nu)$ of the convergence rate ν at the iterations of estimation and then determine the probability. The probability that EMD convergence rate at the t–th iteration will exceed a given threshold ν_{tv} is:

$$P_t = 1 - \int_{-\infty}^{\nu_{\text{tv}}} w_t(\nu) d\nu . \quad (4)$$

In this case, the distribution $w_t(\nu)$ can be found as the difference DPD of EDM on adjacent iterations:

$$w_t(\nu) = r(w_{t-1}(r) - w_t(r)),$$

conditionally accepting for a unit of time a dimensionless time between iterations.

In this case, the convergence rate can be estimated as at each iteration, as after a certain number of k iterations:

$$w_t(\nu) = r(w_{t-1}(r) - w_t(r))$$

Figure 4a shows an example of the DPD convergence rate of the EDM at 60 iterations at $\mu = 1$. At the same time, threshold value ν_{tv} is equal to 0.21 and the probability (4) of exceeding (shaded domain) is equal to 0.68. Figure 4b shows the dependence of probability exceeding the convergence rate of the EMD of the selected threshold value on LSS. Clearly, if you increase volume, then the probability increases, and reaches at $\mu = 5$ value 0.99.

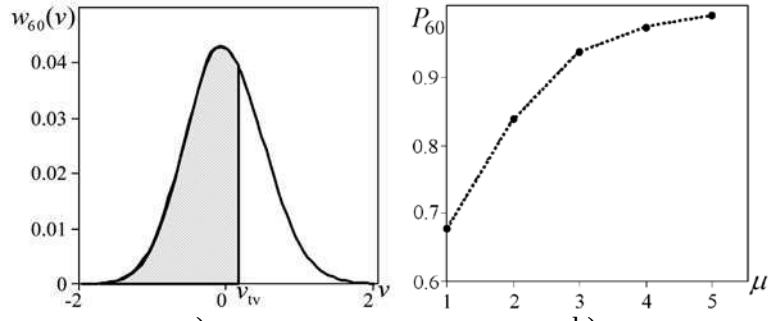

a) b)

Figure 4. DPD convergence rate and probability of exceeding the threshold value.

3.3. Confidence interval of the EMD

The change in the boundaries of the confidence interval at adjacent iterations is used as the numerical value of the deformation estimates of the confidence interval of EMD for a given confidence probability:

$$\Delta r_{\text{ci}} = r_{\text{lt}} - r_{\text{l}(t+1)} + r_{\text{rt}} - r_{\text{r}(t+1)}, \quad (5)$$

where the indices “l” and “r” mean left and right limits of the confidence intervals, respectively. Ratio (6) explains figure 5, where l_t and l_{t+1} are confidence intervals, respectively, in the t-th and $(t+1)$-th iterations.

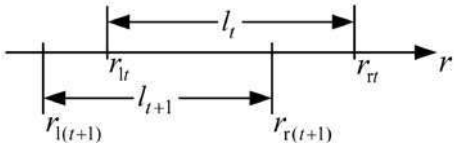

Figure 5. Changing the boundaries of the confidence interval.

Similarly, through the boundaries of the confidence intervals, one can describe the change in the vector of estimates with increasing LSS from $\mu = m$ to $\mu = m + k$:

$$\Delta r_{\text{ci}}(+k) = r_{\text{lt}}\big|_{\mu=m} - r_{\text{lt}}\big|_{\mu=m+k} + r_{\text{rt}}\big|_{\mu=m} - r_{\text{rt}}\big|_{\mu=m+k}. \quad (6)$$

Note that expressions (5) and (6) are written down with taking into account that the value of EMD cannot be non-negative. It is also necessary to take into account the mismatch signs of the current estimate $\hat{\alpha}_t$ and the exact parameter values α, when analyzing the measurement of boundaries of the confidence intervals of individual deformation parameters (such as the angle of rotation, parallel shift, etc.), which can be equal to positive and negative values:

$$\Delta r_{\text{ci}} = \left(r_{\text{lt}} - r_{\text{l}(t+1)} + r_{\text{rt}} - r_{\text{r}(t+1)}\right) sign\ (\hat{\alpha}_t - \alpha),$$

$$\Delta r_{\text{ci}}(+k) = \left(r_{\text{lt}}\big|_{\mu=m} - r_{\text{lt}}\big|_{\mu=m+k} + r_{\text{rt}}\big|_{\mu=m} - r_{\text{rt}}\big|_{\mu=m+k}\right) sign\ (\hat{\alpha}_t - \alpha)_t.$$

4. Conclusion

The paper presented numerical description of image geometric deformations parameters estimates behavior at iterations of non-identification relay stochastic gradient estimation. As initial information for solving the problem, we consider the probability distribution of parameter estimates. As an argument of numerical characteristics that describe the convergence rate of estimates of geometric deformation parameters of images, the distribution of EMD probabilities is used. They form numerical values, which made it possible to ensure invariance to the set of parameters of the used inter-frame geometric deformations model.

The mathematical expectation of EMD change, probability of exceeding the convergence rate of a given threshold value and confidence interval of EMD at a given confidence level are investigated as numerical characteristics. The investigated characteristics can be used to optimize the volume and plan of the local sample according to various criteria. In particular, when using the probability of exceeding a given threshold value of the convergence rate to optimize the LSS, and after calculating the DPD of EMD, the task is reduced to finding the LSS which ensures that probability (4) exceeds a given probability threshold.

Results showed that the confidence interval is a less informative parameter in comparison with mathematical expectation of change and with probability of exceeding a given threshold value of the convergence rate EMD. This is due to the fact that the probability distribution of EMD significantly changes from iteration to iteration. Therefore, on adjacent iterations, the change in the limits of the confidence interval does not always characterize the improvement of the estimates vector.

5. References

[1] Fursov V A, Gavrilov A V, Goshin Ye V and Pugachev K G 2017 Conforming identification of the fundamental matrix in the image matching problem *Computer Optics* **41(4)** 559-563 DOI: 10.18287/2412-6179-2017-41-4-559-563

[2] Tashlinskii A G, Smirnov P V and Tsaryov M G 2017 Pixel-by-pixel estimation of scene motion in video *International Archives of the Photogrammetry Remote Sensing and Spatial Information* **XLII-2/W4** 61-65

[3] Maksimov A I and Gashnikov M V 2018 Adaptive interpolation of multidimensional signals for differential compression *Computer Optics* **42(4)** 679-687 DOI: 10.18287/2412-6179-2018-42-4-679-687

[4] Moritz P, Nishihara R and Jordan M 2016 A linearly-convergent stochastic L-BFGS algorithm *Proc. of the 19th Int. Conf. on Artificial Intelligence and Statistics* 249-258

[5] Dmitriev E A and Myasnikov V V 2018 Comparative study of description algorithms for complex-valued gradient fields of digital images using linear dimensionality reduction methods *Computer Optics* **42(5)** 822-828 DOI: 10.18287/2412-6179-2018-42-5-822-828

[6] Tsypkin Ya Z 1995 Information theory of identification (Moscow: Fizmatlit) 336 (in Russian)

[7] Tashlinskii A G 2003 Computational expenditure reduction in pseudo-gradient image parameter estimation *Lecture Notes in Computer Science* **2658** 456-462

[8] Tashlinskii A G 2007 Pseudogradient estimation of digital images interframe geometrical deformations *Vision Systems: Segmentation and Pattern Recognition* (Vienna: I Tech Education and Publishing) **25** 465-494
[9] Tashlinskii A G 2008 Optimization of goal function pseudogradient in the problem of interframe geometrical deformations estimation *Pattern Recognition Techniques, Technology and Applications* (Vienna: I Tech Education and Publishing) **10** 249-280
[10] Tashlinskii A G and Zhukova A V 2017 Effectiveness of correlation and information measures for synthesis of recurrent algorithms for estimating spatial deformations of video sequences *CEUR Workshop Proceedings* **1901** 235-239
[11] Tashlinskii A G and Tichonov V O 2001 Methods for analyzing the error of pseudogradient measurement of the parameters of multidimensional processes *Izvesyiya vuzov: Radioelectronika* **44(9)** 75-80 (in Russian)

Acknowledgments
The reported study was funded by RFBR and Government of Ulyanovsk Region according to the research project № 18-01-730006 and № 18-41-730009.

Comparative analysis of segmentation algorithms for the allocation of microcalcifications on mammograms

Yu A Podgornova[1], S S Sadykov[1]

[1]Murom Institute (branch) Federal state budgetary Educational Institution of Higher Education" Vladimir State University named after Alexader Grigoryevich and Nickolay Grigoryevich Stoletovs", Orlovskaya street, 23, Murom, Russia, 602264

e-mail: yuliyabulanova@yandex.ru

Abstract. Breast cancer is the most common disease of the current century in the female population of the world. The main task of the research of most scientists is the detection of this pathology at an early stage (the tumor size is less than 7 mm) when a woman can still be helped. An indicator of this disease is the presence of small-point microcalcifications, located in groups within or in the immediate circle of the tumor. Microcalcification is a small-point character at cancer, reminding grains of sand of irregular shape which sizes are from 100 to 600 microns. The probability of breast cancer increases with the increase in the number of microcalcifications per unit area. So, the probability of cancer is 80% if more than 15 microcalcifications on 1 sq. cm. The microcalcifications are often the only sign of breast cancer, therefore, their detection even in the absence of a tumor node could be a harbinger to cancer. Image segmentation is one way to identify microcalcifications. The conducted research allowed us to choose the optimal segmentation algorithms of mammograms to highlight areas of microcalcifications for further analysis of their groups, sizes, and so on.

1. Introduction

The mammary gland is a complex, sensitive organ that requires constant monitoring due to the annual increase in the incidence of breast cancer and its "rejuvenation" [1]. Often a symptom of serious diseases is small-point calcification, called microcalcifications (deposits of calcium) [1]. Usually, isolated microcalcifications or clusters are small in size, so they do not self-identify. For detection of this pathology is required to carry out hardware diagnostics such as ultrasound and mammography.

Mammography is a noninvasive method for the detection of pathologies of mammary glands [2].

Microcalcinates differ in localization, size, shape, concentration, quantity. Examples of microcalcifications are presented in figure 1. To assess all of these parameters will need to find and select the picture mammography. To evaluate all the specified parameters, it is necessary to find and highlight them in the mammography image. The process of finding homogeneous areas in an image is called segmentation. It is the first step in image analysis. Thus, segmentation [3] plays an important role in the processing of medical images. The main idea of the segmentation process is as follows: each pixel of the image can be associated with some visual properties, such as brightness, color, and texture. Within one object or one part of an object, these attributes change relatively little, whereas when crossing the border from one object to another, there is usually a significant change in the above attributes.

At the moment many image segmentation algorithms are developed [4], therefore the main task of this paper is the analysis of existing methods of segmentation and selection of an optimal algorithm for detection of microcalcifications in mammographic images.

There is the following classification of image segmentation algorithms [5]: threshold methods, region-based methods, edge detection methods, and clustering-based algorithms. Edge detection methods are not used in this work, as most are used to highlight the contours of the image. This article explores the following segmentation algorithms: algorithm FloodFill, the watersheds, MeanShift, and k-means.

Figure 1 shows examples of mammograms with different microcalcifications, in Figure 1(c), in addition to microcalcifications, there is also a malignant neoplasm that has fuzzy spiciform contours, i.e. a star-shaped knot with thin strands extending from it, which are called spicules.

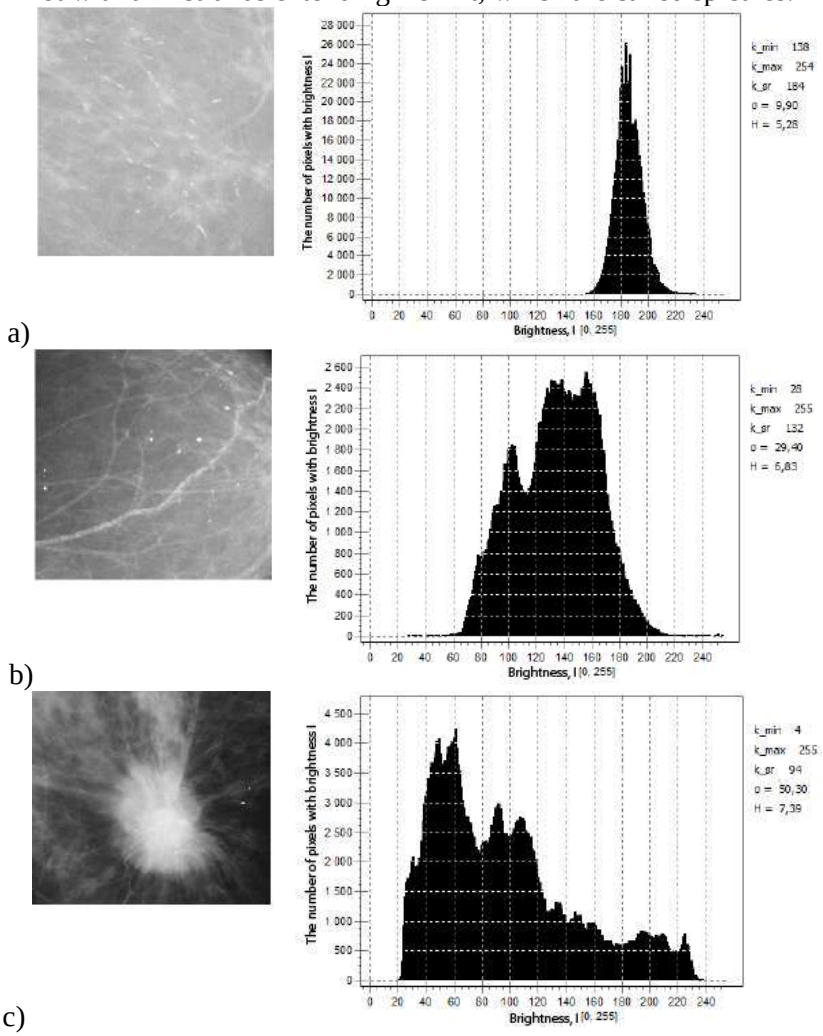

Figure 1. Examples of forms, localization, and the number of microcalcifications on mammograms.

2. Overview of segmentation algorithms

2.1. Watershed method

The concept of watershed [7, 8, 9, 10] is based on the representation of the image as a three-dimensional surface defined by two spatial coordinates and the level of brightness as the height of the surface (relief). In this "topographical" interpretation, three types of points are considered: (a) points of the local minimum; (b) points located on the slope, i.e. from which water rolls down to the same local minimum; and (C) points located on the crest or peak, i.e. from which water is equally likely to roll down more than one such minimum. When applied to a specific local minimum, a set of points

that satisfy condition (b) is called a basin (or catchment area) of this minimum. The sets of points that satisfy condition (c) form the ridge lines on the surface of the relief and are called the watershed lines.

One of the most important applications of segmentation by watersheds is the selection of objects of uniform brightness in the background (in the form of spots). Areas characterized by small changes in brightness have small gradient values. Therefore, in practice, there is often a situation when the method of segmentation by watershed is applied not to the image itself, but to the gradient of this image. Under such conditions, the local minima of the basins agree well with the small gradient values, which usually corresponds to the objects of interest.

2.2. MeanShift segmentation

The main idea of this method [11, 12] is that the input image can be used to construct a nuclear estimate for the probability density of data distribution in the RGBXY feature space. Next, a natural assumption is made that the local maxima of the probability density corresponding to the cluster centers. From the necessary condition of a local extremum, an expression is determined for the shift vector *m(p)* of the feature space $p \in$ RGBXY, applying which iteratively to the point p we get a sequence of points converging to the local maximum of the probability density estimate (i.e. to the center of the nearest cluster):

$$m(p) = \frac{\sum_{i=1}^{n} p_i \cdot g_i}{\sum_{i=1}^{n} g_i} - p,$$

where $g_i = g\left(\left\|\frac{(p - p_i)}{h}\right\|^2\right)$, $g(v) = -k'(v)$, h is smoothing parameter, *K(v)=ck(v)* is kernel estimates of a density.

2.3. FloodFill algorithm

Using the FloodFill method [11, 13, 14] it is possible to select areas of uniform color. To do this, select the starting pixel and set the interval for changing the color of neighboring pixels relative to the original. The interval can be asymmetric. The algorithm will combine pixels into one segment (filling them with one color) if they fall within the specified range. The output is a segment filled with a certain color and its area in pixels.

Such an algorithm can be useful for filling an area with weak color swings with a homogeneous background. One of the ways to use FloodFill is to detect damaged edges of the object. For example, if the algorithm fills neighboring regions by filling homogeneous areas with a certain color, then the integrity of the border between these areas is violated.

2.4. k-means algorithm

k-means segmentation [15, 16, 17, 18] is the most popular clustering method. The algorithm is aimed at minimizing the total quadratic deviation of cluster points from the centers of these clusters. Thus, this is an iterative algorithm that divides a given set of pixels into k clusters of points, which are as close as possible to their centers, and the clustering itself occurs due to the displacement of these same centers. It is necessary to take into account the fact that the k-means method is very sensitive to noise, which can significantly distort the results of clustering.

3 Experimental results

As criteria for evaluation of work of algorithms of segmentation, it is possible to use quality of background suppression and selection of objects in the form of connected areas.

Because microcalcifications are a complex object, it is impossible to demand accurate determination of the object consisting of several parts of different brightness as a single connected region.

For the analysis methods were taken real pictures of microcalcifications on mammograms. Images differ in the number and type of microcalcifications, brightness of the background and objects, and the presence of repetitive textures.

Figures 2-4 show the results of the algorithms on the original images. Only the FloodFill algorithm coped with the allocation of microcalcifications, all other algorithms have identified too many connected regions. Such experimental results suggest the need for using pre-processing methods before using segmentation.

Next to the images were applied contrasting methods, described in detail in [2].

Figures 5-7 show examples of studies of segmentation algorithms on contrasted mammograms.

The results of the experiments are as follows:

1) the watershed algorithm is not suitable for the solution of a task at all;
2) the MeanShift algorithm is able to allocate the required objects only in images without tumors on the background of fatty involution;
3) the k-means algorithm showed results similar to the previous method.

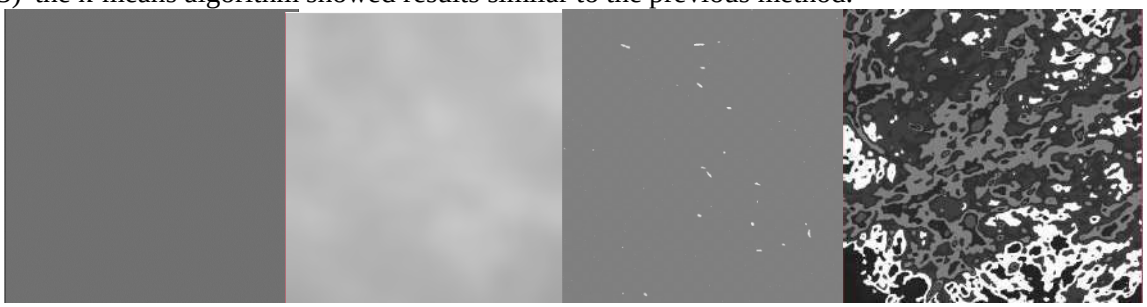

a) b) c) d)

Figure 2. Examples of image segmentation shown in Figure 1(a): (a) watershed method, (b) MeanShift algorithm, (c) FloodFill algorithm, (d) k-means segmentation.

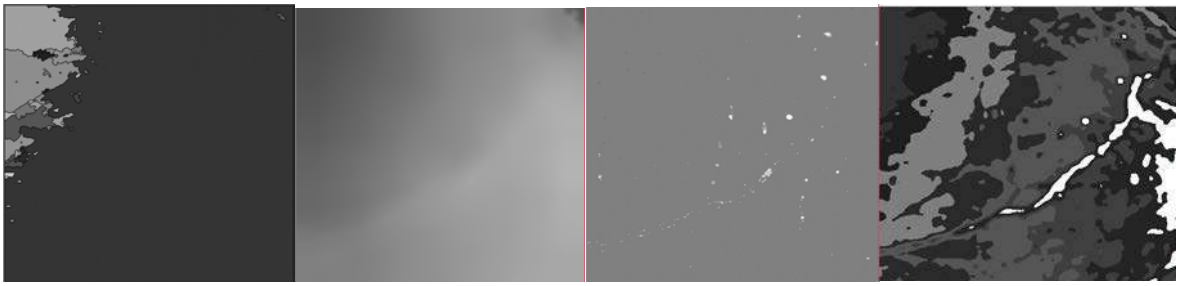

a) b) c) d)

Figure 3. Examples of image segmentation shown in Figure 1(b): (a) watershed method, (b) MeanShift algorithm, (c) FloodFill algorithm, (d) k-means segmentation.

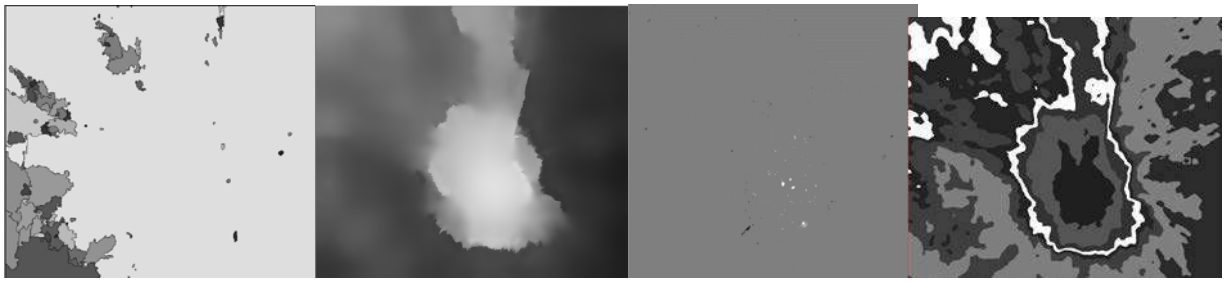

a) b) c) d)

Figure 4. Examples of image segmentation shown in Figure 1(c): (a) watershed method, (b) MeanShift algorithm, (c) FloodFill algorithm, (d) k-means segmentation.

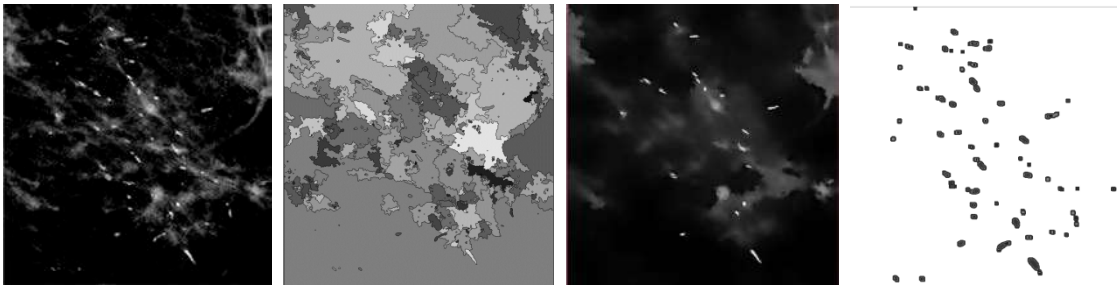

a) b) c) d)

Figure 5. Examples of image segmentation shown in Figure 1(a): (a) changing the brightness/contrast of the image, (b) the watershed algorithm, (c) – the MeanShift algorithm, (d) the k-means segmentation.

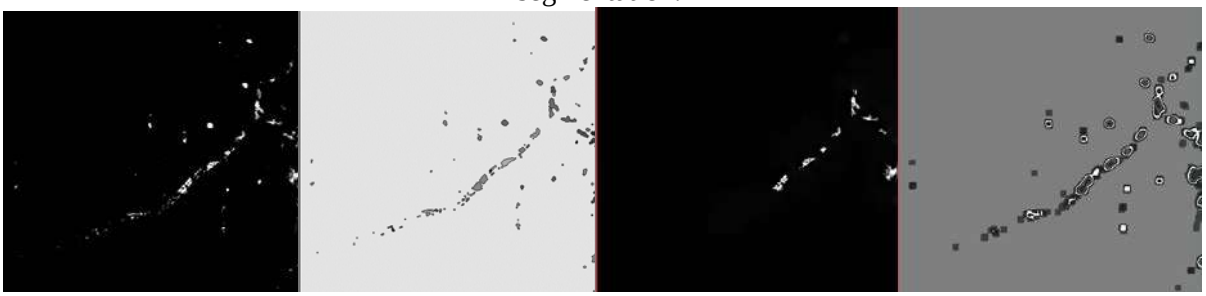

a) b) c) d)

Figure 6. Examples of image segmentation shown in Figure 1(b): (a) changing the brightness/contrast of the image, (b) the watershed algorithm, (c) the MeanShift algorithm, (d) the k-means segmentation.

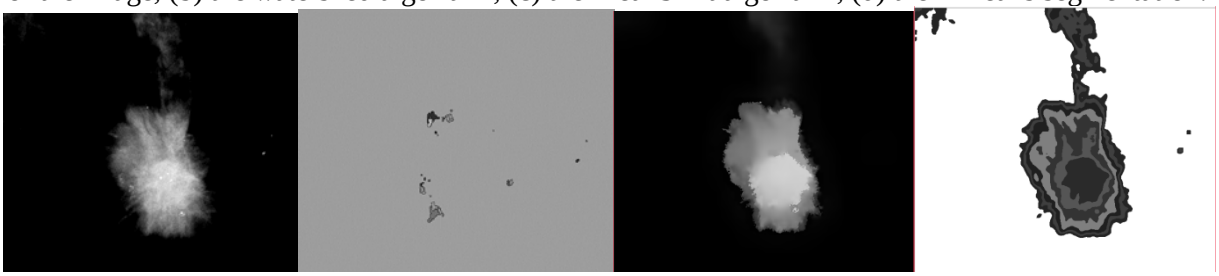

a) b) c) d)

Figure 7. Examples of image segmentation shown in Figure 1(c): (a) changing the brightness/contrast of the image, (b) the watershed algorithm, (c) the MeanShift algorithm, (d) the k-means segmentation.

The study of the work of the algorithms was carried out on 250 mammograms from the MIAS [2] database. Empirically managed to achieve the results presented in Table 1 and 2.

Table 1. The results of the segmentation algorithms on the original mammograms.

Algorithm	Number of correct detections (% of total images)	Number of false detections (% of total images)
Watershed algorithm	15 (6%)	235 (94%)
MeanShift algorithm	213 (85,2%)	37 (14,8%)
FloodFill algorithm	178 (71,2%)	72 (28,8%)
k-means segmentation	89 (35,6%)	161 (64,4%)

Table 2. The results of the segmentation algorithms on the processed mammograms.

Algorithm	Number of correct detections (% of total images)	Number of false detections (% of total images)
Watershed algorithm	45 (18%)	205 (82%)
MeanShift algorithm	98 (39,2%)	152 (60,8%)
k-means segmentation	107 (42,8%)	143 (57,2%)

4. Conclusion

Comparative analysis of different methods of image segmentation applied to the problem of allocation of microcalcifications in mammographic images. To compare segmentation methods, criteria were used based on the expert's assessment (based on visual analysis) of the quality of background suppression and the selection of objects as connected areas. Through experimental studies, it was found that the method of watersheds incorrectly finds the boundaries of objects and is not acceptable in solving the problem.

The best segmentation result was obtained using the FloodFill algorithm, which consists of the selection of areas of uniform color. During the experiments, it was found that to improve the quality of mammogram segmentation, it is advisable to pre-process the images. It provides a reduction in the number of analyzed areas by combining segments and removing irrelevant fragments from the point of view of the problem. Using the same segmentation algorithms after processing the images showed that the MeanShift algorithms and k-means are able to highlight microcalcifications only on the images without tumors on the background of fatty involution.

It should be noted that further research is needed to improve the methods of thematic segmentation, taking into account the spatial properties of areas and providing the best compromise between insufficient and excessive segmentation.

The obtained results allow us to outline the prospects of using segmentation algorithms in the construction of automatic cancer detection systems on mammograms at an early stage.

5. References

[1] Korzhenkova G P 2004 *Comprehensive X-ray Sonographic Diagnosis of Breast Diseases* (Moscow: Firma STROM) p 128
[2] Sadykov S S, Bulanova Yu A and Zaharova E A 2014 Computer diagnosis of tumors in mammograms *Computer Optics* **38(1)** 131-138
[3] Eddaoudi F and Regragui F 2011 Microcalcifications detection in mammographic images using texture coding *Applied Mathematical Sciences* **5** 381-393
[4] Panchenko D S and Putyatin E P 1999 Comparative analysis of image segmentation methods *Radio electronics and informatics* **4** 109-114
[5] Whitey D J and Koles Z J 2008 A review of Medical Image segmentation: Methods and available software *International Journal of Bioelectromagnetism* **10** 125-148
[6] Doskolovich L L, Kharitonov S I, Petrova O I and Soifer V A 1998 A gradient method for design of multiorder varied-depth binary diffraction gratings – a comparison *Opt. And Lasers in Eng.* **29** 249-259
[7] Sadykov S S, Bulanova Yu A, Zaharova E A and Yashkov V S 2013 Marker watershed study to isolate the breast cancer area *Algorithms, methods and data processing systems* **1** 56-64
[8] Hagyard D and Razaz M 1996 Analysis of watershed algorithms for gray scale images *IEEE conf on image processing* **3** 41-44
[9] Gauch J M 1999 Image segmentation and analysis via multiscale gradient watersheds *IEEE trans on image processing* **8** 69-79
[10] Myasnikov E V 2017 Hyperspectral image segmentation using dimensionality reduction and classical segmentation approaches *Computer Optics* **41(4)** 564-572 DOI: 10.18287/2412-6179-2017-41-4-564-572
[11] Comaniciu D, Ramesh V and Meer P 2000 Real-Time Tracking of Non-Rigid Objects Using Mean Shift *Conference on CVPR* **2** 1-8
[12] Dingding Liu, Bilge Soran, Gregg Petrie, and Linda Shapiro 2019 *A Review of Computer Vision Segmentation Algorithms* (Washington: University of Washington)
[13] Comaniciu D and Meer P 2002 Mean Shift: A Robust Approach toward Feature Space Analysis *IEEE Trans. Pattern Analysis and Machine Intelligence* **24** 603-619
[14] Charles J J, Kuncheva L I, Wells B and Lim I S 2006 An Evaluation Measure of Image Segmentation Based on Object Centres *International Conference Image Analysis and Recognition ICIAR 2006: Image Analysis and Recognition* (Springer: Verlag Berlin Heidelberg)

[15] Inaba M, Katoh N and Imai H 1994 Applications of weighted Voronoi diagrams and randomization to variance-based k-clustering *Proceedings of 10th ACM Symposium on Computational Geometry* 332-339 DOI:10.1145/177424.178042
[16] Steven J 2002 Acceleration of K-Means and Related Clustering Algorithms *Lecture Notes in Computer Science* (Springer Berlin Heidelberg) 166-177 DOI:10.1007/3-540-45643-0_13
[17] Nameirakpam D 2015 Image Segmentation Using K-means Clustering Algorithm and Subtractive Clustering Algorithm *Procedia Computer Science* **54** 764-771
[18] Tatarnikov V V, Pestunov I A and Berikov V B 2017 Centroid averaging algorithm for a clustering ensemble *Computer Optics* **41(5)** 712-718 DOI: 10.18287/2412-6179-2017-41-5-712-718

Acknowledgments
Podgornova Yu A expresses her sincere gratitude to her academic advisor, Dr. of Tech. Sci., Professor Sadykov S S for his help at the research conduct, valuable recommendations in relation to their planning and article preparation as well as for his moral support.

Development of the technique for automatic highlighting ranges of interest in lungs x-ray images

N Yu Ilyasova[1,2], T A Chesnokova[2]

[1]Image Processing Systems Institute of RAS - Branch of the FSRC "Crystallography and Photonics" RAS, Molodogvardejskaya street 151, Samara, Russia, 443001
[2]Samara National Research University, Moskovskoe Shosse 34A, Samara, Russia, 443086

e-mail: ilyasova.nata@gmail.com, c_taya@mail.ru

Abstract. In this paper, information technology has been developed for highlighting ranges of interest in lung x-ray images, based on the calculation of textural properties and classification of k-means. In some cases, the highlighted objects can describe not only the current patient's condition but also specific characteristics regarding age, gender, constitution, etc. While using the k-means method, the relationship between the segmentation error and fragmentation window size was revealed. Within the study, both a visual criterion for evaluating the quality of the segmentation result and a criterion based on calculating the clustering error on a large set of fragmented images were implemented. The study also included image pre-processing techniques. Thus, the study showed that the technology provided key objects highlighting error at 26%. However, the equalizing procedure has lessened this error to 14%. X-ray image clustering errors for fragmentation windows of 12x12, 24x24 and 36x36 were presented.

1. Introduction

Lungs X-ray is commonly performed in pulmonology. As chest x-ray is relatively fast and easy, it is particularly useful for screening respiratory diseases such as pneumonia and tuberculosis. According to medical studies, the mass of the lungs, being unevenly distributed in the chest, and has a higher density in the lower lobes. In addition, the lung mass increases with a fibrosis degree because of conjunctive tissue diffusing [1]. Many diseases can be distinguished at early stages due to the lung size screening and the ribs changes monitoring. Nowadays, there are no clinical methods to measure the density of the lungs directly. High-resolution computed tomography as the clinical standard in pulmonary fibrosis diagnostics, considers specific emission decreasing in lung tissue [2, 3]. These changes can be distinguished through the lungs x-ray image analysis.

A technique based on textural features selection has been suggested for the x-ray image analysis. Earlier, textural features had shown good results for the recognition and further diagnostics of biomedical images [4-9]. Considering the relevance of the problem, the researchers have come up with a number of solutions based on feature generation via discriminative analysis [10], followed by image segmentation [11-13]. The well-known MaZda library [14, 15] was used to calculate the textural features. The work [16] explores the detection of pathologies using blood cells images through textural characteristics of different classes of the source images in various colour subspaces; and as recent studies have shown, textural analysis is very well suited for highlighting the ranges of interest in medical pictures [4-8].

In this paper, a technology enhancing the ranges of interest, using the k-means classification methods has been proposed. The main benefit of the method is an opportunity to highlight the regions of interest by their textural features. The level of interaction between the signs, expressed by the value of correlation coefficients [10], may serve as additional information, which helps to improve the quality of the x-ray pictures of the lungs diagnosis. If the correlation between the signs is strong enough, the question arises about the appropriateness of using these signs and the possibility to reduce the dimension of feature space either by abandoning some of them and using only one of the associated signs or by identifying common properties. In the first case, we reduce the number of calculations, leaving the best feature values of any criterion. In the second case, the ability to obtain a new, more effective feature for classification appears. This technique was used in the work [17] and ensured high precision segmentation of fundus images. The presented results indicate that the proposed technology seems to be the most effective for x-ray image analysis.

The prime objective of this paper is to introduce a novel approach to identifying the lungs and background using clustering methods. In fact, as we specify it below, our approach is more than simply clustering. It is evident from the get-go that blindly using nondeterministic clustering algorithms, which typically produce (unmanageably) large numbers of local optima, would introduce great variability into the result. On the other hand, deterministic algorithms such as agglomerative hierarchical clustering typically are (substantially) slower and require essentially “guessing” the initial clustering, which in practical applications can often turn out to be suboptimal.

2. The technique for highlighting the lungs on x-ray images based on images pre-processing and k-means clustering

In this paper, we analyze the selection of the lungs at the chest x-ray images using automatic image segmentation. This method is widely used in the processing of biomedical images for various purposes, for example, for the detection of lung or liver cancer [18]. Every time we learn new about cancer, the motivation to help patients increases. Cancer differs from other diseases. It is not caused by any physical damage or biochemical imbalance. If we can identify all the major signs of the disease, this can greatly facilitate progress in understanding the origin and development of cancer. Therapeutically, if different types of cancer possess common basic structures, then the remedy for one type of cancer may be used on others. For the study, it was necessary to form a set of features that could provide the most accurate classification of x-ray images. There was a large number of textural features. In the work [19], they were divided into three groups, e.g., features based on the measurement of spatial frequencies; features based on statistical characteristics of the levels of intensity of the elements of decomposition; and features based on the description of structural elements.

Within this study, the “MaZda” program calculated 287 features. An approach based on the adjacency matrix was used [15, 19] for the formation of the features introducing a mutual disposition of pixels within the floating window. In addition, some textural properties based on the description of structural elements were considered. From the group of features based on the series lengths the following features were used, e.g. moment, inverse moment, distribution of gray levels, distribution of lengths of lines of constant optical density, the relative number of lines of constant optical density. The features mentioned above form one of the subsets out of all textural properties. Figure 1 shows the scheme for highlighting the regions of interest using the k-means method; we will describe each point in detail.

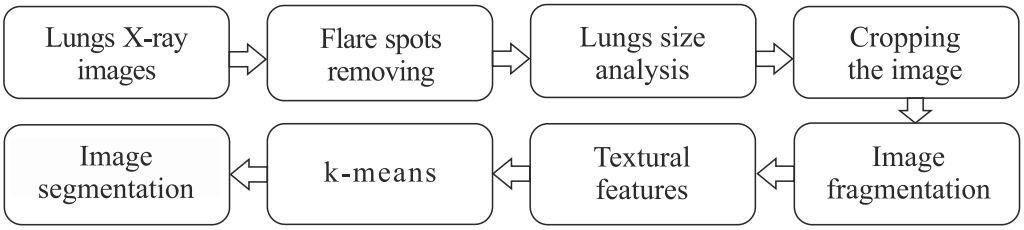

Figure 1. Technology for the regions of interest highlighting using the k-means method.

To recognize the individual objects at the x-ray picture, the following steps were undertaken. The original image was preliminary processed (Figure 2a) as follows: the flare spots with inappropriate, informative part of the image were removed; then the image was fragmented for textural features by 12 × 12, 24 × 24, 36 × 36 windows; and a set of textural features of fragmented images and clustering images based on the generated informative features was formed. For enhancing the lungs area, the initial image was preliminarily equalized. After that, the threshold processing was performed at 160, the amount of the threshold being set up experimentally. For the resulting image, see Figure 2c. An assessment of the height and width of each lung was performed, and in accordance with the data obtained (Figure 2b), nonilluminated images were cropped to leave only the parts with the lungs images being in the range of interest of the physician (Figure 2d). Next, the image was fragmented and the textural properties were calculated for every pixel by the MaZda program.

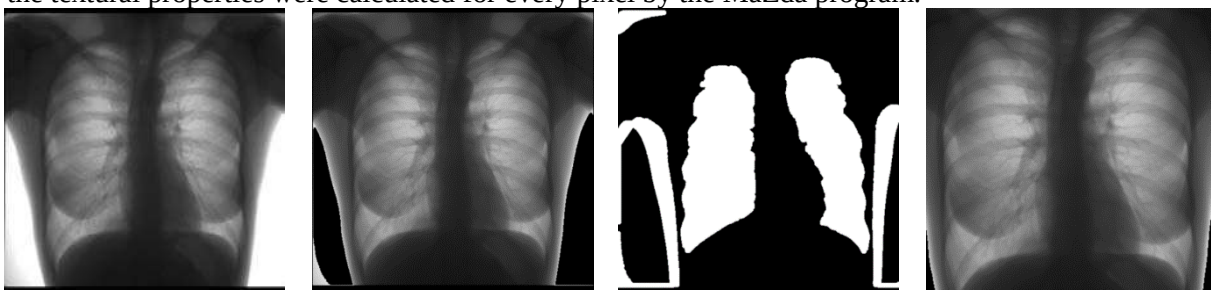

a) b) c) d)

Figure 2. Image preprocessing results: (a) source image; (b) nonilluminated image; (c) equalized image with highlighted lungs and a flare spot; (d) image with the ranges of interest.

Having performed the space of features, clustering was performed based on the k-means method. The results of this procedure are illustrated in Figure 3.

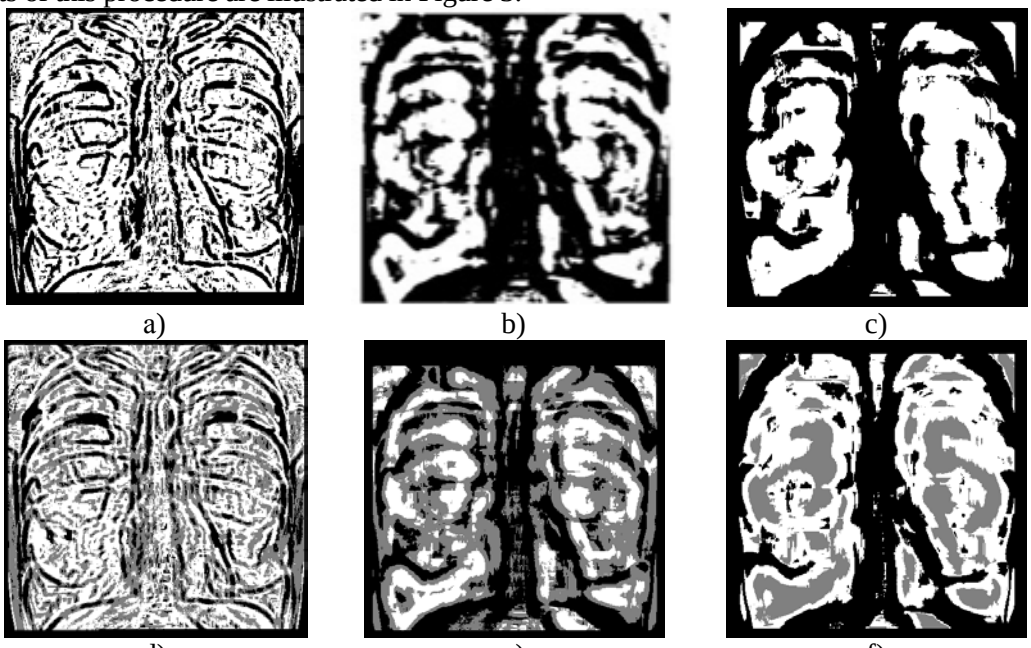

a) b) c)

d) e) f)

Figure 3. Results of X-ray image segmentation according to the presented technology: (a) k = 2, fragmentation 12 × 12; (b) k = 2, fragmentation 24 × 24; (c) k = 2, fragmentation 36 × 36; (d) k = 3, fragmentation 12 × 12; (e) k = 3, fragmentation 24 × 24; (f) k = 3, fragmentation 36 × 36.

In the figure, the clustering of k-means on the lungs according to the textural attributes highlighted the ranges of interest incompletely. To improve the quality of the lung highlighting on X-ray pictures, the second technology based on morphological methods was considered. This technology is presented in Figure 4.

A drawback of k-means is that it is not a deterministic algorithm. Typically, there are copious local minima; and the algorithm guarantees that it will converge to a local minimum rather than to a global one. Being an iterative algorithm (as the initial centers are not pre-set in advance), k-means starts with a random set of centers at the initial iteration and converges to a different local minimum in every run. There is no magic bullet in practical applications, typically, trying to guess the location of initial centers is not easier as guessing where, for example, the global minimum is. In fact, it is acceptable in many applications. However, in the context of extracting of lungs signatures it might result in an exercise in futility. We need a way to eliminate or greatly reduce indeterminism, so we propose the second technique.

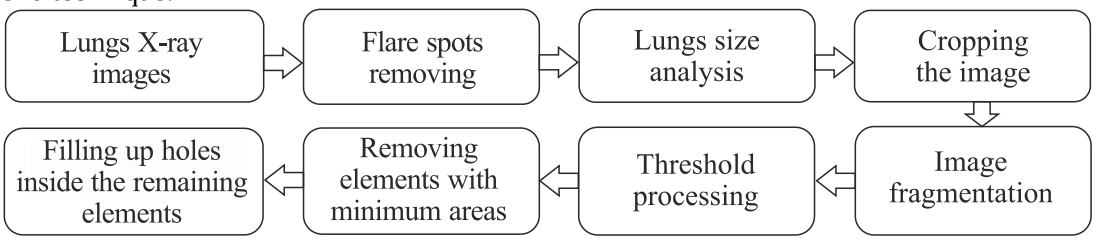

Figure 4. Technology for the selection of the ranges of interest according to the morphological methods.

At the first step, similar to the technology based on the k-means method, the original image was cropped to avoid processing fragments that were out of interest. This method contained the following steps: equalization of the original image; removing the elements with the smallest areas (while two elements, i.e. the lungs, remain); filling in holes inside the remaining elements. For the image processing result, see Figure 5.

a) b)

Figure 5. Results of x-ray image processing: (a) processing by morphological operations; (b) lungs highlighted by an expert.

A comparative analysis of the results of the research methods was carried out and the corresponding errors were calculated, i.e. the k-means clustering error and the segmentation error of the equalization method. To analyze the obtained results, the image of the lungs highlighted by the expert (Figure 5b) was considered a reference. The clustering errors were calculated separately for each class, i.e. for the lungs and for the background; in case of the lungs, the error was calculated as a ratio of the number of incorrectly classified image fragments to the total number entering the region of the lungs. For the results of the analysis, see Table 1.

The total clustering error with the k-means method was 38.49% for 12×12 fragmentation, 30.61% and 28.06% for fragmentation 24×24 and 36×36 respectively. For the equalization, the error was noticeably smaller and amounted to 13.90%, and all the pixels corresponding to the segmentation error were located at the boundaries of the range of interest; that fact simplified further improvement of the algorithm.

3. Conclusion

The present study considers the application of the k-means method for the detection of images of individual objects, such as the lungs and background.

The information technology for automatic highlighting the ranges of interest on lung X-rays has been proposed. The article presents the relationship between the segmentation error and the fragmentation window size. The analysis of the obtained images was carried out, and the clustering error was found. Regarding the first method of lung X-ray, the result was less effective and revealed the objects of certain classes with an error of 28.06%, whereas technology based on the morphological methods highlighted lungs with an error of 13.90%. The clustering error of the x-ray image for the fragmentation windows of 12×12, 24×24 and 36×36 has also been found. The selection of the range of interest on the lungs x-ray in accordance with the equalization was considered preferable. The high error of the first clustering method was associated with the choice of feature space; in our case, image processing was conducted for all features calculated using MaZda software. In the future, we are planning to improve the results by the use of discriminant analysis for texture features.

Table 1. Clustering error.

	1 class (lungs)	2 class (background)	Total error
Number of correct fragments 1nd method (12×12)	97 951	40 321	
Segmentation errors 1nd method (12×12, %)	29.16	56.70	38.49
Number of correct fragments 1nd method (24×24)	64 119	74 153	
Segmentation errors 1nd method (24×24, %)	33.2	27.83	30.61
Number of correct fragments 1nd method (36×36)	78 915	59 357	
Segmentation errors 1nd method (36×36, %)	40.93	17.69	28.06
Number of correct fragments, 2nd method (equalization)	73 582	72 176	
Segmentation errors 2nd method (%)	24.26	0	13.90

4. References

[1] Boran Z, Xiaoming Zh 2018 Lung mass density analysis using deep neural network and lung ultrasound surface wave elastography *Ultrasonics* 173-177
[2] Mathieson J R, Mayo J R, Staples C A and Müller N L 1989 Chronic diffuse infiltrative lung disease: comparison of diagnostic accuracy of CT and chest radiography *Radiology* **1** 111-116
[3] Verschakelen J A 2010 The role of high-resolution computed tomography in the work-up of interstitial lung disease *Curr Opin Pulm Med* **5** 503-510
[4] Ilyasova N, Paringer R and Shirokanev A 2017 A smart feature selection technique for object localization in ocular fundus images with the aid of color subspaces *Procedia Engineering* **201** 736-745
[5] HeiShun Yu, Tischler B, Qureshi M M, Soto J A, Anderson S, Daginawala N, Li B and Buch K 2016 Using texture analyses of contrast enhanced CT to assess hepatic fibrosis *European Journal of Radiology* 511-517
[6] Ilyasova N, Kupriyanov A and Paringer R 2018 Particular Use of BIG DATA in Medical Diagnostic Tasks *Pattern Recognition and Image Analysis* 114-121
[7] Acharya U R, Ng E Y, Tan J H, Sree S V and Ng K H 2012 An integrated index for the identification of diabetic retinopathy stages using texture parameters *Journal of Medical Systems* 2011-2020
[8] Hajek M, Dezortova M, Materka A and Lerski R 2006 Texture Analysis for Magnetic Resonance Imaging *Med4publishing* 234
[9] Ilyasova N Yu 2013 Methods for digital analysis of human vascular system. Literature review *Computer Optics* **37(4)** 517-541
[10] Ilyasova N, Kupriyanov A and Paringer R 2014 Formation of features for improving the quality of medical diagnosis based on discriminant analysis method *Computer Optics* **38(4)** 851-855

[11] Ilyasova N Yu 2014 Evaluation of geometric features of the spatial structure of blood vessels *Computer Optics* **38(3)** 529-538
[12] Shirokanev A S, Kirsh D V, Ilyasova N Yu and Kupriyanov A V 2018 Investigation of algorithms for coagulate arrangement in fundus images *Computer Optics* **42(4)** 712-721 DOI: 10.18287/2412-6179-2018-42-4-712-721
[13] Khorin P A, Ilyasova N Yu and Paringer R A 2018 Informative feature selection based on the Zernike polynomial coefficients for various pathologies of the human eye cornea *Computer Optics* **42(1)** 159-166 DOI: 10.18287/2412-6179-2018-42-1-159-166
[14] Strzelecki M, Szczypinski P, Materka A and Klepaczko A 2013 A software tool for automatic classification and segmentation of 2D/3D medical images *Nuclear Instruments and Methods In Physics Research Section A: Accelerators, Spectrometers, Detectors and Associated Equipment* 137-140
[15] Strzelecki M, Szczypinski P, Materka A, Klepaczko A 2009 MaZda – A software package for image texture analysis *Computer Methods and Programs in Biomedicine* 66-76
[16] Nikitaev V, Flury B 2010 The way to recognize images of cell texture *Biometrika* 33-41(in Russian)
[17] Ilyasova N, Kupriyanov A and Paringer R 2017 Intelligent feature selection technique for segmentation of fundus images *7th International Conference on Innovative Computing Technology, INTECH* 138-143
[18] Kakushadze Z, Willie Y 2017 *K-means and cluster models for cancer signatures *Biomolecular Detection and Quantification* 7-31
[19] Andreev G A, Bazarskiy O V, Glauberman A S, Kolesnikov A I, Korzhik O V and Hlyavich Ya L 1984 Analysis and synthesis of random spatial textures *Foreign radio electronics* 3-33

Acknowledgments
This work was financially supported by the Russian Foundation for Basic Research under grant No. 16-41-630761, No. 17-01-00972, No. 19-29-01135 and by the Ministry of Science and Higher Education within the State assignment to the FSRC “Crystallography and Photonics” RAS No. 007-GZ/Ch3363/26 (theoretical results).

Development of a Method of Terahertz Intelligent Video Surveillance Based on the Semantic Fusion of Terahertz and 3D Video Images

A A Morozov[1], **O S Sushkova**[1], **I A Kershner**[1] and **A F Polupanov**[1]

[1]Kotel'nikov Institute of Radio Engineering and Electronics of RAS, Mokhovaya 11-7, Moscow, Russia, 125009

e-mail: morozov@cplire.ru, o.sushkova@mail.ru, ivan kershner@mail.ru

Abstract. The terahertz video surveillance opens up new unique opportunities in the field of security in public places, as it allows to detect and thus to prevent usage of hidden weapons and other dangerous items. Although the first generation of terahertz video surveillance systems has already been created and is available on the security systems market, it has not yet found wide application. The main reason for this is in that the existing methods for analyzing terahertz images are not capable of providing hidden and fully-automatic recognition of weapons and other dangerous objects and can only be used under the control of a specially trained operator. As a result, the terahertz video surveillance appears to be more expensive and less efficient in comparison with the standard approach based on the organizing security perimeters and manual inspection of the visitors. In the paper, the problem of the development of a method of automatic analysis of the terahertz video images is considered. As a basis for this method, it is proposed to use the semantic fusion of video images obtained using different physical principles, the idea of which is in that the semantic content of one video image is used to control the processing and analysis of another video image. For example, the information about 3D coordinates of the body, arms, and legs of a person can be used for analysis and proper interpretation of color areas observed on a terahertz video image. Special means of the object-oriented logic programming are developed for the implementation of the semantic fusion of the video data, including special built-in classes of the Actor Prolog logic language for acquisition, processing, and analysis of video data in the visible, infrared, and terahertz ranges as well as 3D video data.

1. Introduction

Recently, the terahertz range of the electromagnetic waves attracts a strong interest of the safety systems developers [1–9]. This interest is caused by a set of special properties of the terahertz radiation. For instance, the terahertz radiation can penetrate dielectric materials like plastic, wood, and ceramics. The terahertz radiation is safe for people and can be used in public places in contrast with the X-radiation. Furthermore, the terahertz range of the electromagnetic waves includes the resonance frequencies of complex molecules and, therefore, the terahertz spectroscopy can be used for the distant detection of explosives, drugs, and other dangerous substances.

The terahertz range of the electromagnetic waves is situated between the microwaves and the infrared radiation (see figure 1). It is accepted that the frequency of the terahertz radiation is about 3 THz – 300 GHz that corresponds to the wavelengths from 0.1 to 1 millimeter. Actually,

the bounds of the terahertz range are conventional; they are defined differently in research papers.

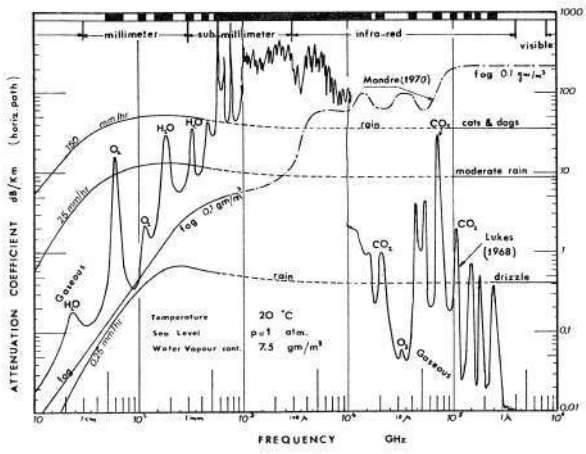

Figure 1. This is the dependence of the attenuation coefficient of the electromagnetic waves penetrated in the atmosphere on the wavelength of the radiation [10]. The terahertz waves are situated between the microwaves and the infrared radiation and correspond approximately to the area of high values of the attenuation coefficient. The abscissa is the frequency [THz] and the ordinate is the attenuation coefficient [dB/Km].

It is significant that the properties of the terahertz radiation and the principles of its usage differ for various sub-ranges of the terahertz waves. In particular, the 0.5-3 THz waves are used for the implementation of the terahertz spectroscopy and detection of dangerous substances [11]. Detection of the weapons and other dangerous objects hidden under the clothing of people is usually based on the usage of terahertz radiation frequencies that are less than 1 THz (so-called sub-terahertz radiation) that correspond to the transparency windows of the clothing. Active, passive, and combined methods of the sounding are used for the detection of the hidden objects.

There is a substantial difference between the images of hidden objects acquired using the active and passive sounding methods. Accordingly, the analysis of the terahertz images of different kinds also requires solving different problems and application of different methods.

The passive terahertz video surveillance is based on the receiving the essential human body radiation. In this case, the extrinsic objects look like dark spots against the background of the intrinsic emission of the human body (see an example in figure 2). Main problems of the passive terahertz image processing are the following ones:

(i) Typical passive terahertz images are fuzzy and unclear. The resolution of the images and the signal-to-noise ratio are low.

(ii) The background of the typical passive terahertz image is dark in comparison with the human body image. The shades of the hidden objects look like dark areas too. Therefore, any mistake in the separation of the foreground and background in the terahertz images automatically leads to the erroneous detection of hidden objects and false alarms.

The active terahertz video surveillance requires a target illumination and the registration of the radiation reflected from the human body (see an example in figure 3). The problems of active terahertz image processing are mostly caused by the fact that the reflection of the external terahertz radiation sources produces flares of different kinds. These flares have often prolonged

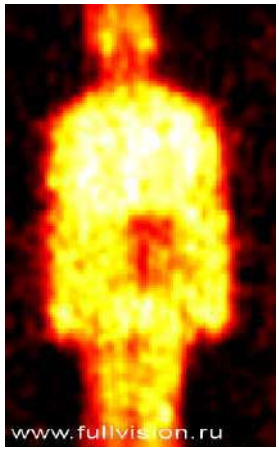

Figure 2. This is a human body image in the terahertz range. The image is acquired using the THERZ-7A industrial passive terahertz video surveillance system (Astrohn Technology Ltd [12]). The frequency range is 0.23–0.27 THz. The TT gun is hidden behind the belt at the back.

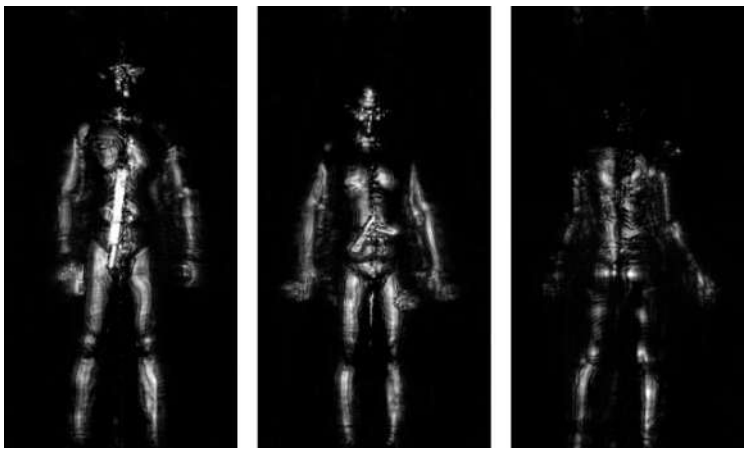

Figure 3. These are examples of human terahertz images taken with an active terahertz video surveillance system [13]. In the figure, there are samples of cold weapon and fire-arms hidden under the clothing of the persons.

shapes that can be mistakenly recognized as a cold weapon or other dangerous objects hidden under the clothing [13].

At present, the main directions of the terahertz video surveillance development are the combination of the active and passive methods of terahertz video acquisition and implementation of 3D terahertz video surveillance. In particular, these problems were addressed recently in the framework of the CONSORTIS European project [14, 15] (see an example in figure 4). Unfortunately, there is still no evidence of the development of fully-automatic hidden objects detection methods that are reliable enough to be used in the industrial terahertz video surveillance systems.

2. Semantic fusion of heterogeneous video images

Fundamentally different methods are necessary for the implementation of the fully-automatic analysis of terahertz video images and recognition of hidden objects. It is necessary to take into account the semantics of the video images including the context of the video scene on the

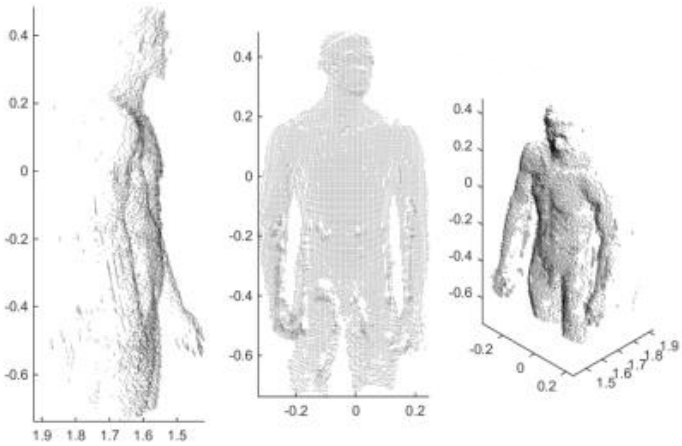

Figure 4. This is an example of 3D terahertz image of a mannequin acquired using the Pathfinder 200 GHz terahertz radar [14].

analogy of how the human operator analyzes the terahertz images. The additional information that is to be taken into consideration includes the coordinates of the body, arms, and legs of the person, multi-spectral video information (video, infrared, terahertz, etc.), time variations of these attributes, etc. The consideration of this information is especially important when the terahertz video surveillance system has to watch the free movements of the persons in a public place. Next, we will call the fully-automatic and semi-automatic terahertz video surveillance systems as terahertz intelligent video surveillance systems by analogy with the conventional intelligent video surveillance systems that operate in the video and/or infrared spectral ranges.

A typical terahertz video image looks like a set of fuzzy spots that can be monochromatic or colored depending on the data analysis method applied. A conventional terahertz video surveillance system displays a video in the visual and/or infrared range simultaneously with the terahertz video. This video information enables to the specially trained operator to interpret the terahertz image in a proper way and to detect objects hidden under the clothing of the visitors. This work of the human operator is a kind of semantic fusion of heterogeneous video images. The idea of the semantic fusion is in that several videos are to be united so that the semantic content of one video image is used to control the processing and analysis of another video image.

It is the authors' opinion that one of the most important data sources for the object recognition in the terahertz video is the positional relationships between the body, arms, and legs of the person and the terahertz video image. It is advisable to use a point clouds and the images of skeletons of the persons acquired by a time-of-flight camera for this purpose. To implement this idea, a set of special built-in classes of the Actor Prolog object-oriented logic language [16–27] were developed: *Astrohn*, *KinectBuffer*, *TEV1*, etc.

The *Astrohn* built-in class implements the terahertz and RGB video data acquisition using the THERZ-7A device [12]. The *Astrohn* class supports the data input from the device as well as reading from and writing to the video file. The *Astrohn* class supports conversion of the terahertz video data to the color video images. In particular, pseudo colors can be used for the terahertz data representation. The *Astrohn* class operates also with RGB video acquired from the internal IP-camera of the THERZ-7A device and can combine this RGB video data with the terahertz video. The *Astrohn* class implements a simple synchronization of the terahertz and RGB video streams. For this purpose, each terahertz frame is coupled with the RGB frame that is the nearest in time. Currently, the *Astrohn* class supports more than 25 high resolution color maps including a set of conventional thermal imaging color maps: Aqua, Blackhot, Blaze, BlueRed,

Gray, Hot, HSV, Iron, Red (Jet), Medical, Parula, Purple, Reptiloid, and Green (Rainbow).

The *KinectBuffer* built-in class acquires 3D video data from the time-of-flight camera of the Kinect 2 device (Microsoft Inc). The reading and recording of 3D video data files are also supported [28]. The following essential functions are implemented in the *KinectBuffer* class:

(i) Creation of the 3D surface based on the 3D point cloud.

(ii) Projection of given texture to the surface using a 3D lookup table [26, 28, 29].

We have used these features of the *KinectBuffer* class to the fusion of 3D and terahertz video images in our experiments. A special method of the speculative reading of the video files is implemented in the *Astrohn* class that enables to synchronize recorded 3D and terahertz video data.

An example of a 3D image that is generated by the fusion of a time-of-flight camera point cloud and a terahertz image is demonstrated in figure 5. The terahertz video is combined with the image of a person's skeleton that was computed by the procedures of the standard Kinect 2 SDK. A 3D lookup table was applied to project the terahertz video to the 3D surface in the real time. In particular, the user can rotate, zoom, and shift the 3D video by the mouse during the demonstration. In the example, the 3D point cloud is recognized as a human body and this information is used for the selection of terahertz image colored areas that are directly related to the objects hidden under the clothing of the person. This is a case of semantic fusion of heterogeneous video information that prevents false detections of background terahertz areas as target hidden objects.

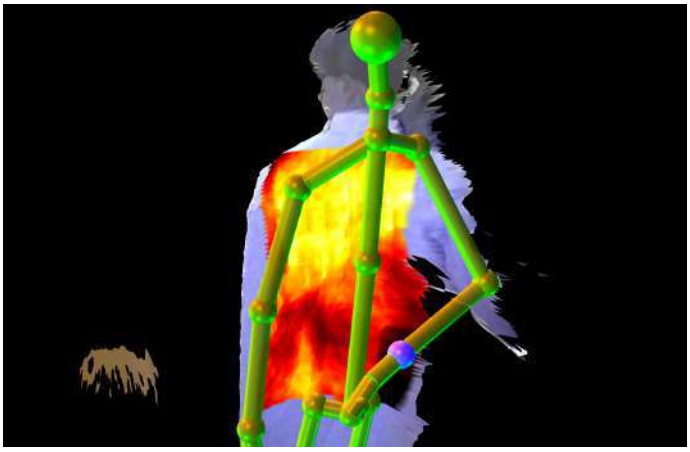

Figure 5. This is an example of 3D and terahertz video data fusion implemented using the *KinectBuffer* and *Astrohn* built-in classes of the Actor Prolog language [24, 28].

3. An example of heterogeneous video data analysis

Let us consider an example of heterogeneous video data analysis. The goal of this experiment is to check whether the terahertz videos contain information enough to teach a convolutional network to distinguish the dangerous and safe objects.

A set of heterogeneous videos was prepared for the experiment (see figures 6 and 7). For that, a special logic program was written in Actor Prolog for multichannel video data acquisition (see figure 8). The video includes 3D point clouds and terahertz images of persons. A calibration procedure [29] was performed to compute a 3D lookup table that establishes relations between the video images of different kinds. Then another logic program was written to project terahertz images to the 3D images of the persons and to generate training/test data sets in the PNG

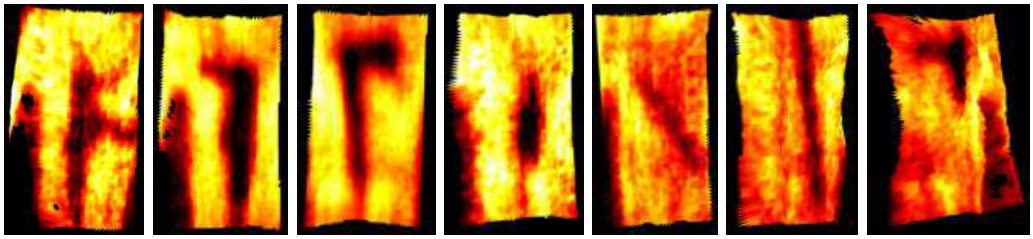

Figure 6. The learning set includes weapon and other dangerous objects (from left to right): the Kalashnikov sub-machine-gun (AK), AK without the magazine, an axe, bottles, a knife, a baton, and guns of different brands.

format. An image generated by this logic program is shown in figure 5. The difference between the image 5 and the images demonstrated in figures 6 and 7 is in that the later images were rotated and normalized to provide the uniform size and angle of view for all frames. Besides, the images of skeletons and RGB video data were eliminated. The frames with inappropriate positions of the person in the view area were automatically discarded. The Hot standard color map was used for the terahertz data visualization.

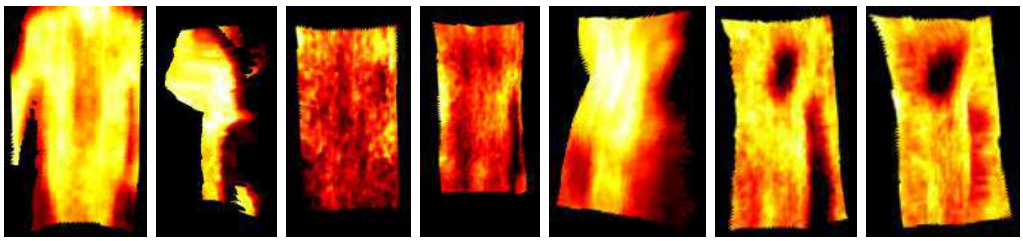

Figure 7. The learning set includes also terahertz images of people dressed in casual clothes and outer clothing. Some images contain ordinary objects like phones and USB disks. The number of these images is balanced with the number of images that contain weapon and dangerous objects.

Convolutional networks of several standard architectures were trained using the data sets: LeNet [30], AlexNet [31], ResNet50 [32], and Darknet19 [33]. The results of the training are reported in table 1. It is not a surprise that the oldest network LeNet yields the worst results and the Darknet19 that is the latest of these four networks yields the best results.

After that, an additional test data set was prepared that includes only the images of a person that keeps the M16 automatic rifle and the images of the person without extra objects (see figure 9). The number of images of different kinds was balanced. Then, the trained networks were used to analyze the video images.

The results of the experiment are reported in table 2. The networks recognize successfully the M16 automatic rifle as a dangerous object. Surprisingly, the AlexNet architecture yields the best results in spite of the fact that this network architecture is quite old and simple. The newest Darknet19 architecture yields unexpectedly the worst results in this test. Probably this is because the recognition and the generalization are different problems and the development of network architectures for the generalization of video data requires a special attention.

These results demonstrate that the neural network approach to the terahertz video data analysis can make generalizations of the hidden object properties and successfully predict that the hidden object is a kind of a weapon and/or dangerous object. It is a promising area for further research to make experiments with heterogeneous video data fusion, standardizing of

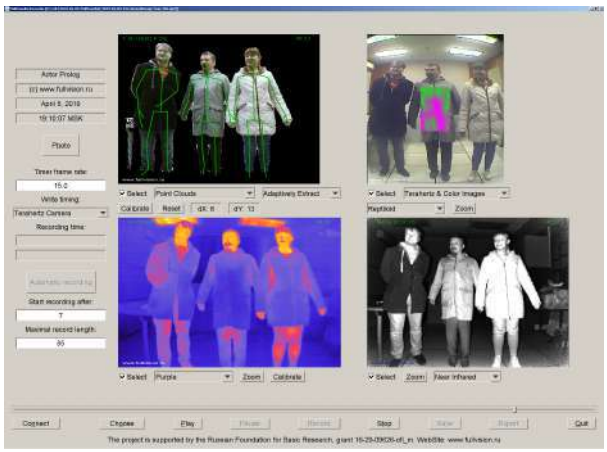

Figure 8. This is the user interface of the logic program written in Actor Prolog for the automation of multichannel video data acquisition. The program controls the video data acquisition simultaneously from the THERZ-7A device (the right window on top), the Kinect 2 device (the left window on top and the bottom right window), and the i3system TE V1 thermal camera (the bottom left window). The video data is recorded in a special Actor Prolog format developed for the multichannel video data processing.

Table 1. These are the results of the training of the convolutional networks of various architectures. The size of the training set is 9173 video frames. The size of the test data set is 2293 frames. The training process includes two stages: 30 epochs (that is 5520 iterations) without transformations and 30 epochs with the flip and warp transformations. The image size is 224×224. The batch size is 50.

Network	Accuracy	Precision	Recall	F1 Score
LeNet	0.8203	0.8224	0.8203	0.8272
AlexNet	0.8543	0.8545	0.8543	0.8558
ResNet50	0.9930	0.9931	0.9930	0.9930
Darknet19	0.9974	0.9974	0.9974	0.9974

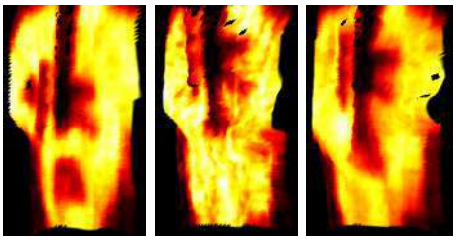

Figure 9. This is terahertz images of a person that keeps the M16 automatic rifle.

video data by non-linear color maps, and development of neural network architectures for the terahertz data analysis.

Table 2. The trained networks recognize the M16 automatic rifle as a dangerous object with the following quality. The size of the test data set is 672 video frames.

Network	Accuracy	Precision	Recall	F1 Score
LeNet	0.8720	0.8981	0.8720	0.8865
AlexNet	0.9970	0.9970	0.9970	0.9970
ResNet50	0.9940	0.9941	0.9940	0.9941
Darknet19	0.7589	0.8373	0.7589	0.8058

4. Conclusion

A method of semantic fusion of heterogeneous video data is proposed as a basis for the implementation of the terahertz intelligent video surveillance. In the framework of this method, 3D video data is used for the analysis and proper interpretation of the terahertz videos. Special logic programming means were developed for the experimenting with the terahertz video surveillance including a set of built-in classes of the Actor Prolog language for terahertz, infrared, and RGB video data acquisition, writing, reading, and synchronization. It was demonstrated that these logical means enable real-time video data acquisition and processing. In particular, the terahertz video can be projected to the 3D human body surface acquired by a time-of-flight camera. This heterogeneous information can be used by video data analysis algorithms to establish the positional relationships between the body, arms, and legs of the person and the colored areas in the terahertz video that helps to improve the detection of the objects hidden under the clothing of the person.

5. References

[1] Federici J F, Schulkin B, Huang F, Gary D, Barat R, Oliveira F and Zimdars D 2005 *Semiconductor Science and Technology* **20** S266
[2] Chan W L, Deibel J and Mittleman D M 2007 *Reports on progress in physics* **70** 1325
[3] Sanders-Reed J N 2015 *Micro- and Nanotechnology Sensors, Systems, and Applications VII* (International Society for Optics and Photonics) **9467** 94672E
[4] Antsiperov V E 2016 Automatic target recognition algorithm for low-count terahertz images *Computer Optics* **40(5)** 746-751 DOI: 10.18287/2412-6179-2016-40-5-746-751
[5] Sizov F 2017 *Semiconductor Physics, Quantum Electronics & Optoelectronics* **20** 273-283
[6] Appleby R, Robertson D A and Wikner D 2017 P*assive and Active Millimeter-Wave Imaging XX* (International Society for Optics and Photonics) **10189** 1018902
[7] Dhillon S S, Vitiello M S, Linfield E H, Davies A G, Hoffmann M C, Booske J, Paoloni C, Gensch M, Weightman P, Williams G P, Castro-Camus E, Cumming D R S, Simoens F, Escorcia-Carranza I, Grant J, Lucyszyn S, Kuwata-Gonokami M, Konishi K, Koch M, Schmuttenmaer C A, Cocker T L, Huber R, Markelz A G, Taylor Z D, Wallace V P, Zeitler J A, Sibik J, Korter T M, Ellison B, Rea S, Goldsmith P, Cooper K B, Appleby R, Pardo D, Huggard P G, Krozer V, Shams H, Fice M, Renaud C, Seeds A, Stohr A, Naftaly M, Ridler N, Clarke R, Cunningham J E and Johnston M B 2017 *Journal of Physics D: Applied Physics* **50** 043001
[8] Chen S, Luo C, Wang H, Deng B, Cheng Y and Zhuang Z 2018 *Sensors* (Basel, Switzerland) **18** 1342
[9] Yuan J and Guo C 2018 *Eighth International Conference on Information Science and Technology (ICIST)* 159-164
[10] Zufferey C H 1972 A Study of Rain Effects on Electromagnetic Waves in the 1-600 GHz Range Master's thesis *The MIMICAD Research Center*
[11] Baker C, Lo T, Tribe W, Cole B, Hogbin M and Kemp M 2007 *Proceedings of the IEEE* **95** 1559-1565

[12] ASTROHN Technology Ltd 2019 URL: http://astrohn.com
[13] Zhang J, Xing W, Xing M and Sun G 2018 *Sensors* **18** 2327
[14] CONSORTIS 2018 *Final Publishable Summary Report* (Teknologian Tutkimuskeskus VTT)
[15] Robertson D A, Macfarlane D G and Bryllert T 2016 *Passive and Active Millimeter-Wave Imaging XIX* 9830 983009
[16] Morozov A A 1999 *IDL* (Paris, France) 39-53
[17] Morozov A A, Vaish A, Polupanov A F, Antciperov V E, Lychkov I I, Alfimtsev A N and Deviatkov V V 2014 *Biodevices Scitepress* 53-62
[18] Morozov A A and Polupanov A F 2014 *CICLOPS-WLPE* (Aachener Informatik Berichte no AIB) 31-45
[19] Morozov A A, Sushkova O S and Polupanov A F 2015 *RuleML DC and Challenge* (Berlin: CEUR)
[20] Morozov A A 2015 *Pattern Recognition and Image Analysis* **25** 481-492
[21] Morozov A A and Sushkova O S 2016 Real-time analysis of video by means of the Actor Prolog language *Computer Optics* **40(6)** 947-957 DOI: 10.18287/2412-6179-2016-40-6-947-957
[22] Morozov A A, Sushkova O S and Polupanov A F 2017 *Advances in Soft Computing* (Cham: Springer International Publishing) **II** 42-53
[23] Morozov A A, Sushkova O S and Polupanov A F 2017 *ISIE* (Washington: IEEE Xplore Digital Library) 1631-1636
[24] Morozov A A, Sushkova O S and Polupanov A F 2019 *Optoelectronics in Machine Vision-Based Theories and Applications* (IGI Global Publications) 134-187
[25] Morozov A A and Sushkova O S 2018 A Virtual Machine for Low-Level Video Processing in Actor Prolog *Journal of Physics: Conference Series* **1096** 012044 DOI: 10.1088/1742-6596/1096/1/012044
[26] Morozov A A and Sushkova O S 2018 *Advances in Artificial Intelligence – IBERAMIA* (Cham: Springer International Publishing) 29-41
[27] Morozov A A and Sushkova O S 2019 *The intelligent visual surveillance logic programming* URL: http://www.fullvision.ru
[28] Morozov A A, Sushkova O S, Petrova N G, Khokhlova M N and Migniot C 2018 *Radioelektronika. Nanosistemy. Informacionnye Tehnologii* **10** 101-116
[29] Morozov A A, Sushkova O S, Polupanov A F, Antsiperov V E, Mansurov G K, Paprotskiy S K, Yanushko A V, Petrova N G and Bugaev A S 2018 *Radioelektronika. Nanosistemy. Informacionnye Tehnologii* **10** 311-322
[30] LeCun Y, Bottou L, Bengio Y and Haffner P 1998 *Proceedings of the IEEE* **86** 2278-2324
[31] Krizhevsky A, Sutskever I and Hinton G E 2012 *Advances in Neural Information Processing Systems* **25** 1097-1105
[32] He K, Zhang X, Ren S and Sun J 2016 *IEEE Conference on Computer Vision and Pattern Recognition (CVPR)* **1** 770-778
[33] Redmon J and Farhadi A 2016 *CoRR* URL: http://arxiv.org/abs/1612.08242
[34] Barmpoutis A 2013 *IEEE Transactions on Cybernetics* **43** 1347-1356

Acknowledgments
Authors are grateful to Renata A. Tolmacheva for the help in the preparation of terahertz/3D video samples and Angelos Barmpoutis for his J4K library [34] which was used for the data collection. Authors thank Dmitry M. Murashov, Feodor D. Murashov, Viacheslav E. Antsiperov, Gennady K. Mansurov, Stanislav K. Paprotskiy, Andrei P. Gorchakov, Alexander V. Yanushko, Nadezda G. Petrova, and Alexander S. Bugaev for cooperation. We are grateful to the Astrohn Technology Ltd and OOO ASoft who provided us with the THERZ-7A terahertz scanning device. The work was carried out within the framework of the state task. This research was partially supported by the Russian Foundation for Basic Research (project number 16-29-09626-ofi-m).

A method of iterative image normalization for tasks of visual navigation of UAVs

M O Elantcev[1], I O Arkhipov[1] and R M Gafarov[1]

[1]Kalashnikov Izhevsk State Technical University, Russian Federation, Izhevsk, Studencheskaya 7, 426069

e-mail: emo-name@hotmail.com, aio1024@mail.ru

Abstract. The work deals with a method of eliminating the perspective distortion of an image acquired from an unmanned aerial vehicle (UAV) camera in order to transform it to match the parameters of the satellite image. The normalization is performed in one of the two ways. The first variant consists in the calculation of an image transformation matrix based on the camera position and orientation. The second variant is based on matching the current frame with the previous one. The matching results in the shift, rotation, and scale parameters that are used to obtain an initial set of pairs of corresponding keypoints. From this set four pairs are selected to calculate the perspective transformation matrix. This matrix is in turn used to obtain a new set of pairs of corresponding keypoints. The process is repeated while the number of the pairs in the new set exceeds the number in the current one. The accumulated transformation matrix is then multiplied by the transformation matrix obtained during the normalization of the previous frame. The final part presents the results of the method that show that the proposed method can improve the accuracy of the visual navigation system at low computational costs.

1. Introduction

This paper is concerned with the development of a method for image normalization that is used in a visual navigation system of unmanned aerial vehicles (UAVs). The navigation system being developed [1] matches images acquired from an UAV onboard camera with the satellite image of the flying area. The matching yields the shift, rotation, and scale values that can be used to transform the input image to the corresponding part of satellite image. Knowing the coordinates of the satellite image and the shift, rotation, and scale parameters of the current input image, it is possible to determine the coordinates of the UAV.

During the flight the tilt of the UAV is unstable, it changes because of weather conditions or when the UAV is making a pivot. It results in perspective distortions of images acquired from the onboard camera, even if a stabilized platform used. The distortions interfere with the correct matching of the images from the camera with the satellite image, which is usually represented in an orthogonal projection. To increase the likelihood of correct matching a method of image normalization for eliminating the perspective distortions is needed. The method should be computationally simple because it is supposed to run on low-power UAV processors.

There are several approaches to solve this problem. The first approach is to calculate the matrix of perspective transformation based on the external parameters of the camera obtained from the UAV

sensors, namely pitch, yaw, roll, and altitude. In [2], the distortion is compensated by determining the orientation of a virtual camera with its optical axis collinear to the normal vector of the shooting plane. This virtual camera provides us with an image without perspective distortions. Therefore, to eliminate the distortions of the input image we need to calculate the homography matrix between the images from the real and the virtual cameras. There are two difficulties with using this approach: the moments of shooting and of external parameters recording should be strictly synchronized, and the surface of the flying area should be flat.

The second approach is to find and analyze the location of the known structural elements in the input image. This approach assumes that each frame from the camera is processed independently. The paper [3] focuses on the distortion elimination for the task of bar code recognition. Its idea is to find four straight lines bounding the quadrilateral barcode area. These lines provide four corner points that are used to calculate the transformation matrix. This approach is difficult to apply to the task of normalizing the UAV images because the shapes of the objects in the images are usually unknown.

The third approach is to find the pairs of corresponding elements in the two images and use their positions to determine the transformation matrix of one image into another. Usually the methods search for the pairs of image points with characteristic local features known as keypoints. Depending on the task, different methods of keypoints extraction and matching can be used [4,5].

Under ideal conditions, four pairs of the keypoints are enough to determine the transformation matrix. However, in practice even the positions of the correctly matched points can be different because of noise. To obtain a more accurate solution a system of equations based on all the matched pairs is constructed. This system is usually solved by the least squares method so as to minimize the given error function (the DLT method [6]). In [7], it is proposed to perform this method iteratively. This method helps to increase the likelihood of image matching by means of eliminating the noise points.

The set of the pairs of corresponding points can also contain mismatched pairs. In this case the DLT method can yield a wrong result and one of the robust methods should be used, such as RANSAC [8, 9]. In this method four pairs of corresponding points are randomly selected among all the matched pairs. Using them the homography matrix is calculated, and then the algorithm checks how many pairs fit this transform (inliers). The process is repeated, and other random pairs are selected from the set of inliers until a solution is found that satisfies the specified number of pairs or the maximum number of iterations is exceeded. Another similar robust method is LMS. It estimates four current selected pairs of points not by the number of inliers but by the median distance among all the pairs of points [6].

The described robust methods require a large number of iterations; therefore, they are not effective on low-power processors. The RHO method [10] aims to solve this problem. Instead of randomly electing four pairs of points at each iteration, the method preliminarily evaluates each pair, selects the most promising ones and then corrects the estimation. This allows to obtain the result in significantly fewer iterations.

The fourth approach is to analyze the input image using a neural network, as it is demonstrated in [11]. It is noted that the advantage of this approach is the ability to work when there is a very small number of the keypoints or when the input images are blurred. However, this method is computationally complex and requires special hardware to work in real time, which makes it difficult to apply to the task of UAV visual navigation.

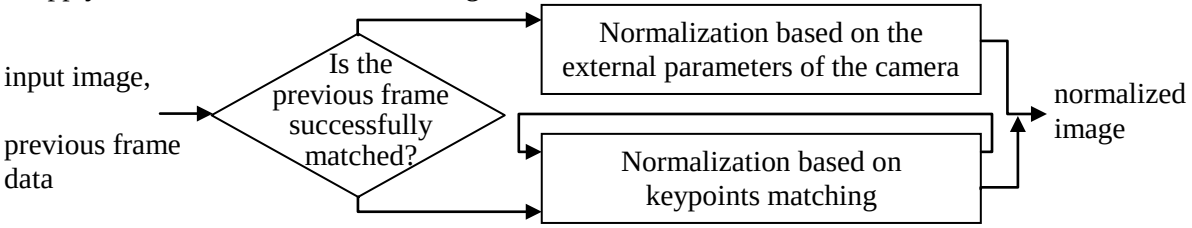

Figure 1. Simplified scheme of the proposed method.

The proposed method of iterative image normalization for tasks of visual navigation of UAVs combines the first and the third approaches. A simplified scheme of the method is shown in Figure 1. Normalization based on the external parameters of the camera (pitch, yaw, roll, and flight altitude) is used either when processing the initial camera frame or in the case where the previous frame has not been successfully matched with the satellite image or the current frame cannot be matched with the previous one. In other cases the iterative method of homography matrix calculation based on matching the keypoints of the previous and the current frames is used.

2. Description of the peculiarities of the task considered

The UAV flies along the given trajectory that contains both straight sections and turns. The considered flight altitude is 250-500m. There is a camera onboard the UAV that is directed strictly downwards. There is no stabilized platform on the UAV. The shooting speed of the camera is enough to provide at least 80% of overlap between the current and the previous frames. The parameters of focal length and the dimensions of the camera's sensor are known.

The UAV is equipped with an accelerometer and a pressure sensor that provide information about the UAV orientation (roll, pitch, and yaw) and the flight altitude. However, according to experiments on real images, the moments of shooting and of parameters recording are not exactly the same. Therefore, strong wind gusts cause inaccuracies in the recorded external parameters of the camera. In addition, the pressure sensor estimates the flight altitude only above sea level. When calculating the flight altitude above ground level the height map of the flying area should be taken into account.

The result of the normalization is the image transformed into the orthogonal projection so that later it can be matched with the satellite image.

3. Normalization based on the external parameters of the camera

The first algorithm of the proposed normalization method is based on the information on the camera orientation and position in space, namely the roll ρ, pitch τ, yaw γ, and flight altitude h_f. In addition, the input information includes the terrain height h_a at the shooting point and the reference altitude h_r at which the shooting scale equals the satellite image scale. The output information is the coefficients of the transformation matrix that eliminates the distortion. The algorithm consists of two stages: the calculation of the transformation coefficients disregarding the scale and the calculation of the scaling factor.

3.1. Calculation of the transformation coefficients disregarding the scale

The camera's field of view can be represented as a pyramid that intersects the earth's surface plane. To simplify the calculation, instead of rotating the pyramid, according to the camera orientation the earth's surface plane is rotated and placed at one of the base vertices of the pyramid, as Figure 2a shows.

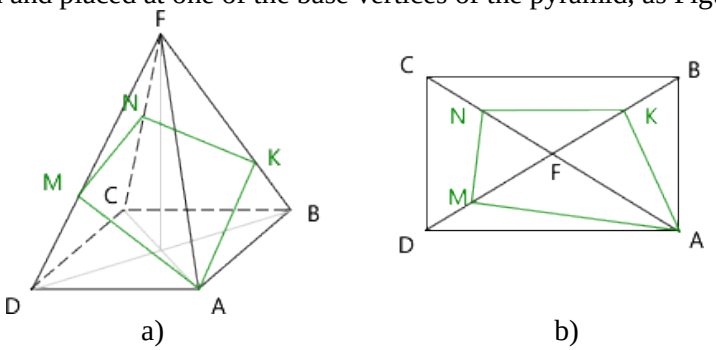

a) b)

Figure 2. The pyramid of vision: (a) a view at an angle, MNK is the section with the earth's surface plane, (b) the top view.

The purpose of the first stage is to calculate the coordinates of the points M, N, K on the top view projection (Figure 2b). These coordinates can be used to calculate the resultant homography matrix T_a by solving an equation system constructed with the coordinates transformation equations of the pairs

of points: A-A, B-K, C-N, D-M. The transformation of each pair of points can be described by two equations [12]:

$$x' = \frac{t_{11}x+t_{12}y+t_{13}}{t_{31}x+t_{32}y+1} \qquad y' = \frac{t_{21}x+t_{22}y+t_{23}}{t_{31}x+t_{32}y+1}, \tag{1}$$

where x and y are the coordinates of the point before the transformation, x' and y' are the coordinates of the point after the transformation, t_{11}, t_{12}, t_{13}, t_{21}, t_{22}, t_{23}, t_{31} и t_{32} are the coefficients of the transformation matrix T_a.

The shape of the pyramid depends on the size of the photo sensor and the focal length. The viewing angles are calculated as follows:

$$\alpha_{\mathrm{x}} = 2\,\mathrm{arctg}\frac{m_{\mathrm{w}}}{2f_{\mathrm{L}}} \qquad \alpha_{\mathrm{y}} = 2\,\mathrm{arctg}\frac{m_{\mathrm{h}}}{2f_{\mathrm{L}}}, \tag{2}$$

where m_w and m_h are the dimensions of the photo sensor, f_L is the focal length. The vertex angles of the pyramid are calculated as follows:

$$\beta_{\mathrm{x}} = \frac{m_{\mathrm{w}}}{m_{\mathrm{h}}}\sin\frac{\alpha_y}{2} \qquad \beta_{\mathrm{y}} = \frac{m_{\mathrm{h}}}{m_{\mathrm{w}}}\sin\frac{\alpha_x}{2} \tag{3}$$

The length of the edge of the pyramid l_e and the diagonal of the base of the pyramid l_d are calculated as follows:

$$l_{\mathrm{e}} = \frac{m_{\mathrm{h}}}{2\sin(\beta_{\mathrm{y}}/2)} \qquad l_{\mathrm{d}} = \sqrt{m_{\mathrm{w}}^2 + m_{\mathrm{h}}^2}, \tag{4}$$

Depending on the orientation of the camera, the earth's surface plane is placed at one of the four base vertices, as shown in Figure 3.

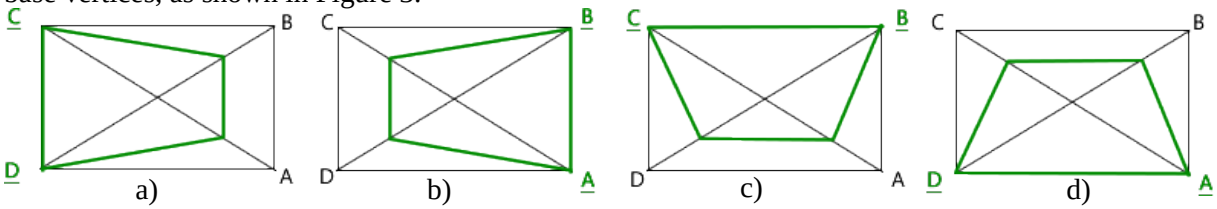

Figure 3. The location of the pyramid section with the earth's surface plane depending on the orientation of the camera: (a) $\tau = 0$, $\rho < 0$, (b) $\tau = 0$, $\rho > 0$, (c) $\tau > 0$, $\rho = 0$, (d) $\tau < 0$, $\rho = 0$.

The vertices are renamed according to the following rule: a vertex that coincides with a section corner is called A', then in anticlockwise direction: B', C ', D'.

The coordinates of the vertex K can be calculated with the following formula:

$$d_{\mathrm{k}} = m_w \frac{\sin\rho}{\cos(\beta_{\mathrm{x}}/2-\rho)}$$
$$\mathrm{K_x} = \left|\mathrm{D'_x} - d_{\mathrm{k}}\frac{m_{\mathrm{w}}}{2l_{\mathrm{e}}}\right| \qquad \mathrm{K_y} = \left|\mathrm{D'_y} - d_{\mathrm{k}}\frac{m_{\mathrm{h}}}{2l_{\mathrm{e}}}\right| \tag{5}$$

The coordinates of the vertex M can be calculated with the following formula:

$$d_{\mathrm{m}} = m_h \frac{\sin\tau}{\cos(\beta_{\mathrm{y}}/2-\tau)}$$
$$\mathrm{M_x} = \left|\mathrm{B'_x} - d_{\mathrm{k}}\frac{m_{\mathrm{w}}}{2l_{\mathrm{e}}}\right| \qquad \mathrm{M_y} = \left|\mathrm{B'_y} - d_{\mathrm{k}}\frac{m_{\mathrm{h}}}{2l_{\mathrm{e}}}\right| \tag{6}$$

The coordinates of the vertex N can be calculated with the following formula:

$$d_{\mathrm{nk}} = m_{\mathrm{h}} - 2d_{\mathrm{k}}\cos\frac{\pi-\beta_{\mathrm{y}}}{2} - \sin\frac{\pi-\beta_{\mathrm{y}}}{2} / \sin(\pi-\tau-\frac{\pi-\beta_{\mathrm{y}}}{2})$$
$$d_{\mathrm{fk}} = d_{\mathrm{e}} - d_{\mathrm{k}} \qquad d_{\mathrm{nfb}} = -2d_{\mathrm{fk}}\cos\beta_{\mathrm{y}} \tag{7}$$
$$d_{\mathrm{nf}} = (\sqrt{d_{nfb}^2 - 4\left(d_{\mathrm{fk}}^2 - d_{\mathrm{nk}}^2\right)} - d_{\mathrm{nfb}})/2$$
$$\mathrm{N_x} = \left|\frac{\mathrm{C'_x}-\mathrm{A'_x}}{2} + d_{\mathrm{nf}}\frac{m_{\mathrm{w}}}{2l_{\mathrm{e}}}\right| \qquad \mathrm{N_y} = \left|\frac{\mathrm{C'_y}-\mathrm{A'_y}}{2} + d_{\mathrm{nf}}\frac{m_{\mathrm{h}}}{2l_{\mathrm{e}}}\right|$$

To align the image with the northward direction, matrix multiplication can be used:

$$T_n = T_a\begin{pmatrix}\cos\gamma & -\sin\gamma & 0\\ \sin\gamma & \cos\gamma & 0\\ 0 & 0 & 1\end{pmatrix} \tag{8}$$

3.2. Calculation of the scale factor

Since the earth's surface plane was placed at one of the base vertices of the pyramid, the obtained transformation matrix disregards the original scale of the image. To calculate the scaling factor the following formula can be used:

$$d_{\mathrm{nd}} = \sqrt{(\mathrm{N_x} - \mathrm{A'_x})^2 + (\mathrm{N_y} - \mathrm{A'_y})^2}$$

$$S_n = \frac{l_{\mathrm{e}} d_{\mathrm{nd}}}{d_{\mathrm{nf}} l_{\mathrm{d}}} \tag{9}$$

To transform the image acquired from the UAV camera to the scale of the satellite image, the transformation matrix should be adjusted using the following scale factor:

$$S_r = S_n \frac{h_{\mathrm{r}} - h_{\mathrm{a}}}{h_{\mathrm{f}} - h_{\mathrm{a}}} \tag{10}$$

3.3. Obtaining the result of the normalization

To obtain the final transformation matrix the following formula should be used:

$$T_r = T_n \begin{pmatrix} S_r & 0 & 0 \\ 0 & S_r & 0 \\ 0 & 0 & 1 \end{pmatrix} \tag{11}$$

Figure 4 shows the result of the method of image normalization based on the external parameters of the camera.

a) b) c)

Figure 4. The result of image normalization based on the external parameters of the camera: (a) the original image, (b) the normalized image, (c) the corresponding part of the satellite image.

4. Normalization based on keypoints matching

The first algorithm of the proposed method eliminates the distortions of the image coarsely, because, as it is mentioned above, the moment of recording the external parameters of the camera not necessarily coincides with the moment of shooting. Moreover, it is rather difficult to accurately take into account the elevation difference of the underlying surface. Therefore, it is used only when the previous frame from the camera cannot be matched with the satellite image. In other cases the second algorithm is used that is based on matching the current frame with the previous frame already normalized.

4.1. Matching the current frame with the previous one

To reduce its complexity, the image matching algorithm analyzes not all the pixels but only the keypoints extracted with the method described in [13].

After the keypoint sets of the both images are found, they are used to determine the shift, rotation, and scale values between the two images using the statistical differentiation method [14]. These parameters form the following transformation matrix [15]:

$$H_{\mathrm{m}} = \begin{pmatrix} s\cos\phi & -s\sin\phi & t_{\mathrm{x}} \\ s\sin\phi & s\cos\phi & t_{\mathrm{y}} \\ 0 & 0 & 1 \end{pmatrix}, \tag{12}$$

where t_x and t_y are the shift values along the X axis and the Y axis respectively, φ is the rotation value, s is the scale value.

4.2. Selecting pairs of corresponding points

After the transformation matrix is found, it is used to determine the pairs of corresponding points. Some point A of the current frame corresponds to some point B of the previous frame when after

applying the transformation matrix to the coordinates of the point A the distance between A and B does not exceed the specified threshold (1-2 pixels).

From the whole set of the pairs of corresponding points four pairs are selected that will be used to calculate the homography matrix (1). The choice is limited by the condition that no three points are collinear. The best case occurs when a quadrilateral of maximum area with as large angles as possible is found. However, the search for such a set of points is a computationally complex operation. The following approaches to selecting the points were tried:

1) the four points nearest to the corners of the image;

2) the four points most distant from the center of mass of the keypoints set and located in different quadrants relative to the center of mass;

3) the first point is the most distant from the center of mass, the second point is the most distant from point 1, the third is the point with the greatest sum of its distances from points 1 and 2, the fourth is the point with the greatest sum of its distances from points 1, 2 and 3;

4) a random selection of points.

If this algorithm finds less than four corresponding pairs, the normalization based on the external parameters of the camera is applied.

4.3. Calculation of the transformation matrix

After the four pairs of the corresponding keypoints are selected, the refined transformation matrix is calculated. This homography matrix matches the projection of the current frame with the projection of the previous frame already normalized.

Then the search for the pairs of corresponding points is repeated using the current frame warped according to the refined transformation matrix. From the found pairs a new set of four pairs is selected and a new refined matrix is calculated. The process is repeated as long as the number of the pairs of corresponding points increases. Experiments show that in most cases two iterations are enough to obtain the solution. The final matrix of the transformation of the original image into the normalized one is determined by the formula:

$$T_{\mathrm{r}} = T_p \prod_{i=1}^{n} H_i \qquad (13)$$

where T_p is the perspective transformation matrix for normalizing the previous frame, H_i are the transformation matrices obtained at each iteration, n is the number of iterations.

Since the previous frame is used to normalize the current frame, the normalization error can accumulate. However, this method is used as a part of the visual navigation system that implies that the next step is to match the normalized image with the satellite image. This matching eliminates the accumulated error.

5. Experiments

To test the proposed method, it has been integrated into the preprocessing stage of the UAV visual navigation system that is being developed. Then a series of experiments using real images of a UAV flight were performed. The trajectory of the UAV flight is shown in Figure 5 and consists of sections of two types: straight sections (270 frames) and turns (70 frames).

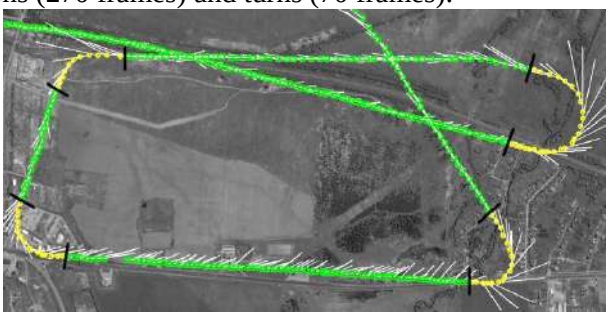

Figure 5. The trajectory used in the experiments. The positions of the UAV at the straight sections are marked with green dots. The positions of the UAV at the turns are marked with yellow dots. The black lines show the boundaries between the sections. The white lines connect the coordinates of the UAV to the corresponding centers of photographing.

The first experiment aims to choose the best algorithm for image normalization based on keypoints matching. The proposed iterative algorithm was tested (with the four variants of selecting the four pairs of points described above), as well as the methods implemented in the OpenCV 3.4.5 library: DLT, RANSCAC, LMS and RHO. To determine the speed of the methods, each input frame was processed 100 times and the average execution time was calculated. Processing was performed on an AMD FX-8320E 3.2 GHz processor without using a graphics accelerator.

Table 1. Comparison of the results of various methods of the homography matrix calculation.

Indicator	Section	Proposed method				DLT	RANSAC	LMS	RHO
		variant 1 of pair selection	variant 2 of pair selection	variant 3 of pair selection	variant 4 of pair selection				
Average number of pairs of corresponding points before processing	straight sections	156.8							
	turns	123.2							
	whole trajectory	150.0							
Average number of pairs of corresponding points after processing	straight sections	173.5	171.5	172.1	158.9	175.0	177.5	**178.3**	178.2
	turns	136 7	133.6	135.0	125.6	138.7	141.3	**142.6**	142.0
	whole trajectory	165.8	163.7	164.5	152	167.5	170	**170.9**	170.7
Average number of iterations of the proposed algorithm	straight sections	1.9	1.8	1.8	1.2	-			
	turns	1.8	1.7	1.7	1.2	-			
	whole trajectory	1.9	1.8	1.8	1.2	-			
Average processing time per one frame (ms)	straight sections	0.06	0.05	0.07	**0.03**	0.33	0.52	2.72	0.313
	turns	0.05	0.04	0.06	**0.03**	0.31	0.57	2.70	0.24
	whole trajectory	0.06	**0.03**	0.06	**0.03**	0.33	0.53	2.72	0.30

Table 1 presents the processing results. The methods were evaluated by the average number of the pairs of corresponding points (greater values are better) and the average processing per one frame (lower values are better). According to the first criterion, the methods implemented in the OpenCV library were the best: RANSAC, LMS, RHO. They increased the number of the pairs of corresponding points by ~ 20 pairs (~ 13% of the initial quantity). However, the speed of processing is critical for the implementation of a UAV navigation system. According to this criterion, the proposed iterative method with the variants 1-3 for the pair selection was the best. It takes ~0.03–0.06ms for processing one frame, which is ~5–10 times faster than the best of the OpenCV methods, with that it increases the number of the pairs of corresponding points by ~15 pairs (~10%). The high speed of the proposed method is due to the fact that in most cases two iterations are enough to obtain the resulting homography matrix. Thus, for the second experiment according to the both criteria the following methods were chosen: the proposed iterative method with the first variant of the pair selection and the RHO method.

The second experiment aims to determine the effect of the integration of the normalization method into the UAV visual navigation system. There were three trials in the experiment: without normalization, with normalization using the proposed method, and using the RHO method. The first criterion was the number of the images from the UAV camera successfully matched with the satellite image. The second criterion was the average distance between the automatically calculated positions of the center of photographing and the manually marked ones. The results of the experiment are shown in table 2.

After analyzing the results of the experiment, we can conclude that the preliminary normalization of the image significantly improves the output of the UAV visual navigation system being developed. It increases the number of the successfully matched frames as well as the accuracy of the calculated coordinates of the UAV. The methods work well both in the straight sections of the flight trajectory and in the sections with turns. The result of the proposed method is not worse than the one of the RHO

method from the OpenCV library, and at that the proposed method performs much faster, which is very important for integrating it into a UAV visual navigation system.

Table 2. The effect of normalization methods on the output of the visual navigation system.

Indicator	Section	Without normalization	Proposed method with variant 1 of pair selection	RHO
Number of frames	straight sections	270		
	turns	70		
	whole trajectory	340		
Number of successfully matched frames	straight sections	226 (83.7%)	**246 (91.1%)**	**246 (91.1%)**
	turns	59 (84.3%)	**64 (91.4%)**	62 (88%)
	whole trajectory	285 (83.8%)	**310 (91.1%)**	308 (90.6%)
Average distance between the found center of photographing and the manually marked one (pixels)	straight sections	16.0	**6.6**	6.8
	turns	7.5	**6.4**	6.7
	whole trajectory	16.0	**6.6**	6.7

6. Conclusion

The proposed method of iterative image normalization successfully solves the task of image preprocessing for developing a UAV visual navigation system. The integration of this method into the navigation system improves the accuracy of matching the images acquired from the onboard camera with the satellite image and reduces the probability of the UAV loss.

Due to using the two normalization approaches the proposed method can eliminate perspective distortions resulting from both the camera orientation and the inclination of the underlying surface. At the same time, this method is computationally simple and can be integrated into the UAV navigation system, which should run on low-power processors.

7. References

[1] Gafarov R M, Arkhipov I O, Korobeynikov A V and Elantsev M O 2017 Application of the method of statistical differentiation for the gridding of aerophoto image to a satellite image *Intellektualnye sistemy v proizvodstve* **15** 109-112 DOI: 10.22213/2410-9304-2017-2-109-112

[2] Kholopov I S 2017 Projective distortion correction algorithm at low altitude photographing *Computer Optics* **41(2)** 284-290 DOI: 10.18287/0134-2452-2017-41-2-284-290

[3] Boriskevich A A 2016 A robust method for normalization of barcode images scanned with a mobile device *Izvestija Nacionalnoj akademii nauk Belarusi. Serija fiziko-tehnicheskih nauk* **4** 106-112

[4] Adel E, Elmogy M and Elbakry H 2014 Image stitching based on feature extraction techniques: a survey *International Journal of Computer Applications* **88** 1-8

[5] Goncharenko M O 2015 Comparative analysis of key points detection methods as a part of video segmentation problem *Bionics of Intelligense* **85** 90-94

[6] Hartley R and Zisserman A 2003 *Multiple View Geometry in Computer Vision* (Cambridge: Cambridge university press)

[7] Efimov A I and Novikov A I 2016 An algorithm for multistage projective transformation adjustment for image superimposition *Computer Optics* **40(2)** 258-265 DOI: 10.18287/2412-6179-2016-40-2-258-265

[8] Agarwal A, Jawahar C V and Narayanan P J 2005 A survey of planar homography estimation techniques *Centre for Visual Information Technology International Institute of Information Technology*

[9] Goshin Y V, Kotov A P and Fursov V A 2014 Two-stage formation of a spatial transformation for image matching *Computer Optics* **38(4)** 886-891 DOI: 10.18287/0134-2452-2014-38-4-886-891

[10] Bazargani H, Bilaniuk O and Laganiere R 2015 A fast and robust homography scheme for real-

time planar target detection *Journal of Real-Time Image Processing* **15** 739-758 DOI: 10.1007/s11554-015-0508-4
[11] DeTone D, Malisiewicz T and Rabinovich A 2016 Deep image homography estimation *arXiv* (Preprint arXiv:1606.03798)
[12] Glasbey C A and Mardia K V 1998 A review of image-warping methods *Journal of applied statistics* **25** 155-171
[13] Arkhipov I O, Mishenkov M A, Shutov A A and Elantsev M O 2018 Algorithm of unmanned aerial vehicle's positioning using sequence of video stream frames *Intellektualnye sistemy v proizvodstve* **16** 66-69 DOI: 10.22213/2410-9304-2018-3-66-69
[14] Gafarov M R, Gafarov R M and Poltanova E S 2015 Determination of geometrical images parameters using statistical differentiation *Intellektualnye sistemy v proizvodstve* **25** 41-44
[15] Chekhlov D O and Ablameyko S V 2004 Normalization of images relating to perspective transformation based on geometric options *Informatika* **3** 67-76

Acknowledgments
The reported study was funded by Kalashnikov ISTU according to the research project № 09.06.01/18 GMM.

Method for reconstructing the real coordinates of an object from its plane image

V N Nesterov[1,2], V M Mukhin[1] and D V Nesterov[1]

[1]JSC «Samara Electromechanical Plant», Stepan Razin street, 16, Samara, Russia, 443099
[2]Samara National Research University, Moskovskoe shosse, 34A, Samara, Russia, 443086

e-mail: nesterov.ntc@gmail.com

Abstract. Original method of reconstructing the real coordinates of moving objects from their plane images is presented. The method uses multidimensional test objects whose parameters are measures and which are known with high accuracy. In order to ensure the process of measuring movements in real space a test object must be connected with a real object and mathematical models of images of multicomponent movements of a test object must be formed. The parameters of test objects that are used in the named mathematical models are vectors. Such models are used in the construction of systems of measurement equations the solution of which gives the desired components movements of a moving object in 3D space. The method was experimentally tested on specially created stand.

1. Introduction

Problem of the impossibility of recovering the real coordinates of objects in three-dimensional space from their plane image is one of the most serious problems in robotics. This problem was discussed in the fundamental work of well-known experts in the field of robotics and technical vision K. Fu, R. González and K. Li [1]. A more modern work provides a broad overview of various approaches that are used to solve this ill-posed problem [2]. Binocular vision is traditionally used to solve this problem in robotics and other areas. However, this solution leads to additional problems concerning the calibration of cameras, their placement in space, special algorithms for processing the received video information, etc. If you look at the problem more broadly, you should mention the works related to geo-informatics [3] or architecture [4]. Currently, geographic information systems are increasingly complemented by tools for working with spatial geometric objects, which allows solving problems of 3D modeling of objects that are spatially referenced to the surface of the Earth. The reconstruction of 3D coordinates of objects from plane projections in photogrammetry is solved by processing stereo pairs of images [5]. To illustrate the problem consider the process of imaging a 3D object on the surface of a video camera image. With some simplifications the imaging circuit is shown on the figure 1.

On the figure 1 the image plane coincides with the plane x, y of the video camera's coordinate system $\{o, \mathbf{x}, \mathbf{y}, \mathbf{z}\}$, and the optical axis, which is set in the center of the lens, is directed along the axis z The center of the image plane is the origin, and the center of the lens has coordinates $(0, 0, \lambda)$.

Denote the coordinates of a point in 3D space located at a distance in front of the lens, as (X, Y, Z). For all points of controlled space: $Z > \lambda$. From consideration of the corresponding right-angled triangles on the figure 1, we can write:

$$\frac{x_0}{\lambda} = \frac{X_1}{\lambda - Z_1}, \qquad \frac{y_0}{\lambda} = \frac{Y_1}{\lambda - Z_1}. \tag{1}$$

Then the relationship between the coordinates of points $M_1(X_1, Y_1, Z_1)$ and $m(x_0, y_0)$ is determined by the functions:

$$x_0 = \frac{\lambda X_1}{\lambda - Z_1}, \quad y_0 = \frac{\lambda Y_1}{\lambda - Z_1}. \tag{2}$$

They can be used to go from the Cartesian coordinates of a point $M_1(X_1, Y_1, Z_1)$ to the coordinates of a point of its image $m(x_0, y_0)$.

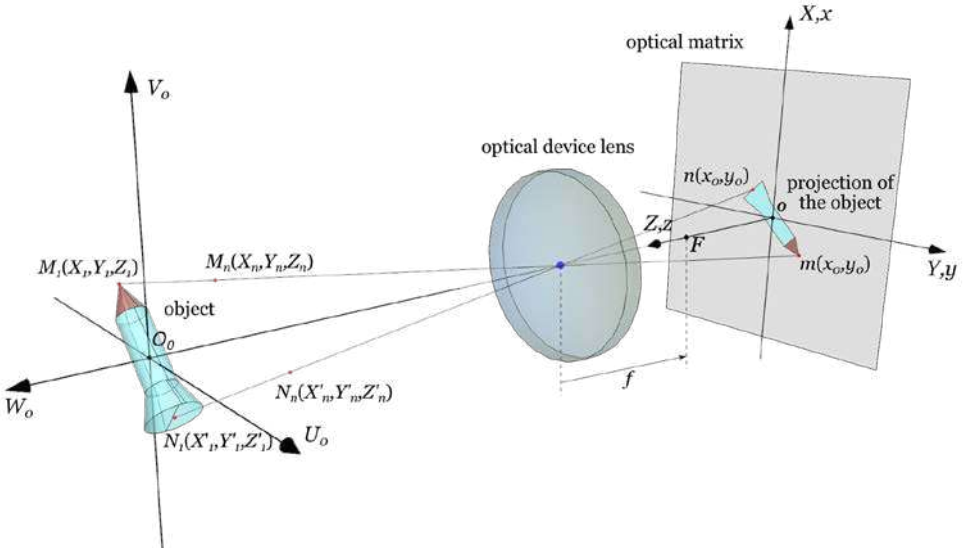

Figure 1. Image formation scheme.

Suppose that the point specified in the image has coordinates $(x_0, y_0, 0)$. In this case, the entire image plane on the z axis has a coordinate $z = 0$. The point of the image $m(x_0, y_0)$ corresponds to all points lying on a line that passes through the points with coordinates $(x_0, y_0, 0)$ and $(0, 0, \lambda)$. The equations of this line in Cartesian coordinates are:

$$X_1 = \frac{x_0}{\lambda}(\lambda - Z_1), \quad Y_1 = \frac{y_0}{\lambda}(\lambda - Z_1). \tag{3}$$

The ambiguity of this transformation is obvious. It is impossible to uniquely reconstruct a point $M_1(X_1, Y_1, Z_1)$ in 3D space by the coordinates of its image $m(x_0, y_0)$.

In all known methods for solving this ill-posed problem, including in the above-mentioned works, information redundancy is organized, for example, by using an additional camera (binocular vision) or using another method of obtaining at least two projections of a real three-dimensional object.

To solve this problem in recent years, the authors develop an original scientific direction, called: the method of multidimensional test objects in optical measurement systems [6].

To ensure the measurement process, a test object must be connected with a real object. And test object must have known geometrical parameters that are used as measures [7, 8]. At the same time, mathematical models of images of multicomponent movements are formed, which contain the parameters of test objects. These parameters are included in the models in the form of vectors and they are called tests. This is the basis of the method. Next we look at the basics of this method in more detail.

2. The main points of the multidimensional test objects method

Note that the following provisions and models have a specific practical orientation and, above all, relate to the restoration of informative movements of 3D objects in space. Therefore, it should be borne in mind certain restrictions on the subject area, although according to the authors' considerations, the provisions of the method can be extended to a wider range of tasks.

Since we are talking about the reconstruction of the components of the multidimensional movement of objects in three-dimensional space, which are vector quantities, the elements of multidimensional test objects included in the models are also vector quantities. A feature of the method is that the parameters of a multidimensional test object reflect the multidimensionality of will be measured movements and are functionally associated with them in the models in the process of forming the corresponding measurement and computational algorithms:

$$\left.\begin{aligned}\mathbf{X}_x(\mathbf{r},\tau)&=\mathbf{F}\left(\mathbf{x}_{1x}(\mathbf{r},\tau),...,\mathbf{x}_{px}(\mathbf{r},\tau),\mathbf{L}_{1x},...,\mathbf{L}_{qx}\right);\\ \mathbf{X}_y(\mathbf{r},\tau)&=\mathbf{F}\left(\mathbf{x}_{1y}(\mathbf{r},\tau),...,\mathbf{x}_{py}(\mathbf{r},\tau),\mathbf{L}_{1y},...,\mathbf{L}_{qy}\right);\\ \mathbf{X}_z(\mathbf{r},\tau)&=\mathbf{F}\left(\mathbf{x}_{1z}(\mathbf{r},\tau),...,\mathbf{x}_{pz}(\mathbf{r},\tau),\mathbf{L}_{1z},...,\mathbf{L}_{qz}\right),\end{aligned}\right\} \quad (4)$$

where $\mathbf{X}_x(\mathbf{r},\tau)$, $\mathbf{X}_y(\mathbf{r},\tau)$, $\mathbf{X}_z(\mathbf{r},\tau)$ are projections of multi-component movements on the axis of the Cartesian coordinate system; $\mathbf{r}$ is radius-vector from the beginning of the base coordinate system to the controlled point of the object under study; τ is time; $\mathbf{F}$ is components link function $\mathbf{x}_{1k}(\mathbf{r},\tau),...,\mathbf{x}_{pk}(\mathbf{r},\tau)$ and $\mathbf{L}_{1k},...,\mathbf{L}_{qk}$ $\mathbf{L}_{1k},...,\mathbf{L}_{qk}$ of the coordinate component $\mathbf{L}_k$ ($k\in\{x,y,z\}$) of the multidimensional test $\mathbf{L}$; $\mathbf{x}_{1k}(\mathbf{r},\tau),...,\mathbf{x}_{pk}(\mathbf{r},\tau)$ are informative components of the k coordinate component of the multicomponent movement $\mathbf{X}(\mathbf{r},\tau)$; p is number of informative components of multicomponent movement; $\mathbf{L}_{1k},...,\mathbf{L}_{qk}$ are components of the k coordinate component $\mathbf{L}_k$ of the multidimensional test $\mathbf{L}$; p is number of components of the k coordinate component $\mathbf{L}_k$ of the multidimensional test $\mathbf{L}$.

As already noted, the principal feature of the model (4) is the introduction of test objects $\mathbf{L}_{1k},...,\mathbf{L}_{qk}$, which must be indicated in vector form as informative components known in it.

Figure 2 shows, as an illustration, a two-dimensional test object, which was obtained by a combination of two one-dimensional.

The test object is located in the plane $O_0X_0Y_0$ and has the following parameters (tests), which are known with high accuracy:

$$\mathrm{AO_i}=nL_{ABx}\ \text{и}\ \mathrm{BO_i}=(1-n)L_{ABx},\ (n=0{,}5);$$
$$\mathrm{CO_i}=nL_{CDy}\ \text{и}\ \mathrm{DO_i}=(1-n)L_{CDy},\ (n=0{,}5);$$
$$\mathrm{EB}=(1-n)L_{ABx}\ \text{и}\ \mathrm{FD}=(1-n)L_{CDy},\ (n=0{,}75).$$

The test object $O_0X_0Y_0$ is a two-dimensional and multicomponent, and its parameters in models (5) are used in a vector form, for example:

$$\mathbf{AO}_\mathrm{i}=n\mathbf{L}_{ABx}=nL_{ABx}\cdot\mathbf{i},\ (n=0{,}5);\ \mathbf{BO}_\mathrm{i}=(1-n)\mathbf{L}_{ABx}=(1-n)L_{ABx}\cdot\mathbf{i},\ (n=0{,}5);$$
$$\mathbf{CO}_\mathrm{i}=n\mathbf{L}_{CDy}=nL_{CDy}\cdot\mathbf{j},\ (n=0{,}5);\ \mathbf{DO}_\mathrm{i}=(1-n)\mathbf{L}_{CDy}=(1-n)L_{CDy}\cdot\mathbf{j},\ (n=0{,}5);$$
$$\mathbf{EB}=(1-n)\mathbf{L}_{ABx}=(1-n)L_{ABx}\cdot\mathbf{i},\ (n=0{,}75);\ \mathbf{FD}=(1-n)\mathbf{L}_{CDy}=(1-n)L_{CDy}\cdot\mathbf{j},\ (n=0{,}75),$$

where $\mathbf{i}$ and $\mathbf{j}$ are basis vectors whose direction coincides with the direction of the axes O_0X_0 and O_0Y_0.

Here the problem is not set to classify or demonstrate the variety of test objects. Here are formulated only the basic requirements for them, which are fundamental.

Let us draw an analogy between the parameters (components) of a multidimensional test object and the components of complex displacements. Then the components of multidimensional tests or their

projections on the coordinate axes will be considered as multicomponent quantities – multicomponent tests, the components of which are also vector quantities.

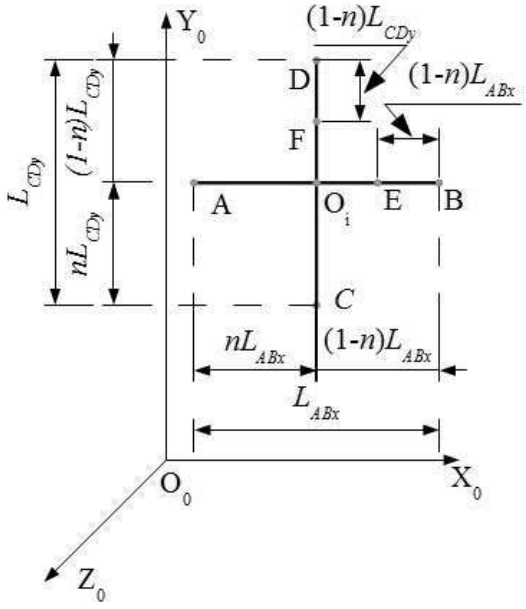

Figure 2. 2D test object ABCD.

Accordingly, the general method of forming multidimensional tests and the function of the connection of their components with multicomponent quantities fall under the basic principles of the concept of vector multicomponent physical quantities [5] and are formulated as follows:

- multidimensional multicomponent tests are considered as functions of the set of their components;
- functions of communication of the named components in models of multicomponent tests are determined by the laws of vector algebra;
- models of vector multidimensional multicomponent tests allow the multivariate representation of these components, depending on the problem being solved.
- models of vector multidimensional multicomponent tests allow to give alternative representation of these components, depending on the problem being solved.

Based on the provisions about the multidimensional test object, we define the type of function of communication $\mathbf{F}$ of informative components $\mathbf{x}_{1k}(\mathbf{r},\tau),...,\mathbf{x}_{pk}(\mathbf{r},\tau)$ and components $\mathbf{L}_{1k},...,\mathbf{L}_{qk}$ of the coordinate component $\mathbf{L}_k$ of the multidimensional test $\mathbf{L}$ in model (4):

$$\mathbf{F}_{ik}\left\{\mathbf{x}_{1k}(\mathbf{r},\tau),...,\mathbf{x}_{pk}(\mathbf{r},\tau),\mathbf{L}_{1k},...,\mathbf{L}_{qk}\right\}=\sum_{k}^{\{x,y,z\}}\sum_{u=1}^{q}v_{iuk}\mathbf{L}_{iuk}+\sum_{k}^{\{x,y,z\}}\sum_{j=1}^{p}\eta_{ijk}\mathbf{x}_{ijk}(\mathbf{r},\tau), \quad (5)$$

where i is the sequence number of the communication function; $k\in\{x,y,z\}$ is the set of coordinate components; u is the serial number of the components of the multi-component test $\mathbf{L}_{iuk}$; j is the sequence number of the informative components of the coordinate component of the multicomponent displacement $\mathbf{X}_k(\mathbf{r},\tau)$; $v_{iuk}\in[0,1]$ are the weights reflecting the absence – 0 – or the presence – $(0,1]$ – the corresponding component of a multicomponent test $\mathbf{L}_{iuk}$ in model (5); $\eta_{ijk}\in[0,1]$ are the weights reflecting the absence – 0 – or the presence – $(0,1]$ – the corresponding informative component $\mathbf{x}_{ijk}(\mathbf{r},\tau)$ in model (5).

Using (5) it is possible to present model (4) in the following form:

$$\left.\begin{aligned}
\mathbf{X}_{ix}(\mathbf{r},\tau) &= \sum_{u=1}^{q} v_{iux}\mathbf{L}_{iux} + \sum_{j=1}^{p} \eta_{ijx}\mathbf{x}_{ijx}(\mathbf{r},\tau);\\
\mathbf{X}_{iy}(\mathbf{r},\tau) &= \sum_{u=1}^{q} v_{iuy}\mathbf{L}_{iuy} + \sum_{j=1}^{p} \eta_{ijy}\mathbf{x}_{ijy}(\mathbf{r},\tau);\\
\mathbf{X}_{iz}(\mathbf{r},\tau) &= \sum_{u=1}^{q} v_{iuz}\mathbf{L}_{iuz} + \sum_{j=1}^{p} \eta_{ijz}\mathbf{x}_{ijz}(\mathbf{r},\tau),
\end{aligned}\right\} \qquad (6)$$

where the vectors $\mathbf{L}_{iux}$, $\mathbf{L}_{iuy}$, $\mathbf{L}_{iuz}$, $\mathbf{x}_{ijx}$, $\mathbf{x}_{ijy}$, $\mathbf{x}_{ijz}$ are defined in one-dimensional spaces that coincide with the corresponding axes of the Cartesian coordinate system.

Such a representation of model (5), while retaining its universal character, provides a mechanism for adaptation to specific practical tasks through the use of a combination of coefficients $v_{iux} \in [0,1]$, $v_{iuy} \in [0,1]$, $v_{iuz} \in [0,1]$, $\eta_{ijx} \in [0,1]$, $\eta_{ijy} \in [0,1]$, $\eta_{ijz} \in [0,1]$ in the field of their definition.

The following is figure 3, which illustrates the process of moving the test object, on the basis of which the model (6) was obtained. It shows the movement in space of a cruciform shape, which is a test object, and the reflection of this movement on a flat matrix of the optical instrument.

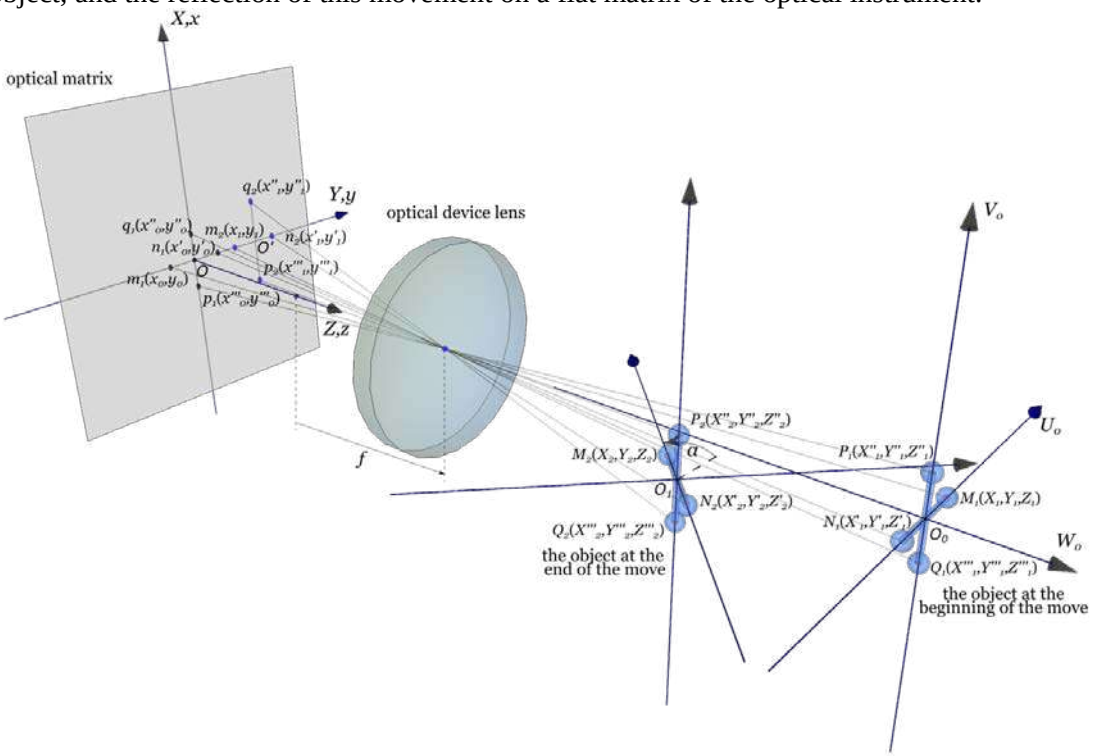

Figure 3. Illustration for model (6).

Any movement, including multicomponent, is described in accordance with the laws and provisions of vector algebra. When considering the projections of vector quantities onto the plane and introducing special agreements, it is possible to significantly simplify the process of synthesizing complex mathematical models by formally generating them, which is necessary to search for appropriate measurement and computational algorithms [9]. The information redundancy embodied in the models in the form of parameters of a multidimensional test object allows us to approach its solution.

3. Physical realizability of the measurement method

Based on the formulated provisions on multidimensional test objects, we list the method-forming features, the implementation of which will solve the problem of the physical realizability of the method:

1. The presence (the ability to form) a system of n equations that are asymmetric with respect to informative components $\mathbf{x}_{1k}(\mathbf{r},\tau), ..., \mathbf{x}_{pk}(\mathbf{r},\tau)$ ($k \in \{x, y, z\}$ is the set of coordinate components) displacements of the corresponding image points of the test object:

$$\left.\begin{array}{c} \mathbf{Y}_1(\mathbf{r},\ \tau) = \Psi_1\left\{\mathbf{F}_1\left\{\mathbf{x}_{1k}(\mathbf{r},\tau), ..., \mathbf{x}_{pk}(\mathbf{r},\tau), \mathbf{L}_{1k}, ..., \mathbf{L}_{qk}\right\}\right\}; \\ ..... \\ ..... \\ \mathbf{Y}_n(\mathbf{r},\ \tau) = \Psi_n\left\{\mathbf{F}_p\left\{\mathbf{x}_{1k}(\mathbf{r},\tau), ..., \mathbf{x}_{pk}(\mathbf{r},\tau), \mathbf{L}_{1k}, ..., \mathbf{L}_{qk}\right\}\right\}, \end{array}\right\} (n \geq p \geq 2), \quad (7)$$

$$\mathbf{F}_1\left\{\mathbf{x}_{1k}(\mathbf{r},\tau), ..., \mathbf{x}_{pk}(\mathbf{r},\tau), \mathbf{L}_{1k}, ..., \mathbf{L}_{qk}\right\} \neq ... \neq \mathbf{F}_p\left\{\mathbf{x}_{1k}(\mathbf{r},\tau), ..., \mathbf{x}_{pk}(\mathbf{r},\tau), \mathbf{L}_{1k}, ..., \mathbf{L}_{qk}\right\}, \quad (8)$$

where $\mathbf{Y}_1(\mathbf{r},\ \tau),..., \mathbf{Y}_n(\mathbf{r},\ \tau)$ are functions of displacement of the corresponding points of the image of the object being monitored relative to the selected on the image of the points of reference; $\mathbf{F}_1\left\{\mathbf{x}_{1k}(\mathbf{r},\tau),..., \mathbf{x}_{pk}(\mathbf{r},\tau), \mathbf{L}_{1k},..., \mathbf{L}_{qk}\right\},..., \mathbf{F}_p\left\{\mathbf{x}_{1k}(\mathbf{r},\tau),..., \mathbf{x}_{pk}(\mathbf{r},\tau), \mathbf{L}_{1k},..., \mathbf{L}_{qk}\right\}$ are vector functions of the set of informative components $\mathbf{x}_{1k}(\mathbf{r},\tau),..., \mathbf{x}_{pk}(\mathbf{r},\tau)$ and components $\mathbf{L}_{1k},..., \mathbf{L}_{qk}$ of the coordinate component $\mathbf{L}_k$ of a multidimensional test object (of the multidimensional test) $\mathbf{L}$.

2. The ability to realization special measuring and computing algorithms:

$$\left.\begin{array}{c} \mathbf{x}_{1k}(\mathbf{r},\tau) = f_1\{\mathbf{Y}_1(\mathbf{r},\ \tau), ..., \mathbf{Y}_n(\mathbf{r},\ \tau)\}; \\ ..... \\ ..... \\ \mathbf{x}_{pk}(\mathbf{r},\tau) = f_p\{\mathbf{Y}_1(\mathbf{r},\ \tau), ..., \mathbf{Y}_n(\mathbf{r},\ \tau)\}, \end{array}\right\} \quad (9)$$

condition of the existence of which, with continuity and differentiability $\mathbf{Y}_1(\mathbf{r},\ \tau),..., \mathbf{Y}_n(\mathbf{r},\ \tau)$ in the whole range of measurement, is the inequality of zero Jacobian:

$$\det\left[\frac{\partial\ \mathbf{Y}_i(\mathbf{r},\ \tau)}{\partial\ \mathbf{x}_{jk}(\mathbf{r},\ \tau)}\right] \neq 0 \quad i = \overline{1,n},\ j = \overline{1,p}\ . \quad (10)$$

The condition (10) is ensured by the implementation of the “asymmetry” of the values $\mathbf{Y}_1(\mathbf{r},\ \tau),..., \mathbf{Y}_n(\mathbf{r},\ \tau)$ relative to their constituent components $\mathbf{x}_{1k}(\mathbf{r},\tau),..., \mathbf{x}_{pk}(\mathbf{r},\tau)$ and $\mathbf{L}_{1k},..., \mathbf{L}_{qk}$, which is expressed by the inequality (8).

Obviously, when using a single-channel optical system, the functions $\psi_1,..., \psi_n$ are the same. If we use the transmission coefficient σ of the optical converter, then the system of equations (7) can be rewritten as follows:

$$\left.\begin{array}{c} \mathbf{Y}_1(\mathbf{r},\ \tau) = \sigma\left\{\mathbf{F}_1\left\{\mathbf{x}_{1k}(\mathbf{r},\tau), ..., \mathbf{x}_{pk}(\mathbf{r},\tau), \mathbf{L}_{1k}, ..., \mathbf{L}_{qk}\right\}\right\}; \\ ..... \\ ..... \\ \mathbf{Y}_n(\mathbf{r},\ \tau) = \sigma\left\{\mathbf{F}_p\left\{\mathbf{x}_{1k}(\mathbf{r},\tau), ..., \mathbf{x}_{pk}(\mathbf{r},\tau), \mathbf{L}_{1k}, ..., \mathbf{L}_{qk}\right\}\right\}, \end{array}\right\} (n \geq p \geq 2). \quad (11)$$

Having considered the system (11) we can understand all the perspectives of the optical measurement method. For a more detailed consideration of the implementation of the proposed method, refer to [6-9]. The originality and novelty of the measurement method is confirmed by patents of the Russian Federation for inventions [10–12]. The method was experimentally tested on specially created stand where the cruciform figure was used as a test object. The details of the experiment and its results are presented in a separate section in paper [6].

4. Conclusions

Summing up, we can conclude that, on the basis of the method of multidimensional test objects, the incorrect problem of reconstructing the coordinates of objects moving in three-dimensional space from their flat image has been solved.

The basics of optical measurements of informative components of multicomponent displacements based on the method of multidimensional test objects, providing information redundancy at the input of an optical image receiver, are also presented. Additional information at the system input in the form of known parameters of multidimensional test objects creates opportunities for improving the quality and quantity of the resulting information.

Separate attention is required for the problem of generating multidimensional test objects, to investigate the effects of their type, quantity and optimization of test components (parameters of a multidimensional test object) on the quality of the measuring system both in the general theoretical aspect and for solving specific applied problems. These questions should be the subject of further research.

5. References

[1] Fu K, Gonzalez R and Lee K 1989 *Robotics* (Moscow: World) p 624
[2] Oswald M R, Toppe E, Nieuwenhuis C and Cremers D 2013 A review of geometry recovery from a single image focusing on curved object reconstruction *Innovations for shape analysis: models and algorithms* (Berlin Heidelberg: Springer-Verlag) 343-378 DOI: 10.1007/978-3-642-34141-0
[3] Kostyuk Yu L, Paramonov A S and Gritsenko V G 1998 The technology of creating 3D models of objects on flat projections and its application in geoinformatics *Geoinformatics: Theory and Practice* (Tomsk: Tomsk University) **1** 96-106
[4] Dzwierzynska J 2016 Reconstructing architectural environment from the perspective image *World multidisciplinary civil engineering-architecture-urban planning symposium, WMCAUS* (ScienceDirect: Proc. engineering) **161** 1445-1451
[5] Kostyuk Yu L 2002 Efficient algorithms for processing and displaying graphic data and their implementation in software packages *Abstract of thesis ... doc. tech. of science* (Tomsk: Tomsk University) p 39
[6] Nesterov V N, Mukhin V M and Meshchanov A V 2013 *The method of multidimensional test objects in optical measurement systems* (Samara: Publishing House of the Samara Scientific Centre of the Russian Academy of Sciences) p 224
[7] Nesterov V N and Meshchanov A V 2006 Models for vector multicomponent physical quantities and a multivariate test method for optical measurement systems *Measurement Techniques* **49(12)** 1182-1188
[8] Nesterov V N and Meshchanov A V 2007 Theoretical principles of optical measurements on the components of multicomponent displacements for mobile objects on the basis of multivariate tests *Measurement Techniques* **50(11)** 1127-1136
[9] Nesterov V N and Zhmurov D B 2007 Formal synthesis of a data-acquisition system for multicomponent physical quantities *Measurement Techniques* **50(9)** 903-907
[10] Nesterov V N, Mukhin V M and Meshchanov A V 2008 The way to measure the components of complex movements of an object *Russian Federation patent No RU2315948* URL: http://www1.fips.ru/fips_servl/fips_servlet?DB=RUPAT&DocNumber=2315948&TypeFile=html
[11] Nesterov V N, Mukhin V M and Meshchanov A V 2012 The method of controlling the accuracy of contour movements of industrial robots *Russian Federation patent No RU 2466858* URL: http://www1.fips.ru/fips_servl/fips_servlet?DB=RUPAT&DocNumber=2466858&TypeFile=html
[12] Nesterov V N, Nesterov D V and Mukhin V M 2017 The way to measure the components of complex movements of an object *Russian Federation patent No RU2610425* URL: http://www1.fips.ru/fips_servl/fips_servlet?DB=RUPAT&DocNumber=2610425&TypeFile=ht

Selection in a 3D microtomographic image the region with the highest quality

A S Kornilov[1,2], I V Safonov[1], A V Goncharova[2] and I V Yakimchuk[1]

[1]Schlumberger Moscow Research, Pudovkina 13, Moscow, Russia, 119285
[2]National Research Nuclear University MEPhI, Kashirskoe shosse 31, Moscow, Russia, 115409

e-mail: kranton94@mail.ru

Abstract. We present an algorithm for processing of X-ray microtomographic (micro-CT) images that allows automatic selection of a sub-volume having the best visual quality for further mathematical simulation, for example, flow simulation. Frequently, an investigated sample occupies only a part of a volumetric image or the sample can be into a holder; a part of the image can be cropped. For each 2D slice across the Z-axis of an image, the proposed method locates a region corresponding to the sample. We explored applications of several existing blind quality measures for an estimation of the visual quality of a micro-CT image slice. Some of these metrics can be applied to ranking the image regions according to their quality. Our method searches for a cubic area located inside regions belonging to the sample and providing the maximal sum of the quality measures of slices crossing the cube across the Z-axis. The proposed technique was tested on synthetic and real micro-CT images of rocks.

1. Introduction

In the last decade, X-ray microtomography (micro-CT) has been actively used for analyzing of rock, soil, granular materials [1] and building their 3D models for a Digital Rock [2]. One of the applications of these digital models is a flow modelling of a multiphase fluid [3]. A typical micro-CT image can have size up to ~4000^3 voxels. Some systems allow getting even larger images. However, the sample under study occupies only part of the image or can be in the holder. For mathematical modelling, researchers often use only a sample fragment of a cubic form with sides from 400 to 1000 voxels. Thus, there is a task of cropping a fragment from a whole micro-CT image, which is suitable and, in some sense, optimal for further analysis. Currently, an operator performs this procedure manually. The quality of the micro-CT image varies in the image volume, individual parts of the sample, for example, dense inclusions, can significantly affect the quality [4]. For a reasonable fragment selection, the operator needs to view several hundred slices of a 3D image. The selection process takes considerable time and depends on the subjective opinion of the operator. So, the development of an automatic quick and formalized algorithm of the fragment selection for mathematical modelling is an important problem.

The complexity of this problem is explained by the huge variety of images that can be on the input of the algorithm. This diversity is caused not only by the variety of scanned samples but also by

features of various microtomographic systems and parameters of image reconstruction algorithms. In addition, certain tomography artifacts can be differently suppressed by various reconstruction software. Frequently, only a part of an original reconstructed tomographic image relates to a sample. And also the software of a micro-CT system reconstructs from shadow projections an image having a bit depth of 8 or 16 bits per voxel.

Figure 1 demonstrates several examples of 2D slices perpendicular to the Z axis. These images were obtained using different micro-CT systems. A granular material is placed in a cylindrical holder, which is completely inside the field of view, non-reconstructed areas in the corners of the image are filled by gray (figure 1a). A cylindrical sample of sandstone is completely in the field of view, the areas in the corners are filled by gray (figure 1b). A cylindrical sandstone sample is completely in the field of view but is off-center; unreconstructed areas are filled by black (figure 1c). Note, the holder is not of interest for further analysis. In the following example, scanning is performed inside a sample, unreconstructed corner areas are darker and blurred (figure 1d) than a center zone. A piece of an arbitrary shape sample is completely in the field of view (figure 1e). A rectangular fragment is cropped from an original reconstructed image (figure 1f). In addition, several dozen slices at the top and bottom of a 3D image may not contain the sample. They can contain a holder or air.

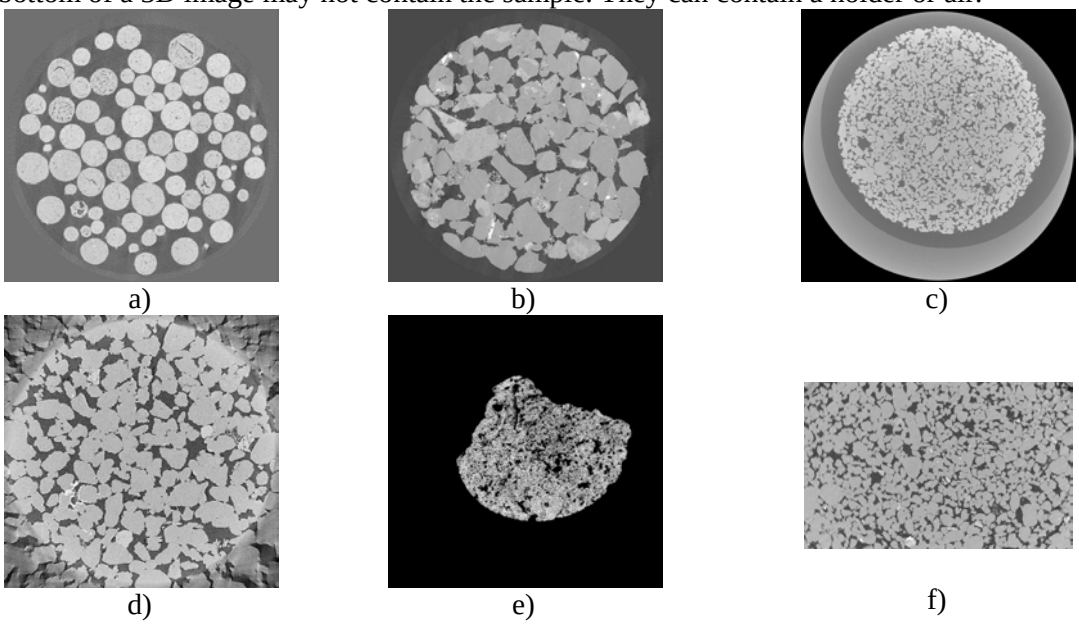

Figure 1. Examples of slices of various micro-CT images.

One more challenge is a formalization of a criterion for a selection of a fragment for further modelling. Which one of the many possible fragments to choose? It is reasonable to crop the fragment optimal from the point of view of some criterion. What can the criterion be in this case? Ideally, the criterion should depend on the objectives of the subsequent modeling. For example, to simulate the fluid flow, the criterion may be based on porosity or coherence of the pore structure. However, regardless of the methods and objectives of the subsequent analysis, we can say that we are interested to determine the most qualitative fragment in terms of visual assessment.

An important requirement for the developed algorithm and software is a high speed of the micro-CT image analysis. The processing time should be substantially less than the time required for the selection of the suitable fragment manually. We propose a fast algorithm that automatically selects from a micro-CT image a fragment of a given size that has the highest visual quality assessment.

2. Algorithm for selection of micro-CT image region

2.1. Main ideas

We propose to select a convex region related to the sample on each slice of the 3D image and evaluate the image quality in this area. Then we determine whether it is possible to inscribe a cube of a given

size into selected regions of consecutive slices and calculate the image quality estimation for the cube, summing up the estimations of slices intersecting the cube. The result of the algorithm is the cube that corresponds to a fragment of the 3D image with the highest image quality assessment. The proposed approach allows organizing parallel processing of the slices to select the regions located inside the sample and to assess the image quality in this area. Image handling in the slice-wise mode is one from approaches to reduce the processing time of a tomographic image [5].

The method of selecting the region related to the sample assumes that there are areas of varying intensity or filled with different textures in the image of the sample, between which there are visible edges. We propose to apply the thresholding of the outcome of the variance filter [6] to detect the edges between regions. At the same time, if on the image of the slice there are only the edges of the holder, then they should be ignored. From the obtained convex regions for the stack of slices, we can easily determine whether the cube of a given size can be inscribed in them. Moreover, we can find the maximum possible size of the inscribed cube using an algorithm that determines the maximum rectangle that fits inside the connected region [7].

Over the past decade, several no-reference (blind) image quality metrics have been proposed [8-11]. Algorithms for calculating these quality metrics were trained and tuned on a set of natural 2D photos. They can assess the quality of 2D grayscale images with a bit depth of 8 bits per pixel. It was assumed that among the existing non-reference quality metrics we can find applicable for characterizing the quality of the slices of micro-CT images.

To use mentioned no-reference image quality metrics, we should convert images from 16 bits per voxel to 8 bits per voxel. Generally, intensities of images having 16 bits per voxel do not occupy the entire dynamic range. Thus, we need to increase the contrast in converting the images to 8 bits per voxel. Sometimes, it is advisable to increase the contrast in case of images with 8 bits per voxel too. The intensities of all 3D image slices should be normalized in the same range. The parameters for normalization are determined by means of analyzing the intensity histogram H of the central part of the 3D image. To calculate the histogram H, we perform a preliminary pass through the central part of the image, for which we indent 25% from each side of the image.

The lower bound l for intensities normalization is calculated using the statement [12]:

$$l = \min\left(\min\left\{i \middle| H[i] \geq H_0\right\}, \min\left\{i \middle| \sum_{k=0}^{i} H[k] \geq C_0\right\}\right), \tag{1}$$

where H_0 is the threshold for the height of the histogram column for dark tones; C_0 is the threshold for the area of the histogram in dark tones, functionally C_0 is equivalent to the percentile of H.

The upper limit u for intensities normalization is calculated with the formula:

$$u = \max\left(\max\left\{i \middle| H[i] \geq H_1\right\}, \max\left\{i \middle| \sum_{k=i}^{2^n-1} H[k] \geq C_1\right\}\right), \tag{2}$$

where H_1 is the threshold for the height of the histogram column for bright colors; C_1 is the threshold for the area of the histogram in bright colors; n is the bit depth, 8 or 16.

Normalization of the intensities of each slice I in the range [0, 255] is performed according to the formula:

$$I(r,c) = \begin{cases} 0 : I(r,c) \leq l, \\ \dfrac{255\left(I(r,c) - l\right)}{(u-l)} : l < I(r,c) < u, \\ 255 : u \leq I(r,c) \end{cases} \tag{3}$$

where (r, c) is the slice pixel coordinates, $r = 0 \ldots N - 1$, $c = 0 \ldots M - 1$; N is the number of rows in the image; M is the number of columns.

2.2. Region of sample selection in 2D slice

The algorithm for selecting the region belonging to the sample searches for a convex region, within which there are distinguishable edges between regions of different intensity. It is important to find the area inside the sample, but it is not necessary to accurately detect the boundary of the sample. Often,

the noise level in micro-CT images is quite high. Therefore, many well-known edge-detection filters are not applicable, as they react to noise. In addition, we are not interested in the edges themselves, but areas where there are changes in intensity. The variance filter allows getting an image in which relatively large values are in the pixels, around which there is a change in the intensity and relatively small values in uniform areas.

The variance filter is defined as [6]:

$$I_{\text{var}}(r,c)=\frac{1}{W^2}\sum_{i=0}^{W-1}\sum_{j=0}^{W-1}\left(I\left(r+i-\left[\frac{W}{2}\right],c+j-\left[\frac{W}{2}\right]\right)-\overline{I_W}(r,c)\right)^2, \quad (4)$$

where [ ] is the operator of taking the integer part; $I(r, c)$ is the intensity of a pixel with coordinates (r, c), $r = [W / 2] \ldots N - [W / 2] - 1$, $c = [W / 2] \ldots M - [W / 2] - 1$; the mean value $\overline{I_W}$ within the window is calculated as:

$$\overline{I_W}(r,c)=\frac{1}{W^2}\sum_{i=0}^{W-1}\sum_{j=0}^{W-1}I\left(r+i-\left[\frac{W}{2}\right],c+j-\left[\frac{W}{2}\right]\right). \quad (5)$$

The window size depends on the slice size, and it is selected about 100 by 100 pixels. Figure 2b shows the result of the variance filter for the slice in figure 1a. Thresholding of the outcome of the variance filter allows obtaining a binary image, in which the pixels are set to value 1 when the intensity varies in the local vicinity. Figure 2b shows the result of the thresholding. It should be noted that after the thresholding, several connected regions may form. To merge them into a single connected region, we use the morphological closing operation [13]. Several small areas can be located near the boundaries of the image. For instance, they can occur on the outer border of the holder. To exclude these undesirable regions from consideration we process only the connected region with the largest area. For this region, we calculate the convex hull and fill it with values 1. The resulting region protrudes approximately half to two-thirds of the size of the variance filter window from the sample region. To ensure that the region is inside the sample region, a morphological erosion filter [13] is applied with the size of the structural element equal to the size of the variance filter window.

Note that the image of the slice may be missing a fragment relating to the sample. The proposed algorithm allows detecting such a situation. We make a conclusion about this situation based on the area and shape of the largest detected region after the application of the closing operation. Also, according to the results of the sample area selection on the slice, the algorithm produces recommendations for the operator of the micro-CT system. For example, if the sample is significantly displaced from the center of the slice, then it is probably possible to reconstruct an image of better quality if you re-shoot the shadow projections by placing the sample in the center.

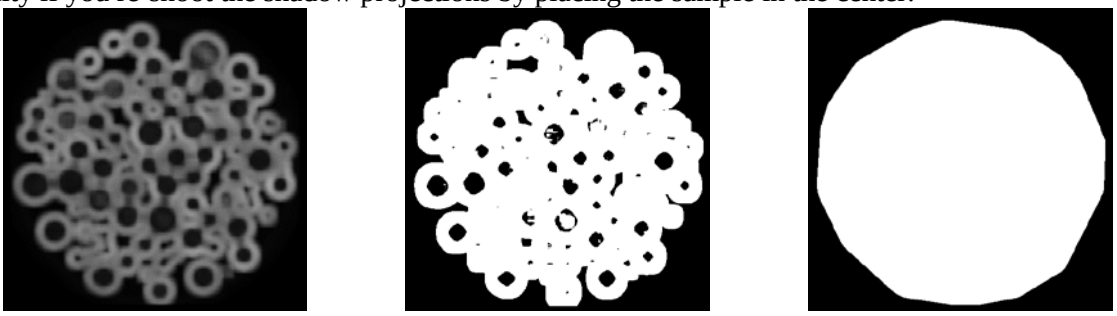

a) b) c)

Figure 2. Illustration of the sample region selection stages for the slice from figure 1a: (a) the result of the variance filter; (b) the result of the thresholding of image from figure 2a; (c) a convex region constructed along the outer boundary of region from figure 2b.

2.3. Analysis of the use of no-reference quality metrics for micro-CT images

At present, a sufficiently big number of no-reference image quality metrics has been proposed. Such metrics make possible to evaluate the quality based on the image only without the reference. Part of the metrics is designed to assess one factor affecting the quality, for example, the blurriness level [14].

Others claim to universality. We evaluated the following algorithms for assessing of quality of slices of micro-CT image: BIQI (Blind Image Quality Index) [8], BRISQUE (Blind Referenceless Image Spatial Quality Evaluator) [9], NIQE (Natural Image Quality Evaluator) [10] and OG-IQA (Oriented Gradients Image Quality Assessment) [11].

The considered algorithms were trained on natural photos, for instance, from the LIVE data set [15]. This data set, in addition to undistorted photos, contains images that have been distorted. Several types of distortion were used: additive white Gaussian noise, Gaussian blur, JPEG and JPEG2000 compression artifacts. However, this dataset is rather idealistic, because only one type of distortion affects an image at the same time. After interviewing many observers, an estimate of quality for each image from the set was calculated based on the pairwise comparison.

The BIQI algorithm [8] implements a two-step approach to assess the quality of the images. This approach is based on a natural scene statistic (NSS) and the assumptions that natural images have certain statistical properties, and distortions change these statistical characteristics in such a way that the type and degree of distortion can be estimated with a high confidence level. The first step in BIQI is an identification of distortion type. The second stage is an estimation of the strength of the distortion. Features for learning are taken from the model of natural scenes in the wavelet domain [16]. The models for classification and regression are trained by support vector machine (SVM) on data from the LIVE dataset. The BRISQUE method [9] uses the features of the NSS model calculated in the spatial domain [17]. A single regression model for all distortion types is trained on images from LIVE dataset using SVM method. The NIQE [10] technique constructs of a multivariate Gaussian distribution (MVG) of statistical features based on the statistical model of natural scenes in the spatial domain [17]. The quality of the estimated image is defined as the distance between the multidimensional normal distribution of this image characteristics and the reference MVG obtained as a result of training on the features of pristine undistorted images. The OG-IQA [11] algorithm analyzes the correlation structure of the gradient orientation in the image. The idea is that the orientation of the local gradients contains significant information about the naturalness of the image, and when distortions appear, this information changes in a certain way. The AdaBoost algorithm is used to train the regression model.

Initially, we assumed that these metrics can be used for an absolute quality assessment of micro-CT images, i.e. regardless of the equipment used and the sample analyzed. However, from the experiments, we saw that the metrics are not applicable for assessing the quality of images for samples of different rocks, because frequently the results did not correspond to the expert's opinion and the physical parameters of the experiments. However, for a comparative quality assessment of slices from one sample, the results were quite reasonable.

To study the applicability of these criteria for the comparative quality assessment of the slices from one sample, we formed a set of 10 images obtained as follows. We obtained six images by scanning the same sample with different exposure times. The noise level is directly dependent on the exposure time. The highest noise level corresponds to the shortest exposure. For two of these six images, we additionally reconstructed two images with a binning and a reduced number of projections. Binning is the process of combining the charges of neighboring pixels on an image sensor into one "superpixel". In tomographic reconstruction, binning is lowering the spatial resolution due to summation the values of neighboring pixels, which leads to an increase in the signal-to-noise ratio. Using fewer projections for reconstruction causes noise-like artifacts.

For these 10 images, it is known how they are ranked according to their quality. For the central part of these images, we calculated the quality assessment by several quality metrics. Table 1 contains the number of errors in image rankings using considering no-reference quality metrics. The number of errors is counted as the number of images that must be removed from the series to obtain a properly sorted sequence by quality. The best result was shown by NIQE metrics, which made two mistakes with images reconstructed with binning.

NIQE advantage was expected. This metrics is less associated with a fixed set of distortions of the LIVE dataset and uses a simpler model which is less tended to overfit. Moreover, for NIQE we built own MVG model of high-quality micro-CT images instead of photos from LIVE dataset. Further adjustment of this model may lead to improved results.

Table 1. The number of errors in the quality ranking of micro-CT images using non-reference quality metrics.

Quality metrics	Errors count
BIQI	4
BRISQUE	4
OG-IQA	6
NIQE	2

2.4. Algorithmic optimization

We achieve a high speed of handling of images due to parallel processing and the use of optimized algorithms. An example of algorithmic optimization is the implementation of a variance filter via integral images. In the integral image *IntI*, each pixel with coordinates (*r*, *c*) is equal to the sum of the pixels of the image *I* located to the left and above (*r*, *c*) [18]:

$$IntI(r,c)=\sum_{\substack{r'\le r\\ c'\le c}} I(r',c'). \tag{6}$$

IntI can be calculated in a single pass through the image *I* by the following statement:

$$IntI(r,c)=I(r,c)+I(r,c-1)+I(r-1,c)-I(r-1,c-1). \tag{7}$$

The sum of the pixels in the square window for the image *I* via the integral image *IntI* is calculated as:

$$\begin{aligned} S(r,c)=&IntI\left(r+\left[\frac{W-1}{2}\right],c+\left[\frac{W-1}{2}\right]\right)+IntI\left(r-\left[\frac{W}{2}\right],c-\left[\frac{W}{2}\right]\right)\\ &-IntI\left(r-\left[\frac{W}{2}\right],c+\left[\frac{W-1}{2}\right]\right)-IntI\left(r+\left[\frac{W-1}{2}\right],c-\left[\frac{W}{2}\right]\right), \end{aligned} \tag{8}$$

where *W* is the window size; the coordinate (*r*, *c*) is in the center of the window.

With the help of integral images, we can quickly perform the operations of the summation and averaging of rectangular image blocks. The area of integral images application is expanded by calculating such images for squares and higher powers of pixel values [19]. If we additionally calculate the integral image of *IntI2* for I^2 (via the formula (7)) and the sum of pixels in the square window S_2 (using formula (8)), then the variance filter can be calculated as:

$$I_{\text{var}}(r,c)=\frac{1}{W^2}\left(S_2(r,c)-\frac{S(r,c)^2}{W^2}\right). \tag{9}$$

Table 2 contains the processing time of a slice of 4000×4000 pixels by three various implementations of variance filter. We estimated the time for a single-threaded C++ program on a laptop with CPU Intel Core i7 2.6 GHz. The slowest approach is the implementation of the filter directly via formulas (4) and (5) in several nested loops. It is much faster to calculate the variance from the histogram, which during the window movement across the image is not recalculated completely but is updated. Finally, the fastest way is to calculate the local variances via integral images. The integral images *IntI* and *IntI2* require a larger amount of memory in comparison with *I*, but in our task, this is not a limitation.

Table 2. The variance filter processing time for a slice of 4000×4000 pixels.

Method	Processing time, s
In several nested loops	4.3
Via histogram	1.1
Via integral images	0.5

3. Results and conclusions

We tested about one hundred 3D micro-CT images that had from 1000 to 2000 slices. The region inside the sample was selected correctly for all cases. The results of the automatic selection of regions for the slices from figure **1** are shown in figure 3.

To test the algorithm for cropping of 3D fragment having the highest visual quality, we developed a software tool for generating a synthetic image of the micro-CT slice (see figure 4). This tool allows adjusting the sample size, the level of additive or multiplicative Gaussian white noise, the contrast, the radius of blurring filter, and the intensity of the holder region. From these synthetic slices, we formed a 3D image in which the noise level increased from the central slice to the top and bottom. For the slices of this 3D image, we calculated inverted and normalized NIQE quality metrics Q. As expected, the quality assessment Q is correlated with the noise level and is decreased from the central slice to top and bottom. Our algorithm identifies the central region as having the highest quality because the sum of quality assessments for the central slices is maximum (see figure 5). Background of the graph is a cross-section of the generated 3D image.

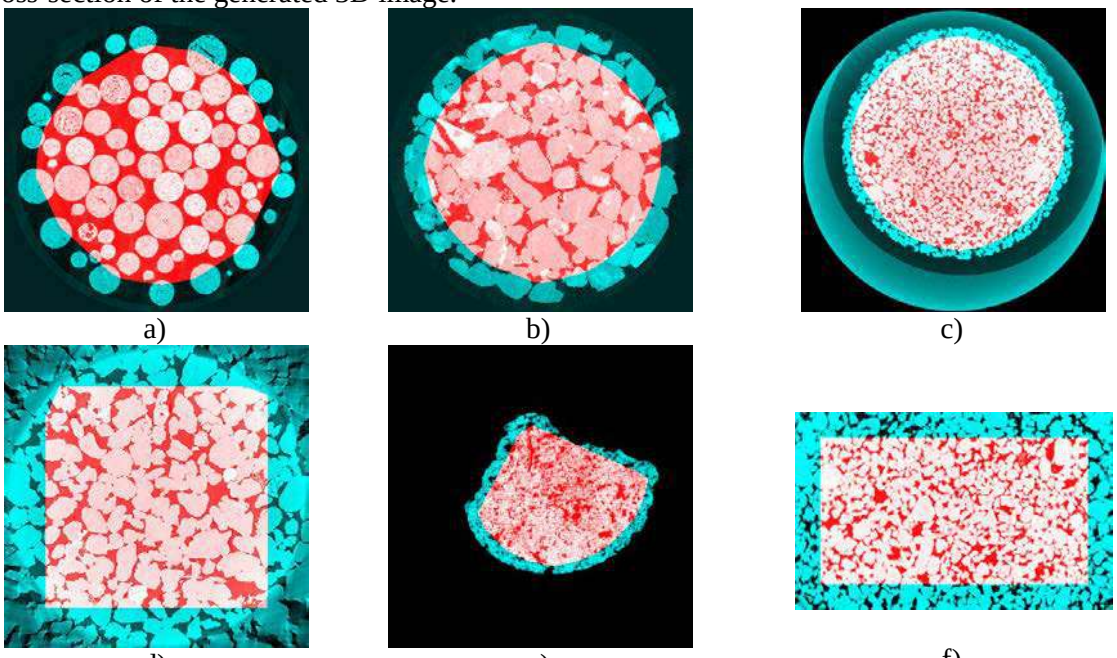

a) b) c) d) e) f)

Figure 3. The results of the algorithm for the selection of areas related to the sample for images from figure 1.

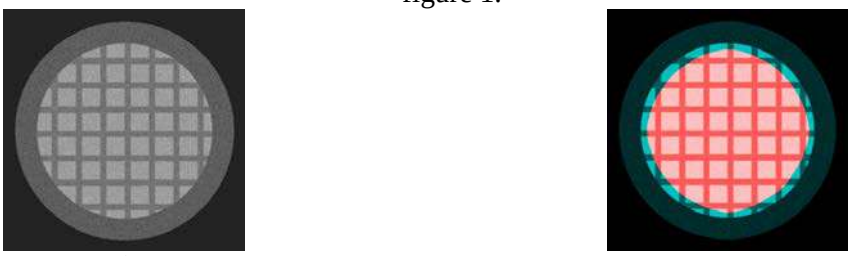

a) b)

Figure 4. Synthetic image of the slice (a) and the result of the area related to the sample selection (b).

Outcomes for real micro-CT images of rocks and granular materials are in good agreement with expert opinion, except regions damaged by X-ray tomography-specific local defects, for example, ring artifacts and intensity distortions due to high-dense inclusions. The existing no-reference image quality metrics can give a relative estimation of the noise level and sharpness for the slices from a single image, but do not consider tomography-specific artifacts. Figure 6 demonstrates a plot with a cross-section of normalized NIQE quality metrics for slices of real micro-CT image.

The processing time of a 4000×4000×2000 voxel 3D image takes less than 6 minutes on a laptop with CPU Intel Core i7 2.6 GHz, 8 Gb RAM, SSD. The use of the proposed algorithm allows reducing the operator's spent time on the selection of a 3D micro-CT image fragment for further modelling and to excludes subjective judgments from this stage.

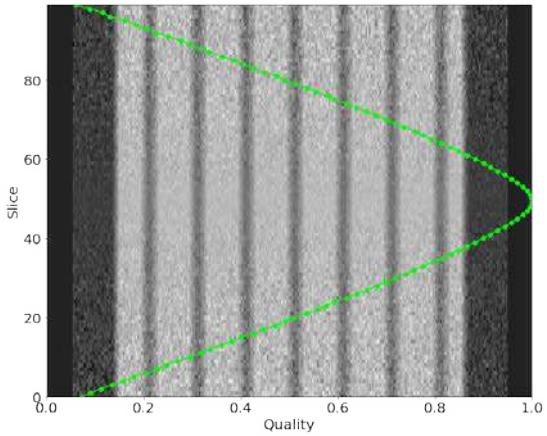

Figure 5. The graph of normalized NIQE quality estimation on the synthetic 3D image slices, where the noise level increases from central slice to top and bottom.

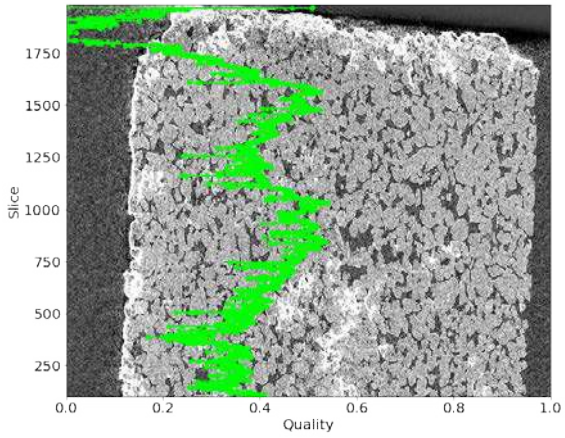

Figure 6. The graph of normalized NIQE metrics for slices of the real 3D image.

4. References

[1] Safonov I, Yakimchuk I and Abashkin V 2018 Algorithms for 3D particles characterization using X-ray microtomography in proppant crush test *J. of Imaging* **4** 134

[2] Koroteev D A, Dinariev O, Evseev N, Klemin D V, Safonov S, Gurpinar O M, Berg S, van Kruijsdijk C, Myers M, Hathon L A, de Jong H and Armstrong R 2013 Application of digital rock technology for chemical EOR screening *Proc. of the SPE Enhanced Oil Recovery Conf.* 165258

[3] Dinariev O and Evseev N 2016 Multiphase flow modeling with density functional method *Computational Geosciences* **20** 835-856

[4] Buzug T M 2008 *Computed Tomography: From Photon Statistics to Modern Cone-Beam CT* (New York: Springer Science & Business Media)

[5] Smelkina N A, Kolsanov A V, Chaplygin S S, Zelter P M and Khramov A G 2017 Pulmonary emphysema recognition by CT scan *Computer Optics* **41(5)** 726-731 DOI: 10.18287/2412-6179-2017-41-5-726-731

[6] Fabijańska A 2011 Variance filter for edge detection and edge-based image segmentation *MEMSTECH*

[7] van Droogenbroeck M and Piérard S 2011 Object descriptors based on a list of rectangles: method and algorithm *Int. Symp. on Mathematical Morphology and Its Applications to Signal and Image Processing*

[8] Moorthy A K and Bovik A C 2010 A two-step framework for constructing blind image quality indices *IEEE Signal processing letters* **17** 513-516

[9] Mittal A, Moorthy A K and Bovik A C 2012 No-reference image quality assessment in the spatial domain *IEEE Transactions on Image Processing* **21** 4695-4708

[10] Mittal A, Soundararajan R and Bovik A C 2013 Making a “completely blind” image quality analyzer *IEEE Signal Processing Letters* **20** 209-212
[11] Liu L, Hua Y, Zhao Q, Huang H and Bovik A C 2016 Blind image quality assessment by relative gradient statistics and adaboosting neural network *Signal Processing: Image Communication* **40** 1-15
[12] Safonov I V, Kurilin I V, Rychagov M N and Tolstaya E V 2018 *Adaptive Image Processing Algorithms for Printing* (Singapore: Springer)
[13] Soille P 2004 *Morphological Image Analysis: Principles and Applications* (New York: Springer Science & Business Media)
[14] Asatryan D G 2017 Image blur estimation using gradient field analysis *Computer Optics* **41(6)** 957-962 DOI: 10.18287/2412-6179-2017-41-6-957-962
[15] Sheikh H R, Sabir M F and Bovik A C 2006 A statistical evaluation of recent full reference image quality assessment algorithms *IEEE Transactions on Image Processing* **15** 3440-3451
[16] Srivastava A, Lee A B, Simoncelli E P and Zhu S C 2003 On advances in statistical modeling of natural images *J. of mathematical imaging and vision* **18** 17-33
[17] Ruderman D L and Bialek W 1994 Statistics of natural images: Scaling in the woods *Advances in neural information processing systems*
[18] Crow F C 1984 Summed-area tables for texture mapping *ACM SIGGRAPH computer graphics* **18** 207-212
[19] Phan T, Sohoni S, Chandler D M and Larson E C 2012 Performance-analysis-based acceleration of image quality assessment *SSIAI* 81-84

Accuracy analysis of 3D object reconstruction using point cloud filtering algorithms

A N Ruchay[1,2], K A Dorofeev[2] and V V Kalschikov[2]

[1]Federal Research Centre of Biological Systems and Agro-technologies of the Russian Academy of Sciences, 9 Yanvarya street, 29, Orenburg, Russia, 460000

[2]Chelyabinsk State University, Bratiev Kashirinykh street 129, Chelyabinsk, Russia, 454001

e-mail: ran@csu.ru, kostuan1989@mail.ru, vkalschikov@gmail.com

Abstract. In this paper, we first analyze the accuracy of 3D object reconstruction using point cloud filtering applied on data from a RGB-D sensor. Point cloud filtering algorithms carry out upsampling for defective point cloud. Various methods of point cloud filtering are tested and compared with respect to the reconstruction accuracy using real data. In order to improve the accuracy of 3D object reconstruction, an efficient method of point cloud filtering is designed. The presented results show an improvement in the accuracy of 3D object reconstruction using the proposed point cloud filtering algorithm.

1. Introduction

The 3D object reconstruction is a popular task in the field of medicine, agriculture, architecture, games, and film industry [1, 2, 3]. Accurate 3D object reconstruction is an important aspect for object recognition, object retrieval, scene understanding, object tracking, virtual maintenance and visualization [4, 5, 6, 7].

RGB-D low-cost sensors such as the Kinect can provide a high-resolution RGB color image with a depth map of the environment [8, 9, 10]. The depth map discontinuity, and a small error around object boundary may lead to significant ringing artifacts in rendered views. Also, the depth map provided by a RGB-D camera is often noisy due to imperfections associated with infrared light reflections, and missing pixels without any depth value appearing as black holes in the maps. Therefore, the point cloud obtained from the depth map inevitably suffers from noise contamination and contains outliers.

The noise and holes can greatly affect to the accurate of 3D reconstruction [11, 12], therefore, noise-reduction and hole-filling enhancement algorithms are intended to serve as a pre-processing step for 3D reconstruction systems using Kinect cameras [13, 14, 15, 16]. To reduce impulsive noise and to fill small holes, the filters [17, 18, 19, 20, 21] are used.

In this paper, we are interested in the design of a filtering algorithm of a poin cloud to improve the quality of the 3D reconstruction. In recent years, a large number of methods contributing to 3D point cloud filtering have been proposed: Normal-based Bilateral Filter [22], Moving Least Square [22], Iterative guidance normal filter [23], Bilateral Filter [24], Density-based Denoising [25], Rolling normal filter [26], Statistical Outlier Removal filter [27], Radius Outlier Removal filter [27], Voxel Grid filter [22], 3D Bilateral filter [28].

In a common approach of noise reduction it is supposed that the raw point cloud contains the ground truth, distorted by artificial noise such as additive [29, 30]. Although this common approach could be used for quantitative comparison (e.g., PSNR, MSE, etc), common methods reduce only artificial noise but not original noise contained in the raw point cloud. In this paper, we consider denoising point cloud algorithms for 3D object reconstruction. We propose a denoising method using a point cloud as the input. We also evaluate the performance of denoising methods on the base of the accuracy of 3D object reconstruction. Actually, RSME errors by ICP algorithm and hausdorf distance [31] between input cloud and filtered cloud are calculated.

General denoising methods are not designed to clean coarse noise contained in the input point cloud. Therefore, our main goal is to evaluate denoising methods in terms of reconstruction accuracy which depends on the quality of the input point cloud.

The paper is organized as follows. Section 2 discusses related denoising point cloud methods. Computer simulation results are provided in Section 3. Finally, Section 4 summarizes our conclusions.

2. Point cloud denoising filters

This section contains information about point cloud denoising filters.

The paper [22] presents a good survey of filtering approaches for 3D point cloud. We compare the following point cloud denoising algorithms in terms of accuracy of 3D object reconstruction: Statistical Outlier Removal filter (SOR) [27], Radius Outlier Removal filter (ROR) [27], Voxel Grid filter (VG) [22], 3D Bilateral filter (3DBF) [28].

2.1. Statistical Outlier Removal filter (SOR)

SOR uses point neighborhood statistics to filter outlier data [27]. Sensor scans typically generate point cloud datasets of varying point densities. Additionally, measurement errors lead to sparse outliers which corrupt the results even more. This complicates the estimation of local point cloud characteristics such as surface normals or curvature changes, leading to erroneous values, which in turn might cause point cloud registration failures. Some of these irregularities can be solved by performing a statistical analysis on each points neighborhood, and trimming those which do not meet a certain criteria. This sparse outlier removal is based on the computation of the distribution of point to neighbors distances in the input dataset. For each point, we compute the mean distance from it to all its neighbors. By assuming that the resulted distribution is Gaussian with a mean and a standard deviation, all points whose mean distances are outside an interval defined by the global distances mean and standard deviation can be considered as outliers and trimmed from the dataset.

2.2. Radius Outlier Removal filter (ROR)

ROR removes outliers if the number of neighbors in a certain search radius is smaller than a given K [27]. We can specifie a number of neighbors which every index must have within a specified radius to remain in the point cloud.

2.3. Voxel Grid filter (VG)

VG filtering method first defines a 3D voxel grid (3D boxes in 3D space) on a point cloud. Then, in each voxel, a point is chosen to approximate all the points that lie on that voxel. Normally, the centroid of these points or the center of this voxel is used as the approximation. The former is slower than the later, while its representative of underlying surface is more accurate. The VG method usually leads to geometric information loss.

2.4. 3D Bilateral filter (3DBF)

3DBF filter denoises a point with respect to its neighbors by considering not only the distance from the neighbors to the point but also the distance along a normal direction [28].

Let us first consider a point cloud M with known normals n_v at each vertex position v. Let $N(v)$ be the 1-ring neighborhood of vertex v (i.e. the set of vertices sharing an edge with v). Then, the filtered position of v is

$$v + \delta v \cdot n_v,$$

where

$$\delta v = \frac{\sum_{p \in N(v)} w_d(\|p - v\|) w_n(|\langle n_v, p - v \rangle|) \langle n_v, p - v \rangle}{\sum_{p \in N(v)} w_d(\|p - v\|) w_n(|\langle n_v, p - v \rangle|)},$$

and w_d and w_n are two decreasing functions. Here vertex v is shifted along its normal toward a weighted average of points that are both close to v in the ambient space and close to the plane passing through v with normal n_v.

3. Experimental results

In this section, we evaluate the performance of the tested denoising methods in terms of reconstruction accuracy which depends on the quality of the input point cloud.

We compare the following point cloud denoising algorithms in terms of the accuracy of 3D object reconstruction and speed: Statistical Outlier Removal filter (SOR) [27], Radius Outlier Removal filter (ROR) [27], Voxel Grid filter (VG) [22], 3D Bilateral filter (3DBF) [28]. SOR, ROR, and VG are available in the Point Cloud Library (PCL). 3DBF was implemented in C++. The experiments are carried out on a PC with Intel(R) Core(TM) i7-4790 CPU @ 3.60 GHz and 16 GB memory.

In our experiments we use the point clouds of a lion and an apollo from dataset [32] and a chair from database [33]. Fig. 1 shows RGB images and depth maps of a lion, an apollo, and a chair.

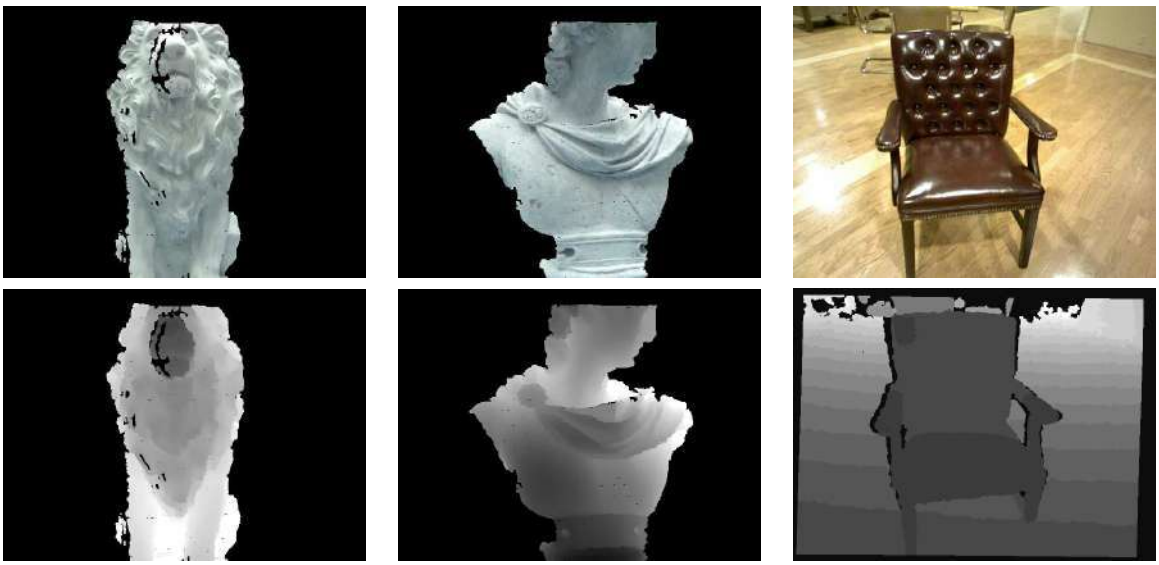

Figure 1. RGB images and depth maps of a lion, an apollo, and a chair are scanned by Kinect sensor.

We construct couples of point clouds for each model using the following steps:

(i) Registration RGB and depth data (Fig. 1).

(ii) Making point clouds (Fig. 2).

(iii) Computing point cloud statistics, such as points count, minimum, maximum and median distance between points in point cloud (Table. 1). Point clouds statistics is required for further calculation of optimum parameters of 3D filters.

(iv) Metric calculation algorithms between couples of frames of point clouds. We calculate transorfmation matrix with standart ICP algorithm and euclidian fitness score (ICP error). Since filtered point cloud can contain different points count of rather initial cloud, we also calculate the hausdorf distance between initial and filtered clouds for estimation of the quality of 3D filtration.

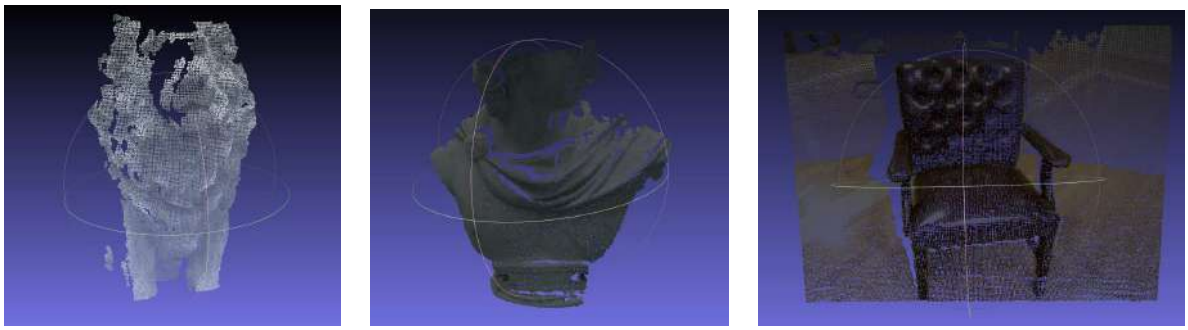

Figure 2. Obtained point clouds of a lion, an apollo, and a chair.

Table 1. Point clouds statistics.

Model	Points count	Min	Max	Median
chair	98593	0.001788	5.962374	0.013808
lion	22603	0.000837	0.670678	0.032839
apolo	30038	0.001030	0.579652	0.010399

Result of calculation and visualization of the hausdorf metric between two frames of chair model shown in Fig. 3.

The metrics between two frames of each model without filtering are presented in Table 2.

Table 2. Calculated metrics between two point clouds of each model without filtering.

Model	ICP error	Hausdorf distance
chair	3.30E-04	0.593978345
lion	6.50E-05	0.078128666
apollo	4.90E-05	0.069139026

The corresponding ICP error and hausdorf distance calculated for chair model with SOR, ROR, VG, 3DBF point cloud denoising algorithms are shown in Table 3. The ROR filter yields the best result in terms of ICP error and hausdorf distance evaluation among all point cloud denoising algorithms. Fig. 4 shows the point clouds of a chair after denoising ROR and SOR filtering.

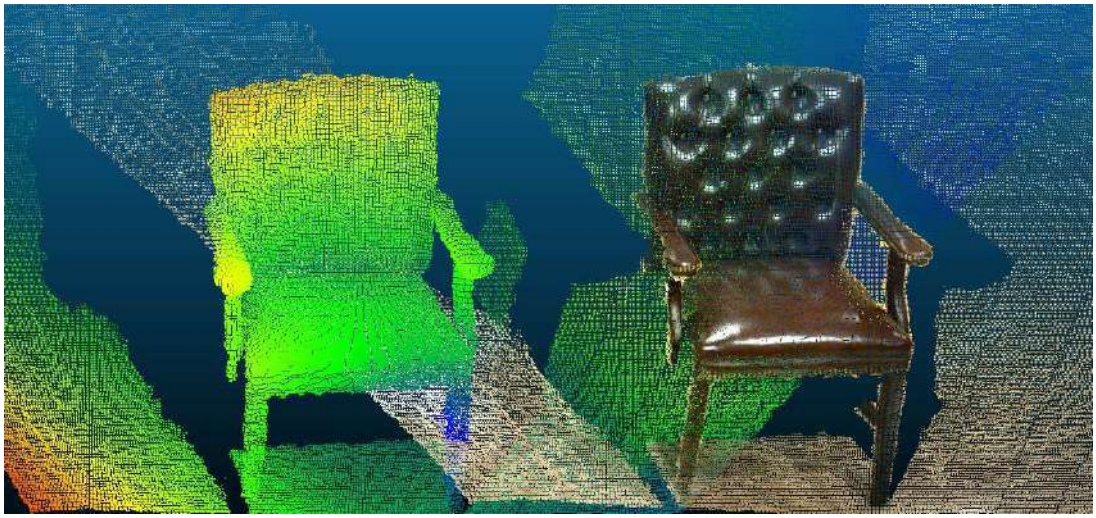

Figure 3. Visualization of hausdorf metric between two point clouds of chair model.

Table 3. Results of measurements using a common ICP algorithm and the hausdorf metric after 3D filtering for chair model.

Filter	Points count	Param1	Param2	ICP error	hausdorf distance
SOR	64405	3	0.11	3.5E-04	0.572
ROR	65448	3	0.007	4.8E-04	0.593
VG	62246	0.009		4.8E-04	0.591
3DBF	87090	0.05	0.001	3.6E-04	0.596

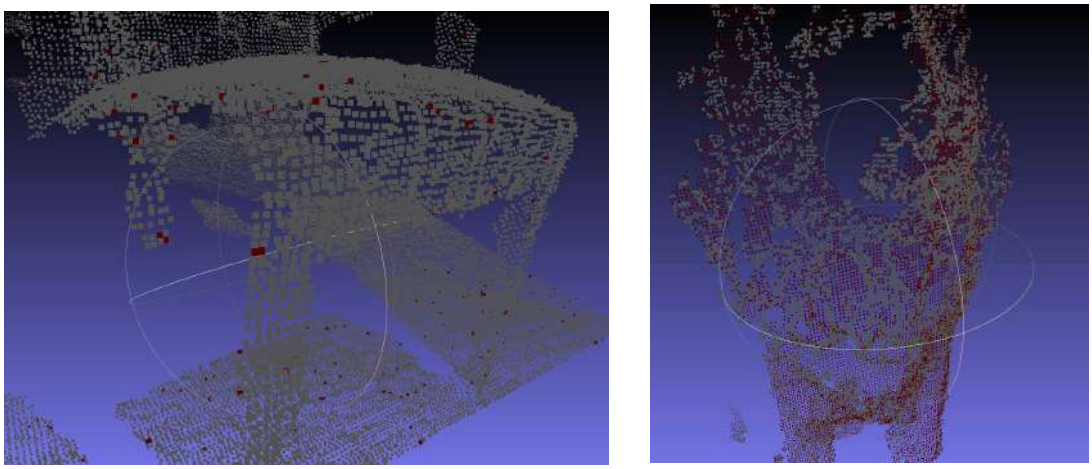

Figure 4. Results of filtering by ROR and SOR filters between two point clouds of chair model.

4. Conclusion

In this paper, we compared various point cloud algorithms in terms of accuracy of 3D object reconstruction using real data from a RGB-D sensor. The experiment has shown that the ROR filter yields the best result in terms of ICP error and hausdorf distance evaluation among all point cloud denoising algorithms.

5. References

[1] Echeagaray-Patron B A, Kober V I, Karnaukhov V N and Kuznetsov V V 2017 *Journal of Communications Technology and Electronics* **62** 648-652
[2] Ruchay A, Dorofeev K and Kober A 2018 *Proc. SPIE* **10752** 1075222-8
[3] Ruchay A, Dorofeev K and Kolpakov V 2018 Fusion of information from multiple Kinect sensors for 3D object reconstruction *Computer Optics* **42(5)** 898-903 DOI: 10.18287/2412-6179-2018-42-5-898-903
[4] Echeagaray-Patron B A and Kober V 2015 *Proc. SPIE* **9598** 95980V-8
[5] Echeagaray-Patron B A and Kober V 2016 *Proc. SPIE* **9971** 9971-6
[6] Ruchay A, Dorofeev K and Kober A 2018 *CEUR Workshop Proceedings* **2210** 82-88
[7] Ruchay A, Dorofeev K and Kober A 2018 *CEUR Workshop Proceedings* **2210** 300-308
[8] Tihonkih D, Makovetskii A and Kuznetsov V 2016 *Proc. SPIE* **9971** 99712D-8
[9] Nikolaev D, Tihonkih D, Makovetskii A and Voronin S 2017 *Proc. SPIE* **10396** 10396-8
[10] Gonzalez-Fraga J A, Kober V, Diaz-Ramirez V H, Gutierrez E and Alvarez-Xochihua O 2017 *Proc. SPIE* **10396** 10396-7
[11] Makovetskii A, Voronin S and Kober V 2018 *Proceedings of SPIE - The International Society for Optical Engineering* **10752** 107522V
[12] Voronin S, Makovetskii A, Voronin A and Diaz-Escobar J 2018 P*roceedings of SPIE - The International Society for Optical Engineering* **10752** 107522S
[13] Makovetskii A, Voronin S and Kober V 2017 *Analysis of Images, Social Networks and Texts* (Cham: Springer International Publishing) 326-337
[14] Tihonkih D, Makovetskii A and Voronin A 2017 *Proc. SPIE* 10396 10396-7
[15] Ruchay A, Dorofeev K, Kober A, Kolpakov V and Kalschikov V 2018 *Proc. SPIE* **10752** 1075221-10
[16] Ruchay A, Dorofeev K and Kober A 2018 *Proc. SPIE* **10752** 1075223-8
[17] Ruchay A and Kober V 2016 *Proc. SPIE* **9971** 99712Y-10
[18] Ruchay A and Kober V 2017 *Proc. SPIE* **10396** 1039626-10
[19] Ruchay A and Kober V 2017 **Proc. SPIE** *10396* 1039627-9
[20] Ruchay A and Kober V 2018 *Analysis of Images, Social Networks and Texts* (Cham: Springer International Publishing) 280-291
[21] Ruchay A, Kober A, Kolpakov V and Makovetskaya T 2018 *Proc. SPIE* **10752** 1075224-12
[22] Han X F, Jin J S, Wang M J, Jiang W, Gao L and Xiao L 2017 *Signal Processing: Image Communication* **57** 103-112
[23] Han X F, Jin J S, Wang M J and Jiang W 2018 *Multimedia Tools and Applications* **77** 16887-16902
[24] Paris S, Kornprobst P and Tumblin J 2009 *Bilateral Filtering* (Hanover, MA, USA: Now Publishers Inc.)
[25] Zaman F,Wong Y P and Ng B Y 2017 *9th International Conference on Robotic, Vision, Signal Processing and Power Applications* (Singapore: Springer Singapore) 287-295
[26] Zheng Y, Li G, Xu X, Wu S and Nie Y 2018 *Computer Aided Geometric Design* **62** 16-28
[27] Rusu R B and Cousins S 2011 *IEEE International Conference on Robotics and Automation* 1-4
[28] Digne J and de Franchis C 2017 *Image Processing On Line* **7** 278-287
[29] Boubou S, Narikiyo T and Kawanishi M 2017 3*DTV Conference: The True Vision - Capture, Transmission and Display of 3D Video (3DTV-CON)* 1-4
[30] Chen R, Liu X, Zhai D and Zhao D 2018 *Digital TV and Wireless Multimedia Communication* (Springer Singapore) 128-137
[31] Alexiou E and Ebrahimi T 2017 *Ninth International Conference on Quality of Multimedia Experience (QoMEX)* 1-3
[32] Lee K and Nguyen T Q 2016 *Mach. Vis. Appl.* **27** 377-385
[33] Choi S, Zhou Q, Miller S and Koltun V 2016 *CoRR* ArXiv: abs/1602.02481

Acknowledgments
This work was supported by the Russian Science Foundation, grant no. 17-76-20045.

Early diagnosis of a developing biosystem using acousto-optic imaging

A B Burlakov[1], A S Machikhin[2], D D Khokhlov[2], V I Kuzmin[3], A F Gadzaov[3], D L Tytik[4], S A Busev[4], V E Kasatkin[4] and L A Sleptsova[1]

[1]Lomonosov Moscow State University, Leninskie Gory, 1, Moscow, Russia, 119991
[2]Scientific and Technological Center of Unique Instrumentation RAS, Butlerova street, 15, Moscow, Russia, 117342
[3]Russian Technological University (MIREA), Vernadsky Avenue, 78, Moscow, Russia, 119454
[4]Frumkin Institute of Physical Chemistry and Electrochemistry RAS, Leninsky Avenue, 31, Moscow, Russia, 119071

e-mail: aalexanderr@mail.ru, demid06101993@gmail.com

Abstract. Studying the embryo development at an early stage is considered. For this, hyperspectral imaging using an acousto-optical microscope-based system is proposed. Acousto-optic visualization of the early developmental stages of the loach Misgurnus fossilis embryo showed a regular change in the spectral characteristics of different image areas corresponding to the tissues and body fluids, depending on the functional state of the embryo. We show that there is a discrete set of maxima in the optical absorption spectrum with a distance of 20 nm and 30 nm between them. Value 20 nm corresponds to the normal development of biological tissue. The appearance of the value 30 nm between the maxima of neighboring optical absorption bands indicates the development of pathological processes in the biosystem. Such deviations from the norm are characteristic of germinal tissues, and they are absent in the perivitelline fluid. Thus, we demonstrated that for the early diagnosis of the physiological state of a developing biosystem, special attention should be paid to optical absorption spectra.

1. Introduction

At present, numerous studies are devoted to the fundamental mechanisms of developmental biology, since changes occurring during lifetime from the moment of fertilization of an ovum to an adult multicellular organism cause many questions related to the formation of a complex multi-level system that is constantly becoming more complex [1-3].

The use of the embryonic model for the research is very promising, since it provides a possibility to analyze the functional features of the various embryogenesis stages, including the initial ones, when within a short period of time many processes that determine the subsequent vital activity of organisms (active cell division, differentiation, morphogenesis) occur. Even the smallest impact in the early development stages may entail the appearance of various delayed effects. In addition, embryonic models have unique advantages for studying the preservation of the completeness of genetic information, which can only be found in early ontogenesis, since many of the most important genes for

population conservation are expressed during this period, and a change in the regulatory mechanisms of gene expression occurs in the initial period of embryogenesis [4,5].

To study these processes, non-invasive methods that allow not to interfere the vital activity of a living biological system are needed. Spectral imaging is one of such methods [6,7]. It allows quantitative characterizing the spatial distribution of spectral properties. In this research, we demonstrate the effectiveness of this technique for early diagnosis of the developing biosystem. For this purpose, we have assembled an experimental setup based on acousto-optic (AO) imaging add-on module installed on a microscope. We measured and analysed the optical absorption spectra of different areas corresponding to fluids and tissues of the loach embryo and showed that this method may be effectively used to define the state of a developing biosystem.

2. Experimental setup

Different approaches and instrumentation are used to obtain spectral images, but the method based on tunable optical filters is most versatile. In comparison to other filters, AO tunable filters (AOTFs) provide a unique combination of features: arbitrary spectral access, high throughput, and the ability of modulating the transmission function, rather high spectral and spatial resolution, small tuning time, while being programmable and totally PC-controlled devices with no need of mechanical adjustment. AOTF is based on anisotropic Bragg diffraction of wideband optical radiation on the ultrasound wave [8]. The central wavelength λ of the filter transmission band is defined by the period of ultrasound wave which is driven by a radio-frequency signal and can be controlled electronically.

Fig. 1 shows an imaging system used for the research. The illumination from the light source is collected by the Koehler illumination system. After passing through the specimen, the light is collected by the objective lens, which forms the image of the specimen in the infinity. After passing the tube lens, the light is divided into two paths by means of a beam-splitting prism. One path leads to the binocular tubes, in which the eyepieces 2 are located. Their front focal planes coincide with the back focal plane of the tube lens. Consequently, the eyepieces 2 form the infinity-located image of the specimen for convenient visual inspection. The other path is intended for digital image acquisition. The tube lens translates the image directly onto the recording plane of color camera 3.

Figure 1. Microscope-based AO spectral imager. 1 – AO spectral imaging unit, 2 – eyepieces for visual observation, 3 – color camera for wideband image registration.

The AOTF-based add-on module 1 is inserted between the microscope body and the trinocular head. It consists of a beam-splitter, an optical coupling system, the AOTF, an imaging objective and a monochrome camera [9]. The device is designed to allow simultaneous visual observation of the

specimen, color image registration and acquisition of spectral image series necessary for the measurement of the absorption spectra distribution.

Strong chromatic drift and spatial aberrations of the filtered image caused by diffraction light by ultrasound can reach several percent of the field of view and make it impossible to obtain accurate spectral measurements using AOTF images. To overcome this problem we to use the tandem AOTF [10].

For precise measurement of the spectral dependence $I(\lambda)$ in any image point x,y, it is necessary to provide repeatable values of the wavelength λ, intensity I and coordinates x,y. That is why, generally spectral imager should have a spectral, amplitude and spatial calibrations, correspondingly [11]. In our case, the specimen may slightly move during a longtime experiments, which leads to the necessity of additional motion correction (Fig. 2).

Spectral calibration is provided using a certified diffraction spectrometer by accurate measurement of the dependence of the selected wavelength λ on the frequency f applied to AOTF piezotransducer. To compensate optics vignetting and illumination non-uniformity, a series of background spectral images $B(x,y;\lambda)$ is acquired. After background correction, correlation techniques are applied to the areas of interest in order to find its offsets $\Delta x(\lambda)$ and $\Delta y(\lambda)$ during the experiment. Only after all these three types of correction are done, the corrected images $I(x,y;\lambda)$ are used for the spectral measurements.

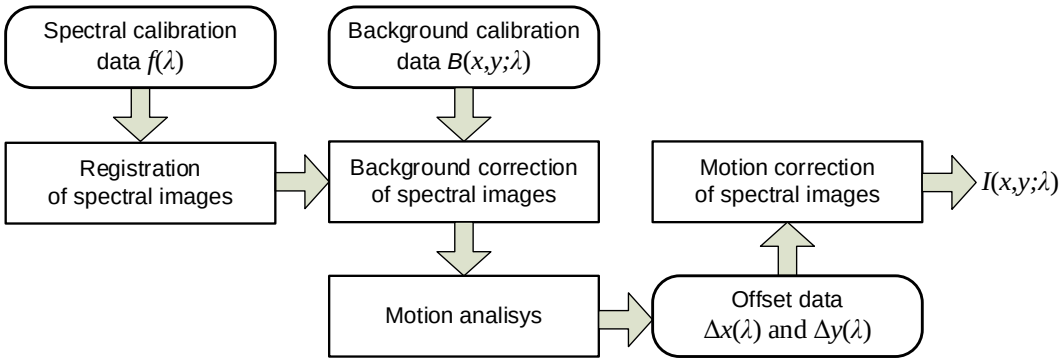

Figure 2. Main stages of image processing.

The experiments were carried with the embryo of the loach Misgurnus fossilis which is considered to be a classical object of developmental biology. Females caught from nature inhabitant were kept in a refrigerator at 4-5°C. Accelerated maturation of females was performed by hormonal stimulation of chorionic gonadotropin at room temperature, the artificial insemination was performed according to the standard method [12]. The fertilized eggs were thoroughly washed with two portions of fresh water. After that some of the embryos (50 pcs) were placed in an isolated storage with a stabilized temperature of 17°C. Development stages were determined according to the tables of normal development of the loach [13,14]. The embryo of a certain developmental stage was thoroughly washed with two portions of fresh water and placed in the object plane of a microscopic spectral imager. Spectral image series of the developing embryo were registered twice a minute for approximately an hour.

3. Results and discussion

Fig. 3 shows one of the spectral images of the loach embryo at 33rd development stage obtained after the correction procedure. The areas used for spectral analysis are highlighted in red. These regions represent different parts of embryo (myotomes, different parts of yolk and perivitelline space).

Fig. 4 summarizes the spectral distributions obtained in different regions of loach embryo. The first feature in the optical absorption spectra for different regions (maxima or their absence) is in the wavelength region nearby 477 nm. Light at this wavelength plays an important role in many physiological processes occurring in all living organisms [15]. For head section (eye area) and yolk in the area of the head section, there is a sharp drop in optical density up to 485 nm. In this case, in different areas of the perivitelline space, a significant increase in the optical density is observed with a

maximum at 477 nm, followed by a sharp drop in optical absorption to the minimum, at 485 nm. We note that in the region of differentiating myotomes, the optical density in this region of wavelengths does not change. A characteristic feature for all spectra is the greatest change in optical density in the wavelength range from 450 to 590 nm. In the wavelength range of 590–720 nm, insignificant changes in the optical density are observed for all selected regions of the loach embryo.

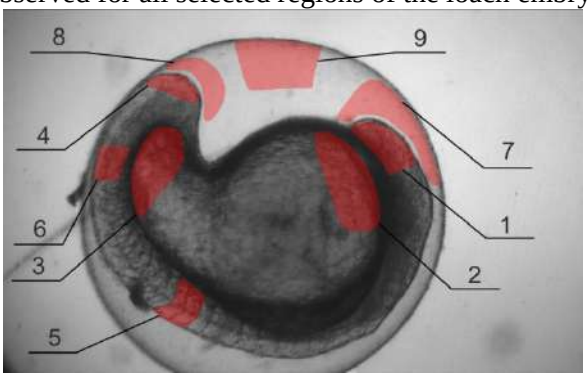

Figure 3. Spectral image of the loach embryo at 33rd stage of development (λ = 635 nm).
1 – head section (eye area); 2 – yolk near the head; 3 – yolk near the tail; 4 – tail section;
5 – differentiated myotomes; 6 – differentiating myotomes; 7 – perivitelline space near the head;
8 – perivitelline space near the tail; 9 – perivitelline space.

More detailed analysis of the spectral features for different regions of the loach embryo emphasizes the simultaneous growth of optical density at a wavelength of 500 nm for all regions of the embryo. In the wavelength region of 580–620 nm, the spectra can be divided into two groups: with a slight change in optical density (perivitelline space and tail region in the tail part of the embryo) and spectra with well-defined maxima (other tissues shown in figures 2 and 4). In the spectral range from 640 to 670 nm, it is possible to conclude about peculiar resonance rearrangements in the tissues of the embryo by the spectra appearance. In the wavelength range 670-720 nm, the spectra are naturally divided into two groups according to the criterion for the presence of a local maximum in the spectrum.

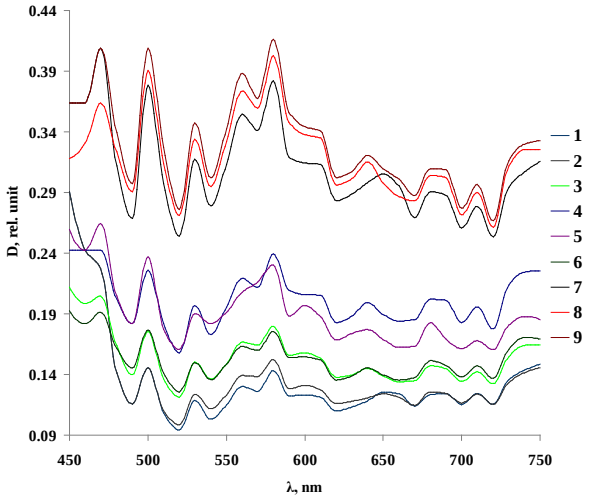

Figure 4. Optical density spectral distributions for different regions.
Curve numbers correspond to the region numbers in Fig. 3.

For each spectrum, a pattern was found in the location of the maximum values of the optical absorption intensity in different regions of the embryo, determined by a discrete set of uniform intervals (the distance between adjacent maxima), among which the values of 20 nm and 30 nm dominate. The intervals of 20 nm correspond to regular sequences of uniform strokes known for the scale of characteristic dominant sizes in natural environments [13,14], while the presence of an interval of 30 nm is associated with the pathological development of a biosystem. Thus, the spectral

measurements have a clear biophysical interpretation. Further applying advanced techniques for spectral image processing may allow to extract much more morphological data [16,17].

4. Conclusion

Our analysis shows that spectral imaging of a developing biosystem is an informative and promising technique. It allows contrast visualisation as well as absorption spectrum measurements in each image pixel. The biggest fluctuations in optical density are observed in the areas of perivitelline space (glycoprotein solution). For the image areas corresponding to the loach embryo tissues (tail section, differentiating myotomes and yolk in the area of the tail section), a stable change in optical density is observed. It is known that the yolk in the tail section is actively consumed for the embryo energy needs and the yolk in the region of the head section is preserved until the late development stages. The difference in spectral characteristics for these areas of the yolk qualitatively confirms its utilization. Thus, the use of an AO spectral imager provides a fast and precise estimation of living system properties as well as a unique opportunity to analyse 61the dynamics of the biochemical processes in a developing embryo by means of processing the time changes of absorption spectra.

5. References

[1] Gilbert S 2000 *Developmental Biology* (Sunderland (MA): Sinauer Associates Inc.)
[2] Cooper G M and Hausman R E 2007 *The Cell: A Molecular Approach* (Sunderland (MA): Sinauer Associates Inc.)
[3] Heams T, Huneman P, Lecointre L and Silberstein M 2015 *Handbook of Evolutionary Thinking in the Sciences* (Berlin: Springer) 265-283
[4] Zhiyuan G and Korzsh V 2006 *Fish Development and Genetics: The Zebrafish and Medaka Models* (Singapore: World Scientific Pub Co Inc.)
[5] Kimmel C B, Ballard W W, Kimmel S R, Ullmann B and Schilling T F 1995 Stages of embryonic development of the zebrafish *Developmental dynamics* **203** 253-310
[6] Li Q, He X, Wang Y, Liu H, Xu D and Guo F 2013 Review of spectral imaging technology in biomedical engineering: achievements and challenges *J. Biomed. Opt.* **18(10)** 100901
[7] Zimmermann T, Rietdorf J and Pepperkok R 2003 Spectral imaging and its applications in live cell microscopy *FEBS Letters* **546(1)** 87-92
[8] Goutzoulis A P and Rape D R 2004 *Design and Fabrication of Acousto-Optic Devices* (Boca Raton: CRC Press)
[9] Polschikova O, Machikhin A, Batshev V, Ramazanova A, Belov A and Pozhar V 2017 AOTF based optical system of a microscope module for multispectral imaging techniques *Proc. SPIE* **10592** 105920H
[10] Machikhin A, Batshev V and Pozhar V 2017 Aberration analysis of AOTF-based spectral imaging systems *J. Opt. Soc. Am.* A **34(7)** 1109-1113
[11] Podlipnov V and Skidanov R 2017 Calibration of an imaging hyperspectrometer *Computer Optics* **41(6)** 869-874 DOI: 10.18287/2412-6179-2017-41-6-869-874
[12] Kostomarova A A 1975 *Objects of developmental biology* (Moscow: Nauka) 309-323
[13] Jirmunsky A V and Kuzmin V I 1990 *Critical levels in the development of natural systems* (Leningrad: Nauka)
[14] Fujimoto T, Kataoka T, Sakao S, Saito T, Yamaha E and Arai K 2006 Developmental stages and germ cell lineage of the loach (Misgurnus anguillicaudatus) *Zoological Science* **23(11)** 977-989
[15] Villamizar N, Vera L M, Foulkes N S and Sánchez-Vázquez F J 2014 Effect of lighting conditions on zebrafish growth and development *Zebrafish* **11(2)** 173-181
[16] Myasnikov E 2017 Hyperspectral image segmentation using dimensionality reduction and classical segmentation approaches *Computer Optics* **41(4)** 564-572 DOI: 10.18287/2412-6179-2017-41-4-564-572
[17] Brianskiy S and Vizilter Y 2018 Morphological conditional estimates of image complexity and information content *Computer Optics* **42(3)** 501-509 DOI: 10.18287/2412-6179-2018-42-3-501-509

Neural network technology to search for targets in remote sensing images of the Earth

N S Abramov[1], A A Talalayev[1], V P Fralenko[1], O G Shishkin[1] and V M Khachumov[1,2]

[1]Aylamazyan Program Systems Institute of Russian Academy of Sciences, Peter the First Street, 4 "a", Veskovo Village, Yaroslavl Region, Russia
[2]The Peoples' Friendship University of Russia, Miklukho-Maklaya Street, 6, Moscow, Russia

e-mail: shishkinog@mail.ru, nikolay.s.abramov@gmail.com

Abstract. The paper introduces how multi-class and single-class problems of searching and classifying target objects in remote sensing images of the Earth are solved. To improve the recognition efficiency, the preparation tools for training samples, optimal configuration and use of deep learning neural networks using high-performance computing technologies have been developed. Two types of CNN were used to process ERS images: a convolutional neural network from the nnForge library and a network of the Darknet type. A comparative analysis of the results is obtained. The research showed that the capabilities of convolutional neural networks allow solving simultaneously the problems of searching (localizing) and recognizing objects in ERS images with high accuracy and completeness.

1. Introduction

Today, there is an upsurge of activity in the field of Earth remote sensing (ERS) data processing: new software systems are being created, high-resolution image processing methods are being modernized. The current situation is characterized by the improvement of the equipment of spacecraft (SC) and ground control stations, the expansion of the functionality and spectrum of the image processing tasks performed. The scope of application of these spacecraft includes monitoring of forest, agricultural and arctic zones, analysis of natural disasters, environmental protection, public safety, etc. The growing volumes of evolving ERS data have significantly increased the requirements for speed and quality of information processing. Recently, artificial neural networks (ANN) and high-performance computing technologies have been increasingly used.

The analysis of modern work on the application of ANN has shown that neural networks are mainly used for searching and recognizing targets that are related to the category of nonrigid [1,2]. The authors of this paper created a scientific and practical groundwork in solving various problems based on intelligent processing of ERS images (multispectral, panchromatic, color) search for rigid objects and zones of interest using the developed spectrographic approach and the generalized metric (fires, inundations, ice conditions assessment, etc.) [3-8]. The proposed paper presents the results of new in-depth studies related to the use of modern convolutional neural networks (CNN) for processing panoramic full-color ERS images obtained from unmanned aerial vehicles (UAVs); some methods and

tools to improve their efficiency and performance during the search and recognition of the objects of military equipment with the necessary completeness and accuracy, which still remains unresolved even with an abundance of software, are proposed. The modern formulation of the task of finding and recognizing an object by a neural network includes the steps of selecting the type, setting the parameters of the ANN and preparing the input data. The multi-class and single-class problems were considered as part of the study. The first task is thought of as the search and recognition of objects of several classes simultaneously. The second task involves the search by a neural network of objects of a single class.

2. Methods, software tools and results of image processing using ANN

Two types of CNN were used to process ERS images: a convolutional neural network from the nnForge library [9] and a network of the Darknet type [10]. Both implementations are distinguished by the support of various types of layers; therewith a flexible configuration is provided and it is possible to change the structure to suit own needs. In addition, the network of the second type not only classifies the target objects but also reports on their positions in the shot. A distinctive feature of the considered CNN is the support of computational speedup using graphics processing units (GPU) both during training and operation. Copies of trained ANN are distributed between the existing GPUs where data are processed independently and asynchronously. A special software complex for designing neural network application systems was used to implement the computational process [11, 12].

A special tool for the automated preparation of training samples has been implemented to improve the quality of the classification. A human expert prepares preliminarily some images with a transparency marker set, where background pixels are set invisible using alpha channel controls. Figure 1 shows the original fragment of the ERS image, on the right: the same fragment is shown after the alpha channel change. For convenience, images with objects of different classes are sorted to different directories.

Figure 1. Images: original and with the alpha channel mask.

Various settings of the ANN from the nnForge library (configurations and characteristics of the layers) can be customized with scaled copies of these images. The scaling factor is chosen so that each target object is placed in a separate scanning window, the size of which coincides with the size of the input ANN window. The experiments were conducted on military equipment images of 6000x4000 pixels, made from a height of 300 meters at the Russia Arms Expo – 2015 (RAE-2015) international exhibition.

The following CNN architecture from the nnForge library was experimentally chosen:

– contrast extraction layer with a 9x9 pixel Gaussian window [13]; the original size of the data window: 39x39;

– convolution layer with the 6x6 feature maps (total 136 maps), the hyperbolic tangent module is used for normalization, the window size after processing is 34x34;

– average subsampling layer with a 2x2 mask, the window size after processing is 17x17;

– convolution layer with the 6x6 feature maps (total 272 maps), the window size after processing is 12x12;

– average subsampling layer with a 2x2 mask, the window size after processing is 6x6;

– convolution layer with the 6x6 feature maps (total 544 maps), the window size after processing is 1x1;

– dropout layer with an adjustable probability of disabling connections between neurons (experimentally set to 0.05);

– convolution layer with the 1x1 feature maps, the number of feature maps corresponds to the number of distinguished classes, the hyperbolic tangent type activation function is used.

The scanning window during the recognition moves through the image in increments of one pixel and is processed by the neural network. The sequential processing of the entire image results in a colored map where the target objects are separated from the background. Figure 2 shows an example of the original image and the result of its processing.

Figure 2. The original image and the result of its processing.

3.626 million objects automatically extracted from 73 images were used for training. The following results have been achieved: Classification completeness: background – 0.9976, materiel – 0.9354. Classification accuracy: background – 0.9392, materiel – 0.9974. Training time: 24 hours on one Nvidia Geforce GTX 1060 and using a single CPU core Intel Core i7 6850K (of the existing 6 cores, 3.6 @ 4.0 GHz). Processing time of ten panoramic images on one GPU: 3051 s; on two GPUs: 1640 s.

As a result of numerous experiments, the developers of the Darknet network have selected a very successful architecture, such that it works on different training / test samples [14, 15]. The network, within certain limits, is resistant to the fact that images of different sizes and subjected to geometric distortions can be input. The main adjustable parameter is the size of the CNN input layer.

The software tool developed as part of this study includes the programs YOLORotate, YOLOAnchors and YOLOGetObjects.

The YOLORotate program is designed to convert images into a format suitable for training the YOLO v2 type ANNs. The data needed for the preparation of a series of our experiments include many panoramic images taken from the UAV. They have four classes of target objects: IFV (infantry fighting vehicles), Military vehicles, SPG (self-propelled gun mounts) and Tanks; information about the coordinates and sizes of each of the objects is pre-assembled and stored in text files. Each such image has a size of not less than 832x832 pixels, where all target objects occupy a relatively small part of the image. YOLORotate rotates images from a training sample with a given step, for example, 15 degrees. At the same time, the maximum possible number of fragment images with target objects is cut out. A total of 4361 fragments for the training sample and 1173 fragments for the test sample were automatically created. It is guaranteed that on each such fragment there is at least one target object. In

order to ensure that the target objects are located in random positions of the received fragment images, a pseudorandom number generator is used. The analysis showed that with the selected size of the source data of 832x832 pixels, up to 20 targets fall into the frame. The YOLOAnchors program uses the k-means method [16] to detect the width and height of typical targets on the output window of a neural network. The program finds several such pairs of sizes, which are used later in the training of the ANN.

The program YOLOGetObjects segments the images into fragments of 832x832 pixels while providing a partial intersection, and each next window captures a quarter of the previous one (both horizontally and vertically). In total, there are 70 fragments per panoramic picture. Further, all fragments are independently processed using a GPU and a general-purpose processor. The next step is to combine information about all the target objects found. Figure 3 shows an example of the result of using a trained ANN.

Figure 3. The result of shot processing by a multi-class ANN.

Table 1. ANN test results with an input window of 416x416 pixels.

		6 images per pack	14 images per pack
Share of target objects found	IFV	0.9346	0.9731
	Military cars	0.9880	0.9983
	SPG	1.0000	1.0000
	Tanks	0.9967	0.9934
Average share of target objects found		0.9798	0.9912
Completeness	IFV	0.7500	0.6885
	Military cars	0.9811	0.9949
	SPG	0.9006	0.9655
	Tanks	0.9058	0.9107
Normalized accuracy	IFV	0.9118	0.8947
	Military cars	0.8627	0.9541
	SPG	0.9990	1.0000
	Tanks	0.8561	0.7672
F1-measure	IFV	0.8230	0.7782
	Military cars	0.9181	0.9741
	SPG	0.9473	0.9825
	Tanks	0.8802	0.8328
Average *F1*-measure		0.8922	0.8919
The ratio of the number of found targets to their total number		0.9869	0.9948
Training time, hours		1.18	2.44
6000x4000 pixels image processing time, seconds		2.13	

Table 2. ANN test results with an input window of 832x832 pixels.

		6 images per pack	14 images per pack
Share of target objects found	IFV	0.9615	0.9538
	Military cars	0.9983	0.9974
	SPG	1.0000	1.0000
	Tanks	0.9967	0.9934
Average share of target objects found		0.9891	0.9862
Completeness	IFV	0.5846	0.6077
	Military cars	0.9657	0.9657
	SPG	0.9290	0.9432
	Tanks	0.9421	0.9322
Normalized accuracy	IFV	0.8630	0.9004
	Military cars	0.9462	0.9160
	SPG	0.9927	0.9724
	Tanks	0.7123	0.7484
F1-measure	IFV	0.6970	0.7256
	Military cars	0.9558	0.9402
	SPG	0.9598	0.9576
	Tanks	0.8113	0.8303
Average *F1*-measure		0.8560	0.8634
The ratio of the number of found targets to their total number		0.9945	0.9925
Training time, hours		4.78	11.11
6000x4000 pixels image processing time, seconds		5.50	

Table 3. ANN test results with an input window of 416x416 pixels and increased number of feature maps.

		6 images per pack	14 images per pack
Share of target objects found	IFV	0.9615	0.9500
	Military cars	1.0000	0.9983
	SPG	1.0000	1.0000
	Tanks	0.9934	0.9983
Average share of target objects found		0.9887	0.9867
Completeness	IFV	0.7846	0.7538
	Military cars	0.9923	0.9966
	SPG	0.9432	0.9473
	Tanks	0.9223	0.9438
Normalized accuracy	IFV	0.8970	0.9230
	Military cars	0.9421	0.9166
	SPG	1.0000	1.0000
	Tanks	0.8510	0.8616
F1-measure	IFV	0.8371	0.8299
	Military cars	0.9665	0.9549
	SPG	0.9708	0.9729
	Tanks	0.8852	0.9008
Average *F1*-measure		0.9149	0.9146
The ratio of the number of found targets to their total number		0.9945	0.9937
Training time, hours		4.69	10.37
6000x4000 pixels image processing time, seconds		3.98	

The batch training where the next step of adjusting the weighting factors is based on information about the results of processing a limited group of images of the training sample was used in all experiments. Each group of images on the new training period is formed randomly; preference is given to the groups with representatives of all classes of target objects. Using batch training allows improve the quality of the neural network and abandon the resource-intensive dropout layer [17]. The best package size is chosen experimentally for each problem to be solved.

Tables 1-3 show the refinement characteristics and the results of the experiments performed in solving a multi-class problem — simultaneous search and recognition of objects of four classes.

Table 4 shows the comparative results of processing the test sample when solving single-class and multi-class problems. The training time of the selected network configuration on each of the four classes of military equipment was 6.84, 13.6 and 26.8 hours when working with groups of 28, 56 and 112 images. In the single-class case, the ANN works with only one class; the user has the opportunity to choose the best option – the network trained using a group of images of the optimal size. In the last column of table 4, the best coefficients for mixed mode are collected, when a network trained for individual classes is used. For instance, a network trained on a package of 56 images is used for IFV, and for the Tanks class – a network trained on a package of 112 images. The average processing time of a 6000x4000 pixels image in one separate single-class neural network is the same as that of a multi-class neural network, that is, four seconds.

Table 4. Experimental data, multi-class and single-class problems.

Class of objects	Share of founded objects and the size of the group of images					
	Multi -class problem		Single-class problem			
	6	14	28	56	112	/
IFV	0.9615	0.9500	0.8577	0.9115	0.8538	0.9115
Military cars	1.0000	0.9983	0.9057	0.8885	0.8954	0.9057
SPG	1.0000	1.0000	0.8276	0.9635	0.9473	0.9635
Tanks	0.9934	0.9983	0.9174	0.9455	0.9521	0.9521
Average share of target objects found	0.9887	0.9867	0.8771	0.9273	0.9121	0.9332
Training time of one separate neural network, hours	4.69	10.37	6.84	13.6	26.8	–

The results of the experiments confirmed the effectiveness of the use of single-class neural networks. However, training a complex of such networks requires more computing resources than those used for training of one multi-class network. An increase in the complexity of the task with the same number of feature maps leads to a decrease in the average share of the found target objects for a single-class ANN.

3. Conclusion

The article presents the results of research related to the use of modern convolutional neural networks for processing panoramic full-color aerial ERS images. Using the nnForge and Darknet CNN, multi-class and single-class problems of searching and classifying targets are solved. Some methods for preparing training samples, optimal configuration, and the use of high-performance computing have been developed to improve the recognition efficiency. A comparative analysis showed that the one-class approach has an advantage in recognition quality but loses in operation time. In general, it should be noted that the capabilities of convolutional neural networks allow solving simultaneously the problems of searching (localizing) and recognizing objects in ERS images with high accuracy and completeness.

4. References

[1] Vizilter Yu V, Gorbatsevich V S, Vorotnikov A V and Kostromov N A 2017 Real-time face identification via CNN and boosted hashing forest *Computer Optics* **41(2)** 254-265 DOI: 10.18287/2412-6179-2017-41-2-254-265
[2] Ivanov A I, Lozhnikov P S and Sulavko A E 2017 Evaluation of signature verification reliability based on artificial neural networks, Bayesian multivariate functional and quadratic forms *Computer Optics* **41(5)** 765-774 DOI: 10.18287/2412-6179-2017-41-5-765-774
[3] Fralenko V P 2010 Spectrographic texture analysis for earth remote sensing data *Artificial Intelligence and Decision Making* **2** 11-15
[4] Fralenko V P 2018 Intelligent analysis of aerospace images using high-performance computing devices *Proceedings of the conference "Artificial Intelligence: Problems and Solutions"* (Moscow region, Patriot Park)
[5] Abramov N S, Agronik A Yu, Emelyanova Yu G, Latyshev A V, Talalaev A A, Fralenko V P and Khachumov M V 2017 Methods, models and software for processing data for space monitoring of the Arctic zone *Aerospace Instrument-Making* **7** 38-51
[6] Fralenko V P 2017 Localization and classification of military equipment in the stream of images from UAVs *Materials of the conference "Fundamental Science for Army" within of the Third International Military-Technical Forum "ARMY-2017"* (Moscow region, Patriot Park)
[7] URL: https://www.science-education.ru/ru/article/view?id=18607
[8] Khachumov V M, Fralenko V P, Chen Guo Xian and Zhang Guo Liang 2015 Construction perspectives of the remote sensing data high-performance processing system *Program Systems: Theory and Applications* **1** 121-133
[9] URL: http://milakov.github.io/nnForge
[10] URL: https://arxiv.org/abs/1612.08242
[11] Talalaev A A and Fralenko V P 2013 The complex of tools for the design of neural network application systems *Scientific and Technical Volga region Bulletin* **4** 237-243
[12] Talalaev A A and Fralenko V P 2013 The architecture of a parallel-pipeline data processing complex for heterogeneous computing environment *Bulletin of Peoples' Friendship University of Russia. Mathematics series. Computer science. Physics* **3** 113-117
[13] URL: https://journals.plos.org/ploscompbiol/article?id=10.1371/journal.pcbi.0040027
[14] Everingham M, Van Gool L, Williams C K, Winn J and Zisserman A 2010 The pascal visual object classes (voc) challenge *International journal of computer vision* **88** 303-338
[15] Lin T-Y, Maire M, Belongie S, Hays J, Perona P, Ramanan D, Dollar P and Zitnick C L 2014 Microsoft coco: Common objects in context *In European Conference on Computer Vision*
[16] Celebi M E, Kingravi H A and Vela P A 2013 A comparative study of efficient initialization methods for the k-means clustering algorithm *Expert Systems with Applications* **40** 200-210
[17] Srivastava N, Hinton G E, Krizhevsky A, Sutskever I and Salakhutdinov R 2014 Dropout: a simple way to prevent neural networks from overfitting *Journal of Machine Learning Research* **15** 1929-1958

Acknowledgements

This work was supported by the Russian Foundation for Basic Research (projects No. 18-29-03011-mk Research and Development of New Methods and Technologies for the Tasks of Intellectual Analysis and Optimization of Processing Large Data Streams of the Earth Remote Sensing and No. 17-29-07003-ofi_m Development of Methods and Models of Dynamic Behavior Planning and Hierarchical Intellectual Motion Control of Unmanned Aerial Vehicles in an Uncertain Environment with Computing Resources Constraints).

Nonlinear analysis of the degree of order and chaos of morphology of porous silicon nanostructures

Z Zh Zhanabaev[1,2,3], T Yu Grevtseva[1,2,3], K A Gonchar[4], G K Mussabek[1,2,5], D Yermukhamed[1,2], A A Serikbayev[2], R B Assilbayeva[6], A Zh Turmukhambetov[2] and V Yu Timoshenko[4,5]

[1]National Nanotechnological Laboratory of Open Type at al-Farabi Kazakh National University, al-Farabi av., 71, Almaty, Kazakhstan, 050040
[2]Al-Farabi Kazakh National University, al-Farabi av., 71, Almaty, Kazakhstan, 050040
[3]Institute of Experimental and Theoretical Physics, al-Farabi av., 71, Almaty, Kazakhstan, 050040
[4]Lomonosov Moscow State University, Leninskie Gory, 1, Moscow, Russia, 119991
[5]National Research Nuclear University "MEPhI", Institute of Engineering Physics for Biomedicine, Laboratory "Bionanophotonics", Kashirskoe sh., 31, Moscow, Russia, 115409
[6]Caspian State University of Technology and Engineering named after Sh. Yessenov, 30 microdistrict, 14/2, Aktau, Kazakhstan, 130000

e-mail: mptl449a@gmail.com, serikbayev.almas@gmail.com

Abstract This work has been done to identify quantitative criteria the degree of order and chaos morphology of porous layers consisting of silicon nanowire arrays. In order to fulfill the work, a method of using metal-assisted chemical etching has been utilized to produce nanowires. There has been done a work of digital processing of porous film images which were extracted by scanning electron microscope. Informational-entropic and Fourier analysis have been applied to quantitatively describe the degree of order and chaos in nanostructure distribution in the layers. Self-similarity of the layer morphology has been quantitatively described via its fractal dimensions by correlation method. The applied approach for image processing allows us to distinguish the morphological features of as-called "black" (more ordered) and "white" (less ordered) silicon layers, which are characterized by minimal and maximal optical reflection, respectively. From all of the methods of digital techniques that we have used the method for determining the conditional information of a chaotic set was proved to be the most informative.

1. Introduction

Recently porous silicon (Si) nanostructures as nanowires (NWs) are intensively studied in view of their possible applications in optoelectronics, photonics, and sensorics [1-5]. Si NWs possess unique electrical and optical properties, which are prospective for biomedicine [6-8] and advanced energy and environment applications [9]. Porous silicon films are of particular interest because the electrical and optical properties of these films depend on their porosity, thickness, size distribution of pores and nanocrystals. In general, a tailoring of the nanostructure morphology seems to be promising for the development of new semiconductor devices for different purposes.

Nanocluster semiconductor films, including porous layers of silicon nanowire (SiNWs) grown in non-equilibrium conditions have scale-invariant, hierarchically self-similar, i.e. fractal and multi-fractal structure [10-13]. The scale invariance of a SiNW film is in their self-similarity (similarity coefficients on different variables are equal to each other) and self-affinity (similarity coefficients are different on different variables, that corresponds to anisotropic structure of the film).

Fractal distribution of nanoclusters and pores in a film, which is grown by wet chemistry method, can be caused by processes of self-organization occurred in non-equilibrium non-linear open systems. The self-organization is considered as appearance of the order from chaos. Description of porous silicon films with partially ordered SiNWs is an interesting scientific problem because the informational entropy and fractal dimension can be used as quantitative characteristics of dynamical chaos. According to the well-known Prigozhin theorem, derivative of entropy with respect to time tends to its minimal value at self-organization. In agreement with Klimontovich's S-theorem [14], entropy decreases at self-organization of a system. Possibility to define the entropy via fractal measure has been described in Ref.[15]. It is noted, that if the order of multifractal moment characterizing a hierarchical system is equal to unity, one can calculate entropy of the system. However, calculation of multifractal moment's order is a stand-along scientific problem. The ordering of different complex systems (universe, galaxies, oscillatory systems, etc.) on different spatial scales also can be described using entropy [16-18]. The informational entropy can be considered as a value containing information about the system [16]. The thermodynamic entropy can be used for the description of organized structures evolution, for example, expansion of Universe [17]. In Ref.[18] it is shown that thermodynamic entropy can be used for control of self-organized criticality by description of nanosized structure of thin film coatings.

The informational entropy is a basic building block of complexity theory including theories of chaos and fractals [19, 20]. To evaluate the informational entropy of nanostructured systems it is required more accurate analysis of surface and bulk nano-thermodynamics. The problem is in the fact that for the description of equilibrium systems, usually Boltzmann entropy is used. For the description of non-equilibrium systems one should consider the Shannon entropy. But in this case we have difficulties related with normalization of entropy, because entropy tends to infinity at decreasing of size of cells to zero. In this paper we will pay attention to this problem.

Fractal analysis of images allows us to detect and describe singularities of cluster structure of films. The fractal analysis is useful for the description of self-affinity of films with different chemical composition and for quantitative description of surface waviness, irregularity, roughness and anisotropy [21]. Calculation of the fractal dimensions of different surface can be used for their optimal position at grinding processes [22].

As usual, distribution of pores in different materials is characterized by fractal regularities. Studies of the relation between fractal dimension and porosity have been described in Refs. [23-25]. Thus, the fractal dimension of porous membranes significantly depends on percentage ratio of components [23]. Calculations of numeric values of the fractal dimension of porous samples are used in computerized tomography for the description of pore structure of rocks [24]. An analysis of the porosity and pore structures by using the fractal and multi-fractal approaches is widely used in geology for oil, gas and geothermal systems [25]. However, in general, the desired relationship between porosity and fractal dimension is ambiguous. Objects containing fractals with different number of iterations of their parts (prefractals) have the same values of fractal dimension but different values of porosity. Note that a description of the physical processes in nanostructures with quantum properties is possible on the base of comprehensive analysis of their scale-invariant (fractal), informational-entropic, topological, and spectral characteristics. The present work is aimed to quantitatively describe the scale-invariant structure of porous SiNWs layers and to develop an adequate technique for distinguishing films of "black" and "white" silicon by their morphology.

2. Experimental

Samples of two types, i.e. so-called "black" and "white" porous layers, were obtained by metal-assisted chemical etching (MACE), which is a "top-down" approach of material processing by dissolution catalyzed with noble metal nanoparticles [6-9]. As a substrate we used (100) oriented p-

type c-Si wafers with resistivity of 1-10 Ω*cm and the treatment was carried out in three stages: 1) deposition of catalyst metal particles on the substrate surface, 2) chemical etching of the substrate and 3) removal of residual metal particles. In our experiments as the catalyst we used silver (Ag) nanoparticles, which were precipitated on the surface of c-Si substrates from a mixture of 0.02 M aqueous solution of AgNO3 and 5M aqueous solution of hydrofluoric acid (HF) in the volume ratio 1:1 for 45 sec. Then the MACE treatment was done by immersing the samples in a mixture of 5M HF and 30% hydrogen peroxide (H2O2) taken in the volume ratio of 10:1. The length of SiNWs (layer thickness) was determined by the etching time. To obtain samples of "black silicon" and "white silicon" the MACE treatment was performed during 1-10 minutes and 0.5-6 hours, correspondingly. After the MACE process, the samples were immersed in 45% concentrated nitric acid (HNO3) for 15 minutes to remove residual Ag particles and then the samples were washed in de-ionized water and dried in air.

The structure properties of the obtained samples were studied by means of the scanning electron microscopy (SEM) using an ULTRA 55 FE-SEM (Carl Zeiss) microscope. Spectra of the total reflection were measured in the optical range from 0.2 to 1.2 μm using a spectrophotometer Lambda 35, Perkin Elmer. The optical measurements were carried out at room temperature in air.

Typical spectra of the total reflectance of SiNW arrays with low (“black”) and high (“white”) level of the reflectance are shown in Figure 1.

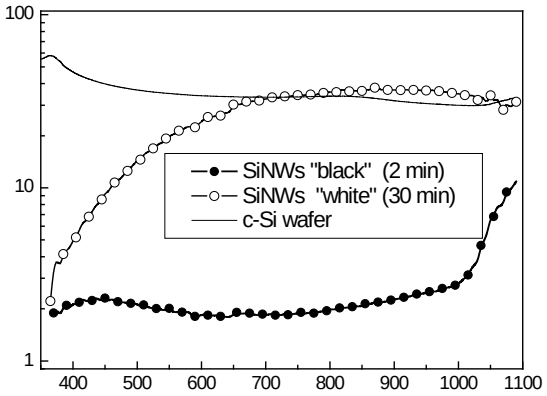

Figure 1. Total reflection spectra of two samples of SiNWs prepared for 2 min (close circles) and 30 min (open circles) as well as for a double-side polished c-Si wafer (solid line).

3. Analysis of SEM images

3.1. Porosity evaluation

Porosity of a SiNW layer can be experimentally determined by gravimetric measurements of the corresponding substrate before and after MACE [7,8]. However, this method is characterized by relatively low accuracy when the mass measurement occurred at a nanoscale. While the porosity of a thin film of SiNWs can be calculated from its optical density [6], it gives only the average porosity and it can be only applied for films with low light scattering.

Different methods can be used for image processing [26-28]. In our work the porosity of the top of SiNW layer was estimated from an analysis of the corresponding top view SEM images. The analysis was done in the following way. At the first stage a square part of a SEM image with sizes 700 × 700 pixels was selected (see for example Figure 2a). At the second step, the selected area (Figure 2(b)) has been subjected to conversion of contrast enhancement. At the third step, the image was converted to the “black and white” format (Figure 2(c)). The corresponding histogram of the brightness distribution of pixel is shown in Figure 2(d). The horizontal axis corresponds to the brightness level, B, in the range from 0 (black pixels) to 255 (white pixels), and the vertical axis represents number N of pixels.

Porosity of the films was calculated as follows

$$\eta = 1 - \frac{N_w}{N_w + N_b}, \tag{1}$$

where N_b and N_w are numbers of black (pores) and white (Si nanocrystal) pixels, correspondently.

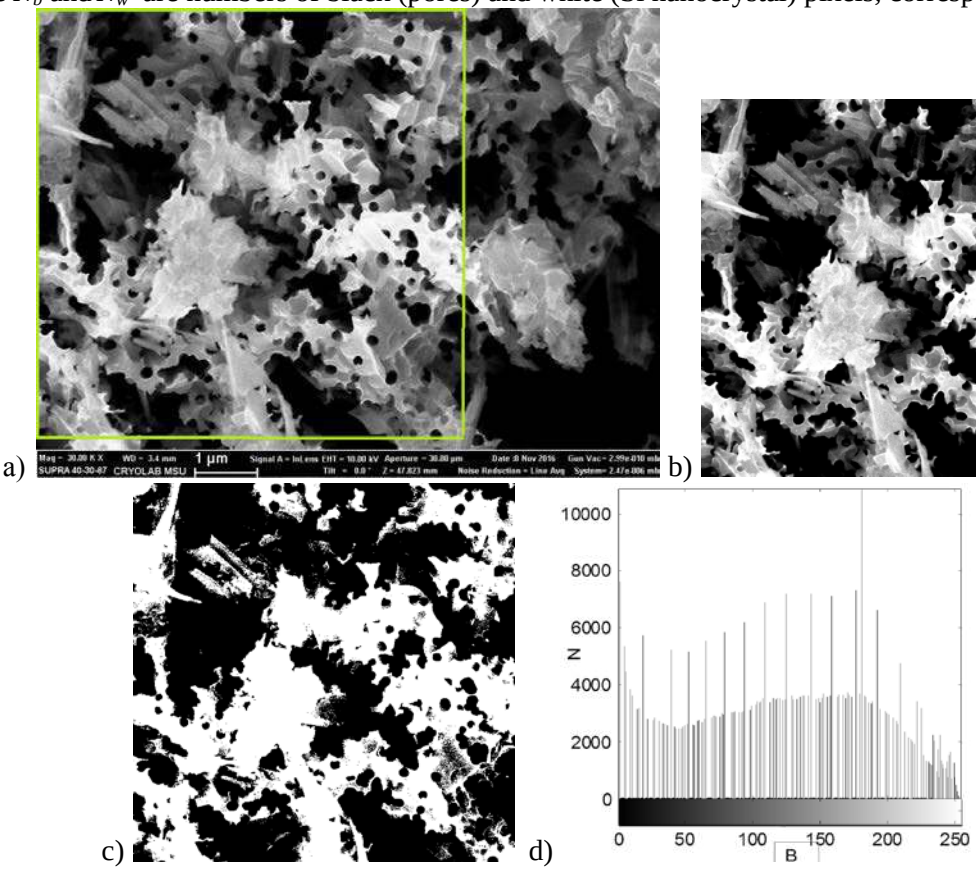

Figure 2. a) SEM image of a porous Si film where green lines select a fragment for the digital analysis; (b) the fragment selected for image processing; (c) the segment image with high contrast containing only white and black pixels; (d) histogram of the distribution of pixel intensities in the image.

3.2. Information entropy analysis

SEM images of investigated silicon films show that these films have porous structure and contain sets of quantum nanowires with complex internal structure. These sets form separated clusters with different shape and chaotic distribution. The information entropy is widely used to characterize the chaotic state of an object. We have defined its numeric value via the following well-known formula:

$$S(x,y) = -\sum_{i=1}^{N}\sum_{j=1}^{N} P_{i,j}(x,y)\ln P_{i,j}(x,y), \tag{2}$$

where $P_{i,j}$ is the probability of pixel with a certain brightness proportional to histogram counts (Figure 2(d)), which correspond to a segment of the original image in (x,y) plane.

Dependence of non-normalized informational entropy on porosity of the films is shown in Figure 3. In case of using the expression *S(x,y)/(S(x)+S(y))* we obtain values of entropy normalized to unit because entropy is maximal if a process is independent on variables *x* and *y*. Surfaces of "white" silicon observed in the vertical direction (top view) have bigger values of porosity than lateral sides of the films. The entropy of a top side of film decreases with increasing of porosity, but entropy of its lateral side increases. It should also be noted that entropy of "black" silicon films is smaller than entropy of "white" silicon films by about 50%. It means that "black" silicon is more ordered than

"white" silicon, i.e. pore sizes are distributed according to some regularity and coherent absorption of photons is possible

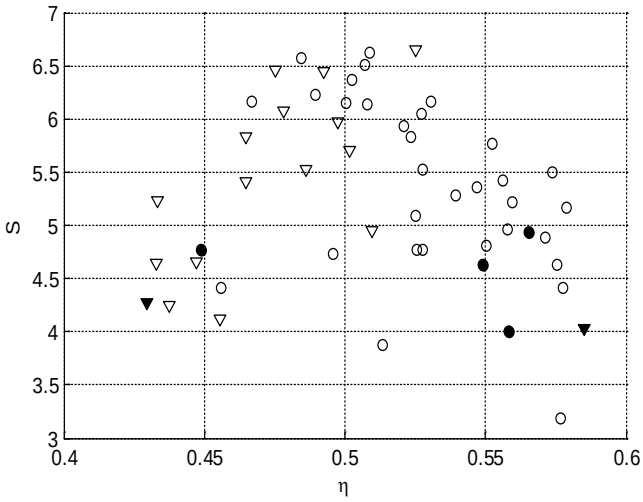

Figure 3. Dependence of the information entropy on porosity of films. Number of cells (pixels is 700 × 700)

○ – "white" silicon (top view);
▽ – "white" silicon (lateral view);
● – "black" silicon (top view);
▼ – "black" silicon (lateral view).

Figure 4 represents a dependence of the information-to entropy ratio (IER) on porosity. The information (*I(x|y)*) has been defined as a difference between full entropy S(x,y) and conditional entropy *S(x|y)* as

$$I(x \mid y) = S(x, y) - S(x|y), \tag{3}$$

where x, y are horizontal and vertical coordinates.

The designation *I(x|y)* corresponds to values of information calculated via variable *x* at known value of *y*. Entropy *S(x|y)* can be defined via conditional probability as *P(x|y)=P(x,y)/P(y)*.

Formula (3) reflects the generally accepted definition of information which meaning is measure of order (certainty) [14]. Conditional entropy (corresponding to some order) is always less then unconditional entropy (absence of order), so, *I(x|y)* is always greater than zero. In the theory of telecommunications formula (3) contains *S(x)* instead of *S(x,y)*. It leads to understated values of *I(x|y)*.

The relation of *I(x|y)/ S(x|y)=IER* (information-to-entropy ratio) is an analog of signal-to-noise ratio *SNR* widely used in radiophysics [29-31]. Difference between these values is in the fact that *SNR* should be calculated at a known noise level, but *IER* can be defined without knowing the noise level. While the entropy of "black" silicon is less than that of "white" one, the information is larger.

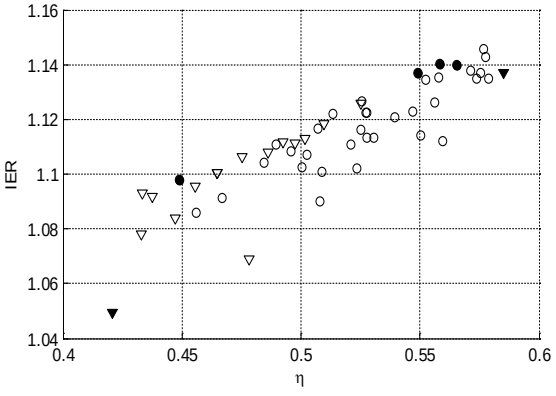

Figure 4. Dependence of the information-to-entropy ratio on porosity of SiNW films

○ – "white" silicon (top view);
▽ – "white" silicon (lateral view);
● – "black" silicon (top view);
▼ – "black" silicon (lateral view).

3.3. Fractal dimension analysis

Fractal dimensions of the films have been defined by use of the *box-counting* method. As expected, due to scale-invariant structure of nanostructured films values of their fractal dimensions differ insignificantly (the values belong to the range 1.80 ÷ 1.95). Although values of fractal dimension vary insignificantly because of presence of prefractals (fractals of different iterations), porosity can vary significantly. This fact is evident from Figure 5 illustrating dependence of the fractal dimension on porosity of the films.

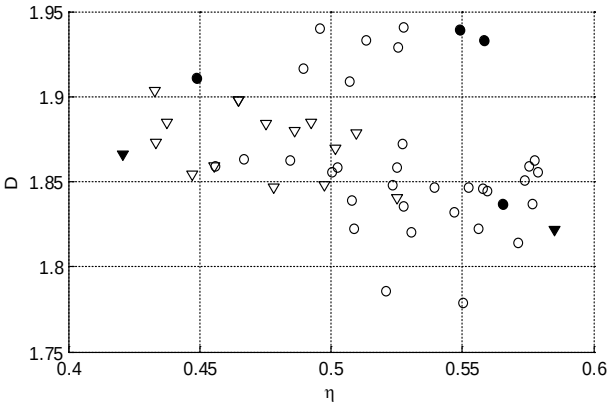

Figure 5. Dependence of fractal dimension of SiNW films on their porosity.

○ – "white" silicon (top view);
▽ – "white" silicon (lateral view);
● – "black" silicon (top view);
▼ – "black" silicon (lateral view).

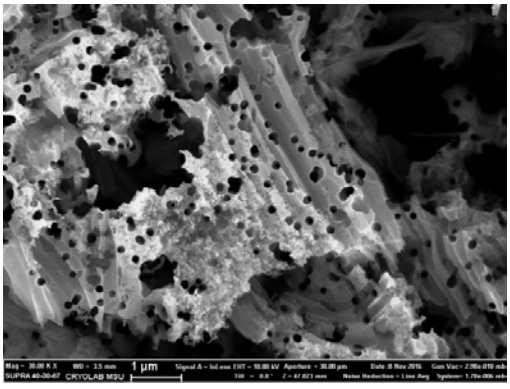

a)

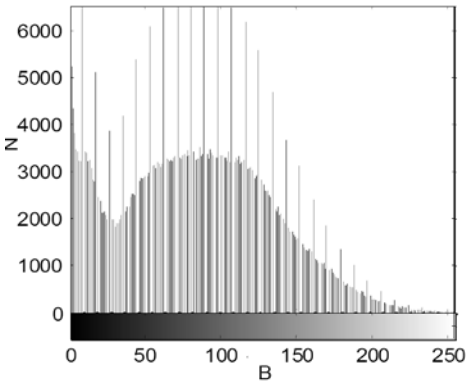

b)

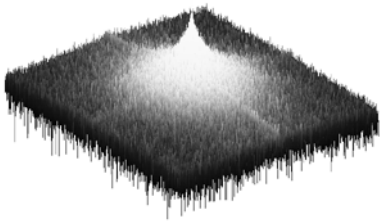

c)

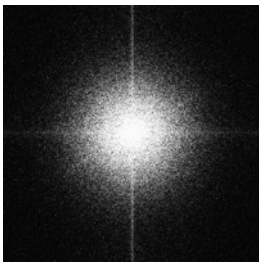

d)

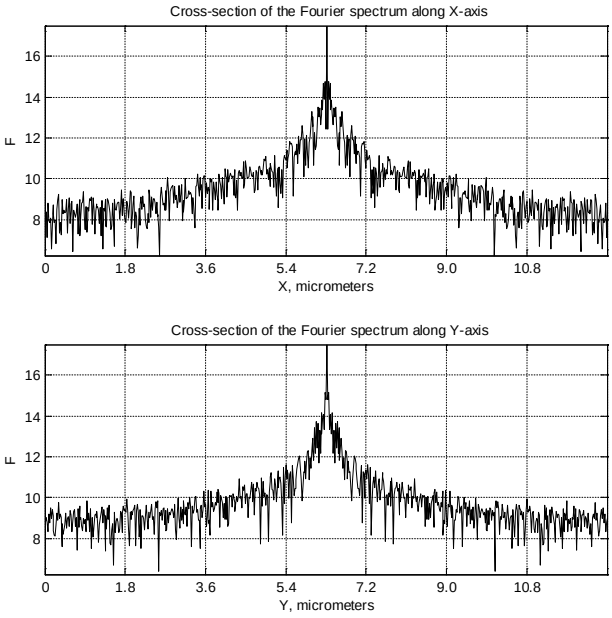

e)

Figure 6. SEM image of "white" silicon film (top view) (a), histogram of pixel intensities of the image (b), three-dimensional Fourier spectrum (c), projection of the Fourier spectrum on the plane (d), cross-section of three-dimensional spectrum along X- and Y-axes (e).

3.4. Fourier analysis of SEM-images

Results of an application of the two-dimension Fourier transform analysis for the description of SEM images of different films are shown in Figures. 6-9. Figure 6 illustrates results obtained at processing of a typical image of "white" silicon film (top view). Figures 7, 8 and 9 describe "white" silicon (lateral view), "black" silicon (top view) and "black" silicon (lateral view), correspondently. The Fourier transform has been applied to elements of matrix describing pixel intensities of an original image. Cross-section lines of three-dimensional Fourier spectra are drawn along the abscissa and ordinate axes in such way that they pass through centers of the graphs. Using two-dimensional Fourier transform let us describe type of silicon films ("black" or "white" silicon). Weak asymmetry in the Fourier spectra corresponds to certain anisotropy of structure of the films caused by experimental conditions.

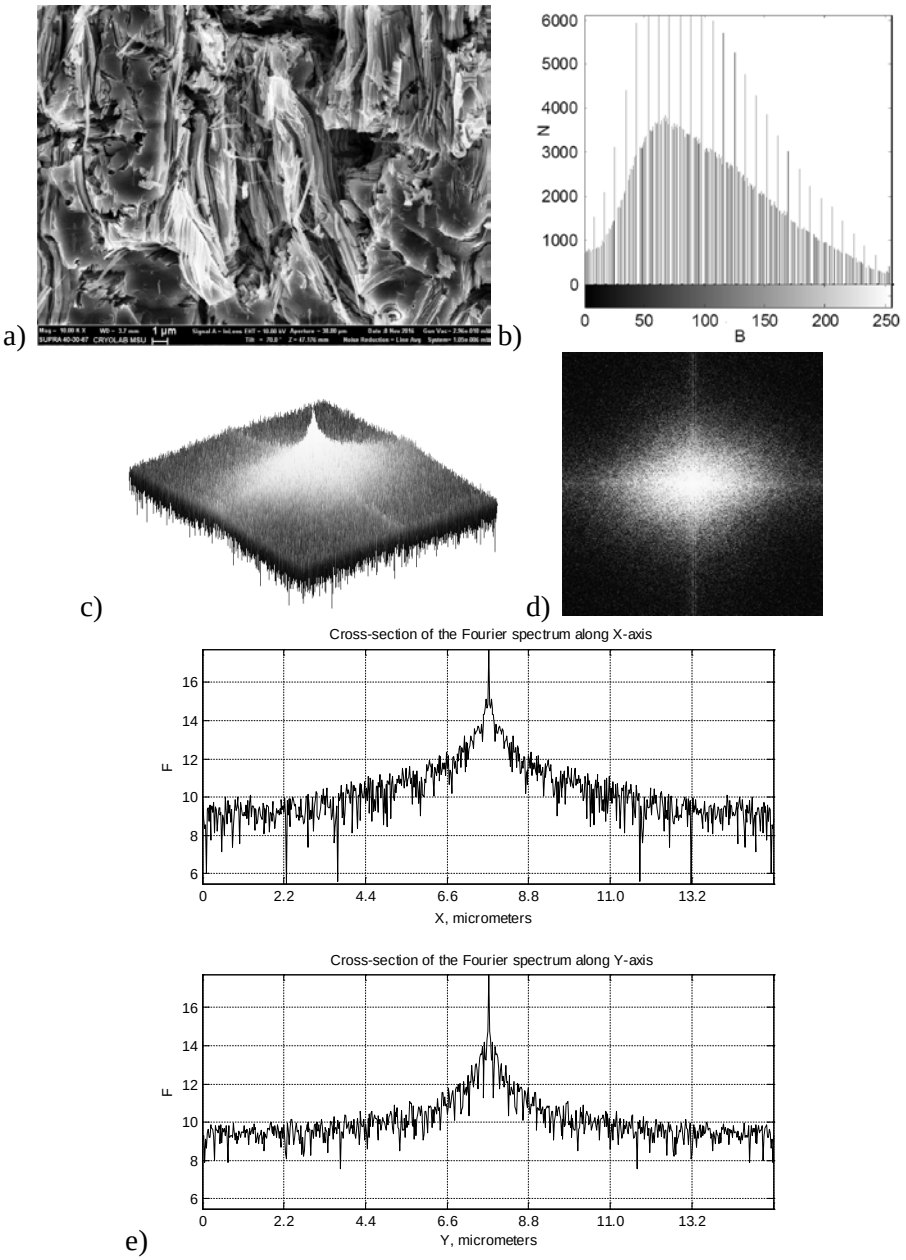

Figure 7. Cross-sectional SEM image of "white" silicon film (lateral view) (a), histogram of pixel intensities of the image (b), three-dimensional Fourier spectrum (c), projection of the Fourier spectrum on the plane (d), cross-section of three-dimensional spectrum along X- and Y-axes (e).

From the presented above graphs we can see that histograms describing distribution of pixel intensities of images of "white" and "black" silicon films are noticeably different: histograms corresponding to "white" silicon are usually solid, but histograms of "black" silicon contain sharp bursts. This difference between histograms of "white" and "black" silicon films indicate to the fact that "black" silicon has more expressed structuredness. These characteristic features of the histograms can be used for classification of silicon films to "white" and "black" silicon.

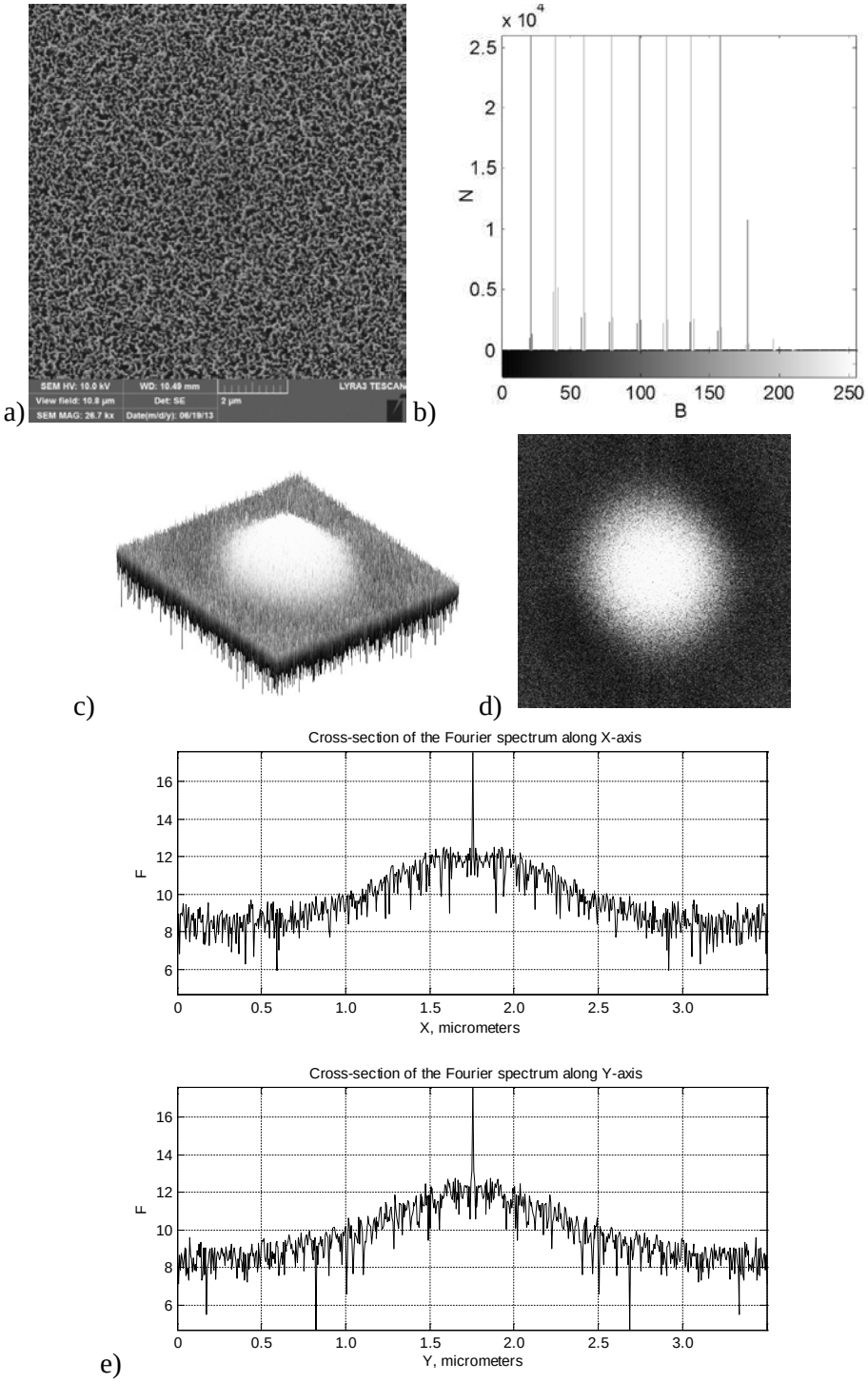

Figure 8. Image of "black" silicon film (top view) (a), histogram of pixel intensities of the image (b), three-dimensional Fourier spectrum (c), projection of the Fourier spectrum on the plane (d), cross-section of three-dimensional spectrum along X- and Y-axes (e).

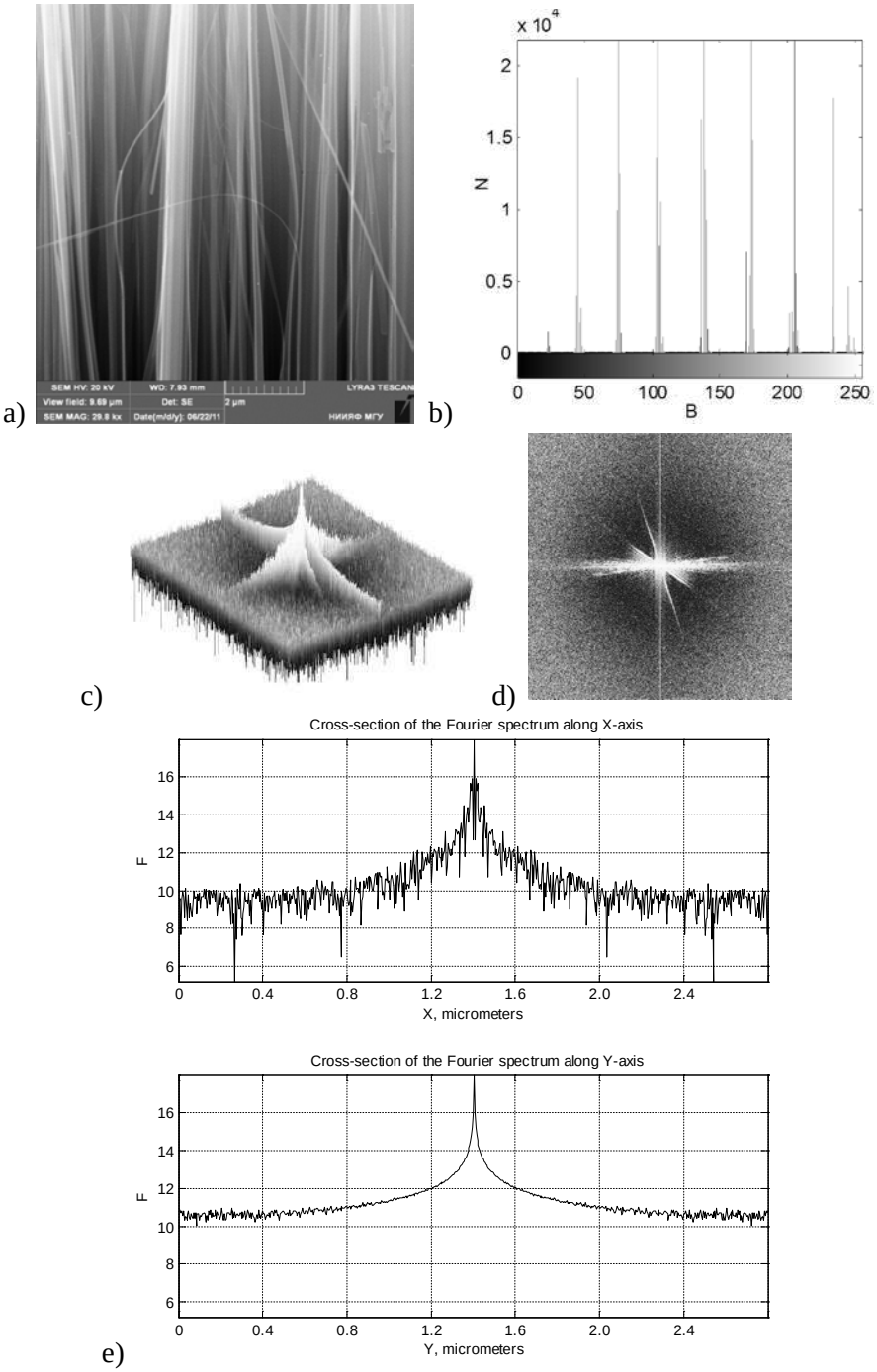

Figure 9. Cross-sectional SEM mage of "black" Si film (lateral view) (a), histogram of pixel intensities of the image (b), three-dimensional Fourier spectrum (c), projection of the Fourier spectrum on the plane (d), cross-section of three-dimensional spectrum along X- and Y-axes (e).

4. Conclusions

The quantitative analysis of SEM images of nanostructured films with properties of "white" and "black" silicon, which were formed by MACE c-Si wafers, allowed us to estimate the porosity varied from 42% to 53% for their lateral sides and from 46% to 58% for their top sides. Thus, the top surfaces of "white" silicon have larger porosity than that for the lateral sides and this fact indicates the gradient of morphology related to the MACE growth of Si NWs accompanied with their gradual chemical dissolution. The revealed difference between information entropy for "black" and "white" Si films shows that the structure of the former is more ordered than that for the latter. The fractal

dimensions of the both types of nanostructured Si layers are different due to the presence of fractals with different iterations. The Fourier analysis of SEM images also indicates that the "white" silicon films are more isotropic than the "black" ones. This fact is confirmed by values of the scaling factor describing colored noise typical for distribution of nanostructures. The distribution histogram of pixel intensities in the SEM images of the top of Si NW arrays reveals the Gaussian function and a power law for the "white" and "black" samples, respectively. Thus, the performed informational-entropic, fractal, spectral, and statistical treatments of the SEM images indicate that the optical properties of "black" and "white" samples are related to the more ordered structure of the former that ensures the stronger effective absorption of light with photon energies below the bandgap.

5. References

[1] Jarimaviciute-Zvalionienea R, Prosycevasa I, Kaminskienea Z and Lapinskas S 2011 Optical properties of black silicon with precipitated silver and gold nanoparticles *Acta Physica Polonica A* **120** 942-945
[2] Koynov S, Brandt M S and Stutzmann M 2006 Black nonreflecting silicon surfaces for solar cells *Applied Physics Letters* **88** 203107
[3] Lua Y T and Barronw A R 2013 Nanopore-type black silicon anti-reflection layers fabricated by a one-step silver-assisted chemical etching *Phys. Chem. Chem. Phys.* **15** 9862-9870
[4] Ravindra N M, Marthi S R and Sekhri S 2015 Modeling of Optical Properties of Black Silicon/Crystalline Silicon *Journal of Scientific and Industrial Metrology* **1(1)** 1-7
[5] Ge M, Rong J, Fang X and Zhou Ch 2012 Porous doped silicon nanowires for lithium ion battery anode with long cycle life *Nano Letters* **12** 2318-2323
[6] Osminkina L A, Sivakov V A, Mysov G A, Georgobiani V A, Natashina U A, Talkenberg F, Solovyev V V, Kudryavtsev A A and Timoshenko V Yu 2014 Nanoparticles prepared from porous silicon nanowires for bio-imaging and sonodynamic therapy *Nanoscale Research Letters* **9(463)** 1-7
[7] Gonchar K A, Osminkina L A, Galkin R A, Gongalsky M B, Marshov V S, Timoshenko V Yu, Kulmas M N, Solovyev V V, Kudryavtsev A A and Sivakov V A 2012 Growth, structure and optical properties of silicon nanowires formed by metal-assisted chemical etching *Journal of Nanoelectronics and Optoelectronics* **7(6)** 602-606
[8] Crescentini M, Rossi M, Ashburn P, Lombardini M, Sangiorgi E, Morgan H and Tartagni M 2016 AC and Phase Sensing of Nanowires for Biosensing *Biosensors* **6(15)** 1-14
[9] Ghosh R and Giri P K 2017 Silicon nanowire heterostructures for advanced energy and environmental applications: a review *Nanotechnology* **28** 012001
[10] Zhanabaev Z Zh, Grevtseva T Yu, Danegulova T B and Assanov G S 2013 Optical processes in nanostructured semiconductors *Journal of Computational and Theoretical Nanoscience* **10(3)** 673-678
[11] Zhanabaev Z Zh and Grevtseva T Yu 2014 Physical fractal phenomena in nanostructured semiconductors *Reviews in Theoretical Science* **2(3)** 211-259
[12] Zhanabaev Z Zh, Grevtseva T Yu and Ibraimov M K 2016 Morphology and electrical properties of silicon films with vertical nanowires *Journal of Computational and Theoretical Nanoscience* **13** 615-618
[13] Fazio B, Artoni P, Iatì M A, D'Andrea C, Faro M J L, Sorbo S D, Pirotta S, Gucciardi P G, Musumeci P, Vasi C S, Saija R, Galli M, Priolo F and Irrera A 2016 Strongly enhanced light trapping in a two-dimensional silicon nanowire random fractal array *Light: Science & Applications* **5** 1-7
[14] Klimontovich Yu L 1998 Information Concerning the States of Open Systems *Physica Scripta* **58(6)** 549-555
[15] Slomczynski W, Kwapier J and Zyczkowski K 2000 Entropy computing via integration over fractal measures *Chaos* **10(1)** 180-188
[16] Hwang W Y 2014 A coherent view on entropy *Natural Science* **6** 540-514
[17] Frautschi S 1982 Entropy in an expanding universe *Science* **217(4560)** 593-599

[18] Fox-Rabinovich G, Paiva J M, Gershman I, Aramesh M, Cavelli D, Yamamoto K, Dosbaeva G and Veldhuis S 2016 Control of self-organized criticality through adaptive behavior of nano-structured thin film coatings *Entropy* **18** 290
[19] Gao J, Liu F, Zhang J, Hu J and Cao Y 2013 Information entropy as a basic building block of complexity theory *Entropy* **15** 3396-3418
[20] Dezso A and Kaptay G 2017 On the Configurational Entropy of Nanoscale Solutions for More Accurate Surface and Bulk Nano-Thermodynamic Calculations *Entropy* **19** 248
[21] Khamesee M B, Kurosaki Y, Matsui M and Murai K 2004 Nanofractal analysis of material surfaces using atomic force microscopy *Materials Transactions* **45(2)** 469-478
[22] Prabhu S and Vinayagam B K 2011 Fractal dimensional surface analysis of AISI D2 tool steel material with nanofluids in grinding process using atomic force microscopy *Journal of the Brazilian Society of Mechanical Sciences and Engineering* **33(4)** 459-466
[23] Wei Q and Wang D. 2003 Pore surface fractal dimension of sol-gel-derived Al2O3-SiO2 membranes *Materials Letters* **57** 2015-2020
[24] Peng R D, Yang Y C, Ju Y, Mao L T and Yang Y M 2011 Computation of fractal dimension of rock pores based on gray CT images *Chinese Sci Bull* **56(31)** 3346-3357
[25] Anovitz L M and Cole D R 2015 Characterization and analysis of porosity and pore structures *Reviews in Mineralogy & Geochemistry* **80** 61-164
[26] Gashnikov M V 2017 Minimizing the entropy of post-interpolation residuals for image compression based on hierarchical grid interpolation *Computer Optics* **41(2)** 266-275 DOI: 10.18287/2412-6179-2017-41-2-266-275
[27] Vizilter Y V, Gorbatsevich V S, Vishnyakov B V and Sidyakin S V 2017 Object detection in images using morphlet descriptions *Computer Optics* **41(3)** 406-411 DOI: 10.18287/2412-6179-2017-41-3-406-411
[28] Myasnikov V V 2018 Description of images using a configuration equivalence relation *Computer Optics* **42(6)** 998-1007 DOI: 10.18287/2412-6179-2018-42-6-998-1007
[29] Seshadri R and Penchalaiah N 2011 Method for reducing of noise by improving signal-to-noise-ratio in wireless Lan *International Journal of Network Security & Its Applications* **3(5)** 115-120
[30] Naylor G and Johannesson R B 2009 Long-term signal-to-noise ratio at the input and output of amplitude-compression systems *Journal of the American Academy of Audiology* **20** 161-171
[31] Abbott B P 2016 Observation of gravitational waves from a binary black hole merger *Physical Review Letters* **116** 061102-061116

Acknowledgments
This work was partially supported by the Committee of Science of the Ministry of Education and Science of the Republic of Kazakhstan (Grant AP05132854, Grant AP05132738). G.K.M. and V.Yu.T. acknowledge the support of the Comprehensive Program of NRNU “MEPhI”.

Analysis of the preferences of public transport passengers in the task of building a personalized recommender system

A A Borodinov[1], V V Myasnikov[1,2]

[1]Samara National Research University, Moskovskoe Shosse 34A, Samara, Russia, 443086
[2]Image Processing Systems Institute of RAS - Branch of the FSRC "Crystallography and Photonics" RAS, Molodogvardejskaya street 151, Samara, Russia, 443001

e-mail: aaborodinov@yandex.ru

Abstract. The paper presents the theoretical and algorithmic aspects for making a personalized recommender system (mobile service) designed for public route transport users. The main focus is on identifying and formalizing the concept of "user preferences", which is the basis of modern personalized recommender systems. Informal (verbal) and formal (mathematical) formulations of the corresponding problems of determining "user preferences" in a specific spatial-temporal context are presented: the preferred stops definition and the preferred "transport correspondence" definition. The first task can be represented as a well-known classification problem. Thus, it can be formulated and solved using well-known pattern recognition and machine learning methods. The second is reduced to the construction of dynamic graphs series. The experiments were conducted on data from the mobile application "Pribyvalka-63". The application is the tosamara.ru service part, currently used to inform Samara residents about the public transport movement.

1. Introduction

The amount of heterogeneous data characterizing the transport situation in the city has increased due to the widespread and active use of modern electronic communications systems, global navigation systems, and various active and passive sensors. Such information is used in navigation and reference systems (services) quite widely [1]. However, along with the development of services and their popularization, the expectations and demands of users and the amount of information that has to be taken into account when planning movements are growing. User demand is individualized from the classic tasks of searching for the “shortest path” [2] or getting a “forecast of arrival at a stop of public transport” [3, 4], shifting expectations from services to Intelligent personal assistants. Although the final decision or choice in such systems remains with the person, the options of the solutions they offer are significantly dependent on the scenario conditions of the request as well as on previous actions and decisions of the user [5, 6]. Accounting for all of the indicated factors is possible in “self-tuning” systems for individual user preferences based on machine learning methods [7]. The imperfection of existing algorithms and the lack of significant experience in the use of machine learning methods in such systems prevents the rapid emergence of such services.

Multimodal routing is determined by the possibility of using several modes of transport in one trip. The analysis of modern literature devoted to recommender systems of multimodal routing [5, 8, 9] allows us to identify some major problems:

– The cold start problem is a well-known and well-researched problem for recommender systems [8, 10]: it is essential to achieve a balance between the accuracy of the recommended routes from system initialization. Thus, the allowable setting time for a personal preference profile should be small.

– The receiving information method from the user is not formalized [11, 12].

– Individual characteristics such as personal income, age, gender, family size, access to public transport influence the choice of the route even for the same purpose of the trip [13].

– User preferences change over time. In addition, context influences user selection [14, 15].

– Typical existing solutions mainly use the Bayesian approach with a sequential parameter recalculation scheme [5, 16].

– It is possible to use transfer learning to improve recommendations [17].

– The problem of determining traffic flow on the vehicle route [18].

This article proposes one of the possible ways of describing and solving the problem of determining individual preferences of users of public route transport and creating a personalized recommender system. The system uses user interaction data with the mobile service as part of the problem of creating a personalized recommender system. The second section of the work formalizes the basic concepts and introduces the basic notation for all objects of interaction. The third section describes the information arising from the public transport user interaction with the mobile application "Pribyvalka-63". Mobile application and service tosamara.ru, are currently used to inform Samara residents about public transport movement and its arrival at the stop. Also in this section are presented the variants of unformalized (verbally described) definitions of "user preferences", suitable for further consideration. The fourth section presents the mathematical formulations of problems, as well as methods and algorithms. Finally, the fifth section presents the results of experimental studies on real data obtained using the mobile application "Pribyvalka-63".

2. Definitions and designations

Let S be the set of public transport stops. Let for each stop $s \in \mathrm{S}$ defined spatial (geographical) coordinates $\mathbf{x}_s \equiv (x_s, y_s, z_s)$ and some unique stop identifier, denoted by *ID*(*s*). Without loss of generality, we can assume that the set S is ordered (for example, by *ID*(*s*)): $S = \{s_1, s_2, \ldots, s_{|S|}\}$.

Let the value *d* determine the calendar date, the value *t* - the time of day, and $w(d) \in W$ - the day of the week, taking values from the set:

$$\begin{aligned} &\mathrm{W}=\mathrm{W}_0 \cup \mathrm{W}_1, \\ &\mathrm{W}_0 \equiv \{MON, TUE, WEN, THU, FRI\}, \quad \mathrm{W}_1 \equiv \{SAT, SUN\}. \end{aligned} \tag{1}$$

Let V determine the set of public transport vehicles, each $v \in \mathrm{V}$ is characterized by the type

$$type(v) \in \{BUS, TRAM, TROL, MARS\}, \tag{2}$$

and has a unique identifier *ID*(*v*) (in practice, the unique identifier may coincide with the vehicle state registration number). For each vehicle at any time, we consider its spatial coordinates to be determined:

$$\mathbf{x}(v,d,t) \equiv (x(v,d,t), y(v,d,t), z(v,d,t)). \tag{3}$$

Denote the routes set of public transport objects as M. In addition, each route $m \in \mathrm{M}$ is characterized by five arguments:

$$m \equiv \left(ID(m), N(m), \mathbf{s}(m), N^*(m), \mathbf{x}(m)\right), \tag{4}$$

where $ID(m)$ - route identifier (in practice, the route number), $N(m)$ - stops number in the route, and $\mathbf{s}(m)$ - stops sequence in an amount $N(m)$ of form:

$$\mathbf{s}(m) = \left(s_1^m, s_2^m, \ldots, s_{N(m)}^m\right), \tag{5}$$

where $s_n^m \in \mathrm{S} \quad \left(m \in \mathrm{M}, n \in \overline{1, N(m)}\right)$. Let $\mathrm{S}(m) \equiv \left\{s_i^m\right\}_{i=\overline{1,N(m)}} \subseteq \mathrm{S}$ be the stops set of the corresponding route, $ind(s,m)$ - stop index s of route m, viz. $ind\left(s_n^m, m\right) = n$. In case $s \notin \mathrm{S}(m)$ the corresponding index is assumed to be "indefinite", and denoted as Δ: $ind(s,m) = \Delta$. Denote the routes set passing through one or a couple stops as follows:

$$\mathrm{M}(s) \equiv \left\{m \in \mathrm{M}: \mathrm{s} \in \mathrm{S}(m)\right\}, \ \mathrm{M}(s1, s2) \equiv \left\{m \in \mathrm{M}: \mathrm{s1} \in \mathrm{S}(m) \wedge \mathrm{s2} \in \mathrm{S}(m)\right\}. \tag{6}$$

More detailed information about the route geometry is represented by a pair $N^*(m), \mathbf{x}(m)$, where the first value determines the number of nodes of the polyline describing the route, and the second is the vector defining the coordinates of these nodes:

$$\mathbf{x}(m) \equiv \left(\mathbf{x}_1^m, \mathbf{x}_2^m, \ldots, \mathbf{x}_{N^*(m)}^m\right). \tag{7}$$

For convenience, we will call the pair $(m,k), \quad \left(k = \overline{1, K(d,m)}\right)$ route implementations (RI) on the appropriate day *d*.

Additionally, we denote $t(d,m,k,s)$ - vehicle arrival time assigned to RI (*m*,*k*) on day *d*, to stop $s \in \mathrm{S}(m)$ (in case $s \notin \mathrm{S}(m)$ we consider the time value as uncertain).

Denote the vehicle assigned to RI *(m,k)* on day *d*, as $v(d,m,k) \in \mathrm{V} \quad \left(k = \overline{1, K(d,m)}\right)$.

In addition to the vehicles, pedestrians and passengers, considered in the paper as the users of transport services, are participants in the traffic. Denote by U the set of users, and we will characterize each specific user $u \in \mathrm{U}$ with a unique identifier *ID*(*u*) (mobile device id or hash code) and spatial coordinates at a specific point in time d, t:

$$\mathbf{x}(u,d,t) \equiv \left(x(u,d,t), y(u,d,t), z(u,d,t)\right). \tag{8}$$

If there is no information about user coordinates, we consider that they have "undefined value" Δ (all three at the same time).

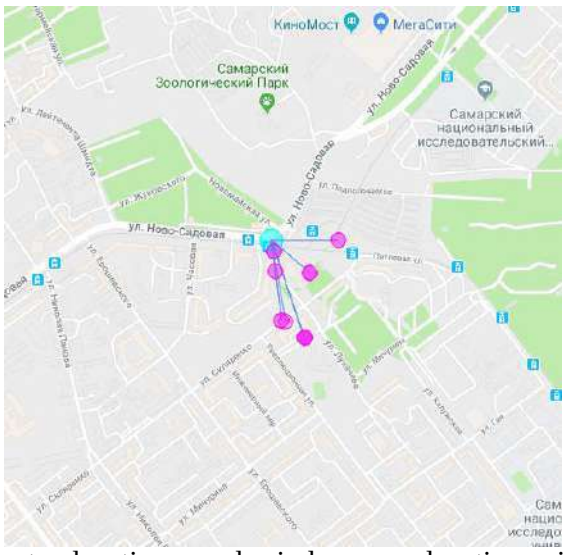

Figure 1. Blue circle – stop location, purple circles – user location points at request time.

3. Mobile application and support service data, «informal preferences» options

For the mobile service "Pribyvalka-63" data for analysis are presented as follows:

- stop data (identifiers and coordinates);
- route information (identifiers and stop identifier list);

- data on the vehicle (identifiers), location coordinates (with a frequency of 2 times per minute), the destination to routes;

- coordinates of users and request parameters are recorded during requests (request results are not saved, since they can be restored from vehicle traffic data) in the form: $ID(s),d,t,\quad ID(u),\mathbf{x}(u,d,t)$;

- user response to the request is not saved.

Based on the presented data, the following two options "user preferences" seem appropriate (we consider the user known):

- user-preferred stops at specific space-time coordinates (Figure 1);

- user-preferred "transport correspondence", also considered in the space-time context. "Transport correspondence" refers to the actual movement from one stop to another, the route chosen and the route vehicle type. Information about the "starting" and "end" stops of a particular user is optional (derived) information (Figure 2).

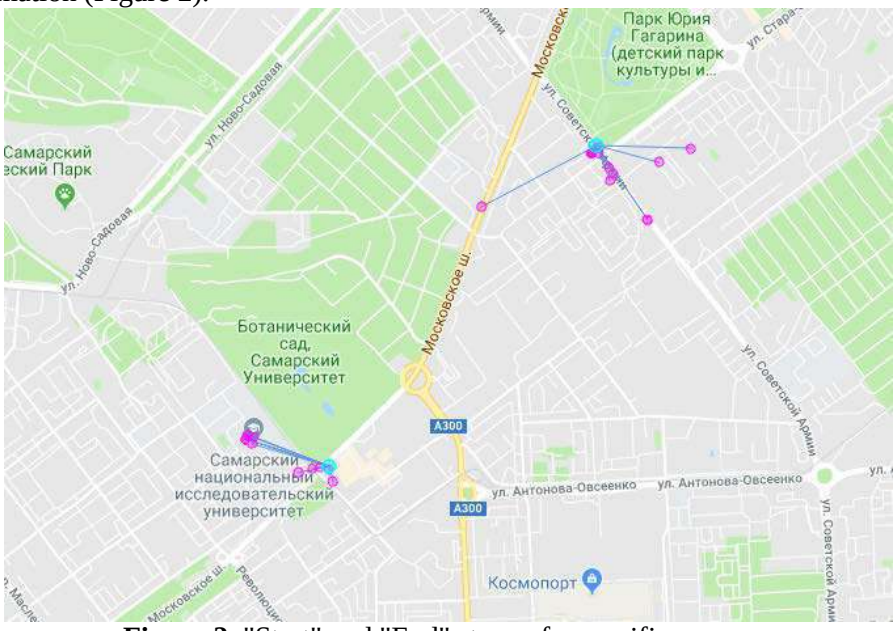

Figure 2. "Start" and "End" stops of a specific user.

4. Methods

4.1 *User-preferred stops*

The task of determining "user-preferred stops" when it is in certain space-time coordinates can be formalized as follows.

Let given precedent set (training examples) for a specific user. Each precedent is a set of space-time context vector-description and the corresponding "answer" (in our case, the stop identifier). It is necessary for the newly received space-time context vector-description of the new situation (which may be absent in the list of precedent examples), to indicate the most "suitable (s) / relevant (s)" answer (s), if necessary, ordering them by degree relevance.

For the case of a single issued response, the described task is a well-known classification theory [19, 20] or machine learning [7, 21], where, according to the object/situation description, the system should indicate the object/situation class as a feature vector. Any recognition algorithm can be represented as two consecutive operators. The first operator translates the description of the object into a numerical value characterizing the "degree of membership" to the class. And the second, according to the indicated value, refers to a specific class [22]. In statistical methods of recognition, the posterior probability [19] is used as a numerical value, in algebraic [23] - estimates, in neural network - the output of the last layer of neurons, etc. Denote the specified numeric value $\Gamma(\mathit{features};\mathit{class})$.

Thus, the formal formulation of the problem for a specific user $u \in \mathrm{U}$ can be represented as follows (where $z \equiv ID(s)$).

Given:

a) precedent set in the form $\{\mathbf{x}_i, d_i, t_i; z_i\}_{i \in \Im}$. (feature vector; answer)

b) feature vector of the new situation $\mathbf{x}, d, t$.

It is necessary: for the specified vector $\mathbf{x}, d, t$ to determine the permutation of objects $\sigma : \mathrm{N}_{|S|} \to \mathrm{N}_{|S|}$ from an ordered set (stops) $\mathrm{S} = \{s_1, s_2, \ldots, s_{|S|}\}$ such that

$$\Gamma\left(\mathbf{x}, d, t; ID\left(s_{\sigma(1)}\right)\right) \geq \Gamma\left(\mathbf{x}, d, t; ID\left(s_{\sigma(2)}\right)\right) \geq \ldots \geq \Gamma\left(\mathbf{x}, d, t; ID\left(s_{\sigma(|S|)}\right)\right). \quad (9)$$

The result for the user is an ordered stops list:

$$s_{\sigma(1)}, s_{\sigma(2)}, \ldots, s_{\sigma(|S|)}. \quad (10)$$

The formal quality measure of the final decision:

$$\Gamma_{\Sigma} = \sum_{i=1}^{|S|} \frac{1}{i} \Gamma\left(\mathbf{x}, d, t; ID\left(s_{\sigma(i)}\right)\right). \quad (11)$$

Solution:

Theory of pattern recognition and machine learning offers a variety of methods for solving the problem. In this paper, we use an approach based on the calculating estimates idea proposed by Yu. I. Zhuravlev [23] and nonparametric estimation of Parzen probability density [19]. Set the value $\Gamma(\mathit{features}; \mathit{class})$, characterizing feature vector belongs to a class

$$\Gamma(\mathbf{x}, d, t; z) = \sum_{i \in \Im} \mu(\mathbf{x}, d, t; \mathbf{x}_i, d_i, t_i) I(z_i = z), \quad (12)$$

where

$$\mu(\mathbf{x}, d, t; \mathbf{x}_i, d_i, t_i) = I\begin{pmatrix} (w(d) \in W_0 \wedge w(d_i) \in W_0) \vee \\ (w(d) \in W_1 \wedge w(d_i) \in W_1) \end{pmatrix} \cdot \exp(-\alpha |t - t_i|) \cdot \exp(-\beta \|\mathbf{x} - \mathbf{x}_i\|). \quad (13)$$

Event indicator:

$$I(a) = \begin{cases} 1, & a = \mathit{true}; \\ 0, & a = \mathit{false}. \end{cases} \quad (14)$$

The values $\alpha, \beta \in \mathbb{R}_+$ - some coefficients, $|t - t_i|$ - a numerical value (for example, the number of seconds), which characterizes the difference between t, t_i. As a result, the algorithm for solving the problem of determining "user-preferred stops" will be as follows:

Step 1. For all stops from the set S calculate the values (12):

$$\Gamma(\mathbf{x}, d, t; ID(s_i)), \quad i = \overline{1, |\mathrm{S}|}. \quad (15)$$

Step 2. The values set obtained in (15) is ordered in descending order — a permutation is formed $\sigma : \mathrm{N}_{|S|} \to \mathrm{N}_{|S|}$ (9).

The resulting permutation is the solution of the problem. An ordered list of stops is provided to the user (10).

«Cold Start» Solution:

To solve the "cold start" problem, the precedent set as follows supplements the initially empty precedent set:

$$\{(\mathbf{x}_i, d0, t0; ID(s_i))\} \cup \{(\mathbf{x}_i, d1, t0; ID(s_i))\}, \quad i = \overline{1, |\mathrm{S}|}, \quad (16)$$

where $t0$="0h00min", $d0$ and $d1$ are the dates, respectively, of the weekend and working days preceding the system launch date, and $\mathbf{x}_i \left(i = \overline{1, |\mathrm{S}|}\right)$ - stop coordinates $s_i \left(i = \overline{1, |\mathrm{S}|}\right)$. Analysis of

expressions (12) - (13) shows that with such "starting" data, the contribution of the time component $\exp\left(-\alpha\left|t-t_i\right|\right)$ in expression (12) will be the same, and the differences in values $\Gamma(\ldots)$ will be completely determined by differences in Euclidean distances from the point $\mathbf{x}$ to the stops coordinates $\mathbf{x}_i\ \left(i=\overline{1,|\mathrm{S}|}\right)$. Thus, the value $\Gamma\left(\mathbf{x},\ldots;ID(s)\right)$ will be more significant when s closer to $\mathbf{x}$.

4.2 User-preferred "transport correspondence"

The task of determining the user-preferred "transport correspondence" can be presented as the task of estimating the probability characteristics (relative frequency) of correspondences. That is, the movements from the stop *s*1 to the stop *s*2, in the space-time context. The following values are important (all characteristics are related to the behavior of a particular user u):

- $p_u\left(t\middle|s1,s2,m,\mathrm{W}_a\right)\ \left(m\in\mathrm{M}(s1,s2),\quad a=\overline{0,1}\right)$ - correspondence time distribution density *s*1→*s*2 with the route choice *m* on the weekday W_a; the density function corresponds to the "boarding time" on the route vehicle, and is indicated to stop *s*1;
- $p_u\left(t\middle|s1,s2,\mathrm{W}_a\right)$ - correspondence time distribution density *s*1→*s*2 on the weekday W_a;
- $P_u\left(s1,s2\middle|\mathrm{W}_a\right)$ - correspondence probability *s*1→*s*2 on the weekday W_a;
- $P_u\left(m\middle|s1,s2,\mathrm{W}_a\right)$ - probability of choosing the route *m* for implementing the correspondence *s*1→*s*2 on the weekday W_a;
- $P_u\left(m\middle|\mathrm{W}_a\right)$ - probability of choosing the route *m* for implementing the correspondence on the weekday W_a;
- $P_u^*\left(s\,|\,\mathrm{W}_a\right)$ - the probability that the stop s is the "end/start".

Additional information about user behavior can be obtained from additional data:

- $p_u\left(\rho\,|\,\mathrm{W}_a\right)$ - distances distribution that the user is able to overcome without using route vehicles;
- $p_u\left(\tau\middle|\rho,\mathrm{W}_a\right)$ - time distribution that the user spends in overcoming the corresponding distance.

All specified values can be calculated on potential user correspondences data collected by the recommender system:

$$\left\{s_i^{start},s_i^{end},m_i^j,k_i^j,t\left(d,m_i^j,k_i^j,s_i^{start}\right),\tau_i^*,\sigma_i^*\right\}_{i\in I_d} \tag{17}$$

for each day *d* and user. Where s_i^{start},s_i^{end} - correspondence data, information about the route m_i^j,k_i^j $t\left(d,m_i^j,k_i^j,s_i^{start}\right)$ - vehicle arrival time RI at the stop $s_i^{start},\tau_i^*,\sigma_i^*$ - mean and standard deviation of potential boarding on the vehicle.

5. Experiments

The presented method software implementation was written in Python. The results were visualized based on Google Maps. The experiments used "Pribyvalka-63" mobile application and tosamara.ru service data.

The database obtained during the experiments, contains information about requests 57190 users. Each user is represented by a unique identifier *ID*(*u*), which is defined by the device ID hash code and is impersonal. The database contains a total of 4103161 user requests for an arrival forecast at a public transport stop. From 1478 stops of the tosamara.ru service, users made requests to 1417 stops.

For the experiments, we selected common user requests that represent the average user of the service. Maps with different parameters $\alpha,\beta\in\mathbb{R}_+$ and request time were built to visualize the results of the proposed approach. The color of the area on the map corresponds to the first stop from the ordered list (10). An example of determining the preferred stop for the user is shown in Figure 3.

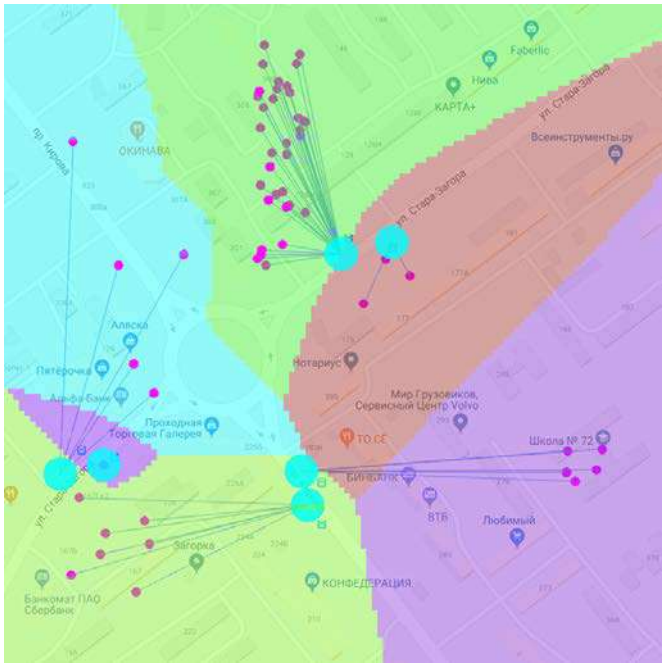

Figure 3. Preferred stops map depending on user location.

Leave-One-Out cross-validation was applied to obtain statistical indicators characterizing the quality of the proposed algorithm. The partitions number $C_{|\Im|}^{1}$ of the user requests set in this case is equal to $|\Im|$, and the classification accuracy is calculated as follows:

$$Accuracy = \frac{1}{|\Im|}\sum_{i\in\Im} I\left(z_i \equiv ID(s_{\sigma_i(1)})\right)\cdot 100\% \tag{18}$$

where the indicator $I(a)$ corresponds to (14).

Also, another method was implemented for comparison with the proposed algorithm, in which the user was offered the nearest stop, without taking into account previous requests. The proposed algorithm accuracy was 93%, for the nearest stop algorithm - 65%.

6. Conclusion

In this paper, we presented the informal and mathematical problem formulations of defining user preferences. Users take public transport route in a personalized recommendation system task. We showed the results of an experimental study. An algorithm was developed using pattern recognition and machine learning methods. The determining the user preferred transport correspondence task was formalized and an approach to its solution was specified.

7. References

[1] Chorus C G, Molin E J E and Van Wee B 2006 Use and effects of Advanced Traveller Information Services (ATIS): A review of the literature *Transport Reviews* **26** 127-149

[2] Agafonov A A and Myasnikov V V 2018 Numerical route reservation method in the geoinformatic task of autonomous vehicle routing *Computer Optics* **42(5)** 912-920 DOI: 10.18287/2412-6179-2018-42-5-912-920

[3] Agafonov A A, Yumaganov A S and Myasnikov V V 2018 Big data analysis in a geoinformatic problem of short-term traffic flow forecasting based on a K nearest neighbors method *Computer Optics* **42(6)** 1101-1111 DOI: 10.18287/2412-6179-2018-42-6-1101-1111

[4] Agafonov A and Myasnikov V 2015 Traffic flow forecasting algorithm based on combination of adaptive elementary predictors *Communications in Computer and Information Science* **542** 163-174

[5] Arentze T A 2013 Adaptive personalized travel information systems: A bayesian method to learn users' personal preferences in multimodal transport networks *IEEE Transactions on Intelligent Transportation Systems* **14** 1957-1966
[6] Nuzzolo A, Crisalli U, Comi A and Rosati L 2015 Individual behavioural models for personal transit pre-trip planners *Transportation Research Procedia* 5 30-43
[7] Portugal I, Alencar P and Cowan D 2018 The use of machine learning algorithms in recommender systems: A systematic review *Expert Systems with Applications* **97** 205-2 27
[8] Campigotto P, Rudloff C, Leodolter M and Bauer D 2017 Personalized and Situation-Aware Multimodal Route Recommendations: The FAVOUR Algorithm *IEEE Transactions on Intelligent Transportation Systems* **18** 92-102
[9] Eiter T, Krennwallner T, Prandtstetter M, Rudloff C, Schneider P and Straub M 2016 Semantically Enriched Multi-Modal Routing *International Journal of Intelligent Transportation Systems Research* **14** 20-35
[10] Mikic Fonte F A, López M R, Burguillo J C, Peleteiro A and Barragáns Martínez A B 2013 A Tagging Recommender Service for Mobile Terminals *Information and Communication Technologies in Tourism* (Springer Berlin Heidelberg) 424-435
[11] G. March J 1978 Bounded Rationality, Ambiguity, and the Engineering of Choice *Bell Journal of Economics* **9** 587-608
[12] Campigotto P and Passerini A 2010 Adapting to a realistic decision maker: Experiments towards a reactive multi-objective optimizer *Lecture Notes in Computer Science (including subseries Lecture Notes in Artificial Intelligence and Lecture Notes in Bioinformatics)* **6073 LNCS** 338-341
[13] Zhang J and Arentze T 2013 Design and implementation of a daily activity scheduler in the context of a personal travel information system *Lecture Notes in Geoinformation and Cartography* 407-433
[14] Braunhofer M and Ricci F 2017 Selective contextual information acquisition in travel recommender systems *Information Technology and Tourism* **17** 5-29
[15] Braunhofer M, Elahi M and Ricci F 2015 User Personality and the New User Problem in a Context-Aware Point of Interest Recommender System *Information and Communication Technologies in Tourism* (Springer International Publishing) 537-549
[16] Guo S and Sanner S 2010 Real-time multiattribute Bayesian preference elicitation with pairwise comparison queries *Journal of Machine Learning Research* **9** 289-296
[17] Pan S J and Yang Q 2010 A Survey on Transfer Learning *IEEE Transactions on Knowledge and Data Engineering* **22** 1345-1359
[18] Myasnikov V V 2012 Method for detection of vehicles in digital aerial and space remote sensed images *Computer Optics* **36** 429-438
[19] Fukunaga K 1990 *Introduction to statistical pattern recognition* (San Diego: Academic Press)
[20] Vorontsov K V *Machine Learning* URL: http://www.machinelearning.ru/wiki/ (date of the application 10.11.18)
[21] Bishop C M 2006 *Pattern Recognition and Machine Learning* (Springer)
[22] Zhuravlev Yu I and Nikiforov V V 1971 Recognition Algorithms Based on Estimation Calculation *Cybernetics* **3**
[23] Zhuravlev Yu I and Gurevich I B 1989 Pattern recognition and image recognition *Recognition, classification, forecast. Mathematical methods and their application* **2**

Acknowledgments
The work was funded by the Ministry of Science and Higher Education of the Russian Federation (unique project identifier RFMEFI57518X0177).

Algorithm for constructing three-dimensional Barcodes to represent nD spatial objects in GIS

D E Andrianov[1], S V Eremeev[1] and Y A Kovalev[1]

[1]Vladimir State University named after Alexander Grigorievich and Nikolai Grigorievich Stoletovs, Gorky street, 87, Vladimir, Russia, 600000

e-mail: yurko02@mail.ru

Abstract. The article describes the algorithm for creating three-dimensional Barcodes to represent nD features. The algorithm is based on computer topology methods using the 3D sweep hull algorithm for computing convex hulls and Delaunay triangulation. The result of the algorithm are 3D Barcodes of features. 3D Barcode graphs were built that reflect their time differences.. The algorithm for constructing 3D Barcodes will allow analyzing spatial nD objects at different time intervals.

1. Introduction

Currently, geographic information systems mainly work with vector 2D maps. But now, the information on 2D maps is not enough for a more detailed analysis of the terrain, so GIS is increasingly beginning to include the ability to process 3D maps.

The relevance of the work lies in the fact that the existing algorithms for processing and storing 3D map data work exclusively with coordinates, which significantly increases the processing time of such objects. It is proposed to apply computer topology methods using the 3D sweep hull algorithm to develop an algorithm for constructing 3D Barcodes that will allow storing and quickly processing data on spatial objects in GIS [1, 2, 3].

There are various algorithms for handling nD features. In [4], an algorithm is presented that allows processing nD objects. The meaning of the algorithm is to simulate n-dimensional characteristics (time and scale) as additional geometric dimensions perpendicular to the spatial objects, creating a higher order model in the use of intervals, on the basis of which 2D models are raised to the following dimensions. These intervals are obtained from the cell complex (topological space) and they are divided into smaller ones. Extrusion is a widely used method in GIS for creating simple 3D models. Starting from the planar partition of the polygons and the height interval associated with each of them, it generates a set of spatially-decomposing rectangular polyhedra, assuming that each polygon exists over its entire segment. For example, a set of building trails and related heights are squeezed into a set of simple prismatic buildings [5, 6, 7].

The authors of [8] were builded the foundation for the integration of five dimensions into one formal presentation of data. The formal definition of geographic data in the 5D conceptual continuum

will most effectively manage and query geographic data using one integrated approach. In addition, it will ensure consistency in scope and time.

This approach led to a new theory and method for geodata, as well as technologies that implement multidimensional partitioning. Integration of multidimensional geodata concepts allows to use of common geometry and embedded topological, temporal and scale structures through full 3D + time + scale splitting.

But these algorithms are based on the use of coordinates of objects, which significantly slows down their processing.

In this work, three-dimensional Barcodes will be built on the basis of data from spatial objects from a 3D map. The resulting Barcodes will be compared with 2D Barcodes for vector maps. The advantages of the developed algorithm can be considered as the speed of work, the ability to work with three-dimensional maps, as well as to store object changes over time.

2. Algorithm for constructing 3D Barcodes for nD features in GIS

The algorithm of building 3D Barcodes is based on the 3D sweep hull algorithm [9]. This algorithm is also called the Newton apple shell, and it functions as follows:

1. Sort a set of points $\{x, y, z\}$ in the sequence $z \to x \to y$.
2. Starting with the first of the sorted points, the points are connected, until a triangle of the area is formed to form an array. The process of connection occurs by building a ball around each point.
3. New points are sequentially added to the array. The edges of the array are triangles, which are represented as a list with information about adjacency. The process of adding a new point to the array includes determining which triangular faces are visible to the new point and replacing them with new triangles made using the new point and closing the edges in terms of the new point.
4. Next, a non-intersecting triangulation of the set of triangles is created.
5. Adjacent pairs of triangles of this triangulation must be “inverted” in order to create Delaunay triangulation from the original non-overlapping triangulation.

The algorithm generates Delaunay triangulation together with a three-dimensional convex hull for a set of points.

The construction of the Barcode itself takes place by analogy with 2D Barcodes as described in [10]. The object barcode $B = \{(x_i, l_i)\}$, where, $i = 1,2\ldots,n$ is the hole number, n is the number of holes, x_i is the coordinate of the beginning of the object’s Barcode hole, l_i is the length of the object’s Barcode hole.

A distinctive feature is the addition of the third component in the Barcode which is a time t. Taking into account the added time, Barcodes for different periods of time are combined on each radius into a single component.

Accordingly, 3D Barcodes, built on the basis of data on nD objects, will look like this: $B = \{(x_i, l_i, t_i)\}$, where t_i is a certain period of time in which the object was changed [11, 12].

Also 3D Barcode can have another third component line, for example, scale s.

Then the Barcode will look like: $B = \{(x_i, l_i, s_i)\}$, where s_i is the scale on which the feature is displayed.

3D Barcode can be built not only for one object, but also for their group. In this case, the coordinates of the entire group of objects will be perceived as a single object.

Consider the construction of 3D Barcode on an example. Figure 1 shows a 3D feature. Figure 2 shows the 3D Barcode for the object shown in Figure 1.

The graph of Figure 2 shows the Barcode length on the axis *x*, the Barcode radius on the axis *y*, and the year of change on the axis *z*.

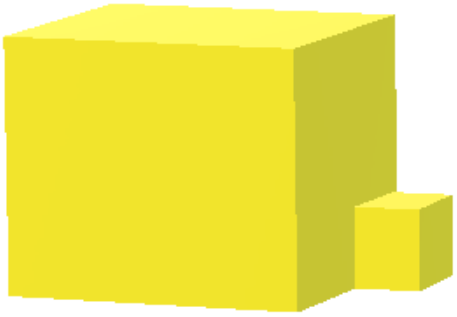

Figure 1. Example of a 3D object.

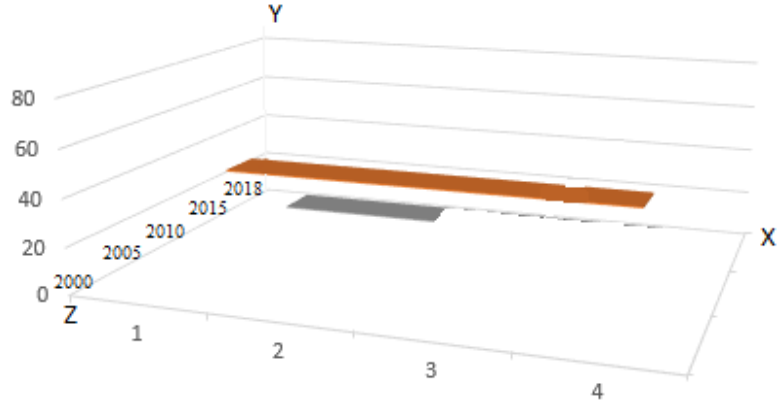

Figure 2. 3D Barcode.

3. The results of the algorithm

To carry out the experiment of building 3D Barcode, a tablet of the 1990s was taken, reflected in Figure 3 (a) with the image of a map of the city's terrain. Some of the objects were built in 3D, and Barcode was built for them. Then the plot from this area was taken from Yandex maps for 2018. This area is reflected in Figure 3 (b). For these objects was also built 3D Barcode shown in Figure 3 (c).

a) 

b) 

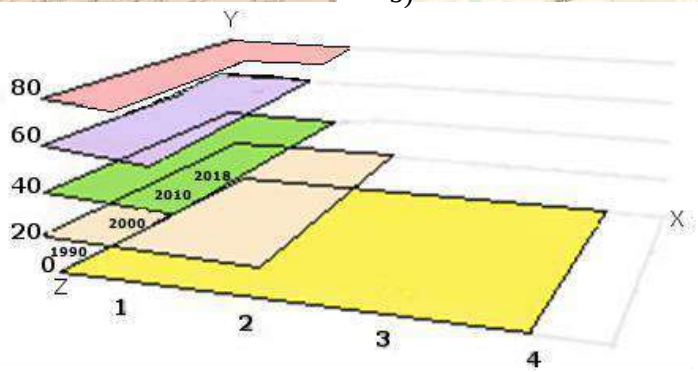

c)

Figure 3. A group of objects and their 3D Barcodes: a-b) Objects that change over time; c) 3D Barcodes of objects in different time intervals.

For comparison, 2D Barcodes were constructed for the objects from Figure 3 (a, b). These Barcodes are shown in Figure 4 (a, b).

a)  b) 

Figure 4. Graph of 2D Barcodes: a) Barcode for objects from figure 3 (a); b) Barcode for objects from figure 3 (b).

When comparing 2D and 3D Barcode graphs, we can conclude that 3D Barcodes are more informative, store more information, and, unlike 2D Barcodes, allow you to quickly access the desired nD object on the map. One of the advantages of the algorithm's performance is the use of Delaunay triangulation for constructing holes of objects, which significantly reduces the processing time of objects.

4. Conclusion

An algorithm for constructing 3D Barcode for nD features developed in the article. It can be applicable to all vector maps, including 3D maps.
Unlike 2D Barcode, this algorithm takes into account an additional characteristic which is a time. This allows to track changes in nD features over the years.
In the future, the algorithm will also be able to use the scale as an additional characteristic, which will significantly reduce labor costs when working with vector maps.
The developed algorithm is also useful in real estate. It will allow to search for the best terrain for building buildings, estimate the time of building objects, as well as analyze areas for missing buildings.

5. References

[1] Eremeev S V, Andrianov D E and Komkov V A 2013 Algorithms for the formation of a graph model of an urban area in a GIS *Geoinformatics* **4** 19-24
[2] Zhilin Li and Qi Zhou 2012 Integration of linear and areal hierarchies for continuous multi-scale representation of road networks *Intern. J. of Geographical Information Science* **26** 855-880
[3] Herbei and Radulov I 2015 Topology of spatial data *In 15th International Multidisciplinary Scientific GeoConference SGEM* **2(2)** 87-94
[4] Arroyo Ohori K, Ledoux H and Stoter J 2015 A dimension independent extrusion algorithm using generalised maps *International Journal of Geographical Information Science* **29(7)** 1166-1186
[5] Myasnikov E V 2017 Hyperspectral image segmentation using dimensionality reduction and classical segmentation approaches *Computer Optics* **41(4)** 564-572 DOI: 10.18287/2412-6179-2017-41-4-564-572
[6] Afanasyev A A 2017 Hybrid methods of automated identification of changes in landscape cover according to the data of remote sensing of the Earth under noise conditions *Computer Optics* **41(3)** 431-440 DOI: 10.18287/2412-6179-2017-41-3-431-440
[7] Pechenkin V V 2017 Optimization of placement of observation tools in a three-dimensional scene in order to minimize “blind zones” *Computer Optics* **41(2)** 245-253 DOI: 10.18287/2412-6179-2017-41-2-245-253
[8] Peter van Oosterom and Jantien Stoter 2014 5D Data Modelling: Full Integration of 2D/3D Space, Time and Scale Dimensions *Techncial University of Delft* **1** 2-16
[9] Dr David A Sinclair 2016 A 3D Sweep Hull Algorithm for computing Convex Hulls and Delaunay Triangulation **1** p 26

[10] Kovalev Y A, Eremeev S V and Andrianov D E 2018 Algorithm for searching for differences in spatial objects that change over time, based on Barcode *International Conference on Soft Computing and Measurements* **1** 481-483
[11] Boissonnat J-D, Srikanta K C and Tavenas S 2015 Building Efficient and Compact Data Structures for Simplicial Complexe *An extended abstract appeared in the proceedings of SoCG* **1** p 230
[12] Edelsbrunner H and Mucke E P 1994 Three-dimensional alpha shapes *ACM Trans Comput Graphics* **13** 43-72

Acknowledgments
The reported study was funded by RFBR and Vladimir region according to the research project № 17-47-330387.

Tree state category identification for boreal area conifers using global features estimation by fuzzy logic approach

A S Pyataev[1,2], A Y Redkin[2] and A V Pyataeva[1,3]

[1]Reshetnev Siberian State University of Science and Technology, Krasnoyarsky Rabochy Av., 31, Krasnoyarsk, Russia, 660037
[2]Brunch of FBI «Russian Centre of Forest Health» – Centre of Forest Health of Krasnoyarsk Krai, Akademgorodok, 50A, building 2, Krasnoyarsk, Russia, 660036
[3]Siberian Federal University, Svobodny pr., 79, Krasnoyarsk, Russia, 660041

e-mail: anna4u@list.ru

Abstract. Tree state category identification allows forecasting forest development in the surveyed area. Tree state category determination process based on global features is subjective and uses concepts such as the degree of density of the crown, the degree of drying of branches, the fall of the bark, the color of the needles, etc. For global features estimation, fuzzy logic is used. To formalize these subjective concepts, linguistic variables and their terms were extracted. The characteristic functions describing the terms were piecewise linear and in this work were approximated by Gaussian functions. Such an approach in conjunction with image processing algorithms that allows to search objects on images or correct images obtained for example from unmanned aerial vehicles could be the basis of a system for automatically determining the forest plantations health state and improve the inspection quality. The study was conducted for coniferous species of the boreal zone. The mathematical model built in this work allows reducing the cost of automation of calculations related to the processing of the data obtained by forest pathological surveys, despite the fact that the accuracy value of fuzzy classification after the approximation of the membership functions remained at the same level.

1. Introduction

Determining the tree state category by a set of visual marks is widely used in forest health diagnostics to estimate sanitary conditions of forest plantations. This estimation based on forest health diagnostics results allows to planning forest protection events system, which contains preventive, protective and exterminatory actions. Tree sanitary condition estimation correctness depends on forest health engineer experience and qualification. Forest health engineer such estimation made uses subjective concepts such as crown density, conifer shades, defoliation grade, etc.

In Russia, eleven categories of tree sanitary status are allocated. This is defined by the Russian Federation Government Resolution No. 607 of May 20, 2017 “On the Rules of Sanitary Safety in Forests”. The paper considers the signs of only the first six tree state categories, since the last five categories are beyond the scope of the research interests, because they characterize fallen trees. Fallen trees include windfall, windbreak, snowbreak and emergency trees. The difficulty of the tree state category determination depends on fuzzy, subjective concepts, on the basis of which the forest health engineer makes conclusions about assigning the tree to one or another category.

To formalize such subjective concepts in our approach we use fuzzy logic. Nowadays, fuzzy logic is widely used in various fields of human activity: from environmental issues [1] to applied problems of disaster impact assessment [2]. In forest development tasks, fuzzy logic is used for estimation of the plants growth potential [3], for forest cuttings types classifications [4], in problems of forest fire forecasting and detection [5, 6], in problems of forest protection [7].

Tree state category division based on symptom analyses, which could be separated by local and global. The presence of hollows, conifer damage, burns, etc. could be classified as local symptoms. At the same time, crown density, conifer shades, growth size, defoliation grade, shrinking branches grade and bark falling could be classified as global symptoms. Global symptoms description subjectiveness generates difficulties and dissensions when tree state categories are being estimated. Global symptoms determination approach based on fuzzy logic designed to fix this problem. Such an approach in conjunction with image processing algorithms that allows to search objects on images [8, 9] or correct images [10] obtained for example from unmanned aerial vehicles could be the basis of a system for automatically determining the forest plantations health state.

2. Theoretical research

In paper [11] were extracted linguistic variables and terms, shown in table 1, to formalize subjective concepts of global symptoms determination. Terms domain and definition are built in cooperation with Krasnoyarsk centre of forest health specialists.

Table 1. Linguistic variables and its terms.

Linguistic variable	Terms
crown density	rich, sparse, openwork, very openwork
growth	normal, reduced, small, very small or nonexistent
shrinking branches grade	nonexistent, dry unitary branches, crown drying out less than 2/3 volume, crown drying out more than 2/3 volume
bark falling	nonexistent, partial, full
conifer shade	green, light green, yellow green, flavescent, yellow, red-brown, gray

The characteristic functions, describes terms, were piecewise linear (figure 1) and specified in tabular form. Such form of function description makes it difficult to automate calculations. One of the problem solutions is to approximate piecewise linear functions by a smooth function.

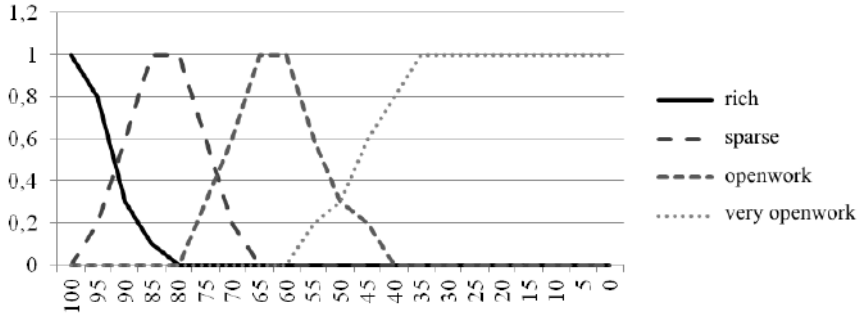

Figure 1. The linguistic variable «crown density» terms graphics.

Approximation methods are actively used in different fields of study to solve various problems. In paper [12] derived a new finite dimensional semidiscrete approximation scheme for systems of linear neutral delay-differential equations and proved convergence results. Paper [13] considers a fuzzy data approximation method defined at a 3D fuzzy data set. A fuzzy smoothing bicubic spline approximation for a given fuzzy data set is defined and the approximation error using similarity measures of fuzzy numbers is estimated. Study [14] considers the use of the convolution method for constructing approximations comprising fuzzy number sequences with useful properties for a general fuzzy number. It shows that this convolution method can generate differentiable approximations in finite steps for fuzzy numbers with finite non-differentiable points. Paper [15] considers a smoothing

method of a set of points to be approximated from a given boundary value problem for the modified Helmholtz equation. In paper [16] the context interpolation algorithms for multidimensional signals in the compression problem are investigated. Interpolation algorithm based on context modeling for the hierarchical compression method for arbitrary dimension signals is proposed. The algorithm is based on optimizing parameters of the interpolating function in a local neighborhood of the interpolated sample. Wherein locally optimal parameters, which, were found for more sparse scale signal levels, are used to interpolate samples of less sparse scale signal levels.

In our paper, we carried out a spline approximation of previously corrected characteristic functions with Gauss functions. The original piecewise linear functions were presented in tabular form. The aim of the approximation made was to find functions that are as close as possible to the original piecewise linear functions, wherein the functions obtained should keep classification quality.

The approximation functions received could be used not only for pine, but for every boreal coniferous species. Gauss function spline approximation result for linguistic variable «crown density» terms graphics shown in table 2.

Table 2. Linguistic variable «crown density» characteristic functions

Term	Characteristic functions
Rich	$f(x)=\begin{cases}1/\exp\left[(x-97)^2/32\right], & x\le 97\\ 1, & x>97\end{cases}$
Sparse	$f(x)=\begin{cases}1/\exp\left[(x-82)^2/50\right], & x\le 82\\ 1, & x\in(82,87)\\ 1/\exp\left[(x-87)^2/32\right], & x\ge 87\end{cases}$
Openwork	$f(x)=\begin{cases}1/\exp\left[(x-55)^2/50\right], & x\le 55\\ 1, & x\in(55,70)\\ 1/\exp\left[(x-70)^2/50\right], & x\ge 70\end{cases}$
Very openwork	$f(x)=\begin{cases}1, & x<40\\ 1/\exp\left[(x-40)^2/50\right], & x\ge 40\end{cases}$

Figure 2 considers approximated graphics for each term. X-axis contains crown density percent and Y-axis describes assurance degree.

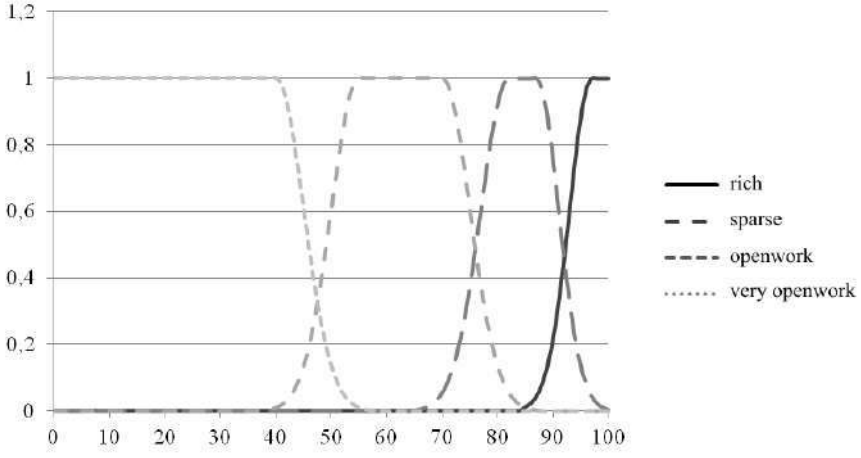

Figure 2. The linguistic variable «crown density» approximated terms graphics.

Characteristic functions approximation made similarly for the rest of linguistic variables. Figure 3 shows previously corrected piecewise linear terms graphics and approximated terms graphics:

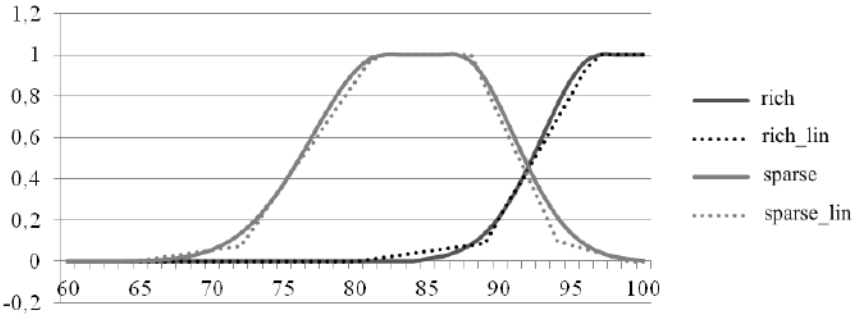

Figure 3. Comparison of the piecewise linear and approximated graphics for terms.

Fuzzy rules knowledgebase has been produced on linguistic variables characteristic functions. Fuzzy rules examples that allow making a conclusion about the state category of the surveyed tree are given below:

- IF («crown density» = «rich») AND («growth» = «normal») AND («shrinking branches grade» = «0») THEN («state» = «healthy»).
- IF («crown density» = «openwork») AND («growth» = «small») AND («shrinking branches grade» = «from 10% to 65%») THEN («state» = «severely weakened»).

According to the approximation results, there was no significant change neither in the clear output value, nor the degree of confidence in the introduction of fuzziness, nor the triggering force of the rules, nor the type of output figure. The reason for this was similarity of the approximating functions and the original piecewise linear functions, so the quality of the fuzzy classification has not been changed.

3. Conclusion

In this paper, a mathematical model is constructed allows describing subjective concepts that influence on the formation of a conclusion about the tree sanitary condition. A spline approximation of the initial characteristic piecewise linear functions by Gauss functions was performed to solve the problem of estimating the category of the coniferous trees of the boreal zone according to global features based on fuzzy logic. The mathematical model built in this work allows reducing the cost of automation of calculations related to the processing of the data obtained by forest pathological surveys, despite the fact that the accuracy value of fuzzy classification after the approximation of the membership functions remained at the same level.

4. References

[1] Saadoud D, Hassani M, Peinado José Martin F and Saïd Guettouche M 2018 Application of fuzzy logic approach for wind erosion hazard mapping in Laghouat region (Algeria) using remote sensing and GIS *Aeolian Research* **32** 24-34

[2] Ahmed S, Abed M and Mebarki A 2018 Post-earthquake assessment of buildings damage using fuzzy logic *Engineering Structures* **166** 117-127

[3] Strnad D, Kohek Š and Kolmanič S 2018 Fuzzy modelling of growth potential in forest development simulation *Ecological Informatics* **48** 80-88

[4] Samec P, Caha J, Zapletal M, Tuček P, Cudlín P and Kučera M 2017 Discrimination between acute and chronic decline of Central European forests using map algebra of the growth condition and forest biomass fuzzy sets: A case study *Science of The Total Environment* **599-600** 899-909

[5] Garcia-Jimenez S, Jurio A, Pagola M, Miguel De L, Barrenechea E and Bustince H 2017 Forest fire detection: A fuzzy system approach based on overlap indices *Applied Soft Computing* **52** 834-842

[6] Lin H, Liu X, Wang X and Liu Y 2018 A fuzzy inference and big data analysis algorithm for the prediction of forest fire based on rechargeable wireless sensor networks *Sustainable Computing: Informatics and Systems* **18** 101-111
[7] Zeng X, Chen C, Liu A, Wei H, Zhang H, Huang G and Wu Y 2018 Planning a sustainable regional irrigated production and forest protection under land and water stresses with multiple uncertainties *Journal of Cleaner Production* **188** 751-762
[8] Zakharov A A, Barinov A E, Zhiznyakov A L and Titov V S 2018 Object detection in images with a structural descriptor based on graphs *Computer Optics* **42(2)** 283-290 DOI: 10.18287/2412-6179-2018-42-2-283-290
[9] Vizilter U V, Gorbatsevich V S, Vishnyakov B V and Sidyakin S V 2017 Object detection in images using morphlet descriptions *Computer Optics* **41(3)** 406-411 DOI: 10.18287/2412-6179-2017-41-3-406-411
[10] Kozak A V, Steinberg B Y and Steinberg O B 2018 Fast restoration of a blurred image obtained by a horizontally rotating camera *Computer Optics* **42(6)** 1046-1053 DOI: 10.18287/2412-6179-2018-42-6-1046-1053
[11] Pyataev A 2018 Tree state category identification for pine based on fuzzy logic by visual data *Proc. Int. Conf. Regional problems of earth remote sensing* (Krasnoyarsk)
[12] Fabiano R H and Catherine Payne 2018 Spline approximation for systems of linear neutral delay-differential equations *Applied Mathematics and Computation* **338** 789-808
[13] Gonzalez P, Idais H, Pasadas M and Yasin M 2018 3D fuzzy data approximation by fuzzy smoothing bicubic splines *Mathematics and Computers in Simulation*
[14] Huang H, Congxin W, Jialian X and Dongxiao Z 2017 Approximation of fuzzy numbers using the convolution method *Fuzzy Sets and Systems* **310** 14-46
[15] Kouibia A, Pasadas M, Reyah L and Akhrif R 2019 Approximation of surfaces by modified Helmholtz splines *Journal of Computational and Applied Mathematics* **350** 262-273
[16] Gashnikov M V 2018 Interpolation based on context modeling for hierarchical compression of multidimensional signals *Computer Optics* **42(3)** 468-475 DOI: 10.18287/2412-6179-2018-42-3-468-475

Automatic search for vanishing points on mobile devices

E V Myasnikov[1,2]

[1]Samara National Research University, Moskovskoe Shosse 34A, Samara, Russia, 443086
[2]Image Processing Systems Institute of RAS - Branch of the FSRC "Crystallography and Photonics" RAS, Molodogvardejskaya street 151, Samara, Russia, 443001

e-mail: mevg@geosamara.ru

Abstract. The vanishing point is a point in the plane of the perspective image, in which the projections of mutually parallel lines of three-dimensional space converge. Automatic search for vanishing points in images is a rather complicated task, the solution of which is not currently possible on mobile devices without introducing additional restrictions. In this paper, a rather simple method is proposed for solving this problem, which operates under two main constraints. One of these limitations is the analysis of the Manhattan scenes. Another is the fusion of information received from mobile device sensors. Modeling was performed using a public open data set to evaluate the characteristics of the proposed solution.

1. Introduction

Vanishing points are some of the most important objects in three-dimensional computer vision. The vanishing points are points in the plane of a perspective image, in which the projections of mutually parallel lines of three-dimensional space converge. The search of vanishing points can be one of the stages in assessing the orientation and position of a camera [1], reconstructing three-dimensional scenes [2], and can be used in many applications related to these tasks [3,4].

Images with corrected geometric distortion are used to search for vanishing points. As a rule, the automatic search for vanishing points is performed in several stages. At the first stage, the line segments are selected on images. On the second stage, the lines are divided into groups corresponding to different vanishing points. Finally, the calculation of the positions of the corresponding points is performed.

Unfortunately, the automatic search for vanishing points is quite a difficult task, the solution of which is not currently possible on mobile devices without introducing additional restrictions. In the present paper, a rather simple method is proposed for solving this problem, which operates under two main constraints. One of these limitations is the analysis of only Manhattan scenes. Another is the presence of an accelerometer on a device, which makes it possible to estimate the gravity vector.

The search for vanishing points in images of Manhattan scenes is performed in order to find three vanishing points: the vanishing points of vertical lines of facades, as well as horizontal lines of main and side facades. In this case, the vanishing points are selected in such a way that the vectors corresponding to the found vanishing points are orthogonal. In general, the proposed method is based on the idea described in [5], according to which the search for horizontal vanishing points can be performed along the horizon line, defined by a plane orthogonal to the direction to the vertical

vanishing point. Modeling was performed using a well-known open data set [6-8] to evaluate the characteristics of the proposed solution.

The paper is organized as follows. Section 2 provides a description of the developed method of searching the vanishing points. Section 3 describes the modeling methodology and experimental studies, which were conducted using an open data set. The paper ends with a conclusion and a list of references.

2. Method

In general, the proposed method consists in the sequential search of three vanishing points, starting from the point corresponding to the vertical lines of the facades.

At the preparatory stage of the method, the image is pre-processed, including the elimination of geometric distortions. After that, a search of line fragments (segments) is performed on the image. For this purpose, the Hough transform can be used; however, in this work, rather a simple approach is used, which is based on the tracing of contours.

Let us assume that the camera is modeled as a regular pinhole camera (see Fig. 1), and the origin of the coordinate system is aligned with the camera. Let the OX and OY axes form a plane parallel to the image plane, and the OZ axis is orthogonal to it. In this case, the relationship between the coordinates of the point $(X, Y, Z)^T$ in the specified coordinate system and the point $(x, y)^T$ in the image plane is expressed in the form:

$$\begin{bmatrix} x \\ y \\ 1 \end{bmatrix} \sim K \begin{bmatrix} X \\ Y \\ Z \end{bmatrix}$$

where K is the matrix of the internal parameters of the camera, which contains information on the focal length, pixel size, skew, and shift of the image center relative to the optical axis.

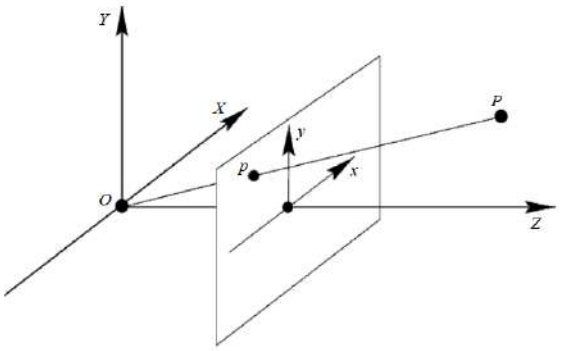

Figure 1. Camera model and coordinate system.

To find the first vanishing point, we use information from the gravity sensor of the mobile device. At this stage, we select such line segments that are in a good agreement with the gravity vector. This selection is carried out by comparing the angle of deviation of each line l_i from the gravity vector g with a predetermined threshold value t:

$$L = \left\{ l_i \left| \arccos\left(\left(l_i^2 - l_i^1\right)^T g \Big/ \left(\left\| l_i^2 - l_i^1 \right\| \|g\| \right) \right) < t \right. \right\}.$$

Here l_i^1 and l_i^2 are the coordinates of the ends of the corresponding line segment l_i.

The selected set of lines L_1 determines the position of the first vanishing point V_1, corresponding to the vertical lines in the image. After finding the first vanishing point, we exclude all the lines corresponding to it from further consideration: $L_2=L/L_1$.

At the second stage of the method, we determine the plane of the horizon line α^h in three-dimensional space as a plane orthogonal to the refined gravity vector (and direction to the first vanishing point) and passing through the origin:

$$V_{11}X + V_{12}Y + V_{13}Z = 0.$$

Next, we define the horizon line Γ in the image plane as the projection of a line passing, for example, through the points with the following coordinates:

$$\Gamma^1 = \begin{bmatrix} -1 \\ (V_{11} - V_{13})/V_{12} \\ 1 \end{bmatrix}, \quad \Gamma^2 = \begin{bmatrix} 1 \\ -(V_{11} + V_{13})/V_{12} \\ 1 \end{bmatrix}.$$

To search for the second vanishing point V_2, we calculate the points p_i of the intersection of all the lines l_i, which were selected on the image $l_i \in L_2$, with the horizon line Γ:

$$p_i = (x_i, y_i),\ p_i \in l_i \wedge p_i \in \Gamma.$$

Then we build the histogram h of the number of intersection points, which fall into different ranges of angles in the polar coordinate system:

$$h_n = \sum_i I\left(\frac{n-1}{N}\pi \le \varphi_i < \frac{n}{N}\pi\right),\ n = 1..N.$$

Here φ_i is the radial coordinate of the intersection point p_i in the plane α^Γ (see figure 2), $\varphi_i = \arccos(\tilde{X}_i)$, and the normalized coordinates $\tilde{P}_i$ are related to the coordinates in the image plane as follows:

$$(\tilde{X}_i, \tilde{Y}_i, \tilde{Z}_i) = (X_i, Y_i, Z_i)/\|(X_i, Y_i, Z_i)\|$$

$$\begin{bmatrix} X_i \\ Y_i \\ Z_i \end{bmatrix} \sim K^{-1} \begin{bmatrix} x_i \\ y_i \\ 1 \end{bmatrix}.$$

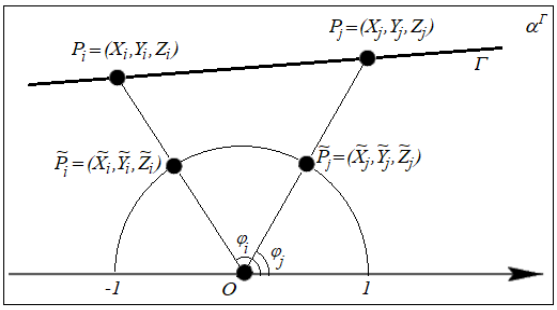

Figure 2. The plain of the horizon line.

An example result of the preparatory stage of the method and the found horizon line are shown in figure 3.

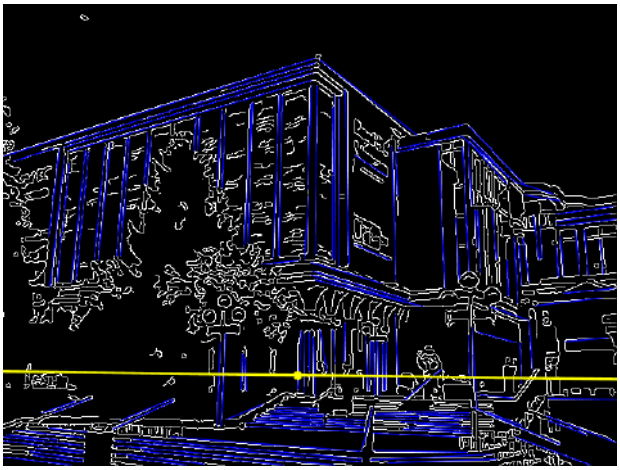

Figure 3. A result of the preparatory stage: the detected contours of the image are shown in white; the selected segments of straight lines are shown in blue. The horizon line found is shown in yellow.

We calculate the approximate position of the second vanishing point as the position of the histogram peak on the horizon line. Further, we refine the position of the second vanishing point using the set of line segments related to the peak on the histogram. Then we exclude the set of lines corresponding to the second vanishing point from further consideration.

The position of the third vanishing point can be found in the same way as the position of the peak on the histogram with the subsequent refinement. However, a faster way to guarantee the orthogonality of the vectors corresponding to the vanishing points is to find a vector, which is orthogonal to the vectors corresponding to the first and second vanishing points:

$$V_3 = V_1 \times V_2 .$$

An example demonstrating the search for the second and third vanishing points is shown in figure 4.

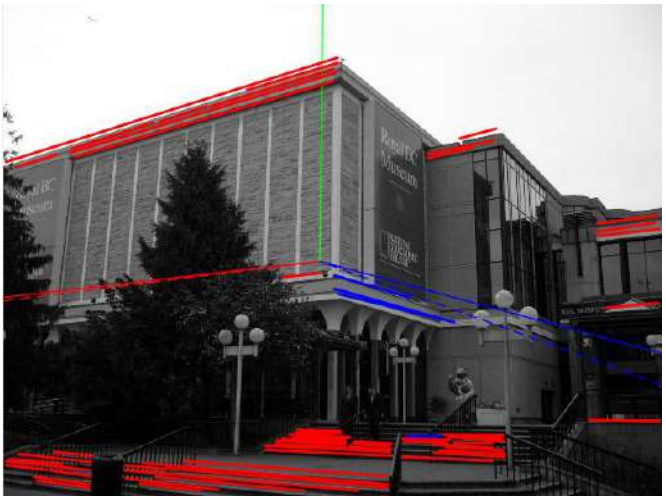

Figure 4. An example of the search for vanishing points: the directions to the true points from the center are shown by thin dashed lines; the directions to the estimated vanishing points are shown in thin solid lines; the segments of lines selected for the second and third vanishing points are shown in bold red and blue lines, respectively.

3. Experiments

This section describes the results of an experimental study of the method described above. For the experiments, we used the public open data set "The York Urban Database" [6-8]. It contains original images and information about camera calibration parameters as well as the true position of vanishing points. The specified data set includes 102 images of urban areas, obtained mainly on the territory of the University of York and in the city of Toronto, Canada.

To estimate the optimal parameters of the developed method, we performed the simulation according to the following scheme:

- for each image of the above data set, we calculated the true gravity vector using the information about the true position of vanishing points;
- we added random vectors (noise) with specified characteristics (uniform distribution in the range [-r; r]) to the obtained gravity vector, and the resulting vector was used as a gravity vector obtained from the sensor of a mobile device;
- we estimated the positions of the vanishing points using the algorithm described above;
- for each vanishing point, we calculated the error as the norm of the vector difference between the estimated and true coordinates of the vanishing points.

The results of the experiments are shown in figure 5 below. Each of the histograms in the figure shows the distribution of the norm of the vector difference between the estimated and true coordinates of the vanishing points. In the ideal case, the histogram has only one leftmost nonzero column, which means minimal deviations of estimated vanishing points from the true values in all experiments. The histogram located in the left column in figure 5.a has a similar appearance.

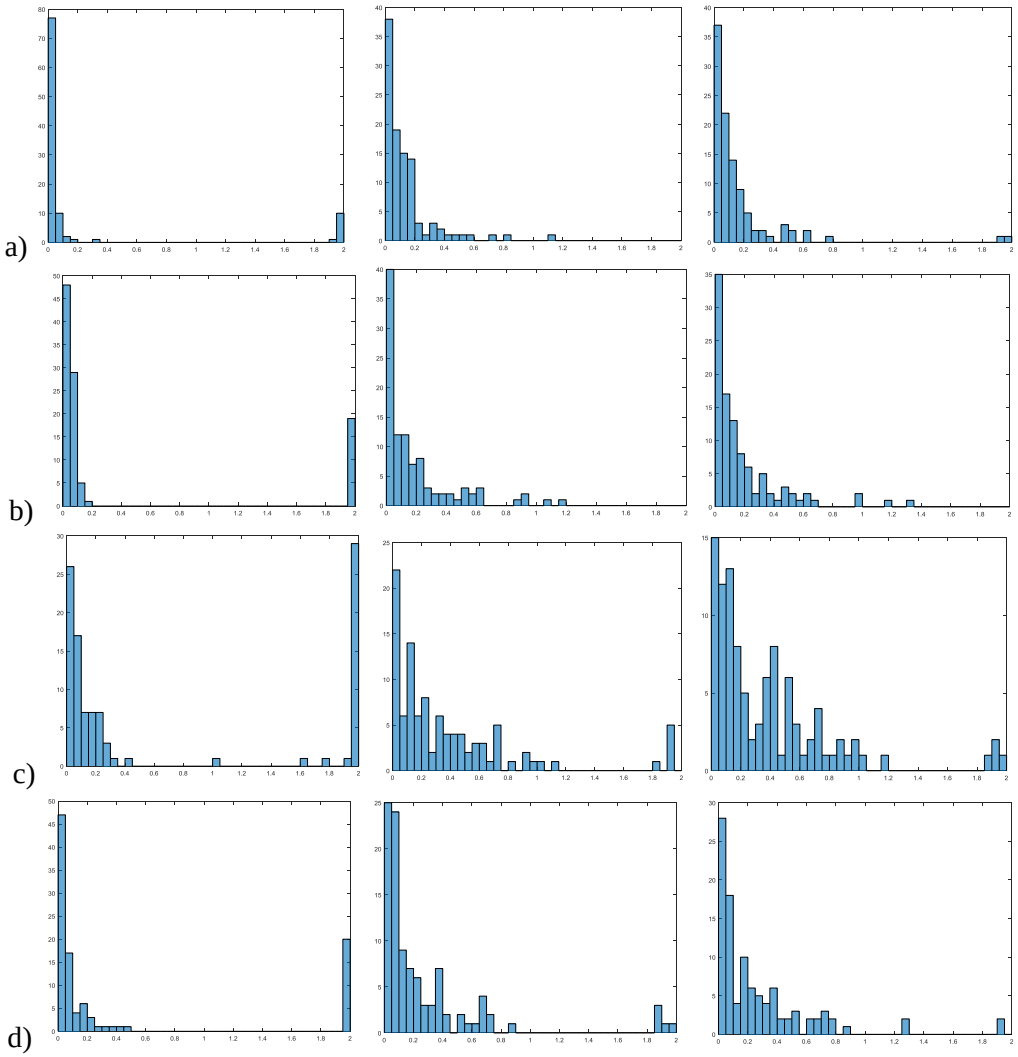

Figure 5. The histogram of deviations of vanishing points. The left column corresponds to the first vanishing point, the middle column corresponds to the second point, and the right column corresponds to the third vanishing point. The rows correspond to different ranges of the noise component: $r = 0$ (a), $r = 0.1$ (b), $r = 0.2$ (c, d). Figures (a)-(c) show the result for more strict selection conditions for line segments: $t = \pi / 50$, $N = 50$. Figure (d) shows the result for soft conditions: $t=\pi/25$, $N=25$.

The presence of a high right column in histograms in figures 5.b and 5.c (left) shows the error in orientation. It means that the direction to the estimated vanishing point is reversed relative to the direction to its true position. Such errors can occur since, for large random deviations of the gravity vector, the algorithm selects lines converging in the opposite direction to the true one.

As can be seen from the results of the experiments, on the one hand, the growth of the noise component causes the expected increase in errors. On the other hand, the growth becomes unacceptable for rather significant random deviations r = 0.2 (see figure 5.c). Such growth can be partially compensated by mitigating the conditions when selecting line segments, as shown in figure 5.d. Here, milder filtering conditions for line segments were used: possible angle deviations were $t = \pi / 25$ compared to the previously used $t = \pi / 50$, and the number of histogram splits was $N = 25$ compared to the previously used $N = 50$.

Thus, the accuracy of the algorithm can be improved in the cases of noisy gravity vector readings by selecting appropriate parameters. Another way to improve the accuracy may consist in the use of previously obtained estimates in the processing of a video stream. This is a subject of future research.

4. Conclusion

The paper proposed and investigated the method of automatic search for vanishing points. This method is based on the combination of information obtained from sensors of mobile devices and images obtained from the camera in the visible range. The simulation was performed using "The York Urban Database" open data set, which allowed evaluating the performance of the method under random deviations in the values of the gravity vector. The method described in the paper is easy to implement and undemanding of computing resources, which allows its use on mobile devices.

In the future, we plan to improve the described method for working with a video stream that allows tracking and refinement of the positions of vanishing points with the aim of evaluating the orientation and position of a camera.

5. References

[1] Caprile B, Torre V 1990 Using vanishing points for camera calibration *International Journal of Computer Vision* **4(2)** 127-139

[2] Lee D C, Hebert M and Kanade T 2009 Geometric reasoning for single image structure recovery *International Conference on Computer Vision and Pattern Recognition (CVPR)* 2136-2143

[3] Xu H, Yang Z, Zhou Z, Shangguan L, Yi K and Liu Y 2016 Indoor localization via multi-modal sensing on smartphones *International Joint Conference on Pervasive and Ubiquitous Computing, ACM* 208-219

[4] Park S, Lee H, Lee S and Yang H S 2015 Line-based single view 3D reconstruction in Manhattan world for augmented reality *International Conference on Virtual Reality Continuum and its Applications in Industry, ACM* 89-92

[5] AngladonV, Gasparini S and Charvillat V 2015 The toulouse vanishing points dataset *Proceedings of the 6th ACM Multimedia Systems Conference (MMSys)* (Portland, United States)

[6] Coughlan J M, Yuille A L 2003 Manhattan world: Orientation and outlier detection by Bayesian inference *Neural Computation* **15(5)** 1063-1088

[7] Denis P, Elder J H and Estrada F 2008 Efficient Edge-Based Methods for Estimating Manhattan Frames in Urban Imagery *Proc. European Conference on Computer Vision* **5303** 197-211

[8] Denis P 2008 Efficient Edge-Based Methods for Estimating Manhattan Frames in Urban Imagery *M.Sc. Thesis* (York University, Canada)

Acknowledgements

The work was partly funded by RFBR according to the research project 17-29-03190 in parts of «2. Method» – «3. Experiments» and by the Russian Federation Ministry of Science and Higher Education within a state contract with the "Crystallography and Photonics" Research Center of the RAS under agreement 007-ГЗ/Ч3363/26 in part of «1. Introduction».

Optimal tuning of the contour analysis method to recognize aircraft on remote sensing imagery

E N Dremov[1], S Yu Miroshnichenko[1] and V S Titov[1]

[1]South-West State University, 50 Let Oktyabrya street, 94, Kursk, Russia, 305040

e-mail: evgeni-dremov@yandex.ru, oldguy7@rambler.ru, titov-kstu@rambler.ru

Abstract. In this paper, we describe the experimental results of aircraft recognition on optical remote sensing imagery using the theory of contour analysis. We propose the a method to calculate optimal values of the contour's items quantity and the classification threshold through measuring within- and between-class distances for all possible training set instances combinations with followed by detection and minimization of the type I and II errors. We discuss the construction of contours' similarity measures combining the principles of finding the most appropriate reference instance and calculating the average value for the whole class. It is shown that the proposed parameters' tuning method and the similarity function make contour analysis capable to train on compact non-uniform datasets and to recognize aircraft on the noisy and less detailed images.

1. Introduction

The mathematical apparatus of contour analysis is an effective approach to solve the problem of objects recognition using their shapes as the distinctive features [1,2].

To reach affine transformation invariance researchers in the field of aircraft recognition use a combination of few features and methods such as contours, Zernike moments and wavelet coefficients in [3], Radon transform, PCA and kNN classification in [4], HOG, graph theory and an object reconstruction in [5].

In contrast, contour analysis uses the single similarity measure of two vector-contours, the module of the normalized dot product (NDP) that is invariant (insensitive) to transfer, rotation, and proportional scaling of the recognized object towards the reference one. The similar recognition methods produce a unique value per each classes pair [6-8] and require an additional clustering procedure to match an object to a certain class. In contrast, the NDP module provides a uniform similarity measure of two contours within the range [0..1] where 1 – denotes the identical instances. Moreover, the NDP itself is a complex-valued number describing contour's scale and rotation angle relatively the reference instance.

Despite the listed above advantages, the NDP has its own limitations, which include the need to select the values of the vector-contour's items quantity and the classification threshold used to decide whether the corresponding object belongs to a certain class.

The first limitation is a consequence of the fact that in order to calculate the NDP value, the compared contours should have the same items' quantity (however, the length of the vector-contours - the sum of its vectors lengths - does not have to be equal). The problem of optimal vector-contour's

items quantity selection is to find a balance between the lower values, smoothing together little-informative details and distinctive features of the recognized object, and higher values, providing more distinctive features but making the instances the single class more unlike [6].

The second limitation arises from the of the classification rule used to decide whether a given vector-contour belongs to one of the classes and consists in the need to select a threshold value corresponding to the minimal similarity value between the reference objects. This value for each class is determined by the differences between the instances in the training dataset.

Comparing to the state-of-the-art convolutional neural networks (CNN) [9, 10], requiring hundreds of images to train, contour analysis's based recognition methods are capable of dealing with compact and nonuniform datasets containing less than 10 instances per class. Moreover, CNNs require transfer learning techniques [11] to operate on images with spectral parameters different from the training ones (for example, created by the sensor of another type). To the contour analysis list of disadvantages, we should write a much shorter range of applications, as the recognition process is driven by the only feature – the object's shape, together with the strong addiction to the segmentation method's quality used to extract the object from an underlying surface [12-15].

This article considers the application of the mathematical apparatus of contour analysis to recognize the aircraft's class on remote sensing imagery. The shape of the aircraft on view from above is the primary distinctive feature determining its class. However, aircraft instances of the same class can have differences in shape due to the following reasons: the presence or absence of the external wing-mounted armament or equipment, the disassembly of aerodynamic surfaces (slats, flaps, rudders), engines and rotary blades, wings with variable geometry, folded wings for naval aircraft. Shape variations can also be caused by the segmentation algorithms that incorrectly react to the boundaries of its illuminated and shaded areas, as well as closely located airfield equipment.

The article has the following structure. Section 2 contains a formal statement of the recognition problem used to determine the list of optimized parameters. Section 3 is devoted to the description of the features of the training and test datasets: the first one serves as a data source to calculate optimal values of the parameters, the second one – to verify results. Section 4 shows the process and the results of the experiment to obtain the value of the classification threshold for each class in training dataset. Section 5 is devoted to the results of the experiment to determine the values of the vector-contour's items quantity required to calculate the NDP value for each class. Section 6 describes the selection of similarity value calculation criterion and the experimental results of the tuned contour analysis method. Section 7 contains a discussion and suggestions for future work.

2. Formalization of the recognition problem

We introduce the following notation:

$\mathbf{C} = \{C_i\}_1^{N_C}$ – is a set of aircraft classes, where C_i – is an aircraft class with index i, N_C – is the number of aircraft classes.

$\mathbf{\Gamma}_i = \left\{\Gamma_{ik}\right\}_{k=1}^{Ni}$ – is a set of reference vector-contours (hereinafter referred to as "references") of *i*-th class, k – is an reference instance index, N_i – is the number of instances in the *i*-th class, Γ_{ik} – instance contour of *i*-th aircraft class with index *k*.

Each instance described by a vector-contour Γ_{ik}, consisting of l complex-valued elements called elementary vectors $\gamma_{ik}(\cdot)$, designated as:

$$\Gamma_{ik} = (\gamma_{ik}(1), \gamma_{ik}(2), ..., \gamma_{ik}(l)).$$

The mathematical apparatus of contour analysis is applicable only to contours with the equal items quantity. In practice, images contain objects that have contours with an arbitrary number of elements. The process to transform the vector-contour to have strictly l elements is called "equalizing" [2]:

$$\Gamma_{ik} \xrightarrow{f_e} \Gamma_{ik}(l), \Gamma_{ik}(l) = \{\gamma_{ik}(n)\}_1^l. \quad (1)$$

The NDP $\eta(\cdot)$ is calculated by the formula:

$$\eta(\Gamma_{ik},\Gamma_{jm},l)=\frac{\left(\Gamma_{ik}(l),\Gamma_{jm}(l)\right)}{|\Gamma_{ik}(l)|\cdot|\Gamma_{jm}(l)|},\ \left(\Gamma_{ik}(l),\Gamma_{jm}(l)\right)=\sum_{n=1}^{l}(\gamma_{ik}(n),\gamma_{jm}(n)), \quad (2)$$

where $\Gamma_{ik}(l)$ and $\Gamma_{jm}(l)$ – are equalized vector-contours, $\left(\Gamma_{ik}(l),\Gamma_{jm}(l)\right)$ – is a vector-contours dot product, $|\Gamma_{ik}(l)|$ and $|\Gamma_{jm}(l)|$ - the norms (lengths) of the corresponding vector-contours.

The operations (2) and (3) with vector-contours are both performed on vectors of complex-valued numbers, which allows achieving the following features [1,3]:

1. The sum of the elementary vectors of a closed contour is zero.
2. Invariance to the transfer (Figure 1): the vector contour does not depend on the parallel transfer within the original image.
3. Invariance to the rotation (Figure 1): rotating an image by a certain angle is equivalent to rotating each elementary vector by multiplying it by a complex factor.
4. Invariance to scaling (Figure 1): changing the image size is equivalent to multiplying each elementary vector by the real scale factor.
5. Changing the starting point leads to a cyclic shift of the vector contour. The NDP is not invariant to the change of the initial point.

The later feature requires to transform the NDP to the cross-correlation function (CCF) of vector-contours, which in addition to the invariance properties of (2) is insensitive to the initial point's shift:

$$\tau(i,j,k,m,l)=\max_{s}\left|\frac{\left(\Gamma_{ik}(l),\Gamma_{jm}^{(s)}(l)\right)}{|\Gamma_{ik}(l)||\Gamma_{jm}(l)|}\right|, \quad (3)$$

where $s=0,...,l-1$ is a shift from to the initial point, $\Gamma_{jm}^{(s)}(l)$ – is a contour obtained from $\Gamma_{jm}(l)$ by the cycle shift of its elementary vectors to *s*-elements.

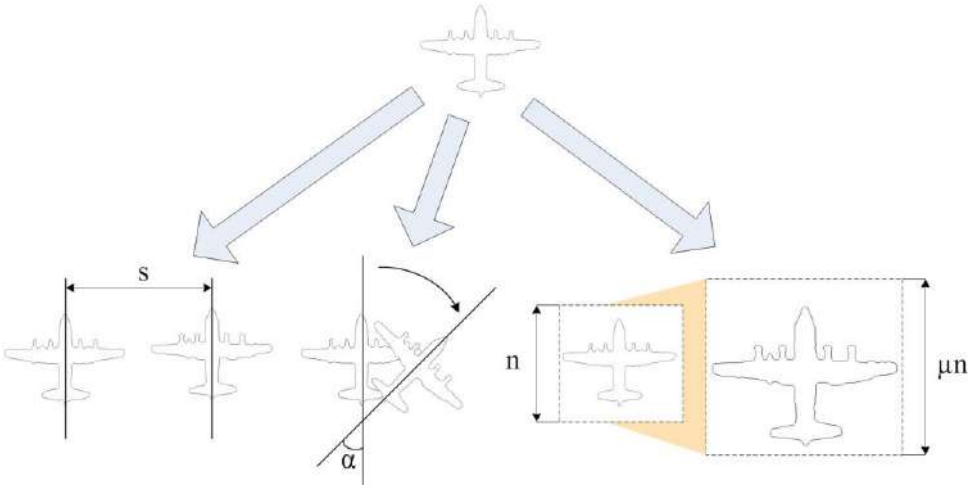

Figure 1. NDP invariance to the transfer, rotation, proportional scaling.

The classification rule to determine the affiliation of a certain contour Γ to C_i class is:

$$C(\Gamma)=\begin{cases}C_i : i=\arg\limits_{i}\left[\max\limits_{i}(f(\Gamma,\mathbf{\Gamma}_i)\geq T_i)\right],\\ \varnothing : \forall i \max\limits_{i} f(\Gamma,\mathbf{\Gamma}_i)<T_i,\end{cases} \quad (4)$$

where T_i – is the classification threshold value for the aircraft of the *i*-th class, $f(\Gamma,\Gamma_i)\in[0,1]$ – is the function for calculation the similarity value of the given vector-contour Γ to the set $\mathbf{\Gamma}_i$ of reference objects.

The function for similarity value calculation can apply one of the two following criteria:

1. Maximum CCF for a vector-contour Γ and one of the reference instances Γ_{ik}:

$$f_1(\Gamma, \mathbf{\Gamma}_i) = \max_{k,s} \left| \frac{\left(\Gamma(l_i), \Gamma_{ik}^{(s)}(l_i)\right)}{|\Gamma(l_i)||\Gamma_{ik}(l_i)|} \right|, \quad (5)$$

where l_i - is the optimal value of the vector-contour's items quantity for *i*-th aircraft class.

2. The mean CCF value for a *i*-th whole class:

$$f_2(\Gamma, \mathbf{\Gamma}_i) = \frac{1}{N_i} \sum_{k=1}^{N_i} \max_{s} \left| \frac{\left(\Gamma(l_i), \Gamma_{ik}^{(s)}(l_i)\right)}{|\Gamma(l_i)||\Gamma_{ik}(l_i)|} \right|. \quad (6)$$

The aim of the article is to create a contour analysis tuning method by the solution of the following problems:

1. Determine the optimal values of the vector-contour's items' quantity $\mathbf{L} = \{l_i\}_{i=1}^{N_C}$ and the classification threshold $\mathbf{T} = \{T_i\}_{i=1}^{N_C}$ in terms of the minimum total number of I and II type errors.

2. Select a criterion to calculate the similarity value of the vector-contour to a set of reference instances $\mathbf{\Gamma}_i$.

3. Dataset details

The dataset we used within the experiment is divided into the training part, used to tune the recognition method's parameters and the test part for the verification.

The training dataset contains aerial images of optical range with a resolution of 0.15 m / pixel displaying the parking of decommissioned and reserved aircraft at the Davis-Monthan airfield [16]. The training dataset is compact and includes 430 images of the aircraft of eight classes: B-1, B-52, C-5, C-37, C-130, C-135, P-3, and S-3.

Figure 2 shows the examples of all 8 aircraft classes of the training dataset. Table 1 lists the characteristics of the classes and the instances' contours.

Figure 2. Image examples of aircraft in the training dataset.

The classes of the training dataset differ significantly from each other both in the number of instances and in the degree of within-class similarity of their contours. An example of a significant difference in the instances is shown in Figure 3 for B-1 class: the nose cone (Figure 3a), the engines (Figure 3b), the slats, flaps, landing shields, rudders, stabilizers (Figure 3c, d) were removed. The other classes (for instance, B-52) have minimal differences in instances.

The described differences in the training dataset require to calculate the optimal values of vector-contours' items quantity and the classification threshold individually for each class.

The test dataset is equivalent to the training one and contains 421 aerial images of three resolution levels: 0.15 (10 images), 0.3 (10 images) and 0.5 meters per pixel (402 images), shot in the Davis-

Monthan and a few operating airfields. Figure 4 shows the examples of the aircraft included in the test dataset (the details of the test dataset are given in Table 2).

Table 1. Characteristics of contours in the training dataset.

Aircraft class	B-1	B-52	C-5	C-37	C-130	C-135	P-3	S-3
Instances count	17	10	20	11	135	81	92	64
Mean items' quantity	1132	1945	2404	1227	1570	1420	1458	1132
Items' quantity histogram	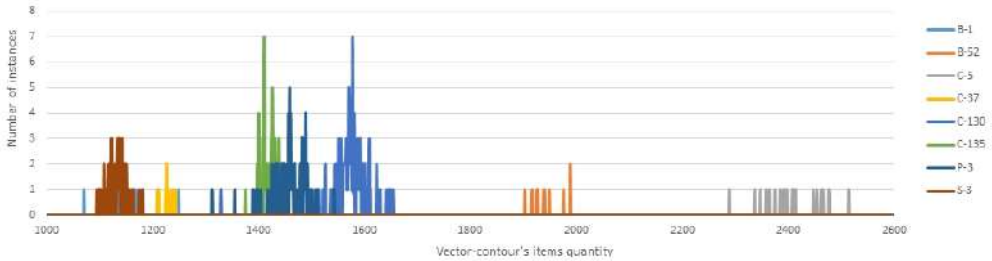							

a)  b)  c)  d) 

Figure 3. Instances of B-1 aircraft having various dismantled elements.

B-1 B-52 C-5 C-37

C-130 C-135 S-3 P-3

Figure 4. Images examples of the aircraft in the test dataset.

Test images of 0.3 and 0.5 meters per pixel (for instance, B-1 and C-130 on Figure 4) have significant visual differences from the training set in contrast and brightness as well as in lighting/shading scheme so the major remaining recognition feature is the shape. Test images of 0.15 meters per pixel were shot on the other season, have greater camera-to-surface angle, differences in color rendition and contain much more noise that seems to be caused by the lossy compression. All the described features of the test dataset strongly affect aircraft contours challenging the robustness of the proposed contour analysis's parameters tuning method.

Table 2. Characteristics of contours in the test dataset.

Aircraft class	B-1	B-52	C-5	C-37	C-130	C-135	P-3	S-3
Instances count	7	6	48	11	57	102	142	49
Mean items' quantity	1263	1884	2441	1177	1483	1315	1345	1084
Items' quantity histogram	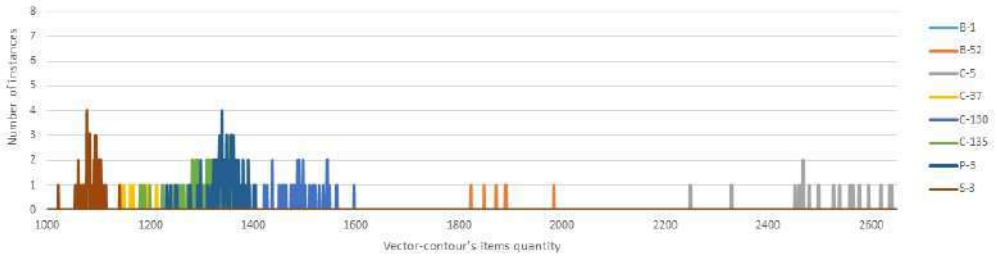							

4. Optimal classification thresholds calculation

To calculate the optimal classification thresholds $\mathbf{T} = \{T_i\}_{i=1}^{N_C}$, the measurements of within-class and between-class distances were made for all possible combinations of training dataset instances.

The measurement of the within-class distance is a calculation of the CCF (3) for a particular non-coincident pair of vector-contours of the same class. The measurement of a between-class distance is a calculation of CCF for a particular pair of vector-contours of different classes.

An error of a within-class distance measuring (type II error or a false negative measure) [17] is the value of within-class distance that is less than the specified value of the classification threshold *T*:

$$e_i(k,m,l,T) = \begin{cases} 1, \tau(i,i,k,m,l) < T \\ 0, \tau(i,i,k,m,l) \geq T \end{cases}. \quad (7)$$

The error in between-class distance measuring (type I error or a false positive measure) [17] is the value of the between-class distance which is greater than the specified value *T*:

$$e_{ij}(k,m,l,T) = \begin{cases} 1, \tau(i,j,k,m,l) > T \\ 0, \tau(i,j,k,m,l) \leq T \end{cases}. \quad (8)$$

It is clear from formulas (7) and (8) that an increase in the threshold value *T* reduces in the number of type I errors but concurrently increases in the number of type II errors and vice versa.

The optimal value for each aircraft class corresponds to the minimum number of type I and II errors for the given range of the vector-contour elements quantity *l*.

The relative type II measurement error (the ratio of the within-class distance measurement errors to their total number) for the *i*-th class with the given *l* and *T* is defined as:

$$E_{IC}(i,l,T) = \frac{N_{IC}(i,l,T)}{N_i \cdot (N_i - 1)}, \quad (9)$$

$$\mathrm{N}_{IC}(i,l,T) = \sum_{k=1}^{N_i} \sum_{m=1, m\neq k}^{N_i} e_i(k,m,l,T), \quad (10)$$

where $\mathrm{N}_{IC}(\cdot)$ – is the number of type II measurement errors.

The relative type I measurement error (the ratio of the between-class distance measurement errors to their total number) is calculated with the formula:

$$E_{BC}(i,l,T) = \frac{N_{BC}(i,l,T)}{N_i \cdot \sum_{j=1, j\neq i}^{N_C} N_j}, \quad (11)$$

$$N_{BC}(i,l,T) = \sum_{j=1, j\neq i}^{N_C} \sum_{k=1}^{N_i} \sum_{m=1}^{N_j} e_{ij}(k,m,l,T), \quad (12)$$

where $N_{BC}(\cdot)$ – is the number of type I measurement errors.

At each classification threshold value, the total relative measurement error $E_{\min}(\cdot)$ is calculated as a minimal sum of relative type I and II measurement errors and represents an objective function [18] to compute an optimal threshold value T for C_i class:

$$E_{\min}(i,T) = \min_{l}\left(E_{IC}(i,l,T) + E_{BC}(i,l,T)\right). \quad (13)$$

The vector-contour elements quantity l varies within the interval $l = [100,...1000]$ with a step of 10. The interval boundaries are explained by the fact that the distinguishing features of the most aircraft in the training dataset are lost at $l < 100$, and $l > 1000$ reaches the minimum quantity of items for some reference instances.

The classification threshold changes within the interval $T = [60,...,80]$ with a step of 1. The interval is chosen according to the following arguments: at $T < 60\%$ many instances of different classes are similar to each other, whereas at $T > 80\%$ a within-class similarity becomes insufficient due to the variety of contour shapes within a single class.

The experimental data was used to create graphs of the total relative measurement error (13) dependence from the classification threshold for each aircraft class. The graphs shown in Figure 5 provide the characteristic features of the most interesting classes of the training dataset. The B-1 class is described by significant differences between its instances, which is confirmed by high values of (13) in the range of 6-12% for the entire graph in Figure 5a with a slight predominance of type II measurement error. The B-52 class graph, on the contrary, demonstrates a rapid decline in type I error at a threshold of 60-70% with the following near-zero type II error on the right side of the graph.

As for the C-130 and P-3 classes of propeller aircraft (Figure 5b), the outwardly similar contours are characterized by close graphs of (13) with the predominance of type I error for C-130 and type II error for P-3.

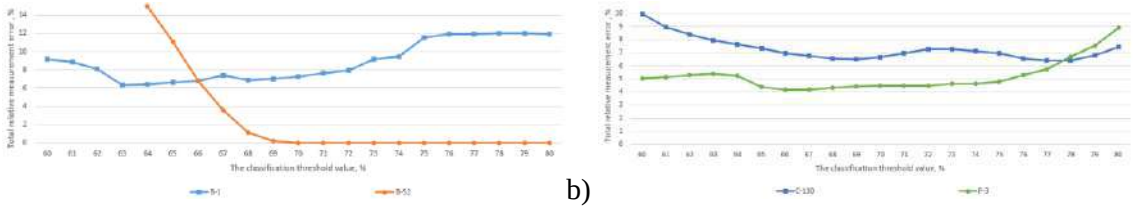

a) b)

Figure 5. Total relative measurement error (13) dependence from the classification threshold for classes B-1 / B-52 (a) and C-130 / P-3 (b).

Formula (13) was used to calculate the optimal classification thresholds $\mathbf{T} = \{T_i\}_{i=1}^{N_C}$ for each class in the training dataset (the results of the calculation are given in Table 3):

$$T_i = \arg\left[\min_{T}(E_{\min}(i,T))\right]. \quad (14)$$

Table 3. Optimal classification thresholds.

Class index	1	2	3	4	5	6	7	8
Class name	B-1	B-52	C-5	C-37	C-130	C-135	P-3	S-3
Optimal value T_i, %	63	71	66	69	69	69	66	74

5. Optimal vector-contour's items quantity calculation

The optimal values of vector-contour's items $\mathbf{L} = \{l_i\}_{i=1}^{N_C}$ for each aircraft class are calculated on the basis of the total relative measurement error using the previously determined threshold $\mathbf{T} = \{T_i\}_{i=1}^{N_C}$.

The sum of the relative measurement errors of type I (9) and II (11) errors represents an objective function to compute an optimal value of the items' quantity l_i for C_i class:

$$E(i,l) = E_{IC}(i,l,T_i) + E_{BC}(i,l,T_i). \quad (15)$$

Graphs (Figures 6-7) show the vector-contour's items optimal quantity corresponding to the minimum of (15) marked with a vertical line. The optimal items quantity for B-1 class (Figure 6a) lies near the intersection of the types I and II error graphs. The errors for a given class vary widely due to

the significant differences in its instances. The B-52 class items optimal quantity (Figure 6b) is determined only by the minimum of type I errors.

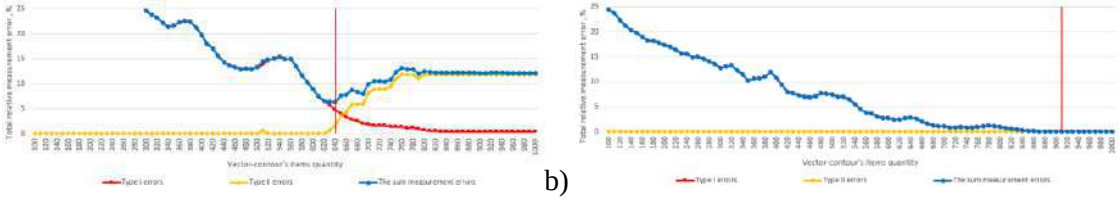

a) b)

Figure 6. Total relative measurement error (15) dependence from the B-1 (a) and B-52 (b) vector-contour's items quantity.

The optimal value of C-130 (Figure 7a) and P-3 (Figure 7b) classes biased towards type II error and is to the right of the intersection of both error graphs. Class C-130 is characterized by a higher total error value compared to P-3 due to more significant differences between the references instances of this class.

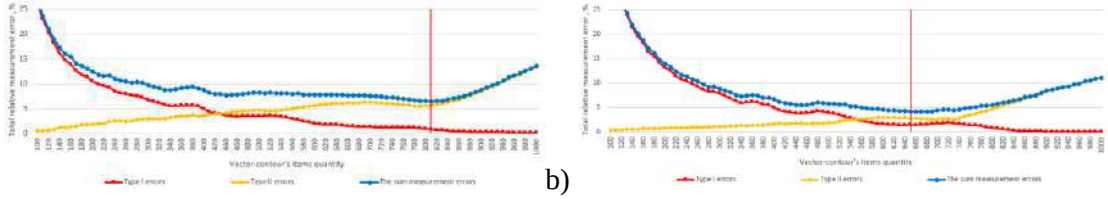

a) b)

Figure 7. Total relative measurement error (15) dependence from the C-130 (a) and P-3 (b) vector-contour's items quantity.

Formula (15) was used to determine the optimal values of vector-contour's items quantity $\mathbf{L} = \{l_i\}_{i=1}^{N_C}$ for each class in the training dataset (the results are presented in Table 4):

$$l_i = \arg\left[\min_{l}(E(i,l))\right]. \quad (16)$$

Table 4. Optimal values of the vector-contour's items quantity.

Class index	1	2	3	4	5	6	7	8
Class name	B-1	B-52	C-5	C-37	C-130	C-135	P-3	S-3
Optimal value l_i	640	910	900	910	810	680	650	580

The proposed optimal items' quantity calculation method was experimentally compared to the most widely used heuristic methods including the use of:

(a) the minimal items' quantity of the certain class's instances to minimize the type II error;

(b) the maximal items' quantity of the certain class's instances to minimize the type I error;

(c) the recognized object's items quantity to retain its actual level of details.

The table 5 represents the total relative measurement error (15) per each aircraft class along with the mean value for all the heuristic methods and the proposed one.

Table 5. The total relative error for the proposed method and for heuristics.

Row name	Total relative error (15), %								
Class index	1	2	3	4	5	6	7	8	Mean error through all classes
Class name	B-1	B-52	C-5	C-37	C-130	C-135	P-3	S-3	
Heuristic (a)	12.18	20.00	38.66	0.09	13.68	7.59	11.97	8.38	14.07
Heuristic (b)	12.18	13.33	26.29	0.09	21.23	3.70	10.00	3.97	11.35
Heuristic (c)	11.49	8.89	19.29	0.15	11.42	2.53	7.32	2.58	7.96
Proposed method	**9.42**	**0.00**	**2.13**	**0.00**	**6.51**	**0.23**	**4.18**	**0.76**	**2.90**

The differences in results of heuristic methods (a-c) for certain classes emphasize the training dataset's irregularity. The best heuristic solution is to use items' quantity of the recognized object, however, the proposed tuning method provides around 3 times less total measurement error.

6. Criterion for similarity value calculation

To estimate the developed parameters tuning method and to select a criterion for the similarity value calculation of a recognized vector-contour Γ to a set of reference instances $\mathbf{\Gamma}_i$, we used the test dataset described in section 2. The test images of 0.3/0.5 meters per pixel resolution are upscaled to 0.15 hence the instances of a certain class have close items' quantities through the whole dataset.

The recognition results for the test datasets obtained by the classification rule (4) in combination with the functions for similarity value calculation f_1 (5) and f_2 (6) are presented in Table 6.

Table 6. The results of test datasets recognition with the classification rule (4) in combination with functions f_1 and f_2.

Class index		1	2	3	4	5	6	7	8	Total
Class name		B-1	B-52	C-5	C-37	C-130	C-135	P-3	S-3	
f_1	Type I errors	0	0	3	0	3	0	1	0	7 (1.66%)
	Type II errors	1	0	0	0	0	0	0	0	1 (0.24%)
	Total errors	*1*	*0*	*3*	*0*	*3*	*0*	*1*	*0*	**8 (1.9%)**
f_2	Type I errors	1	0	2	0	0	29	0	0	32 (7.6%)
	Type II errors	5	5	6	11	45	39	31	1	143 (33.9%)
	Total errors	*6*	*5*	*8*	*11*	*45*	*68*	*31*	*1*	**175 (41.5%)**

Function (5) performs much better than (6) that is explained by the fact our parameters tuning method uses a similar to (5) pair-wise within-class and between-class distance calculation rule to define type I and II measurement errors.

To reduce errors number we modified the classification rule (4) to combine the functions (5) and (6), integrate their merits and mutually compensate shortcomings. The modified classification rule becomes the following:

$$C(\Gamma)=\begin{cases} C_i : i=\arg\left[\max_i(f_2(\Gamma,\mathbf{\Gamma}_i)\ge T_i)\right], \\ C_i : i=\arg\left[\max_i(f_1(\Gamma,\mathbf{\Gamma}_i)\ge T_i)\right],\ \forall i\ \max_i f_2(\Gamma,\mathbf{\Gamma}_i)<T_i\ , \\ \varnothing : \forall i\ \max_i f_1(\Gamma,\mathbf{\Gamma}_i)<T_i, \end{cases} \tag{17}$$

The results of the test datasets recognition with the modified classification rule (17) are presented in Table 7.

Table 7. Test dataset recognition results with modified classification rule (17).

Class index		1	2	3	4	5	6	7	8	Total
Class name		B-1	B-52	C-5	C-37	C-130	C-135	P-3	S-3	
$f_1 + f_2$	Type I errors	0	0	1	0	0	0	0	0	1 (0.24%)
	Type II errors	1	0	0	0	0	0	0	0	1 (0.24%)
	Total errors	*1*	*0*	*1*	*0*	*0*	*0*	*0*	*0*	**2 (0.48%)**

The remaining type II error for the contour analysis method belongs to class B-1 and indicates the need to expand its training dataset with instances of the operating (non-disassembled) aircraft. The type I error for C-5 is explained by the segmentation algorithm fault.

7. Conclusion and discussion

In this paper, we presented the results of the experiment aimed to tune the contour analysis method to recognize aircraft on aerial imagery. We calculated optimal values of the vector-contour's items quantity and the classification threshold through measuring within- and between-class distances for all possible training set instances combinations with the following detecting and minimization of type I and II errors. It is shown that each class has its own optimal values of these parameters due to the features of the reference instances of the training dataset. We proposed a classification rule that combines the merits of functions based on the best instance match and the mean CCF for class respectively.

The vectors of further research are the development of new segmentation methods that allow solving the aircraft edges detection problem upon the conditions of camouflage, poor contrast with the underlying surface, illuminated and shaded areas, as well as close-lying airfield equipment.

8. References

[1] Furman Ya A, Krevetskii A V and Peredreev A K 2002 *An Introduction to Contour Analysis: Applications to Image and Signal Processing* (Moscow: Fizmatlit) p 592
[2] Furman Ya A, Yuriev A N and Yanshin V V 1992 *Digital Methods for Processing and Recognizing Binary Images* (Krasnoyarsk: Publishing House of Krasnoyarsk University) p 248
[3] Hsieh J W, Chen J M, Chuang C H and Fan K C 2005 Aircraft type recognition in satellite images *Vision, Image and Signal Processing* **152** 307-315
[4] Liu G, Sun X, Fu K and Wang H 2013 Aircraft recognition in high-resolution satellite images using coarse-to-fine shape prior *IEEE Geoscience and Remote Sensing Letters* **10** 573-577
[5] Wu Q, Sun H, Sun X, Zhang D, Fu K and Wang H 2015 Aircraft recognition in high-resolution optical satellite remote sensing images *IEEE Geoscience and Remote Sensing Letters* **12** 112-116
[6] Veltkamp R C 2001 Shape matching: similarity measures and algorithms *Proc. Int. Conf. on Shape Modeling and Applications* (Geneva: SMI) 188-197
[7] Gostev I M 2010 Geometric correlation methods for the identification of graphical objects *Physics of Particles and Nuclei* **41** 27-53
[8] Zakharov A A, Barinov A E, Zhiznyakov A L and Titiv V S 2018 Object Detection in Images with a Structural Descriptor Based on Graphs *Computer Optics* **42(2)** 283-290 DOI: 10.18287/2412-6179-2018-42-2-283-290
[9] Ronneberger O, Fischer P and Brox T 2015 U-net: convolutional networks for biomedical image segmentation *Int. Conf. on Medical Image Computing and Computer-Assisted Intervention* **9351** 234-241
[10] He K, Zhang X, Ren S and Sun J 2016 Deep residual learning for image recognition *Conf. on Computer Vision and Pattern Recognition* (Las Vegas: Conference Publishing Services) 770-778
[11] Pan S J and Yang Q 2010 A survey on transfer learning *Transactions on Knowledge and Data Engineering* **22** 1345-1359
[12] Miroshnichenko S Yu, Degtyarev S V and Titov V S 2009 Detection of object edges in aerospatial cartographic images *Machine Graphics & Vision* **18** 427-437
[13] Gorbachev S V, Emelyanov S G, Zhdanov D S, Miroshnichenko S Y, Syryamkin V I, Titov D V and Shashev D V 2018 *Digital Processing of Aerospace Images* (London: Red Square Scientific, Ltd) p 244
[14] Gonzales R and Woods R 2002 *Digital Image Processing* (London: Pearson Education) p 793
[15] Blokhinov Y B, Gorbachev V A, Rakutin Y O and Nikitin A D 2018 A Real-Time Semantic Segmentation Algorithm for Aerial Imagery *Computer Optics* **42(1)** 141-148 DOI: 10.18287/2412-6179-2018-42-1-141-148
[16] Wikipedia Davis-Monthan Air Force Base URL: https://en.wikipedia.org/wiki/Davis–Monthan_Air_Force_Base (01.02.2019)
[17] Flach P 2012 *Machine Learning: the Art and Science of Algorithms that Make Sense of Data* (Cambridge University Press) p 396

[18] Singiresu S R 2009 *Engineering Optimization: Theory and Practice* (John Wiley & Sons) p 840

Acknowledgments
The authors gratefully acknowledge support by CodLix LLC.

Recognition of forest and shrub communities on the base of remotely sensed data supported by ground studies

A Y Denisova[1], L M Kavelenova[1], E S Korchikov[1], A V Pomogaybin[1], N V Prokhorova[1], D A Terentyeva[1], V A Fedoseev[1,2] and N V Yankov[1]

[1]Samara National Research University, Moskovskoe Shosse 34A, Samara, Russia, 443086
[2]Image Processing Systems Institute of RAS - Branch of the FSRC "Crystallography and Photonics" RAS, Molodogvardejskaya street 151, Samara, Russia, 443001

e-mail: denisova_ay@geosamara.ru

Abstract. The forest and shrub communities are important components of the environment and provide a wide spectrum of ecological services. In the Samara region the forest and shrub cover is dispersed on the territory what makes its monitoring difficult. The forest areas are limited by natural and anthropogenic reasons since Samara region is a forest-steppe territory with a high level of human activity. The shrub communities are mostly the secondary ecosystems incorporated in natural grassy communities, agricultural fields or enclosing to forests. These specific ecosystems can be recognized on remote sensing data including satellite images supported by preliminary ground surveys. In this article, we present the study of the forest and shrub communities recognition using remote sensing images and ground surveys in the Samara region. We describe a process of the test site selection for remote sensing data verification and discuss the results of applying the author's classification technology for multispectral remote sensing composites to classify forest communities in the Samara region.

1. Introduction

Forest ecosystems are effectively involved in biosphere stabilization, planetary biodiversity conservation, environmental management provision being a valuable part of the natural wealth of the Russian Federation. In Russia, forest conservation is better organized than in other countries of the world. However, the forests of the Russian Federation European part show clear negative changes associated with deterioration of their qualitative composition, age and species structure as well as the forest formation changes and the biodiversity reduction [1]. This fact provides the hopefulness of forest communities monitoring using remote sensing (RS) imagery aiming to obtain operational and independent observations of the current territory state.

In Russian Federation forest monitoring results are used at different management levels. At the state level, forest monitoring tasks include "... operational monitoring of changes in the forest fund conditions caused by the forest use, natural and man-made impacts on forests, processing and analysis of these data, making forecasts for the forest protection and conservation, the forest resources rational use and the sustainable development of the forest sector of the Russian economy". The legal basis for forest monitoring is the Establishment of the Council of Ministers of the Russian Federation dated November 24, 1994 N 1229 entitled "On the creation of a unified state system of environmental

monitoring" and the decision of the Interdepartmental Commission on Environmental Safety of the Security Council of the Russian Federation dated June 16, 1994 N 8, which recognized the need of forest monitoring system development and implementation a as part of a unified state system of environmental monitoring [2]. At the regional level, the functions of forest monitoring include the development and adaptation of methodology and software for organizing and conducting forest monitoring taking into account the specific features of the region [3]. In the Samara region, the forest monitoring tasks can be formulated as the regional verification of the RS data and the development of the forest communities classification technology according to the regional Forest Plan.

This article describes an approach to solve these problems. The approach was developed by the experts in ecology and geoinformatics of Samara University. The approach takes into account the plant communities peculiarities of the Samara region. The article presents the results of the global statistics analysis made using the open information sources about the nature of forest and shrub communities changes in the region. The article describes the steps of the ground control polygons selection for the regional verification of remote sensing data. The article considers the authors' technology of the supervised spatial classification based on seasonal composites of multispectral remote sensing data to define tree species for the test sites. The experimental results of classification technology testing for a territory with a known Forest Plan are also provided. Finally, the article includes some results on the analysis of the Forest Plan classification using verified remote sensing data in order to identify plant community changes.

2. Forest and shrub communities characteristics in Samara region

The tree species dominance in mature forests is determined by geographic latitude changes. There are three main forest regions in Russia such as boreal, hemiboreal and nemoral. The north-eastern part of the Samara region belongs to nemoral forest region. For a nemoral region, the deciduous forests and the forest-steppe landscapes are the most typical [4,5].

According to the climatic conditions, the Samara region is a territory where the transition from forest-steppe to steppe takes place [6]. Since 1996 all the region forests were transferred to the first ecological group corresponding to the ecological situation [7]. In accordance with the forest vegetation zones approved by the order of the Ministry of Agriculture of Russia dated March 9, 2011 No. 61, the forests of the Samara region are assigned to the forest-steppe zone of the forest-steppe region of the European part of Russian Federation. All forests in the region belong to the protected areas in order to preserve the different types of natural resources. The forests play an important sanitary, hygienic, health and other useful roles [8] in the region.

Due to the peculiarities of the regional natural conditions as well as the high anthropogenic transformation of the region, the areas covered with forest are highly fragmented. The whole forest coverage of the Samara region is about 12.8% of the total region area. The forest coverage for the different municipal subregions varies from 2% or less in the southern areas to 22-25% in the northern and northwestern areas [8,9].

From the beginning of the 19th century, the general forests change trends in the Samara region reflect a significant forest transformation. Forest area reduced in more than two times. A clear species composition changes including oak participation decreased and the aspen forests area increased as well as the tree age structure changes were detected. For example, the relict upland forest area and oak forest area continue to decrease in Zhiguli [10].

Figure 1 demonstrates the official statistical data characterizing the general indicators of the forests in the Samara region in recent years. The statistical data reflect a slight decrease and a subsequent return of the forest area indicators to the 2004 level. The more important point of the qualitative forest changes is the reduction in the young and middle-aged forests fraction as well as the increase in the fraction of ripe and over-mature forests.

Figure 1 demonstrates that the species composition changes show the tendencies of the aspen and oak-occupied areas decrease and the simultaneous increase in the fraction of maple, ash, elm, poplar and shrubs-occupied areas.

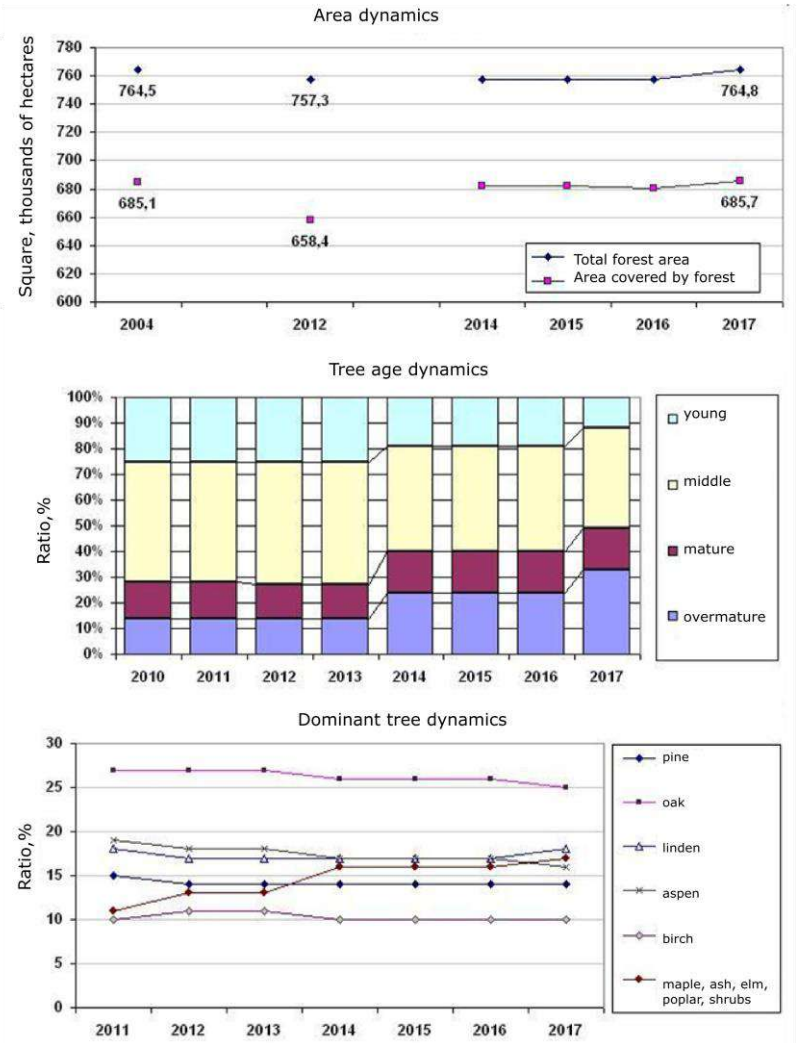

Figure 1. Overall dynamics of forests indicators in the Samara region in recent years (compiled according to the State reports from 2004 to 2017 [6,9-16]).

Thus, the peculiarities of the forest plant communities in the Samara region are:

1. The originality of the vegetation cover in terms of its ecosystem diversity, orographic localization, geology and soil characteristics;
2. The presence of natural forests in the regional forest fund as well as the anthropogenic forests of various types and the secondary forest ecosystems developing during the revitalization of the disturbed areas and fallow lands;
3. The significant heterogeneity of tree plantations in terms of area, localization, species and age composition, increasing due to succession changes;
4. The considerable fragmentation and different affiliation of regional forest fund components.

These peculiarities approve the necessity of a ground reference polygons network with a detailed description in order to classify the regional forest and shrub communities. The reference polygons network will be subsequently used for verification of the methods and algorithms applied to remote sensing data obtained for the territory of the Samara region.

3. Test site selection for remote sensing data verification

To verify the results of manual decryption of remote sensing images and their automatic classification, the reference data must be available. For this reason, the regional network of the ground control polygons is needed to ensure the possibility of the remote sensing data verification and to set up the algorithms and technologies for the remote sensing data analysis taking into account the regional

specifics, i.e. the features of the territory composition and climatic features in the region. Since 2017, the specialists from Samara University have been working on the creation of the ground reference polygons network in the Samara Region. The target vegetation types include plant communities valuable for the regional biological diversity conservation.

In 2018, a group of ecologists from this article authors' team carried out a survey of the new ground control polygons belonging to the category of forest and shrub communities. The ground control polygons are located in the Krasnosamarsky and Novosemeikinsky forests of Samara region. A ground survey was carried out on the homogeneous species composition for these sites that can serve as a refugiums of protected species. For example, the oak and birch forests are the areas where the rare species of orchids and ferns grow.

Three ground control polygons were selected. They are shown in Figure 2. Polygon No. 1 is covered by birch, Polygons No. 2-3 correspond to the oak forests. Polygon No. 2 contains also insignificant birch impurities with the concentration less than 1%. Polygon No. 3 is characterized by the presence of birch and aspen impurities with the impurity concentration up to 10%. Due to the weather conditions in 2018 such as a long and cold spring with a rapid vegetation onset upon the hot weather beginning, the summer field surveys did not capture the phenological moment of the most distinguishable deciduous tree species and this fact was limited the number of surveys in this direction.

Figure 2. Ground control polygons for birch and oak forests (initial ground survey).

The survey of the shrub communities was carried out in the same period and allowed us to identify six polygons in the Bolshechernigovsky and Kinelsky districts of the Samara region. The centers of the selected polygons are shown in Figure 3.

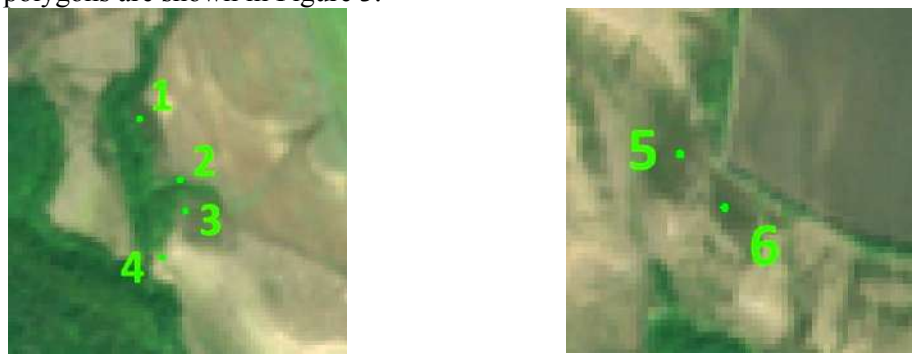

Figure 3. The centers of the ground reference polygons of shrub communities.

In Figure3, Polygon No. 1 and No. 2 represent an unbroken shrub steppe with a projective cover of shrub crowns about 50%. The Polygon No. 1 is characterized by the predominance of Cytisus ruthenicus and Caragana frutex, for the Polygon No. 2 is dominated by Caragana frutex and Amygdalus nana. Polygon No. 3 is a closed shrub steppe with the projective cover of shrub crowns equal to 100% with a predominance of Caragana frutex. Polygon No.4 is the slope with feather grass steppe and does not contain shrubs. Polygon No. 5 is characterized by uneven overgrowing with shrubs with the average projective cover about 80-90%. Polygon No. 5 is characterized by shrubs of Caragana frutex as a monodominant and by an admixture of individual Ulmus foliaceae trees. Polygon No. 6 corresponds to a shrub steppe with the high crowns closeness and projective cover of shrubs

over 80%. The shrubs presented in Polygon No. 6 are 80% of Caragana frutex and 20% of Amygdalus nana. All selected shrub communities were presented by small areas of the size 100 × 100 m and less. Most of the shrub communities were located on the slopes with a noticeable height difference from 3 to 20 m and arranged along the borders of more massive forest and steppe communities.

A survey of shrub communities has shown that due to their secondary nature it is difficult to select fairly large homogeneous areas for them, Figure 4.

Figure 4. General view of the shrub communities, June-July 2018 (upper photos - Bolshechernigovsky, lower photos - Kinelsky district of the Samara region).

In addition, the field surveys have confirmed that shrub communities are poor by rare species of higher plants. However, shrub communities deserve further study because, due to agricultural landscapes environment around, they actually become the shelters for the fauna representatives including protected species of mammalian, birds and insects.

It is obvious that the volume of allocated ground control polygons does not allow confident recognition of the forest and shrub communities due to the small size and the insufficient number of the test sites. However, the information about these polygons can be used to refine the classification results that were obtained by the training based on the geo-information data sources, for example, the maps of the protected natural territories and Forest plan. These data sources cannot be used without clarification due to the long period of update of geo-information data sources and paper cartographic materials. Thus, the clarification using ground control polygons will lead to an increase in the classification accuracy by means of the classification results verification.

4. Supervised local classification technology for detailed forest classification using multi-temporal remote sensing data

In this section, we describe a forest classification technology developed earlier by the part of the authors' team and deliver the results of its application to the forest classification. We selected forest communities as the object of our experimental research because there are available regional Forest Plan data of the 2013-2014 years. The regional Forest Plan gives detailed information on tree species fraction for each forest parcel and can be used to train the classifier. As for the shrub communities, there were not enough amount of detailed ground truth data and the selected ground control polygons were too small to get the proper classification accuracy. Moreover, the small size of the shrub communities requires high-resolution images to be used for classification. But there were no available

high-resolution images at the moment of the research for the test site. Thus, we left the shrub classification for future research.

The classification technology applied in this paper uses the multi-temporal remote sensing image composites as input. From the point of view of the plant-community analysis, the composites of multi-temporal multispectral images obtained during the vegetation season provide a more comprehensive vegetation description because they reflect the differences in vegetation phenology. The classification is based on the spatial processing methods and the pixel-wise classification methods investigated in [17-18]. Originally, the technology was tested for the vegetation classification using hyperspectral data. This fact confirms its applicability to the multidimensional datasets.

4.1. Classification technology

The classifier applies a composite of medium-resolution multispectral images, a training sample mask at the training stage and a test sample mask at the classification stage as input data. The image composite includes all spectral channels of all available cloudless images obtained during the vegetation season. The spectral bands necessarily include the channels related to the near-infrared (NIR) and red (R) spectral ranges characterizing the presence and density of green vegetation. The training sample mask represents an image of class labels defined for the image parts with the known classification. The test sample mask marks the pixels to be classified by the value “1” and “0”, otherwise. The classifier output is an image containing the class labels for each pixel.

The overall classification technology involves the following stages:

1. Feature extraction.
2. Spatial preprocessing.
3. Clustering.
4. Segmentation.
5. Supervised pixel-wise classification.
6. Merging classification and segmentation results.
7. Spatial post-processing.

The feature extraction is performed by the dimension reduction using principal component analysis (PCA) method [19] and data normalization. The latter is used to place the features into the range [-1,1] that simplifies the further pixel-wise classification.

Spatial preprocessing aims to reduce the level of noise in data keeping the edges in image as most as possible. We carry out spatial preprocessing using the median filter of the small size $N \times N$.

Clustering is used to find the groups of pixels with a similar feature description regardless of their spatial arrangement. In this paper, we applied the generalized expectation-maximization (GEM) clustering algorithm to implement this step [20]. GEM algorithm estimates the cluster count and cluster parameters according to the Gaussian mixture model of the data distribution. The algorithm assigns cluster labels according to the maximum conditional probability rule.

During the segmentation stage, a spatial connectivity analysis of the clustering results is provided to obtain the segments that are homogenous in both spatial and feature domains. It is likely that each particular image segment entirely corresponds to one vegetation class. Both stages segmentation and clustering may be implemented as a single segmentation process adapted to the seasonal data processing, for example, using the method [21].

To implement the supervised pixel-wise classification we selected the support vector machine classification with the radial basis functions (SVM-RBF)[22]. This algorithm is one of the best pixel-wise classifiers tested with the hyperspectral images of vegetation [23]. The algorithm is trained using the training sample mask and the training feature image. The classification model obtained after training is used for the further test sample classification.

At the next stage, we perform merging of the pixel-wise classification and segmentation results. For this purpose, the majority voting is used by the segments, i.e. the final class label is the same for all pixels belonging to the same segment and it is defined as the most frequent class label for this segment. The resulting image is spatially much more homogenous than the image after pixel-wise classification.

Finally, spatial post-processing is performed. This kind of spatial post-processing was proposed in [18]. It is organized as the sliding window filter of size $M \times M$ and threshold T. For each window position, the dominant class is defined. If the number of pixels belonging to the window and corresponding to the dominant class exceeds the threshold T and the class label of the current pixel differs from the dominant class label, the current pixel class is substituted by the dominant class label. This spatial post-processing algorithm is an analogue of the median filtration and tends to minimize the amount of singular misclassified pixels.

4.2. Forest classification using the proposed technology

To train our classifier we applied the available Forest plan data as the ground truth information. These data represent a vector map of the forest parcels with the detailed tree species description. However, the last available Forest plan was made during the 2013-2014 years. Since the situation is likely to be changed for the past 5 years, the training sample obtained from the Forest plan might contain errors and lead to the classification inaccuracies as a result.

To estimate the classification accuracy more precisely we performed our study in the following way. We divided the available Forest plan data into the training and control sets. Both sets included the forest parcels occupied mostly with one type of tree species and the dominant tree species fraction was more than 80%. Then, we trained the classifier using the training set and applied it to the control set to estimate the basic achievable classification accuracy. After that, we extracted the largest parcels that were classified differently from the Forest plan data. Extracted parcels were used for the ground survey to discover the reasons for misclassification. Finally, we corrected training and control sets using the ground truth data obtained by the survey and estimated the classification accuracy using the corrected ones.

The experimental research was conducted for the Krasnosamarskoye forestry as a test site. It is the largest forest area in the Samara region. The remote sensing data included 17 cloud-free and atmospherically corrected Sentinel-2 [24] images obtained for the period from April to October 2018. The multi-temporal image composite derived from these images contained 136 components in 8 spectral bands. The spatial resolution of the image composite was 10 meters. We omitted the spectral channels with the original spatial resolution of 60 meters and applied an image sharpening to convert 20-meters channels into 10-meters representation using Scanex Image Processor software [25].

The forest parcels extracted from the Forest plan data included 9 tree classes: birch, elm, oak, willow, maple, aspen, pine, poplar and ash. The vector objects of forest parcels were converted into compatible raster representation i.e. the mask image with the class labels had the same spatial resolution as the remote sensing image composite.

The training and control mask images were generated separately and composed two different pixel sets with empty intersection. We formed our training set by the random selection of pixels from the northern part of the forest. To avoid the classifier adaptation to the particular class distribution, we included the fixed number of pixels per each class into the training set. As a result, our training set contained 2000 pixels per each class. The parcels from the southern part of the forest constituted the control set.

To obtain the classification results we applied the classification technology described above with the following parameters. The number of PCA components used as features was 40 and the pre-processing and post-processing spatial filtration parameters were $N = 3, M = 3, T = 5$. The achieved classification accuracy for the control set was 0.8160. Figure 5 demonstrates the largest 43 misclassified forest parcels. For these parcels, the classification results mismatched the original Forest plan data.

4.3. Classification error analysis

The forest parcels defined as the ground polygons for remote sensing data verification confirmed the correct classification of these parcels using the proposed classification methodology. A large area of these parcels explaines the long-term resistance of their vegetation communities to significant changes. This fact allows us to conclude that the selected ground polygons are suitable for verification

of remote sensing data in a wide time interval if the changes caused by emergency and anthropogenic activities remain minimal for these polygons.

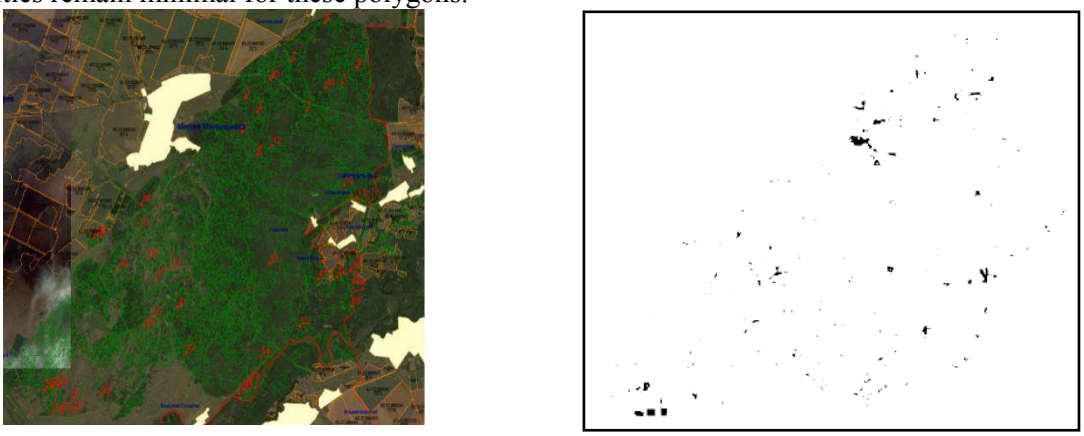

Figure 5. 43 largest forest parcels with classification errors: the map (left) and the mask (right).

As for the forest parcels with an erroneous classification for which the Forest plan data do not coincide with the classification results, we made an additional analysis to identify the causes of the erroneous classification. 13 of the 43 largest forest parcels were selected to be verified by the ground survey that was conducted in the autumn of 2018. The survey included an assessment of the tree species composition and a determination of the current ecosystem status.

The survey demonstrated that 8 from 13 visited parcels have unsatisfactory Forest plan data that do not correspond to the current state of the forest. Figure 6 shows the examples of the changes occurred in the observed forest parcels.

Figure 6. The changes in forest parcels of the Krasnosamarskoye forestry: the loss of old trees and the introduction of young ones (upper images); burned conifer areas (bottom images).

The discovered reasons for the Forest plan data inconsistency are listed below

1. The loss of old trees and the introduction of young ones of other tree species into the emerging places leading to a partial change of the dominant tree species and the spatial distribution pattern of the forest.
2. The burning down of the tree layer as a result of fires in recent years leading to parcel overgrowing by aspen and birch.
3. The young age of conifer in some parcels leading to the different spectral reflection in comparison with the ripe conifer.
4. The inaccuracies in forest parcel partition in the Forest plan used.

5. Conclusion

The research presented in this paper deals with the problem of forest and shrub vegetation communities estimation using remote sensing data in the Samara region. The paper addresses such issues as the ground control polygons selection for the remote sensing data verification, the classification accuracy assessment for the regional forest sites and the reasons for possible misclassification. We conducted our study in three stages including a preliminary ground survey, remote sensing data classification and the classification error analysis supplemented by the final ground survey.

As a result of the preliminary ground survey, a set of ground control polygons corresponding to different forest and shrub communities was selected. These polygons were included in the regional ground control polygons network that can be used for remote sensing data verification in the natural vegetation studies in the Samara region. For the selected polygons, up-to-date description of the vegetation state was described.

During the classification stage, we applied the earlier developed original classification technology. The training and control sets were defined using the available Forest plan data. The classification accuracy achieved was 0.8160.

The classification results analysis made for the selected ground control polygons of forest vegetation showed that the selected polygons are resistant to significant changes over the past 5 years and, therefore, they represent the sustainable plant communities that can be used to verify other classification methods and algorithms of these communities in the Samara region.

To analyze the discrepancy between the classification results and the Forest Plan, an additional ground survey of the largest sites with discrepancies was made. The survey revealed that the classification errors mostly deal with the inaccuracies in the forest parcel boundary of the Forest plan and with the significant changes in the dominant species composition within these areas. Overall classification error analysis confirmed the effectiveness of the forest classification by the technology regarded in this paper since the classification errors highlight the forest parcels with significant tree species changes.

As for the shrub communities, it was found that in the Samara region these communities are arranged in the small places with the significant elevation difference (from 3 to 20 meters). Therefore, the study of shrub communities requires the use of high-resolution remote sensing instruments or unmanned aerial vehicles to obtain the representative remote sensing dataset. The future research is planned to involve these types of data for the shrub communities investigations.

6. References

[1] 2002 *National Strategy for the Biodiversity Conservation of Russia* (Moscow: Ministry of Natural Resources of the Russian Federation) p 129
[2] 1995 *Regulation on forest monitoring. Letter dated 11.29.95, N MG-1-17-6 / 287* (Moscow: Federal Service of Forestry of Russia)
[3] Tarankov V I 2006 *Monitoring of forest ecosystems* (Voronezh: Publishing house of the Voronezh State Forestry Academy) p 299
[4] Smirnova O V 1994 *Eastern European deciduous forests* (Moscow: Nauka) p 364
[5] Smirnova O V, Bobrovsky M V and Khanina L G 2017 *European Russian Forests* (Springer) p 572
[6] 2014 *State report on the state of the environment and natural resources of the Samara region for 2013* (Samara) **24** p 283
[7] Polievktova E V 2007 *Economic Encyclopedia of Russian Regions. Samara Region* (Moscow, CJSC "Economy") p 396
[8] 2018 *Report on the environmental situation in the Samara region for 2017* (Samara) **28** p 226
[9] 2017 *State Report on the State of the Environment and Natural Resources of the Samara Region for 2016* (Samara) **27** p 198
[10] 2015 *State report on the state of the environment and natural resources of the Samara region for 2014* (Samara) **25** p 298
[11] 2005 *State Report On the State of the Environment of the Samara Region in 2004* (Samara) **15** p

214
[12] 2010 *State Report on the State of the Environment and Natural Resources of the Samara Region for 2010* (Samara) **21** p 336
[13] 2012 *State report on the state of the environment and natural resources of the Samara region for 2011* (Samara) **22** p 343
[14] 2013 *The State Report on the State of the Environment and Natural Resources of the Samara Region for 2012* (Samara) **23** p 397
[15] 2016 *State Report on the State of the Environment and Natural Resources of the Samara Region for 2015* (Samara) **26** p 296
[16] 2017 *State Report on the State of the Environment and Natural Resources of the Samara Region for 2016* (Samara) **27** p 198
[17] Borzov S M and Potaturkin O I 2014 Vegetation cover type classification using hyperspectral remote sensing *Vestnik NSU. Series: Information Technologies* **12** 13-22
[18] Fedoseev V A 2018 Hyperspectral satellite image classification using small training data from its samples *Journal of Physics: Conference Series* **1096** 012042
[19] Wold S, Esbensen K and Geladi P 1987 *Principal Component Analysis Chemometrics and intelligent laboratory systems* **2** 37-52
[20] Denisova A Y and Sergeyev V V 2018 EM clustering algorithm modification using multivariate hierarchical histogram in the case of undefined cluster number *Proceedings of SPIE* **10806** 108064H
[21] Plotnikov D E, Kolbudaev P A and Bartalev S A 2018 Identification of dynamically homogeneous areas with time series segmentation of remote sensing data *Computer Optics* **42(3)** 447-456 DOI: 10.18287/2412-6179-2018-42-3-447-456
[22] Zhang T 2001 An Introduction to Support Vector Machines and Other Kernel-based Learning Methods *AI Magazine* **22** 103-104
[23] Bibikov S A, Kazanskiy N L and Fursov V A 2018 Vegetation type recognition in hyperspectral images using a conjugacy indicator *Computer Optics* **42(5)** 846-854 DOI: 10.18287/2412-6179-2018-42-5-846-854
[24] Drusch M, Del Bello U, Carlier S, Colin O, Fernandez V, Gascon F, Hoersch B, Isola C, Laberinti P, Martimort P, Meygret A, Spoto F, Sy O, Marchese F and Bargellini P 2012 Sentinel-2: ESA's optical high-resolution mission for GMES operational services *Remote sensing of Environment* **120** 25-36
[25] 2019 *Scanex Image Processor* URL: http://www.scanex.ru/upload/iblock/c16/c16cb3ad6f737ff7dc13271fb4c9e335.pdf

Acknowledgements
The research was supported by RFBR projects 16-29-09494 ofi_m, 18-07-00748 a, 19-07-00357 a and the Russian Federation Ministry of Science and Higher Education within a state contract with the "Crystallography and Photonics" Research Center of the RAS under agreement 007-ГЗ/Ч3363/26.

Image clustering by autoencoders

A S Kovalenko[1], Y M Demyanenko[1]

[1]Institute of mathematics, mechanics and computer Sciences named after I.I. Vorovich, Milchakova street, 8a, Rostov-on-Don, Russia, 344090

e-mail: alexey.s.russ@mail.ru, demyanam@gmail.com

Abstract. This paper describes an approach to solving the problem of finding similar images by visual similarity using neural networks on previously unmarked data. We propose to build special architecture of the neural network - autoencoder, through which high-level features are extracted from images. The search for the nearest elements is realized by the Euclidean metric in the generated feature space, after a preliminary decomposition into two-dimensional space. Proposed approach of generate feature space can be applied to the classification task using pre-clustering.

1. Introduction

Nowadays there are a large number of approaches to solving the classification problem [1]. But as a rule, they all resolve into the use of a model class with a teacher-learning-based algorithm. All of them are united by one major drawback - the requirement of marked data for training. When a new task arises in the field of computer vision, as a rule, the marked data is missing, and it is necessary to spend money on their marking.

If we consider approaches based on methods of uncontrolled learning, such as clustering algorithms, they are usually focused on working with data of small dimensions. If we consider images as processed data, they usually have a high dimension. Lowering the dimension of space, for example, by the method of principal components, still does not give space to which clustering algorithms can be effectively applied.

There is a need to build a map acting from the image space Ω (1) into a certain feature space of these images, to which you can effectively apply decomposition methods and directly produce clustering and search for nearby objects by visual component.

2. Latest work

The most frequently used approach to solving the problem of reducing the dimension is the method of principal components. But it can be applied only to rectilinear data. If we consider objects of large sizes, the probability of their good separation becomes small. But if they constitute a mixture of objects belonging to normal distributions with different parameters, they can be separated using the t-SNE algorithm (Laurens van der Maaten Visualizing Data using t-SNE) [2]. In most cases, there is work with data that does not meet these requirements. There is a need to build a mapping from the current space of objects into the space of their descriptive features, which will be imposed the requirement of their distribution under the normal law. Such a problem is considered in the paper on variational autoencoders (Doersch C. Tutorial on Variational Autoencoders) [3].

In our work, for this purpose an encoder was built and trained, which is the necessary mapping into the space of attributes of images distributed according to the normal law. Further, the t-SNE algorithm can be applied to the resulting space to further decompose the space into dimensions, where clustering algorithms will work well.

3. Building of encoder

For training and testing of models, a set of images "MNIST", which contains the images collection of handwritten numbers. An example of the data is shown in the figure 1.

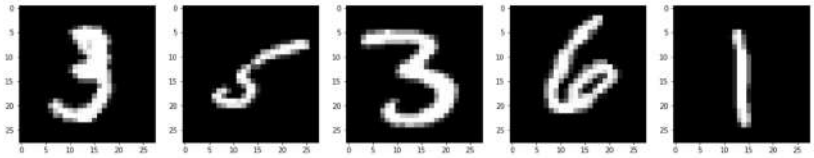

Figure 1. MNIST example.

Autoencoder was built with the architecture shown in the figure 2. For the general concept of architecture in more detail see [3].

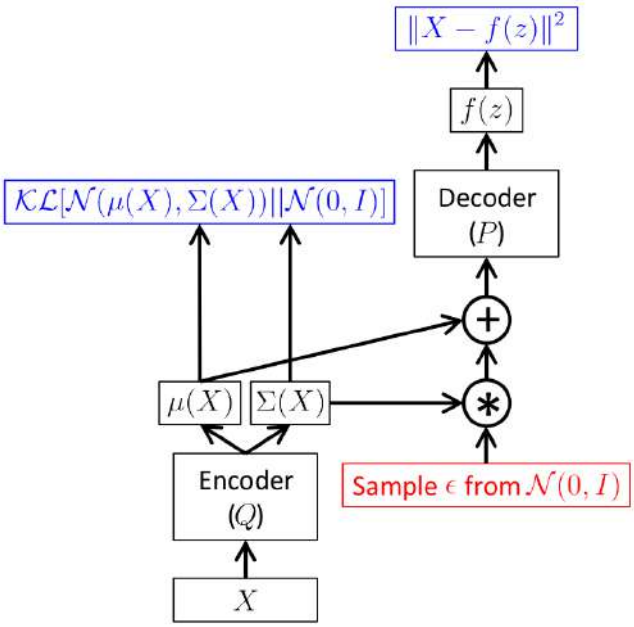

Figure 2. General block diagram of the auto encoder model, where the blue blocks indicate error functions.

During the experiments, the following architectures of the neural networks of the encoder (Q) and decoder (P) networks, built only on fully connected layers and convolutional networks, were used. The parameter for these networks was the dimension of the hidden space.

A detailed description of the architectures of these models in the form of flowcharts is in the repository attached to the work. A brief description of the models is shown in the pictures 3 and 4.

Layer (type)	Output Shape	Param #
input_15 (InputLayer)	(None, 28, 28, 1)	0
Encoder (Model)	(None, 10)	237972
Decoder (Model)	(None, 28, 28, 1)	237456

Total params: 475,428
Trainable params: 473,892
Non-trainable params: 1,536

Figure 3. Summary for a model built on fully connected layers.

Layer (type)	Output Shape	Param #
input_9 (InputLayer)	(None, 28, 28, 1)	0
Encoder (Model)	(None, 10)	25385
Decoder (Model)	(None, 28, 28, 1)	24924

Total params: 50,309
Trainable params: 50,309
Non-trainable params: 0

Figure 4. Summary for a model built on convolutional layers.

Both models were trained on the above 60000 data set. The Adam [4] optimization algorithm was used for training. Number of learning epochs is 500. Keras framework: keras with backend tensorflow was used for building and learning.

At the output, the encoder returns two vectors: the vector of the mean value for the distribution to which the object belongs and the vector of the covariance matrix in a diagonal form. To construct the set H, we use the average value, since it characterizes the cluster centroid in the space of hidden features, where Ω - original objects set (1), g - encoder.

$$\Omega = \{I_m\}_{m=1}^{N} \tag{1}$$

After training encoder, we construct the desired set H as follows:

$$H = \{g(x)|x \in \Omega\}. \tag{2}$$

Now we lower the dimension of the set H using the algorithm of distributed stochastic selection of neighbors (t-SNE):

$$\hat{H} = \text{t-SNE}(H),\ \forall h \in \hat{H} \Rightarrow dim(h) = 2. \tag{3}$$

On the other hand, you can set the dimension of the hidden space of the variational auto encoder, equal to 2, and then we get a set of objects of the desired dimension. But in this case, the loss of information increases when the object is encoded by an encoder, and the results of decomposition with this approach are worse.

4. Experiments

Was took 5000 elements from the " MNIST " data set and under exposure of the encoder using the t-SNE algorithm, we get the set $\hat{H}$ (3). Consider the examples of $\hat{H}$ sets obtained using the g encoder model with various parameters of the hidden space size. Figure 5 depicts the set $\hat{H}$ when using the dimension of the hidden space equal to 2, without further using t-SNE.

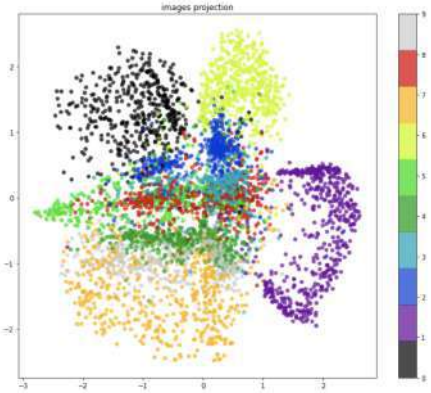

Figure 5. Visualization of the hidden space of dimension 2, obtained by a fully connected encoder.

Figure 6 depicts the set $\hat{H}$ constructed using a fully meshed model with a hidden space dimension parameter of 10 using the t-SNE algorithm.

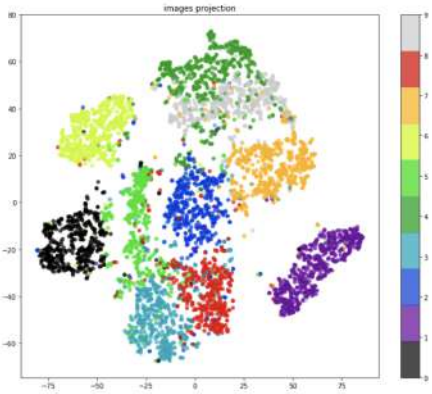

Figure 6. Hidden space of dimension 10, obtained by a fully connected encoder, followed by t-SNE.

Figure 7 depicts the set $\hat{H}$ constructed using the convolutional model with the parameter of the dimension of the hidden space equal to 10 using the t-SNE algorithm.

It can be observed that when using the hidden space of a higher dimension and the subsequent action on it by the t-SNE algorithm, the classes become better separable, picture 6. This is due to the fact that the auto encoder better restores the image at the output and, as a result, the space of hidden features becomes more representative. When using convolutional architecture,

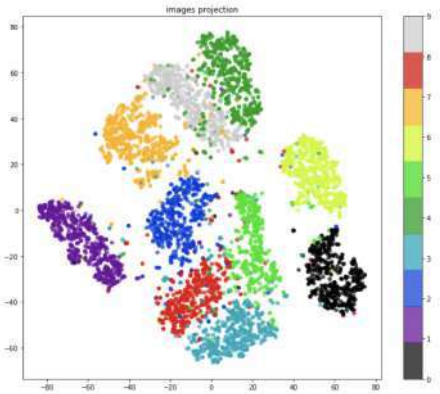

Figure 7. Hidden space of dimension 10, obtained by a convolutional encoder, followed by t-SNE.

visual separability of classes shows similar results, picture 7, and the number of parameters for this architecture is an order of magnitude smaller than that of the whole consisting of fully connected layers. Since when training a variational autoencoder, the encoder tends to predict the parameters of the normal distribution to which the object should belong, then when considering the set of predicted average values, we get the space of normally distributed values. The t-SNE algorithm uses the proximity metric of objects in the normal distribution, which results in a good decomposition result. There is also a method for reducing the dimension of space, based on the selection of the main components (PCA) [5], but it shows the worst results when applied to this set of hidden features, picture 8.

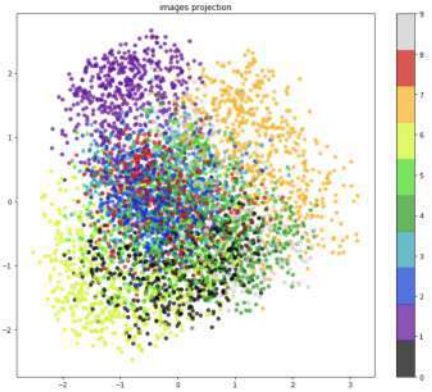

Figure 8. Visualization of the space obtained by the action of the encoder consisting of fully connected layers, after decomposition by PCA.

4.1. Search of nearest images and clustering

Random elements from the set $\hat{H}$ (3) are taken as an example of searching for the nearest images by visual similarity, for which 5 nearest elements from the same set are found using the Euclidean

metric, pictures 9 and 10.

Since in the set $\hat{H}$ (3) the data clusters have a random non-linear form, the clustering algorithm DBSCAN [6] is applied. After splitting the set into clusters, 10 representatives of each class are taken and the voting method selected labels for each class from the available data markup. After that, the classification accuracy is evaluated. It is 82.2%. If you reduce the space to dimension 2 only with an encoder, the accuracy is 75.9%.

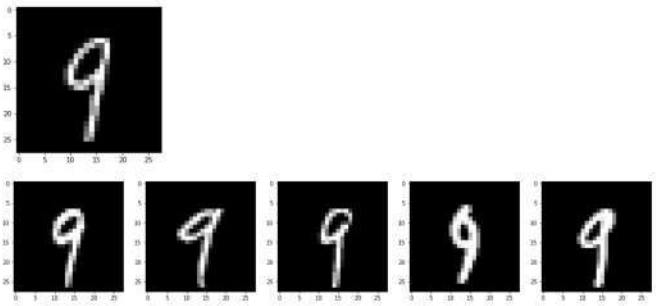

Figure 9. Original image (top) and 5 closest (bottom).

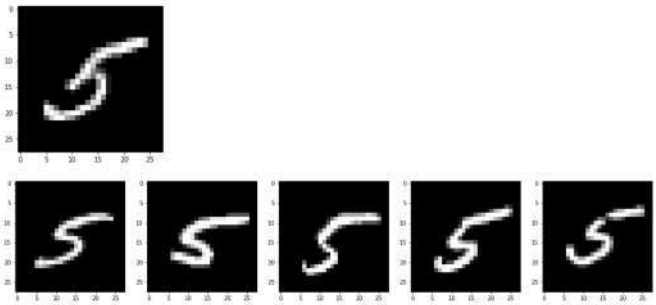

Figure 10. Original image (top) and 5 closest (bottom).

5. Results

In this work, a variational auto encoder model was built, trained on the MNIST task data set. The experiment shows that the described approach of using a larger dimension of the hidden space with its further decomposition using the t-SNE method gives better separability of classes compared to reducing the dimension only by the auto encoder, and gives higher accuracy when clustering the set, 82.2% instead of 75.9%.

6. Conclusion

The considered approach allows us to solve the classification problem on previously unallocated data and search for the closest ones based on visual similarity.

You can also select the nearest elements to the cluster centroids, which will be more likely to be correctly classified during clustering, and train the classifier based on the [7] neural network, which may allow you to classify all the input data with better precision.

7. Applications

Link to GitHub repository with implementation: Clustering-by-VAE

8. References

[1] Kotsiantis S 2007 *Supervised Machine Learning: A Review of Classification Techniques* (Peloponnese: Department of Computer Science and Technology University of Peloponnese) 249-268
[2] Maaten L 2008 Visualizing Data using t-SNE *Journal of Machine Learning Research* **9** 2579-2605
[3] Doersch C 2016 Tutorial on Variational Autoencoders *CoRR* ArXiv: abs/1606.05908 (28.05.2019)
[4] Kingma D 2015 Adam: A method for stochastic optimization *Scottsdale: ICLR* ArXiv: abs/1412.6980 (28.05.2019)
[5] Shlens J 2014 A Tutorial on Principal Component Analysis *CoRR* ArXiv: abs/1404.1100 (28.05.2019)
[6] Ester M 1996 *Density-Based Algorithm for Discovering Clusters in Large Spatial Databases with Noise* (AAAI Press) 226-231
[7] Wu H 2017 *CNN-Based Recognition of Handwritten Digits in MNIST Database* (Berlin: Springer)

The peculiarities of interaction between the end-user and the remote sensing system for spatial objects detection and recognition

R V Brezhnev[1], Yu A Maglinets[1], K V Raevich[1] and G M Tsibulsky[1]

[1]Siberian Federal University, Institute of Space and Information Technology, Kirenskogo St., 26, Krasnoyarsk, Russia, 660074

e-mail: brejnev.ruslan@gmail.com, ksenia_248@mail.ru

Abstract. The paper discusses the requirements for the system of remote sensing (hereinafter referred to as "System") which is focused on the end user (EU), based on the concepts of object-oriented monitoring. The classification of simple queries generated with interactive tools in the context of the end user's subject area is presented. The research investigates the features of the System needed for maintaining task-setting interaction, such as the subject ontology, including knowledge about the object of interest, its static and dynamic properties, the hierarchy of vector layers that describe spatial objects, the updated image database. The authors indicate the resources necessary for solving specific tasks, including spatial data repository and specification of computational procedures capable of interpreting the query in terms of decision operators. Specifically, the paper considers the structure of task-setting interaction tools, which ensures the object space-time localization, finding its meaning in semantic space, performance specification parameters measured one time or in dynamics, requirements for the visualization of the results and the activity of the System in relation to the end user in the monitoring process. The solutions presented were tested on monitoring the condition of agricultural lands in the multi-task space monitoring system of the Institute of Space and Information Technology, Siberian Federal University, Krasnoyarsk.

1. Introduction

At present there is an intrinsic gap between the existing interfaces of geographic information systems and the information need of the end user, who, as a rule, operates within a closed professional environment. New tools are needed to reconcile the mental model of the end user, on the one hand, and the totality of the processed data, the algorithms of data assimilation, presentation and processing on the other. They should provide the end user with an interactive environment where he could set monitoring tasks in the usual terms of objects, attributes, classifiers, indicators, charts, graphs, etc. The most intuitive in this sense is the object-oriented paradigm to analyze complex subject areas, which is often used in practice to set the task of implementing software solutions that perform specific functions [1,2]. The paper discusses the possibility to use this concept for organizing interaction with an end user, when it does not arise between the problem originator and the system analyst, but

between the problem originator and the decision system itself. At present, ontological approach, which reflects many aspects of the object-oriented view on representing geographic knowledge, is widely used in intellectual systems. However, due to the high degree of this approach formalization, direct interaction between the end user and the systems such as, for example, Protégé [3] is cumbersome as it involves intermediary – knowledge engineer. Next, we consider the issues of building an interactive environment focused on the end user and supporting the capabilities of the System within the object-oriented monitoring concept developed by the team of the authors.

2. Initial data for the task setting process

The main variables discussed in setting the task of spatial object remote research are: the localization of the object of interest (context) and the informative characteristics to be determined.

The object is localized in the coordinate system of the earth's surface, in time, and in semantic space.

Spatial localization can be carried out based on the use of a priori information about the study object (SO) position, represented as a pair of points defined in space by coordinates (x, y), which identify rectangular search area, or a polygonal vector object represented in one of the GIS- formats. In addition, the position of the object can be specified by the user directly, based on substrate maps, or by specifying the elements of the existing vector maps, for example, administrative or cadastral division, departmental affiliation, land use maps, etc. The position of an object can also be specified indirectly, based on its non-spatial properties, defined by the user and applying the knowledge of the System.

Localization in time can also be stated either explicitly, by specifying a time reference or interval, or indirectly, based on the characteristics of the object life cycle. Depending on the nature of the problem being solved, the following time localization options are possible: "now", "exact date in the past", "last measurement results", "forecast" (for a future date), "monitoring" (a series of measurements with a specified interval).

The process of localization in semantic space, which, unlike the previous two methods of localization, depends essentially on the nature of the object and the subject area of research, is characterized by the greatest variability. In the first approximation, we assume that the specified process comes to choosing one or more classes from a predetermined set of domain classifiers. The examples presented in the article are given for the subject area of detecting agricultural land (AL) use with remote sensing.

Substantive characteristics to be determined can be divided into static, dynamic and structural. Depending on the nature of the problem being solved, it can be formulated as an object recognition task, a measurement task, or a prediction of the numerical value of one or more object attributes, a segmentation task (for heterogeneously structured objects). In the latter case, it is also possible to set the task of recognition or measurement for each of the selected segments. The recognition task requires the assignment of the observed object to a class defined in one of the domain classifiers. The statement of the measurement (forecasting) task requires the correlation of the measured property with the corresponding element of the attribute classifier.

3. The structure of interaction dialogue frames for the problem setting

Formally, the structure of interaction on setting the object monitoring task can be represented as a directed graph:

$$Gr = (P,V), \tag{1}$$

where P is the set of vertices defining the nature of the action (operation) in the interaction, V is the set of directed edges defining the execution paths for operations. The set of the graph vertices consists of two subsets:

$$P = S \bigcup EU, \tag{2}$$

where S is a subset of the operational vertices of the system, EU is a subset of the operational vertices of the user.

The main stages of the task setting: 1) defining the context; 2) clarifying the goal; 3) developing the requirements for representation of findings.

The object is localized along three “axes” of interaction: in the coordinate system of the earth’s surface, in time and in semantic space, each of which is related to an interaction frame. The preferred direction of interaction is determined by the user. For example, when choosing a spatial axis, the user can specify the spatial coordinates of the desired point of the monitored object. If the object is recognized by the system, it notifies the user about the main characteristics of this object, thereby setting localization indirectly in the semantic space. In another possible scenario, the user can select one of the object classifiers and specify the required classifier vertex. When switching to a frame with a geospatial representation, the areas corresponding to the selected vertex at the current time are activated. When switching to the time frame, the user can select the observation interval. If an interval in the past is selected, corresponding changes should occur in the spatial frame, displaying the required period of the object observation.

In the general case, various localization results are possible, affecting the further course of the task solution process. Thus, the result of localization in space is the exact fixation of a single spatial object (AL), a set of objects (AL sets) united by common features, for example, spring wheat fields of “MAYAK" agricultural company, or indication of the region of interest where these objects can be located. When setting the time interval, we determine the need for: a) obtaining immediate information; b) obtaining retrospective information; d) monitoring; c) forecasting.

3.1. Clarifying the goal

For an object (class of objects) defined during the previous stage of interaction, we determine the set of characteristics to be evaluated. A set of characteristics available for selection depends on the model for describing semantic characteristics used in the System. In our example, these are properties associated with the corresponding nodes of the objects classifiers, such as “area”, “degree of heterogeneity” [4], “phytomass volume assessment”, “yield assessment”, “integral characteristic of the crops condition”, “germination percentage", "surface layer temperature ", etc. Structural analysis is possible for agricultural fields, with a high degree of heterogeneity during the field season, caused, for example, by partial nonemergence of crops, or by extreme values of soil moisture in the local areas of the field [5]. It includes segmentation of the zone of interest with the selection of homogeneous areas. For each of the selected areas it is also possible to specify the properties required for measurement.

When setting the forecasting problem in the subject area under consideration, as a rule, we assume the expected phytomass volumes, or the yield per unit area. At the considered stage of interaction, the appropriate forecast model is selected from those available in the System.

When setting the monitoring task, as well as the task of current observation, one or more characteristics to be monitored, as well as the method of organizing the monitoring process, are determined.

3.2. Developing the requirements for representation of findings

At this stage of interaction, the forms of findings representation on request are refined - numerical values, tables, elements of business graphics, thematic maps, and atlases. Since there is no complete formalization of tasks in practice, the resulting images of the study objects are also of interest to the user. They can be analyzed together with the information structured above.

When setting the monitoring task, particular interest consists in defining the probability of the System prompt response to the anomalous behaviours of the study object, detected during the analysis of timely remote sensing data. For example, when monitoring fallow lands, these are the excessive values of vegetation indices, indicating the presence of phytomass in the field and, indirectly, the use of inadequate tillage methods. The active method of monitoring provides for the possibility to notify the user about negative scenarios of agricultural lands dynamics immediately when such information is obtained by the System.

4. Problem solution utilities of the System

A subject knowledge base pre-formed in the System, which restricts the class of study objects defining the area of study and information about their spatial localization, is a prerequisite for organizing an interaction. The research relies on the ontology-based approach to describe and extract the semantics of agriculture objects, developed in [6,7]. To localize objects in the semantic space, a system of thematic classifiers is presented there. To describe the measured attributes, the ontology properties are used, which are characterized by the name, unit of measurement, allowable range of values and computational measurement procedure.

The other necessary components of the system are: a cartographic base and a set of vector layers characterizing the spatial localization of objects and their attribute characteristics describing factual information. To organize monitoring, the System should have access to space survey data that arrives at the intervals determined by the characteristics of the object's life cycle. Accordingly, it is crucial to maintain a constantly updated database of remote sensing, which has assimilation, preprocessing, indexing, storage utilities and access to the specified data, as described in [8]. The alternative is to use web services that provide processing of information at place of its obtaining and delivering the results of processing to the consumer (see for example, [9–16]).

For each of the attributes calculated in the system, we should present a computational procedure to determine the sequence of spatial data processing operators and the conditions for their use [12]. This functionality is supported by the availability of spatial information processing modules in the System repository.

For active monitoring, as a supporting capability we need a formalized model of the object development over time. Thus, the crops vegetation period includes an interconnected series of phenophases changes, anthropogenic (farming operations) and environmental influences, which can be interpreted as positive or negative in a specific context [13]. With software prototyping we designed the interactive tools developed. The prototype is implemented as an additional module of the multi-task space monitoring system of the Institute of Space and Information Technology, Siberian Federal University, Krasnoyarsk [8,14].

5. Experimental Testing

The main provisions of the concept of man-machine interaction for setting and solving different tasks of spatial objects remote monitoring were implemented for obtaining the crops condition information, taking into account their uneven growth over time. Within the structure of interaction tools described above, the task setting process can be decomposed into the following steps (Figure 1):

5.1. Design of a subject classifier by a knowledge engineer

The stage allows introducing priori descriptions in the form of thematic sub-classifiers containing the monitoring feature classes, as well as their unary and binary properties. For the task in question, the structure of the classifier is formally as follows [13]:

$$c_i = < ID, \{x, y\}, \Phi, K, E, Tm, F, NS, NP, T, \overline{N} >, \quad (3)$$

where c_i is the classifier of the AL objects, $c_i \in C$, C is the global taxonomy classifier; ID – is object identifier; $\{x, y\}$ – is the set of geographic coordinates of the object in a given projection; K – is the set of agricultural crops (property-object); Φ is the set of phenological phases throughout the growing season; E – is the sequence of planned farming operations (FO); Tm is the set of reference time intervals $e_i \in E$, $e_i(k_i, tm_i)$ and $\varphi_i \in \Phi$, $\varphi_i(k_i, tm_i, \overline{N}_i)$, where tm_i is the time of measurement, and $k_i \in K$; $\overline{N}$ - is the set of reference intervals of vegetation index values, associated with phenological phases, allowing to interpret the current condition of vegetation; F is the set of the object conditions. The relation $f_i(\overline{N}_i)$ is defined. In addition, the measured properties include NS, NP, T – area, perimeter and thickness, respectively.

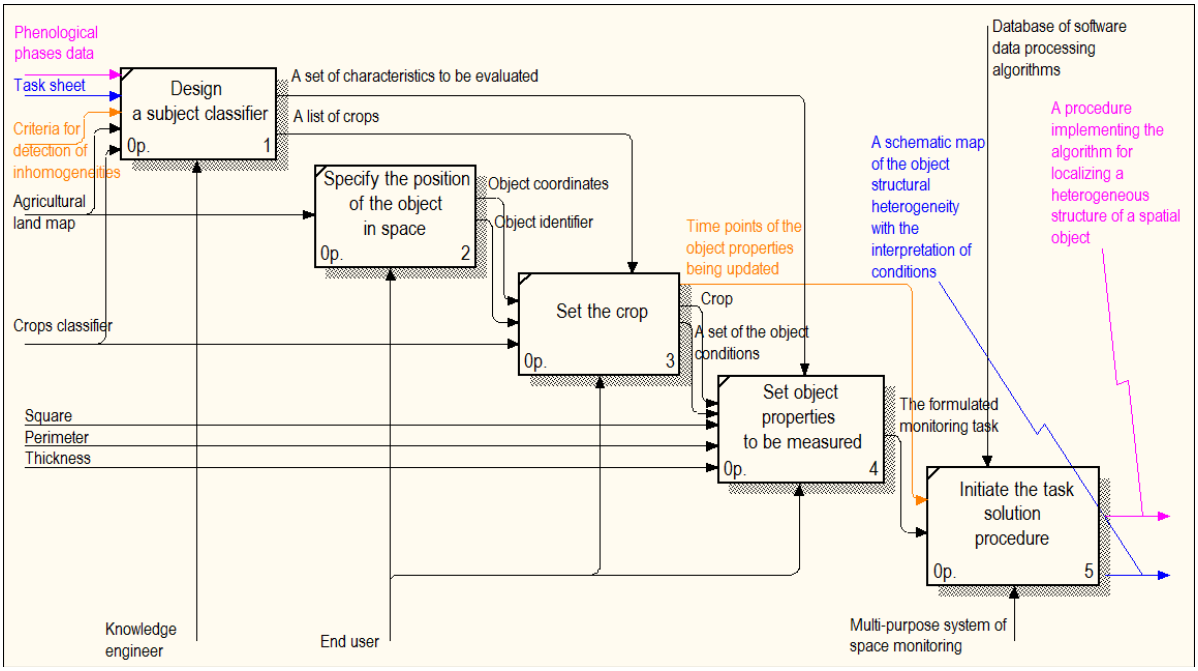

Figure 1. The task decomposition pattern (Monitoring crop growth conditions throughout the growing season, taking into account uneven growth over time).

5.2. Setting the position of an object in space

Setting the position of an object in space is the part of interaction. Based on (1) and (2), its model, can be represented as a graph Gr_1 (Figure 2). The object localization model includes the following specific steps:

- The system displays a map of the "AL" objects (S_1^1).
- The end user localizes an object (or objects, by multiple selection) on the basis of the “AL” object map (EU_1^1).
- The system identifies an object on the map visually (S_2^1).
- The system displays an object operation panel (S_3^1).
- The end user assigns the object to its agricultural company (AC) (EU_2^1).
- The Information System (IS) sets the ID_j of the assigned object, fixes its coordinates $\{x_i, y_i\}$ (S_4^1).
- The Information System displays a map of selected objects «AL» (S_5^1).

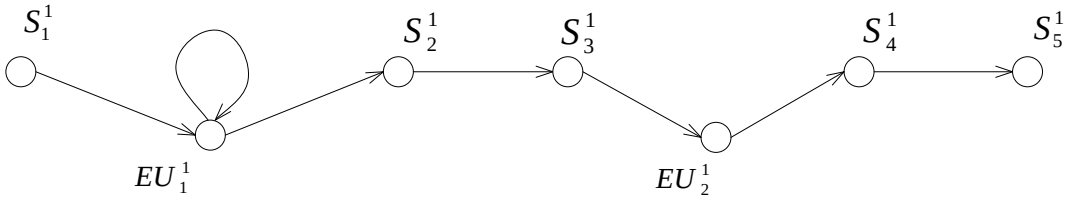

Figure 2. Graph Gr_1: Spatial localization of an object.

5.3. The interaction of assigning a crop

The interaction of assigning a crop can be represented as a graph Gr_2 (Figure 3), which includes the following steps:

- The system displays a map of the “AL” objects assigned to the agricultural company (S_1^2).
- The end user localizes an object (or objects, by multiple selection) on the basis of the object map of the company's agricultural lands (EU_1^2).
- The system identifies the object on the map visually (S_2^2).
- The system displays an object operation panel (S_3^2).
- The end user assigns the crop k_i with the normative time points Tm for updating the state of the object, i.e. measurement frequency of specified characteristics to the selected object (EU_3^2) on the basis of a given classifier. Each object can have individual time intervals between the state changes, which are measured from the actual sowing date.
- The system displays a map of "AL" objects with the given crops (S_6^2).

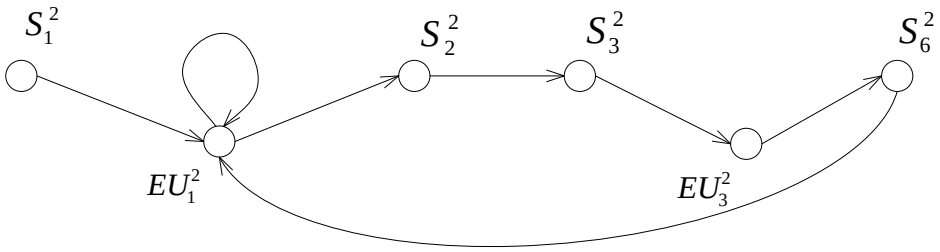

Figure 3. Graph Gr_2: Assigning a crop.

5.4. The process of setting the properties of an object

The interaction graph Gr_3 depicts the process of setting the properties of an object to be monitored (Figure 4). The main steps of interaction are:

- The system displays a map of "AL" objects assigned to the agricultural company (S_8^3).
- The end user localizes an object (or objects, by multiple selection) on the basis of the “AL” objects assigned to AC (EU_1^3).
- The system identifies the object on the map visually (S_2^3).
- The system displays an object operation panel (S_7^3).
- The end user sets restrictions on the values of size NS (EU_4^3) and form (EU_5^3) parameters to be calculated.
- The end user confirms the request (EU_6^3).

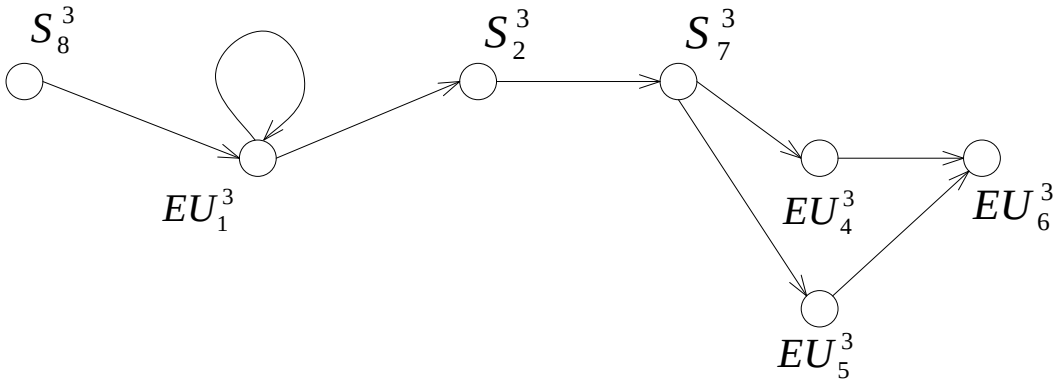

Figure 4. Graph Gr_3: The interaction for setting the object properties to be monitored.

5.5. The task solution stage

The task solution stage is considered as an information request which is impossible without prior training a multi-task monitoring system. The learning processes lie outside the framework of the considered interaction and consist in establishing the relation between subject classifiers and pre-programmed algorithm being program modules. The modular architecture implements the principle of reusing system components for solving various tasks, including those in parallel mode. At the physical level, this approach enables to represent a given operation for processing or analyzing data as a separate module, and a set of operations as a set of logically interrelated software modules running in a given sequence, with a given set of input parameters, at a specified time.

Thus, when choosing an object of a certain class, the System knows in advance which algorithm is required to be executed. If several algorithms are available for a class of objects, then we should provide steps how to choose the relevant one. At the same time, taking into account the fact that this interaction is user-focused, it is possible to use the natural language form of the search algorithm, which will in essence have the form of interaction "NL request - function".

So, in the considered task of monitoring crops condition, taking into account their uneven growth over time, the object class "AL" is connected with an algorithm for localizing a spatial object with heterogeneous structure. The practical result of this task solution is a series of "AL" object maps displaying structural heterogeneity with the interpretation of conditions, some of which are presented in Figure 5. The results are visualized to the user as vector layers in the Monitoring System. On the one hand the number of the formed layers is limited by the number of time points of the object properties being actualized, on the other hand, by remote sensing data, which are available under favorable weather conditions.

21.05.2018 25.06.2018 03.07.2018

Figure 5. The time series of maps displaying the AL object inhomogeneous structure (*ID = 164*).

6. Conclusion

The paper proposes a concept of designing an interaction environment for the end user of the remote sensing system for spatial objects detection and recognition within the paradigm of object-oriented monitoring. The following issues were considered in detail: 1) Initial data and constraints for the problem setting, which are grouped into the following categories: the representation of the object of interest in time, in the coordinate system of the Earth's surface, in semantic space, and in the target characteristics. 2) Interaction dialogue frames needed for a System to interact with the end user, including knowledge base for the subject area of research, a set of vector layers characterizing the spatial localization of objects and their attribute characteristics, the remote sensing data stream, implemented in the form of regularly updated image database or web-services, as well as functionality for measuring the required properties of the object. 3) The process of task setting in terms of interaction steps, which help to define the necessary context; goal clarification; development of requirements for representation of findings.

The interactive tools were developed based on software prototyping within the project "Multi-task space monitoring system of the Institute of Space and Information Technology, Siberian Federal University, Krasnoyarsk".

«This study was supported by the Russian Foundation for Basic Research (grant №: 18-47-242002 p_mk), the Government of the Krasnoyarsk Territory, the Krasnoyarsk Regional Science Foundation as a part of the research project titled "Development of technology for creating intelligent information systems of object-oriented monitoring of territories based on remote sensing data".

7. References

[1] Nedoluzhko I V, Eremenko V S and Eremenko A S 2016 *Modern problems of remote sensing* (Moscow) p102
[2] Korets M A 2014 *Regional problems of Earth remote sensing* (Krasnoyarsk) 294-298
[3] Brezhnev R V and Maltsev E A 2015 *Pattern Recognition and Image Analysis* **25** 201-208
[4] Shukilovich A Yu, Fedotova E V and Maglinets Yu A 2016 *J. Sib. Fed. Univ.* **9(7)** 1035-1044
[5] Brezhnev R V and Maglinets Yu A 2017 *CEUR Workshop Proceedings* **2033** 247-251
[6] Raevich K V, Maglinets Yu A and Tsibulsky G M 2016 *J. Sib. Fed. Univ.* **9** 1025-1034
[7] Maglinets Yu A, Raevich K V and Tsibulsky G M 2017 *Proc. Eng.* **201** 331-340
[8] Brezhnev R V, Maglinets Yu A, Maltsev E A, Perfilyev S E, Sidorov A Yu, Tsibulsky G M and Shocol A S 2012 *J. Sib. Fed. Univ.* **5** 340-352
[9] Bartalev S A and Lupyan E A *Current problems in remote sensing of the earth from space* **10** 197-214
[10] Tolpin V A, Lupyan E A, Bartalev S A, Plotnikov D and Matveev A M 2014 *Optics of the atmosphere and the ocean* **27** 581-586
[11] Lupyan E A, Bartalev S A, Tolpin V A, Zharko V O, Krasheninnikova Yu S and Oksyukevich A Yu 2014 *Current problems in remote sensing of the earth from space* **11** 215-232
[12] Brezhnev R V and Perevalova A A 2018 *Regional problems of Earth remote sensing* (Krasnoyarsk) 40-43
[13] Brezhnev R V, Maglinets Yu A, Raevich K V and Tsibulsky G M *CEUR Workshop Proceedings* **2210** 316-322
[14] Maglinets Yu A, Tsibulsky G M and Noskov M V 2016 *J. Sib. Fed. Univ.* **9** 1012-1018
[15] Plotnikov D E, Kolbudaev P A, Bartalev S A 2018 Identification of dynamically homogeneous areas with time series segmentation of remote sensing data *Computer Optics* **42(3)** 447-456 DOI: 10.18287/2412-6179-2018-42-3-447-456
[16] Varlamova A A, Denisova A Y, Sergeev V V 2018 Earth remote sensing data processing for obtaining vegetation types maps *Computer Optics* **42(5)** 864-876 DOI: 10.18287/2412-6179-2018-42-5-864-876

The image series forgery detection algorithm based on the camera pattern noise analysis

N I Evdokimova[1] and V V Myasnikov[1,2]

[1]Samara National Research University, Moskovskoe Shosse 34A, Samara, Russia, 443086
[2]Image Processing Systems Institute of RAS - Branch of the FSRC "Crystallography and Photonics" RAS, Molodogvardejskaya street 151, Samara, Russia, 443001

e-mail: nadezh.evdokimova@gmail.com, vmyas@geosamara.ru

Abstract. In the paper, the image series forgery detection algorithm based on the analysis of camera pattern noise is proposed. Distribution characteristics of the camera pattern noise are obtained by extracting the noise component of images from the non-tampered image series. A noise residual of a forgery image is compared with the camera pattern noise. We compare various noise filtering algorithms to choose the one that achieves the best performance of the proposed method. The proposed algorithm is tested both on examples of copy-move forgeries and forgery fragments which were inserted from an image not included in the image series.

1. Introduction

Image time series describes a scene dynamic. Analysis of image series allows predicting an image that may be next in the image series, as well as to conclude the authenticity of the image. There are several approaches to detect forged images. These approaches can use temporal and spatial correlations [1], unique artifacts of compression, and, finally, unique artifacts left by the camera. Methods using temporal and spatial correlations are divided into two categories. The methods belonging to the first category are based on pixel analysis of images [2-5] while the methods from the second category use the object level of images [6].

In the conditions of availability of many graphic editors and ease of their use, even an ordinary user does not require specialized knowledge and skills to falsify images. Forgeries can be made to add a new object to the scene captured by the camera or to hide the existing ones. Image series forgery detection has its distinctive features as compared to images matching since each image of an image series captures a scene at different moments. Two neighboring images of an image series can be captured under different lighting, weather or seasonal conditions. This paper proposes a forgery detection algorithm that is invariant to the conditions for obtaining images of a series.

This work consists of three parts. The first part deals with the model of the camera sensor noise and presents a method for extracting pattern noise. In the second part of the work, an algorithm for image forgery detection is proposed. The third part contains an experimental result of the proposed algorithm effectiveness. Experiments are focused on copy-move detection (fragments duplicated within one image) and copy-paste detection (fragments inserted from an image not included in the image series).

2. Model of a camera's sensor noise

When the camera sensor captures a uniformly lit scene, the output image will contain a certain number of pixels, slightly different in brightness from the rest. This fact is related to random noise components, such as readout noise (the magnitude of the matrix signal fluctuations relative to the average signal value) or shot noise (random fluctuations of voltages and currents relative to their average value), and a deterministic component - pattern noise. Pattern noise is present in each image, fixed by the sensor, and remains approximately the same for different images captured by the sensor.

The output image of the camera can be represented as follows [7]:

$$y(i,j) = f_{i,j}\left(x(i,j) + \eta(i,j)\right) + c(i,j) + \varepsilon(i,j) \quad (1)$$

where $\eta = \eta(i,j)$ is shot noise, $\varepsilon = \varepsilon(i,j)$ is readout noise, $c = c(i,j)$ is fixed pattern noise (FPN), $x = x(i,j)$ is image of the scene in the absence of any noise and $f_{i,j}$ is a multiplicative coefficient characterizing photo-response nonuniformity (PRNU).

2.1. Extraction of sensor pattern noise

To reduce the contribution of the random noise $\varepsilon = \varepsilon(i,j)$ and $\eta = \eta(i,j)$ to the determined noise component, an image time series $I_i(n,m), i = \overline{1,L}, n = \overline{1,N}, m = \overline{1,M},$ of the same scene captured by the same camera is used.

A F noise filter is used [8], [9] to extract the high-frequency component of camera noise. For each image of the sequence $I_i(n,m)$, it is possible to define the pattern noise matrix $W_i(n,m)$ as follows:

$$W_i(n,m) = I_i(n,m) - F\left(I_i(n,m)\right). \quad (2)$$

Estimation of pattern noise matrices $W_1(n,m), W_2(n,m), ..., W_L(n,m)$ set can be performed using a matrix of per-element expected values and a matrix of per-element dispersion values. These matrices can be calculated using (3) and (4), respectively. Both the matrix of expected values and the matrix of dispersion values have the same dimensions and depth as the pattern noise matrix $W_i(n,m)$ and the original images $I_i(n,m)$ accordingly.

$$E\{W_0, W_1, ..., W_L\} = E(n,m) = \frac{1}{L} \cdot \sum_{i=0}^{L-1} W_i(n,m). \quad (3)$$

$$D\{W_0, W_1, ..., W_L\} = D(n,m) = \frac{1}{L} \cdot \sum_{i=0}^{L-1} \left(W_i(n,m) - E(n,m)\right)^2. \quad (4)$$

Expected values and dispersion are calculated for every pixel of every dimension.

2.2. Selection of a noise extraction filter

The main requirement for a noise filter is the high quality of filtering areas around the edges of objects. This requirement is imposed so that the noise matrices contain the least amount of scene traces. The median filter, the Lee filter [10], the Gauss filter, the non-local mean filter [11] and the bilateral filter were chosen in the work.

3. Forgery detection algorithm

After obtaining pattern noise distribution characteristics of the camera, the noise component of the suspicious image distortion is extracted. Let $I_F(n,m)$ be a suspicious image that captures the same scene with the same camera. The image is not included in the image series used in (3) and (4). The pattern noise matrix of the suspicious image is determined as follows:

$$W_F(n,m) = I_F(n,m) - F\left(I_F(n,m)\right). \quad (5)$$

The image forgery detection algorithm can be introduced as follows:

- Obtaining pattern noise distribution characteristics of the camera using an image series;
- Obtaining the pattern noise matrix of the suspicious image. It is needed to use the same noise filter with the same parameters;

- Evaluation of similarity between the pattern noise of the suspicious image and the pattern noise of the camera;
- Creating of binary mask and post-processing of it.

Pattern noise distribution characteristics of the camera are obtained in the way described in the previous part of this work.

3.1. Calculation of similarity between the noise of suspicious image and camera pattern noise

The pattern noise matrix of the suspicious image $W_F(n,m), n=\overline{1,N}, m=\overline{1,m}$ is calculated using the formula (2). If images of the image series $I_i(n,m), i=\overline{1,L},$ have three channels, then every element of the pattern noise matrix can be presented as a vector $\mathbf{w}_{i,j}=\left(w_{ij}^R, w_{ij}^G, w_{ij}^B\right)^T, i=\overline{1,N}, j=\overline{1,M}$. The similarity between the noise of the suspicious image and camera pattern noise distribution is characterized by the Mahalanobis distance. The Mahalanobis distance is calculated for every element $\mathbf{w}_{i,j}$ of pattern noise matrix and the corresponding element $\boldsymbol{\mu}_{i,j}=E(i,j)=\left(\mu_{ij}^R, \mu_{ij}^G, \mu_{ij}^B\right)^T$ of expected values matrix using (6).

$$d_M(\mathbf{w}_{i,j}, \boldsymbol{\mu}_{i,j})=\sqrt{\left(\mathbf{w}_{i,j}-\boldsymbol{\mu}_{i,j}\right)^T \mathbf{B}_{ij}^{-1}\left(\mathbf{w}_{i,j}-\boldsymbol{\mu}_{i,j}\right)}, \quad (6)$$

where $\mathbf{B}_{ij}$ is a covariance matrix.

Set of Mahalanobis distance $d_M(\mathbf{w}_{i,j}, \boldsymbol{\mu}_{i,j})$ calculated for every $\mathbf{w}_{i,j}$ forms a Mahalanobis distance matrix $\mathbf{D}_M\{\mathbf{W}_F, \mathbf{E}\}$. Next, the matrix $\mathbf{D}_M$ is averaged in the window whose size does not exceed the size of the forged region to carry off peak values caused by random noise.

3.2. Creating a binary mask based on the distance matrix

The task of creating a binary mask is solved by choosing a threshold and threshold processing on the Mahalanobis distance matrix.

The threshold is selected based on the analysis of the Mahalanobis distance matrices total histogram. The cumulative histogram is created by aggregating Mahalanobis distance matrices histograms of authentic images $I_i(n,m), i=\overline{1,L}$.

Neyman-Pearson criterion is used to select a value of the threshold T. The probability of a false-positive p_0 is fixed, and the value of the threshold T is chosen to minimize the probability of a false-negative p_1.

3.3. Binary mask post-processing

In the work, post-processing of a binary mask includes selecting connected regions on the mask [12] and filtering them by size. A connected area is considered forged if its square exceeds $1/1000$ of the original image square. A minimal convex hull is constructed around each of forged region. Then the space inside the minimal convex hulls is filled.

4. Experiments

The experiments were carried out on a standard PC (Intel Core i5-4460, 16 GB RAM).

Ten image time series were used as the object of experiments. Every image series includes 15 authentic images and two forged images. All images were represented in the RGB space. One forged image included a copy-move and a fragment of another image was inserted into the second image. All images had a size of 4032×3024.

Figure 1 illustrates the camera pattern noise extracted by: (a) - the median filter, (b) - the Lee filter, (c) - the Gauss filter, (d) - the non-local mean filter and (e) - the bilateral filter. The images of camera pattern noise have been converted to grayscale and transformed by linear enhancement to the range of $[0,255]$.

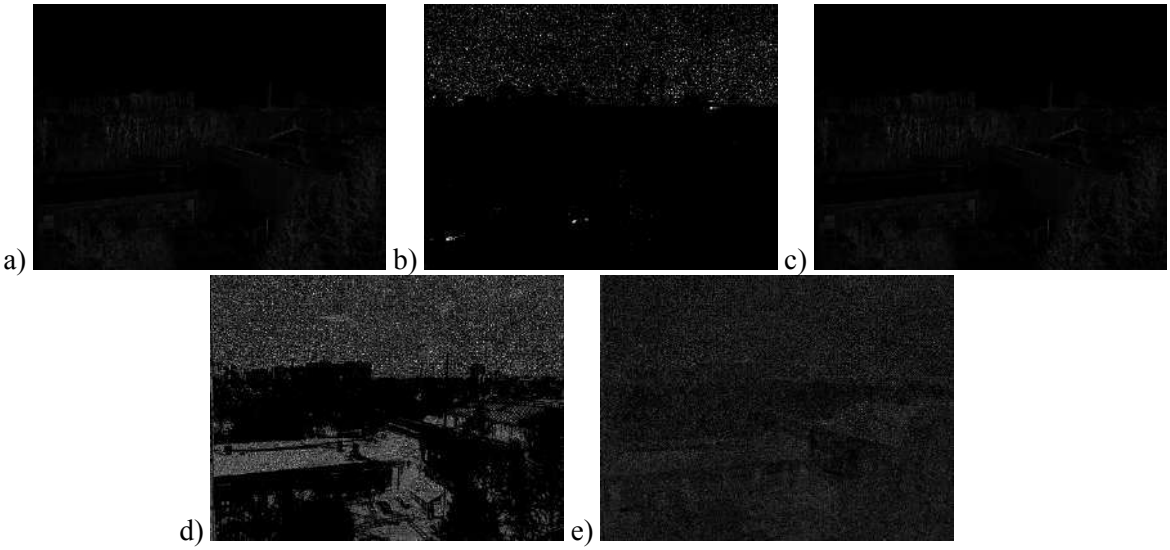

Figure 1. Camera pattern noise extracted by: a - the median filter; b - the Lee filter; c - the Gauss filter; d - the non-local mean filter and e - the bilateral filter.

The first part of the experiments was aimed at determining the effectiveness of the copy-move detection by the proposed algorithm.

4.1. Effectiveness of copy-move detection

The results of experiments aimed at detecting copy-move fragments are shown in Table 1. An example of an image containing copy-move, as well as the result of detecting it using a bilateral filter, is shown in Figures 2 (a) and 2 (b), respectively.

Table 1. F1 metric value of copy-move detection.

#	Median filter	Lee filter	Gauss filter	Non-local mean filter	Bilateral filter
1	0.24	0.03	0.56	0.46	0.87
2	0.36	-	0.43	0.64	0.93
3	0.29	-	0.37	0.25	0.77
4	0.44	0.02	0.42	0.33	0.69
5	0.38	0.01	0.30	0.15	0.86
6	0.42	-	0.14	0.14	0.87
7	-	0.03	0.19	0.31	0.74
8	0.49	-	0.27	0.21	0.94
9	-	-	0.07	0.07	0.92
10	0.53	0.01	0.86	0.00	0.92

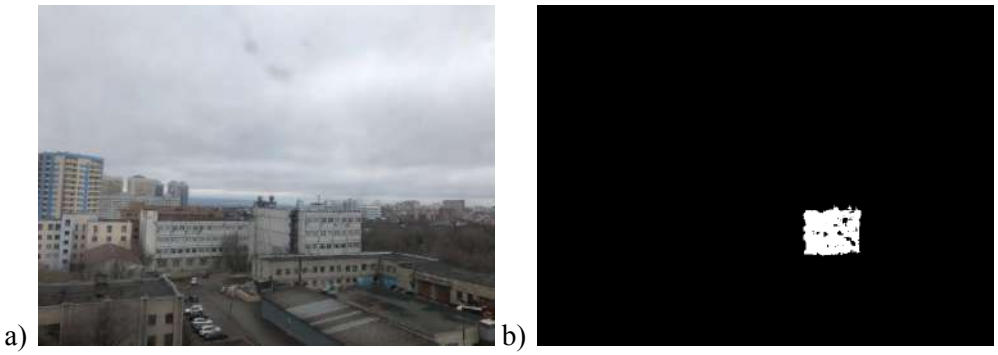

Figure 2. The result of copy-move detection in the image.

4.2. Effectiveness of copy-paste detection

The results of experiments aimed at detecting copy-paste fragments are shown in Table 2. An example of an image containing copy-paste, as well as the result of detecting it using a bilateral filter, is shown in Figure 3 (a) and 3 (b), respectively.

Table 2. F1 metric value of copy-paste detection.

#	Median filter	Lee filter	Gauss filter	Non-local mean filter	Bilateral filter
1	0.25	-	0.30	0.21	0.95
2	0.44	-	0.43	0.15	0.96
3	-	-	0.54	0.28	0.87
4	0.37	-	0.36	0.13	0.54
5	0.22	-	0.27	0.17	0.92
6	-	-	0.01	0.01	0.95
7	0.21	-	0.26	0.30	0.91
8	0.13	-	0.47	-	0.86
9	0.81	-	0.83	0.21	0.93
10	-	-	0.39	0.17	0.83

a)  b) 

Figure 3. The result of copy-paste detection in the image.

5. Conclusion

The image series forgery detection algorithm based on the camera pattern noise analysis has been proposed in the paper. The conducted research has allowed determining the most suitable noise filter in the sense of the selected metric F1 - bilateral filter. Also, experiments have shown the Lee filter is not suitable for solving the problem of copy-move and copy-paste fragments detection. The proposed algorithm allows detecting copy-move fragments with the average F1 value of 0.85 if the bilateral noise filter was used for pattern noise extraction. The average F1 value of 0.87 is reached for copy-paste fragments detection with the bilateral noise filter also.

6. References

[1] Christian A and Sheth R 2016 Digital Video Forgery Detection and Authentication Technique - A Review *International Journal of Scientific Research in Science and Technology* **2** 138-143

[2] Evdokimova N I and Kuznetsov A V 2017 Local patterns in the copy-move detection problem solution *Computer Optics* **41(1)** 79-87 DOI: 10.18287/2412-6179-2017-41-1-79-87

[3] Kuznetsov A V and Myasnikov V V 2016 A copy-move detection algorithm based on binary gradient contours *Computer Optics* **40** 284-293 DOI: 10.18287/2412-6179-2016-40-2-284-293

[4] Kuznetsov A V and Myasnikov V V 2014 A fast plain copy-move detection algorithm based on structural pattern and 2D rabin-karp rolling hash *Lecture Notes in Computer Science (including subseries Lecture Notes in Artificial Intelligence and Lecture Notes in Bioinformatics)* **8814** 461-468

[5] Evdokimova N I and Myasnikov V V 2018 Detecting forgery in image time series based on anomaly detection *CEUR Workshop Proceedings* **2210** 184-192
[6] Hussain M, Chen D, Cheng A, Wei H and Stanley D 2013 Change detection from remotely sensed images: From pixel-based to object-based approaches *ISPRS Journal of Photogrammetry and Remote Sensing* **80** 91-106
[7] Lukáš J, Fridrich J and Goljan M 2006 Detecting digital image forgeries using sensor pattern noise *Proceedings of SPIE - The International Society for Optical Engineering* **6072**
[8] Fahmy M F and Fahmy O M 2016 A new morphological based forgery detection scheme *National Radio Science Conference, NRSC, Proceedings* 212-216
[9] Chen M, Fridrich J, Goljan M and Lukáš J 2008 Determining image origin and integrity using sensor noise *IEEE Transactions on Information Forensics and Security* **3** 74-90
[10] Soifer V A, Chernov A V, Chernov V M, Chicheva M A, Fursov V A, Gashnikov M V, Glumov N I, Ilyasova N Y, Khramov A G and Korepanov A O 2009 *Computer Image Processing* (VDM Verlag Dr. Müller)
[11] Buades A, Coll B and Morel J-M 2005 A non-local algorithm for image denoising *Proceedings IEEE Computer Society Conference on Computer Vision and Pattern Recognition, CVPR* **II** 60-65
[12] Solomon C and Breckon T 2011 Morphological *Processing Fundamentals of Digital Image Processing* (John Wiley & Sons, Ltd) 197-234

Acknowledgments
This work was supported by RFBR according to the research project № 18-01-00748-a in part of "Introduction" and (2) "Model of a camera's sensor noise" and RF Ministry of Science and Higher Education within the State assignment to the FSRC «Crystallography and Photonics» RAS (Agreement 007-Г3/43363/26) in part of (3) "Forgery detection algorithm" - (4) "Experiments".

Automatic detection of constructions using binary image segmentation algorithms

E A Dmitriev[1], A A Borodinov[1], A I Maksimov[1] and S A Rychazhkov[1]

[1]Samara National Research University, Moskovskoye shosse, 34, Samara, Russia, 443086

e-mail: dmitrievEgor94@yandex.ru, aaborodinov@yandex.ru

Abstract. This article presents binary segmentation algorithms for buildings automatic detection on aerial images. There were conducted experiments among deep neural networks to find the most effective model in sense of segmentation accuracy and training time. All experiments were conducted on Moscow region images that were got from open database. As the result the optimal model was found for buildings automatic detection.

1. Introduction

The automatically detecting objects in Earth remote sensing (RS) images task is one of the most difficult tasks. An example of a solution to the problem under consideration is [1]. Currently, one of the most effective approaches is semantic segmentation algorithms usage. In other words, for each image pixel, the object class to which it belongs is determined.

The segmentation of remote sensing images is used in many industries: geoinformatics, the creation of maps, analysis of land use, etc. At the moment, many segmentation process stages are solved manually with the help of operators, which leads to high economic costs in temporary resources, as well as some inaccuracies in the markup due to the human factor.

Currently, there are many algorithms for image segmentation [2, 3, 4], but the most effective are approaches using convolutional neural networks (CNN) [5]. For almost all computer vision tasks, convolutional networks provide more efficient results than other algorithms.

In recent years, various approaches have been proposed for the CNN models formation, which at the output give an original image segmentation map. One of the most effective methods is based on the use of fully connected neural networks [5]. Unlike the convolutional networks that are used for classification, there is no subnet of the multilayer perceptron for classification in fully connected networks.

The CNN architecture for semantic segmentation can be divided into two parts: the encoder and the decoder. The output coder produces feature maps with a smaller size than the input image. A decoder is used to restore the size of the feature maps. In the original versions of models of fully convolutional networks, the decoder was a geometric transformation to increase the size of images with various interpolation methods [5]. Currently, an approach is used where the decoder subnetwork is constructed symmetrically to the encoder's subnetwork with the exception of pooling layers. Instead of pooling layers, transposed layers [6] or unpooling layers [7] can be used.

The paper discusses 4 convolutional networks for detecting buildings with different encoder and decoder architectures. As the criteria for the algorithms effectiveness, network learning time and segmentation accuracy are used.

The work is organized in the following order. The second section describes the considered neural network architectures. The third section presents the experimental studies results on real images of the Moscow region. The final section summarizes the results and tells about the future research direction in the field of semantic segmentation algorithms.

2. Methods

As algorithms for binary semantic segmentation, we used SegNet neural networks [7], a model with an encoder from the ResNet-50 network [8] and a decoder in the form of a geometric transformation with bilinear interpolation, U-Net [9], LinkNet [6].

The SegNet network model is a classic encoder-decoder architecture. The SegNet encoder network consists of 13 convolutional layers which correspond to the first 13 convolutional layers in the VGG-16 network. The decoder architecture is almost symmetrical to the encoder's subnetwork, with the exception of pooling layers. In this paper, unpooling layers are used. The SegNet network model is shown in Figure 1.

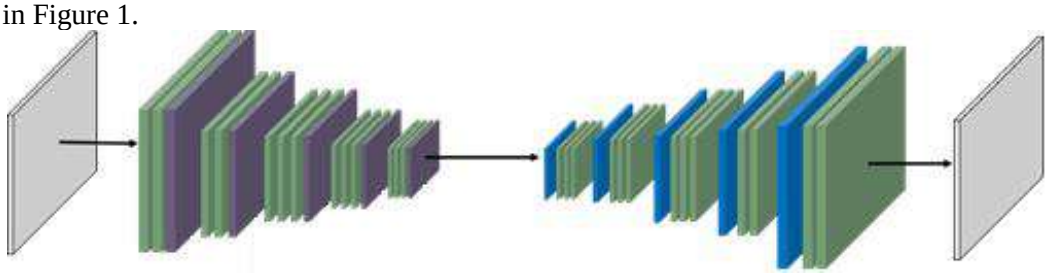

Figure 1. SegNet model.

The paper also considered a convolutional neural network for segmentation with an encoder based on ResNet-50. A feature of the ResNet-50 network is the use of residual connections, which make it possible to effectively solve the problem of a damped gradient arising with an increase in the number of neural network layers. The network model is shown in Figure 2.

The next neural network architecture under consideration is U-Net. The U-Net model feature is the feature maps concatenation on the lower and upper neural network levels. This approach is very similar to the residual connections in the ResNet-50 network, but in the case of U-Net, deeper connections are used. The network model is shown in Figure 3.

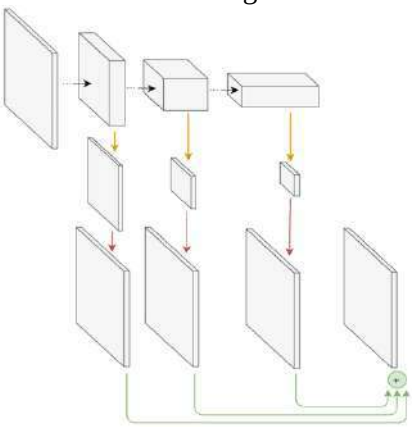

Figure 2. Fully convolutional network model based on ResNet-50.

LinkNet is an evolution of the U-Net model. The encoder and decoder are divided into several sub-blocks. LinkNet requires less computational resources in comparison with the considered models due to the rapid decrease in the size of attribute maps. At the network input, a decrease in feature maps occurs at the expense of pooling and convolution with a step equal to 2, and in the encoder block, at

the expense of convolution instead of pooling. In the decoder, transposed convolutional layers are used to restore the size of the images. The network model is shown in Figure 4.

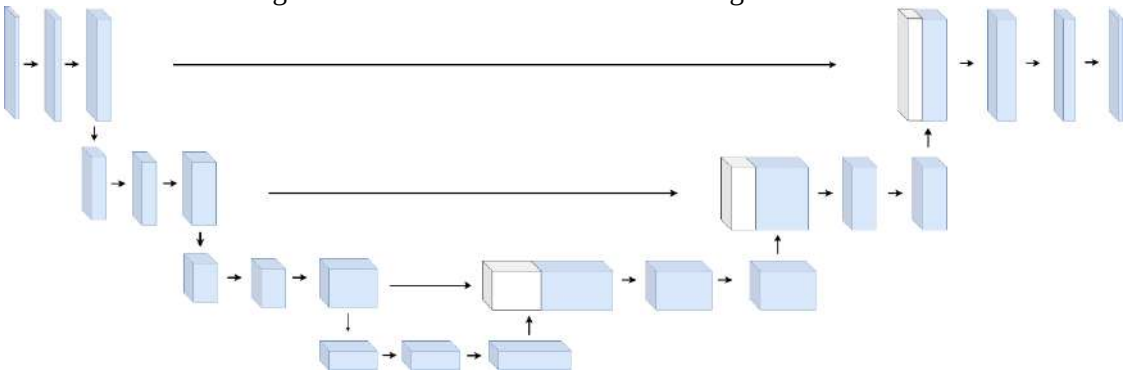

Figure 3. U-Net model.

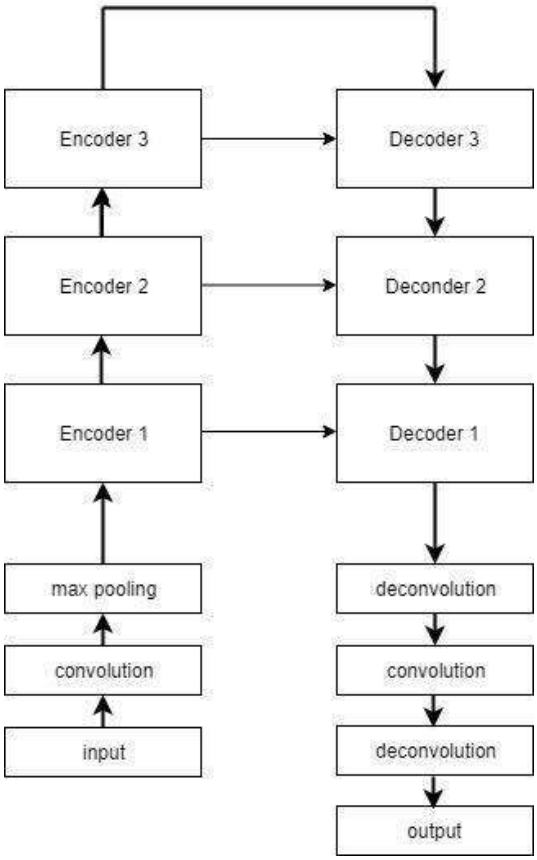

Figure 4. LinkNet model.

Cross-entropy was used as a loss function. According to [11], in the classification problem, the cross-entropy usage as a loss function allows achieving a better local minimum from the classification accuracy viewpoint with random algorithm parameters initialization compared to the standard deviation.

Let $I(n_1, n_2, n_3)$ – digital image applied to the input of the neural network, wherein $(n_1, n_2, n_3) \in \mathbf{D}$, $\mathbf{D} = \{(n_1, n_2, n_3) : n_1 = \overline{0, N_1 - 1}, n_2 = \overline{0, N_2 - 1}, n_3 = \overline{0, N_3 - 1}\}$, N_1, N_2 – the size of images, and N_3 – the number of channels in the input image. Let $Y(n_1, n_2, n_3)$ – mask the true segmentation, the dimensions of which coincide with the input image, and the number channels equal to the classes number. Each channel corresponded to a specific class. The classes were the buildings and the background. The values $Y(n_1, n_2, n_3)$ in the channels were 0 or 1, depending on the pixel class in the input image. Let

$O(n_1, n_2, n_3)$ – the image obtained at the neural network output whose size and the channels number coincide with the image markup. Let $y(n_3), o(n_3)$ – pixels with the same positions on the spaced and output images. Then the loss function as follows:

$$H(y,o) = -\sum_{i=0}^{N_3-1} y(i) \log o(i). \quad (1)$$

The target function performed functional mean error of the neural network training set. Let X^G – set with training images, where G – amount of elements, and w – neural network weights. Then the mean error is as follows:

$$Q(w, X^G) = \frac{1}{G} \sum_{i=0}^{G-1} \sum_{j=0}^{N_1-1} \sum_{k=0}^{N_2-1} H(O(i,j), Y(i,j)) \quad (2)$$

All models were trained using an adaptive stochastic gradient algorithm [12]. During the network training, the reducing technique the training coefficient was used in the event that the network quality value on the validation sample did not increase.

3. Experiments

The work considered photographs of settlements of the Moscow region [13]. RGB images of 512 × 512 size were fed to the network input. The number of shots was 3323. The ratio of the number of elements in the training sample to the number of elements of the test sample was 80:20. In the role of classes were the buildings and the background. An example of the image and mask is shown in Figure 5.

Figure 5. An example image and the mask part of the Moscow region settlement.

As can be seen from Figure 5, there were cases when the mask did not fully match the input image. Despite this, the inclusion of such images in the training sample made it possible to increase the metric value used in test images with an ideal mask even without a preprocessing stage.

The segmentation accuracy was used as a metric. The segmentation accuracy corresponds to the percentage of correctly classified pixels from the total number of pixels. The models were trained using the Nvidia GTX 1080 Ti graphics card. The experiments results are presented in table 1.

Table 1. The considered NN results.

Model	Training time, h	Segmentation accuracy, %
SegNet	4	96.7
Network based on ResNet 50	1.3	96.2
U-Net	2	96.9
LinkNet	**0.5**	**97.2**

According to the results of the experiments, it can be concluded that the approaches using transposed layers in the decoder used in LinkNet and the concatenation of the upper and lower feature maps used in the LinkNet and U-Net network allow to obtain higher generalizing abilities compared to other considered architectures. An example of the output image of the LinkNet network is shown in Figure 6.

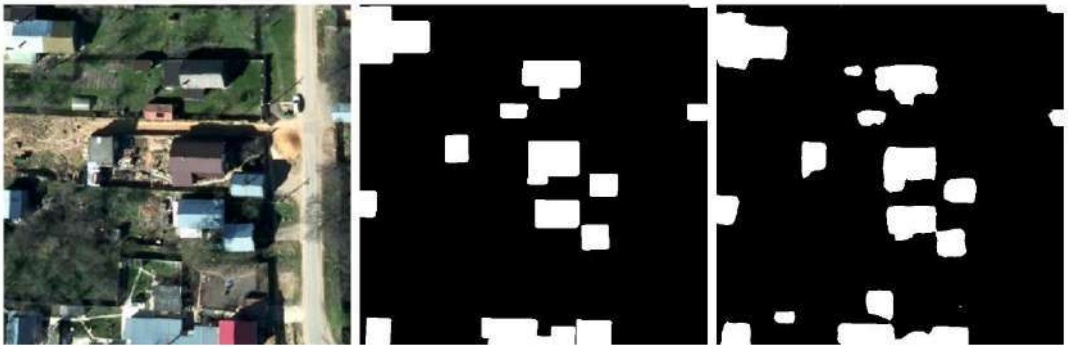

Figure 6. A test image example, markup and mask, obtained using LinkNet.

4. Conclusion

In this article, various convolutional neural networks architectures were investigated for the detection of structures in remote sensing images.

An experiments series was conducted, during which the optimal neural network architecture was identified in terms of training time and segmentation accuracy. Further research is planned on the use of conditional random fields to improve the segmentation quality.

5. References

[1] Myasnikov V V 2012 Method for detection of vehicles in digital aerial and space remote sensed images *Computer Optics* **36(3)** 429-438
[2] Kuznetsov A V and Myasnikov V V 2014 A comparison of algorithms for supervised classification using hyperspectral data *Computer Optics* **38(3)** 494-502
[3] Blokhinov Y, Gorbachev V A, Rakutin Y O and Nikitin A D 2018 A real-time semantic segmentation algorithm for aerial imagery *Computer Optics* **42(1)** 141-148 DOI: 10.18287/2412-6179-2018-42-1-141-148
[4] Cortes C and Vapnik V 1995 Support-vector networks *Machine Learning* **20** 273-297
[5] Long J, Shelhamer E and Darrell T 2016 Fully convolutional networks for semantic segmentation *The Pattern Analysis and Machine Intelligence* **324** 100-108
[6] Chaurasia A and Culurciello E 2017 Linknet: Exploiting encoder representations for efficient semantic segmentation *IEEE Conference on Computer Visionand Pattern Recognition* **362** 234-247
[7] Badrinarayanan V, Kendall A and Cipolla R 2017 Segnet: A deep convolutional encoder-decoder architecture for image segmentation *IEEE Conferenceon Computer Vision and Pattern Recognition* **353** 125-145
[8] He K, Zhang X, Ren S and Sun J 2016 Deep residual learning for image recognition *IEEE Conference on Computer Vision and Pattern Recognition* **123** 235-247
[9] Ronneberger O, Fischer P and Brox T 2015 U-net: Convolutional networks for biomedical image segmentation *Medical Image Computing and Computer-Assisted Intervention – MICCAI* **345** 234-241
[10] Russakovsky O, Deng J, Su H, Krause J, Satheesh S, Ma S, Huang Z, Karpathy A, Khosla A, Bernstein M, Berg A C and Fei-Fei L 2015 ImageNet large scale visual recognition *IEEE Conference on Computer Vision and Pattern Recognition* **243** 121-136
[11] Golik P, Doetsch P and Ney H 2013 Cross-entropy vs. squared error training: a theoretical and experimental comparison *Proceedings of the Annual Conference of the International Speech Communication Association, INTERSPEECH* 1756-1760
[12] Kingma D and Ba J 2014 Adam: A Method for Stochastic Optimization *International Conference on Learning Representations*
[13] Regional geographic information system of the Moscow region URL: https://rgis.mosreg.ru

Acknowledgments

This work was supported by the Russian Foundation for Basic Research (RFBR) № 18-01-00748-a.

A technique for detecting concealed objects in terahertz images based on information measure

D M Murashov[1], A A Morozov[2] and F D Murashov[3]

[1]Federal Research Center "Computer Science and Control" of RAS, Vavilov str., 44-2, Moscow, Russia, 119333
[2]Kotel'nikov Institute of Radio Engineering and Electronics of RAS, Mokhovaya, 11-7, Moscow, Russia, 125009
[3]Moscow Aviation Institute (National Research University), Volokolamskoe Shosse, 4, Moscow, Russia, 125993

e-mail: d_murashov@mail.ru, morozov@cplire.ru

Abstract. In this paper, a new technique for detecting concealed objects in the images acquired by a passive THz imaging system is proposed. The technique is based on a method for mutual information maximization successfully used for image matching. For reducing computational expenses, we propose to analyze the mutual information at local maxima of the cross-correlation function computed in the Fourier domain. The proposed technique does not require parameter tuning. A computing experiment approved the efficiency of the proposed technique and the possibility of its implementation in security systems.

1. Introduction

One of the areas of public safety protection is the development of concealed object detection systems in images obtained in the terahertz band (300 GHz - 3 THz). As a rule, these images are characterized by a low signal-to-noise ratio, low resolution, low contrast, and fuzziness of objects (see Figure 1 (a)).

One of the approaches to solving the problem for detecting concealed objects in the terahertz images consists of image segmentation and recognition of selected objects. Many of the proposed segmentation methods are based on the assumption that there are three areas in the terahertz image (background, a human body, and hidden objects) characterized by their radiometric temperature range corresponding to the ranges of gray tone levels. Gaussian mixture models are usually used to represent the images. The authors of works [1-3] used these models as the basis for developing multi-level segmentation algorithms. Noise suppression algorithms are applied at the preprocessing stage to improve the segmentation quality. For example, the anisotropic diffusion algorithm and the nonlocal means (NL-means) algorithm are used in [1]. In paper [3], the authors developed a multi-level EM algorithm to localize objects. At the first level, the algorithm segments two objects: the background and the human body. At the second level, the EM algorithm highlights the hidden object over the body. In [4], the author proposed an algorithm based on the maximum likelihood method for recognizing hidden objects. In order to reduce the effects of noise and low contrast, it may be useful to combine images taken in different spectral ranges. To increase the performance of the concealed

objects detection, the authors of work [5] combined images obtained in the terahertz and visible spectral bands. In [6], the objects hidden under clothes are localized using the images obtained in four channels of a system operating in 3- and 8-millimeter wavelengths with vertical and horizontal polarization. A multilevel segmentation algorithm combines the k-means algorithm, the EM algorithm for estimating the parameters of a Gaussian mixture, and the Bayesian classifier. An alternative approach to object detecting in terahertz images is to use matching the template image of an object and the input image. In [7], a method based on the localization of the maximum of the correlation coefficient was applied to detect objects. In this paper, for detecting objects in terahertz images, we propose to apply an image matching method based on the mutual information maximization [8].

2. Problem statement

Suppose there is a set of images of objects that should be detected under the clothes of people, using a passive terahertz camera. Objects that are visible in the image should be compared with the templates, and it is necessary to make a decision about their identity or difference. Suppose there are N template images of objects U_n, $n=1,2,...,N$. Let the image V be the input image. It is necessary to identify the object U_n located in the image V.

To solve such a problem, the segmentation of the input image is usually preliminarily performed, feature descriptions of the images of objects U_n are formed, and then in the feature space, the separating surfaces between the classes of the objects under consideration should be found.

The properties of terahertz images listed above complicate the segmentation of objects. Therefore, it is preferable to use methods that do not require segmentation. In this paper, we propose to solve the object detection problem as an image matching problem [9]. Let the similarity measure of the template and the objects in the image V be the criterion $J(U_n,V)$. Then the problem can be formulated as follows. It is necessary to find a template image V which provides the maximum value of the similarity measure $J(U_n,V)$:

$$U_m = \arg\max_{U_n}\{J(U_n,V)\},\ n=1,2,...,N. \quad (1)$$

Several methods that do not require segmentation of images are known, in particular, methods based on the maximization of the cross-correlation function values, maximization of the correlation coefficient [7,9], and maximization of the mutual information [8,10]. These methods do not require a priori knowledge about the relationship between the input image and the template as well as information on the statistical characteristics of the images. However, the correlation matching of terahertz images fails in some cases (see Figure 1). The mutual information is calculated directly from the joint distribution of the gray levels of these images and involves the data contained in the compared images more completely than the correlation parameters. The mutual information is a quantitative characteristic of the statistical dependence of images. The greater similarity of the template and the input image produces a greater value of the mutual information. In this work, the mutual information is used as a similarity measure to solve the problem (1).

To apply the information-theoretic approach, a stochastic model of the dependency between the template image and the input image is necessary. Let the grayscale values in the compared images at the point $\mathbf{x}$ with coordinates (x,y) be described as discrete random variables $U(\mathbf{x})$ and $V(\mathbf{x})$ with values u and v quantized into a finite number of levels K and L respectively. If images $U(\mathbf{x})$ and $V(\mathbf{x})$ represent the same scene, there is a relationship between the variables $U(\mathbf{x})$ and $V(\mathbf{x})$. We will use a model similar to that proposed in [8,11]:

$$V(Tr(\mathbf{x})) = F(U(\mathbf{x})) + \eta(\mathbf{x}), \quad (2)$$

where Tr is a coordinate transformation (for registered images $V(Tr(\mathbf{x}))=U(\mathbf{x})$); F is a grayscale value conversion function that simulates the relationship between two images of an object; $\eta(\mathbf{x})$ is a random variable that simulates noise. Model (2) can be considered as a model of a discrete stochastic information system with the input U and the output V.

a) b) c)

Figure 1. The result of the correlation image matching: (a) an image of a human with a hidden object obtained from the THERZ-7A complex; (b) the image of the template object; (c) the result of an erroneous correlation matching. The contour of the template is shown in red.

The mutual information between the system input and output is defined by the expression:

$$I(U;V)=\sum_{k=1}^{K}\sum_{l=1}^{L}p(u_k,v_l)\log\left[\frac{p(u_k,v_l)}{p(u_k)p(v_l)}\right], \quad (3)$$

where the functions $p(u)$, $p(v)$, and $p(u,v)$ define one-dimensional and two-dimensional discrete probability distributions of the gray tone levels of the images U and V. If mutual information (3) is used as a similarity measure, the problem (1) can be formulated as follows. It is necessary to find an image of the template U_n maximizing the criterion (3):

$$U_m=\arg\max_{U_n}\{I(U_n;V)\}. \quad (4)$$

In the next section, an algorithm for solving the problem is proposed.

3. Comparison of the template images with the images obtained in the terahertz spectral band

The direct computing of the mutual information values on the set of pixels corresponding to the intersection of the images U_n and V at different positions of U_n relative to V requires large computational expenses. Therefore, in practice, methods for accelerated computing of the mutual information magnitude are necessary. For example, in [8], a differential equation was obtained for searching for the extremum of function (3) in the image matching problem.

In this paper, we propose to compute the mutual information values $I(U_n;V)$ at the points of the input image V corresponding to the local maxima of the cross-correlation function [9], where the content of the input image V matches the template image U_n. The number of the local maxima is significantly less than the number of pixels in the input image V and the cross-correlation function of the images can be rapidly computed in the frequency domain. These circumstances make it possible to significantly speed up the computing of mutual information and, accordingly, solving the problem (4). Since the cross-correlation function is sensitive to changes in the amplitudes of the grayscale levels in the compared images, we will use contour preparations of the U_n and V images for its computing because the boundaries of the objects have a fairly stable high grayscale value in the contour preparations. The cross-correlation function is determined as follows:

$$c_{Un,V}(x,y)=\sum_{s}\sum_{t}C_{Un}(s,t)C_V(x+s,y+t), \quad (5)$$

where C_{Un} and C_V are the contour preparations of the images U_n and V, x and y are the spatial coordinates of the points of the image C_V, s and t are the coordinates of the points in the intersection area of the images C_{Un} and C_V. Given the high noisiness of terahertz images, masks of

stochastic gradients [12] for signal-to-noise ratio SNR = 1 will be used to obtain contour preparations. The computing of the function (5) will be carried out in the frequency domain.

Thus, the search algorithm on the terahertz images of an object corresponding to condition (4) includes the following operations: (a) smoothing the image V and obtaining contour preparations C_{U1} and C_V of the images U_n and V respectively; (b) calculating the cross-correlation function of the contour preparations C_{U1} and C_V by the formula (7); (c) finding the points of local maxima of the $c_{U1,V}(x,y)$ function; (d) calculating the mutual information $I(U_1;V)$ at the $c_{U1,V}(x,y)$ local maxima points; (e) finding the maximum of mutual information $I_{\max}(U_1;V)$; (f) repeating steps (a) – (e) for the images U_1, ..., U_N; finding the maximum of the mutual information $I_{\max}(U_m;V)$ among the values of $I_{\max}(U_1;V)$, $I_{\max}(U_2;V)$, ..., $I_{\max}(U_N;V)$ and the corresponding template image U_m which will be the solution of the problem (4). It should be noted that an operation of impulse noise filtering [13] can be applied at step (a) for input image enhancement.

The proposed algorithm has no parameters and does not require tuning. Figure 2 illustrates the main stages of localizing the objects. The input image captured by the THERZ-7A complex is shown in Figure 2 (a), and the image of the template object is given in Figure 2 (b). Contour preparations of these images are presented in Figures 2 (c) and 2 (d). Figure 2 (e) visualizes the cross-correlation function of the contour preparations. The figure shows the local maxima of the surface formed by the function $c_{Un,V}(x,y)$. The result of localizing the object in the input image is shown in Figure 2 (f).

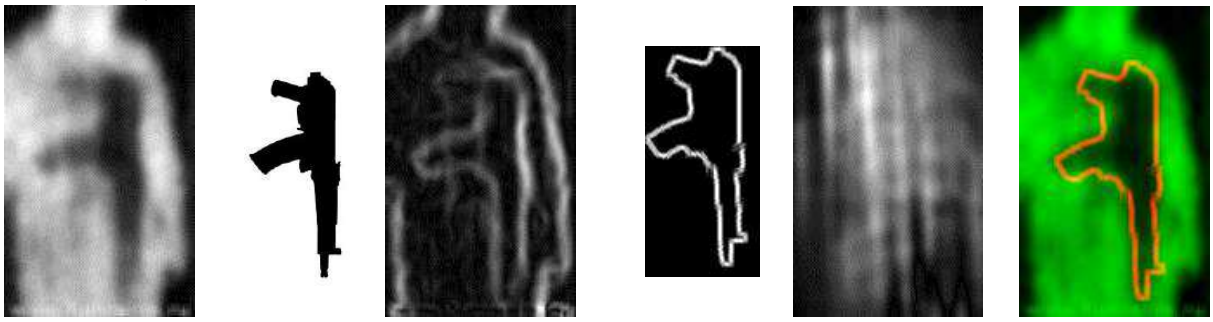

a) b) c) d) e) f)

Figure 2. The main stages of localizing the objects: (a) image captured by the THERZ-7A complex; (b) the image of the template object; (c) the contour preparation of the input image; (d) the contour preparation of the template image; (e) visualized cross-correlation function of contour preparations $c_{Un,V}(x,y)$; (f) the result of localizing the object in the input image, corresponding to the maximum of the mutual information $I(U_n;V)$.

4. Experiment

To estimate the applicability of the above approach to solve the problem of localizing and identifying concealed objects, a computational experiment was carried out. The experiment was organized as follows. We obtained template images of objects, which should be detected in images captured at the output of the terahertz imaging system. Template images are shown in Figure 3.

a) b) c)

Figure 3. Images of template objects: (a) Kalashnikov submachine gun (AK); (b) TT handgun; (c) Walther handgun.

We consistently placed objects under the clothes of a person and recorded image sequences using the THERZ-7A system. Using the proposed method, we compared the template images shown in Figure 3 (a) with frames of the obtained video sequences and fixed the values of the similarity measure (3). The shooting range was about 1.5 meters and varied slightly, so the template images were used with the constant value of the scale factor. The cross-correlation function and the mutual information are not invariant with respect to rotation. Therefore, it is also necessary to analyze the rotated and flipped variants of the template images. The results of the object localizing are shown in Figures 4 (a-e), and the computed values of mutual information are presented in Table 1. It follows from Figure 4 and Table 1 that concealed objects are successfully localized by the proposed method based on a combination of correlation matching and the mutual information maximum matching.

From the data in Table 1, we can draw the following conclusion. When comparing images with concealed objects obtained at the output of the terahertz imaging system and the images of template objects, the maximum of the mutual information is achieved if the template corresponds to the concealed object. Consider an example. Suppose a terahertz image is obtained in which a hidden object is visible (for example, a Walther handgun). This image is matched with the AK submachine gun, TT handgun, and Walther handgun templates. The computed values of the mutual information between the matched images are given in the third row of Table 1. The maximum value of the mutual information is obtained when comparing the input image and the Walther template. The system then makes a decision that the concealed object is a Walther handgun. From this, it follows that the proposed method can be used to detect and recognize prohibited concealed objects in security systems. To eliminate false alarms, the calculated maximum value of the mutual information is compared with a predetermined threshold value. If the found maximum of the criterion (3) is less than the threshold, then the decision is made that the prohibited object is not found. The threshold value is determined empirically.

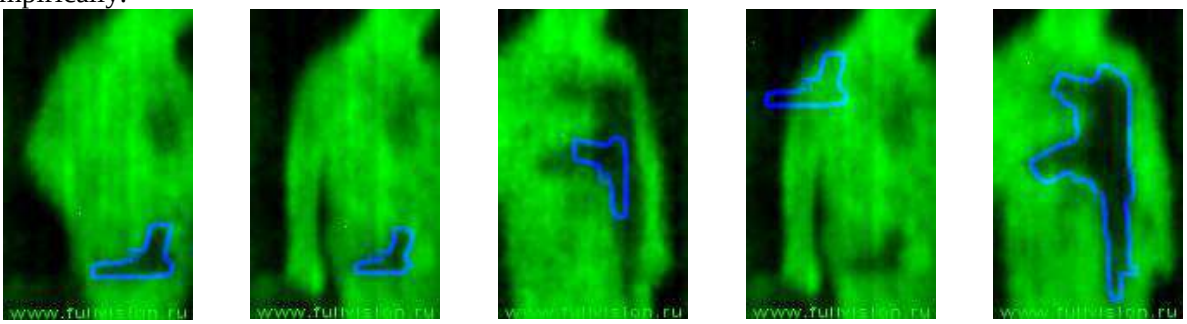

a) b) c) d) e)

Figure 4. The result of the matching images of template objects and the images of hidden objects: (a) TT handgun hidden under the clothes and its template; (b) hidden Walther handgun and its template; (c) hidden AK submachine gun and TT template; (d) hidden Walther handgun and TT template; (e) hidden AK submachine gun and its template.

Table 1. The values of the mutual information computed when matching the template images and the images of concealed objects.

Concealed object	Template objects		
	AK	TT	Walther
AK	**0.307398**	0.295407	0.276332
TT	0.191471	**0.404531**	0.345492
Walther	0.162791	0.267373	**0.342771**

5. Conclusions

The paper proposes a new algorithm for localization and identification of objects in images taken using the passive terahertz imaging system. The proposed algorithm combines matching methods based on maximizing the value of the cross-correlation function and the mutual information magnitude. To reduce computational expenses, the criterion of the mutual information maximum is

analyzed at points of local maxima of the cross-correlation function computed in the frequency domain. The proposed algorithm does not require parameter tuning. Future research will be aimed at improving the quality of detection and recognition of concealed objects using preprocessing of terahertz images and applying detection methods that are invariant to geometric transformations.

6. References

[1] Shen X, Dietlein C R, Grossman E, Popovic Z and Meyer F G 2008 *IEEE transactions on Image Processing* **17** 2465-2475
[2] Lee D S, Yeom S, Son J Y and Kim S H 2010 *Optics Express* **18** 10659-10667
[3] Martinez O, Ferraz L, Binefa X, Gomez I and Dorronsoro C 2010 Concealed object detection and segmentation over millimetric waves images *IEEE Computer Society Conference on Computer Vision and Pattern Recognition-Workshops* 31-37
[4] Antsiperov V E 2016 Automatic target recognition algorithm for low-count terahertz images *Computer Optics* **40(5)** 746-751 DOI: 10.18287/2412-6179-2016-40-5-746-751
[5] Kowalski M, Palka N, Piszczek M and Szustakowski M 2013 *Acta Physica Polonica* A **124**
[6] Yeom S, Lee D, Lee H, Son J and Gushin V P 2013 *Progress in Electromagnetics Research* **39** 169-180
[7] Trofimov V A, Trofimov V V, Shestakov I L and Blednov R G 2016 Concealed object detection using the passive thz image without its viewing *Passive and Active Millimeter-Wave Imaging XIX* (International Society for Optics and Photonics) **9830** 98300E
[8] Viola P and Wells III W M 1997 *International journal of computer vision* **24** 137-154
[9] Gonzalez R C and Woods R E 2008 *Digital Image Processing* (New Jersey: Pearson Education, Inc)
[10] Maes F, Collignon A, Vandermeulen D, Marchal G and Suetens P 1997 *IEEE transactions on Medical Imaging* **16** 187-198
[11] Escolano F, Suau P and Bonev B 2009 *Information theory in computer vision and pattern recognition* (Springer Science & Business Media)
[12] Jain A K 1989 *Fundamentals of digital image processing* (Englewood Cliffs, NJ: Prentice Hall)
[13] Chervyakov N I, Lyakhov P A and Orazaev A R 2018 Two methods of adaptive median filtering of impulse noise in images *Computer Optics* **42(4)** 667-678 DOI: 10.18287/2412-6179-2018-42-4-667-678

Acknowledgments

Authors are grateful to the Astrohn Technology Ltd and OOO ASoft who provided us with the THERZ-7A terahertz scanning device. This research was supported in part by the Russian Foundation for Basic Research (grants No 18-07-01295 and No 16-29-09626).

Creation of digital elevation models for river floodplains

A Klikunova[1], **A Khoperskov**[1]

[1]Volgograd State University, Volgograd, Russia, 400062

e-mail: klikunova@volsu.ru

Abstract. A procedure for constructing a digital elevation model (DEM) of the northern part of the Volga-Akhtuba interfluve is described. The basis of our DEM is the elevation matrix of Shuttle Radar Topography Mission (SRTM) for which we carried out the refinement and updating of spatial data using satellite imagery, GPS data, depth measurements of the River Volga and River Akhtuba stream beds. The most important source of high-altitude data for the Volga-Akhtuba floodplain (VAF) can be the results of observations of the coastlines dynamics of small reservoirs (lakes, eriks, small channels) arising in the process of spring flooding and disappearing during low-flow periods. A set of digitized coastlines at different times of flooding can significantly improve the quality of the DEM. The method of constructing a digital elevation model includes an iterative procedure that uses the results of morphostructural analysis of the DEM and the numerical hydrodynamic simulations of the VAF flooding based on the shallow water model.

1. Introduction

A high-resolution 3D topographic model for the large areas is essential to solving a variety of applied problems in the geosciences that are associated with modeling and monitoring the environment. The progress of computer technology and numerical methods gives us new opportunities for modeling fluid dynamics in certain territories. Such problems include storm surges, spring floods in river valleys, flooding due to heavy rainfall [1, 2]. Hydrodynamic models allow technical and environmental expertise in the design of hydrological structures [3, 4]. The important tasks are the determination of the watersheds' boundaries [5], the creating tools to help authorities respond to emergency situations [6].

One important research area is the creation of decision support systems (DSS) for solving various hydrological problems, and the effectiveness of these DSS is determined by the quality of the applied digital elevation models (DEM) [7, 8, 9]. Such DSS belong to the class of Spatial Decision-Support System, which combine standard decision-making tools with geographic information systems, providing new opportunities for water resources management [4, 10], city and regional planning, real-time decision-making for land management [11], transportation engineering [12], protecting the natural resources in conditions of increasing human pressures on the ecosystem.

A quality DEM is a critical component for all these tasks [13]. The terrain is a major physical factor that influences the dynamics of water. Unfortunately, the accuracy of best topographic maps is not high enough for numerical simulations. In addition, new problems appear on small spatial scales, and they are associated with changes in the surface of the relief caused by natural

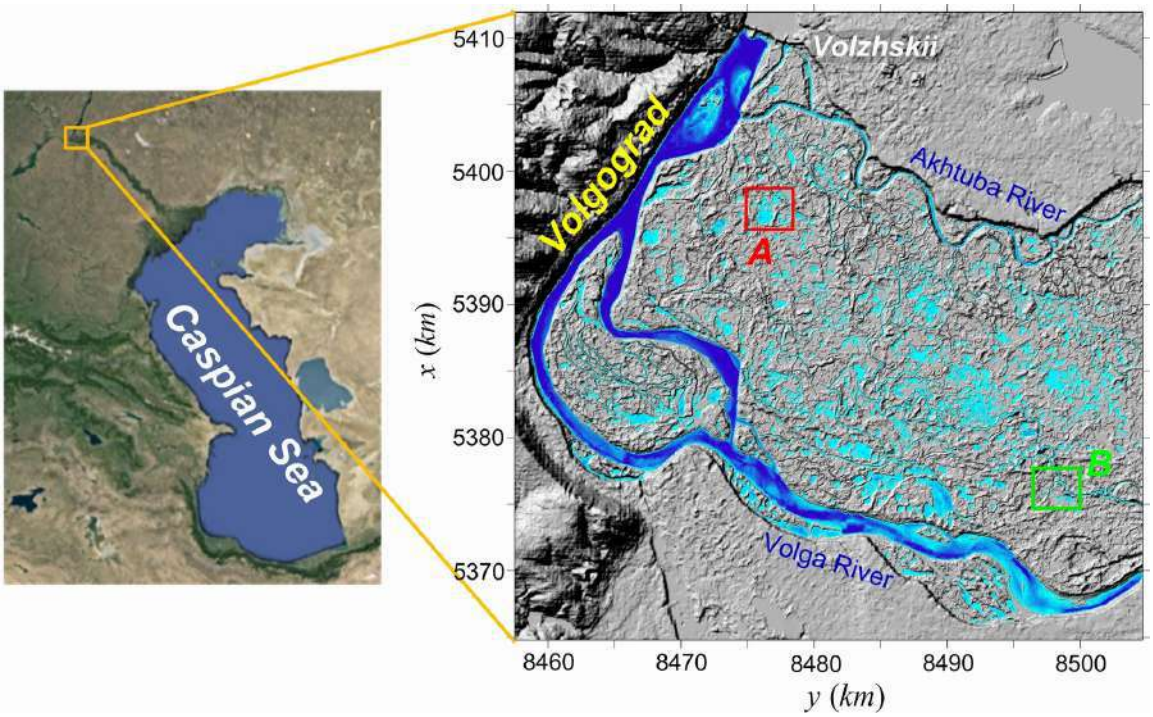

Figure 1. The northern part of the Volga-Ahtuba floodplain.

and man-made factors [14, 15]. Changes in the profile of the bottom and adjacent areas are a continuous process due to active sediment transfer and erosion processes, which require the use of the self-consistent model of water and sediment dynamics and regular updating of the DEM also [16].

In this paper, we describe the key stages of creating a DEM for river systems based on the synthesis of various spatial data using the example of the northern part of the Volga-Akhtuba floodplain (VAF). The Volga Hydroelectric Station controls the flow of water downstream of the Volga River and the moisture reserves for the entire floodplain. The volume flow of water through the dam is called discharge $Q(t)$ ($\mathrm{m}^3{\cdot}\mathrm{sec}^{-1}$) and it varies between $Q(t) \simeq 4000 - 30000\,\mathrm{m}^3{\cdot}\mathrm{sec}^{-1}$ during the year.

Important components of our methodology are the use of observational data on the dynamics of the coastlines of numerous small reservoirs in the interfluve during the spring flood and the verification of DTM using hydrodynamic modeling. Observations of the coastlines motions for a large number of reservoirs during the spring flooding are a source of very accurate local topography data. These water reservoirs are the results of the passage of spring water and they usually disappear in early summer. Thus, the water surface area in the territory of VAF varies strongly during a few weeks from 2-5% before flooding (low water) up to a maximum value of 20-40%, which depends on the specific conditions in each year. In late summer, the water basin area is smaller than in the early spring period before the flood, that connected with high summer temperature and lack of rain. The coastline coincides with the contour line (isoline) of the heights' distribution with very high accuracy at each time point. Thus, the local DEM may be the result of processing the monitoring data of the coastlines dynamics for a large number of small reservoirs during the spring flood. These local DEMs are high-resolution data for the most critical areas in terms of hydrology as a part of global DEM for the northern territory of the Volga-Akhtuba floodplain (Fig. 1).

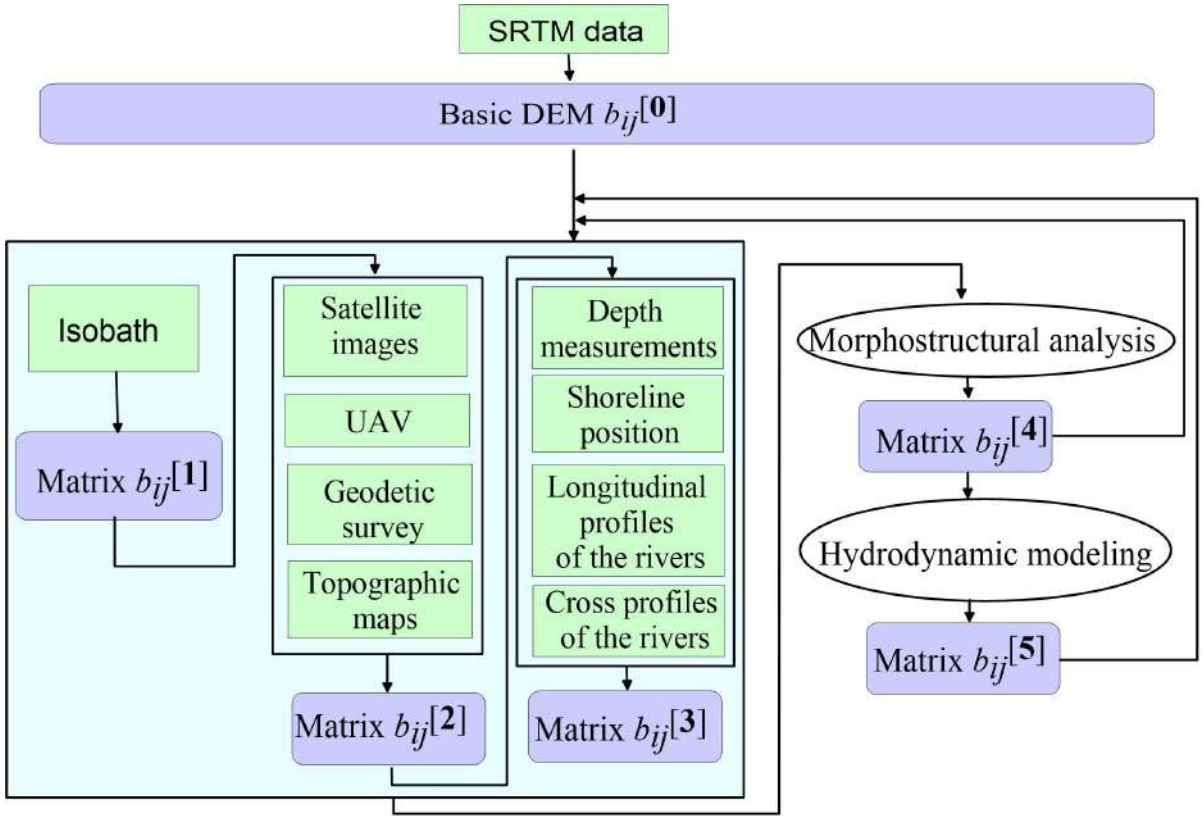

Figure 2. Stages and sequence of DEM creation.

2. Iterative process of creating DEM

2.1. Main stages of creating DEM

Figure 2 shows the general scheme for constructing a digital elevation model and highlights the most significant steps which we will discuss below. Our DEM is based on the height matrix $b_{ij} = b(x_i, y_j)$ for nodes of the Pulkovo 95 coordinate system with step $\Delta x = \Delta y$: $x_i = x_0 + i\Delta x$, $y_j = y_0 + j\Delta y$ ($i = 1, 2, ..., N_x$, $j = 1, 2, ..., N_y$). We take the SRTM3 SRTMGL1 data $b_{ij}^{[SRTM]}$ as the initial height matrix. The professional GIS "Panorama" tools allow us to recalculate the matrix by a smaller step ($\Delta x = 15$ m, 10 m, 5 m) using the weighted average interpolation in 16 directions. Such matrix $b_{ij}^{[0]}$ will be called the basic digital elevation model.

The main stages of the transformation matrix $b_{ij}^{[0]}$ are discussed below.

1) To clarify the model of the bottom of the Volga River and the Akhtuba River, we use **Sailing Directions (shipping charts) and water depth maps**. To refine the bottom model of the Volga River and the Akhtuba River, we use Sailing Directions (shipping charts) and reservoir depth maps, and then we obtain the matrix $b_{ij}^{[1]}$ after digitizing and embedding this data into the basic DEM $b_{ij}^{[0]}$.

2) A unique feature of the VAF is a complex system of small channels in the interfluve (the so-called eriks), which form a hierarchical system of channels between River Akhtuba and River Volga (Fig. 3). We use the **satellite images** of the "RESURS-P" series and UK-DMC 2, the DigitalGlobe's satellite constellation (Google Earth services) to vectorize the linear objects of this channel system for subsequent introduction into the DEM matrix of $b_{ij}^{[1]}$. UAV images and geodesic data are an important source for clarifying the location of small channels (Fig. 5). As

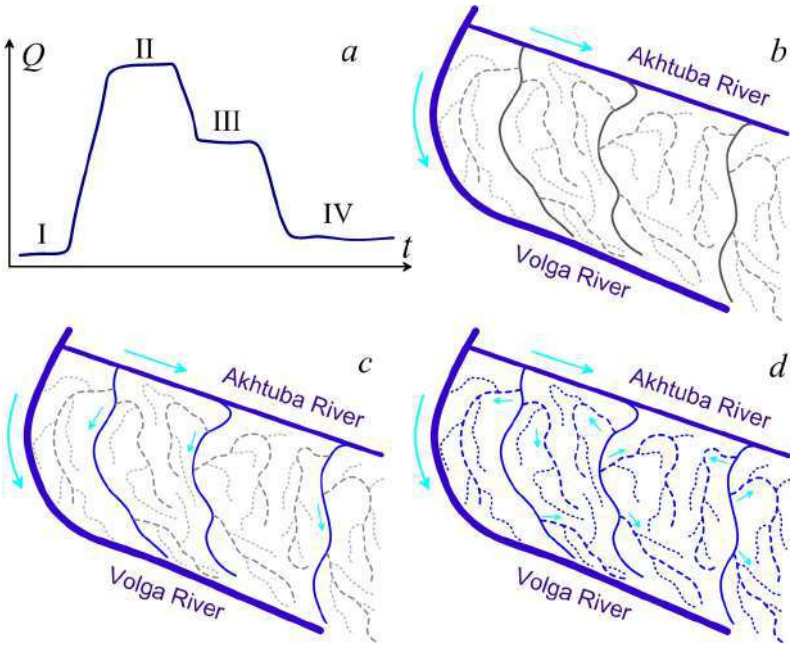

Figure 3. *a* — Typical dependence of discharge $Q(t)$. *b, c, d* — The hierarchical structure of the hydrological system in the VAF at different stages of flooding.

a result, we have the matrix $b_{ij}^{[2]}$, which contains the system of small channels.

3) To update the Volga River bottom model, we use the data of the last **depth measurements** ranging from the Volga hydroelectric power station to the Svetly Yar settlement. These data are very sparse and after approximation to all our grid nodes we have the matrix $b_{ij}^{[3]}$ with the height data of the river bed.

4) We use data on **dynamics of coastlines** of transient reservoirs, which are filled with water at the stage of interfluve flooding (April – May) and dry out in the summer (Figure 4). These measurements provide an additional set of lines with a constant level of relief with very high accuracy. The refined matrix $b_{ij}^{[3]}$ is the result of binding these isolines to heights. Our studies have shown the effectiveness of the UAVs use to obtain data on the boundaries of water bodies (Fig. 5). UAVs provide a more detailed sequence of isolines at the initial stage of flooding rise, which is almost unattainable for satellite data. However, this approach is local and does not allow to cover large areas.

Figure 4 shows vertical profiles along the AB and CD segments for the $b_{ij}^{[2]}$ matrix, indicating the positions of the corresponding intersections of coastlines with these segments. The points for the same coastline on opposite slopes of the reservoir have different elevation levels, which indicates the need to update the matrix $b_{ij}^{[2]}$. For example, the height difference is $\Delta b = 0.5\,\mathrm{m}$ for a pair of points (1a, 1b) in the figure 4 b and $\Delta b = 1\,\mathrm{m}$ for (2a, 2d) in the figure 4 c.

5) Then we calculate the standard set of **morphostructural analysis** parameters [17]: the profile curvature $k_t(x_i, y_j)$, the tangential curvature $k_s(x_i, y_j)$ and the tilt angles $s(x_i, y_j)$ (Figure 6):

$$s = \frac{360^o}{2\pi} \arctan \sqrt{b_x^2 + b_y^2}\,, \tag{1}$$

$$k_t = \frac{b_{xx} b_y^2 - 2 b_{xy} b_x b_y + b_{yy} b_x^2}{p\sqrt{q}}\,, \tag{2}$$

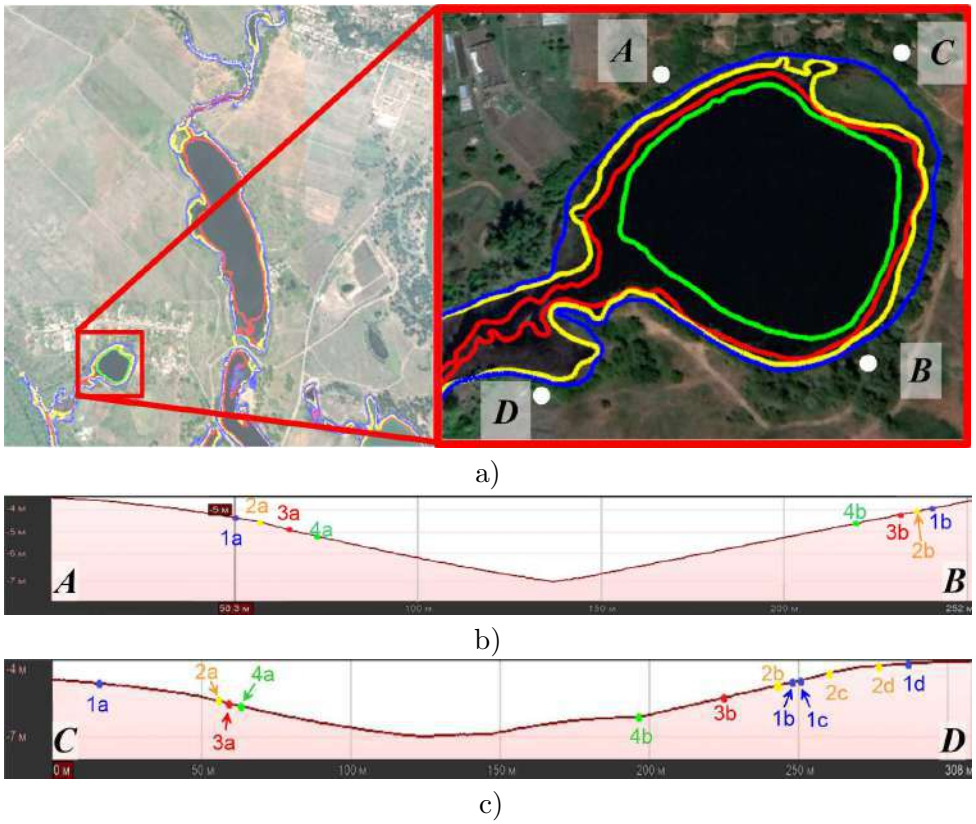

Figure 4. The position of coastlines at different points in time for small bodies of water near the village Zonal'nyj.

$$k_s = \frac{b_{xx}b_y^2 + 2b_{xy}b_xb_y + b_{yy}b_x^2}{p\sqrt{q^3}}, \tag{3}$$

$b_x = \dfrac{\partial b}{\partial x}$, $b_y = \dfrac{\partial b}{\partial y}$, $b_{xx} = \dfrac{\partial^2 b}{\partial x^2}$, $b_{yy} = \dfrac{\partial^2 b}{\partial y^2}$, $b_{xy} = \dfrac{\partial^2 b}{\partial x \partial y}$, $p = b_x^2 + b_y^2$, $q = 1 + p$.

We often encounter two types of artifacts:

a) Strong local errors of heights on the $b_{ij}^{[0]}$ matrix are strongly highlighted against the background of a rather flat territory. These errors are often caused by data processing problems for small forests and small water reservoirs.

b) The second difficulty is related to the detection of small channels connectedness.

There are problems with the automatic selection of objects even in images for urbanized areas, the morphology of which is simpler compared to the wooded marsh landscape of the floodplain [18]. Analysis of the hyperspectral observational data for various platforms allows us to improve the classification of objects [8], but this approach is algorithmically complex [19]. The spatial distributions of the parameters (1) – (3) help identify areas with artifacts, first of all, areas with a violation of hydrological connectedness of watercourses on the digital elevation model. The morphostructural analysis of the DEM allows simple means to detect possible errors and promptly correct them, refining the hydrological network [20, 21].

6) Hydrodynamic modeling is carried out at the final stage (Fig. 3*a*, *b*), reproducing the spring flooding of the interfluve territory in accordance with the procedure described in [1, 3, 22]. This allows you to check the channels connectedness of the hydrological system in addition to the morphostructural analysis. Comparison of simulation results with observational data is a

Figure 5. The vectorization of water bodies images with UAV. The colored lines show the boundaries of the reservoirs.

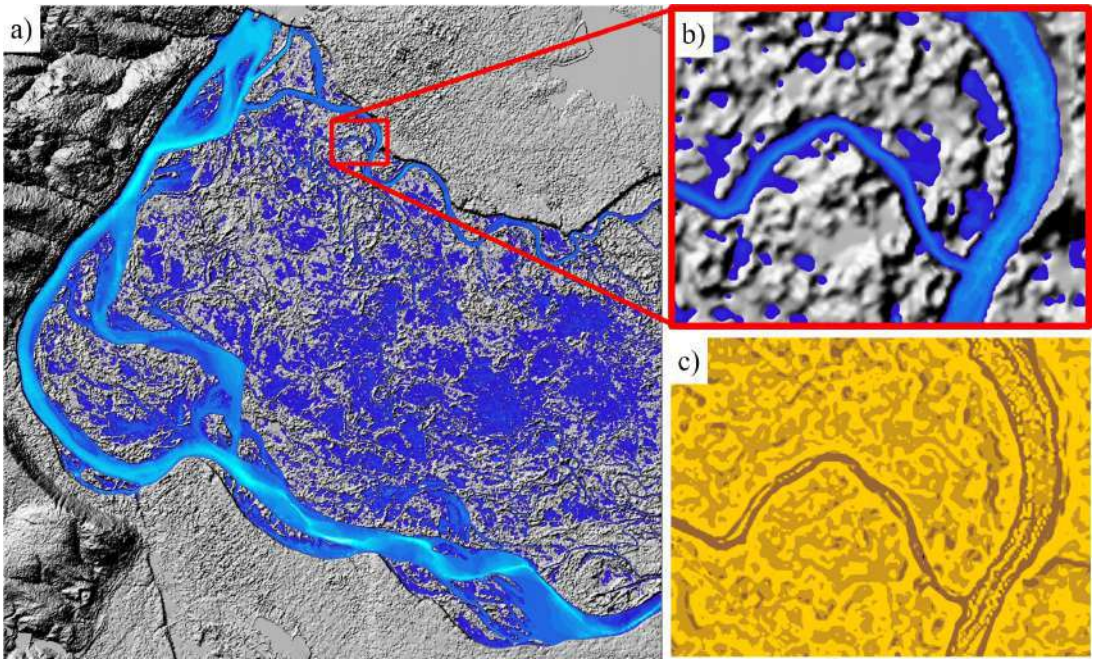

Figure 6. *a*) The general structure of the VAF flooding is based on the results of our numerical hydrodynamic modeling. *b*) The distribution of water for the specified area of the frame. *c*) The distribution of the morphometric index k_s for the same zone.

powerful tool for updating the DEM for the most important zones, which primarily provide for the formation of vast reservoirs of the lake type due to the water outflow from small canals (eriks).

Such verification based on hydrodynamic modeling is the most resource-intensive procedure. For hydrodynamic simulations, we use the software for the numerical solution of the shallow water equations described in [1, 22] and taking into account the parallel implementation for GPUs [23].

2.2. Assimilation of local spatial data by the DEM matrix

One essential feature of building a digital model of river bed is the source data sparseness, which include:

(i) There are two coastlines with water level mark $L_1^{coast}(\vec{r})$, $L_2^{coast(\vec{r})}$.

(ii) There are several depth curves on topographic maps of $L_i^{bed}(\vec{r})$ $(i = 1, ..., m_B)$. We have only $m_B \sim 3 - 4$ even for the largest rivers.

(iii) Several soundings show, as a rule, only the deepest points on a topographic map.

(iv) Depth measurements using echo sounders require new field studies.

All these data form set of points $\mathcal{P}$ on the height matrix b_{ij}.

We used an iterative procedure to build a river bottom DEM:

$$b_{n,m}^{p+1} = \begin{cases} b_{n,m}^{p} + \alpha \left[b_{n+1,m}^{p} - 2b_{n,m}^{p} + b_{n-1,m}^{p} \right] + \alpha \left[b_{n,m+1}^{p} - 2b_{n,m}^{p} + b_{n,m-1}^{p} \right], & P_{n,m} \notin \mathcal{P} \\ b_{n,m}^{(exp)}, & P_{n,m} \in \mathcal{P}, \end{cases} \tag{4}$$

where $b_{n,m}^{(exp)}$ is the depth at the points $\mathcal{P}_{n,m}$, α is the parameter that determines the convergence of the iterative procedure (4). The formula (4) is the finite-difference analog of the diffusion equation. We obtain the solution to the Poisson's equation in the case of converging iterations (4). Figure 7 shows the results of the construction of the DEM of the Volga River area, based on the approach described above.

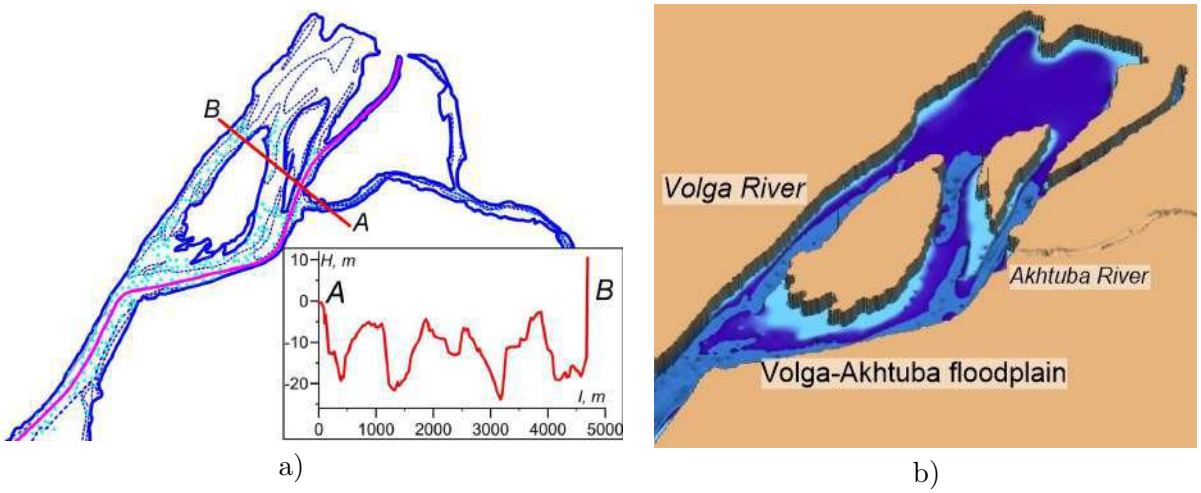

a) b)

Figure 7. *a*) Vector map of the River Volga. *b*) Digital elevation model of riverbed of the Volga downstream from the hydroelectric dam.

2.3. Coastlines dynamics as factor in improving DEM

Fig. 3 shows a schematic diagram of the hydrological regime in the VAF. Water flows from the Volga River to the Akhtuba River in a low water period in the case $Q \simeq 5 - 9$ thousands $m^3 \cdot sec^{-1}$, but it is not enough to fill the channels and besides the moisture reserve is very small

in the area between the rivers. All channels are quickly filled with the increase of Q up to 23–30 thousands $m^3 \cdot sec^{-1}$ and the water is poured onto the flat part of VAF. The water level is maintained by the powerful moistening at the third stage with $Q = 16000 - 20000\,m^3 \cdot sec^{-1}$. In late spring, there is a change to low-water and the total moisture content decreases in the territory.

There is a large number of shallow lakes on the flat territory between the large and small channels in spring and early summer. The coastlines of such reservoirs are moved on considerable distances in a short time period (Fig. 8 and See Fig. 4). Measuring the position of coastline at different points in time can help us determine an additional set of contour lines (isolines of heights) of the terrain for critical zones.

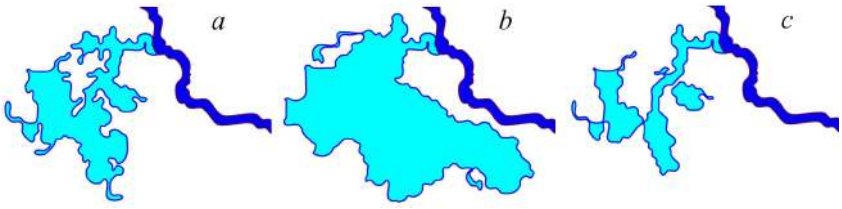

Figure 8. Shallow lake near the Bulgakov Channel at various stagesof the flooding in 2014 is shown: a) start the flooding (May 6), b) maximum the flooding (May 8), c) the dissipation of the reservoir (May 18).

2.4. Verification based on the results of hydrodynamic simulations

Fig. 9 shows the results of hydrodynamic simulations in the floodplain of the small river at various stages of the DEM refinement:

(i) We use the DEM after embedding the riverbed in the SRTM matrix and assignment the coastlines, the fairway line and the river slope (Fig. 9*a*).

(ii) Panel *b* in the figure demonstrates the water distribution in the river channel after processing the DEM in the "Construction of horizontals by elevation matrix" service in the GIS Panorama.

(iii) The next iteration involves the DEM rebuilding taking into account the geodetic transverse profiles of the river valley, which are obtained as a result of field measurements (Fig. 9*c*).

(iv) The final step involves updating the digital model on a small scale at the high water stage (Fig. 9*d*).

3. Conclusions

The object of our study is the valley between the River Volga and River Akhtuba, the ecosystem of which is unique on Earth due to the special hydrological regime. We propose the iterative procedure for creating the DEM for special floodplain areas with a large number of transient reservoirs. The initial data are the SRTM matrix, the space images from the "Resource-P " and UK-DMC-2 satellites, the topographic maps, the geodetic measurements of the elevation profiles, the depth measurements. The morphostructural analysis and the numerical simulations of surface water dynamics on realistic topography can be powerful tools for verification of the digital elevation model.

The observed dynamics of coastlines allows building elevation levels along the boundaries of water bodies, and this approach is actively used to construct the DEM. However, this method acquires special value in the case of periodically flooded areas, since the moving coastlines

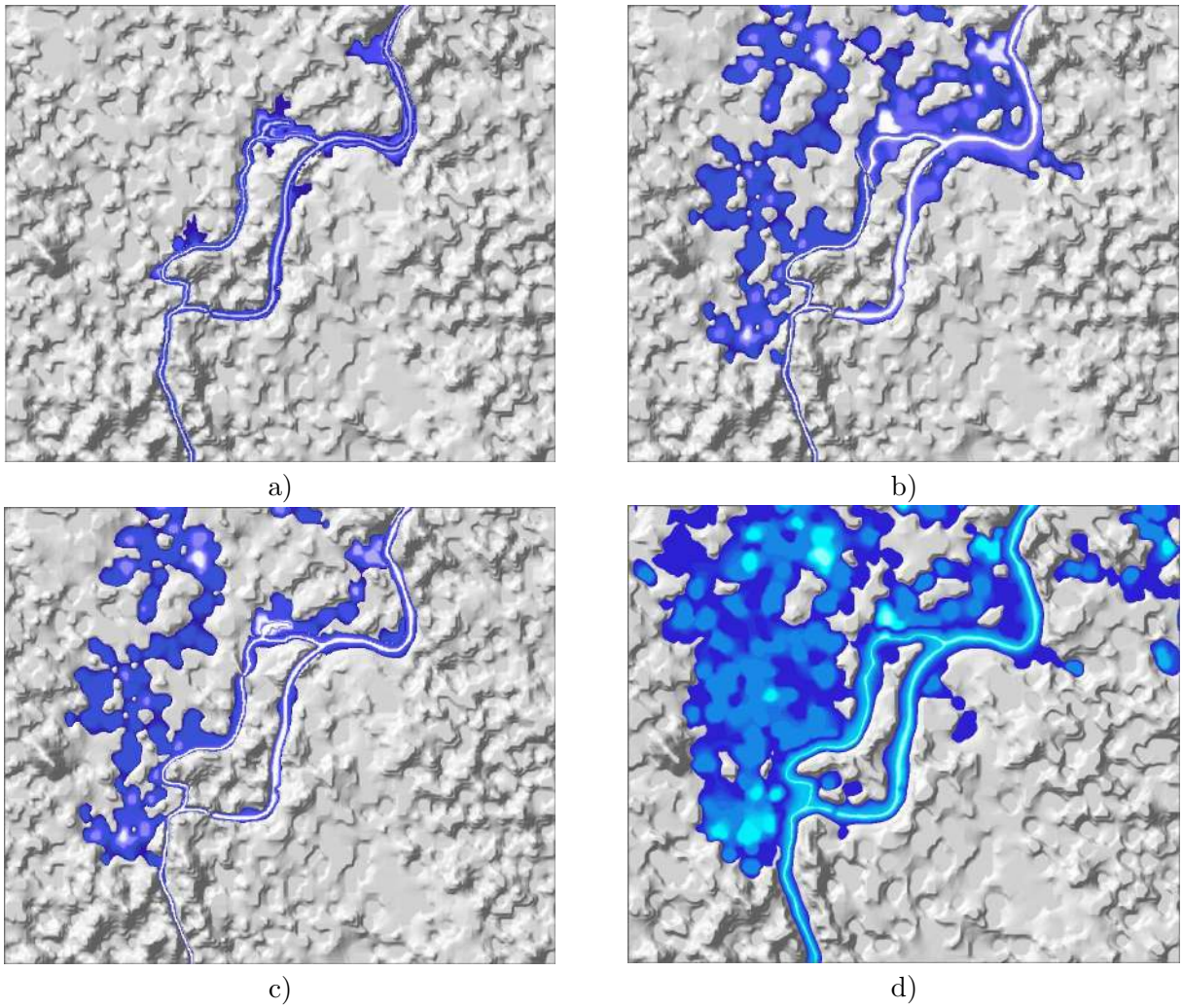

Figure 9. Results of local DEM refinement for the small river valley using hydrodynamic simulations. By identifying the shortcomings of the DEM, we provide flooding in the model for the nearest areas in accordance with the observations.

provide detailed sets of contour lines, being the basis for a very high-quality and relevant digital elevation model.

4. References

[1] Khrapov S S, Pisarev A V, Kobelev I A, Zhumaliev A G, Agafonnikova E O, Losev, A G and Khoperskov A V 2013 *Advances in Mech. Engineering* **5** 78708
[2] Madadi M R, Azamathulla H M and Yakhkeshi M 2015 *Earth Sci. Informatics* **8** 627-638
[3] Agafonnikova E O, Klikunova A Y and Khoperskov A V 2017 *Bul. of the South Ural State Univ. Ser.: Mathem. Modelling, Program. and Comp. Software* **10** 148-155
[4] Jafary P, Sarab A A and Tehrani N A 2018 *Environmental Processes-an International J* **5(4)** 807-831
[5] Ermolaev O P, Mal'tsev K A and Ivanov M A 2014 *Geography and Natural Resources* **35(3)** 222-228
[6] Efremova O A, Kunakov Yu N, Pavlov S V and Sultanov A K 2018 An algorithm for mapping flooded areas through analysis of satellite imagery and terrestrial relief features *Computer Optics* **42(4)** 695-703 DOI: 10.18287/2412-6179-2018-42-4-695-703
[7] Voronin A, Isaeva I, Khoperskov A and Grebenuk S 2017 *Communications in Comp. and Inform. Sci.* **754** 419-429

[8] Boori M S, Paringer R, Choudhary K and Kupriyanov A 2018 Comparison of hyperspectral and multi-spectral imagery to building a spectral library and land cover classification performance *Computer Optics* **42(6)** 1035-1045 DOI: 10.18287/2412-6179-2018-42-6-1035-1045
[9] Keenan P B and Jankowski P 2019 *Decision Support Syst.* **116** 64-76
[10] Jonoski A and Seid A H 2016 Decision support in water resources planning and management: the Nile basin decision support system *Real-World Decision Support Systems* (Cham: Springer) 199-222
[11] Grima N, Singh S J and Smetschka B 2017 *Land use policy* **67** 73-85
[12] Bagloee S A, Tavana M, Di Caprio D, Asadi M and Heshmati M 2017 *Modern Transportation* **25** 59-73
[13] Satge F, Bonnet M P, Timouk F, Calmant S, Pillco R, Molina J, Lavado-Casimiro W, Arsen A, Cretaux J F and Garnier J 2015 *Int. J. of Remote Sensing* **36(2)** 465-488
[14] Ahmed M F, Rogers J D and Ismail E H 2014 E*urop. J. of Remote Sensing* **47** 343-373
[15] Reichenbach P, Rossi M, Malamud B D, Mihir M and Guzzetti F 2018 *Earth-Science Reviews* **180** 60-91
[16] Sidoryakina V V and Sukhinov A I 2017 *Computational Math. and Math. Phys.* **57(6)** 978-994
[17] Nikiforov S L, Sorokhtin N O, Lobkovsky L I and Koshel S M 2018 *Oceanology* **58(2)** 266-272
[18] Michaelsen E 2018 On the automation of gestalt perception in remotely sensed data *Computer Optics* **42(6)** 1008-1014 DOI: 10.18287/2412-6179-2018-42-6-1008-1014
[19] Myasnikov E V 2017 Hyperspectral image segmentation using dimensionality reduction and classical segmentation approaches *Computer Optics* **41(4)** 564-572 DOI: 10.18287/ 2412-6179-2017-41-4-564-572
[20] Rueda A, Noguera J M and Martinez-Cruz C 2013 *Comp. & Geosciences* **59** 116-123
[21] Elmahdy S I 2015 *Applied Geomatics* **7(1)** 1-11
[22] Khoperskov A and Khrapov S. 2018 A *Numerical Simulation of the Shallow Water Flow ona Complex Topography Numerical Simulations in Engineering and Science* (InTechOpen) 237-254
[23] Dyakonova T A, Khoperskov A V and Khrapov S S 2016 *Communications in Comp. and Inform. Sci.* **687** 132-145

Acknowledgments
The work has been supported by the Ministry of Science and Higher Education (government task no. 2.852.2017/4.6). The research is carried out using the equipment of the shared research facilities of HPC computing resources at Lomonosov Moscow State University. The authors are grateful to E. Agafonnikova, S. Khrapov, A. Pisarev, K. Tertychny for their help and assistance in carrying out this project. A. Klikunova thanks for the support of the Russian Federal Property Fund and the Administration of the Volgograd region (grant 18-47-340003).

A technique for detecting diagnostic events in video channel of synchronous video and electroencephalographic monitoring data

D Murashov[1], Yu Obukhov[2], I Kershner[2] and M Sinkin[3]

[1]Federal Research Center "Computer Science and Control" of Russian Academy of Sciences, Moscow, Russia, 119333
[2]Kotel'nikov Institute of Radio Engineering and Electronics of RAS, Mokhovaya str., 11-7, Moscow, Russia, 125009
[3]N.V. Sklifosovsky Research Institute for Emergency Medicine of Moscow Healthcare Department, Bolshaya Sukharevskaya square, 3, Moscow, Russia, 129090

e-mail: d_murashov@mail.ru

Abstract. In this paper, a technique for automated detecting diagnostic events in the video channel of video and electroencephalographic monitoring data is presented. The technique is based on the analysis of the quantitative features of facial expressions in images of video data. The analysis of video sequences is aimed at detecting a group of frames characterized by high activity of frame regions. For detecting the frames, a criterion computed from the optical flow is proposed. The preliminary results of the analysis of real clinical data are presented. The intervals of synchronous muscle and brain activity, which may correspond to an epileptic seizure, are detected. These intervals can be used for diagnosing epileptic seizures and distinguishing them from non-epileptic events. Requirements for video shooting conditions are formulated.

1. Introduction

This paper is aimed at the solution of the problem for automated detecting diagnostic events in the video channel of synchronous video and electroencephalographic monitoring data. Video-electroencephalographic (VEEG) monitoring is a method for long-term synchronous registration of electroencephalography (EEG) and video image. Simultaneous video recording the clinical condition of the patient and the bioelectric activity of the brain (i.e. EEG) allows one to diagnose epileptic seizures reliably and distinguish them from events of non-epileptic nature [1, 2].

The duration of EEG monitoring is usually 24 hours or more, and if used in intensive care units it can last for weeks. Visual analysis of large amounts of data obtained during the long-term VEEG monitoring requires huge labor costs and special training of clinical neurophysiologists. This determines the urgency of developing new methods for detection, quantitative analysis, and classification of diagnostic objects and the exception of artifacts in long-term VEEG monitoring of patients.

The methodology of EEG analysis is traditionally based on the visual analysis of curves. Experts identify non-artifact fragments of the record and analyze its background structure, single (epileptiform) graph elements and their special patterns, which are specific for different clinical conditions [3]. In most cases, the algorithmic capabilities of the software for video EEG instruments are limited to preprocessing multi-channel EEG signals, indicating the likelihood of record artifacts, calculating inter-channel coherence and sources of electrical activity. To simplify the assessment of large volumes of visual information, a mathematical analysis of the oscillations with a graphical presentation of the results, notably a quantitative EEG (qEEG), is used [4]. However, the method of visual presentation of quantitative EEG in the form of trends and histograms does not take into account many artifacts, in particular, chewing and movement of the patient's head. When detecting high-amplitude plots on the qEEG histogram, the physician needs to revise the in video record a fragment of interest for visual assessment and differentiation of an epileptic and artifact event. For this purpose, they use not only the electrographic pattern but also the analysis of the video. In this case, trained EEG technical and medical staff visually scanning all VEEG data and marking specific events [2].

Recently, a number of methods for automatic detecting seizures according to EEG data have been proposed [3, 5-7]. However, all of them use only the native EEG without taking into account the video image, and their accuracy is insufficient for widespread clinical practice. The analysis of publications in periodicals and monographs in the subject domain showed the lack of publications on methods for automatic recognition of epileptic seizures in video sequences obtained during the video-EEG monitoring. Therefore, it is necessary to develop methods and algorithms for automated detection of diagnostic events in long-term video-EEG recordings, which will improve the reliability of their classification and significantly reduce the time for analyzing large amounts of video EEG data and increase their diagnostic significance.

In this paper, we propose a technique for detecting diagnostic events in the video channel of the video-EEG monitoring data of patients in coma.

2. Detecting events in VEEG data

When developing a technique for automated detection of diagnostic events in VEEG data, it is assumed that the decision on event detection is made when the specific features are detected simultaneously in EEG and video channels. This will make it possible to avoid false alarms caused by activity in only one of the data channels. For example, if the camera fixed the movement of a patient, which is not associated with convulsions, or the appearance of medical staff in the frame.

In this case, it is necessary to analyze informative areas in patient images with visible particular muscle contractions. Informative areas are usually associated with the details of a person’s face (eyes, nose, and mouth). Analysis of video sequences with recorded seizures showed a variety of appearance of these seizures. For example, in the case of a non-convulsive attack, only rather weak muscular contractions are observed in the region of the patient’s mouth. At the same time, the rest of the facial muscles remain motionless. In another case, more intense contractions of the muscles of the mouth and periodic movements of the head with immobile muscles in the eye area can be observed. In a number of cases, intense contractions of the muscles are visible all over the face, and contractions of the neck muscles and head movements are also possible. In the absence of seizures, the frames of the video data are relatively static for the studied group of patients.

One of the possible approaches for detecting events in a video channel can be associated with an analysis of the dynamics of the details of a person’s face (eyes, nose, mouth). The literature presents a wide range of methods for localizing these details [8-10]. It should be noted that the images of video sequences obtained during VEEG monitoring have the following features. First, an arbitrary angle of video recording the patient's face (see Figure 1). This feature eliminates methods based on the property of facial symmetry, and methods that require a full frontal image of the face. Second, medical equipment, partially covering the details of the face (see Figure 1(a)). This circumstance also complicates the task of localizing diagnostically important regions. Third, informative regions may not be associated with characteristic points of the face (eyes, corners of the mouth, etc.). Such regions, for example, may be neck areas. Therefore, conventional methods for localization of characteristic points

and details of the face may not be applicable. In paper [11], the authors proposed to use displacement vectors of scene objects, which are calculated as projections of the optical flow vectors onto the floor plane, for abnormal behavior detection in the video surveillance systems. This method has demonstrated efficiency in a wide range of operating conditions and scenes.

In this paper, we propose to detect diagnostic events using the magnitude of the criterion characterizing the degree of activity of the region of interest. The region of interest will be the part of the frame that includes the patient's face, head, and neck areas (see Figure 1). As a criterion of the activity of the region of interest, the total optical flow calculated for each frame of the video sequence is used:

$$J(i)=\sum_{x=0}^{W-1}\sum_{y=0}^{H-1}\sqrt{V_x^2(x,y,i)+V_y^2(x,y,i)}+\delta(i),\ i=1,...,N, \tag{1}$$

where $J(i)$ is a criterion value calculated in the frame number i; W, H are the frame width and height; $V_x(x,y,i)$ and $V_y(x,y,i)$ are the optical flow values in axial directions X and Y in the frame number i at a pixel with coordinates (x,y); $\delta(i)$ is a noise.

a) b)

Figure 1. Frames from long-term VEEG records.

Since the noise component is present in the model (1), the smoothed value of the activity criterion $\hat{J}(i)$ should be used to detect events. The smoothed $\hat{J}(i)$ value is obtained using a discrete version of the Kalman-Bucy filtering algorithm [12]. We apply the Kalman-Bucy algorithm since it provides the optimal estimate in the sense of minimum error variance. The decision to fix a diagnostic event is made according to the threshold rule. To avoid false alarms of the detector due to short-term spikes, the decision about the occurrence of an event is made if the value of $\hat{J}(i)$ exceeds a predetermined threshold in a sequence of frames not shorter than M. Thus, the decision rule is formulated as follows:

$$Event=\begin{cases}1,\ if\ \ \hat{J}(i)\ge T\ u\ i-i_0\ge M;\\ 0,\ if\ \ \hat{J}(i)<T\ or\ i-i_0<M,\end{cases} \tag{2}$$

where $Event$ is an event indicator, T is a threshold value, i_0 is a frame number from which the inequality $\hat{J}(i)\ge T$ is taking place, M is the length of the sequence of frames required to make a decision about the appearance of a diagnostic event. The threshold value is defined as follows:

$$T=\hat{J}_0+k\sigma, \tag{3}$$

where $\hat{J}_0$ is computed as a mean value of $\hat{J}(i)$ in a fragment of video sequence with low dynamics of the scene, σ is a standard deviation of $\hat{J}(i)$, k is a coefficient.

Thus, the algorithm for detecting diagnostic events in the video channel of VEEG monitoring data consists of the following steps.

1. Reading frame number 1 of a video sequence.

2. Computing the total optical flow in the region of interest in the video sequence frame according to the formula (1).
3. Computing the smoothed value of the activity index $\hat{J}(i)$.
4. Checking conditions (2) and (3). If the condition $\hat{J}(i) \geq T$ is satisfied, the current frame number $i_0 = i$ is stored. If the condition is not satisfied, go to step 1.
5. Repeating steps 1–3. If the conditions $\hat{J}(i) \geq T$ and $i - i_0 \geq M$ are satisfied, an event is detected. If not, go to step 1.

In the next section, an experiment aimed at testing the proposed technique is described.

3. Experiment

The developed technique is implemented in the MatLab software environment. For computing $V_x(x,y,i)$ and $V_y(x,y,i)$ in (1), Lucas–Kanade algorithm [13] is applied. This algorithm for computing the optical flow is chosen from the condition of the highest performance in comparison with other methods. The magnitude of the smoothed activity index $\hat{J}(i)$ is estimated using a discrete version of the Kalman-Bucy filtering algorithm [12]. The values of the filtering algorithm parameters are selected when processing test video sequences, and based on the best ratio of the error and speed values.

The developed technique was applied to five videos of patients in a coma. In three records epileptic seizures are detected, including non-convulsive ones. For each of the five video sequences, the parameters of the decision rule (2), (3) were determined from fragments with low scene dynamics. The number of frames corresponding to the shortest event duration in condition (2) was chosen equal to 75, which corresponds to a time interval of 2.5 seconds. The value of the coefficient in (3) was selected as $k = 1.1$. Examples of graphs of the criterion $J(t)$ and its smoothed value $\hat{J}(t)$, as well as the event indicator $Event$ for two fragments of the VEEG monitoring of the patient shown in Figure 1(a) are given in Figures 2 and 3. Here and below, instead of the variable i designating the frame number, we use the variable $t = i / FrameRate$, where t is the time, and $FrameRate$ is the frame rate of the video. In the experiment, we processed videos with a frame rate equal to 30 frames per second. Figure 2 (a) demonstrates the detection of diagnostic events. For the videos, corresponding to the graphs shown in Figures 2 (a) and 3, the parameters in expression (3) for determining the threshold value T were found to be equal to $\hat{J}_0 = 1604$ and $\sigma = 127.9$.

Figures 2 (b, c) show the graphs of the processed EEG signals from the synchronous recording of VEEG monitoring. Figure 2 (b) shows the projection of the ridge of the wavelet spectrogram on the power spectral density (PSD) and time axes. Using an adaptive threshold, the ridge points (maximum values of the power spectral density at each time point), which lie above this threshold, were calculated. Close points of the ridge, lying above the threshold, were combined into clusters - fragments of the ridge, marked in black on the graph. These ridge fragments are interpreted as episodes of suspicious activity, similar to an epileptic seizure [7].

Figure 2 (c) shows the EEG signal in one of the channels, filtered by a Butterworth filter of the 8th order with a passband from 5 to 22 Hz and notch filters at frequencies multiple of 50 Hz. The sampling frequency of the signal is equal to 500 Hz. The black color indicates the suspicious intervals obtained by analyzing the ridges of the wavelet spectrograms. From Figures 2 (a-c) one can see the intervals of synchronous muscle and brain activity, which may correspond to epileptic seizures. These intervals are found between 75 and 130 seconds, 144 and 147 seconds, 165 and 175 seconds, and between 202 and 207 seconds.

The graphs in Figure 3 correspond to video record without seizures.

A fragment of VEEG data from another patient recorded a non-convulsive epileptic seizure. Figure 4 shows the results of processing synchronous video and EEG channels of this recording. Figure 4 (a)

demonstrates the detection of diagnostic events in the video channel of the VEEG record. This figure shows manifestations of seizure, which is poorly expressed, but distinguishable in $\hat{J}(t)$ graph.

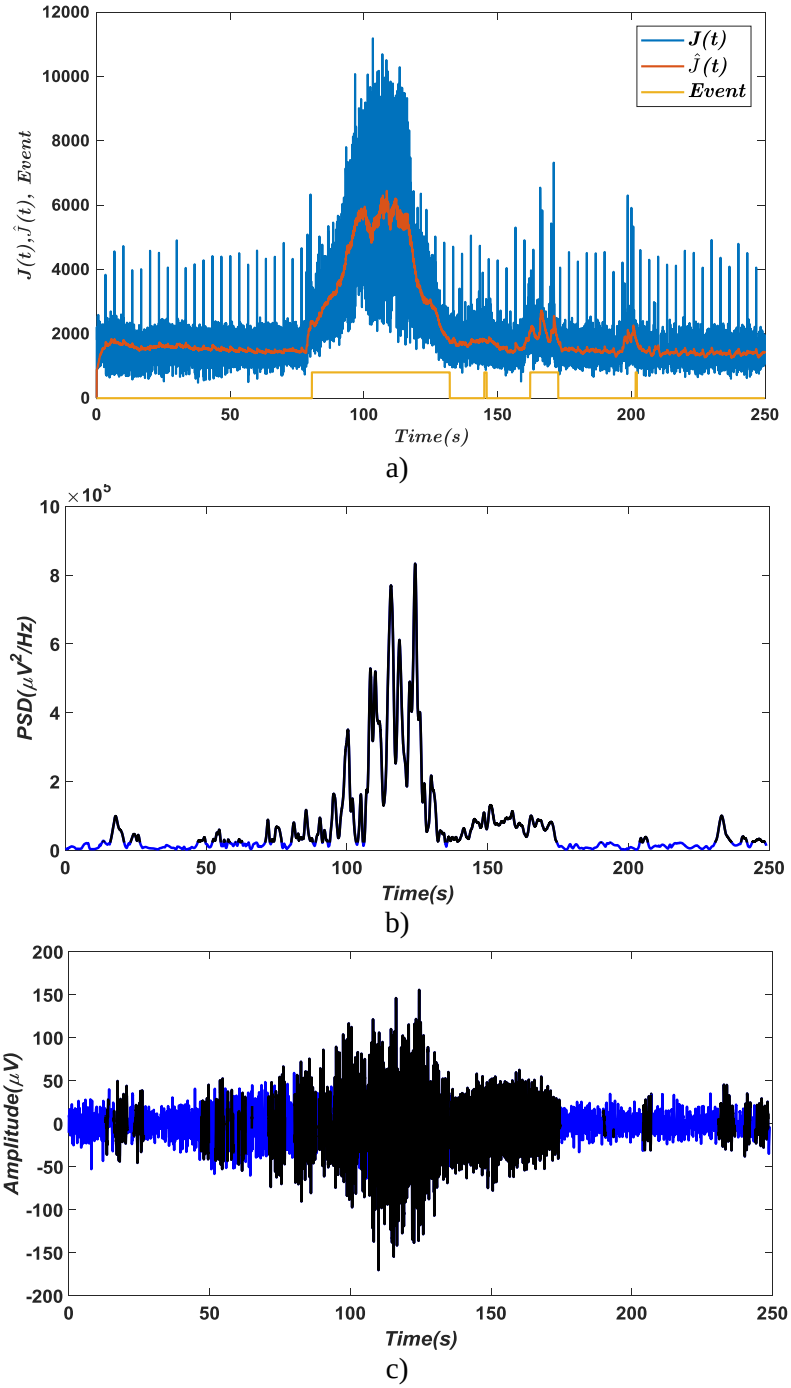

Figure 2. Graphs obtained from VEEG monitoring data illustrating detection of diagnostic events: (a) graphs of the criterion $J(t)$, estimate $\hat{J}(t)$, and event indicator *Event*; (b) projection of the ridge of the wavelet spectrogram on the power spectral density (PSD) and time axes; (c) EEG signal in one of the channels, filtered by a Butterworth filter of the 8th order and notch filters.

Figure 4 (b) shows the projection of the ridge of the wavelet spectrogram on the power spectral density (PSD) and time axes. Figure 4 (c) illustrates the EEG signal in one of the channels, filtered by a Butterworth filter of the 8th order and notch filters.

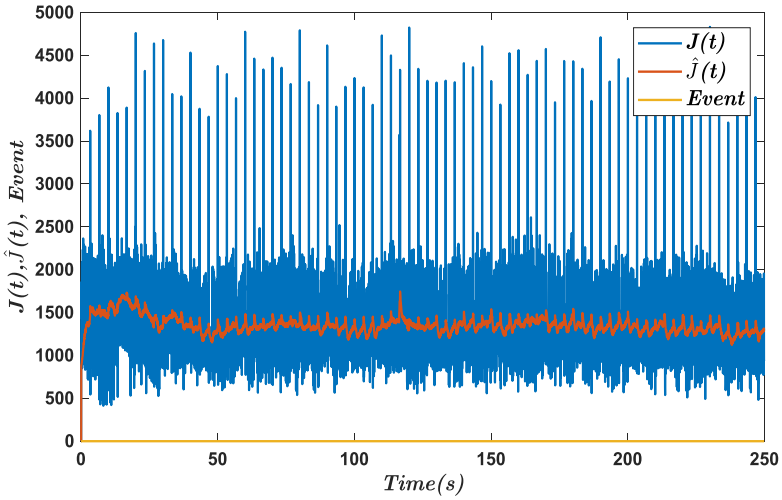

Figure 3. Graphs of the criterion $J(t)$, smoothed estimate $\hat{J}(t)$, and event indicator $Event$. The analyzed video does not contain seizures.

In Figures 4 (a-c) the intervals of synchronous muscle and brain activity, which may correspond to an epileptic seizure, can be seen. These intervals are visible between 7 and 45 seconds, 50 and 53 seconds, and between 95 and 98 seconds.

For the video, corresponding to the graphs shown in Figure 4 (a), the parameters in expression (3) for the threshold value T were computed equal to $\hat{J}_0 = 670.44$ and $\sigma = 12.29$.

It follows from Figures 2, 3, and 4 that diagnostic events can be detected using the criterion (1) and the rule (2)-(3) at different angles of shooting and with partial occlusion of the patient's face with medical equipment.

4. Requirements for recording video data of VEEG monitoring

Requirements for recording video data of VEEG monitoring are derived from the need for reliable detection of diagnostic events. For this, the field of view must be selected so as to provide the necessary dynamic range of values of the criteria used for event detecting. In the field of view of the camera should not get the details of the scene, generating a strong noise background. Essential for the video channel is the immobility of the camera. In the video sequence captured by the unfixed camera, the event cannot be detected due to the high level of noise in the optical flow caused by camera movement. Camera resolution should allow fixing facial expressions and muscle contractions of small amplitude. Based on the analysis of the video channel of the video EEG monitoring data, the following requirements for the video shooting parameters are formulated. First, the field of view of the video camera should cover the patient's head and neck. Secondly, the camera should be fixed. Thirdly, the resolution of the camera matrix should not be lower than HD.

5. Conclusions

A technique for automatic detection of diagnostic events based on the analysis of the quantitative characteristics of the patient's activity in video records is proposed. Analysis of video sequences is aimed at detecting a group of frames with high scene dynamics. A criterion computed from the optical flow magnitude is applied. The preliminary results of the analysis of real clinical data for patients in a coma are presented. The results of the analysis showed the efficiency of the proposed algorithm at different angles of shooting and partial occlusion of the patient's face with the details of medical equipment. The comparison of the results of diagnostic event detection from the video record with data obtained from the synchronous EEG showed the possibility of reliable diagnosing epileptic seizures and distinguishing them from non-epileptic events. Future research will be aimed at applying

pattern classifiers for detecting epileptic seizures based on a joint analysis of synchronous EEG and video channels.

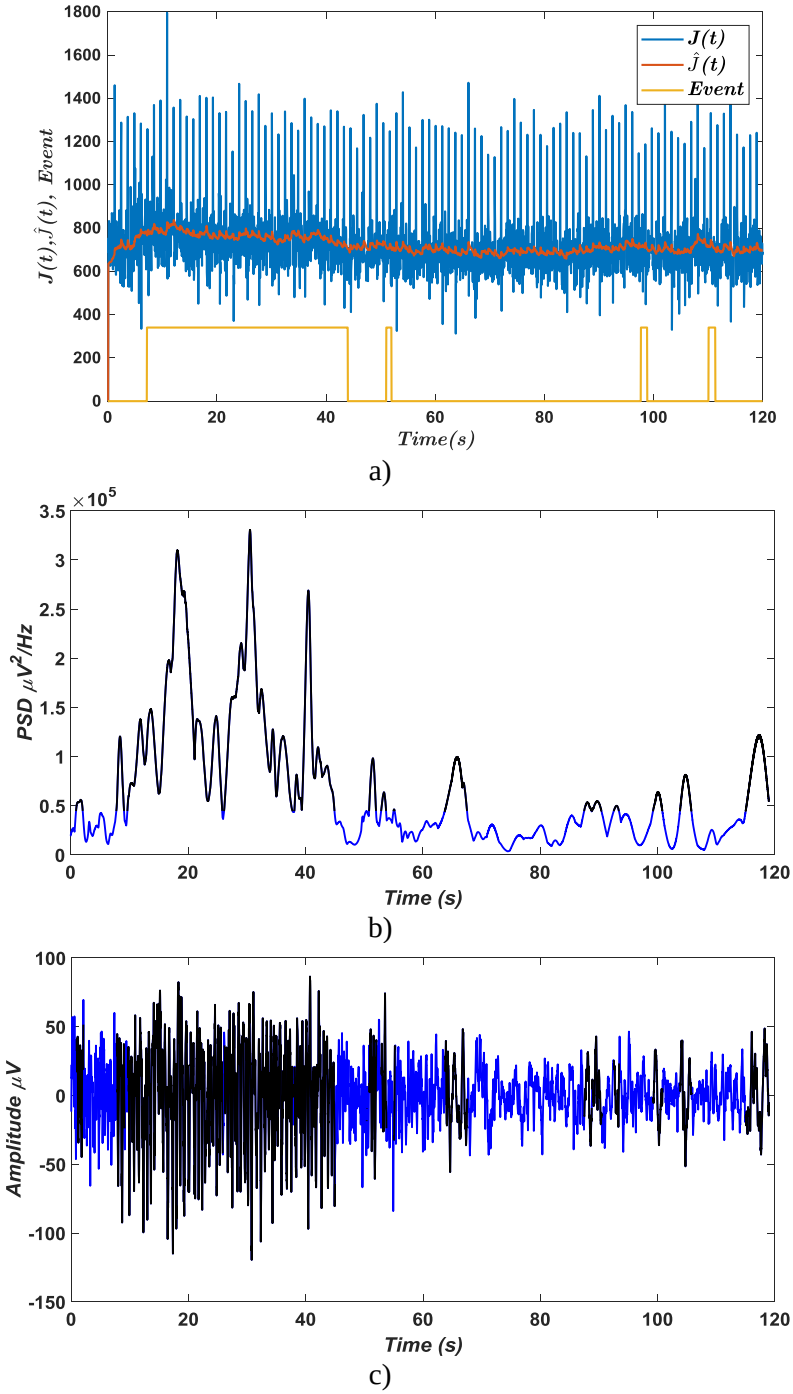

Figure 4. Graphs obtained from VEEG monitoring data illustrating detection of non-convulsive seizure: (a) graphs of the criterion $J(t)$, estimate $\hat{J}(t)$, and event indicator *Event*; (b) projection of the ridge of the wavelet spectrogram on the PSD and time axes; (c) EEG signal in one of the channels, filtered by a Butterworth filter of the 8th order and notch filters.

6. References

[1] Gravino G, Galea B, Soler D, Vella N and Aquilina J 2016 Video-EEG Long Term Monitoring as a new service at Mater Dei Hospital *Malta Medical Journal* **28** 46-54

[2] Lee Y Y, Lee M Y, Chen I A, Tsai Y T, Sung C Y, Hsieh H Y and Wu T 2009 *Chang Gung Med J* **32** 305-312
[3] Hirsch L, Brenner R 2011 *Atlas of EEG in critical care* (John Wiley & Sons)
[4] Duffy F H, Hughes J R, Miranda F, Bernad P and Cook P 1994 *Clinical Electroencephalography* **25** VI-XXII
[5] Tzallas A T, Tsipouras M G and Fotiadis D I 2007 *Computational Intelligence and Neuroscience* **2007** 80510
[6] Antsiperov V E, Obukhov Y V, Komol'tsev I G and Gulyaeva N V 2017 *Pattern Recognition and Image Analysis* **27** 789-803
[7] Obukhov K, Kershner I, Komol'tsev I and Obukhov Y 2018 *Pattern Recognition and Image Analysis* **28** 346-353
[8] Yow K C and Cipolla R 1997 *Image and vision computing* **15** 713-735
[9] Viola P and Jones M J 2004 *International journal of computer vision* **57** 137-154
[10] Singh A, Patil D, Reddy M and Omkar S N 2017 Disguised face identification (DFI) with facial keypoints using spatial fusion convolutional network *IEEE International Conference on Computer Vision* 1648-1655
[11] Shatalin R A, Fidelman V R, Ovchinnikov P E 2017 Abnormal behavior detection method for video surveillance applications *Computer Optics* **41(1)** 37-45 DOI: 10.18287/2412-6179-2017-41-1-37-45
[12] Kalman R E, Bucy R S 1961 *Journal of basic engineering* **83** 95-108
[13] Lucas B D, Kanade T 1981 *IJCAI81* 674-679

Acknowledgments
This research is partially funded by RFBR, grant № 18-29-02035.

Possibility estimation of 3D scene reconstruction from multiple images

E A Dmitriev[1], V V Myasnikov[1,2]

[1]Samara National Research University, Moskovskoe Shosse 34A, Samara, Russia, 443086
[2]Image Processing Systems Institute of RAS - Branch of the FSRC "Crystallography and Photonics" RAS, Molodogvardejskaya street 151, Samara, Russia, 443001

e-mail: DmitrievEgor94@yandex.ru, vmyas@geosamara.ru

Abstract. This paper presents a pixel-by-pixel possibility estimation of 3D scene reconstruction from multiple images. This method estimates conjugate pairs number with convolutional neural networks for further 3D reconstruction using classic approach. We considered neural networks that showed good results in semantic segmentation problem. The efficiency criterion of an algorithm is the resulting estimation accuracy. We conducted all experiments on images from Unity 3d program. The results of experiments showed the effectiveness of our approach in 3D scene reconstruction problem.

1. Introduction

3D-scene reconstruction is a classic computer vision problem. Algorithms for 3D-scene reconstruction are prevalent in many spheres like robotics, architecture, design, Earth remote sensing, automated driving systems.

There are several methods for solving considered problem [1, 2]. Binocular stereo vision is one of such methods [1]. This method calculates a disparity between conjugate points on rectified stereo images. The main problem is to find conjugate points. A possible solution is searching key points on stereo images, then getting points descriptors and matching points by metrics values between descriptors [4]. There are more modern approaches that use convolutional neural networks [3, 4, 5].

3D-scene reconstruction using multiple images is a computationally expensive problem [2]. The current level of technology development doesn't make it possible to reconstruct 3D-scenes in real time with good quality.

This article proposes an algorithm for possibility estimation of 3D-scene reconstruction using several frames of a video sequence in real time. This procedure helps to evaluate images number to get good quality 3D points cloud. The algorithm estimates conjugate pairs number from multiple images using a deep convolutional neural network. The article presents a model of a neural network with a quite small amount of weights. The model is possible to use on mobile devices with a graphical accelerator in real time. We conducted all experiments on images from Unity 3d program.

The article is structured as follows: the second section describes the main terms. Next section describes the model of neural network. The fourth section presents the results of experiments. Finally, we summarize results and tell about future researches.

2. Main terms

Let $I_k^s(n_1,n_2)$ be an RGB image from camera k and scene s, where $(n_1,n_2)\in\mathbf{D}$, $\mathbf{D}=\{(n_1,n_2): n_1=\overline{0,N_1-1}, n_2=\overline{0,N_2-1}\}$, $k=\overline{0,K-1}$, $s=\overline{0,S-1}$, N_1,N_2 are height and width of image from camera, K is number of cameras on scene and S is number of scenes. Every scene differs from each other by objects types or relative positions of objects. Let l be the index of the fixed camera and we call the image from this camera as *a relative image*. Let $R_k^s(n_1,n_2)$ be discrete function whose values are points coordinates in space. Every value of $R_k^s(n_1,n_2)$ is projected on the correspondent position of the image plane $I_k^s(n_1,n_2)$. $R_l^s(n_1,n_2)$ is a function whose values are projected on relative image s. To form elements of train and test datasets we consider the following function:

$$P_j^s(n_1,n_2)=\begin{cases}0, R_j^s(n_1,n_2)\neq R_l^s(n_1,n_2)\\ 1, R_j^s(n_1,n_2)=R_l^s(n_1,n_2)\end{cases} \quad (1)$$

Let $X^G=(x_i,y_i)_{i=0}^{G-1}$ be a dataset, x_i is a tensor, passed through the neural network, y_i is a label tensor and G is the size of the dataset. We form tensor x_i by concatenating $m<K$ different images $I_k^s(n_1,n_2)$ with the relative image from scene s. We choose m less than K in order to form more input and label tensors from one scene. Number of elements from one scene is C_{K-1}^{m-1}.

To get label tensor we consider the following function:

$$A_i^s(n_1,n_2)=\sum_{\substack{j=0\\ j\neq l}}^{m-1}P_j^s(n_1,n_2)\ , \quad (2)$$

where j is index of camera. $A_i^s(n_1,n_2)$ values show frames number in set of m images from input tensor (without considering relative image), that contain projection of $R_j^s(n_1,n_2)$ point. We represent all values of $A_i^s(n_1,n_2)$ function in one hot encoding with m bits to get final y_i label tensor. Our task is similar to semantic segmentation task or pixel classification problem.

3. Model description

We considered several fully convolutional neural networks whose output tensor has the same width and height as input tensor [6]. Such networks are used in semantic segmentation task and show good performance. Some of these networks are U-Net [7], SegNet [8]. These networks have comparable number of weights.

Another considered network is LinkNet [9]. This model exploits all features of U-Net and has a smaller number of weights. Specific feature of LinkNet is using several encoders and decoders. Original model consists of four blocks with 11.5 million parameters number.

In this work we use 3 decoder and encoder blocks to make network run faster in real time. We reduced size of max pooling kernel to 2×2 with stride 1 instead of kernel 3×3 with stride 2. This change in size of max pooling kernel doesn't allow feature maps to decrease fast to save more information. Our model has 3 million number of parameters. Figure 1 shows proposed model while figure 2 and figure 3 demonstrate architecture of encoder and decoder blocks respectively.

We used cross entropy as a loss function. According to [10], cross entropy loss function allows to get local minimum that gives bigger accuracy than mean square distance loss function using random weights initialization.

Let v be an output tensor of neural networks that has the same shape as label tensor. Loss function looks as follows:

$$H\left(y(n_1,n_2),v(n_1,n_2)\right)=-\sum_{i=0}^{m-1}y(n_1,n_2,i)\log v(n_1,n_2,i)\ . \quad (3)$$

Loss on whole dataset can be calculated as follows:

$$Q(X^G) = -\frac{1}{G}\sum_{i=0}^{G-1}\sum_{j=0}^{N_1-1}\sum_{k=0}^{N_2-1}\sum_{t=0}^{m-1} y_i(j,k,t)\log\left(v_i(j,k,t)\right) \quad (4)$$

We used an adaptive stochastic gradient descent Adam as optimization method [11, 12]. We also decreased learning coefficient value if loss on test set remained the same or less than on previous epoch.

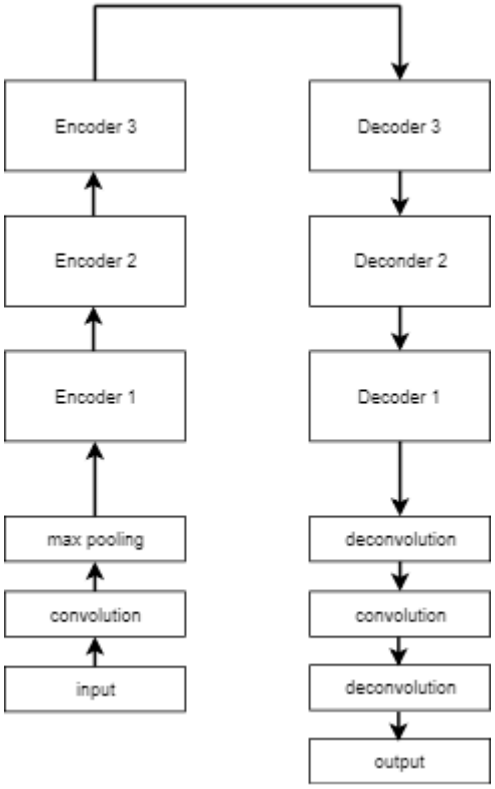

Figure 1. Neural network model.

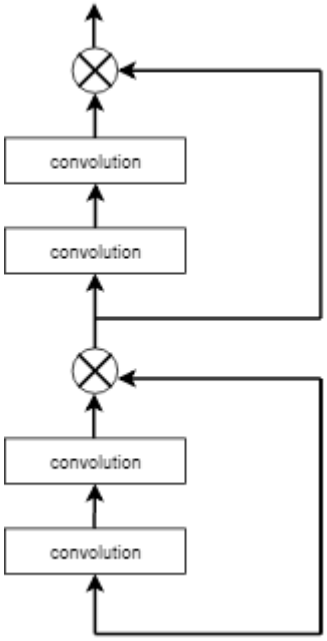

Figure 2. Encoder architecture.

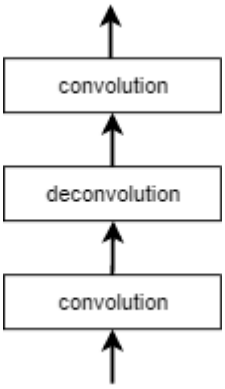

Figure 3. Decoder architecture.

4. Results of experiments

We trained and tested model on dataset of Unity 3d images. Number of cameras K was 8, number of scenes was 23 and number of RGB images m in input tensor was 5. Number of images in dataset was 805. Size of image was 300×300. We split images on 70/30 percent for train and test dataset respectively.

Input tensor contained 15 channels in third dimension. First 3 channels belonged to relative image. Relative image, with non-relative image, label tensor and output tensor are presented on figures 4, 5, 6, 7. Intensity on images 6 and 7 depends on number of conjugate pairs in input tensor.

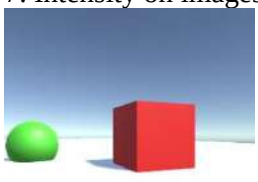

Figure 4. Relative image.

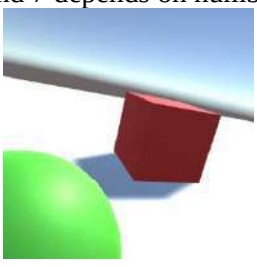

Figure 5. Non-relative image.

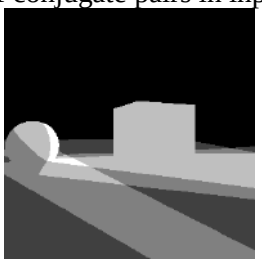

Figure 6. Label tensor.

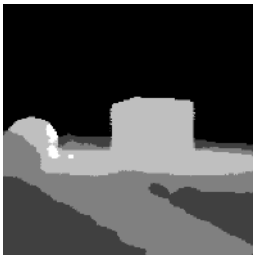

Figure 7. Output tensor.

We used accuracy metric for results estimation. Accuracy metric looks as follows:

$$M = \frac{1}{N_1 N_2 O} \sum_{t=0}^{O-1} \sum_{i=0}^{N_1-1} \sum_{j=0}^{N_2-1} \left(\arg\max_u v_t(i,j,u) == \arg\max_l y_t(i,j,l) \right), \quad (5)$$

where O is number of images in test dataset, u and l are indexes for output and label tensors respectively.

After training neural network on train dataset accuracy on test dataset was 0.96.

5. Conclusions

In this paper, we presented a new approach for possibility estimation of 3D-scene reconstruction using convolutional neural network. Our model can estimate conjugate pairs number from multiple images.

We conducted experiments and showed effectiveness of our approach. The aim of future researches to propose a method for camera-world rotation matrix and translation vector estimation.

6. References

[1] Horn B 1986 *Robot Vision* (Cambridge: MIT Press)
[2] Choy C B, Xu D, Gwak J Y, Chen K and Savarese S 2016 3D-R2N2: A unified approach for single and multi-view 3D object reconstruction *Lecture Notes in Computer Science (including subseries Lecture Notes in Artificial Intelligence and Lecture Notes in Bioinformatics)* **9912 LNCS** 628-644
[3] Savchenko A V 2017 Maximum-likelihood dissimilarities in image recognition with deep neural networks *Computer Optics* **41(3)** 422-430 DOI: 10.18287/2412-6179-2017-41-3-422-430
[4] Lowe D G 2004 Distinctive image features from scale-invariant keypoints *International Journal of Computer Vision* **60** 91-110
[5] Žbontar J and Le Cun Y 2015 Computing the stereo matching cost with a convolutional neural network *Proc. of the IEEE Computer Society Conference on Computer Vision and Pattern Recognition* 1592-1599
[6] Shelhamer E, Long J and Darrell T 2017 Fully Convolutional Networks for Semantic Segmentation *IEEE Transactions on Pattern Analysis and Machine Intelligence* **39** 640-651
[7] Ronneberger O, Fischer P and Brox T 2015 U-net: Convolutional networks for biomedical image segmentation *Lecture Notes in Computer Science (including subseries Lecture Notes in Artificial Intelligence and Lecture Notes in Bioinformatics)* **9351** 234-241
[8] Badrinarayanan V, Kendall A and Cipolla R 2017 SegNet: A Deep Convolutional Encoder-Decoder Architecture for Image Segmentation *IEEE Transactions on Pattern Analysis and Machine Intelligence* **39** 2481-2495
[9] Chaurasia A and Culurciello E 2018 LinkNet: Exploiting encoder representations for efficient semantic segmentation *IEEE Visual Communications and Image Processing* 1-4
[10] Golik P, Doetsch P and Ney H 2013 Cross-entropy vs. Squared error training: A theoretical and experimental comparison *Proceedings of the Annual Conference of the International Speech Communication Association, INTERSPEECH* 1756-1760
[11] Kingma D P and Ba J 2014 Adam: A Method for Stochastic Optimization *ArXiv: 1412.6980*
[12] Nikonorov A V, Petrov M V, Bibikov S A, Kutikova V V, Morozov A A and Kazanskiy N L 2017 Image restoration in diffractive optical systems using deep learning and deconvolution *Computer Optics* **41(6)** 875-887 DOI: 10.18287/2412-6179-2017-41-6-875-887

Acknowledgements

The reported study was funded by RFBR according to the research projects 18-01-00748, 17-29-3190.

Optimization of computational complexity of lossy compression algorithms for hyperspectral images

L I Lebedev[1], A O Shakhlan[2]

[1]Lobachevsky State University of Nizhny Novgorod, Ulyanov st., 10, Nizhny Novgorod, Russia, 603005
[2]Bauman Moscow State Technical University, 2nd Baumanskaya st., 5/1, Moscow, Russia, 105005

e-mail: lebedev@pmk.unn.ru

Abstract. In this paper, we consider the solution of the problem of increasing the speed of the algorithm for hyperspectral images (HSI) compression, based on recognition methods. Two methods are proposed to reduce the computational complexity of a lossy compression algorithm. The first method is based on the use of compression results obtained with other parameters, including those of the recognition method. The second method is based on adaptive partitioning of hyperspectral image pixels into clusters and calculating the estimates of similarity only with the templates of one of the subsets. Theoretical and practical estimates of the increase in the speed of the compression algorithm are obtained.

1. Introduction

The main idea of compression methods using recognition methods is to replace the original description of a pixel (signature) $\mathbf{y} = (y_1, y_2, ..., y_n)$ in a constant length Υ record with the values of parameters obtained during recognition. On average, as a rule, there are quite many pixels that are similar to $\mathbf{y}$, and the description $\mathbf{y}$ is much larger than the description Υ, which ensures the efficiency of the HSI compression. We shall consider the methods of comparison with templates as the main recognition methods. Recognition based on comparison with templates consists in establishing the similarity (proximity) of a certain pixel $\mathbf{y}$ to the equivalence class $K(\mathbf{y}^{\mathbf{e}}, A)$ generated by the template $\mathbf{y}^{\mathbf{e}}$ and given by the transformation operator A. As an estimate of the proximity $\varepsilon_m(A)$ of the pixel $\mathbf{y}$ to the template $\mathbf{y}^{\mathbf{e}}$, the minimum mean square error $\varepsilon(A)$ (NSE) is used with respect to the parameters of the operator A:

$$\varepsilon_m(A) = \min_A \varepsilon(A) = \frac{1}{n} \cdot \left\| \mathbf{y} - A(\mathbf{y}^{\mathbf{e}}) \right\|^2 = \frac{1}{n} \cdot \sum_{i=1}^{n} \left(y_i - A(y_i^{\mathbf{e}}) \right)^2 . \quad (1)$$

The HSI compression algorithm is based on recognition by the methods of comparison with templates. This type of recognition is used in the self-learning mode, when a set of templates is formed on the basis of unrecognized signatures. With different transformation operators A, it is possible to obtain several criteria for similarity estimates by solving the optimization problem (1). On their basis, several recognition methods will be obtained.

2. Criteria for assessing the proximity of signatures

Let us consider some criteria for calculating similarity estimates:

$$\begin{gathered} A(\mathbf{y}^{\mathbf{e}}) = \mathbf{y}^{\mathbf{e}}: \quad \varepsilon_m^{nt} = \mathrm{M}(\mathbf{y}^{\mathbf{e}})^2 + \mathrm{M}\,\mathbf{y}^2 - 2\cdot \mathrm{M}\,\mathbf{y}^{\mathbf{e}}\mathbf{y}\ ; \\ A(\mathbf{y}^{\mathbf{e}}) = \mathbf{y}^{\mathbf{e}} + \Delta y^{\mathrm{e}}: \quad \varepsilon_m^{ot} = \mathrm{D}\,\mathbf{y}^{\mathbf{e}} + \mathrm{D}\,\mathbf{y} - 2\cdot \mathrm{cov}(\mathbf{y}^{\mathbf{e}},\mathbf{y})\ ,\ \Delta y^{\mathrm{e}} = \mathrm{M}\,\mathbf{y} - \mathrm{M}\,\mathbf{y}^{\mathbf{e}}\ ; \\ A(\mathbf{y}^{\mathbf{e}}) = k_m\cdot \mathbf{y}^{\mathbf{e}}: \quad \varepsilon_m^{st} = \mathrm{M}\,\mathbf{y}^2 - \mathrm{M}^2(\mathbf{y}^{\mathbf{e}}\mathbf{y})/\mathrm{M}(\mathbf{y}^{\mathbf{e}})^2\ ,\ k_m = \mathrm{M}(\mathbf{y}^{\mathbf{e}}\mathbf{y})/\mathrm{M}(\mathbf{y}^{\mathbf{e}})^2\ ; \\ A(\mathbf{y}^{\mathbf{e}}) = k_m\cdot \mathbf{y}^{\mathbf{e}} + \Delta y^{\mathrm{e}}: \quad \varepsilon_m^{at} = \mathrm{D}\,\mathbf{y} - \mathrm{cov}^2(\mathbf{y}^{\mathbf{e}},\mathbf{y})/\mathrm{D}\,\mathbf{y}^{\mathbf{e}}\ ,\ k_m = \mathrm{cov}(\mathbf{y}^{\mathbf{e}},\mathbf{y})/\mathrm{D}\,\mathbf{y}^{\mathbf{e}}\ ,\ \Delta y^{\mathrm{e}} = \mathrm{M}\,\mathbf{y} - k_m\cdot \mathrm{M}\,\mathbf{y}^{\mathbf{e}}\ . \end{gathered} \tag{2}$$

In the above formulas, $\mathrm{M}\mathbf{y}$, $\mathrm{M}\mathbf{y}^{\mathbf{e}}, \mathrm{M}\mathbf{y}^2, \mathrm{M}(\mathbf{y}^{\mathbf{e}})^2$ denote the initial moments of the first and second orders of the current signature and template; $\mathrm{M}\mathbf{y}^{\mathbf{e}}\mathbf{y}$ is the mixed covariance moment; $\mathrm{D}\mathbf{y}$, $\mathrm{D}\mathbf{y}^{\mathbf{e}}$ denote the dispersion of the signature and the template; $\mathrm{cov}(\mathbf{y}^{\mathbf{e}},\mathbf{y})$ is the correlation moment; Δy^{e}, k_m are the bias and the scale factor [1-3].

3. Recognition algorithm with self-learning

Based on the proximity estimates (2), in accordance with the recognition algorithm, for each template pixel $\mathbf{y}^{\mathbf{e}}$ and the current signature $\mathbf{y}$, the value $\varepsilon_m(\mathbf{y},\mathbf{y}^{\mathbf{e}})$ is calculated; among these values, the smallest one, $\varepsilon_{\min}(\mathbf{y})$ is found. If this estimate is greater than a given threshold $\varepsilon_{\min}(\mathbf{y}) > \delta$, then a new template is formed on the basis of the signature description $\mathbf{y}$. When $\varepsilon_{\min}(\mathbf{y}) < \delta$, the pixel is considered to be recognized and using the parameters obtained, a corresponding record in the output file is made. For all the similarity estimates (2), a template number must be assigned, which is recorded in a 2-byte field (or a 4-byte field if the number of templates exceeds 65536). The values Δy^{e} and k_m are given by real variables, which are recorded in 4-byte fields. Therefore, the length of the structures for writing the parameters depending on the similarity estimate used will be equal, respectively, to 2, 6, 6 and 10 bytes (or 4, 8, 8 and 12 bytes)..

4. Optimization of computations in the HSI compression algorithm

Let us consider two possibilities for increasing the speed of the compression algorithm under consideration. It follows from the recognition algorithm that the number of obtained templates depends on the threshold value δ, which in turn is determined by the error limited to a certain percentage σ of the current signature. Then the recognition and, therefore, the compression will be performed using an adaptive threshold $\delta = (0.01\cdot\sigma)^2\cdot \mathrm{M}\mathbf{y}^2$. From the analysis of formula (2), it follows that when compressing a HSI with a similarity estimate ε_m^{at}, the number of templates will be the smallest among all compression algorithms using the remaining proximity estimates. In turn, compression algorithms based on proximity estimates ε_m^{st} and ε_m^{ot} have some advantages in terms of speed over the algorithm using the proximity estimate ε_m^{nt}. Similarly, the greater the value σ, the less templates will be obtained in the recognition process and thus the shorter the HSI compression time. Therefore, in order to reduce compression time required by more time-consuming algorithms, it is necessary to use the results of compression provided by faster compression algorithms. The modification of the compression algorithm in this variant consists in calculating the estimate of similarity only with the templates generated by the template of the high-speed algorithm. The second modification of the compression algorithm is based on the current clustering of signatures being recognized and forming own templates in each cluster. Therefore, if the current signature is assigned to a cluster, the similarity estimate will be formed on the basis of the templates of this cluster. The clustering is carried out in the space of the features, which can be easily obtained by calculating the initial moments of the first and second orders of the current pixels.

Let us estimate the computational complexity of recognition methods based on the proposed similarity estimates. Let the function describing the dependence of the number of templates used on the current number of the pixel being recognized be given by the formula $v = [f(u)]$, with

$m = f(N)$, $f(0) = 0$, where N is the number of pixels of the image, and m is the number of templates obtained during image compression. The function $v = [f(u)]$ is piecewise constant and, therefore, an increase in the number of templates per unit occurs during the compression of pixels with the numbers $u = N_i$. Hence, $f(N_i) - f(N_{i-1}) = 1$, and from this expression one can find the numbers of pixels N_i. Then the computational complexity of the HSI compression algorithm will be determined by the formula:

$$C = \sum_{i=1}^{m} i \cdot (N_i - N_{i-1}) \cdot O(n), \quad (3)$$

where $O(n)$ is the complexity of obtaining the estimate of similarity of a pixel with the template. If we assume that $f(u)$ is a linear function of (L), then $C(L) = [N \cdot (m+1)/2] \cdot O(n)$, since $N_i - N_{i-1} = N/m$. However, as a rule, the number of templates increases faster at the initial stage of compression and slows down closer to the completion of the HSI pixel recognition process. If we take the parabola (P) $u = N \cdot v^2/m^2$ as a function approximating the plot of the number of templates depending on the number of pixels processed, then it follows from the expression $m \cdot \sqrt{N_i/N} - m \cdot \sqrt{N_{i-1}/N} = 1$ that $N_i - N_{i-1} = N/m^2 \cdot (2 \cdot i - 1)$. Hence, the computational complexity of the HSI compression algorithm in this case can be estimated by the value $C(P) = [N \cdot (m+1) \cdot (4 - 1/m)/6] \cdot O(n)$, and therefore, $C(P)/C(L) \approx 4/3$. In the case of the cubic dependence (K) $u = N \cdot v^3/m^3$, the computational complexity is equal to $C(K) = [N \cdot (m+1) \cdot (3 - 1/m)/4] \cdot O(n)$, and $C(K)/C(L) \approx 3/2$. For the proposed approximation functions, the computational complexity of the recognition algorithm is proportional to $N(m+1)$ and, therefore, if the number of templates is $M > m$, then while maintaining the same distribution law, the HSI compression time will increase by a factor of M/m. Note that an increase in the HSI compression time does not depend on the distribution law.

5. Experimental research

Experiments on solving recognition problems were performed on the f100520t01p00-12 HSI file of the AVIRIS spectrometer based on 224 frequencies with wavelengths in the range from 365.9298 to 2496.236 nm. The original HSI was represented by a matrix of 813×2109 pixels with a resolution of 17.3 m. A two-byte format for representing the spectrum amplitude values was used. At the beginning, filtering (correction of values) of spectral images of the original HSI was performed. Its purpose was to replace the negative values of the signature with the data obtained by piecewise linear approximation with the closest positive values. Signatures with completely negative or positive component values were not adjusted. The number of pixels with completely negative values was 207055 of the total number 1714617 (≈12%).

By using compression with an adaptive threshold, calculated for the value $\sigma = 2$ for the similarity estimates listed in (2), we obtained 2582, 1841, 976 and 785 templates, respectively. Since it can be expected that the computational complexity of compression is proportional to the number of templates obtained in the course of recognition, the running time of the algorithm may vary up to 3.3 times when using different similarity estimates. Figure 1 shows the graphs of the number of templates used depending on the current number of a HSI pixel being recognized for various similarity estimates. Figure 2 shows the graphs of various functions a) - c) approximating the dependence of the number of templates used on the current number d). Figure 3 shows a histogram of the number of signatures recognized by each template when using the estimate ε_m^{st}. It can be concluded from these graphs that the bulk of the pixels is encoded on the basis of the first third of the templates. However, the remaining pixels will use in the coding almost the entire set of templates, which leads to an increase in the running time of the algorithm. When using a modification of the compression algorithm utilizing

the results obtained in recognition with the estimate ε_m^{st}, each signature will be compared on average with only three templates.

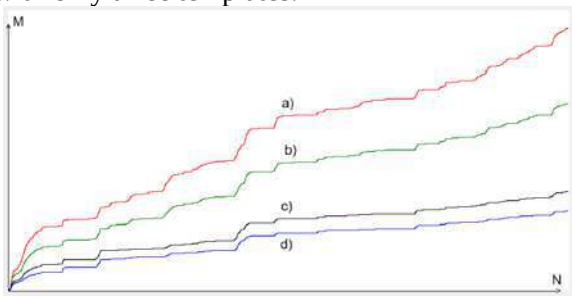

Figure 1. The number of templates used vs. the current number of the HSI pixel when compressed with estimates: a) $-\varepsilon_m^{nt}$; b) $-\varepsilon_m^{ot}$; c) $-\varepsilon_m^{st}$; d) $-\varepsilon_m^{at}$.

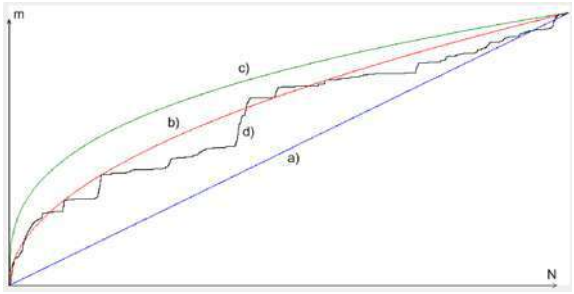

Figure 2. Approximation of the initial dependence $m = f(N)$ obtained for compression with the estimate ε_m^{st} - plot d), functions: a) – linear; b) $m = k \cdot \sqrt{N}$; c) $m = k \cdot \sqrt[3]{N}$.

As a result, compression with the estimate ε_m^{nt} was obtained tens of times faster than with the use of the original algorithm. The use of a modified algorithm for compressing HSI using the same estimate ε_m^{st} with the parameter $\sigma = 1$ was even more efficient since the number of templates in this case increases to 12232.

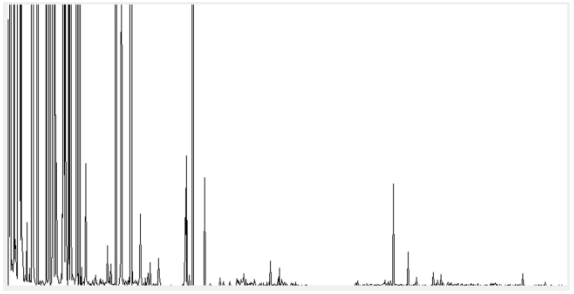

Figure 3. Histogram of the number of recognized HSI pixels vs. the template number.

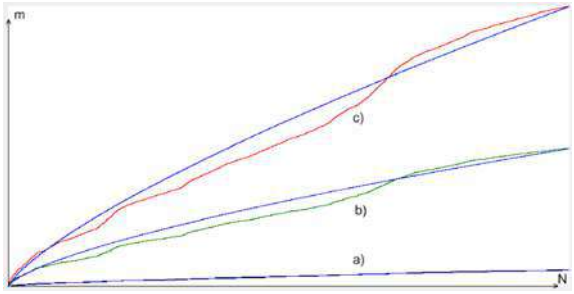

Figure 4. The number of templates vs. the pixel number for different thresholds: a) $\sigma = 10$; b) $\sigma = 6$; c) $\sigma = 5$ and their approximation by the functions $m = k \cdot N^{\mu}$.

The second modification was based on identifying clusters in the space of features, which were obtained on the basis of groups of pixels. There are many examples of the application of clustering and segmentation methods for solving practical problems [4-6]. However, for the purpose of modification, clustering algorithms must have computational complexity that is an order of magnitude smaller than that of the original compression methods. Therefore, to solve the clustering problem, one can use the original compression algorithms for large values of the parameter σ, which will provide the necessary speed. As a result, for $\sigma = 5$, about three dozen clusters with different sets of templates were obtained to get the similarity estimate ε_m^{at} for the given hyperspectral image, thus making it possible to reduce by an order of magnitude the execution time of the compression algorithm. Let us consider the efficiency of solving the problem of computational complexity optimization by the proposed compression algorithms for more variable data, both in terms of the representation of various types of underlying surfaces on the HSI, and the values of spectral scatter. This MoffettField HSI of the same AVIRIS spectrometer was represented by a matrix of 753 × 1924 pixels with a resolution of 17.0 m. 68335 out of 1448772 pixels represent fragments that have not been covered by the scan band. The templates obtained by compressing the HSI for $\sigma = 10$ with the similarity estimate ε_m^{st} were used as cluster representatives. As a result, 764 templates were obtained within the time ≈ 10 minutes. The computational complexity was 675863990 operations for computing similarity estimates. For $\sigma = 5$, the number of operations amounted to 10300082029 and the original compression algorithm produced

12891 templates for the time ≈ 160 minutes. The execution time of the proposed compression algorithm for $\sigma = 5$ with the account of the time for obtaining clusters was ≈ 13 minutes, which corresponds to theoretical estimates. Figure 4 shows the plots of the number of templates used to obtain the same similarity estimate depending on the current HSI pixel number for various compression thresholds and their approximation by analytical functions.

6. Conclusion

Experiments performed on hyperspectral images have confirmed the estimates of the expected increase in the speed of the modified recognition algorithms based on self-learning recognition. It was established that the speed of the modified compression algorithms is more than an order of magnitude higher than their original counterparts. A further increase in speed can be achieved by parallelizing the computations at each step of the two-step compression algorithm proposed.

7. References

[1] Lebedev L I 2018 Recognition and classification of objects in a hyperspectral image *Proceedings of the 5th International Scientific Conference «Regional problems of remote sensing of the earth»* (Krasnoyarsk: Siberian Federal University) 138-143
[2] Lebedev L I and Shakhlan A O 2018 Spatial analysis of hyperspectral images *Proceedings of the 25th International Scientific Conference* (Tomsk: Tomsk Polytechnic University) 150-153
[3] Lebedev L I 2013 *Correlation - extreme contour recognition methods. Theoretical foundations: A study manual* (Nizhny Novgorod: Nizhny Novgorod State University) p 113
[4] Tatarnikov V V, Pestunov I A and Berikov V B 2017 Centroid averaging algorithm for a clustering ensemble *Computer Optics* **41(5)** 712-718 DOI: 10.18287/2412-6179-2017-41-5-712-718
[5] Myasnikov E V 2017 Hyperspectral image segmentation using dimensionality reduction and classical segmentation approaches *Computer Optics* **41(4)** 564-572 DOI: 10.18287/2412-179-2017-41-4-564-572
[6] Varlamova A A, Denisova A Y and Sergeev V V 2018 Earth remote sensing data processing technology for obtaining vegetation types maps *Computer Optics* **42(5)** 864-876 DOI: 10.18287/2412-6179-2018-42-5-864-876

Acknowledgements

This work was supported by the Russian Science Foundation, project No. 16-11-00068.

Multi-channel data storage format definition for visualization tasks on the example of SPOT-4 images

N Yu Sevastianova[1] and N S Vinogradova[1]

[1]Ural Federal University, Mira street, 19, Ekaterinburg, Russia, 620002

e-mail: n.u.sevastianova@mail.ru

Abstract. One of the features of a remote sensing data storage is the widespread utilization of large-capacity disk arrays. Emergency situations arising from the use of arrays can lead to the fact that the remote sensing data, usually stored in uncompressed form, may become partially damaged. But even with incomplete recovery, this kind of data can be used in the future to solve production problems. However, this recovery is sometimes hampered by incomplete knowledge of the format of the corrupted data. The article describes an approach to automatic recognition of multichannel data interleaving type (BIP, BIL or BSQ) and its application to a recovery of SPOT-4 remote sensing data stored in the segment format "SEG", which were damaged after a disk array failure.

1. Introduction

SPOT is a commercial high-resolution optical satellite earth observation system, which operated in 1998-2013 and aimed at solving environmental and agricultural problems, as well as used in such fundamental areas, as climatology and oceanography [1,2,3,4]. The SPOT-4 device was a multispectral observation system that carried out the survey in four spectral ranges (listed in table 1).

Table 1. SPOT-4 spectral bands [1].

Imaging Band	Spatial Resolution	Wavelength
panchromatic	10 m	0.61–0.68 μm
B1: green	20 m	0.50–0.59 μm
B2: red	20 m	0.61–0.68 μm
B3: near-IR	20 m	0.78–0.89 μm

In 2011-2012, the Space monitoring center of the Ural Federal University received a signal from the SPOT-4 spacecraft and accumulated more than 1 TB of survey data in the original "raw" format (RAW) and the post-processed «SEG» format. After the accident of disk storage in 2016, the data were temporarily lost, but preliminary analysis of the results of the repair work showed that only a part of the data that was stored on failed devices (3 hard disks out of 20) was finally lost. At the same time, the storage file system remained weakly damaged, which made it possible to recover most of the files (including SEG), and the chains of lost fragments have preserved their localization within the file, but were written as zero bytes. Since SPOT-4 data is currently actively used in the educational process, the

question of the visualization possibility and further use of this data turned out to be extremely relevant. In the course of solving this problem, among others, a problem of identifying the method of storing multichannel data have arisen. Different recovering methods for corrupted data are developed last time propose the approaches for recovering different remote sensing data types [5,6], i.e. hyperspectral data [7] and SAR data [8], but the peculiarity of a problem considered here is that data are multispectral and they have the specific corruption type (randomly located horizontal stripes of zeros pixels). There are three main ways to record data in multichannel images [9]:

- BIL (byte interleaving by line): channels separated by lines;
- BIP (byte interleaving by pixel): pixel-by-pixel recording of spectral channels;
- BSQ (band sequential): per-channel recording.

The presented storage methods have an associated header, which is usually represented in ASCII encoding. This header contains basic information about the image, such as the format, the number of rows and columns, the presence of a color map, can also contain auxiliary information, such as geographic reference, authorship, imaging time.

BIL uses a method of recording multi-channel images in which rows of values for each channel are written sequentially. For example, in the case of a three-channel image, all three data channels are first written to the first row, then to the second row, and so on until the last row of the image is written.

BIP method implies that the data for each pixel is written sequentially. For example, when you record a three-channel image, the data for the first, second, and third channels is recorded for the first pixel of the first column; then the channel data is written for the first pixel of the second column, and so on.

For per-channel recording (BSQ), the information for each channel is recorded sequentially. In other words, the data of all pixels of the first channel is recorded first, then all pixels of the second channel are recorded and so on [9]. Automatic recognition of correct data interleaving type makes it possible to organize the on-flow damaged data recovery.

2. The algorithm for the SPOT-4 data analysis

As reference information, the sizes of images in bytes (which can be completely different) and the number of SPOT-4 channels equal to four are used. For data analysis in MATLAB, an algorithm is developed that allows you to select and analyze the method of multispectral data storage. At the first stage, factorization of file size into the prime factors was performed, which allowed splitting the image size to determine the number of columns and rows. It showed, that line size for SEG data is a multiple of 3057, where the first 57 bytes of each channel contains metadata. Another approach may imply the one-dimensional Fourier transform and spectral peaks analysis. The peaks positions correspond to the image number of columns, and the latter makes it possible to determine the image size, but the determination of interleaving type may be inconveniently.

In order to set the desired data storage method, the images are opened with all three possible options. Visual comparison of opened images revealed significant spatial differences (figure 1).

The image that is opened in the assumption that the data stored as BIL, contained stripes along the image columns, which deal with the violation of pixels interleaving method. The image, opened under the assumption of BSQ way, also carries an incorrect pixel striping, that can be observed in the figure 1c (more stripes along image diagonals). An image opened under the assumption that the data is stored in a BIP manner represents the correct striping (figure 1a). Thus, for SPOT-4 remote sensing data, the BIP is the correct way to store multispectral data.

2.1. Analysis of the characteristics of the BIL format

As noted earlier from the visual mapping, an image opened under the assumption using the BIL storage method, has expressed bars in the direction of the image columns. In order to emphasize the bands, spatial filtering methods were used. The following types of spatial filters have been tested [10,11,12]:

- Laplace filters;
- line detection filters;
- Sobel operator;

• Roberts cross filter.

The results are shown in figure 2.

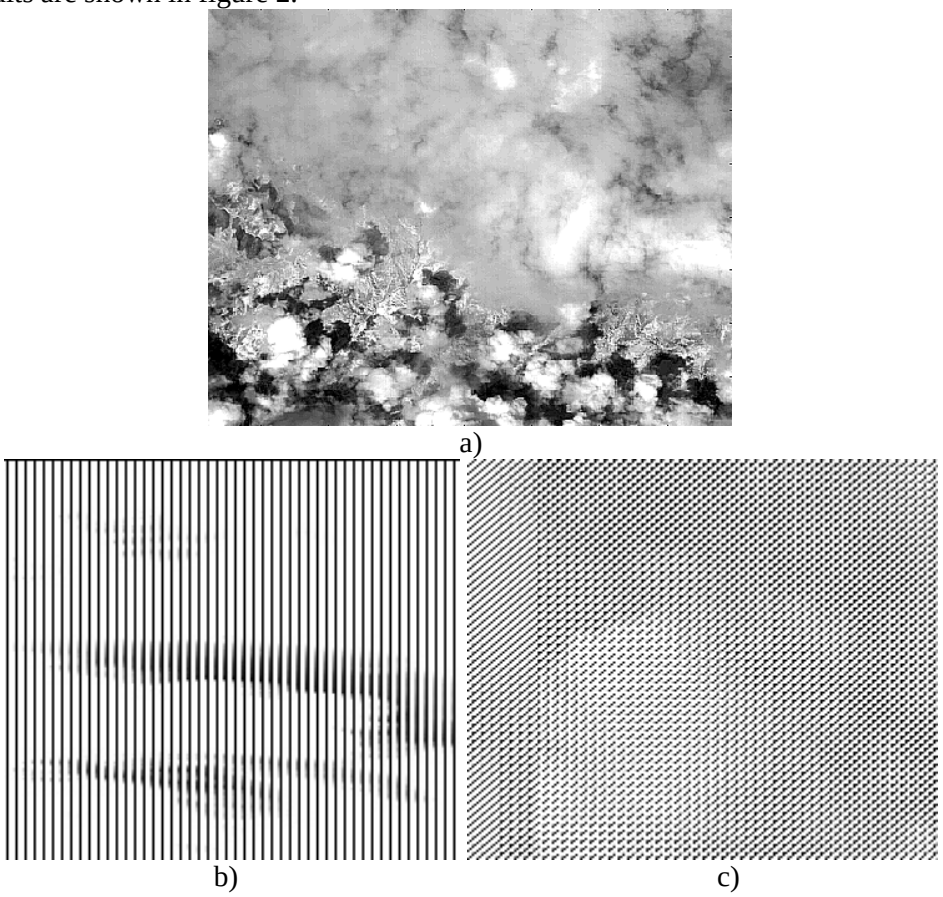

a)

b) c)

Figure 1. Image fragment: a – opened as BIP; b – opened as BIL; c– opened as BSQ.

Variance is calculated for all filtering results (for different channels and different fragments). The variance along the row characterizes the spread of image brightness, thus being a quantitative indicator of the presence of bands oriented along the columns of the image that occurs when the image is opened under the assumption that the storage method is BIL. The maximum variance value is obtained by using the Sobel filter. Figure 3 presents the results of variance calculation for images that are open in the assumption of BIP and BSQ, with the application of the Sobel operator. The maximum variance of the image opened in assumption correct method of storage, do not exceed any fragments the maximum variance of another image opened in the assumption is a wrong way to storage. As can be seen, the image variance, opened with the correct pixel alternation method, does not have sharp changes in comparison with the open with the help of BIL and seems to be smoother. Thus, on the basis of visual comparison and analysis of variance, one can conclude that the Sobel operator is the best filter in the problem of line selection in the direction of image columns.

Figure 4 shows fragments of filtered images using the Sobel operator. The image opened in the assumption method of BIP storing, has no sharp boundary changes, while the image that is open in the BIL assumption, shows sharp stripes in the column direction, which is expressed quantitatively in the calculation of the variance of the image. Thus, this feature can be used as an indicator of identification of the storage format correctness for SPOT-4 data and, possibly, other remote sensing data types.

2.2. Analysis of the BSQ format characteristics

As noted earlier, the image, which is opened under the assumption of the BSQ storage method, an arbitrary pixel alternation is expressed, which looks like a strip along the diagonals. In order to emphasize the stripes, spatial filtering methods are also used. In the course of the work the various filters presented earlier were tested, as well as others, such as gradient filters and filtration using

homogeneity filter (Figure 5). Since the Sobel Operator and the Robinson cross operator are only used to highlight horizontal or vertical lines, the image was rotated 45 degrees after filtering. The angle four-channel data is 45 degrees.

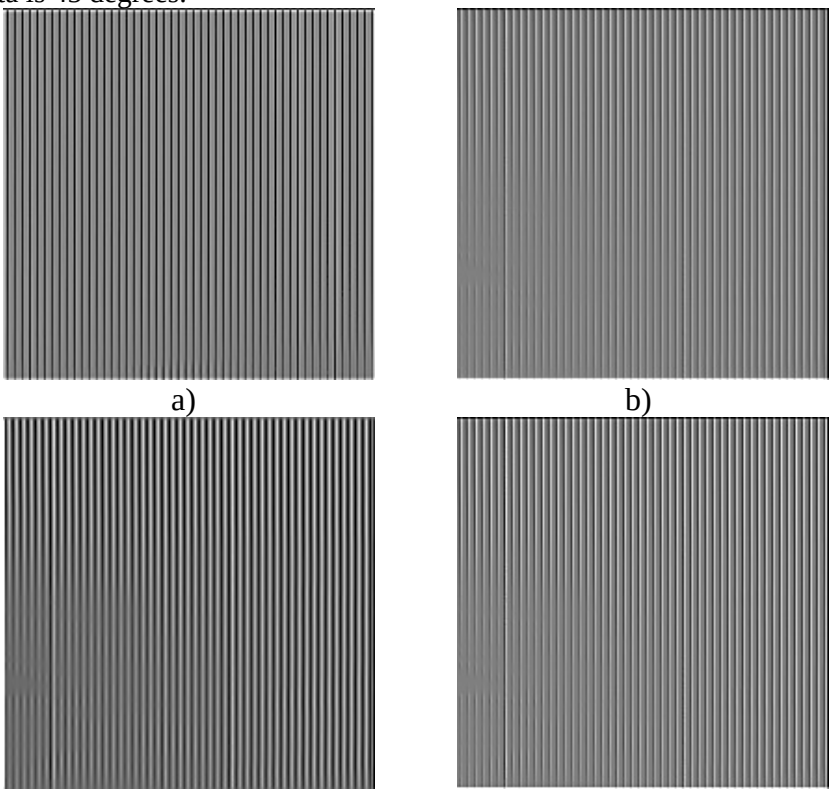

Figure 2. Image filtering result (BIL): a) Laplace filter; b) line detection filter; c) Sobel filter; d) Roberts cross operator.

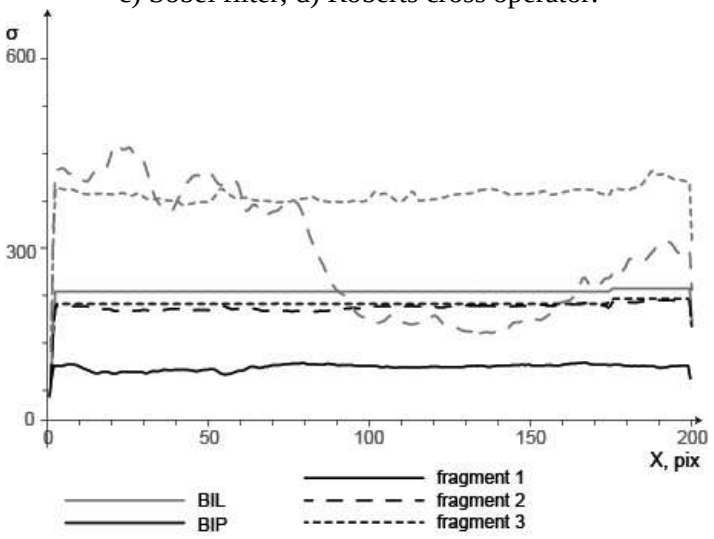

Figure 3. Variance calculations for different fragments opened as BIP and BIL.

For all filtering results, the variance is also calculated, which shows that the Sobel operator provides maximum contrast between the images opened under the assumption of BIP and BSQ. Figure 7 presents the results of variance calculation for images that are opened in the assumption BIP and BSQ, with the help of the Sobel operator. The variance of a data fragment opened by the BIP method is smoother than the variance of another method. Thus, on the basis of visual comparison and analysis of variance, it can be concluded that the Sobel operator in this case also emphasizes the selection of

lines in the direction of the image columns. Figure 6 shows the image fragments filtered by the Sobel operator. The image opened in the assumption with the BSQ method, has vertical stripes, and for the other image that is opened in the assumption with BIP, this is not observed.

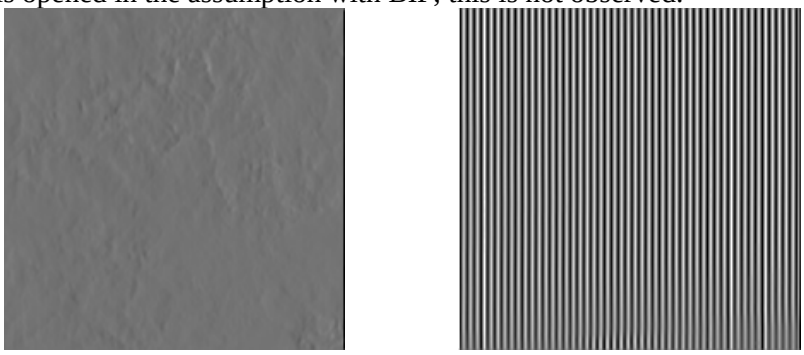

a) b)

Figure 4. Application of Sobel operator: a – image opened as BIP; b – image opened as BIL.

The example of SPOT-4 recovered data is shown in figure 8. The horizontal black stripes correspond to the data segments, which were located at the damaged disk drives. Vertical stripe at the left edge has the width about 57 bytes (per channel) and contains service information and metadata. The relative number of damaged stripes is about 13.8%, and it fits the number of damaged disks (3 of 20).

3. Results

An algorithm was developed and implemented in MATLAB, that allows one to determine automatically the correct way to multispectral data storage method in terms of pixel interleaving. The algorithm was tested on the example of SPOT-4 remote sensing data stored in post-processed SEG-format. The algorithm is based on Sobel spatial filtering, which emphasizes the geometric features of the image opened in the correct way. In case of an incorrect way, the variance calculated along the line of the image gives inflated values, thus it becomes possible to identify an adequate way of data interleaving type. The algorithm shows reliable results on eighty-seven different fragments of SPOT-4 remote sensing data in four different channels. The proposed algorithm was used for SPOT-4 data restoration after the disk storage failure.

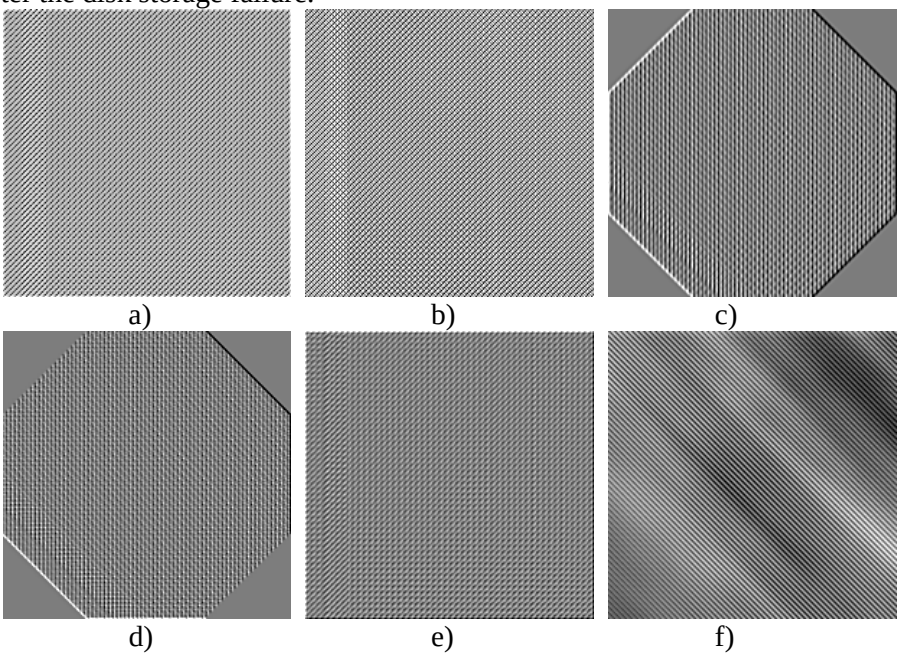

a) b) c)

d) e) f)

Figure 5. Scene filtration results: a) Laplace filter; b) lines detection filter; c) Sobel operator; d) Roberts cross operator; e) gradient filter; e) homogeneity operator.

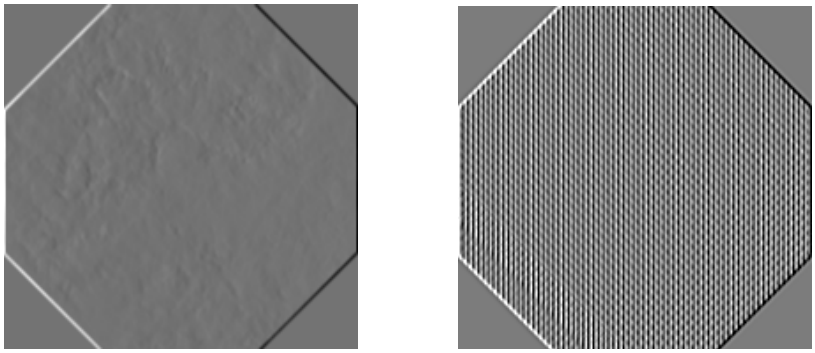

а) б)

Figure 6. Application of Sobel operator: a) for scene opened as BIP; b) for scene opened as BSQ.

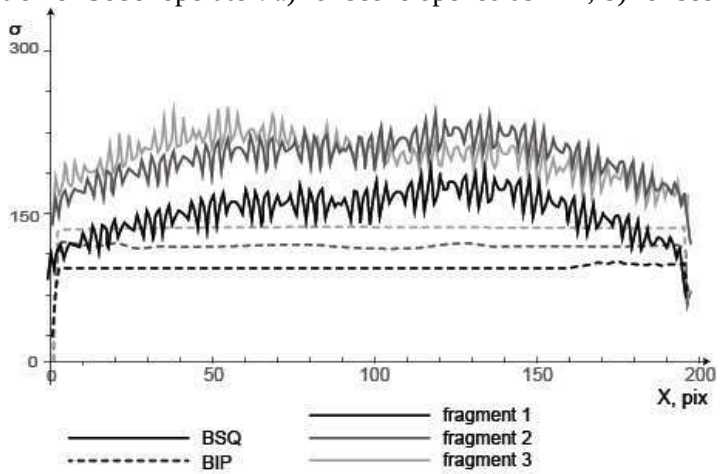

Figure 7. Scene variances through the image column for BIP and BSQ interleaving.

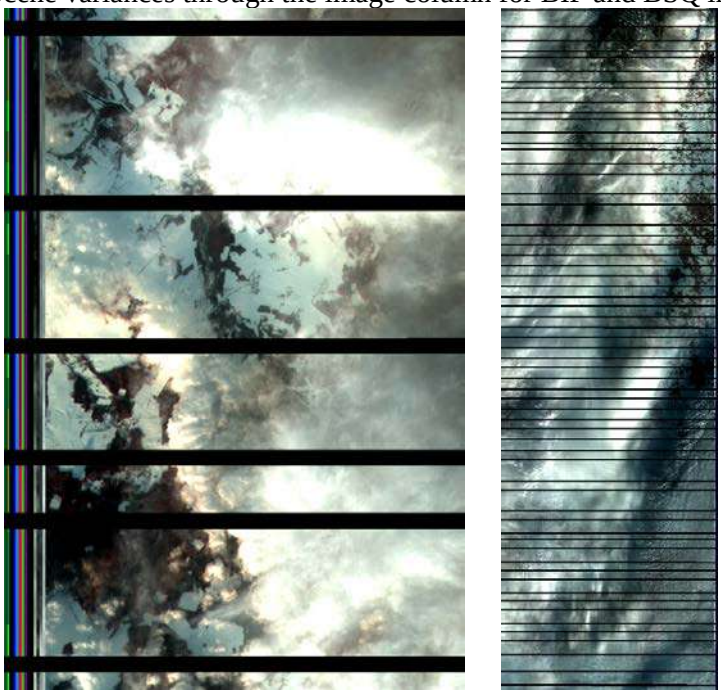

Figure 8. SPOT-4 recovering: a) image fragment; b) full scene.

4. References

[1] Arnaud M, Leroy M 1991 *ISPRS Journal of Photogrammetry and Remote Sensing* **46(4)** 205-215

[2] Yurikova E A, Kokutenko A A and Sukhinin A I 2008 Research of opportunities of application of data SPOT-4 for interpretation the areas of vegetation damaged by fires *Vestnik Sibirskogo gosudarstvennogo aerokosmicheskogo universiteta im. akademika M.F. Reshetneva* **4** 75-78
[3] Plotnikov D Y, Kolbudaev P A and Bartalev S A 2018 Identification of dynamically homogeneous areas with time series segmentation of remote sensing data *Computer Optics* **42(3)** 447-456 DOI: 10.18287/2412-6179-2018-42-3-447-456
[4] Boori M S, Paringer R, Choudhary K and Kupriyanov A 2018 Comparison of hyperspectral and multi-spectral imagery to building a spectral library and land cover classification performance *Computer Optics* **42(6)** 1035-1045 DOI: 10.18287/2412-6179-2018-42-6-1035-1045
[5] Dong J, Yin R, Sun X, Li Q, Yang Y and Qin X 2019 Inpainting of Remote Sensing SST Images with Deep Convolutional Generative Adversarial Network *IEEE Geoscience and Remote Sensing Letters* **16(2)** 173-177
[6] Chang Y, Yan L, Wu T and Zhong S 2016 Remote Sensing Image Stripe Noise Removal: From Image Decomposition Perspective *IEEE Transactions on Geoscience and Remote Sensing* **54(12)** 7018-7031
[7] Eason D, Andrews M 2014 Compressed hyperspectral image recovery via total variation regularization assuming linear mixing *IEEE International Conference on Image Processing* 620-624
[8] Biondi F 2017 Recovery of Partially Corrupted SAR Images by Super-Resolution Based on Spectrum Extrapolation *IEEE Geoscience and Remote Sensing Letters* **14(2)** 139-143
[9] Bossler J D 2010 *Manual on geospatial science and technology. Second edition* (Boca Raton: CRC Press) p 832
[10] Sirota A A, Solomatin A I 2008 Statistical algorithms for detecting the boundaries of objects in the image *Vestnik VGU* **1** 58-64
[11] Gruzman I S 2012 Synthesis of optimal differentiators for the locally oriented texture detection algorithm *Computer Optics* **36(1)** 109-115
[12] Zhuravel Y N, Fedoseev A A 2013 The features of hyperspectral remote sensing data processing under environment monitoring tasks solution *Computer Optics* **37(4)** 471-476

Analysis and object markup of hyperspectral images for machine learning methods

V P Gromov[1], L I Lebedev[1] and V E Turlapov[1]

[1]National Research State University named after NI Lobachevsky, Gagarin Ave., 23, Nizhny Novgorod, Russia, 603950

e-mail: vadim.turlapov@itmm.unn.ru

Abstract. The development of the nominal sequence of steps for analyzing the HSI proposed by Landgrebe, which is necessary in the context of the appearance of reference signature libraries for environmental monitoring, is discussed. The approach is based on considering the HSI pixel as a signature that stores all spectral features of an object and its states, and the HSI as a whole - as a two-dimensional signature field. As a first step of the analysis, a procedure is proposed for detecting a linear dependence of signatures by the magnitude of the Pearson correlation coefficient. The main apparatus of analysis, as in Landgrebe sequence, is the method of principal component analysis, but it is no longer used to build classes and is applied to investigate the presence in the class of subclasses essential for the applied area. The experimental material includes such objects as water, swamps, soil, vegetation, concrete, pollution. Selection of object samples on the image is made by the user. From the studied images of HSI objects, a base of reference signatures for classes (subclasses) of objects is formed, which in turn can be used to automate HSI markup with the aim of applying machine learning methods to recognize HSI objects and their states.

1. Introduction

To successfully develop the application of hyperspectral images (HSI), a certain level of automation for their processing is required, which is demonstrated today by some examples of the successful application of deep learning methods. However, the success of deep learning methods is to a significant extent determined by the completeness of the research and formalization of HSI objects to be recognized and quantified in each applied task. All this makes it relevant to study classes of HSI objects in order to form an effective set of the HSI object descriptors and the knowledge bases (or libraries of the HSI objects and their states as the sets of signature instances) providing the stages of machine learning and using the artificial intelligence methods.

A necessary function of such a class library of HSI objects should be the function of automatic marking of objects on each training HSI for a new application task. In a number of applied tasks, the HSI objects have the states and properties that depend on season and time, which greatly complicates the task, and requires the creation of a tool capable of distinguishing small changes of the object being classified. One of the possible candidates for such a tool may be the principal component analysis (PCA) method, which is widely used today in HSI processing to minimize the dimension of the basis for the representation of the class being studied. In this paper, we discuss the HSI analysis apparatus,

which is capable of providing an adequate description of the HSI class hierarchy, as well as developing, implementing and demonstrating the performance of algorithms and software for these purposes.

2. Review of publications on the research topic

The content of this work is determined by a number of publications in recent years. However, we would like to start with the publication [1] of 20 years ago, in which the author, D.Landgrebe, summarizes the more than the 20-year period of his work in the study of Earth remote sensing (ERS). Landgrebe began research with Earth's multispectral imaging (MSI) and is one of the two authors of the well-known open-source MultiSpec software for processing ERS data, which was then extended to HSI processing and remains popular in the world to the present. This software complex is used in Russia, for example, in the GIS Lab at the Moscow State University. The latest version of the complex is available on the website of its authors' university (https:// engineering.purdue.edu/~biehl/MultiSpec/).

In [1], Landgrebe establishes, as a result of the MSI and HSI study, the priority of the spectral features of an object over features associated with the neighborhood pixels, as they do not require the study of such a neighborhood. Here he formulated the requirements for the optimal definiteness of the class, and therefore for the tool (software package) with which this certainty is achieved. The Landgrebe-optimal definiteness of the class requires that the class definitions (attributes) be:

- *Exhaustive*. There must be a logical class to assign each pixel in the scene to.
- *Separable*. The classes must be separable to an adequate degree in terms of the spectral
- features available.
- *Of informational value*. The classes must be ones that meet the users needs.

In the same paper, Landgrebe proposed a nominal sequence of steps for analyzing hyperspectral images from 4 steps, which, if necessary, can be repeated iteratively:

1) Classes Delineation and Training Samples Designation.
2) Feature Extraction and Preliminary Classification.
3) Final Class Description Determination.
4) Classification.

At the first step, on the basis of visual perception and selection of samples of homogeneous objects belonging to a class (subclass), the features of each class are formed, maximally utilizing spectral features.

The second step practice assumes that the training sets defined for the class may be small. From which it is concluded that it is useful to exclude features that are ineffective for a particular set of classes, and at the same time reduce the dimension of features without losing information. A preliminary classification is a criterion for the success of feature extraction and can guide the expansion of both the composition of the features and the training set. As the main procedure for the formation of a set of features, the PCA method was used as one of the main ways to reduce the data dimension by losing the least amount of information. The nominal sequence of steps proposed by Landgrebe for analyzing HSI basically remains relevant to the present.

However, the most important result of many years of Landgrebe’s research in our opinion is the conclusion that, due to the influence of the atmosphere, the best HSI accuracy that we can count on is from 2% to 5% (not the accuracy of the HSI fixation equipment, but the accuracy compliance of the recorded reflection of the earth's surface with the real reflection), which cannot be compared even with the measurement level of 0.1%, implied by 10-bit data. Unfortunately, Landgrebe does not specify the rules for estimating these 2-5%, but it gives hope that in many cases it would be possible to confine one-byte representation of HSI instead of two-byte, and speaks about the usefulness of having a tool for evaluating the noise component along with other HSI analysis tools. Such a tool can be based, for example, on the empirical mode decomposition method [2].

At the same time, recent publications are turning to the construction of libraries of reference spectral signatures HSI, which provide automation of the classification of HSI objects in applied problems. Thus, the publication [3] of 2014 emphasizes the need to create a database of reference spectral signatures of HSI for objects with different types of pollution. This is planned to be used to

create classification maps of polluted sites and environmental monitoring according to HSI data. The classification "with training" uses a database of pollutant signatures, which greatly speeds up and simplifies further work. A test was conducted to identify areas with the presence of oil pollution. In the publication [4] of 2017, the authors supplemented the method with a two-stage partitioning into clusters within each class: at the first stage, the algorithm clusterizes the regions of interest, maximizing the likelihood function for a mixture of Gaussian distributions; in the second, it performs clustering using Mahalanobis distances to cluster centers as a feature space.

Detection of anomalies in hyperspectral images is very similar to the task of detecting various states of an object. In the publication [5] of 2014, a number of new algorithms for detecting anomalies on HSI were proposed: spectral mismatch algorithms (spatial-spectral and adaptive spectral with modification) and an algorithm for probabilistic anomaly detection. Algorithms of spectral mismatch are used to determine the fact of "abnormality" mismatch of the statistics of the inner window data with the outer window data. The probabilistic anomaly detection algorithm uses a re-quantization of the spectral data of the signatures to a significantly smaller number of levels (for example, to 4 levels). A comparison of the proposed algorithms with widely used variants of the RXD algorithm (global and local), which showed a convincing superiority of the proposed algorithms.

The article [6] of 2016 is devoted to the development of information technology for the early recognition of crop types based on a set of MODIS satellite images in the region’s territories. Early recognition is carried out in the first half of the planting season and is characterized by a lack of ground and space data to adjust the recognition algorithms. A two-step solution is proposed. At the first stage, models and databases of time series of agricultural crops and agro-seasons are formed according to data for the past years, at the second stage, data of the current year are added to detect the initial state (agro-season) for crop monitoring objects and a training sample is generated for the entire current season based on the models and DB.

In the article [7] of 2016, a comparative analysis of algorithms for recognition of forest cover objects and some other natural and man-made objects on hyperspectral aerospace images is given. For example, in one of the tasks, there are seven main classes: water surface; road surface; soils; meadow vegetation; Pine; Birch tree; aspen. For forest cover, the species composition and age were studied. The spectral dimension of the problem is limited by the PCA method to four principal components. Each class is further characterized by a reference pattern and parameters of the Gaussian distribution. The best of the participating methods turned out to be the Bayes classifier (BC) based on Gaussian mixtures, while the worst one, the metric classifier. The method of K-weighted neighbors showed the accuracy commensurate with the accuracy of nonlinear optimal classifiers and can be used along with them for the recognition of forest cover of different species composition and age. To build a class standard in the considered problems, 4 principal components were sufficient.

In [8], 2018, the use of imaging hyperspectrometers for precision farming in a field experiment to determine the humidity index of soil covered with vegetation is considered. It is shown that the humidity index at each point of the hyperspectral image, where greens are present, is determined by the ratio of $I_{0,9}$ to $I_{0.97}$, where $I_{0.9}$ is the spectral brightness at a wavelength of 0.9 μm, and $I_{0.97}$ is at a wavelength of 0, 97 microns.

In the publication [9] of 2018, focused on the use of high-resolution multispectral images (1-5m), an information technology for processing ERS data for estimating plant habitats, based on the calculation of local signs, was proposed and investigated. The basic stages of the proposed technology are a super-pixel segmentation (the selection of connected areas of local homogeneity in the multi-channel image), the calculation of the segments' parameters, clustering of the segments, the estimates of plant habitats. The stages of calculating parameters and superpixel segmentation are combined into one process. This process allows obtaining both splitting into locally homogeneous sections and their parameters in one pass through the image, reducing the computational complexity of the algorithm and the complexity of producing the training set by the operator. The parameters include minimum and maximum brightness values of superpixels, the mathematical expectation of their brightness for each channel, and superpixel's areas. The data from ground studies of 4 elementary vegetation classes are used: 1) sparse grass vegetation; 2) low-grass vegetation; 3) tall grass; 4) trees and shrubs. These data

are used to form the parameters of classes in the synthesis of model images, as well as for training sets construction and classifying ERS images of plant habitats.

Publication [10], also in 2018, demonstrates the potential of hyperspectral and multispectral data for monitoring and assessing land cover across the Russian Federation region, and highlights the development of a spectral library for land cover classes with the construction of a standardized classification system.

The study used 1 hyperspectrometer (Hyperon) and 2 multi-spectrometers (ALI and OLI). For all three images, the following were applied: 1) the k-nearest-neighbor algorithm (KNN) as supervized learning method for a classification; 2) the method of migrating means clustering (MMC) as unsupervized learning method. Training set data are collected on the basis of field works and supported by the reference to topographic maps. Initially, 27 subclasses were allocated along with training sites for them, which were then combined into 8 classes: 1. Water; 2. Vegetation; 3. Settlement; 4. Wetlands; 5. Naked land; 6. Transportation; 7. Bare rocks; 8. Sand dunes. Field measurements were performed on a FieldSpec 3 ASD portable spectroradiometer (range: VNIR, visible, near-infrared, and SWIR, shortwave infrared, between 350 and 2500 nm; accuracy: 1 nm) and GPS (Trimble PRO XRS) with a reference accuracy of 1 m. 7-8 measurements were made for each class, in random points of 60 zones of each image. The classification accuracy assessment experiment confirmed the expected that supervised classification is better than unsupervised classification for all three images (Hyperion, ALI, and OLI), and hyperspectral images are more informative than multispectral ones. The main thing, however, is that the automatic classification via the collected reference samples was quite effective for both HSI and MSI.

All considered publications of recent years ultimately confirm the relevance of work on creating databases of standards of HSI objects and standards of states of these objects for different tasks of territorial management, as well as the relevance of developing the HSI analysis methods that ensure the information content of the standards. The same applies to multispectral images, which are easier, due to greater availability, to be used in the practice of managing territories, but for them more often you have to use, along with spectral, to textural attributes of the classification objects' states.

3. Methods of analysis and markup of HSI objects

The survey noted that the nominal sequence of steps for analyzing HSI proposed by Landgrebe [1] largely remains relevant to the present. This is true, however, there are features in the described scheme that lead to the loss of essential HSI information. Actually, the use of PCA to significantly reduce the data dimension initially implies a loss of information. The main question is what information we agree to lose. It is also important that the result of PCA depends on the content of a particular image. In this regard, we would like to clarify the place of the PCA method in the nominal sequence of steps for analyzing HSI in cases requiring really “fine” analysis. Consider the first two steps of the Landgrebe nominal HSI analysis sequence.

The first step is “Classes Delineation and Training Samples Designation”. Recall that Landgrebe-optimal classes should be: exhaustive (can be specified to each HSI pixel); separable; informationally valued. It is recommended, if possible, to build a set of classes divided by spectral features. At this step, the number of classes must be predetermined and sets of training samples for each class must be selected. The analysis process always begins with a visual review of HSI. It usually uses 3-color coloration of the visible and infrared ranges, or some other combination of channels, which are useful for preliminary visual classification to be separated by color. This operation is useful in any cases and tasks, and of course must be present as a mandatory HSI analysis tool. In the same way, we should welcome the desire to maximally ensure the spectral separability of classes, which we will be able to check by the separability in trying to mark class samples automatically via spectral features.

The second step: "Feature Extraction and Preliminary Classification". At this step, it is intended to significantly reduce the dimension of the HSI space by applying the PCA method or a method similar in capabilities and choosing the number of principal components (m) corresponding to the specified accuracy. After this, we can verify that the class samples are separable in the space of m principal components from the point of view of linear discriminant analysis (LDA). This can be monitored visually by observing clusters of color-labeled samples on the coordinate planes of the principal

component basis. If any classes are inseparable, additional components are introduced into the basis. Checking whether the list of classes is sufficiently comprehensive is carried out by checking for the presence of pixels that are not assigned to any of the classes. If there are any, unclassified pixels are marked manually with labels of existing classes, to which they should belong, or labels of additional classes. An example of markup using HSI analysis tools included in the Terra Plus GIS [11] is shown in Figure 1.

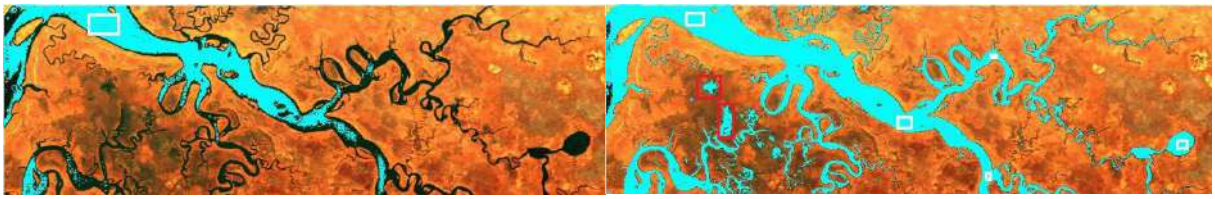

Figure 1. The choice of one sample (1440 pixels, window with white frame) for marking the river on HSI and the area of the river (24935 pixels) are automatically colored in cyan in response to this choice (on the left); selection of 5 samples (4191 pixels), which ensured complete filling of the main watercourse, all tributaries and lakes (95,935 pixels, on the right). In both cases, only one recognition basis is constructed. Cases of over-marking zones (wetlands) are marked with red outlines.

The data source for Figure 1 is HSI Suwannee_0609-1331_ref.dat: wetlands of the Suwannee River Basin in Florida, USA, Spectir spectrometer, the number of channels $n = 360$.

The efficiency of the procedure of the second step has been repeatedly tested by practice. However, we consider it necessary to introduce some development into it. First, we insist on the complete preservation of the reference HSI pixel signatures, regardless of the number of channels that are necessary for the current classification in a particular application (perhaps with the exception of completely noisy channels). This will allow us to build a classification, which is not so much dependent on the conditions of a specific task and a specific HSI, but is reusable and is supported by reference (standard) signatures, which were confirmed in field tests, as in [3], [4], [6-10].

3.1. The role of signatures, their linear dependence and the values of standard deviations in the classification procedure

In [10], an example of classification of 27 subclasses of 8 dissimilar classes is shown, showing the similarity of the signatures of all 27 subclasses in the range of 82-96 channels of the Hyperion spectrometer. This, on practical material, indicates the importance of detecting the fact of a linear relationship between signatures and using the scale factor of this relationship as a feature of a class and a subclass. In our practice, the presence of a linear dependence of class signatures is regular. Figure 2 shows an example of such pixel signatures for points randomly selected on the river area and on the land area in HSI Suwannee_0609-1331_ref.dat (see also figure 1).

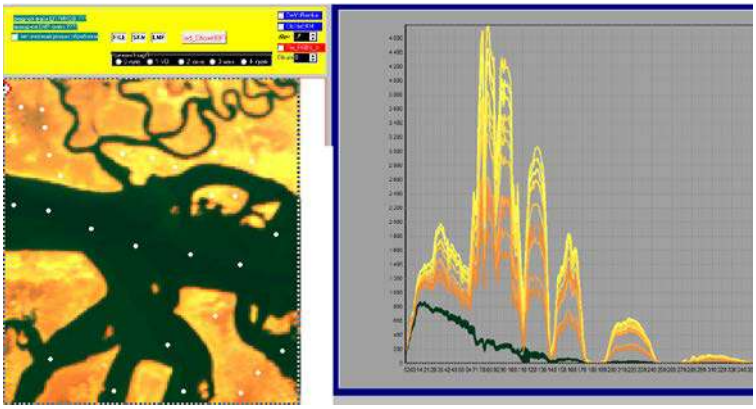

Figure 2. 28 pixels of HSI Suwannee for different parts of the river and land (on the left, white dots) and their signatures, demonstrating a linear relationship within the class (the color of the graph curve corresponds to the color of the marked pixel in the original image).

Covariance (1)

$$\mathrm{cov}(\mathbf{x},\mathbf{y}) = E[(\mathbf{x} - E\mathbf{x})(\mathbf{y} - E\mathbf{y})], \quad (1)$$

and the Pearson correlation coefficient (2)

$$r(\mathbf{x},\mathbf{y}) = \mathrm{cov}(\mathbf{x},\mathbf{y})/(\sigma\mathbf{x}\cdot\sigma\mathbf{y}) = \mathrm{cov}(\mathbf{x},\mathbf{y})/(\sqrt{D\mathbf{x}}\cdot\sqrt{D\mathbf{y}}), \quad (2)$$

where E is the moment of the first order, D is the variance, σ is the standard deviation, can be used as a detector of the linear relationship between the **x** and **y** signature vectors of two HSI pixels, with the number of channels n.

To detect a linear relationship with reference signatures, we need the unbiased values of the signatures of the current HSI, so we assume in (1) $E\mathbf{x} = E\mathbf{y} = 0$, after which we have:

$$\mathrm{cov}(\mathbf{x},\mathbf{y}) = (\mathbf{x}\cdot\mathbf{y})/n; \quad r(\mathbf{x},\mathbf{y}) = (\mathbf{x}\cdot\mathbf{y})/(|\mathbf{x}|\cdot|\mathbf{y}|), \quad (3)$$

where |**x**| and |**y**| are modules of vectors **x** and **y**.

The Pearson correlation coefficient turns into a normalized scalar product of signature vectors and seems to us to be a more interesting detector, since arccos (r) can be used as a measure of the angular deviation of the signature **x** from the signature **y**. The values of standard deviations $\sigma\mathbf{x}$, $\sigma\mathbf{y}$ (4)

$$\sigma\mathbf{x} = \sqrt{D\mathbf{x}} = \sqrt{E[(\mathbf{x} - E\mathbf{x})^2]}, \quad (4)$$

their ratios

$$s = \sigma\mathbf{x}/\sigma\mathbf{y}, \quad (5)$$

or quantized values will be used as the feature of a class (subclass).

With this approach, the reference (standard) class signature (or time series of standards) becomes the real basis for the classification, and changes in this role the PCA method of the Landgrebe nominal sequence, which depends on the content of a particular hyperspectral image.

Thus, the procedure for detecting linear dependencies between signatures by the value of the Pearson correlation coefficient becomes a necessary procedure of the second step and applied before the PCA. To the same extent, this is also necessary in the first step of the Landgrebe nominal sequence.

3.2. The role of the PCA method in the classification procedure

However, the PCA method does not lose its significance as an effective HSI analysis tool. We consider it necessary to apply it to a local homogeneous sample, which determines the local standard of the object class on the sample area. If sample homogeneity is provided by a qualified expert, then we can set the local standard of the class equal to the average of the sample signature, which corresponds to the PCA procedure. A ready-made standard can also be used as a local standard. Further, the PCA procedure provides orthogonality and statistical independence for the components of the decomposition. This is expressed in the diagonality of the covariance matrix, with the result that the expression of the Mahalanobis distance between two signatures takes the form (6):

$$d(\mathbf{x},\mathbf{y}) = \sqrt{\sum_{i=1}^{n}(x_i - y_i)^2/\sigma_i^2}, \quad (6)$$

where σ_i is standard deviation of x_i from y_i in the sample, d is the normalized Euclidean distance. As a result, each of the principal components gets in σ_i value its own scale to solve the problem of linear discriminant analysis (LDA).

The main task of applying the PCA method on a homogeneous sample is, in our opinion, a “fine” analysis: identifying subclasses of local classification that have an applied meaning. For clarity, when assessing the applied value of selected subclasses, it is advisable to use standard techniques: 1) visualization of different subclasses with different color and brightness; 2) visualization of the projections of the signature samples on the coordinate planes of the principal components for evaluating their clustering and LDA capabilities (Figure 3).

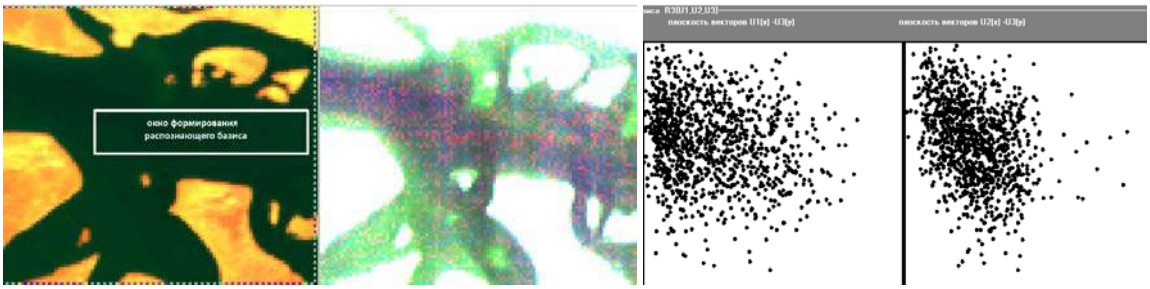

Figure 3. Color-luminance illustration of the discriminant properties of a three-component basis constructed using the PCA method (middle) for a sample of river pixels with the window shown on the left. The dark area of the color-brightness illustration corresponds to the signature of the local class and the deeper part of the river, the green - to the subclass of the shallow part of the river. Projections of 1155 sample pixels on 2 basis planes (right).

Depending on the degree of homogeneity of the sample, PCA may give different results. Figure 3 shows an example of the analysis of HSI Suwannee_0609-1331_ref.dat, which represents a fairly frequent situation when choosing an area that is completely homogeneous in appearance (the rectangle in the left image). The dark area of the color-brightness illustration (in the second image from the left) corresponds to the signature of the local class and the deeper part of the river, the green one to the subclass of the shallow part of the river, the cyan is the shallowest part; the red component is the noise. The projections of 1155 pixels of the sample on 2 base planes (on the right) are presented in two images on the right and, by visual impression, are inseparable by the LDA method before PCA is applied. We can also face the case when PCA on a uniform sample can only give noise components, which, together with an estimate of their standard deviations, is also very useful in determining the threshold values for classification error.

Figures 4-5 show an example of analyzing a fragment of the water surface of the San Francisco Bay at HSI Moffett Field. This bay is known as the first wetland sanctuary within the United States urban area (Don Edwards San Francisco Bay National Wildlife Refuge). It is characterized by a large variety of classes and subclasses of wetland areas, visited by 280 bird species. In particular, in Figure 4 for the study a fragment of heterogeneous tidal pollution is highlighted for the study. According to this sample, water areas belonging to the class specified by the fragment are distinguished.

Figure 4. HSI Moffett Field with automatic classification by training window (shown with white frame on the left side of the image).

In Figure 5 (left), the selected fragment and the surrounding area of interest are shown with zoom to increase the accuracy of selection (Zoom tool). The right shows the color reproduction of the result of the PCA method for the 3 principal components. Blue (in the middle) and green (on edges) colors correspond to the bulk of pollution. The open water corresponds to the red color (a small part of the pixels in the selection window). The right side shows the projections of 2030 pixels of the selection

window on 3 coordinate planes of the principal components: classification clusters are noticeable, and are quite distinctly separated by color.

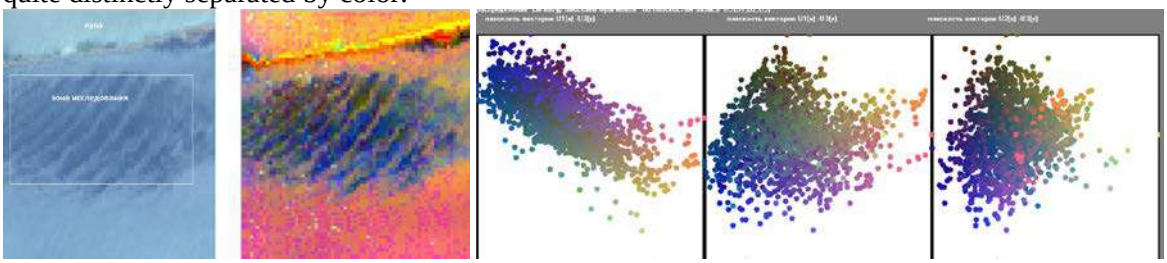

Figure 5. Fragment of the bay with a selection window (on the left, white frame); visualization of orthogonal components of the basis of the classification constructed by the PCA method with different colors (blue and green colors correspond to pollution, red to free water of the bay, the road along the dam separating the bay and the salt lake above the road is yellow). The right side shows the pixel projections of the selection window on the 3 coordinate planes of the principal components: classification clusters are noticeable, which are quite distinctly separated by color.

4. Discussion of the results

Feature extraction is one of the most important operations in the classification of hyperspectral images. This operation must be performed before the classification and best of all should be based on the analysis of the classified HSI. In the case of using standard signatures from the database, or when such standards are developed on the HSI under study, the first necessary analysis step is the procedure for detecting the linear dependence between signatures by the Pearson correlation coefficient (see Figure 2). This procedure is an adequate tool for cluster analysis of HSI by the criterion of the angular deviation of signatures already on the first step of the nominal HSI analysis sequence.

So, in the second step of the Landgrebe sequence, the procedure for detecting a linear dependence of signatures precedes the use of a fine analysis of a homogeneous area via PCA. In the experiments shown above, the PCA method was used as a method for studying the existence of subclasses in HSI object classes, which have been defined by homogeneous image fragments. The use of PCA in conjunction with the visual and quantitative assessment of the principal components allows you to see whether the constructed principal components have real application value or they reflect the noise component of the image, as in Figures 3 and 5.

Components with small standard deviations can have useful information for distinguishing classes in the classification process and for detecting different states of an object of the same class in space and time, which can make even the smallest values of standard deviations noticeably significant.

5. Conclusion

The paper discusses the development of methods for recognizing objects of hyperspectral images (HSI) in the direction of creating and using banks of reference (standard) signatures for objects of applied tasks of environmental monitoring. This direction needs modification of the Landgrebe nominal sequence of steps for analyzing HSI.

In this modification, the HSI pixel is considered as an n-dimensional vector of the signature, which stores all spectral features of both the object and its state. And HSI is generally viewed as a two-dimensional field of signatures. For these reasons, the modification is built on per-signature analysis of HSI rather then on per-channel analysis.

The modification of the nominal sequence of HSI analysis according to Landgrebe also consists in the fact that as a first step of the analysis a procedure is proposed for detecting a linear dependence of signatures by the magnitude of the Pearson correlation coefficient. This procedure is also the basis of HSI clustering performed in the first step. The primary feature of a class and the clustering criterion is the angular proximity to the standard signature of the class. The secondary feature of a class (subclass) is the value of the standard deviation of the class standard signature **y**, and the ratio $s = \sigma\mathbf{x} / \sigma\mathbf{y}$ for the class instances.

In the second step of the Landgrebe-nominal sequence HSI analysis, the PCA method remains the main tool along with clustering. However, it is no longer used to build classes, and is applied to investigate the presence in the class of subclasses essential for the applied area. This turns PCA into a multivariate differential analysis tool.

The content is illustrated by results of analysis tools for the study of homogeneous fragments of hyperspectral images that are contained in the GIS Terra Plus [11]. Experimental material includes such objects as water, swamps, and wetlands, soil, vegetation, concrete, salt, tidal pollutions. Selection of object samples on the image is made by the user. From the studied images of objects of hyperspectral images in the GIS Terra Plus, a base of standard signatures for classes (subclasses) of objects is formed, which, in turn, can be used to automate HSI markup with the aim of using machine learning methods to recognize HSI objects and their states.

6. References

[1] Landgrebe D 1999 Information extraction principles and methods for multispectral and hyperspectral image data *Information Processing for Remote Sensing* (River Edge, NJ: World Scientific Publishing Company) **1** 3-38

[2] Pakhomov P A, Borusyak A V and Turlapov V E 2018 Investigation of hyperspectral image pixel signatures by the empirical mode decomposition method *CEUR Workshop Proceedings* **2210** 352-364

[3] Ramenskaya E V, Guryanova A O, Mandra A G and Ermakov V V 2014 Obtaining of support spectral signals during hyperspectral survey *Ecology and Industry of Russia* **10** 44-47 (in Russian)

[4] Ramenskaya E V, Kuznetsov M P, Ermakov V V, Barkova O R and Bran A A 2017 Hyperspectral image classification using cluster data structure *Sovremennye problemy distantsionnogo zondirovaniya Zemli iz kosmosa* **14(7)** 9-19 (in Russian)

[5] Denisova A Yu and Myasnikov V V 2014 Anomaly detection for hyperspectral imaginary *Computer Optics* **38(2)** 287-296

[6] Vorobiova N S, Sergeyev V V and Chernov A V 2016 Information technology of early crop identification by using satellite images *Computer Optics* **40(6)** 929-938 DOI: 10.18287/2412-6179-2016-40-6-929-938

[7] Kozoderov V V, Kondranin T V and Dmitriev E V 2016 Comparative analysis of recognition algorithms for forest cover objects on hyperspectral aerospace images *Issledovanie Zemli iz kosmosa* **6** 45-55 (in Russian)

[8] Podlipnov V V, Shchedrin V N, Babichev A N, Vasilyev S M and Blank V A 2018 Experimental determination of soil moisture on hyperspectral images *Computer Optics* **42(5)** 877-884 DOI: 10.18287/2412-6179-2017-42-5-877-884

[9] Varlamova A A, Denisova A Y and Sergeev V V 2018 Earth remote sensing data processing for obtaining vegetation types maps *Computer Optics* **42(5)** 864-876 DOI: 10.18287/2412-6179-2018-42-5-864-876

[10] Boori M S, Paringer R, Choudhary K and Kupriyanov A 2018 Comparison of hyperspectral and multi-spectral imagery to building a spectral library and land cover classification performance *Computer Optics* **42(6)** 1035-1045 DOI: 10.18287/2412-6179-2018-42-6-1035-1045

[11] Lebedev L I, Yasakov Yu V, Utesheva T Sh, Gromov V P, Borusjak A V and Turlapov V E 2019 Complex analysis and monitoring of the state of the environment based on Earth sensing data *Computer Optics* **43** (in press)

Acknowledgments

This work was supported by the grant of the Russian Science Foundation No. 16-11-00068.

Application of vision systems to improve the effectiveness of monitoring compliance with technical safety requirements at industrial facilities

A A Ekimenko[1], E A Ekimenko[1] and S V Shavetov[1]

[1]ITMO, Kronverksky prospect, 49, Saint Petersburg, Russia, 197101

e-mail: ekimenkoanton@mail.ru, modest3005@yandex.ru

Abstract. According to the Federal State Statistics Service for 2017, over 25,000 injuries at work were registered in Russia, of which 1,138 were fatal. Studies have shown that most of the injuries in the workplace due to non-compliance with technical safety rules, namely the lack of personal protective equipment or their improper use. To improve the efficiency of monitoring compliance with the rules of technical safety at industrial facilities, this paper discusses the use of vision systems for automatic control of the availability of personal protective equipment at workers in the area of industrial work.

1. Introduction

Construction is a high-risk activity that requires builders to lift heavy construction materials, work in uncomfortable poses, and perform high-intensity operations that are key factors leading to workplace injuries [1]. The consequences of head and neck injuries are the most serious, and often fatal [2]. Wearing a helmet is an effective protection measure to minimize the risk of traumatic brain injury. Helmets protect workers, prevent the penetration of sharp objects, absorb impact from blunt objects and reduce the risk of electric shock. Despite the vital role of helmets in the protection of life, most of the workers who received head injuries at the time of the incident did not have head protection [3].

The method of automated monitoring of personal protective equipment(PPE) on workers can improve safety at the production site. However, the currently existing methods of detecting the absence of helmets on workers have significant limitations, and many cannot be used in real-time monitoring systems. Some existing methods have proven themselves to work in the near field, but they are not very effective in detecting people at a long distance. This is due to the fact that the resolution of the workers in the image is too small to extract facial features that are clearly visible in near-field frames. [4]

Most surveillance cameras of construction sites are installed at the border of the construction site, at high altitude. Long-distance video is distinguished by the low resolution of workers (the area not more than 30 pixels) in the image, a wide background and various poses of people [5,6], which is a serious problem when detecting people without a hard hat on construction sites.

This article discusses the method of recognizing people without helmets in the far field on open production sites.

In order to test the robustness of the method to the changing conditions of the construction site, this study also analyzes various visual factors that have a negative effect on the detection process.

2. Existing PPE control methods

Currently, research into the detection of the absence of a hard hat can be divided into two categories: tag(sensors), based detection methods and computer vision-based detection methods (RFID). In 2013, A. Kelm [7] proposed a mobile radio frequency identification method to verify the compliance of personnel equipment with technical safety requirements. In the proposed method, the monitoring system of personal protective equipment consists of a set of RFID tags associated with the worker's respective PPE, such as hard hats, goggles, respirators, etc., and a user interaction module performing the task of reading RFID tags, which by the presence of the appropriate labels determine what kind of PPE the worker is equipped with. To determine the state of the user's protective equipment, the set of reading items are compared with the previously saved list of PPE that worker must have to be able to enter the facility. Since RFID readers were located at the entrance to the construction site, this system can only guarantee that some worker entered the construction site with the necessary PPE. This system does not allow controlling the use of PPE by a worker after passing a checkpoint at the production site. In addition, marking the PPE with an RFID tag only indicates that distance between the worker and the PPE is close, but does not guarantee that PPE is used properly by the worker. Later, S. Barro-Torres proposed a new monitoring system for PPE that allows for monitoring the use of PPE throughout the production site. Instead of checking PPE at the entrance, it was proposed to equip workers with devices that collect information about the presence of PPE locally and transmit this information to the data aggregation server using a wireless data channel such as WI-FI, Bluetooth or mobile communication. This system also, like the previous one, does not allow determining whether the worker is wearing a hard hat on the head or it is just next to it [9]. A pressure sensor is installed in the hard hat to determine if the hard hat was worn, the collected information is transmitted via Bluetooth wireless communication to the monitoring system server. If the employee goes beyond the permissible range of data transmission from the receiver device for a long period — the data may be lost, since the data storage volume locally on the sensor is limited and has a period of overwriting, which makes it impossible to determine the presence of PPE in some time intervals, information about which did not have time to be transferred to the server. In addition, these devices must be charged regularly. The need for a regular charge can limit its use and damage the widespread use of this technology.

In view of the above, the use of existing methods of detecting and tracking PPE based on tags and sensors is limited by the need for each builder to use tags or sensors. This can be considered as an obsessive requirement for workers, besides the use of this technology requires large financial investments in additional equipment, such as tags, sensors, readers and transmitters. Many workers do not want to wear such equipment because of possible health problems or privacy issues.

Methods for monitoring PPE based on image recognition have become more common, thanks to more extensive monitoring capabilities. RGB-D cameras, such as Kinect and XTION, are one of the most popular tools for analyzing the deviant behavior of employees [10-12]. However, the range of operation of these cameras is strongly limited by the distance from 1 to 4 m [13], which does not allow their use in open areas. Also, sensors of this type are susceptible to interference from sunlight and ferromagnetic radiation, which makes them unsuitable for detecting the absence of hard hats on construction sites [14]. In this regard, the use of conventional cameras, especially single camera, has a competitive advantage for practical use. However, there are still problems with automatic detection systems for the absence of hard hats using one or more cameras. For example, S. Du offers a method for detecting the absence of hard hats, based on facial features, information about movement and color [15]. Color-based face recognition methods have two important assumptions: all workers turn to face the camera while working, and all hard hats have the same color. In practice, these two assumptions may not be fulfilled on a real construction site. K. Shresta suggests using edge detection algorithms to recognize the edges of objects in the upper area of the face, where the hard hat can be recognized [16]. This method also depends on facial recognition and does not produce a positive result if the employee does not face the camera. A. H. Rubayat proposes a method for detecting the absence of hard hats,

using histograms of oriented gradients (HOG) and Hough transform to obtain characteristics of workers and hard hats [17,18]. Like the previous ones, this method is also based on facial features detection and has similar limitations. To solve the limitations of the above methods, this article proposes an algorithm for automatic detection of the absence of hard hats, based on the Faster R-CNN. The R-CNN Faster algorithm takes less time to process an image and has higher precision than previous methods.

3. The proposed method of control of personal protective equipment

Open production sites are very complex environments. A variety of weather events, changes in light, changes in the distance to the object, the occurrence of overlaps and changes in people's poses can have a significant impact on the quality of worker detection in a long-distance observation system.

Based on the analysis of existing solutions made in Chapter 2, we can conclude that existing methods of detection based on computer vision are limited in their practical application in real-world scenarios.

Thus, the overall goal of this work is to develop a new method for monitoring the use of workers' PPE on open production sites and assess the possibility of using the proposed method to detect the absence of hard hats in various conditions.

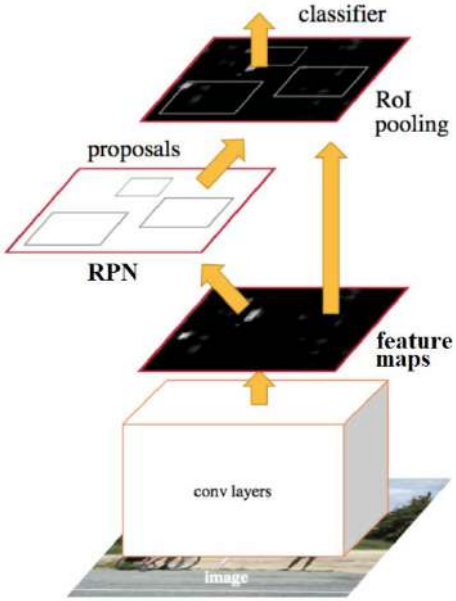

Figure 1. Faster R-CNN algorithm.

Faster R-CNN is a neural network object detection method proposed by S. Ren in 2015 [19]. In Faster R-CNN, the Region Proposal Network (RPN) is introduced instead of the slow selective search algorithm, that can generate high-quality candidate regions that are used to detect and classify objects. Faster R-CNN allows processing up to 5 frames per second, that, in combination with high precision, allows using this method in real object detection systems.

Faster R-CNN consists of three main steps, as shown in Figure 1. The first step to obtain a feature map of the objects, the original image is fed to the input of the CNN network represented by multiple layers of the convolutions and layers under the samples (MaxPooling). The next step is a fully convolutional RPN network, in which the obtained features are used to form candidate regions. Since the whole picture contains many unnecessary objects, and people always appear very small, it is difficult to draw a conclusion based on the feature map, whether a person wears a helmet or not. Therefore, only foreground areas will be used to recognize the absence of hard hats. The third step is represented by the Fast R-CNN classifier, which uses the obtained regions and the corresponding attributes to determine whether the given region contains a person without hard hats. Compared to other methods used to detect the absence of helmets, the Faster R-CNN has three advantages:

- Faster R-CNN is more reliable in working with complex scenes of open industrial sites. In particular, the previously used methods work only if the person is in a standing position. While the Faster R-CNN method is capable of reliably operating in the independence of human pose, workplace position, light, visibility range, and partial overlaps.
- Faster R-CNN has a higher precision that meets the requirements of engineering problems. As a result of testing the method on the Pascal VOC 2012[20] dataset, the precision of 89.6% was obtained, while for the HOG — 10.2 % [21].
- Thirdly, this method has a high speed of operation, which allows creating a system of monitoring the absence of hard hats, working in real time.

Thus, on the basis of the above, we conclude that Faster R-CNN method has higher rates of robustness, precision, and speed compared with the previously used, meeting the practical requirements for safety monitoring at various industrial facilities.

3.1 Performance metrics

The effectiveness of the method was evaluated based on its precision, speed, and robustness as follows. To assess the quality of work, we will use the following metrics: precision — the ability of the method to distinguish this class (workers without hard hats) from other classes, recall – the ability of the algorithm to detect workers without hard hats, miss rate (probability of skipping) – the opposite of recall indicates what percentage of workers without helmets was skipped by the method.

$$precision = \frac{TP}{TP + FP}$$
$$recall = \frac{TP}{TP + FN} \quad (1)$$
$$miss\,rate = 1 - recall = \frac{FN}{TP + FN}$$

where TP — number of correctly accepted hypotheses (workers without hard hats), FP — number of incorrectly accepted hypotheses (workers in hard hats), FN — number of incorrectly rejected hypotheses (workers without hard hats are not detected).

The speed of the method will be estimated as the amount of time required to detect the worker without a hard hat for one image.

Robustness represents the degree of stability of the method when working on various images. Open production sites usually contain many workers, equipment and building materials. Also, on open production sites, changes in weather, lighting, visibility often occur, there are partial overlaps of the object of detection. These factors have a significant impact on the visual perception of such scenes and, accordingly, on the results of detection. A good algorithm should be resistant to such changes.

4. Experiments and results

Training and testing of the method were carried out on a data set of 100,000 objects representing images from various open production sites. The training set is made up of 80,000 randomly selected images, testing was conducted on the remaining 20,000 images.

The effectiveness of the method was evaluated using the above-described metrics of quality, speed, and robustness. To calculate these metrics, all images in the test data set were divided into several categories (Table 1) – external factors, impacting the correct detection, such as weather changes, lighting, people's poses, range, and overlap. The next step was calculating the above-mentioned metrics for each category.

The Faster R-CNN model returns a probabilistic value for each detected object. The probability value here is defined as the probability that an object is a worker without hard hats. For example, a probability value of 0.9 means that probability that an object is a worker without a hard hat is 90%. An event is considered positive if the resulting probability exceeds the specified probability threshold. Therefore, the probability threshold value affects the classification of positive and negative events.

As shown in figure 2, a high probability threshold allows excluding ambiguous events from the results, which leads to high precision, but low recall, while low threshold allows more ambiguous events, which gives a high level of recall but low precision. For optimal results, both in precision and recall, a probability threshold of 0.7 was chosen.

Table 1. Information about image datasets for different categories.

Categories	Subcategories	Number of workers without hard hats	Number of images
Weather	Sunny	3134	1000
	Cloudy	2783	1000
	Rainy	1559	1000
	Foggy	2217	1000
Light	8:00 - 10:00	2831	1000
	10:00 - 13:00	3125	1000
	13:00 - 16:00	2952	1000
	16:00 - 18:00	2127	1000
Pose	Standing	2542	1000
	Bending	1762	1000
	Squatting	1275	1000
	Sitting	1128	1000
Distance	Short	2136	1000
	Medium	2854	1000
	Long	2916	1000
Overlap	Whole body visible	1924	1000
	Upper body visible	1015	1000
	Head visible	1393	1000
	Part of head visible	1067	1000

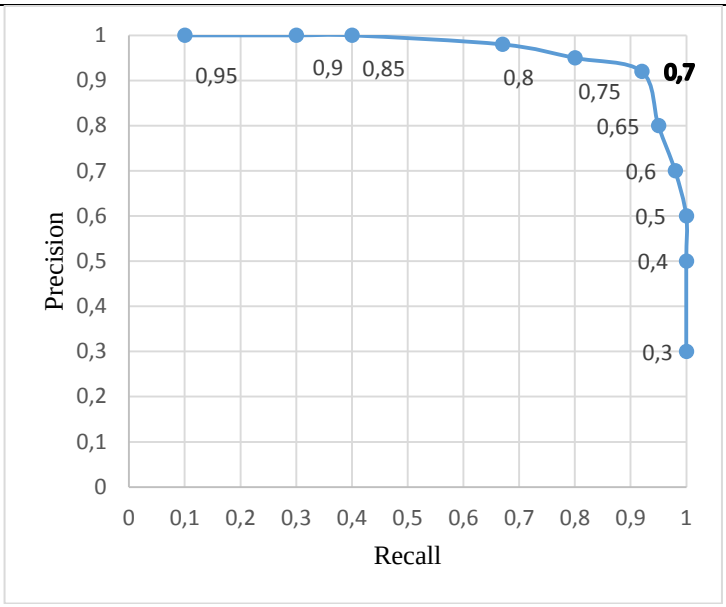

Figure 2. The curve of precision depending on the recall.

Due to the fact that video surveillance cameras are placed in various places on construction sites, and the trajectory of the workers is random, the images of workers on the frames can be of different resolution. The shooting distance is inversely proportional to the number of pixels in the image occupied by the worker's representation in the frame, as well as the number of features that can be extracted from the given image. From where we can conclude that at a long distance it is difficult to

recognize the object in the image. To evaluate the method's performance with objects of different resolutions, the images of the test sample were divided into three categories depending on the distance to the target object: long, medium and short distance. 1000 images from the test dataset were selected for each category. The results are presented in table 2.

Despite the fact that as the distance between the camera and the workers increased, the classifier's performance metrics deteriorated, the overall precision of the classifier remained above 90%. Consequently, the trained model proved to be robust in detecting objects with various resolutions. Changes in weather conditions have a significant influence on the quality of classification of images obtained in open production sites. Since, in heavy rain, snow and fog work on construction sites is usually suspended, it can be excluded from consideration. Then we need to test the method on images taken under the following weather conditions: sunny, cloudy, rainy and foggy. The test results (Table 3) showed the robustness of the method to weather changes. However, the best results were obtained in sunny weather (precision — 96%), the worst in rainy (precision — 93%). To test the effect of light on the results of the method, we divided the frames from the test dataset into four categories: images taken from 8:00 to 10:00, from 10:00 to 13:00, from 13:00 to 16:00, from 16:00 to 18:00.

The test results showed that the method works robustly under different lighting conditions. From table 3 it can be seen that decrease in light, the speed, and precision of the method changed slightly.

Table 2. Performance metrics of the system depending on the distance to the object.

Category	Subcategories	Precision (%)	Recall (%)	Miss rate (%)	Time (s)
Distance	Short	98.4	95.9	4.1	0.204
	Medium	95.8	95.3	4.7	0.207
	Long	93.7	92.3	7.7	0.212

Table 3. Performance metrics of the system depending on weather conditions.

Category	Subcategories	Precision (%)	Recall (%)	Miss rate (%)	Time (s)
Weather	Sunny	96.7	95.2	4.8	0.204
	Cloudy	95.7	95.8	4.2	0.202
	Rainy	93.7	94.2	5.8	0.209
	Foggy	94.7	93.0	7.0	0.210

Table 4. Performance metrics of the system depending on the light at different times of the day.

Category	Subcategories	Precision (%)	Recall (%)	Miss rate (%)	Time (s)
Light	08-10	95.6	94.6	5.4	0.209
	10-13	96.6	95.8	4.2	0.207
	13-16	97.0	95.5	4.5	0.208
	16-18	96.9	93.7	6.3	0.210

Depending on the type, place of work and the tool used, workers have to take different poses. Thus, to test the quality of the algorithm were selected images containing workers in the positions: standing, bending, squatting and sitting. Each category was represented by 1000 images. The test result (table 5) shows high precision at various poses of workers. (more than 90%). The worst results were obtained in the squat position (93% Precision).

Table 5. Performance metrics of the system depending on poses.

Category	Subcategories	Precision (%)	Recall (%)	Miss rate (%)	Time (s)
Poses	Standing	96.8	96.9	3.1	0.209
	Bending	95.6	94.0	6.0	0.208
	Squatting	93.7	93.5	6.5	0.205
	Sitting	94.6	98.4	1.6	0.207

Construction sites are usually occupied by many workers, equipment and building materials. On the frames obtained from CCTV, the images of the workers were often overlapped by various obstacles: equipment, building materials, etc. Therefore, on many frames, workers are only partially

visible. To test the effect of partial overlaps, we classify the degree of overlap into four categories: “whole body visible”, “upper body visible”, “head visible”, and “part of head visible” (Table 6). The test results showed that precision for the first three categories was more than 95%. For part of the heads, the detection precision was 90%, but the recall is only 64%.

Table 6. Performance metrics of the system depending on the presence of overlaps.

Category	Subcategories	Precision (%)	Recall (%)	Miss rate (%)	Time (s)
Overlap	Whole body visible	95.5	95.3	4.8	0.205
	Upper body visible	96.2	97.8	2.2	0.206
	Head visible	96.0	95.2	4.8	0.204
	Part of head visible	90.1	61.3	38.8	0.209

5. The discussion of the results

The article proposes a new method for detecting workers without hardhats on construction sites. The proposed method can monitor in real time with high accuracy and robustness to various scene changes. Thus, this method can provide early information about the absence of PPE on the worker while on the production site. This article discusses various methods for detecting hard hats and object detection technologies in general. Previous studies have used methods to solve this problem with limitations on robustness and practical applicability in the conditions of the open production site. We looked at the limitations of each of these methods and discussed the development of vision-based methods in the history of computer vision. Existing sensor-based detection methods, including RFID-based methods, are limited by the need for a physical tag or sensor that each builder must wear. Sensors that transmit data via Bluetooth require regular charging, which affects the practicality of its use in an open production site. In addition, these systems are more dependent on the actions of employees, and their implementation requires large investments. Given the limitations of HOG in practical use and the high efficiency of methods using deep learning, the proposed method can significantly improve the quality of automatic detection of the absence of hard hats on workers. When choosing a method for use on construction sites, we analyzed the characteristics of images, open production sites, and a number of factors that affect the detection of the absence of hard hats. The Faster R-CNN algorithm was chosen as this method. To test the robustness of the method, we tested the work of the Faster R-CNN on various images of the construction site. As a test data set, 20,000 images were collected. The test data set covers a variety of visual changes that can occur on outdoor production sites, including weather, lighting, worker poses, and overlaps. The results obtained in the course of experimental testing prove the robustly of the Faster R-CNN method for revealing the absence of hard hats in various visual conditions. Recognition precision and recall in all cases exceeded 90%, except low recall for the case of visibility of the upper part of the head — which is the expected result, because even none of the previously known algorithms does give an accurate result in this case. However, given the ability of the Faster R-CNN operate in real time and frequent changes in the poses of workers, we can assume that with a high probability the image of the worker will get completely into the frame at the next moment of time, where the head will be visible.

6. Conclusion

Construction remains one of the most dangerous employment sectors in the world. Despite the fact that hard hats provide significant protection from falling objects and from blows to the head, they do not always prevent accidents on the spot, resulting to head injury. For effective safety management at production sites, it is essential to improve the monitoring of workers without hard hats. This paper proposes a method for detecting the absence of hard hats, capable of operating in real time in changing conditions of open production sites, based on the neural network method of classification of objects Faster R-CNN. The results of testing the method showed that the proposed method was able to successfully detect workers without hard hats under different conditions with an average precision and recall of 95.7% and 94.9%, respectively. High metrics of precision and recall show that the proposed

method can be effectively used in video surveillance systems to detect workers without hard hats in real time.

7. References

[1] Schneider S, Susi P 1994 Ergonomics and construction: a review of potential hazards in new construction *Am. Ind. Hyg. Assoc. J* **55(7)** 635-649
[2] Jeong B Y 1998 Occupational deaths and injuries in the construction industry *Appl. Ergon.* **29(5)** 355-360
[3] Park M-W, Elsafty N and Zhu Z 2015 Hardhat-wearing detection for enhancing on-site safety of construction workers *J. Constr. Eng. Manag.* **141(9)** 04015024
[4] Paul M, Haque S M and Chakraborty S 2013 Human detection in surveillance videos and its applications-a review *EURASIP J. Adv. Signal Process* **1** 176
[5] Tian Y, Feris R S, Liu H, Hampapur A and Sun M-T 2011 Robust detection of abandoned and removed objects in complex surveillance videos *IEEE Trans. Syst. Man Cybern. Part C Appl. Rev.* **41(5)** 565-576
[6] Huang X, Hinze J 2003 Analysis of construction worker fall accidents *J. Constr. Eng. Manag.* **129(3)** 262-271
[7] Kelm A, Lombardi D A, Verma S K, Brennan M J and Perry M J 2013 Factors influencing worker use of personal protective eyewear *Accid. Anal. Prev.* **41(4)** 755-762
[8] Flin R, Mearns K, O'Connor P and Bryden R 2000 Measuring safety climate: identifying the common features *Saf. Sci.* **34(1)** 177-192
[9] Barro-Torres S, Fernández-Caramés T M, Pérez-Iglesias H J and Escudero C J 2012 Real-time personal protective equipment monitoring system *Comput. Commun.* **36(1)** 42-50
[10] Dong S, He Q, Li H and Yin Q 2015 Automated PPE Misuse Identification and Assessment for Safety Performance Enhancement *ICCREM* 204-214
[11] Han S, Lee S 2013 A vision-based motion capture and recognition framework for behavior-based safety management *Autom. Constr.* **35** 131-141
[12] Han S, Lee S and Peña-Mora F 2013 Comparative study of motion features for similarity-based modeling and classification of unsafe actions in construction *J. Comput. Civ. Eng.* **28(5)** A4014005
[13] Ray S J, Teizer J 2012 Real-time construction worker posture analysis for ergonomics training *Adv. Eng. Inform.* **26(2)** 439-455
[14] Starbuck R, Seo J, Han S and Lee S 2014 A stereo vision-based approach to marker-less motion capture for on-site kinematic modeling of construction worker tasks *Comput. Civ. Build. Eng.* 1094-1101
[15] Liu M, Hong D, Han S and Lee S 2016 Silhouette-Based On-Site Human Action Recognition in Single-View Video *Construction Research Congress* 951-959
[16] Du S, Shehata M and Badawy W 2011 Hard hat detection in video sequences based on face features, motion and color information *3rd International Conference on Computer Research and Development* **4** 25-29
[17] Rubaiyat A H, Toma T T, Kalantari-Khandani M, Rahman S A, Chen L, Ye Y and Pan C S 2016 Automatic Detection of Helmet Uses for Construction Safety *WIC/ACM International Conference on Web Intelligence Workshops (WIW)* 135-142
[18] Myasnikov V V 2017 Description of images using model-oriented descriptors *Computer Optics* **41(6)** 888-896 DOI: 10.18287/2412-6179-2017-41-6-888-896
[19] Ren S, He K, Girshick R and Sun J 2015 Faster R-CNN: towards real-time object detection with region proposal networks *Adv. Neural Inf. Process. Syst.* 91-99
[20] PASCAL VOC 2017 *Detection results: VOC2012*
[21] Ott P, Everingham M 2009 Implicit Color Segmentation Features for Pedestrian and Object Detection *12th International Conference on Computer Vision* 723-730

The regression model for the procedure of correction of photos damaged by backlighting

A V Goncharova[1], I V Safonov[1] and I A Romanov[1]

[1]National Research Nuclear University MEPhI (Moscow Engineering Physics Institute), Kashirskoe Shosse, 31, Moscow, Russia, 115409

e-mail: alen.gon4arowa@gmail.com

Abstract. In the paper, we propose an approach for selection a correction parameter for images damaged by backlighting. We consider the photos containing underexposed areas due to backlit conditions. Such areas are dark and have poorly discernible details. The correction parameter controls the level of amplification of local contrast in shadow tones. Besides, the correction parameter can be considered as a quality estimation factor for such photos. For an automatic selection of the correction parameter, we apply regression by supervised machine learning. We propose new features calculated from the co-occurrence matrix for the training of the regression model. We compare the performance of the following techniques: the least square method, support vector machine, random forest, CART, random forest, two shallow neural networks as well as blending and staking of several models. We apply two-stage approach for the collection of a big dataset for training: initial model is trained on a manually labeled dataset containing about two hundred of photos, after that we use the initial model for searching for photos damaged by backlit in social networks having public API. Such approach allowed to collect about 1000 photos in conjunction with their preliminary quality assessments that were corrected by experts if it was necessary. In addition, we investigate an application of several well-known blind quality metrics for the estimation of photos affected by backlit.

1. Introduction

A lot of photos are affected by various defects and need to be enhanced in an automatic manner to be more pleasant for observers. The most noticeable defects are the following: various issues with brightness and contrast, color misbalance, blurring and shaking, compression artifacts, high noise level, red eyes and other artifacts due to flash, color fringing, and geometrical distortions [1]. There are numerous methods for noise suppression (e.g. [2]), red-eye correction (e.g. [3]), and image sharpening (e.g. [4]), but there are just a few publications devoted to correction photos damaged by backlit. Photos taken in backlighting conditions has high global contrast, but local contrast in areas of shadow tones is quite low. Figure 1 demonstrates the photo affected by backlighting. One can see poorly distinguishable details in shadows. It is important to develop a method for enhancement of such images.

Paper [5] describes the technique for the correction of photos damaged by backlit. That method is based on a contrast stretching and alpha-blending of brightness of the initial image and an estimated reflectance. In the majority cases, the technique provides good visual outcomes, nevertheless, it has

shortcomings. The most important parameter of the method is factor k_s, which controls the amplification of local contrast in shadows. This factor is calculated by means of decision tree based on features that originated from brightness histogram. The decision tree allows to obtain for k_s just five discrete values. Sometimes it leads to significant changes in correction power due to insignificant alterations in an image. Such effect is undesirable. Also, that decision tree was created based on several heuristic assumptions and was not verified on the big number of sample photos. Is that solution general for plenty of photos affected by backlit?

The aim of our paper is overcoming of disadvantages of the method from [5] by the development of a regression model for the estimation of k_s based on machine learning techniques. It is worth to note, also factor k_s can be treated as blind metrics for assessment of the visual quality of photos damaged by backlighting. In the paper, we discuss three subjects: an approach for collection of a representative dataset; a selection of method for creation of regression model; algorithms for calculation and selection of informative features for the model.

Figure 1. Example of photo damaged by backlit.

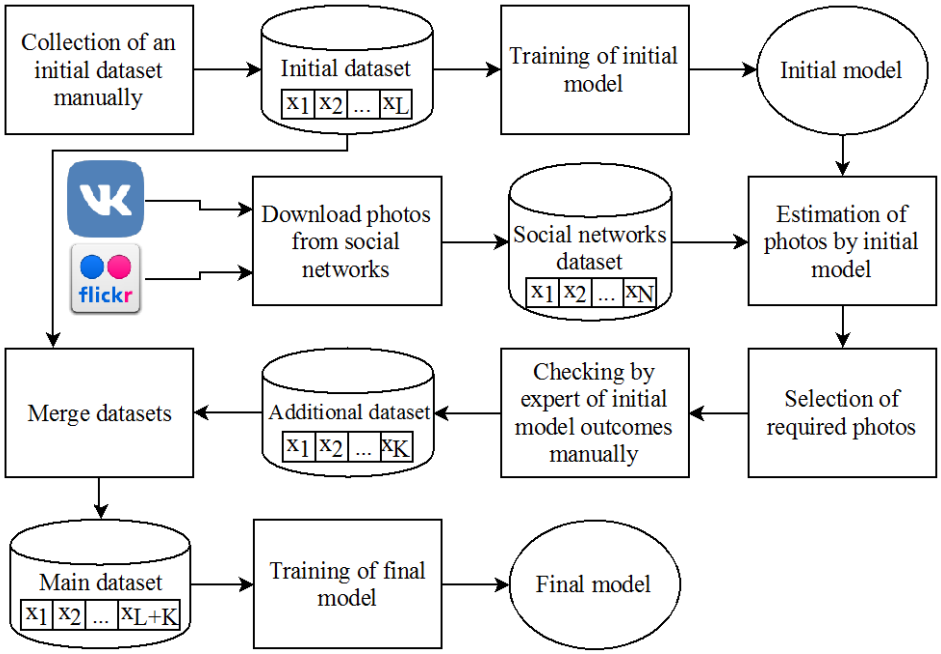

Figure 2. The scheme for dataset collection.

2. Collection of a dataset

In the best of our knowledge, there is no publicly available dataset containing photos deteriorated by backlighting. Moreover, a collection of a big dataset is a tiresome task because a relatively small number of such photos are in the Internet and social networks, so, manual search requires many efforts and a long time. We employ a concept of semi-supervised learning and self-training [6] for the

collection of the representative dataset. An initial dataset containing about two hundred of photos was collected and labeled manually. We trained the initial regression model using the initial dataset and random forest technique [7]. Nowadays many social networks provide an application interface for downloading of photos. We made a software tool for download of photos from flickr.com and vk.com [8]. The initial regression model estimates the downloaded photos and collects photos having required k_s to provide uniform distribution of images by the correction factor. Evidently, the initial model is not ideal, so, an expert checks outcome and makes re-labeling if it is necessary. Further, we add validated photos to the main dataset. Photos from the initial dataset are added to the main dataset as well. In this way, we collected about 1000 labeled images. The final model was trained on the main dataset. Figure 2 illustrates our approach for the dataset collection.

3. Analysis of methods for creation of a regression model

We have analyzed the application of the following methods for creation of regression model:

- linear least squares (LLS);
- support vector machine for regression (SVR) [9];
- k-nearest neighborhoods for regression (k-NN) [10];
- classification and regression tree (CART) [11];
- random forest [7];
- feedforward neural network [12];
- single-layer neural network [13];
- averaging of outcomes of enumerated above methods;
- blending [14]
- averaging of several outcomes of blending;
- stacking [15].

There are several measures to evaluate the performance of the regression models. We calculated the following five measures that evaluate conformance of outcomes of the regression model with experts' judgments.

1. Mean absolute error (*MAE*):

$$MAE(y,f) = \frac{1}{N}\sum_{i=1}^{N}|y_i - f_i|\,; \tag{1}$$

where N is the number of elements, f_i is the predicted value, and y_i is the true value.

2. Mean squared error (*MSE*):

$$MSE(y,f) = \frac{1}{N}\sum_{i=1}^{N}(y_i - f_i)^2. \tag{2}$$

3. Median absolute error (*MedAE*):

$$MedAE(y,f) = median(|y_1 - f_1|,..,|y_N - f_N|). \tag{3}$$

4. Pearson correlation coefficient (r):

$$r(y,f) = 1 - \frac{\sum_{i=1}^{N}(y_i - \bar{y})(f_i - \bar{f})}{\sqrt{\sum_{i=1}^{N}(y_i - \bar{y})^2}\sqrt{\sum_{i=1}^{N}(f_i - \bar{f})^2}}. \tag{4}$$

where $\bar{y} = \frac{1}{N}\sum_{i=1}^{N} y_i$, $\bar{f} = \frac{1}{N}\sum_{i=1}^{N} f_i$.

5. Normalized area under regression error characteristic curve (*AUC REC*) [16].

We used 5-fold cross-validation with stratification. All models were trained using the features from [5]. Table 1 contains the performance measures of different regression models. For *MAE*, *MSE* and *MedAE* smaller is better. For r and *AUC REC* larger is better. Random forest and SVR have the highest performance measures. However, the distribution of residuals of the regression model via random forest looks normal in comparison with residuals by SVR. In addition, random forest has a relatively small number of parameters for model adjustment. Thus, we have selected random forest for the creation of regression model for the estimation of amplification factor k_s.

Table 1. Performance measures of different regression models.

	MAE	*MSE*	*MedAE*	*r*	*normAUC*
LLS	15.2	350	13.3	0.59	0.694
SVR	15.1	377	**12.1**	0.54	**0.727**
k-NN	16.7	453	14.0	0.38	0.709
CART	18.5	559	15.3	0.41	0.723
Random forest	**14.8**	**334**	13.1	**0.61**	0.711
Feedforward neural network	15.0	350	12.9	0.59	0.706
Single-layer neural network	15.0	344	12.9	0.59	0.692
Averaging of methods	**14.8**	340	12.7	0.59	0.708
Blending	15.0	350	13.2	0.58	0.721
Averaging of several blendings	14.9	340	13.2	0.60	0.718
Stacking	14.9	339	13.4	0.60	0.714

4. Features for the description of photos damaged by backlit

In the paper [5] feature set for estimation of amplification factor k_s is described. Those features are calculated from brightness histogram *H*. Typical histogram of a photo damaged by backlighting has relatively high peaks in shadow and/or highlights, but a gap in middle tones. Besides, the histogram in dark tones is asymmetric. To characterize such shape of histogram the following features were proposed: parts of the tones in the shadow and middle tones; parts of tones in the first and second halves of dark tones; the ratios of the histogram maxima in shadows, middle, and highlight tones per the global histogram maximum; locations of the histogram maxima in shadows and highlights. The entire dynamic range was divided uniformly on shadow, middle tones, and highlights.

However, there are high-quality images that have values of those features close to values for photos affected by backlit. Sometimes normal images have a histogram that has peaks near the boundaries of dynamic range and a valley between them. Figure 3 shows an example of such pristine photo and its histogram of brightness. The method from [5] makes dark areas in the photo a lighter. It is necessary to prevent the modification of dark tones in normal images. To overcome the undesirable correction of high-quality photos, we propose to use another set of features. We modify histogram-based features from [5] and introduce new features originated from the co-occurrence matrix.

In figure 3 one can see that peaks in the left and right parts of the histogram are shifted towards to middle tones. We propose to treat as shadow tones a quarter of the leftmost part of the dynamic range instead of one third. Highlight tones are a quarter of the rightmost part of the dynamic range. Middle tones occupy half of the range. Solid lines in histogram in figure 3 demonstrate this division for dark, middle and light tones. Dashed lines show a similar differentiation in [5]. This simple alteration of sub-ranges for shadow, highlights, and middle tones allows to decrease considerably the number of falsely corrected pristine images even by usage similar to [5] features.

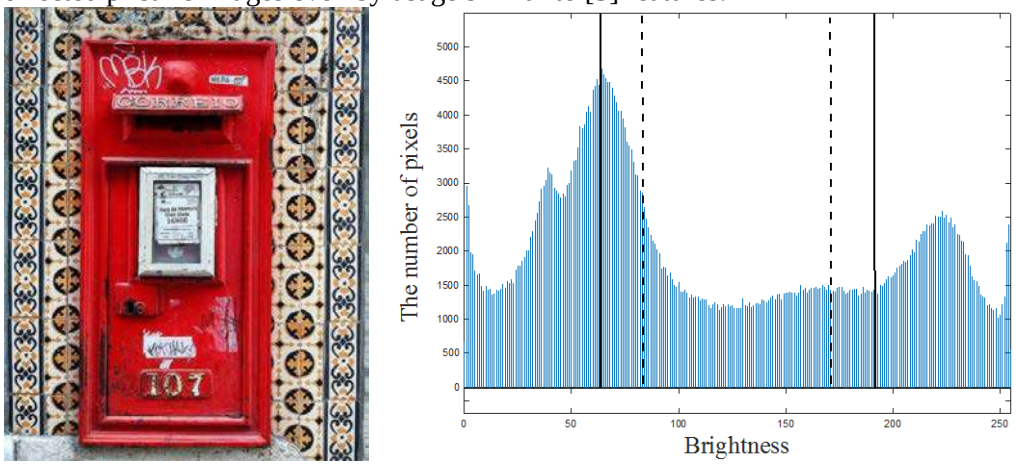

Figure 3. The high-quality photos and corresponding brightness histogram which looks like the histogram of a photo damaged by backlit.

One more opportunity is a division of range on more than three sub-ranges and the calculation of features for each range. We propose to employ nine evenly distributed sub-ranges.

We argue that extraction of features from the co-occurrence matrix is a prospective approach for the description of photos affected by backlit. Neighboring pixels of natural images have close values, and non-zero elements locate along the main diagonal of the co-occurrence matrix, as a rule. For photos damaged by backlighting, the co-occurrence matrix has the highest concentrations of elements in left-top or right-bottom corners as well as gaps in the central part of the main diagonal. Figure 4 shows the co-occurrence matrices for undistorted and damages by backlighting photos.

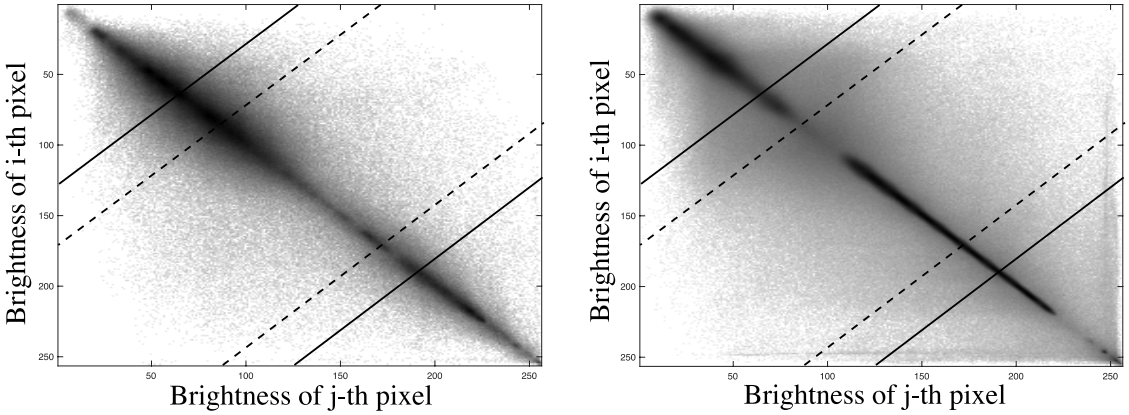

Figure 4. Co-occurrence matrices for undistorted (left) and damages (right) photos.

We propose to divide the co-occurrence matrix into three parts orthogonally to the main diagonal similar to shadow, middle tones and highlights sub-ranges in a histogram. It is possible to divide the main diagonal in three equal parts (see dashed lines in figure 4), but it is preferable to set range of middle tones twice larger than for dark and bright tones (see solid lines in figure 4). The following features are calculated from the co-occurrence matrix *G*, where pixels situated in distance 3 pixels in column is considered. Fractions of *G* in dark, light, and middle tones:

$$S_1 = \sum_{i=0}^{127} \sum_{j=0}^{127-i} G(i,j)/(M \times N) \tag{5}$$

$$S_2 = 1 - (S_1 + S_3), \tag{6}$$

$$S_3 = \sum_{i=128}^{255} \sum_{j=383-i}^{255} G(i,j)/(M \times N) \tag{7}$$

where *M* is the number of rows and *N* is the number of columns of the image.

Fractions of *G* in sub-regions of dark tones:

$$S_{11} = \sum_{i=0}^{63} \sum_{j=0}^{63-i} G(i,j)/(M \times N) \tag{8}$$

$$S_{12} = S_1 - S_{11}. \tag{9}$$

Ratios of maxima in dark tones and maxima in bright tones to global maxima:

$$M_1 = \max_{\substack{i=0\ldots127,\\ j=0\ldots127-i}} (G(i,j)) \Big/ \max_{\substack{i=0\ldots255,\\ j=0\ldots255}} (G(i,j)), \tag{10}$$

$$M_3 = \max_{\substack{i=128\ldots255,\\ j=383-i\ \ldots255}} (G(i,j)) \Big/ \max_{\substack{i=0\ldots255,\\ j=0\ldots255}} (G(i,j)). \tag{11}$$

Locations of the matrix *G* maxima in the left and in the right parts:

$$P_1 = \max_{\substack{i=0\ldots127,\\ j=0\ldots127-i}} (G(i,j)), \tag{12}$$

$$P_3 = \max_{\substack{i=128\ldots255,\\ j=383-i\ldots255}} (G(i,j)). \tag{13}$$

The following features are the number of elements of co-occurrence matrix G, which are the greater than the threshold which equals to the average value of G:

$$thres(y, G_0) = \begin{cases} 1 | \ y \geq G_0 \\ 0 | \ y < G_0 \end{cases}, \tag{14}$$

$$G_0 = M \times (N-3)/256^2, \tag{15}$$

$$A_1 = \sum_{i=0}^{127} \sum_{j=0}^{127-i} thres(G(i,j), G_0), \tag{16}$$

$$A_2 = \sum_{i=0}^{127} \sum_{j=127-i}^{255} thres(G(i,j), G_0) + \sum_{i=128}^{255} \sum_{j=0}^{383-i} thres(G(i,j), G_0) \tag{17}$$

$$A_3 = \sum_{i=128}^{255} \sum_{j=383-i}^{255} thres(G(i,j), G_0). \tag{18}$$

where M is the number of rows and N is the number of columns.

Also, we calculate the ratios of the last three features:

$$R_1 = A_2/A_1, \tag{19}$$

$$R_2 = A_2/A_3, \tag{20}$$

$$R_3 = A_1/A_3. \tag{21}$$

Additionally, the same features (5-21) can be extracted from big fragments of image. We divide a photo into 2 equal parts vertically and 3 parts horizontally. Totally we calculate about two hundred of features from the histogram and the co-occurrence matrix for the entire image and its fragments.

5. Enrichment of feature set

To enrich our feature set we applied a combination of features with the following feature selection. The idea of combining features is based on the assumption that some of the combinations, for example, sum, product, ratio of different features and their squaring, can provide an improvement to the regression model. Therefore, it is advisable to try as many such combinations as possible.

In an ideal case, features should be informative that is they should have a high correlation with amplification factor k_s from the ground truth. Obviously, informativeness of various features is very different. A use of non-informative features can lead to the worsening of the regression model. It is necessary to select “good” features and drop “bad” ones. For feature selection, we employed a greedy addition of features to random forest regression model. If the addition of a feature to model leads to decreasing of MAD, then we remain the feature, otherwise, we drop it.

6. Results

We tested and compared to each other all feature sets described above. In the paper, we do not show intermediate outcomes, because they have a huge size. The best result demonstrates model which uses features $S_3, S_{11}, M_1, M_3, P_1, P_3, A_2, A_3, R_1$ and ratio S_{12}/M_1, where the features are calculated for whole image as well as its fragments.

As was mentioned, the amplification factor for dark tones k_s can be treated as blind quality factor for images damaged by backlit. At present, a sufficient number of blind image quality metrics have been proposed. Such metrics make possible to evaluate the quality based on the image only without the reference. Part of the metrics is developed to assess the single factor affecting the quality, for example, the blurriness level [17]. Other ones claim to be universal. We compared the correlation coefficient r between experts’ judgments about k_s and several measures for quality assessment.

The following existing algorithms for non-reference quality assessment were analyzed. Blind Image Quality Index (BIQI) [18] implements a two-step approach to assess the quality of photographs. This method is based on usage of features originated from natural scene statistics (NSS) in the wavelet domain and assumptions that photos of natural scenes have determined statistic characteristics, these characteristics are changed due to distortions, and type and strength of distortion can be predicted. The first stage of BIQI is a classification type of defect. The second one is a numerical quality assessment

by means of the regression model. Support vector machine (SVM) is applied for training classification and regression models. Blind/Referenceless Image Spatial Quality Evaluator (BRISQUE) [19] uses features from NSS in the spatial domain. One regression model for all distortions is trained by SVM. Oriented Gradients Image Quality Assessment (OG-IQA) method [22] analyzes the correlation of oriented gradients in the spatial domain. It was speculated, orientations of local gradients change predictably for distorted images of natural scenes. One regression model for all distortions is trained via Adaptive Boosting for decision trees. Natural Image Quality Evaluator (NIQE) [20] does not use distorted images for training. In this method, multivariate Gaussian (MVG) model based on NSS features in the spatial domain is calculated for pristine photos only. The quality of the estimated image is estimated as the distance between its MVG and pre-calculated MVG of several undistorted images. Integrated Local Natural Image Quality Evaluator (IL-NIQE) [21] algorithm exploits the same idea as NIQE, but IL-NIQE operates with color channels of photo in salient local patches.

Table 2. Correlation coefficient between experts' judgments and measures for quality assessment.

	Decision tree, [5]	BIQI	BRISQUE	NIQE	ILNIQE	OG-IQA	Proposed
Correlation coefficient, r	0.47	-0.22	0.05	0.13	0.23	0.13	**0.69**

Table 2 contains the correlation coefficient between ground truth and measures for quality evaluation. Amplification factor k_s serves as quality metrics for algorithm from [5] and for proposed regression model. Our method provides the best conformance to experts' judgments. Well-known universal image quality measures have low correlation with ground truth and cannot be used for quality characterizing of photos damaged by backlighting.

Table 3 contains outcomes of comparison of three methods for the estimation of amplification factor k_s. We analyzed decision tree from [5] as a baseline, regression model by means of random forest trained in features from [5], and random forest model trained on proposed features. According to all performance measures our technique outperforms considered alternatives.

Table 3. Comparison of methods for estimation of k_s.

	MAE	*MSE*	*MedAE*	*r*	*normAUC*
Decision tree from [5]	21.5	800	17.0	0.47	0.700
Random forest with features from [5]	14.8	334	13.1	0.61	0.711
Random forest with proposed features	**13.5**	**282**	**11.7**	**0.69**	**0.724**

7. Conclusion

Photos taken by backlighting conditions need to be enhanced to improve their pleasantness. There is a technique for the correction of dark tones. The automatic adjustment of the parameter for amplification of dark tones is needed for that method. For this purpose, we propose a feature set, extracted from the co-occurrence matrix, and regression model via random forest. For the collection of training dataset, we employed semi-supervised paradigm for obtaining of required photos from social networks. The regression model developed outperforms the baseline method. In addition, our model produces smooth continuous values of amplification factor rather than step-wise discrete values in the existing method. The proposed algorithm is intended for photo enhancement software.

8. References

[1] Safonov I V, Kurilin I V, Rychagov M N and Tolstaya E V 2018 *Adaptive Image Processing Algorithms for Printing* (Singapore: Springer Nature)

[2] Thang P C and Kopylov A V 2018 Tree-serial parametric dynamic programming with flexible prior model for image denoising *Computer Optics* **42(5)** 838-845 DOI: 10.18287/2412-6179-2018-42-5-838-845

[3] Safonov I V, Rychagov M N, Kang K and Kim S H 2008 Automatic red eye correction and its quality metric *Proc. of SPIE* **6807** 68070W

[4] Safonov I V, Rychagov M N, Kang K and Kim S H 2008 Adaptive sharpening of photos *Proc. of SPIE* **6807** 68070U
[5] Safonov I V 2006 Automatic correction of amateur photos damaged by backlighting *Proc. of GraphiCon* 80-89
[6] Triguero I, García S and Herrera F 2015 Self-labeled techniques for semi-supervised learning: taxonomy, software and empirical study *Knowledge and Information systems* **42(2)** 245-284
[7] Breiman L 2001 Random forests *Machine learning* **45(1)** 5-32
[8] Goncharova A V 2018 No-reference metrics for the quality of images damaged by backlighting *Proc. of DSPA* **2** 568-572
[9] Drucker H, Burges C J, Kaufman L, Smola A J and Vapnik V 1997 Support vector regression machines *Proc. of NIPS* 155-161
[10] Altman N S 1992 An introduction to kernel and nearest-neighbor nonparametric regression *The American Statistician* **46(3)** 175-185
[11] Breiman L, Friedman J, Stone C J and Olshen R A 1984 *Classification and regression trees* (Boca Raton: CRC Press)
[12] MATLAB feedforwardnet URL: https://www.mathworks.com/help/deeplearning/ref/feedforwardnet.html (01.04.2019)
[13] MATLAB linearlayer URL: https://www.mathworks.com/help/deeplearning/ref/linearlayer.html (01.04.2019)
[14] Jahrer M, Töscher A and Legenstein R 2010 Combining predictions for accurate recommender systems *Proc. of ACM SIGKDD* 693-702
[15] Wolpert D H 1992 Stacked generalization *Neural networks* **5(2)** 241-259
[16] Bi J and Bennett K P 2003 Regression error characteristic curves *Proc. of ICML* 43-50
[17] Asatryan D G 2017 Image blur estimation using gradient field analysis *Computer Optics* **41(6)** 957-962 DOI: 10.18287/2412-6179-2017-41-6-957-962
[18] Moorthy A K and Bovik A C 2010 A two-step framework for constructing blind image quality indices *IEEE Signal processing letters* **17(5)** 513-516
[19] Mittal A, Moorthy A K and Bovik A C 2012 No-reference image quality assessment in the spatial domain *IEEE Transactions on Image Processing* **21(12)** 4695-4708
[20] Mittal A, Soundararajan R and Bovik A C 2013 Making a “completely blind” image quality analyzer *IEEE Signal Processing Letters* **20(3)** 209-212
[21] Zhang L, Zhang L and Bovik A C 2015 A feature-enriched completely blind image quality evaluator *IEEE Transactions on Image Processing* **24(8)** 2579-2591
[22] Liu L, Hua Y, Zhao Q, Huang H and Bovik A C 2016 Blind image quality assessment by relative gradient statistics and adaboosting neural network *Signal Processing: Image Communication* **40** 1-15

Combined usage of the optical and radar remote sensing data in territory monitoring tasks

V N Kopenkov[1]

[1]Samara National Research University, Moskovskoe Shosse, 34A, Samara, Russia, 443086

e-mail: vkop@geosamara.ru

Abstract. At the present time, a lot of problems in a sphere of fundamental sciences as well as technical and applied tasks can be solved only with the use of satellite images, since their usage reduces material, financial and time costs significantly in comparison with traditional methods. One of the modern integrated approach remote sensing processing is to join the measurements obtained from the various sources, such as optical and radar sensors, allowing to achieve a gain in comparison with independent processing due to the extension of the information volume and the opportunities of data acquisition (weather conditions, spectral ranges, etc.). However, methods of digital processing and interpretation of radar data, as well as qualitative and proven methods and algorithms for joint processing of optical and radar satellite images, has not sufficiently been well developed yet. Therefore, the development of new methods and information technology of joint analysis and interpretation of optical and radar data which are a major issue of the current paper, are certainly relevant. The paper presents an information technology for joint processing of optical and radar satellite imagery, based on training the processing procedure based on the reference values of data from sensors of the one type (optical data), followed by applying to both data types: optical and SAR data.

1. Introduction

Today, a lot of problems of fundamental sciences, as well as technical and applied tasks can be solved effectively only with help of space vehicles, since their usage significantly reduces the material, financial and time costs compared with traditional methods. Recently, it is possible to receive multi-spectral aerospace information in the optical and radio bands in a regular way. At the same time, the tasks of determining various characteristics of the earth's surface, monitoring and analyzing of emergency, classifying and analyzing of territories as a whole are becoming increasingly important. A special place is occupied by the task of classifying the underlying surface and species composition. Conventionally, to solve this task images obtained in the optical range of the electromagnetic spectrum used as input data. Classic approaches which are successfully used for the processing of optical images do not give positive results when working with data obtained by synthetic aperture radars. The recognition of vegetation types, borders of territories, the detection and classification of objects on the base of radar images is practically not performed, because approaches to processing and thematic interpretation of radar data are not sufficiently well developed and investigated. For example, all known algorithms for automatic classification are adapted to the Gaussian model of the distribution of additive noise arising only on optical images. High-resolution radar images formed by synthetic

aperture radars as a result of irradiating the surface of the Earth with coherent waves are usually distorted by multiplicative noise, known as speckle noise. This kind of noise is a serious problem during the processing of radar images on the base of classic methods. Therefore, we need image processing and analysis methods adapted to the physical and technical features of radar imaging.

2. The scheme of combining the radar and optical data

Traditionally, the technology of combining and processing of mixed remote sensing data consists of 3 main subtasks: independent preliminary processing, matching and combining satellite images obtained by various sensors in the optical and microwave ranges, detecting differences and further processing of remote sensing data.

Within the framework of the first task, the well-known solutions combine the methods of interpolation of data on a non-uniform grid, image reconstruction frequency methods, adaptive filtering [1], radiometric, geometric and polarimetric calibration (for polarimetric radar data) [2], image enhancement operations [1], reduction of speckle noise on a radar image, orthotransformation taking into account a digital elevation model, etc. Existing approaches ordinarily solve this task using assumptions about the same characteristics of imaging systems, which have similar spatial resolution and the same spectral ranges of signal acquisition and receiving.

The task of matching heterogeneous images are needed for the realization of a further goal – joint analysis of radar and optical satellite imagery refers to the data processing and analysis area [3-5]. In this case, special attention should be paid to the choice of the merging method. Because the type and amount of preliminary data preparation depend on it. For example, in the case of point-oriented methods, high-precision geocoding and the further combination of all images is very important. In the case of object processing the preliminary detection, selection and, possibly, recognition of objects on images, as the objects observed on radar images often look completely different than on optical ones, since the scattering of the radio signal and sunlight by objects can differ significantly. Radar and optical observations are complementary, and this fact may have a different nature depending on the problem being solved. Their joint processing improves the ability to detect certain objects and measure the parameters of the underlying territory. The general classical scheme of combining radar and optical data is shown in Figure 1.

Herewith, to solve practical tasks, in most cases, the combination of optical and radar data is implemented in two ways.

In a situation where optical data is not available, radar data can be a good alternative. For joint processing, in this case, data is orthotransformed, and reduced to comparable resolution (or the optical image may have a lower resolution since the imaging capabilities of such images are higher). After that, points or objects in both images are analyzed to solve the problem of identifying differences and unchanged regions, as well as for further analysis of remote sensing data.

The second data matching approach is based on the RGB ↔ HIS conversion, which allows you to combine terrain information obtained in two different ranges on one output image. First, the three most informative spectral channels RGB → HIS (brightness-saturation-hue color) are converted, then the brightness is replaced with a radar image on the resulting image and the inverse transformation is performed, which requires a balanced stretching of the channels to improve the quality of the final representation in RGB. Using such images, it is possible to determine the roughness (low/high vegetation, flooded/not-flooded area), and the structure of the territory, which is necessary for geological tasks.

However, both the first and second version of the data combination is not suitable for the qualitative solution of the underlying surface classification and analysis tasks.

3. The technology of joint processing of optical and radar data based on a training dataset

Analysis and processing of images obtained by dissimilar remote sensing sensors, with spatial and spectral resolution improving, usually involves the formation of individual models of observation for each of the sensors, which is not always possible and requires a large amount of additional a priori information about the observation model. In addition, it is extremely difficult to develop an automatic

adaptive technology for processing dissimilar remote sensing data on the basis of a variety of particular observation models.

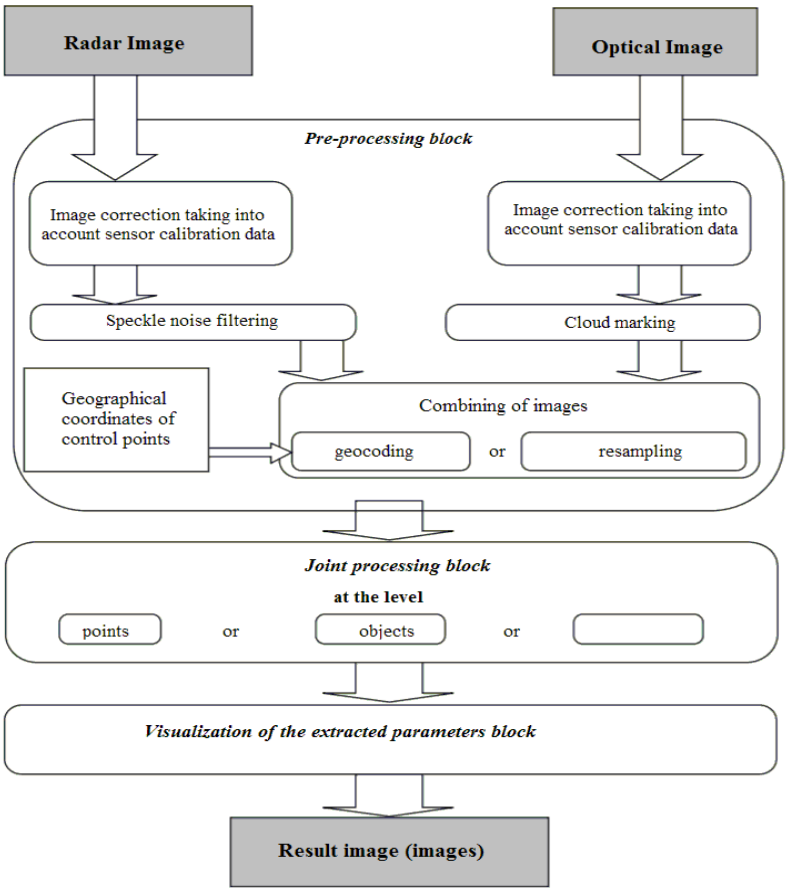

Figure 1. The classical scheme of combining radar and optical data.

Therefore, the methods of nonlinear analysis and data interpretation, such as neural networks or hierarchical structures or Approximate Local Correlation Integral (aLOCI) are of the greatest interest for investigation. These methods can be used without definite assumptions about the source data. In addition, aLOCI uses quadtrees to increase the efficiency of calculations in the multidimensional case. Among these methods in our task we intend to use a multidimensional classification based on optical data, since the solution of the microwave signal analysis problem in the general case can be made in the form of a classification with training, based on features in the form of optical data, observation results and a priori information about the underlying surface [6-7].

At the same time, it is advisable to use standard methods for extracting features and classification algorithms for multidimensional data, because the interest in improving the quality of evaluation of thematic classification. These methods most often include features obtained as a result of the principal component method (PCA) and the Nonparametric Weighted Feature Extraction (NWFE) method, and such classifiers as the Support Vector Method (SVM) and Random Forest (RF) [5-6]. The developed algorithm for the local processing of satellite images based on hierarchical regression [6] allows us to accelerate data processing by using hierarchical data structures and in a multidimensional case, the performance is comparable to or superior to other classification methods, in particular, neural networks. Finally, the assessment of the quality of the results of classification and detection of changes in the territory by received dissimilar satellite images relates to the field of image analysis based on the values of one remote sensing sensor using the values of another sensor (for example, calculating of the regression function) [7,10-11].

Thus, the construction of the technology is supposed to be carried out in three stages: data preparation, combination and analysis of the image sequence. At the first stage, the use of sensor-

dependent methods of processing and combining (spatial) data is assumed, i.e. features of the source of satellite images (optical or radar) are taken into account, but it is assumed that the observed territory is the same. After that, the radar images "are brought to the kind" of optical (or optical images "are brought to the kind" of radar, depending on the task) based on the features and non-linear regression models. And finally, a sequence of images with similar spectral characteristics is formed that makes it possible to implement the solution of thematic processing tasks such as classification, change detection and etc.

In this paper, to form an aggregate set of satellite images that are suitable as source data for classification and analysis of changes, we propose a technology for converting (point-by-point processing based on reference values) data of the one type (conceivably radar) based on a training sample consisting of a data set of another type (optical images). Regression models of processing based on a decision tree for merging extracted SAR (Synthetic-aperture radar) radars and optical sensor values are assumed to be used here. Hierarchical structures in the form of a decision tree are not parametric and therefore do not require an unambiguous description of the desired classes. Herewith, the final processing procedure consists of a set of explicit hierarchical conditions (rules, thresholds of functions) applied to the input data intervals, in our case SAR and optical functions, as reference values. This allows classifying the pixels (area sampling) of the radar image as a function of optical data. Decision tree classifiers have been successfully applied to classify the underlying surface. The general scheme of data conversion (in the process of applying the processing procedure), oriented on a priori information about the desired processing result (presented in [6, 10]), is illustrated by the diagrams presented in Figure 2.

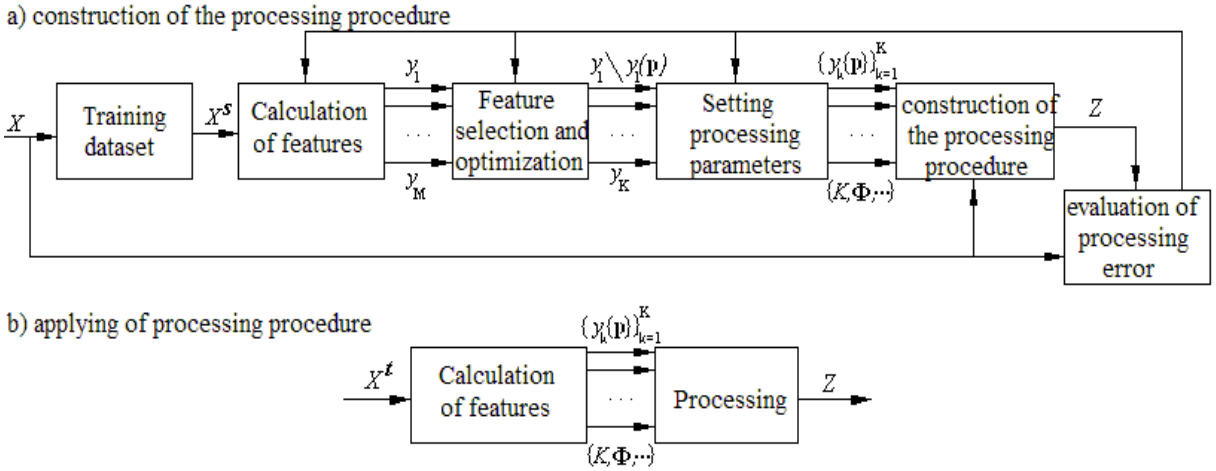

Figure 2. The scheme of training and usage of processing procedures, based on the training dataset.

Considering a large number of matched pairs of image pixels (z_i, x_i) as a training sample, we build the signal processing procedure **Φ**, which associates the feature vector $\{y_k(n,[\mathbf{p}])\}_{k=0}^{K-1}$ calculated on the base of discrete samples of the input signal *X*, the output value of the signal *Z*. The sets of features, parameters of the processing procedure construction, as well as the type of functions of the elementary regression in the terminal nodes can be adjusted according to the results of the evaluation of the quality of processing.

To evaluate the generalization ability of the constructed procedure, the full sliding control functional is used:

$$Q^{st}(\mu(\Omega),\Omega) = \frac{1}{N}\sum_{n=1}^{N} \nu(\mu(\Omega_n^s),\Omega_n^t),$$

where Ω is the final set of objects for learning (dataset), $\mu(\Omega)$ is the algorithm (method) of training on a dataset Ω, (Ω_n^s,Ω_n^t), $n=1,2,...,N$ are the variants of dividing the dataset into training and control parts.

$\nu(\mu(\Omega_n^s),\Omega_n^t)$ is the error rate of the algorithm $\mu(\Omega_n^s)$, constructed on the base of the set Ω_n^s and checked by using the set Ω_n^t.

Receiving information from different sensor types leads to a shift in the position of sensor cells relative to objects due to the differences in the orbital parameters of the satellites and due to the difference in the physical laws of pixel formation in the image (resolution is dissimilar for optical and radar data). It is obvious that individual sensors cover the observed area with grids with different parameters that can be described as a relative motion within the coordinate system of the observed scene. As for the coordinate system of the observed scene, you can use some projection coordinate system in which each pixel is represented as an area of finite size, assuming that the coordinates of the image pixel are the coordinates of the center of the pixel. This view does not contradict the processing technology based on decision trees since the latter can use the integral values in the spectral channels over the local window as attributes for the input and output pixels.

In this way, the technology of forming a sequence of consistent and combined dissimilar remote sensing images is used to obtain features for the tasks of land use classification according to remote sensing data, as well as for analyzing changes on the sequence of images.

4. Evaluation of the training dataset volume and experimental research

Is quite logical is the fact that when working with images solution of the problem of constructing the processing procedures taking into account all combination of training and testing dataset is unrealizable in practice because of the giant of busting on various combinations of datasets. Therefore, it is necessary to develop a method to determine the possibility of stopping a forming, or the need to continue training and testing datasets generation on the base of a finite number of them. It is obvious that for every task there is an optimal complexity of the model, at which the best quality of generalization is achieved.

In paper [10], the technology of decision making about stopping the process of generating various combinations of training and control datasets was proposed, according to which to make a decision of stopping generation of various combinations of training and control datasets, and about the transition to the next subset of features it is necessary to calculate confidence intervals for the expectation of a Poisson distribution with parameter λ: $Bin(n,\lambda/n) \approx P(\lambda)$ for the functional full cross-validation on a datasets N_1 and N_2 in the form:

$$\left[\lambda_1 - \frac{\tau_{1-\alpha/2}\sqrt{\lambda_1}}{\sqrt{N_1}}, \lambda_1 + \frac{\tau_{1-\alpha/2}\sqrt{\lambda_1}}{\sqrt{N_1}}\right]\left[\lambda_2 - \frac{\tau_{1-\alpha/2}\sqrt{\lambda_2}}{\sqrt{N_2}}, \lambda_2 + \frac{\tau_{1-\alpha/2}\sqrt{\lambda_2}}{\sqrt{N_2}}\right],$$

where $\tau_{1-\alpha/2}$ – quantile of distribution $N_{0,1}$ for level $1-\alpha/2$ ($\alpha = 1-\gamma$).

The decision of stopping of a generation of various combinations of datasets and about the transition to the next subset of features is taken at a time when a separation of calculated confidence intervals on adjacent steps is achieved. The presented technology of decision about stopping the brute force bust process allows estimating the amount and possible combinations of training and control data sets used in experimental studies.

As data used as training and control datasets, we used sets of images (free data) from Landsat-7 and Sentinel 1-2 satellites for different time periods, as well as Radarsat-2 data available at the center of remote sensing data of Samara University. Datasets from Landsat-7, Spot 6/7, Aist, Resurs-P, Pleiades and coverage with Google and Yandex data were used as reference data in the optical range.

Experimental study on the applicability of the technology to dissimilar datasets (optical and radar data) are in progress, so the final results are not presented in this article. Experimental studies of the feasibility of individual stages of processing, classification and analysis of remote sensing data on the basis of hierarchical structures built in accordance with the principles of learning "by precedent" are presented in the author's works [6, 10, 11].

To carry out our experimental studies, we used sets of images from such space vehicles as Spot 7, Aist-2D, Resurs-P, Sentinel-2 in the optical range (more than 40 test images) and radar images from

the Radarsat2 and Sentinel-1 satellites (more than 20 scenes). All data were obtained in the spring-summer period in 2010-2018. All images were radiometric and geometrically corrected, brought to a similar resolution and matched (geographically bounded) with an accuracy of about 1 to 2 pixels. All pre-processing and low-level processing task was implemented in ScanEx ImageProcessor software. Examples of images from different spacecraft are shown in Figure 3.

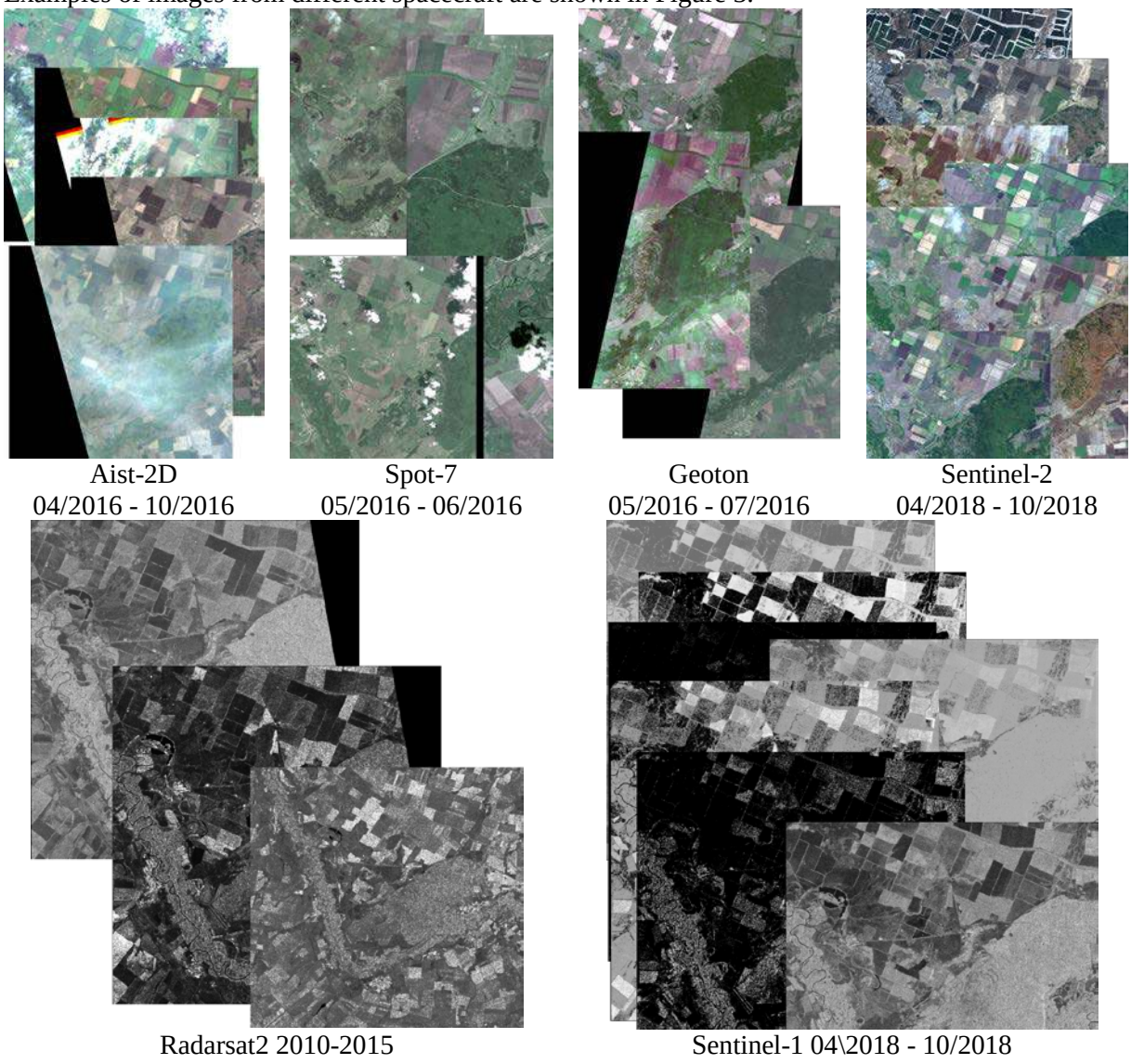

Figure 3. Training and testing datasets in a form of images from different spacecrafts.

All experimental studies can be divided into 3 groups:

1) Optical data as a training sample, and optical data from the same satellite as test data.

2) Optical data from different satellites as a training sample, and optical data from another satellite as test data.

3) Optical and radar data from different satellites as a training sample, and optical data from another satellite as test data.

The results of experimental studies of the quality of the pixel-by-pixel classification are shown in Table 1. In general, it can be noted that the technology of joint processing of optical and local data based on hierarchical structures with training on a priori information is quite efficient.

At the same time, we note that if the training sample contains data of the same type as that used as a test data, then the quality of the classification is quite high. It should be noted that the classification based on radar data shows a very low quality of classification since the features in the form of the

original image pixels are not sufficiently informative. Therefore, it is necessary to use other features in the form of generalized coefficients over a certain local image area. Selection and optimization of such features is the goal of further work.

Table 1. Quality of per-pixel classification.

	Images for test			
Training dataset	Sentinel-2	Aist-2D	Spot-7, Geoton	Radarsat2, Sentinel-1
Sentinel-2	96-98%	72-87%	67-79%	
Sentinel-2 (70%) + Aist-2D	93-98%	90-95%	72-84%	
Sentinel-2 (50%) + Aist-2D + Spot-7 + Geoton	89-97%	86-94%	84-91%	
Sentinel-2 (80%) + Radarsat2 + Sentinel-1	93-98%	76-84%	62-78%	46-72%
Optical satellites (80%) + Radarsat data (20%)	90-97%	87-92%	78-84%	52-74%
Optical satellites (50%) + Radarsat data (50%)	86-92%	76-82%	76-80%	57-82%

No experiments were carried out to restore (classify) pixels of optical images by using the pixel values only of radar images because it is impossible to obtain adequate results for various spectral channels (RGB) from radar data only.

5. Conclusion

This article presents a new information technology for joint processing of optical and radar satellite imagery. The technology is based on learning procedure that uses the data from sensors of the one type (optical in the basic approximation) as reference values and then the technology is applied to the data of both types: the same one (optical) and the another data type (radar data). Experiments on testing of the developed regression models of processing based on a decision tree for joint processing of data obtained in the optical and SAR ranges confirm the efficiency and effectiveness of the technology. That, as a result, allows classifying the samples (areas of pixels) of the radar image as a function of optical data. The earlier experiments [6, 10, 11], as well as experiments in the framework implemented in this paper, showed the efficiency of using decision trees as classifiers of the underlying surface and demonstrated a high quality of classification, which suggests the possibility of applying this approach to the problem of joint analysis of optical and radar data.

6. References

[1] Wan X, Yang Y 2010 Super-resolution image reconstruction *Computer Application and System Modeling (ICCASM)* **8** 351-355
[2] Nikolsky D B 2016 Methods for processing radar data *Geomatics* URL: http:// geomatica.ru/clauses/48/ (10/01/2018)
[3] Kopenkov V N, Sergeev V V, Soifer V A and Chernov A V 2017 Remote sensing of the Earth and geographic information systems *Bulletin RFBR* **95(3)** 78-96 DOI: 10.22204/2410-4639-2017-095-03-78-96
[4] Zakharova L N, Zakharov A I, Sorochinsky M V, Ryabokon G P and Leonov V M 2011 Joint data analysis of optical and radar sensors: opportunities. restrictions, prospects *Radio engineering and electronics* **56(1)** 5-19
[5] Schmitt M, Tupin F and Xiang Zhu X 2017 Fusion of SAR and optical remote sensing data — Challenges and recent trends *IEEE International Geoscience and Remote Sensing Symposium (IGARSS)* DOI: 10.1109/IGARSS.2017.8128239
[6] Kopenkov V N 2013 Designing a procedure for local image processing based on hierarchical regression designed for processing satellite images tasks *Collection of scientific articles "Modern problems of remote sensing of the Earth from space*" **10** 2284-2295

[7] Hughes L H, Auer S and Schmitt M 2018 Investigation of joint visibility between SAR and optical images of urban environments *ISPRS Annals of the Photogrammetry, Remote Sensing and Spatial Information Sciences* (Riva del Garda, Italy) **IV-2**
[8] Mandanici E, Bitelli G 2016 Preliminary Comparison of Sentinel-2 and Landsat 8 Imagery for a Combined Use *Remote Sensing* **8(12)** 1014
[9] Kopenkov V N 2014 The method of stopping the process of building hierarchical regression in the implementation of computational procedures for local image processing *Computer Optics* **38(2)** 351-355
[10] Bagautdinov R S, Kopenkov V N, Myshkin V N, Sergeev V V and Tribunsky S A 2015 Investigation of the possibility of using satellite images to identify archaeological objects *Computer Optics* **39(3)** 439-444 DOI: 10.18287/0134-2452-2015-39-3-439-444
[11] Kopenkov V N, Myasnikov V V 2016 Development of Algorithm for automatic construction of computational procedure of local image processing, based on the usage of hierarchical regression *Computer Optics* **40(5)** 713-720 DOI: 10.18287/2412-6179-2016-40-5-713-720

Acknowledgments
The reported study was funded by RFBR according to the research project № 16-29-09494 ofi_m, 17-29-03190 ofi, 18-07-00748, as well as the Ministry of Science and Higher Education of the Russian Federation as part of the work on the State task of the Federal Research Center "Crystallography and Photonics" of the Russian Academy of Sciences (agreement № 007-GZ/Ch3363/26).

Surface recognition of machine parts based on the results of optical scanning

M A Bolotov[1], V A Pechenin[1], N V Ruzanov[1] and E J Kolchina[2]

[1]Samara National Research University, Institute of Engines and Power Plants, Moskovskoe Shosse, 34A, Samara, Russia, 443086
[2]Stock company «RKC «Progress», Zemeca street, 18, Samara, Russia, 443009

e-mail: vadim.pechenin2011@yandex.ru

Abstract. To predict the quality parameters of products (in particular, the assembly parameters) mathematical models were implemented in the form of computer models. To ensure the adequacy of calculations, it is necessary to have information about the actual geometry of the parts, which can be obtained using noncontact measurements of parts of the assembly. As a result of measuring parts and components using optical or laser scanner, a large dimension array of measured points is formed. After standard processing (e.g. noise removal, combining the scans, smoothing, creating triangulation mesh), the recognition of individual surfaces of parts becomes necessary. This paper presents a neural network model that allows the recognition of elements based on an array of measured points obtained by scanning.

1. Introduction

The least automated step in the industry is the assembly of single and serial products characterized by medium and high complexity. These products include aircraft engines. The considered products are not made in large quantities as cars; they are characterized by a high degree of optionality and increased requirements for complexity and accuracy. The share of labour-consuming assembly in the total labour-intensiveness of products is up to 25% and largely determines their quality. There are several reasons that make it difficult to fully automate the assembly of these products. One of the significant reasons is the difficulty of determining the parameters of the operations performed by robots, which are guaranteed to ensure the specified accuracy and quality of products. The assembly of medium and high complexity products is a unique operation, during which the course of operations is changed according to the results of measurements and the geometric analysis of the assembled parts. Measurement of geometry is made by both contactless and contact methods.

To partially automate engine assembly processes, it is necessary to recognize both the individual parts and the surfaces of the parts along which the assembly will take place. Face recognition is possible using computer vision approaches [1,2,3]. The aim of this work is to create a model based on the use of neural networks, designed to recognize the surfaces of engineering parts after their measurement using an optical or laser scanner.

2. Object of research

To test the model, a real engine parts simulator was designed and manufactured: spacers in the turbine of an aircraft engine. A detail drawing is shown in Figure 1. The part contains cylindrical and flat edges, as well as threaded holes.

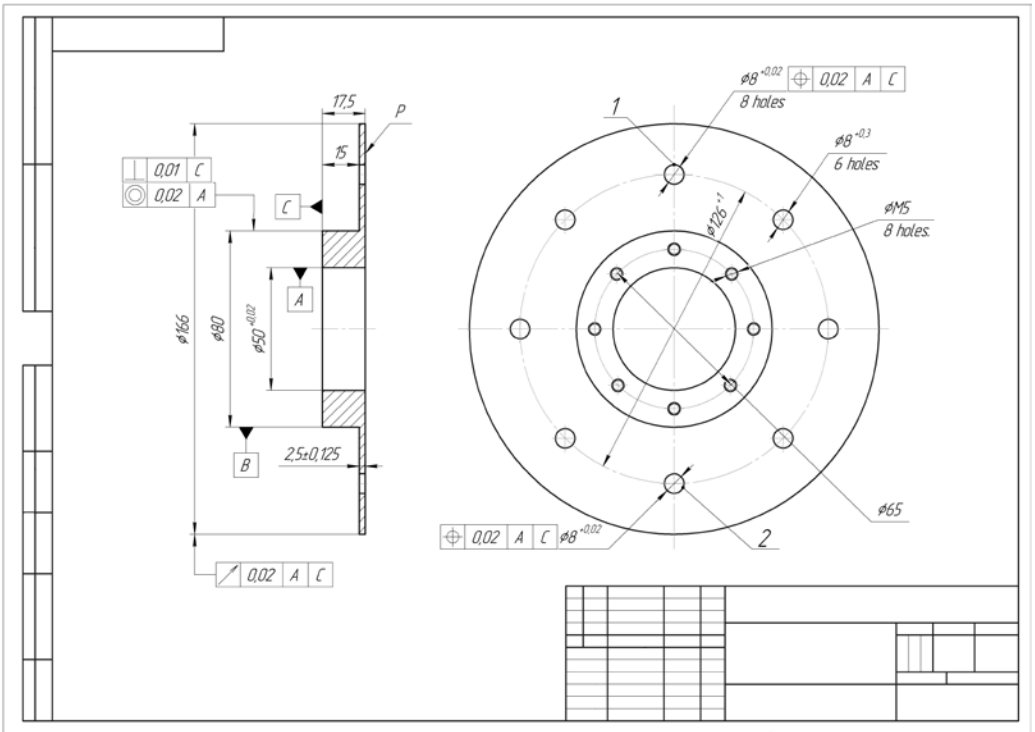

Figure 1. Drawing part "spacer simulator".

Automated element (surface) recognition of measured parts using neural networks solves two tasks: 1) segmentation of a part's components into types of surfaces (plane, cylinder, cone, etc.) 2) additional refinement of the boundaries of triangulation surfaces based on deviations of the facet normal vectors. To solve the first problem, a convolutional neural network was used.

3. Neural network model of surface recognition

Convolutional neural networks (CNN) are a very wide class of architectures which main idea is to reuse parts of the neural network to work with different small, local input areas [4]. The main area of application of convolutional architectures is image processing [5, 6].

At present, many approaches have been developed for recognizing three-dimensional objects in works devoted to computer vision. These approaches can be divided into two groups: recognition of elements, directly working on their own three-dimensional representations of objects, such as polygonal grids, voxel representations and arrays of points, and approaches based on signs and metrics that describe the shape of a three-dimensional object, "what it looks like" in the collection 2D projections [7].

Except for the recent work by Wu et al. [8], who studied form descriptions from a voxel-based object representation through three-dimensional convolutional networks, the previous three-dimensional shape descriptions were mostly "manually developed" according to a specific geometric property of the shape surface or volume. For example, shapes can be represented by histograms or models with total signs of surfaces consisting of normals and curvatures [9], distances, angles, areas of triangles or volumes of tetrahedra calculated for sample points of surfaces [10], properties of spherical functions defined in volumetric grids [11], local shape diameters measured on tightly selected surface points [12], and thermal core signatures on polygonal grids [13, 14]. The development of controlled machine learning algorithms on top of such descriptions of three-dimensional figures creates several problems. First, the size of organized databases with annotated 3D models is rather limited compared

to image data sets. For example, ModelNet contains about 150 thousand objects. In contrast, the ImageNet database [15] already includes tens of millions of annotated images. Secondly, the additional features and metrics of three-dimensional figures tend to be very multidimensional, which makes the algorithms prone to retraining.

One of the latest works on the problems of object classification and the segmentation of individual parts, in which an array of measured points is used directly at the entrance to the network, is [16]. Developed by authors from Stanford University, the network is named PointNet, the main idea of the approach is to memorize the spatial features of each point and then merge all the individual features into a marked general point cloud. The network is based on a convolutional architecture. The main disadvantage of the reduced network is that at the input it is necessary to always have the same number of points for all objects, which in practice is not possible and you will have to resort to an artificial "distortion" of the data.

Based on the literature review and the specifics of the problem being solved, the decision was made to use an approach based on the use of 2D projections of objects in solving the current problem. In this approach, a convolutional neural network, U-net [17], is used for segmentation.

We will reveal the main idea and stages of the developed model for the segmentation of individual faces. The main idea is to create projections (pictures) for the faceted model of measured data, segmentation of faces on projections and identification of facets by segmented images. The stages of the approach are shown in Figure 2.

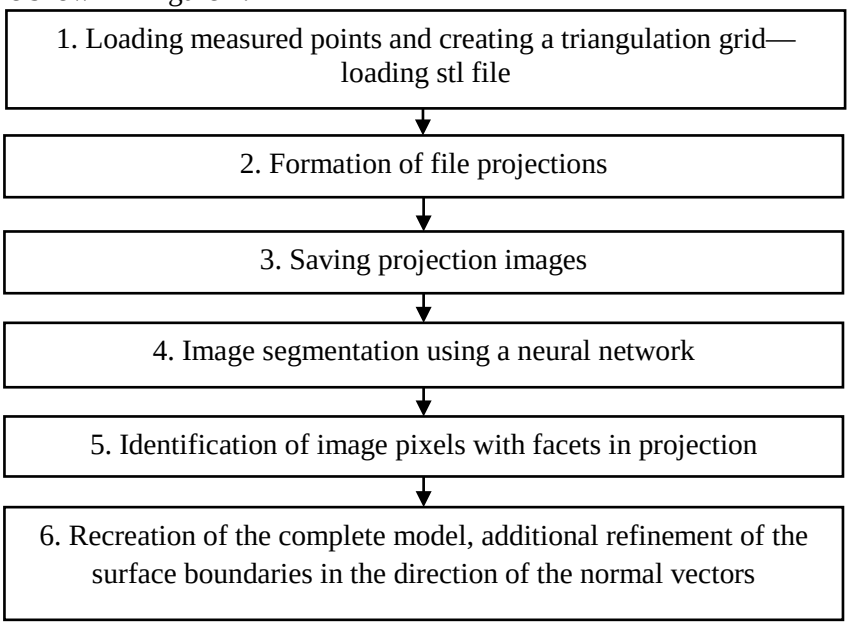

Figure 2. A flowchart of the face recognition model using projections of measured data.

Consider the face recognition steps in more detail.

3.1. Loading measured points and creating a triangulation grid—loading stl file

As noted in the introduction, the model is designed to recognize geometry after measurement using optical and laser scanners. After measurement using the scanner and preliminary data processing, a file is created with the coordinates of points united into a facet surface of the *.stl format. The file contains the following data: $\mathbf{V}_{g\times3}$ (matrix of coordinates of the vertices of the grid stl-model), $\mathbf{F}_{m\times3}$ (matrix of combinations of three vertices forming the facets of the surfaces), $\mathbf{N}_{m\times3}$ (matrix of coordinates of facet normals).

3.2. Formation of file projections

To enable semantic segmentation of the facets into separate surfaces using deep neural networks, it is necessary to create projections of 3D surfaces on coordinate planes. To prepare the projections, Roberts' algorithm was used [18].

Roberts' algorithm is the first known solution to the problem of removing invisible lines. This is a mathematically elegant method that works in object space. The algorithm primarily removes from each body the edge or edges that are screened by the body itself. Then each of the visible edges of each body is compared with each of the remaining bodies to determine which part or parts, if any, are shielded by these bodies. Therefore, the computational complexity of Roberts' algorithm grows, theoretically, with the square of the number of objects.

The operation of Roberts' algorithm takes place in two stages:

1. Definition of non-face faces for each body separately.
2. Identify and remove invisible edges.

To prepare the data, only the first stage of the algorithm was used. The second stage is not necessary for further decision; it is more complex and requires additional facets.

When creating projections on coordinate axes, orthogonal projections in the visual plane are obtained. For example, when projected on the *XOY* plane, the structure $\mathbf{F}_{m\times3}$ is preserved, and the matrix of the vertices $\mathbf{V}_{g\times3}$ is converted into $\mathbf{V}_{g\times2}$, having only coordinates along the *x*- and *y*-axes. Bypassing the vertices of the obtained projections of the facets in the same sequence as in the original, you can divide them into two types: those that are oriented counter-clockwise, which means that we are looking at the facet from the outside of the body and those that are oriented clockwise, which means that we are looking at the facet from the inside. The order of the vertices determines the direction of the normal. Thus, if the component of the normal vector of the projection plane (in this example, the component along the *z*-axis) is negative, we look at the facet from the inside. Since the object is bounded by a closed surface, we cannot observe the faces from the inside—they are invisible. Thus, it is necessary to exclude the facets identified by the above method from the $\mathbf{F}_{m\times3}$ structure, obtaining the projection structure $\mathbf{F}_{m1\times3}$, where $m_1<m$.

3.3. Saving projection images

Image saving is performed using STL work libraries (functions of the *stltools* package by Pau Micó) and MATLAB graphics saving tools. The sizes of the pictures are saved, as are all projections. Using the same tools, training projection images are saved, where objects for recognition are highlighted in different colours (Figures 3 and 4).

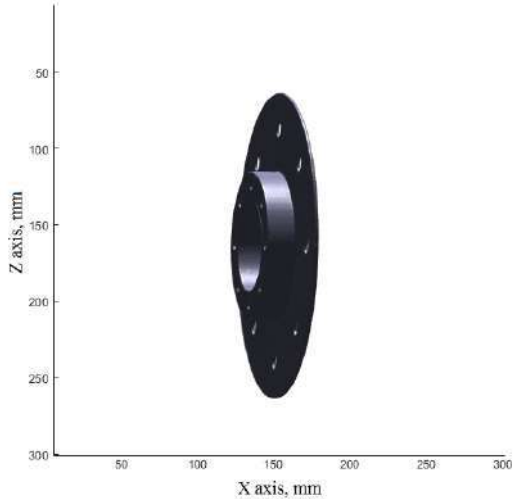

Figure 3. Stl file details "spacer simulator".

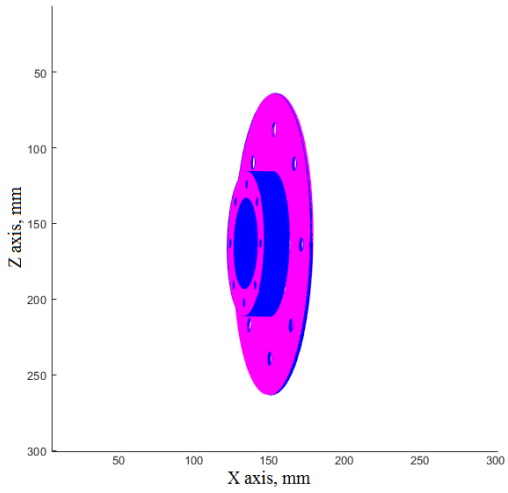

Figure 4. Part projection used for segmentation.

Nevertheless, segmentation requires clear boundaries, so images stored in the *.png format are imported into MATLAB (variable loading matrix RGB-colour) and converted to grayscale using the expression:

$$\mathbf{I}_{gray} = 0,299 \cdot \mathbf{R} + 0,587 \cdot \mathbf{G} + 0,114 \cdot \mathbf{B}, \quad (1)$$

where $\mathbf{I}_{gray}$ is the grayscale image matrix and $\mathbf{R}, \mathbf{G}, \mathbf{B}$ are the matrix components of the RGB system.

Multidimensional matrixes of images are saved to a *.mat file. A total of six projections remain. The object is placed as if in a cube whose faces are parallel to the planes of the coordinates. The dimensions of the cube are such that it includes all the measured objects in the sample. Projections are accordingly made on the faces of the cube: two on the faces parallel to the *XOY* plane; two parallel to *XOZ* and two parallel to *YOZ*.

3.4. Image segmentation using a neural network

The U-Net network architecture is shown in Figure 5.

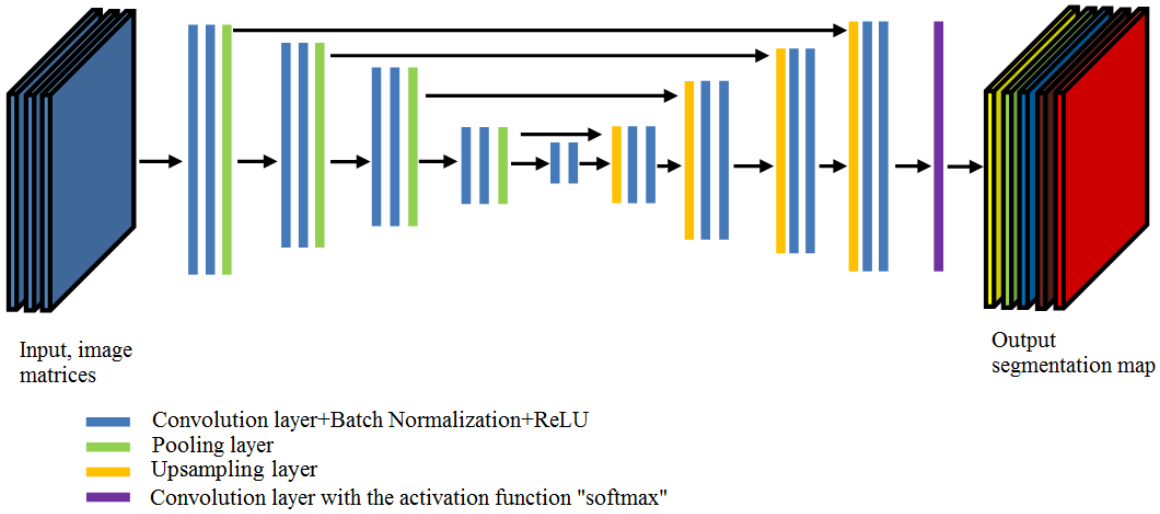

Figure 5. U-Net neural network architecture for image segmentation.

The network architecture is a sequence of layers of convolution and pooling, which first reduce the spatial resolution of the image, and then increase it by first merging it with the image data and passing it through other layers of the convolution. Thus, the network serves as a kind of filter.

The first half of the network contains layers of convolution with the activation function *ReLu*, normalization by mini-batch and layers of pooling (sub-sampling) and it is called a compressing path. The second part is an expanding path.

The upsampling layer is a reverse pooling layer that expands the feature map, followed by a convolution, which reduces the number of feature channels. Then comes the concatenation (“pasting” of linear objects) with an appropriately cut map of features from the compressive path and two convolutional layers.

On the last layer, convolution with a 1x1 core is used to bring each 64-component feature vector to the required number of classes. The activation function on the last layer is “softmax”.

The network was reproduced in the Python software environment.

3.5. Identification of image pixels with facets in projection

After the image is segmented, its pixels are compared to the coordinates of the corresponding projection. For matching, pixels are converted to points on the corresponding face of the cube described in Section 3.3. The values of the image pixels lie in the interval from 0 to 255. Accordingly, in order to identify the pixels responsible for a certain edge, values of a certain intensity are searched for in the image matrix. In this case, the search is made with a certain tolerance. The position of the found pixels in the matrix (row-column) is translated, taking into account the scale, into space coordinates (two coordinates from the image, the third—the coordinate of the corresponding cube face). In addition, in Section 3.2, the faces closed by others were not deleted. Therefore, when matching, a point of an object in an image can fall on two or more projection facets. In this case, the facet that is closest to the viewpoint is selected.

3.6. Recreation of the complete model, additional refinement of the surface boundaries in the direction of the normal vectors

The previous steps were necessary for preliminary automated recognition of only a fraction of the measured points. After identifying the vertices and facets to different surfaces, they are compared with the full set of vertices (search by equality of point coordinates). Points close to the geometric centre of the surface are selected. On the top in the geometric centre, a facet is selected that belongs to a specific face of the body. At the next stage, the algorithm for searching and refining facets of one face is used. We briefly describe the steps of the algorithm for searching for facets belonging to a specific face [19]:

1) input parameters are set: $\mathbf{V}_{g\times 3}$, $\mathbf{F}_{m\times 3}$, $\mathbf{N}_{m\times 3}$, $\vec{p}$ (coordinate vector of a point on the surface whose facets are to be selected), $\vec{t}$ (normal at point p), and α (angle tolerance to find matching facets).

2) search for the facet that owns point p (intersection point of the beam and the facets).

3) search for all facets for which the normal vector is different from the normal vector $\vec{t}$ by no more than a value α (the scalar product of normal vectors is used to check the angles).

Facets are selected, from all the facets found that are suitable in the direction of the normal, that are associated with the first and among themselves common vertices.

4. Recognition results

To measure the details an optical 3D scanner RANGEVISION Pro2M was used. Figures 6 and 7 show photographs of the process of measuring the “spacer simulator” part (drawing in Figure 1).

Figure 6. One scan measurement of the part.

Figure 7. Group of measurement scans of the part.

To assess the quality of segmentation, you can use the modified loss function given in [20]. It is proposed to calculate the error in determining the parameters of a rectangle when recognizing faces and images in a picture using the intersection over union (IoU) metric, which is equal to the ratio of the area of intersection of the rectangle obtained as a result of detection and the rectangle from the mark-up to the area of their union.

In our case, we work with body facets, so instead of squares, we can operate on the number of facets. Therefore, a coefficient δ_{segm} is calculated that is equal to the ratio of the number of facets $N_{p\cap\partial}$ that are the intersection of the set of facets of the surface, obtained as a result of recognition, and actually belong to the surface of the facet to the $N_{p\cup\partial}$ set of facets, which is their union:

$$\delta_{segm} = N_{p\cap\partial} / N_{p\cup\partial}. \quad (2)$$

Thus, the value of the coefficient lies in the interval [0; 1]. If there are several recognizable surfaces, then a generalized coefficient can be calculated δ_{segm} for all recognizable body faces.

The number of measured facets of the part m was 622130. For training the neural network, a sample of 1000 cases of the stl-model of the considered part, aligned in different ways in space, corresponding to a total of 6000 projections, was formed. For formation of the training set, a nominal model of the part was used, which was saved in the *.stl format.

Recognized flat and cylindrical faces of the “spacer simulator” detail measured with the scanner using all six projections are shown in Figures 8 and 9.

Table 1 shows the calculated coefficients δ_{segm} of the measured cylindrical, flat and combined recognizable faces.

Table 1. Facet recognition errors.

Object of evaluation	Cylindrical faces	Flat edges	All recognizable faces
Value of δ_{segm}	0.76	0.95	0.91

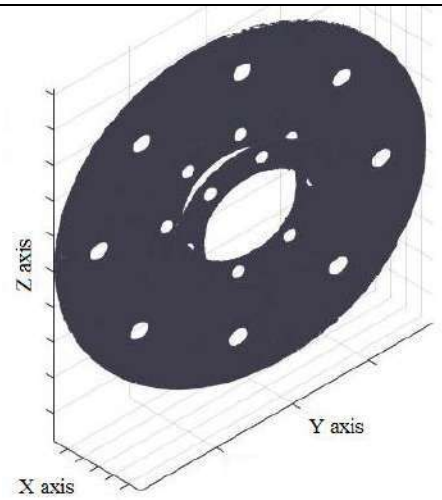

Figure 8. Recognized flat faces

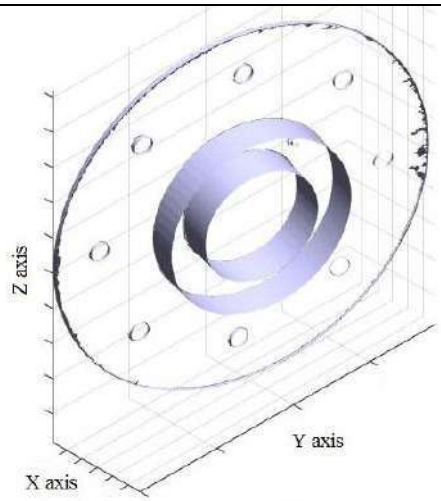

Figure 9. Recognized cylindrical faces.

The recognition error of cylindrical faces is higher than flat ones. Although all cylindrical faces were identified, there were facets belonging to flat faces, as well as some facets from the threaded holes. The overall ratio exceeded 90%, which is associated with a much larger number of facets of flat faces compared to cylindrical.

5. Conclusion

The model presented in this paper allows you to quickly recognize cylindrical and flat surfaces of parts using a trained neural network and face facet search algorithm from previously recognized facets. The developed model is needed for further prediction of the assembly parameters of the product based on computer modelling [21]. Using digital prediction will allow robotic assemblers to function without human intervention.

6. References

[1] Zakani F R, Bouksim M, Arhid K, Aboulfatah M and Gadi T 2018 Segmentation of 3D meshes combining the artificial neural network classifier and the spectral clustering *Computer Optics* **42(2)** 312-319 DOI: 10.18287/2412-6179-2018-42-2-312-319

[2] Blokhino Y B, Gorbachev V A, Rakutin Y O and Nikitin A D 2018 Development of an algorithm for semantic segmentation of real-time aerial photographs *Computer Optics* **42(1)** 141-148 DOI: 10.18287/2412-6179-2018-42-1-141-148

[3] Nikitin M U, Konushin V S and Konushin A S 2017 Neural network model for video-based face recognition with frames quality assessment *Computer Optics* **41(5)** 732-742 DOI: 10.18287/ 2412-6179-2017-41-5-732-742

[4] Nikolenko S I, Kadurin A and Arkhangelskaya E 2018 *Deep learning* (SPb: Peter)

[5] Hubei D H 1988 *Eye, Brain, and Vision* (New York: Scientific American)

[6] Webvision: The Organization of the Retina and Visual System URL: http:// webvision.med.utah.edu/book/

[7] Su H, Maji S, Kalogerakis E and Learned-Miller E 2015 Multi-view Convolutional Neural Networks for 3D Shape Recognition *ICCV* **7410471** 945-953
[8] Wu Z, Song S, Khosla A, Yu F, Zhang L, Tang X and Xiao J 2015 3D ShapeNets: A deep representation for volumetric shape modeling *In Proc. CVPR* 1-9
[9] Horn B K P 1984 Extended gaussian images *Proc. of the IEEE* **72(12)** 1671-1686
[10] Osada R, Funkhouser T, Chazelle B and Dobkin D 2002 Shape distributions *ACM Transactions on Graphics* **21(4)** 807-832
[11] Kazhdan M, Funkhouser T and Rusinkiewicz S 2003 Rotation invariant spherical harmonic representation of 3D shape descriptors *Proceedings of the Eurographics/ACM SIGGRAPH symposium on Geometry processing* 156-164
[12] Chaudhuri S and Koltun V 2010 Data-driven suggestions for creativity support in 3D modeling *ACM Transactions on Graphics* **29(6)** 183
[13] Bronstein A, Bronstein M, Ovsjanikov M and Guibas L 2011 Shape Google: Geometric words and expressions for invariant shape retrieval *ACM Transactions on Graphics* **30(1)** 1
[14] Kokkinos I, Bronstein M, Litman R and Bronstein A 2012 Intrinsic shape context descriptors for deformable shapes *Proceedings of the IEEE Conference on Computer Vision and Pattern Recognition (CVPR)*
[15] Deng J, Dong W, Socher R, Li L-J, Li K and Fei-Fei L 2009 Imagenet: A large-scale hierarchical image database *Proceedings of the IEEE Conference on Computer Vision and Pattern Recognition (CVPR)*
[16] Qi C R, Su H, Mo K and Guibas L J 2016 PointNet: Deep learning on point sets for 3d classification and segmentation *ArXiv preprint arXiv:1612.00593* 652-660
[17] Ronneberger O, Fischer P and Brox T 2015 U-net: Convolutional networks for biomedical image segmentation *Lecture Notes in Computer Science (including subseries Lecture Notes in Artificial Intelligence and Lecture Notes in Bioinformatics)* **9351** 234-241
[18] Roberts L G 1965 Machine perception of three-dimensional solids *Optical and Electro-Optical Information Processing* (Cambridge: MIT Press) 159-197
[19] Stepanenko I S, Pechenin V A, Ruzanov N V and Khaimovich A I 2018 Technique of increasing the accuracy of GTE parts manufactured by selective laser melting *Journal of Physics: Conference Series* **1096(1)** 012143 DOI: 10.1088/1742-6596/1096/1/012143
[20] Yu J, Jiang Y, Cao Z and Huang T 2016 UnitBox: An Advanced Object Detection Network *INNS*
[21] Bolotov M A, Pechenin V A and Murzin S P 2016 Method for uncertainty evaluation of the spatial mating of high-precision optical and mechanical parts *Computer Optics* **40(3)** 360-369 DOI: 10.18287/2412-6179-2016-40-3-360-369

Acknowledgements
The work was supported by the Ministry of Education and Science of the Russian Federation in the framework of the program to improve the competitiveness of the Samara University among the world's leading research and educational centers for 2013–2020 and partly by the Russian Federation President's grants (project code СП-262.2019.5). Experimental studies were carried out on the equipment of the center for the collective use of CAM technologies of the Samara University (RFMEFI59314X0003).

Improving the accuracy of detecting the edges of texture objects in remote sensing images

E V Medvedeva[1], A I Evdokimova[1]

[1]Vyatka State University, Moskovskaya str., 36, Kirov, Russia, 610000

e-mail: emedv@mail.ru, alenaevdokimova0@gmail.com

Abstract. The authors offer a method for detecting the edges of texture objects in remote sensing images. This method is based on the evaluation of textural and brightness attributes. It is proposed to use transition probabilities for three-dimensional Markov chains with two states as texture features, averaged within a sliding window. It makes possible to improve the detection accuracy of texture objects on multichannel or multi-time snapshots. To reduce the computational resources, it is proposed to determine the signs by the bit planes of the senior, most informative digits of the digital image. The simulation results confirm the effectiveness of the proposed method.

1. Introduction

Multispectral remote sensing images are of high spatial resolution and have rich information about texture. Information about the texture allows to determine the types of the earth's surface (rocks, soil, vegetation, water, etc.), to estimate the area of flooding, land use, forestry, wildfires, oil pollution, ice, etc.

The ability to detect, identify, and classify texture objects is based on the fact that objects of different types reflect and absorb electromagnetic radiation in different wavelengths in different ways. When combining different channels, one can find out information about rocks, vegetation cover, state of reservoirs, types of agricultural crops, etc. For example, in the visible red spectral channel (wavelength 0.63–0.69 μm), it is possible to distinguish many plant varieties, boundaries of the soil and geological delineation (deposits of the ore body, oil fields) [1,2]. One can track the dynamics for several pictures of the same area, taken at different times, for example changing the size of the area of the segments corresponding to oil pollution, or changing the forest area.

The basic operation for detecting the edges of texture objects is segmentation, the quality of which is determined by the effectiveness of the selection of a textural feature. There are various approaches to the selection of textures. They are [3-9]:

- based on the calculation of the statistical characteristics of the gradient, density of differences, adjacency matrices of brightness levels, etc.,
- based on the description of textures as primitives with some properties (average intensity of elements, perimeter, area, orientation, etc.) and comparing them with a template for each texture,
- based on signal processing algorithms for extracting texture features (discrete cosine and wavelet transforms),
- based on models, including the autoregression model, Markov random fields, fractal methods, etc.

One of the new approaches in the selection of textures is the joint use of spectral and textural features [10,11].

Many of these methods require large computational resources and do not accurately separate the attribute space. The quality of the selection of texture objects depends on the choice of the most appropriate characteristics of the task and approaches to the development of algorithms. In addition, as multispectral images have a high spatial resolution, an important factor in the detection of textures is to reduce the computational complexity of algorithms. In this regard, the use of known methods is not always advisable.

As the texture regions on images occupy extended space with homogeneous statistical characteristics and different for different regions, the method based on the mathematical apparatus of Markov chains [12] is very effective in this case. Its complexity depends on the dimension of the transition probability matrices.

Works [13,14] propose to solve the computational complexity reduction problem using representation of g - bit digital images (DI) as a set of g - bit binary images (BBI) and approximate them with Markov chains with two states and 2 × 2 transition probability matrices. Assuming that the most informative are the binary images belonging to the senior bits of DI, it is proposed to use one of the BBIs of the senior bits of DI to select textures. This solution reduces computational resources in the allocation of textures.

When using the mathematical apparatus of Markov chains, textural features are probabilistic characteristics between elements of images. Works [14–16] present the method of texture segmentation of DI based on a two-dimensional Markov chain with two states. With probabilities of transitions between elements different by 0.15 for different texture areas, the segmentation error did not exceed 6%.

Considering that there is a large statistical dependence between separate areas of images taken in different spectral ranges (channels), it is proposed to use the nature of the statistical connection not only between the elements inside the DI, but also the inter-channel DI. The use of the transition probability for three-dimensional Markov chains as a textural attribute improves the accuracy of prediction of image elements and, accordingly, the quality of the selection of textures. Also, an approach based on three-dimensional Markov chains can be applied to detect changed texture regions in time-varying DIs.

Real remote sensing DIs contain objects in which the pixel brightness changes slightly (water bodies, fields of different crops, etc.). Therefore, to improve the quality of detection of texture objects for which the probabilistic characteristics between the elements are close to unity, it is advisable to take into account the brightness characteristics determined by BBI of the senior bits DI.

The aim of the article is to develop a method of segmentation of multi-channel digital images with high spatial resolution based on the mathematical apparatus of three-dimensional Markov chains, which allows to increase the accuracy of detecting the edges of texture objects while reducing computational resources.

2. Mathematical model of the texture image

A special case of multichannel images can be considered color RGB images. Therefore, the proposed method will be considered for the case of three-component DI with R, G, and B color channels. Each RGB color component of an image is a g-digit digital halftone image. There is a significant statistical relationship between the elements of individual DI areas belonging to different color channels. For example, objects of yellow color are well expressed on green and red components, and objects of white color are seen on all three components. Therefore, taking into account the statistical connection between the elements inside DI and between individual color channels, we can assume that RGB images allow them to be approximated by a three-dimensional Markov chain with several states, and BBI with a three-dimensional Markov chain with two states and horizontal transition matrixes ${}^{1}\mathbf{\Pi} = \left\| {}^{1}\pi_{ij}^{(l)} \right\|_{2\times 2}$, vertical ${}^{2}\mathbf{\Pi} = \left\| {}^{2}\pi_{ij}^{(l)} \right\|_{2\times 2}$ and ${}^{4}\mathbf{\Pi} = \left\| {}^{4}\pi_{ij}^{(l)} \right\|_{2\times 2}$

between channels. The introduction of the inter-channel matrix ${}^4\mathbf{\Pi} = \left\| {}^4\pi_{ij}^{(l)} \right\|_{2\times 2}$ will make it possible to get rid of the segmentation of the separate components and identify the changed areas in the images.

Figure 1 shows a fragment of a three-dimensional binary Markov field corresponding to a fragment of an BBI of a two-channel DI.

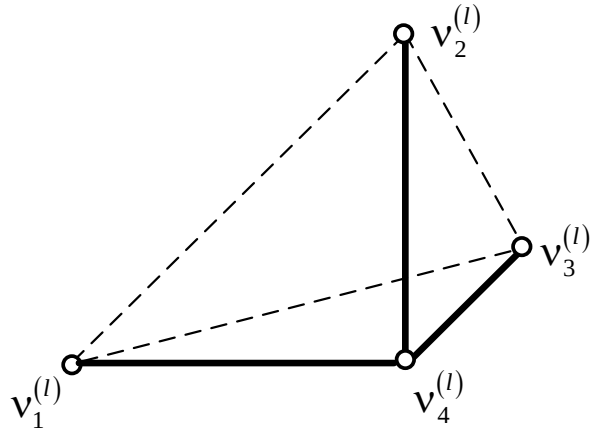

Figure 1. Fragment of a three-dimensional binary Markov field.

The amount of information in the element $\nu_4^{(l)}$ relative to the elements of the nearest neighborhood $\Lambda_{i,j,k} = \left\{\nu_1^{(l)}, \nu_2^{(l)}, \nu_3^{(l)}\right\}$, in accordance with the mathematical model of the three-dimensional random Markov process presented in [13], is determined by the formula:

$$I\left(\nu_4^{(l)} \middle| \nu_1^{(l)}, \nu_2^{(l)}, \nu_3^{(l)}\right) = -\log \frac{\prod_{i=1}^{3} w\left(\nu_4^{(l)} \middle| \nu_i^{(l)}\right) w\left(\nu_4^{(l)} \middle| \nu_1^{(l)}, \nu_2^{(l)}, \nu_3^{(l)}\right)}{\prod w\left(\nu_4^{(l)} \middle| \nu_i^{(l)}, \nu_j^{(l)}\right)}, \quad (1)$$

where $w\left(\nu_4^{(l)} \middle| \square\right)$ is the probability density of transitions in Markov chains of various dimensions; the products in (1) are calculated for all possible non-coinciding combinations of various subscript indices.

The probability density of transitions in a three-dimensional binary Markov chain $w(\nu_4^{(l)} \mid \Lambda_{i,j.k}^{(l)})$ can have the form:

$$\begin{aligned} w(\nu_4^{(l)} \mid \Lambda_{i,j,k}^{(l)}) = \sum_{i,\ldots,r=1}^{2} \pi(\nu_4^{(l)} = M_i^{(l)} \mid \nu_1^{(l)} = M_j^{(l)}; \nu_2^{(l)} = M_k^{(l)}; \\ \nu_3^{(l)} = M_r^{(l)}) \times \delta(\nu_1^{(l)} - M_j^{(l)}) \delta(\nu_2^{(l)} - M_k^{(l)}) \delta(\nu_3^{(l)} - M_r^{(l)}). \end{aligned} \quad (2)$$

where $\delta(\cdot)$ is the delta function.

The probabilities of the states $\pi_{iiii}^{(l)}$ of an element $\nu_4^{(l)}$ are determined by the argument of expression (1) and for various combinations of neighboring elements $\Lambda_{i,j,k}^{(l)}$ can be calculated using the formulae presented in Table 1, where ${}^r\pi_{ii}^{(l)}\left(r = \overline{1,7}\right)$ are elements of transition probability matrices in one-dimensional Markov chains with two states of three main - ${}^1\mathbf{\Pi}^{(l)}$, ${}^2\mathbf{\Pi}^{(l)}$, ${}^4\mathbf{\Pi}^{(l)}$ and four related matrices - ${}^3\mathbf{\Pi}^{(l)} = {}^1\mathbf{\Pi}^{(l)} \times {}^2\mathbf{\Pi}^{(l)}$; ${}^5\mathbf{\Pi}^{(l)} = {}^1\mathbf{\Pi}^{(l)} \cdot {}^4\mathbf{\Pi}^{(l)}$; ${}^6\mathbf{\Pi}^{(l)} = {}^2\mathbf{\Pi}^{(l)} \cdot {}^4\mathbf{\Pi}^{(l)}$; ${}^7\mathbf{\Pi}^{(l)} = {}^3\mathbf{\Pi}^{(l)} \cdot {}^4\mathbf{\Pi}^{(l)}$.

Table 1. Expressions for calculating conditional probabilities.

$v_1\, v_2\, v_3 \to v_4$	Expressions
$000 \to 0$	$\pi^{(l)}_{iiii} = \frac{{}^1\pi^{(l)}_{ii} \cdot {}^2\pi^{(l)}_{ii} \cdot {}^4\pi^{(l)}_{ii} \cdot {}^7\pi^{(l)}_{ii}}{{}^3\pi^{(l)}_{ii} \cdot {}^5\pi^{(l)}_{ii} \cdot {}^6\pi^{(l)}_{ii}},$
$001 \to 0$	$\pi^{(l)}_{iiji} = \frac{{}^1\pi^{(l)}_{ii} \cdot {}^2\pi^{(l)}_{ii} \cdot {}^4\pi^{(l)}_{ij} \cdot {}^7\pi^{(l)}_{ij}}{{}^3\pi^{(l)}_{ii} \cdot {}^5\pi^{(l)}_{ij} \cdot {}^6\pi^{(l)}_{ij}},$
⋮	⋮
$111 \to 0$	$\pi^{(l)}_{jjji} = \frac{{}^1\pi^{(l)}_{ij} \cdot {}^2\pi^{(l)}_{ij} \cdot {}^4\pi^{(l)}_{ij} \cdot {}^7\pi^{(l)}_{ij}}{{}^3\pi^{(l)}_{ii} \cdot {}^5\pi^{(l)}_{ii} \cdot {}^6\pi^{(l)}_{ii}},$ (3)
$000 \to 1$	$\pi^{(l)}_{iiij} = \frac{{}^1\pi^{(l)}_{ij} \cdot {}^2\pi^{(l)}_{ij} \cdot {}^4\pi^{(l)}_{ij} \cdot {}^7\pi^{(l)}_{ij}}{{}^3\pi^{(l)}_{ii} \cdot {}^5\pi^{(l)}_{ii} \cdot {}^6\pi^{(l)}_{ii}},$
$001 \to 1$	$\pi^{(l)}_{iijj} = \frac{{}^1\pi^{(l)}_{ij} \cdot {}^2\pi^{(l)}_{ij} \cdot {}^4\pi^{(l)}_{ii} \cdot {}^7\pi^{(l)}_{ii}}{{}^3\pi^{(l)}_{ii} \cdot {}^5\pi^{(l)}_{ij} \cdot {}^6\pi^{(l)}_{ij}},$
⋮	⋮
$111 \to 1$	$\pi^{(l)}_{jjjj} = \frac{{}^1\pi^{(l)}_{ii} \cdot {}^2\pi^{(l)}_{ii} \cdot {}^4\pi^{(l)}_{ii} \cdot {}^7\pi^{(l)}_{ii}}{{}^3\pi^{(l)}_{ii} \cdot {}^5\pi^{(l)}_{ii} \cdot {}^6\pi^{(l)}_{ii}},$

3. Texture 3D Segmentation Algorithm

Allocation of extended textures in multichannel (or multi-temporal) DI was reduced to calculating estimates of transition probabilities horizontally ${}^1\hat{\pi}^{(l)}_{ii}$, vertically ${}^2\hat{\pi}^{(l)}_{ii}$, between channels ${}^4\hat{\pi}^{(l)}_{ii}$ and estimation $\hat{\pi}^{(l)}_{iiii}$ using formulas (3), as well as estimating brightness in BBI of the senior, most informative DI digits.

Taking into account the local changes in the probability and brightness characteristics on multichannel images, a three-dimensional sliding window was used for calculation.

The texture features were the average estimates corresponding to the central element of the window - $\tilde{\pi}^{(l,r,k)}_{iiii}$ of probability of transitions in the three-dimensional Markov chain and the brightness $\tilde{L}^{(l,r,k)}$ of the BBI:

$$\tilde{\pi}^{(l,r,k)}_{iiii} = \frac{1}{m \times n} \sum_{r=1}^{m} \sum_{k=1}^{n} \hat{\pi}^{(l,r,k)}_{iiii}. \quad (4)$$

$$\tilde{L}^{(l,r,k)} = \frac{1}{m \times n} \sum_{r=1}^{m} \sum_{k=1}^{n} \hat{L}^{(l,r,k)}. \quad (5)$$

The pixel belonging to one or another texture object in the image of the k- channel was carried out on the basis of the analysis of the texture feature histogram. The number of peaks in the histogram corresponded to the number of texture objects with different probabilistic characteristics. The threshold value was chosen as the minimum value between two adjacent peaks of the histogram. When

evaluation $\tilde{\pi}_{iiii}^{(l,r,k)}$ was close to 1, the averaged brightness $\tilde{L}$ was additionally used to decide whether a pixel belongs to one or another object. Each texture object was assigned its own label.

The authors combined images of different channels in order to increase the information content of texture objects.

4. Experimental results

Artificial and real DI were used for experimental studies. Artificial binary images were generated by a given markup using a mathematical model based on a two-dimensional Markov chain and the algorithm given in [13]. The images were formed in such a way that they contained areas with coincident and different statistical characteristics for different channels.

To assess the accuracy of the selection of the edges of texture objects, the authors compared the segmented image with the ideal markup and then calculated the number of erroneously segmented elements:

$$ESE = \frac{1}{h \cdot w} \sum_{i=1}^{h} \sum_{j=1}^{w} F(i, j) \quad (6)$$

where *h*, *w* are image height and width; *F* is a value that is equal to zero when the image element is segmented correctly, and equal to 1 if otherwise.

Examples of the results of segmentation of artificial images are shown in Figure 2: (a) an image containing two areas with different statistical characteristics; (b) the result of a segmentation algorithm based on a three-dimensional Markov chain with a difference between the probabilities $\Delta\tilde{\pi}_{iiii}$ of segments in 0.25; (в) an image with three objects; (d) the result of a segmentation algorithm based on an estimation of probability $\tilde{\pi}_{iiii}^{(l,r,k)}$ and brightness $\tilde{L}$.

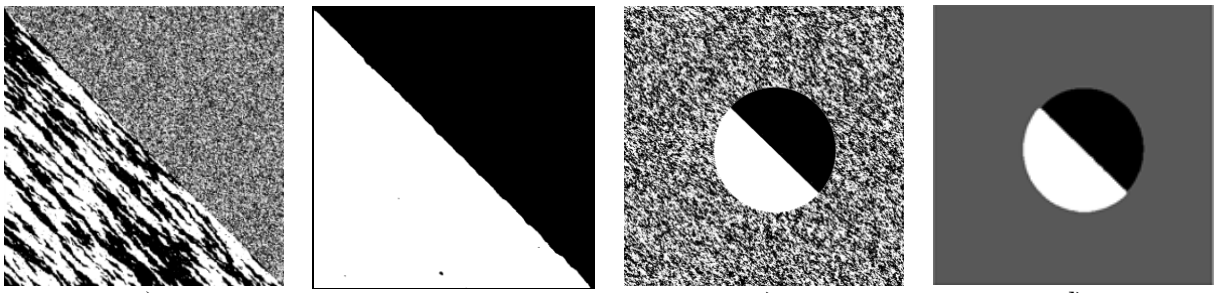

a) b) c) d)

Figure 2. Results of the segmentation of artificial images.

Table 2 presents the estimates of the ESE criterion for segmented artificial images containing two texture regions (similar to Figure 2a). A sliding window of 11x11 size was used to calculate the probability estimations $\tilde{\pi}_{iiii}$.

Table 2. Estimation of segmentation results by ESE criterion.

Value of transition probabilities ${}^{1}\pi_{ii} = {}^{2}\pi_{ii}$		Value ESE, %	
in the first segment	in the second segment	Algorithm based on a two-dimensional Markov chain	Algorithm based on a three-dimensional Markov chain
0.5	0.95	0.32	0.21
0.6	0.85	0.79	0.29
0.7	0.95	0.54	0.28
0.8	0.9	6.31	5.88

Three-dimensional segmentation for all values of the transition probabilities gave a segmentation error less than segmentation based on two-dimensional Markov chains. The worst segmentation result

was obtained when the difference between the probabilities of the segments was 0.1. As this difference increases, the segmentation error is a fraction of a percent.

Table 3 presents the estimates of the ESE criterion for segmented binary images, similar to Fig. 2c. Three-dimensional segmentation was performed on the basis of estimates of probability and brightness characteristics within a sliding window of 11x11.

Table 3. Estimation of segmentation results by ESE criterion.

Probabilities between elements in the texture area ${}^1\pi_{ii} = {}^2\pi_{ii}$	ESE,%	
	Without brightness	With brightness
0.6	8.3182	0.61
0.7	8.285	0.5738
0.8	8.1621	0.4429

Accounting for the brightness of the image in a given example allowed to reduce the segmentation error by up to 18 times.

An example of real image remote sensing segmentation, containing four types of objects (urban buildings, forest and fields planted with different crops) is shown in Figure 3: (a) - RGB image; (b) and (c) - BBI of the 7th category of channels R and B, which were used to select the edges of texture objects; (d) and (d) are the results of two-dimensional segmentation of the image of the R and B channels, respectively; (e) - the result of three-dimensional segmentation of channel R relative to channel B.

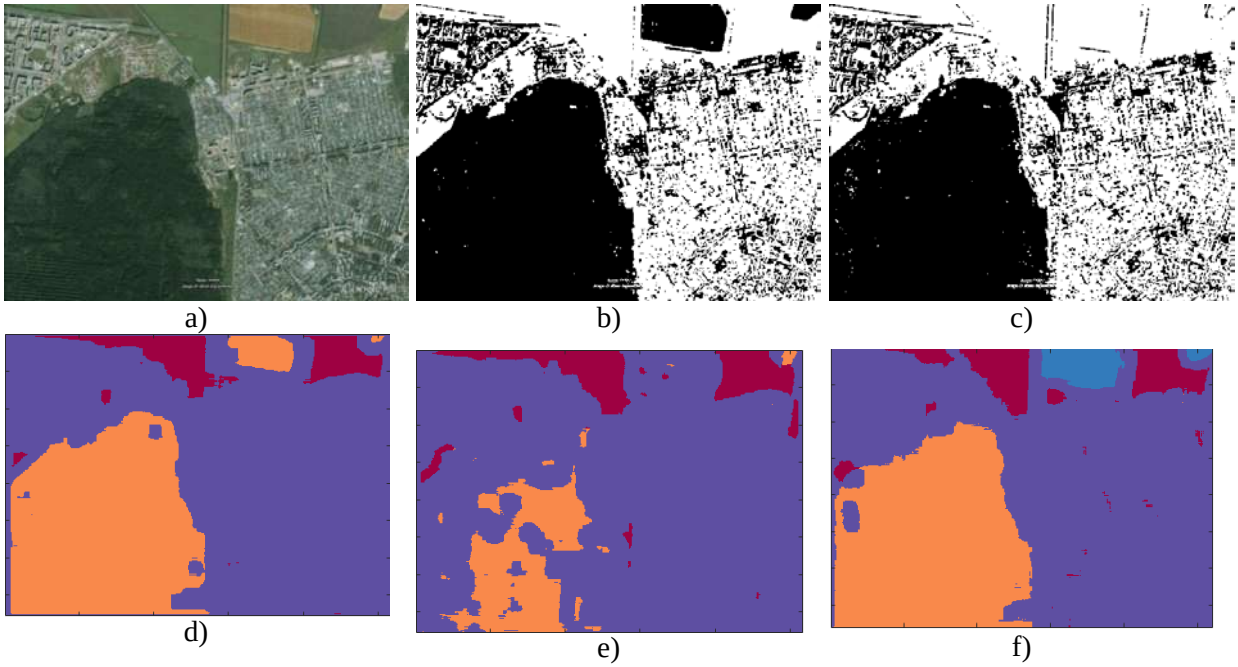

Figure 3. The result of detecting the edges of texture objects in the remote sensing image.

Two-dimensional segmentation in the images of the R and B channels allowed to detect only 3 objects. The introduction of the matrix of probabilities of transitions between color components ${}^4\mathbf{\Pi} = \left\| {}^4\pi_{ij}^{(l)} \right\|_{2\times 2}$ allowed to get rid of the segmentation of the separate components and to detect another object. The proportion of erroneously segmented elements is 7.8%.

Figure 4 shows an example of detecting texture objects on multi-temporal images: (a) and (b) - multi-temporal images; (c) - the result of the detection of a modified object (felled forest) by a three-dimensional segmentation algorithm; (d) - the combined image of the modified object with the original one (a).

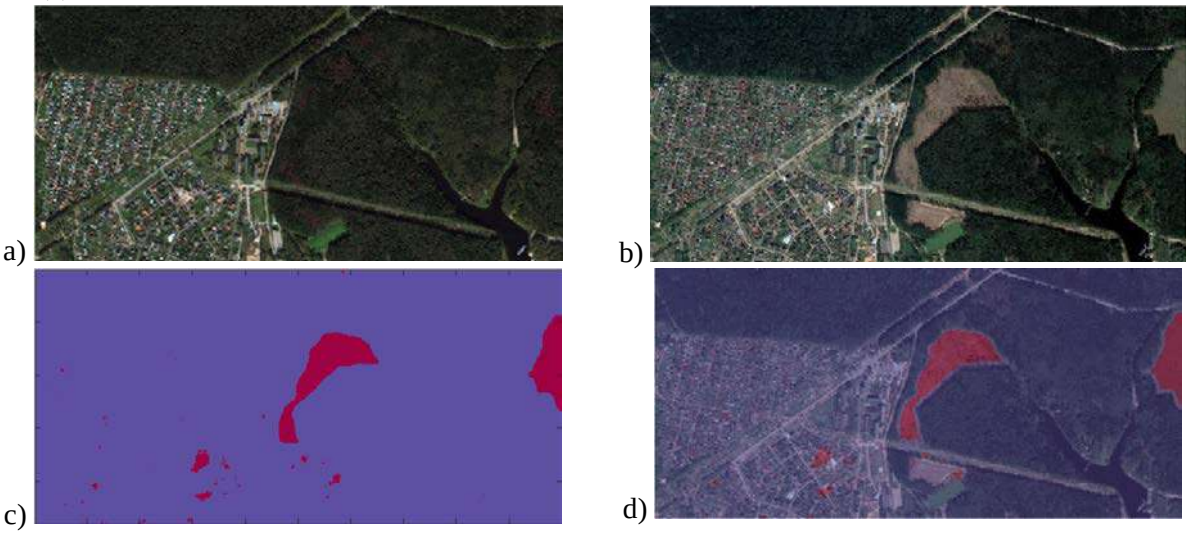

Figure 4. The result of detecting the edges of the modified texture objects in multi-time shots.

5. Conclusion

The developed segmentation method, based on an estimate of transition probabilities for three-dimensional Markov chains and luminosity, improved the accuracy of detecting the edges of extended texture objects on multichannel and time-varying images compared to the two-dimensional segmentation algorithm proposed in [14]. In addition, the evaluation of texture features by bit binary images allows to reduce computational resources for the implementation of the segmentation algorithm.

6. References

[1] Schovengerdt R A 2010 *Remote sensing. Models and methods of image processing* (Moscow: Technosphere) p 594
[2] Ivanov E S 2016 Some applications of remote sensing image segmentation *Modern problems of remote sensing of the Earth from space* **13(1)** 105-116
[3] Gonzalez R, Woods R 2012 *Digital Image Processing* (Moscow: Technosphere) p 1104
[4] Haralick R M 1979 Statistical and structural approaches to texture *Proceedings of the IEEE* **67(5)** 786-804
[5] Li M, Zang S, Zhang B, Li S and Wu C A 2014 Review of Remote Sensing Image Classification Techniques: the Role of Spatio-contextual Information *European Journal of Remote Sensing* **47** 389-411
[6] Borne F 2017 Texture-based classification for characterizing regions on remote sensing images *Journal of Applied Remote Sensing* **11(3)** 16
[7] Su W, Zhang C, Yang J, Wu H, Deng L, Ou W, Yue A and Chen M 2012 Analysis of wavelet packet and statistical textures for object-oriented classification of forest-agriculture ecotones using SPOT 5 imagery *International Journal of Remote Sensing* **33(11)** 3557-3579
[8] Plotnikov D E, Kolbudaev P A and Bartalev S A 2018 Identification of dynamically homogeneous areas with time series segmentation of remote sensing data *Computer Optics* **42(3)** 447-456 DOI: 10.18287/2412-6179-2018-42-3-447-456
[9] Blokhinov Yu B, Gorbachev V A, Rakutin Yu O and Nikitin A D 2018 A real-time semantic segmentation algorithm for aerial imagery *Computer Optics* **42(1)** 141-148 DOI: 10.18287/ 2412-6179-2018-42-1-141-148

[10] Yuan J, Wang D L 2014 Remote sensing image segmentation by combining spectral and texture features *IEEE Transactions on geoscience and remote sensing* **52(1)** 16-24
[11] Zhang J, Gao Y W, Feng S W, Chen Z H and Yuan Y B 2015 Image segmentation with texture clustering based JSEG *Proc. International Conference on Machine Learning and Cybernetics (ICMLC)* **2** 599-603
[12] Stan Z L 2009 *Markov Random Field Modeling in Image Analysis* (Springer-Verlag London Limited) p 569
[13] Petrov E P, Trubin I S, Medvedeva E V and Smolskiy S M 2013 Mathematical Models of Video-Sequences of Digital Half-Tone Images *Integrated models for information communication systems and net-works: design and development* 207-241
[14] Medvedeva E V, Kurbatova E E 2015 Image Segmentation Based on Two-Dimensional Markov Chains *Computer Vision in Control Systems-2. Innovations in Practice* (Springer International Publishing Switzerland) 277-295
[15] Medvedeva E V, Kurbatova E E 2017 A combined algorithm of isolation texture areas in noisy images *6th Mediterranean Conference on Embedded Computing* 155-158
[16] Medvedeva E V, Kurbatov E E and Okulova A A 2017 Textural segmentation of noisy images of the Earth's surface *Modern problems of remote sensing of the Earth from space* **14(7)** 20-28

Geometric modeling of raster images of documents with weakly formalized description of objects

D Yu Vasin[1], V P Gromov[1] and S I Rotkov[2]

[1]National Research Lobachevsky State University of Nizhny Novgorod, Gagarin Ave., 23, Nizhny Novgorod, Russia, 603950
[2]Federal State Budgetary Educational Institution of Higher Education Nizhny Novgorod State University of Architecture and Civil Engineering», Ilyinskaya St., 65, Nizhny Novgorod, Russia, 603950

e-mail: dm04@list.ru, rotkovs@mail.ru

Abstract. In this paper, we analyze graphic documents with a weakly formalized description of objects (WFGD) and reveal their main features that influence the choice of models, methods and algorithms for processing such documents. In the framework of the development of the combinatorial-geometric approach, a geometric model for describing WFGDs with a pronounced orientation of linear objects is proposed. We also propose a technology for vectorization of raster images of WFGDs in the presence of noise in the source data. The effectiveness of an extended class of vector models (linear and segment-node models) used for describing WFGDs with a distinctive linear orientation of objects is shown, which was revealed during practical experiments on real WFGDs.

1. Introduction

In recent years, increasing importance has been given in video information analysis to the development of mathematical methods for constructing a formalized structured description of input video information. The tasks related to obtaining formal descriptions are addressed by studying the internal structure, and content of elements or objects of a simpler nature (non-derivative elements, objects identified in the images being processed at various processing levels, etc.) [1-3].

In this paper, only the images of large-format, semantically rich graphic documents with a complex structure (LFGD) are considered as source information. In this case, the source data, as a rule, are graphic images (GI) on paper, while digital documents must be produced in the terms of the respective problem area. Such documents contain symbols of four classes of objects: point (discrete), linear, two-dimensional (areal), and symbol images. Taken together, these symbols make up spatially-distributed data (SDD) [4 - 9].

The analysis of LFGDs shows that a significant proportion of such documents was produced in a manner inconsistent with the rules for nomenclature description of objects. We shall distinguish such LFGDs as a subclass of documents with a weakly formalized description of objects (WFGD). This subclass includes: engineering drawings, diagrams, floor plans for buildings, topographic maps and nautical charts, data on the Earth's surface obtained from satellites, etc. The main features of WFGDs,

which influence the choice of representation models and methods for their processing, are considered in [4–9]. Taking these features into account places greater demands on the geometric modeling of this class of graphic documents (GD).

2. The problems of creating automatic technologies and systems for WFGD processing

In order to automate WFGD input, various information technologies have been proposed in recent years. They are based on heuristic procedural methods, as well as on recognition methods with learning, and are effective for a limited set of objects with strict limits on their size and orientation. It should be noted that the technology of automatic analysis of WFGD is a complex multi-stage process that involves a large number of processing methods and algorithms: filtering, compression, storage and search, analysis and decision making. For effective operation of this "pipeline", it is very important to ensure that all mathematical models, methods, algorithms and data representation structures are interconnected and mutually effective: it is obvious that even the highest efficiency at some particular stage of processing can be offset by low performance at other stages.

Huge information redundancy of raster images of WFGD (RIWFGD) certainly places greater demands on automatic processing algorithms. The problem becomes even more serious, if we take into account that automatic processing of RIWFGD at lower levels of the hierarchy should be carried out in real time and with limited memory resources, and the models and methods being developed should be integrated into existing technologies and systems.

Consequently, the models and methods for processing RISFGD must be technologically advanced and must meet the general efficiency requirements for graphic image analysis as a whole [4, 5, 9]:

- technological effectiveness;
- high efficiency in terms of speed and memory;
- natural integrability in the general processing scheme.

It should be noted that vector models of WFGDs obtained by means of automatic procedures do not always produce objects that correspond to their reference description and that are not always specific, both in terms of their composition and the methods for setting them. Besides, the practice of processing WFGDs, especially WFGDs taken from archives, has revealed some new serious problems associated with the transition from the lower (pixel) level of representation to the vector level. This results in a further dramatic increase of complexity of the procedures for automatic recognition of objects in WFGDs and inevitably reduces the time efficiency of the entire processing technology for this class of documents due to the requirement of mandatory interactive control and editing of possible errors.

To avoid multiple duplication in the development of systems for solving various tasks of WFGD processing, it is useful to have a basic system that can be considered as a tool for solving two main tasks: on the one hand, it would be the basis for developing systems specialized in a specific subject area, and on the other hand, it would be an automated workplace for the development and research of algorithms for WFGD processing.

The combinatorial-geometric approach (CGA) proposed in the 1980s for processing raster images of graphic documents (RIGD) in spatially distributed data [4] can become the core of such a system. This approach is based on the hierarchy of mathematical models of image description, the hierarchy of data representation structures, a set of fast and memory-efficient algorithms for solving problems of computational geometry, as well as specialized algorithms for processing video data. The essence of the approach is as follows: a contour image model (CIM) or a linear-contour image model (LCIM) is constructed from the initial RIGD, i.e. the initial RIGD is assigned a set of points, polygons and broken lines. Based on this representation, a hierarchy of interrelated mathematical models of description, structures for representation and decision making is built, where objects are also considered as points, polygons, broken lines and their collections. The objects of the hierarchy of image models are built using a system of logical – geometric predicates (decision rules) that calculate the characteristics and relationships between objects: dimensions, distances, nesting, junction, intersection, and other types of mutual arrangement relationship, characteristics of objects and their parts.

As a result, the entire complex set of tasks related to the analysis of video data is considered from a unified point of view of building a hierarchy of interrelated mathematical models for description, representation and decision-making structures. At the lower level of this hierarchy, raster information from the original source of visual data is processed, while the upper level corresponds to the description of graphic data at the level of content in the user's terms [4].

Therefore, it is important to further increase the intelligence of information technologies for automatic processing of RIWFGD, and, consequently, to further develop the CGA and the hierarchy of description models and appropriate RIWFGD processing methods and algorithms.

3. Effective models for WFGD description

In the framework of the CGA, the mathematical model of the image is understood as a triplet of the form $M_v^\alpha = \left\{E_v^\alpha, C_v^\alpha, R_v^\alpha\right\}$, where: $E_v^\alpha = \left\{e_1^\alpha, e_2^\alpha, ..., e_s^\alpha\right\}$ is the set of non-derivative elements of the rank α model; $C_v^\alpha = \left\{c_1^\alpha, c_2^\alpha, ..., c_n^\alpha\right\}$ is the set of permissible relations between the non-derivative elements of the rank α model; $R_v^\alpha = \left\{r_1^\alpha, r_2^\alpha, ..., r_n^\alpha\right\}$ is the set of characteristics of non-derivative elements of the rank α model; α = 1,2,3, ... *N* is the rank (level) of the model [4].

An image model will be considered invariant with respect to a certain set of classes of GD images, if:

- the model can be built for any document from this set;
- the original image can be restored using a model with known accuracy.

Initially, to automate LFGD processing, mathematical models were proposed for the lower levels of the hierarchy to describe images. In these models, graphic images were presented in the form of a raster (set of pixels), a collection of lines, contours and points (CIM, LCIM). At the same time, LCIM was considered as the base model for all subsequent levels of models. Models of higher levels were built on the basis of CIM or LCIM. For these models, effective computational geometry methods (the general-to-specific method on the basis of hierarchical structures of vector data representation), methods for graphic objects recognition (the correlation extremal method), etc., were developed [4-9].

The practice of automated WFGD processing required the extension of the existing class of models for their description. The original extended classes of raster and vector models for describing RIGD are discussed in detail in [6–9]. In particular, at the raster level, original models of raster simple objects (RSO) and raster composite objects (RCO) were proposed. RSO are divided into raster linear objects (RLO) and raster areal objects (RAO). The class of vector models was extended by introducing linear (LIM) and segment–node (SNIM) models. In this case, CIM is in one-to-one correspondence with RIWFGD, it can be used as an independent model, but it can also be considered as a preparatory stage for producing a linear-contour model, and LIM can be considered as a degenerate case of LCIM. SNIM is a vector model that describes the entire image as a group of connected sets.

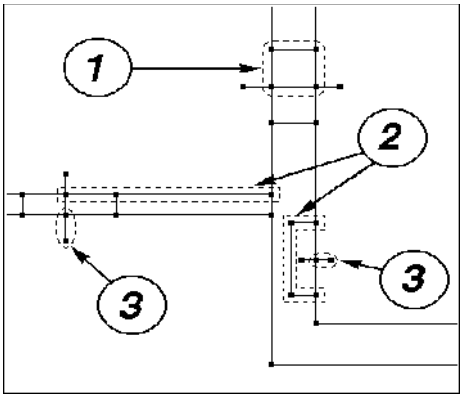

Figure 1. An example of a WFGD represented in the form of SNIM.

Figure1 shows a fragment of the WFGD represented in the form of SNIM. The segment is a broken line, but in particular cases it is a leg between intersections of this line with other lines in the image (Figure 1, positions 1, 2). In this case, the segments are often the boundary between two contour objects. For a section of the line limited by the intersection with another line only on one side, the concept of a segment with a free end was introduced (Figure 1, position 3). In general, Figure 1 shows a fragment of a segment-node image model of a WFGD containing the image of the elements described above that are characteristic of the vector representation of the WFGD.

With a view to a more rigorous description, it is advisable to associate a formalized representation of the SNIM with graph theory [10, 11]. If we impose the restriction that the SNIM segment is exclusively a straight line space bounded on both sides by nodes, then the term “segment” can be considered synonymous with the term “link”. Thus, the SNIM graph is a set $\boldsymbol{G} = \boldsymbol{\{U, S\}}$ consisting of two subsets. The subset $\boldsymbol{U}$ consists of elements of the “node” type: $\mathbf{U} = \boldsymbol{\{U_1, U_2, \ldots, U_p\}}$, and the subset $\boldsymbol{S}$, of the elements of the “link” type: $\boldsymbol{S = \{S_1, S_2, \ldots, S_q\}}$. When each vertex of the graph $\boldsymbol{G}$ is assigned its identifying number, it will be possible to refer this graph to the class of labeled graphs.

Another feature of the SNIM graph is its original characteristic for each of its nodes/vertices: the coordinates *(X, Y)* of the node's location on the plane. This feature makes it possible to uniquely map the graph $\boldsymbol{G}$ on the plane, which distinguishes it from most other graphs of arbitrary nature, for which the specific form of the schematic image (graph diagram) is often not essential. Complete certainty when mapping the SNIM graph on a plane allows us to speak of this model as an image model.

The use of SNIM is especially effective when processing WFGDs with a distinct topological load on linear geometric elements of the image [7–9]. In this case, the topological model is determined by the presence and storage of sets of interrelations, such as interconnected arcs at intersections, an ordered set of segments forming the boundary of each contour, etc. The topological properties of the figures do not change with any deformations that occur without breaks or connections. The topological feature of the WFGD is the presence of a large number of raster rectilinear objects forming mutual intersections. The image of the graph chart has similar features, and due to this the application of SNIM, which is also described in terms of graph theory, is particularly effective precisely for this kind of documents.

Unlike object vector WFGD models, SNIM does not contain objects in the usual sense, such as contours, vectorized lines, segments, etc. The transition from SNIM to the level of object vector models is a separate task. CIM, LCIM and LIM are associated with different vectorization algorithms and provide geometric interpretation of images in the tasks of scene analysis and recognition, as well as the metric description of the information components of the raster [4, 5, 7-9].

4. Problem statement

Vectorization is a basic operation in most processing and analysis systems for graphic images. If a RIWFGD consists mainly of interacting linear extended objects (diagrams, technical drawings and plans, hydrographic maps and plans) with a clearly defined direction of their orientation, then in the case of significant amounts of initial raster data, the dashed form of representation allows reducing them and building simple and reliable algorithms for vectorization and, if necessary, geometric segmentation into linear and area raster objects. It means that effective geometric modeling of RIWFGD can be achieved, and in the case of small volumes of source raster data it is possible to build sufficiently time-effective algorithms directly from RIWFGD in pixel form.

If the RIWFGD of vectorized objects do not contain distortions and noise, then the existing local vectorization algorithms can cope with this task quite well, although it must be borne in mind that the vectorized objects that are being obtained require additional smoothing or approximation. However, it is not always possible to meet the requirements of the metric accuracy of the approximation and the geometric accuracy of a vectorized object at the same time [4, 5, 7–9].

In the framework of this research, the source data for the proposed vectorization technology is a binary raster image (BRIWFGD) with geometric dimensions N x M, which is the description of the RIWFGD source document as a two-layer pixel object:

$$R_{ij} = \begin{cases} 1, \text{if the pixel belongs to the sign layer;} \\ 0, \text{if the pixel belongs to the background layer;} \end{cases} \quad i = 1, \ldots, N; \quad j = 1, \ldots, M$$

We will look for the sought-after geometric model as a collection of sets of non-derivative geometric elements: topological nodes U, segments S, and contours K (Figure 2):

Figure 2. Non-derivative elements of the geometric model of the image.

$U = \{U_i\}$, $i=1, 2, 3, \ldots, N_u$;
$S = \{S_i\}$, $i=1, 2, 3, \ldots, N_s$;
$K = \{K_i\}$, $i=1, 2, 3, \ldots, N_k$).
Figure 2 shows these elements against the background of RIWFGD, where:

- areas 1 define the background raster layer;
- areas 2 define the sign raster layer;
- lines and nodes 3 define topological nodes and short segments;
- lines 4 define segments of centerlines;
- lines 5 define contours of polygon objects.

5. Original procedures and operations for producing a geometric model of WFGD

We propose a set of improved and original algorithms for WFGD vectorization based on a low-level model for describing RIWFGD.

The composition of the sets of non-derivative geometric elements is described below.

A topological node is described by a set of numerical characteristics $U\{x, y, swT, spN\}$, where: x, y are the raster coordinates of the node, with the node pixel always belonging to the sign layer; $swT = \{0, 1, \ldots, v\}$ is the coefficient of topological connectivity, which determines the number of segments originating from the node; $spN = \{N_1, N_2, \ldots, N_s\}$ is the list of segment numbers originating from this node.

The segment $S=\{x_1, y_1, \ldots, x_t, y_t\}$ is an inter-node fragment of the centerline. It consists of a collection of connected pixels of the sign layer belonging to the centerlines of the RLO, where t is the number of linear approximation nodes of the set of connected pixels of the inter-node intervals of the centerline.

The contour $K=\{x_1,y_1,\ldots, x_k,y_k\}$ is a description of the RAO boundaries by a collection of connected boundary pixels of the sign layer, where k is the number of nodes of the linear approximation of the set of boundary RAO pixels.

Using a two-layer model of raster pixel data and the chosen vector description model, it is easy to extend existing methods and algorithms for a vector description of a set of raster composite objects (RCO) of multicolor documents, including full-color raster images of Earth remote sensing, as well as raster hyperspectral images (HSI) that have undergone color (spectral) layering (clustering).

Structural analysis of the sign layer of BRIWFGD shows that this layer contains the following RCOs:

- noise objects of quite small geometric dimensions (“snow”);
- small-sized objects, which are images of elements of a set of discrete signs;
- large-sized objects, which are isolated linear and areal signs, or a conglomerate of the results of the superposition (merger, tangency) of linear, discrete and areal signs.

Within the framework of CGA, the original hierarchical model proposed by the authors for the representation of raster and vector SDD and as our contribution to the development of existing methods and algorithms, we propose the following sequence of original procedures and operations for constructing a WFGD geometric model based on the collection of raster composite objects (RCO) of BRIWFGD, providing a high level of confidence during the semantic interpretation of the document.

Stage 1 Construction of a RCO model from the sign layer of BRIWFGD.

1.1 Compiling a list of sign pixels in the sign layer Z of the raster R_1: ListZP = $\{Pix_i=1\}(i=1, 2,\ldots, Nz)$, where: Pix_i is the sign pixel with the coordinates x_i,y_i; Nz is the number of sign pixels of the Z layer.

1.2 While the ListZP is not empty, the next, not yet clustered pixel is extracted from it, and, starting from it, the RCO is formed by clustering along the 8 - connected neighborhood.

1.3 After completing the clustering procedure, the set of pixels constituting the next RCO are converted into a vector contour (stage 2) and are deleted from the ListZP list.

1.4 If the ListZP is empty, then the stage of construction of the RCO model is considered complete.

Stage 2 Contour analysis of the RCO model.

2.1 Selecting a set of boundary pixels G from the raster sign layer for each RCO.

2.2 Construction of the CIM by following (based on pixels G) the boundaries of the RCO that make up the layer *Z*.

2.3 Parametrization of all contours constructed, by measuring for each contour the following geometrical characteristics: p_1 is the contour length along its perimeter; p_2, p_3 are the width and height of the minimum area rectangle circumscribing the contour, with its sides parallel to coordinate axes; p_4 is the contour area; $p_5 = p_4 / p_1^2$ is the external aspect of the contour.

2.4 Segmentation of contours depending on parameters $p_1 - p_5$ into: noise contours, which are subsequently removed from the initial layer *Z*; discrete signs; isolated areal objects; small-length linear segments and producing from them the set **V** with the subsequent removal of the corresponding RCOs from the initial layer *Z*.

Thus, the output result of the stage is a CIM containing vectorized elements of the *Z* layer and a modified raster $\widetilde{R}_1$ which contains no RCOs that describe vectorized objects.

Stage 3 Splitting of large-sized RCOs of the sign layer into areal and linear signs and their description by a set of geometric elements such as nodes, segments and contours.

3.1 Splitting the modified sign layer of pixels $\widetilde{R}_1$ using its skeleton model [12] into the following types: “linear” pixels belonging to the centerlines of the RLO; "areal" pixels belonging to RAO; “nodal” pixels belonging to the nodal points of the RLO and RAO intersection.

The operation is performed by the method of sequential, parametrically controlled D - multiple morphological pixel operations of diffusion and dilation [12], where D is the half-thickness of the RLO.

The classification of pixels into the types listed above is carried out on the basis of the original recognition mask filters, which make it possible to identify, at a pixel level, certain types of graphic situations with a high degree of confidence.

3.2 For “nodal” pixels, their coordinates are measured and they are entered into the set **V** of vector data as a vector description of the topological nodes of the desired geometric model.

3.3 By using “linear” pixels, the inter-node gaps of the center line are tracked, it is linearly approximated, and the tracking results are entered into the **V** set as LRO segments.

3.4 For “areal” pixels, the procedure of D-multiple “spraying” and the subsequent construction of the contour of the areal object are performed, followed by linear approximation and entering the approximated contour into the set **V**.

3.5 For nodal pixels, their topological characteristics are calculated, based on the constructed metric of nodes, segments and contours: the connectivity coefficients K_{sw} and the list of numbers of segments originating from the nodes.

Thus, after completing all operations, the set of vector data **V** will be formed, consisting of vector elements of the following types: node points, contours, segments that uniquely define the desired geometric model of the original WFGD.

The targeted parametric control of the input parameter D for the whole procedure (LRO half-thickness) can be obtained from the skeleton of the RIWFGD.

Figure 2 shows an adequate geometric model where objects are split into contour (areal) and linearly extended ones, with topological characteristics of their interaction (tangency or intersection).

To support the whole variety of algorithms for classification of signs in graphic documents, the set of vector elements **V** thus obtained is supplemented for the current document with a description of its sign pixel layer **Z** in a dashed format, which allows constructing character recognition algorithms based on their combined and consistent synchronous description (vector and pixel). This feature distinguishes the proposed methods and algorithms for describing RIWFGD from the existing ones.

Figure 3 shows a fragment of a geometric model of a WFGD in a terrain map with a large number of linear objects. The model was obtained by applying the proposed technology.

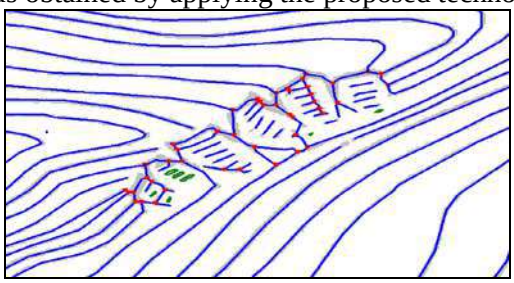

Figure 3. A fragment of a geometric model of a WFGD in a terrain map with a large number of linear signs.

6. Conclusion

In the course of our research, documents of the WFGD type were analyzed, and their main features that determine the choice of models, methods and algorithms for their processing were identified. The effectiveness of the extended class of vector models (LIM and SNIM) for the description of WFGDs with a distinctive linear orientation of objects was confirmed during practical experiments on real WFGDs.

7. References

[1] Vasin Yu G and Yasakov Yu V 2016 Distributed database management system for integrated processing of spatial data in a GIS *Computer Optics* **40(6)** 919-928 DOI: 10.18287/2412-6179-2016-40-6-919-928

[2] Khafizov R G, Okhotnikov S A and Yaranceva T V 2016 Models of the image of object contours with geometrical distortions *Computer Optics* **40(3)** 404-409 DOI: 10.18287/2412-6179-2016-40-3-404-409

[3] Belim S V and Kutlunin P E 2015 Boundary extraction in images using a clustering algorithm *Computer Optics* **39(1)** 119-124 DOI: 10.18287/0134-2452-2015-39-1-119-124

[4] Vasin Yu G, Bashkirov O A and Chudinovich B M 1987 Combinotary geometric approach in complex graphic data analysis tasks *Automation of complex graphic information processing: Inter-university collection* (Gorky: Gorky State University) (in Russian)

[5] Vasin Yu G and Bashkirov O A 1984 Mathematical models for structured description of graphic images *Automation of complex graphic information processing: Inter-university collection* (Gorky: Gorky State University) 92-117 (in Russian)

[6] Vasin D Yu 2015 Automation of characters input based on low-level models of graphic images description *Privolzhsky Science Magazine* **3(35)** 109-115 (in Russian)

[7] Vasin Yu G, Vasin D Yu, Gromov V P and Rotkov S I 2018 Robust vectorization of graphic documents with distinctive orientation of linear objects *Proc. of International Scientific Conference in Computing for Physics and Technology* (Tsargrad, Moscow region) 313-317 (in Russian)

[8] Vasin D Yu, Gromov V P and Rotkov S I 2018 Formation of segment and nodal model of graphic documents with distinctive orientation of linear objects *Proc. of International Scientific Conference in Computing for Physics and Technology* (Tsargrad, Moscow region) 265-280 (in Russian)

[9] Vasin Y, Vasin D, Utesheva T, Lebedev L and Kustov E 2017 Increasing the effectiveness of intelligent information technology for producing digital graphic documents with weakly formalized description of objects *Procedia Engineering Proc.* **201** 341-352 DOI: 10.1016/j.proeng.2017.09.642

[10] Harary F 1996 *Theory of graphs* (London: Addison-Wesley) p 274

[11] Christofides N 1986 *Graph theory: an algorithmic approach* 4th (London: Academic Press) p 400

[12] Gonzalez R and Woods R 2018 *Digital image processing* (New York: Pearson) p 1019

Acknowledgements
This work was supported by the Russian Foundation for Basic Research, RFBR grants No. 17–07–00543 and No. 18–07–00715.

Watermarking algorithms for JPEG 2000 lossy compressed images

V Fedoseev[1,2], T Androsova[1]

[1]Samara National Research University, Moskovskoe Shosse 34A, Samara, Russia, 443086
[2]Image Processing Systems Institute of RAS - Branch of the FSRC "Crystallography and Photonics" RAS, Molodogvardejskaya street 151, Samara, Russia, 443001

e-mail: vicanfed@gmail.com

Abstract. In the paper, we propose two watermarking algorithms for semi-fragile data hiding in JPEG 2000 lossy compressed images. Both algorithms are based on the concept of quantization index modulation. These methods have a property of semi-fragility to the image quality. It means that the hidden information is preserved after high-quality compression, and is destroyed in the case of significant degradation. Experimental investigations confirm this property for both algorithms. They also show that the introduced embedding distortions in terms of PSNR and PSNR-HVS are in almost linear dependence on the quantization parameter. It allows us to control the quality at an acceptable level when information embedding.

1. Introduction

The JPEG 2000 image compression format, despite being less popular compared to JPEG, can provide better compression and is therefore widely used in remote sensing systems, medical imaging, and some other areas [1]. This fact underscores the importance of the task of protecting JPEG 2000 images from unauthorized changes. For example, the recipient of remote sensing data must have confidence in the absence of their falsification, as well as the doctor who makes the diagnosis based on the digital image must be convinced of its authenticity and in the absence of distortions caused by lossy data compression.

One of the common approaches for the problem of protecting images from changes is embedding of semi-fragile digital watermarks, which are preserved in images while minor changing and destroyed after significant modifications. However, only a small number of semi-fragile watermarking methods for JPEG 2000 can be found in the literature [2]-[4]. Specifically, such class of methods includes one by Sun et al. [2] based on the EBCOT encoding procedure and the two algorithms by Maeno et al. [3], which do not allow to control quality factor. One more algorithm by Preda [4] is not linked with JPEG 2000 parameters. In this paper, we propose such a method for lossy JPEG 2000 compression mode, based on the quantization index modulation technique (QIM) [5].

The paper is organized as follows. In Section 2, we briefly describe the quantization procedure specified in the JPEG 2000 lossy compression standard. Section 3 presents the developed watermarking method while Section 4 investigates it.

2. JPEG 2000 lossy compression procedure

The flowchart of the compression algorithm is shown in Figure 1. At the first stage of compression, the brightness of each component is reduced by 128 [6]. Then the image color space is converted from RGB to YCbCr. The resulting image is subjected to discrete wavelet transform (DWT) with the Daubechies filter bank (9, 7) for the partition of the image into low-frequency and high-frequency areas (subbands), also called as the approximation and the details [6].

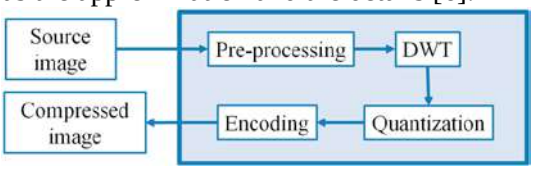

Figure 1. JPEG 2000 coding flowchart.

After the transformation, each coefficient $a_b(u,v)$ of subband b is quantized by the formula:

$$q_b(u,v) = \left\lfloor \frac{a_b(u,v)}{\Delta_b} \right\rfloor * sign(a_b(u,v)), \quad (1)$$

where $a_b(u,v)$ are quadrant coefficients and Δ_b is the quantization step.

The quantization step is represented by two bytes: 11-bit mantissa μ_b and 5-bit exponent ε_b and is determined by the following formula:

$$\Delta_b = 2^{R_b-\varepsilon_b}\left(1+\frac{\mu_b}{2^{11}}\right), \quad (2)$$

where R_b is the nominal dynamic range of subband b.

According to [7, 8], two modes of calculating the values Δ_b for various b are possible, which are expounded quantization and derived quantization. In the first mode, the values (ε_b, μ_b) are explicitly transmitted by the way similar to q-table in JPEG coding. In the second mode, which is considered in this paper, (ε_b, μ_b) values are calculated from the given values $(\varepsilon_0, \mu_0) \triangleq (\varepsilon, \mu)$, defined for the LL-subband, using the following equations:

$$\varepsilon_b = \varepsilon - N_L + n_b;\ \mu_b = \mu, \quad (3)$$

where N_L is the total number of decomposition levels and n_b is the level number corresponding to subband b [8].

The final step of the compression process is the error-free coding of quantized coefficients using the arithmetic coding based on bit-planes. The JPEG 2000 decoder reverses the given operations.

3. Embedding information based on QIM

To embed the watermark, we modified the quantization operation (1) according to the QIM concept. Specifically, we used two forms of QIM embedding rules: Simple-QIM [9]

$$y(k) = 2\Delta\left\lfloor \frac{x(k)}{2\Delta} \right\rfloor + \Delta \cdot W(k), \quad (4)$$

where $x(k)$ are quantized values, and $W(k)$ are the embedded bits, and DM-QIM (Dither Modulation – Quantization Index Modulation) [5]. The latter one assumes the use of two dither vectors $d_0(k), d_1(k)$ that are consistent with each other and used when embedding bits “0” and “1”:

$$d_0(k), d_1(k) \epsilon \left[-\tfrac{\Delta}{2}; \tfrac{\Delta}{2} - 1\right], k \in [0, K-1],$$

where K is the number of quantized values. Information embedding in DM-QIM is carried out as follows:

$$y(k) = \Delta \cdot round\left(\frac{x(k) + d_{W(k)}(k)}{\Delta}\right) - d_{W(k)}(k). \quad (5)$$

To use (4)-(5) in our adaptations for JPEG 2000, the embedded watermark should be robust against the JPEG 2000 quantization operation (1). To achieve the robustness, we modified (4) to

$$y(k) = \text{sign}(x(k)) \cdot \left(2\Delta\left\lfloor \frac{|x(k)|}{2\Delta} \right\rfloor + \Delta \cdot W(k)\right), \quad (6)$$

and (6) – to

$$y(k) = sign\big(x(k)\big) \cdot \left(\Delta \cdot \left\lfloor \frac{x(k) + 0.5 \cdot \Delta \cdot sign\big(x(k)\big) + d_{W(k)}(k)}{\Delta} \right\rfloor - d_{W(k)}(k) \right), \quad (7)$$

In the compression process, the values $a_b(u,v)$ are used as $x(k)$, and Δ_b are used as the quantization steps Δ (see (1)). The obtained quantized values $y(k)$ would be the values $q_b(u,v)$.

The dependence of the embedding rule on the quantization step Δ makes it possible to provide semi-fragility of the embedded information: it will be preserved under compression with quantization steps smaller than Δ and lost for steps greater than Δ.

4. Experiments

To verify the developed watermarking techniques, we embedded a watermark in the *Lenna* image. Figure 2 shows the original image on the left and images with hidden information in the center and on the right. Visual distortions caused by embedding are not noticeable.

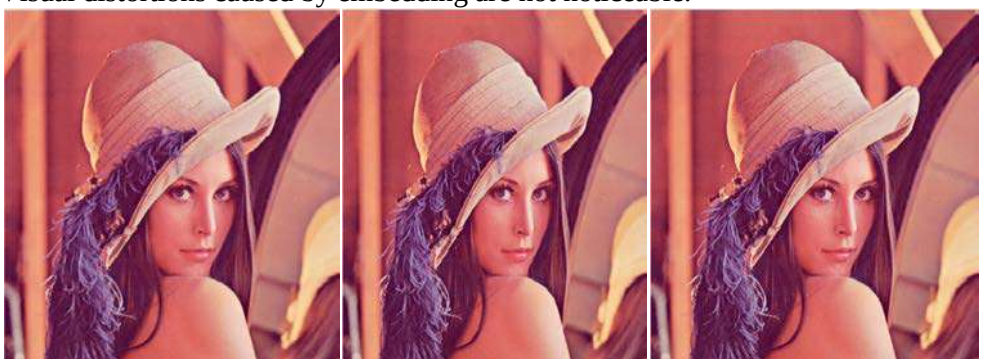

Figure 2. Original image (left), and watermarking results: by the modified Simple-QIM (center, PSNR=64.94) and by the modified DM-QIM (right, PSNR=68.69); quantization parameters $\mu = 8.5$, $\varepsilon = 9$.

Next, we should make sure that the watermark has the property of semi-fragility. Let W be the embedded information and W^R be the extracted information. Then the extraction accuracy will be calculated by the formula:

$$\rho = 1 - BER = 1 - \frac{1}{K}\sum_{k=0}^{K-1} XOR(W(k), W^R(k)), \quad (8)$$

where BER is Bit Error Rate.

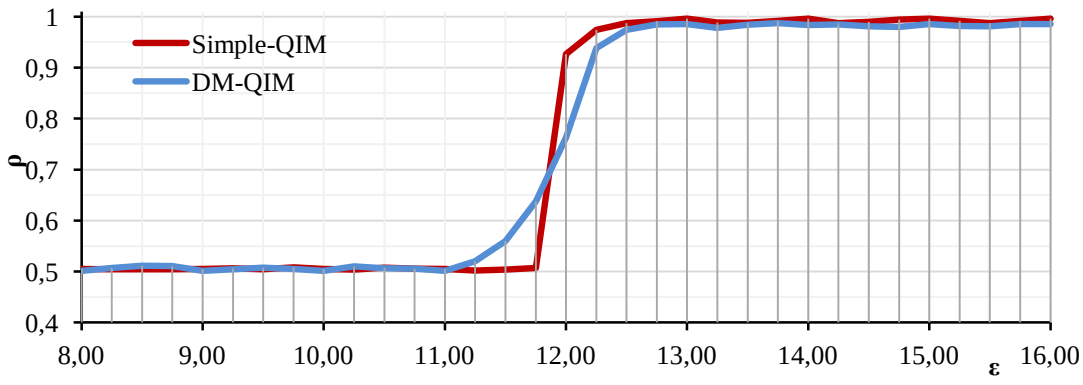

Figure 3. Dependence of the extraction accuracy from ε (the embedding parameters are $\mu = 8.5$, $\varepsilon = 12$).

In the second experiment, we compressed images with embedded information (similar to one shown in Figure 2) using JPEG 2000 standard with different quantization steps Δ_b determined by ε values according to the formulas (2)-(3) (at the fixed $\mu = 8.5$). After compression, we attempted to

extract information and to estimate the accuracy using expression (8). The results illustrated in Figure 3 show that the hidden data is preserved at a smaller quantization step (corresponding to a larger value of ε than that used in compression). Thus, both algorithms have shown their efficiency in terms of providing semi-fragility to JPEG 2000 lossy compression. But if we compare two algorithms, we may conclude that the Simple-QIM graph jump is sharper, i.e., it is closer to the ideal shape. Therefore, the Simple-QIM modification is more accurate than DM-QIM at the acceptable quantization step border.

Next, we investigated the distortions introduced by information hiding. For this purpose, we used PSNR and PSNR-HVS metrics. The second one measures image quality from its perception by the person [10]. Figures 4-5 show the results of this experiment for the image "Lenna" at various ε (μ is fixed and equal to 8.5). The results confirm that the image does not undergo significant degradation, and also that image quality is directly related to ε (the dependence is approximately linear). Thus, the achieved semi-fragility by ε can be expressed as semi-fragility by the specified level of PSNR or PSNR-HVS.

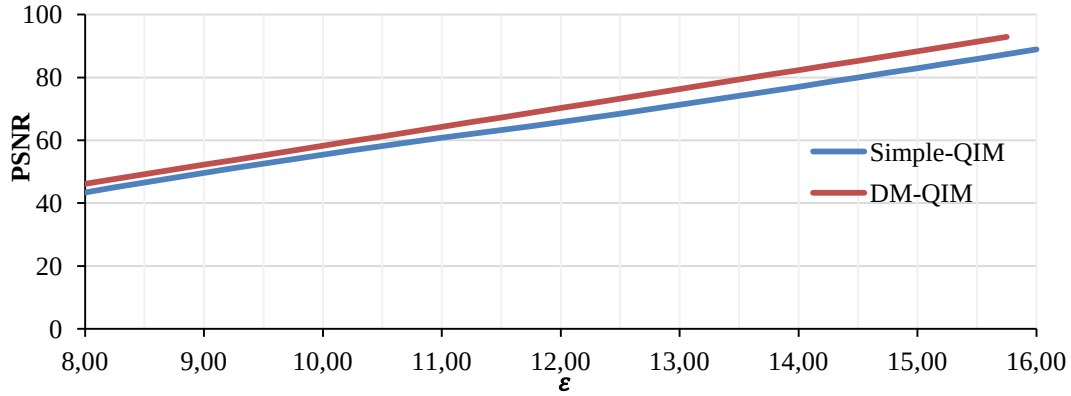

Figure 4. Dependence of PSNR of images with embedded information on the parameter ε that determines the quantization step when embedding a watermark ($\mu = 8.5$).

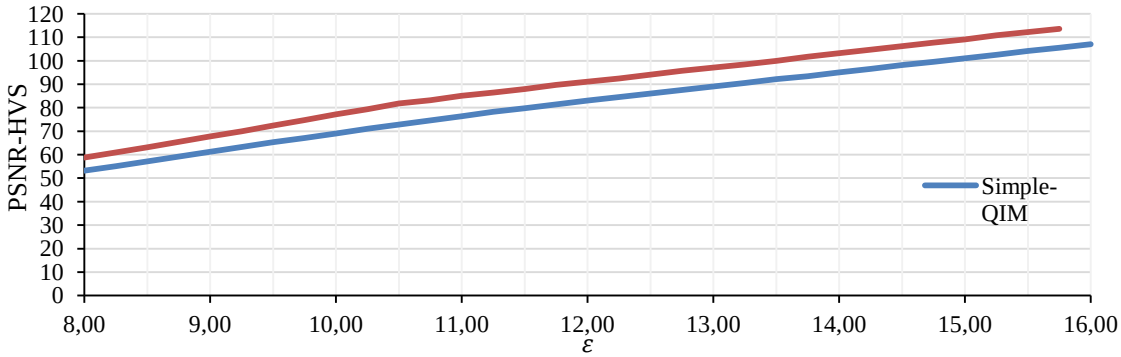

Figure 5. Dependence of PSNR-HVS of images with embedded information on the parameter ε that determines the quantization step when embedding a watermark ($\mu = 8.5$).

5. Conclusion

In this paper, we proposed two watermarking algorithms for semi-fragile data hiding in JPEG 2000 based on QIM concept: Simple-QIM and DM-QIM. Our investigations have shown that both algorithms provide semi-fragililty property to JPEG 2000: a watermark is preserved under compression with quality parameters greater than the specified one and is deleted when the compression quality is reduced. Visually, the distortions caused by embedding the CEH are not noticeable. Moreover, the measurements of these distortions using PSNR and PSNR-HVS show that the values are in almost linear dependence on the parameter ε. It is a very important property which allows us to control the quality at an acceptable level when information embedding.

6. References

[1] Gonzalez R C and Woods R E 2009 *Digital Image Processing* (Pearson Education)
[2] Sun Q, Chang S-F, Kurato M and Suto M 2002 A quantitative semi-fragile JPEG2000 image authentication system *Proceedings International Conference on Image Processing* **2** II–II
[3] Maeno K, Sun Q, Chang S-F and Suto M 2006 New semi-fragile image authentication watermarking techniques using random bias and nonuniform quantization *IEEE Transactions on Multimedia* **8** 32-45
[4] Preda R O 2013 Semi-fragile watermarking for image authentication with sensitive tamper localization in the wavelet domain *Measurement* **46** 367-373
[5] Chen B and Wornell G 2001 Quantization Index Modulation: A Class of Provably Good Methods for Digital Watermarking and Information Embedding *IEEE Transaction on Information Theory* **47** 1423-1443
[6] Schelkens P, Skodras A and Ebrahimi T 2009 *The JPEG 2000 suite* (John Wiley & Sons)
[7] Rabbani M and Joshi R 2002 An overview of the JPEG 2000 still image compression standard *Signal Processing: Image Communication* **17** 3-48
[8] Marcellin M W, Lepley M A, Bilgin A, Flohr T J, Chinen T T and Kasner J H 2002 An overview of quantization in JPEG 2000 *Signal Processing: Image Communication* **17** 73-84
[9] Mitekin V A and Fedoseev V A 2018 New secure QIM-based information hiding algorithms *Computer Optics* **42(1)** 118-127 DOI: 10.18287/2412-6179-2018-42-1-118-127
[10] Egiazarian K, Astola J, Ponomarenko N, Lukin V, Battisti F and Carli M 2006 New full-reference quality metrics based on HVS *Proceedings of the Second International Workshop on Video Processing and Quality Metrics* **4**

Acknowledgments
This work was supported by the Russian Science Foundation under grant 18-71-00052.

Evaluation of different embedding methods for JPEG authentication watermarking

A A Egorova[1], V A Fedoseev[1,2]

[1]Samara National Research University, Moskovskoe Shosse 34A, Samara, Russia, 443086
[2]Image Processing Systems Institute of RAS - Branch of the FSRC "Crystallography and Photonics" RAS, Molodogvardejskaya street 151, Samara, Russia, 443001

e-mail: varlamova.anna.95@mail.ru

Abstract. This paper considers the applicability of different data embedding methods for semi-fragile watermarking systems used for JPEG image authentication. The methods include Least Significant Bit watermarking and various versions of Quantization Index Modulation. In our investigations, we tested the semi-fragility property against JPEG and compared the visual quality of the watermarked images. We also checked the watermark fragility to unacceptable modifications like median filtering, blurring, and adding Gaussian noise. Finally, we analyzed the provided tampering localization error.

1. Introduction

One of the ways to protect an image from tampering is to embed a fragile or a semi-fragile digital watermark, a barely visible and removable component, whose presence in the image may testify its authenticity [1]. Fragile watermarks are destroyed after any image modifications and are usually used for the data integrity verification. If a specific set of modifications is considered to be acceptable, semi-fragile watermarks are applied to authenticate the data. They are robust against permitted transformations and fragile to any other. As a rule, these permitted transformations include modifications that do not affect image content and structure, for example, weak distortions caused by lossy compression.

The most common standard for lossy image compression is JPEG. More than 20 semi-fragile JPEG watermarking systems have been developed since 2000. The most widespread among them are those that embed a watermark in the frequency domain, namely in the Discrete Cosine Transform (DCT) coefficients before or after quantization [2-15]. The watermarks embedded by such systems are visually imperceptible and JPEG-resistant even at low values of the quality factor.

The effectiveness of a particular semi-fragile system depends mostly on its data embedding method. For this reason, in this paper, we investigate the influence of different embedding methods on the performance of the JPEG semi-fragile watermarking. We consider and compare the methods that are commonly applied in JPEG-resistant watermarking. They include Least Significant Bit (LSB) watermarking [1], Quantization Index Modulation (QIM) [16], and its versions (Sign-QIM [17], MOD-QIM [18], and DM-QIM [16]). In the experimental part, we test their applicability to semi-fragile JPEG watermarking and compare the Peak Signal-to-Noise (PSNR) values of the obtained watermarked images. We also verify the fragility of the considered embedding methods to

unacceptable distortions (exemplified by median filtering, blurring, and adding white Gaussian noise) and analyze the tampering localization error.

The rest of this paper is organized as follows. In Section 2, the lossy JPEG compression scheme is described. In Section 3, the description of considered data embedding methods is given. Section 4 presents the experimental results.

2. Lossy JPEG compression scheme

The JPEG lossy compression algorithm consists of the following key steps (also shown in Figure 1) [17].

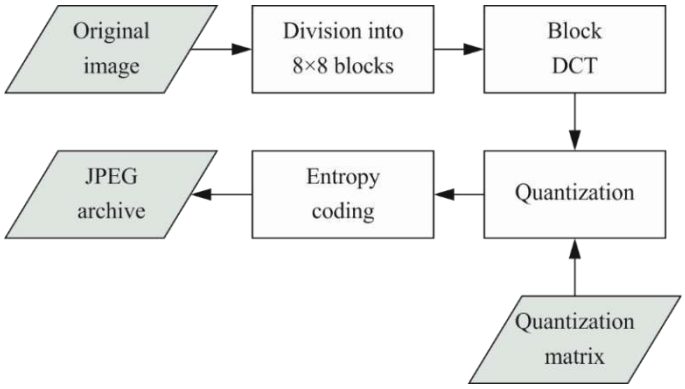

Figure 1. Lossy JPEG compression scheme.

1. Division of the original $N_1 \times N_2$ image I into 8×8 nonoverlapping blocks I_i, where $i = 1,..,N$ and $N = N_1 N_2 / 64$ is the total number of nonoverlapping blocks in the image.
2. Calculating blockwise DCT. DCT decomposes the image values into different frequencies. We denote each obtained block of DCT coefficients as $B_i(m_1, m_2)$. The coefficients in the upper left corner (Figure 2) characterize the low frequency component.
3. Quantization of each block B_i using the quantization matrix Q_{QF} of size 8×8, corresponding to the predetermined compression quality factor QF (from 1 to 100).

$$D_i(m_1, m_2) = round\left(\frac{B_i(m_1, m_2)}{Q_{QF}(m_1, m_2)}\right). \quad (1)$$

The smaller QF is, the higher the values of coefficients of the quantization matrix Q_{QF}, more zeros among quantized DCT coefficients $D_i(m_1, m_2)$, and the smaller the size of the resulting archive.

4. Scanning each block $D_i(m_1, m_2)$ in zigzag order, as shown in Figure 2, and entropy coding. Further, we denote DCT coefficients shortly as $D_i(j)$, where $j = 1..64$ is the index of an element in zigzag order.

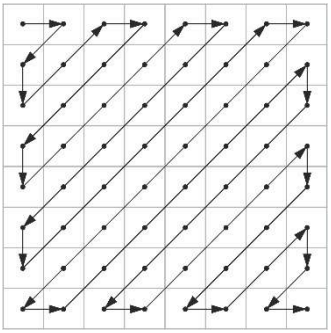

Figure 2. Zigzag scanning of a DCT block.

3. Data embedding methods used in JPEG-resistant watermarking

Data embedding is a key step of any JPEG semi-fragile watermarking system. It determines the way of modifying the spectral components. The most common data embedding methods actively used in JPEG-resistant watermarking are the LSB [1] and QIM variations [16-18].

It is worth mentioning the loss of information in the JPEG algorithm occurs at the DCT coefficients quantization stage. For this reason, frequency domain watermarking systems embed the watermark either at the quantization step or immediately after it.

LSB embedding in JPEG semi-fragile systems is performed after the quantization by replacing one or more of the quantized DCT image coefficients with watermark bits [4, 5]. Let us assume that the number of modified DCT coefficients in each block is equal to the number of bits to be embedded per block N_W. We also assume that inter-coefficient relationships are not taken into account during the watermark embedding process. We denote the positions of the modified DCT coefficients in zigzag order as j_k, where $k = 1..N_W$. In general, they are defined by the secret key. Then the LSB method embeds the watermark by changing the quantized DCT coefficients located in the j_k positions:

$$D_i^W(j_k) = 2\lfloor D_i(j_k)/2 \rfloor + W_{i,k}, \tag{2}$$

where $W_{i,k}$ is the k^{th} bit of information that is embedded in the i^{th} quantized DCT block. All coefficients excluding j_k remain unchanged. The watermark extraction procedure for this method is obvious.

LSB is actively used [3-5] because it does not require high computational cost, simple to implement, and makes possible to hide a sufficiently large amount of information. However, its application in the DCT frequency domain may cause significant distortions.

The QIM-based methods usually lead to smaller distortions of the watermarked image. Unlike LSB, QIM-based techniques embed a watermark while quantizing DCT coefficients. They modulate the DCT coefficients by the watermark bits [16]. In the JPEG semi-fragile systems, various versions of QIM are in use [6-9]. At first, we consider the method applied in the Preda & Vizireanu watermarking system [7]:

$$B_i^W(j_k) = round\left(\frac{B_i(j_k)}{2Q_{QF}(j_k)} - W_{i,k}\right)2Q_{QF}(j_k) + W_{i,k}Q_{QF}(j_k), \tag{3}$$

$$W_{i,k} = round\left(B_i^W(j_k)/Q_{QF}(j_k)\right)(\mathrm{mod}\,2). \tag{4}$$

Note that (3) is similar to LSB. As in the case of LSB, the components $B_i^W(j_k)$ are multiples of the quantization steps $Q_{QF}(j_k)$. The second QIM-based method we consider in this paper is Sign-QIM – a simple modification of the method by Preda & Vizireanu. Its distinctive feature lies in the fact that the watermark component sign depends on the direction to which the modified DCT coefficient is rounded off at the quantization stage. Due to this, the error in the coefficient j_k caused by information embedding does not exceed $Q_{QF}(j_k)$:

$$B_i^W(j_k) = Br_i(j_k) + S_i(j_k)\cdot W_{i,k}\cdot Q_{QF}(j_k), \tag{5}$$

where

$$Br_i(j_k) = round\left(\frac{B_i(j_k)}{2Q_{QF}(j_k)}\right)2Q_{QF}(j_k). \tag{6}$$

The third method is DM-QIM, which is the most known QIM version [16]. It subtracts the noise-like component, which is previously added to the host image components, to avoid a mean value shift instead of adding the remainder of dividing by the quantization step:

$$B_i^W(j_k) = round\left(\frac{B_i(j_k) + d_{W_{i,k}}(j_k)Q_{QF}(j_k)}{2Q_{QF}(j_k)}\right)2Q_{QF}(j_k) - d_{W_{i,k}}(j_k)Q_{QF}(j_k), \tag{7}$$

where $d_0(j), d_1(j) \in \mathbf{R} \cap [-1;1)$ are two pseudorandom arrays used to modulate watermark bits, and

$$d_1(j) = d_0(j) - sign\left(d_0(j)\right).$$

One more QIM-based embedding method was proposed in paper [18] by Glumov & Mitekin. It has a wider range of obtained values than Preda & Vizireanu. This method is not intended to provide robustness against JPEG compression, so the embedding is performed in the spatial domain. Another distinction of [18] from [7] is that it conducts the *floor* operation $\lfloor x \rfloor$ instead of $round(x)$. Thus, the embedding a single bit w into a single image component x by [18] is as follows:

$$x^W = \lfloor x/2\delta \rfloor 2\delta + w\delta + x\left(\mathrm{mod}\,\delta\right), \tag{8}$$

where δ is the quantization step. In (8), the last summand provides exactly the extension of the range of x^W values. We denote this QIM-based method as MOD-QIM.

To incorporate MOD-QIM method with the JPEG compression procedure, we bring in modifications to the rounding function keeping the remainder as follows:

$$B_i^W(j_k) = Br_i(j_k) + S_i(j_k) \cdot W_{i,k} Q_{QF}(j_k) + M_i(j_k), \tag{9}$$

where

$$Br_i(j_k) = round\left(\frac{B_i(j_k)}{2Q_{QF}(j_k)}\right) 2Q_{QF}(j_k),$$

$$S_i(j_k) = sign\left(B_i(j_k) - Br_i(j_k)\right) = \begin{cases} 1, & Br_i(j_k) \geq B_i(j_k) \\ -1, & else \end{cases},$$

and $M_i(j_k)$ is the value $Br_i(j_k) \mathrm{mod}\left(Q_{QF}(j_k)\right)$ shifted to the range $\left[-Q_{QF}(j_k)/2, Q_{QF}(j_k)/2 - 1\right]$. Watermark extraction is carried out by (4).

4. Experimental part

In the experimental research, we implemented and tested the selected embedding methods using different criteria. All experiments were carried out using the images from the University of Waterloo repository [20].

4.1. Efficiency of the embedding methods in JPEG semi-fragile watermarking

The first experiment assesses the efficiency of the considered methods in JPEG-resistant semi-fragile watermarking. In this experiment, we embedded $N_W = 4$ bits into the DCT coefficients in the fixed positions (low, medium and high frequency coefficients were modified). For data embedding, we used $QF = 50$. Then the watermarked images were compressed to JPEG using various quality factors QF^*, both lower and higher than QF.

After that, we extracted the hidden bits from each obtained image and estimated the bit error rate (BER) as:

$$BER = \frac{1}{N \times N_W} \sum_{i=1}^{N} \sum_{k=1}^{N_W} XOR\left(W_{i,k}, W_{i,k}^R\right). \tag{10}$$

The results of the experiment averaged by the dataset are presented in Figure 3 and Table 1.

Table 1. Integral BER deviations from theoretical values (after JPEG compression with all possible QF^* values).

Embedding method	err_{FN}	err_{FP}
LSB	8.486	0.042
Preda-QIM	8.543	0.041
Sign-QIM	8.540	**0.037**
DM-QIM	**5.446**	0.066
MOD-QIM	8.282	1.286

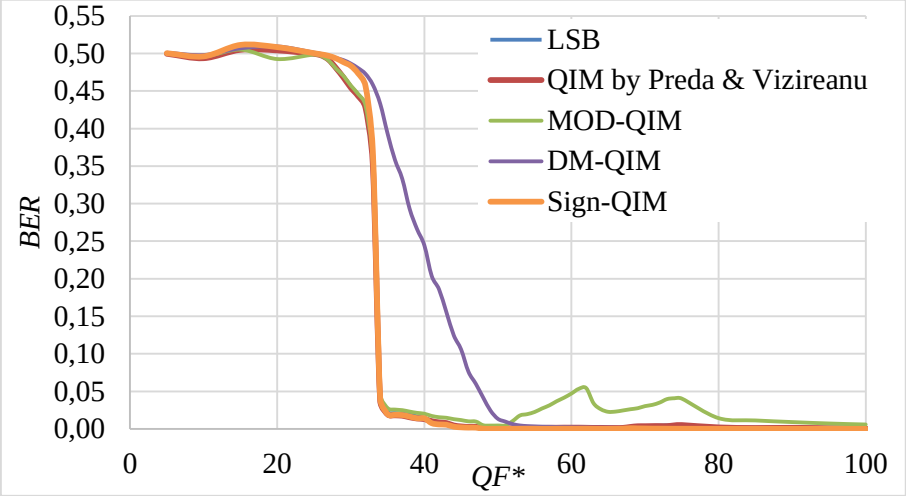

Figure 3. BER after JPEG compressions with different QF^*.

In the ideal case, BER should be close to 0 for $QF^* \geq QF$. For smaller QF^*, BER should be close to 0.5 that corresponds to random guessing. In practice, there is an inevitable transition phase where BER gradually decreases from 0.5 to 0. Figure 3 shows that it is true for all the considered methods. The shorter the transition phase, the better the method.

Besides, there may be nonzero values of BER at $QF^* \geq QF$ due to the rounding of pixel values after the inverse DCT that cause distortions of the spectral components.

To assess the deviation of the obtained curves from the ideal case (a step function), we used the following heuristic measures:

$$err_{FN} = \sum_{QF^*=QF-25}^{QF-1} \left(0.5 - BER\left(QF^*\right)\right), \tag{11}$$

$$err_{FP} = \sum_{QF^*=QF}^{QF+24} BER\left(QF^*\right). \tag{12}$$

These two expressions characterize the integral BER deviation from their theoretical values. The obtained err_{FN} and err_{FP} values are presented in Table 1. The table demonstrates that in terms of err_{FN} measure, DM-QIM considerably outperforms the rest methods. However, DM-QIM provides a high err_{FP} value. LSB, Preda-QIM, and Sign-QIM are very close in err_{FN} values, while MOD-QIM has a large number of errors at $QF^* \geq QF$.

4.2. Investigation of introduced distortion level

In the second experiment, we estimated how the quality of the resulting image depends on the number of embedded bits and the positions of the modified coefficients. For this purpose, we calculated the Peak Signal-to-Noise (PSNR) measure.

The numbers of modified coefficients in each frequency domain were predetermined, but their positions were random. We considered coefficients 2-14 in the zigzag scan as the low frequency domain, 15-35 coefficients as the medium frequency domain, and 36-64 coefficients as the high frequency domain. As in the first experiment, QF was equal to 50. The results of the second experiment are presented in Table 2.

Table 2 shows that LSB, MOD-QIM and Preda-QIM provide quite close quality of the watermarked images. DM-QIM showed the best results. Analysis of various configurations of modified frequency domains showed that it is better to embed information into low frequency components. For instance, if 10 bits are embedded in the low frequency coefficients using DM-QIM,

the quality of the resulting image is higher than if we embed one bit in the high frequency coefficients by any method.

Table 2. Averaged PSNR of watermarked images after watermark embedding by different methods.

Number of bits per block, N_W	Number of modified AC coefficients per domains (LF-MF-HF)	PSNR				
		LSB	Preda-QIM	Sign-QIM	DM-QIM	MOD-QIM
1	1-0-0	43.95	42.92	45.87	47.03	44.74
1	0-1-0	33.85	33.74	34.68	37.72	33.97
1	0-0-1	28.93	28.94	29.23	31.67	28.96
2	2-0-0	41.55	40.55	43.56	44.12	42.17
2	0-2-0	31.84	31.70	32.69	34.68	31.98
2	0-0-2	26.42	26.43	26.74	28.76	26.45
4	4-0-0	38.85	37.87	40.92	41.15	39.42
4	0-4-0	29.32	29.18	30.23	31.71	29.50
4	0-0-4	23.68	23.68	24.02	25.75	23.72
4	1-1-2	25.64	25.62	26.05	28.13	25.70
10	10-0-0	34.90	33.93	36.99	37.22	35.45
10	0-10-0	25.78	25.62	26.69	27.70	25.97
10	0-0-10	20.04	20.03	20.40	21.80	20.09
10	2-3-5	22.12	22.08	22.56	24.15	22.55
10	3-3-4	22.85	22.80	23.31	24.88	22.19
10	2-4-4	22.68	22.62	23.15	24.73	22.76
10	1-3-6	21.49	21.46	21.91	23.50	21.56
Mean		**29.05**	**28.77**	**29.94**	**31.45**	**29.27**

4.3. Investigation of watermark fragility to unacceptable distortions

The considered data embedding methods should be fragile to typical distortions corrupting image content. To verify this property, we performed median filtering and image blurring with a sliding window of size from 3×3 to 15×15, and additive white Gaussian noise with variance values from 400 to 1000. The results are presented in Figures 4, 5, and 6, respectively ($QF = 50$, the number of embedded bits per block $N_W = 4$). Since all these distortions are unacceptable, the relative extraction error (BER) should ideally be close to 0.5, which corresponds to the probability of random guessing of the correct bit.

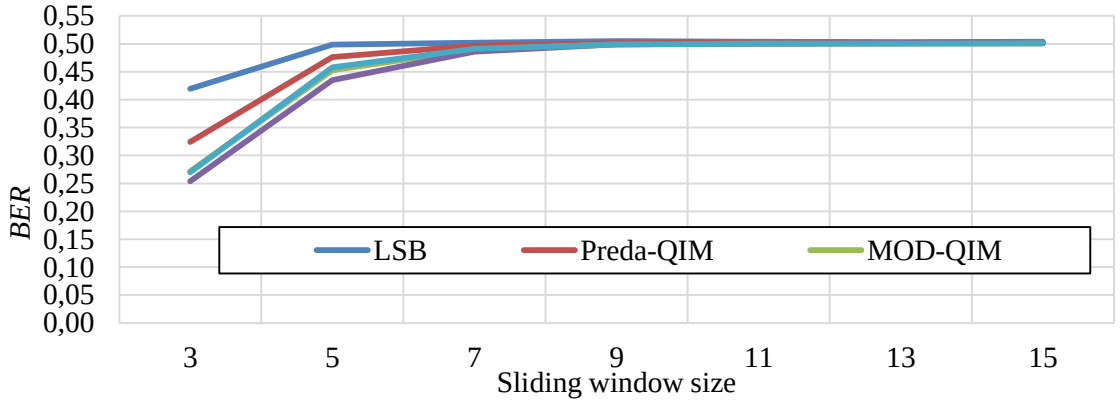

Figure 4. The effect of median filtering on the extraction error.

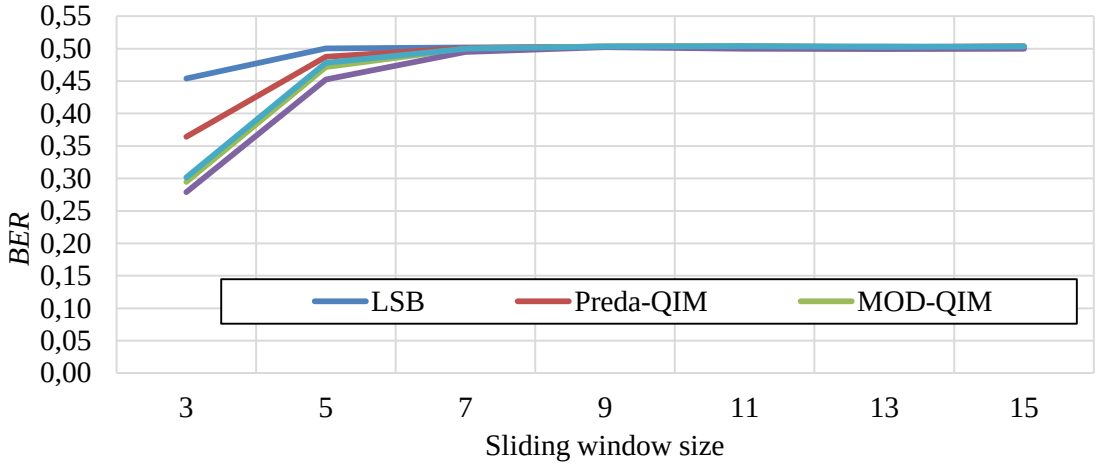

Figure 5. The effect of blur on the extraction error.

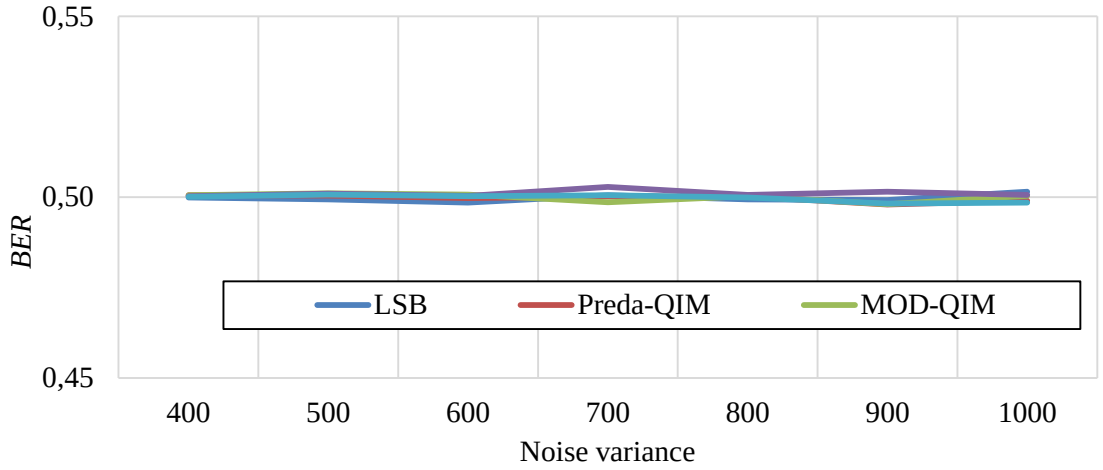

Figure 6. The effect of additive noise on the extraction error.

Figures 4-5 show that LSB slightly outperforms QIM-based methods. However, QIM-based methods also provide the *BER* that exceeds 0.4 after nonlinear and linear filtering even with a window size of 5×5, which is a very good result. With a 3×3 window, the error is also high enough, so the considered methods are fragile to the distortions. After adding noise to the watermarked image, almost all methods behave perfectly.

Thus, according to the experimental results, it can be concluded that the considered data embedding methods are fragile to these three types of distortions.

4.4. Investigation of tampering localization error

Some watermarking systems used for authentication perform content-based watermark generation aimed to raise tampering localization accuracy. One of such systems is proposed in paper [7] Preda & Vizireanu. For each block, it calculates a hash value of a pseudo-random sequence and block coordinates and uses the obtained code as a watermark. This technique protects the image from copy-move attacks. However, in this research, we did not apply any technique improving localization accuracy, because we just aimed to compare the embedding methods.

Therefore, we constructed the watermark in a pseudo-random manner, so the localization error was overestimated. Theoretically, the probability of skipping a distorted block, in this case, should be close to $1/2^N$, where N is the number of bits embedded in each block. Thus, for example, if $N_W = 4$, the percentage of error should be about 6.25%.

The dependence of the fraction of falsely detected blacks on the fraction of tampered blocks is presented in Figure 7. It illustrates that the graphs for different methods, as expected, are very close to

each other and correspond to the theoretical estimation. The only exception is MOD-QIM that provides a high error and does not depend strongly on the number of tampered blocks. Consequently, this method cannot be applied for JPEG semi-fragile watermarking.

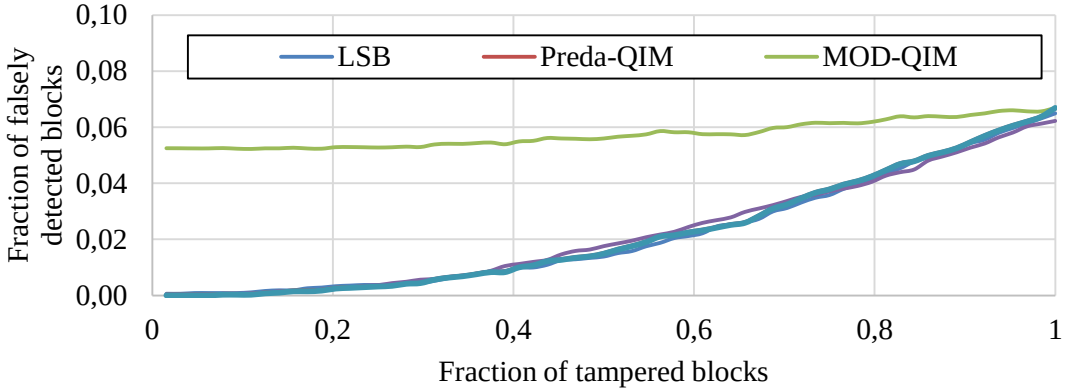

Figure 7. The influence of the number of modified blocks on the tampering localization error (the watermark is randomly generated).

5. Conclusion

In the paper, we investigated the different data embedding methods that are usually used in JPEG semi-fragile watermarking systems such as LSB and various QIM versions (MOD-QIM, Sign-QIM, and DM-QIM). The evaluation of their performance showed that all considered methods could be applied to embed a JPEG semi-fragile digital watermark in the frequency domain apart from MOD-QIM. The study of the quality of the images formed by the watermark embedding process showed the superiority of the DM-QIM method over the others. We also showed that visual distortions of the watermarked image are more visually imperceptible when the watermark is embedded in the low frequency DCT coefficients. As JPEG semi-fragile watermarks must be destroyed with any image modifications, apart from JPEG, we checked the fragility of the considered methods to the distortions: median filtering, blurring and white Gaussian noise. Finally, we carried out that the error of tampering localization coincides with theoretical value for all considered methods excluding MOD-QIM.

6. References

[1] Cox I 2008 *Watermarking and Steganography* (Morgan Kaufmann) p 624
[2] Lin C Y and Chang S F 1999 Issues and solutions for authenticating MPEG video *Proceedings of SPIE* 54-65
[3] Lin C Y and Chang S F 2000 Semifragile watermarking for authenticating JPEG visual content *Security and Watermarking of Multimedia Contents* II **3971** 140-151
[4] Ho C K and Li C T 2004 Semi-fragile watermarking scheme for authentication of JPEG images *ITCC* **1** 7-11
[5] Huang L Y 2013 Authentication watermarking algorithm resisting JPEG compression based on preliminary quantization *Information Technology Journal* **12** 3723-3728
[6] Ye S, Zhou Z, Sun Q, Chang E and Tian Q 2003 A quantization-based image authentication system *Proceedings of the 2003 Joint* **2** 955-959
[7] Preda R O and Vizireanu D N 2015 Watermarking-based image authentication robust to JPEG compression *Electronics Letters* **51** 1873-1875
[8] Wang H, Ho A and Zhao X 2011 Novel fast self-restoration semi-fragile watermarking algorithm for image content authentication resistant to JPEG compression 72-85
[9] Fan C H, Huang H Y and Hsu W H 2011 A Robust Watermarking Technique Resistant JPEG compression *J. Inf. Sci. Eng* **27** 163-180
[10] Fallahpour M and Megias D 2016 Flexible image watermarking in JPEG domain *ISSPIT* 311-316
[11] Mursi M, Assassa G M R, Aboalsamh H and Alghathbar K 2009 A DCT-based secure JPEG image authentication scheme *World Academy of Science, Engineering and Technology* **53** 681-

687
[12] Lin E T, Podilchuk C I and Delp E J 2000 Detection of image alterations using semifragile watermarks *Security and Watermarking of Multimedia Contents* II **3971** 152-164
[13] Al-Mualla M E 2007 Content-adaptive semi-fragile watermarking for image authentication *14th IEEE International Conference on Electronics, Circuits and System* 1256-1259
[14] Wong P H W, Au O C L and Wong J W C 2001 Data hiding technique in JPEG compressed domain *Security and Watermarking of Multimedia Contents* III **4314** 309-320
[15] Xiao J, Ma Z, Lin B, Su J and Wang Y 2010 A semi-fragile watermarking distinguishing JPEG compression and gray-scale-transformation from malicious manipulation *IEEE Youth Conference on Information, Computing and Telecommunications* 202-205
[16] Chen B and Wornell G 2001 Quantization index modulation: a class of provably good methods for digital watermarking and information embedding *IEEE Transaction on Information Theory* **47** 21
[17] Egorova A A and Fedoseev V A 2019 A classification of semi-fragile watermarking systems for JPEG images *Computer Optics* **43** (in print)
[18] Glumov N I and Mitekin V A 2011 A new semi-fragile watermarking algorithm for image authentication and information hiding *Computer Optics* **35(2)** 262-267
[19] Wallace G K 1992 The JPEG still picture compression standard *IEEE Transactions on Consumer Electronics* **38** xviii–xxiv
[20] Image repository *The waterloo fractal coding and analysis group* URL: http://links.uwaterloo.ca/Repository.html

Acknowledgment
The work was partly funded by the Russian Federation Ministry of Science and Higher Education within a state contract with the "Crystallography and Photonics" Research Center of the RAS under agreement 007-ГЗ/Ч3363/26 (in part of JPEG implementation) and by the RFBR grant # 18-71-00052 (in parts of review and investigations).

Defuzzification of the initial context in Formal Concept Analysis

D E Samoilov[1,2], V A Semenova[2,3] and S V Smirnov[2]

[1]Samara National Research University, Moskovskoe Shosse, 34A, Samara, Russia, 443086
[2]Institute for Control of Complex Systems of RAS, Sadovaya Str., 61, Samara, Russia 443020
[3]Samara State Technical University, Molodogvardeyskaya Str., 244, Samara, Russia, 443100

e-mail: smirnov@iccs.ru

Abstract. The research field is the problem of extracting from the initial empirical material the formal concept lattice, which can serve as the basis of the formal ontology of the studied subject domain. The initial empirical material, i.e. the data of multidimensional observations and experiments, is characterized by incompleteness and inconsistency, conditioned by realities of empirical information accumulation. This leads to the fact that required for lattice building formal context can be previously presented only within the framework of some multi-valued logic. It needs to be approximated in binary logic, since effective methods for derivation of formal concepts are developed only for unambiguous (binary) formal contexts. The exact solution of this problem, considering the properties existence constraints of objects in the studied subject domain, is difficult and in a certain sense is inadequate to expectations of subject exploring the subject domain. For defuzzification of the initial formal context heuristic was proposed, idea of which is to localize the approximation task of "soft" context within every group of dependent properties of each object of learning sample. The model reflecting such restrictions is formed as hierarchy of groups of dependent properties, which predetermines the recursive and multi-pass nature of the developed defuzzification algorithm.

1. Introduction

Standardly, protocols of observations and experiments are drawn up as tables “object-properties” (TOP) [1, 2]. Most often, TOP contains the results of measuring the values of the certain properties set of objects that are in the field of researcher view. Such TOPs are called multi-valued formal contexts (FCs) for data analysis tasks [3]. At the same time a very popular method of “object-properties” type data mining now is the formal concept analysis (FCA) [3-7], which deals only with binary (single-valued) FCs:

$$(G^*, M, I)$$

where $G^* = \{g_i\}_{i=1,\dots,r}$, $r = |G^*| \geq 1$ – is the set of observed objects: $G^* \subseteq G$, G – all hypothetically conceivable set of objects of the studied knowledge domain (KD), $M = \{m_j\}_{j=1,\dots,s}$, $s = |M| \geq 1$ – set of measurable properties of the objects; $I \subseteq G^* \times M$ – the binary relation described by the incidence matrix “object-properties”, each element of which is a truth estimate of basic semantic propositions (BSP) about the studied KD:

b_{ij} = «oobject $g_i \in G^*$ has the property $m_j \in M$»,
i.e. $I = (\|b_{ij}\|)_{i=1,\ldots,r;\, j=1,\ldots,s}$, $\|b_{ij}\| \in \{\textbf{Truth}, \textbf{False}\}$.

The main purpose of FCA is to extract clusters called formal concepts from tabular data. A partially ordered set of all formal concepts is called a lattice of concepts, which can be considered as a "skeleton" of the formal ontology of the studied KD [8-10].

A single-valued FC can be obtained by a certain granulation of the information of a multi-valued FC with help of the conceptual scales [11, 12]. Process of granulation depends on the objectives of the KD studying. This granularity generation tool is similar to the linguistic variables introduced by Zadeh [13]. Fuzzy conceptual scaling [14, 15] leads to FC of the form (1) with a fuzzy relation I. A slightly different approach to conceptual scaling that forms a fuzzy relation I was studied in [16].

In works [17-19], the genesis of a non-strict (in particular, fuzzy) FC (NFC) is considered from more general positions and is generally associated with incompleteness and inconsistency of the primary information about the studied KD. At the same time, it was established that fuzzy logic for describing "soft" correspondence of "object-properties" is less adequate than more sophisticated multi-valued logics. In [18, 19], in order to form the truth estimates of the BSP, it was proposed to use vector logic [20], namely, V^{TF} logic, which can be considered as the simplest generalization of Zadeh's fuzzy logic.

Constructive use of a NFC is based on its α-approximation, i.e. replacing in (1) fuzzy (or non-strict in the case of using vector logics) relation I with its α-section $I^{(\alpha)}$ [12, 14-19]. Unfortunately, in the general case a single-valued correspondence $I^{(\alpha)}$ in the problem of formal concept analysis turns out to be incorrect, because the standard α-section procedure does not take into account the existential dependencies between the measurable properties: incompatibility and conditionality of the objects properties of the studied KD [19, 21, 22]. A comprehensive model of a system of measurable properties (SMP) with restrictions on their existence was justified in [23, 24]. This work is devoted to the development of an algorithm for rational α-approximation of a NFC, which takes into account the complex organization of a SMP in FCA problems.

2. Truth evaluation of the propositions about the object properties

In V^{TF} logic the truth of BSP b_{ij} is estimated by the vector ⟨Truth, *False*⟩ (figure 1):

$$\|b_{ij}\| = \langle b^+_{ij}, b^-_{ij}\rangle;\ b^+_{ij}, b^-_{ij} \in [0, 1];\ (b^+_{ij} + b^-_{ij} \equiv 1) = \textbf{False}.$$

Each object of the training sample $g_i \in G^*$, $i = 1,\ldots, r$, is characterized in a NFC by the set of truth vectors $\{\|b_{ij}\|\}_{j=1,\ldots,s}$ (figure 2). V^{TF}-threshold of trust $\alpha = \langle \alpha^+, \alpha^-\rangle$ determines two regions in the existence space of truth vectors. Location of the vector $\|b_{ij}\|$ in one of these regions is interpreted as falsity, and for other region it is interpreted as truth of the corresponding BSP (figure 3). On the other hand, in the specified space for each vector $\|b_{ij}\|$ two regions are defined, location of the trust threshold α in one of them means falsity, and in the other - the truth of the BSP b_{ij} (figure 4).

3. Patterns of groups of conjugate properties

According to [23, 24], the SMP is a hierarchies set of groups of conjugate properties (GCP), which is formed as a product of subject hypothesizing about the structure of the conceptual description of the studied KD. Each GCP hierarchy is formed by replacing in a supergroup one or more measurable properties with a subgroup of such properties. The highest supergroup in the GCP nesting hierarchy is proto-property, the lower subgroups in the hierarchy are the "leafy" GCP, that are matched to measured properties.

In [23, 24] it was established that there are three and only three basic patterns of subgroups (subGCP) that replace one property in a supergroup:

- a group of two measurable properties, in which one property *conditiones* another;
- a group of $n > 1$ *incompatible* measurable properties;
- a group of $n > 1$ mutually conditioned properties.

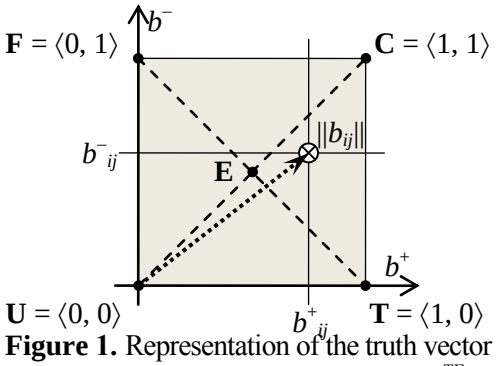

Figure 1. Representation of the truth vector $\|b_{ij}\| = \langle b^+_{ij}, b^-_{ij} \rangle$ and truth constants of V^{TF} logic «True», «False», «Uncertainty», «Contradiction», «Equivocal» (**T**, **F**, **U**, **C**, **E**).

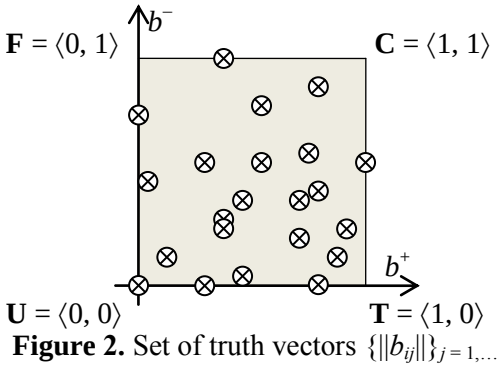

Figure 2. Set of truth vectors $\{\|b_{ij}\|\}_{j=1,\ldots,s}$, characterizing in a non-strict formal context BSP about object $g_i \in G^*$.

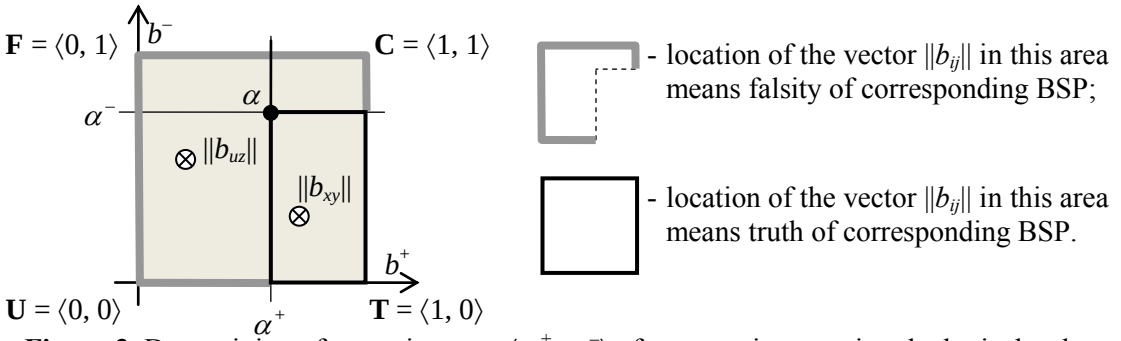

Figure 3. Determining of α-section; $\alpha = \langle \alpha^+, \alpha^- \rangle$ of a non-strict set using the logical order (or verisimilitude) for truth vectors in V^{TF} logic: $\|b_{xy}\| > \alpha$, if $b^+_{xy} \geq \alpha^+$, $b^-_{xy} \leq \alpha^-$.

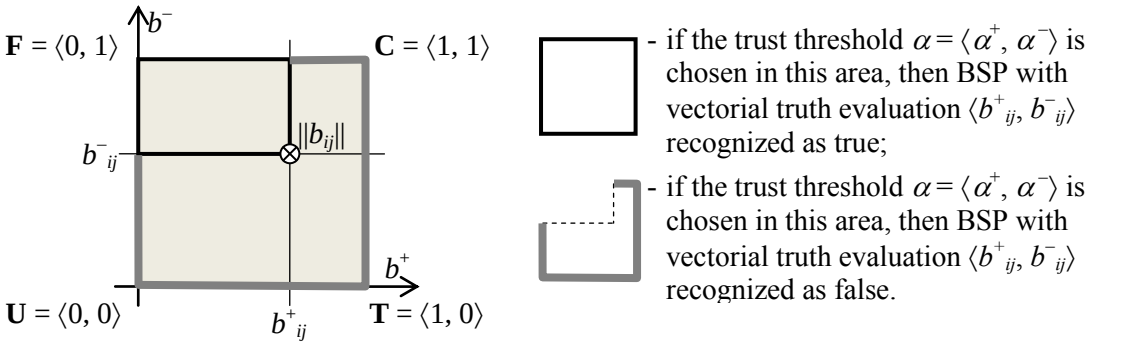

Figure 4. Regions of choice of the trust threshold for the source data $\alpha = \langle \alpha^+, \alpha^- \rangle$, determining the approximate truth estimate in the scale {**True**, **False**} of the BSP, which vectorial truth estimation is $\langle b^+_{ij}, b^-_{ij} \rangle$.

The nature of properties conjugacy in such GCP can be clearly reflected in the existence space of truth vectors by connecting its points with appropriate arcs (figure 5a-c).

Similarly can be represented two complex patterns of subgroups, which replace several properties in a supergroup according to fixed rules (only in supergroups, where all properties are mutually conditioned):

- a group of properties with several conditionalities (figure 6a);
- a group of properties with several incompatibilities and conditionalities (figure 6b).

4. Rational α-section of a non-strict formal context

So, in order to apply effective FCA methods to extract formal concepts from a NFC, it is necessary to ensure its correct α-approximation in the presence of properties existence constraints (PEC).

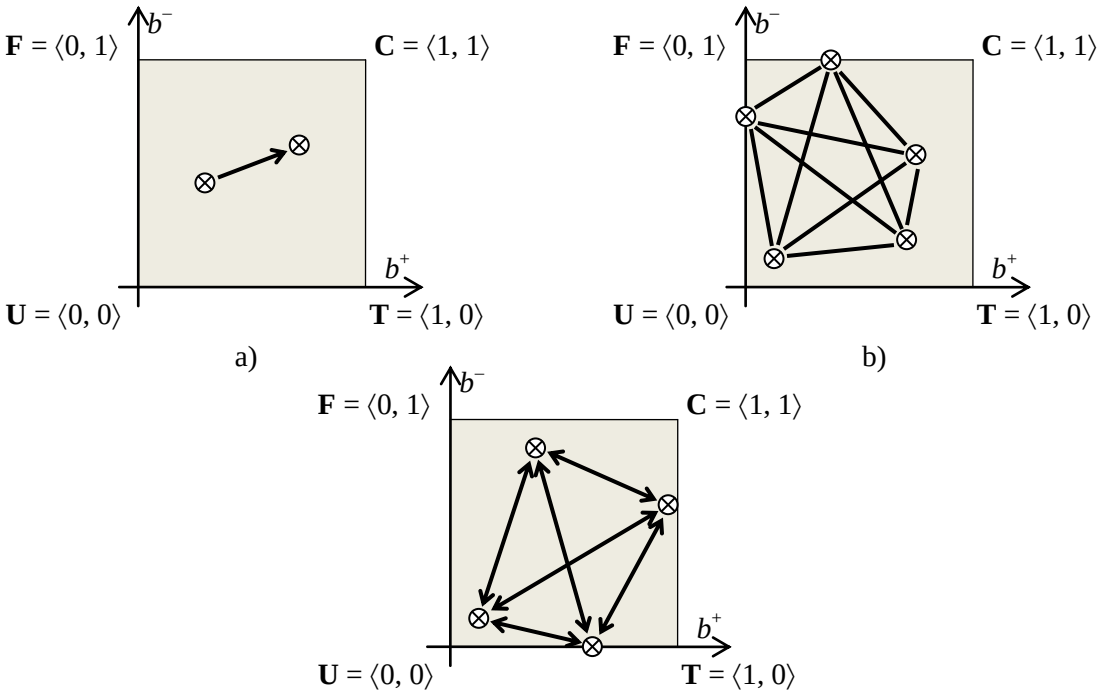

Figure 5. Examples of combined diagrams of properties conjugacy and truth estimates of BSP corresponding to these properties for *basic* GCP patterns: (a) a group where one property conditiones another (C-group); (b) a group of incompatible properties (I-group); (c) a group of mutually conditioned properties (MUC-group).

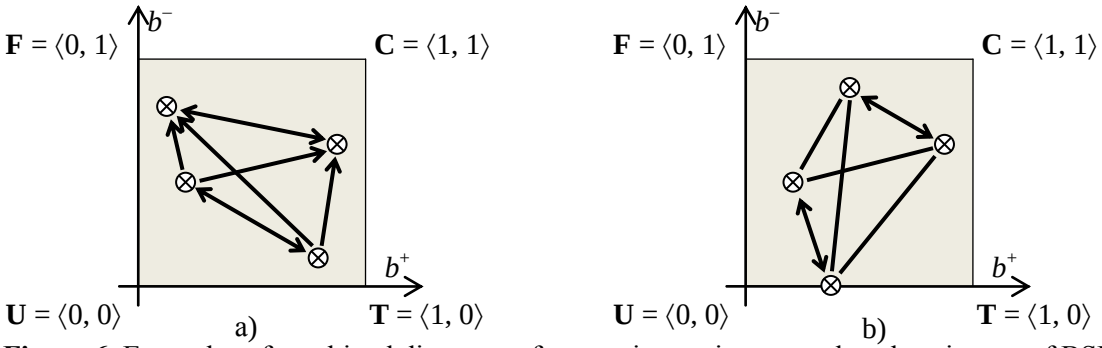

Figure 6. Examples of combined diagrams of properties conjugacy and truth estimates of BSP corresponding to these properties for *mixed* GCP patterns (M-group): (a) a group that includes subGCP-pairs of properties with conditionalities (C-pairs); (b) a group including subGCP-pairs of properties with incompatibilities (I-pairs) and C-pairs.

4.1. Search of region of acceptable values of the trust threshold for the source data

Formally, the problem can be reduced to constructing a single predicate "α-section is correct" with a vectorial argument $\alpha = \langle \alpha^+, \alpha^- \rangle$, $\alpha^+, \alpha^- \in [0, 1]$, where condition for confirming the truth of each empirical BSP b_{ij}:

$$b^+_{ij} \geq \alpha^+ \wedge b^-_{ij} \leq \alpha^-$$

(or, on the contrary, the necessary falsity of this BSP) should be combined with the implementation of all relevant PEC. And then find the region (possibly, it will be empty) of existence of trust thresholds α that deliver the value **True** to such predicate.

In the general case, to build such predicate and identify the specified region is very difficult; an example of constructing such predicate for the case when PEC is caused by incompatibility of some part of measurable properties can be found in [25]. However, even assuming the possibility of such a

decision, it is very *impractical* to bind the subject who studies the KD with a need to select a threshold only from *a limited region*. For example, with this approach the subject may not meet the intuitive expectations from softening or tightening the trust threshold for the data representing the KD [25].

4.2. *Heuristic approach*

Instead of the described search the following heuristic is proposed:

- the subject is free to choose a threshold (the choice of α-threshold is *arbitrary*);
- determined by a threshold α and, in general, the unacceptable composition of *each* object properties of the sought-for single-valued FC (in figure 2 this corresponds to the emphasizing of part of estimates $\|b_{ij}\|$ according to the rule illustrated by figure 3) should be consistently reduced due to the sequential cutting off of properties that violate PEC;
- the cut-off mechanism consists in local tightening of the trust threshold within each GCP in the SMP.

For unambiguous choice of "best" among trust thresholds - $\beta = \langle \beta^+, \beta^- \rangle$, - which tighten the threshold α chosen by the subject and provide the necessary reduction of the GCP composition of the object $g_i \in G^*$, following criterias are proposed (figure 7):

- *tightening vector length (in a rectangular metric)*
$$|\beta^+ - \alpha^+| + |\beta^- - \alpha^-| = (\beta^+ - \alpha^+) + (\alpha^- - \beta^-) \to \mathbf{min};$$
- *truth region area* of the tightened trust threshold
$$(1 - \beta^+) \times \beta^- \to \mathbf{max};$$
- *reliability* [20] of the tightening vector ("in coordinates of the tightening")
$$t_{\beta^+} - t_{\beta^-} = (\alpha^- - \beta^-) - (\beta^+ - \alpha^+) \to \mathbf{max}.$$

The first and third criterias define two manifolds that are mutually perpendicular segments (figure 7). This fact guarantees an unambiguous choice of β at consistent application of criterias for the reduction of GCP members.

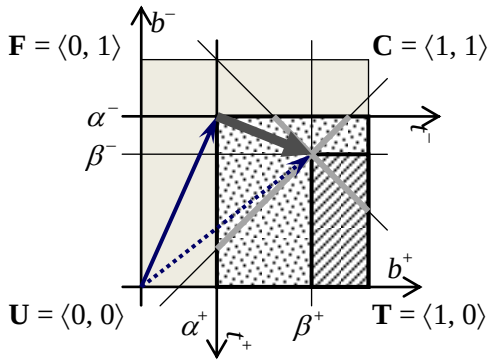

Figure 7. The vector tightening (bold arrow) which sets the shift of trust threshold $\alpha = \langle \alpha^+, \alpha^- \rangle$ by threshold $\beta = \langle \beta^+, \beta^- \rangle$; ⊡ – the truth region of threshold α, ▨ – the truth region of threshold β.

The proposed heuristic method for obtaining the correct unambiguous approximation of a NFC is *effective*.

Indeed, the method is implemented for each object of the training sample *separately*, and at some step one of following conditions will arise:

- either the properties set of an object g_i begins to satisfy PEC (note that an empty set of properties satisfies such constraints, but then an object with such properties "set" must be qualified as unidentified by introducing a new property "unidentified object" into the sought-for FC);
- or it will be stated that there is a *ineradicable contradiction* between the initial context and PEC: there are BSP about object g_i with the truth estimate $\|b_{ij}\| = \langle 1, 0 \rangle$ (i.e. true in classical two-valued logic), but violating PEC.

4.3. *Defuzzification algorithm of a non-strict formal context*

The algorithmization complexity of proposed heuristics is due to the multi-hierarchical structural organization of the SMP [23, 24] - q.v. Section 3. At the same time, it is clear that the work begins with the input by a subject of the trust threshold for the source data $\alpha = \langle \alpha +, \alpha - \rangle$ that suits him and performing the standard α-section of the correspondence "object-properties" of a NFC. The algorithm core is the correction cycle of the obtained α-approximation of a NFC, performed for each object $g_i \in G^*$. Therefore, in the further description of "corrective steps" we will omit the mention of the object being processed, implying by default this uniqueness characteristic of the considered GCPs. But first we note the following:

- A GCP is excluded from the desired FC when all nested GCP (and all "leafy" sub-GCP which are matched to measured properties) are excluded from it. The local (for the GCP) trust threshold for the source data that implements such an *elimination* will be called the *absence*-, or GCP *a*-threshold (figure 8);
- A GCP will be included in the desired single-valued FC if it retains/preserves at least one GCP in it (and, therefore, at least one "leafy" sub-GCP associated with the measured property). The local (for the GCP) trust threshold for the source data that implements such an *inclusion* will be referred to as the GCP *presence*- or *p*-threshold (figure 9).

The NFC defuzzification will be completed when each GCP in the SMP will have its own value of *p*-threshold. For the object $g_i \in G^*$ in the desired single-valued FC, only those BSP will be recognized as true which are related to the measurable properties matched to the preserved "leafy" GCP.

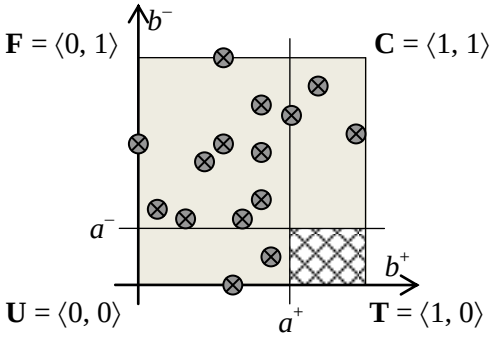

Figure 8. Definition of GCP *a*-threshold $\langle a^+, a^- \rangle$: ▨ – truth region of *a*-threshold; ⊗ – eliminated truth vectors of BSPs corresponding to the measured properties, which (in turn) are matched to the "leafy" subGCP of the excluded GCP.

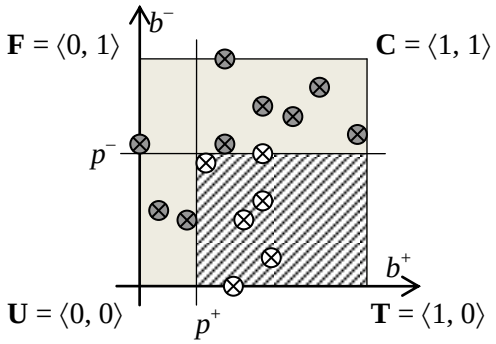

Figure 9. Definition of GCP *p*-threshold $\langle p^+, p^- \rangle$: ▨ – truth region of *p*-threshold; ⊗ – eliminated and ⊗ – retained truth vectors of BSP corresponding to the measured properties, which (in turn) are matched to the "leafy" subGCP of the considered GCP.

4.3.1. Detection of GCP a-thresholds

At the first step of the correction cycle *heuristically optimal* a-threshold of *each* GCP is detected.

For the GCP, the recursive identification of all its "leafy" subGCPs mapped to the measured properties is implemented, and an actual set of truth vectors of the corresponding BSPs which are saved as a result of standard NFC α-section is generated.

Of course, the actual set of GCP truth vectors may turn out to be empty (figure 10), and, therefore, the considered GCP is excluded from the desired FC as a result of the standard α-section of a NFC. In this case, the identification of the optimal GCP a-threshold does not make sense, and some "disabling" of the GCP *p*-threshold may be a sign of this GCP cut-off. Assigning to *p*-threshold abscissa a negative value may serve as example of such disabling.

The heuristically optimal GCP *a*-threshold can be detected only with a non-empty actual set of GCP truth vectors, and, as it is not difficult to understand, the members of the southeast Pareto-front of this set will serve as reference vectors for determining the optimal GCP *a*-threshold (figure 11). GCP *a*-threshold itself should be searched (for example, by brute force) at the intersection of lines which are parallel to the coordinate axes and passing through the reference vectors (see rhombs in figure 11):

- intersections of lines $x = b^+_X$ and $y = b^-_Y$, respectively, of the first and second members of each pair of neighboring truth vectors $\langle b^+_X, b^-_X\rangle$ и $\langle b^+_Y, b^-_Y\rangle$ of the Pareto-front;
- the intersection of the $x = b^+_N$ line of the "northern" truth vector $\langle b^+_N, b^-_N\rangle$ of the Pareto-front with the $y = \alpha^-$ line;
- the intersection of the $y = b^-_S$ line of the most "southern" – the truth vector $\langle b^+_S, b^-_S\rangle$ of the Pareto-front with the $x = \alpha^+$ line.

An intersection that is "best" in terms of the proposed criterias is accepted as the heuristically optimal GCP *a*-threshold. In the further analysis of the data, it is taken into account that indeed optimal GCP *a*-threshold is more plausible, but it infinitely small differs from the heuristically optimal one.

4.3.2. Detection of GCP p-thresholds

At the second (and final) step of the correction cycle, *a heuristically optimal p*-threshold of *each* GCP is detected. The main work is performed by:

- a recursive procedure of local GCP correction (with the detection of its heuristically optimal *p*-threshold). One of the procedure input parameters is the "current *p*-threshold";
- a recursive procedure of GCP exclusion from the desired FC (with the disabling of its *p*-threshold).

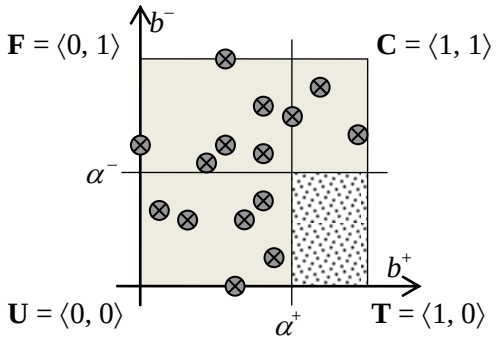

Figure 10. Elimination of GCP from the desired FC as a result of the standard α-section of the source context (the designation of the region and the truth vectors is the same as in figures 7 and 8).

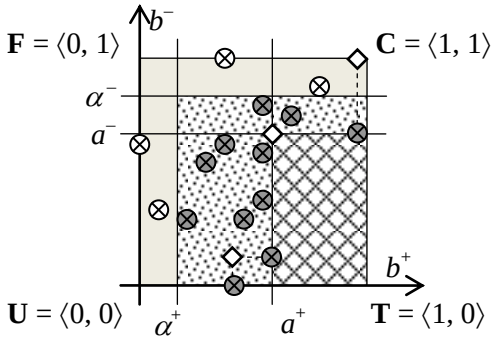

Figure 11. Determination of the optimal GCP a-threshold based on the reference truth vectors and their "intersections" (the designation of vectors and trurh regions is the same as in figures 8-10).

The first procedure is sequentially launched for the "root" GCP with the current threshold equal to α. Recursively, possibly with reiteration of passes, it performs correction of the "root" GCP and all its subGCP. The second procedure plays an auxiliary role in execution of the first one, but exactly at an attempt to exclude the GCP ineradicable contradiction of the initial context and PEC can be found (q.v. Subsection 4.2).

Let's explain these actions.

In relation to any GCP, the trust threshold for the data $\beta = \langle \beta^+, \beta^-\rangle$ either excludes or retains it in the desired FC.

In the first case, GCP *p*-threshold is disabled (i.e., the GCP exclusion from the desired FC is fixed) and, if the GCP is not "leafy", *p*-thresholds of all embedded subGCPs of the considered GCP are disabled.

In the second case, if the given GCP is "leafy", then the *p*-threshold is equal to β. Otherwise, the execution of local PEC is checked at threshold β:

- first, all embedded sub-GCPs of the considered GCP are corrected recursively (with detection of *p*-thresholds);
- secondly, *according to the rules that depend on the type* of a given GCP, its *p*-threshold is revealed.

Here are these rules:

- GCP – MUC-group (see figure 5c). If at least one subGCP has a *p*-threshold disabled, then *p*-threshold of the MUC-group and *p*-thresholds of all its subGCP are disabled. Otherwise, the *p*-threshold of the MUC-group is set to β;
- GCP – C-group or C-pair (see figure 5a or figure 6). If the conditioned subGCP is excluded, then the *p*-thresholds of the C-group/C-pair and the conditioning subGCP are disabled. Otherwise, the *p*-threshold of the C-group/C-pair is set to β;
- GCP – I-group or I-pair (see figure 5 and figure 6b). All non-excluded subGCP are incompatibility *violators*. From violators we select subGCP with a "best" (from the position of the proposed criterias) *a*-threshold, which is assigned as new β. Correction of the considered I-group/I-pair is repeated. Reiterations continue as long as two or more non-excluded subGCPs retain. As a result, the *p*-threshold of the I-group/I-pair will be either disabled or equated to the current β.
- GCP – M-group (see figure 6). Members which violates conditionality and incompatibility (i.e. certain subsubGCP) are selected from non-excluded subGCP-pairs. Then subsubGCP with the "best" *a*-threshold is selected from them and this a-threshold is assigned as new β. Correction of the considered M-group is repeated. Reiterations continue as long as there are violators. As a result, the *p*-threshold of the M-group will be either disabled or equated to the current β.

5. Conclusion

The proposed heuristic method and the developed algorithm of defuzzification of the initial context allows one to take into account the complex organization of the SMP of the studied KD in problems of the FCA. The obtained result "closes" the main section of the hypothetical-deductive theory of ontological data analysis developed by authors [17-19, 23-25].

It is important to study the effectiveness of the developed algorithm depending on the parameters characterizing the SMP of the studied KD and the initial non-strict context of FCA problem.

The presented method and algorithm are focused on the unambiguous approximation of non-strict formal contexts and the derivation of "crisp" concepts. A promising task is the development of an appropriate method and algorithm, the end result of which is a system of "fuzzy" concepts.

6. References

[1] Barsegyan A A, Kupriyanov M S, Holod I I, Tess M D and Elizarov S I 2009 *Data and Process Analysis* (St. Petersburg: BHV-Petersburg)
[2] Zagoruyko N G 2013 *Cognitive data analysis* (Novosibirsk: Sobolev Institute of Mathematics, SB RAS)
[3] Ganter B and Wille R 1999 *Formal Concept Analysis. Mathematical foundations* (Springer-Verlag Berlin-Heidelberg)
[4] Formal Concept Analysis Homepage URL: http://www.upriss.org.uk/fca/fca.html (15.05.2019)
[5] Ganter B and Obiedkov S 2016 *Conceptual Exploration* (Springer-Verlag Berlin Heidelberg)
[6] Ignatov D I 2015 Introduction to Formal Concept Analysis and Its Applications in Information Retrieval and Related Filds *Information Retrieval. Revised Selected Papers 8th Russian Summer School* (Nizhniy Novgorod, Russia, Springer International Publishing) 42-141
[7] Carpineto C and Romano G 2004 *Concept Data Analysis: Theory and Applications* (Wiley)
[8] Obitko M, Snasel V and Smid J 2004 *Proc. of the CLA 2004 International Workshop on Concept Lattices and their Applications* (Ostrava, Czech Republic) 111-119
[9] Smirnov S V 2001 Ontological analysis of modeling domain *Bulletin of the Samara Scientific Center of RAS* **3** 62
[10] Godin R, Mili H, Mineau G W, Missaoui R, Arfi A and Chau T T 1998 Ontology Design with Formal Concept Analysis *Theory and Application of Object Systems (TAPOS)* **4(2)** 117
[11] Ganter B and Wille R 1989 Conceptual scaling *Applications of Combinatorics and Graph Theory to the Biological and Social Sciences* (New York Springer-Verlag) 139
[12] Wolff K E 1998 Conceptual Interpretation of Fuzzy Theory *6th European Congress on Intelligent Techniques and Soft Computing* (Germany, Aachen) **1** 555-562

[13] Zadeh L A 1975 The concept of a linguistic variable and its application to approximate reasoning *Information Science* **8** 199 (Part I), **8** 301 (Part II), **9** 43 (Part III)
[14] Belohlavek R and Konecny J 2007 Scaling, Granulation, and Fuzzy Attributes in Formal Concept Analysis *The IEEE International Conference on Fuzzy Systems* (London) 918
[15] Yang K M, Kim E H, Hwang S H and Choi S H 2008 Fuzzy Concept Mining based on Formal Concept Analysis *Int. J. of Computers* **2** 279
[16] Pollandt S 1996 *Fuzzy-Begriffe: Formale Begriffsanalyse unscharfer Daten* (Springer-Verlag Berlin Heidelberg)
[17] Smirnov S V 2007 Fuzzy formal contexts in building of ontologies based on the formal concepts analysis: genesis and use *Proc. All-Russian Conf. "Knowledge–Ontologies–Theories"* (Novosibirsk, Sobolev Institute of Mathematics, SB of RAS) **2** 17-25
[18] Smirnov S V 2014 Multi-valued and fuzzy logic in ontological data analysis *Proc. 3rd Int. scientific conf. "Information technology and systems"* (Publishing House of Chelyabinsk State University) 90-91
[19] Semenova V A and Smirnov S V 2016 Intelligent analysis of incomplete data to building formal ontologies *CEUR Workshop Proceedings* **1638** 796-805
[20] Arshinskii L V 2007 Substantial and formal deductions in logics with vector semantics *Automation and Remote Control* **68(1)** 139
[21] Pronina V A and Shipilina L B 2009 Using relationships between attributes to build a domain ontology *Control sciences* **1** 27
[22] Lammari N and Metais E 2004 Building and maintaining ontologies: a set of algorithms *Data & Knowledge Engineering* **48(2)** 155
[23] Samoylov D E, Semenova V A and Smirnov S V 2018 Multilevel recursive model of properties existence constraints in machine learning *Journal of Physics: Conf. Series* **1096** 012096
[24] Samoylov D E, Semenova V A and Smirnov S V 2018 The structure of measured properties system for objects of multidimensional observation and experiments *Bulletin of the Samara State Technical University Series "Technical Sciences"* **3(59)** 56
[25] Ofitserov V P, Smirnov V S and Smirnov S V 2014 Method of the alpha-section of non-strict formal contexts in the formal concepts analysis *Proc. of the 16th Int. Conf. Problems of Control and Modeling in Complex Systems* (Samara: Samara Scientific Center of RAS) 228

Forecasting using predictor selection from a large set of highly correlated variables

A Yu Timofeeva[1] and Yu A Mezentsev[1]

[1]Novosibirsk State Technical University, K. Marksa Avenue, 20,Novosibirsk, Russia 630073

e-mail: a.timofeeva@corp.nstu.ru

Abstract. The potential of correlation-based feature selection has been explored in selecting an optimal subset from a set of highly correlated predictors. This problem occurs, for example, in time series forecasting of economic indicators using regression models on multiple lags of a large number of candidate leading indicators. Greedy algorithms (forward selection and backward elimination) in such cases fail. To obtain the globally optimal solution, the feature selection problem is formulated as a mixed integer programming problem. To solve it, we use the binary cut-and-branch method. The results of simulation studies demonstrate the advantage of using the binary cut-and-branch method in comparison with heuristic search algorithms. The real example of the selection of leading indicators of consumer price index growth shows the acceptability of using the correlation-based feature selection method.

1. Introduction

Big data analytics includes the feature selection task [1, 2] for predictive modelling [3]. In many practical applications, candidate predictors correlate strongly. An example is the task of time series forecasting using leading indicators [4].

Lagged predictors are highly correlated. Fast and scalable univariate feature selection methods are not suitable under a given situation. They evaluate features individually, so the final subset includes many redundant strongly correlated features.

Multivariate methods take into account feature dependencies and try to discard not only irrelevant variables (which do not affect the response), but also redundant ones. Most often, the predictors are selected simultaneously with the construction of predictive models using embedded methods such as LASSO regression [4, 5]. It provides a sparse solution that includes only relevant features, which, however, is very sensitive to the regularization parameter.

In addition, stepwise regression is often used in time series forecasting [6]. It refers to the so-called "wrapper" methods. They select the optimal subset of features from all possible candidates simultaneously with the model estimation. Generally, this problem has exponential complexity in the number of features. In practice, to solve it, search approaches use greedy algorithms [7]. However, they do not usually produce an optimal solution, but approximate a globally optimal solution in a reasonable amount of time.

Finally, filter methods select variables regardless of the model. A Correlation-based Feature Selection is a well-known multivariate filter algorithm [8]. This approach is proposed for solving

classification problems. Its applicability for predictor selection with a highly correlation of candidate predictors, in particular when selecting leading indicators, is poorly studied. This is the gap that we will attempt to address in our article. For this purpose, we first transform a correlation-based heuristic evaluation function optimization problem into a mixed integer programming problem. But in this problem the number of variables and constraints depends on the square of the number of features. With a branch and bound algorithm, the amount of computation becomes large. Therefore it is proposed to use the previously developed binary cut-and-branch method.

2. Correlation-based Feature Selection

Correlation-based Feature Selection (CFS) ranks feature subsets according to a correlation-based heuristic evaluation function [8]. The best subset contains predictors highly correlated with the response, yet uncorrelated to each other. Thus, the problem of feature selection is formulated as the following optimization problem:

$$\frac{\sum_{i \in S_k} R_i}{\sqrt{k + 2 \sum_{i,j \in S_k, i \neq j} r_{ij}}} \to \max_{S_k}, \tag{1}$$

where R_i is an absolute value of correlation coefficient between the response and the *i*-th feature, r_{ij} is an absolute value of correlation coefficient between the *i*-th and the *j*-th features, S_k is a subset of *k* features.

As for the time series of economic indicators, both the response and the predictors are usually quantitative. Therefore the Pearson product-moment correlation coefficient is applicable.

We reformulate the problem (1) as a problem of nonlinear integer programming:

$$\frac{\sum_{i-1}^{n} R_i^2 x_i + 2 \sum_{i \neq j} R_i R_j x_i x_j}{\sum_{i-1}^{n} x_i + 2 \sum_{i \neq j} r_{ij} x_i x_j} \to \max_{x_1, \ldots, x_n}, \tag{2}$$

where $x_i \in \{0,1\}, i = 1,...,n$, n is the number of features. If $x_i = 1$ then the optimal subset contains the *i*-th variable, and $x_i = 0$, otherwise.

The problem (2) is a polynomial fractional programming problem. Based on the transformation of feature selection problem proposed in [9], we replace the denominator in (2) by a positive continuous variable *u*. It leads to the equivalent polynomial problem. In addition, we convert a maximization problem into a minimization one. Thus, the problem is represented as follows:

$$-\sum_{i-1}^{n} R_i^2 x_i u - 2 \sum_{i \neq j} R_i R_j x_i x_j u \to \min_{x_1, \ldots, x_n, u}$$

$$\sum_{i-1}^{n} x_i u + 2 \sum_{i \neq j} r_{ij} x_i x_j u = 1,$$

$$u > 0,\ x_i \in \{0,1\}.$$

Based on a linearization technique proposed in [10] to transform the terms $x_i u$, $x_i x_j u$, we introduce variables z_i, $i = 1,...,n$, v_{ij}, $i = 1,...,n$, $j = 1,...,n$, $i \neq j$. Then we obtain the following mixed integer linear programming problem:

$$-\sum_{i-1}^{n} R_i^2 z_i - 2 \sum_{i \neq j} R_i R_j v_{ij} \to \min_{\substack{x_1, \ldots, x_n, u, \\ z_1, \ldots, z_n, v_{11}, \ldots, v_{nn}}} \tag{3}$$

$$z_i \geq 0,\ v_{ij} \geq 0,\ u > 0,\ x_i \in \{0,1\},$$

$$\sum_{i-1}^{n} z_i + 2 \sum_{i \neq j} r_{ij} v_{ij} = 1,$$

$$M\left(x_i-1\right)+u\le z_i\le M\left(1-x_i\right)+u,\ z_i\le Mx_i,$$
$$M\left(x_i+x_j-2\right)+u\le v_{ij}\le M\left(2-x_i-x_j\right)+u,\ v_{ij}\le Mx_i, v_{ij}\le Mx_j,$$

where M is a large positive value.

Finally, the initial nonlinear problem (1) is reduced to a high-dimensional linear programming (LP) problem. The number of the new continuous variables is $(n^2+n+2)/2$. They are added to the initial n binary variables. The number of constraints also depends on n^2 and is $(2n^2+n+2)$.

3. Binary cut-and-branch method

The binary cut and branch method (BCBM) was originally developed to solve LP problems with Boolean variables [11] and then extended to the case of the General linear programming problem with mixed variables (milp) [12]. Any such problem, the special case of which is (3), can be represented as:

$$\gamma(x)=c^{1T}x+c^{2T}y+const\to\max, \tag{4}$$
$$A^1x+A^2y\le b,\ \bar{0}\le x\le\bar{1},\ y\ge\bar{\bar{0}}, \tag{5}$$
$$x\in I_2^{n^1}, \tag{6}$$

which is a milp problem with Boolean variables x and continuous variables y. Conditions (3) specify that the solution components x belong to one of the vertices of the unit hypercube of dimension n^1; $c^1, x, \bar{0}, \bar{1}$ are vectors of the same dimension; $\bar{0}$ is a zero vector; $\bar{1}$ is a vector of ones; *const* is a constant; and $c^1\ge\bar{0}$. The vectors $c^2, y, \bar{\bar{0}}$ have dimension n^2. Condition $x\in I_k^n$ indicates that x belongs to the set of vectors of dimension n, the elements of which take integer values from the range $[0\div k-1]$. Conformity of statements (4-6) and (3): Boolean variables $x\in I_2^{n^1}$ have the same meaning in both statements, continuous variables $y\ge\bar{\bar{0}}$ have the meaning of variables $z_i\ge 0, v_{ij}\ge 0, u>0$ in statement (3). Matrices A^1 and A^2 in the constraints (4) are formed from the coefficients of the constraints in the problem (3).

In fact, any milp problem and a considerable part of mip problems can be compactly reduced to (1)–(3); see, e.g., [11].

Suppose x^0, y^0 is the solution of the relaxed problem (4)–(5); $[\cdot]$ is the integer part of number; and $\beta_0=\hat{\alpha}^Tx^0$, where $\hat{\alpha}_j\in\{0,\ 1\}$, $j=\overline{1,n}$. Then any inequality of the form

$$\hat{\alpha}^Tx\le\hat{\beta}_0,\ \hat{\alpha}_j\in\{0,\ 1\},\ j=\overline{1,n},\ \hat{\beta}_0=[\beta_0],\ \beta_0=\hat{\alpha}^Tx^0, \tag{7}$$

is called a binary cut (BC) for problem (4)–(5).

If x^0 is part of the solution x^0, y^0 of the relaxed problem (4)–(5), then

$$\varsigma^Tx\le\phi_0,\ \phi_0=\varsigma^Tx^0. \tag{8}$$

Relation (8) can be a generating inequality if $\varsigma_j=\sum_{i\in I^B}\lambda_ia_{ij}$, $\lambda_i\ge 0$, where $a_{ij}, i\in I^B$ are the coefficients of the basis part A^1 and λ_i are the weights of the basis constraints. Specifically, if λ_i are dual estimates for constraints (5), then $\varsigma_j=c_j$, $j=\overline{1,n}$. A complementary system of BCs to constraints (5) is defined as

$$\mathrm{A}^{1D}x\le\beta, \tag{9}$$

where $\mathrm{A}^{1D}=\left\|\hat{\alpha}_j^i\right\|_{m^D\times n^1}$, $\hat{\alpha}_j^i\in\{0,\ 1\}$, $j=\overline{1,n}$ is the coefficient matrix of the complementary system and the vector β composed of the right-hand part of the constraints is defined from (7).

There are several ways to find out whether the BCs are valid [9,10]. Specifically, the binary cut and branch algorithm (BCBA) uses the following feature. We now define

$$\bar{\alpha}^T x \geq \beta(x^0)+1, \tag{10}$$

where $\beta(x^0)=\left[\bar{\alpha}^T x^0\right]$ and x^0 is part of the optimal solution x^0, y^0 of problem (4), (5), and (9).

If problem (4), (5), and (10) has a solution, then the cut $\bar{\alpha}^T x \leq \beta(x^0)$ is invalid. Contrary wise, if problem (4), (5), and (10) has no solution due to the conflicting conditions (5) and (10), then $\bar{\alpha}^T x \leq \beta(x^0)$ is a valid BC. This is the underlying feature of the BC synthesis procedure called *selection in a set of the nearest cuts* (SSNC) [11, 12]. We now describe this procedure.

We define an inequality ensuing from the basis system (5) and (9) through a permutation by arranging ς in a descending order (denoted by $\vec{\varsigma}$). We consider a totality of n^1 vectors, of dimension n^1:

$$\bar{\alpha}^1=(1,0,...,0),\ ...,\ \bar{\alpha}^j=(1,1,...,1,0,0,...,0)\ (\ j\ \text{original ones}),\ ...,\ \bar{\alpha}^{n^1}=(1,1,...,1).$$

Each $\bar{\alpha}^j$ is set in correspondence with the value $cs(\bar{\alpha}^j)=\dfrac{\vec{\varsigma}^T\bar{\alpha}^j}{|\varsigma|_2\left|\bar{\alpha}^j\right|_2}$, $j=\overline{1,n^1}$.

The discrete function $cs(\bar{\alpha}^j)$ has a strict maximum and uniquely defines the priority of each of the alternative cuts with the coefficients $\bar{\alpha}^j$. Adding the entire totality of these BCs to (9) and solving (4), (5), and (10), we can find out conflicting conditions (if there are any) to identify valid cuts. Then, if there are valid BCs, we select a single cut with the maximum value of $cs(\bar{\alpha}^j)$. If there are no valid cuts, we select a BC that corresponds to the maximum of $cs(\bar{\alpha}^j)$, $j=\overline{1,n^1}$.

Another important feature of BCs is their radicality measure, which characterizes the depth of a cut of a given type. For a BC $\bar{\alpha}^T x\leq\bar{\beta}_0$, $\bar{\alpha}_j\in\{0,1\}$, $j=\overline{1,n}$, $\bar{\beta}_0=[\beta_0]$, $\beta_0=\bar{\alpha}^T x^0$, we define the radicality r as the number of vertices of the unit hypercube cut off by the BC (BC system), assuming that the cut is valid.

In the general case, $\hat{a}^T x\leq b$, $b\in I_k^1, x\in I_2^{n^1}, \bar{a}\in I_2^{n^1}$, $k=\sum_{j=1}^{n^1}\bar{a}_j, 1\leq k\leq n^1$ or $\sum_{j=1}^{n^1}\bar{a}_j x_j\leq b, x_j\in I_2^1, j=\overline{1,n^1}$, where $\bar{a}_j\in\{0,1\}$ are the cut-off coefficients.

For an arbitrary $b\in I_1^k$, $k=\sum_{j=1}^{n^1}\bar{a}_j, 1\leq k\leq n^1$, and $C_k^l=\dfrac{k!}{l!(k-l)!}$, we define

$$r_k^b=2^{n^1-k}\sum_{l=b+1}^{k}C_k^l\to\max \tag{11}$$

Relation (11) considers the unit hypercube vertices lying above the level $\hat{a}^T x\leq b$, i.e., belonging to the hyperplanes $\hat{a}^T x=l$ with the right-hand parts ($b+1, b+2, ..., k$). The $\hat{a}^T x=b$ hyperplane itself contains $2^{n^1-k}C_k^b$ vertices. The *maximum radical BC* is derived from (11) and $\bar{\alpha}_j=1, j=\overline{1,n^1}$ with the possible exclusion of the minimum order relative to $\vec{\varsigma}$ if the sum of the coefficients in the left-hand part of the BC $\hat{a}^T\tilde{x}\leq b$ without this exclusion is an integer number.

Regardless of which measure—closeness to the generating inequality or radicality is considered as a priority, the BCBA is as follows.

3.1. Binary Cut-and-Branch Algorithm

1. Suppose that we have obtained the solution of the original relaxed problem (4), (5), and (7): x^0, y^0 and $\gamma(x^0, y^0)$. If x^0 are integers, the algorithm stops. Otherwise, it goes to step 2.

2. At step $t(1,2,...)$, we select a probing vertex with the maximum estimate $\gamma(x^q, y^q)$, $q \in (1,2,...,t-1)$. If the list of vertices is empty, the problem has no integer solution. The algorithm stops. If the vertex with the maximum estimate $\gamma(x^q, y^q)$ contains integer x^q, the solution (x^q, y^q) is the optimal one. The algorithm stops. Otherwise:

3. We create two new candidates for each of which we supplement the current matrix A^{1D} for the step q with BCs (7) and (10) by the cut selection procedures (by the value of $cs(\tilde{\alpha}^j)$ or by radicality (11)): $(\tilde{\alpha}^{(t+1)})^T x \le \beta(x^q)$ и $(\tilde{\alpha}^{(t+1)})^T x \ge \beta(x^q)+1$, respectively.

4. We solve a pair of alternative subproblems with the cuts $(\tilde{\alpha}^{(t+1)})^T x \le \beta(x^q)$ and $(\tilde{\alpha}^{(t+1)})^T x \ge \beta(x^q)+1$.

5. We save their solution components $\underline{x}^{t+1}$ and $\bar{x}^{t+1}$ and the estimates $\gamma(\underline{x}^{t+1}, \underline{y}^{t+1})$ and $\gamma(\bar{x}^{t+1}, \bar{y}^{t+1})$ by adding them to a list of the tree vertices. If any of the candidates has no solution, it is withdrawn from the list of the vertices.

6. We increase the step number ($t := t+1$) and go to step 2.

4. Simulation study results

The applicability of the CFS method to variable selection with a highly correlation of candidate predictors was investigated using the following model example.

The relevant features $x_1^{(m)}, x_2^{(m)}, x_3^{(m)}, x_5^{(m)}, x_6^{(m)}$ were modeled as independent random variables with a standard normal distribution. The relevant features $x_4^{(m)}, x_7^{(m)}$ were computed as follows:

$$x_4^{(m)} = x_3^{(m)} + e_1, x_7^{(m)} = x_5^{(m)} + x_6^{(m)} + e_2,$$

where e_1, e_2 are independently standard normally distributed.

The response was defined as

$$y = \sum_{i=1}^{7} x_i^{(m)} + e_3$$

where e_3 is a normally distributed random variable independent of e_1, e_2 and of $x_i^{(m)}$ with zero expectation and standard deviation equal to 0.1.

The redundant variables were modeled correlated with the main predictors:

$$x_i^{(r)} = x_i^{(m)} + \varepsilon_i,\ i = 1,...,7,$$
$$x_i^{(r)} = x_{i-7}^{(m)} + \varepsilon_i,\ i = 8,...,14,$$

where $\varepsilon_1,...,\varepsilon_{14}$ are independently standard normally distributed. The irrelevant features $\xi_1,...,\xi_5$ were also modeled as random noise. In addition, the noise candidates include $\varepsilon_1,...,\varepsilon_4$.

For each random variable, samples of size 1,000 were drawn. As a result, the set of features for selection included

- the relevant predictors, on the basis of which the response was calculated, $x_1^{(m)},...,x_7^{(m)}$;
- the redundant variables correlated with the relevant one, $x_1^{(r)},...,x_{14}^{(r)}$;
- the irrelevant features $\xi_1,...,\xi_5$, $\varepsilon_1,...,\varepsilon_4$.

A total number of variables was thirty. Simulation studies were repeated 1,000 times. The mixed integer linear programming problem contained 496 variables and 1,832 constraints. In order to solve the problem, greedy algorithms were used as an alternative: forward selection and backward elimination [13]. Their implementation in the R environment was used: the forward.search and

backward.search functions provided by the FSelector package. The variable subset was evaluated by the objective function from (1).

Table 1 presents the results of simulation studies, the proportion of cases in which each variable is included in the subset. The irrelevant features were not included in the subset in any experiment. The following notation is used: forward — the forward selection, backward — the backward elimination, BCBM — the binary cut-and-branch method.

Table 1. Predictor selection results.

	Method				Method		
Variable	forward	backward	BCBM	Variable	forward	backward	BCBM
$x_1^{(m)}$	0.219	0.955	0.927	$x_4^{(r)}$	0.049	0.938	0.613
$x_2^{(m)}$	0.216	0.945	0.929	$x_5^{(r)}$	0.006	0.716	0.024
$x_3^{(m)}$	0.258	0.991	0.962	$x_6^{(r)}$	0.013	0.742	0.036
$x_4^{(m)}$	0.954	0.996	0.98	$x_7^{(r)}$	0.217	0.997	0.915
$x_5^{(m)}$	0.208	0.993	0.977	$x_8^{(r)}$	0	0.046	0.006
$x_6^{(m)}$	0.204	0.995	0.969	$x_9^{(r)}$	0	0.061	0.003
$x_7^{(m)}$	1	1	0.999	$x_{10}^{(r)}$	0	0.069	0.005
$x_1^{(r)}$	0.011	0.462	0.057	$x_{11}^{(r)}$	0.012	0.37	0.053
$x_2^{(r)}$	0.013	0.504	0.066	$x_{12}^{(r)}$	0.001	0.065	0.002
$x_3^{(r)}$	0.012	0.642	0.053	$x_{13}^{(r)}$	0	0.048	0.001

From table 1 it can be seen that the forward selection often does not include the redundant predictors. However, the final subset almost does not get a significant part of the relevant features. Only $x_4^{(m)}, x_7^{(m)}$ correlated with the other significant predictors are constantly included in the subset. This has a negative effect on the objective function values, which are far from optimal. The evaluation function values are displayed as a boxplot in figure 1. From figure 1, it can be concluded that the variation of the objective function values in the simulations is very large, and the average value is much smaller than that achieved by the backward elimination and the binary cut-and-branch method.

Both the backward elimination and the binary cut-and-branch method include all relevant features in the subset of predictors. But the backward elimination often leaves too many redundant predictors in the subset. Compared to this, for the BCBM results, such cases are relatively rare. Only a few redundant attributes $x_4^{(r)}, x_7^{(r)}$ are often included in the subset. This is because they are related to the relevant predictors $x_4^{(m)}, x_7^{(m)}$ which are correlated with the other significant predictors. Nevertheless, despite this problem, the binary binary cut-and-branch method provides the best values of the objective function compared to the backward elimination (figure 1).

The multicollinearity problem described is evidently difficult for the CFS method. It is a problem of the method itself, rather than optimization algorithms. This may have a negative effect on its applicability in practice.

5. Selection of leading indicators of consumer price index growth

Let us verify the applicability of the Correlation-based Feature Selection method using a real example. For this purpose, the task of forecasting the consumer price index was chosen. From economic research [14] it is known that one of the leading indicators of price changes during a business cycle is the industrial materials price index. The data provided by the unified interdepartmental informational-statistical system [15] include the monthly time series of the price index for the acquisition of machines and equipment for investment purposes. Indices are grouped by type of economic activity and regions of the Russian Federation. Further, the territory of the Russian Federation as a whole is selected.

The period from June to November 2010 was chosen as the test time interval. During that period, there was a sharp increase in the base price index in percent compared to the corresponding period of the previous year. The training dataset was taken from January 2006 to May 2010. It was used to fit the ARIMA model. But it naturally predicts the continuing fall in prices, as shown in figure 2. Let us verify whether this forecast can be improved by using leading indicators.

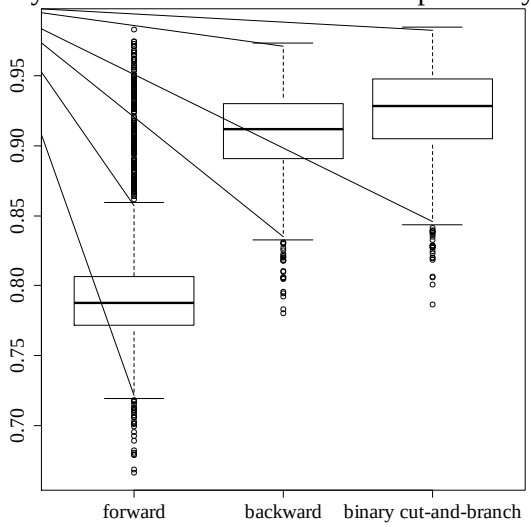

Figure 1. Boxplot for the values of the objective function obtained in simulation studies.

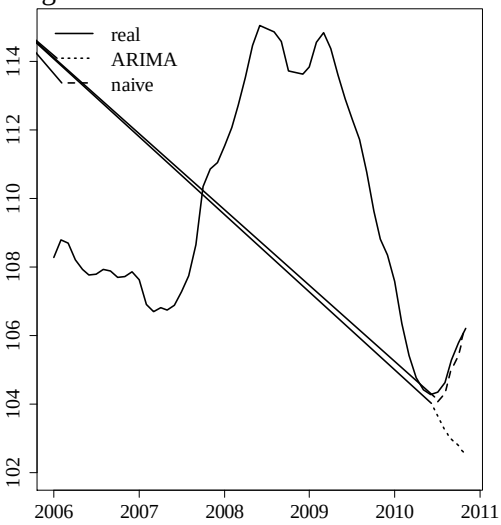

Figure 2. Real and forecast values of the base consumer price index, in percent compared to the corresponding period of the previous year.

For the time period used to train the model, there are the data on price indices for the acquisition of machines and equipment for investment purposes for 92 types of economic activity, including 16 sections of Classification and a total index for all types of activity. The values of indices are in percent compared to the corresponding period of the previous year.

First, a naive approach was used, suggesting that the best predictor is the total index for all activities. The CFS method was used for optimal lags selection only. Lags from 0 to -6 were considered as candidates. As a result, lags -4 and -6 are chosen. This approach led to a rather low value of the objective function F^* (table 2).

Next, the price indices for the acquisition of machines and equipment for investment purposes by economic activity, taken with lags from 0 to -6, were considered as candidate predictors for the application of greedy algorithms. Thus, the total number of predictors n was 644. The obtained optimal number n^* is presented in table 2.

Table 2. The results of solving the optimization problem.

Method	n	n^*	F^*
naive	7	2	0.857957
forward selection	644	4	0.954952
backward elimination	644	39	0.963451
forward selection	119	4	0.942901
backward elimination	119	18	0.950590
binary cut-and-branch	119	7	0.954994

Finally, the number of predictors was reduced to indices by sections and the total index, that is, 17 indices. The total number of variables was 119 taking into account the possible lags. Table 2 shows the optimal values of the objective functions F^* and the number of predictors n^* obtained using the methods of forward selection, backward elimination, and binary cut-and-branch.

In both cases, the forward selection method leaves very few predictors. The values of the objective function are the lowest. The method of backward elimination selects a lot of variables, which, of course, are redundant. The binary cut-and-branch method provides the best value of the objective function.

In order to compare the forecasting performance on test data, regression models were estimated on the training set with the inclusion of selected variables with selected lags. For this, the dynlm package of the statistical environment R was used.

The future predictor values should be available in order to build a forecast for six months ahead. It was assumed that their real values are available only until May 2010. If later values were needed, then the predictor values were forecasted based on the ARIMA model. For the automatic selection of the structure of the ARIMA model, the auto.arima function of the forecast package was used. It is implemented in the R environment. For forecasting, the forecast function from the same package was used. Forecasting based on the results of the predictor selection by the backward elimination method was not performed, since the number of variables (39 and 18) is clearly redundant for estimating a model of 47 months (taking into account the earliest lag -6).

Table 3 presents the deviations of the real values of the consumer price index from its forecasts. The smallest absolute differences are in bold. It is revealed that the naive approach gives a good result. Graphically, it is shown in figure 2.

Table 3. Consumer price index forecast results.

Method	June	July	August	September	October	November
ARIMA	0.22	0.68	1.39	2.31	2.98	3.73
naive	**-0,07**	0.28	0.30	0.27	**0.36**	**-0.18**
forward selection, 92 indices	-1,6	-0.9	-0.67	**0.18**	0.71	0.6
forward selection, 17 indices	-0.08	0.53	0.37	0.84	1.06	0.69
binary cut-and-branch, 17 indices	-0.86	**0.13**	**0.29**	0.93	1.22	1.13

This means that the Correlation-based Feature Selection approach can be recommended for choosing the optimal lags of predictor variables in a time series model. The simultaneous selection of price indices for the acquisition of machines and equipment for investment purposes by economic activity and their lags is more complicated. The time series of indices are very similar (some are even almost identical). Hence there is a very high correlation between the variables. At the same time, the lagged values of the indices are also highly correlated. This is similar to the case of multicollinearity from the model example considered in the previous section. As it was revealed above, in such a model, the achievement of optimum in problem (1) does not guarantee that only relevant features will be selected. In the structure of the solution, a certain proportion of redundant predictors is allowed.

Evidently, this problem also occurs in the selection of indices as leading indicators. As a result, the optimal solution obtained using the binary cut-and-branch method provides the best forecast performance for the medium term (2-3 months) only. In the long term, 5-6 months ahead, forecasts are worse than when selecting optimal lags for the total index only.

This effect is clearly visible when compared the results of selection by forward selection and binary cut-and-branch method for 17 indices. The results of forward selection give a smaller number of predictors and better predict for the long term. This can be explained by the overfitting effect, since using the binary cut-and-branch method, a greater number of predictors have been selected, some of which may be redundant.

6. Conclusions and recommendations

Thus, the Correlation-based Feature Selection method is applicable for selecting leading indicators in the time series forecasting. The candidate predictors are highly correlated. From simulation studies, it is revealed that greedy heuristics optimization algorithms in such cases do not give satisfactory results.

The forward selection does not include many relevant features; the backward elimination leaves many redundant predictors in the subset. The binary cut-and-branch method gives the best result. However, the CFS method is not perfect: the optimal value of the heuristics does not guarantee that only all relevant predictors will be selected, and the inclusion of redundant variables is possible. This happens when the relevant features correlate with each other and with redundant variables. To avoid this, it is recommended by forming the initial set of candidate predictors to pre-exclude duplicate indicators and indicators with very similar dynamics.

7. References

[1] Gaidel A V and Krasheninnikov V R 2016 Feature selection for diagnosing the osteoporosis by femoral neck X-ray images *Computer Optics* **40(6)** 939-946 DOI: 10.18287/2412-6179-2016-40-6-939-946
[2] Kutikova V V and Gaidel A V 2015 Study of informative feature selection approaches for the texture image recognition problem using the Laws' masks *Computer Optics* **39(5)** 744-750 DOI: 10.18287/0134-2452-2015-39-5-744-750
[3] Bolón-Canedo V, Sánchez-Maroño N and Alonso-Betanzos A 2015 *Knowledge-Based Systems* **86** 33-45
[4] Sagaert Y R, Aghezzaf E H, Kourentzes N and Desmet B 2018 *European Journal of Operational Research* **264** 558-569
[5] Tibshirani R 1996 *Journal of the Royal Statistical Society. Series B (Methodological)* **58** 267-288
[6] Fite J T, Don Taylor G, Usher J S, English J R and Roberts J N 2002 *International Journal of Physical Distribution & Logistics Management* **32** 299-308
[7] Flach P 2012 *Machine learning: the art and science of algorithms that make sense of data* (Cambridge University Press)
[8] Hall M A 1999 *Correlation-based feature selection for machine learning* PhD thesis (Hamilton: University of Waikato)
[9] Nguyen H, Franke K and Petrovic S 2009 *Proc. of the NIPS 2009 Workshop on Discrete Optimization in Machine Learning: Sub modularity, Sparsity & Polyhedra (DISCML)* (Vancouver, Canada)
[10] Chang C-T 2001 *European Journal of Operational Research* **131** 224-227
[11] Mezentsev Y A 2016 Binary Cut-and-Branch Method for Solving Linear Programming Problems with Boolean Variables *CEUR Workshop Proceedings* **1623** 72-85
[12] Mezentsev Y 2017 *Constructive Nonsmooth Analysis and Related Topics (dedicated to the memory of V.F. Demyanov) (CNSA)* (St. Petersburg, Russia) 1-3
[13] Sutter J M and Kalivas J H 1993 *Microchemical journal* **47** 60-66
[14] Klein P A and Moore G H 1983 *Journal of forecasting* **2** 119-135
[15] Unified interdepartmental informational-statistical system URL: https://fedstat.ru/

Acknowledgments

The reported study was funded by Russian Ministry of Education and Science, according to the research project No. 2.2327.2017/4.6.

Analysis of stable functioning of objects using machine learning

V N Klyachkin[1], D A Zhukov[1] and E A Zentsova[1]

[1]Ulyanovsk State Technical University, Severny Venets street, 32, Ulyanovsk, Russia, 432027

e-mail: v_kl@mail.ru, zh.dimka17@mail.ru

Abstract. Stable functioning of the technical objects is estimated using methods of the statistical process control. However this approach does not always provide the timely detection of violations. It is suggested using machine learning methods for the binary classification of object states (stable or unstable). A program has been developed for calculation in the Matlab environment which allows for analysis of impact of the learning method, classification quality criteria, method of validation set as well as methods of selection of significant indicators on the object's stable functioning forecast precision. Stable operation of the water treatment management system, stable vibration of the hydraulic unit, machining operation process are taken as examples.

1. Introduction

Stable functioning of the technical object is estimated using methods of the statistical process control. However, this approach does not always provide the timely detection of violations [1-2]. It is suggested using machine learning methods for the binary classification of object states (stable or unstable). Alongside with that, the statistical control history can be used as base data for the object state forecasting using machine learning methods. Values of test items and the object operation state are known for every sample.

The binary classification quality depends very heavily on the series of factors. Firstly, it is the selected machine learning method. For example, basic (the naive Bayesian classifier, the neural network and etc.), compositional (various forms of bagging or boosting) and also aggregated methods can be used [3-6]. Secondly, the diagnostic quality depends on the selected criterion. The most commonly used criteria are the error rate in the control sample, *F*-criterion and the area AUC under the ROC-curve [7-8]. Technical objects are characterized by samples with a small volume of non-operating states. In this case the *F*-criterion is the most efficient one. Learning results depend on selection methods of significant criteria of the object operation (using of low-priority criteria can lead to incorrect results), on the forming method of the control sample and on the scope of the control sample [9].

The research objective is to design a program for estimating the stable functioning of the technical object. This program shall analyze the influence of the machine learning method, forming method of the control sample and the selection of significant criteria on the precision of stability forecasting and on carrying out of the numerical analysis of the stable functioning of real objects.

2. Preparation of base data

The statistical process control involves the identification of non-accidental violations connected with so-called special reasons [10-12]. For example, as far as the mechanical processing is concerned these reasons can be the edge wear or its unfastening, composition changes of the cutting fluid and etc.
The main advantage of this approach lies in the fact that violation is identified before the test item oversteps the limits. In addition to the above, statistical methods (control charts are usually used for monitoring of the middle level and the dispersion process) show the violation of its stability (when test features overstep the confidence limit).

Control charts are one of the most efficient tools for the analysis, process monitoring and its preservation in the statistically controlled state. Plotting involves the determination of parameters: volume of the instantaneous sample, time intervals between the sample taking and the position of control limits. Efficiency factors of the control chart are expenditures for carrying out the control procedure; the time interval till the signal collection about the process violation and the probability level of the false alarm.

As far as the multi-parameter process is concerned firstly of all correlation relationships among object performance indicators are examined. Then control facilities are selected and their parameters are specified.

Shewhart charts (when the middle level and its dispersion are controlled described in terms of the range or the standard deviation) are used for independent indicators in accordance with standards. Chart can be combined. For example, charts with average values and chart with ranges; charts with average values and charts with standard deviations, charts with individual observations and charts with moving ranges. The last option is used when measurements are too labor-intensive or expensive. In this case, for the control the result of one measurement is used instead of the instantaneous sample.

Gain in the sensitivity of these charts (reduce the time or the sample volume from the moment when the process violated till the moment when this violation was identified) is possible by using the preventative border and searching for so-called non-accidental structures in the chart. For example, multiple successive increasing or decreasing points indicate the process trend. Multiple points located checker-wise are the indicator of cyclical process fluctuations, etc. Charts of cumulative sums or exponentially weighted moving averages are sometimes used to specify the process stability issue [1-2, 12].

Stability of correlation indicators is estimated using Hotelling algorithms and the generalized variance [13-17]. The Hotelling chart is used to estimate the middle level stability of the multi-variate process. The null-hypothesis of the fact that the mean vector fits the requirements is tested. The generalized dispersion chart is a tool for monitoring of the multi-variate spreading. The hypothesis of the fact that the correlation matrix fits the requirements is tested.

Which controlled indicator or which subrange of indicators is responsible for the process violation? Causes of violations under the multi-variate process control can be identified using the Hotelling partial criterion or the down-weighting of plotted charts. For example, if we control three indicators, then three Hotelling charts shall be plotted for each pair of indicators. This approach is not always correct but in practice it often leads to the identification of the needed indicator. The similar approach can be also used with the generalized variance chart.

Preventative borders , searching for non-accidental structures and charts of multi-variate exponentially weighted moving averages based on both the Hotelling statistics and the generalized variance can be used to improve the efficiency of the multi-variate control.

Let's assume that N samples upon d performance indicators were examined. Control charts identified the stability process violation in k samples. By doing so, the multitude N of precedents is formed $(x^{(i)}, y^{(i)})$, $i = 1 \ldots N$: objects with preset d performance parameters $x = (x_1, x_2, \ldots, x_d)$ and corresponding states y taking one of two possible values (0,1); $y = 0$ corresponds to the unstable state (the number of such precedents is k), $y = 1$ corresponds to the stable state (the number of such precedents is $N - k$). Based on these data it is necessary to restore the dependence between performance indicators and the object state.

3. Object state diagnostics

The implementation of machine learning methods is possible based on the tool library Statistics and Machine Learning Toolbox in the pack Matlab. Taking into consideration research objectives, we designed a program which:

- uses various basic and compositional methods and plots aggregated classifiers of three types: with the aggregation by the average value, by the median or the voting [18-19],
- using various classification quality criteria: error rates in the control sample, *F*-criterion and the area AUC under the ROC-curve,
- selecting significant object performance indicators by plotting the regression model for the dependence of the object state y on performance indicators x_j ($j = 1 \ldots d$) and checking the significance of indicators upon the Student criterion,
- varies the forming method of the control sample (the random selection or the specified base data) and its volume [9].

The base data sample is introduced to diagnose the state stability of the technical object. The machine learning is carried out using all basic and compositional methods integrated in Matlab. In this case, the classification quality is estimated using the cross-validation under the *F*-criterion. Significant performance indicators are selected. Than this procedure is checked whether it improves the quality of the model or not. The sample volume providing the best criterion value is selected by varying the control sample volume from 5 to 25% in comparison with the original sample. Aggregated classifiers are plotted for this very option. The classifier providing the maximum *F*-criterion is selected. If necessary, there is also an opportunity to minimize the error rate in the control sample when plotting aggregated classifiers.

In Fig. 1 shows a flow cyart of the corresponding algorithm.

4. Numerical examination

The statistical control of the mechanical processing stability of the axis (grinding of four cylindrical surfaces) was carried out using 400 samples. All four controlled indicators (axis step diameters) turned out to be correlated with each other. The Hotelling chart was used to control the middle level of the process. The generalized variance chart was used to control the multi-variate dispersion. Fig. 2 shows the results of the statistical control for the first 51 samples. The critical value of the Hotelling statistics was 10.830. The critical value of the generalized variance was $0.45*10^{-8}$. Charts were plotted using the system Statistica.

It is apparent that process violations (overstepping the limits) in the Hotelling chart happened in three samples: 38, 45 and 47. Process violations in the generalized variance chart happened in two samples: 33 and 34. As can be seen from the above, violations of the controlled process happened in 5 cases of 51 precedents.

Table with base data was prepared upon all 400 observations. When carrying out the examination using the designed program it was found that all four indicators were significant. The maximum value of the *F*-criterion (0.874) was measured for the control sample of the volume 15% in comparison with the original sample when using the aggregated classifier by the average value including the support vector machine and the decision tree bagging. In addition to the above, the value of the *F*-criterion was boosted by 8%. The best classifier by separate methods (the decision tree bagging) was considered as the standard approach.

During the second test the vibration stability of the hydraulic aggregate was estimated by values of 10 gauges in 5000 observations [20]. The multitude of 10 values was divided into four sub-multitudes. Two values turned out to be uncorrelated with others. Three correlated values formed the third group. Five correlated values formed the forth group. First two independent values were controlled using Shewhart charts for average values and standard deviations. The Hotelling and the generalized variance charts were plotted for the third and the forth groups. According to the results of the statistical control the sample of base data was formed. The machine learning was carried out using this sample. Seven indicators out of ten turned out to be significant. The aggregated classifier by the median including the gradient boosting and the logistic regression turned out to be the best. The

volume of the control sample was 20%. The increase of the *F*-criterion (up to the value 0.904) was 18%.

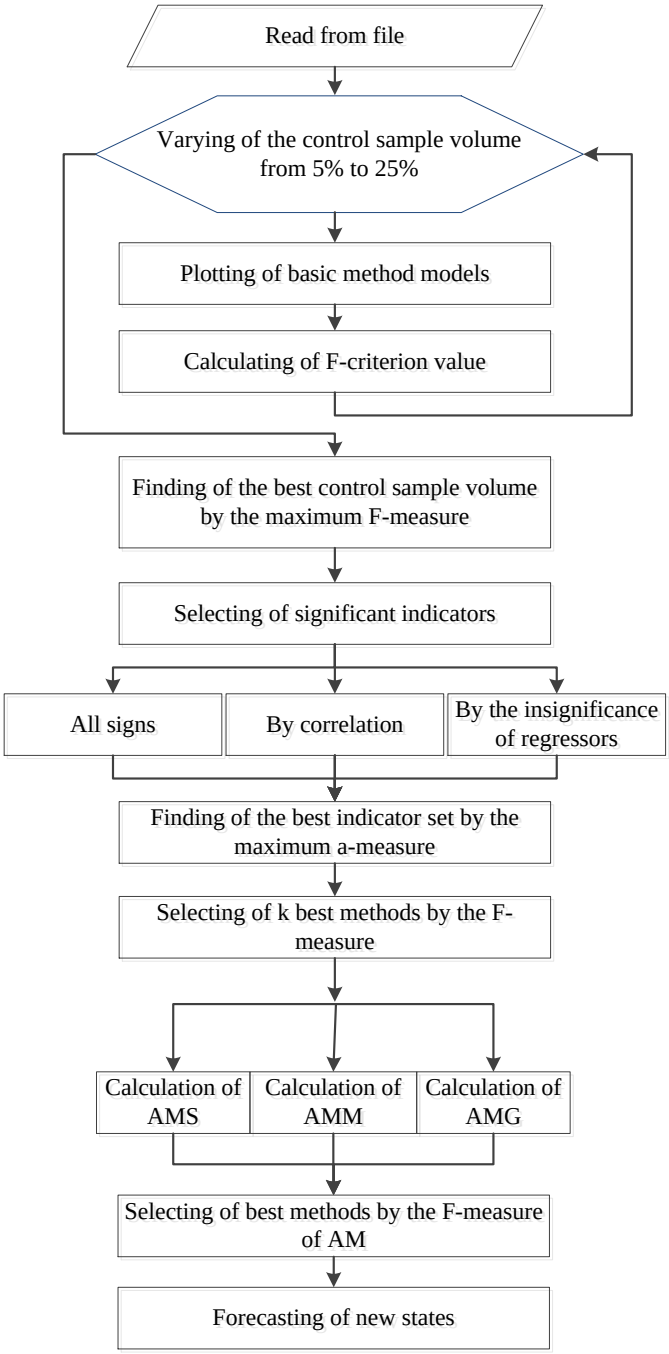

Figure 1. Flow chart of the algorithm for stability forecasting.

When analyzing the stable functioning of the water purification system by eight quality indicators of the potable water results of 1557 observations (operating state was registered in 1204 cases) were used. Six indicators turned out to be significant. Maximum value of the *F*-criterion was when aggregating the neural network and the decision tree bagging. During this test the increase of the criterion value in comparison with the neural network (the best separate classifier) was negligible: from 0.879 to 0.881. In addition to the above, the volume of the control sample was 10%.

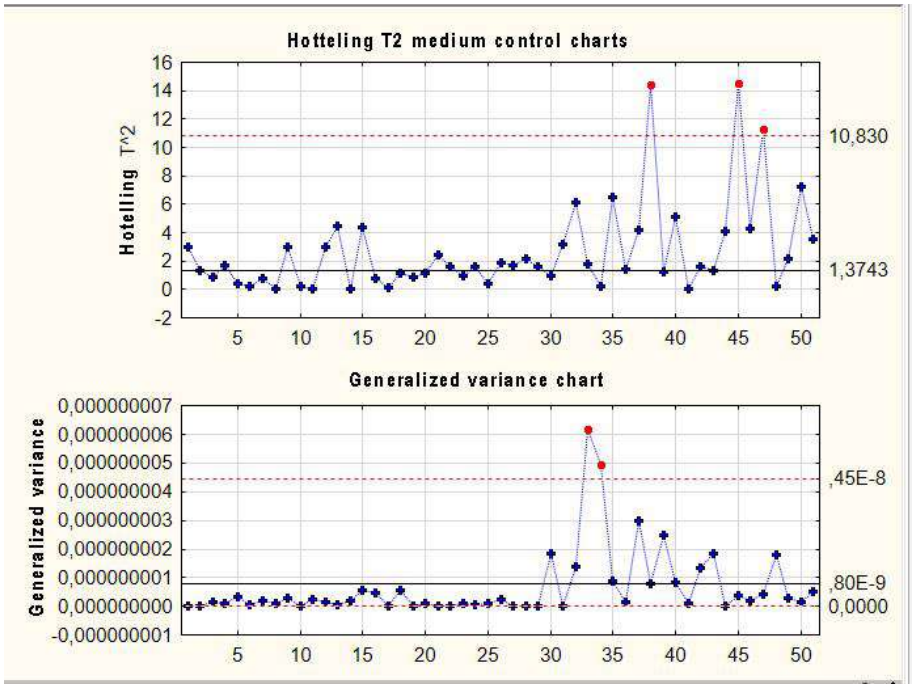

Figure 2. The Hotelling and the generalized variance charts.

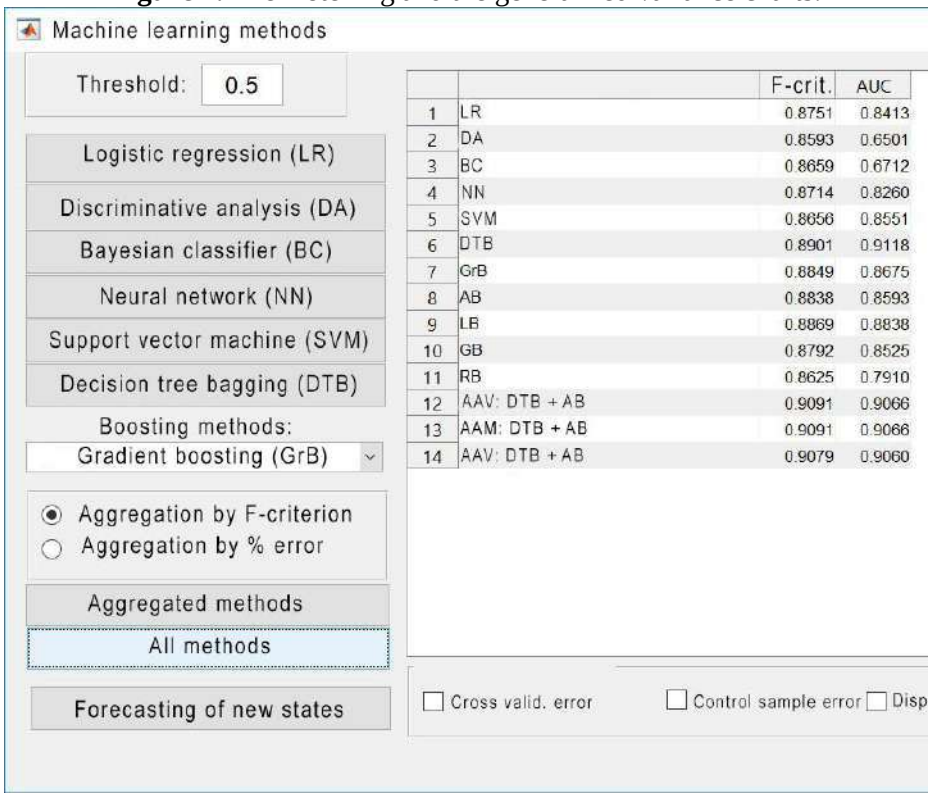

		F-crit.	AUC
1	LR	0.8751	0.8413
2	DA	0.8593	0.6501
3	BC	0.8659	0.6712
4	NN	0.8714	0.8260
5	SVM	0.8656	0.8551
6	DTB	0.8901	0.9118
7	GrB	0.8849	0.8675
8	AB	0.8838	0.8593
9	LB	0.8869	0.8838
10	GB	0.8792	0.8525
11	RB	0.8625	0.7910
12	AAV: DTB + AB	0.9091	0.9066
13	AAM: DTB + AB	0.9091	0.9066
14	AAV: DTB + AB	0.9079	0.9060

Figure 3. Calculation results.

Fig. 3 shows the program window with one calculation options. It is apparent that in this very case the value of the *F*-criterion for basic binary classification methods falls in the range from 0.8593 for the discriminative analysis and up to 0.8901 for the decision tree bagging. All aggregated methods have one and the same structure (this happens by no means always) and include two basic methods: the decision tree bagging and AdaBoost. In the general case the number of basic methods can be even greater. Please note that the best of basic classifiers (the decision tree bagging) is almost always

included in the structure of the aggregated classifier. The value of the *F*-criterion by aggregated methods is some greater then by any basic classifiers. For the aggregation by the average value and by the median it is equal and amounts 0.9091.

Alongside with that, the decision tree bagging showed the greatest AUC - area under the error curve (0.9118). Like for the *F*-criterion, the closer is this value to 1, the higher is the classification quality. The maximum value by aggregated methods (0.9066) turned out to be somehow less.

5. Conclusion

The carried out research showed that the stable functioning analysis of the technical object can be carried out both using methods of the statistical process control, widely used during the technological process control, and using the binary classification of object states based on the machine learning. Previous results of the statistical control can be used as base data and precedents.

Shewhart charts are used for the middle level process control and its dispersion when exercising control over independent indicators of the object operation. The stability of correlated indicators is estimated using the Hotelling and the generalized variance algorithms. The Hotelling chart is used to estimate the middle level stability of the multi-variate process. The generalized variance chart is used as the tool for monitoring of the multi-variate dispersion.

The base data sample is introduced to diagnose the state stability of the technical object using the machine learning. Learning of the binary classification model is carried out using all basic and compositional methods integrated in Matlab. In this case, the classification quality is estimated using the cross-validation under the *F*-criterion. The diagnostics precision can be increased due to the aggregation of methods, the selection of significant indicators and changing of the control sample volume.

The designed program provides the automatic searching for the best diagnostic option of the object state by the preset criterion. As examples, the stable functioning of the water purification control system, the hydraulic aggregate vibration stability and the technological procedure of mechanical processing were considered.

6. References

[1] Klyachkin VN and Karpunina I N 2018 Statistical methods for assessing the stability of functioning of technical systems *Reliability and Quality of Complex Systems* **2** 36-42
[2] Klyachkin V N 2008 The static control system for multivariate manufacturing process *Instruments and Systems: Monitoring, Control, and Diagnostics* **10** 30-33
[3] Witten I H and Frank E 2005 *Data mining: practical machine learning tools and techniques* (San Francisco: Morgan Kaufmann Publishers) p 525
[4] Merkov A B 2011 *Pattern recognition.Introduction to statistical learning methods* (Moscow: Editorial URSS) p 256
[5] Voronina V V, Miheev A V, Yarushkina N G and Svyatov K V 2017 *Machine learning: theory and practice* (Ulyanovsk: UlSTU) p 290
[6] Voroncov K V URL: https://yadi.sk/i/FItIu6V0beBmF
[7] Sokolov E A URL: https://github.com /esokolov/ml-course-hse/blob/master/2018-fall/lecture-notes/lecture04-linclass.pdf
[8] D'yakonov A M URL: https:// dyakonov.org/2017/07/28/auc-roc-ploshchad'-pod-krivoj-oshibok/#more-5362
[9] Zhukov D A and Klyachkin V N 2018 The Effect of the Control Sample Volume on the Quality of Diagnostics of the Technical Object State *Automation of Control Processes* **2** 90-95
[10] Wheeler D and Chambers D 1992 *Understanding Statistical Process Control* (SPC Press) p 409
[11] Montgomery D C 2009 *Introduction to statistical quality control* (New York: John Wiley and Sons) p 754
[12] Maksimov A I and Gashnikov M V 2018 Adaptive interpolation of multidimensional signals in differential compression *Computer Optics* **42(4)** 679-687
[13] Yumaganov A S and Myasnikov V V 2017 The method of searching for similar code sequences in executable binary files using the unmarked approach *Computer Optics* **41(5)** 756-784

[14] Klyachkin V N and Bubyr' D S 2014 Forecasting of technical object state based on piecewise linear regressions *Radioengineering* **7** 137-140
[15] Klyachkin V N and Karpunina I N 2017 The analysis of technical object functioning stability as per the criterion of monitored parameters multivariate dispersion *CEUR Workshop Proc.* **1903** 28-31
[16] Salmasnia A, Kaveie M and Namdar M 2018 An integrated production and maintenance planning model under VP-T2 Hotelling chart *Computers & Industrial Engineering* **18** 89-103
[17] Franceschini F, Galetto M and Genta G 2015 Multivariate control charts for monitoring internal camera parameters in digital photogrammetry for LSDM (Large-Scale Dimensional Metrology) applications *Precision Engineering* **42** 133-142
[18] Klyachkin V N, Kuvayskova Yu E and Zhukov D A 2017 The use of aggregate classifiers in technical diagnostics, based on machine learning *CEUR Workshop Proc.***1903** 32-35
[19] Klyachkin V N and Shunina Yu S 2015 System for borrowers' creditworthiness assessment and repayment of loans forecasting *Herald of Computer and Information Technologies* **11** 45-51
[20] Kropotov Yu A, Proskuryakov A Yu and Belov A A 2018 A method for predicting changes in the parameters of time series in digital information control systems *Computer Optics* **42(6)** 1083-1100

Acknowledgments
This surveying was carried out with the financial support from the Russian Foundation for Basic Research (RFBR) and the Government of Ulyanovsk region, the project 18-48-730001 should be used.

Adaptive algorithm of conforming image matching

V A Fursov[1,2], Ye V Goshin[1,2] and K G Pugachev[1]

[1]Samara National Research University, Moskovskoe Shosse 34A, Samara, Russia, 443086
[2]Image Processing Systems Institute of RAS - Branch of the FSRC "Crystallography and Photonics" RAS, Molodogvardejskaya street 151, Samara, Russia, 443001

e-mail: pugachev_k.g@mail.ru

Abstract. This paper presents an adaptive algorithm of conforming image matching based on the principle of conformity. The algorithm consists of several main stages. At the first stage, we find the corresponding points using a minimum value of conformity as the measure of points' similarity. We define a conformity function as the sum of all possible combinations of squared differences of pixel intensity values on the fragments that are matched. Then, we perform an adaptive procedure of errors correction considering an intensity gradient distribution. An important feature of the algorithm is the finding of error points using a criterion of maximum value of samples' conformity for every fragment of the disparity map. The results of experiments on the "Teddy" test images are shown.

1. Introduction

Image matching is the most important and difficult step in computer vision applications, such as image stitching, the creation of three-dimensional models of objects or scenes by a sequence of frames etc. At least three approaches to solve image matching problem are known: area-based (1), feature-based (2), and symbolic (3) approach. In the framework of the area-based approach [1], which is used in this paper, for the fragments of the first image, the most similar fragment is need to be found.

The choice of fragments similarity measure is very important, when the area-based approach is used. There are many similarity measures. The absolute differences (AD) and squared differences (SD) and the sum of absolute differences (SAD) are the most commonly used to compute matching cost. Also, the sum of squared differences (SSD), normalized cross correlation (NCC), rank transformation (RT), and census transformation (CT) are the popular methods to aggregate matching cost. In detail, these methods were described in paper [2].

In paper [3] Wang et al. applied the AD algorithm to real-time image matching using GPU. The results show that AD algorithm is not capable of producing a smooth disparity map in highly textured images. To overcome it, Min et al. [4] and Pham and Jeon [5] implemented truncated absolute differences (TAD) algorithm, which uses the colour and gradient values in pixels matching to improve its robustness against variations in illumination.

SD algorithm was applied to subpixel image matching by Yang et al. [6]. To improve the flattening of edges and to smooth areas, they used a bilateral filter. In paper [7] Miron et al. researched various matching cost functions. They concluded that the SD algorithm produces the largest error.

Lee and Sharma [8] implemented the real time image matching algorithm using the SAD algorithm to calculate matching costs via GPU. In paper [9] Gupta and Cho proposed a technique, which uses two different sizes of correlation windows in the SAD algorithm. As denoted in [2], the SAD algorithm is fast, but the quality of the initial disparity map is low because of the noise at object boundaries and in homogeneous regions.

In paper [10] Fusiello et al. used the SSD algorithm with multiple fixed window blocks to reduce the incidence of occlusion errors. In paper [11] the SSD algorithm with multiple windows was implemented by Yang and Pollefeys using GPU.

Low-dimensional image features matching method using NCC was proposed in [12] by Satoh. This method achieves a high accuracy, but requires a lot of computational resources. Cheng et al. [13] proposed to calculate matching cost using a zero mean normalized cross correlation (ZNCC).

An image matching algorithm using the RT algorithm was proposed by Gac et al. [14]. The method provides a reliable initial disparity map by using a careful selection of the window sizes. A new RT algorithm was developed in paper [15] to reduce matching ambiguity using a Bayesian model. This model considers similarity between the first and the second image pixels and the level of ambiguity within each image independently.

To improve image matching accuracy, some researchers tried using combinations of various cost functions. For instance, Mei et al. [16] implemented a combination of the AD and CT algorithms to compensate their limitations. They showed that CT algorithms produce incorrect matches in regions with repetitive local structures, and the AD algorithm does not work well in the large regions without texture.

The combination of the SAD and CT algorithms led to higher performance, but computational complexity has become higher as well [17]. The SAD and CT cost measures were obtained individually. The final cost function was calculated as a linear combination of SAD and CT cost measures based on a weighting factor.

Zhang et al. [18] has improved the matching accuracy by using a combination of SAD and the arm length differences (ALD) methods. Lee et al. [19] used combination of CT and gradient difference methods. However, due to similar or repetitive texture patterns, matching ambiguity can appear in some regions.

In paper [20] Perez-Patricio et al. has proposed a fuzzy logic method using the various cost functions simultaneously and decision-making based on membership functions. The method uses both local and global information to reduce errors' count in homogeneous areas and to preserve the edges near discontinuities.

When the area-based approach is used, many points with wrong disparity value can appear in disparity map. In our previous papers we have tried to solve this problem by using a new criterion of similarity. In particular, in papers [21, 22] a new fragments' similarity criterion was presented. Although we have obtained the results comparable and in some cases are better than results of semi-global block matching, however, this problem was not fully solved.

The traditional way of noise removal is smoothing filtering of image representing disparity map. This method can give visually better image, however this smoothing procedure unavoidably distorts into disparity map points with true value of disparity. Consequently, the three-dimensional coordinates of the scene, which are calculated using these points, can also be distorted. So, the problem of filtering procedure creating, which performs error correction without affecting the other points with high reliability, is actual task.

2. Problem statement

In this paper we develop an approach based on the principle of fragments conformity. The method was proposed in [21, 22]. Let us state that F_1 and F_2 are two images, which are obtained by multi-view shooting. For every point of these images we can specify a rectangular fragment with size of $K \times L$, K and L are odd. In general case, $K \neq L$. Every fragment of the first image F_1 can be presented in the form of vector $\mathbf{f}_1$, obtained by scanning by rows or columns.

Let's specify rectangular search area with size of $N \times M$ on the second image F_2 for every point of the first image F_1. For every point in search area we can form vector $\mathbf{f}_2$ with the same size in a similar way.

The task is to find corresponding point (central point of $\mathbf{f}_2$, the most similar for some measure) in the search area of the second image F_2 for every point (central point of $\mathbf{f}_1$) of first image F_1. For certainty, we assume that fragments sizes are odd and the search area is a set of points, which can be used as centres of fragments.

For points of the first image with coordinates (*k*, *l*) and $N \times M$ points in search area in second image vectors of differences are calculated:

$$\Delta\mathbf{f}(n,m) = \mathbf{f}_2(n,m) - \mathbf{f}_1(k,l), \quad n = \overline{1,N},\ m = \overline{1,M}, \tag{1}$$

where N and M are count of rows and columns of the search area.

Then conformity function is calculated as:

$$W(n,m) = \sum_{\substack{i,j=1,\\ i<j}}^{S} (\Delta f_i(n,m) - \Delta f_j(n,m))^2, \tag{2}$$

where Δf_i is i^{th} element of vector (1), $S = K \times L$ is elements count of $\mathbf{f}_1$ and $\mathbf{f}_2$ vectors, $n = \overline{1,N}, m = \overline{1,M}$. Point (n^*, m^*) in search area of the second image with minimum value of conformity function is chosen as corresponding point for point (*k*, *l*) at the first image:

$$W(n^*, m^*) = \min_{\forall n,m} W(n,m) \tag{3}$$

We have used this criterion in papers [21, 22], where we have shown that this criterion allows improving an accuracy of image matching. The important feature is that all possible combinations of fragments samples differences are used. So, this criterion gives much more information about pixel intensity distribution of image fragment and provides a high reliability of image matching. However, as we mentioned above r, the points with wrong calculated disparity can occur in the areas with low values of gradient function.

Proposed filter, which allows overcoming it, is also based on the principle of samples conformity. The main idea is to use the conformity function like (2) to find error point and replace its value by values of neighbouring points. But the points without errors are not will be affected. This method allows avoiding errors in image areas with low values of pixel intensity gradient.

3. Method of error correction

We develop an error correction algorithm for areas of disparity map image with low values of pixel intensity gradient. Let us state that F_d is image representing obtained disparity map. Let's choose fragment of this image with size of $P \times Q$, P and Q are odd. In general case $P \neq Q$.

For every point (p, q) we calculate value of local conformity with other points of this fragment:

$$W(p,q) = \sum_{\substack{i=1,P,\\ j=1,Q\\ i\neq p,\, j\neq q}}^{S-1} (f(p,q) - f(i,j))^2, \tag{4}$$

where $f(p,q), \quad f(i,j)$ are values of fragments samples in points (p,q) and (i,j), and $S = P * Q$.

Now S functions of local conformity are calculated. We search point (p^*, q^*) with the maximum value of local conformity and assume it as error point:

$$W(p^*, q^*) = \max_{\forall p,q} W(p,q). \tag{5}$$

This statement is bases on an assumption that all points of this fragment are in areas with low value of pixel intensity gradient. So, the three-dimensional coordinates of elements of the same objects can't be too different from neighbouring points, because the objects don't contain any tears of surface.

To correct the value of error point (p^*, q^*), an error value is replaced by mean value of variational range of fragment samples. In case, when count of errors in disparity map is low, it's useful to compare an error value with mean value of variational range. If the difference is low and can be compared with possible differences in coordinates of surface elements, this replacement will not change anything. It can be seen that all points will remain the same. So, the coordinates of surface can be calculated accurately using the values of obtained disparity map.

On the fragments with objects edges this procedure will not work because the values of conformity function (4) will be high due to the difference between fragments samples of different objects. So, these image areas should be excluded from consideration. Moreover, this filter work efficiently, when count of error points on the fragment is low.

In view of the above, the next section proposes a multistage technology with adaptation to the features of the various parts of the disparity map, ensuring the efficient correction of error points.

4. Overall technology of disparity map forming

The technology consists of several main stages:

1. Disparity map forming using a method of conforming estimates;
2. Preliminary disparity image processing, single errors' correction;
3. Object edges detection and binary template construction;
4. Error points correction on the areas with the low value of gradient function (on the objects surface).

Let us describe briefly these stages of technology.

At the first stage we form disparity map using method and algorithm which are described in [21, 22]. The main idea of this method was described in Section 2.

Preliminary disparity image processing is performed to correct values of single error points. The algorithm is implemented by several iterations (by rows and columns) on the image. For each point of the image difference from neighbouring points (by vertical or horizontal) and the difference between neighbouring points are calculated. If the first difference is higher than threshold value and the second value is low, this point is chosen as an error point. Then, the value of the central pixel is replaced by half-sum of neighbouring pixels values. Similar procedure can be used to correct double, triple and etc. errors.

To construct a binary template with detected edges, various methods can be used to find the differences, similarities [23] and image segmentation [24]. In this paper we use the simplest and widely used approach. We use a median filter to blur images and Sobel operator to form the field of gradients. Then we perform the contrasting and binarization procedures.

At the last stage, we perform iterative error correction in the areas of disparity map with low value of gradient. We divide disparity image into disjoint fragments with size of $P \times Q$ and iteratively perform an error correction using method, which is described in Section 3. If the fragment contains objects edges, an error correction is not performed. When the fourth stage is performed, some clusters of failed points can be "transformed" into the single error points. Therefore, the second stage correction can be repeated without loss of accuracy.

5. Results of experiment

The described technology was used to form a disparity map for a set of multi-view test images «Cones» [25]. Test images are presented at Figure 1. For these test images, the disparity map shown at Figure 2a was obtained using method and algorithm described in [21, 22]. Search window with the size of 5×7 and search area with the size of 1×65 were used. Then median intensity of pixels was set as 128. It can be seen that disparity map contains many points with the wrong disparity. The most of them, as expected, are in the area without any local features (textures, symbols etc.).

Figure 2b shows a disparity map obtained after several iterations of single, double and triple error's removal (Stage 2). Also, correction of big areas with errors was performed. We can see, that this disparity map is still consists of many errors. Moreover, most of these points are contained in the areas of the test images with a small value of gradient.

a) b)

a) left image; b) right image

Figure 1. Test images.

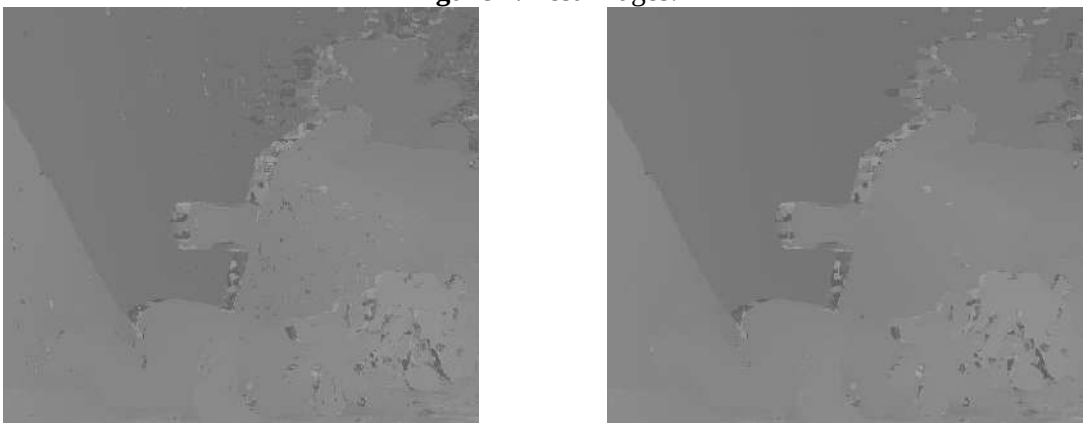

a) b)

a) Obtained disparity map (first stage); b) Processed disparity map (second stage)

Figure 2. Disparity maps.

Figure 3a shows disparity map obtained using our error correction algorithm, which is described in Section 3. To compare the obtained results with the other methods and algorithms, we have constructed a disparity map using semi-global block matching method [26]. We have used the implementation of this method from OpenCV library [27] with parameters:

1) minDisparity=0;
2) numberOfDisparities=80;
3) SADWindowSize=5;
4) disp12MaxDiff=1;
5) preFilterCap=31;
6) uniquenessRatio=5;
7) speckleWindowSize=5;
8) speckleRange=5.

Disparity map obtained by semi-global block matching is shown at Figure 3b. Figure 3c shows the ground-truth disparity map. It can be seen that semi-global matching smooth errors. However, this method also smooths edges of objects.

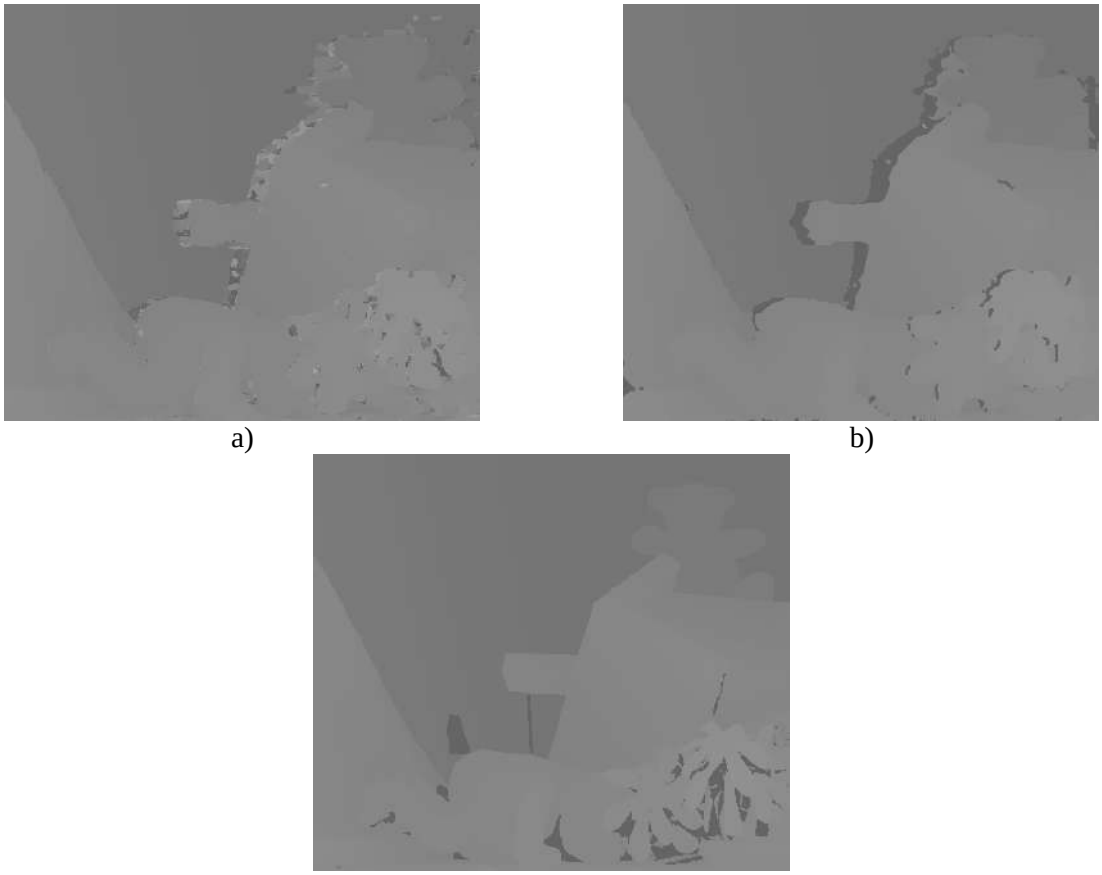

a) b)

c)

a) Filtered disparity map (fourth stage); b) Disparity map, obtained using Semi-Global Block Matching; c) Ground-truth disparity map

Figure 3. Disparity maps.

Accuracy comparison for semi-global matching method and our performed technology was performed. For both methods an error of image matching was calculated using the formula:

$$\sigma = \sqrt{\frac{1}{NM}\sum_{i,j=1}^{N,M}\left(I^{1}_{i,j} - I^{2}_{i,j}\right)}.$$

Calculation was performed for points, where disparity value is known. So, for our proposed method error value is 5,22 before processing. After processing error value became 3,98. For semi-global matching error value is equal to 4,00. We can see that proposed method of error correction can significantly reduce the number of errors in the disparity map.

6. Conclusion

A new method and algorithm of error correction on the areas with low value of pixel intensity gradient are proposed. The important feature is that an algorithm allows removing only point with the wrong disparity value. The other points of fragment are not affected. This feature is very useful for disparity maps formation, which affects the three-dimensional models calculation of coordinates. The constructed technology, including this algorithm, has a high accuracy.

7. References

[1] Guk A P and Altsyntsev M A 2017 Automatic identification of corresponding points for aerial images of forest areas *Vestnik of SSUGT* **22** 68-77

[2] Rostam A H and Haidi I 2016 Literature Survey on Stereo Vision Disparity Map Algorithms *J. Sens.* 8742920

[3] Wang L, Gong M, Gong M and Yang R 2006 How far can we go with local optimization in real-time stereo matching *Proc. 3rd Int. Symp. 3D Data Proc. Vis. Trans.* (Chapel Hill, NC, USA/ IEEE) 129-136
[4] Min D, Lu J and Do M N 2011 A revisit to cost aggregation in stereo matching: how far can we reduce its computational redundancy? *Proc. IEEE Int. Conf. Comp.Vis. (ICCV '11)* (Barcelona, Spain/IEEE) 1567-1574
[5] Pham C C and Jeon J W 2013 Domain transformation-based efficient cost aggregation for local stereo matching *IEEE Trans. Circ. Sys. Vid. Tech.* **23** 1119-1130
[6] Yang Q, Yang R, Davis J and Nistrer D 2007 Spatial-depth super resolution for range images *Proc. IEEE Conf. Comp. Vis. Pat. Rec. (CVPR)* (Minneapolis, Minn, USA/IEEE) 1-8
[7] Miron A, Ainouz S, Rogozan A and Bensrhair A 2014 A robust cost function for stereomatching of road scenes *Pat. Rec. Let.* **38** 70-77
[8] Lee S H and Sharma S 2011 Real-time disparity estimation algorithm for stereo camera systems *IEEE Trans. Cons. Electr.* **57** 1018-1026
[9] Gupta R K and Cho S Y 2013 Window-based approach for fast stereo correspondence *IET Comp. Vis.* **7** 123-134
[10] Fusiello A, Castellani U and Murino V 2001 Relaxing symmetric multiple windows stereo using Markov Random Fields *Computer Vision and Pattern Recognition of Lecture Notes in Computer Science* **2134** 91-105
[11] Yang R and Pollefeys M 2003 Multi-resolution real-time stereo on commodity graphics hardware *Proc. IEEE Comp. Soc. Conf. Comp. Vis. Patt. Rec.* **1** 211-217
[12] Satoh S 2011 Simple low-dimensional features approximating NCC-based image matching *Pat. Rec. Let.* **32** 1902-1911
[13] Cheng F, Zhang H, Yuan D and Sun M 2014 Stereo matching by using the global edge constraint *Neurocomp.* **131** 217-226
[14] Gac N, Mancini S, Desvignes M and Houzet D 2008 High speed 3D tomography on CPU, GPU, and FPGA *EURASIP J. Emb. Sys.* 930250
[15] Zhao G, Du Y K and Tang Y D 2011 Anew extension of the rank transform for stereo matching *Adv. Eng. Forum* **2-3** 182-187
[16] Mei X, Sun X, Zhou M, Jiao S, H. Wang and Zhang X 2011 On building an accurate stereo matching system on graphics hardware *Proc. IEEE Int. Conf. Comp. Vis. Work.* (Barcelona, Spain/IEEE) 467-474
[17] Cigla C and Alatan A A 2013 Information permeability for stereo matching *Sig. Proc.: Im. Com.* **28** 1072-1088
[18] Zhang N, Wang H and Cr J 2013 A near real-time color stereo matching method for GPU *Proc. 3rd Int. Conf. on Adv. Comm. Comp.* (Lisbon, Portugal/ IARIA) 27-32
[19] Lee S, Lee J H, Lim J and Suh I H 2015 Robust stereo matching using adaptive random walk with restart algorithm *Im. Vis. Comp.* **37** 1-11
[20] Pérez-Patricio M, Aguilar-González A, Camas-Anzueto J-L and Arias-Estrada M 2015 A Fuzzy Logic Approach for Stereo Matching Suited for Real-Time *Proc. Int. J. Comp. App.* **113** 9
[21] Fursov V A, Gavrilov A V, Goshin Ye V and Pugachev K G 2018 The technology of image matching by the criterion of conformity of image fragments samples *Inf. Tech. and Nanotech.* (Samara, Russia/ New Engineering Ltd.) 2299-2305
[22] Fursov V A, Gavrilov A V, Goshin Ye V and Pugachev K G 2018 The technology of image matching by the criterion of conformity of image fragments samples *J. Phys.: Conf. Ser.* **1096** 012084
[23] Plotnikov D E, Kolbudaev P A and Bartalev S A 2018 Identification of dynamically homogeneous areas with time series segmentation of remote sensing data *Computer Optics* **42(3)** 447-456 DOI: 10.18287/2412-6179-2018-42-3-447-456
[24] Lebedev M A, Rubis A Yu, Vizilter Yu V and Vigolov O V 2018 Detecting image differences based on reference EMD-filters *Computer Optics* **42(2)** 291-296 DOI: 10.18287/2412-6179-2018-42-2-291-296

[25] University of Tsukuba Computer Vision Laboratory URL: http://www.cvlab.cs.tsukuba.ac.jp/dataset/tsukubastereo.php
[26] Hirschmüller H 2008 Accurate and efficient stereo processing by semi-global matching and mutual information *CVPR, PAMI* **30(2)** 328-341
[27] OpenCV Library URL: http://opencv.org

Acknowledgments
The work was funded by the Russian Federation Ministry of Education and Science (project # 2.891.2017) and RFBR (projects # 17-29-03112).

The electrocardiogram signal morphology analysis based on convolutional neural network

M Zavoyskih[1], A Korobeynikov[1,2], A Menlitdinov[2], V Lyuminarskiy[1] and Yu Kuzelin[3]

[1]Kalashnikov Izhevsk State Technical University, Studencheskaya 7, Izhevsk, Russia, 426069
[2] IzhTeleMed Ltd., Lenina, 110, Izhevsk, Russia, 426009
[3] Republican Clinical Diagnostic Center, Lenina 87B, Izhevsk, Russia, 426009

e-mail: grizz8575@gmail.com, kav33@inbox.ru

Abstract. The analysis of electrocardiogram signal morphology based on convolutional neural network is considered. Input data is obtained by splitting the signal into cardiac cycles. The calculation the average cycle is performed to exclude the artefacts. The Haar wavelet transform of the average cycle is performed. The images of size 200x6 are input data for the recognition system: 200 – number of counts constituting the cycle; 6 – number of Haar transform time scales. This work is a reconsideration of the previous work of the authors. The training samples base of marked cardiac cycle segments is the same (1500 cycles): the average cycle and the segment's start and end indexes. In the previous work, the original composite system consisting of several modules was used as a recognition system. In current work it is proposed to use the convolutional neural network with the special structure: 4 convolutional layers, 2 dense layers, and 200 outputs for every of 3 segment. The recognition system based on neural network showed results slightly superior to the previous system. The percent of acceptable localization of the segments is the following: P – 82.2%, QRS – 88.7%, and T – 85.4%. The proposed system effectively solves the problem using the standard modules of modern artificial neural networks.

1. Introduction

Among the many methods of research, observation and monitoring of human condition, the leading place belongs to electrocardiography (ECG). The need to monitor the ECG during anesthesia, resuscitation, intensive care and diagnosis is beyond all doubt. The ECG signal carries a large amount of information, and a detailed automatic analysis of the patient's ECG signal allows to timely generate alarms that prevent death, as well as to make prognostic conclusions.

When processing the ECG signal, taking the advantages of modern computing resources, it is required to automatically analyze the shape of the ECG signal cycle (cardiocycle), i.e. automatically recognize the characteristic segments and determine their time and amplitude parameters. [1]

An example of the ECG signal cardiac cycle shape and it's characteristic points is shown in Fig. 1. It is common in cardiology to analyze the segments, i.e. the regions between the characteristic points: the segment of P (points P_0… P_1), QRS segment of a point (Q...S), and the segment T (point T_0… T_1). The morphology analysis input receives information obtained at the stage of splitting the ECG signal into cycles: an array of cardiocycle signals accumulated over a some period of time. [2-3]

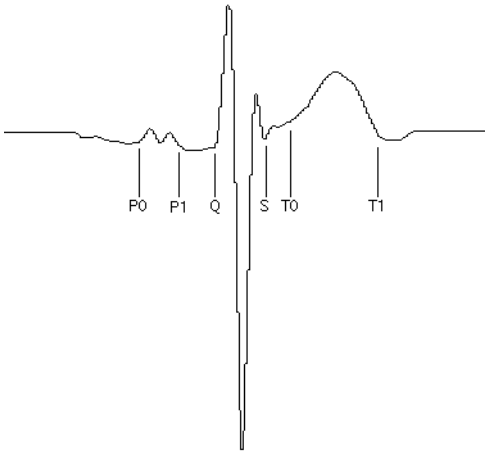

Figure 1. The average shape of the cardiac cycle.

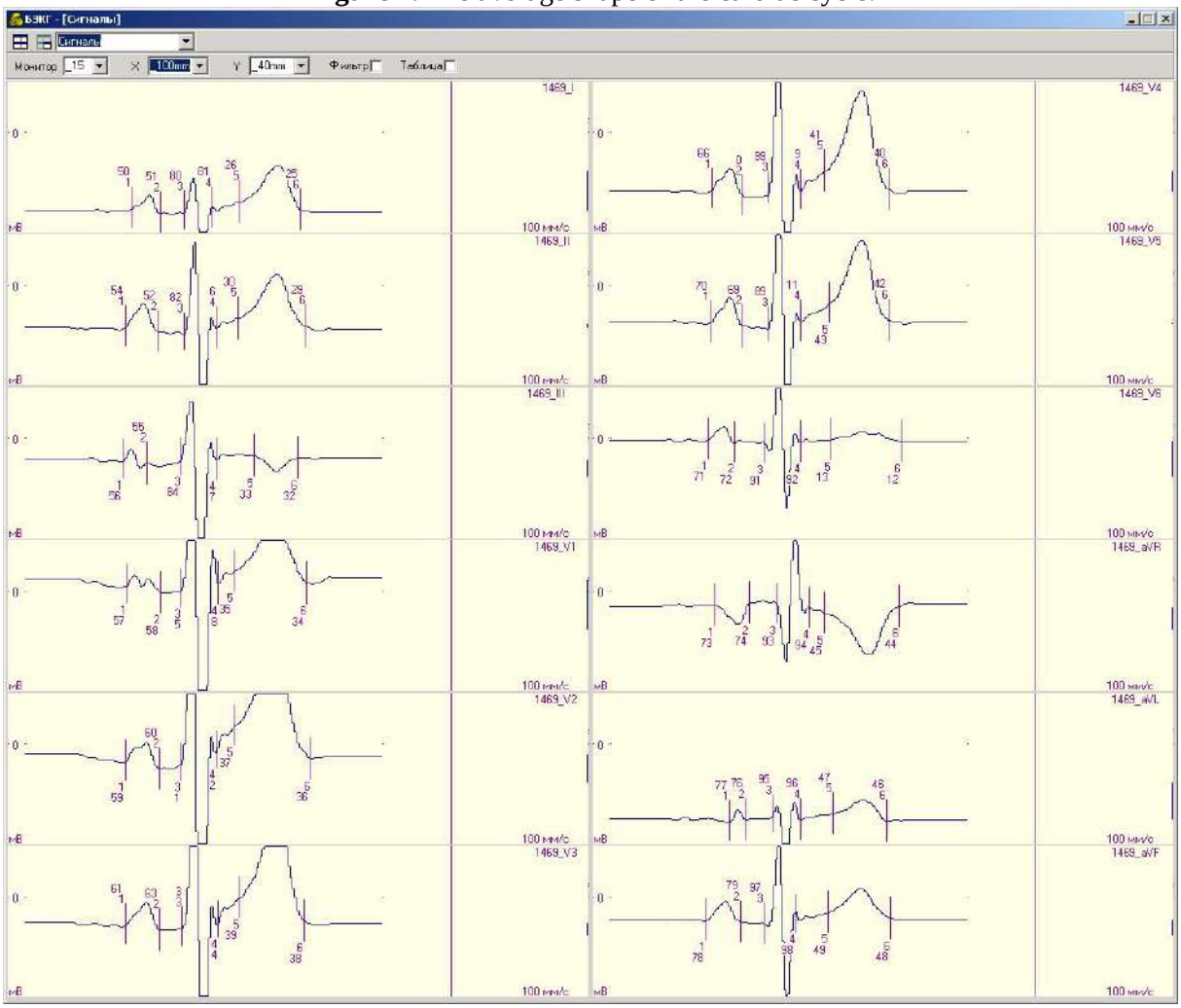

Figure 2. The software used to obtain the training sample base of marked cardiac cycles segments.

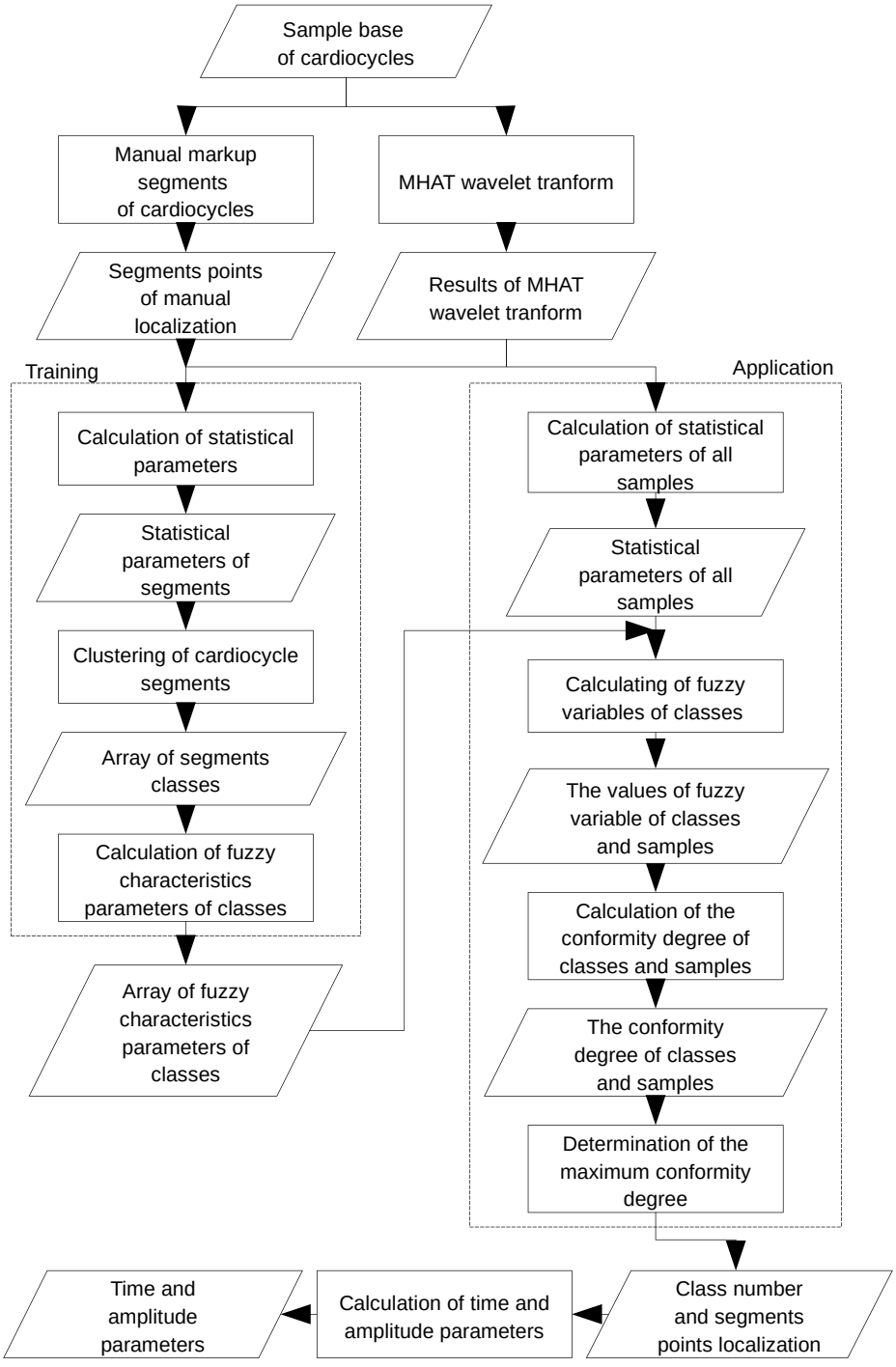

Figure 3. The stages of the previous version of the cardiac cycle morphology analysis.

2. The previous version of the cardiac cycle morphology analysis

Based on the fact that the normal cardiocycle shape changes slowly over time and each current cardiocycle can be distorted by artifacts and noises, it makes sense to recognize the characteristic segments of average cardiocycle shape. The average cardiocycle of several (5-20) cardiocycles having a high correlation coefficient with each other is calculated. Then the selected cardiocycles are averaged pointwise. An example of the obtained signal is shown in Fig. 1 [2]. In the following stages, the shape (characteristic points and segments) of the cardiocycle is recognized.

The training of the recognition system is performed on the basis of the information provided after the manual cardiocycle marking, i.e. the localization of the start and end indexes of the segments P, QRS, and T is known. Such information can be formed using specially developed software. Marking of cardiocycles segments should be made by a medical specialist in this area. The screenshot example of the software developed by LLC Izhtelemed for performing of such marking is presented on Fig. 2. [4]

In [2] it was proposed to use a special algorithm based on the pattern recognition of the ECG signal (Fig. 3.). An original composite system consisting of several modules was developed.

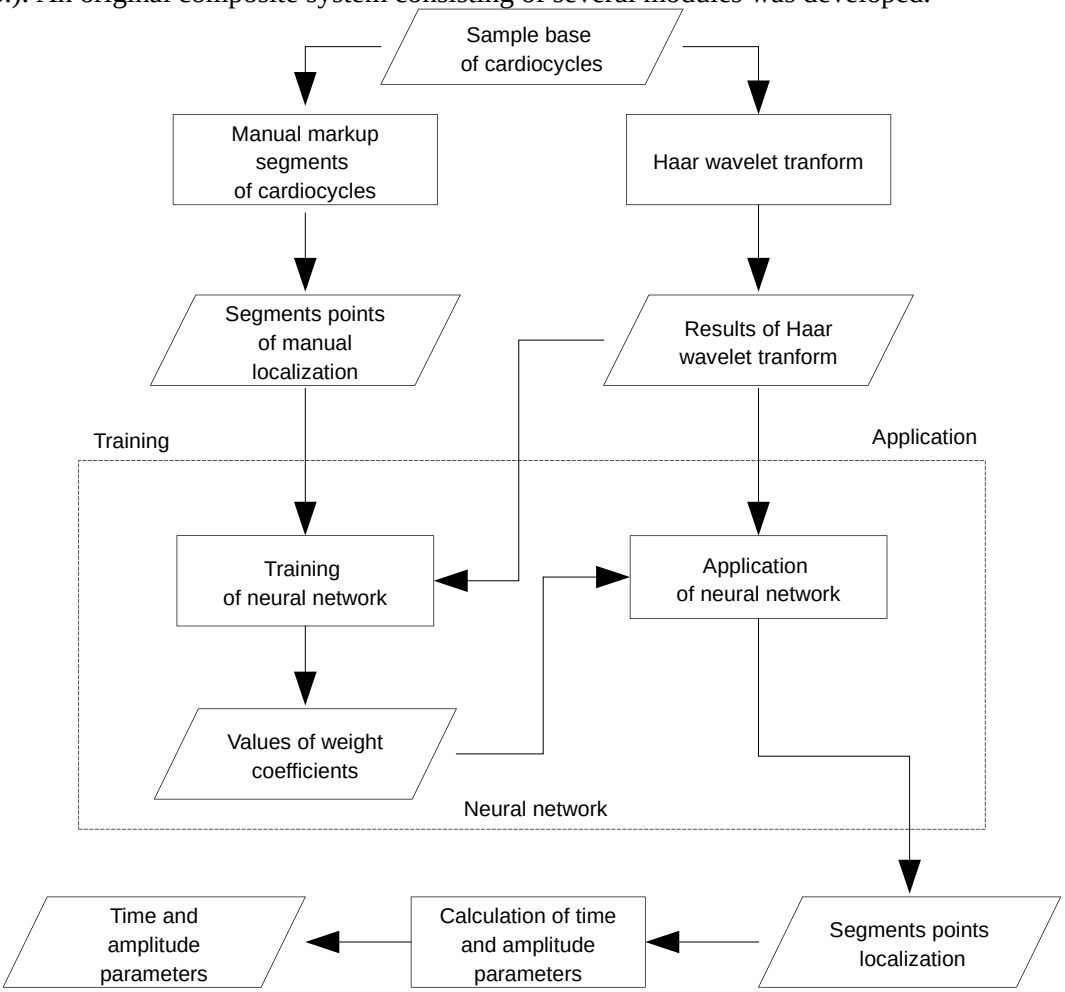

Figure 4. The stages of the cardiac cycle morphology analysis based on neural network.

3. The cardiac cycle morphology analysis based on neural network

In this paper, a reconsideration of the approach based on the pattern recognition of the cardiocycle morphology is carried out, and it is proposed to use an artificial neural network (ANN) as a recognition system of cardiocycle segments. Fig. 4 presents the stages of morphology analysis based on convolutional ANN.

Currently, most studies on ECG analysis algorithms use wavelet transform [5-7]. In the course of the study in [2] it was found that the wavelet transform application of the signal simplifies the ECG cardiac cycle segmentation. In this paper, in contrast to the previous work [2], the Haar wavelet transform of the average cardiocycle was chosen due to the simplicity of its implementation [8]:

$$d^{k+1}{}_i = \frac{x^k{}_{2i} - x^k{}_{2i+1}}{2},\ x^{k+1}{}_i = \frac{x^k{}_{2i} + x^k{}_{2i+1}}{2}, \quad (1)$$

where x is the signal for which the wavelet transform of the next time scale is calculated; d is the result of the wavelet transform calculation; k is the time scale number; i is the signal point index.

As a result of wavelet transform of each cardiocycle at different time scales, a matrix of half-differences is obtained based on which the image is formed. This image then will be fed to the ANN input layer. A total of 6 time scales of transformation is used, an example is shown on Fig. 7.

At the moment, most researchers in signal, speech and image recognition algorithms use a neural network [9-13]. Some researchers combine wavelets and neural network [14-15].

To solve the problem of cardiocycle segments localization based on the wavelet transform results, the apparatus of convolutional ANN (which have been successfully used for image processing in recent years) was chosen.

The first convolutional ANN (which borrowed for computer science the ideas embodied by nature in the visual cortex) was the ANN of Kunihiko Fukushima (Neocognitron, 1975-1980) [16]. The convolutional network in already quite modern form appeared in the works of Yann LeCun (LeNet, 1989). [9]

The input data for the ANN in this paper are the Haar wavelet transform results performed on the average cardiocycle, presented in the form of images of size 200x6, where 200 – the number of counts constituting the cardiocycle (1 second), 6 – the number of time scales of the Haar wavelet transform.

The base of the cardiac cycle segments recognition system are the modules of the convolutional ANN. The special structure of the developed ANN is shown on Fig. 5.

The main modules of the proposed ANN structure are convolutional layers. To avoid the network overfitting problem to the ANN it is added the layers of random transmission shutoffs of the particular outputs (dropout) with a probability of outputs disconnection equal to 25%.

The last two layers of ANN are dense (fully connected) layers. A formed structure of the ANN outputs based on the requirements of the solved problem is following: an array of 200 outputs for each segment (P, QRS, T), i.e. total of 600 outputs.

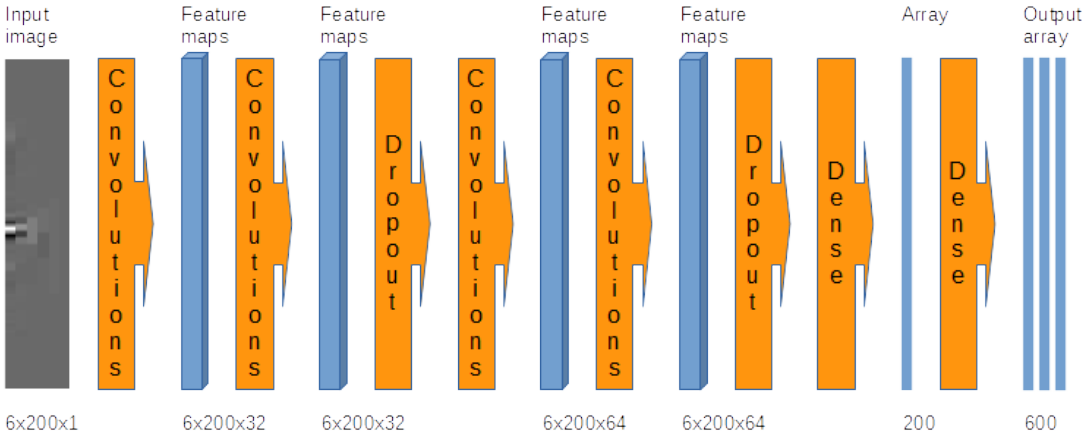

Figure 5. The structure of proposed convolutional artificial neural network.

4. Experiments

To train the recognition system, it is necessary to form a correct training sample base. Each training example should include the following: the image obtained as a result of the Haar wavelet transform of the average cardiocycle, as well as the coordinates of the start and end indexes of the segments (P, QRS, T) which was marked by the expert.

Before training the ANN, it was necessary to modify the training sample to bring the format of target responses for each training example in accordance with the ANN outputs. On the basis of a set of 6 coordinates of 3 segments from each cardiac cycle allocated by the cardiologist 3 array of outputs target values for each segment separately are formed according to the following formula (2):

$$t^{m_i} = \begin{cases} 1, i \in [i^{m_0}, i^{m_1}] \\ 0, i \notin [i^{m_0}, i^{m_1}] \end{cases}, \quad (2)$$

where i = {1...200} is the ANN's output index and the coordinate on the average cardiac cycle; t^m_i is the target output value; m is the segment number; i^m_0 and i^m_1 is the indexes of the start and end of the segment marked by the expert.

After obtaining a set of outputs for each segment by using ANN it is necessary to interpret them. Each training example after transformation by formula (2) contain an image of the wavelet transform result of the average cardiocycle and an array of 600 values, the localization of each segment in which will be allocated units (Fig. 7).

The mean square error (MSE) is chosen as the optimization criterion in this work. The ANN's output MSE is the difference between the desired result (target) and the actual output. In the process of ANN fitting the regression problem is solved, i.e. the values of all outputs obtained during the work of ANN should match with all target outputs values in the training sample. To measure the recognition quality we use the standard error function:

$$\mathrm{MSE} = \frac{1}{m \cdot i} \sum_m \sum_i (e^{m_i})^2 = \frac{1}{m \cdot i} \sum_m \sum_i (t^{m_i} - y^{m_i})^2, \quad (3)$$

where e^m_i is the error value of the segment's m output i; y^m_i is the output obtained by ANN (depends on the ANN's current weights values and the input example); t^m_i is the target output value.

The ANN learning process is reduced to correcting the ANN weights, so as to minimize the MSE. The gradient descent method is generally used to minimize the MSE. In this work, an adaptive Adam algorithm based on gradient descent with smoothed versions of the mean and standard gradients is used to optimize MSE. [17]

Training samples base consisting of 1500 elements was used to fit the ANN. All samples were divided into training and test subsamples with the ratio of 80% by 20%, i.e. training subsample contains 1200 examples and the test subsample contains 300 examples.

The average period of the ANN's training was 1 hour and 40 minutes on Lenovo G505s laptop (CPU AMD A10-5750M, RAM 4 GB). The graph of the error function obtained during ANN training is shown on Fig. 6, where the abscissa axis is the learning epoch number.

Training error displays the ANN's fitting accuracy on a training subsample. However, it does not give a full confidence that the trained model will also be working well on a new data that was not in the training subsample. The model accuracy on the new data is the ANN generalizing ability. To estimate the model generalization ability, the generalization error obtained on the test subsample was used (Fig. 6).

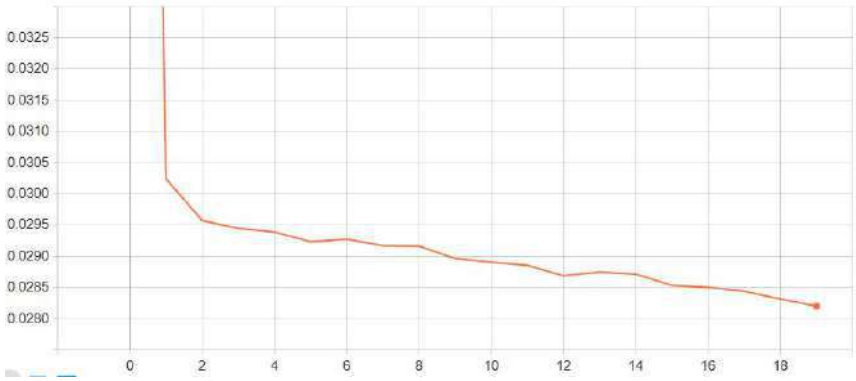

a) the training subsample error

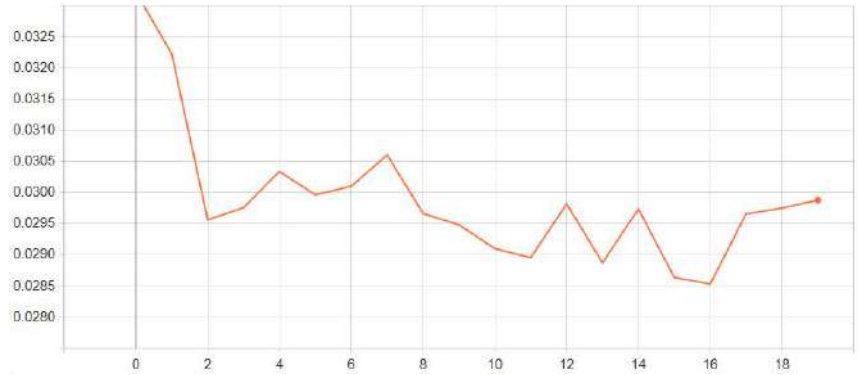

b) the generalization error

Figure 6. Changing an errors when training ANN.

The ANN learning process is iterative. Each iteration is called an epoch. During one epoch, all the examples from the training subsample are submitted to the ANN input. It is also possible to validate the fitting error on the test subsample. As can be seen on the charts, the error function reaches a minimum at epoch 19.

After the ANN training phase, it is possible to use the cardiac cycle segments recognition system on unknown signals. During operation, as well as during training, the wavelet Haar transform of the average cardiocycle is applied, and then the resulting image is fed to the ANN input. The ANN was localized precisely enough the P and QRS segments on the EGG signal which neither was in the training nor in the test subsample (Fig. 7). Segment T localization error could be the result of an inaccurate marking by the expert.

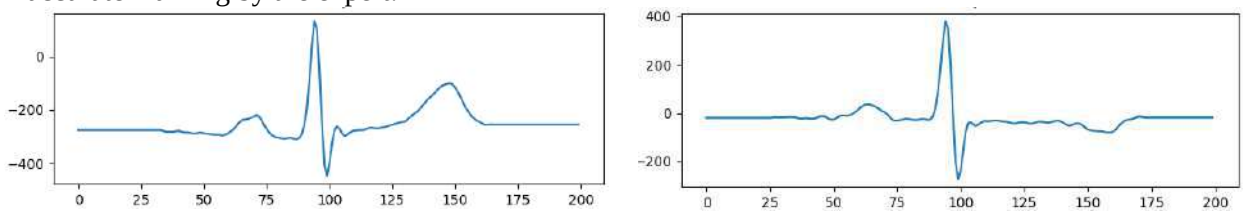

a) the average cardiac cycle signal

b) the Haar wavelet transform result (ANN input)

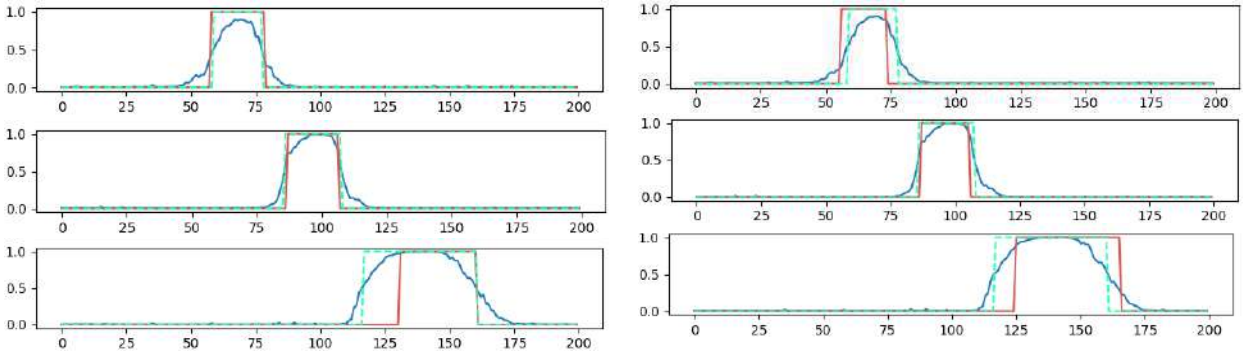

c) the segments recognition result (ANN outputs)

Figure 7. The example of segments localization results.

To perform experiments with the ECG morphology analysis system based on the proposed ANN, the Keras library was used – an open-source ANN library written in Python. It is capable of running on top of the Deeplearning4j, TensorFlow, or Theano frameworks. In this work, Keras was used along with TensorFlow – an open-source software library for machine learning. [18-19]

The Table 1 is showing the results of practical comparison of the proposed cardiocycle segments recognition system (based on convolutional ANN) and the previous version of recognition system proposed in [2] (pattern recognition algorithm) both carried out on the same signals sample (1500 samples). Column names mean the following:

a) e_{limit} is the absolute difference between manual marking and automatic recognition of a segment coordinate, the error expressed in counts;

b) *point* is the name of the cardiac cycle characteristic points: P_0, P_1, Q, S, T_0, T_1;

c) % is percentage of samples satisfying the value e_{limit}.

According to the clinical requirements for the quality of the algorithms results for the cardiocycles segments localization on real signals, a maximum error of no more than 40 MS is allowed. In our case, when the quantization frequency is of 200 Hz, maximum allowable error is equal 8 counts.

According to these requirements, the recognition system based on ANN with a maximum allowable error of 8 counts showed satisfactory results for the following segments (rows in table 1 marked are grayed out): P – 82.18 % of samples, QRS – 88.74 % of samples, and T – 85.36 % of samples. The

system based on the pattern recognition proposed in [2] showed a satisfactory results for the following segments: P – 81.44 % of samples, QRS – 89.20 % of samples, and T – 80.50 % of samples.

Table 1. The results of the recognition systems comparison.

		%	
e_{limit}	point	pattern recognition [2]	convolutional ANN
2	P_0	39.77	34.15
2	P_1	41.59	39.31
2	Q	58.76	46.25
2	S	60.64	57.18
2	T_0	43.46	45.69
2	T_1	43.62	41.27
4	P_0	58.33	53.28
4	P_1	60.89	56.34
4	Q	76.76	73.56
4	S	77.93	68.93
4	T_0	64.58	62.80
4	T_1	61.58	60.56
8	P_0	81.44	84.93
8	P_1	83.35	82.18
8	Q	90.38	90.82
8	S	89.20	88.74
8	T_0	84.65	86.15
8	T_1	80.50	85.36
16	P_0	93.54	96.93
16	P_1	93.95	92.99
16	Q	95.31	94.53
16	S	95.31	95.18
16	T_0	94.56	93.62
16	T_1	94.15	92.23

5. Conclusion

The system based on convolutional ANN proposed in this paper showed results slightly superior to the previous system based on pattern recognition [2] and similar to the work [20].

The proposed system effectively solves the problem used the standard modules of modern convolutional ANN, which simplifies the development of signal and image analysis systems.

The obtained results should be considered as satisfactory given that the training sample was formed mainly on the basis of the ECG from the functional diagnosis cardiological department with large percentage of it were pathological ECG [3].

In the future researches it is possible to modify the developed ANN structure by adding new layers to ANN. It is also necessary to increase the variety and volume of training sample signals. Thus, it is possible to improve the recognition system and use it in a clinical practice.

6. References

[1] Velic M, Padavic I. and Car S 2013 Computer aided ECG analysis - State of the art and upcoming challenges *IEEE EUROCON International conference on computer as a tool* DOI:10.1109/EUROCON.2013.6625218

[2] Korobeynikov A V 2004 *Algorithms and software of computer monitoring systems for analysis of electrocardiograms morphology and rhythm* (Doctoral dissertation, ISTU, Izhevsk, Russia)

[3] Kalyadin N I, Lemenkov V A, Korobeinikov A V, Perevozchikov S M, Odiyankov E G, Rodionov A N and Kotkov S M 2002 Development and Clinical Experience with a Computer

Monitoring System Used at the Intensive Cardiological Care Unit. *Biomedical Engineering* **36(1)** 44-49 DOI: 10.1023/a:1015417424098
[4] *IzhTeleMed Ltd.* (n.d.). URL: http://izhtelemed.ru/
[5] Li W 2019 Wavelets for Electrocardiogram: Overview and Taxonomy *IEEE Access* **7** 25627-25649 DOI: 10.1109/access.2018.2877793
[6] Lannoy G D, Frenay B, Verleysen M and Delbeke J 2009 Supervised ECG Delineation Using the Wavelet Transform and Hidden Markov Models *IFMBE Proceedings 4th European Conference of the International Federation for Medical and Biological Engineering* 22-25 DOI: 10.1007/978-3-540-89208-3_7
[7] Zaniol C, Varriale M C and Manica E 2018 Apnea Recognition with Wavelet Neural Networks *TEMA (São Carlos)* **19(2)** 277 DOI: 10.5540/tema.2018.019.02.277
[8] Mallat S G, Peyré G 2009 *A wavelet tour of signal processing: The sparse way* (Amsterdam: Academic Press)
[9] LeCun A and Bengio Y 1995 *Convolutional Networks for Images, Speech, and Time-Series, in Arbib* (The Handbook of Brain Theory and Neural Networks, MIT Press)
[10] Özbay Y, Ceylan R and Karlik B 2006 A fuzzy clustering neural network architecture for classification of ECG arrhythmias *Computers in Biology and Medicine* **36(4)** 376-388 DOI: 10.1016/j.compbiomed.2005.01.006
[11] Ronneberger O, Fischer P and Brox T 2015 U-Net: Convolutional Networks for Biomedical Image Segmentation *Lecture Notes in Computer Science Medical Image Computing and Computer-Assisted Intervention* 234-241 DOI: 10.1007/978-3-319-24574-4_28
[12] Hinton G, Deng L, Yu D, Dahl G, Mohamed A, Jaitly N and Kingsbury B 2012 Deep Neural Networks for Acoustic Modeling in Speech Recognition: The Shared Views of Four Research Groups *IEEE Signal Processing Magazine* **29(6)** 82-97 DOI: 10.1109/msp.2012.2205597
[13] Deng L, Hinton G and Kingsbury B 2013 New types of deep neural network learning for speech recognition and related applications: An overview IEEE International Conference on Acoustics, Speech and Signal Processing DOI: 10.1109/icassp.2013.6639344
[14] Efitorov A and Dolenko S 2018 A New Type of a Wavelet Neural Network *Optical Memory and Neural Networks* **27(3)** 152-160 DOI: 10.3103/s1060992x18030050
[15] Shoaib M, Shamseldin A Y, Melville B W and Khan M M 2016 Hybrid Wavelet Neural Network Approach *Artificial Neural Network Modelling. Studies in Computational Intelligence* 628
[16] Wasserman P D 1989 *Neural computing: Theory and practice* (New York, NY: Van Nostrand Reinhold)
[17] Goodfellow I, Bengio Y and Courville A 2017 *Deep Learning* (MIT Press) URL: http://www.deeplearningbook.org
[18] TensorFlow (n.d.) URL: https://www.tensorflow.org/
[19] Pattanayak S 2017 Introduction to Deep-Learning Concepts and TensorFlow *Pro Deep Learning with TensorFlow* 89-152 DOI: 10.1007/978-1-4842-3096-1_2
[20] Sampath A and Sumithira T 2016 ECG Morphological Marking using Discrete Wavelet Transform *Intelligent Decision Technologies* **10(4)** 373-383 DOI: 10.3233/idt-160264

Game-theoretic model of wide social groups' behavior with stimulation of volunteering activities

M I Geraskin[1]

[1]Samara National Research University, Moskovskoe Shosse, 34, Samara, Russia, 443086

e-mail: innovation@ssau.ru

Abstract. The problem of developing tools for the stimulation system of socially optimal actions (volunteering) is considered. Based on the study of the population's differentiation according to the propensity to an altruism, the game-theoretic model of the social group's behavior is formed, accounting for the incentives for volunteering. In the cases of the linear decreasing incentive function and the linear cost functions of agents, the Cournot-Nash equilibrium mechanism in the corresponding game is proved. An existence of the equilibrium actions and an impact of incentives on the volunteers' time distribution are confirmed by the simulation of the volunteers' behavior in Russia.

1. Introduction

In Russia, in recent years, volunteering has been developing, because in 2016 a number of the volunteers was 1.435 million[1], i.e., 1% of the population. The volunteering is realized in the performance of actions that maximize the collective utility function, that is, socially optimal actions. The volunteers do not receive income, therefore, these actions do not correspond to the criterion of individual rationality. The Russian statistics demonstrates that moral motivation is effective for a narrow social group of altruistic people. Among the broad masses of the population, trends of individual rationalism [1,2] are exist. The state programs [3,4] implement for overcoming of these trends. In addition, the expansion of volunteering can be provided by the system of stimulation of these actions on the base of the state information system [5].

The interconnection algorithms of the stimulation system and the information system [6,7] enable to solve the problems of personalized registration of citizens' actions, the distribution of the state incentive fund, the monitoring of the of the stimulation effectiveness.

The methodological basis for the development of incentive systems includes the following mechanisms: the competitive mechanism is Pareto-efficient and optimal by the criterion of the additive utility function under non-coalition [8] and coalition [9] agents' behavior; the mechanism of sequential resource distribution (MSRD) [10,11]; the mechanisms of direct and reverse priorities [12]. For MSRD the existence and the uniqueness were proved [13]; according to MSRD, the incentive is distributed [14] as a minimum of the agent's message about its action and the average undistributed rest of incentives. MSRD satisfies [15] the conditions of individual rationality, Pareto efficiency and

[1] Labor and employment in Russia 2017: Statistic compilation / Rosstat. Moscow. 2017. 261 p. http://www.gks.ru/free_doc/doc_2017/trud_2017.pdf

non-manipulability. MSRD is not applicable in a system with independent and simultaneous agents' actions, because the MSRD implies the sequential registration of the agent' actions and the distribution of incentives. Therefore, we use the compensatory linearly decreasing stimulation function, for which these conditions were proved [6,7]. The simulation of the social management [16,17] on the basis of the large groups of population demonstrated the effectiveness of this approach. The utility functions of agents can take into account the symmetry and asymmetry of their awareness [18], which is provided by analyzing the correlation of information flows between social groups [19,20].

The stimulation system of socially optimal actions provides the following results:

- an increase in a number of the volunteers and the time fund of these actions;
- the cross-impact of the altruism and the individual rationality on the behavior of the population groups;
- an emergence of the contradictions between the interests of large social groups, differentiated by a degree of the propensity to the altruism.

Consequently, the model of the population behavior can be formed as the non-cooperative game of the social groups (hereinafter, the agents). The utility functions of these agents include both the incentives for performing socially optimal actions and the loss of the income due to the redistribution of available time, which is a constraint.

2. Methods

We assume that, for the *k*th agent, a continuous function $\zeta_k(\bullet)$ is defined, and we denote the socially optimal actions time interval in the absence of stimulation as a_k. The function $\zeta_k(\bullet)$ expresses the dependence of a_k on the available time fund, and the function has the following form:

$$a_k = \zeta_k(D) = D^{\delta_{ak}}, \delta_{ak} \in [0,1], D >> 1, k \in K, \quad (1)$$

where *D* is the disposable time fund, i.e., the physical time fund with the exception of the rest time; δ_a is the elasticity coefficient of the "charitable" time to *D*, which characterizes the propensity to the altruism; *K* is the set of agents; a_k is the component of the socially optimal actions vector $\mathbf{A} = \{a_k, k \in K\}$.

Definition: the altruism (the propensity to the charity) of the kth agent is called the type of agent, for which $\delta_{ak} > 0{,}5$ *in function (1).*

We introduce the hypothesis of the influence of the propensity to the altruism on the agent's behavior: an increase in the propensity to the altruism leads to a decrease in the utility of the wage, i.e.,

$$U'_{\delta_a}(p_d) < 0, \quad (2)$$

where *d* is the working time interval; p_d is the price (the tariff rate) of the working time; $U(\bullet)$ is the continuously differentiated utility function of the agent.

In the case of the stimulation, the model of the agents' actions choice includes the utility function and the stimulation function. We describe these components of the model.

The agent's utility function is the difference between the sum of the incentives and the costs of the working time loss:

$$U_k(a_k) = p_a a_k - p_d^{1-\delta_{ak}} a_k, k \in K, \quad (3)$$

where p_a is the sum of the insensitive, i.e., the price of a unit of "charitable" time. Formula (3) corresponds to hypothesis (2), because, with a growth of δ_a, the influence of the working time price and the working time fund on the agent's utility decreases.

The stimulation function determines the price of the insensitive as follows [7]:

$$p_a(\mathrm{A}) = b_1 - b_2 \sum_{k \in K} n_k a_k, k \in K, b_1, b_2 > 0, \quad (4)$$

where n_k is the number of agents in *k*th social group, which is constant in the current period; b_1, b_2 are the constant coefficients, calculated by the following formulas

$$b_1 = p_d \frac{A^0}{A^0 - A^D}, b_2 = \frac{p_d}{A^0 - A^D}, A^0 = \sum_{k \in K} a_k^0, A^D = \frac{D}{2} \sum_{k \in K} n_k \,. \tag{4a}$$

The coefficients b_1, b_2 depend on the of agents' actions vector in the previous period $\mathbf{A}^0 = \left\{ a_k^0, k \in K \right\}$. Formulas (4a) are obtained on the basis of the following conditions[1]: 1) in the absence of incentives (i.e., for $p_a(\mathrm{A}) = 0$), the total number of the socially optimal actions is equal to $\sum_{k \in K} a_k^0$; 2) when the price of the incentive is equal to the average wage p_d , the disposable time fund is divided equally between the working time and the "charitable" time (i.e., $\frac{D}{2}$).

We consider the problem of searching for the Nash equilibrium vector **A** from the maximum of the utility function (3) under condition (4) in the case of the constancy of the agents' number in all social groups (i.e., $\frac{\partial n_k}{\partial p_a} = 0 \forall k \in K$).

3. Results and discussion

The equilibrium conditions are formulated as the following assertion.

Assertion 1[2]. *The actions vector* ***A****, satisfying the following conditions*

$$b_1 - b_2 \sum_{j \in K} n_j a_j - b_2 n_k a_k \left(1 + \sum_{j \in K \setminus k} \frac{\partial a_j}{\partial a_k} \right) - p_d^{1-\delta_{ak}} = 0 \,, \tag{5}$$

$$\sum_{j \in K \setminus k} \frac{\partial a_j}{\partial a_k} > -2, k \in K \,, \tag{6}$$

is the Nash equilibrium in problem (3), (4).

In the case of the Cournot hypothesis [21], all agents symmetrically do not change the selected actions in response to the environment's actions, i.e.

$$\frac{\partial a_j}{\partial a_k} = 0, \, j \in K \setminus k \,, \tag{7}$$

which corresponds to the simultaneous and independent choice of actions.

Under condition (7), system (5) has the following form

$$2 n_k a_k + \sum_{j \in K \setminus k} n_j a_j - \alpha_k = 0, \alpha_k = \frac{b_1 + p_d^{1-\delta_{ak}}}{b_2}, k \in K \,, \tag{8}$$

The solution of the system (8) by the Kramer's method can be written as follows:

$$a_k^* = \frac{n\alpha_k - \sum_{j \in K \setminus k} \alpha_j}{(n+1) n_k}, k \in K \,, \tag{9}$$

where the symbol "*" denotes the equilibrium values, *n* is the number of agents in the system. For the Cournot-Nash equilibrium (9), conditions (6) are satisfied considering (7).

---

[1] In the case of these conditions, the system of equations $b_1 - b_2 A^0 = 0, b_1 - b_2 A^D = p_d$ leads to the solution (4a).

[2] Proof of assertion 1. Function (3) under (4) has the form $U_k(a_k) = \left(b_1 - b_2 \sum_{k \in K} n_k a_k \right) a_k - p_d^{1-\delta_{ak}} a_k$. Therefore, the extremum necessary condition $U'_{a_k} = 0$ can be written in the form (5). The sufficient maximum condition $U''_{a_k} < 0$ leads to (6).

We simulate the equilibrium (11) using the example of the social groups of Russian volunteers (Table 1). The actual propensity to the altruism is calculated by the formula $\delta_{ak}(a)=\frac{\ln a_k}{\ln D}$ that follows from formula (1), where the weekly time fund is taken equal to D=112 hours; the graph of the function $\delta_{ak}(a)$ is shown in Fig. 1. The actual distribution function of the population in groups with different propensities to the altruism is calculated by the formula $f_k(a)=\frac{n_k}{\sum_{k\in K} n_k}$.

Table 1 Analysis of the volunteers in 2016.

		Including time worked per week, hours								
Indicator	Total	<9	9 – 15	16 – 20	21 – 30	31 – 40	41 – 50	>51		
The average "charitable" time *a*, hours	8.6	2.35	15	20	30	40	50	60	70	80
The population n_k, thousand	1435	997	243	82	48	23	11	9.8	9	8
The total "charitable" time *A*, thousand hours	12398	2343	3645	1640	1440	920	550	588	630	640
The structure of "charitable" time, %	100	18.90	29.40	13.23	11.62	7.42	4.44	4.74	5.08	5.16
$\delta_{ak}(a)$	0.181	0.181	0.574	0.635	0.721	0.782	0.829	0.868	0.900	0.929
$f_k(a)$		0.070	0.018	0.005	0.000	0.000	0.000	0.000	0.000	0.000
The agent's index		1	2	3	4	5	6	7	8	9

The model of the probability distribution of volunteers according to the "charitable" time has the form of the normal law with certain values of the kurtosis and the asymmetry [7]:

$$f(a)=\frac{1}{\sigma_a\sqrt{2\pi}}e^{-\frac{w\left(a-\bar{a}^{l}\right)^2}{2\sigma_a^2}}, \qquad (10)$$

where $\bar{a},\sigma_a$ are the mathematical expectation and the standard deviation of the initial distribution of the random variable of the "charitable" time; l is the coefficient taking into account the asymmetry (l>1 is the left asymmetry, l<1 is the right asymmetry) in comparison with the normal law (l = 1); w is the coefficient taking into account the kurtosis (w<1 is a more uniform distribution, w> 1 is a less uniform distribution) in comparison with the normal law (w = 1).

According to a degree of the propensity to the altruism, the model of the distribution density of volunteers has a similar form (10), but because the function $\delta_{ak}(a_k)$ is calculated through a logarithmic relationship, instead of formula (10), the following formula is used:

$$f(\delta_a)=\frac{1}{e^{\sigma_\delta}\sqrt{2\pi}}e^{-\frac{e^{w_1}\left(e^{\delta_a}-\left(e^{\bar{\delta}}\right)^{l_1}\right)^2}{2\left(e^{\sigma_\delta}\right)^2}}, \qquad (11)$$

where $\bar{\delta},\sigma_\delta$ are the mathematical expectation and the standard deviation of the initial distribution of the random value of the propensity to the altruism, the parameters w_1,l_1 are similar to the parameters w, l for the distribution (10).

Using the least squares algorithm implemented in the MSExcel processor, the following values of the coefficients of functions (10), (11) are obtained: $\bar{a}=8{,}6,\sigma_a=0{,}57$, $w=0{,}007,l=0{,}58$, $\bar{\delta}=0{,}18,\sigma_\delta=-0{,}65$, $w_1=0{,}43,l_1=0{,}08$. The statistical estimates of regressions (for function (10)

$R^2 = 0{,}99, F = 257$, for function (11) $R^2 = 0{,}99, F = 218$) prove their adequacy. Therefore, the distributions of volunteers according to the time and the propensity to the altruism correspond to the right branch of the Gauss function, that is, the mathematical expectations of the time and the propensity to the altruism are close to the minimum of these indicators. Functions (10), (11) with regard to the indicated coefficients are shown in Fig. 1.2.

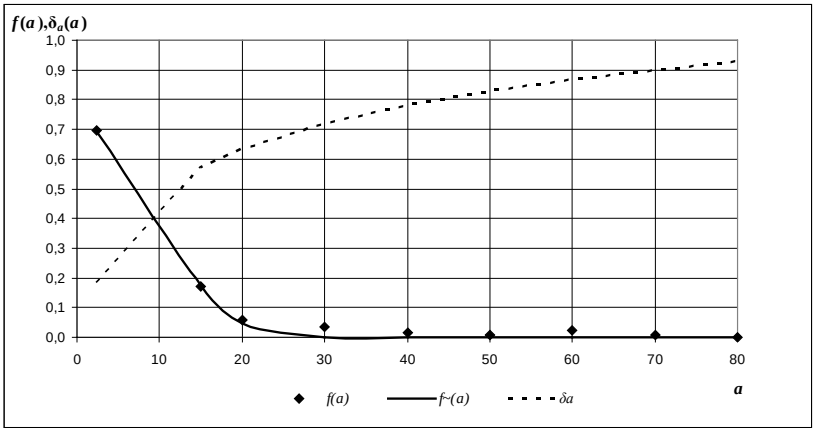

Figure 1. Density distribution function of volunteers by the time and the propensity to altruism.

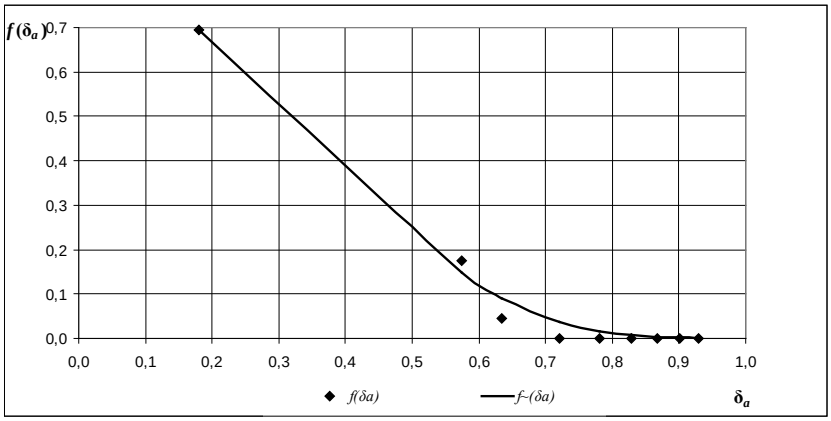

Figure 2. The density function of the distribution of volunteers by the degree of propensity to altruism.

Consider the Cournot-Nash equilibrium (9) for agents, which are indexed in accordance with Table. 1. In Fig. 3 the distribution functions of the time depending on a degree of the propensity to the altruism with different insensitives are shown. In Fig. 4 the dependence of the volunteers' time on the insensitive is demonstrated.

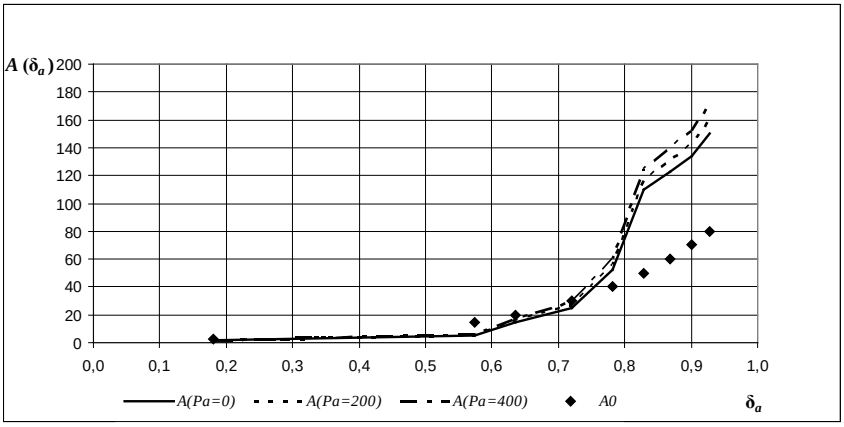

Figure 3. The distribution of the volunteers' time depending on the insensitive.

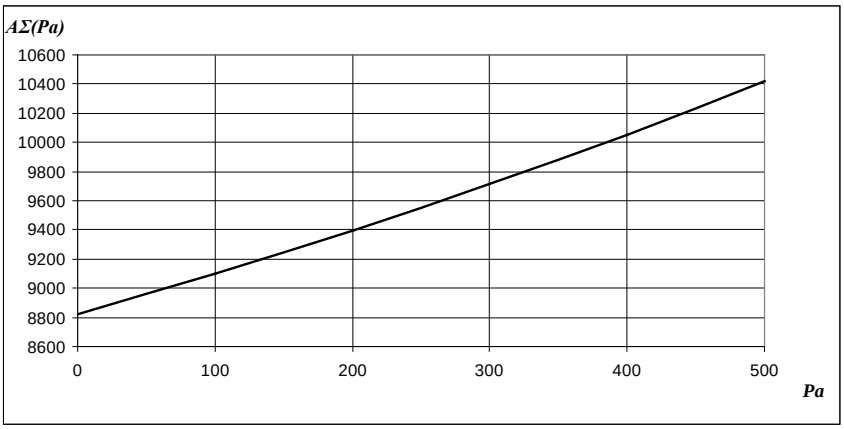

Figure 4. The dependence of the total volunteers' time on the insensitive.

The analysis of the Cournot-Nash equilibria simulation leads to the following conclusions.

First, the distribution of "charitable" time is closest to the real distribution for Pa=0, but the calculated equilibrium actions are lower than the actual values for the agents with low propensity to the altruism, and higher than the actual values for the agents with high propensity to the altruism. Moreover, the volunteers' time at Pa=0 is lower than the actual value. However, the average deviation of the total time for each agent from the total actual time is 4%. Consequently, in the developed equilibrium model, the influence of the population's propensity to the altruism on the volunteers' time is slightly exaggerated.

Second, in the case of the equilibrium distribution, the agents with the highest propensity to the altruism make the greatest contribution to the volunteers' time.

Third, with a growth of the insensitive, the distribution of "charitable" time becomes increasingly uneven, that is, the "charitable" time increases slightly for the agents with low propensity to the altruism and increases sharply for the agents with high propensity to the altruism. Therefore, the agents with high propensity to the are the most sensitive to stimulation.

Fourth, with an increasing in the incentive, the total "charitable" time grows, i.e., the stimulation influences on the involvement in volunteering for high and low altruistic agents.

4. Conclusion

The problem of the developing the information tools for the system of the volunteering stimulation is considered. In the article, the following main results are obtained.

The game-theoretic model of the social groups' behavior is developed, taking into account the stimulation of volunteering, based on the differentiation of the population according to the altruism and the individual rationality.

In the case of the linear diminishing incentive function and the linear agents' cost functions, the Cournot-Nash equilibrium mechanism in the corresponding game is proved.

The simulation of the volunteers' behavior in Russia demonstrates the adequacy of the model, the existence of the equilibrium actions vector and the effect of the stimulation on the volunteers' time.

The analysis shows that the stimulation system has the greatest effect on the agents with high propensity to altruism, but the growth of socially optimal actions is manifested in all social groups.

5. Literature

[1] Roland G 2000 *Transition and Economics. Politics, Markets, and Firms* (Cambridge: MIT Press) p 840

[2] Braguinsky S, Yavlinsky G 2000 Incentives and Institutions. Transition to a Market Economy in Russia (NJ.: Princeton University Press) p 420

[3] RF Government Decree of 30.12.2015 N 1493 "On State program" Patriotic Education of Citizens of the Russian Federation for 2016-2020"

[4] RF Government Decree of December 27, 2012 N 2567-r "On the state program of the Russian Federation" Development of Culture and Tourism "2013-2020"
[5] RF Government Decree of 15.04.2014 N 313 (as amended on 10.21.2016.) "On approval of the Russian Federation, the state program" Information Society (2011-2020)"
[6] Geraskin M I 2017 Algorithms of the information stimulation system of Russian citizens' socio-optimal actions *CEUR Workshop Proceedings* **1903** 92-99
[7] Geraskin M I 2018 Analysis of the influence of citizens' altruism on the effectiveness of the socially-optimal actions stimulation system *CEUR Workshop Proceedings* **2212** 431-439
[8] Burkov V N, Danev B, Enaleev A K, Nanev T B, Podvalny L D and Yusupov B S 1988 Competitive mechanisms in problems of distribution of scarce resources *Avtomatika i telemekhanika* **11** 142-153
[9] Burkov V N, Enaleev A K and Kalenchuk V F 1989 Coalition with the competitive mechanism of resource distribution *Avtomatika i telemekhanika* **12** 81-90
[10] Burkov V N, Enaleev A K and Lavrov Y G 1992 Synthesis of optimal planning and incentive mechanisms in the active system *Avtomatika i telemekhanika* **10** 113-120
[11] Burkov V N, Iskakov M B and Korgin N A 2010 Application of generalized median schemes for the construction of non-manipulable mechanism multicriterion active expertise *Automation and Remote Control* **71(8)** 1681-1694
[12] Korgin N A 2009 Equivalence of non-manipulable and non-anonymous priority resource distribution mechanisms *Upravleniye bol'shimi sistemami* **26.1** 319-347
[13] Burkov V N, Gorgidze I I, Novikov D A and Yusupov B S 1997 *Models and cost and revenue distribution mechanisms in the market economy* (Moskva: Institut problem upravleniya) p 356
[14] Korgin N A 2010 Use of intersection property for analysis of feasibility of multicriteria expertise results *Automation and Remote Control* **71(6)** 1169-1183
[15] Burkov V N, Korgin N A and Novikov D A 2016 Problems of aggregation and decomposition mechanisms of management of organizational and technical systems *Problemy upravleniya* **5** 14-23
[16] Khaimovich I N, Ramzaev V M and Chumak V G 2016 Use of big data technology in public and municipal management *CEUR Workshop Proceedings* **1638** 864-872
[17] Khaimovich I N, Ramzaev V M and Chumak V G 2015 Challenges of data access in economic research based on Big Data technology *CEUR Workshop Proceedings* **1490** 327-337
[18] Faizliev A R, Korotkovskaya E V, Sidorov S P, Smolov F M and Vlasov A A 2018 Utility Maximization for an Investor with Asymmetric Attitude to Gains and Losses over the Mean-Variance Efficient Frontier *Journal of Physics: Conference Series* **1141(1)** 012017
[19] Sidorov S, Faizliev A and Balash V 2017 Measuring long-range correlations in news flow intensity time series *International Journal of Modern Physics C* **28(8)** 1750103
[20] Kulikovskikh I M 2017 Anomaly detection in an ecological feature space to improve the accuracy of human activity identification in buildings *Computer Optics* **41(1)** 126-133 DOI: 10.18287/2412-6179-2017-41-1-126-133
[21] Cournot A A 1960 *Researches into the Mathematical Principles of the Theory of Wealth* (London: Hafner)

Analysis of the credit turnover in the "Retailer-Bank-Insurer" system with variations in market factors

M I Geraskin[1], O A Kuznetsova[1]

[1]Samara National Research University, Moskovskoye shosse, 34A, Samara, Russia, 443086

e-mail: olga_5@list.ru

Abstract. The article considers the possible states of the "Retailer-Bank-Insurer" system. The Pareto-efficient agents' strategies, which maximize the total profit of the system, are described. The agents' models parameters influence on the change in the state of the system is analyzed. Additionally, the influence of the complementarity effect on the change in the retailer's optimal sales volume is investigated. The values of the agents' parameters, which cause the transition of the system from one state to another are determined.

1. Introduction

The integrated organizational systems in the economy are formed in the event that the buyer's demand for one product is conditional upon the fact of purchasing another product. A typical example of such integration is the "retailer-bank-insurer" system, which is formed in the framework of the retailer's credit turnover. Hereinafter, the retailer, the bank, and the insurer are called the agents. The demand for retailer products encourages customers to apply for loans from banks and insurance services to insurers, and the possibility of obtaining credit resources, in turn, expands the demand for retailer products [1]. Therefore, the complementary demand leads to the integrated systems emergence [2].

The integrated system is tightly coupled [5], if the utility function (profit) of agent depends on its action and on the actions of the environment, i.e., other agents [3, 4]. In particular, the agents' costs of the "retailer-bank-insurer" system are interdependent (non-separable), since the system stability is ensured through mutual payments (commissions, discounts, etc.). The system agents revenues can be interdependent, if the system has a mechanism for the aggregate utility distribution [6, 7]. In this case, the agents' utilities can be considered as transferable.

As a result of the agents heterogeneity in economic activity, the problem of coordinating the agents' interests in the integration is considered. The agents, whose goods initiate demand for the goods of other agents, have prevailing economic activity. One of these agents is called the meta-agent. The meta-agent status is realized in the awareness about other agents' utility functions and the utility values. The meta-agent chooses the distribution mechanism of the aggregated system utility. In the "retailer-bank-insurer" system the retailer is the meta-agent. The Pareto efficient [8] algorithm for the transferable utility distribution for the tightly coupled system was developed in [9].

In this paper, we use this algorithm to investigate the influence of the market environment parameters on the states of the "retailer-bank-insurer" system. Two types of states can be implemented in the system [10]. First, the meta-agent dominates, when the meta-agent's optimal sales volume is

less than other agents' optimums; as a result, the environment agents reduce their volumes of sales to the meta-agent's volume. Second, the environment dominates, when the meta-agent's optimum exceeds other agents' optimums. Hence, there are two options of coordinating: either the meta-agent reduces sales to the volume of the environmental optimum level, or the environment increases sales to the meta-agent's optimum. The choice of these options is carried out in the system consistently [11, 12], according to the maximum of the total profit criterion. Consequently, the state of the system has a significant effect on the equilibrium after the agents' total profits distribution [13].

The subject of the paper is to study the influence of the agents' market demand functions parameters on the resulting system states and to determine the boundary values of these parameters, which cause transitions from one state to another.

2. Methods and materials

We consider the "retailer-bank-insurer" system. The utilities of agents are calculated by the following formulas [3]:

$$\pi_k(Q_k) = \bar{p}_{k(n)} Q_k^{b_{k(n)}+1} - c_k Q_k, k \in K, \quad (1)$$

where $\bar{p}_k = a_k - u_k - \rho_k > 0, k \in K$; $\pi_k(Q_k)$ is the agent's profit function; $p_{k(n)}$ is the price of k-th agent's goods; u_k is k-th agent's integration costs; ρ_k is k-th agent risk; $a_{k(n)}$, $b_{k(n)}$ are the price function coefficients for the n-th system state (n = 1 is the integrated system with $Q_{-l}^* > Q_l^*$, n = 2 is the integrated system with $Q_{-li}^* > Q_l^* > Q_{-lj}^*$, n = 3 is the integrated system with $Q_{-l}^* < Q_l^*$); K is the agents' set; the meta-agent is denoted by the symbol «l», the environment is denoted by the symbol «–l», the symbol «*» denotes the optimum of the agent; Q_k is k-th agent sales; ρ_k is direct costs per unit of k-th agent.

The system states are classified as follows:

$$n = \begin{cases} 1, \text{если } Q_l^* < Q_{-l}^*, \\ 2, \text{если } Q_l^* > Q_{-l}^*, \\ 3, \text{если } Q_l^* \in (Q_{-l1}^*, Q_{-l2}^*), \end{cases} \quad (2)$$

where the symbols Q_{-l1}^*, Q_{-l2}^* denote the environmental agents of the meta-agent.

The meta-agent is an agent, which profit exceeds the total profit of the environment for the optimal strategy. The meta-agent is determined by the following criterion:

$$\pi_l(Q_l^*) > \sum_{k \in K \setminus l} \pi_k(Q_k^*). \quad (3)$$

The risk costs characterize the share of probable losses of the agent's average revenue from the price. The risk cost of the retailer is the bank's arrears on loans for goods sold. The bank's risk exposure is the overdue debt on loans issued, which is taken into account by the discount rate. The insurer's risk costs are payments for insured events, which are taken into account by the probability of their occurrence. In the case of $u_k > 0$, the integration costs are interpreted as discounts or commissions in price of agent with greater economic activity. In the case of $u_k < 0$ the integration costs represent the income of the more active agent as a transfer in the form of price premiums or commissions from other agents for participation in the integrated system.

The agents' optimums are calculated by the following formulas [3]:

$$Q_k^* = \left[\frac{c_k}{\bar{p}_{k(n)}(b_{k(n)}+1)}\right]^{\frac{1}{b_{k(n)}}}, k \in K, n = 1,2,3 \quad (4)$$

The complementary demand is taken into account as follows: the meta-agent sales volume through its demand function coefficient depends on the environment sales volume:

$$a_1 = a_{lk} a_{l0} Q_k^*, k \in K \setminus l, a_{lk} = \begin{cases} a_{lk(1),n=1}, \\ a_{lk(2),n=2}, \\ a_{lk(3),n=3}. \end{cases} \quad (5)$$

where α_{lk} is the complement ratio of k-th and l-th goods, $\alpha_{lk(1)} > \alpha_{lk(2)} > 0$ are constants. The complementarity effect is expressed as follows: the growth in lending leads to a faster growth in

retailer's turnover under low interest rate (n = 1), and it leads to a slow increase under high interest rate (n = 2).

The boundary values of the demand functions parameters are determined in the form of the following conditions:

$$Q_l^*(\tilde{a}_l) = min\{Q_k^*(\tilde{a}_k), k \in K \setminus l\}, Q_l^*(\tilde{\tilde{a}}_l) = max\{Q_k^*(\tilde{\tilde{a}}_k), k \in K \setminus l\},$$
$$Q_l^*(\tilde{b}_l) = min\{Q_k^*(\tilde{b}_k), k \in K \setminus l\}, Q_l^*(\tilde{\tilde{b}}_l) = max\{Q_k^*(\tilde{\tilde{b}}_k), k \in K \setminus l\},$$

where $\tilde{a}_k, \tilde{\tilde{a}}_k, \tilde{b}_k, \tilde{\tilde{b}}_k, k \in K$ are the values of the demand functions coefficients under which the transition occurs between the states n = 1, 2 (denoted by the symbol "~") and n = 2, 3 (denoted by the symbol "≈"). Because the system is tightly coupled, that is, the profits redistribution between agents is possible, the equilibrium is selected according to the agents' total profits criterion:

$$Q^p = \{Q_k^p, k \in K\} = \arg\max_{Q \geq 0} \pi_\Sigma(Q), \pi_\Sigma = \sum_{k \in K} \pi_k(Q_k^*) \quad (6)$$

where Q^p is the Pareto-efficient (equilibrium) vector of the agents' actions Q_k^p; π_Σ is the total system profit.

We consider the problem of searching for the Pareto-effective strategies (i.e., actions) in the possible states of the "retailer-bank-insurer" system.

3. Results

Assertion 1. The Pareto-effective strategies of agents are as follows:

$$Q^p = \{Q_k^p, k \in K\} \begin{cases} = Q_l^*, n = 1, \\ \in [Q_{-l}^*, Q_l^*], n = 2, \\ \in [Q_{-l1}^*, Q_{-l2}^*], n = 3. \end{cases}$$

Proof of assertion 1: for n = 1, by criterion (6) we get $Q^p = \{Q_k^p, k \in K\} = \arg\max_{Q \geq 0} [\pi_l(Q_l^*) + \pi_{-l1}(Q_{-l1}^*) + \pi_{-l2}(Q_{-l2}^*)]$; because in this case, according to (2), $Q_l^* < Q_{-l}^*$, then, accounting (3), we can get $Q_k^p = Q_l^*, k \in K$. When n = 2, by criterion (6) we get $Q_{-l}^* \leq Q_k^p \leq Q_l^*, k \in K$. When n = 3, we get $Q_{-l1}^* \leq Q_k^p \leq Q_{-l2}^*, k \in K$.

In order to simulate the Pareto-effective strategies, we consider the "retailer-bank-insurer" system, in which the initiator of the coordination is the retailer. The parameters of the system are presented in Table 1.

Table 1. System parameters.

Parameters	Retailer	Bank	Insurer
a_k	49000	0,785	0,35
u_k	-3230	0,031	0,018
ρ_k	0	0,001	0,077
p_k	$49000Q_1^{0,09}$	$0,785Q_2^{0,19}$	$0,35Q_3^{0,165}$
c_k	1500	0,053	0,03
b_k	-0,09	-0,19	-0,165

As follows from table 1, the maximum price of the retailer's product and its costs exceed the prices and costs of other agents, therefore, according to the maximum profit criterion, the retailer acts as a the meta-agent. The retailer receives additional income in the integration, because the integration costs of the retailer are negative.

In Figure 1, agent the profits dependence on sales volumes are plotted. It should be noted that due to the large difference in the prices of agents, the realtor's profit is estimated on the right scale, and the bank's profit and the insurer's profit are presented on the left scale.

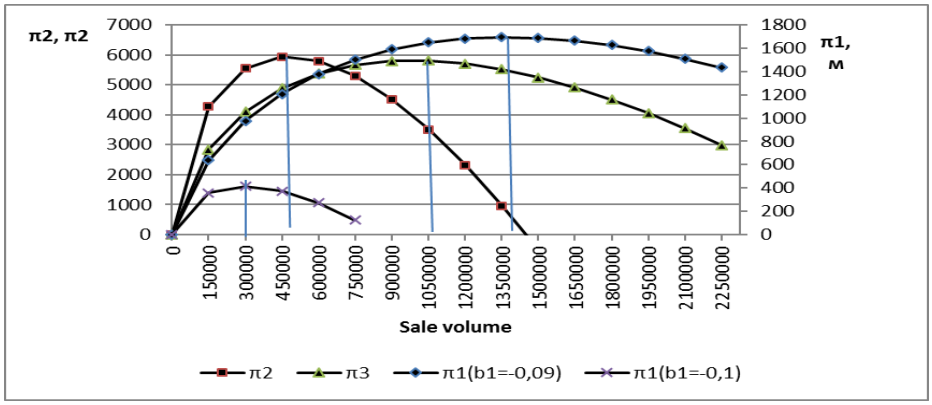

Figure 1. Dependence of agent profits on sale volumes.

In Figure 1, the following notation is used: $\pi_{1(b1 = -0,1)}$ is the retailer's profit, when its optimum is less than that of other agents; $\pi_{1(b1 = -0,09)}$ is the retailer's profit, when its optimum greater than that of other agents; π_2 is the bank's profit, π_3 is the insurer's profit.

The criterion for solving the problem is determined as the total profit of the system. In Figure 2, the total profit coincides with the retailer's profit due to its significant superiority over other agents. Thus, the total profit of the system is approximately equal to the retailer's profit. Consequently, the optimal sales volume of the system is determined by the retailer's model.

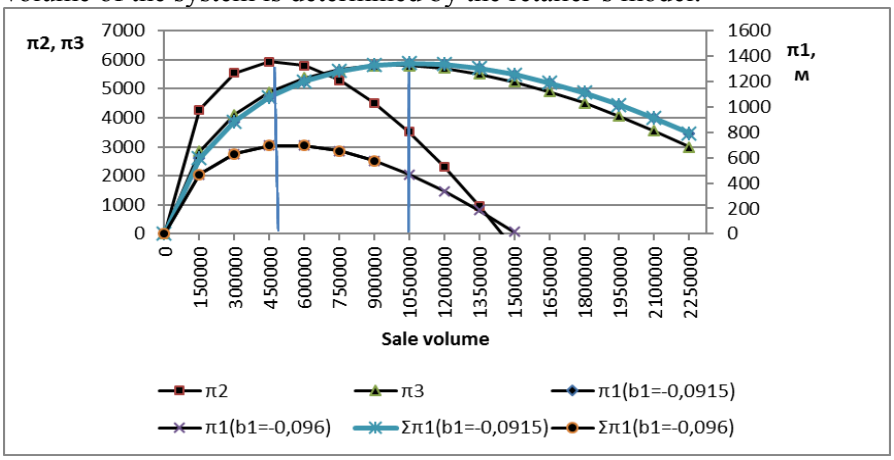

Figure 2. Dependencies of agent profits and total system profits.

In Figure 2, the following notation is used: $\pi_{1(b1 = -0,1)}$ is the retailer's profit, when its optimum less than that of other agents; $\pi_{1(b1 = -0,09)}$ is the retailer's profit, when its greater than that of other agents; π_2 is the bank's profit, π_3 is the insurer's profit, $\pi_{\Sigma 1(b1 = -0,0915)}$ is the total profit of non-integrated agents, when the optimal retailer's volume is greater than the optimal volumes of other agents, $\pi_{\Sigma 1(b1 = -0,096)}$ s the total profit of non-integrated agents, when the optimal retailer's volume is less than the optimal volume of other agents.

The changing in the market parameters leads to a variety of system states, which is characterized by the position of Q_l* relative to other agents. In Figure 2, the set of the possible states reflects its boundary states, when $Q_{l(1)}$*= Q_2* and $Q_{l(1)}$*= Q_3*. Accordingly, it is possible to distinguish three intervals: Q_l*< Q_2* < Q_3*, Q_2* < Q_l*< Q_3*, Q_2*< Q_3* < Q_l*.

Provided that the agent optimal volume depends on b_1, it is possible to determine the boundary values b_1. The situation Q_l*= Q_2* < Q_3* is realized, when b_1 = -0,098. The situation Q_2*< Q_3* = Q_l* is reached, when b_1 = -0,098. In the situation (b_1 = -0,1) the retailer's optimal volume $Q_{l(1)}$* is less than the optimal volumes of other agents Q_2*, Q_3*. In the situation (b_1 = -0,09) the retailer's optimal volume $Q_{l(1)}$* is greater than the optimal volumes of other agents Q_2*, Q_3*. Because the retailer's profit significantly exceeds other agents' profit, the total profit of agents in a non-integrated system

almost coincides with the retailer's profit. Accordingly, it is possible to determine the optimum of the system as the optimum of the retailer.

We carry out the factor analysis of the market parameters influence a_1, b_1, a_2, b_2 on Q_1*.

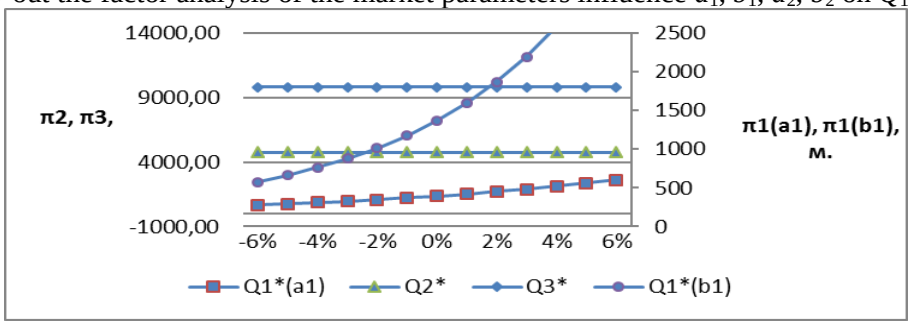

Figure 3. Dependencies of agents' optimal volumes on market factors a_1, b_1.

We consider the following initial market environment parameters : a_1= 49000, b_1= -0,019. When changing the market parameters a_1, b_1, the complementarity effect does not arise, because the sales volumes of other agents do not change. Accordingly, the parameter α_{lk} in formula (5) is not taken into account. At the same time, it is obvious that an increase in a_1 is accompanied by a less sharp change in the retailer's optimal volume, than with a change in b_1. Thus, an increase in a_1 from 0 до 4% provides that it enters the zone Q_2*<Q_1*<Q_3*. An increasing in a_1 by more than 4% provides that the retailer's volume a switch to the zone Q_1*>Q_3*. At the same time, as a_1 decreases, the retailer's optimal volume decreases, and the situation Q_1*<Q_2* arises.

An increasing in b_1 from 3% to 4% provides that the retailer's volume is in the zone Q_2*<Q_1*<Q_3*. An increasing in b_1 more than 4% provides that the retailer's volume is in the zone Q_1*>Q_3*. A decreasing in b_1 leads to the retailer's optimum reducing, and a situation Q_1*<Q_2* arises.

When the market parameters a_2, b_2 change, the value of the bank's optimal volume changes, and the complementary effect arises that affects the retailer's sales. The calculation of the parameter a_1 by the formula (3) leads to an increase in Q_1* with increasing Q_2*.

An increase in the a_2 leads to changes in the optimal volumes of the bank and the retailer. An increasing in a_2 from -2% to -1% leads to transition of the retailer's optimum in the zone Q_2* < Q_1* < Q_3*. An increasing in a_2 from -1% to +∞ provides the retailer's volume transition to the zone Q_1* > Q_3*. While decreasing in a_2 more than 2%, the retailer's optimal volume is reduced, and a situation Q_1* < Q_2* arises.

Table 2. Characteristic intervals.

n = 1 Q1*< Q2*	n = 2 Q2*< Q1*< Q3*	n = 3 Q1* > Q3*
$\Delta a_1(-\infty,0\%)$, $\Delta b_1(-\infty,3\%)$ $\tilde{a}_1 = 49171{,}5$, $\tilde{b}_1 = -0{,}08964$	$\Delta a_1(0\%,-4\%)$, $\Delta b_1(3\%,4\%)$	$\Delta a_1(-4\%,+\infty)$, $\Delta b_1(4\%,+\infty)$ $\tilde{\tilde{a}}_1 = 54341$, $\tilde{\tilde{b}}_1 = -0{,}084$
$\Delta a_2(-\infty,-2\%)$, $\Delta b_2(-\infty,-1\%)$ $\tilde{a}_2 = 0{,}766$, $\tilde{b}_2 = -0{,}188$	$\Delta a_2(-2\%,-1\%)$, $\Delta b_2(-1\%,1{,}6\%)$	$\Delta a_2(-1\%,+\infty)$, $\Delta b_2(1{,}6\%,+\infty)$ $\tilde{\tilde{a}}_2 = 0{,}778$, $\tilde{\tilde{b}}_2 = -0{,}0164$

A changing in b_2 from -1% to 1,6% provides that the retailer's optimum is the zone Q_2* < Q_1* < Q_3*. An increasing in b_2 more than 1,6% provides that the retailer's optimum switches to the zone Q_1*> Q_3*. When b_2 decreases more than 1%, the retailer's optimal sales volume decreases and the situation Q_1* < Q_2* arises.

The situation n = 1 denotes that the retailer's sales volume is in the interval $Q_1^* < Q_2$. In this situation, the retailer's sales volume is the least in the system, hence, the retailer is interested in reducing the volume of other agents to Q_1.

The situation n = 2 denotes that the retailer's sales volume is in the interval $Q_2^* < Q_1^* < Q_3^*$. In this situation, the retailer's optimal volume is greater than the bank's optimum, but less than the insurer's optimum. The retailer encourages the bank to increase its sales, and it encourages the insurer to reduce its sales.

Situation n = 3 denotes that the retailer's sales volume is in the interval $Q_1^* > Q_3^*$. In this situation, the optimal sales volume of the retailer is greater than other agents' optimums, therefore, it is interested to encourage them to increase the sales.

The emergence of each situations is a result of a change in the parameters of the retailer: the maximum price of its product and the ratio of sales volume change to the price. Additionally, due to the complementarity effect, the change in bank's parameters through the coefficient of the demand function affects the change in the retailer's volume. Hence, the retailer's parameters are determined: the maximum price and the change in sales volume, when the transition from one situation to another occurs.

4. Conclusion

The paper considers the "retailer-bank-insurer" system. The system takes into account the integration costs and the joint influence of agents' sales volumes on each other. Several frontier positions have been defined, under which the Pareto-effective system strategy changes.

The zones $Q_1^* < Q_2^*$, $Q_2^* < Q_1^* < Q_3^*$, $Q_1^* > Q_3^*$ are selected. In the first zone, the retailer, in order to increase its profit, is interested in encouraging the bank and the insurer to reduce their sales volumes to Q_1^*. In the second zone, to achieve the same result, the bank must increase its sales volume, and the insurer must decrease. In the third zone, both the bank and the insurer must increase their sales to achieve Q_1^*.

The influence of market factors a_k, b_k on the optimal sales volume of agents is analyzed. An increase in these parameters leads to an increase in the optimal sales volumes of agents of the relevant market. At the same time, the change in the bank's parameters has an impact on the change in retailer's sales volume. The change in the retailer's optimum is more sensitive to changes in the bank's parameters.

5. References

[1] Kulikovskikh I M 2017 Anomaly detection in an ecological feature space to improve the accuracy of human activity identification in buildings *Computer Optics* **41(1)** 126-133 DOI: 10.18287/2412-6179-2017-41-1-126-133
[2] Geraskin M I and Manakhov V V 2015 Optimization of interactions in a multi-agent, tightly linked "retailer-bank-insurer" system *Problemy upravleniya* **4** 9-18
[3] Continuity and stimulating compatibility in cardinal voting mechanisms URL: https://papyrus. bib.umontreal.ca (15.07.2017)
[4] Novikov D A 2012 *Theory of management of organizational systems*
[5] Shao R and Zhou L 2016 Voting and optimal provision of public goods *Journal of Social Economics* **134** 3-41
[6] Burkov V N, Gorgidze I I and Novikov D A 1997 *Models and mechanisms for the distribution of costs and revenues in a market economy* (Moscow: ICS RAS)
[7] Moulin H 2017 Designing a single mechanism *Theoretical economics* **12(2)** 587-619
[8] Ventura A, Kafiero K and Montibeller M 2016 Pareto Efficiency, Coase's Theorem and External Effects: A Critical Look *Journal of Economic Problems* **50(3)** 872-895
[9] Geraskin M I, Kuznetsova O 2017 Agents' Interaction algorithm in a strongly coupled system with a transferable utility *CEUR Workshop Proceedings* **1904**
[10] Geraskin M I 2017 Optimal mechanism for the distribution of the effect in an integrated strongly coupled system of anonymous agents with a transferable utility *Problemy upravleniya* **2** 27-41
[11] Pattanyk P K, Salles M 2016 *Social choice and welfare* (Elsevier science)

[12] Bondarik V N, Kordin N A 2012 Resource allocation mechanisms based on non-maximum, symmetric, anonymous voting procedures with delegation *Management problems* **5** 26-32
[13] Korgin N A, Korepanov V O 2016 Effective solution to the problem of resource allocation with the Groves-Lediar mechanism for portable utility *Automation and remote control* **77(5)** 914-942

Performance comparison of machine learning methods in the bus arrival time prediction problem

A A Agafonov[1] **and A S Yumaganov**[1]

[1]Samara National Research University, Moskovskoye shosse, 34, Samara, Russia, 443086

e-mail: ant.agafonov@gmail.com, yumagan@gmail.com

Abstract. The problem of predicting the movement of public transport is one of the most popular problems in the field of transport planning due to its practical significance. Various parametric and non-parametric models are used to solve this problem. In this paper, heterogeneous information affecting the prediction value is used to predict the arrival time of public transport, and a comparison of the main machine learning algorithms for the public transport arrival time forecasting is given: neural networks, support vector regression. An experimental analysis of the algorithms was carried out on real traffic information about bus routes in Samara, Russia.

1. Introduction

Public passenger transport is an important part of the transport system. Efficient use of passenger transport will help to reduce road congestion by reducing the use of personal vehicles, as well as cut down fuel consumption and reduce environmental pollution. To improve the quality of passenger transport service, among other things, it is necessary to provide passengers with information about the exact arrival time of vehicles at stops. This information is important for passengers because it allows them to choose alternative routes and reduce the waiting time for vehicles.

The arrival time of vehicles at stops can be considered as stochastic, since it depends on many factors, including the passing time of road segments, the time spent at stops and the delay time at intersections. Furthermore, such factors as traffic congestion, incidents and weather conditions must be taken into account to predict the arrival time. Thus, the development of prediction model that takes into account various spatial-temporal factors is a difficult task.

Despite the popularity of the above mentioned problem, many papers consider only individual factors (for example, speed of the vehicle on the current and previous road segments) to predict the arrival time at stop. Moreover, the comparison of algorithms in those papers is carried out on different sets of data that often include information about only one or a few routes.

In this paper, a comparison of different public transport arrival time prediction models including artificial neural networks, support vector regression and linear regression is made. Heterogeneous information describing the transport situation is used for prediction. Comparison of algorithms is carried out on the traffic data of bus network in Samara, Russia.

2. Related works

There are a large number of studies devoted to the problem of public transport arrival prediction. All existing works can be divided into several categories according to the type of used models and algorithms: parametric and non-parametric regression models, Kalman filters based models, artificial neural networks, the support vector machine, hybrid models.

Linear regression models [1, 2] are constructed as regression functions from a set of independent variables. The applicability of these models to transport systems is limited due to the strong correlation of the variables of the regression function. Nonparametric regression, in particular, the k-nearest-neighbor method, was used to solve the prediction problem in the papers [3, 4, 5]. However, the requirement of a large sample size imposes a restriction on the use of this method in real time. In [6], a clustering algorithm was used to determine the distribution of the travel time of the road segment.

Models based on the Kalman filter [7] allow to estimate the future values of the dependent variables based on the recursive procedure, taking into account the stochastic nature of the process and the noise of the measurements. Models of artificial neural networks (ANN) [8, 9] are the most commonly used approaches for predicting arrival time. Prediction model presented in [8] combines two models of neural networks trained using two sets of data respectively: travel times dataset and arrival time at stops dataset. Authors of [9] used the Bayesian approach to combine several neural networks to build a prediction.

The support vector regression (SVR) is a set of similar learning algorithms with a teacher used for classification and regression analysis problems [11, 12]. In [12], the travel time of the current and next road segments was used for prediction. In [11], the authors used a genetic algorithm to select SVR parameters. The authors of [13] used a prediction model that combines two SVR models.

Hybrid models are also used to reduce the forecast error [14, 15, 16]. These models combine several heterogeneous methods and algorithms. The travel time prediction problem is necessary to solve other complex problems, such as reliable path finding [17] or autonomous vehicles routing [18].

The results of a comparison of several regression models and machine learning methods are presented in [19], the best result was shown by the SVR model. Inverse results were obtained in [20], the best results were shown by the neural network model.

In most works, the best results of the public transport arrival time prediction were shown using machine learning methods: neural network models and SVR. However, the choice of a particular model depends on the used input data.

3. Basic notation and problem formulation

A transport network is considered as a directed graph, the vertices of which correspond to the stops and the edges denotes segments of the transport network between the stops.

Let's s denotes a bus stop from set S; w_{ij} denotes the segment of the transport network between the stops $i \in S$ and $j \in S$ with length $|w_{ij}|$; r denotes public transport route from set R; R_{ij} denotes the set of routes passing through segment w_{ij}; n denotes a vehicle from set N; N_r denotes a set of vehicles with route $r \in R$.

The problem of arrival time prediction for the vehicle $n \in N$ with route $r \in R$ at the stop $j \in S$ can be formulated as:

$$t_j^{arr,n} = t_i^{dep,n} + T_{ij}^{travel,n}, \tag{1}$$

where $t_j^{arr,n}$ denotes the arrival time at the stop j, $t_i^{dep,n}$ denotes the departure time from the stop i, $T_{ij}^{travel,n}$ denotes the travel time between stops i and j.

Then the problem of the arrival time prediction is reduced to the problem of travel time prediction $T_{ij}^{travel,n}$ or, equivalently, problem of vehicle's speed v_{ij}^{n} prediction.

The problem can be formulated as follows:
using the transport network graph, as well as statistical and real-time data, predict a speed $\hat{v}_{ij}^{n}(t_c, t)$ *at the time* t*, considering that the prediction is calculated at time* t_c*.*

4. Proposed model

4.1. Factors of prediction

In order to obtain a speed prediction $\hat{v}_{ij}^{n}$ of a vehicle $n \in N$ running the route $r \in R$, various factors affecting the predicted value can be taken into account. In contrast to the works known to the authors, this article proposes the use of heterogeneous information describing the transport situation. This information defined as follows:

- The speed v_{ij}^{n} of the vehicle $n \in N$ on the segment w_{ij};
- The weighted average speed $v_{ij}^{route,r}$ of vehicles running the route $r \in R$ on the segment w_{ij}:

$$v_{ij}^{route,r}(t) = \frac{\sum_{k \in N_r} \omega\left(t - t_i^{dep,k}\right) v_{ij}^{k}}{\sum_{k \in N_r} \omega\left(t - t_i^{dep,k}\right)},$$

  where $\omega(t)$ is a kernel

$$\omega(t) = \begin{cases} \exp(-\alpha t), & t \le \Delta_{max}, \\ 0, & t > \Delta_{max}; \end{cases}$$

  Δ_{max} is a time interval for which estimates of speed are considered.
- The weighted average speed v_{ij}^{all} of vehicles with any route on the segment w_{ij}:

$$v_{ij}^{all}(t) = \frac{\sum_{r \in R_{ij}} \sum_{k \in N_r} \omega\left(t - t_i^{dep,k}\right) v_{ij}^{k}}{\sum_{r \in R_{ij}} \sum_{k \in N_r} \omega\left(t - t_i^{dep,k}\right)};$$

- The average hourly traffic flow speed v^{hour};
- The average daily traffic flow speed v^{day};
- The historical average speed $v_{ij}^{stat}(t)$ of vehicles with any route on the segment w_{ij} at time interval t;
- The average traffic flow speed $v_{ij}^{flow}(t)$ on the segment w_{ij} at the time point t;
- The traffic flow speed v_{ij}^{fNow} on the segment w_{ij} at the current time.

It is assumed that the average hourly and average daily speeds reflect the current seasonal and weather situation indirectly, the average speed of the traffic flow reflects the changes in the traffic situation and the occurrence of congestion.

4.2. The basic model of an artificial neural network

In [20], the neural network model with one hidden layer containing 5 neurons was used as a prediction model. Three factors were used to predict the travel time of the vehicle $n \in N$ with the route $r \in R$ on the road segment w_{ij}:

- the weighted speed of vehicle with the same route on the road segment $v_{ij}^{route,r}(t)$;
- the weighted speed of vehicle with any route on the road segment $v_{ij}^{all}(t)$;
- the vehicle speed on the previous segment $v_{i-1,i}^{n}$.

We denote this model as $\mathrm{ANN}^{3,5,1}$.

4.3. Support vector regression model

The support vector regression (SVR) method is a special class of algorithms characterized by the use of kernels. The most common kernels are linear, polynomial, radial basis function, sigmoid. In this work a radial basis function is used in the following form:

$$k(\mathbf{x}, \mathbf{x}') = \exp(-\gamma \|\mathbf{x} - \mathbf{x}'\|^2),$$

where $\gamma > 0$ is a model parameter, $\mathbf{x}$ and $\mathbf{x}'$ are the input data of the model. The three above mentioned factors are used as an input data.

4.4. Extended model of artificial neural network

We proposed to use an extended model of the neural network to predict the speed $\hat{v}_{ij}^n(t_c, t)$ of a vehicle $n \in N$, running the route $r \in R$. The input data includes all the factors described in Section 4.1, and it can be written as a vector:

$$\mathbf{V} = \Big(v_{i-1,i}^n, v_{ij}^{n1}, v_{ij}^{n2}, v_{ij}^{route,r}(t), v_{ij}^{all}(t), v_{ij}^{stat}(t_c), v_{ij}^{stat}(t), \\ v_{ij}^{flow}(t_c), v_{ij}^{flow}(t), v^{hour}(t), v^{day}(t), v_{ij}^{fNow}\Big).$$

where $n1$ is a preceding vehicle of the route r which passed the transport segment w_{ij}, $n2$ is a preceding vehicle of any route which passed the road segment w_{ij}.

The neural network model of the following form is used for prediction: one input layer (12 neurons), one hidden layer (13 neurons) and one output layer (1 neuron). The Adam [21] method was used as the optimization method.

4.5. Experiments

Experimental studies of models were carried out on traffic data of bus routes in the transport network of Samara, Russia, for two months, from August 1, 2018 to September 30, 2018. The forecast was performed for 837 vehicles on 176 routes.

The comparison of the linear regression model LR, basic neural network model $\text{ANN}^{3,5,1}$, support vector regression model SVR and the extended neural network model ANN^{ext} was made.

In order to evaluate the prediction quality of each prediction model, two standard metrics were used: mean absolute percentage error (MAPE) and mean absolute error (MAE).

$$\text{MAPE} = \frac{1}{n} \sum_{t=1}^{n} \frac{|v_t - \hat{v}_t|}{v_t} \times 100\% \tag{2}$$

$$\text{MAE} = \frac{1}{n} \sum_{t=1}^{n} |v_t - \hat{v}_t| \tag{3}$$

where v_t is a real value and $\hat{v}_t$ is a predicted value.

Table 1 shows the comparison of prediction models for one of the routes of the analysed transport network.

Table 1. Comparison of prediction models.

	LR	$\text{ANN}^{3,5,1}$	SVR	ANN^{ext}
MAPE	29.58	29.76	34.75	27.75
MAE	1.76	1.77	2.20	1.60

In this case, the size of the input data used for training and forecasting was limited to the size of selected route's data. Data obtained on a given day were used as a test data, all the rest data were used as a train data. The table shows the average MAE and MAPE values obtained for 7 days. From the obtained results it can be seen that the average value of the prediction error for one road segment is quite high. The best result is demonstrated by the extended model of an artificial neural network.

However, more interesting are the results of predicting the arrival time of vehicles at distant stops. For experimental studies of the dependence of MAPE and MAE on the forecast horizon, the full volume of data on the vehicles movement was used. The studies were carryed out for one day and all routes, while the data obtained for the entire above-mentioned period of time except the selected day were used as archival data. The time spent on training the SVR model amounts to tens of hours for such a significant amount of input data and the results obtained above show the superiority of other models. Thus the SVR model was not used on these experimental studies.The dependence of MAPE and MAE on the forecast horizon are shown in Figure 1.

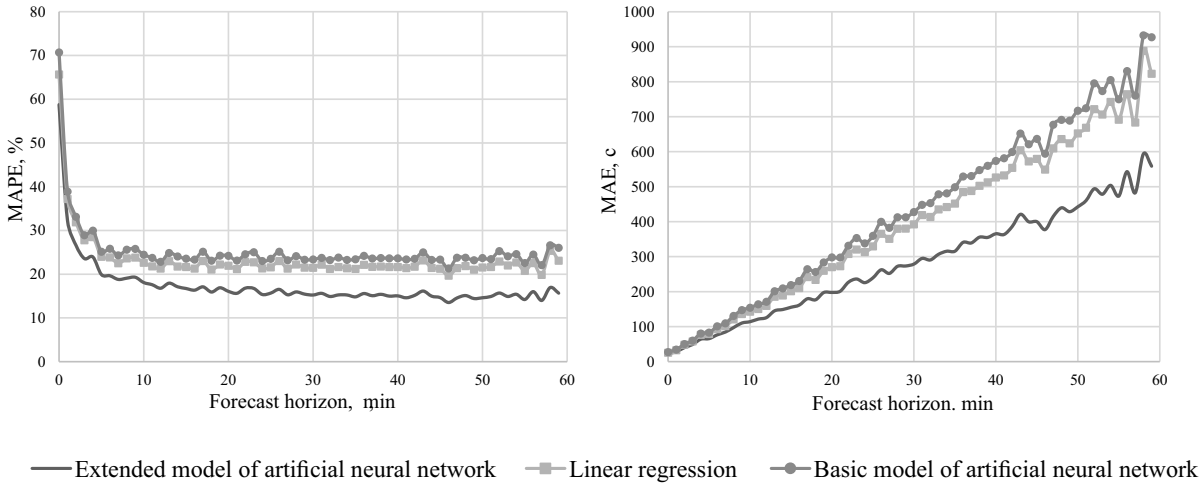

Figure 1. The dependence of MAPE and MAE on the forecast horizon.

Based on the obtained results, it can be concluded that the prediction quality of the extended model of an artificial neural network is higher throughout the forecast horizon than the prediction quality of the other models . The worst result was obtained using the basic model of the artificial neural network. At the same time, the value of MAPE decreases for all considered models with an increase in the forecast horizon value. The prediction quality of the vehicles arrival time at distant stops is significantly higher than the prediction quality for the nearest stops.

5. Conclusion

This paper proposed an extended model of the neural network which takes into account heterogeneous information to predict the arrival time of the public transport. The experiments were carried out on real traffic information about bus routes in the Samara, Russia. The proposed model showed the best results compared to linear regression model, support vector regression model and the basic model of the artificial neural network.

The proposed model can be used to predict the arrival time of public transport in real time.

The possible direction of further research includes the usage of different models for individual routes or periods of the day.

6. References

[1] Agafonov A A, Sergeyev A V and Chernov A V 2012 Forecasting of the motion parameters of city transport by satellite monitoring data *Computer Optics* **36(2)** 453-458
[2] Jeon R and Rilett L 2005 Prediction model of bus arrival time for real-time applications *Transportation Research Record* **1927** 195-204
[3] Chanh H, Park D, Lee S, Lee H and Baek S 2010 Dynamic multi-interval bus travel time prediction using bus transit data *Transportmetrica* **6** 19-38
[4] Smith B, Williams B and Keith Oswald R 2002 Comparison of parametric and nonparametric models for traffic flow forecasting *Transportation Research Part C: Emerging Technologies* **10** 303-321
[5] Agafonov A A, Yumaganov A S and Myasnikov V V 2018 Big data analysis in a geoinformatic problem of short-term traffic flow forecasting based on a K nearest neighbors method *Computer Optics* **42(6)** 1101-1111 DOI: 10.18287/2412-6179-2018-42-6-1101-1111
[6] Xu H and Ying J 2017 Bus arrival time prediction with real-time and historic data *Cluster Computing* **20** 3099-3106
[7] Chen M, Liu X, Xia J and Chien S 2004 A dynamic bus-arrival time prediction model based on APC data *Computer-Aided Civil and Infrastructure Engineering* **19** 364-376
[8] Chien S J, Ding Y and Wei C 2002 Dynamic bus arrival time prediction with artificial neural networks *Journal of Transportation Engineering* **128** 429-438
[9] van Hinsbergen C, van Lint J and van Zuylen H 2009 Bayesian committee of neural networks to predict travel times with confidence intervals *Transportation Research Part C: Emerging Technologies* **17** 498-509
[10] Jeong R and Rilett L 2004 Bus arrival time prediction using artificial neural network model *Proc. of the 7th International IEEE Conference on Intelligent Transportation Systems* **1** 988-993
[11] Yang M, Chen C, Wang L, Yan X and Zhou L 2016 Bus arrival time prediction using support vector machine with genetic algorithm *Neural Network World* **26** 205-217
[12] Bin Y, Zhongzhen Y and Baozhen Y 2006 Bus arrival time prediction using support vector machines *Journal of Intelligent Transportation Systems: Technology, Planning, and Operations* **10** 151-158
[13] Yu B, Yang Z Z and Yu B 2009 Hybrid model for multi-stop arrival time prediction *Neural Network World* **19** 321-332
[14] Agafonov A and Myasnikov V 2015 Traffic flow forecasting algorithm based on combination of adaptive elementary predictors *Communications in Computer and Information Science* **542** 163-174
[15] Yu B, Yang Z Z, Chen K and Yu B 2010 Hybrid model for prediction of bus arrival times at next station *Journal of Advanced Transportation* **44** 193-204
[16] Zheng W, Lee D H and Shi Q 2006 Short-term freeway traffic flow prediction: Bayesian combined neural network approach *Journal of Transportation Engineering* **132** 114-121
[17] Agafonov A A and Myasnikov V V 2016 Method for the reliable shortest path search in time-dependent stochastic networks and its application to GIS-based traffic control *Computer Optics* **40(2)** 275-283 DOI: 10.18287/2412-6179-2016-40-2-275-283
[18] Agafonov A A and Myasnikov V V 2018 Numerical route reservation method in the geoinformatic task of autonomous vehicle routing *Computer Optics* **42(5)** 912-920 DOI: 10.18287/ 2412-6179-2018-42-5-912-920
[19] Yu B, Lam W and Tam M 2011 Bus arrival time prediction at bus stop with multiple routes *Transportation Research Part C: Emerging Technologies* **19** 1157-1170
[20] Yin T, Zhong G, Zhang J, He S and Ran B 2017 A prediction model of bus arrival time at stops with multi-routes *Transportation research procedia* **25** 4627-4640
[21] Kingma D P and Ba J L 2014 Adam: A Method for Stochastic Optimization *Computing Research Repository* **15**

Acknowledgments
This work was supported by the RFBR (research projects N18-29-03135-mk, N 18-07-00605 A).

The detection of conflicts in the requirements specification based on an ontological model and a production rule system

M Sh Murtazina[1] and T V Avdeenko[1]

[1]Novosibirsk State Technical University, Karla Marksa ave., 20, Novosibirsk, Russia, 630073

e-mail: murtazina@corp.nstu.ru; tavdeenko@mail.ru

Abstract. The paper presents an approach to organizing the detection of conflicts between requirements based on an ontological model and a system of production rules. Requirements in the form of plain text are converted to instances of OWL ontologies for analysis. There are three basic elements "subject", "action" and "object" in the requirements. These elements become classes of the ontology. The object properties between instances of the same classes are defined in the ontology. In the system of rules it is determined that one of four types of relations can be established between a pair of the requirements: isConflict, isDuplicate, isInterconnect, isNotInterconnect. We develop the software product in the Python language for building and applying production rules system for classes and property objects of the ontology. Protégé 5.2 is used to work with the ontology. Also Python library PySwip and development environment SWI-Prolog 7.6.4 are used in the work. The paper also considers the issues of extracting requirements ontology instances from the automated processing results of textual requirements. The UDPipe with Russian language model is used for text processing

1. Introduction

Essential precondition for successful implementation of the software products is the preliminary development of high-quality software requirements specification (SRS). The latter task is solved during requirements engineering (RE) process, in which inaccurate and incomplete ideas about what services should the software product provide in order to solve the potential users' problems are converted into a formal SRS. Moreover, it is necessary to take into account the limitations under which the software product should be implemented and work. According to SEBoK (version1.9.1) a set of requirements must satisfy the following characteristics: complete, consistent, feasible, comprehensible and able to be validated.The completeness means that the set of requirements need not be further refined. The consistency criterion assumes that the requirement set does not contain conflicting requirements, the requirements are not duplicated, and the same term is used for the same element in the whole set of requirements. The feasibility criterion means that a solution can be developed for a set of requirements that meets the requirements taking into account the limitations of the project (for example, cost) with an acceptable level of risk. The comprehensibility criterion implies that a set of requirements has to be formulated so that to give a clear idea of what is expected of the software product, and in what way it relates to the whole system. The validability criterion implies that

it should be possible to prove that the set of requirements will lead to the user needs satisfaction under existing constraints of the project [1].

For the agile software development approach, the requirements specification is usually not a single document, but logical structure filled with requirements to the software product. The creation of such specifications is usually preceded by the development of a document called «Vision and scope», which gives an overview of the developed software product in terms of the key needs and constraints under which the project will be implemented. Then, the work begins on the creation of the product backlog containing prioritized list of requirements. The major feature of an agile approach is permanent readiness to change the requirements, therefore only those elements of the product backlog that have the highest priorities are worked out in detail at the current time. The requirements with low priorities remain in the product backlog, where they can be added, removed, or changed at any time. Under conditions of variability of the requirements their coordination becomes one of the most difficult problems in the requirements engineering.

Requirements negotiation involves detection and resolution of conflicts. Therefore, it seems that at the stage of collecting the product backlog elements, the most important of the above quality characteristics is to ensure the consistency of the set of product backlog elements. In this paper we will consider the main component of this quality characteristic, namely, conflict-free set of requirements. The proposed approach can be used as part of the intellectual support of the engineering process based on ontological models. The ontology data of requirements can be processed together with the data of other ontologies in the field of requirements engineering described by us in works [2-4].

The paper is organized as follows. Section 2 provides an overview of publications on the research theme. In section 3 we propose an approach to converting text requirements into the ontology. In section 4, we describe the developed software based on production model to search for conflicts between the requirements represented by instances of the ontology. Section 5 concludes on the prospects of the proposed approach.

2. Theoretical background

The paper [5] describes a prototype of the «Oz» design system, which provides automated methods for conflict detection, generation of conflict resolution variants, and explanation of the decision choice. So the experimental tool «Oz» is designed to develop harmonized requirements. Requirements from different stakeholders are presented in the form of scenarios. The «Oz» prototype includes requirements language, specification language, specification planner, and requirements negotiation tools. The work [6] of the same authors presents an approach to the identification and resolution of conflicts between the requirements within the framework of the paradigm of Conflict-Oriented Requirements Analysis (CORA). Requirements ontology is used to describe the structure of the requirements, which providing formulation of the requirements and their interaction. Conflicts between the requirements are presented in the requirements ontology as types of interaction. The interactions between the requirements are determined directly from the requirements concept description. Conflict resolution is based on the generation of alternative requirements' variants resolving the conflict.

The authors of [7] mentioned that manually produced conflict-analysis of the requirements needs considerable effort and is prone to the errors. They propose to use semantic technologies as a basis for automating the analysis of conflicts between the requirements implementing ontological approach OntRep. In [7] three types of conflicts are distinguished: conflicts between the requirements and the constraints, conflicts between the requirements and the guidelines (for example, on formalization of requirements), conflicts between the requirements. Conflicts between the requirements are divided into two groups: simple (between two requirements) and complex (between several requirements). To implement the conflict analysis approach, all terms used in the requirements must be formulated as Glossary terms in the ontology OntRep, and the requirements must be formulated using a specific structure. The OntRep tool consists of two basic components. The first component is an instance collector that takes input data. For example, these might be requirement tickets from the project management tool and bug tracking in Trac software. A ticket in this system means a virtual card with a description of the requirement (task) or the error that needs to be corrected. The OntRep tool instance

collector analyzes the contents of the ticket and assigns categories of the requirements (classes) defined in the ontology (for example, security requirement). The second component of OntRep tool is intended to generate a report on conflicts between the requirements [8].

The paper [9] describes an automated tool EA-Analyzer for revealing conflicts. This tool is designed to identify conflicts in aspect-oriented requirements specified in natural language text. Requirements are written using RDL (Requirements Description Language), which uses XML tags to annotate the natural language specification. The main elements of the language are <subject>, <object> and <relationship> tags. The <subject> tag grammatically corresponds to the subject of the sentence, the <object> tag corresponds to the object to which the action applies, and the <relationship> tag defines the action performed by the subject over the object. There can be several objects in one sentence. Classification of verbs in RDL is based on semantic categories proposed in the works of R. Dixon [10]. Also RDL uses categories of degrees (for example, showing the differences between the modal verbs), reflecting the importance degree of the requirement. Contamination (merging heterogeneous factors) consists of three sub-elements: constraint, basic requirement and result. In EA-Analyzer, the conflict detection problem is formulated as a classification problem that is a well-studied machine learning problem. The EA-Analyzer tool uses annotated requirements in RDL to decide if there are inconsistencies in the requirements [9].

The paper [11] proposes a set of rules for conflict analysis of class diagrams. The conflict-analysis process is a four-step cycle: modeling a priori knowledge, modeling new requirements, identifying conflicts, and resolving conflicts. The rules process four possible types of conflicts: inconsistency, redundancy, overriding, and missing parts.

The paper [12] deals with the definition of cooperation and conflicts between the requirements. The requirements conflict if they contain conflicting statements about common software attributes, and they are in a cooperative state if they complement each other's statements about attributes. The approach proposed in [12] includes manual transformation of the requirements into the software attributes, automatic detection of conflicts and cooperation between the requirements based on their attributes, automatic tracing of dependencies between the requirements.

In [13] an approach is proposed that allows comparing the stakeholder’s points of view on the subsystems of the information system. Requirements of stakeholders, written in natural English language, are processed with the help of the syntactic StanfordParser and the tool TreeTagger for morphological tagging of texts. On the basis of the analysis of the received semantic-syntactic relations on a set of rules the ontology of functional requirements is created. The concepts of the resulting ontologies are collated using external resources such as WordNet and string matching methods such as the N-gram method. As a result of comparison between the concepts of two textual descriptions of the requirements the following semantic relations are determined: the concepts are equivalent, one concept is more or less general against another concept, two or more concepts belong to the same subset or not.

The paper [14] proposes an approach to the automatic building the ontology out of a set of user stories. SpaCy library is used for processing texts in natural English language that allows to make parsing sentences based on the dependency tree, searching named groups, extracting registered entities, as well as permitting coreference. The problem of extracting knowledge in a natural language for further reflection in the ontology of a subject area is reflected in [15].

Thus, the conducted analysis of publications on the topic of the study allows us to conclude that one of the promising areas in search for conflicts between the requirements are approaches involving presentation of text requirements in the form of ontology instances. This can be done manually and semi-automatically. Automatic construction of ontologies from the texts of requirements is currently extremely relevant and still not well covered topic. The considered papers on the construction of ontologies from the texts of requirements does not directly affect the problem of conflict determination, but the ideas used in them can be used as a basis for extracting from the results of automatic text processing of requirements of instances of ontology, structured for the task of finding conflicts between requirements.

3. The conversion of textual requirements into ontology instances

In a sentence that expresses a requirement, regardless of the requirements recording technique used (for example, requirements can be written in the IEEE 830 or user stories style), three main parts can be distinguished: the subject, the action, and the object on which the action is directed. Each requirement must be represented in the ontology as a set of instances of these three classes. The object properties between pairs of instances for each class must be determined. For each requirement it is necessary to create an instance of the class "Requirement", which will be associated with corresponding instances of the classes "subject" ("actor"), "action" and "object". It is also necessary to determine the possible relations between instances of classes. It should be noted that a class, the elements of which grammatically correspond to the subjects of sentences with requirements, in an ontology may be called differently, for example, "actor" or "functional user role". In the example below which illustrates the proposed approach the term "actor" will be used to designate the subject.

First, in the Protégé 5.2 environment, the structure of classes was implemented and the object properties between them were set. Figure 1 shows the object properties of ontology, their domains and ranges.

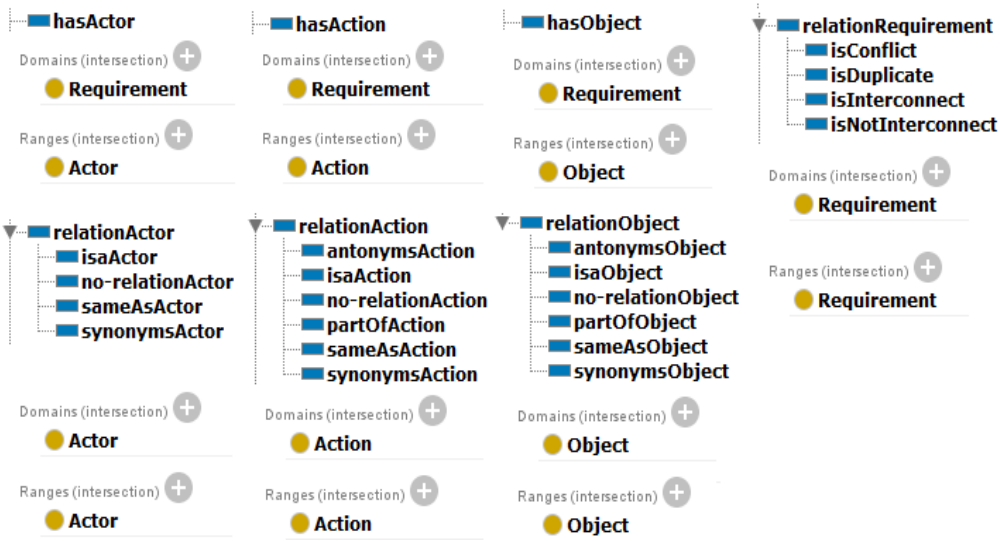

Figure 1. Object properties of ontology, their domains and ranges.

The object properties between instances of the same class "Actor" are grouped into the object properties class "relationActor". Also, the relations between the instances of the classes "Action" and "Object" are grouped into object properties classes "relationAction" and "relationObject".

The object properties of the "sameAsActor", "sameAsAction", "sameAsObject" are set up between instances of the corresponding classes if one name is used for the elements of two requirements or the full name is in one and an abbreviation in the second. These properties are symmetric. For example, instances of the class "Actor" with the values "senior manager" ("sr. manager") and "senior manager" will be connected by the object property "sameAsActor". Also, each of them will be connected with itself by this property. It is necessary for comparing two requirements without including duplicates of the same instances of the class "Actor" in the ontology (see Figure 2).

The object properties "isaActor", "isaAction" and "isaObject" are used to setting hierarchical relations. For example, the "senior manager" is a "manager".

The object properties "synonymsActor", "synonymsAction" and "synonymsObject" are set if the values of the corresponding requirements elements have a synonymous value. For example, the action "to view" records is synonymous with the action "to list" records.

The object properties "antonymsAction" and "antonymsObject" are set between instances of the corresponding classes if they have the opposite meaning. For example, the object "my comment" and the object "someone else's comment".

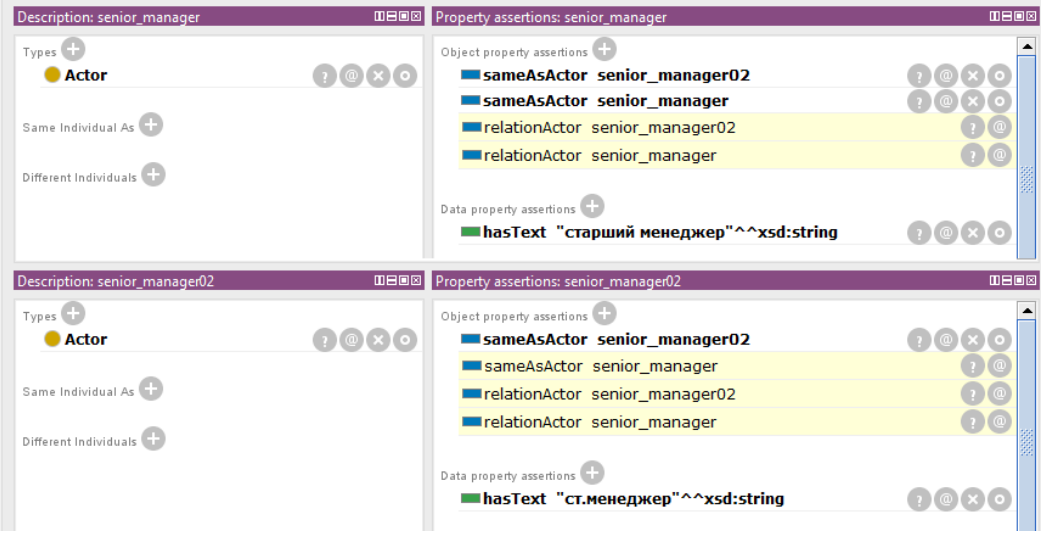

Figure 2. Object property for individuals «senior manager».

The object properties “partOfAction” and “partOfObject” are set between instances of the respective classes if one is part of the other. For example, the “product” object is part of the object “shopping basket”. Or, for example, the “delete” action is part of the “edit” action.

In all other cases, it is considered that the corresponding elements of the requirements are bound by the object properties “no-relationActor”, “no-relationAction” and “no-relationObject”. In other words, the relation between them is not revealed.

Figure 3 shows an example of requirement elements transformed into ontology instances.

Requirements:

User story 01: Как *менеджер*, *Я* могу удалить только *добавленные мною описания товаров*…
As a *manager*, I can only delete the *product descriptions I added* ...

User story 02: Как *менеджер*, *Я* могу редактировать *описания всех товаров из каталога*….
As a *manager*, I can edit *descriptions for all products from the catalog* ....

It should be noted that the conversion of textual requirements into ontology instances can be carried out in semi-automatic mode using automatic text processing tools. The UDPipe with the Russian language model can be used for processing of textual requirements in Russian. The UDPipe parses the proposal and provides the results in the format CoNLL-U.

The following fields are used to describe the annotation of text token (word, punctuation mark, or special character) of a sentence in the CoNLL-U format:

1) ID: token index
2) FORM: word form or punctuation symbol,
3) LEMMA: lemma of word form,
4) UPOSTAG: universal part of speech tag,
5) XPOSTAG: language tag of a part of speech (if not, a dash is indicated),
6) FEATS: list of morphological features from the universal feature inventory or from a specific language extension,
7) HEAD: number of the parent token or zero for the root token,
8) DEPREL: universal dependency relation to parent token (set to “root” if HEAD = 0),
9) DEPS: list of secondary dependencies
10) MISC: additional information.

Figure 4 illustrates the presentation in the CoNLL-U format of the sentence “Как менеджер, Я хочу удалять товар из каталога” (“As a manager, I want to remove product from the catalog”).

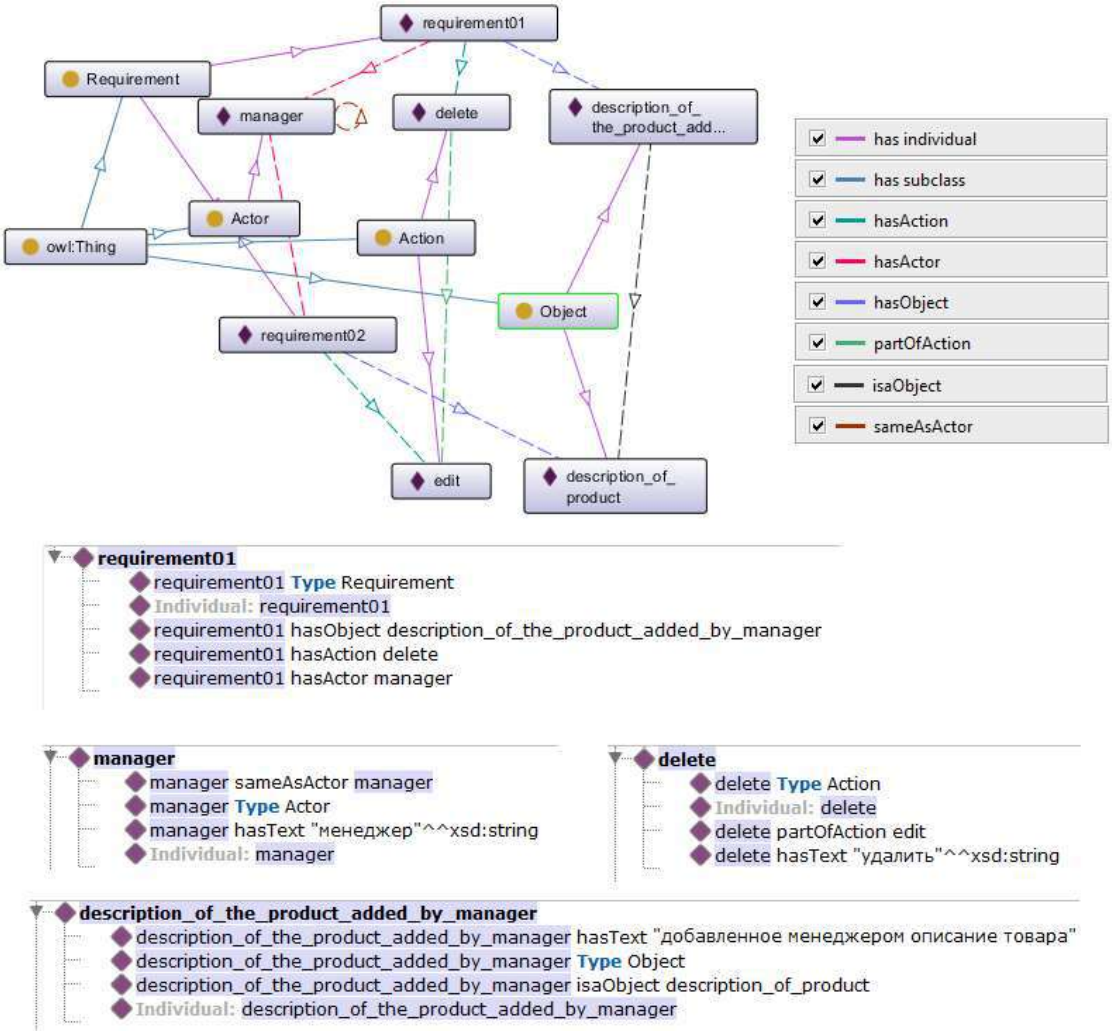

Figure 3. Fragment of ontology in Protégé.

Id	Form	Lemma	UPosTag	XPosTag	Feats	Head	DepRel	Deps	Misc
# newdoc									
# newpar									
# sent_id = 1									
# text = Как менеджер, Я хочу удалять товар из каталога.									
1	Как	как	SCONJ	_	_	2	mark	_	_
2	менеджер	менеджер	NOUN	_	Animacy=Anim|Case=Nom|Gender=Masc|Number=Sing	5	parataxis	_	SpaceAfter=No
3	,	,	PUNCT	_	_	2	punct	_	_
4	Я	я	PRON	_	Case=Nom|Number=Sing|Person=1	5	nsubj	_	_
5	хочу	хотеть	VERB	_	Aspect=Imp|Mood=Ind|Number=Sing|Person=1|Tense=Pres|VerbForm=Fin|Voice=Act	0	root	_	_
6	удалять	удалять	VERB	_	Aspect=Imp|VerbForm=Inf|Voice=Act	5	xcomp	_	_
7	товар	товар	NOUN	_	Animacy=Inan|Case=Acc|Gender=Masc|Number=Sing	6	obj	_	_
8	из	из	ADP	_	_	9	case	_	_
9	каталога	каталог	NOUN	_	Animacy=Inan|Case=Gen|Gender=Masc|Number=Sing	6	obl	_	SpaceAfter=No
10	.	.	PUNCT	_	_	5	punct	_	SpaceAfter=No

Figure 4. Phrase parsing done by the UDPipe tool.

A subject (actor), an action and an object can be automatically extracted from the results of a sentence analysis, provided that the sentence with the requirement is formulated simply enough, that is does not contain a lot of speech turns (see Figure 5).

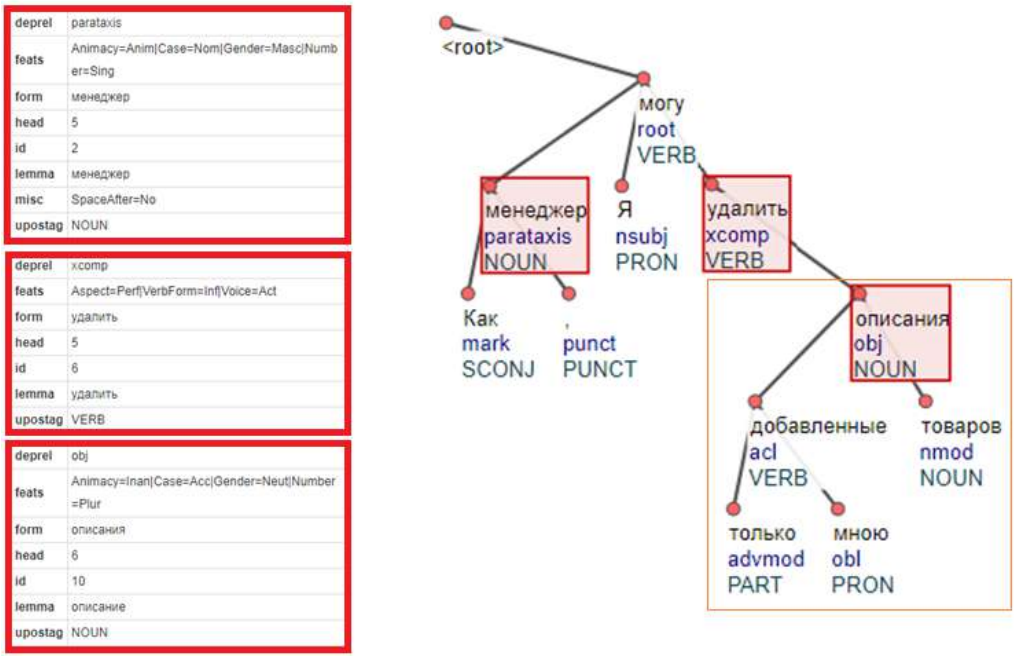

Figure 5. Dependency tree obtained by UDPipe.

The setting of object properties between instances of requirements elements can also be performed in semi-automatic mode. For example, using regular expressions, modal verbs and negatives can be searched. The linguistic ontologies like WordNet can be used to search for synonyms. It should be said that the search for antonyms with the help of linguistic ontologies for verbs can lead to undesirable results, since, for example, the actions “add” and “delete” can be viewed as antonyms, however, the verb phrases “can remove” and “cannot remove” will have an antonymous meaning .

Production rules can be applied for processing the parser results of sentences. For example: If X is an animated noun (UPOSTAG = NOUN and FEATS: Animacy = Anim), then this is a subject (actor). Next, it is necessary to check whether the noun has a definitive in order to extract the whole name of the subject. For example, if the actor “senior manager” is used instead of the actor “manager” then the actor is described as an animated noun (ID = 3, UPOSTAG = NOUN, FEATS: Animacy = Anim) and definitive “senior” (ID = 2, UPOSTAG = ADJ, DEPREL = amod, HEAD = 3). The universal dependence relation “amod” indicates that the adjective “senior” serves as a definitive for the noun “manager”. In the case of user story, the case of actor search is simplified due to a certain position of the actor in the sentence, so the actor can be extracted even without the use of special tools.

To extract the «action», it is necessary to analyze the tokens that are defined as verbs (UPOSTAG = VERB). At the same time, attention should be paid to the morphological features of the token in order to separate the verbs from the participles (FEATS: VerbForm = Part) and the adverbial participles (FEATS: VerbForm = Conv). In the example in Figure 5, the words «“want” (UPOSTAG = VERB, FEATS: VerbForm = Fin) and “delete” (UPOSTAG = VERB, FEATS: VerbForm = Inf) are the verbs. The phrase “I want” in the user Story is predefined, therefore, we extract the word “delete” as an action.

The object will be a noun associated with the word-action. In this example, this is the word “description” (ID = 11, UPOSTAG = NOUN, DEPREL = obj, HEAD = 6). The universal dependence relation “obj” indicates that the noun “description” plays the role of a direct object for the verb “delete”. Next, it is need to check whether the word “description” has attribute relations with other words of a sentence in order to extract the whole object.

Determining object properties between the instances of the requirements elements can also be performed in semi-automatic mode. For example, modal verbs and negatives can be searched using regular expressions. Besides, the linguistic ontologies like WordNet can be used to search for synonyms. It should be noted that the search for antonyms of verbs with the help of linguistic

ontologies can lead to undesirable results. For example, the actions “add” and “delete” can be viewed as antonyms, however, the verb phrases “can delete” and “cannot delete” will have an antonymous meaning in terms of the problem to be solved.

4. An approach to detection of conflicts between the requirements

To determine the type of relationship between the requirements, a system of production rules of the following form can be generated:

IF ObjectProperty_between_class_instances (Actor1, Actor2)
AND ObjectProperty_between_class_instances (Action1, Action2)
AND ObjectProperty_between_class_instances (Object1, Object2)
THEN Objectproperties_between_class_instances (Requirement1, Requirement2)

For the ontology with the properties of objects presented in figure 1, 144 rules were formed with the proposed approach. Below we give some examples of conflict detection rules:

1. **IF** isaActor (Actor1, Actor2) **AND** antonymsAction (Action1, Action2)
AND isaObject (Object1, Object2) **THEN** isConflict (Requirement1, Requirement2)

2. **IF** isaActor (Actor1, Actor2) **AND** antonymsAction (Action1, Action2)
AND partOfObject (Object1, Object2) **THEN** isConflict (Requirement1, Requirement2)

3. **IF** isaActor (Actor1, Actor2) **AND** partOfAction (Action1, Action2)
AND antonymsObject (Object1, Object2) **THEN** isConflict (Requirement1, Requirement2)

Depending on the used rule, one of the following four relations between the requirements are detected: “conflicting requirements”, “requirements are duplicates”, “requirements are related” or “connection is not detected”.

To implement the proposed approach, an application with a graphical interface in Python was developed. The application provides the following functions:

- building a system of production rules to process relations between instances of ontology classes and saving them as a model into XML file;
- editing the system of production rules previously saved as a model;
- application of the model rules to the requirements, presented in the form of class instances of OWL ontology.

To implement the first function, a constructor was created that helps the user to build a system of rules for analyzing the relations between the requirements elements in a few «clicks». The constructor allows you to select a file with OWL ontology for which the model was built. In the next steps of working with the designer, you can define which ontology classes correspond to the elements «actor», «action» and «object», as well as select the properties of objects that will be used for analysis. This allows the end user to create their own rules for processing the data they have. At the last step of working with the application, the generated combinations of antecedents for the production rules are issued. The user needs to define rule consequents by selecting the type of relation between the requirements for each rule. Semi-automatic rule generation does not allow the user to skip any rule because it covers all possible combinations for rule antecedents. Figure 6 shows the last step in building the model.

Further we consider two examples for rules obtained from the ontology described above. The first example analyzes the requirements in the form of user stories; the second example analyzes the requirements in the form of simple statements.

Example 1:
IF sameAsActor(Actor1, Actor2)
AND partOfObject(Action1, Action2)

AND isaObject(Object1, Object2)
THEN isConflict(Requirement1, Requirement2)
Substitution of data into the rule:
IF sameAsActor(«менеджер», «менеджер»)
AND partOfAction(«удалить», «редактировать»)
AND isaObject(«добавленное менеджером описание товара», «описание товара в каталоге»)
THEN isConflict(Requirement1, Requirement2)

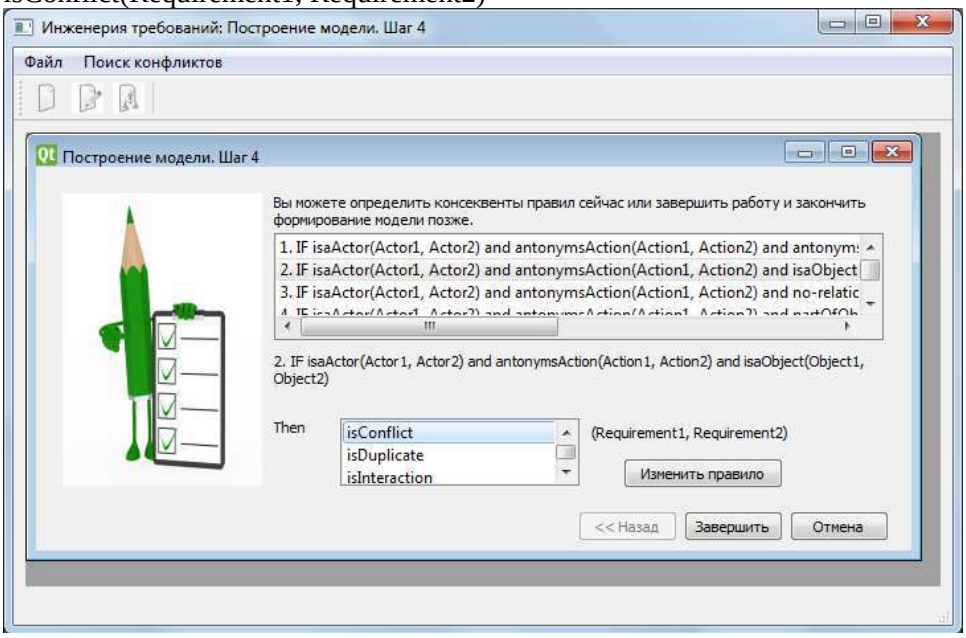

Figure 6. Constructor form screen.

Example 2:
IF sameAsActor(Actor1, Actor2)
AND antonymsAction(Action1, Action2)
AND sameAsObject(Object1, Object2)
THEN isConflict(Requirement1, Requirement2)

Requirements*:*
R1: Пользователь может удалять комментарии.
The user can delete comments
R2: Пользователь может только просматривать комментарии.
The user can only view comments.

Substitution of data into the rule:
IF sameAsActor(«пользователь», «пользователь»)
AND antonymsAction(«может удалять», «может только просматривать»)
AND sameAsObject(«комментарии», «комментарии»)
THEN isConflict (Requirement1, Requirement2)

In the first example, the Manager on the one hand can edit the descriptions of any goods (regardless of whether he added them or not), and on the other hand he has a ban on editing the descriptions of goods added not by him. In the second example, we see a contradiction in the actions of the user on one object “comments”, which also requires clarification and correction, because it is not clear what kind of comments we mean: only the comments created by the user himself, or all the comments to the objects created by the user in the system. And at first glance, “understandable flaws” can lead to the implementation of functionality that does not correspond to the original idea.

In the course of requirements analysis, data in the form of classes' instances and relationships between them are imported into the database of facts in Prolog language, the generated production rules are imported into Prolog Rules. Then the Prolog Inference Engine is used to detect conflicts between the requirements. The results of the requirements analysis are saved into a text file. Python library PySwip and SWI-Prolog 7.6.4 development environment were used to implement this functionality.

5. Conclusion

The paper proposed an approach to detection of conflicts in the set of requirements based on an ontological model and a production rules system. To organize the processing of textual requirements, it was proposed to extract from the textual requirements the subject (actor), the action and the object on which the action is directed and save them in the form of ontology instances. It was also proposed to establish relations between instances of classes belonging to a pair of requirements that are defined in the ontology as object properties. The production rules system for determining the type of relation between a pair of requirements is based on these object properties. The developed toolkit to be able to facilitate the process of detection conflicting requirements since it performs the matching of requirements in a semi-automatic mode, which contributes to the detection of seemingly minor inaccuracies in the requirements formulation. It should be noted that the application of this approach requires the recording of textual requirements in the form of simple sentences that can be partially processed automatically, since it is quite labor-intensive to completely manually convert textual requirements into ontology instances.

6. References

[1] SEBoK *Guide tothe Systems Engineering Body of Knowledge* (Version 1.9.1)
[2] Murtazina M S and Avdeenko T V 2018 Ontology-Based Approach to the Requirements Engineering in Agile Environment *Proc. of 14th International Scientific-Technical Conference on Actual Problems of Electronic Instrument Engineering* **8546144** 496-501
[3] Avdeenko T and Murtazina M 2018 Intelligent Support of Requirements Management in Agile Environment *Studies in Computational Intelligence* **803** 97-108
[4] Murtazina M Sh and Avdeenko T V 2019 An ontology-based approach to support for requirements traceability in agile development *Procedia Computer Science* **150** 628-635
[5] Robinson W N and Volkov S 1998 Supporting the Negotiation Life Cycle *Communications of the ACM* **41(5)** 95-102
[6] Robinson W N and Volkov S 1999 Requirement Conflict Restructuring *GSU CIS Working Paper* **99-5** 1-47
[7] Heindl M, Moser T, Winkler D and Biffl S 2011 Automating the Detection of Complex Semantic Conflicts between Software Requirements: An empirical study on requirements conflict analysis with semantic technology *Proc. Int. Conf. on Software Engineering and Knowledge Engineering* (Miami Beach: USA Knowledge Systems Institute Graduate School) 729-735
[8] Moser T,Winkler D, HeindlM and Biffl S 2011 Requirements Management with Semantic Technology: An Empirical Study on Automated Requirements Categorization and Conflict Analysis *Proc. Int. Conf. on Advanced Information Systems Engineering* 3-17
[9] Sardinha A, Chitchyan R, Araújo J, Moreira A and Rashid A 2013 Conflict identification with EA-Analyzer *Aspect-oriented requirements engineering* 209-224
[10] Chitchyan R, Rashid A, Rayson P and Waters R 2007 Semantics-Based Composition for Aspect-Oriented Requirements Engineering *Proc. Int. Conf. on Aspect-oriented software development* 36-48
[11] Liu C-L and Huang H-H 2015 Ontology-Based Requirement Conflicts Analysis in Class Diagrams *Proc.of the World Congress on Engineering* **1** 471-476
[12] Egyed A and Grunbacher P 2004 Identifying Requirements Conflicts and Cooperation: How Quality Attributes and Automated Traceability Can Help *IEEE Software* **21(6)** 50-58
[13] Assawamekin N, SunetnantaT and Pluempitiwiriyawej C 2010 Ontology-based

multiperspective requirements traceability framework *Knowledge and Information Systems* **25(3)** 493-522
[14] Robeer M, Lucassen G, van der Werf J M E M, Dalpiaz F and Brinkkemper S 2016 Automated Extraction of Conceptual Models from User Stories via NLP *Proc. Int. Requirements Engineering Conf.* 196-205
[15] Mikhaylov D V, Kozlov A P and Emelyanov G M 2016 Extraction the knowledge and relevant linguistic means with efficiency estimation for formation of subject-oriented text sets *Computer Optics* **40(4)** 572-582 DOI: 10.18287/2412-6179-2016-40-4-572-582

Acknowledgments
The reported study was funded by Russian Ministry of Education and Science, according to the research project No. 2.2327.2017/4.6.

Application of convolution neural networks in eye fundus image analysis

N Y Ilyasova[1,2], A S Shirokanev[1,2] and I A Klimov[1]

[1]Samara National Research University, Moskovskoe Shosse 34A, Samara, Russia, 443086
[2]Image Processing Systems Institute of RAS - Branch of the FSRC "Crystallography and Photonics" RAS, Molodogvardejskaya street 151, Samara, Russia, 443001

e-mail: ilyasova.nata@gmail.com, alexandrshirokanev@gmail.com, klimov.ilya.05@gmail.com

Abstract. In this work, we proposed a new approach to analyzing eye fundus images that relies upon the use of a convolutional neural network (CNN). The CNN architecture was constructed, followed by network learning on a balanced dataset composed of four classes of images, composed of thick and thin blood vessels, healthy areas, and exudate areas. The learning was conducted on 12x12 images because an experimental study showed them to be optimal for the purpose. The test error was no higher than 4% for all sizes of the samples. Segmentation of eye fundus images was performed using the CNN. Considering that exudates are a primary target of laser coagulation surgery, the segmentation error was calculated on the exudate class, amounting to 5%. In the course of this research, the HSL color system was found to be most informative, using which the segmentation error was reduced to 3%.

1. Introduction

A severe consequence of diabetic retinopathy (DRP) is vision loss. DRP affects all parts of the retina, leading to macular edema, which in turn causes fast worsening of eyesight [1]. The accurate and early diagnosis alongside an adequate treatment can prevent the vision loss in more than 50 % of cases [2-3]. There are a number of approaches to treating DRP, one of which involves laser photocoagulation [4]. During this procedure, a number of retina areas where edema occurs are cauterized with a laser. The procedure is conducted via coagulating near-edema zones. The development of diagnostic systems enabling an automatic identification of the edema zone is currently a relevant task [5]. For the laser coagulation procedure to be automated [6, 7], objects in the eye fundus image need to be classified [8-11], which can be done in a number of ways [12].

Convolutional neural networks are the choice of preference when dealing with object classification [13]. Such is the conclusion members of the research community involved in medical image analysis have come to in the course of their research. Techniques for medical data analysis are often among research topics at international conferences and symposia. May 2006 has seen the publication of the first issue of IEEE Transaction on. The first detailed review to be published on the use of deep learning for medical image analysis appeared in 2017 [5]. Nowadays an active trend for the development of digital medicine is seen.

In Ref. [14], a classification model based on a convolutional neural network was used for diagnosing the H. Pylori infection. In the work, an architecture specially tailored for a particular task was utilized. The authors came to the conclusion that the particular disease was possible to diagnose based on endoscopic images obtained using CNN. In Ref. [15], diagnosing an early-stage hypertension retinopathy was discussed. The onset of the disease in the eye retina is prompted by blood hypertension. The classifier proposed in Ref. [15] offered a 98.6 percent accuracy. In Ref. [16], a toolkit was developed for the automated analysis of psoriasis-affected skin biopsy images, which is of considerable significance in clinical treatment. The paper is a pioneering attempt into automatic segmentation of psoriasis-affected skin biopsy images. The study resulted in a practical system based on the machine analysis. CNN training on a prepared dataset was demonstrated, intended for further analysis of input images.

In this work, we study a class of eye fundus images with pathological changes that can be found at different stages of the disease. Manifestations of the diabetic retinopathy include exudates, which cause the retina thickening (Figure 1). In general, the image of an eye fundus with pathology contains four classes of objects, such as thick and thin blood vessels, healthy areas and exudate zones.

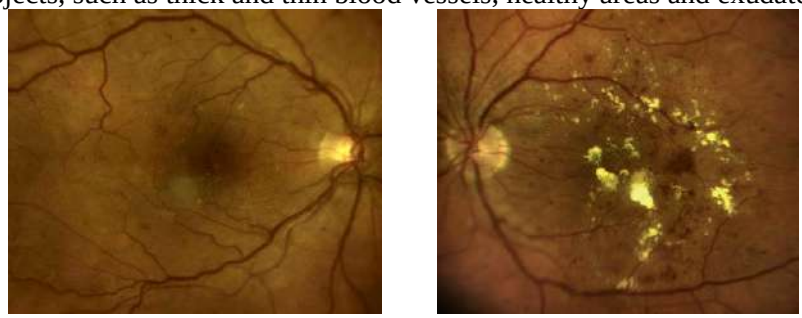

Figure 1. Illustration of diagnostic eye fundus images: healthy eye (left) and affected eye (right).

2. Training the convolutional neural network

The initial data for analysis contained 11 training datasets of various size. All datasets were balanced and in total contained 534 images. For the purposes of the present work, the CNN training was conducted on four above-described classes of eye fundus images. The initial dataset consisted of 75 percent of training images and 25 percent of test images. To prevent overtraining, a control dataset was also used. A 3x3 convolution kernel was chosen because it is optimal for 12x12 images. The CNN architecture was constructed empirically so as the required accuracy of no less than 96 % is ensured. Table 1 gives architecture of the empirically constructed convolutional neural network. With this architecture, a recognition accuracy of 99.3% was attained, which is the best recognition result for the four above-mentioned classes of images. Figure 2 depicts a plot for training the CNN model in each training epoch.

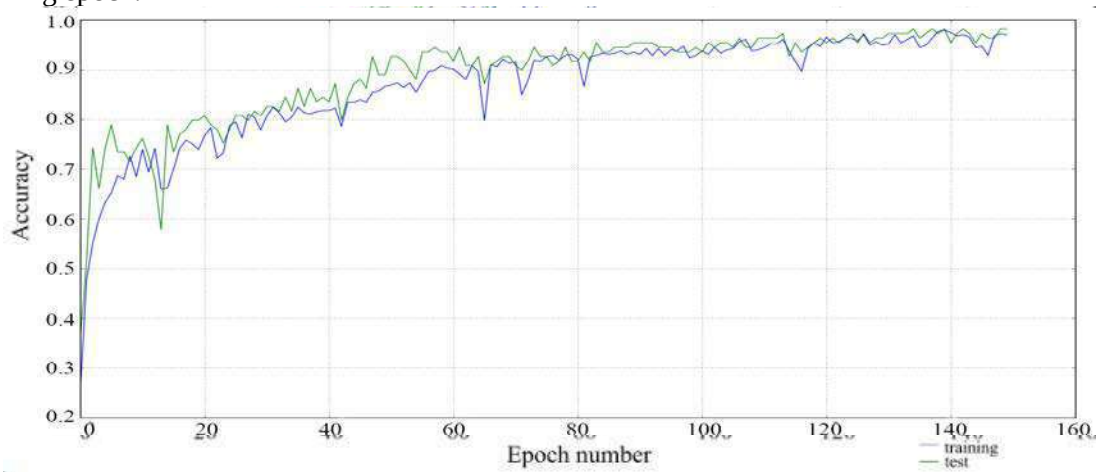

Figure 2. The dependency of learning accuracy on the number of epochs.

Table 1. Architecture of the convolutional neural network.

Layer number	Layers	Parameters	Layer number	Layers	Parameters
1	Convolutional	300 neurons	3	Activation	Function: RELU
1	Activation	Function: RELU	4	Convolutional	150 neurons
2	Convolutional	300 neurons	4	Activation	Function: RELU
2	Activation	Function: RELU	4	MaxPooling	Size: 2×2
2	Dropout	0.5	4	Dropout	0.5
2	MaxPooling	Size: 2×2	5	Fully-connected	4
3	Convolutional	150 neurons	5	Activation	softmax

To attain a recognition certainty of 95 %, the CNN was put through 120 training runs on the initial images of all sizes. Figure 3 shows an average training result for each image size.

The results in Figure 2 show that the highest classification accuracy is attained for 12x12 images.

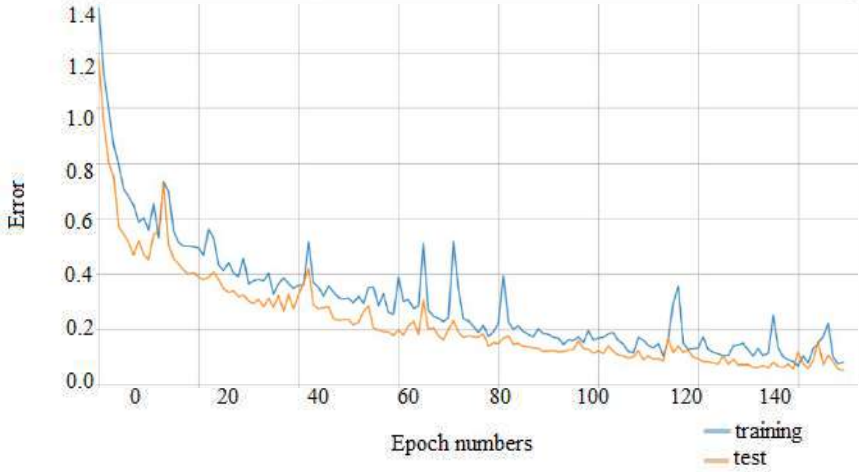

Figure 3. The dependency of learning error on the number of epochs.

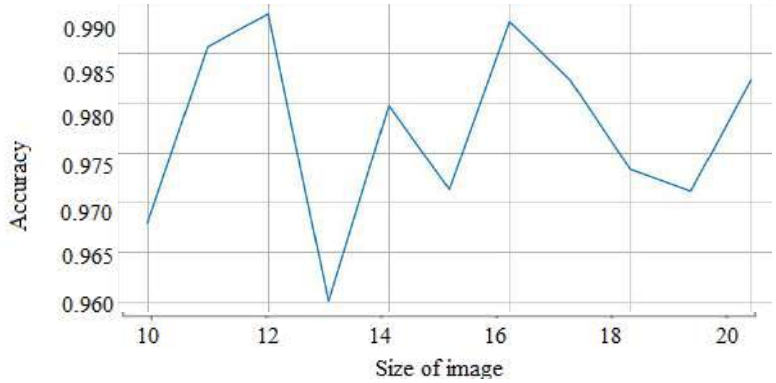

Figure 4. The dependence of accuracy on the size of images in the training set.

3. Experimental study

For the experiments, datasets were formed containing four above-described classes of 12x12 images, using which the best result of CNN testing is achieved (Figure 3). In this study, the segmentation of eye fundus images was conducted via deep learning. Shown in Fig. 4b is the result of CNN-aided image segmentation. With a view of estimating the CNN-aided segmentation error, a manual segmentation by an expert ophthalmologist was introduced as a reference image (Figure 4c). The study was conducted on the exudates class, which had been singled out into a separate image (Figure 4d). The error of CNN-aided segmentation of the said exudate areas was calculated relative to the expert estimate. The result of comparison of the exudation areas highlighted by CNN and the expert is shown in Table 2. Using the data from Table 2, a CNN-aided segmentation error for the exudates was

defined as $E = (k + t)/NM$ and amounted to 7% (where N×M is the image size, k is the number of expert-highlighted pixels that CNN failed to recognize as exudates, t is the number of exudate pixels recognized by CNN but missing from the expert's image). The error of first kind, defined as $E_1 = l/F$, where l is the number of falsely recognized exudates classes and F is the total number of exudate-containing pixels in the expert's image, amounted to 5%.

In the process of exudates area identification, color plays a key role. The segmentation error can be significantly reduced by operating in particular color spaces. It has been established [17] that color models YUV, RGB and HSL are most close to color perception of the human eye. However, the models RGB and YUV have a number of hardware limitations with certain video-systems. In further research, we used the HSL color model as the one that most adequately renders the color characteristics of blood vessels and exudates. Figure 5 shows pathological areas highlighted by the expert in different HSL color channels.

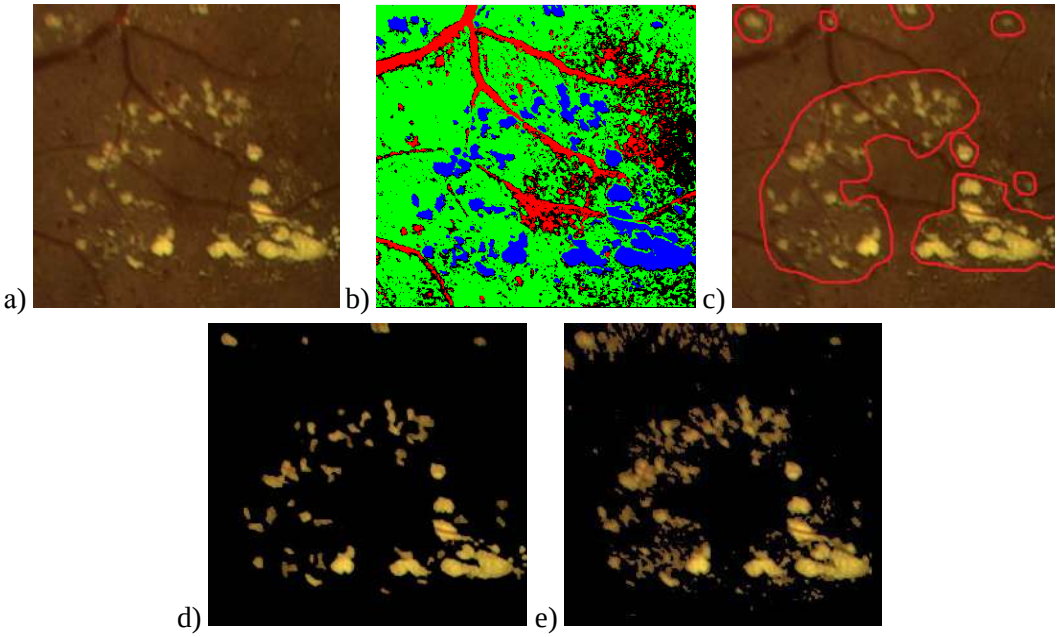

Figure 4. (a) The original eye fundus image; (b) four classes of objects highlighted in the image using CNN; (c) exudates areas manually outlined by an expert; exudates areas highlighted by (d) an expert and (e) using the CNN technique.

Table 2. Percentage of exudates areas in the image.

Areas	Percentage of exudates area, %
Exudates area in the expert's image	9
Exudates area in the CNN-aided image	15
Total exudates area	95.6
Expert's exudates areas omitted by CNN	0.4
CNN-highlighted exudates areas missing in the expert's image	6

Veracity of CNN-aided exudate highlighting has been confirmed by comparison of histograms of CNN-aided and expert's images (Figure 4), which were superimposed for each corresponding channel of HSL color system, with the expert-based histograms marked as green bars, and the CNN-based histograms marked red (Figure 6). The expert-based histograms define an interval of values for the affected fundus areas. From the histograms, the CNN-aided interval of exudates area is seen to be narrower than that obtained based on expert's estimates. The histogram regions corresponding to the false CNN-aided classification are within intervals shown by rectangles (Figure 6). Table 3 gives segmentation errors calculated for each channel of the HSL color model. The data in Table 3 suggest that the H channel is the most informative channel with the least segmentation error.

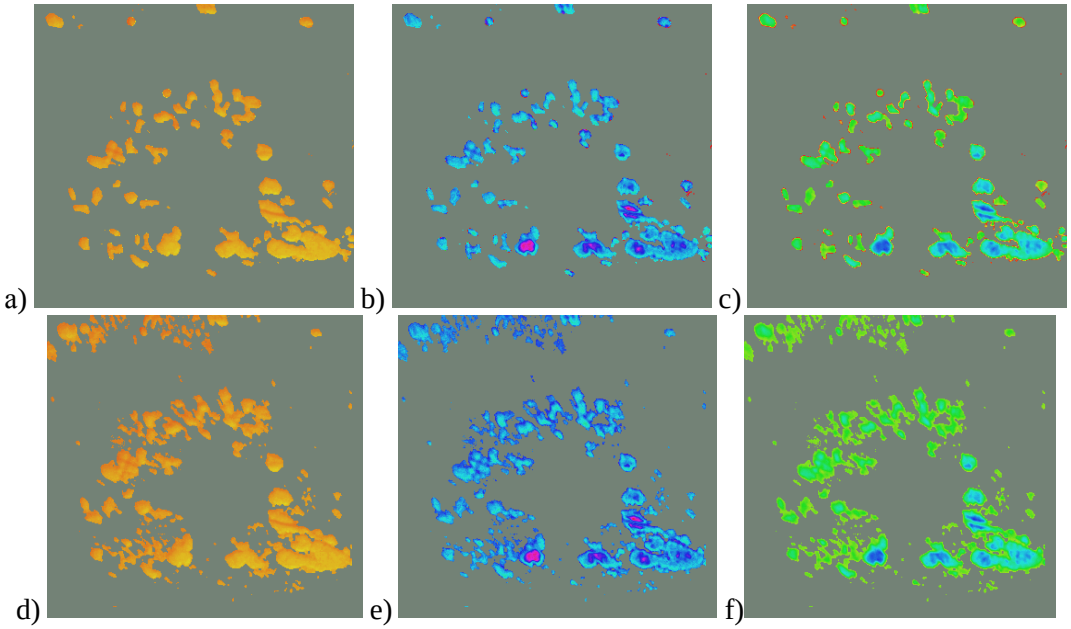

Figure 5. Expert-highlighted affected fundus areas for the HSL color model for the channel (a) H, (b) S, and (c) L; CNN-highlighted affected fundus areas for the HSL color model for the channel (d) H, (e) S, and (f) L.

Table 3. Segmentation error for each channel.

Channel	H	S	L
Segmentation error for the exudates class, %	3	9	9.8

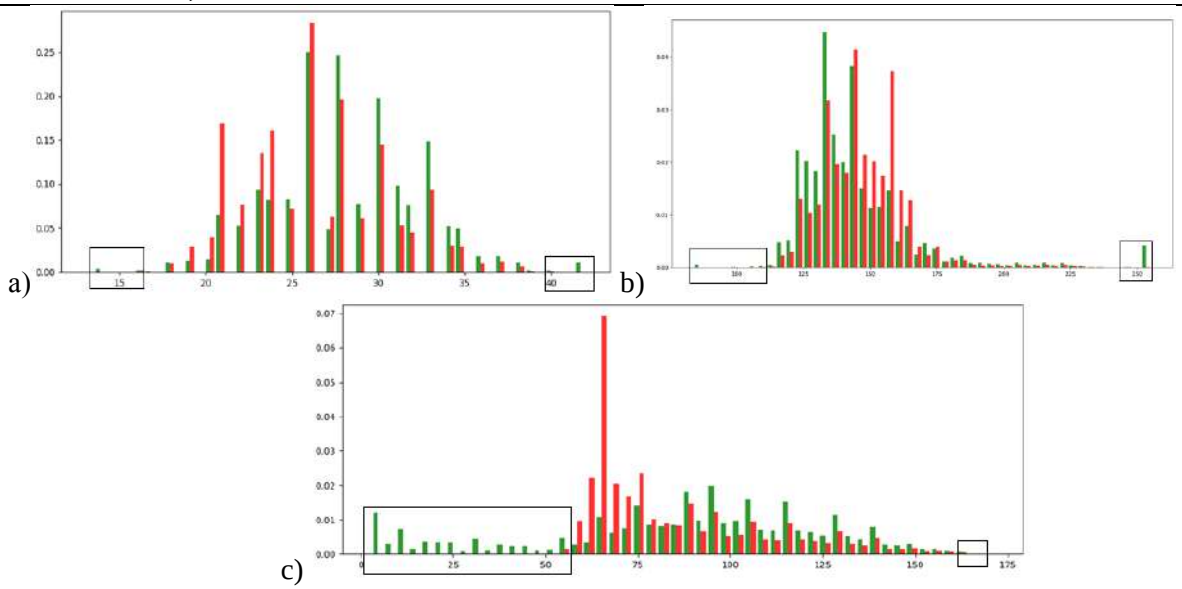

Figure 6. Image histograms obtained by using an expert opinion and CNN: a) H channel, b) S channel, and c) L channel.

4. Conclusion

In this work, a convolutional neural network (CNN) has been applied to the analysis of an eye fundus image. CNN architecture has been constructed, allowing a testing error of no more than 4% to be attained. Based on a 3x3 convolution kernel, CNN training was conducted on 12x12 images, thus enabling the best result of CNN testing to be achieved. CNN-aided segmentation of the input image conducted in this work has shown the CNN to be capable of identifying all training dataset classes

with high accuracy. The segmentation error was calculated on the exudates class, which is key for laser coagulation surgery. The segmentation error on the exudates class was 7 %, with the error of first kind being 5 %.

In the study, we utilized the HSL color model because it renders color characteristics of eye blood vessels and exudates most adequately. We have demonstrated the *H* channel to be most informative, with the segmentation error amounting to 3 %.

5. References

[1] Shadrichev F E Diabetic retinopathy *Territorial Diabetes Center* 8-11
[2] Ilyasova N Yu 2014 Evaluation of geometric features of the spatial structure of blood vessels *Computer Optics* **38(3)** 529-538
[3] Khorin P A, Ilyasova N Yu and Paringer R A 2018 Informative feture selection based on the Zqrnike polynomial coefficients for various pathologies of the human eye cornea *Computer Optics* **42(1)** 159-166 DOI: 10.18287/2412-6179-2018-42-1-159-166
[4] Astakhov Y S, Shadrichev F E, Krasavira M I and Grigotyeva N N 2009 Modern approaches to the treatment of diabetic macular edema *Ophthalmologic sheets* **4** 59-69
[5] Litjens G A 2017 Survey on deep learning in medical image analysis *Medical Image Analysis* **42** 60-88
[6] Ilyasova N, Kirsh D, Paringer R, Kupriyanov A and Shirokanev A 2017 Coagulate map formation algorithms for laser eye treatment *IEEE Xplore* 1-5
[7] Shirokanev A S, Kirsh D V, Ilyasova N Yu and Kupriyanov A V 2018 Investigation of algorithms for coagulate arrangement in fundus images *Computer Optics* **42(4)** 712-721 DOI: 10.18287/2412-6179-2018-42-4-712-721
[8] Ilyasova N, Kirsh D, Paringer R and Kupriyanov A 2017 Intelligent feature selection technique for segmentation of fundus images *Seventh International Conference on Innovative Computing Technology (INTECH)* 138-143
[9] Shirokanev A S, Ilyasova N Yu and Paringer R A 2017 A smart feature selection technique for object localization in ocular fundus images with the aid of color subspaces *Procedia Engineering* **201** 736-745
[10] Ilyasova N, Paringer R and Kupriyanov A 2016 Regions of interest in a fundus image selection technique using the discriminative analysis methods *Lecture Notes in Computer Science (includingsubseries Lecture Notes in Artificial Intelligence and Lecture Notes in Bioinformatics)* **9972** 408-417
[11] Ilyasova N Yu, Kupriyanov A V and Paringer R A 2014 Formation of features for improving the quality of medical diagnosis based on descriminant analysis methods *Computer Oprics* **38(4)** 851-855
[12] Ilyasova N Yu 2013 Methods for digital analysis of human vascular system. Literature review *Computer Optics* **37(4)** 517-541
[13] Guido S, Andreas C 2017 Introduction to machine learning with python. *O`Reilly Media* 392
[14] Shichijo S 2017 Application of Convolutional Neural Networks in the Diagnosis of Helicobacter pylori Infection Based on Endoscopic Images *The LANCET* **25** 106-111
[15] Bambang K T 2017 The Classification of Hypertensive Retinopathy using Convolutional Neural Network *ICCSCI* 166-173
[16] Anabik P 2018 Psoriasis skin biopsy image segmentation using deep convolutional neural network *Computer Methods and Programs in Biomedicine* **159** 59-69
[17] Nikitaev V G 2004 Experimental study of color models in automated image analysis tasks *Scientific session MIFI* **1** 253-254

Acknowledgements
This work was financially supported by the Russian Foundation for Basic Research under grant # 19-29-01135, # 17-01-00972 and by the Ministry of Science and Higher Education within the State assignment to the FSRC “Crystallography and Photonics” RAS.

Description and formation of the database perimeter for systematisation and storage of multi-structured data

A A Nechitaylo[1], O I Vasilchuk[2] and A A Gnutova[1]

[1]Samara National Research University, Moskovskoe Shosse, 34A, Samara, Russia, 443086
[2]Volga Region State University of Service, Gagarin st., 4, Togliatti, Russia, 445677

e-mail: alik.51@mail.ru, lola_red@mail.ru

Abstract. For storage of big data, as a rule, relational databases are used. For multilateral research and analysis of the processes occurring in large economic systems, financiers, economists and other technical specialists use graphs with actual names of enterprises, cities, regions, etc. to move from the physical names of the studied regions to the corresponding parameters of relational databases.

1. Introduction

"Big data" envisages the process of managing and analysing large amounts of data, which began to develop rapidly in the world since 2011, while data analysis tools began to receive information from more diversely structured sources, which is caused by the widespread introduction of digital technologies in various fields (business, medicine, entertainment, etc.). Thus, in particular, according to the Forecast of the socio-economic development of the Russian Federation for the period up to 2036, "the health care system will operate within a single digital circuit based on a unified state health information system (EGISZ), which will enable us to collect, store, process ("Big data") and analyse large amounts of information [2]. One of the final goals of this work includes the processing and intellectual analysis of big data parallel computations to create decision-making systems in real time. To solve such problems, it is necessary to determine not only the relationships (algorithms, models, etc.) of the final goal with the means to achieve it and the existing constraints, but also the forms for describing and forming the database perimeter.

2. Formulation of the problem

The task of synthesising rational schemes for choosing alternatives and evaluating their quality is to choose the best (optimal) one from the set of competing strategies for solving a certain problem, based on the analysis of the conditions and consequences of its implementation. A significant addition to what has been said is that by conditions we mean not some fixed picture of today, but also conditions that can arise during the implementation of the strategy. Accepting well-grounded optimal solutions is impossible without the steady and efficient acquisition of reliable large data arrays [8].

Taking into account the above and taking into account recent trends, in the near future the main sources of information will be Internet of Things (IoT), social media, meteorological data, GPS signals from vehicles, location data of mobile network subscribers, Google Trends, search sites work and other alternative sources of information.

3. Experimental research

The authors conducted a study on the Internet about the availability of programmes working with "big data" in the Russian-speaking community. The study showed that large users (such as Sberbank, Pyaterochka, etc.) are developing such services for their own purposes [10]. As for small business, we have not even identified the formulation of tasks, which determines the relevance of the goal of this work.

In Russia, the Central Bank of the Russian Federation and the Federal Tax Service of the Russian Federation give particular attention to systematisation and storage of multi-structured data. In this regard, the business has to solve a number of systemic and technological issues that prevent the implementation of big data analysis in everyday practice. Among these issues is the lack of strategies for companies to use the methods and data of big data analysis, the lack of modern technological solutions, and the lack of relevant skills and understanding of the key streams of data generation [9].

The study of the problems associated with the implementation of "big data" in the activities of economic entities aimed at ensuring economic security and business development shows that the strengthening of control by the Central Bank of the Russian Federation and the Federal Tax Service of the Russian Federation is directed, first of all, to the formation of a database perimeter for systematisation and storage of multi-structured data of legal entities in a single information space.

Central banks around the world have created or created departments for working with big data ("big data") in order to better understand the economy that they manage in the hope of one day getting technologies that allow them to monitor the state of the economy in real time. The current global trend is presented in table 1.

Table 1. Activities of the Central Bank of countries to promote "big data".

Region	Description of the activities of the Central Bank of the country to promote "big data"
Russia	The Bank of Russia published the first study on analysis based on "Big data". The report "Evaluation of economic activity based on textual analysis" presents a method for calculating a leading indicator of economic activity in Russia, which is based on daily contextual analysis of news sites using machine learning. A news monitoring system has been created; big data can predict consumer behaviour over a long period of time.
Japan	The Bank of Japan has been using big data since 2013 to analyse economic statistics, which helps the regulator build more accurate forecasts. It is planned to use big data for direct collection of economic data, instead of relying on survey results.
China	The People's Bank of China will more actively use "big data", artificial intelligence and cloud computing to increase its ability to recognise, prevent and reduce inter-industry and intermarket financial risks. In China, big data is interested in the context of tracking consumers and, mainly, to control debtors. One of the main problems of China is the rapid formation of "bubbles" and the tendency of the population to participate in financial pyramids. In May, the local Central Bank announced that it plans to use big data together with artificial intelligence to track such risks.

USA	In monetary policy decision making, the regulator continues to rely on traditional data sets. Economists at the Federal Reserve System (FRS) often use “big data” when studying specific issues, such as spending dynamics after hurricanes. Nevertheless, the Fed sees many shortcomings in big data, especially limited periods of time that cover these supersaturated data sets. This significantly reduces their value for forecasting. In addition, data sets are often produced by private companies that focus on something other than economic analysis. This can make big data less reliable, and the Fed is wary of using it for policy development. However, in individual projects, big data is already used, for example, to analyse consumer and government spending after hurricanes. The problem of big data, according to economists, is the too shallow depth of the sample, which significantly reduces the possibility of analysis. In addition, data is often collected by private companies that pursue their own interests. (Commercial banks: More than 60% of banks in North America believe that big data gives a competitive advantage, more than 90% that the one who copes with big data will win in the future, only 37% of banks have working projects)
Eurozone	The ECB has been exploring big data since 2013. Information on approximately 40 thousand daily transactions in the money market will become the basis of the alternative rate, since traditional benchmarks are becoming unreliable. The regulator has also acquired a large set of pricing data for actual consumer purchases and is exploring ways to measure inflation in real time. ECB analysts track Google Trends to assess unemployment change, and use algorithms to analyse media reports to assess whether the rhetoric of the regulator is viewed as “hawkish” or “pigeon”. However, the ECB remains cautious. Just as there are concerns about fake news that dominates social media, there is a risk that fake news or at least low quality statistics will crowd out better data in public discourse. Information about 40 thousand daily transactions will form the basis of an alternative discount rate. The ECB has also acquired data on the prices of real citizens' purchases and is looking at ways of online scraping to measure real-time inflation.
United Kingdom	The Big Data Board, now called the Data Management Team, has been created, as well as the data laboratory and analytical unit. Bank of England analysts recently used big data to gauge the effects of exchange rate changes. They also created a platform for these trading repositories.
India Singapore Indonesia	India faces security and privacy concerns, so the country's central bank is more concerned about cybersecurity in the context of big data. Singapore has created a Data Analysis Group, whose task is to collect large data, which will be analysed manually, without the use of AI technology. The main task, as in India, is the fight against money laundering and terrorism. The Statistics Department of the Bank of Indonesia explores social networks, news sites and other sources to analyse consumer sentiment. They recently began receiving data from online stores.

Figure 1 below illustrates the use of “big data” by banks to predict US home sales through Google Trends. The technique is based on the fact that people are looking for houses much more immediately before shopping [7].

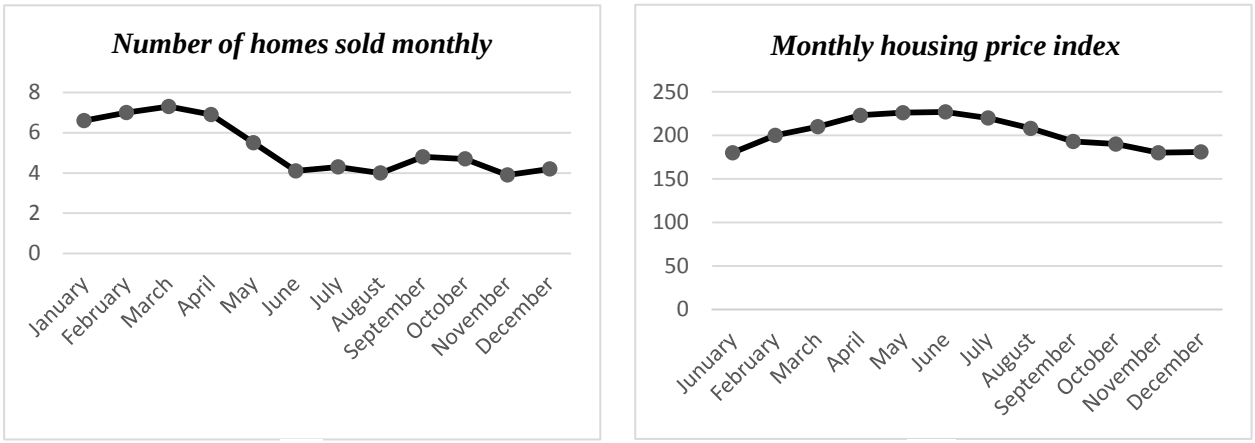

a) b)

Figure 1. Illustration of changes in prices and the number of homes sold in the United States: a) The number of homes sold monthly; b) monthly price index for housing.

As can be seen, managerial decisions are formed based on the information received and the method of its transfer along the functional units of the organisation. Quality, reliability, timeliness will definitely influence the effectiveness of the management decision.

The age of information technology allows us to form, consolidate, modernise information, and therefore there are problems that lead to an excess of information and a deterioration of its quality [6].

According to experts, the amount of useful information in relation to all the information received will be reduced from year to year. It is believed that by far not all of the data is valuable - according to IDC estimates, by 2020 the share of useful information will be only 35% of the total generated [4].

4. Solution description

In order for the use of information that a manager receives to be effective, it is necessary to determine correctly whether the information obtained is useful and whether it will be important for making management decisions, and only after that choose the right toolkit (algorithms, models, systems, competence, etc.). Experimental comparison of relational and non-relational databases, conducted by the authors, confirms expert assessments of specialists that managing thousands of attributes that are required for economic research in relational databases is inefficient [11].

In this connection, the problem of describing and forming the perimeter of the database for systematizing and storing multi-structured documentary data becomes very relevant for the economy. A schematic representation of this is shown in Figure 2.

Document databases are intuitive to developers, since data at the application level is usually presented as a JSON document. Developers can save data using the same document model that they use in the application code. In a document database, all documents may have the same or different data structure. Each document is self-describing (that is, it contains a schema that can be unique) and does not necessarily depend on any other document. Documents are grouped into “collections,” which are similar in function to tables in relational databases.

For example, a JSON file for describing a book element in a simple book database may look like the following code.

```
[
   {
      "year" : 2013,
      "title" : "Turn It Down, Or Else!",
      "info" : {
         "directors" : [ "Alice Smith", "Bob Jones"],
         "release_date" : "2013-01-18T00:00:00Z",
         "rating" : 6.2,
```

"genres" : ["Comedy", "Drama"],
"image_url": "http://ia.media-imdb.com/images/N/O9ERWAU7FS797AJ7LU8HN09AMUP908RLlo5JF90EWR7LJKQ7@@._V1_SX400_.jpg",
"plot" : "A rock band plays their music at high volumes, annoying the neighbors.",
"actors" : ["David Matthewman", "Jonathan G. Neff"]
}
},
{
"year": 2015,
"title": "The Big New Movie",
"info": {
"plot": "Nothing happens at all.",
"rating": 0
}
}
]

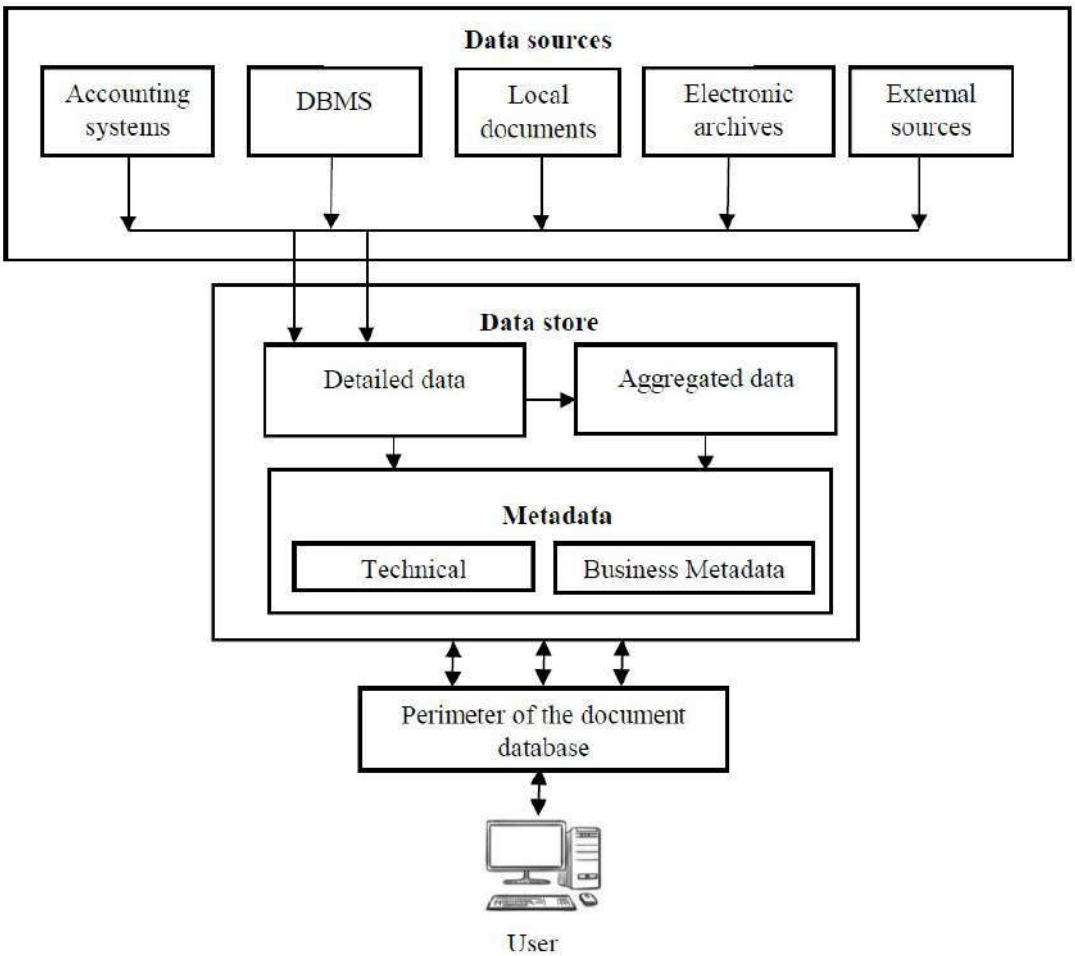

Figure 2. Illustration of the perimeter structure of the database on the systematization and storage of multi-structured data in the economy.

П when using a document database, each entity monitored by the application can be stored as a separate document. The document database allows the developer to conveniently update the application as requirements change. In addition, if you need to change the data model, then only the documents affected by this change need to be updated. To make changes there is no need to update the

schema and interrupt the database. When using a document database, the attributes of each transaction can be described in one document, which simplifies management and improves reading speed. Changing the attributes of one transaction will not affect other transactions.

Analysis of popular document databases: Amazon DocumentDB (compatible with MongoDB), Amazon DynamoDB, MongoDB, and Couchbase, based on literature and expert opinions, showed the promise of using MongoDB Documentation AWs to solve economic problems using the AWS MongoDB Quick solution, Start (also available in PDF format) for deploying a MongoDB cluster in the AWS cloud.

In solving the problems of organising modern production, it is necessary to take into account an increasing number of factors of different natures, which are the subject of research in various fields of knowledge. Under these conditions, one person cannot decide on the choice of factors influencing the achievement of a chain, and cannot determine the essential interrelationships between goals and means; in the formation and analysis of the decision-making model, there should be involved development teams consisting of specialists from various fields of knowledge, between whom interaction and mutual understanding should be organised; and the problem of decision making becomes a problem of collective choice of goals, criteria, means and options for achieving the goal, i.e. the problem of collective decision-making based on modern methods of processing big data. This leads to the fact that the formulation of the problem becomes a problem itself, for the solution of which it is necessary to develop special approaches, techniques, methods. In such cases, it is necessary to determine the scope of the decision-making problem (problem situation); identify the factors influencing its decision; choose techniques and methods that allow you to formulate or set the task so that the decision was made.

If it is possible to obtain an expression (algorithm, methodology, etc.) connecting the goal with the means, then the problem is almost always solved. These expressions can represent not only simple relations, similar to those considered, but also more complex, composite criteria (indicators) of additive or multiplicative form. Of course, in this case, computational difficulties may arise, which, if overcome, may require recourse to the formulation of the problem. However, the obtained formalised representation of the task allows us to apply further formalised methods for analysing the problem situation.

Decision making is a scientific direction that began to take shape in the middle of the last century. The task of this direction is the synthesis of rational schemes for choosing alternatives and evaluating their quality, which consists of choosing the best (optimal) one from the set of competing strategies for solving a certain problem. A significant addition to the last phrase is that the terms are understood not as some frozen picture of “today”, but also those conditions that may arise during the implementation of the strategy.

This scientific direction is distinguished by the fact that the choice of the optimality criterion must be approached creatively. According to this approach, the optimality criterion is not a kind of extremum of a function of one variable, but is an area of multidimensional feature space in which some particular parameters may be non-optimal. It is implied that we are talking about the fact that not all particular utility functions are considered as equilibrium, but as a hierarchically ordered system of utility functions with different weights (the choice of which, along with the choice of the functions themselves, is actually the content of the decision-making process).

Thus, in order to make a decision, it is necessary to obtain an expression associating the goal with the means of achieving it using the input criteria for assessing the attainability of the goal and evaluating the means. If such an expression is obtained, then the problem is solved.

5. Conclusion

In the classical theory of decision making, the central question is associated with the axioms of "rational" choice. As a result, when referring to the methods of the classical theory of decision making, the choice is reduced to binary preference relations. However, the classical rational bases of choice are not universal, but represent only a limited part of the grounds on which reasonable and natural decision-making mechanisms can be built. In order to simplify the construction and interaction of

these mechanisms (algorithms, techniques, etc.) for different sectors of the national economy, it is advisable to build typical perimeters (possibly interfaces) of big data collection and storage bases.

The number and complexity of such problems, for which it is impossible to get the performance criterion in analytical form immediately, but as the degree of development of civilisation increases the price of the wrong decision also increases. For problems of decision making, as a rule, a combination of qualitative and quantitative methods is characteristic. Decision-making in industrial control systems is often associated with a lack of time: it is better not to make the best decision, but in the required time, because otherwise the best solution may no longer be needed. Therefore, the decision often has to be taken in the context of incomplete information (its uncertainty or deficit), and it is necessary to ensure that the most relevant decision-making information and the most objective preferences underlying the decision-making can be determined as quickly as possible.

6. References

[1] Central banks use big data to form financial policy URL: http://www.vestifinance.ru/articles/95398 (20.12.2018)
[2] Forecast of the socio-economic development of the Russian Federation for the period up to 2036 URL: http://economy.gov.ru/wps/wcm/connect/9e711dab-fec8-4623-a3b1-33060a39859d/prognoz2036.pdf?MOD=AJPERES&CACHEID=9e711dab-fec8-4623-a3b1-33060a39859d (15.11.2018)
[3] How big is the internet? URL: https://geektimes.ru/company/asus/blog/275032/ (25.10.2018)
[4] How Central Banks Are Using Big Data to Help Shape Policy URL: https://www.bloomberg.com/news/articles/2017-12-18/central-banks-are-turning-to-big-data-to-help-them-craft-policy (15.11.2018)
[5] The Future of Prediction: How Google Searches Foreshadow Housing Prices and Sales URL: http://papers.ssrn.com/sol3/papers.cfm?abstract_id=2022293 (05.11.2018)
[6] The problems of making effective management decisions URL: https://cyberleninka.ru/article/n/problemy-prinyatiya-effektivnogo-upravlencheskogo-resheniya (25.10.2018)
[7] Vashko T A 2011 Information duplication technology as a means of improving the quality of decision making *Problems of the modern economy* **4** 137-141
[8] Kazanskiy N L 2017 Efficiency of deep integration between a research university and an academic institute *Procedia Engineering* **201** 817-831 DOI: 10.1016/j.proeng.2017.09.604
[9] Kazanskiy N L, Protsenko V I and Serafimovich P G 2017 Performance analysis of real-time face detection system based on stream data mining frameworks *Procedia Engineering* **201** 806-816 DOI: 10.1016/j.proeng.2017.09.602
[10] Protsenko V I, Seraphimovich P G, Popov S B and Kazanskiy N L 2016 Software and hardware infrastructure for data stream processing *CEUR Workshop Proceedings* **1638** 782-787 DOI: 10.18287/1613-0073-2016-1638-782-787
[11] Kazanskiy N L, Protsenko V I and Serafimovich P G 2014 Comparison of system performance for streaming data analysis in image processing tasks by sliding window *Computer Optics* **38(4)** 804-810

Neural network model in digital prediction of geometric parameters for relative position of the aircraft engine parts

M A Bolotov[1], V A Pechenin[1], N V Ruzanov[1] and D M Balyakin[1]

[1]Samara National Research University, Moskovskoe Shosse, 34A, Samara, Russia, 443086

e-mail: vadim.pechenin2011@yandex.ru

Abstract. The quality of aircraft and rocket engines depends primarily on the geometric accuracy of assembly units and parts. Mathematical models implemented in the form of computer models are used to predict quality indicators (in particular, assembly parameters). Direct modeling of the conjugation process using numerical conjugation and finite-element models of assemblies requires significant computational resources and is often accompanied by problems convergence of solutions. In order to solve the above problems, it is possible to use neural network models describing the main regularities of the pairing process based on the accumulated results. The work presents a neural network model for predicting assembly parameters of the parts based on the use of actual surfaces of the parts obtained as a result of mathematical modeling. Assembly on conical surfaces is considered. A convolutional neural network was used to predict assembly parameters.

1. Introduction

Complex industrial and knowledge-intensive products are characterized by high requirements to geometrical accuracy of the parts and assembly units. These products include modern aircraft engines which are subject to high requirements for reliability, minimum weight, cost effectiveness and durability. These characteristics are also achieved through improvement of the technology for manufacturing parts and units. While manufacturing and assembling, dimensional accuracy is ensured. The ways to achieve dimensional accuracy are determined at the stage of design and technological preproduction [1,2,3]. The solution of these tasks at each of the stages can be simplified due to availability of mathematical models [4] and means allowing to predict and determine the actual value of geometric parameters [5,6] characterizing achievable accuracy.

The work proposes a model based on the use of neural networks allowing to predict assembly parameters of the parts when conjugating them on flat, cylindrical and conical surfaces with dimensions specific to the gas turbine engine parts.

2. Object of research

The assembly of two conical rings is considered as an object. Figure 1 shows the assembly model for conical items.

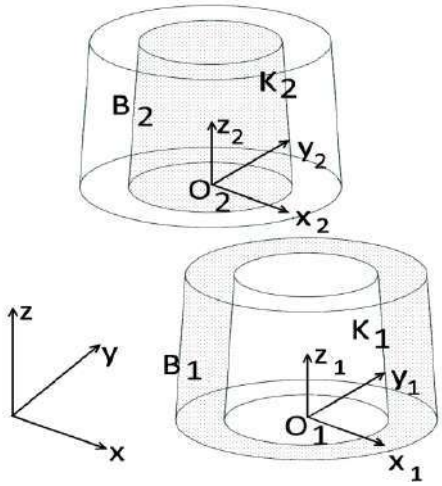

Figure 1. Mechanical system model for assembling two cone rings.

In Figure 1, the cone rings K_1 and K_2 are defined as the local design coordinate systems R_1 and R_2. Conjugation of the parts occurs on surfaces B_1 and B_2. Each surface is defined in the local coordinates of the part. One ring is male and deprived of six degrees of freedom, the second one is female and movable [7]. The assembly parameters of two cone rings are the coordinate of axis intersection with the top end face of the movable ring. The coordinates of the point in a plane perpendicular to the axis of the cone are represented by the polar coordinate system and is characterized by a polar radius ρ_c and corresponding polar angle φ_c, varying from 0 up to 360º. The coordinate along the rotation axis describes the displacement δ_o along the corresponding vector of the end surfaces of the outer ring relative to the inner ring. Axle distortions are negligible in this case of assembly.

In order to create a neural network model for predicting assembly parameters, it is necessary to create training sets and to check the quality of network operation on the test data. This requires either accumulating sufficiently large statistics of measured data (from several thousand cases) or augmenting data from fewer statistics. At the same time, it is necessary to calculate the assembly parameters, that will be predicted, accurately. Let's consider in more detail the stages for creating a neural network model for predicting geometric parameters of the relative position of the parts.

3. Neural network model in digital prediction of geometric parameters for relative position of the conical rings

In general, the contact of the surface pairs respectively conjugated occurs on a finite set of points. These tasks are contact ones [8]. Analytical solutions of contact tasks of surfaces, that do not have shape deviation, are known. In general, the finite element method is used to model contact tasks of surfaces with shape deviations. This method allows to take into account the surface geometry features and to solve the tasks for predicting the assembly.

The developed model includes the following stages:

1. Creating valid part models.
2. Creating triangulation grids on the part surfaces.
3. Performing a virtual analysis of a part assembly, saving the results.
4. Training of the neural network, estimation of prediction errors.

3.1. Creating valid part models

The actual part models were created in the following sequence. At the first stage, the finite set of nominal points for the parts conjugated was formed. At the second stage, the actual (model) conjugated point surfaces were calculated based on the coordinates of nominal points, form deflection functions, and location deviation parameters.

In order to describe the form deviation, a harmonic sequence is selected with the help of which it is possible to describe the discrete sequence of deflection data, obtained from the measured geometry, accurately. Harmonic sequence has the following form:

$$\delta_n(x) = \sum_{k=1}^{+\infty} A_k \sin(k \cdot (2 \cdot \pi \cdot x / \tau + \theta_k) + \left(1 + (-1)^k\right) \cdot \pi / 2), \quad (1)$$

being A_k is an amplitude set of the harmonic sequence members;

θ_k are phases of the harmonic sequence members;

k is a frequency of the harmonic sequence members;

τ is a function period (curve length);

x is a current curve length from the start point up to the current point (angle).

The parts considered represent rotation bodies. The conjugated panes having geometry deviation are swept ones: they can be obtained by moving an object, such as a section, a broker line, or a curve along a guide curve, over a distance.

The coordinate vector of each point of the section curve guide for a cone face, the axis of which is perpendicular to *XOY*, can be described using the expression:

$$\vec{p}_u = \left|(r_c - \delta r_h + \delta r_c + \delta_n(\chi)) \cdot \cos(\chi) \quad (r_c - \delta r_h + \delta r_c + \delta_n(\chi)) \cdot \sin(\chi) \quad h\right| + \vec{t}, \quad (2)$$

being r_κ is a nominal radius of section points;

δr_c is a constant value of the radius deviation from the nominal value;

χ is a polar angle of the point p_u;

δ_n is a simulated deflection of the form by means of sequence (1) at the point p_c;

h is a section height.

δr_h is a the height change of the cone radius. Calculated by the formula:

$$\delta r_h = h \cdot tg(90 - \gamma / 2), \quad (3)$$

being γ is an angle at the cone top.

3.2. Creating triangulation grids on the part surfaces

Accordingly, the curve, that will move along the resulting guide, represent a line. Thus, the points of cone faces may be defined using two equations (2), respectively, at the minimum and maximum heights h. Then sets of three adjacent points (two on one section and one on the other) form facets of the finite-element model.

3.3. Performing a virtual analysis of a part assembly, saving results

In order to solve the contact task with using the developed finite element model, an iterative algorithm was developed, allowing to calculate the conjugation of the parts without taking into account the deformations of the parts in the assembly process described in detail in [9]. Algorithm for finding the conjugated state assumes iterative movement of one conjugated surface relative to another with the application vector of the surface assembly force $\vec{D}_1$. The concept of the gap function is introduced $G(\vec{V})$ which specifies achievement of the conjugate state of the surfaces of the parts and depends on the vector of mutual arrangement of surfaces $\vec{V}$. In order to calculate the function $G(\vec{V})$, the best combination of the conjugated surfaces is performed at each stage. Iteration algorithm (ICP) of the nearest points [10, 11] is used to perform the best alignment procedure. According to this algorithm, at each iteration by methods of nonlinear optimization search, the angles of rotation and displacement are calculated along the coordinate axes. In order to exclude intersections of two surfaces, the system of inequalities presented in work [12] is used, which imposes limitations on the gap function $G(\vec{V})$. In consequence of the algorithm, the rotation matrix and movement vector of the moving part are

calculated determining the transformation of its initial coordinate system into the coordinate system in assembled state:

$$\vec{p}_{as} = \vec{p}_p \cdot \mathbf{R}_{as} + \vec{t}_{as}, \quad (4)$$

being $\vec{p}_{as}$, $\vec{p}_{\partial}$ are vectors of coordinates of points (*x*, *y*, *z*) of the part respectively after the assembly and in the initial state;

$\mathbf{R}_{as}$, $\vec{t}_{as}$ are the rotation matrix and the point coordinate movement vector that $\vec{p}_p$ specify the movement of the part during the assembly.

The proposed algorithm makes it possible to calculate the conjugations of parts, when their deformations during the assembly process are more than three times as compared with deviations of the geometry. The parameters for assembly of cone rings ρ_c, ϕ_c and δ_o because the axis distortions are negligible small, are contained in the displacement vector $\vec{t}$ from the equation (4).

3.4. Training of the neural network, estimation of prediction errors

The neural network for prediction is a sequence of interconnected layers starting with a convoluted layer and ending with a regression layer (Figure 2).

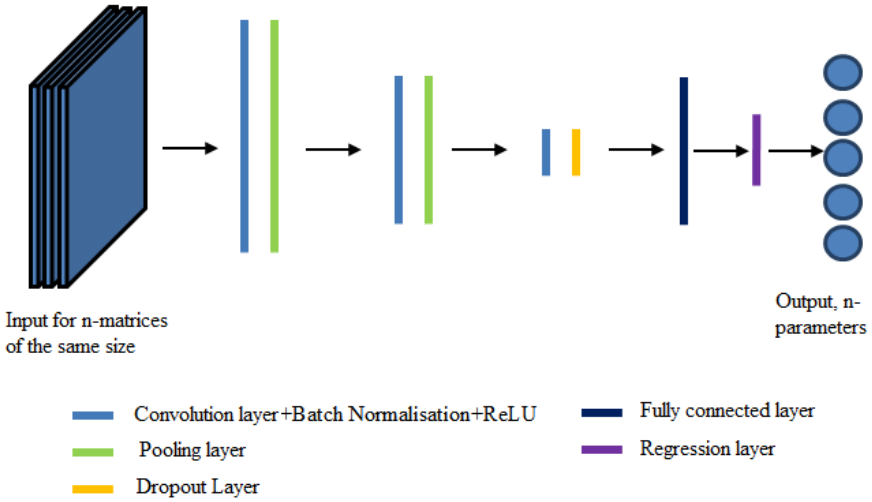

Figure 2. The architecture of a convolutional neural network for predicting parameters.

A set of rectangular matrices of equal size numbers is supplied to the network input. Let us give a brief description to the layers of the network considered.

The convolutional layer is the main block of the convolutional neural network. The convolution layer includes its own filter for each channel, the convolution kernel of which processes the previous layer by fragments (summarizing the results of the matrix product for each fragment).

The scalar result of each convolution falls on the activation function which is a kind of nonlinear function. The activation layer is usually logically combined with the convolution layer (believe that the activation function is embedded in the convolution layer). The piecewise linear *ReLu* function is selected.

Normalization of mini-batches (batch normalization) is described for example in [13], from the Russian sources in [14]. Mini Batch is a small collection of data that is usually selected from the entire training set randomly. Batch normalization solves the problem of gradient mismatches at different network levels, preventing effective training by normalizing the input data in such a way as to get zero mathematical expectation and unit variance. Normalization is performed before entering each layer.

The pulling layer (otherwise subsampling, downsampling) is a nonlinear sealing of the feature map, with a group of pixels (usually 2×2) compacted to one pixel, passing a nonlinear transformation. The averaging function used in this network is most commonly used.

Dropout Layer [15]. Dropout is a method for regulating neural networks. Each neuron (except the most recent one, output layer) is set to a certain probability *p* which it will be thrown out of the

network with. The training algorithm changes in this way: on each new training example, each neuron with probability *p* is either used as usual or its output is set strictly to zero. Everything happens then with no changes; zero at the output causes the neuron to drop actually out of the computation graph: and direct calculation, and the reverse spread of the gradient stop at this neuron and do not go further.

A fully connected layer. After several passages of image convolution and compaction using pulling, the system is rebuilt from a specific high-resolution pixel grid to more abstract feature maps, usually the number of channels increases on each next layer and the image size decreases in each channel. After all, there is a large set of channels storing a small number of data (even one parameter) that are interpreted as the most abstract concepts identified from the original image.

These data are combined and transmitted to a normal fully connected neural network which can also consist of several layers. At the same time, fully connected layers already lose the spatial structure of pixels and have a relatively small size (relative to the number of pixels of the original image).

The last layer is a regression layer that uses the *MSE loss function* (mean-square error). Accordingly, the assembly parameters are calculated directly at the network output.

In case of assembly of two planes and cone rings at the input, it is sufficient to supply a single matrix of distances representing the initial gap in the connection. The initial gap is a matrix of distances between points of one surface (a fixed part in a connection) and the adjacent surface of another (a moving part) when the parts are in the nominal position. Or the moving part is shifted to some short distance from the fixed part along one of the axes.

To estimate the prediction results for the parameters of assemblies and to specify the structure of the selected neural network model, it is necessary to estimate prediction errors. Estimation of prediction error parameters shall be made according to two criteria:

1 Proportion of the predicted values within the permissible tolerance δ_{add} .

2 Mean-square error (*RMSE*) of predicted and actual parameters.

Here is a sequence of calculations for these values:

1 Calculate the tolerance between the predicted and the actual parameters:

$$\Delta_n = \Pi_{pr} - \Pi_a . \quad (5)$$

2 The number of errors within the permissible area shall be counted $N_{\Delta add}$. The permissible area of errors shall be calculated as a percentage of the maximum value of the predicted parameter — 10%.

3 Prediction accuracy shall be calculated as the ratio of quantity $N_{\Delta add}$ to the total sample size:

$$\delta_{add} = N_{\Delta add} / N_{com} . \quad (6)$$

4 The mean-square error value shall be calculated by the formula:

$$RSME = \sqrt{\Delta^2 / N_{com}} . \quad (7)$$

4. Results of virtual assembly application for prediction of assembly parameters

The points of two cone surfaces are modeled using formulas (1-3). 10,000 sets of points in total were modeled for two types of cones (5,000 of each type). Each set contains 720 points (360 points belonging to two guide curves). Nominally, the guide points lie in planes parallel to *XOY*. Table 1 shows the statistical characteristics (mathematical expectation $\overline{X}$ and standard deviation σ) of the geometric deviations of the two cones.

Table 1. Value of deviation parameters for points of two conjugated cones.

Parameter	The first cone				The second cone			
	A_k , mm	k	θ_k , rad	δr_c , mm	A_k , mm	k	θ_k , rad	δr_c , mm
$\overline{X}$	0.0041	5.9	1.9783	0.0665	0.0010	5.8	1.9556	0.0001
σ	0.0067	2.3	1.8823	0.0219	0.0009	2.3	1.8308	0.0085

The height of the cones h is 40 mm; the radius at the base r_c is 27,36 mm; the angle at the top is γ 6 degrees.

Statistical characteristics and minimal and maximal values of assembly parameters for cone rings obtained in consequence of simulation using formed sets of measured points of the connected parts are shown in Table 2.

Table 2. Assembly parameters of two cone rings.

Parameters	$\overline{X}$	σ	Min	Max
ϕ_c, deg	131.0174	75.8793	0.0652	359.9210
ρ_c, mm	0.0104	0.0068	0.0001	0.0453
δ_o, mm	-0.4318	0.7330	-2.3640	0.9730

Figure 3 shows an example of one of the initial gaps in connections of cone surfaces.

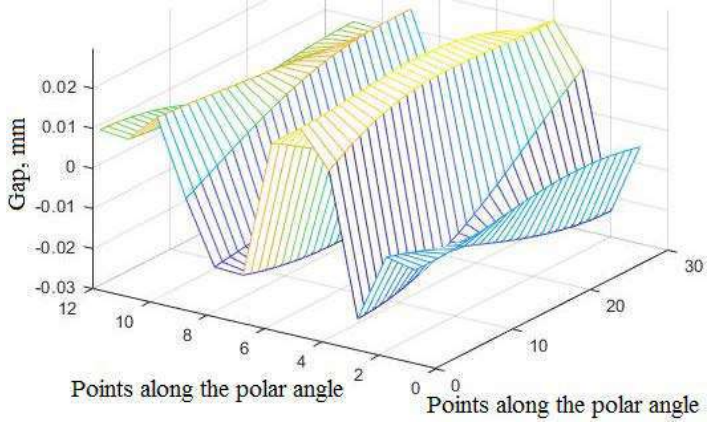

Figure 3. Initial gap in connection of two cones.

The matrix sizes are 12×30 points for the cone rings. Since there are no inclination angles of the rolling ring at the initial stage of assembly, during and at the end of assembly, the gap will be the same in height in zero position. Therefore, a gap in one section (360 points) has been taken and in order to perform several convolution operations, one row is divided into 12 rows for 30 values each. After calculation of all matrices, their values are normalized into the range [0 1].

Selected parameters of a convolutional neural network with a regression layer are: network depth , characterized by the number of convolution subnets N_{CNN} including convolutional layers, layer downsampling layers; the size of the convolution kernel ($N_k \times N_k$); the number of convolution channels M_c ; the probability *p* in dropout . The window size in pulling does not change — 2×2. After selecting the network architecture, the network training process is optimized according to the following parameters: packet size (batch) of data during training N_b ; number of learning epochs N_{ep} ; number of epochs to reduce learning speed N_{ELS} ; reduction factor of learning speed F_{LS} (varies from 0 to 1); training algorithm (“SGDM” [16, 17] or “RMSProp” [18]).

Table 3 shows the prediction results for the assembly of two planes and two cone rings.

Table 3. Network performance assessment.

Parameters	Cone rings		
	φ_c	ρ_c	δ_o
δ_{add}	0.864	0.866	0.998
RMSE	0.647	0.003	0.056

Table 4 shows the network parameters that achieve the maximum accuracy in predicting assembly parameters.

As it appears from the results given in Table 3, the value δ_{add} of the parameter δ_0 is the highest one, the polar coordinates of the center are determined with less smaller accuracy. It should be taken into account that the value ρ_c is almost 19 times smaller indicator *RMSE* than δ_0, since the values of the center offset in the plane perpendicular to the axis of rotation are significantly lower than its offset along the axis of rotation.

Table 4. Optimal parameters of the networks for predicting assembly of the cone rings.

Parameter	N_{CNN}	N_k	M_c	p	N_b	N_{ep}	N_{ELS}	F_{LS}	Training algorithm
Value	2	4	6	0.4	40	70	30	0.1	“SGDM”

5. Conclusion

The work presents a model for predicting conjugation accuracy of the parts according to the geometry measurement results based on the use of digital models and a convolutional neural network. Connecting of two conical rings is selected as the object for calculations. The data obtained by simulation are used to train a convoluted neural network allowing to predict assembly components based on geometry deviations maps of measured surfaces connection parameters. Evaluation of the accuracy of the results leads to the conclusion about the adequacy of the developed neural network model. The adequacy of the developed model depends on the accuracy of the mathematical description of the actual geometry of the parts, the rigidity of the material and the design and size of the training set. Optimal parameters of the network may depend on the considered object.

6. References

[1] Soifer V A, Kazanskiy N L and Kharitonov S I 1998 *Optics and Lasers in Engineering* **29(4-5)** 237-247
[2] Kazanskiy N L, Stepanenko I S, Khaimovich A I, Kravchenko S V, Byzov E V and Moiseev M A 2016 Injectional multilens molding parameters optimization *Computer Optics* **40(2)** 203-214 DOI: 10.18287/2412-6179-2016-40-2-203-214
[3] Doskolovich L L, Kazanskij N L, Pavel'ev V S and Sojfer V A 1995 *Avtometriya* **1** 114-119
[4] Deng X and Wang J 2017 *Academic Journal of Manufacturing Engineering* **15(1)** 64-71
[5] Zakharov O V and Kochetkov A V 2016 *Measurement Techniques* **58(12)** 1317-1321
[6] Pechenkin M V, Abzalov A R and Shustov V E 2017 *Bulletin IzhSTU them. M.T. Kalashnikov* **20(2)** 87-90
[7] Pechenin V A, Bolotov M A, Ruzanov N V, Grachev I A and Shcherbakov I A 2017 *Russian Engineering Research* **37(8)** 739-743
[8] Kovalenko P, Perepelkina S and Korakhanov T 2017 *Tribology in Industry* **39(2)** 192-197
[9] Bolotov M A, Pechenin V A and Murzin S P 2016 Method for estimating the uncertainty of the spatial mating of high-precision optical and mechanical parts *Computer Optics* **40(3)** 360-369 DOI: 10.18287/2412-6179-2016-40-3-360-369
[10] Besl P J and Mckay N D 1992 IEEE *Transactions on Pattern Analysis and Machine Intelligence* **14(2)** 239-256
[11] Tian H, Yang P, Su C and Dong Z 2015 *International Journal of Security and its Applications* **9(12)** 47-56
[12] Pierce R S and Rosen D 2007 *Journal of Computing and Information Science in Engineering* **7(4)** 314-321
[13] Ioffe S Y and Szegedy C 2015 Batch Normalization: Accelerating Deep Network Training by Reducing Internal Covariate Shift *Proc. 32nd ICML* 448-456
[14] Nikolenko S I, Kadurin A and Arkhangelskaya E 2018 *Deep learning* (St. Petersburg: Peter) 153-163

[15] Srivastavaetal N 2014 *Journal of Machine Learning Research* **15(1)** 1929-1958
[16] Sutskever I, Martens J, Dahl G and Hinton G 2013 *Proceedings of the 30th international conference on machine learning (ICML-13)* **28** 1-14
[17] Chabanenko V D 2016 *Modifications of the stochastic gradient descent method for machine learning problems with large data volumes* (Moscow: Lomonosov Moscow State University / Faculty of Computational Mathematics and Cybernetics / Department of Mathematical Methods of Forecasting)
[18] Tijmen T and Hinton G 2012 Lecture 6.5-rmsprop: Divide the gradient by a running average of its recent magnitude *COURSERA: Neural Networks for Machine Learning* **4** 26-31

Acknowledgments
This work is supported by the Ministry of Education and Science of the Russian Federation in the framework of the implementation of the Program State Assignment for 2019. The project code is 9.11978.2018/11.12.

Optimization of urban freight transportation based on evolutionary modelling

E A Gladchenko[1], O N Saprykin[1] and A N Tikhonov[1]

[1]Samara National Research University, Moskovskoe Shosse 34A, Samara, Russia, 443086

e-mail: liz-ok_033@mail.ru, saprykinon@ssau.ru

Abstract. Logistics problems require special attention, because every year they become more complicated and multivariable. On the one hand, a supply chain management includes incessant monitoring of such issues as requests elaboration, paths determination, routing of shipments, multimodal choice, set up of transhipments, fleet choice and maintenance, warehousing, packaging and others. On the other hand, dozens of people are involved in the logistics process. All these moments complicate the decision-making that is why data driven decisions are required nowadays. As well as shipment problems are NP-hard, the heuristic methods should be applied to resolve them. In this article we propose a genetic algorithm to solve the complex problem that consists of the Travelling Salesman Problem combined with the Knapsack Problem. We have developed an urban freight transportation model which is focused on the minimization of the underway time as well as on the maximization of the truck's loading. A significant contribution in our method is the census of traffic frequency by using traffic zoning. The developed approach has been implemented using the Python programming language in the Zeppelin environment. The first version of the system has been approved in the city of Samara (Russia) with test demand dataset.

1. Introduction

Nowadays, the competition between logistics companies is extremely high. To stay alive each of them competes for clients, strives to reduce costs, improve quality and efficiency of work, in other words they try to optimize the process. In the 21st century, such technological advances as Big Data or Internet of Things [1], are available to be used for the above listed purposes. The potential of Big Data techniques with state-of-the-art software can significantly enhance the data-driven decision-making process.

Logistics optimization is a complex and dynamic problem that requires a systematic approach. On the one hand, this is determined by the large membership involved in the process: shippers, carriers, recipients, third party logistic managers and others. Their decisions and actions should be well coordinated, that is why it is necessary to have a good communication. On the other hand, the supply chain consists of several stages. The first is a distribution that includes tracking the demand level and types of commodities, booking and consolidation of requests. Transportation operations take place at the second stage which includes layout of the route, fleet choice, schedule preparing and adjustment, organization of the multimodal transshipment. This is the most sensitive and vast part of the logistics process, because of the wide variety of stochastic issues that need to be predicted. Warehousing, with

the best depots locations, as well as using the interior automation equipment and mechanic means, is the third stage. The last one is packaging, which is especially considerable in perishable, fragile and out of gauge goods shipments.

Outlined stages are not independent and affect each other. Thus, routing is NP-hard optimization problem that can be formally solved only in limited cases and has low performance. To avoid these limitations, heuristic methods are commonly applied. This paper is focused on the genetic analysis in terms of integrated transportation optimization.

The rest of the paper is organized as follows. Section 2 gives a brief background to the recent research, both theoretic and empirical; and problem statement. Section 3 contains basic model's features, presents methodological description, including genetic analysis. In Section 4 the implementation is displayed. Section 5 concludes and summarizes the paper.

2. Background

2.1. Literature Review

There is a huge amount of research related to supply chain optimization. For example, M. Grazia Speranza [1] outlines the main tendencies in the logistics management, one of which is the complex data handling. The author points out three directions of the extension: systemic direction (the most applicable for this research), collaborative direction and dynamic direction. The paper presents some feasible ways of using Big Data in terms of transportation process optimization. Big Data technologies make possible to build predictive models of transportation processes too [2]. Generally, articles which describe different methodologies, rested on the model formulization. For instance, Shui Lam and Burkhard Englert [3] represent a basic mathematical model, which takes into account only two shipment offers. The proposed method compares shipment schedules, transportation cost and terminal charges that helps to find out optimal deliveries.

Nevertheless, heuristic analysis allows estimating multiple decisions applying Genetic Algorithms [4]. Zbigniew Michalewicz [5] describes the processes of evolving with the parents' selection and the producing of offspring. This study contains several modes of application Mutation and Crossover operators, as well as the representation in matrix encoded data. For example, genetic analysis, with the unique combination of operators, was used by Gintaras Vaira [6] to solve the Rich Vehicle Routing Problem (RVRP). The general VRP is different from the typical VPR, because it restricts extra constraints for a task, a vehicle, a cargo and so on. The genetic algorithm allows resolving VRP with pick-up and deliveries as well as VRP with time windows.

As we have already noted the supply chain optimization is a complex subject that is why solving only the routing problem apart from real life constraints is not efficient. The next research tries to take this fact into account. The aim of the next model is not to create new optimal routes, but to find the best combination of existing routes and services in maritime transportation. Anantaram Balakrishnan and Christian Vad Karsten [7] report the LP-based heuristic procedure for containerized cargo that may require the transshipment during the delivery. The approach is based on a selection from the limited number of possible transshipments using the augmented multi-commodity flow network.

Another complicated problem for freight operators is to control the booking rate to provide the maximum profit and execute all shipments when the product demand and resource capacities are not determined. The stochastic resource allocation problem which is formulated by Xinchang Wang [8] as a stochastic programming (STOC) model that incorporates three important features: random resource capacities, stochastic product demands, and network effects. The algorithm embeds a nonlinear optimization solver that uses an iterative-search type algorithm.

Furthermore, there is a strong relationship between the shipment size and fleet size. Lots of papers propose various models to find the optimal mapping function. One of them is based on the discrete-continuous econometric model where the shipment size is a continuous variable and the size of the vehicle fleet is a discrete variable [9]. Results that are represented in the paper prove a hypothesis: with the increase of the distance and total demand it is become more efficient to exploit heavier, except for old vehicles.

Latent Class Analysis (LCA) is also applicable to shipment size optimization. Raphael Piendl, Gernot Liedtke and Tilman Matteis [10] combine LCA and minimization of the total logistics costs. The proposed model divides transport cases into classes according to similar response patterns. Four homogeneous segments were identified which were integrated as an additional component to the systematic framework of the total logistics cost formulation. Concepción Román, Ana Isabel Arencibia, María Feo-Valero [11] represent fascinating research, that outlines the quantification of attribute cut-offs combined with the estimation of taste heterogeneity through the Latent Class Model (LCM). The analysis is based on the empirical data about decision-making in the area of logistics management and based on the specification of the penalized utility.

Another application of the heuristic algorithm was introduced by Wu-Yang Liu and Li-Ning Xing [12] to reduce costs in the processing of express logistics system as a type of capacitated arc routing problem (CARP). The first step in the model is performing architecture optimization. The second step is assuming extended random path-scanning (drawing between 5 Rules). The paper illustrates the dependence between the number of depots, vehicles, total cost and different characteristics, as vehicles load, speed, acquisition cost, depot construction post, maximum service time, etc.

Nevertheless, when the optimal number of deports is identified it can be not conformed to the best way between stores and final destinations, their location should be taken into account in this case. Xiang Hua, Xiao Hu and Wuwei Yuan [13] present a mean to solve this problem by applying the Adaptive particle swarm optimization (APSO). The APSO is a supplement of nonlinear inertia weight as well as time-varying acceleration coefficients as opposite to the Particle swarm optimization (PSO), which is a common method of decision-making. This fact allows a quick and accurate finding of the global optimum. As a result, the best locations may be determined using the knowledge of customer's locations and demand. However, logistics managers more often deal with existing depots, so the real problem is to create optimal paths under existing circumstances.

To achieve the maximum effect, the logistic problem should be solved as a complex task, involving different aspects of the transportation process. One of the papers that consider this conception is a review written by Pieter Vansteenwegen, Wouter Souffriau and Dirk Van Oudheusden [14]. The authors outline different combinations of logics problems, which are put together into the Orienteering Problem (OP). They investigate in more detail three of them (Team OP, OP with time windows, Team OP with time windows), give several examples of their mathematical formalisations and ways of solving. Another example of solving the complex logistic task is the study of Mohamed El Yafrani and Belaïd Ahiod [15]. They look into the Travelling Thief Problem (TTP) which includes two interdependence combinatorial optimization subproblems: the Travelling Salesman Problem (TSP) and the Knapsack Problem (KP). The authors compare iterative neighborhood algorithms to other methods, present deterministic procedures for each problem combination reinforce their assumptions by experimental results.

However, recent research in the considered area does not take into account city traffic flows. This constraint is very vital for modern cities with high motorization level. Our study extends the described above conception, and focused on the routing of the city freight trucking in urban traffic conditions. To solve this problem the transportation planning techniques were involved in a model and combined with an evolutionary approach.

2.2. Problem statement

The study addresses the following problem: identify the optimal route from the distribution center to destination points with the fleet's capacity constraint and taking into account urban traffic. The problem differs from a typical TSP, because the route is based on the road traffic. This supplement promises to minimize the delivery time and consequently the total logistics costs. In addition, the described problem requires combining the TSP with KP.

To solve the described above problem we propose the evolutionary approach that is based on a modified genetic algorithm. This approach allows reflecting the latent organizing process of a complex technical system that is close to nature system [16]. The input data for the algorithm are city transport infrastructure and transportation demand. The idea is that we have a city where vehicle density is varying in different time-windows and districts. It means that the underway time of one route during

various times of the day will be different. This information can be provided by modelling system that is based on the origin-destination matrices.

Therefore, the algorithm takes into account origin and destination locations, schedule time, transportation demand, fleet capabilities. Moreover, to find the optimal loading the KP is solving on every iteration of TSP algorithm. The KP algorithm is based on the genetic approach too. The overall solution represents the combination of two genetic algorithms: the KP genetic algorithm is nested into the TSP genetic algorithm.

3. Methodology

3.1. Mathematical Model

The model describes the city freighting planning for helping logistics managers in decision-making, i.e. to optimize the whole route (TSP), with maximum trucks loading (KP). A solution consists of determining the final routes of delivery with the sequence of destination points which start and end in the depots. The goal is to minimize the underway time and to maximize the truck's loading.

To get an accurate and realistic solution the impact of the urban vehicle density should be taken into account. However, traffic datasets for most of the cities are unobtainable. For this reason, we use Transport Zoning and macroscopic transport simulation to make our model more flexible.

The process of transportation simulation of the city is based on the gravity law. Marc Barthelemy [17] presents detailed information about creating origin-destination matrices and processing mobility networks. Simulation allows estimating the flow value between different areas in the city by using population and infrastructure datasets. Figure 1 shows a visual representation of the model that takes into account traffic zones. The micromodel that is based on this traffic zones allocation shows different transportation velocity on different branches of the road network. We propose the space-time model because the velocity depends on time-windows too. Therefore, we can predict the average velocity of trucks during transportation.

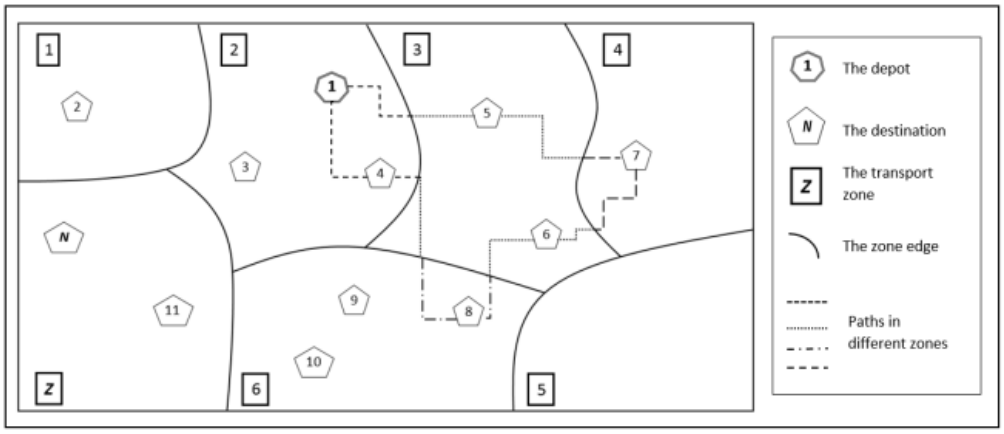

Figure 1. Example of the delivery route that starts and ends in the depot (1-5-7-6-8-4-1).

In our paper we are using the following designation indicators:

- N is the number of destination points.
- i is the origin point, (i=1…N).
- j is the destination point, (j=1…N).
- d_j is the quantity demand in the point j, (j=2…N).
- l_{ij} is the distance between i and j, (i=1…N), (j=1…N).
- $l_{ij} = 0$ if $i = j$, which means there is no distance between the same origin-destination points.
- ts is the average service time that is needed for unloading one package, is a set value, e.g. $ts = 2$ min.
- te is the average extra time in the destination point, for instance drawing up of documents etc., is a set value, e.g. $te = 7$ min.

- c is the capacity of the truck.
- z is the transport zone of the city (z=1…Z).
- $\overline{V_z^i}$, $\overline{V_z^j}$ is the average speed in z-th zone.
- M_k is the matrix chromosome with the whole route, (k=1…K).
- x_{ij} is the variable for the matrix.
- P_k is the vector form of the matrix's chromosome (k=1…K).
- p_n^P is the value (number) of the destination point, where n is an atomic number of the gene in the P-th chromosome.

The fitness function (FF) for the TSP is T_k shows the total underway time of the route, where the sequence of m is a reverse sequence of loading the kth truck in the depot. FF1 for TSP looks like:

$$T_k = (\sum_{j=p_1}^{p_{n-2}} \sum_{z=1}^{Z} \left(\frac{2 \times l_{j,j+1}}{\overline{V_z^j} + \overline{V_z^{j+1}}} + d_{j+1} \times ts + te \right) + \frac{2 \times l_{p_{n-1},p_n}}{\overline{V_z^{p_{n-1}}} + \overline{V_z^{p_n}}} \rightarrow min \quad (1)$$

The constraint is:

$$\sum_{j=p_2}^{p_{n-1}} d_j \leq c \quad (2)$$

It means that the total quantity of freight during one route cannot exceed the capacity of a truck. To relate the points to transport zones (z), we assign a zone number to each origin and destination points.

The fitness function for the Knapsack Problem (FF2):

$$\sum_{j=p_2}^{p_{n-1}} d_j \rightarrow max \quad (3)$$

(3) can be treated as the more loading leads to a better economic effect for the final logistics costs.

3.2. Genetic Algorithm

To solve the designated in Section II B problem we adopted genetic analysis which is based on the evolutionary process. Genetic modelling is one among many heuristic ways in decision-making that uses encoded information, where variables have discrete values 0 and 1. Basic stages of the program are chromosomes generation and selection. Genotypes consist of genes with straight positions. When the first population is built, these potential solutions are tested by the fitness function, where the best ones are selected for the following iterations using mutation and/or crossover operators.

We randomly create the first K "parents" populations that are shaped into Binary Matrixes Chromosomes. Each matrix represents the encoded route, includes rows i and columns j, if x_{ij}=1 there is a sub-path between i and j, otherwise x_{ij}=0. Matrices are completed with some special conditions, such as:

$$x_{ij} \in \{0,1\}; \quad i = 1 \dots N, j = 1 \dots N, \quad (4)$$

$$x_{1j} = x_{i1} = 1; \quad i = 1 \dots N, j = 1 \dots N, \quad (5)$$

$$x_{ij} = 0; \ \forall (i = j); \quad i = 1 \dots N, j = 1 \dots N, \quad (6)$$

$$\sum_{i=1}^{N} x_{ij} \leq 1; \quad \forall j = 1 \dots N, \quad (7)$$

$$\sum_{j=1}^{N} x_{ij} \leq 1; \quad \forall i = 1 \dots N. \quad (8)$$

For example, figure 2 displays the matrix for M_1.

The route from figure 1 can be treated as vector P_1: (1-5-7-6-8-4-1), where $p_1^P = p_n^P = 1$ in any way. It is because the delivery is always started and ended in the depot, which number is $i = j = 1$.

i \ j	1	2	3	4	5	6	7	8	…	N-1	N
1	0	0	0	0	1	0	0	0		0	0
2	0	0	0	0	0	0	0	0		0	0
3	0	0	0	0	0	0	0	0		0	0
4	1	0	0	0	0	0	0	0		0	0
5	0	0	0	0	0	0	1	0		0	0
6	0	0	0	0	0	0	0	1		0	0
7	0	0	0	0	0	1	0	0		0	0
8	0	0	0	1	0	0	0	0		0	0
…											
N-1	0	0	0	0	0	0	0	0		0	0
N	0	0	0	0	0	0	0	0		0	0

Figure 2 Example of the Binary Matrix (M_1).

After that, the FF1 (1) is calculated for all K individuals, and the algorithm checks the constraint (2). Some of the structures from the first population will be removed due to inconsistency with the capacity limitation.

After these steps, the standard algorithm may proceed to the next iterations, but our approach contains additional KP step. The rest of K vectors are estimated by FF2 (3). Figure 3 shows an example of one of the possible solutions of the KP task.

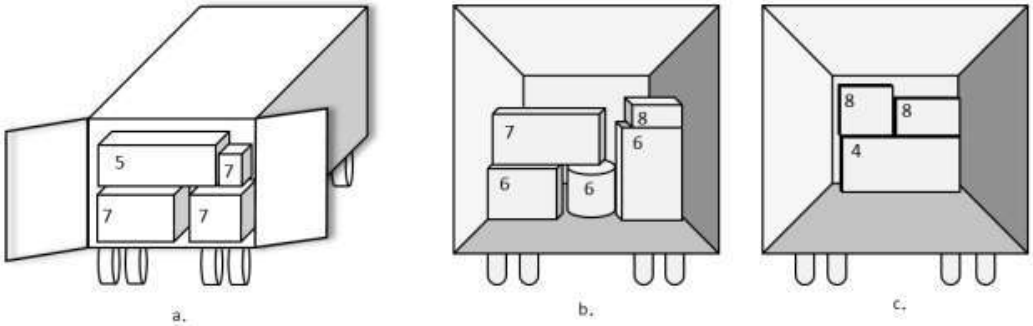

Figure 3. Example of the truck loading for the route (1-5-7-6-8-4-1): a) the third layer of loading; b) the second layer of loading; c) the first layer of loading.

Subsequently the best representatives P_k are selected for further simulations with M_k using the crossover operator. The outcome of this procedure is the new offspring, which is used for the next loop iteration. Figure 4 represents the schema of the proposed genetic algorithm.

4. Implementation

The solution is implemented as Python notebook that allows working with the model iteratively and improving it step by step. As a host environment, we are using Zeppelin, because it provides capabilities to build scalable interactive notebooks with a rich user interface. The developed software is implemented as a Docker container, which contains all configured modules and packages and can be deployed on most common operating systems. The developed scripts and notebooks are stored in the Bitbucket git repository. Figure 5 presents the architecture of the developed solution.

The Python programming language is a flexible tool for systems prototyping. There are a lot of packages for solving different applied and scientific problems. To work with spatial data in our project the following Python packages were used:

- Shapely (low level processing of geometries).
- GeoPandas (processing of data frames with geometry column).
- NeworkX (working with spatial graphs).
- OSMnx (loading network for some region from OpenStreetMap resource).
- Matplotlib (power tool for plotting with supporting of geographic maps).

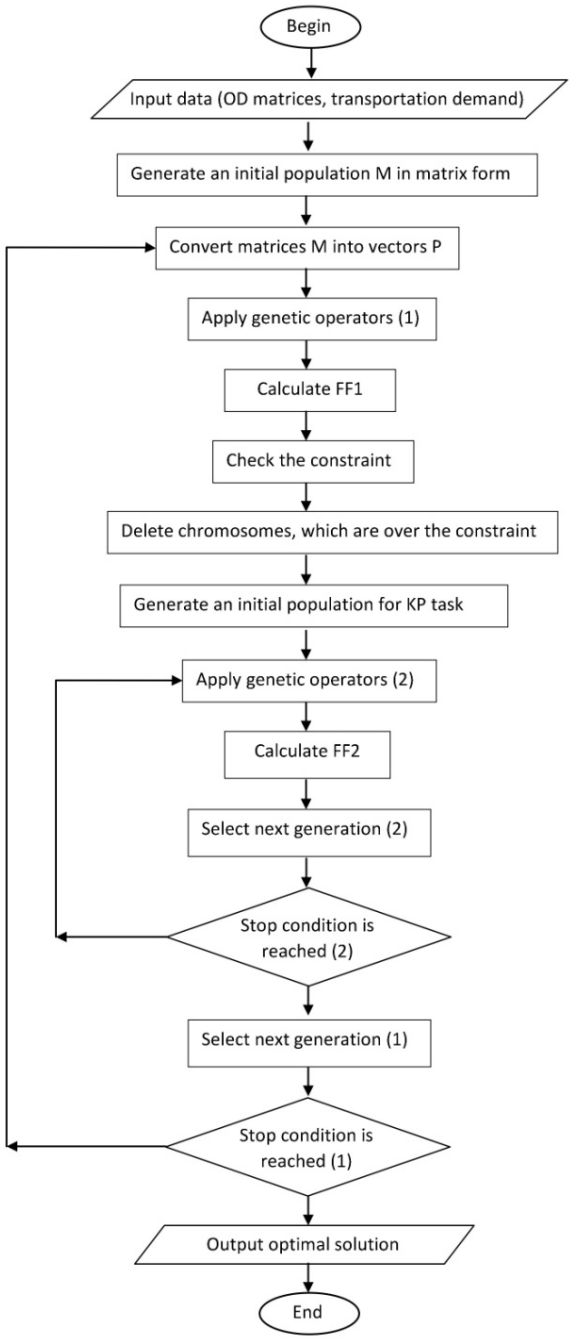

Figure 4. The schema of the heuristic algorithm.

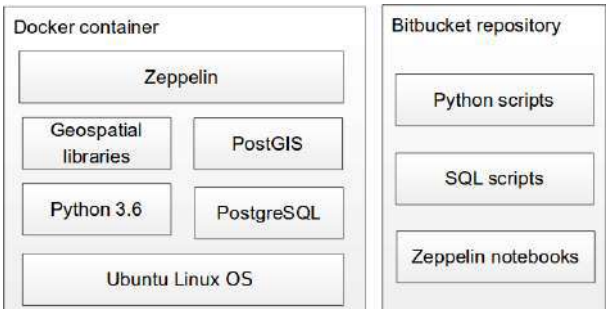

Figure 5. Schema of the solution environment.

A genetic algorithm was implemented using Deap package that contains genetic operators and means to construct any evolutional model. Fitness function (1) was implemented as a custom function and registered in Deap framework as “evaluate” parameter. Inside the main evolution loop that solves TSP task, we have added the nested evolution loop that solves KP task for each “individual” that is selected as a population for the next generation. Therefore, the developed Python script fully implements the method proposed in Section III.

The solution was debugged using the map of the city of Samara (Russia). The information about dividing the city into traffic zones and building Origin-Destination matrices was taken from the previous study [18]. For other task parameters (origin and destination points, transportation demand, freight fleet and its capacity) we have used the test data. We have used SUMO as a simulation engine in our research (figure 6).

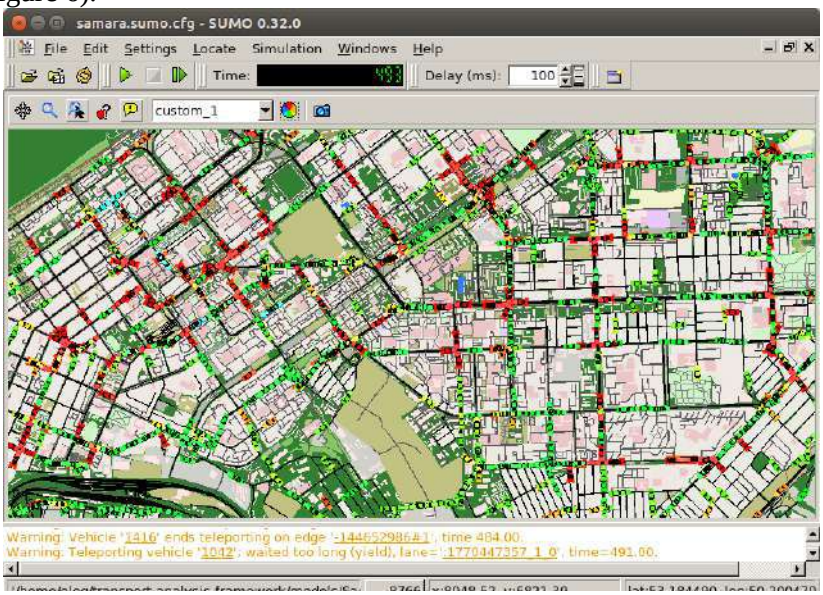

Figure 6. Simulation of transportation flows in Samara.

5. Conclusion

The genetic analysis is used as a tool for freight transportation decision making support. The urban freight transportation model allows us to determinate the optimal origin-destination route of the delivery by minimizing underway time and maximizing truck’s loading. The main advantage of the proposed approach is applying of transport zoning, which promises to bring solutions closer to the real-life situation.

The further research may take into account time windows of deliveries and fleet capability differences. Moreover, the genetic algorithm requires tuning to get optimal execution performance. Additionally, the simulation stage should be used to test the model performance within the urban traffic circumstances.

6. References

[1] Speranza M G 2016 Trends in transportation and logistics *European Journal of Operational Research* **264** 830-836
[2] Agafonov A A, Yumaganov A S and Myasnikov V V 2018 Big Data analysis in a geoinformatic problem of short-term traffic flow forecasting based on a k nearest neighbors method *Computer Optics* **42(6)** 1101-1111 DOI: 10.18287/2412-6179-2018-42-6-1101-1111
[3] Lam S and Englert B 2009 Cost-Based Optimization of Shipment Scheduling *IFAC Proceedings Volumes* **42(15)** 143-148
[4] Mokshin A V, Mokshin V V and Sharnin L M 2019 Adaptive genetic algorithms used to analyze behavior of complex system *Communications in Nonlinear Science and Numerical Simulation* **71** 174-186
[5] Michalewicz Z 1996 *Genetic Algorithms + Dara Srtuctures = Evolution Programs* (Spring-Verlag Berlin Heidelberg, New York)
[6] Vaira G 2014 Genetic algorithm for vehicle routing problem *Doctoral Dissertation, Technological Sciences, Informatics Engineering* (Vilnius)
[7] Balakrishnan An and Karsten C V 2017 Container shipping service selection and cargo routing with transshipment limits *European Journal of Operational Research* **263** 652-663
[8] Wang X 2016 Stochastic resource allocation for containerized cargo transportation networks when capacities are uncertain *Transportation Research Part E* **93** 334-357
[9] Abate M and Jong G 2013 The optimal shipment size and truck size choice – The allocation of trucks across hauls *Transportation Research Part A* **59** 262-277
[10] Piendl R, Liedtke G and Matteis T 2016 A logit model for shipment size choice with latent classes – Empirical findings for Germany *Transportation Research Part A* **102** 188-201
[11] Román C, Arencibia An Is and Feo-Valero M 2016 A latent class model with attribute cut-offs to analyse modal choice for freight transport *Transportation Research Part A* **102** 212-227
[12] Liu W-Y and Xing L-N 2013 The double layer optimization problem to express logistics systems and its heuristic algorithm *Expert Systems with Applications* **41** 237-245
[13] Hua X, Hub X and Yuan W 2016 Research optimization on logistics distribution centerlocation based on adaptive particle swarm algorithm *Optik* **127** 8443-8450
[14] Vansteenwegen P, Souffriau W and Oudheusden D V 2010 The orienteering problem: A survey *European Journal of Operational Research* **209** 1-10
[15] Yafrani E M and Ahiod B 2016 A local search based approach for solving the Travelling Thief Problem: The pros and cons *Applied Soft Computing* **52** 795-804
[16] Saprykina O and Saprykin O 2017 Transport Infrastructure Optimization Method Based on a Memetic Algorithm *Proceedings of the IEEE 20th International Conference on Intelligent Transportation Systems* (Yokohama, Japan) 1636-1641
[17] Barthelemy M 2010 Spatial Networks *Physics Reports* **499** 1-101
[18] Saprykina O and Saprykin O 2017 Validation of Transport Infrastructure Changes via Microscopic Simulation: A Case Study for the City of Samara, Russia *Proceedings of the 5th IEEE International Conference on Models and Technologies for Intelligent Transportation Systems* (Naples, Italy) 788-793

Local approximation of discrete processes by interpolation polynomials

A A Kolpakov[1], Yu A Kropotov[1]

[1]Vladimir State University named after Alexander and Nicholay Stoletovs, Orlovskaya street, 23, Murom, Vladimir Region, 602264

e-mail: desT.087@gmail.com

Abstract. This paper discusses the structure of the devices and their defining formulas used for local approximation using power-algebraic polynomials when the observed data are known exactly. A multichannel system for processing discrete sequences is considered. On the basis of the considered system the research of acceleration of calculations in the system from specialized computational modules is carried out. The carried out researches have shown, that the developed model of multichannel data processing system allows to reduce essentially time for data processing.

1. Introduction

Organization of calculations or processing of data on the observed samples of the process carried out with the help of the representation of algebraic polynomials refers to the class of methods of analytical representation and signal processing. This paper discusses the structure of the devices and their defining formulas used for local approximation with the help of power algebraic polynomials, when the observed data are known exactly.

2. Multi-channel system for processing discrete sequences

The representation of the functions of the observed data can be referred to the issues of interpolation with the help of polynomials on linearly independent systems of functions and are considered later as the issues of coordination of local interpolation functions on smoothness in the nodes of their conjugation [2, pp. 146-194].

The approximation of the processes on the observed samples can be carried out with the help of algebraic polynomials, for example, the point method of least squares or methods of local interpolation, which belong to the class of methods of analytical representation of signals. Here we consider algebraic models and methods of the need to solve local satisfaction with the conditions of smooth coupling, approximation by discrete data.

Thus, at first it is assumed that all sample values of the process and its derivatives in the interpolation and coupling nodes are known.

Let's denote an interpolation polynomial through $P_i(t)$, which provides the approximation of the process $y(t)$ at the interval $[\bar{t}_i, \bar{t}_{i+1})$, $\bar{t}_i < \bar{t}_{i+1}$, $i = 0, 1, \ldots$, by some number of known values of this

process $y(t_{ij}) = y_{ij}$, $j = 0, 1, \ldots, n$, and, possibly, its derivatives $y^{(r)}(t_{ij}) = y_{ij}^{(r)}$, $r = 0, 1, \ldots, m_j$ and $y_{ij}^{(0)} \equiv y_{ij}$.

The moments $\bar{t}_i$ of the pairing of polynomials $P_{i-1}(t)$ and $P_i(t)$ will be referred to points or nodes in the pairing, and the moments t_{ij}, at which sample values y_{ij} and $y_{ij}^{(r)}$ are taken, will be referred to interpolation nodes. The intervals $[\bar{t}_{i-1}, \bar{t}_i]$ and $[\bar{t}_i, \bar{t}_{i+1}]$, called interpolation intervals, are obviously areas of definition for polynomials $P_{i-1}(t)$ and $P_i(t)$. Interval boundaries, within which interpolation nodes t_{ij} are located, are denoted as moments $\bar{\bar{t}}_i$ and $\bar{\bar{t}}_{i+1}$, so interval $[\bar{\bar{t}}_i, \bar{\bar{t}}_{i+1}]$ is the area where the observed data used in interpolation formula construction or mapping $P_i(t) : [\bar{\bar{t}}_i, \bar{\bar{t}}_{i+1}] \to [\bar{t}_i, \bar{t}_{i+1}]$ are defined.

Interpolation polynomial $P_i(t)$ by the system of algebraic functions t^k, $k = 0, 1, \ldots, N$, i.e. polynomial $P_i(t) = a_{i0} + a_{i1}t + a_{i2}t^2 \cdots + a_{iN}t^N$, can be written in the form

$$P_i(t) = \sum_{j=0}^{n} \sum_{r=0}^{m_j} L_{ij}^r(t) y_{ij}^{(r)}, \tag{1}$$

where $L_{ij}^0(t) \equiv L_{ij}(t)$ and $L_{ij}^r(t)$ is polynomials satisfying the conditions in the interpolation nodes

$$L_{ij}(t) \mid_{t=t_{ik}} = \delta_{jk}, \quad \frac{d^l}{dt^l} L_{ij}^r(t) \mid_{t=t_{ik}} = \delta_{jk}\delta_{lr}, \quad l = 0, 1, \ldots, m_j, \tag{2}$$

where δ_{jk} is Kroneker's symbol.

It should be taken into account that the system of functions t^k refers to the class of generalized Chebyshev systems, which by definition should have a non-zero determinant

$$U^* \begin{pmatrix} 0 & 1 & 2 & \cdots & N \\ t_0 & t_1 & t_2 & \cdots & t_N \end{pmatrix} = \begin{vmatrix} 1 & 0 & \cdots & 0 & \cdots & 1 & \cdots & 0 \\ t_0 & 1 & \cdots & 0 & \cdots & t_n & \cdots & 0 \\ \cdot & \cdot & \cdot & \cdot & \cdot & \cdot & \cdot & \cdot \\ t_0^N & t_0^{N-1} & \cdots & t_0^{N-m_0} & \cdots & t_n^N & \cdots & t_n^{N-m_n} \end{vmatrix} \neq 0. \tag{3}$$

In this case, we can conclude that there is an interpolation polynomial at any location of interpolation nodes and, in particular, the existence of fundamental polynomials $L_{ij}^r(t)$, and hence the possibility of approximation of observed data using the (1).

The essential point of this conclusion is that in each node of interpolation there should be known the values of both the process and all its derivatives up to a given maximum order. However, if the physical features of the problem as the initial data in the construction of the interpolation polynomial are sample values of the process and its derivatives, measured at different moments of time, and interpolation polynomial instead of (1) is given by the expression

$$P_i(t) = \sum_{j=0}^{n} \sum_{r \in \mathrm{M}_j} L_{ij}^r(t) y_{ij}^{(r)}, \tag{4}$$

where M_j is a subset of multiple integers $(0, 1, \ldots, m_j)$. The fundamental polynomials satisfy the conditions

$$\frac{d^l}{dt^l} L_{ij}^r(t) \mid_{t=t_{ik}} = \delta_{jk}\delta_{lr}, \quad l, r \in \mathrm{M}_j. \tag{5}$$

It can be shown that the problem of constructing polynomials (4) and (5) in some combinations of interpolation nodes may not have a solution.

This can be shown in a simple example of building a second-degree polynomial $P(t) = a_0 + a_1 t + a_2 t^2$ a using the values specified in the interpolation nodes $P(t_0) = y_0$, $P(t_1) = y_1$, $P(t_2) = y_2$. The coefficients of this polynomial, taking into account the given conditions, should satisfy the system of linear algebraic equations

$$\begin{pmatrix} 1 & t_0 & t_0^2 \\ 0 & 1 & 2t_1 \\ 1 & t_2 & t_2^2 \end{pmatrix} \begin{pmatrix} a_0 \\ a_1 \\ a_2 \end{pmatrix} = \begin{pmatrix} y_0 \\ \dot{y}_1 \\ y_2 \end{pmatrix}. \quad (6)$$

The determinant of this system is $(t_2 - t_0)(t_2 + t_0 - 2t_1)$. In case of equidistant nodes, when $t_2 + t_0 = 2t_1$, it is equal to zero. At the same time, the solution of the system and, accordingly, the solution of the interpolation problem does not exist, except for the unlikely case of a multi-digit solution, when the ranks of the main and extended matrices coincide.

Such a situation, although not necessarily, may arise in general. Therefore, if there is a need to use formulas of the type (4), (5), the selected interpolation scheme should be checked for the existence of a solution to the problem of interpolation polynomial construction. Apart from this condition, no other restrictions are imposed on the application of these formulas.

Using formula (1), the approximation $\hat{y}(t)$ of process $y(t)$ on the entire time axis can be written as

$$\hat{y}(t) = \sum_{i=0}^{\infty} P_i(t) I_i(t) = \sum_{j=0}^{n} \sum_{r=0}^{m_j} \sum_{i=0}^{\infty} I_i(t) L_{ij}^r(t) y_{ij}^{(r)}. \quad (7)$$

Sampling values y_{ij} and $y_{ij}^{(r)}$, which clearly define interpolation and fundamental polynomials (1; 4), can be divided into two classes: the actual measured values, the values of process $y(t)$ and its derivatives $y^{(r)}(t)$ in the interpolation nodes t_{ij}, and the values that represent their estimation from indirect data. This estimation can be obtained, for example, by calculating the values of polynomial $P_{i-1}(t)$ representing the process at the previous step of interpolation, and the values of its derivatives $P_{i-1}^{(r)}(t)$ in the required interpolation nodes. On the interpolation schemes, such values will be marked with an asterisk in the future so that they can be distinguished from the measured values.

To ensure the required smoothness of the interpolation formula (7) in the interval nodes $[\bar{t}_i, \bar{t}_{i+1})$, nodes $\bar{t}_i$ should obviously be included in the set of interpolation nodes t_{ij} for the given index value i, if they are no longer included in their number by definition. In this case, nodes $\bar{t}_{i+1}$ do not have to belong to this set.

When considering the case where the layout of the interpolation nodes and the length of the segments $[\bar{t}_i, \bar{t}_{i+1})$ do not depend on the number i of the interpolation step, i.e.

$$\bar{t}_{i+1} - \bar{t}_i = \Theta \quad \text{and} \quad t_{ij} = t_j + i\Theta, \quad (8)$$

and if you enter the discrete time $t = \tau + k\Theta$, the interpolation formula (7) can be written as

$$\hat{y}(t) \equiv \sum_{k=0}^{\infty} \hat{y}_k(t) = \sum_{k=0}^{\infty} \sum_{j=0}^{n} \sum_{r=0}^{m_j} I(t - k\Theta) L_j^r(t - k\Theta) y_{kj}^{(r)}, \quad (9)$$

where $L_j^r(\tau) \equiv L_{0j}^r(\tau)$ – the fundamental polynomials defined in interval $[\bar{t}_0, \bar{t}_1)$, $L_j^0(\tau) \equiv L_j(\tau)$ and the time window $I(t - k\Theta) \equiv I_k(t)$. Further on, for the sake of certainty, it is also believed that $\bar{t}_0 \equiv t_{0q} = 0$.

The interpolation of processes in the multidimensional space represented by a discrete function is done in a similar way, if the formula (9) is applied separately to each vector component. When interpolating the trajectories or boundaries of objects in a multidimensional space, the question arises

of choosing the most natural coordinate system, in which the curve under consideration takes a smoother form or is described by simpler equations.

From the above studies and according to [8], it is clear that the use of dot MNAs is fully justified, since this method allows us to obtain the lowest number of coefficients compared to other interpolation methods, such as spline functions, interpolation polynomial Lagrange, etc., with the same value of error.

3. Study of acceleration of calculations in the system of specialized computational modules

The expression (9) corresponds to the function of the multichannel data processing system model, which looks like

$$\hat{y}(t) = \sum_{l=1}^{l} F_l^r y(t)\Phi_0 = \sum_{l=1}^{l} F_l^r y_{kl}\,, \tag{10}$$

where l is a number of specialized calculators with processor function F_l^r. Structural scheme, which implements the model of multichannel system of processing discrete data sequences, is shown in Figure 1.

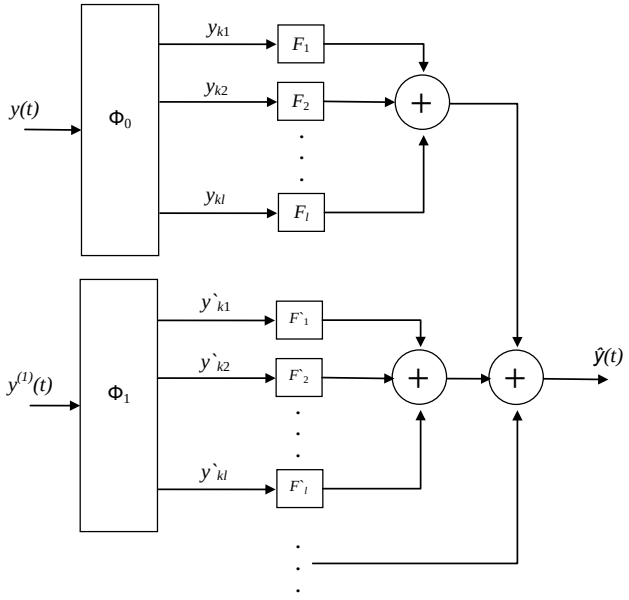

Figure 1. Multi-channel model of data processing system.

As can be seen from Figure 1 and in accordance with (10), each channel of the data processing system is characterized by the function of a processor F_l. At the same time, input information in the form of a sequence $y_{kl}^{(r)}$ on a finite interval of N samples is used as input actions in these channels, which is obtained as a result of sampling of the process by switching devices $\Phi_0, \Phi_1, \ldots$. Taking into account that the specified sequences are defined by the expression

$$y_{kl}^{(r)} = y^{(r)}(t_k + \Theta), \quad k = 0, 1, 2, \ldots, N\text{-}1, \tag{11}$$

where $r \in \{0,1,2\}$. In the case of equidistant interpolation nodes forming a periodic sequence of reference points with the period T and taking into account $\Theta = dT$, expression (11) takes the form

$$y_{kj}^{(r)} = y^{(r)}((j + dk)T), \quad k = 0, 1, 2, \ldots, N\text{-}1. \tag{12}$$

where d is thinning, $d \in \{0, 1, 2, \ldots, N\text{-}1\}$,

j is sequence offset, $j \in \{0, 1, 2, \ldots, N\text{-}1\}$.

An evenly distributed sequence can be represented depending on offset j in the form of

$$y_{kj}^{(r)} = \begin{cases} y^{(r)}[d(k-j)T], \text{ j} < \text{k}, \\ y^{(r)}[dkT], \text{ j} = \text{k}, \\ y^{(r)}[d(k+j)T], \text{ j} > \text{k}. \end{cases} \quad k = 0, 1, 2, \ldots, N\text{-}1. \tag{13}$$

In practical terms, the expressions (12) and (13) describe situations, where the nodes of the interface respectively coincide with the reference points of process $y(t)$ and its derivatives.

It should also be noted that the *l*-th channel of the model of multichannel data processing system with the function of the data generator F_l is a set of filters $F_{li}^r(S)$ in the form of

$$F_l = \sum_{i=1}^{n} F_{li}(S),$$

which form the structural scheme presented in Figure 2. with the transfer function in the form of

$$F_{li}^r(S) = \sum_{l=1}^{l} \sum_{i=1}^{n} \frac{1}{S_{li}} (a_{jil}^r - c_{jil}^r e^{-S\Theta}), \tag{14}$$

where c is series coefficients.

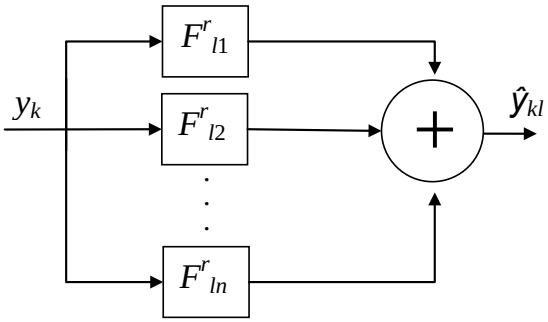

Figure 2. Filter block diagram.

After transformation of expression (14) relative to S_i with regard to the limitations of the equality type

$$r = 0, d = 1, j = 0, c = 0, \tag{15}$$

the solution of determining the acceleration of computational operations depending on the number of specialized calculators and on the volume coefficient of parallel calculations a is carried out by the formula

$$S_l = \frac{l}{l(1-a)+a}. \tag{16}$$

We can see from expression (16) that the increase of calculation efficiency depends on the algorithm of the task, when restricting the type $a < 1$, which allows us to estimate the efficiency of parallelization of the algorithm and the conclusion about the necessary number of specialized calculators [1, 5].

Dependence of the growth of computational operations' acceleration on different number of specialized calculators on the size coefficient of parallelized calculations a is shown in Figure 3.

Figure 3 shows that the increase of computation speed for the computer system from *l* specialized calculators can be obtained at the value of parameter a according to the condition $0.25 \le a \le 0.75$.

The results of the research of the dependence of the acceleration of calculations on the number of specialized calculators *l* are shown in Figure 4.

Figure 4 shows that with the coefficient $a = 0.75$ in the algorithm, the increase in the number of parallelized cores of specialized calculators up to the value of $l \ge 16$ leads to a significant increase in

performance, in particular, the use of a single quad-core GPU as a specialized calculator increases the performance by more than 2 times.

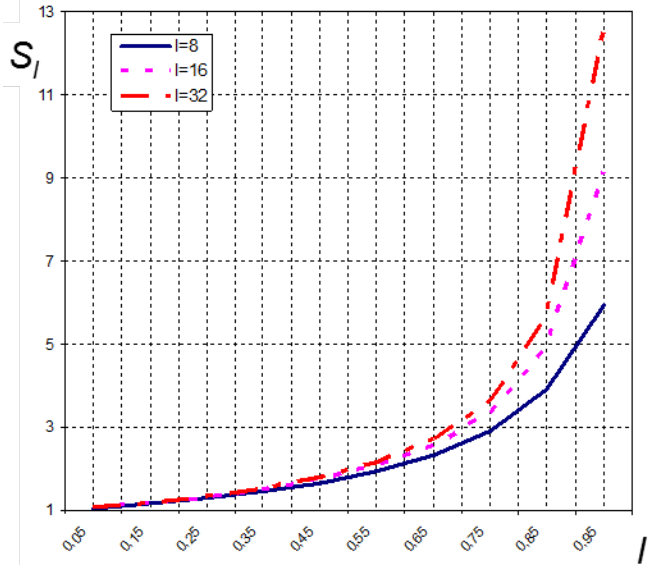

Figure 3. Dependence of calculations acceleration in the system from l specialized calculators on the value a.

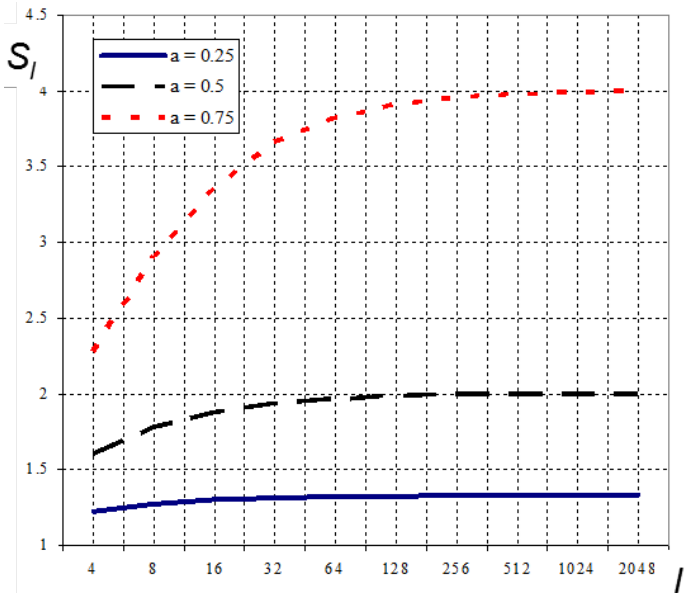

Figure 4. Dependence of calculations acceleration S_l in the system from specialized calculators on the value of l.

The developed model of multichannel data processing system was used for research and development of the algorithm of advanced audio stream mixing in telecommunication systems [10]. Application of the developed algorithm in a heterogeneous computer system reduces the time for data processing to 0.2226×10^{-3} sec. instead of 1.351×10^{-3} sec. – the time of data processing by the base algorithm.

4. Conclusions

Studies have shown that the increase in calculation efficiency depends on the algorithm of the task when limiting the a < 1 type. It allows you to estimate the efficiency of algorithm parallelization and make a conclusion about the necessary number of specialized calculators. Thus, the increase of calculation acceleration for a computer system from l specialized calculators can be obtained with the

value of parameter a in accordance with the condition $0{,}25 \leq a \leq 0.75$. At the same time, the increase of the number of parallelized cores of specialized calculators up to the value of $l = 16$ at the value of the coefficient $a = 0.75$ in the algorithm leads to a significant increase in performance, but with a further increase up to $l > 256$ it does not bring any significant results, which is consistent with the main provisions of Amdal and Graham's researches.

5. References

[1] Bakhvalov N S and Voevodin V B 2005 *Modern problems of computational mathematics and mathematical modeling T. 1: Computational mathematics* (Moscow: Science) p 342
[2] Kulbak S 1967 *Information theory and statistics* (Moscow: Science) p 408
[3] Ljung L 1991 *System identification. Theory for the user* (Moscow: Science) p 432
[4] Brillinger D R 1990 A study of second- and third-order spectral procedures and maximum likelihood in the identification of bilinear systems *IEEE Trans. on Acoustics, Speech and signal processing* **38(7)** 1238-1245
[5] Pupkov K A, Kapalin and V I Yushchenko A S 1976 *Functional rows in non-linear systems theory* (Moscow: Science) p 448
[6] Bakhvalov N S, Zhidkov N P, and Kobelkov G M 2008 *Numerical methods* (Moscow: BINOM Knowledge Lab) p 640
[7] Helman, D R and JaJa J 1999 Designing Practical Efficient Algorithms for Symmetric Multiprocessors *Lecture Notes in Computer Science, International Workshop ALENEX'99* **1619** 37-56
[8] Formalev V F and Reviznikov D L 2004 *Numerical methods* (Moscow: FISMATLYT) p 400
[9] Kropotov Y A and Proskuryakov A Y 2007 Mathematical model of probability law for the amplitudes of speech waveforms in the exponential basises *17th International Crimean Conference - Microwave and Telecommunication Technology, CRIMICO* 364-366
[10] Kolpakov A A and Kropotov Y A 2017 Advanced mixing audio streams for heterogeneous computer systems in telecommunications *CEUR Workshop Proceedings* **1902** 32-36
[11] Kropotov Y A, Belov A A and Proskuryakov A Y 2018 Method for forecasting changes in time series parameters in digital information management systems *Computer Optics* **42(6)** 1093-1100 DOI: 10.18287/2412-6179-2018-42-6-1093-1100

Creating methods and algorithms of adaptive control in biotechnical complexes of corrective action on human respiratory system

N V Ivakhno[1], S I Zykin[1]

[1]Federal State Budgetary Educational Institution of Higher Education "Tula State University", Lenina Ave., 92, Tula, Russia, 300012

e-mail: natalia_iv@list.ru

Abstract. The article describes methods of adaptive control of the preset resistance in the respiratory complexes with regard to changes in the human condition based on the results of identifying the respiratory system parameters, as well as on the results of modeling of the respiratory system presented as a combination of airway generations, the last of which ends with alveoli. The presented algorithms lay the basis for building intelligent medical systems involving adaptive corrective action.

1.Introduction.

Creating adaptive training complexes is a rather complicated theoretical problem [1,2,3]. That is due first of all to the complexity and variability of the processed signals. Since the equipment produces a controlling effect, it is necessary to simultaneously diagnose the state of the person's respiratory system, process the results in real time, and adjust the load. The solution to this problem is to create a well-validated methodology and to determine the technical parameters of adaptive-type corrective action equipment having new qualitative characteristics in order to ensure the full diversity of applications in curative, restorative and sports medicine.

For the load on the respiratory muscles to be selected, the patient breathes through the complex, which is operating in various modes (Figure 1).

In the process of breathing, the adjustable resistance in the breathing tube connected to the mouthpiece is used to measure by means of sensors the pressure in the breathing tube $P(t)$, which is then transmitted to the monitoring and control unit through the analog signal processing unit [2].

As a result of analysis of the pressure curve, the input parameters of detection (amplitude of the useful signal as, variance σ^2 and the average noise value $a0$) are adjusted for implementing the signal processing model with the purpose of timely recognition of respiratory activity and ensuring a high degree of synchronization between the person's respiration and the complex [4,5,6].

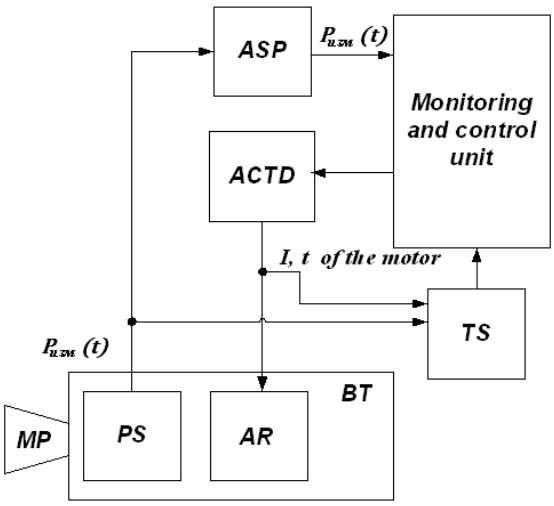

MP – mouthpiece, PS – system of pressure sensors; AR – adjusted resistance preset by changing cross-sectional area; BT – breathing tube;
ASP – analog signal processing unit; ACTD – actuating device;
TS – technical self-diagnosis unit

Figure 1. A generalized functional structure diagram for complexes of corrective action on respiratory system.

The respiratory system condition diagnosis unit that employs parametric analysis methods is used to generate control signal sent to the actuating device, which carries out the adjustment and adaptation of the load (resistance/switching pressure) in the breathing circuit according to the predetermined law and taking into account the patient's individual condition and changes in it [4,5,6,7]. Also, for the purposes of long-term prediction and for determining limitations on the action, mathematical modeling of processes in the respiratory system is performed.

2. The criterion used to determine the type of controlling action on the basis of diagnostic matrices.

In this structure, the self-diagnosing circuit protects the actuating device from overload, analyzing the temperature *t* and the current *I* of its electric motor, and allows the failure to be extrapolated by correcting the controlling action. At the same time, the pressure in the breathing tube is analyzed during operation both in the partial load and the peak load mode, which prevents barotrauma [3, 8]. The anticipatory alert power assessment unit makes it possible to predict a decrease in or failure of the supply voltage level, to save current data in a timely manner, and to ensure the restart and recovery of the system.

Thus, the variable parameters characterizing the state of the person's respiratory system when exposed to different resistances and at different switching pressures $R_1,...,R_N$, $P_1,...,P_N$ are as follows: inspiration / expiration phase duration $T_1,...,T_N$, slope angle of the approximation curve at the first observation stage $\alpha_1,..,\alpha_i..,\alpha_N$, slope angle for the approximation function decrease β_i (for load in the form of resistance), the coefficient of the approximation function in the third observation interval $\beta p_1,...,\beta p_N$ (for load in the form of switching pressure), the rise time of the pressure curve to the maximum $t_{H1},...,t_{HN}$, characteristics of the pressure curve during free respiration $\alpha_0,\beta p_0,t_{H0},T_0$ (load by switching pressure), $\alpha_0,\beta_0,t_{H0},T_0$ (load by resistance) [1,6,7,8].

Then, the generalized matrices characterizing the state of the person and the level of their training when exposed to resistance and pressure are described as follows:

$$M = \begin{bmatrix} \alpha_0 & \beta_0 & t_{H0} & T_0 \\ . & . & . & . \\ \alpha_i & \beta_i & t_{Hi} & T_i \\ \alpha_N & \beta_N & t_{HN} & T_N \end{bmatrix}, \quad M1 = \begin{bmatrix} \alpha_0 & \beta p_0 & t_{H0} & T_0 \\ . & . & . & . \\ \alpha_i & \beta p_i & t_{Hi} & T_i \\ \alpha_N & \beta p_N & t_{HN} & T_N \end{bmatrix}.$$

The general criterion allowing to establish the type of controlling action is determined on the basis of a set of parameters that make up the matrices of states M and M1:

$$K1_j^2 = \begin{cases} \frac{1}{N} \sum_{k=0}^{s-1} \sum_{i=1}^{N} c_k \cdot \left(\frac{M1_{ik} - M1_{i^* k}}{M1_{0k}} \right)^2 \; npu \; j = 1, \\ \\ \frac{1}{N} \sum_{k=0}^{s-1} \sum_{i=1}^{N} c_k \cdot \left(\frac{M_{ik} - M_{i^* k}}{M_{0k}} \right)^2 \; npu \; j = 0. \end{cases}$$

where c_1, c_2, c_3, c_4 are weight coefficients characterizing the importance of each indicator, as determined by experts; j is the variable that determines the type of action, k is the parameter number ($k = 0,...,S-1$, S is the number of parameters, i is the action level $i = 1,...,N$, and $i^* = i - 1$ is the previous action level) [4,5,9].

Then, the task of finding the method of action by load in the breathing circuit in the admissible set of possible options will be reduced to finding such parameters of controlling the actuating device that will provide the best value of the target vector function:

$$Q_i = \begin{cases} \sqrt{\sum_{k=0}^{S-1} c_k \frac{(M_{ik} - MZ_{ik})^2}{MZ_{ik}^2}}, npu \quad j = 0 \\ \\ \sqrt{\sum_{k=0}^{S-1} c_k \frac{(M1_{ik} - MZ1_{ik})^2}{MZ1_{ik}^2}}, npu \quad j = 1 \end{cases}$$

where MZ_{ik}, $MZ1_{ik}$ are the matrices of the required characteristics of the human respiratory system at the given load in the form of resistance and switching pressure, respectively.

Adaptation will be carried out in two circuits: the 1st circuit is responsible for the work of the mathematical model of the respiratory system and the apparatus, the 2nd circuit is responsible for presetting the initial load and for the choice of the value at which the smallest deviation from the reference characteristic is achieved [1,4,10].

3. The mathematical model of the biotechnical complex "corrective action equipment – human respiratory system".

For the monitoring and timely adjustment of the load, we will consider a mathematical model of the biotechnical complex "corrective action equipment – human respiratory system" [5, 6].

In this model, the structure of the lungs was represented as a set of generations of the airways (channels), the latter of which ends in alveoli. It was assumed that the airways branch out according to the principle of correct dichotomy, that is, two conjugates have the same size and are branched from their parent at equal angles; the empirical equations of the air channels of the average person were taken into account [6,11,12].

The mathematical model of the biotechnical complex “corrective action equipment – human respiratory system” is represented by three main blocks:
- equations of the gas dynamics of the lungs and of the dynamics of the muscles:

$$\begin{cases} \dfrac{dPl_0(t)}{dt} = \dfrac{G_0(t)\cdot\dfrac{Rb\cdot T^*}{M} - Pl_0(t)\cdot\dfrac{dV_0(t)}{dt}}{V_0(t)}, \\ \ldots \\ \dfrac{dPl_{im}(t)}{dt} = \dfrac{G_{im}(t)\cdot\dfrac{Rb\cdot T^*}{M} - Pl_{im}(t)\cdot\dfrac{dV_{im}(t)}{dt}}{V_{im}(t)}, \\ \ldots \\ \dfrac{dPl_{nm}(t)}{dt} = \dfrac{G_{nm}(t)\cdot\dfrac{Rb\cdot T}{M} - Pl_{nm}(t)\cdot\dfrac{dV_n(t)}{dt}}{V_{nm}(t)}, \\ \lambda\cdot\rho\cdot\dfrac{d^2u(t)}{dt^2} = Pl_{nm}(t) - P_a - \left(E_1\cdot\dfrac{u(t)}{Dc} - \sigma_1(t)\right)\cdot\dfrac{\lambda}{r(t)} - k\cdot\dfrac{du(t)}{dt}\cdot\dfrac{\lambda}{r(t)Dc}, \\ \lambda\cdot\rho\cdot\dfrac{d^2w(t)}{dt^2} = Pl_{nm}(t) - P_a - \left(E_2\cdot\dfrac{w(t)}{L} - \sigma_2(t)\right)\cdot\dfrac{2r(t)\lambda+\lambda^2}{r^2(t)} - k\cdot\dfrac{dw(t)}{dt}\cdot\dfrac{2r(t)\lambda+\lambda^2}{r^2(t)L}; \end{cases}$$

- equations of medium mass transfer rates by the generation level:

$$\begin{cases} G_i(t) = \dfrac{M}{Rb\cdot T^*\cdot R^*_{im}}\cdot\Big[\left(Pl_{im-1}(t) - Pl_{im}(t)\right)^2\cdot sign\left(Pl_{im-1}(t) - Pl_{im}(t)\right) + \\ \qquad + 2\left(Pl_{im+1}(t) - Pl_{im}(t)\right)^2\cdot sign\left(Pl_{im+1}(t) - Pl_{im}(t)\right)\Big], \\ G_0(t) = \dfrac{M}{Rb\cdot T^*\cdot R^*_0}\cdot\Big[\left(P_{km}(t) - Pl_0(t)\right)^2\cdot sign\left(P_{km}(t) - Pl_0(t)\right) + \\ \qquad + 2\left(Pl_1(t) - Pl_0(t)\right)^2\cdot sign\left(Pl_1(t) - Pl_0(t)\right)\Big]; \end{cases}$$

where $V_{im}(t)$ is the current volume of the *im*-th channel; *nm* is the last level of the airways ($nm = 23$); *Rb* is Boltzmann’s constant; *M* is the molar mass of gas; $\Omega_i(t)$ is the volumetric flow rate of gas in the *i*-th channel; $Pl_{im}(t)$ is the pressure of gas in the *im*-th channel; $P_{km}(t)$ is the pressure in the tube of the training apparatus; P_a is the atmospheric pressure; $Pl_0(t)$ is the tracheal pressure; $Pl_1(t)$ is the pressure at the 1st level of the airways (AW); $u(t)$ is the radial displacement of the cylinder wall; $Pl_{nm}(t)$ is the current pressure in the cylinder; $\sigma_1(t)$ is the preset transverse muscular tension; $\sigma_2(t)$ is the preset longitudinal muscular tension; λ is the thickness of the cylinder wall; *k* is the viscosity coefficient of the material; E_1 is the transverse modulus of elasticity of the material; E_2 is the longitudinal modulus of elasticity of the material; $r(t)$ is the current inner radius of the cylinder; *Dc* is the inner radius of the cylinder in undeformed state; ρ is the density of

environment element; $w(t)$ is the longitudinal displacement of the face of the cylinder; L is the length of the undeformed cylinder; R^*_{im} is the resistance of the *im*-th AW; $G_{im}(t)$ is the mass air flow rate in the i-th AW; $G_0(t)$ is the mass air flow rate in the trachea; the process of respiration occurs at a constant body temperature $T^* = 310\ K$;

- the model of automatic switching of respiratory muscles, implemented by means of setting special functions $\Theta_1(t)$, $\Theta_2(t)$, $\Theta_3(t)$ and $\Theta_4(t)$, which provide for automatic activation of muscles when the lungs in the process of expiration achieve the minimum preset volume $V_{\min}$ and for disactivation thereof at the moment when the lungs achieve the maximum preset volume $V_{\max}$:

$$10^{-5}\left(\frac{d\Theta_1(t)}{dt}\right) = \left(1 + \Theta_2(t) - \Theta_1(t)\right)\times$$
$$\times\left(\varsigma\left(\delta_V - \left|V_{\min} - V(t)\right|\right) + \varsigma\left(\delta_V - \left|V_{\max} - V(t)\right|\right)\right),$$
$$10^{-5}\left(\frac{d\Theta_2(t)}{dt}\right) = \left(\Theta_1(t) - \Theta_2(t)\right)\times$$
$$\times\left(1 - \varsigma\left(\delta_V - \left|V_{\min} - V(t)\right|\right) - \varsigma\left(\delta_V - \left|V_{\max} - V(t)\right|\right)\right),$$

$$0{,}5\frac{d\Theta_3(t)}{dt} = \Theta_4(t)\cdot\left(1 - \Theta_3(t)\right) - 0{,}7\cdot\Theta_3(t)\cdot\left(1 - \Theta_4(t)\right),$$
$$0{,}001\frac{d\Theta_4(t)}{dt} = 0{,}5 + 0{,}5\cdot(-1)^{ceil\left(\Theta_1(t) - \Theta_4(t)\right)},$$
$$\varsigma(\arg) = 0{,}5 + 0{,}5\cdot sign(\arg),$$

where $\Theta_1(t), \Theta_2(t), \Theta_3(t), \Theta_4(t)$ are unknown functions, δ_V is the absolute error of registering the moment when the volumes become equal, *ceil* is the rounding function, $\varsigma(\arg)$ is the switching function (if the argument is positive, it equals 1, if the argument is negative, it equals 0).

The developed mathematical description of the mass transfer process in the complex system of branching pathways ensures a higher level of detail of the respiration process on the whole, making it possible to study the influence of any changes in the structural level of a specifically selected generation, to the extent of actually assigning given properties to specific airways [6,7,8].

The obtained system of ordinary nonlinear differential equations was solved numerically using Rosenbrock method. An analysis of the experimental graphs of changes in the pressures, volumetric and mass flow rates described in [6,12] shows that the obtained results of modelling provide highly accurate qualitative and quantitative reflection of the biomechanics of a number of processes accompanying respiration. Consequently, this model can be used to analyze the adequacy of and to set limitations on the preset adaptive loads on the respiratory system in various training modes using the CACRS.

A generalized structure diagram of the mathematical model is presented in Figure 2.

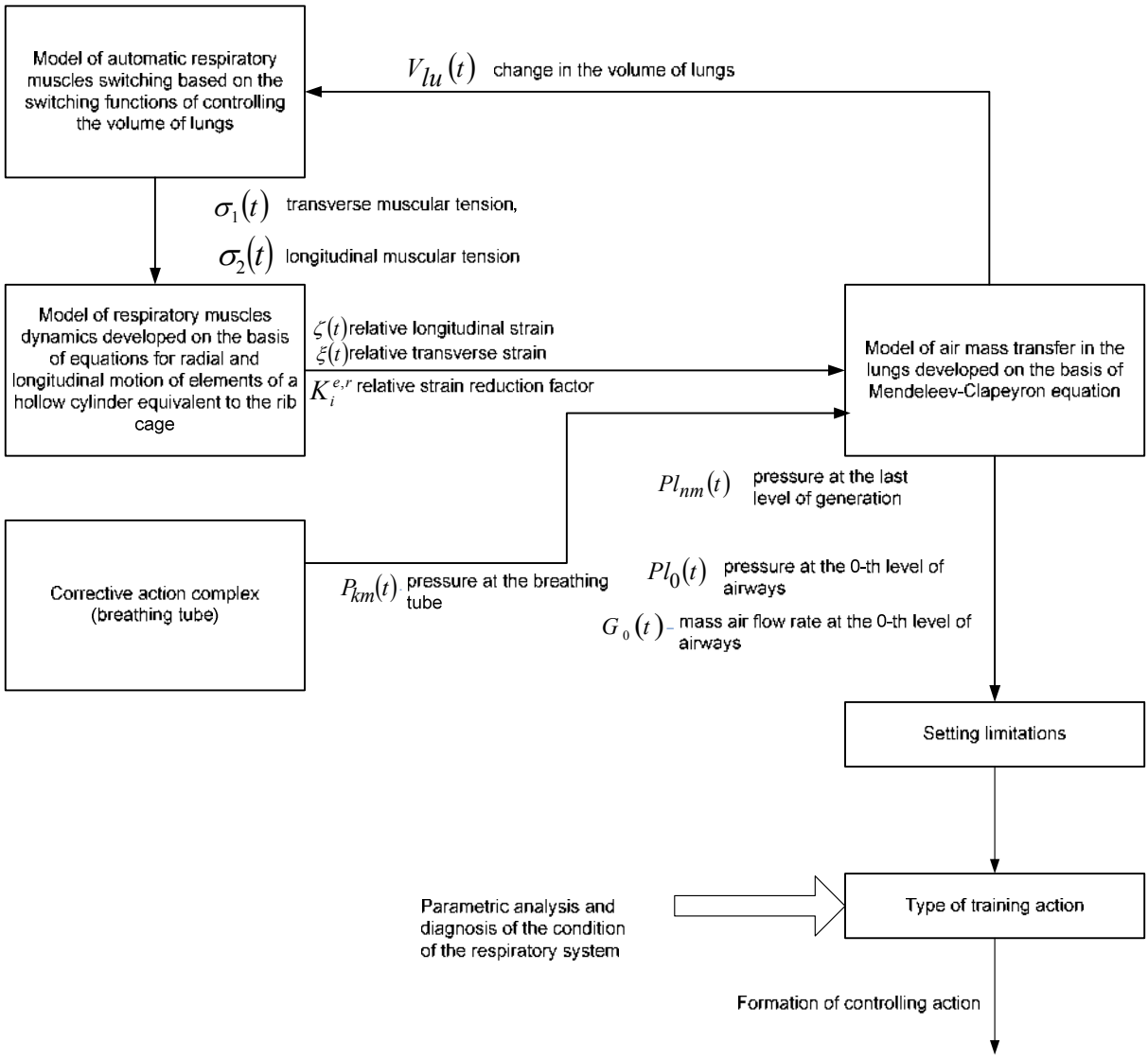

Figure 2. A generalized structure diagram of the model of the biotechnical system "corrective action complex – respiratory system".

4. Algorithm of load adaptation based on the data of diagnostic condition matrices

The 2nd circuit operates in search mode with automatic load adjustment, as the parameters of human respiratory system are changing (Figure 3); NA is the number of load alteration levels [3,11,12].

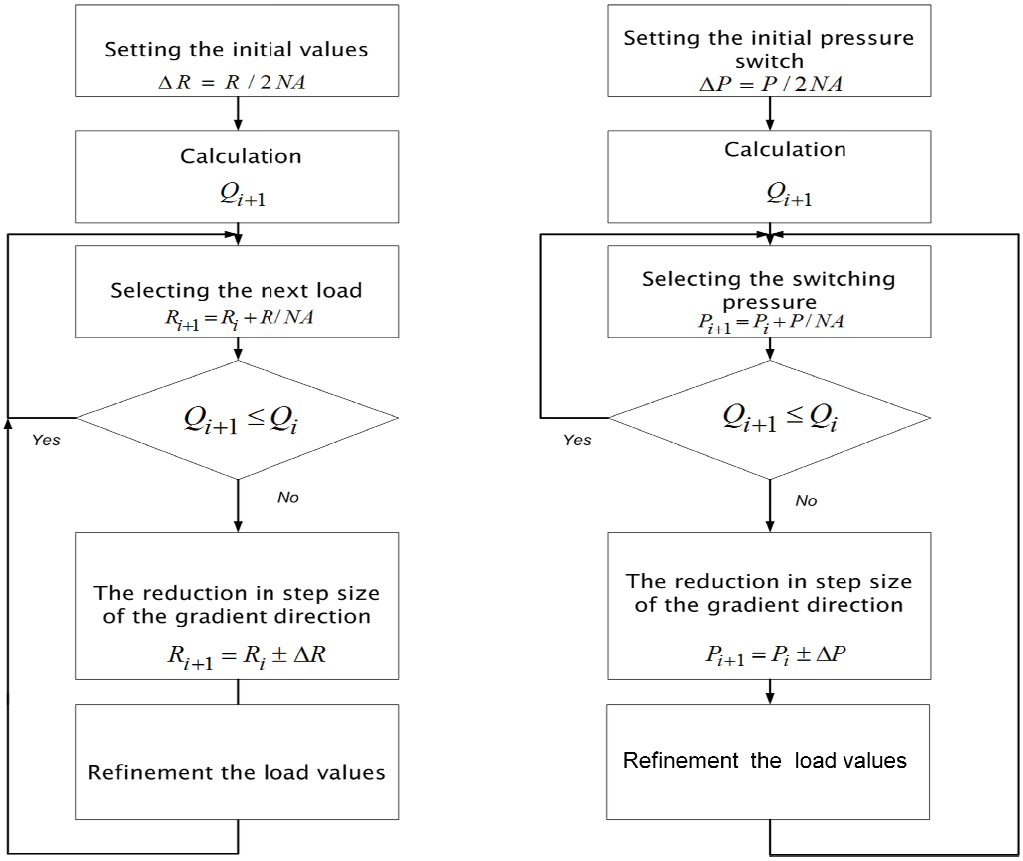

a) b)

a – adjustment of load – resistance of the circuit;
b – switching pressure adjustment

Figure 3. A diagram of work of corrective action complexes adaptation algorithm (2nd circuit).

Load correction based on changes in the target function is illustrated by the graph in Figure 4. On the *x*-axis there is every step corresponding to presetting the load for the next inspiration/expiration

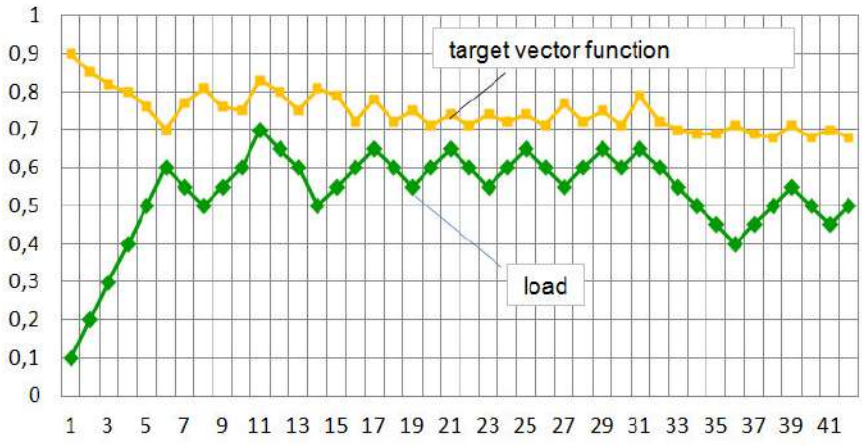

Figure 4. Experimental characteristics of the results of work of the 2nd adaptation circuit (load in the form of resistance).

5. Conclusions

Based on the experimental and analytical assessment of changes in pressure parameters during various types of action on the respiratory system, the problem of automated identification of indicators characterizing the change in the condition of the human respiratory system when working with corrective action complexes has been solved, and a set of algorithms providing timely self-adjustment of the controlling action has been developed.

The task of controlling the actuating device in real time with simultaneous complex signal processing can be accomplished using high-performance microcontrollers.

The above methods and algorithms are the basis for the development of a new class of medical devices: automated complexes of corrective action on the human respiratory system ensuring adaptive signal processing, modeling of biological processes, and real-time control of the actuating device, which increases the efficiency of treating patients with bronchial asthma and chronic obstructive bronchitis, as well as of rehabilitation programs in patients with movement disorders.

6. References

[1] Ivakhno N V, Merkulova V 2011 Respiratory muscles simulator *Utility model patent No. 115668. Russian Federation. Priority date 20.09.2011*

[2] Kravtsova N S, Paringer R A and Kupriyanov A V 2017 Parallel implementation of the informative areas generation method in the spatial spectrum domain *Computer Optics* **41(4)** 585-588 DOI: 10.18287/2412-6179-2017-41-4-585-587

[3] Gaidel A V 2016 Matched polynomial features for the analysis of grayscale biomedical images *Computer Optics* **40(2)** 232-240 DOI: 10.18287/2412-6179-2016-40-2-232-239

[4] Ivakhno N V, Tyagin D 2008 Artificial pulmonary ventilation machine *Invention patent No. 2375034. Russian Federation. Priority date 04.06.2008*

[5] Ivakhno N V, Fedorov S S 2014 Principle of construction of mathematical model of process of signal processing in the detection of respiratory activity in systems of intellectual fitness effects *Biotechnosphere* **5(35)** 19-22

[6] Ivakhno N V 2015 The structure and algorithm circuit self-diagnosis of the intellectual equipment of respiratory muscles *Biotechnosphere* **3(39)** 40-44

[7] Chafonova V G, Gazeeva I V and Tihomirova G V 2016 Automatic control and digital correction of scale and rotation mismatch in stereo pairs *Computer Optics* **40(1)** 112-121 DOI: 10.18287/2412-6179-2016-40-1-112-120

[8] Ivakhno N V, Antsibor S V 2015 Parametric analysis of respiration characteristics under the relay action *Proceedings of the Tula State University. Technical sciences* **5(2)** 78-84

[9] Gaidel A V, Zelter P M, Kapishnikov A V and Khramov A G 2014 Computed tomography texture analysis capabilities in diagnosing a chronic obstructive pulmonary disease *Computer Optics* **38(4)** 843-851

[10] Ilyasova N Yu, Kupriyanov A V and Paringer R A 2014 Formation of features for improving the quality of medical diagnosis based on discriminant analysis methods *Computer Optics* **38(4)** 851-856

[11] Smelkina N A, Kosarev R N, Nikonorov A V, Bairikov I M, Ryabov K N, Avdeev A V and Kazanskiy N L 2017 Reconstruction of anatomical structures using statistical shape modeling *Computer Optics* **41(6)** 897-904 DOI: 10.18287/2412-6179-2017-41-6-897-904

[12] Antsiperov V E 2016 Automatic target recognition for low-count terahertz images *Computer Optics* **40(5)** 746-751 DOI: 10.18287/2412-6179-2016-40-5-746-751

Algebras of finitary relations

V P Tsvetov[1]

[1]Samara National Research University, Moskovskoe Shosse 34A, Samara, Russia, 443086

e-mail: tsf-su@mail.ru

Abstract. Algebras of finitary relations naturally generalize the algebra of binary relations with the left composition. In this paper, we consider some properties of such algebras. It is well known that we can study the hypergraphs as finitary relations. In this way the results can be applied to graph and hypergraph theory, automatons and artificial intelligence.

1. Introduction

It is obvious that graphs and binary relations are closely related. We often use the facts of the binary relations theory in graph theory to solve some algorithmic problems. In the same way, we can consider hypergraphs as finitary relations. This could be a good idea for IT and AI, especially for pattern recognition and machine learning [1-13].

By now it has become common to use universal algebras [14] in various applications [15]. Algebraic methods can also be efficiently applied in graph theory. For example, the shortest path problem can be solved by transitive closure algorithm for binary relation [16].

In this way, and following by [17], we are going to study hypergraphs as elements of algebraic structures.

At first, we define a (*n*-uniform) hypergraph as a finitary relation on finite set U, in other words, as a subset of U^n. In case of $n=2$ this leads to graph as a binary relation. Boolean algebras $\left\langle 2^{U\times U},\left(\cup,\cap,\bar{},\varnothing,U\times U\right)\right\rangle$ and $\left\langle 2^{U^n},\left(\cup,\cap,\bar{},\varnothing,U^n\right)\right\rangle$ are well known to us.

It is less trivial to define the inverse operation and the left composition for finitary relations. We have to start from inverse operation, left and right compositions for binary relations:

$$R^{-1}=\left\{\left(u_2,u_1\right)\mid\left(u_1,u_2\right)\in R\right\}, \tag{1}$$

$$R_1\circ R_2=\left\{\left(u_1,u_2\right)\mid\exists u_0\left(u_1,u_0\right)\in R_1\wedge\left(u_0,u_2\right)\in R_2\right\}, \tag{2}$$

$$R_1\circ R_2=R_2\circ R_1=\{(u_1,u_2)\mid\exists\ u_0(u_0,u_2)\in R_1\wedge(u_1,u_0)\in R_2\} \tag{3}$$

Note that $\left\langle 2^{U\times U},(\circ,I)\right\rangle\sim\left\langle 2^{U\times U},(\bullet,I)\right\rangle$ are isomorphic monoids, where I is identity relation on U. By the way, we can define operations

$$R_1\circ_1 R_2=R_1^{-1}\circ R_2, \tag{4}$$

$$R_1\bullet R_2=R_2\circ R_1, \tag{5}$$

$$R_1\circ_2 R_2=R_1\circ R_2^{-1}, \tag{6}$$

$$R_1 \bullet_2 R_2 = R_2 \circ R_1^{-1} \quad (7)$$

$$R_1 \circ_3 R_2 = R_1^{-1} \circ R_2^{-1}, \quad (8)$$

$$R_1 \bullet_3 R_2 = R_2^{-1} \circ R_1^{-1}. \quad (9)$$

This makes it possible to set the following pairs of isomorphic magmas. $\left\langle 2^{U\times U}, (\circ_1, I)\right\rangle \square \left\langle 2^{U\times U}, (\square_1, I)\right\rangle$ are isomorphic magmas with left identity elements. $\left\langle 2^{U\times U}, (\circ_2, I)\right\rangle \square \left\langle 2^{U\times U}, (\square_2, I)\right\rangle$ are isomorphic magmas with right identity elements. $\left\langle 2^{U\times U}, (\circ_3)\right\rangle \square \left\langle 2^{U\times U}, (\square_3)\right\rangle$ are isomorphic magmas without identity elements.

It is easy to see that in the symmetric case $R = R^{-1}$ all of monogenic monoids $\left\langle \left\{R^n\right\}_{n=0}^{\infty}, (\circ, I)\right\rangle$, $\left\langle \left\{R^n\right\}_{n=0}^{\infty}, (\square, I)\right\rangle$, $\left\langle \left\{R^n\right\}_{n=0}^{\infty}, (\circ_i, I)\right\rangle$, $\left\langle \left\{R^n\right\}_{n=0}^{\infty}, (\square_i, I)\right\rangle$ ($i \in 1..3$) are equal.

The monogenic monoid $\left\langle \left\{R^n\right\}_{n=0}^{\infty}, (\circ, I)\right\rangle$ and distributive algebraic structure $\left\langle \left\{R^n\right\}_{n=0}^{\infty}, (\circ, \cup, I, \varnothing)\right\rangle$ are useful to treat all-pairs shortest path problem [16]. We are going to define and study hypergraph operations similar to (1)-(9).

2. Algebras of finitary relations

Let us consider the underlying set of finitary relations 2^{U^n}, and define the following unary and binary operations for $i \neq j$

$$R^{(ij)} = R^{(ji)} = \left\{\left(u_1,..,u_j,..,u_i,..,u_n\right) \middle| \left(u_1,..,u_i,..,u_j,..,u_n\right) \in R\right\}, \quad (10)$$

$$R_1 \circ_{ij} R_2 = \left\{\left(u_1,..,u_i,..,u_j,..,u_n\right) \middle| \exists u_0 \left(u_1,..,u_0,..,u_j,..,u_n\right) \in R_1 \wedge \left(u_1,..,u_i,..,u_0,..,u_n\right) \in R_2\right\}. \quad (11)$$

Obviously, the operation (10) is an involution.

$$\left(R^{(ij)}\right)^{(ij)} = R. \quad (12)$$

Moreover,

$$R_1 \circ_{ij} R_2 = R_2 \circ_{ji} R_1. \quad (13)$$

It is easy to prove that operation (11) is associative. Actually,

$$\left(u_1,..,u_i,..,u_j,..,u_n\right) \in R_1 \circ_{ij} \left(R_2 \circ_{ij} R_3\right) \Leftrightarrow \exists u_0 \left(u_1,..,u_0,..,u_j,..,u_n\right) \in R_1 \wedge \left(u_1,..,u_i,..,u_0,..,u_n\right) \in R_2 \circ_{ij} R_3 \Leftrightarrow$$

$$\Leftrightarrow \exists u_0 \left(u_1,..,u_0,..,u_j,..,u_n\right) \in R_1 \wedge \left(\exists u_0' \left(u_1,..,u_0',..,u_0,..,u_n\right) \in R_2 \wedge \left(u_1,..,u_i,..,u_0',..,u_n\right) \in R_3\right) \Leftrightarrow$$

$$\Leftrightarrow \exists u_0' \left(\exists u_0 \left(u_1,..,u_0,..,u_j,..,u_n\right) \in R_1 \wedge \left(u_1,..,u_0',..,u_0,..,u_n\right) \in R_2\right) \wedge \left(u_1,..,u_i,..,u_0',..,u_n\right) \in R_3 \Leftrightarrow$$

$$\Leftrightarrow \exists u_0' \left(u_1,..,u_0',..,u_j,..,u_n\right) \in R_1 \circ_{ij} R_2 \wedge \left(u_1,..,u_i,..,u_0',..,u_n\right) \in R_3 \Leftrightarrow$$

$$\Leftrightarrow \left(u_1,..,u_i,..,u_j,..,u_n\right) \in \left(R_1 \circ_{ij} R_2\right) \circ_{ij} R_3.$$

Then we set

$$I_{ij} = \left\{\left(u_1,..,u_i,..,u_j,..,u_n\right) \middle| k \in 1..n \wedge u_k \in U \wedge u_j = u_i\right\} \in 2^{U^n}. \quad (14)$$

It is easy to see

$$\left(u_1,..,u_i,..,u_j,..,u_n\right) \in I_{ij} \circ_{ij} R \Leftrightarrow \exists u_0 \left(u_1,..,u_0,..,u_j,..,u_n\right) \in I_{ij} \wedge \left(u_1,..,u_i,..,u_0,..,u_n\right) \in R \Leftrightarrow$$

$$\Leftrightarrow \exists u_0 \left(u_1,..,u_i,..,u_0,..,u_n\right) \in R \wedge u_j = u_0 \Leftrightarrow \left(u_1,..,u_i,..,u_j,..,u_n\right) \in R,$$

and similarly

$$\left(u_1,..,u_i,..,u_j,..,u_n\right) \in R \circ_{ij} I_{ij} \Leftrightarrow \exists u_0 \left(u_1,..,u_0,..,u_j,..,u_n\right) \in R \wedge \left(u_1,..,u_i,..,u_0,..,u_n\right) \in I_{ij} \Leftrightarrow$$

$$\Leftrightarrow \exists u_0 \left(u_1,..,u_0,..,u_j,..,u_n\right) \in R \wedge u_i = u_0 \Leftrightarrow \left(u_1,..,u_i,..,u_j,..,u_n\right) \in R.$$

Thus,

$$I_{ij} \circ_{ij} R = R \circ_{ij} I_{ij} = R . \quad (15)$$

Hence we have just proved the

Lemma 1. $\left\langle 2^{U^n}, \left(\circ_{ij}, I_{ij}\right)\right\rangle$ is a monoid.

Note that

$$\left(u_1,..,u_i,..,u_j,..,u_n\right) \in \left(R_1 \circ_{ij} R_2\right)^{(ij)} \Leftrightarrow \left(u_1,..,u_j,..,u_i,..,u_n\right) \in R_1 \circ_{ij} R_2 \Leftrightarrow$$
$$\Leftrightarrow \exists u_0 \left(u_1,..,u_0,..,u_i,..,u_n\right) \in R_1 \wedge \left(u_1,..,u_j,..,u_0,..,u_n\right) \in R_2 \Leftrightarrow$$
$$\Leftrightarrow \exists u_0 \left(u_1,..,u_i,..,u_0,..,u_n\right) \in R_1^{(ij)} \wedge \left(u_1,..,u_0,..,u_j,..,u_n\right) \in R_2^{(ij)} \Leftrightarrow$$
$$\Leftrightarrow \left(u_1,..,u_i,..,u_j,..,u_n\right) \in R_1^{(ij)} \circ_{ji} R_2^{(ij)} \Leftrightarrow \left(u_1,..,u_i,..,u_j,..,u_n\right) \in R_2^{(ij)} \circ_{ij} R_1^{(ij)} .$$

In that way

$$\left(R_1 \circ_{ij} R_2\right)^{(ij)} = R_1^{(ij)} \circ_{ji} R_2^{(ij)} = R_2^{(ij)} \circ_{ij} R_1^{(ij)} . \quad (16)$$

Hence the bijective function $f\left(R\right) := R^{(ij)}$ is an isomorphism of monoids $\left\langle 2^{U^n}, \left(\circ_{ij}, I_{ij}\right)\right\rangle$ and $\left\langle 2^{U^n}, \left(\circ_{ji}, I_{ji}\right)\right\rangle$.

Moreover,

$$\left(u_1,..,u_i,..,u_k,..,u_j,..,u_n\right) \in \left(R_1 \circ_{ik} R_2\right)^{(ij)} \Leftrightarrow \left(u_1,..,u_j,..,u_k,..,u_i,..,u_n\right) \in R_1 \circ_{ik} R_2 \Leftrightarrow$$
$$\Leftrightarrow \exists u_0 \left(u_1,..,u_0,..,u_k,..,u_i,..,u_n\right) \in R_1 \wedge \left(u_1,..,u_j,..,u_0,..,u_i,..,u_n\right) \in R_2 \Leftrightarrow$$
$$\Leftrightarrow \exists u_0 \left(u_1,..,u_i,..,u_k,..,u_0,..,u_n\right) \in R_1^{(ij)} \wedge \left(u_1,..,u_i,..,u_0,..,u_j,..,u_n\right) \in R_2^{(ij)} \Leftrightarrow$$
$$\Leftrightarrow \left(u_1,..,u_i,..,u_j,..,u_n\right) \in R_1^{(ij)} \circ_{jk} R_2^{(ij)} \Leftrightarrow \left(u_1,..,u_i,..,u_j,..,u_n\right) \in R_2^{(ij)} \circ_{kj} R_1^{(ij)} .$$

From which we obtain

$$\left(R_1 \circ_{ik} R_2\right)^{(ij)} = R_1^{(ij)} \circ_{jk} R_2^{(ij)} = R_2^{(ij)} \circ_{kj} R_1^{(ij)} . \quad (17)$$

Hence we have proved the

Lemma 2. Monoids $\left\langle 2^{U^n}, \left(\circ_{ik}, I_{ik}\right)\right\rangle$ and $\left\langle 2^{U^n}, \left(\circ_{jk}, I_{jk}\right)\right\rangle$ are isomorphic, as well as monoids $\left\langle 2^{U^n}, \left(\circ_{ij}, I_{ij}\right)\right\rangle$ and $\left\langle 2^{U^n}, \left(\circ_{ji}, I_{ji}\right)\right\rangle$.

Let us set an algebraic structure $\left\langle 2^{U^n}, \left(\circ_{ij}, \circ_{ik}, I_{ij}, I_{ik}\right)\right\rangle$ and then we can write the following logical consequences:

$$\left(u_1,..,u_i,..,u_j,..,u_k,..,u_n\right) \in R_1 \circ_{ij} \left(R_2 \circ_{ik} R_3\right) \Leftrightarrow \exists u_0 \left(u_1,..,u_0,..,u_j,..,u_k,..,u_n\right) \in R_1 \wedge$$
$$\wedge \left(u_1,..,u_i,..,u_0,..,u_k,..,u_n\right) \in R_2 \circ_{ik} R_3 \Leftrightarrow \exists u_0 \, \exists u_0' \left(u_1,..,u_0,..,u_j,..,u_k,..,u_n\right) \in R_1 \wedge$$
$$\wedge \left(u_1,..,u_0',..,u_0,..,u_k,..,u_n\right) \in R_2 \wedge \left(u_1,..,u_i,..,u_0,..,u_0',..,u_n\right) \in R_3 \Leftrightarrow$$
$$\exists u_0' \, \exists u_0 \left(u_1,..,u_0,..,u_j,..,u_k,..,u_n\right) \in R_1 \wedge \left(u_1,..,u_0',..,u_0,..,u_k,..,u_n\right) \in R_2 \wedge$$
$$\wedge \left(u_1,..,u_i,..,u_0,..,u_0',..,u_n\right) \in R_3 \Rightarrow$$
$$\exists u_0' \left(\exists u_0 \left(u_1,..,u_0,..,u_j,..,u_k,..,u_n\right) \in R_1 \wedge \left(u_1,..,u_0',..,u_0,..,u_k,..,u_n\right) \in R_2\right) \wedge$$
$$\wedge \left(\exists u_0 \left(u_1,..,u_i,..,u_0,..,u_0',..,u_n\right) \in R_3\right) \Leftrightarrow \exists u_0' \left(u_1,..,u_0',..,u_j,..,u_k,..,u_n\right) \in R_1 \circ_{ij} R_2 \wedge$$
$$\wedge \left(\exists u_0 \left(u_1,..,u_i,..,u_0,..,u_0',..,u_n\right) \in R_3 \wedge \left(u_1,..,u_0,..,u_j,..,u_0',..,u_n\right) \in 1_R\right) \Leftrightarrow$$
$$\Leftrightarrow \exists u_0' \left(u_1,..,u_0',..,u_j,..,u_k,..,u_n\right) \in R_1 \circ_{ij} R_2 \wedge \left(u_1,..,u_i,..,u_j,..,u_0',..,u_n\right) \in R_3 \circ_{ij} 1_R \Leftrightarrow$$
$$\Leftrightarrow \left(u_1,..,u_i,..,u_j,..,u_k,..,u_n\right) \in \left(R_1 \circ_{ij} R_2\right) \circ_{ik} \left(R_3 \circ_{ij} 1_R\right) .$$

This means that the following Lemma is true.

Lemma 3. In an ordered algebra $\left\langle 2^{U^n},\left(\circ_{ij},\circ_{ik},\subseteq,I_{ij},I_{ik},0_R,1_R\right)\right\rangle$, the pseudo distributive law holds

$$R_1\circ_{ij}\left(R_2\circ_{ik}R_3\right)\subseteq\left(R_1\circ_{ij}R_2\right)\circ_{ik}\left(R_3\circ_{ij}1_R\right). \tag{18}$$

According to [17], we use the notation $1_R:=U^n$ and $0_R:=\varnothing$.

Then look at composition

$$\begin{gathered}\left(u_1,..,u_i,..,u_j,..,u_n\right)\in R\ \circ_{ij}R^{(\mathrm{ij})}\Leftrightarrow\exists u_0\left(u_1,..,u_0,..,u_j,..,u_n\right)\in R\ \wedge\left(u_1,..,u_i,..,u_0,..,u_n\right)\in R^{(\mathrm{ij})}\Leftrightarrow\\ \Leftrightarrow\exists u_0\left(u_1,..,u_0,..,u_j,..,u_n\right)\in R\ \wedge\left(u_1,..,u_0,..,u_i,..,u_n\right)\in R\ .\end{gathered} \tag{19}$$

Definition 1. The finitary relation R is called a function from *i*-th to *j*-th argument if

$$\forall u_1,...,u_i,..,u_j,u_j',..,u_n\left(u_1,..,u_i,..,u_j,..,u_n\right)\in R\ \wedge\left(u_1,..,u_i,..,u_j',..,u_n\right)\in R\ \to u_j=u_j'. \tag{20}$$

We can obtain from (19) - (20) the following set inclusion

$$\left(u_1,..,u_i,..,u_j,..,u_n\right)\in R\ \circ_{ij}R^{(\mathrm{ij})}\Rightarrow u_i=u_j\Leftrightarrow\left(u_1,..,u_i,..,u_j,..,u_n\right)\in I_{ij}\Leftrightarrow R\ \circ_{ij}R^{(\mathrm{ij})}\subseteq I_{ij}. \tag{21}$$

Definition 2. The finitary relation R is called a surjection from *i*-th argument if

$$\forall u_1,...,u_{i-1},u_{i+1},..,u_j,..,u_n\ \exists u_0\left(u_1,..,u_0,..,u_j,..,u_n\right)\in R\ . \tag{22}$$

From (21) - (22) we can get the reverse set inclusion

$$I_{ij}\subseteq R\ \circ_{ij}R^{(\mathrm{ij})}. \tag{23}$$

Thus, in the case of R is a surjective function from *i*-th to *j*-th argument we have the equality

$$R\ \circ_{ij}R^{(\mathrm{ij})}=I_{ij}. \tag{24}$$

Similarly, in the case of R is a surjective function from *j*-th to *i*-th argument we have the equality

$$R^{(\mathrm{ij})}\circ_{ij}R\ =I_{ij}. \tag{25}$$

Let us denote the set of surjective functions from both (*i*-th to *j*-th and *j*-th to *i*-th) arguments as F_{ij}. It is easy that F_{ij} is closed by $\circ_{ij}$, and hence we have proved the

Lemma 4. $\left\langle F_{ij},\left(\circ_{ij},I_{ij}\right)\right\rangle$ is a subgroup of the monoid $\left\langle 2^{U^n},\left(\circ_{ij},I_{ij}\right)\right\rangle$.

As well as binary relations, finitary relations have the following properties [17]

$$R_1\circ_{ij}\left(R_2\cup R_3\right)=\left(R_1\circ_{ij}R_2\right)\cup\left(R_1\circ_{ij}R_3\right), \tag{26}$$

$$\left(R_2\cup R_3\right)\circ_{ij}R_1=\left(R_2\circ_{ij}R_1\right)\cup\left(R_3\circ_{ij}R_1\right), \tag{27}$$

$$R_1\circ_{ij}\left(R_2\cap R_3\right)\subseteq\left(R_1\circ_{ij}R_2\right)\cap\left(R_1\circ_{ij}R_3\right), \tag{28}$$

$$\left(R_2\cap R_3\right)\circ_{ij}R_1\subseteq\left(R_2\circ_{ij}R_1\right)\cap\left(R_3\circ_{ij}R_1\right), \tag{29}$$

and so we can set an algebraic structures $\left\langle F_{ij},\left(\circ_{ij},I_{ij}\right)\right\rangle$, $\left\langle 2^{U^n},\left(\cup,\cap,\circ_{ij},\circ_{ik},^{(\mathrm{ij})},\subseteq,0_R,1_R,I_{ij},I_{ik}\right)\right\rangle$ that have properties (12)-(18), (24)-(29).

3. Conclusion and examples

We have defined algebraic structures of finitary relations as a common case of well-known algebraic structures of binary relations. We have considered the algebraic structures on an underlying set 2^{U^n} and sometimes called a finitary relation $R\in 2^{U^n}$ by a (*n*-uniform) hypergraph. The operation $\circ_{ij}$ can be called the "straightening the edges" or "deleting shared intermediate vertices". Let us take an example.

Example 1 (algebraic). Let us set $U=\left\{u_0,u_1,u_2,u_3\right\}$, $\left\langle 2^{U^3},\left(\circ_{23},I_{23}\right)\right\rangle$, and $R=\left\{\left(u_1,u_0,u_3\right),\left(u_1,u_2,u_0\right)\right\}$. Now we can get

$$I_{23}=\begin{Bmatrix}(u_0,u_0,u_0),(u_0,u_1,u_1),(u_0,u_2,u_2),(u_0,u_3,u_3),\\(u_1,u_0,u_0),(u_1,u_1,u_1),(u_1,u_2,u_2),(u_1,u_3,u_3),\\(u_2,u_0,u_0),(u_2,u_1,u_1),(u_2,u_2,u_2),(u_2,u_3,u_3),\\(u_3,u_0,u_0),(u_3,u_1,u_1),(u_3,u_2,u_2),(u_3,u_3,u_3)\end{Bmatrix},$$

$$R\circ_{23}R=\{(u_1,u_2,u_3)\},$$

$$R\circ_{23}R\circ_{23}R=\varnothing.$$

Despite its simplicity, operation $\circ_{23}$ has some interesting applications. In examples 2, 3 we are going to denote 3-tuple $(u_{i_1},u_{i_2},u_{i_3})$ as a word $u_{i_1}u_{i_2}u_{i_3}$.

Example 2 (feature selection). Let $R=\{u_1u_0u_0,u_1u_1u_0,u_1u_2u_0,u_1u_2u_1,u_1u_2u_3,u_1u_3u_0\}$ be a set of words, and $R_f=\{u_1u_0u_3\}$, $R_f^{(23)}=\{u_1u_3u_0\}$ are filters. First, apply the filter R_f

$$R_f\circ_{23}R=\{u_1u_0u_3,u_1u_1u_3,u_1u_2u_3,u_1u_3u_3\}.$$

Then apply the filter $R_f^{(23)}$

$$R_f^{(23)}\circ_{23}R_f\circ_{23}R=\{u_1u_0u_0,u_1u_1u_0,u_1u_2u_0,u_1u_3u_0\}.$$

Example 3 (crossover). Let $R=\{u_1u_0u_0,u_1u_1u_0,u_1u_2u_1,u_1u_3u_2\}$ be a population. Let us define the evolution operator $\mathrm{E}(R)=R\cup R\circ_{23}R$ and start a first step of evolution

$$\mathrm{E}(R)=\{u_1u_0u_0,u_1u_1u_0,u_1u_2u_0,u_1u_2u_1,u_1u_3u_1,u_1u_3u_2\}.$$

In example 4 we are going to denote 3-tuple $(u_{i_1},u_{i_2},u_{i_3})$ as an implies $u_{i_1}\to(u_{i_2}\to u_{i_3})$.

Example 4 (AI). Let $R=\{u_1\to(u_1\to u_1),u_1\to(u_1\to u_2)\}$ be a base set of AI premises. Let us define the semantic closure of R as $[R]=\bigcup_{k=1}^{\infty}\left(R\cup R^{(23)}\right)^k$, where $R^{k+1}=R^k\circ_{23}R$ and $R^1=R$. By definition we have

$$[R]=\{u_1\to(u_1\to u_1),u_1\to(u_1\to u_2),u_1\to(u_2\to u_1),u_1\to(u_2\to u_2)\}.$$

Note that $((u_1\to(u_0\to u_3))\wedge(u_1\to(u_2\to u_0)))\to(u_1\to(u_2\to u_3))$ is tautology, so the inference rule $u_1\to(u_0\to u_3),u_1\to(u_2\to u_0)\vdash u_1\to(u_2\to u_3)$ preserves truth.

We also note that $(((u_1\to u_0)\to u_3)\wedge((u_1\to u_2)\to u_0))\to((u_1\to u_2)\to u_3)$ is tautology, too.

It makes perfect sense to use an indicator function $\chi_R:U^n\mapsto\{0,1\}$ for $R\in 2^{U^n}$, that is defined as

$$\chi_R(u_1,..,u_n)=\begin{cases}1,(u_1,..,u_n)\in R\\0,(u_1,..,u_n)\notin R\end{cases}.$$

In the case of finite set $U=\{u_1,..,u_m\}$, we can use this function to define a join-vertices logical array $\psi^R:(1..m)^n\mapsto\{false,true\}$ for (n-uniform) hypergraph. Let $f:1..m\mapsto U$ be a total bijection and $R\in 2^{U^n}$. We define

$$\psi^R_{k_1,..,k_n}=\psi^R(k_1,..,k_n)=\begin{cases}true, & \chi_R(f^{-1}(k_1),..,f^{-1}(k_n))=1\\false, & \chi_R(f^{-1}(k_1),..,f^{-1}(k_n))=0\end{cases}.$$

Let us denote $\{false,true\}$ as D and a set of logical array defined above as $\mathsf{D}^{(1..m)^n}$.

We also can set a logical algebra that generalized adjacency matrices algebra. In this way we define a binary operation $*_{ij}$ on $\mathsf{D}^{(1..m)^n}$

$$\psi^1_{k_1,..,k_n} *_{ij} \psi^2_{k_1,..,k_n} = \bigvee_{s=1}^{m} \psi^1_{k_1,..,k_{i-1},s,k_{i+1},..,k_j,..,k_n} \wedge \psi^2_{k_1,..,k_i,..,k_{j-1},s,k_{j+1},..,k_n}.$$

By our construction semigroups $\left\langle 2^{U^n}, \left(\circ_{ij}\right)\right\rangle$ and $\left\langle \mathsf{D}^{(1..m)^n}, \left(*_{ij}\right)\right\rangle$ are isomorphic.

More interesting is the case of algebraic structures on an underlying set $\bigcup_{n=1}^{\infty} 2^{U^n}$ and operations from 2^{U^n} to 2^{U^m}. For example, let us define the operations "gluing edges" $\circ_g$ and "replacing chains" $\circ_r$.

$$R_1 \circ_g R_2 = \left\{\left(u_1,..,u_{m-1},u'_2,..,u'_n\right) \mid \exists u_0 \left(u_1,..,u_{m-1},u_0\right) \in R_1 \wedge \left(u_0,u'_2,..,u'_n\right) \in R_2\right\},$$

$$R_1 \circ_r R_2 = \left\{\left(u_1,..,u_{i-1},u'_{j+1},..,u'_n\right) \mid \exists u_0 \exists i \exists j \left(u_1,..,u_{i-1},u_0,..,u_m\right) \in R_1 \wedge \left(u'_1,..,u_0,u'_{j+1},..,u'_n\right) \in R_2\right\}.$$

For the finitary relation $R = \left\{\left(u_1,u_0,u_3\right),\left(u_1,u_2,u_0\right)\right\}$ from Example 1 we can get

$$R^{(13)} = \left\{\left(u_3,u_0,u_1\right),\left(u_0,u_2,u_1\right)\right\},$$

$$R \circ_g R^{(13)} = \left\{\left(u_1,u_0,u_0,u_1\right),\left(u_1,u_2,u_2,u_1\right)\right\},$$

$$R \circ_r R = \left\{\left(u_1\right),\left(u_0,u_3\right),\left(u_1,u_0\right),\left(u_1,u_2\right),\left(u_1,u_3\right),\left(u_2,u_0\right),\left(u_1,u_2,u_3\right)\right\}.$$

It is clear that even in the case of finite set U we would never make a finite representation for such algebraic structures. But in particular cases, maybe we can. This case is of interest.

4. References

[1] Hein M, Setzer S, Jost L and Rangapuram S S 2013 The total variation on hypergraphs-learning on hypergraphs revisited *Advances in Neural Information Processing Systems* 2427-2435

[2] Ricatte T, Gilleron R and Tommasi M 2014 Hypernode graphs for spectral learning on binary relations over sets *Joint European Conference on Machine Learning and Knowledge Discovery in Databases* 662-677

[3] Louis A 2015 Hypergraph markov operators, eigenvalues and approximation algorithms *Proceedings of the Forty-Seventh Annual ACM on Symposium on Theory of Computing* 713-722

[4] Zhang C, Hu S, Tang Z G and Chan T H 2017 Re-revisiting Learning on Hypergraphs: Confidence Interval and Subgradient Method *Proceedings of the 34th International Conference on Machine Learning, in PMLR* **70** 4026-4034

[5] Pu L, Faltings B 2012 Hypergraph learning with hyperedge expansion *Machine Learning and Knowledge Discovery in Databases* 410-425

[6] Yu J, Tao D and Wang M 2012 Adaptive hypergraph learning and its application in image classification *IEEE Transactions on Image Processing* **21(7)** 3262-3272

[7] Panagopoulos A, Wang C, Samaras D and Paragios N 2013 Simultaneous cast shadows, illumination and geometry inference using hypergraphs *IEEE Transactions on Pattern Analysis and Machine Intelligence* **35(2)** 437-449

[8] Wang M, Wu X 2015 Visual classification by l1-hypergraph modeling *IEEE Transactions on Knowledge and Data Engineering* **27(9)** 2564-2574

[9] Zhou D, Huang J and Scholkopf B 2007 Learning with Hypergraphs: Clustering, Classification, and Embedding *Advances in Neural Information Processing Systems: Proceedings of the 2006 Conference* **19** 1601-1608

[10] Ghoshdastidar D, Ambedkar D 2014 Consistency of Spectral Partitioning of Uniform Hypergraphs under Planted Partition Model *Advances in Neural Information Processing Systems 27: Annual Conference on Neural Information Processing Systems* 397-405

[11] Ghoshdastidar D, Ambedkar D 2015 A Provable Generalized Tensor Spectral Method for Uniform Hypergraph Partitioning *Proceedings of the 32nd International Conference on Machine Learning, ICML* 400-409
[12] Ghoshdastidar D, Ambedkar D 2017 Consistency of spectral hypergraph partitioning under planted partition model *Ann. Statist.* **45(1)** 289-315
[13] Chien I, Lin C and Wang I 2018 Community Detection in Hypergraphs: Optimal Statistical Limit and Efficient Algorithms *Proceedings of the Twenty-First International Conference on Artificial Intelligence and Statistics, in PMLR* **84** 871-879
[14] Mal'tsev A I 1973 *Algebraic systems* (Springer) p 319
[15] Chernov V M 2018 Ternary number systems in finite fields *Computer Optics* **42(4)** 704-711 DOI: 10.18287/2412-6179-2018-42-4-704-711
[16] Tsvetov V P 2014 On a syntactic algorithm on graphs *Proceedings of the International Conference Advanced Information Technologies and Scientific Computing* (Samara, Russia) 235-238
[17] Tsvetov V P 2018 Dual ordered structures of binary relations *Proceedings of the International Conference Information Technology and Nanotechnology. Session Data Science* (Samara, Russia) 2635-2644

Distributed image processing based on the same IP-cores in FPGA-architecture

V M Zakharov[1], S V Shalagin[1] and B F Eminov[1]

[1]Kazan National Research Technical University named after A.N. Tupolev, Karl Marks, 10, Kazan, Russia, 420111

e-mail: sshalagin@mail.ru

Abstract. The problem of processing images, i. e., two-dimensional data arrays, was solved through implementing two-dimensional fast Fourier transform (FFT) when using single-type hardware modules – IP-cores in the Virtex-6 FPGA architecture. We have shown the possibility of the parallel implementation of each stage in the two-dimensional FFT, based on four "butterfly"-type transforms (BTr) over four elements of the data array being processed. Estimations were obtained regarding time- and hardware complexity of the IP-core implementing BTrs and used in implementing the one-dimensional FFT. The results obtained can be used in estimating hardware and time consumption when performing a two-dimensional FFT over an array of the pre-defined dimensionality in using existing and forthcoming distributed programmable-architecture systems.

1. Introduction

The problem of real-time image processing is topical today. Software implementation of algorithms employing this problem on a general-purpose computer are limited by the features of the von Neumann architecture.

A way out of the current situation is using special-purpose computers, particularly those embedding the hardware accelerators, both ASIC and FPGA.

This paper discusses the distributed implementation of two-dimensional fast Fourier transform (FFT) based on single-type IP-cores in FPGA-architecture. Based on the estimates of hardware complexity and IP-cores functioning delay time, estimates of hardware and time complexity have been obtained regarding the execution of two-dimensional FFT for an image of a given dimensionality.

There is a known algorithm for the calculation of a two-dimensional FFT, based on the one-dimensional FFT procedure [1 – 4]. A weak point of that algorithm is the fact that it is executed in two stages. At the first stage, the patterns are computed for rows, while at the second stage for columns. Or vice versa, columns at the first stage and rows at the second one. In any case, until all operations have been performed for the first stage, one cannot go to executing the operations at the second stage. Algorithm proposed in this paper does not have this weak point: Operations are performed over the elements of a two-dimensional data array in parallel, without being divided into stages.

The results obtained can be used to solve the problems of the distributed real-time processing of images via the use of special-purpose graphical accelerators based on both existing and promising FPGAs.

Furthermore, in solving the distributed image processing problems, a promising trend is to apply to them distributed programmable-architecture systems [5], the elements of which architecture are FPGAs, such as in [6]. FPGAs allow organizing the distributed data processing at the level of binary data operations, which makes the above hardware platform match with the distributed implementation of a two-dimensional FFT.

We show this in the present paper.

2. Two-dimensional fast Fourier transform

Let us consider the two-dimensional discrete Fourier transform (DFT) for number array $\{x_{mn}\} = X$ sized $N \times N$, $N = 2^a$.

It can be represented as follows [1, 2]:

$$G_{uv} = N^{-2} \sum_{n=0}^{N-1} \sum_{m=0}^{N-1} x_{mn} \cdot W_N^{mu+nv}, \quad (1)$$

where $W_N^{mu+nv} = \exp\left(-2\pi j \frac{mu+nv}{N}\right)$, $u = \overline{0, N-1}$, $v = \overline{0, N-1}$, and $\{G_{uv}\}_{N \times N} = G$ is a pattern for X. Similarly, the reverse two-dimensional DFT is executed:

$$x_{mn} = \sum_{u=0}^{N-1} \sum_{v=0}^{N-1} G_{uv} \cdot W_N^{mu+nv}, \quad m = \overline{0, N-1}, \quad n = \overline{0, N-1}.$$

Note 1. In computing a two-dimensional FFT, low frequencies will be concentrated in the corners of the above matrix, which is not very convenient for further processing the information obtained. To get a representation of the two-dimensional FFT, in which low frequencies would be concentrated within the center of the matrix, a simple procedure can be performed, which consists in multiplying the initial data array by the value of $(-1)^{m+n}$.

Figure 1 and 2 show the initial image and its Fourier-pattern computed according to (1), taking Note 1 into consideration.

The system indicated (1) can be represented similarly to one-dimensional FFT, as follows:

$$G_{uv} = N^{-2} \left[S_{2n_1, 2m_1} + W_N^u \cdot S_{2n_1+1, 2m_1} + W_N^v \cdot S_{2n_1, 2m_1+1} + W_N^{u+v} \cdot S_{2n_1+1, 2m_1+1} \right], \quad (2)$$

where $u = \overline{0, N-1}$, $v = \overline{0, N-1}$, and $S_{2n_1, 2m_1} = \sum_{n_1=0}^{N/2-1} \sum_{m_1=0}^{N/2-1} x_{2n_1 2m_1} \cdot W_N^{2(n_1 u + m_1 w)}$.

As a result, the two-dimensional FFT can be implemented based on single-type operations executed over the elements of matrices D sized $2^d \times 2^d$, submatrices $\{x_{mn}\}$, $m = \overline{0, N-1}$, $n = \overline{0, N-1}$, $d = \overline{1, a}$, $a = \log_2 N$:

$$D_{u,v} = \left[D_{u,v} + W_N^u \cdot D_{u+2^{d-1},v} + W_N^v \cdot D_{u,v+2^{d-1}} + W_N^{u+v} \cdot D_{u+2^{d-1},v+2^{d-1}} \right],$$

$$D_{u+2^{d-1},v} = \left[D_{u,v} - W_N^u \cdot D_{u+2^{d-1},v} + W_N^v \cdot D_{u,v+2^{d-1}} - W_N^{u+v} \cdot D_{u+2^{d-1},v+2^{d-1}} \right],$$

$$D_{u,v+2^{d-1}} = \left[D_{u,v} + W_N^u \cdot D_{u+2^{d-1},v} - W_N^v \cdot D_{u,v+2^{d-1}} - W_N^{u+v} \cdot D_{u+2^{d-1},v+2^{d-1}} \right],$$

$$D_{u+2^{d-1},v+2^{d-1}} = \left[D_{u,v} - W_N^u \cdot D_{u+2^{d-1},v} - W_N^v \cdot D_{u,v+2^{d-1}} + W_N^{u+v} \cdot D_{u+2^{d-1},v+2^{d-1}} \right], \quad (3)$$

where $u = \overline{0, 2^{d-1}-1}$ and $v = \overline{0, 2^{d-1}-1}$.

Figure 1. Initial image as number array *X*.

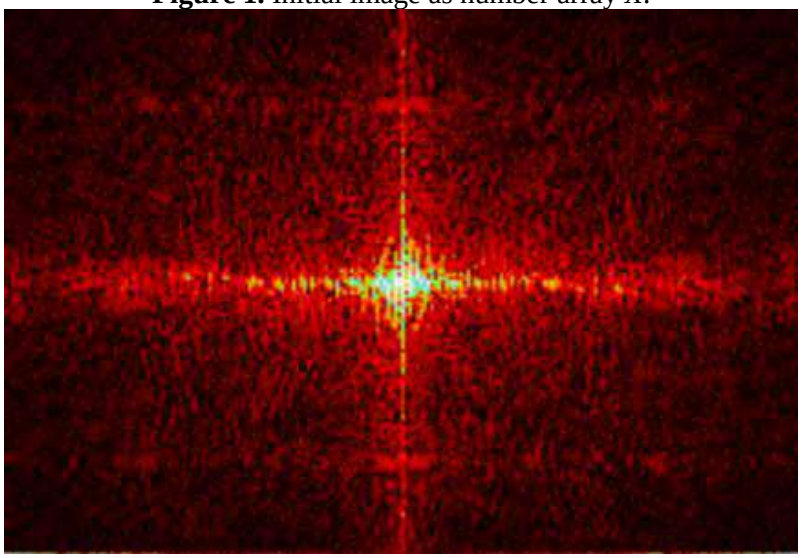

Figure 2. Fourier-pattern of the image shown in figure. 1 above.

Note 2. Number of matrices *D* sized $2^d \times 2^d$ was found to be 4^{a-d}, $d = \overline{1, a}$, $a = \log_2 N$.

Let us represent the system indicated (3) in matrix form as a complex of single-type "butterfly" transforms (BTr) used in computing the one-dimension FFT:

$$\begin{pmatrix} D_{u,v} \\ D_{u,v+2^{d-1}} \end{pmatrix} = \begin{pmatrix} 1 & W_N^v \\ 1 & -W_N^v \end{pmatrix} \cdot \begin{pmatrix} A_1 \\ B_1 \end{pmatrix},$$

$$\begin{pmatrix} D_{u+2^{d-1},v} \\ D_{u+2^{d-1},v+2^{d-1}} \end{pmatrix} = \begin{pmatrix} 1 & W_N^v \\ 1 & -W_N^v \end{pmatrix} \cdot \begin{pmatrix} A_2 \\ B_2 \end{pmatrix},$$

$$\begin{pmatrix} A_1 \\ A_2 \end{pmatrix} = \begin{pmatrix} 1 & W_N^u \\ 1 & -W_N^u \end{pmatrix} \cdot \begin{pmatrix} D_{u,v} \\ D_{u+2^{d-1},v} \end{pmatrix},$$

$$\begin{pmatrix} B_1 \\ B_2 \end{pmatrix} = \begin{pmatrix} 1 & W_N^u \\ 1 & -W_N^u \end{pmatrix} \cdot \begin{pmatrix} D_{u,v+2^{d-1}} \\ D_{u+2^{d-1},v+2^{d-1}} \end{pmatrix}. \quad (4)$$

As a result, to perform one operation indicated (3) over four elements of number array X, according to (4), four BTrs are required. The above operations must be performed over an array of N^2 elements $\log_2 N$ times. According to (3) and (4), the following statements hold true:

Statement 1. Implementing a two-dimensional FFT over number array X sized $N \times N$ requires executing $a \cdot N^2/4$ operations indicated (3) or $a \cdot N^2$ BTrs.

Statement 2. Single-type operations indicated (4) over number array X sized $N \times N$ can be performed in parallel.

Statements 1 and 2 substantiate the applicability of special-purpose computers implementing a single-type operation indicated (3) or (4).

IP-cores implementing BTrs act as a single-type calculator:

$$\begin{pmatrix} Y_1 \\ Y_2 \end{pmatrix} = \begin{pmatrix} 1 & W \\ 1 & -W \end{pmatrix} \cdot \begin{pmatrix} X_1 \\ X_2 \end{pmatrix}.$$

This operation is a basic one in performing an FFT, both one- and multi-dimensional. Therefore, the complexity of performing BTrs determines the complexity of implementing one- and multi-dimensional FFTs. In this study, we confine ourselves with considering the implementation of a two-dimensional FFT based on BTr.

3. Complexity of implementing the single-type butterfly transform on FPGAs

Let us consider the implementation of a hardware module implementing BTr (hereinafter, the "Module") as an IP-core in FPGA-architecture (figure 3). The Module allows handling 18-digit numbers. The functional logic diagram of the Module implemented in ISE Design Suite 14,7, a sheet-oriented CAD editor manufactured by Xilinx, Inc., includes:

- A unit multiplying complex numbers by a constant (ComplexNumMultiplier), shown in figure 4,
- Four adders, two of which perform additions and the resting ones perform subtractions in diminished complements, and
- Registers to ensure pipelined data processing.

An additional register bit serves for storing the sign bit.

Diagram of the ComplexNumMultiplier includes four multipliers (MULT18x18), two 16-bit adders, one of which implements subtractions, and six 16-bit registers to store intermediary results (figure 4).

The Module is implemented on FPGA XC6VLX240t-1FF1156 (Virtex-6 family manufactured by Xilinx, Inc.) that comprises *D*-triggers, generators of Boolean functions of six variables (LUTs), and input/output units (I/O units).

The following is involved in the Module implementation:

- 210 of 301,440 *D*-triggers available (less than 0.1 %);
- 199 of 150,720 LUTs (about 0.13 %), of which 161 were used to implement Boolean functions, while 38 ones as interconnections;
- 83 of 37,680 Slices (about 0.22 %) comprising four LUTs each, implementing Boolean functions of five or six variables and eight *D*-triggers; and
- 130 of 600 I/O units (about 21.7 %), of which 64 are allocated for inputs and 64 for outputs, and 2 more for clock signal and for resetting triggers, respectively.

The maximum function delay time of the Module is 10.438 ns. Values at outputs are computed three clock periods upon the relevant values having arrived at the input.

A structural diagram implementing a BTr is shown in figure 3. The pre-defined transform is implemented in a pipelined manner, within three clock periods, as follows.

At the zeroth clock period, two operands are fed to the Module input, namely complex numbers X_1 and X_2. Operand for multiplying, X_2, is represented by two numbers, eight bits each, while the operand for addition, X_1, is represented as two 16-bit numbers. The first number is for the real part and the second one for the complex part of the number.

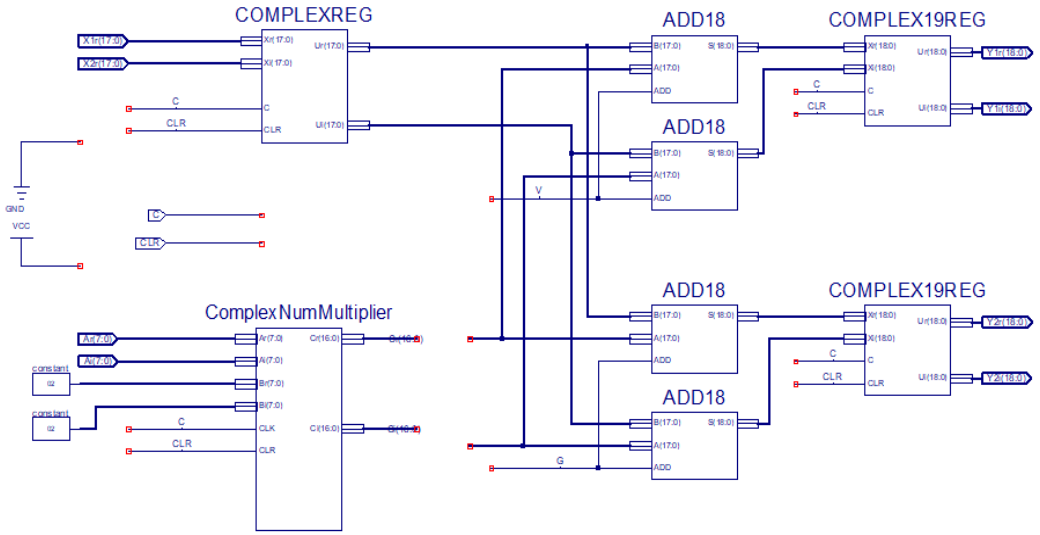

Figure 3. Single-type module diagram to perform a single-type "butterfly" transform.

At the first and second clock periods, the operation of multiplying complex numbers by the pre-defined constant, *W*, is performed with operand X_2, as well as operand X_1 is saved for the complex number addition operation.

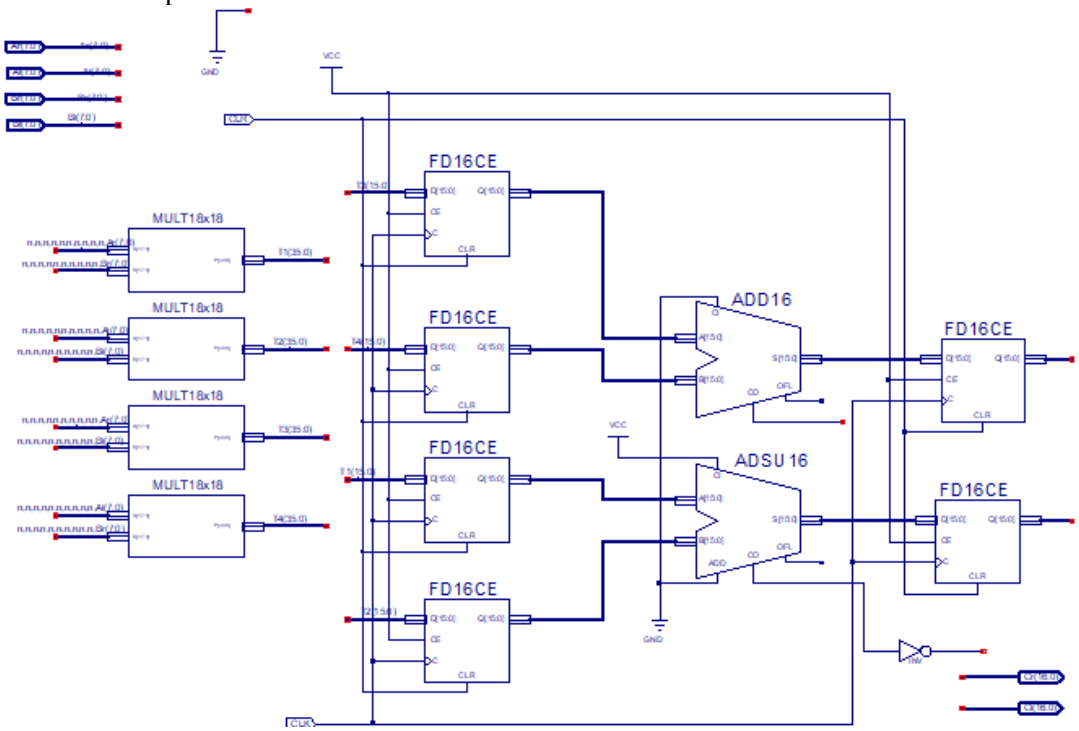

Figure 4. Diagram of multiplying a complex number by constant ComplexNumMultiplier.

At the third clock period, two addition operations are performed: That of operand X_1 and the product of multiplication operation, $W \cdot X_2$, and its values signed minus. Besides, at this stage, the results, Y_1 and Y_2, are saved in registers.

Eventually, the result of BTr is computed in a pipelined manner, within three clock periods, with a frequency that does not exceed 95.8 MHz. The slowest operation is the operation of multiplying complex numbers. Therefore, this operation is performed within two clock periods, intermediary results being saved by organizing the pipelined data processing (figure 4).

4. Discussion

According to [7, 8], a FPGA-based combinational circuit close to the optimal implementation requires involving at most 0.5 of the resources of each type, i.e., *D*-triggers, LUTs, Slices, and input/output units.

According to the complexity estimates obtained, no more than two Modules can be placed on one FPGA of the Virtex-6 family. Limiting factor is the number of I/O units.

$a \cdot N^2/4$ FPGAs of the Virtex-6 family are required to calculate a two-dimensional FFT for a number array sized $N \times N$. Moreover, to calculate the operation described according to (4), one FPGA of the above family is required, each of which accepts at the input and returns by four elements ($D_{u,v}$, $D_{u+2^{d-1},v}$, $D_{u,v+2^{d-1}}$, and $D_{u+2^{d-1},v+2^{d-1}}$), and implements four BTrs. Estimating the operation frequency of a distributed programmable-architecture system (DPAS) [5] that includes this number of FPGAs makes at least 95.8 MHz. Number of delay periods in computing the values of elements $D_{u,v}$, $D_{u+2^{d-1},v}$, $D_{u,v+2^{d-1}}$, and $D_{u+2^{d-1},v+2^{d-1}}$, according to (4), has been $6a$ since the elements to be processed arrived at the input. Generally, true is

Statement 3. To process an array sized $N \times N$ on a DPAS comprising *P* FPGAs that receive for processing *q* elements per clock period and implement a transform indicated (4) per *T* clock periods, *z* time units each, at least $\log N \cdot \left(\left\lceil N^2/(q \cdot P) \right\rceil + T - 1 \right) \cdot z$ time units are required.

For example, let us find the lower estimate of time required to process a number array sized $N \times N$, $N = 2^{10} = 1024$. We will perform the two-dimensional FFT in 10 stages, at each of which $N \times N = 2^{20}$ elements are required. Each Virtex-6 FPGA accepts four elements to be processed, i.e., $q = 4$. If there are *P* of the above-mentioned FPGA in DPAS, then the stage is computed within $\left\lceil N^2/(4 \cdot P) \right\rceil + 5$ clock periods. If we set the number of Virtex-6 FPGAs to 512, as in modern DPASes [5], the one stage of the two-dimensional FFT is implemented within 517 clock periods 10.438 μs each, while 10 stages within 5,170 clock periods, which makes about 5.40 μs to process one stage and about 54 μs to process the entire array. About 18.5 thous of arrays sized 1,024 by 1,024 can be processed within one second.

In case of processing an array sized 2,048 by 2,048 on a DPAS comprising 512 Virtex-6 FPGAs, the lower estimate of processing time, according to Statement 3, is 235 μs, while about 4,255 arrays of the above size can be processed within one second.

Let us compare the two-dimensional FFT implementation proposed, to its known implementation based on "one-dimensional" FFTs [1, 2] denoted as "FFT1," by hardware consumption, i.e., by the number of Virtex-6 FPGAs. In executing *N* FFT1s by the columns of a number array sized $N \times N$, $a \cdot N^2/2$ BTrs are required. The same number of BTrs are required to implement 1FFT to the strings of the number array. Thus, it is necessary to execute $a \cdot N^2$ BTrs, for which $a \cdot N^2/2$ Virtex-6 FPGAs are required, each of which implements two BTrs. As a result, executing a two-dimensional FFT based on the algorithm proposed requires two times fewer Virtex-6 FPGAs due to connecting the algorithmic data to be processed at the FPGA input to the output data according to (4), which allows implementing four BTrs instead of two within the logic resources of one FPGA of the said family, such as *D*-triggers, LUTs, and Slices.

Due to the parallel-serial input of number array *X* into the FPGA, the number of the IP-cores implementing the Module and configured on the Virtex-6 FPGA can be increased significantly.

For the Module implemented on FPGA XC6VLX240t-1FF1156, an additional 64-bit register must be allocated to store the elements of number array *X*. The limiting factor is still the number of Slices involved in implementing the Module. In this case, 227 IP-cores implementing the Module can be placed on the above FPGA. Thus, on one FPGA, $\lfloor 227/4 \rfloor = 56$ operations indicated (4) can be implemented. However, it will additionally require $224a$ clock periods to arrange the serial input of the *X* array elements into FPGA. According to Statement 3, if $P = 512$, $q = 4$, $T = 230$, and

$z = 10.438\ \mu s$, the lower estimate of the processing time of the number array sized $N \times N$, $N = 2^{10} = 1024$, is about 77.4 μs. Within one second, about 12.9 thousand of arrays sized 1,024 by 1,024 can be processed. In case of processing an array sized 2,048 by 2,048, the lower estimate of the operation time is 238 μs, and about 4,202 arrays of that size can be processed within one second.

Note 3. Function delay-time estimate for the operations represented as (4) and performed on a DPAS per a time unit is the lower estimate computed without considering the delay times of communication lines between the FPGA crystals within the DPAS.

5. Conclusion

Currently, much attention is paid to solving a wide variety of problems in using multiprocessor computer systems, the elements of which are the general-purpose processor elements [9-13]. At the same time, the matters of implementing distributed algorithms on DPAS, the elements of which are FPGAs, have been studied insufficiently. Particularly, this is true for the two-dimensional FFT algorithms widely used in image processing, including in the real-time mode. It should also be noted that DPASes are originally intended for the distributed implementation of various algorithms at different times. The present study fills this gap.

Based on estimating the time and hardware complexity of the Module as a single-type IP-core in the FPGA-architecture of the Virtex-6 family, we have evaluated the function delay time and the hardware complexity of a device implementing the pipelined computing of a two-dimensional FFT accompanied by time decimation on DPAS. Relevant estimates for the Module were executed using a special-purpose FPGA CAD, ISE Design Suite 14,7.

A set of single-type IP-cores implementing the two-dimensional FFT allows the implementation of the two-dimensional FFT when placing on the DPAS elements. The estimates of the two-dimensional FFT implementation time have been obtained, depending on the number of FPGAs included in a given DPAS, on the number of Modules implemented on a single FPGA, on the number of timed pulses, within which the Module implements the transform represented as (4), and on the duration of the said timed pulses.

The results obtained in this study allow us to estimate the potential implementation of a two-dimensional FFT on DPASes, both existing and promising ones.

6. References

[1] Gonzalez R C, Woods R E 2007 *Digital Image Processing* (Prentice-Hall) p 976
[2] Dudgeon D, Mersereau R and Merser R 1983 *Multidimensional Digital Signal Processing* (Prentice Hall) p 400
[3] Bailey D H 1988 A High-Performance FFT Algorithm for Vector Supercomputers *International Journal of Supercomputer Applications* **2(1)** 82-87
[4] Cooley J W and Tukey J 1965 An algorithm for the machine calculation of complex Fourier series *Math. Comput.* **19** 297-301
[5] Dordopulo A I, Kalyaev I A and Levin I I 2010 High-Performance Reconfigurable Computer Systems *Supercomputers* **3(3)** 44-48 (in Russian)
[6] Virtex-7. Highest Performance and Integration at 28 nm 2017 (Xilinx, Inc.) URL: https://www.xilinx.com/products/silicon-devices/fpga/virtex-7.html
[7] Shalagin S V 2004 Computer evaluation of a method for combinational-circuit synthesis in FPGAs *Russian Microelectronics* **33(1)** 46-54
[8] Shalagin S V 2016 *Implementing digital devices in FPGA architecture when using distributed computing in Galois fields* (Kazan, KNRTU-KAI Press) p 228 (in Russian)
[9] Raikhlin V A, Vershinin I S, Gibadullin R F and Pystogov S V 2013 Reliable Recognition of Masked Binary Matrices. Connection to Information Security in Map Systems *Lobachevskii Journal of Mathematics* **34(4)** 319-325
[10] Gibadullin R F, Vershinin I S and Minyazev R Sh 2018 Development of Load Balancer and Parallel Database Management Module *4nd International Conference on Industrial Engineering, Applications and Manufacturing*

[11] Gibadullin R F, Vershinin I S and Minyazev R Sh 2017 Realization of replication mechanism in PostgreSQL DBMS *International Conference on Industrial Engineering, Applications and Manufacturing*
[12] Raikhlin V A, Vershinin I S, Gibadullin R F and Pystogov S V 2016 Reliable Recognition of Masked Cartographic Scenes During Transmission over the Network *International Siberian Conference on Control and Communications (SIBCON)*
[13] Pavelyeva E A 2018 Image processing and analysis based on the use of phase information *Computer Optics* **42(6)** 1022-1034 DOI: 10.18287/2412-6179-2018-42-6-1022-1034

Acknowledgements
This work was supported by RFBR Grant 18-01-00120a, "Specialized devices for generating and processing data sets in the architecture of programmable logic devices class FPGA."
The authors also acknowledge L.Yu. Bakiev and I.A. Pesoshin, master's students at KNRTU-KAI, for their help in obtaining experimental data.

Blockchain technology in the pharmaceutical supply chain: researching a business model based on Hyperledger Fabric

S R Bryatov[1], A A Borodinov[1]

[1]Samara National Research University, Moskovskoye shosse, 34, Samara, Russia, 443086

e-mail: aaborodinov@yandex.ru

Abstract. Pharmaceutical companies that manufacture, ship and supply products face difficulties in tracking their products, allowing counterfeiters to inject counterfeit drugs into the system. This situation is observed, in particular, in the Russian market of turnover of pharmaceutical products, although the problem has long been global. The ability of blockchain systems to pinpoint the origin of data makes them particularly suitable for pharmaceutical supply chain applications. The data stored in the blockchain distributed register on the identification of drugs produced by the plant, as well as records of their movements throughout the supply chain, can accurately determine the authenticity of pharmaceutical products lying on the shelves of pharmacies. The development and implementation of such a system can be a big step towards winning the exhausting fight against the easy availability of counterfeit drugs and medical products. In the first part of this work, the main characteristics and features of the functioning of blockchain systems will be studied. In the second and final part, the designed concept of the pharmaceutical turnover control system based on the blockchain technology Hyperledger Fabric using the Hyperledger Composer development environment will be investigated.

1. Introduction

In a recent report by the world health Organization, drug counterfeiting has been identified as a global problem. It estimates that in low- and middle-income countries, every 10th drug in market circulation is counterfeit or has a poor quality [1]. The use of such substandard products may have a negative impact on the mortality rate.

Medicines move through a supply chain in which several participants participate. These usually include the manufacturer, wholesaler and retailer. They are engaged in the production, transportation and sale of these products. Also in these systems, there is a key participant - the regulating authority responsible for each stage of the movement of batches of products throughout the chain. In particular, at the state level, this participant may be some authorized body of the state apparatus, for example, a special Agency for the control of turnover of medicinal products. Its main task is to delegate the rights to manufacture medicines according to state standards, as well as to control the movement of all units of goods ever produced.

As for the consumer, there is another problem - the control of drugs, issued only by prescription. Dispensing without a prescription is illegal, however, the control of honesty of retailers, as well as with counterfeit medicines, is not easy and requiring a special approach.

Some pharmaceutical companies have already started implementing blockchain technology in drug supply chain management [2]. Blockchain is an electronic cryptographic registry based on a decentralized network model in which information is distributed and synchronized between all nodes in the network. This functionality is provided by a consensus algorithm deployed in the system to eliminate the problem of duplicate transactions, allowing nodes to verify the truth of information before it is directly written to the registry. In addition, this system has a high fault tolerance. The threshold for the number of failed nodes before a complete network failure depends on the total number of nodes connected to the network. Thus, the more nodes are functioning in the blockchain network, the less the probability of a complete system failure.

A properly designed system based on blockchain technology can significantly simplify the process of drug turnover control for authorized state bodies [3-5]. At the same time, a decentralized approach has a number of advantages that increase the information security of such systems compared to centralized counterparts [6].

In section 1 of this work, the main characteristics and methods of functioning of blockchain systems will be studied. Section 2 is devoted to the study of the concept of the designed system for the control of drug turnover with regulation at the state level.

2. Blockchain networks

2.1 Blockchain technology

Blockchain is a continuous chain of blocks containing information built according to certain rules. Most often, copies of block chains are stored on many different computers independently of each other. [2]

The set of such computers assembled into a network operating under a single Protocol for adding new blocks to the chain, i.e. for conducting transactions, forms a Blockchain network [3].

Thus, the Blockchain network is a distributed information system that contains information about all transactions ever performed in the past and working on a pre-selected Protocol that determines the course of conducting and validating transactions, and the work of the entire network and its participants [4]. In addition, this network is usually called a distributed registry, as data about each transaction of such a network is stored on each node operating in it.

There are three types of blockchain systems:

1. Public Blockchain (Permissionless Blockchain)
2. Consortium Blockchain
3. Private Blockchain

In the public blockchain, each participant has the opportunity to see and verify any transaction taking place on the network, and can also participate in the consensus-building process. There is no administrative node in the public blockchain that checks transactions, the validity is achieved by consensus between the participants. Bitcoin and Ethereum are vivid examples of this type of networks.

In the consortium blockchain there is an administrative node, which is selected by the network participants initially based on the optimal ways to achieve their business goals, for example, in the case of a partnership. Data in such networks can be public and private (for example, confidential information), so the network itself can be regarded as partially decentralized. An example of such a network is the Hyperledger platform.

A private blockchain is similar to the previous type except for one aspect. All data of such a distributed registry is strictly closed to the public. Only members authorized by the administrative node can access the information stored on blockchain. Multichain or Hyperledger platforms can be used to build such solutions [5][6].

The choice of a particular type of network depends on the task. For example, for small businesses where accounting is maintained by a separate institution, a suitable option would be to use a private blockchain network in which a distributed registry would become a single source of truth. However, in a situation, for example, with the supply chain, where the consumer wants to know everything about the product, a consortium network will approach. Product data would be available to read by all

participants, but only authorized nodes, for example, the seller, the factory and the supplier of raw materials, may record it.

2.2 Functioning of blockchain systems. Consensus mechanisms.

A group of transaction in blockchain networks are combined into blocks of transactions that are connected to each other in the chain using the hash of the record of the previous block (figure 1).

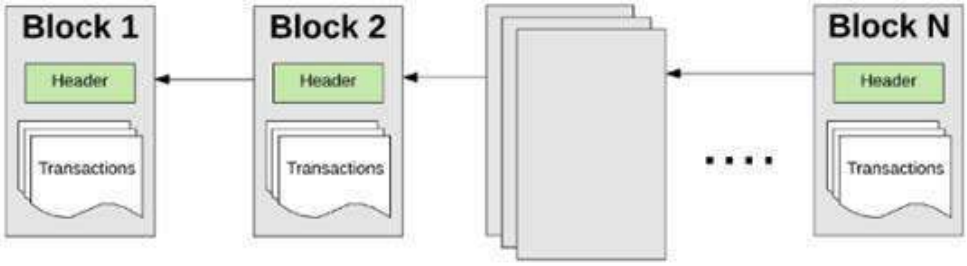

Figure 1. Blockchain systems chain structure

Thus, the basic security mechanism of blockchain networks is implemented as a property of immutability. The farther the block is located along the chain (the older it is), the more protected from changes is the data enclosed in it. If an attacker tries to modify any of the blocks, the local registry will automatically cease to be valid, because the hash values inside the headers of the next blocks will be completely different, based on the mechanism of hash functions.

The Blockchain system does not require a trusted third person for reliable registration of the transaction in the registry. Instead, decentralized consensus mechanisms are used to ensure that transactions are properly executed. In existing blockchain networks, the following are among the most popular [13]:

1. Proof of Work (PoW)
2. Proof of Stake (PoS)
3. Practical Byzantine Fault Tolerance (PBFT)
4. Delegated Proof of Stake (DPoS)

In practice, solutions might also be a combination of such mechanisms.

In the framework of the study we will focus on the algorithm Practical Byzantine Fault Tolerance (PBFT), which is based on the well-known problem of Byzantine generals [14]. To reach agreement in the network, this algorithm assumes that no more than 1/3 nodes will be unfriendly. The whole process can be divided into three stages: pre-training, prepared status and consensus-building. At each stage, a node enters the next phase if it receives votes from more than 2/3 of all nodes. Therefore, PBFT requires that each node is pre-known in the network. As a result, the final decision on the validation of the block is given to the third nodes trusted by the results of the general voting process.

The Hyperledger Fabric platform[15], which will be discussed in the next Chapter, uses PBFT as a consensus algorithm.

3. Designing the information system of drug turnover control

3.1 Hyperledger Fabric platform

The state plays a key role in the supply chain of medicines, as a universal regulator of interaction between the participants of the system. Only the state has the right to establish norms of relations between organizations and consumers, as well as only its bodies can be engaged in the registration of medicines and the issuance of licenses for their production, as well as the sale and issuance of prescriptions. Therefore, when designing a system for controlling the circulation of medicines, it was decided to take a private model of the blockchain network and make it administrated by some state-controlled agency. Thus, the Hyperledger Fabric platform, which offers a wide range of tools for building solutions based on private blockchain networks, became the basis of this project.

Because Hyperledger Fabric-based networks are private, all of their nodes have different roles in the system. There are three types of such nodes:

- Client peers. They are end users and have the right to place a transaction execution order.
- Endorser peers. This type of node manages the execution and validation of transactions. However, not all nodes of this type are directly involved in the execution of the code of smart contracts [16-18]. To do this, there are special nodes-guarantors, which are selected based on the terms of the contract.
- Ordering peers. Are engaged in formation of blocks of transactions and updating of the state of the distributed register. Also used in the configuration of the transaction by the network administrators. Created to simplify the change of consensus algorithm in the network if necessary.

The current project is based on the Hyperledger Composer framework, created to simplify the development of blockchain-based systems based on Hyperledger Fabric. With it, you can get a single system configuration file, which can then be used by the administrator to reprogram the behavior of the entire network. Four different sources are required to successfully create the configuration:

1. Model files.
2. Transaction scripts.
3. Access control lists.
4. Query scripts.

Model files define the structure of the main entities that are created in the distributed registry: assets, members, and transaction descriptions. Assets are digital property and documents, in this case it can be units of medicines, licenses and contracts between the participants of the turnover. Participants are the assets that contain basic information about the users of the system and their belonging to other assets.

Transaction scripts describe smart contract code (chaincode) executed by proxy nodes. In this framework, scripts should be written in the popular JavaScript language.

Access control lists define the rights of participants to access certain system resources, to read, write, and modify assets, as well as to execute the both system transactions and transactions created based on transaction scripts.

Using query scripts, data can be easily extracted from the blockchain registry. They are usually used to display data in front-end applications or in the code of generated transaction scripts, thereby increasing the efficiency of re-use of already developed code.

3.2 Architecture of the proposed solution

The following diagram shows the interaction of network participants with the designed distributed registry.

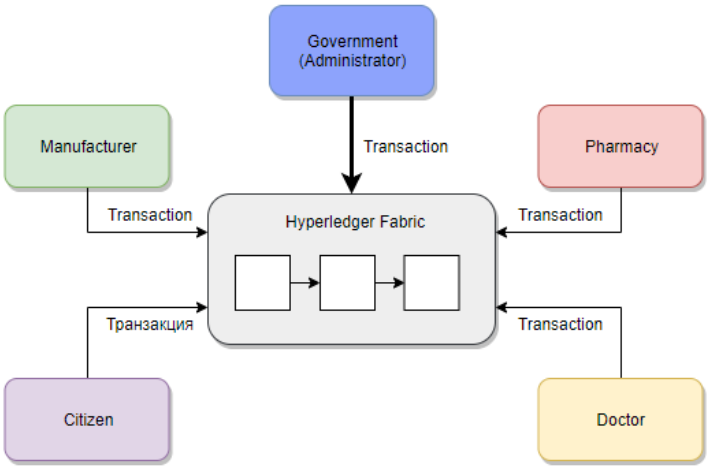

Figure 2. The information exchange participants

Each member of the system has its own specific rights to read data from the registry and perform transactions to modify it. To access a member card, the client application operator must be identified in the system based on private and public keys.

Thus, the following types of information exchange participants can be distinguished in the developed system:

1. Government. It is both the administrator and the developer of the network and it owns all registry nodes. The Government account has the ability to register the other members of the network and make transactions for the issuance of licenses for the production of drugs to manufacturers. It also registers new drugs in the information system.

2. Manufacturer. Produces goods and takes orders from the pharmacy. The manufacturer's account has the ability to register units of medicines in the system based on a unique identifier (uuid), as well as to create transactions on the transfer of ownership of a unit of medicine to the pharmacy.

3. Pharmacy. Sells goods to citizens. Pharmacy account has the ability to create a transaction for the transfer of ownership of drugs to the citizen. If the drug is available without a prescription, make a note of the fact that the drug was sold, in another case, undertakes to pay to the registry information about the sale of drugs to the citizen, the account which has the right to buy a certain type of medication. The transaction is approved by the nodes if there is a doctor's prescription in the system with a link to this type of medicine and the buyer's account, as well as the number of possible purchases of units of drugs in the prescription is greater than 0. With each sale, this counter decreases.

4. Doctor. Writes a prescription to his patients (citizens), in which he makes a mark on the types of drugs and their quantity necessary for healing, as well as a link to the citizen's account and enters these data in the distributed register of Hyperledger Fabric.

5. Citizen. When buying prescription drugs, must present his virtual ID, referring to his account in the state register. Thus, the end of the lifecycle of the drug unit resource in the system is a mark by the pharmacy on the sale of a certain unit in the virtual doctor's prescription, as well as a mark on the unit of the drug of the last owner - a Citizen or the Government, if the drug was sold without a prescription.

The following is a simplified relational model of connections between the system assets (figure 3):

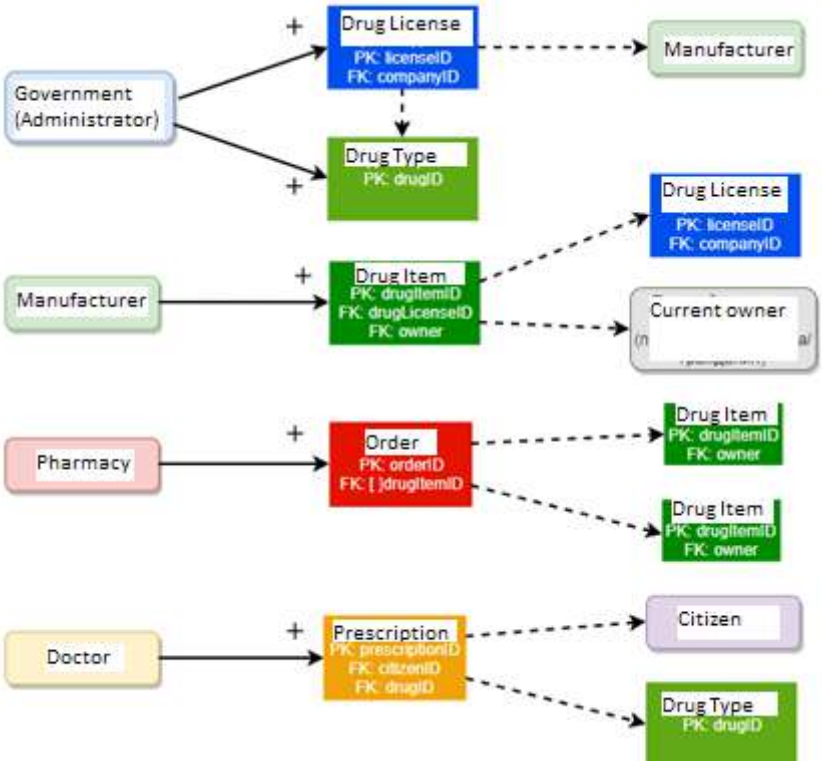

Figure 3. Simplified relational model of the proposed solution.

The arrows with the “+” sign in the diagram above define transactions that create a specified asset by a specific network member. Dashed arrows indicate the relationship between the assets by the foreign key.

3.3 Principles of operation of the designed information system. Strengths and weaknesses

The drug control system is still under development, so it is not possible to provide a final list of the main transactions of the system at this stage. However, we can distinguish the main ones, giving an approximate picture of the functioning of the working prototype. For clarity, we will follow the full lifecycle of the pharmaceutical product:

1. The Governement develops the specification of the medicinal product and registers the new medicinal product in the distributed register by means of the transaction of creation of the “Type of medicinal product” asset. In order to enable production, it also registers a “production License” and issues it to the registered participant-manufacturer, indicating a link to his account. If it revokes a license, a transaction marks the license as “invalid”. There is also a need for a transaction to prolongate it.

2. The Manufacturer creates a “Medicine”, identifying it with a unique code, puts a link to the “Type of medicine” and fills in the fields on the expiration date.

3. The Pharmacy produces the “Order” and notes the amount of the desired product and its type. During the execution of the order, the manufacturer binds to this asset links to the unique unit numbers of the goods from the warehouse. It also makes transactions to change the status of the order. Upon delivery, the "owner” field on the drug unit becomes equal to the ID of the recipient, i.e. pharmacy.

4. The Doctor writes out a “Prescription” to his patient. A Citizen buys medicine, providing his digital medical policy, which in this case is tied to the asset of his account. It also contains a link to the provided recipe. In the pharmacy, a sale transaction takes place, which becomes successful only in the case of the non-zero balance of the counter for this type of drug in the client's prescription. The Citizen becomes the owner of both real and virtual unit of medicine.

Thus, each licensed unit of medicine leaves a unique trace in the register, which can be easily tracked in the event of disputes.

The application of this system in practice should simplify the process of control over the official supply chains of medicines. Transparency of the system will motivate its participants to comply with the rules established by the law.

The weaknesses of this project include the following limitations:

- The proposed system is able to detect only the movement of drugs, which follow an official supply chains, which are known to the regulatory agency. It cannot track counterfeit drugs that are distributed along routes outside the official chains.
- The proposed system will be developed and tested in a controlled simulated network; therefore, the results of the following studies may not reflect actual performance in real-world deployment.

4. Conclusion

At this stage, a relational model is implemented, the main participants of the system and their roles are thought out. Development of the project continues. The next stage will be the development of smart contract transaction scripts and access control lists. After completing the development of a prototype model of the system, it is expected to conduct several tests on virtual machines running Ubuntu 18.04. If successful, the next step will be the creation of a front-end architecture for easy access of users to the designed system.

Blockchain technologies are still quite young and it is impossible to say with accuracy whether they will take root in the future due to many of their conceptual limitations. However, such studies, as a system of control over the circulation of medicines, can later become an example for the emergence of more advanced solutions for automating the processes of the state apparatus with the maximum level of information security on the processing of data.

5. References

[1] World Health Organization. 1 in 10 medical products in developing countries is substandard or falsified: WHO urges governments to take action URL: http://www.who.int/en/news-room/detail/28-11-2017-1-in-10-medical-products-in-developing-countries-is-substandard-or-alsified

[2] Kim H M and Laskowski M 2018 Toward an ontology-driven blockchain design for supply-chain provenance *Intelligent Systems in Accounting, Finance and Management* **25** 18-27
[3] De Filippi P and Hassan S 2016 Blockchain technology as a regulatory technology: From code is law to law is code *First Monday* **21**
[4] Bocek T, Rodrigues B B, Strasser T and Stiller B 2017 Blockchains everywhere - A use-case of blockchains in the pharma supply-chain *Proceedings of the IM IFIP/IEEE International Symposium on Integrated Network and Service Management* 772-777
[5] Rodrigues U R 2019 Law and the blockchain *Iowa Law Review* **104** 679-729
[6] Plotnikov V and Kuznetsova V 2018 The Prospects for the Use of Digital Technology "blockchain" in the Pharmaceutical Market *MATEC Web of Conferences* **193**
[7] Wikipedia, Blockchain URL: https://en.wikipedia.org/wiki/Blockchain
[8] Dennis R, Owenson G and Aziz B 2016 A temporal blockchain: A formal analysis *International Conference on Collaboration Technologies and Systems* 430-437
[9] Singh S, Singh N 2016 Blockchain: Future of financial and cyber security *2nd International Conference on Contemporary Computing and Informatics* 463-467
[10] Hackernoon URL: https://hackernoon.com/3-popular-types-of-blockchains-you-need-to-know-7a5b98ee545a
[11] Zheng Z, Xie S, Dai H, Chen X and Wang H 2017 An Overview of Blockchain Technology: Architecture, Consensus, and Future Trends *IEEE 6th International Congress on Big Data, BigData Congress* 557-564
[12] Sylim P, Liu F, Marcelo A and Fontelo P 2018 Blockchain technology for detecting falsified and substandard drugs in distribution: Pharmaceutical supply chain intervention *Journal of Medical Internet Research* **20**
[13] Zheng Z, Xie S, Dai H, Chen X and Wang H 2016 Blockchain challenges and opportunities: A survey *Internat. J. Web Grid Serv.*
[14] Wikipedia, Byzantine fault tolerance URL: https://en.wikipedia.org/wiki/ Byzantine_fault_tolerance
[15] Hyperledger Project URL: https://www. hyperledger.org/
[16] Werbach K and Cornell N 2017 Contracts ex machina *Duke Law Journal* **67** 313-382
[17] Casado-Vara R, González-Briones A, Prieto J and Corchado J M 2019 Smart Contract for Monitoring and Control of Logistics Activities: Pharmaceutical Utilities Case Study *Advances in Intelligent Systems and Computing* **771** 509-517
[18] Jaccard G O B 2017 Smart contracts and the role of law *Jusletter IT*

The words separation in old Cyrillic texts with fuzzy search method

M N Mokrousov[1]

[1]Kalashnikov Izhevsk State Technical University, Studencheskaya str., 7, Izhevsk, Russia, 426069

e-mail: maxmok@mail.ru

Abstract. The article describes a solution to the problem of word separation in old Cyrillic texts after the stage of graphic character recognition on scanned documents. The article proposes an algorithm for fuzzy text search using the grammatical dictionary of the Old Russian language, with the completeness and accuracy of search results evaluate. To assess the relevance and ranking of the search results, a method for calculating the rank of the symbol recognition variant based on the TF-IDF metric is developed. The article also presents a software system of automated word search, presents the results of experiments that prove the effectiveness of the developed algorithms and programs.

1. Introduction

The urgency of the task of translating ancient Cyrillic manuscripts from graphic representation into text form is due to their exceptional value for historical and linguistic research, which is most effective using the methods of automatic text analysis and recognition of electronic-graphic representation of manuscripts. For maximum process digitization automation of ancient texts requires the involvement pattern recognition methods. A relatively small publications count on recognition systems of handwritten and old-printed Cyrillic texts of the X–XVIII centuries suggests the need to improve methods and technologies to solve this problem.

Almost all researches on the problem of historical documents recognition, says that the existing commercial OCR-system (Optical Character Recognition) do not cope well with the recognition of ancient texts. Researchers from Macedonia [1-2] proposed two ways of recognizing old-printed Cyrillic symbols: on the basis of decision trees and by fuzzy classification. Both methods operate with statistical and simple structural features of symbols. The experimental system recognizes symbols in each method with an average accuracy and completeness of 70-80%. The reducing issue of the recognition result based on information about neighboring characters (the use of a dictionary, etc.) in the work is not affected. In [3] the optical recognition of historical texts is made by whole words, not by individual symbols. At the same time, the recognition process is adaptive; during the work it adjusts itself to the processed historical document. The book of the XVIII century, written in the old German Gothic script, the developed software system correctly recognized 86.6%, which is 4.1% higher than the traditional OCR-system. In [4] the search system in text images produces a pre-selection of words in the archival texts, using such parameters as the minimum possible row height,

margins, relative threshold of the brightness of the background in a separate line, etc. Search in the text based on comparison of the sample image with all images words or symbols that are pre-allocated by the system. The estimation of word images similarity is based on the calculation of the modified Hausdorff distance [5]. It is indicated that the search process takes a long time due to the high computational complexity of the comparison based on the Hausdorff distance.

In [6] describes the automatic text recognition capabilities of neural network models specifically trained to recognize different styles of Church Slavonic handwriting within the software platform Transkribus. Computed character error rates of the models are in the range of 3 to 4 percent; real-life performance shows that specifically trained models, basically, recognize simple (non-superscript) characters correctly most of the time. Error rate is higher with superscript letters, abbreviations, and word separation.

In our opinion, the approaches of word recognition are poorly applicable to Cyrillic texts, because in these texts words are not separated from each other, and there is a relatively large distance between the letters. The individual words selection in such texts is not an easy task. To automatically solve this problem, it is necessary to recognize individual characters, conduct lexical and syntactic analysis of the document.

This paper describes the stage of "Clarify with a dictionary" after graphic recognition of individual characters stage, described in [7]. This step involves the use of fuzzy algorithm to search the dictionary of different combinations of characters variants and the subsequent automated words and symbols selection.

One of the most suitable search methods in this case is the pattern search algorithms, which belong to the group of search methods for substring in a string. For example [8-9] describes and includes implementations the most famous of them: Knuth–Morris–Pratt (KMP) algorithm, Boyer–Moore string-search algorithm, Rabin–Karp algorithm and etc. The use of regular expressions allows expanding the capabilities of the standard text search. In [10] presents two new techniques for regular expression searching, which permit fast searching for regular expressions than any existing algorithm. In this paper the main focus is on the speed of search but not quality.

Almost all fuzzy search algorithms have software implementations in different programming languages. For example, this site [11] provides fuzzy string search tools in text and dictionary written in Java. It contains the most commonly used algorithms and auxiliary utilities for fuzzy string search in large dictionaries. The site includes implementations for Levenshtein Distance, Damerau-Levenshtein Distance, Extension (Spell-checker) Method, N-Gram Method, Signature Hash Method, Bitap, Burkhard-Keller (BK) Trees, Skip algorithm.

However, full borrowing of software solutions to solve the problem is difficult for several reasons, which were identified by the author personally as the analysis result scanned manuscripts on the project *Manuscripts.ru* [21].

First, old-printed Cyrillic texts do not have delimiters (punctuation marks), which complicates the process of singling out individual words in the source text. The maximum length of a word in the dictionary is 26 characters, the minimum is 1 character, which can mean a number. The number of variants for each symbol after graphic recognition can be in the range from 1 to 6. Taking into account the maximum length of the word, the number of possible characters chains, taking into account the maximum length of 26 characters, is determined by the combinatory product rule of probability theory. In this case, the maximum number of search queries for one potentially long word only will be 6^{26}, which is unnecessarily much.

Secondly, after graphic recognition process of low quality images, with various spots, scuffs, page breaks, followed by gluing, the consequences of printed documents restoration, the result of recognition may have the following errors:

1) one character is recognized as two or three;
2) two or three consecutive characters are recognized as one;
3) omission of characters when the recognition program could not pick up the options; most often this case occurs in the presence of a dark spot or scratches;
4) there is no correct variant in the sequence of character recognition probabilities;
5) the word is not in the dictionary.

At the moment, these "noise" problems can be solved only with the use of manual editing the graphic recognition results.

Thirdly In Slavonic-Russian manuscripts simple or alphabetic titles abbreviations are used and such abbreviations are difficult for analysis and search. Such abbreviations were most often used to refer to words related to God and the Church (God, Amen, Trinity, etc.), as well as to other words (maiden, wisdom, memory, etc.).

Fourth, it is necessary to take into account the morphological rules of character conversion and replacement. These are different rules for equating individual letters and their variants or letter combinations at the end of the word form, after certain vowels, consonants or taking into account the position of the characters in the text.

Fifth, a separate item that makes it difficult to fully automate the character recognition process is the presence of a drop cap (initial) – the first capital letter of the text or Chapter, depicted as the miniature.

Author decided to use a recursive search method based on regular expressions, which would take into account the symbol position in the word when evaluating the search relevance. Such fuzzy *positional* search will allow to abstract from possible graphic recognition *errors* and give more freedom to the expert who manages the search.

2. Fuzzy "positional" dictionary search algorithm

To reduce the number of symbols variants obtained after the graphic recognition stage, it is necessary to search for words in the grammatical dictionary of the Old Russian language created within the framework of the project *Manuscripts.ru* [12]. For this purpose, a recursive search algorithm based on regular expressions is used.

2.1. Pre-processing of the input text

The input text is a sequence of characters with variants after graphical recognition. Each character is represented by the following structure:

<Symbol>::=‘[’[<Coordinates>’,’{<Value Variant>’;’}]’]’

<Coordinates>::=<X>’,’<Y>’,’<Width>’,’<Height> *<Variant Value>::=<Value>’,’<Relevance>[’,’<Number_diactric>],*

where *<Coordinates>* are the coordinates of the rectangular area in which the symbol is enclosed in the original image; *<X>,<Y>* are the upper left corner coordinates of the symbol rectangular area in the image; *<Width>,<Height>* are the width and height of the rectangular area of the symbol in the image; *<variant Value>* is the variant of the symbol value; *<Value>* is the percentage of the variant relevance after the graphic recognition stage; *<Number_diactrika>* is the number of previous characters, which is covered by the diactric symbol.

Example:

[(422,1281,64,71),в,89;б,92;г,98;н,81;п,80][(506,1280,50,70),л,97;а,94;в,83;,82]

[(473,1316,72,18)◌̀,100,2][(583,1268,17,18),,78][(0,0,0,0),]

As you can see, the text may contain diactric symbol:

[(473,1316,72,18)◌̀,100,2]

In this case, after the relevancy percentage indicates how much the previous characters covered by this accented character. Also, there may be omissions of characters that could not be determined after graphic recognition stage.

The source text is converted to a table form, where each table column contains variants of the symbol value. The columns number is equal to the characters number.

2.2. Generation of regular expressions and a recursive search in the dictionary

The next is the regular expressions generation and recursive search in the dictionary. This step analyzes variant characters combinations from 1 to 10 (configured in the search options). Each combination is a regular expression that is inserted into the SQL-query:

*SELECT * FROM Dictionary WHERE word like N'[нн]|[сс]|[к]|[сс]|[ннп]'*

The result of the query is a words set found by this expression. If the words count is greater than the threshold value (the default is 100), this result is not considered.

The input to the search algorithm

$Table is an characters variants array after the graphic recognition that are received from the original text;

|$Table| is the number of characters in the input text.

$maxWordLength is the maximum length of the considered symbols combinations.

$maxWordCount is the maximum words count in the query result.

The output

$Result is the resulting array with words sets for each character.

The main dictionary search cycle

```
$b ← 0
$e ← 0
Repeat
{
        RecognizeNextWord( $b, output $e);
        $b ← $e;
} While ($b < |$Table|);
```

Recursive search function

```
RecognizeNextWord( $b, output $e)
{
        $d ← $e – $b + 1;
        While (($d <= $maxWordLength) AND ($e < |$Table|))
        {
                $reg ← GenerateRegularExpression($b, $e);
                $symbol ← $Table[$b];
                if (IsQueryResultAlreadyExists($reg, $symbol) = FALSE)
                {
                        $res ← ExecuteQuery($reg, $symbol);
                        SaveWordSet($res)
                        $Result ← $Result ∪ $res;
                        if (|$res| > 0) AND (|$res| <= $MaxWordCount))
                        {
                                $e2 ← $e +1;
                                RecognizeNextWord($e + 1, output $e2);
                        }
                }
                $e++;
                $d ← $e - $b + 1;
        }
}
```

where *$b* is the character index from which the scan starts;

$e is the character index that ends the scan;

$d is the current length of the scanned character combination;

$reg is the regular expression for the current character combination;

$symbol is the first character of the current combination;

$res is the words set of the current symbols combinations;

GenerateRegularExpression($b, $e) is a function that returns a regular expression for the current character combination;

IsQueryResultAlreadyExists ($reg, $symbol) is a function that returns *True* if for the regular expression *$reg* and the symbol *$symbol* already exists a words set, and *False* otherwise;

ExecuteQuery($reg, $symbol) is a function that searches words in the dictionary by the regular expression *$reg* and the first character *$symbol* and returns a words set;

SaveWordSet($res) is a function that saves a words set *$res* in working memory.

After executing the main algorithm, an array with sets of words for each character combination not exceeding the set threshold will be formed.

Thus, the fuzzy search algorithm consists of two main steps:

1) the original text transformation into table form;

2) the recursive search in the dictionary for character variants combinations using regular expressions.

3. Reducing the number of character recognition options based on the fuzzy search algorithm

The variants number reducing method after graphic character recognition based on the fuzzy search algorithm results is to assess the relevance of the symbols variants by calculating the weights of each symbol variant on such data as:

- frequency of the symbol occurrence in the fuzzy dictionary search results;
- frequency of the symbol occurrence in the fuzzy dictionary search results, taking into account the position in the word and the length of the word;
- frequency of the symbol occurrence in the dictionary;
- frequency of the symbol occurrence in the dictionary, taking into account the position in the word and the length of the word.

The metric TF-IDF [4] adapted for this task is used to calculate the weight of the variant. It was proposed to use a symbol variant (hereinafter the symbol) as a word in this metric, and sets of words as documents. Thus, SF (symbol frequency) – the symbol importance, in the context of the word sets in which the symbol participated, is estimated by the formula:

$$SF(s,W) = \frac{\left|(s \in w_i)\right|}{\left|W\right|},$$

where $|s \in w_i|$ is the occurrences count of a character s in a set of words derived from regular expressions involving this character; $|W|$ is the total words count in the sets obtained from regular expressions involving this character. IDF (*inverse dictionary frequency – inverse frequency of the dictionary*) is the inversion of the frequency which some character s occurs in the dictionary D. There is only one *IDF* value for each character within the dictionary:

$$IDF(s,D) = \log\frac{\left|D\right|}{\left|(s \in d_i)\right|},$$

where $|D|$ is the words count in the dictionary (1846721); $|s \in d_i|$ is the dictionary words count in which the symbol s occurs.

In order to take into account the position p of the symbol s and the length of the words l in the sets W, in which the symbol in question is present, the calculation formulas *SF* and *IDF* can be written as follows:

$$SF(s,W,l,p) = \frac{\left|(w_i(l,p,s) \in W)\right|}{\left|(w_i(p,s) \in W)\right|},$$

where $w_i(l,p,s)$ is the *i-th* word in sets W of length l at position p of which stands the symbol s; $w_i(l,p,s) \in W$ is the words count $w_i(l,p,s)$ in the sets W; $w_i(p,s)$ is the *i-th* word in sets W at position p of which stands the symbol s; $w_i(p,s) \in W$ is the words count $w_i(p,s)$ in the sets W.

$$IDF(s,D,l,p) = \log\frac{\left|(d_i(s,p) \in D)\right|}{\left|(d_i(s,p,l) \in D)\right|},$$

where $d_i(s,p)$ the *i-th* word of the dictionary *D* at position *p* of which stands the symbol *s*; $|d_i(s,p) \in D|$ is the words count $d_i(s,p)$ in the dictionary *D*; $d_i(s,p,l)$ is the *i-th* word of the dictionary D of length *l* at position *p* of which stands the symbol *s*; $|d_i(s,p,l) \in D|$ is the words count $d_i(s,p,l)$ in the dictionary *D*.

Thus, the weight (relevance) of a symbol is estimated in two ways:

1) based on the character occurrences count in word sets derived from regular expressions involving that character:

$$Weight(s) = SF(s,W) * IDF(s,D)$$

2) taking into account the symbol position and the words length in the sets in which the analyzed symbol is present:

$$Weight(s,l,p) = IDF(s,D,l,p) * SF(s,W,l,p)$$

So, in word sets *W*, the symbol *s* can occur at different positions *p* in words of different lengths *l*, the total weight of the symbol, taking into account these parameters, is calculated as the sum of the weights:

$$WeightSum(s,l,p) = \sum_{i=1}^{n} Weight_i(s,l,p),$$

where *n* is the number of weights of the symbol *s*, taking into account the different positions and the word length in the word sets in which the symbol participates.

The total symbol variant weight is calculated as the sum of the weights, taking into account the symbol occurrences count in the word sets and taking into account the position and length of words:

$$WeightTotal(s) = Weight(s) + WeightSum(s,l,p)$$

The next, the $Rank(s_i)$ of each s_i variant of the symbol *s* is calculated as the ordinal number in the variant weights array sorted in descending order. For each symbol variant, there are tree ranks calculated for each weight: $Rank(Weight(s_i))$, $Rank(WeightSum(s_i,l,p))$, $Rank(WeightTotal(s_i))$. Total rank *RankTotal* for the symbol variant is computed as the harmonic mean of the character variant ranks. Each character variant is ranked by accounting *RankTotal*. As the rank was calculated by the variant symbol position in the sorted weight arrays, the lower the rank, the higher the relevance.

4. Experiment description

The graphic recognition variants reduction of the text "Ostromir gospel" was carried out by the following method:

1) selected fragment of the text;
2) a fuzzy dictionary search was performed for the selected text fragment;
3) calculated weight and the symbols variants ranking on the basis of search results;
4) correct the characters variants were set by manual word confirmation found from the dictionary search results;
5) Precision, Recall and completeness were calculated and recorded in the table.

Figure 1. The "Ostromir gospel" fragment with graphic recognized symbols.

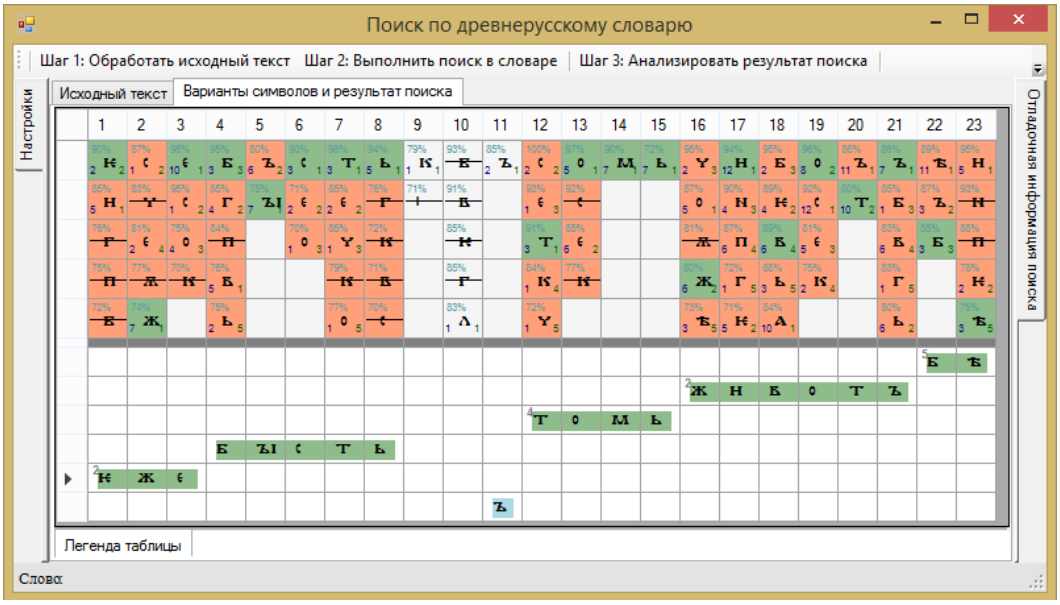

Figure 2. Analysis results of the text 9-10 lines "Ostromir gospel".

The words searching result in the dictionary after graphic recognized text (9-10 lines of "Ostromir gospel" [14], Figure 1), followed by confirmation of the words is shown in Figure 2.

The symbol variant rank is indicated in the lower right corner of the cell with the symbol variant, the variant occurrence frequency in the search results is shown in the lower left corner, and the graphic recognition relevance percentage is shown in the upper left corner. If the symbol variant does not occur in the found word sets, it is crossed out (frequency of occurrence – 0).

In the lower part of the table the words confirmed by the expert are highlighted in green. The number in the upper left corner of the word shows how many words were found in the dictionary by the combination of options (the words count in the set).

Figure 3 shows the process of assembling a sentence from words obtained by searching the dictionary and then confirming the correct word from the search results set. Each symbol and each word in the process of the software system operation can be viewed on the original image. During the sentence assemble the expert can manually add the missing characters and words.

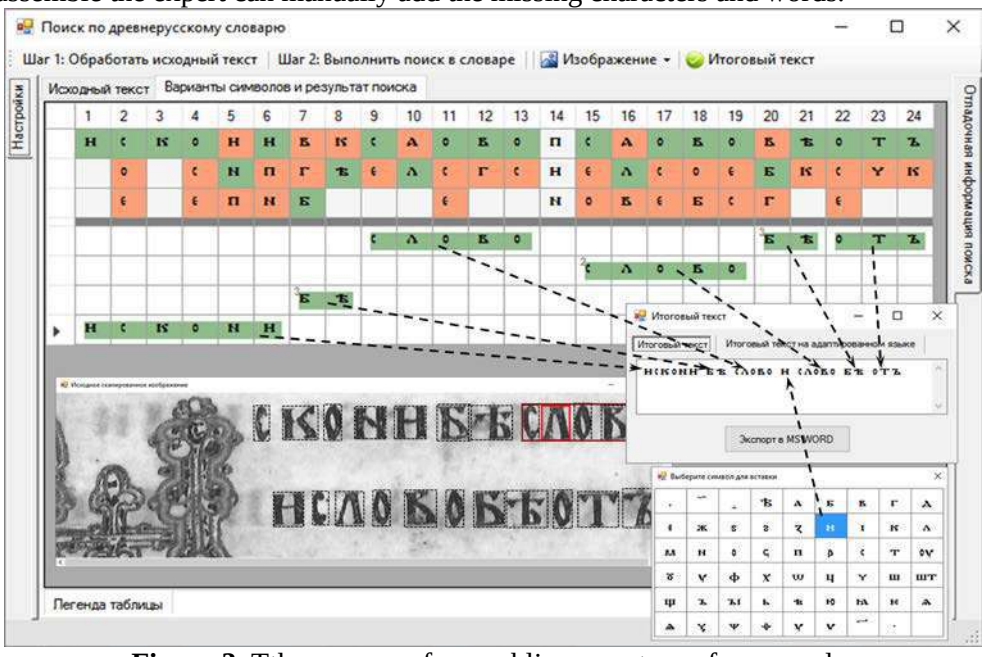

Figure 3. Tthe process of assembling a sentence from words.

The Precision and Recall of the reduction results were evaluated for the highest ranked options (1 and 2).

Let ***S*** be a set of options of characters from the input text; $S^+ \subset S$ is a subset of the symbols that have the highest rank; $S^+ \subset S$ is a subset of the symbols that were used in the formation of words sets (not the strikethrough options); $S^E \subset S$ is a subset of the characters that have been confirmed by the expert (highlighted in green); S' is a lot of characters in the input text (number of columns). In addition to Precision and Recall, the percentage of Reduction the number of symbol variants that did not participate in search queries was estimated.

$$Precision = \frac{\left|S^+ \cap S^E\right|}{\left|S'\right|},\ Recall = \frac{\left|S^+ \cap S^E\right|}{\left|S^E\right|},\ Reduction = \frac{\left|S\right| - \left|S^\Sigma\right|}{\left|S\right|}$$

Table 1. Precision and Recall of the results of reducing the variants character count.

Experiment №	Precision of up to 1 variant	Recall of up to 1 variant	Precision of up to 2 variants	Recall of up to 2 variants	Reduction
1	0.67	0.67	0.9	0.9	0.15
2	0.57	0.67	0.86	1	0.18
3	0.52	0.79	0.62	0.93	0.27
4	0.52	0.52	0.83	0.83	0.17
5	0.52	0.6	0.7	0.8	0.26
6	0.77	0.77	0.86	0.86	0.31
7	0.55	0.55	0.83	0.83	0.26
8	0.36	0.45	0.64	0.8	0.14
9	0.24	0.67	0.32	0.89	0.44
10	0.5	0.59	0.62	0.73	0.14
Average	0.52	0.63	0.72	0.86	0.23

The calculated parameters of Precision and Recall were summarized in a table (Table 1). The Precision and Recall of up to one variant means that only one symbol variant, whose rank is 1 and which is marked as correct by the expert advisor, was taken into account in the calculation. The Precision and Recall of up to two variants means that the calculation took into account two symbol variants with the highest rank, among which there is a variant marked as correct by the expert advisor.

5. Conclusion

The experiments conducted to reduce the symbols variants count based on the fuzzy search algorithm show that the proposed variants reducing method to one variant gives an accuracy rate of 52%, and completeness – 63%, to two variants – 72% and 86%, respectively. Given that one of the symbol variants was graphically recognized correctly, the completeness of reducing variants method in combination with graphic recognition results tends to 100%.

In the future, it is planned to conduct experiments with the use of N-grams, built according to the Old Russian dictionary and the results of expert search using the algorithm described in this article. Author hopes to obtain statistical data about frequency of the letter combinations in old Cyrillic texts, to obtain regularities of language models for old Cyrillic texts, which will improve the efficiency of words search and words selection in such texts.

6. References

[1] Klekovska M, Martinovska C, Nedelkovski I and Kaevski D 2012 Comparison of Models for Recognition of Old Slavic Letters *ICT Innovations* 129-139

[2] Bande C M, Klekovska M, Nedelkovski I and Kaevski D 2014 Feature Selection for Classification of Old Slavic Letters *Control Engineering and Applied Informatics* 16(4) 81-90

[3] Kluzner V, Tzadok A, Shimony Y and Walach E 2009 Antonacopoulos. Word-Based Adaptive OCR for Historical Books *Proceedings of the 10th International Conference on Document Analysis and Recognition* 501-505
[4] Kirov N 2008 A software tool for searching in binary text images *Pregled NCD* **13** 9-16
[5] Dubuisson M-P, Jain A 1994 A Modified Hausdorff Distance for Object Matching *Proc. 12th Int. Conf. Pattern Recognition* 566-568
[6] Rabus A *Recognizing handwritten text in Slavic manuscripts: A neural-network approach using Transkribus* URL : https://www.academia.edu/38835297
[7] Kuchuganov A V and Kasimov D R 2016 Automation of recognition of old-printed characters with the help of descriptive logic *Rašytinis palikimas ir skaitmeninės technologijos: VI tarptautinė mokslinė konferencija* (Vilnius; Iževskas) 104-109
[8] Borivoj M, Holub J and Polcar J 2005 Text Searching Algorithms. Volume I: Forward String Matching **1(2)** URL: http://stringology.org/athens/TextSearchingAlgorithms
[9] Introduction to Pattern Searching Algorithms *Tutorialspoint. The Biggest Online Tutorials Library* URL : https://www.tutorialspoint.com/introduction-to-pattern-searching-algorithms
[10] Navarro G, Raffinot M 2005 New Techniques for Regular Expression Searching *Algorithmica* **41(2)** 89-116 DOI: 10.1007/s00453-004-1120-3
[11] Fuzzy search tools *Google code archive* URL: https://code.google.com/archive/p/fuzzy-search-tools/
[12] The Portal "Manuscript" URL: http://manuscripts.ru/
[13] Jurafsky D and Martin J 2000 *Speech and Language Processing: An Introduction to Natural Language Processing, Computational Linguistics, and Speech Recognition* (New Jersey: Prentice Hall) p 934
[14] Ostromir gospel. Manuscript sheets *Russian national library* URL: http:// www.nlr.ru/exib/Gospel/ostr/ill.html

Acknowledgments
The author expresses gratitude to the Department of the information processing system staff from Kalashnikov Izhevsk State Technical University: Kasimov Denis Rashidovich, Kuchuganov Alexander Valerievich, Kuchuganov Valeriy Nikonorovich for valuable advice and recommendations, and preparation of experimental data.

Data-driven profiling of traffic flow with varying road conditions

O K Golovnin[1]

[1]Samara National Research University, Moskovskoe Shosse 34A, Samara, Russia, 443086

e-mail: golovnin@ssau.ru

Abstract. The article describes the road, institutional and weather conditions that affect the traffic flow. I proposed a method for traffic flow profiling using a data-driven approach. The method operates with macroscopic traffic flow characteristics and detailed data of road conditions. The article presents the results of traffic flow speed and intensity profiling taking into account weather conditions. The study used road traffic and conditions data for the city of Aarhus, Denmark. The results showed that the method is effective for traffic flow forecasting due to varying road conditions.

1. Introduction

Modern technical traffic control systems integrate the means of collecting, storing and analyzing data coming from various technical devices (vehicle sensors, radar detectors, video cameras, road weather stations) into a monitoring system. The monitoring system continuously takes into account a number of parameters: the speed and presence of vehicles, air and roadway temperature, speed and direction of the wind. The data collected in the automatic mode are used for adaptive control of the traffic flow using various traffic flow models, which allow the profiling of changes in the traffic flow characteristics from certain influences [2].

There are three classes of traffic flow models. The macroscopic model describes the traffic flow in terms of averaged characteristics [3]: density, intensity, average speed. With this approach, the traffic flow, moving along the road network, is modeled as a fluid movement [4]. Microscopic models describe the traffic flow as detailed as possible [5]: the movement of each vehicle is calculated individually. The microscopic model allows to achieve high adequacy of the traffic flow description compared to the macroscopic model, but it will require large computational resources [6]. An intermediate place is occupied by mesoscopic models [7], in which the traffic flow is described as consisting of an individual vehicle, but the characteristics of their movement are averaged. An important property of mesoscopic traffic flow models is based on both micro and macro indicators [8].

To study the behavior of traffic flow in various situations, the complexity of the traffic flow model is introduced by injecting additional parameters [9]. The described traffic flow models focus on the study of traffic flow in a separate straight section of the street-road network, while the cause of traffic jams, according to [10], are “bottlenecks” formed not only by the street-road network structure but also various road conditions. Therefore, it is important to use the traffic flow model that adequately describes the traffic flow behavior during the passage of “bottlenecks”.

For example, to study the behavior of the traffic flow when a density of saturation and congestion is reached, a parameter describing the passage time of the street-road network equal to the length of the vehicle moving with free movement speed is introduced [11]. For solving the tasks of ensuring traffic safety, an equivalent distance can act as an additional parameter, which decreases with increasing speed (at the same density), indicating the situation becomes more complicated. In [12], a traffic flow model was proposed, based on the Tanaka model, but taking into account the speed limit in the city to meet the safe traffic requirements. In [13], a prediction model based on the composition of machine learning and time series was proposed. In [14], an approach was proposed to take into account the influence of several static bottlenecks on the traffic flow.

With the growing number and composition of data used by modern innovative traffic management tools, traffic flow models should be modified [15]. Thus, traffic flow models begin to depend on data and be controlled by them (data-driven) [16]. The purpose of the work is to systematically analyze data obtained from various sources (traffic flow sensors, weather stations, video cameras, open media, etc.) to profile the impact of road, organizational and weather factors on the traffic flow characteristics.

2. Profiling of the road conditions impact on traffic flow

2.1. Road conditions

On a large scale, road conditions directly or indirectly affecting traffic flow are shown in figure 1. All other weather, organizational and road conditions, one way or another, are reduced to aggregated conditions.

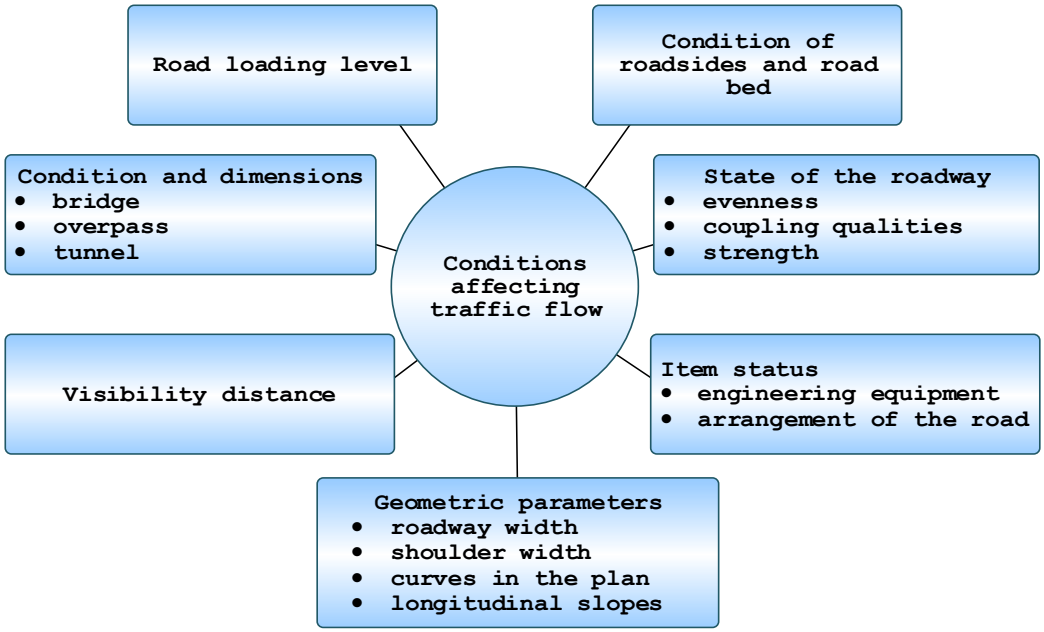

Figure 1. Road conditions affecting traffic flow.

The variety of road conditions and their influence on the traffic flow characteristics is taken into account using a function:

$$Y = \alpha_0 \prod_{i=1}^{n} x_i^{\lambda_i}, \quad (1)$$

where Y is the parameter characterizing the traffic flow (average speed, intensity, density); x_i – the street-road network characteristic or road conditions affecting the final indicator Y; λ_i – degree of influence of the x_i characteristic on Y; α_0 – reduction parameter.

2.2. Traffic flow

In the task of profiling the impact of road conditions on the traffic flow, it is not necessary to isolate a separate vehicle from the stream, since aggregated conditions affect the traffic flow generally, which causes the use of a macroscopic model.

In a macroscopic model, the traffic flow parameters are interconnected by the basic equation displayed by the fundamental diagram, the dependence function of the three main macroparameters: average speed $v(t,x)$, intensity $I(t,x)$, density $k(t,x)$:

$$v(t,x) = \frac{I(t,x)}{k(t,x)}, \tag{2}$$

$$I(t,x) = \frac{\partial Q}{\partial t}, \tag{3}$$

$$k(t,x) = \frac{\partial Q}{\partial x}, \tag{4}$$

$$I(t,x) = f(k(t,x)), \tag{5}$$

where Q is the number of vehicles approaching the street-road network section.

The used fundamental diagram is shown in figure 2 [10, 17].

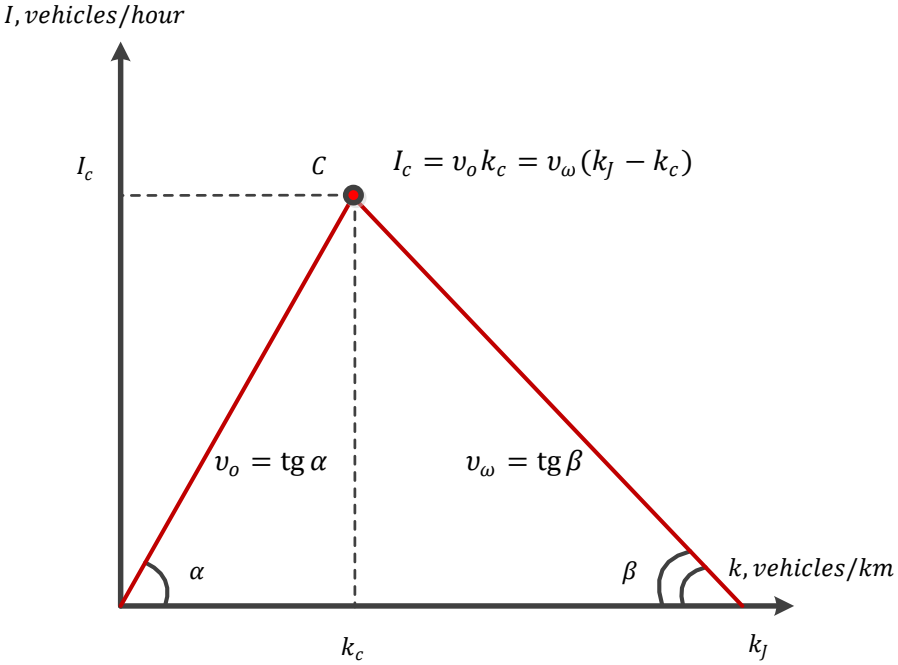

Figure 2. Fundamental traffic flow diagram.

2.3. Method of profiling the impact of road conditions on traffic flow

The method of profiling the impact of road conditions on traffic flow consists of the following steps (figure 3).

Step 1. Formation of a street-road network model.

The model is formed from a variety of areas $\Theta = \{\theta_i^X\}$ of different types with a single set of attributes (spans Θ^L, intersections Θ^S, tunnels Θ^U, overpasses Θ^O, railroad crossings Θ^R, pedestrian crossings Θ^P), multiple arcs $\tilde{E} = \{\tilde{e}_i\}$ and multiple nodes $\tilde{V} = \{\tilde{v}_i\}$.

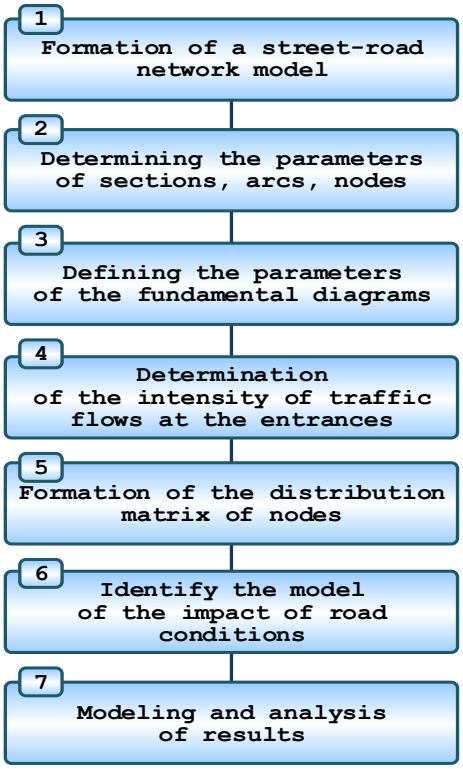

Figure 3. Steps of profiling the impact of road conditions on traffic flow.

Step 2. Determining the parameters of sections, arcs, nodes.

The parameters of the graph street-road network, shown in figure 1, are identified.

Step 3. Defining the parameters of the fundamental diagrams.

Determination of flow macromodel (2)–(5) for identification of fundamental diagrams (triads $I_C^{\tilde{e}_i}, v_0^{\tilde{e}_i}, v_w^{\tilde{e}_i}$ or $I_C^{\tilde{e}_i}, k_C^{\tilde{e}_i}, k_J^{\tilde{e}_i}$) for arcs $\tilde{e}_i \in \tilde{E}$ of the street-road network graph. This step is performed using the street-road network and technical means of monitoring, such as sensors and video monitoring systems, databases of field surveys, radar detectors and presence vehicle detectors.

For arcs of the street-road network $\tilde{e}_i \in \tilde{E}$, where the data on the traffic flow parameters are missing or unreliable, the main traffic flow parameters are defined as follows. The maximum intensity value $I^{\tilde{e}_i}$ on the arc $\tilde{e}_i$ among the available measurement (observation) results of intensity $I^{\tilde{e}_i} \in \tilde{I}^{\tilde{e}_i}$ is selected as the arc bandwidth $I_C^{\tilde{e}_i}$.

Free flow speed on an arc $v_0^{\tilde{e}_i}$ is equal to the maximum speed of movement in this street-road network section defined by the Road Traffic Regulations or other regulatory documents of the location country.

Critical density $k_C^{\tilde{e}_i}$ traffic flow on an arc is calculated by:

$$k_C^{\tilde{e}_i} = \frac{I_C^{\tilde{e}_i}}{v_0^{\tilde{e}_i}}. \quad (6)$$

Maximum traffic flow density on the arc $k_J^{\tilde{e}_i}$ is established by estimating the maximum number of vehicles $Q^{\tilde{e}_i}$ that can fit on the arc $\tilde{e}_i$:

$$k_J^{\tilde{e}_i} = \frac{Q^{\tilde{e}_i}}{l^{\tilde{e}_i}}. \quad (7)$$

This method of estimating the maximum density $k_J^{\tilde{e}_i}$ can be applied with a high degree of accuracy in the presence of aerial photographs obtained using remote Earth sensing methods, on which a congestion state is recorded. An example of an arc throughput calculation is shown in Figure 4.

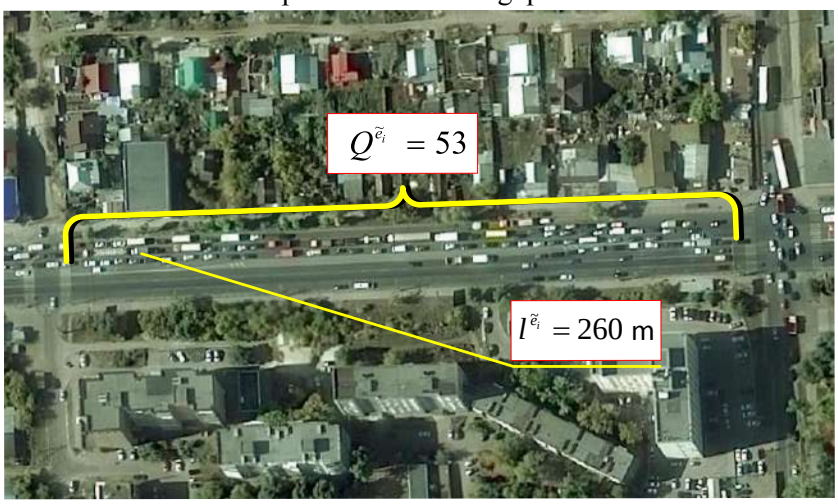

Figure 4. Arc throughput calculation example.

If the intensity, density or average speed sensors are installed on the street-road network, then using the least squares method applied to points with known traffic flow intensity and density in the fundamental diagram, I find the speed of free flow $v_0^{\tilde{e}_i}$ and the speed of propagation of the traffic jam $v_w^{\tilde{e}_i}$ along the arc.

If the parameters of the traffic flow in the surveyed area street-road network cannot be established, then I use the parameters of the traffic flow from the neighboring sections street-road network to synthesize the missing data.

Step 4. Determination of the intensity of traffic flows at the entrances.

To determine the intensity of the traffic flow at the entrances $I_E^{\tilde{e}_i}(t) = I_R^{\tilde{e}_i}(t)$ to the street-road network, I use an algorithm that generates values according to Poisson's law and takes into account the number of inhabitants and the level of motorization in the transport area.

Step 5. Formation of the distribution matrix of nodes.

Formation of distribution matrices $\mathrm{B}^{\tilde{v}_i}$ for all nodes street-road network $\tilde{v}_i \in \tilde{V}$ will be performed using an algorithm analyzing the sets of traffic flow intensity values $\tilde{I}^{\tilde{e}_m}$, $\tilde{I}^{\tilde{e}_n}$ on arcs $\tilde{e}_m$ entering the node $\tilde{v}_i$ and arcs $\tilde{e}_n$ leaving the node $\tilde{v}_i$ under study, respectively.

Step 6. Identify the model of the impact of road conditions.

The model of the impact of road conditions is implemented according to (1).

Step 7. Modeling and analysis of results

By changing the parameters of the fundamental diagrams of arcs $I_C^{\tilde{e}_i}$, $v_0^{\tilde{e}_i}$, $v_w^{\tilde{e}_i}$, $I_C^{\tilde{e}_i}$, $k_C^{\tilde{e}_i}$, $k_J^{\tilde{e}_i}$ I simulate weather phenomena, incidents, control actions. Changes in the intensity at the arcs of entrances $I_R^{\tilde{e}_i}(t)$ simulate fluctuations in transport demand arising from the effects of attraction points. By changing the distribution matrix $\mathrm{B}^{\tilde{v}_i}(t) = \left(\beta_{m,n}(t)\right)_{m=1.n=1}^{M,N}$ in the node $\tilde{v}_i$, the traffic flow redirection is modeled, for example, due to the use of information support tools for traffic participants.

3. Results

3.1. Identification of the traffic flow model

Due to the simplicity of identification, I use the fundamental diagram proposed by [10, 17], which is determined by the maximum road capacity I_C, the free flow speed v_0 and the speed of propagation of the traffic jam v_w (figure 2).

Basic traffic flow diagrams, built on the well-known classical models for experimental data, I present in figure 5. All models assume a saturation point, where the intensity reaches its maximum value. With a further increase in traffic flow density, the intensity decreases.

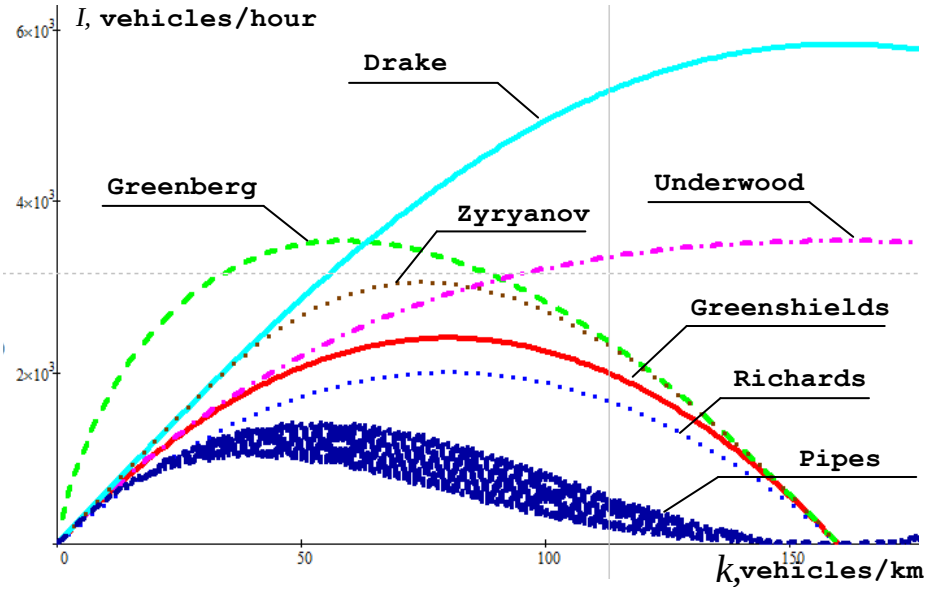

Figure 5. Comparison of the fundamental diagrams of macromodels.

I use the data on average speed and intensity (vehicle number per time) of traffic flow, on the basis of which the density of the traffic flow can be calculated.

3.2. Software implementation

Software that implements the proposed method operates in the .NET Framework 4.5 and is written in C#. The graphical user interface is based on WinForms and integrates into the attribute-driven network-centric intelligent transport system [18]. The interaction with the services of the intelligent transport system was accomplished through the SOAP protocol using WCF technology.

Data on traffic flow and road conditions for analysis are obtained from the CityPulse road database for the city of Aarhus, Denmark [19, 20]. Data are presented in CSV and JSON format. Interval of measurement of traffic flow characteristics – 5 minutes. I take environmental measurements every 1st, 20th and 50th minute.

A traffic flow entry contains data:

- measurement status (presence of errors);
- average time of passage of the site street-road network (s);
- average speed (km/h);
- vehicle count.

The road conditions record contains weather data:

- dew point (°C);
- humidity (%);
- atmospheric pressure (millibar);
- temperature (°C);

- direction of the wind (°);
- wind speed (km/h).

Data are converted into developed software using continuous integration and import feature that provides control over data integrity and consistency [21, 22]. Data are accompanied by associated attribute data, which are the semantics of real-world objects. For systems operating on the basis of the platform with an electronic map, the attribute data are basic, the geodata provide a spatial reference. Data are presented in the form of domain objects (Domain Object pattern) or data transfer objects (DTO pattern). To load related data in these objects, I use the Lazy Load design pattern, which works through WCF using SerializationSurrogate, which is attached by metaprogramming methods.

3.3. Application results

In the developed software, a series of experiments were conducted with the obtained data set consisting of 25 million records. The results obtained using the proposed method allowed me to establish weather conditions that would help to achieve maximum I_{max} = 1538 vehicles/h and minimum I_{min} = 12 vehicles/h values of intensity and maximum V_{max} = 150.5 km/h and minimum V_{min} = 11.6 km/h values of average speed (table 1).

Table 1. Weather conditions for extremes of the traffic flow characteristics.

	Dew point (°C)	Humidity (%)	Pressure (millibar)	Temperature (°C)	Wind direction (°)	Wind speed (km/h)
$\boldsymbol{I_{max}}$	1	87	1003	3	140	7.4
$\boldsymbol{I_{min}}$	17	88	1012	19	280	11.1
$\boldsymbol{V_{max}}$	11	73	1013	15	180	5.6
$\boldsymbol{V_{min}}$	9	88	1013	11	210	5.6

The influence results of individual weather conditions on the traffic flow: in table 2 – the effect of the dew point deficit, in table 3 – the atmospheric pressure effect, in table 4 – the wind speed. The smallest (Min), highest (Max) and average (Avg) values describing the influence of weather conditions on the traffic flow are considered. In this case, the maxima and minima of the values of the average speed and intensity are distinguished in the calculation of the section street-road network.

Table 2. The effect of the dew point on the traffic flow characteristics.

	Minimum intensity (vehicles/h)	Average intensity (vehicles/h)	Maximum intensity (vehicles/h)	Minimum average speed (km/h)	Average speed (km/h)	Maximum average speed (km/h)
Min	14	38	1284	18.1	45.8	149.0
Avg	14	28	456	16.3	45.5	145.1
Max	13	25	300	14.2	44.1	138.6

Thus, the effect of the dew point (table 2) is significant: a decrease in the deficit leads to an increase in throughput (average speed and intensity) of traffic flow.

Table 3. The effect of atmospheric pressure on the traffic flow characteristics.

	Minimum intensity (vehicles/h)	Average intensity (vehicles/h)	Maximum intensity (vehicles/h)	Minimum average speed (km/h)	Average speed (km/h)	Maximum average speed (km/h)
Min	15	23	180	18.8	46.0	149.4
Avg	16	36	600	17.5	44.2	127.1
Max	16	72	1068	15.3	40.3	113.2

An increase in atmospheric pressure (table 3) leads to an increase in the traffic flow intensity, but at the same time, the values of average speed decrease, which allows concluding that the traffic flow is in a state of obstructed movement, which increases the density of the streams according to (2).

Table 4. The effect of wind speed on the traffic flow characteristics.

	Minimum intensity (vehicles/h)	Average intensity (vehicles/h)	Maximum intensity (vehicles/h)	Minimum average speed (km/h)	Average speed (km/h)	Maximum average speed (km/h)
Min	15	41	604	0	46.7	150.0
Avg	15	38	600	0	46.6	149.2
Max	1	3	84	0	38.4	137.7

Wind speed (table 4) has a significant effect at maximum values: a decrease in intensity and speed is observed. Experiments were carried out to take into account the joint influence of road conditions on the traffic flow characteristics. For the formation of a dangerous winter slipperiness type of ice, which reduces the average speed and intensity, the following weather conditions are necessary: air temperature from 0 to -10 °C, an increase in the dew point deficit, and regular changes in wind direction and speed. The greater the wind speed, the more intense the ice. For all sections of the road network, weather conditions were identified under which the likelihood of ice formation increases (table 5).

Table 5. Weather conditions for the occurrence of ice and its consequences.

	Dew point (°C)	Temperature (°C)	Wind direction (°)	Wind speed (km/h)	Intensity reduction (%)	Average speed reduction (%)
Viby Ringvej	3	0	180	11.5	23	16
Christian X's Vej	4	1	140	15.7	27	18
Marselis Boulevard	4	-2	140	12.8	30	22
Vestre Ringgade	5	-1	180	10.1	22	16

4. Conclusion and discussion

Thus, I propose a method for profiling the impact of road, organizational and weather conditions on traffic flow using a data-driven approach. The method operates with macroscopic characteristics of traffic flow and detailed data on road conditions, represented by the models of objects, processes, and phenomena of the real world. The proposed method is implemented as a software module for the intelligent transport geographic information system. I give the results of the analysis of data on the speed and intensity of traffic flow depending on environmental conditions.

The environment has the greatest adverse effect in winter, characterized by a decrease in the length of daylight, low air temperatures, and road surface. Mutual combination of strong side wind and slippery coating leads to loss of stability in open areas of the street-road network. Winter slippery conditions, snow drifts reduce the speed, reduce the width of the carriageway due to the formation of snow deposits, reduce the throughput capacity of the street-road network. Precipitation, fogs, blizzards lead to the limitation of the visibility distance, which also entails a decrease in speed and a decrease in throughput.

The results of the analysis showed that the method is effective for profiling and predicting the changes taking place in the traffic flow, with a change in the affecting road conditions.

5. References

[1] Buch N, Velastin S A and Orwell J 2011 A review of computer vision techniques for the analysis of urban traffic *IEEE T-ITS* **12(3)** 920-939

[2] Qian Y, Zeng J, Wang N, Zhang J and Wang B 2017 A traffic flow model considering influence of car-following and its echo characteristics *Nonlinear Dynamics* **89(2)** 1099-1109
[3] Lighthill M J and Whitham G B 1955 On kinematic waves: II. Theory of traffic flow on long crowded roads *Proc. R. Soc. London Ser. A* **229** 281-345
[4] Drew D R 1968 *Traffic Flow Theory and Control* (New York: McGraw Hill Text) p 467
[5] Lukanin V N, Buslaev A P, Trofimenko Yu V and Yashina M V 1998 *Road traffic and environment* (Moscow: INFRA-M) p 408
[6] Kurzhanskij A B, Kurzhanskij A A and Varajya P 2010 The role of macromodelling in the active management of the transport network *MIPT proceedings* **2(4)** 100-118
[7] Burghout W, Koutsopoulos H N and Andreasson I 2005 Hybrid mesoscopic-microscopic traffic simulation *TRR: Journal of the Transportation Research Board* **1934(1)** 218-255
[8] Hoogendoorn S P and Bovy P H L 2001 State-of-the-art of vehicular traffic flow modelling *Proc. of the Institution of Mechanical Engineers I: Journal of Systems and Control Engineering* **215(4)** 283-303
[9] Cheng R, Ge H and Wang J 2017 An extended macro traffic flow model accounting for multiple optimal velocity functions with different probabilities *Physics Letters A* **381(32)** 2608-2620
[10] Newell G F 1993 A simplifed theory of kinematic waves in highway traffic II: Queueing at freeway bottlenecks *Transp. Res. B* **27** 289-303
[11] Wang F Y 2010 Parallel control and management for intelligent transportation systems: Concepts, architectures, and applications *IEEE Transactions on Intelligent Transportation Systems* **11(3)** 630-638
[12] Kolesov V I, Gulyaev M L and Osipenko A M 2011 Identification of the real model of traffic flow in the city *Vestnik of the Orenburg State University* **10(129)** 43-48
[13] Agafonov A A and Myasnikov V V 2014 An algorithm for traffic flow parameters estimation and prediction using composition of machine learning methods and time series models *Computer Optics* **38(3)** 539-549
[14] Tang T Q, Li P and Yang X B 2013 An extended macro model for traffic flow with consideration of multi static bottlenecks *Physica A: Statistical Mechanics and its Applications* **392** 3537-3545
[15] Zhang J, Wang F Y, Wang K, Lin W H, Xu X and Chen C 2011 Data-driven intelligent transportation systems: A survey *IEEE Transactions on Intelligent Transportation Systems* **12(4)** 1624-1639
[16] Johansson M and Gunnar A 2006 Data-driven traffic engineering: techniques, experiences and challenges *3rd Int. Conf. on Broadband Communications, Networks and Systems, IEEE* 1-10
[17] Daganzo C F 1994 The cell transmission model: A dynamic representation of highway traffic consistent with the hydrodynamic theory *Transportation Research Part B: Methodological* **28(4)** 269-287
[18] Golovnin O K and Mikheeva T I 2018 Attribute-driven network-centric urban transport process control system modeling *Journal of Physics: Conference Series* **1096(1)** 012199
[19] URL: http://iot.ee.surrey.ac.uk:8080/datasets.html
[20] Ali M I, Gao F and Mileo A 2015 CityBench: A configurable benchmark to evaluate RSP engines using smart city datasets *Int. Semantic Web Conf.* 374-389
[21] Ostroglazov N, Golovnin O and Mikheeva T 2018 System analysis and processing of transport infrastructure information *CEUR Workshop Proc.* **2298** 144071
[22] Golovnin O, Stolbova A and Ostroglazov N 2019 An analysis of road traffic flow characteristics using wavelet transform *Studies in Systems, Decision and Control* **199** 433-445

Research on the use of artificial neural networks for the myocardial infarction diagnosis

P I Katkov[1], N S Davydov[1,2], A G Khramov[1,2] and A N Nikonorov[1,2]

[1]Samara National Research University, Moskovskoe Shosse 34A, Samara, Russia, 443086
[2]Image Processing Systems Institute of RAS - Branch of the FSRC "Crystallography and Photonics" RAS, Molodogvardejskaya street 151, Samara, Russia, 443001

e-mail: katkov.p.i@gmail.com, alexander.khramov@gmail.com

Abstract. In this paper, the use of artificial neural networks for the myocardial infarction diagnosis is investigated. For the analysis, 169 ECG records were taken from the database of the Massachusetts University of Technology, of which 80 correspond to healthy patients and 89 correspond to patients who have a myocardial infarction. Each signal has been pre-processed. The result of preprocessing each signal is a common segment consisting of 1000 samples. To detect myocardial infarction, a convolutional neural network consisting of two convolutional layers was used. For accuracy of the neural network leave-one-out cross-validation was used. The best results of the experiments are obtained with the neural network for leads V1, V2, AVF.

1. Introduction

Artificial neural networks are now widely used in different clinical research and its clinical use shows high quality results especially in signal analysis such as electrocardiogram (ECG) signals. Cardiovascular diseases are the main cause of health loss in most developed countries, therefore the premature detection of cardiovascular diseases is a very important issue. One of the most dangerous among cardiovascular diseases is myocardial infarction. In order to detect myocardial infarction, the doctor analyzes the results of electrocardiography.

There are many different methods for analyzing ECG signals. For example, methods based on blind signal separation [1], the multilayer method of support vectors [2], and others.

The main objective of this study is to study the applicability of artificial neural networks for the diagnosis of myocardial infarction by electrocardiogram. The main problems of every myocardial infarction detection method are complexity and a poor theoretical basis and these problems need to be solved for future developments and studies.

We compare our method of myocardial infarction detection with several others such as Blind Signal Separation (BSS) method [1]. BSS was used for the extraction of the raw signal and Naive Bayes classifier was used for myocardial infarction detection. In that study the algorithm gave 96.77%

of accuracy, but it is hard to recreate this result using the information which is given in the paper. The second study is based on the conversion of ECG signal to 3D image and the using of multilayer support vector machine for classification [2]. However, it is also possible to reconstruct the structure of ECG signal in order to filter the signal with a risk of data loss [3]. The ECG signal represents anatomical structure of the heart, its parts and the process of working. One of the last developed method of myocardial infarction detection is based on wavelet transformation[4]. This new approach allows to do fast and accurate classifications using information from energy level of wavelet transformation.

In this paper, we proposed the new approach based on discrete wavelet transformation during pre-processing stage and convolutional neural network in the classification stage. At the first stage, there is a selection of the cardiac cycle in order to reduce the total amount of data and bring all the data to one template form. This is done with use of an algorithm that is based on a discrete wavelet transform of the original signal [5, 6, 7].

At the second stage, the binary classification problem is solved using a convolutional neural network. This is where the architecture for the neural network is composed and its learning takes place. The patient data set was taken from the database of the Massachusetts Institute of Technology [8].

Also in this paper, to get the result of the classification close to what can be obtained by the practical application of the algorithm, a leave-one-out cross validation technique was used.

2. Signal preprocassing

2.1 Segmantation

The first step in bringing the signal to the required form is its segmentation into cardiac cycles, which will allow you to continue working not with the whole signal, but only with its part containing the most important information about the patient. Segmentation is performed using discrete wavelet transform.

2.1.1 Trend removal and signal filtering using discrete wavelet transform

The raw signals used in this study have different lengths and amplitudes. Each of them also has a wandering trend line, which affects the position of each cardiac cycle and can cause unwanted distortions during further processing. An example of a raw ECG signal with a wandering trend line present is shown in Figure 1.

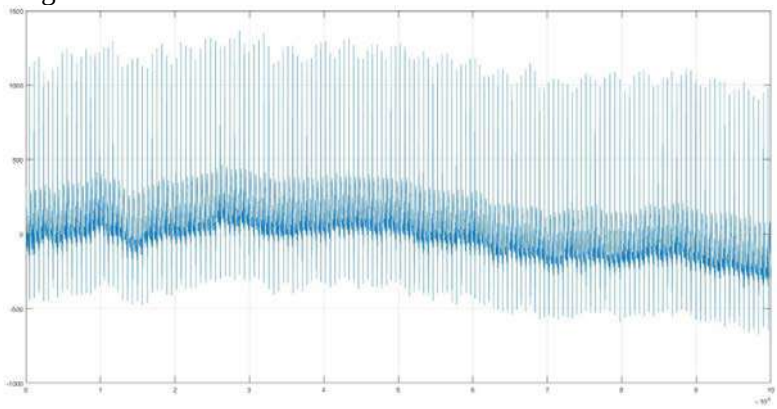

Figure 1. Raw ECG signal.

The wandering of the trend line of the ECG signal is associated with physical movements of the chest in the process of breathing the patient. This noise is low-frequency physical noise and its elimination is necessary for obtaining a stable signal and its subsequent processing.

The frequency range of the trend line is between 0 and 0.5 Hz. The method used to remove a wandering trend line is based on decomposition using discrete wavelet transform into 8 levels and the subsequent restoration of the signal to 8 levels without using additional level coefficients. Due to the

fact that the signal was restored from those coefficients that contain all the main details of the source signal, except for the trend line, the signal shown in Figure 2 will be received at the output of the inverse transform.

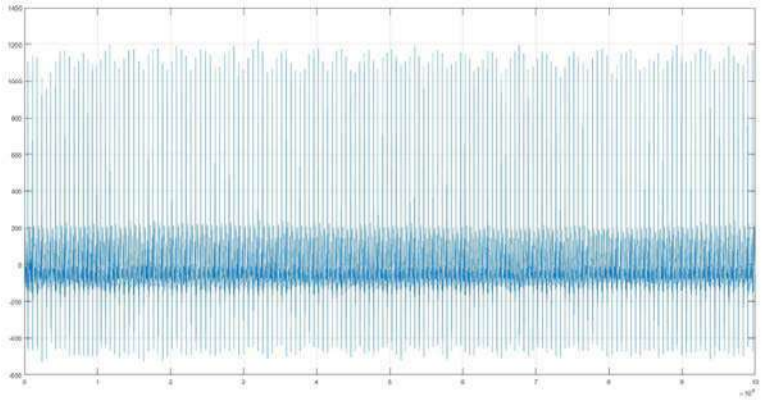

Figure 2. The raw signal without a trend.

Also, to prepare the signal for further processing, it is necessary to remove high-frequency noise. This can be done by decomposing the signal into 3 levels of discrete wavelet transform and restoring the signal according to the coefficients of the third and additional levels, thereby removing high-frequency noise from the signal.

2.1.2 R-peak detection and signal segmentation

To proceed the signal segmentation, it is required to select the most important point of each cardiac cycle – the R-peak. The frequency range corresponding to the QRS complex and R-peak is between 3 and 40 Hz, which means that the signal will require decomposition into 5 levels of discrete wavelet transform and the subsequent restoration of the signal using coefficients 4 and 5 levels.

After the signal is restored, it will contain only peak values at those positions which correspond to the R-peaks in the original signal. Peaks are detected by successively searching for a maximum with a window width of half the sampling frequency and a maximum of at least 10% of the amplitude of the maximum point in the reconstructed signal. The result of projecting the found points on the original signal is shown in Figure 3.

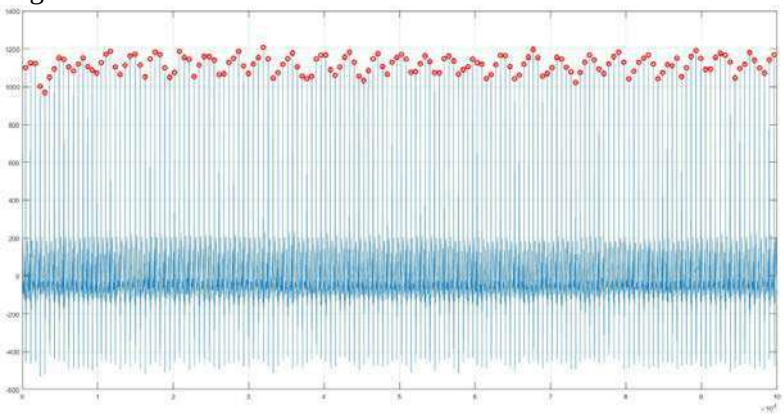

Figure 3. Detected R-peaks.

The final step of segmentation of the ECG signal will be the cutting of the signal into cardiac cycles relative to the R-peak. The length of the cardiac cycle of each patient is different and depends on his pulse and how long the electrocardiogram was taken. Therefore, the following formula was developed to calculate the length of the patient's cardiac cycle:

$$L = \frac{LengthOfSignal}{Pulse}.$$

After calculating the length of the cardiac cycle, it is necessary to distinguish it relative to each R-peak. To do this, take an interval equal to half of the length of the entire cycle to the left of the R-peak and an the same interval to the right of the R-peak.

Thus, the signal will be evenly divided into cardiac cycles of the same length, but for each patient this length will be different. The entire set of segments obtained as a result of dividing the ECG signal is shown in Figure 4.

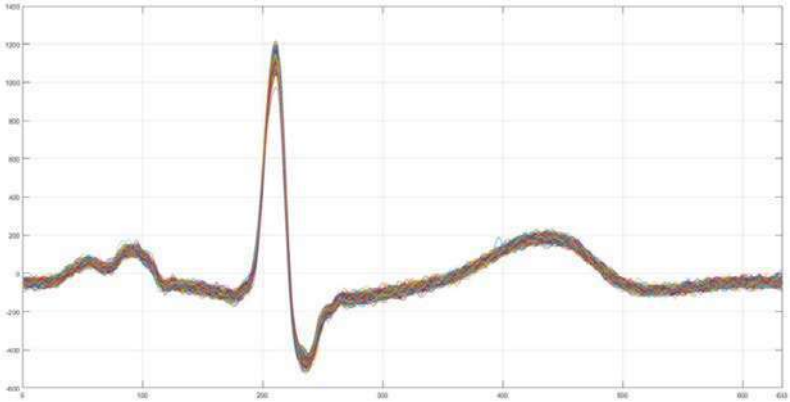

Figure 4. A set of cardiac cycles obtained from a raw ECG signal.

2.2 Calculation of a common standard ECG signal segment

The final step in converting the ECG signal to the common standard segment will be averaging the set of selected segments. This procedure is necessary in order to obtain the general shape of the entire set of segments and drown out low-frequency noises. It is worth mentioning that this step may drown out erroneously identified cardiac cycles that are not. For example, if in the process of ECG removal any physical noise was recorded with a frequency equal to the frequency of the QRS complex, then it can be defined as part of the heartbeat. In this regard, averaging will significantly reduce the contribution of the defective clock to the overall information segment of the signal. Also in the case of pathological signals, various heart sounds and heart damage can affect the waveform. However, the detection of damage data can be based on the selection of the shape - the average standard segment, and the subsequent finding of the greatest deviation from this segment.

The result of the final stage of processing is shown in Figure 5.

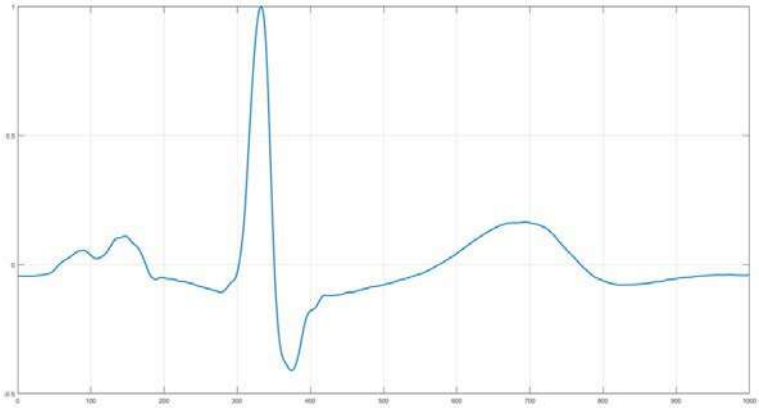

Figure 5. Common mean segment ECG signal.

3. Architecture of the convolutional neural network

After preprocessing signals for all 169 input records, we obtain an array of dimension (169, 600, N), where N is the number of leads taken. This array will be fed to the input of our neural network along with the array, which contains the answers to each entry (1, if the patient is healthy, 0, if he has a posterodiaphragmatic myocardial infarction). We implement the neural network using the Keras library in the Python language.

The following figure 6 shows the architecture of the convolutional neural network.

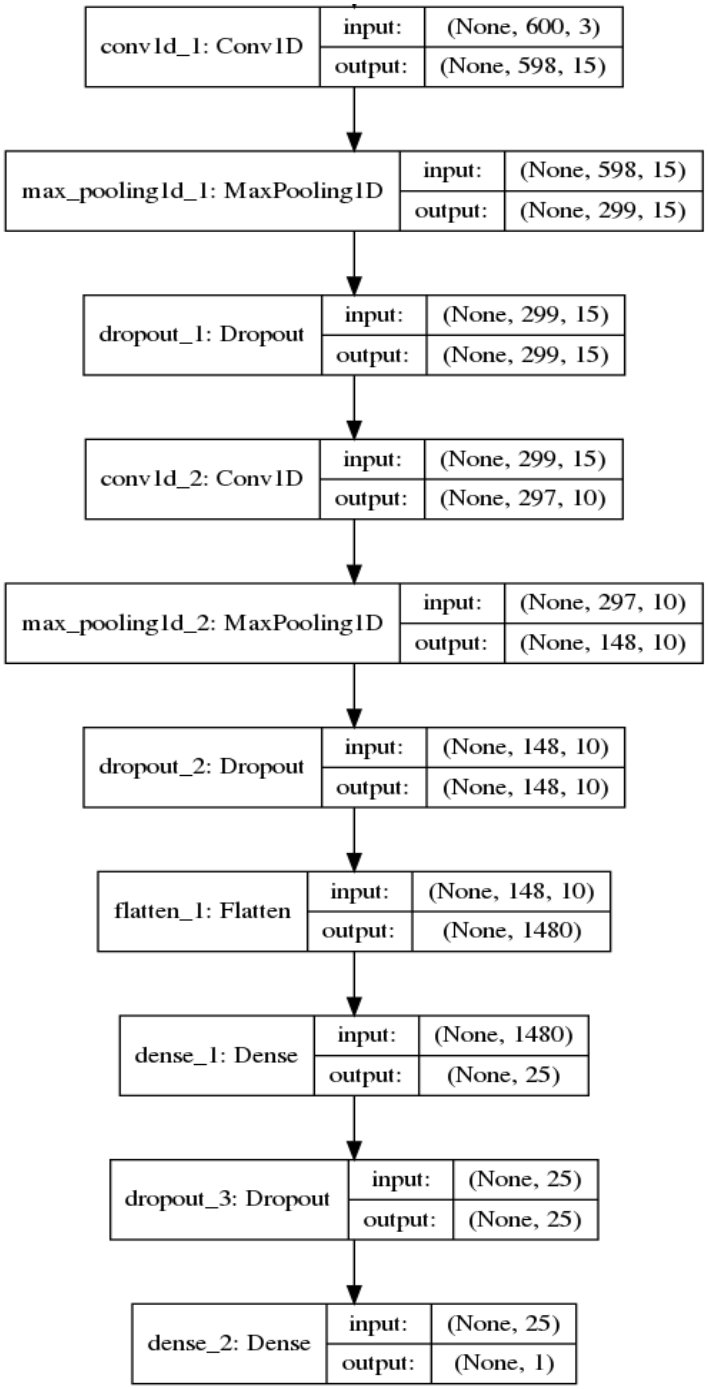

Figure 6. Architecture of the convolutional neural network.

A convolutional layer is a set of feature maps. The number of attribute cards is determined experimentally. If you take a large number of cards, the recognition quality will increase, but the computational complexity will increase too. Two convolutional layers were chosen because, with a smaller choice of layers, the accuracy of the network becomes noticeably worse, and with a larger choice of layers, it is not noticeably better. Each convolutional layer is 15 and 10 feature maps, respectively. To reduce the dimensions of the maps of the previous layer, we use the subsample operation MaxPooling. In order to prevent retraining of the neural network on each convolutional layer, the Dropout method is used. The fully connected part of the network includes two levels. All weights were chosen experimentally.

The network is trained using the error back-propagation algorithm and is optimized in accordance with the Adam optimization algorithm.

The Adam method converts a gradient as follows:

$$S_t = \alpha \cdot S_{t-1} + (1-\alpha) \cdot \nabla E_t^2;\ S_0 = 0;$$
$$D_t = \beta \cdot D_{t-1} + (1-\beta) \cdot \nabla E_t;\ D_0 = 0;$$
$$g_t = \frac{D_t}{1-\beta} \cdot \left(\frac{1-\alpha}{S_t}\right)^{1/2};$$
$$\Delta W_t = \eta \cdot (g_t + \rho \cdot W_{t-1}) + \mu \cdot \Delta W_{t-1},$$

where η – learning rate, ∇E_t - loss function gradient, μ - moment ratio, ΔW_{t-1} –weights changing in the previous iteration, ρ - regularization coefficient, W_{t-1} – weights on the previous iteration, α =0.999, β =0.9.

Since we are solving a binary classification problem, the logistic error function was chosen as the error function, which looks like this:

$$E(w) = -\sum_{i=1}^{N} (y_i ln a_i + (1-y_i) \ln(1-a_i)) \rightarrow min,$$

where y – target vector, a – output vector.

4. Results

For an experimental study, a program was launched for a data set consisting of 169 records with different numbers of leads. Pre-processing was performed for each input signal. In order to test how successfully our model is able to work in practice, element-by-element cross-validation was performed. In this case, a separate observation is used as a test set of data, and the remaining observations from the initial set are used as a training one. The cycle repeats until each observation is used once as a test. Table 1 shows the learning results of the neural network depending on the leads taken.

Table 1. The results of the neural network, depending on the different leads.

Leads	Sensitivity	Specificity	Accuracy
II, V1, V2, AVF	0.8315	0.7375	0.7870
II, III, AVF	0.7416	0.6500	0.6982
V1, V2	0.8876	0.7625	0.8284
II, III, V1, V2, AVF	0.7640	0.8250	0.7929
AVF	0.8315	0.8000	0.8166
V1, V2, AVF	**0.9213**	**0.8500**	**0.8876**

After launching the program with different input leads, the neural network showed the best results when the input data are leads V1, V2, AVF.

Compare the results with other methods of detecting myocardial infarction. It should be noted that in different articles different methods are used to extract signs from the ECG signal, and in some of them the entire signal is analyzed, and therefore a direct comparison of the classification result with each of them is not completely correct. Also, the difference between the presented feature extraction algorithm can be that the algorithm considers three ECG leads of twelve.

The first algorithm considered for comparison is based on quantization of the learning vector [6]. LVQ can be understood as a special case of an artificial neural network. LVQ-network has 2 layers: competing and linear. The competing layer performs clustering of vectors, and the linear layer relates clusters to the target classes specified by the user. Before giving a signal to the input of the neural network, it is pre-processed and extracted from it the cardiac cycle. However, the article does not explain how many leads were taken to analyze the results of the electrocardiogram, and there is no accuracy value in that paper.

The following algorithm is based on the blind signal separation method [1]. The problem of blind signal separation (BSS) and noise is an extremely relevant and complex mathematical problem, but its

solution is non-trivial and the material of the article does not explain how this problem was solved and whether the data was cross-validated. Algorithms based on the support vector method have different directions. In one of the considered articles, the ECG signal is converted to a three-dimensional view and the calculation of three-dimensional signs of the disease and the subsequent application of the multi-layer support vector machine (MSVM) [2].

The results of the comparison of various approaches to the detection of myocardial infarction are shown in Table 2.

Table 2. Comparison with other methods.

Methods	Sensitivity	Specificity	Accuracy
This study	0.9213	0.8500	0.8876
LVQ	0.8700	0.8300	–
BSS	0.9837	0.9404	0.9677
MSVM	0.8682	0.9105	0.8543

5. Conclusion

In this paper, the possibility of using convolutional neural networks to determine myocardial infarction was demonstrated. A preliminary selection of data and its preparation for training was done. A convolutional neural network consisting of two convolutional layers was constructed and trained. An experimental study was conducted, which showed that the neural network shows the best results when the input data are leads V1, V2, AVF. On these leads, the neural network showed results: accuracy - 0.8876, sensitivity - 0.9213, specificity - 0.8500. The classification was carried out using the element-wise cross-validation method to obtain a result that most adequately shows the operation of the algorithm in practical application.

6. References

[1] Devika M G and Aneesh R P 2016 Myocardial infarction fetection using hybrid BSS method *International Conference on Communication Systems and Networks* **1** 167

[2] Dhawan A, Wenzel B, George S, Gussak I, Bojovic B and Panescu D 2012 Detection of acute myocardial infarction from serial ecg using multilayer support vector machine *34th Annual International Conference of the IEEE EMBS* **1** 2704

[3] Smelkina N A, Kosarev R N, Nikonorov A V, Bairikov I M, Ryabov K N, Avdeev A V and Kazanskiy N L 2017 Reconstruction of anatomical structures using statistical shape modeling *Computer Optics* **41(6)** 897-904 DOI 10.18287/2412-6179-2017-41-6-897-904

[4] Swain S, Patra D 2018 Multiscale energy based suitable wavelet selection for detection of myocardial infarction in ECG 1 *Healthcare Technology Letters* **6** 1

[5] Davydov N S, Khramov A G 2018 Myocardial infarction detection using wavelet analysis of ECG signal *CEUR Workshop Proceedings* **2212** 31-37

[6] Haddadi R, Abdelmounim E and Hanine M 2014 Discrete wavelet transform based algorithm for recognition of qrs complexes *World of Computer Science and Information Technology Journal* **4** 127

[7] Chandel S and Singh K 2016 ECG denoising using wavelet transform and soft thresholding *International Journal of Advanced Research in Computer Science and Software Engineering* **6** 370

[8] The PTB Diagnostic ECG Database 2016 URL: https://physionet.org/physiobank/database/ptbdb/ (09.03.2019)

[9] Loginov D S 2011 Methods and tools for computer processing of electrocardiogram for the diagnosis of myocardial infarction: *Dis. Cand. tech. Sciences: 05.11.17* (Penza) p 134

Acknowledgments

With support of RFBR grants (projects 19-29-01235-mk, № 18-07-01390-A), and the state assignment of the IPSI RAS - a branch of the Federal Scientific-Research Center "Crystallography and Photonics" of the RAS (agreement № 007-ГЗ/Ч3363/26).

Detection of spam using email signatures

E V Sharapova[1] and R V Sharapov[1]

[1]Vladimir State University, Orlovskaya street, 23, Murom, Russia, 602264

e-mail: info@vanta.ru

Abstract. Currently, unwanted emails are actively sent to the Internet. Millions copies of e-mails are sent simultaneously to various users. Often e-mails undergo minor modifications to complicate the detection of spam. The paper proposes options for determining the signature of e-mails that allow identify letters with the same content and structure. Content signature of the letter includes the basic phrases in the text of the e-mail with the exception of names, numeric codes, suspicious words that are not included in the dictionary. Structure signatures incorporate the same type of e-mails, such as paragraphs, tables, images. The paper shows the results of using signatures to detect e-mail spam.

1. Introduction

E-mail is one of the most popular services in the Internet. The ability to quickly communicate using electronic messages made e-mail used by billions people. However, users are faced with such a negative phenomenon as receiving unwanted e-mails. Currently, unwanted emails are actively sent to the Internet. These messages contain advertising of various goods and services, political advertising, are used for phishing and the spread of viruses. According to the Kaspersky Lab, at the beginning of 2019 the share of spam in e-mail traffic in Russia amounted to 54%. In other words, more than half of e-mail messages are spam.

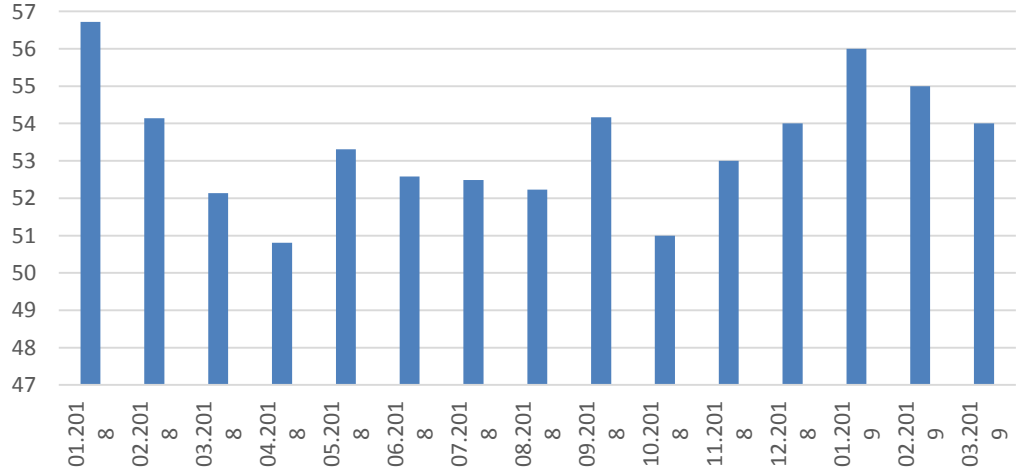

Figure 1. The share of spam in e-mail traffic in Russia.

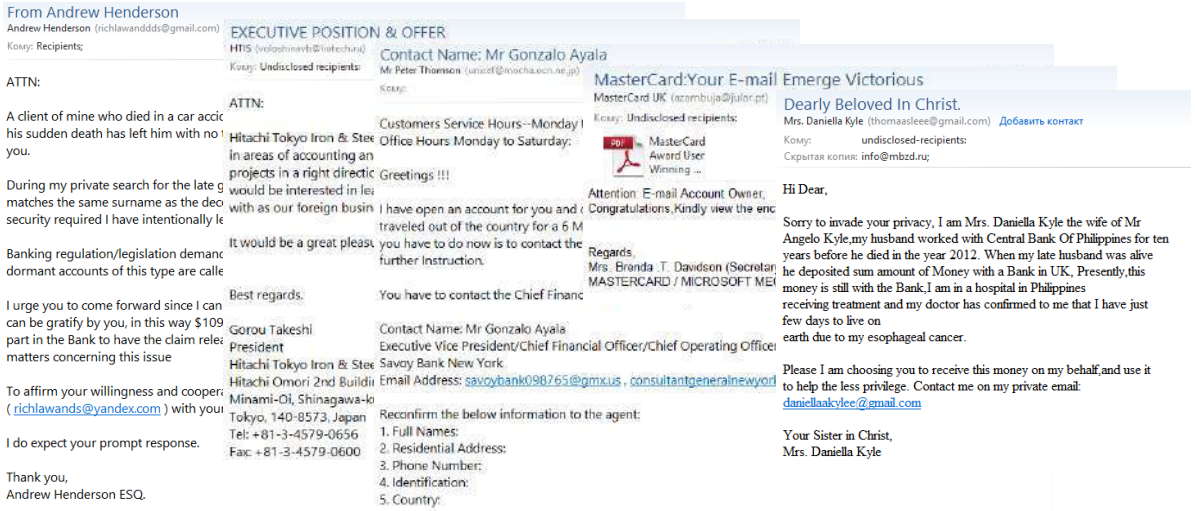

Figure 2. E-mail spam.

Spam is unsolicited mass mailing anonymous e-mail. Millions of e-mails copies are simultaneously sent to different users. Often copies differ from each other with a greeting (for example, an automatic indication of the sender's name from the dictionary - Leonty Lyudvigovich, Yadviga Svyatoslavovna) or a chain of characters (for example, 1c3790b4b8ad11e8aa21e41d2d101530).
The share of Russia in e-mail spam traffic is about 6% in 2019. Greater volume of spam is sent only in China (15%) and the USA (12%).

The uniqueness of messages is provided automatically, that is, random sequences of characters, greetings, etc. [1]. Thus, such messages can be considered as fuzzy duplicates [2], the detection of them is not a trivial task.

2. Analysis of the problem

Breaking e-mail spam has been known for a long time. More than 20 years, people are trying to stop receiving unwanted e-mail messages. This struggle is accompanied by varying success. E-mail filters are constantly improving. But to get around them, spammers come up with new ways.

Let's look at the main ways to combat a spam. Large mail services and information security companies use distributed anti-spam methods [3]. Companies collect information about the mail traffic passing through them and exchange this data between themselves. In this way, they get a full picture of the actions of spammers and can develop and select effective anti-spam defenses [4].

Another group of anti-spam methods is local. It does not use a data from external services, but works only with received messages. Local methods are used by both mail servers and final recipients. Often they are used to filter mail organizations [5, 6, 7].

Authentication of the sender and analysis of e-mail headers is carried out to spam detect. To do this, check information about the sending host, its IP address, server response codes, etc., are analyzed [8].

Often, trap addresses are used for checking - mailboxes intended solely for receiving mail spam and not used in normal life. Machine learning methods are successfully used in the fight against a spam. So, methods Bayesian filtering [9], decision trees [10], support vector machine [11], rule-based methods [12], etc., became popular.

Many works are devoted to the extraction and subsequent analysis of the distinctive properties and characteristics of e-mail items [13, 14, 15]. Various characteristics of messages are considered: visual, structural, system. In [16] it is proposed to use the dynamic property space of e-mail messages.

A number of papers related to the analysis of the text content of the e-mail [17, 18]. In [19] text information placed in images is analyzed. In [20] it is proposed to use social networks to combat with spam.

One of the ways to combat with spam is based on the use of various signatures. The way is based on counting e-mail checksums using various methods to detect duplicate e-mails.

Signatures are widely used in various tasks. They are widely used in information retrieval, in image processing. In [21] discusses methods for detect similar texts (fizzy duplicates).

Hash signature is easiest way to compare two messages. For this, the e-mail checksum is calculated using the MD5 or CRC32 algorithm. TF signature is based on counting the frequency of occurrence of words in a TF document. The signature is based on several most frequent words. The signature used is a CRC32 string checksum consisting of selected words arranged alphabetically. TF*IDF signature involves counting the weight of words not using the TF formula, but using the TF*IDF equation [22]. In this case, not only the word frequency in the document is taken into account, but also the total occurrence of words in all documents in the collection.

TF*RIDF signature based on the combination of the word frequency TF and the residual inverse frequency of the RIDF documents [23]. TF*IDF Optimal signature is a modified version of the TF*IDF signature. The modification consists in changing the principle of calculating the IDF value based on the so-called “optimal frequency”.

Long string signature built on the basis of the two longest sentences, makes it possible to find similar documents quite well. For this, the text contains the two longest sentences and concatenates into one line in alphabetical order. For the string, the control code CRC32 is calculated, which is the signature. Heavy string signature is based on a similar principle. Two sentences are selected from the text. However, sentences are selected on the basis of the sum of weights (calculated using the TF*IDF equation) of its words. The two sentences with the largest sum of weights are ordered alphabetically, concatenated into one line, for which the control code CRC32 is calculated.

I-Match signature is based on the calculation of the value of the I-Match function proposed in [24, 25]. A dictionary of words with an average IDF is compiled for the entire collection of documents (words with too large or small IDF values are not included in the list). For each document, a set of words is formed and its intersection with the dictionary is determined. When crossing some threshold, the hash function SHA1 (I-Match signature) is calculated for the set of words.

To calculate the Super Shingles signature for the entire set of shingles of the document, 84 different hash functions are calculated. Further, according to the criterion of the maximum or minimum of each function, 84 shingle are selected, which are divided into 6 groups, for each of which 6 super shingles are built [26].

MegaShingles signature is similar to no previous. 84 shingles are calculated. They are divided into 6 groups, for each of which 6 super shingles are built. The signature consists of 15 numbers (megashings), representing all possible pair combinations of the 6 super singles.

The signatures of Rabin [22] allow counting fuzzy checksums of letters. The signature of Winnowing [28] is local algorithms for document fingerprinting. The signature ensures that if there is at least one sufficiently long common substring in two files, then at least one label in their sets will match.

The Nilsimsa signatures [29] present the e-mail message by locality-sensitive hash. A Nilsimsa code is something like a hash, but unlike hashes, a small change in the message results in a small change in the Nilsimsa code.

However, improved spamming techniques make existing signatures ineffective. Thus, it becomes necessary to modify the structure of signatures to more effectively detect duplicate letters.

3. Signatures of content and structure

Different e-mail signatures can be used to identify messages with the same content and structure. The signature of the contents of the letter SigData includes the main phrases in the text of the e-mail, with the exception of names, numeric codes, suspicious words that are not included in the dictionary. The difficulty lies in the degree of filtration content. With a weak filtering in the text may remain elements used to uniquely test the letter. With strong filtering (for example, taking into account only nouns or the most frequent words), different letters may be mistakenly recognized as identical.

According to the results of the experiments, it was decided to normalize the text and include in the signature word forms obtained after processing the AOT package by the LEMMATIZER module. At the same time, a package of candidate words for inclusion in the signature was programmatically generated from an e-mail and lemmatization was performed for each word using the AOT API

functions. In the absence of a candidate word in the dictionary, it was not included in the signature. The Russian Morphological Dictionary of A.A. Zaliznyak was used as a dictionary, including 161 thousand lemmas. Thus, it is possible to identify messages that have passed through the uniqueness (that is, fuzzy duplicates of letters). The signature of the message content SigData (see Fig. 3) is a hash code calculated for the text of the electronic message processed above by the indicated method.

A client of mine who died in a car accident a few months ago leaving behind an estate/capital (US$183M) in a Bank, his sudden death has left him with no time to appoint a next of kin to his estate/capital and for this reason I contact you. During my private search for the late gentle man relatives your name and email contact was among the findings that matches the same surname as the deceased who died intestate with no Will or next of kin. To maintain the level of security required I have intentionally left out the final details. Banking regulation/legislation demand that the fiscal authorities should be notified after a statutory time period when dormant accounts of this type are called in by the monetary regulatory bodies if nobody applies to claim the funds. I urge you to come forward since I can provide you with the details needed for you to claim the

↓

SigData: 146bffd75c4c0a40cfb92df1a78395e0

Figure 3. Signature of content.

Massively distributed messages may have minor differences in content, but they do not differ in the design and arrangement of text elements. In other words, the structure of such messages is the same.

The signature of the structure SigStr includes structural elements of an e-mail type, such as paragraphs, tables, images. In this case, the content of the message is not taken into account. For the structure thus obtained, a hash code is calculated (see Fig. 4). Md5 algorithm is used to calculate the hash codes. Messages with the same internal structure will have the same hash codes.

<html><head><title></title></head><body>

 <table border="0" cellspacing="1" cellpadding="0" width="820" height="1200"><tbody><tr><td colspan="2" style="width: 820px;"></td></tr><tr><td style= "border-right-width: 1px; border-right-color: rgb(79, 129, 189); border-right-style: solid; width: 180px; text-align: center; vertical-align: top;" rowspan="2">

<font size="2">
/font></font

↓

SigStr: d1b37003288e83c5fdf5e34f0af0a252

Figure 4. Signature of the structure.

It should be noted that the signature of the structure may not always be applied. Many messages are plain text. Accordingly, the structure will not contain any markup tags. Similarly, some messages are very short and contain only a few tags, for example, new line breaks. The use of such structures as signatures will lead to incorrect accounting of various messages as identical. For this reason, messages that have more than 100 characters of markup tags are used to calculate the structure signature. For other messages, the value of the structure signature is taken equal to 0 and is not taken into account in comparison.

It should be noted that signatures for e-mail messages are calculated once. Further verification is carried out according to calculated signatures.

Although the structure and content signatures are similar to the receipt of the checksum of the message, there is a significant difference. Upon receipt of the checksum, the entire content is taken into account and even minor changes lead to different values of the checksum. The division of the

message into structure and content allows to take into account the individual characteristics of the messages, as well as to find mass mailings with varying content.

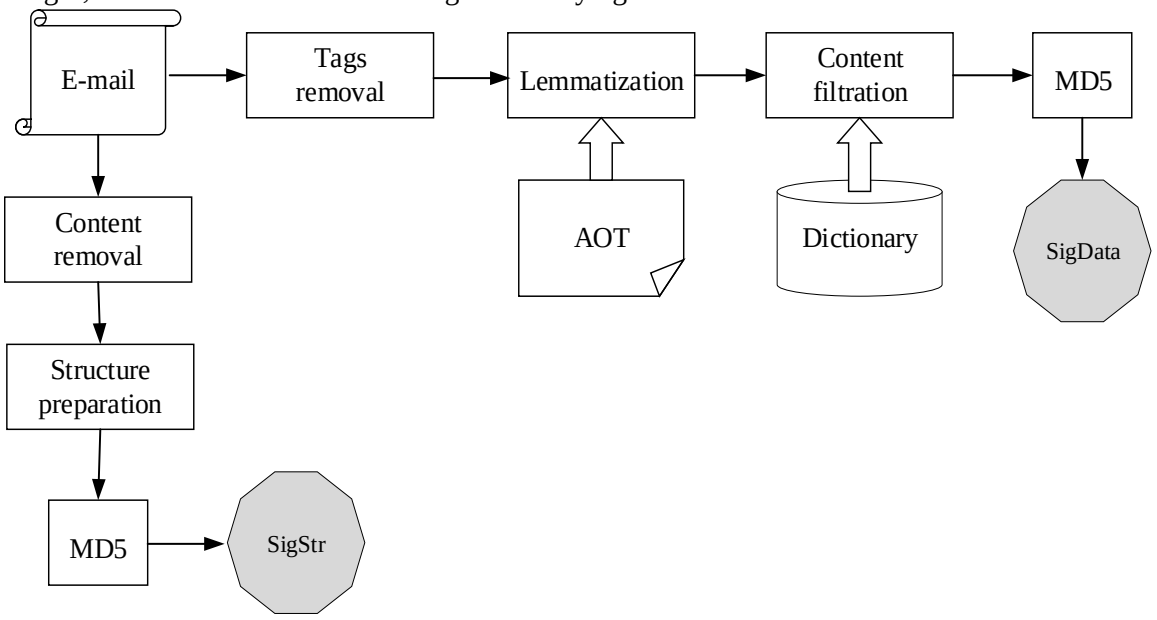

Figure 5. Calculation of signatures.

4. Using signatures to detect e-mail spam

The proposed signatures were used to detect e-mail spam arriving at the e-mail addresses of the Murom Institute of Vladimir State University mivlgu.ru and Internet resource addresses located on the commercial hosting Majordomo.ru (with the spam filter disabled). Mail messages that come to the addresses of popular mail services (gmail.com, yandex.ru, mail.ru, etc.) successfully pass spam filtering and cannot be used as a source of data for research.

A total of 30,000 e-mails were manually selected, which are e-mail spam. It should be noted that more than half of the messages (18638) were represented by several copies. The task was to detect such letters - letters that are fuzzy copies of other documents. In addition, 30,000 e-mails from real senders (that is, non-spam) were added to the message base.

At the beginning, an attempt was made to compare letters by body - content with the exception of a system header containing the sender, recipient, mail server address and other system information. Hash codes were calculated for each mail message. Messages with the same hash codes were recognized as duplicates. The number of identical messages turned out to be small - only 130 letters. The remaining letters have differences in structure and content.

When using the SigData content signature, 12237 similar messages were detected. In addition, due to the characteristics of content filtering when counting signatures (deleting non-informative elements) 42 messages were mistakenly counted as copies of other messages.

When using the signature of the SigStr structure, 14226 similar messages were detected. Due to the use of similar templates in the formation of e-mail messages, as well as messages in the form of unformatted text, 844 messages were mistakenly counted as copies of other messages.

When using the bundle of signatures content-structure SigData + SigStr, 15244 similar messages were found and 886 messages were mistakenly counted as copies of other messages.

The next metrics were used to assess the quality of work:

- Recall:

$$Recall = \frac{\text{Number of spam e-mails marked as spam}}{\text{Total number of spam e-mails}}$$

- Precision:

$$Precision = \frac{\text{Number of spam e-mails marked as spam}}{\text{Number of e-mails marked as spam}}$$

- F-measure:

$$F_1 = 2 \times \frac{Precision \times Recall}{Precision + Recall}$$

The results of using signatures to detect spam are shown in table 1.

Table 1. Results of using signatures to detect spam.

Signature	Recall	Precision	Number of errors	F-measure
Content	0.007	1	0.993	0.014
SigData	0.656	0.996	0.332	0.791
SigStr	0.763	0.944	0.311	0.844
SigData+ SigStr	0.818	0.945	0.260	0.877

As can see, the greatest completeness is 0.818 and the smallest number of errors is 0.260 when using the content-structure signature bundle. The highest accuracy rates are achieved with a full comparison of the content of the letters, but fuzzy duplicates are not determined.

As a practical implementation, it was proposed to use the SigData and SigStr signatures in the spam filter of the mail server of the authors managed service hosted on a commercial hosting. For these purposes, signature counting scripts were implemented and new rules were added to the spam filter. The analysis showed that spam letters of the same content come to different recipients of the server with a frequency of several fractions of a second for several days. In addition, many mailings are repeated at intervals of several weeks to several months. For this reason, it was decided to store the signatures of each letter for three months and use them to decide on the spam membership of the newly received letters. It should be noted that the letters are marked as spam by the filter if at least one of the SigData and SigStr signatures match.

The results of practical use (see Fig. 6) showed the viability of the proposed method of combating postal spam. SigData and SigStr signatures began to be used from October (in September, another spam filter was used). As information accumulated and the system was adapted, it was possible to significantly reduce the number of not detected spam messages (from 42% in October 2018 to 18% in January 2019).

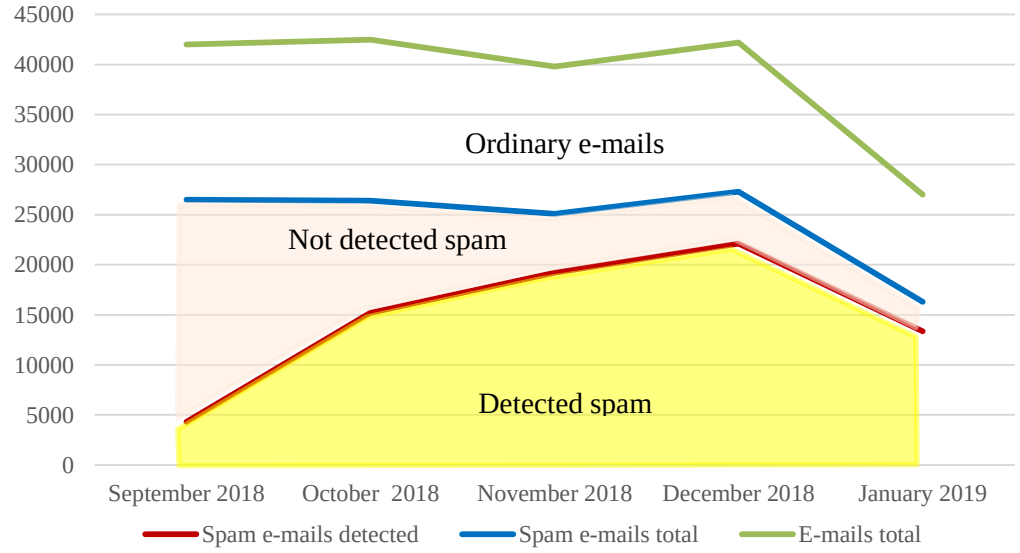

Figure 6. E-mail server spam filtering results.

During testing it was found that the fullness of spam detection increases with the number of pending mailboxes. When considering only the one mailbox address, number of detected spam is low,

because not often identical letters come several times. However, when considering the tens of mailboxes, the number of detected spam increases strongly. For this reason, the use of the proposed signature is justified when considering a group of mailboxes, such as a mail server.

5. Conclusion

The proposed content signatures and structures can be used to detect mass spam mailings, even if mailing is unique. Signatures can be used both individually and in pairs with each other. In the latter case, the best result is achieved in terms of completeness and the smallest number of errors.

To improve the quality of spam filtering, signatures can be used in conjunction with other methods for determining unwanted messages. The proposed signatures can also serve as separate message properties used as components in the application of machine learning methods.

6. References

[1] Lyapicheva N G 2018 Anti-spam issues: impact of cloud technologies *Bulletin of the Central Economics and mathematics Institute RAS* **1**
[2] Sharapov R and Sharapova E 2018 The problem of fuzzy duplicate detection of large texts *CEUR Workshop Proc.* **2212** 270-277
[3] Kovalev S S and Shishaev S S Modern methods of protection against unwanted mailings *Proc. of the Kola Scientific Center of the Russian Academy of Sciences* **7** 100-111
[4] Terentjev A M 2013 The corporate version of the implementation of Doctor Web antivirus packages in scientific institutions: implementation *National interests. Priorities and safety* **19** 40-45
[5] Baranchikova E A 2009 A method for filtering e-mail messages *Bulletin RGRTU* **2** 56-60
[6] Mironenko A N and Belim S B 2011 Multi-level spam filtering system *Information systems and technologies* **3** 125-128
[7] Mironenko A N and Belim S B 2011 Model filtering spam in email traffic *Bulletin of Computer and Information Technologies* **11** 34-36
[8] Subramaniam T, Jalab H A and Taqa A Y 2010 Overview of textual anti-spam filtering techniques *Int. J. Phys. Sci.* **5** 1869-1882
[9] Metsis V, Androutsopoulos I and Paliouras G 2006 Spam Filtering with Naive Bayes - Which Naive Bayes? *Proc.of 3 Conference on Email and Anti-Spam CEAS*
[10] Carreras X and Márquez L 2001 Boosting trees for anti-spam email filtering *Proc. of 4 international conference on recent advances in natural language processing* 1-8
[11] Drucker H, Wu D and Vapnik V 1999 Support vector machines for spam categorization *IEEE Transactions on Neural Networks* **10** 1048-1054
[12] Cohen W 1996 Learning rules that classify e-mail *Proc. of the AAAI spring symposium on machine learning in information access* 18-25
[13] Lee S M, Kim D S and Park J H 2010 Spam detection using feature selection and parameters optimization *Proc. of International Conference on Complex, Intelligent and Software Intensive Systems (CISIS)* 883-888
[14] Wu C T and Cheng K T 2005 Using visual features for anti-spam filtering *Proc. of IEEE International Conference on Image Processing* 509-512
[15] Beiranvand A and Shadgar B 2012 Spam Filtering By Using a Compound Method of Feature Selection *Journal of Academic and Applied Studies* **2** 25-31
[16] Zhou Y, Mulekar M S and Nerellapalli P 2005 Adaptive spam filtering using dynamic feature space *Proc. of 17th IEEE international conference on tools with artificial intelligence* 302-309
[17] Sasaki M and Shinnou H 2005 Spam detection using text clustering *Proc. of international conference on cyberworlds* 316-319
[18] Chirita P A, Diederich J and Nejdl W 2005 Mailrank:using ranking for spam detection *Proc. of the 14th ACM international conference on information and knowledge management* 373-380
[19] Fumera G, Pillai I and Roli F 2006 Spam filtering based on the analysis of text information embedded into images *Journal of Machine Learning Research* **7** 2699-2720

[20] Boykin P and Roychowdhury V 2005 Leveraging social networks to fight spam *Computer* **38** 61-68
[21] Zelenkov Y and Segalovich I 2007 Comparative analysis of methods for fuzzy duplicate detection for Web-documents *Proc. of 9-th Russian Scientific Conference «Digital Libraries: Advanced Methods and Technologies, Digital Collections»* 166-174
[22] Salton G and Buckley C 1988 Term-weighting approaches in automatic text retrieval *Information Processing & Management* **24** 513-523
[23] Church K and Gale W 1995 Poisson mixtures *Natural Language Engineering* **1** 163-190
[24] Chowdhury A, Frieder O, Grossman D and McCabe M 2002 Collection statistics for fast duplicate document detection *ACM Transactions on Information Systems (TOIS)* **20** 171-191
[25] Kolcz A, Chowdhury A and Alspector J 2004 Improved Robustness of Signature-Based Near-Replica Detection via Lexicon Randomization *Proc. of the tenth ACM SIGKDD international conference on Knowledge discovery and data mining* 605-610
[26] Fetterly D, Manasse M and Najor M 2003 A Large-Scale Study of the Evolution of Web Pages *ACM* 669-678
[27] Rabin M 1978 Digitalized signature as intractable as factorization. Technical Report MIT/LCS/TR212 *MIT Laboratory for Computer Science*
[28] Schleimer S, Wilkerson D S and Aiken A 2003 Winnowing: Local Algorithms for Document Fingerprinting *Proc. of ACM SIGMOD International Conference on Management of Data*
[29] Damiani E, De Capitani di Vimercati S, Paraboschi S and Samarati P 2004 An open digest-based technique for spam detection *Proc. of the International Workshop on Security in Parallel and Distributed Systems* (San Francisco, CA USA)

Acknowledgments
The reported study was funded by RFBR according to the research project № 19-07-00692.

Using genetic algorithm for generating optimal data sets to automatic testing the program code

K E Serdyukov[1], T V Avdeenko[1]

[1]Novosibirsk State Technical University, Marksa avenue, 20, Novosibrsk, Russia, 630073

e-mail: tavdeenko@mail.ru

Abstract. In present paper we propose an approach to automatic generation of test data set based on application of the genetic algorithm. We consider original procedure for computation of the weights of code operations used to formulate the fitness function being the sum of these weights. Terminal objective and result of fitness function selection is maximization of code coverage by generated test data set. The idea of the genetic algorithm application approach is that first we choose the most complex branches of the program code for accounting in the fitness function. After taking the branch into account its weight is reset to zero in order to ensure maximum code coverage. By adjusting the algorithm, it is possible to ensure that the automatic test data generating algorithm finds the most distant from each other parts of the program code and, thus, the higher level of code coverage is attained. We give a detailed example illustrating the work and advantages of considered approach and suppose further improvements of the method.

1. Introduction

One of the most important stages in developing software products is testing. The terminal goals of the testing phase are compliance of the developed program with the specified requirements, ensuring right logic while data processing and, as a result, obtaining the correct final results.

Scaling of the software development stimulated the processes of creating huge software systems by diverse development teams, each of which has its own programming style and different competencies. Despite the fact that in parallel with this process there appeared programs allowing for a high level of collaborative development, control over changes and the ability to check the quality of the code, the final product does not always meet the requirements specified at the planning stage.

For this reason, the need for quality and comprehensive testing increases significantly. It is necessary not only to find errors in the code, but also logical inconsistencies. In order to test both the program as a whole and its parts as thoroughly as possible, not only a team of testers is needed, but also preparatory activities – the formation of a set of input data that would test certain parts of the program [2].

Based on the above, we can conclude that automation of testing, or at least automatic test generation, can significantly reduce not only the time but also the cost of development. There are other

advantages of that are not so obvious – a high probability of finding small errors, transparency of test development, testing simultaneously with the development of the program, etc. [1].

Testing is not a standardized process, it depends on many factors, most of which vary from one program to another. In addition, improvement of methods for automatic verification and validation of program code occur quite slowly. Development of most types of designs and templates for testing is often done manually, without use of any intelligent software. Therefore, the testing process becomes incredibly complex and time-consuming, as well as costly, if the ultimate goal is indeed the creation of high-quality software product. In such cases the testing phase can take up to 50% of the whole development time. In this regard, it seems appropriate to use methods developed in the field of artificial intelligence.

One of the most important problems to be solved at the beginning is to identify one of the most complex branches of the code. Based on the solution of this initial problem, we can further build an algorithm for finding test data set that provides coverage of the most complex branches (as many as possible) of the code. In this paper we are trying to derive a solution to this local problem of finding one the branch with most operations of the program.

Various methods have been proposed for solving the problem of automatic test generation. The paper [3] compares various methods for generating test data, including genetic algorithms, random search method, and other heuristic approaches. In [4] it is proposed to use programming based on the constraint logic programming and symbolic execution to solve this problem. In [5] constraint handling rules are used to assist in the manual verification of problem points in the code.

Some researchers use heuristic methods with the help of visualization instruments to automate the process of testing, such as data flow diagram. Studies of automation methods using this diagram have been proposed in [6-9]. In the article [6] it is proposed to additionally use genetic algorithms to determine new input test data sets based on previously used ones.

The articles [10-13] consider integrated approaches for generating test data. In [12] an approach is used that combines strategies of random search and dynamic symbolic computations. The article [13] proposes a theoretical description of a search testing strategy using a genetic algorithm. Approaches to search for local and global extremes on real programs are considered. A hybrid approach for generating test data is proposed - a memetic algorithm.

Approach in [14] uses a hybrid intelligent search algorithm to generate test data. In the proposed algorithm, the method of branch and bound and hill climbing) are used with the use of intellectual search.

Also, there is investigate of approaches for generating test data based on the machine learning [15]. The proposed approach uses the neural network structure with user-configured clustering of input data for sequential learning. There are approaches based on the meta-heuristic algorithm of the cuckoo [16].

For the convenience of generating test data, the UML diagrams are also used. [17, 18]. The articles propose to use genetic algorithms for generating triggers for UML diagrams, which will allow finding the critical path in the program. In article [19] an improved genetic algorithm-based method is proposed for selecting test data for multiple parallel paths in UML diagrams.

In addition to UML diagrams, the program can be displayed as a classification tree method developed by Grochtmann and Grimm [20]. In paper [21] discusses the problem of tree building and proposes an integrated classification tree algorithm, and in [22] the developed ADDICT prototype (abbr. AutomateD test Data generation using the Integrated Classification-Tree methodology) is investigated for an integrated approach

There are many different researches on theme of generation of test data. Most often, to solve this problem, heuristic approaches are used, since they are allowed to select data with not a complete enumeration of possible options. The approach proposed in this article is based on a genetic algorithm with a modification of the calculation of the function of adaptation, which allows to generate data based on a program code without reference to any testing and development systems. This allows to generate data directly only by specifying restrictions on the input variables.

2. Genetic algorithm

Genetic algorithm is a heuristic method, more precise, one of the types of the evolutionary algorithms, that uses the idea and terminology of evolution of the nature. Its goal is not to find the optimal and best solution, but to find one that is close enough to it. Therefore, genetic algorithm is not recommended to apply if there are already fast and well-developed optimization methods. But at the same time, the genetic algorithm perfectly shows itself in solving non-standardized tasks, problems with incomplete data or if it impossible to use other optimization methods because of the complexity of implementation or the duration of execution [23, 24].

A genetic algorithm is considered completed if a certain number of iterations are passed (it is desirable to limit the number of iterations, since the genetic algorithm works on the method of trial and error, which is quite a long process), or if the satisfactory value of the fitness function was obtained. Generally, the genetic algorithm solves the problem of maximizing or minimizing and the adequacy of each decision (chromosome) is assessed using the fitness function.

Genetic algorithm works according by the following principle:

- *Initializing.* Establishing fitness function. Forming the initial population. Classically, the initial population creating by random filling of genes in the chromosomes. However, to increase the convergence rate, the initial population can be filling in specific way, there the values can be analyzed in advance for exclusion of definitely unsuitable genes.
- *Evaluation of population.* Each of the chromosomes is evaluated by the fitness function. Based on specified requirements, chromosomes acquire a certain value in accordance with the solution of the problem [25].
- *Selection.* After each chromosome obtain its own value, the selection of the best chromosomes take place. Selection can be done by different methods, for example, take the first n chromosomes sorted by value of the fitness function, or only chromosomes with maximum value of the fitness function, etc.
- *Crossover*. The first significant difference from conventional methods and one of the most important stages of the algorithm. After selection and retrieving the suitable chromosomes to solve the problem, they crossover with each other. Randomly selected chromosomes generate new chromosomes. Crossover occurs based on the selection of a specific position in the two chromosomes and mutual replacement of parts. After filling the required number of chromosomes to create a new population, the algorithm proceeds to the next step [26].
- *Mutation.* This is also a step characteristic for GA only. In random order, a random gene can change values to a random one. The main purpose of the mutation is the same as in biology – the introduction of genetic diversity in the population. The main goal of mutation is to obtain solutions that could not be produced with existing genes. This will allow, firstly, to avoid falling into local extremes, since the mutation may allow the algorithm to go a completely different path, and secondly, to “dilute” the population in order to avoid a situation where there are only identical chromosomes in the entire population that will not move towards a global solution.

After all stages of the genetic algorithm have been completed, it is estimated whether the population has reached the desired accuracy of the solutions, or whether a certain number of populations have been reached. If these conditions have been met, the algorithm stops working. Otherwise, the cycle is repeated with the new population until the conditions are reached.

3. The test data generation with genetic algorithm

The use of genetic algorithms in the testing process makes it possible to ensure that we will determine the most complex parts of the program code in which the risks due to making mistakes are the greatest. Evaluation is executed through the use of the fitness function, the parameters of which have the different weights of each individual operation [27].

To date, many types of diagrams have been developed that allow us to represent the structure of a program code not as a set of actions, but as diagrams with a specific structure. The most widely used are diagrams (graphs) of control flows which allow representing the whole variety of ways to run a

program. The main purpose of such diagrams falls on the task of creating the program code which includes determining the program complexity, verifying the program logic, and directly writing the code. However, from the problem of generating test data point of view, this type of diagrams built on the already written program code, permits to assess the quality of the developed code and, within the scope of the task, to assess the importance, or complexity, of certain program paths.

Based on the possibility of presenting the program code in the structural form, an approach was developed through which it would be possible to evaluate the program code and to determine such a set of test data that would allow one to "walk" through the largest number of operations and the greatest number of paths. The first step in the proposed method is to consider the structural elements of the code. For ease of presentation, we can use flow diagrams to visualize the structure of the code and to understand in what way the program is executed.

Each operation of the code is assigned its own separate graph node, and as a link is the direction in which the code is executed. For example, a condition is denoted with one graph node, but two branches of the code will come out of it. Each transition between the graph nodes is assigned a certain weight depending on which part of the code the operation is in, whether any complex structural elements precede it, etc. [28].

The problem of generating the input test data consists of three subproblems:

1) Search for the input data for traversing one of the most complex code branches;
2) Elimination or reduction of the weights of operations lying on this branch of the code at the rate of subsequent branches;
3) Search for a set of test data for traversing multiple branches at once.

The limitation on the size of the input data set is established after the development stage and allows one to concentrate on certain branches in which the largest number of operations is performed.

The whole algorithm is executed cyclically. First the procedure of searching the input data for one branch is started, then the operations in this branch are excluded from further computations and the data search for one branch is started again.

Search for a single path in the program code works as follows:

- The first operation is assigned a weight, for example, 100.
- Each subsequent operation is also assigned a weight – if there are no conditions or cycles, the weight is equal to the weight of the previous operation.
- Weight of the condition is assigned in accordance with the following rule. If the condition contains only one branch (only if ...), then the weight of each operation is reduced on 0,8. If the condition is divided into several branches (if ... else ...), then the weight is divided into equivalent parts - for two branches 50 / 50, for three 33/ 33 / 33, etc.
- Weights of operations in the cycle remain the same, but can also be multiplied by a certain weight, if it is necessary to increase the significance of the cycles during testing.
- All nested restrictions are taken into account, for example, for two nested conditions, the weight of operations will be equal to 80 * 80 = 64 percent

In Figure 1 we present an example on the basis of which the algorithm was tested.

As a result of the above procedure we obtain the weights that can be used to develop test variants using genetic algorithm, that is, to estimate how much calculated weight falls on here or another branch for certain values of input parameters.

For convenience, we introduce the following notation:

X – data sets; m – population size, i.e. the number of different variants of input data values; r(i) – the weight of a single operation i; F (X) – the value of the fitness function for each data set depending on the calculated weights.

The problem is to select the maximum of the objective function, i.e.

$$F(X) = \sum_{i=0}^{m} r(\mathrm{i}) \rightarrow max \qquad (1)$$

```
0.  public static void Main(int m, int i, int n) {
1.  intsum = 0, avg = 0;
2.  if (m <i)
3.  {
4.  use_m = m;
5.  }
6.  int[] a = new int[m];
7.  Console.WriteLine("Enter the Array Elements ");
8.  for (j= 0; j< m; j++)
9.  {
10. a[j] = i;
11. if (a[j] > n)
12. {
13. a[j] = n
14. }
15. }
16. for (k= 0; k < m; k++)
17. {
18. sum += a[k];
19. }
20. avg = sum / m;
21. Console.WriteLine("Average is {0}", avg);
22. Console.ReadLine();
23. }
```

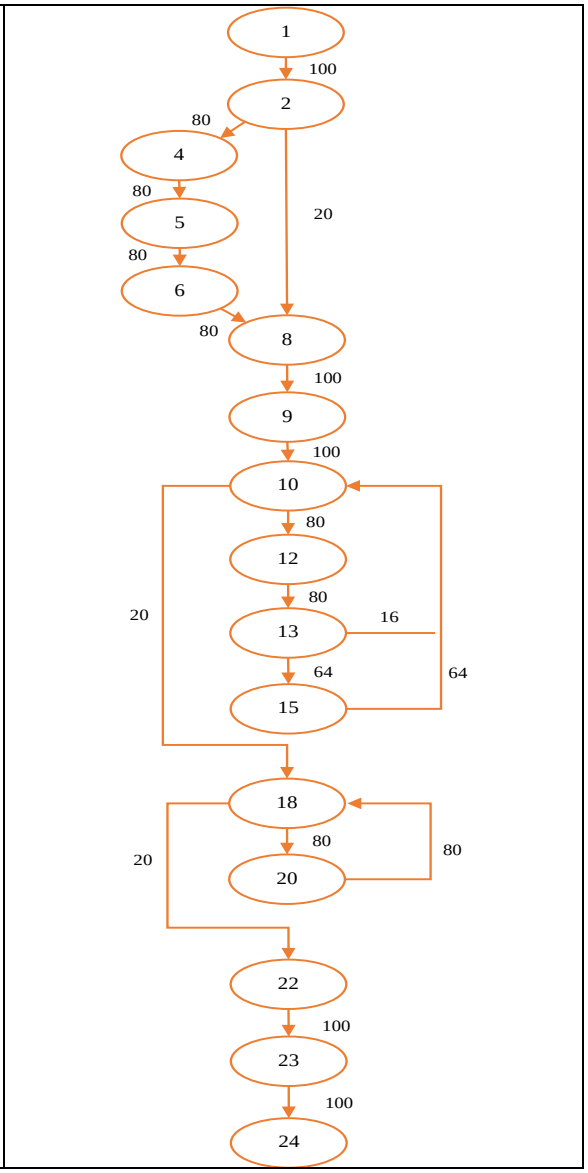

Figure 1. Program code and sequence of graph nodes for the analyzed program code.

4. Results

For a more detailed consideration of the algorithm we use simple test options and carry out each of the steps manually with a detailed description of the pro. At the initialization stage we will generate the following data sets – (10,5,12); (3,4,10); (25,30,11); (5,3,17).

Table 1 presents these sets, the calculated target value of the fitness function and the rank corresponding to the best set.

Table 1. Initial dataset options.

№	Sets X	F(X)	Rank
1	(10,5,12)	896	3
2	**(3,4,10)**	**1196**	**2**
3	**(25,30,11)**	**1308**	**1**
4	(5,3,17)	896	3

From the table we can see that the better options for the selection are 2nd and 3rd options. In order to obtain additional two new variants, their values will be mixed with a certain probability of mutation.

In the crossover stage the division of data sets occur in the first and second positions. For example, when crossing (R1, R2, R3) and (G1, G2, G3), the variables are obtained - (R1, R2, G3), (R1, G2, G3), (G1, R2, R3) and (G1, G2, R3). Parental values remain in the set-in order to keep the crossing clean, i.e. compared to the zero generation there will be added 2 new sets. Thus, in the subsequent generations, six data sets will be used. It is worth mentioning that, depending on the settings of the genetic algorithm, the parental chromosomes can be excluded from consideration.

Mutation will occur with a probability of 0,1 for the chance of changing the value from 1 to the specified value in both directions. Under these conditions, the maximum possible value added during a mutation is 5. As a result of crossing, the data sets will be obtained, shown in Table 2.

Table 2. New datasets obtained by crossing.

№	X	Y	New set	**Mutation**
1	(3,4,10)	(25,30,11)	(3,4,11)	**(3,4,13)**
2	(3,4,10)	(25,30,11)	(3,30,11)	**(3,30,11)**
3	(3,4,10)	(25,30,11)	(25,4,10)	**(25,4,10)**
4	(3,4,10)	(25,30,11)	(25,30,10)	**(25,30,10)**

As a result, two more variants will be added to the additional two parent sets - (3,4,13) and (25,30,10). Table 3 shows all the new variations of the test data set.

Table 3. The first generation of test data.

№	Sets X	F(X)	Rank	Generation
1	(3,4,10)	1196	2	0
2	(25,30,11)	1308	1	0
3	(3,4,13)	1196	2	1
4	(3,30,11)	1308	1	1
5	(25,4,10)	896	3	1
6	(25,30,10)	1308	1	1

If the two variants have the same rank, priority will be given to the option from the newer generation. In the last generation we obtained three data sets, which test the majority of the whole set of program paths - (25,30,11), (3,30,11) and (25,30,10). The first set was obtained from the first generation, so it will be excluded and there will remain only two options - (3,30,11) and (25,30,10).

Because of the small initial sample and a small code, the data sets quickly came to finding overlapping values - 30 in the second position and 10 or 11 in the third. Therefore, to continue to carry out iterations ceases to make sense - already in the next generation, the data will consist mainly of repeating sets.

For the current program code you can use test data sets obtained in the latest generation. Priority depends on rank received.

Thus, using genetic algorithms, one can find such initial test initial values, which would fully check all the paths of the program.

5. Improving the algorithm

The algorithm allows not only to evaluate which program paths will be used for certain data, but also how the data changes and whether duplicate values are preserved for the best chromosomes between populations.

This not only makes it possible to determine the initial test suite, but also, on the basis of data analysis, to draw conclusions about the presence of logic in the program that corresponds to the planned one.

Four additional tests were performed to present the results.In the algorithm, the first population is formed randomly. Certain settings were made for testing – each population contains 100 chromosomes; the total number of populations also equals 100. This will make it possible to form a sufficient number of different variants.

Table 4 presents 4 runs of the method with the first random population, two middle populations and the final one, from which the first chromosome is taken and counted as the final generated data set. For convenience, only the 5 "best" chromosomes in each population will be reflected.

Table 4. Comparison of results.

Population	Test 1	Test 2	Test 3	Test 4
0	1: 78, 23, 35	1: 97, 3, 6	1: 92, 97, 28	1: 15, 67, 26
	2: 62, 36, 95	2: 82, 77, 64	2: 38, 66, 52	2: 32, 27, 83
	3: 52, 35, 27	3: 24, 47, 57	3: 63, 76, 64	3: 37, 52, 64
	4: 17, 77, 73	4: 90, 13, 82	4: 7, 24, 56	4: 70, 49, 64
	5: 75, 9, 96	5: 81, 69, 24	5: 57, 48, 8	5: 67, 29, 94
20	1: 95, 64, 54	1: 97, 80, 4	1: 99, 13, 10	1: 99, 71, 45
	2: 95, 64, 29	2: 97, 80, 53	2: 99, 13, 11	2: 99, 71, 15
	3: 95, 64, 54	3: 97, 80, 28	3: 99, 13, 11	3: 99, 71, 3
50	1: 95, 64, 54	1: 97, 80, 29	1: 99, 13, 10	1: 99, 71, 60
	2: 95, 64, 29	2: 97, 80, 4	2: 99, 13, 11	2: 99, 71, 3
	3: 95, 64, 54	3: 97, 80, 53	3: 99, 13, 11	3: 99, 71, 3
Final (100)	**1: 95, 64, 54** **2: 95, 64, 29**	**1: 97, 80, 4** **2: 97, 80, 29**	**1: 99, 13, 10** **2: 99, 13, 11**	**1: 99, 71, 60** **2: 99, 71, 45**

At least two different final sets of test data were formed in each of the variants, in which the operations in the considered program code will have the greatest weight. In addition, there is certain patterns in the results - the first value is always the maximum (random values are limited to a maximum of 100 to increase convergence), the second value is less than the first, but more than the third.

For additional analysis, we will check how the speed of the algorithm changes depending on the genetic algorithm settings. In the graphs below it can be seeing how the duration of the program varies depending on the size of the population, i.e. the number of chromosomes, and the total number of populations. During the study of changes in the size of populations, the number of populations was equal to 100. And vice versa, during the study of the dependence on the number of populations, the number of chromosomes was equal to 100.

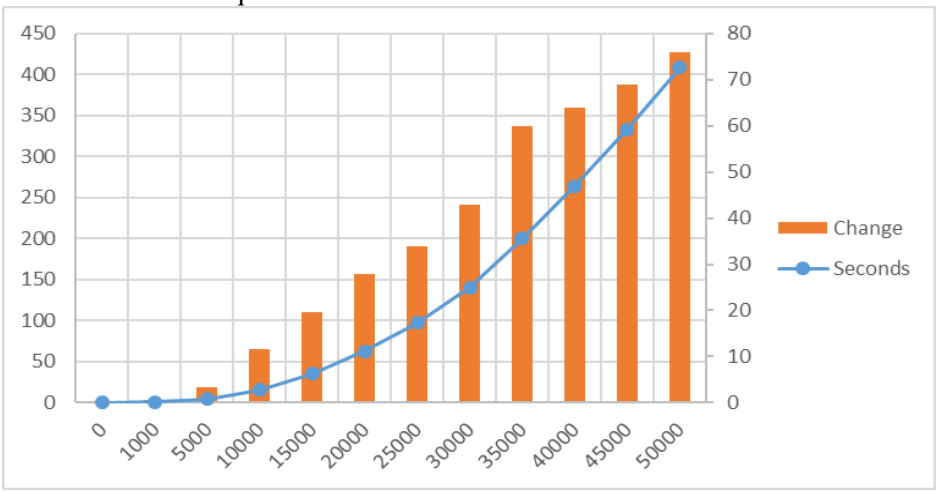

Figure 2. Dependence of execution duration on population size.

Figure 2 shows the dependence on the number of chromosomes in the population. Based on it, it can be concluded that with an increase number of chromosomes in a population, the duration of the algorithm increases significantly, and more, exponentially.

Figure 3 shows the dependence on the number of populations.

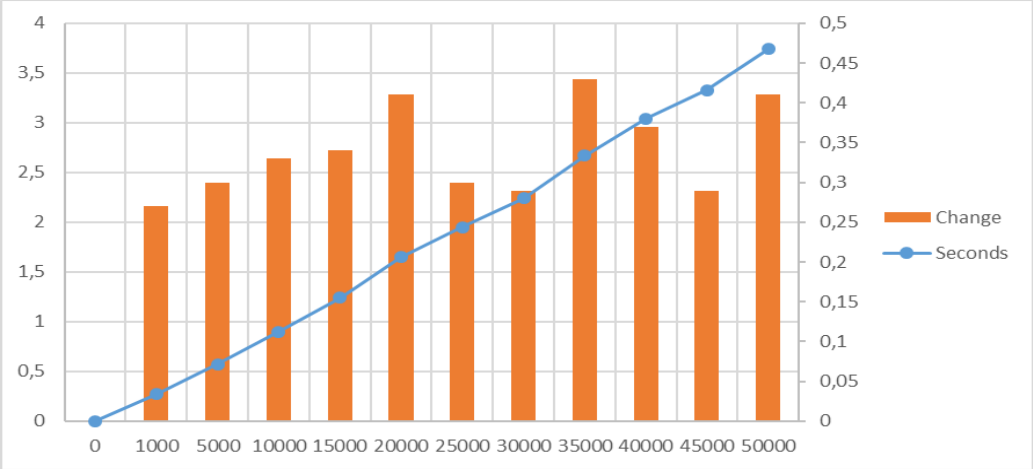

Figure3. Dependence of execution duration on the number of populations.

It becomes obvious that with a change in the number of populations, the duration of the algorithm increases, but in a linear progression. At the same time, there are noticeable fluctuations in the gain in both directions, which remain ap-proximately at the same level.

Despite the fact that in both cases total number of chromosomes remained the same, changes in the duration of work are considerably different. An increase in population size significantly increases the duration of work — the number of chromosomes in the population from 1,000 to 50,000 increased 50 times, but the duration increased 750. When the number of populations changed 50 times, the time increased only 14 times.

This is due to the fact that the most complicated operations from the point of view of loading occur in calculating the fitness function and searching for optimal chromosomes for crossing. Because the search for the best chromosomes depends on the number of chromosomes in the population, so the current search algorithm, i.e. sorting chromosomes in population from best to worst, significantly loads the power of computer systems and increases the speed of work exponentially to the size of the population.

The number of chromosomes in one population allows for a variety of options, i.e. more likely to find more suitable options. An increase in the number of populations leads to a more accurate result, but only with a large number of chromosomes. If the chromosomes are small enough, the algorithm will quickly come to one repeated value.

Based on the foregoing, the number of chromosomes in one population has the greatest influence on the result. At the same time, an increase in the number of chromosomes significantly increases the execution time. But in order to ensure the better end result, the total number of populations should also be increased with an increase in the number of chromosomes.

6. Conclusion

Evolutionary methods work in such a way as to find the best solutions in the problems that are impossible or too costly to solve using standard optimization methods. They do not always work fast or qualitatively, but they show superiority in tasks with non-standard approaches.

The method based on the genetic algorithm will automate the method of selection of input data, while significantly increasing the speed of data retrieval. The algorithm is fully automatic (with the exception of some restrictive settings), so it does not require additional testers or developers work. The resulting data set can be directly used for the testing process and, if necessary, be re-assembled at no additional cost.

In the future, it is reasonable to conduct investigations of the influence of various metrics on the final result and the amount of code coverage, in order to provide such data sets that would allow testing the code as efficiently as possible and with the maximum number of operations.

7. References

[1] Zanetti M C, Tessone CJ, Scholtes I and Schweitzer F 2014 Automated Software Remodularization Based on Move Refactoring. A Complex Systems Approach *3th international conference on Modularity* 73-83
[2] Crispin L, Gregory J 2010 *Agile Testing: A Practical Guide for Testers and Agile Teams* (Pearson Education) p 576
[3] Maragathavalli P, Anusha M, Geethamalini P and Priyadharsini S 2011 Automatic Test-Data Generation For Modified Condition/ Decision Coverage Using Genetic Algorithm *International Journal of Engineering Science and Technology* **3(2)** 1311-1318
[4] Meude C 2001 AT Gen: Automatic Test Data Generation using Constraint Logic Programming and Symbolic Execution *Software Testing Verification and Reliability*
[5] Gerlich R 2014 Automatic Test Data Generation and Model Checking with CHR *11th Workshop on Constraint Handling Rules*
[6] Moheb R 2005 Automatic Test Data Generation for Data Flow Testing Using a Genetic Algorithm *Journal of Universal Computer Science* **11(6)** 898-915
[7] Weyuker E J 1984 The complexity of data flow criteria for test data selection *Inf. Process. Lett.* **19(2)** 103-109
[8] Khamis A, Bahgat R and Abdelaziz R 2011 Automatic test data generation using data flow information *Dogus University Journal* **2** 140-153
[9] Singla S, Kumar D, Rai H M and Singla P 2011 A hybrid pso approach to automate test data generation for data flow coverage with dominance concepts *Journal of Advanced Science and Technology* **37** 15-26
[10] Luger F G 2009 *Artificial Intelligence Structures and Strategies for Complex Problem Solving* (University of New Mexico) p 679
[11] Berndt D J, Fisher J, Johnson L, Pinglikar J and Watkins A 2003 Breeding Software Test Cases with Genetic Algorithms *Proceedings of the Thirty-Sixth Hawaii International Conference on System Sciences* **36**
[12] Liu Z, Chen Z, Fang C and Shi Q 2014 Hybrid Test Data Generation / State Key Laboratory for Novel Software Technology *Companion Proceedings of the 36th International Conference on Software Engineering* 630-631
[13] Harman M, McMinn P 2010 A Theoretical and Empirical Study of Search-Based Testing: Local, Global, and Hybrid Search *IEEE Transactions on Software Engineering* **36(2)** 226-247
[14] Xing Y, Gong Y Z, Wang Y W and Zhang X Z 2015 A Hybrid Intelligent Search Algorithm for Automatic Test Data Generation *Mathematical Problems in Engineering* **2015** 15
[15] Paduraru C, Melemciuc M C 2018 An Automatic Test Data Generation Tool using Machine Learning *13th International Conference on Software Technologies, ICSOFT* 472-481
[16] Panda M, Sarangi P and Dash S 2015 Automatic Test Data Generation using Metaheuristic Cuckoo Search Algorithm *International Journal of Knowledge Discovery in Bioinformatics* **5(2)** 16-29
[17] Doungsa-ard C, Dahal K, Hossain A G and Suwannasart T 2007 An automatic test data generation from UML state diagram using genetic algorithm *IEEE Computer Society Press* 47-52
[18] Sabharwal S, Sibal R and Sharma C 2011 Applying Genetic Algorithm for Prioritization of Test Case Scenarios Derived from UML Diagrams *IJCSI International Journal of Computer Science* **8(3/2)**
[19] Doungsa-ard C, Dahal K, Hossain A and Suwannasart T 2008 GA-based Automatic Test Data Generation for UML State Diagrams with Parallel Paths *Advanced design and manufacture to gain a competitive edge: New manufacturing techniques and their role in improving enterprise performance* 147-156
[20] GrochtmannM, GrimmK 1993 Classification trees for partition testing. Software Testing *Verification and Reliability* **13(2)** 63-82

[21] Chen T Y, Poon P L and Tse T H 2000 An integrated classification-tree methodology for test case generation *International Journal of Software Engineering and Knowledge Engineering* **10(6)** 647-679
[22] Cain A, Chen T Y, Grant D, Poon P, Tang S and Tse T H 2004 An Automatic Test Data Generation System Based on the Integrated Classification-Tree Methodology *Software Engineering Research and Applications, Lecture Notes in Computer Science* **3026** 15
[23] Serdyukov K, Avdeenko T 2017 Investigation of the genetic algorithm possibilities for retrieving relevant cases from big data in the decision support systems *CEUR Workshop Proceedings* **1903** 36-41
[24] Yang HL, Wang C S 2008 Two stages of case-based reasoning - Integrating genetic algorithm with data mining mechanism *Expert Systems with Applications* **l 35** 262–272
[25] Mühlenbein H 1992 *How genetic algorithms really work: Mutation and hill climbing* (Parallel Problem Solving from Nature 2, North−Holland)
[26] Spears W M 1993 *Crossover or mutation? Foundations of Genetic Algorithms 2*
[27] Praveen RS, Tai-hoon K 2009 Application of Genetic Algorithm in Software Testing *International Journal of Software Engineering and Its Applications* **3(4)** 87-96
[28] Coyle L, Cunningham P 2004 Improving recommendation ranking by learning personal feature weights *Proc. 7th European Conference on Case-Based Reasoning* 560-572

Acknowledgments
The work was supported by a grant from the Ministry of Education and Science of the Russian Federation in the framework of the project part of the state task, the project № 2.2327.2017/4.6.

Visual-inertial odometry algorithms on the base of thermal camera

A P Alekseev[1,2], E V Goshin[1,2], N S Davydov[1,2], N A Ivliev[1,2] and A V Nikonorov[1,2]

[1]Image Processing Systems Institute of RAS - Branch of the FSRC "Crystallography and Photonics" RAS, Molodogvardejskaya street 151, Samara, Russia, 443001
[2]Samara National Research University, Moskovskoe Shosse, 34A, Samara, Russia, 443086

e-mail: goshine@yandex.ru, artniko@gmail.com

Abstract. A trajectory building based on a camera data is one of the most popular tasks in the field of machine vision. In particular, this task appears when it is necessary to navigate in the absence of signals from global navigation systems such as GLONASS and GPS. In this work, study of existing methods of visual odometry for the flight trajectory restoration by shooting an infrared camera of the thermal range were conducted. To improve the accuracy, it is proposed to use the data from inertial sensors. As a result, it is shown that the proposed solution allows to successfully solve the problem of trajectory reconstruction.

1. Introduction

Nowadays, there is a need to create methods for building navigation systems based on the usage of video data, which would be based on cheap off-the-shelf hardware and software. One of the fundamental tasks in the field of mobile robots and unmanned vehicles is the localization of the object or vehicle. Along with existing systems, such as pulsed laser systems (e.g. LiDAR [2, 7], IMU [5], GPS, radar [6]), visual odometry methods are of great interest. These methods use the video stream of the camera installed on the object. Due to its low cost in comparison to most other technical means and the availability of algorithms capable of qualitatively converting photometric information into location information, this approach turns out to be quite promising. Of course, this method has disadvantages. Poor illumination of the scene can adversely affect the assessment of movement, besides, it is necessary to dominate the environment of static objects for better correct comparison.

Visual odometry in the case of infrared (IR) shooting has additional difficulties. The low contrast of the image from the infrared camera make it necessary to do an additional processing, which affects its speed. Sharpness of objects in the IR range is low. In addition, there are fundamental geometric constraints for determining the precise rotation and movement of a camera through images. For many systems, however, this is the most promising approach, its combinations with the use of other additional sensors (LiDAR, IMU, etc.) are not uncommon. Modern researches are far advanced in easing restrictions for the applicability of this method. Such researches are based on several 3D reconstruction techniques, which are widely useful in other applications e.g. [8], [9]. This paper shows the result of testing modern approaches of visual odometry in relation to data from a monocular IR camera.

In this article, a comparison of the existing approaches to the trajectory building with the use of a video sequence from an IR camera is made, the optimal approach has been chosen and a conclusion

has been made about its applicability for solving the problem of visual odometry. An approach to improving the accuracy of IR odometry through the use of inertial sensor readings is also proposed.

2. Monocular visual inertial odometry methods

Most monocular visual odometry algorithms for small UAVs are based on the technology of parallel tracking and mapping of PTAM (Parallel Tracking and Mapping) [3]. The PTAM technology is based on the method of simultaneous localization and mapping of the SLAM (simultaneous localization and mapping) map. SLAM provides reliability by tracking and displaying hundreds of control points and it works in real time. A special feature is the simultaneous execution of the task of displaying destinations and estimating the displacement, taking into account a rather effective correction based on processing images from different viewing angles. PTAM technology was developed for augmented reality applications in small spaces. There are several modifications of it, for example, with a limited number of personnel, which ensures its full-fledged work in the conditions of spaces with urban-type buildings [1].

According to research [4, 8]:

Nowadays the following methods are applied:

• single chamber (monoVO)

• multichamber (stereoVO, RGBD-vo)

Methods using data from one camera:

Direct:

• direct distributed (DSO - direct sparse odometry)

• semidirect (SVO - semi-direct odometry)

Indirect:

• method of key points (feature-base visual odometry)

• half-line

A comparison of the approaches is presented in Table 1, the details are analyzed in detail in [4, 8].

Table 1. The comparison of approaches to the construction of the trajectory.

Feature-based	**Direct**
Use only features (for example, angular)	Use the whole image
Faster	Slower (but can be well parallelized)
Easy to remove noise (outliers)	Not easy to remove noise
Resistant to rolling shutter	Not resistant to rolling shutter
Use a small amount of information from the images	Use more complete information
Do not require complex initialization	Require complex initialization
Sensitive to image intensity distortions	Less sensitive to image intensity distortions
Over 20 years of intensive development	About 4 years of research

All monocular algorithms have a set of similar requirements and limitations:

1. The need for accurate camera calibration. Less critical for feature-based algorithms.

2. The inability to determine the scale without the help of external sensors or user.

3. Camera requirements: high shooting speed and wide viewing angle. These parameters are associated with each other, and with the maximum speed of movement of the camera.

For the solvable problem of odometry using IR video streams, some of the drawbacks of indirect methods are critical, for example, when IR shooting, the sensitivity of the method to changes in intensity is essential. That is why the choice was made in favor of the algorithm DSO.

2.1. Description of the direct visual odometry method

The semi-direct odometry model is associated with a dense model, however, it will be shown later that sparse depth information is sufficient to obtain a rough estimate of the motion and the search function of control points [4]. As soon as the control points and the initial position of the camera are found, the

algorithm will use only control points. This explains its name - “semidirect”. This technique allows you to quickly set the processing frame in the new image. The Bayesian filter, which explicitly removes erroneous measurements, also evaluates the depth and positions of the control points. That is, a point is plotted on a three-dimensional map only when the accompanying depth filter has given convergence, which requires multiple measurements. The result of the work is a three-dimensional map with control points, whose reliability has been verified

The speed of the DSO algorithm significantly increases if the control points are not extracted from all frames, but only the key ones. Accuracy is also increased when using the sub-pixel checkpoint extraction function. Unlike direct methods, many small sections are used here, rather than several large flat sections, which positively affects the speed of the algorithm and its reliability.

As part of the project, the task was to form the trajectory of the infrared camera with reference to the objects of the terrain. The first stage is the assessment of existing approaches for solving this problem in the visible range. Despite the various methods of counting, common to all methods is the conversion of the processed image into shades of gray. Further actions take place with a monochromatic image.

Direct sparse odometry is based on continuous optimization of the photometric error over the last frame window, taking into account the photometrically calibrated imaging model. Unlike existing direct methods, all the involved parameters are jointly optimized here (built-in cameras, external cameras and inverse depth values), effectively performing the photometric equivalent of adjusting a window sparse beam. The geometric representation used by other direct approaches is preserved, that is, the points are represented as the inverse depth in the frame of reference (and, thus, have the same degree of freedom).

2.2. Visual inertial odometry

This paper proposes a modification of the DSO, which allows to take into account the data of inertial sensors when restoring the trajectory. According to [4], the key procedure in the DSO algorithm is to minimize the photometric error E_{pj} between the neighborhood of a point $\mathbf{p}$ in the reference frame I_i and the neighborhood of the corresponding point $\mathbf{p}'$ in the target frame I_j:

$$E_{pj} = \sum_{p \in N_p} w_p \left\| \left(I_j(\mathbf{p}') - b_j \right) - \frac{t_j e^{a_j}}{t_i e^{a_i}} \left(I_i(\mathbf{p}) - b_i \right) \right\|_\gamma . \quad (1)$$

Here, $N_\mathbf{p}$ neighborhood of the point where minimization is performed, $t_j e^{a_j}$ and $t_j e^{a_j}$ describe the exposure of the relevant frames, $\| \|_\gamma$ Huber rate, w_p keyframe weight.

In the original DSO point $\mathbf{p}'$ is found as a back projection of a point $\mathbf{p}$ in the reference frame:

$$\mathbf{p}' = \Pi_c \left(\mathbf{R} \Pi_c^{-1}(\mathbf{p}, d_\mathbf{p}) + \mathbf{t} \right), \quad (2)$$

where $d_\mathbf{p}$ inverse point depth, **R** and **t** rotation matrix and translation vector.

In this work, it is proposed to replace the rotation matrix and translation vector in formula (2) with their estimates obtained using inertial sensors. The results of experiments showed, that a visual-inertial modification of the DSO algorithm allowed to significantly increase the accuracy of visual odometry.

3. Results

3.1. IR Camera Calibration

For successful calculations and trajectory construction, it is necessary to calibrate the camera. For cameras of the visual range there are special scales (Figure 1).

The infrared camera requires the same calibration board with contrast fields. After a series of experiments, the substrate material was selected, the printing method and the ink composition for the

areas absorbing infrared radiation, and a coating with maximum contrast was found by selecting materials. Figure 1 on the right shows the finished layout of the board for calibrating the IR camera.

Figure 1. Layout of the calibration scale.

3.2. Experiment

To check the quality of the developed algorithms for visual inertial odometry, a full-scale survey was conducted from a hydroplane using two cameras, an IR and a visible range. As the infrared camera used camera thermal range COX 1000 with a resolution of 1024 * 768. A suspension was made for the field survey (Figure 2). For the control shooting used camera GoPro3. The pitch of both cameras is the same. The platform was fixed on the front wing of the wing to eliminate the structural elements of the aircraft from falling into the frame (Figure 2).

To control the accuracy of the constructed trajectory during the flight, the GPS coordinates were recorded using a mobile navigator. The trajectory of the flight experiment built on GPS is shown in Figure 3. The inertial sensor readings were taken from a mobile phone.

Figure 2. COX-1000 IR camera and its mounting on the same platform with GoPro box.

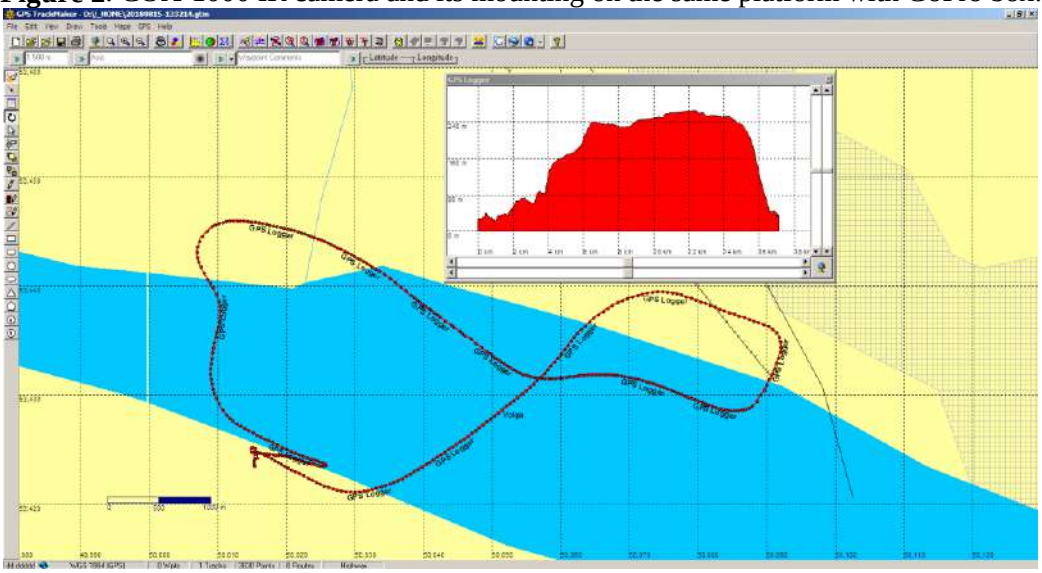

Figure 3. The trajectory and altitude map of the flight experiment recorded by GPS.

3.3. Accuracy of trajectory recovery using visual inertial odometry methods

In some areas of the flight, it was possible to build a fairly accurate flight trajectory. This selectivity is due to the characteristics of the infrared camera matrix, as well as the presence in the frame of fairly large areas with a uniform surface (water, forest). On such sites, the restoration of the trajectory is difficult. Examples of frames where trajectory recovery was completed successfully are shown in Figure 4.

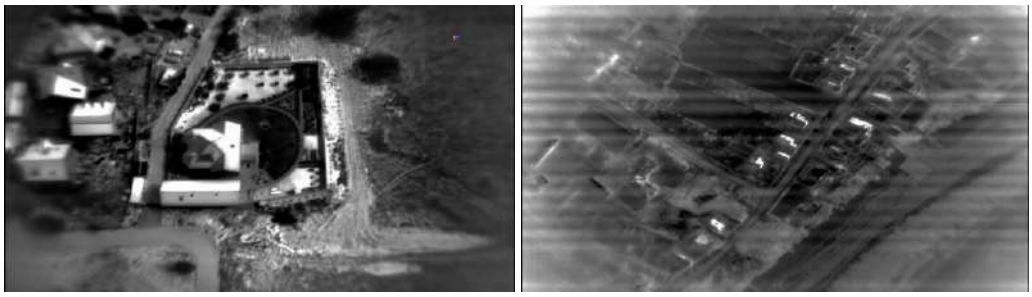

Figure 4. Examples of frames in video stream.

The proposed adjustment of the visual odometry algorithm through the use of inertial sensor data has significantly improved the accuracy of trajectory recovery. Figure 5 shows a comparison of the obtained trajectory sections with GPS data. The average deviation in the studied areas did not exceed 20 meters, which confirms the efficiency of the proposed approach.

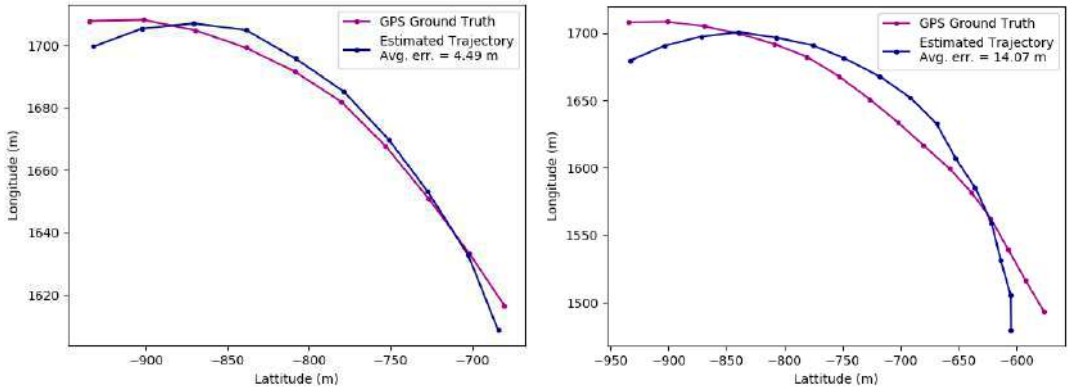

Figure 5. Comparison the trajectory reconstructed by visual odometry with trajectory recorded by GPS.

4. Conclusion

In this work, direct and indirect visual odometry methods for the problem of trajectory recovery from a sequence of frames taken in the thermal infrared range are investigated. For the experimental study, the IR camera was calibrated, a test bench was built, a test laboratory was assembled, full-scale video recordings were carried out with a camera installed on a small aircraft, under various lighting conditions and in different temperature conditions. The methods of direct visual odometry showed acceptable results on the quality of the hydroplane trajectory recovery in comparison with the GPS data. The modification proposed in this paper, which makes it possible to use inertial sensor data to clarify visual odometry, has provided a significant increase in the trajectory recovery accuracy.

5. References

[1] Baker S, Matthews I 2004 Lucas-kanade 20 years on: A unifying framework *International journal of computer vision* **56(3)** 221-255

[2] Cole D M, Newman P M 2006 Using laser range data for 3D SLAM in outdoor environments *Robotics and Automation, ICRA Proceedings IEEE International Conference* **1** 1556 DOI 10.1109/ROBOT.2006.1641929

[3] Engel J, Schöps T and Cremers D 2014 LSD-SLAM: Large-scale direct monocular SLAM *Computer Vision – ECCV* **1** 834-849
[4] Engel J, Koltun V and Cremers D 2018 Direct Sparse Odometry *IEEE Transactions on Pattern Analysis and Machine Intelligence* **40(3)** 611 DOI 10.1109/TPAMI.2017.2658577
[5] Yi J, Zhang J, Song D and Jayasuriya S 2007 IMU-based localization and slip estimation for skid-steered mobile robots *Intelligent Robots and Systems, IROS IEEE/RSJ International Conference* **6** DOI: 10.1109/IROS.2007.4399477
[6] Checchin P, Gérossier F, Blanc Ch, Chapuis R and Trassoudaine L 2010 Radar scan matching SLAM using the Fourier-Mellin transform *Field and Service Robotics* **1** 151-161 DOI: 10.1007/978-3-642-13408-1_14
[7] Hess W, Kohler D, Rapp H and Andor D 2016 Real-time loop closure in 2D LIDAR SLAM *Robotics and Automation (ICRA) IEEE International Conference* **1** 1271 DOI: 10.1109/ ICRA.2016.7487258
[8] Fursov V A, Goshin Ye V and Kotov A P 2016 The hybrid CPU/GPU implementation of the computational procedure for digital terrain models generation from satellite images *Computer Optics* **40(5)** 721-728 DOI: 10.18287/2412-6179-2016-40-5-721-728
[9] Smelkina N A, Kosarev R N, Nikonorov A V, Bairikov I M, Ryabov K N, Avdeev A V and Kazanskiy N L 2017 Reconstruction of anatomical structures using statistical shape modeling *Computer Optics* **41(6)** 897-904 DOI: 10.18287/2412-6179-2017-41-6-897-904

Acknowledgment
Methods and algorithms were designed and developed with the support of RFBR grants (projects 19-29-01235-mk, 16-29-11744-ofi_m, № 16-29-09528- ofi_m, № 17-29-03112- ofi_m, № 18-07-01390-A, № 18-37-00457-mol_a), optics and experimental studies - in the framework of the state assignment of the IPSI RAS - a branch of the Federal Scientific-Research Center "Crystallography and Photonics" of the RAS (agreement № 007-ГЗ/Ч3363/26).

Trap method in ensuring data security

D A Shkirdov[1], E S Sagatov[1] and P S Dmitrenko[2]

[1]Samara National Research University, Moskovskoe Shosse, 34A, Samara, Russia, 443086
[2]V.I. Vernadsky Crimean Federal University, Prospekt Vernadskogo, 4, Simferopol, Russia, 295007

e-mail: sagatov@ya.ru

Abstract. This paper presents the results of data analysis from a geographically distributed honeypot network. Such honeypot servers were deployed in Samara, Rostov on Don, Crimea and the USA two years ago. Methods for processing statistics are discussed in detail for secure remote access SSH. Lists of attacking addresses are highlighted, and their geographical affiliation is determined. Rank distributions were used as the basis for statistical analysis. The intensity of requests to each of the 10 installed services was then calculated.

1. Introduction

Today network and information technologies determine largely both the current standard of living and the possibilities for the future development of society. Unfortunately, modern telecommunications are inseparable from the attempts of intruders to disrupt their stable operation. These attempts have long been undertaken not by individual criminals, but by well-organised groups of hackers. In recent years, accusations of destructive actions are increasingly heard against states.

Under these conditions, the protection of telecommunications and information infrastructure becomes the most important task for both public services and private companies. For the needs of protection, a special infrastructure is created. This paper will focus on creating one of the types of such an infrastructure, known as a network of honeypot servers.

Network attacks can be divided into two large classes [1]:

• Attacks aimed at disabling the telecommunications infrastructure due to the increased load associated with a large number of calls. Overflow can concern both communication channels and the number of requests to a service. These are the so-called denial of service (DoS) attacks.

• Attacks aimed at intercepting telecommunications and information infrastructure management. These attacks are characterised by penetration into the software of the control system with a subsequent acquisition of superuser rights. It should be emphasised that all attempts to take control are carried out exclusively through network requests.

This classification suggests a way to deal with network threats. In order to successfully counter intrusions aimed at denial of service due to the increased load on the network, it is necessary to uncover the sources of the attack and block them.

To combat control interception, it is necessary to create an infrastructure that allows for recording attacking network requests and analysing them. This is necessary to fully understand the mechanism of attack. In turn, attacking requests can come in two forms. The first type is based on the human

factor. This may be the appointment of a simple password for a standard login. The human factor includes a banal betrayal associated with the transfer of information about the features of the protective infrastructure and password system, etc.

Sometimes software failures are used to intercept control, including specially opened backdoors, which are left at the insistence of special services [2]. Attacking requests of this type also need to be studied and classified.

To detect attacking requests, a special approach was proposed known as the honeypot method [3].

A lot of requests are made to the usual resources on the Internet, both legal and malicious. It is simply impossible to recognise attacking requests in the general stream. However, we can make such a resource [4], to which an ordinary user will not be accessed because there will be no content on this server. In addition, this server should not be offered to search engines for scanning. In this case, all requests can be considered suspicious.

After highlighting information about attacking requests and their sources, we can build a defensive infrastructure. First, the most vulnerable network services will be allocated based on data on the number of requests to them. Secondly, the mechanisms and frequency of using any software vulnerabilities that attackers use will become known. Thirdly, databases of attacking addresses will be formed, which will simplify their blocking. Fourthly, it will be possible to carry out active measures to investigate botnets by artificially infecting a honeypot server and tracking the further actions of intruders [5].

Finally, data on the intrusion model will allow for the formulation of relevant rules for conducting an audit of network security [6]. Moreover, these rules will be updated as data is updated from the honeypot servers. Based on the rules for auditing, appropriate software should be developed that could work in local networks and conduct preliminary testing of the most important network resources.

2. Honeypot device and measuring infrastructure

Measuring infrastructure is required for primary data collection. This infrastructure should include geographically dispersed servers. This is necessary to further verify the data and exclude random calls from the general list of attacking requests. The probability of accidental access to two or more geographically separated honeypot [7] servers is extremely small. In addition, installing multiple honeypot servers allows you to increase the database, as attacking requests, and their sources.

Our network of honeypot servers consists of 4 units. Three of them are in the European part of Russia, while one of the servers is installed on a hosting in the USA. When choosing placements, we were guided by the simplicity of the installation process and low-cost hosting. This choice is due to the fact that the data of this study was intended to create protective mechanisms in the Russian segment of the Internet. In addition to coverage, our research also distinguishes a rather long time of collecting statistics, which was more than two years.

The choice of applications installed on the honeypot server was determined by their popularity with users. All honeypot servers have the GNU Debian/Linux operating system installed. A list of protocols, services, associated software, types of attacks, and log files with their location is given in Table 1.

Table 1. Basic parameters of the honeypot server.

№	Network protocol or service	Installed software	Possible attack types	Path to the data file
1	VoIP SIP, Internet telephony	Asterisk	Password selection Incoming call to search for existing number	/var/log/asterisk/messages
2	HTTP, web service	Apache, Nginx	Attempt to find admin panel phpmyadmin, CMS WP, Joomla Attempt to access node	/var/log/nginx/*
3	POP3, IMAP, email	Dovecot, exim	Password selection	/var/log/mail.log

4	MySQL, database management system	MySQL	Password selection	/var/log/MySQL/*
5	SMB, universal service to access network resources	Samba	Password selection	/var/log/Samba/*
6	Proxy, reseller server with redundancy	Squid	Password selection	/var/log/squid3/access.log
7	SSH, secure remote access	OpenSSH	Password selection	/var/log/auth.log
8	FTP, File Transfer Protocol	vsftpd	Password selection	/var/log/vsftpd.log
9	DNS, domain name service	Bind9	DNS vulnerabilities	/var/log/named.log
10	Firewall	iptables	Port scan	/var/log/iptables

Standard ports were used to configure network protocols and services. A list of all active ports open on each of the honeypot servers is given in Table 2. The netstat command was used to output data.

Table 2. List of open ports on a honeypot server.

List of open TCP IPv4 ports on a honeypot server.

```
Active Internet connections (only servers)
Proto Recv-Q Send-Q Local Address           Foreign Address         State       PID/Program name
tcp        0      0 0.0.0.0:21              0.0.0.0:*               LISTEN      532/vsftpd
tcp        0      0 91.222.129.204:53       0.0.0.0:*               LISTEN      478/named
tcp        0      0 127.0.0.1:53            0.0.0.0:*               LISTEN      478/named
tcp        0      0 0.0.0.0:22              0.0.0.0:*               LISTEN      480/SSHd
tcp        0      0 127.0.0.1:953           0.0.0.0:*               LISTEN      478/named
tcp        0      0 0.0.0.0:58201           0.0.0.0:*               LISTEN      463/rpc.statd
tcp        0      0 0.0.0.0:445             0.0.0.0:*               LISTEN      1127/smbd
tcp        0      0 0.0.0.0:3306            0.0.0.0:*               LISTEN      1035/mysqld
tcp        0      0 0.0.0.0:139             0.0.0.0:*               LISTEN      1127/smbd
tcp        0      0 127.0.0.1:5038          0.0.0.0:*               LISTEN      1422/asterisk
tcp        0      0 0.0.0.0:110             0.0.0.0:*               LISTEN      494/dovecot
tcp        0      0 0.0.0.0:143             0.0.0.0:*               LISTEN      1/init
tcp        0      0 0.0.0.0:111             0.0.0.0:*               LISTEN      453/rpcbind
tcp        0      0 0.0.0.0:2000            0.0.0.0:*               LISTEN      1422/asterisk
tcp        0      0 0.0.0.0:8080            0.0.0.0:*               LISTEN      660/apache2
tcp        0      0 0.0.0.0:80              0.0.0.0:*               LISTEN      577/nginx -g daemon
```

List of open TCP IPv6 ports on a honeypot server.

```
tcp6       0      0 :::22                   :::*                    LISTEN      480/SSHd
tcp6       0      0 :::3128                 :::*                    LISTEN      618/(squid-1)
tcp6       0      0 :::57115                :::*                    LISTEN      463/rpc.statd
tcp6       0      0 :::445                  :::*                    LISTEN      1127/smbd
tcp6       0      0 :::139                  :::*                    LISTEN      1127/smbd
tcp6       0      0 :::110                  :::*                    LISTEN      494/dovecot
tcp6       0      0 :::143                  :::*                    LISTEN      1/init
tcp6       0      0 :::111                  :::*                    LISTEN      453/rpcbind
```

List of open UDP IPv4 ports on a honeypot server.

```
udp        0      0 0.0.0.0:4520            0.0.0.0:*                           1422/asterisk
udp        0      0 0.0.0.0:4569            0.0.0.0:*                           1422/asterisk
```

```
udp        0      0 0.0.0.0:16892           0.0.0.0:*                           1422/asterisk
udp        0      0 0.0.0.0:16893           0.0.0.0:*                           1422/asterisk
udp        0      0 0.0.0.0:625             0.0.0.0:*                           453/rpcbind
udp        0      0 127.0.0.1:639           0.0.0.0:*                           463/rpc.statd
udp        0      0 0.0.0.0:5000            0.0.0.0:*                           1422/asterisk
udp        0      0 0.0.0.0:5060            0.0.0.0:*                           1422/asterisk
udp        0      0 0.0.0.0:13254           0.0.0.0:*                           1422/asterisk
udp        0      0 0.0.0.0:13255           0.0.0.0:*                           1422/asterisk
udp        0      0 0.0.0.0:42003           0.0.0.0:*                           618/(squid-1)
udp        0      0 0.0.0.0:12030           0.0.0.0:*                           1422/asterisk
udp        0      0 0.0.0.0:12031           0.0.0.0:*                           1422/asterisk
udp        0      0 0.0.0.0:53099           0.0.0.0:*                           463/rpc.statd
udp        0      0 91.222.129.204:53       0.0.0.0:*                           478/named
udp        0      0 127.0.0.1:53            0.0.0.0:*                           478/named
udp        0      0 0.0.0.0:111             0.0.0.0:*                           453/rpcbind
udp        0      0 0.0.0.0:10368           0.0.0.0:*                           1422/asterisk
udp        0      0 0.0.0.0:10369           0.0.0.0:*                           1422/asterisk
udp        0      0 91.222.129.255:137      0.0.0.0:*                           1104/nmbd
udp        0      0 91.222.129.204:137      0.0.0.0:*                           1104/nmbd
udp        0      0 0.0.0.0:137             0.0.0.0:*                           1104/nmbd
udp        0      0 91.222.129.255:138      0.0.0.0:*                           1104/nmbd
udp        0      0 91.222.129.204:138      0.0.0.0:*                           1104/nmbd
udp        0      0 0.0.0.0:138             0.0.0.0:*                           1104/nmbd
udp        0      0 0.0.0.0:18630           0.0.0.0:*                           1422/asterisk
udp        0      0 0.0.0.0:18631           0.0.0.0:*                           1422/asterisk
udp        0      0 0.0.0.0:10442           0.0.0.0:*                           1422/asterisk
udp        0      0 0.0.0.0:10443           0.0.0.0:*                           1422/asterisk
udp        0      0 0.0.0.0:14582           0.0.0.0:*                           1422/asterisk
udp        0      0 0.0.0.0:14583           0.0.0.0:*                           1422/asterisk
```

List of open UDP IPv6 ports on a honeypot server.

```
udp6       0      0 :::625                  :::*                                453/rpcbind
udp6       0      0 :::38513                :::*                                618/(squid-1)
udp6       0      0 :::111                  :::*                                453/rpcbind
udp6       0      0 :::57514                :::*                                463/rpc.statd
```

3. General statistics on ports

To process the primary data from log files with statistics, special scripts were written that operated with regular expressions and extracted the data we needed.

First, we present the data on traffic by ports, which was obtained by analysing NetFlow data for the month. The data on the most loaded ports, depending on the type of protocols, is summarised in the following Table 3.

It should be noted that Table 3 shows data only for the first 10 ports for each type of protocol. The number of flows in the column shows the number of completed flows that transmitted data on a given port. A stream can be viewed as a single connection between devices with fixed IP addresses and ports.

It should be noted that requests were made to all TCP ports without exception, and the number of requests to the most unpopular port exceeded 10 in one month. Requests on the UDP protocol were fixed only to 16743 ports, and 74.5% of UDP ports were not used.

The collected statistics allow us to rank the popularity of attacks for various types of Internet services, which were discussed in Section 3. Table 4 highlights the top ten of the most popular services for hacking.

Here, Winbox is an application for managing MikroTik RouterOS, and rpcbind is a remote procedure call service.

4. Statistics processing rules on the example of SSH service

In this section, the paper will present the basic data obtained after processing statistics from the honeypot servers. We emphasise once again that the data in this section is based on the log files of the installed services. Log files in turn contain only the response of the service to external requests. In this

section, we attempt to classify threats based on these responses. The full content of the request in most cases remains unknown to us.

Table 3. Data on the number of requests by ports.

№	TCP		UDP		ICMP	
	Port number	Number of flows	Port number	Number of flows	Request type	Number of flows
1	22	284 452	5060	280 161	8.0	23 829
2	80	84 934	137	45 550	3.3	11 989
3	23	43 213	111	4 509	3.10	1 797
4	75	32 984	523	2 397	3.2	1 121
5	3306	32 738	0	2 262	11.0	787
6	8291	32 473	53413	1 400		
7	139	13 504	1900	1 065		
8	21	11 277	123	643		
9	8080	10 798	53	596		
10	111	10 676	11211	406		

Table 4. List of popularity of services.

№	Service type	Ports
1	SSH	22
2	SIP	5060
3	HTTP	80
4	Samba	137, 139
5	Telnet	23
6	MySQL	3306
7	Winbox	8291
8	FTP	21
9	Alternate HTTP	8080, 8088, 8888, 8081, etc
10	rpcbind	111

At the beginning of the section, we will show how data is processed using the SSH server as an example. This is a remote-control service of the operating system, each session of which is protected using encryption, including the transfer of a password for user identification. Data was collected during 2017-2019, with the total period exceeding one year. Information about the size of the collected data is available in Table 5.

Table 5. Sizes of collected data.

Crimea	Rostov on Don	Samara	USA
1.20 Gb	0.46 Gb	1.15 Gb	2.53 Gb

Since the data on the honeypot server was not announced in any way (either through DNS, or registration in a search engine, or in IP telephony, etc.), all requests to the specified IP address can be considered suspicious. More suspicious are calls to the SSH server installed as part of the honeypot.

Attacking requests can be divided into two categories. The first of these should include requests for the selection of a pair: username and password. If the password is the simplest, then there is a chance to get access to the system management via a small search. The second category of attacking requests attempts to exploit the identified vulnerabilities of software implementing the server-side of the SSH protocol. It should be noted that such requests are quite difficult to identify using the analysis of log files, since this one contains only system responses.

Table 6 contains data on the number of unique addresses that sent requests to the honeypot server.

A comparison of the data in Tables 6 and 7 shows that IP addresses are sending requests unevenly. Among them are random devices that send requests by mistake, and they should be removed from the

final blacklist. In order to understand how irregularly the various devices perform requests, we constructed a rank distribution. Using specially written scripts, we will determine how many times n_i requests were sent from one IP address or another during the statistics collection period. Then we arrange these addresses in descending order of the number of requests n_i before enumerating these addresses according to the resulting queue. The dependence of the number of requests n_i on the place in the ordered list i is the rank distribution. Usually it is depicted on a graph with logarithmic axes $\lg(n_i)$ and $\lg(i)$. The resulting graph can be found in Figure 1.

Table 6. The number of IP addresses involved in requests to the SSH server.

	Crimea	Rostov on Don	Samara	USA
Total	15 970	15 527	16 486	15 909

Table 7 contains data on the total number of requests.

Table 7. Number of requests to the SSH server.

	Crimea	Rostov on Don	Samara	USA
Total	10 352 958	3 221 026	9 002 497	21 875 655

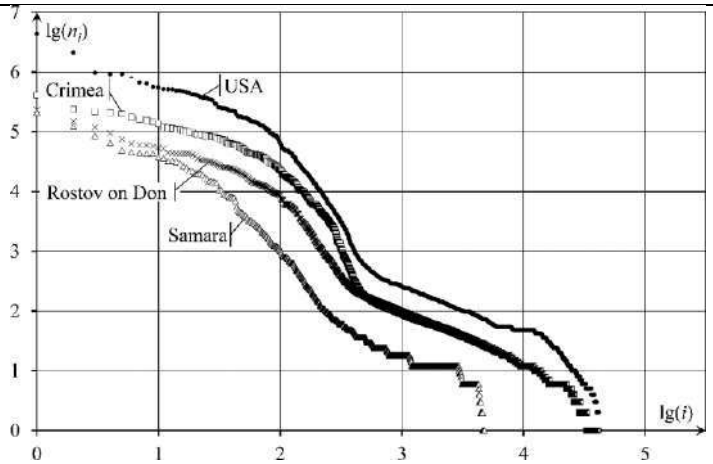

Figure 1. Rank distribution for the number of requests for SSH.

The most active IP addresses managed to send about a million requests to the SSH server. At the same time, a significant part of the addresses turned out once.

The next part of the analysis is devoted to the coincidence of attacking nodes for a geographically distributed network of honeypot servers.

Table 8 shows data on the number of matched IP addresses sending requests to SSH for each pair of honeypot servers.

Table 8. The number of matched IP for two servers.

	Crimea	Rostov on Don	Samara	USA
Crimea	15 970	17%	16%	15%
Rostov on Don	4560	15 527	16%	15%
Samara	4414	4373	16 486	14%
USA	4201	4099	4051	15 909

The total number of unique addresses that sent requests to this honeypot is on the diagonal. The number of matching IP addresses for the two honeypot servers is indicated in the cell below the diagonal. Above the diagonal is the corresponding percentage.

Table 9 shows data on the number of addresses from which requests were sent to three and four traps.

Table 9. The number of matched IP addresses for three or more traps.

Crimea, Rostov on Don, Samara	3 079
Crimea, Rostov on Don, USA	2 874
Crimea, Samara, USA	2 793
Rostov on Don, Samara, USA	2 717
Crimea, Rostov on Don, Samara, USA	2 235

However, the graph from Figure 1 shows that the number of requests from a single IP address can vary greatly. We need to understand how this number is distributed and how many requests are the same for two, three and four honeypots. Table 10 shows the pairwise matching of requests for honeypot servers.

Comparing the data in Tables 8 and 9 shows that matching requests originate from IP addresses from the top of the rank distribution. That is, the same attacking servers make the selection of the password, while the addresses from the tail of the rank distribution most likely accessed only one honeypot server, and only then by chance.

Table 10. The number of matching requests.

	Crimea	Rostov on Don	Samara	USA
Crimea	10 352 958	61%	56%	40%
Rostov on Don	8 277 703	3 221 026	57%	38%
Samara	10 856 564	6 978 442	9 002 497	46%
USA	13 021 228	9 485 649	14 235 002	21 875 655

Table 11 contains data on the number of matching requests for 3 and 4 honeypot servers. The greatest correlation between attacking requests is observed on Russian honeypots.

Table 11. Matching requests for 3 and 4 honeypot servers.

	Request number	The ratio of the total number of requests
Crimea, Rostov on Don, Samara	11 854 523	53%
Crimea, Rostov on Don, USA	13 383 641	38%
Crimea, Samara, USA	15 314 147	37%
Rostov on Don, Samara, USA	12 295 278	36%
Crimea, Rostov on Don, Samara, USA	15 832 904	36%

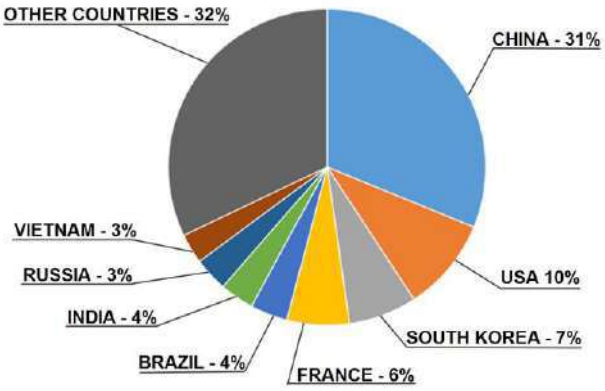

Figure 2. Distribution of IP Addresses by Country.

In conclusion, we would like to discuss the question of the criteria for including an address in the blacklist of attacking addresses. Based on these criteria, a blacklist should be made.

The criteria are based on two basic properties: the repeatability of the attacking actions and their geographical distribution. That is, from an IP address listed in the blacklist, attacks must be made at least three times. The target of these attacks should be at least two honeypot servers. As a result of data processing, 7 475 addresses were included in the blacklist.

The diagram in Figure 2 shows the distribution of IP addresses from the blacklist by country.

The diagram in Figure 3 shows the distribution of attacking requests by country.

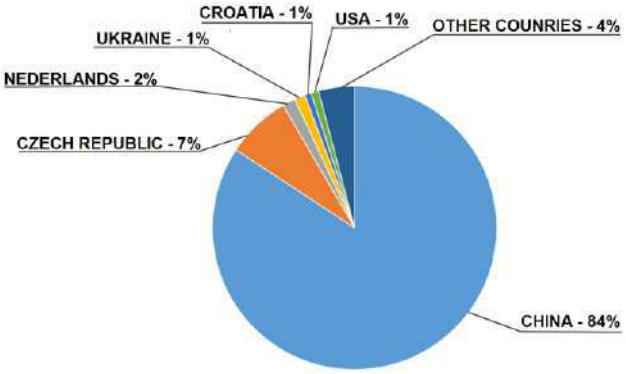

Figure 3. Distribution of attack requests by country.

The ordinate axis delayed the number of requests to the Samba service for the week. Data was taken from a honeypot server located in the USA. The intensity of the attack has increased dramatically since November 2017. Since September 2018, the intensity of the attacks has returned to background values. More than 860 thousand IP addresses sent requests to the American honeypot. In Russia, the intensity of the attacks was an order of magnitude less, and the greatest activity of the attacks was recorded in Rostov on Don.

5. General statistics for Internet services

After the log files for all ten Internet services are processed, we would like to see the comparative tables for the main types of variables that characterise the attacks. The first of these tables should contain data on the number of addresses in the blacklist for each service installed as part of the honeypot.

Table 12. The number of addresses in the blacklist.

№	Service type	The number of addresses in the black list
1	iptables	76 278
2	Samba	66 262
3	Web	7 870
4	SSH	7 475
5	SIP	1 914
6	MySQL	1 039
7	DNS	657
8	Mail	387
9	FTP	360
10	Squid	279

Naturally, the largest list of attacking addresses can be obtained by using a firewall. It detects a request on any ports and types of protocols, and therefore the size of its blacklist is the most complete. It contains the attacking addresses of all network protocols. It is surprising that the second place in the number of attacking addresses is the Samba service, which allows us to access disks and printers from various operating systems.

Another useful type of information on the structure of intrusions is the analysis of countries attacking requests and their IP addresses can be linked back to. Such information is compiled in

Tables 13 and 14. In these tables, the first three countries from the intrusion rating are given for each of the Internet services. Table 14 is based on data by IP addresses, and Table 14 contains data on the number of requests. In each cell, where the country is indicated, data on its percentage contribution to the general structure of attacking requests is also given.

Table 13. Leading Countries by Number of Attacking Addresses.

№	Service type	Countries whose IP addresses are under attack		
1	iptables	China (14%)	USA (14%)	India (7%)
2	Samba	Russia (14%)	Vietnam (12%)	Indonesia (12%)
3	Web	USA (13%)	China (8%)	India (6%)
4	SSH	China (31%)	USA (10%)	Republic of Korea (7%)
5	SIP	France (24%)	USA (22%)	Germany (16%)
6	MySQL	China (82%)	USA (9%)	Brazil (1%)
7	DNS	USA (26%)	China (19%)	Russia (8%)
8	Mail	USA (41%)	France (11%)	Russia (10%)
9	FTP	USA (30%)	France (15%)	Russia (11%)
10	Squid	Russia (18%)	China (17%)	USA (16%)

The data in these tables convincingly indicates from which country the vast majority of attacks are carried out. France, China and the USA can be attributed to the top three of such countries.

Also, the data of Tables 12, 13, 14 allow us to distinguish the main types of intrusions. Password pickup is the greatest threat (a simple password is up to 90% of all hacking incidents). Software flaws are the second most common threat. Data analysis shows that the largest number of holes can be found in the Samba service, but critical vulnerabilities can also occur in web servers, databases and mail servers.

Table 14. Leading Countries by the Number of Attacking Requests.

№	Service type	Countries whose IP addresses are under attack		
1	SIP	France (41%)	Netherlands (24%)	Germany (9%)
2	iptables	France (40%)	Germany (24%)	Russia (14%)
3	SSH	China (83%)	Czech (7%)	Netherlands (2%)
4	Samba	Russia (13%)	Vietnam (11%)	India (8%)
5	DNS	China (90%)	Netherlands (2%)	USA (2%)
6	Web	Ukraine (24%)	USA (20%)	France (18%)
7	MySQL	China (82%)	USA (9%)	Hong Kong (2%)
8	Mail	USA (41%)	France (11%)	Russia (10%)
9	Squid	France (38%)	Russia (12%)	Lithuania (11%)
10	FTP	Lithuania (77%)	France (10%)	USA (8%)

6. Conclusions

In this paper, we presented a series of results that were obtained using the honeypot method. By honeypot we mean a server on which 10 of the most popular Internet services are installed. This server is installed anonymously, without notification and registration, but on a public IP address. Therefore, repeated requests to the honeypot server can be considered suspicious.

Analysis of the log files of the network of honeypots, whose servers are scattered around the world, allow us to make a network intrusion model. This model consists of a number of elements. This paper presents the statistics of calls by ports and protocols and analyses the popularity of installed Internet services.

The processing of the received data is considered in detail using the example of the operating system remote control service SSH. First of all, the rank distribution is constructed for the number of requests to SSH. There is also a correlation between addresses attacking geographically distributed

honeypot servers. The rules for blacklisting the IP addresses of attacking addresses are discussed and fixed.

In addition to statistics for one of the services, data is presented for honeypot servers as a whole. The sizes of blacklists for all 10 services are compared, and the intensity of requests to each of the services is given. Separately, we analysed the geographical affiliation of attacking addresses and requests. For each of the services, the first 3 countries are allocated, the IP addresses of which provide the largest number of attacking requests.

The volume of data obtained is quite large, and in this paper only a small part of the results is given. We expect in the near future to provide new statistics obtained during the processing of the data.

7. References

[1] Gu Y, McCallum A and Towsley D 2005 October Detecting anomalies in network traffic using maximum entropy estimation *Proceedings of the 5th ACM SIGCOMM conference on Internet Measurement* 32-32

[2] Evsyutin O, Kokurina A and Mescheriakov R 2019 A review of methods of embedding information in digital objects for security in the internet of things *Computer Optics* **43(1)** 137-154 DOI: 10.18287/2412-6179-2019-43-1-137-154

[3] Spitzner L 2003 The honeynet project: Trapping the hackers *IEEE Security & Privacy* **99(2)** 15-23

[4] Wang R, Liu Z, Tao M and Zhang L 2015 Identifying Internet background radiation traffic based on traffic source distribution *Journal of High Speed Networks* **21(2)** 107-120

[5] Bhuyan M, Bhattacharyya D and Kalita J 2015 Towards Generating Real-life Datasets for Network Intrusion Detection *IJ Network Security* **17(6)** 683-701

[6] Ryoo J, Rizvi S, Aiken W and Kissell J 2013 Cloud security auditing: challenges and emerging approaches *IEEE Security & Privacy* **12(6)** 68-74

[7] Watson D and Riden J 2008 April The honeynet project: Data collection tools, infrastructure, archives and analysis *Workshop on Information Security Threats Data Collection and Sharing* 24-30

Acknowledgements

The work was done with the financial support of the Ministry of Science and Higher Education of the Russian Federation within the framework of state task No. 2.974.2017/4.6.

Using the bag-of-tasks model with centralized storage for distributed sorting of large data array

S V Vostokin[1], I V Bobyleva[1,2]

[1]Samara National Research University, Moskovskoe Shosse, 34A, Samara, Russia, 443086
[2]Joint Stock Company Space Rocket Center Progress, Zemetsa str., 18, Samara, Russia, 443009

e-mail: easts@mail.ru, ikazakova90@gmail.com

Abstract. The article discusses the application of the bag of tasks programming model for the problem of sorting a large data array. The choice is determined by the generality of its algorithmic structure with various problems from the field of data analysis including correlation analysis, frequency analysis, and data indexation. The sorting algorithm is a block-by-block sorting, followed by the pairwise merging of the blocks. At the end of the sorting, the data in the blocks form an ordered sequence. The order of sorting and merging tasks is set by a static directed acyclic graph. The sorting algorithm is implemented using MPI library in C ++ language with centralized storing of data blocks on the manager process. A feature of the implementation is the transfer of blocks between the master and the worker MPI processes for each task. Experimental study confirmed the hypothesis that the intensive data exchange resulting from the centralized nature of the bag of task model does not lead to a loss of performance. The data processing model makes it possible to weaken the technical requirements for the software and hardware.

1. Introduction

The article studies the possibility of using a model of distributed computing, called the bag of tasks [1], for solving problems of analysis and processing a large data array.

To solve the problems involving the processing and analysis of data, expensive specialized hardware and software are commonly used. However, in companies or institutions where such processing is carried out, there is already a large fleet of desktop computers, workstations, laptops of employees, and even cluster systems, whose resources are not fully used in normal operating conditions. Therefore, from the point of possible reduction in equipment costs, the use of the entire available hardware infrastructure not originally dedicated for data processing is promising in solving data intensive problems [2].

For making calculations on non-dedicated equipment, special programming models and software platforms supporting them are used [3]. One of these programming models is the bag of tasks model. This model has a star-like communication topology of processes. It consists of one master process and a group of worker processes. The worker processes execute tasks that come from the master process and when return the result back to the master process. Worker processes do not have a state. The state

of the calculations, the so-termed the bag of tasks, is monitored by the master process. This state can be updated after the current tasks in worker process is completed and returned to the master process.

The definition of parallel computations in the terms of the bag of tasks model has a number of advantages when distributed application is running on unreliable heterogeneous hardware and software environment.

First, the application has a single point of failure, namely the master process. Worker process failure is not critical.

Second, only the master process is required to accept connections, worker process can only support outgoing connections.

Third, to define a new algorithm in the bag of tasks model, it is sufficient to define 4 sequential procedures. These procedures are (1) checking whether the task to the worker process is available in the current state of the bag; (2) creation of a new task and the bag state update; (3) processing of task in the worker process; (4) receiving the task result and the bag state update. The other parts of the code are reused in every bag-of-tasks applications.

Fourth, the control scheme in the bag of tasks model in most cases does not require special methods of load balancing. This is convenient for programmers because the performance of computers on the network can vary significantly.

While having the above mentioned advantages, the bag of tasks model has one potential drawback. The master process may be a bottleneck in the case of intensive data exchange. Therefore, the applicability of the model in a particular case is determined by the joint characteristics of the problem and the equipment that is used to solve it. That is why a study is required before applying the bag of tasks model to data processing problems.

The goal of our research was to test experimentally the applicability of the bag of tasks model for making calculations on cluster systems without optimization of traffic between the master and the worker processes in solving the block sorting problem.

2. Related work

Our research relates to the field of algorithmic skeletons. This technique of building parallel algorithms allows us to separate the algorithmic (sequential) part of the code from the parallel part. Details of the algorithmic skeletons are described in the review [4].

Algorithmic skeletons are widely used in data processing. An example of such a skeleton is the MapReduce [5]. We focused on another well-known skeleton called Bag-of-tasks [1]. The reason is the “star” communication graph, which is typical both for the Bag-of-tasks skeleton and desktop grid computing in general [6]. The MapReduce skeleton does not apply to desktop grids, as it requires a network with a one-to-one communication graph.

We use a cluster system as a model of desktop grid systems. Computer clusters were successfully used as components of the desktop grids in many studies. A good example is parallel image processing, which is discussed in detail in the article [7]. The the technique of combining BOINC grid [8] and clusters with Torque and Slurm batch systems was shown in [9].

Parallel paired data processing is a frequently used algorithmic technique. It was automated in the algorithmic skeleton called AllPair [10]. Our implementation of pairwise processing is different in that we have limitations on parallel-running pairs and the order in which pairs are processed. The introduction of these restrictions allows us to obtain the sorting algorithm. The sorting algorithm is a block version of the bubble sort. The efficiency of the algorithm compared to the quick sorting we studied earlier in [11]. Block algorithms allow to optimize performance in different areas of computing then heterogeneous and/or distributed hardware is in use [12].

The applied objective of the study is to extend the set of algorithms for managing tasks in the Everest platform [3]. For the platform, the authors had previously developed a variant of the Map skeleton [13].

3. Method of the experimental study

In the study, we use the block sorting problem as a reference problem from the data processing domain. The choice of the block sorting problem is determined by the commonality of its algorithmic

structure with various problems of data analysis, including correlation analysis, frequency analysis, and data indexing.

The block sorting algorithm sorts each data block and then makes the pairwise merging of sorted blocks in the round-robin tournament manner. At the end of the block sorting algorithm, the data in all the blocks form an ordered sequence. Two types of tasks are placed in the bag of tasks: sorting of one block and merging of two blocks. Both types of tasks modify the content of blocks by rearranging elements, while the total number of blocks and their size does not change. The order of merging tasks is defined by the DAG (directed acyclic graph in Fig.1), which is interpreted by the master process in the course of calculations.

The peculiarity of the algorithm implementation is the transferring large blocks of data from the master process to the worker processes and back to the master process for each task. In the study, we deliberately did not use assistive technologies that optimize traffic, such as block caching on worker processes or direct data exchange between worker processes.

As a model of the computing equipment in the experiments we used "Sergey Korolev" cluster system of collective use that installed at Supercomputer center of Samara University (hpc.ssau.ru). The choice is due to the simplicity of programming of the distributed sorting in the bag of tasks model using MPI technology and C++ language. Also the deployment of sorting application components to compute nodes using the Torque batch system is simple too.

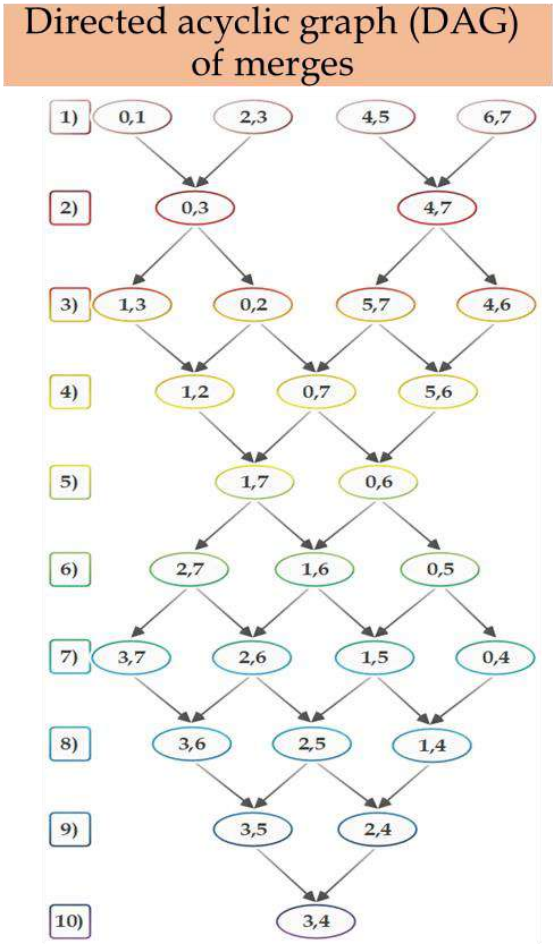

Figure 1. The DAG of merging tasks.

A cluster system has the greatest capacities in the computing infrastructure of any company or institution. A positive test result of block sorting using the bag of tasks model (the speedup of calculations) on the "Sergey Korolev" cluster opens up the possibility of further research on another type of non-dedicated computing equipment available on enterprise network.

4. Results and discussion of the block sorting experiment

The experimental study of the sorting algorithm confirmed the hypothesis that intensive data exchange in cluster system (which is a consequence of the implementation of block sorting algorithm according to the bag of tasks model) nether the less gives the possibility to speedup the calculations.

In the experiment, an array consisted of 8 blocks of 50 million 8-byte integers in each block. The 8 “sorting one block” tasks were performed with standard C ++ std::sort library algorithm and then 28 “merging two blocks” tasks were performed with standard C ++ std::merge algorithm.

The multilevel structure of the DAG had 10 tiers (Fig.1), a maximum of 4 parallel calls to std::merge in one tier. The programming and control of computational experiments on the cluster was performed on the TempletWeb system [14]. The results of experimental study are presented in Table 1 and Fig. 2.

Sequential sorting time of the entire array of 8 blocks on one cluster node (http://hpc.ssau.ru/node/6) using std::sort standard C++ library algorithm was about 110.8 seconds. The sequential sorting time on one cluster node for the block sorting program adapted to the bag of tasks model was about 118.9 seconds. In the parallel version of the program, when the master process and 8 worker processes were deployed on separate nodes of the cluster, the time of execution became 23.6412 seconds (the best result). This result corresponds to nearly five times speedup.

Table 1. Times in seconds of sequential and parallel execution of the block sorting test depending on the number of nodes.

№	Nodes	SEQ	PAR
1	2	118,986	126,947
2	3	118,988	64,4385
3	4	118,996	48,493
4	5	118,99	35,7863
5	6	125,063	39,0551
6	7	124,8	38,1016
7	8	128,148	37,1677
8	9	118,987	23,6412

A series of experiments was carried out in which different variants of the program deployment on the nodes of the cluster system were investigated. It was discovered that despite the fact that the nodes of the cluster support minimum 8 hardware threads, the deployment of all processes on a single node gives the worst result (~35,6 seconds) compared with the deployment of processes under the scheme 1 process on 1 node. The overhead of competing between processes for a shared data bus on a node was even greater than the overhead of transferring data between nodes.

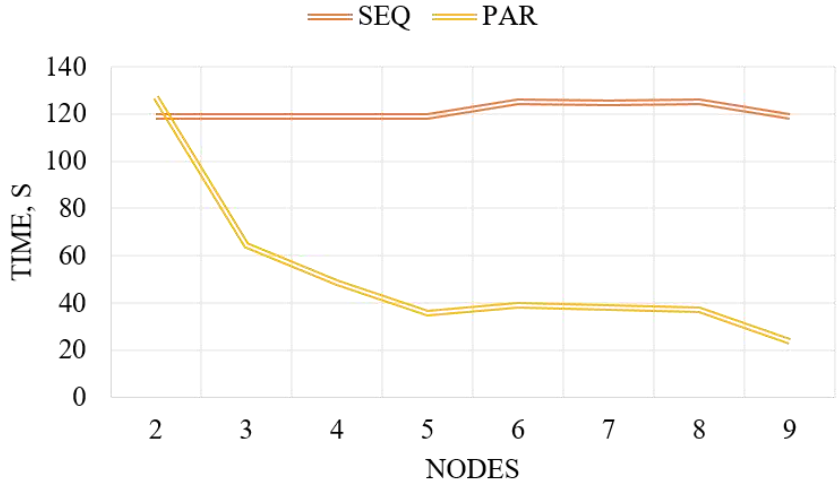

Figure 2. Comparison of sequential and parallel execution depending on the number of nodes.

5. Conclusion

The experiments confirmed the suitability of the bag of tasks model for computing on cluster systems even without using algorithmic techniques to optimize the traffic between the master process and the worker processes in solving the block sorting problem of large data array.

Thus, the bag of tasks model allows to reduce technical requirements for hardware and can be used to solve applied problems of analysis and processing of large information arrays on existing computing networks of companies or institutions.

6. References

[1] Senger H and da Silva F 2012 Bounds on the Scalability of Bag-of-Tasks Applications Running on Master-Slave Platforms *Parallel Processing Letters* **22**
[2] Ivashko E E 2015 Enterprise Desktop Grids *CEUR Workshop Proceedings* **1502** 16-21
[3] Sukhoroslov O and Volkov S 2015 Web-Based Platform for Publication and Distributed Execution of Computing Applications *14th International Symposium on Parallel and Distributed Computing (ISPDC)* 175-184
[4] González-Vélez H and Leyton M 2010 A survey of algorithmic skeleton frameworks: high-level structured parallel programming enablers *Software: Practice and Experience* **40(12)** 1135-1160
[5] Dean J and Ghemawat S 2008 MapReduce: simplified data processing on large clusters *Communications of the ACM* **51(1)** 107-113
[6] Cérin C and Fedak G 2012 *Desktop grid computing* (Paris: CRC Press)
[7] Volotovsky S G, Kazanskiy N L, Popov S B and Serafimovich P G 2010 Performance analysis of image parallel processing applications *Computer Optics* **34(4)** 567-572
[8] Anderson D P 2004 BOINC: A system for public-resource computing and storage *Proceedings - IEEE/ACM International Workshop on Grid Computing* 4-10
[9] Afanasyev A P and Lovas R 2011 Increasing the computing power of distributed systems with the help of grid systems from personal computers *Proceedings of the conference "Parallel Computational Technologies* 6-14
[10] Moretti C and Bulosan J 2008 All-pairs: An abstraction for data-intensive cloud computing *IEEE International Symposium on Parallel and Distributed Processing* 1-11
[11] Vostokin S V and Kazakova I V 2018 Implementation of stream processing using the actor formalism for simulation of distributed insertion sort *Journal of Physics: Conference Series* **1096(1)**
[12] Yablokova L V and Golovashkin D L 2018 Block algorithms of a simultaneous difference solution of d'Alembert's and Maxwell's equations *Computer Optics* **42(2)** 320-327 DOI: 10.18287/2412-6179-2018-42-2-320-327
[13] Volkov S and Sukhoroslov O 2015 Running Parameter Sweep Applications on Everest Cloud Plat-form *Computer Research and Modeling* **7(3)** 601-606
[14] Vostokin S V and Artamonov Y S 2018 Templet Web: the use of volunteer computing approach in PaaS-style cloud *Open Engineering* **8** 50-56

Acknowledgments

This work is partially supported by the Ministry of Education and Science of the Russian Federation in the framework of the State Assignments program (#9.1616.2017/4.6).

An investigation of machine learning method based on fractal compression

E Y Minaev[1,2]

[1]Samara National Research University, Moskovskoe Shosse, 34A, Samara, Russia, 443086
[2]Image Processing Systems Institute of RAS - Branch of the FSRC "Crystallography and Photonics" RAS, Molodogvardejskaya street 151, Samara, Russia, 443001

e-mail: eminaev@gmail.com

Abstract. In this article the method of machine learning with cyclic fractal coding and the use of domain block dictionary, adapted for use on mobile platforms, with optimization of performance and volume of stored fractal images is investigated. The main idea of the method is to use the fractal compression method based on iterated function systems to reduce the dimension of the original images, and to use cyclic fractal coding to represent the class of images. As a result of research of the method it was found that the share of correctly recognized objects on MSTAR averages 0.892, the recognition time averages 254 ms. The achieved results are acceptable for use in mobile platforms, including UAVs and ground autonomous robots.

1. Introduction

The problem of using existing fractal compression algorithms on mobile hardware and software platforms is noted in [1]. Traditionally, fractal compression methods have high computational complexity, and methods and algorithms for optimizing performance developed for desktop hardware platforms are not always applicable for mobile platforms [2] [3]. Modern performance solutions are based on the use of user-programmable gate arrays (FPGAs) and the use of GPUs, which makes it difficult to use these approaches for most mobile platforms. At the same time, the urgency of using fractal compression methods for mobile devices is emphasized in the article [4].

2. Implementation of machine learning method based on cyclic fractal compression

One of the promising approaches to the implementation of the classifier based on fractal compression is proposed in [5]. When we trained the classifier described in [6], the main problem was that the images forming the training sample of one class were compressed independently of each other, and were combined together only at the stage of construction of the support subspaces. At the same time, the recognition stage raises problems associated with the possible intersection of the support subspaces. Accordingly, it is necessary to apply methods that provide spatial separability, which further increases the computational complexity. In [7], a fractal compression scheme using several

different images is proposed. In this article, it is proposed to apply this scheme on cyclic sequence of images from the training set, with the formation of a dictionary of rank and domain blocks [8] and the corresponding transformations. Classic compression IFS algorithm searches the best affine transformation from domain to range block for every range block (Figure 2). As a result, an input image is coded by several affine transformations:

$$\begin{aligned} \mathbf{I}^* &= F\left(\mathbf{I}\right) = \mathbf{C}_{1,4}\mathbf{I} + \mathbf{c}_{5,6}, \\ u^*_{i,j} &= c_7 \cdot u_{i,j} + c_8, \end{aligned} \tag{1}$$

where $\mathbf{I}^* = (i^*, j^*)^T$, $\mathbf{I} = (i, j)^T$ –) is the coordinates of pixel from domain and range block accordingly, $\mathbf{C}_{1,4} = \begin{bmatrix} c_1 & c_2 \\ c_3 & c_4 \end{bmatrix}$, $\mathbf{c}_{5,6} = \begin{bmatrix} c_5 \\ c_6 \end{bmatrix}$ – transformation coefficients, $u^*_{i,j}$, $u_{i,j}$ – is the pixel brightness from range and domain area, a c_7, c_8 – contrast and brightness shift parameter.

We use eight different sets of parameters for fractal image transformation:

$\mathbf{C}_{1,4} = \begin{bmatrix} 0.5 & 0 \\ 0 & 0.5 \end{bmatrix}$, $\begin{bmatrix} 0 & -0.5 \\ 0.5 & 0 \end{bmatrix}$, $\begin{bmatrix} -0.5 & 0 \\ 0 & -0.5 \end{bmatrix}$, $\begin{bmatrix} 0 & 0.5 \\ -0.5 & 0 \end{bmatrix}$, $\begin{bmatrix} 0.5 & 0 \\ 0 & -0.5 \end{bmatrix}$, $\begin{bmatrix} -0.5 & 0 \\ 0 & 0.5 \end{bmatrix}$, $\begin{bmatrix} 0 & 0.5 \\ 0.5 & 0 \end{bmatrix}$, $\begin{bmatrix} 0 & -0.5 \\ -0.5 & 0 \end{bmatrix}$. c_5, c_6 – shift coefficients of affine transformations.

These parameters correspond to different kinds of transformations, such as rotation, domain area mapping and compression with a rate of 0.5.

The transformation is conducted in a class of contraction mapping to obtain a unique and stable fractal image (the maximum of the transformation matrix eigenvalue is less than 1). Parameters of transformations $c_1 - c_8$ are computed by IFS fractal compression algorithm: $c_1 - c_4$ are selected from the possible sets, c_5, c_6 are calculated in the process of searching the best affine transformation from domain to range block, c_7, c_8 – are calculated on the average brightness of domain and range blocks.

Set of transformations for every range block can be written as:

$$I_1 = \bigcup_i F_i(I_0). \tag{2}$$

Using the Hutchinson operator, it can be written shortly as:

$$I_1 = FI_0, \tag{3}$$

where I_0 – initial image, F – Hutchinson operator, representing set of affine transformations, I_1 – result image. The scheme of cyclic sequence of transformations for several images of training set is presented in Figure 1.

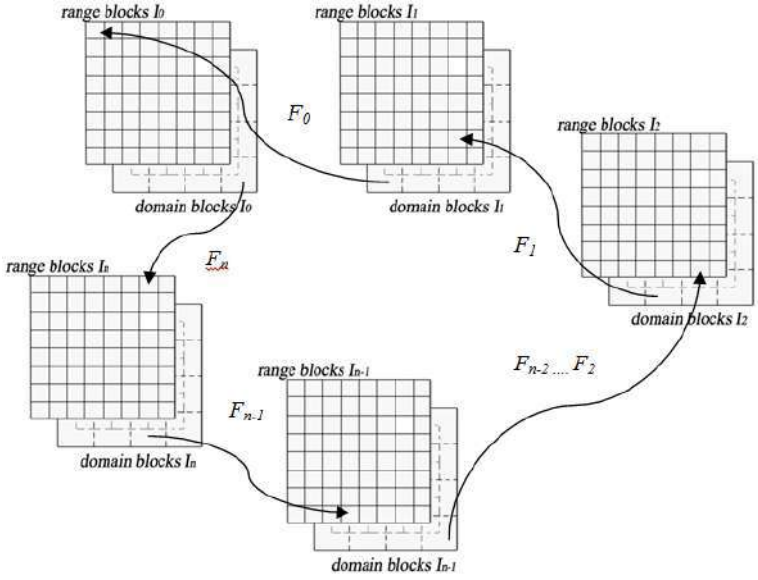

Figure 1. Scheme of cyclic sequence of transformations.

After searching the best affine transformation from domain to range block for every range block, we can compose the dictionary, including information concerning class number, range blocks division, images of range, and domain blocks with transformation coefficients, and with every class of image with different range blocks division training independently (Figure 2).

3. Classification process

Using the dictionary, we can realize the fractal coding of input images by this procedure. At first, the input image is divided into square non-overlapping range blocks. Then, for every range block we search similar appropriate range blocks with domain block and transformation for every class. As a result, we obtain a set of transformations and its initial data for every class of images. Using Hutchinson operator, it can be represented as $F_1^*, F_2^* ... F_m^*$, for *m* classes. The distance between input image and each class can be written as:

$$D_i = \frac{d(F_i^* I^*, I^*)}{I_w^* I_h^*} = \frac{\left\| F_i^* I^* - I^* \right\|_2}{I_w^* I_h^*}, \quad (4)$$

where I^* – initial image, I_w^*, I_h^* – width and height of initial image, F_i^* – Hutchinson operator for transformations of *i* class, *d* - Euclidean norm. Class with minimal distance to input image is the result of classification.

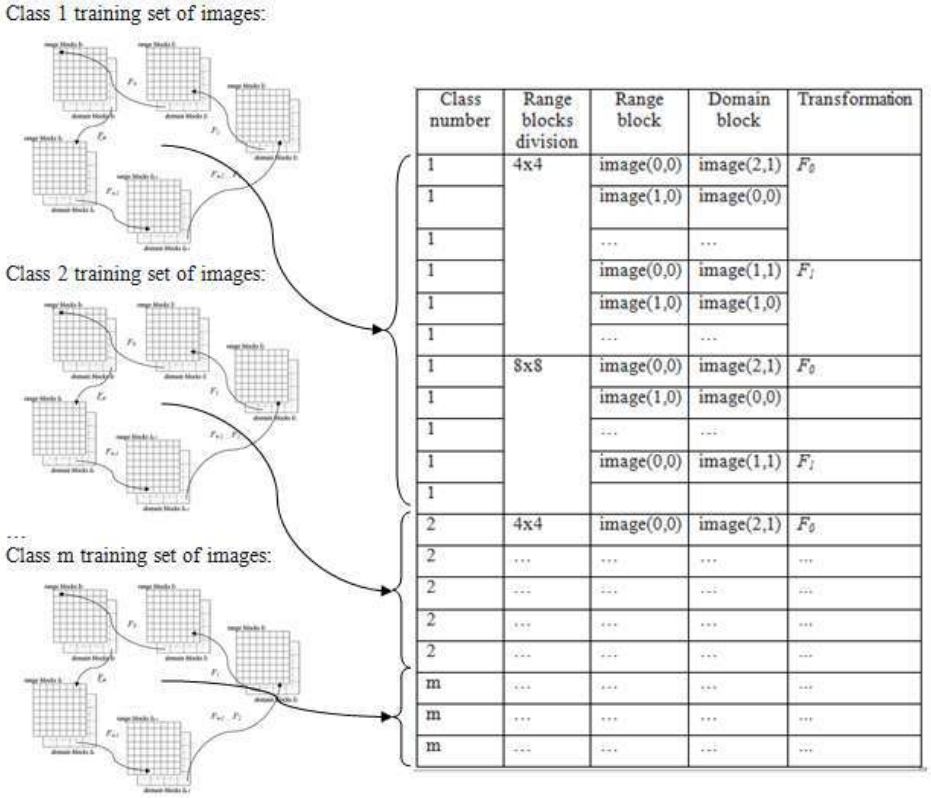

Class number	Range blocks division	Range block	Domain block	Transformation
1	4x4	image(0,0)	image(2,1)	F_0
1		image(1,0)	image(0,0)	
1		...	...	
1		image(0,0)	image(1,1)	F_1
1		image(1,0)	image(1,0)	
1		...	...	
1	8x8	image(0,0)	image(2,1)	F_0
1		image(1,0)	image(0,0)	
1		...	...	
1		image(0,0)	image(1,1)	F_1
1				
2	4x4	image(0,0)	image(2,1)	F_0
2	...	...	...	...
2	...	...	...	...
2	...	...	...	...
2	...	...	...	...
m	...	...	...	...
m	...	...	...	...
m	...	...	...	...

Figure 2. Scheme of training process.

The details of whole information technology are as follows:

(1) Classifier training. For images set representing one of the classes, we obtain an acyclic sequence of transformations. The results are written to dictionary.

(2) Repeat step (1) for all classes, and all variants of range blocks division (4×4, 8×8, etc.) for multi-scale recognition.

(3) Input test image is divided into square non-overlapping range blocks. For every range block, we search similar range blocks with domain block and transformation from the part of dictionary of class and certain range blocks division.

(4) Compute the distance between input image and class.
(5) Repeat steps (3), (4) for all classes, and all variants of range blocks division.
(6) Find class with minimal distance to input test image.
(7) Repeat steps (3), (4), (5), (6) for other input image.

4. Experiments results

In our recognition experiments, we used the MSTAR (moving and stationary target acquisition and recognition) public dataset. Objects BMP2, BTR70, T72 were used, and training and test samples were employed for each object from the dataset. These SAR images are collected using an X-band SAR sensor at two different depression angles (15◦ and 17◦). The total number of SAR images in training set is 689, whereas it is 1365 in test set. At the stage of fractal compression, a different number of range blocks were used 16 (4×4), 64 (8×8), 256 (16×16), 1024 (32×32), and accordingly, domain blocks 9 (3×3), 49 (7×7), 225 (15×15), 961 (31×31). Examples of the obtained fractal images are shown in Figure 3.

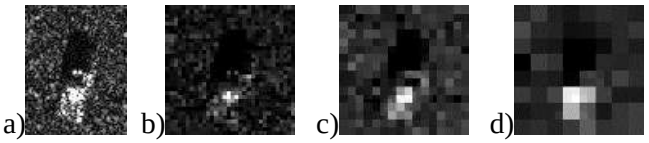

Figure 3. Examples of fractal images of an object, a – original image, b, c, d – fractal image for range blocks 32×32, 16×16, 8×8, accordingly.

An investigation of the object recognition method with cyclic fractal coding using domain blocks dictionary was tested on three-class classification task, with objects BMP2, BTR70, T72 (Table 1).

Table 1. Multiclass recognition results for 3 objects.

Class name	Share of correctly recognized objects	
	Proposed method	Saliency Attention and SIFT[11]
BMP2	0.891	0.64
BTR70	0.882	0.75
T72	0.904	0.74

The proposed method was compared with another experimental method [9]. The experimental conditions in this work are quite similar. The performance of the recognition method on mobile platforms based on the Qualcomm Snapdragon 625, 2 GHz processor was also investigated. It was found that the average recognition time of objects on the MSTAR dataset is 254 ms, which generally corresponds to the speed of processing in real time.

In another experiment we used the MNIST image database. The MNIST database (Modified National Institute of Standards and Technology database) is a large database of handwritten digits that is commonly used for training various image processing systems. The MNIST database contains 60,000 training images and 10,000 testing images (Figure 4). The purpose of the experiment is to show the stability of the object recognition method with cyclic fractal coding using domain blocks dictionary on the data with a large number of instances of the class.

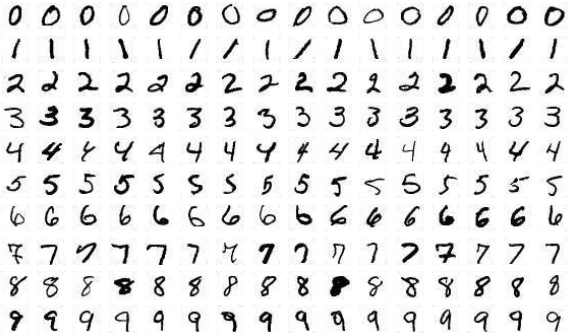

Figure 4. Sample images from MNIST test dataset.

The results of comparison with other classical recognition algorithms (without boosting, preprocessing and a combinations of several methods[10]) are given in the table 2.

Table 2. Multiclass recognition results for 10 objects.

Method name	Test error rate(%)
pairwise linear classifier	7.6
K-nearest-neighbors	2.83
SVM, Gaussian Kernel	1.4
Proposed	2.45

The results show that the proposed method shows comparable results for large databases. A promising direction of future research is to improve the quality of recognition due to additional combinations of methods of boosting, preprocessing, augmentation and reduction of dimensionality.

5. Conclusion

As a result of investigation of the machine learning method with cyclic fractal coding and using the domain block dictionary, it was found that the share of correctly recognized objects on the MSTAR dataset averages 0.892, the recognition time averages 254 ms. The achieved results are acceptable for use in mobile platforms, including UAVs and ground autonomous robots.

6. References

[1] Srivastava S, Lall B 2015 Superresolution based Medical Image Compression for Mobile Platforms *Workshop on Machine Learning for HealthCare* 01436138
[2] Chen D, Singh D 2013 Fractal video compression in OpenCL: An evaluation of CPUs, GPUs, and FPGAs as acceleration platforms *Design Automation Conference (ASP-DAC)* 297-304
[3] Son T N, Hoang T M, Dzung N T and Giang N H 2014 Fast FPGA implementation of YUV-based fractal image compression *Communications and Electronics (ICCE)* 440-445
[4] Lima V, Schwartz W and Pedrini H 2011 Fast low bit-rate 3D searchless fractal video encoding *Graphics, Patterns and Images (Sibgrapi)* 189-196
[5] Minaev E 2018 Object recognition based on fractal coding using domain blocks dictionary *Journal of Physics: Conference Series* **1096(1)** 012099
[6] Minaev E, Fursov V A 2016 Support subspaces method for fractal images recognition *CEUR Workshop Proceedings* **1638** 379-385
[7] Ozawa K 2008 Dual fractals *Image and Vision Computing* **26** 622-631
[8] Sun Y, Xu R, Chen L, Kong R and Hu X 2014 A Novel Fractal Coding Method Based on MJ Sets *PloS one* **9(7)** e101697
[9] Karine A, Toumi A, Khenchaf A and El Hassouni M 2017 Saliency attention and sift keypoints combination for automatic target recognition on MSTAR dataset *International Conference Advanced Technologies for Signal and Image Processing (ATSIP)* 1-5
[10] The MNIST Database of handwritten digits URL: http://yann.lecun.com/exdb/mnist/ (2019-05-25)
[11] Dmitriev E A, Myasnikov V V 2018 Comparative study of description algorithms for complex-valued gradient fields of digital images using linear dimensionality reduction methods *Computer Optics* **42(5)** 822-828 DOI: 10.18287/2412-6179-2018-42-5-822-828

Acknowledgments

The reported study was funded by RFBR according to the research projects No. 17-29-03112-OFI-m, 19-29-01235-mk, experimental studies - in the framework of the state assignment of the IPSI RAS - a branch of the Federal Scientific-Research Center "Crystallography and Photonics" of the RAS (agreement № 007-ГЗ/Ч3363/26).

Dynamic game task of executors incentives in projects for the development of new production in continuous time

O V Pavlov[1]

[1]Samara National Research University, Moskovskoye shosse, 34, Samara, Russia, 443086

e-mail: pavlov@ssau.ru

Abstract. The article explores the incentive problem of executors of the new products development project at the industrial enterprise in continuous time. In the process of developing new products, the learning curve effect manifests itself, which leads to a reduction in labor intensity, depending on the cumulative volume of production. The project for the new products development is considered as a managed hierarchical dynamic system, consisting of a project management board (principal) and executors (agents). The interaction of project participants is formalized as a hierarchical differential game. To solve the formulated dynamic problem of material incentives, the well-known principle of cost compensation was applied. The original problem is divided into the task of coordinated incentives and the task of coordinated planning. The study showed that the task of coordinated dynamic planning is for the principal to determine the optimal planned production volumes in order to minimize the labor cost of agents. The initial dynamic problem of material incentives was reduced to the optimal control problem. The problem of optimal control with continuous time was solved analytically using the Pontryagin maximum principle. The study identifies a condition to determine the optimal production volumes for coordination of the interests of the principal and agents.

1. Introduction

The article explores the incentive problem of executors of the new products development project at the industrial enterprise in continuous time. In the process of developing new products, the learning curve effect manifests itself, which means that labor time (labor intensity) is reduced to perform repetitive manufacturing operations. The project for the development of new products is considered as a managed hierarchical dynamic system consisting of the project management (principal) and executors (agents). The dynamics of a controlled dynamic production system depends only on the actions of the agents, and the principal affects the target function of the agents by choosing the material incentive function. The state of the hierarchical dynamic system in each time period depends on its position and the actions of the participants in the previous period. Production activity in the project for the development of new production is characterized by the diverging interests of the principal and agents, which leads to a decrease in the economic efficiency of the entire production system. To find a solution of these contradictions is possible by coordinating management mechanisms that encourage agents to choose actions that are beneficial to the principal.

Dynamic models of the interaction of unequal players are considered in the active systems theory [1–2], hierarchical information systems theory [3–5] and dynamic games theory [6–8].

The dynamic incentives task of agents in terms of the dynamic games theory is called the inverse Stackelberg game. A review of reverse Stakelberg games models has been carried out in scientific publications [9–12]. In the hierarchical information systems theory [3–5] the dynamic incentives task was called the Germeier's game Γ_2.

The theory of active systems [1] develops the approach based on the principle of cost compensation. The principal compensates the agent's costs in the case of choosing the optimal planned trajectory and does not pay material compensation in other cases. The original problem is divided into the task of coordinated incentives and the task of coordinated planning. The task of coordinated planning is reduced to the problem of optimal control. The recent study [13] explores the results that generalize the theorems in the monograph [1].

The hierarchical systems theory [3–5] suggests the approach that used the choice of the principal of the program of joint actions with the agent and punishment for deviation from this program. As a result, the initial problem is transformed into the optimization problem.

In the dynamic games theory [7], the principal plan is implemented using trigger strategies. The basic idea is that agents agree to follow a certain trajectory and punish any deviated agent.

The current study formulates and analytically solves the dynamic incentives task of agents in the conditions of learning-by-doing within the framework of the approach proposed in the monograph [1].

2. Dynamic game task of executors incentives in projects for the development of new production

2.1. The general statement and decision algorithm of a task of executors incentives in projects for the development of new production

In this dynamic game model there are dynamics of decision making and dynamics of the managed system. The inequality of participants is fixed by the moves order, the first move is made by the principal. It is assumed that agents are not linked to each other and perform actions independently.

The incentive problem is formalized dynamic game in positional strategies for two players with feedback on management:

$$J_p = \int_0^T e^{-\delta t}\{ pu(t) - \sigma(x(t)\}dt \to max,$$

$$J_a = \int_0^T e^{-\rho t}\{ \sigma(x(t)) - C(x(t),u(t))\}dt \to max,$$

$$\frac{dx(t)}{dt} = u(t),$$

$$0 < u(t) \le x_0 + R - x(t), \; t = 0,T,$$

$$x(0) = x_0,$$

$$x(T) = x_0 + R.$$

where J_p is the decision making criteria of principal, J_a is the decision making criteria of agent, δ is principal discount rate, *u(t)* is production volume of agent at time point *t, p is* product price, $\sigma(x(t))$ is incentive function of principal, *x(t)* is the cumulative production volume, *T* is the project's planning horizon, ρ is agent discount rate, $C(x(t),u(t))$ is the function of the agent's labor costs in the production of products (costs at time point *t*), x_0 is the production volume produced by the agent before starting the project, *R* is the production volume to be produced by the time point *T*.

The function of the agent's labor costs in production (costs at time point *t*) in monetary terms is defined as the product of labor intensity $c(x(t))$, production volume *u(t)* and the cost of one hour rate *s*:

$$C(x(t),u(t)) = sc(x(t))u(t). \quad (1)$$

The change dynamics in labor intensity of products from the cumulative production volume is described by different models of the learning curve. The most typical models are power, exponential and logistic ones, which are described in the scientific literature [14–17].

The degree model of the learning curve has the following form:

$$c(x(t)) = ax(t)^{-b}. \tag{2}$$

where a are costs of the first product production, b is learning index.

The learning index characterizes the speed of decrease in the unit costs of product with an increase in the cumulative production volume.

Exponential model of the learning curve:

$$c(x(t)) = k + \beta e^{-\alpha x(t)}.$$

where α is learning index k, β are parameters of the exponential model.

Logistic model of the learning curve:

$$c(x(t)) = c_{min} + (c_{max} - c_{min})\left[\frac{1}{1+\beta e^{\alpha x(t)}}\right],$$

where $c_{\min}$, $c_{\max}$ are minimum and maximum values of unit costs in product manufacturing, α is learning index, β is logistic model parameter.

To solve the formulated problem of incentives, the principle of cost compensation is applied [1].

In accordance with the principle of cost compensation, it is enough for the principal to compensate the agent costs to encourage it to choose a planned trajectory:

$$\sigma(x(t)) = C(x(t), u(t)). \tag{3}$$

Taking into account (3) and (1), the goal function of the principal is written:

$$J_p = \int_0^T e^{-\delta t}\{[p - sc(x(t))]u(t)\}dt \to max.$$

Given that the price of part p is a constant value, the maximization of the integral income of the principal can be replaced by minimizing the integral labor costs of the agent:

$$J_p = \int_0^T e^{-\delta t} C(x(t), u(t))dt \to min.$$

The solution algorithm consists of dividing the original problem into the task of coordinated incentives and the task of coordinated planning.

1. The task of coordinated dynamic incentives.

The principal chooses a compensatory incentive system, which consists of compensating the agent's costs in case that the principal's optimal planned trajectory is chosen and there are no material payments otherwise:

$$\sigma(x(t)) = \begin{cases} C(x(t), u(t)), & если\ x(t) = x^R(t), для \forall t \in [0,T] \\ 0, & если\ x(t) \neq x^R(t), для \forall t \in [0,T]. \end{cases}$$

2. The task of coordinated dynamic planning.

The optimal planned principal trajectory is determined from the solution of the optimal control problem:

$$J_p = \int_0^T e^{-\delta t} C(x(t), u(t))dt \to min. \tag{4}$$

$$\frac{dx(t)}{dt} = u(t), \tag{5}$$

$$0 < u(t) \le x_0 + R - x(t), \ t = 0,T, \tag{6}$$

$$x(0) = x_0, \tag{7}$$

$$x(T) = x_0 + R. \tag{8}$$

The task of the principal is to select the optimal production volumes of parts $u(t)^{opt}$ satisfying the constraint (6), which transfer the production process (5) from the initial state (7) to the final state (8) and minimize the integrated discounted labor costs of the agent (4).

2.2. Solution of the dynamic production planning problem

To solve the formulated optimal control problem with continuous time (4)-(8) we apply the Pontryagin maximum principle [18]. The direct application of the Pontryagin maximum principle to the formulated optimal control problem is impossible, since in this case there is a special control [19].

As the principal's optimality criterion, we consider the criteria of minimizing the integral discounted rate of the labor cost function of agent *C(t)*, which is close in economic terms:

$$J_p = \int_0^T e^{-\delta t} \frac{\dot{C}(t)}{C(t)} \mathrm{d}t \to min.$$

where $\frac{\dot{C}(t)}{C(t)} = [\ln C(t)]'$ is the logarithmic derivative of the labor cost function, which has the economic meaning of the rate of labor cost function.

Statement 1

For a positive and absolutely continuous function *C(t)*, the maximization (minimization) of the following functional

$$\tilde{J} = \int_0^T e^{-\delta t} \frac{\dot{C}(t)}{C(t)} \mathrm{d}t \tag{9}$$

is equivalent to the functional maximizing (minimizing):

$$J = \int_0^T e^{-\delta t} \ln C(t) \mathrm{d}t. \tag{10}$$

The proof of the statement is given in the Appendix.

Taking into account this statement, we take minimization of the total discounted logarithmic function of labor costs as the criteria of optimality (10). We substitute the expression for the labor cost function (1) into the functional (10):

$$J_p = \int_0^T e^{-\delta t} \ln[sc(x(t))u(t)] \mathrm{d}t. \tag{11}$$

To solve the formulated optimal control problem (5)-(8), (11), we apply the Pontryagin maximum principle [18]. Hamiltonian function is stated below:

$$H(t,x,\psi,u) = \psi(t)u(t) - e^{-\delta t}s - e^{-\delta t} \ln[c(x(t))] - e^{-\delta t} \ln[u(t)],$$

where $\psi(t)$ is an auxiliary variable that satisfies the following conjugate equation:

$$\frac{\mathrm{d}\psi}{\mathrm{d}t} = -\frac{\partial H}{\partial x} = e^{-\delta t} \frac{\partial \{\ln[c(x(t))]\}}{\partial x}.$$

In accordance with the Pontryagin maximum principle, at each point of the optimal trajectory the Hamiltonian function reaches its maximum with respect to the control parameters. The maximum of the control Hamiltonian is found from the condition:

$$\frac{\partial H}{\partial u} = 0. \tag{12}$$

We define the optimal control from the condition (12):

$$u(t)^{opt} = \frac{e^{-\delta t}}{\psi}. \tag{13}$$

The system of conjugate equations can be written as follows:

$$\begin{cases} \dfrac{\mathrm{d}x}{\mathrm{d}t} = \dfrac{e^{-\delta t}}{\psi} \\ \dfrac{\mathrm{d}\psi}{\mathrm{d}t} = e^{-\delta t}\,\dfrac{\partial\{ln[\,c(\,x(t\,))]\}}{\partial x} \end{cases} \tag{14}$$

From the equations of system (14) it follows:

$$\mathrm{d}t = e^{\delta t}\psi dx. \tag{15}$$

$$\mathrm{d}t = e^{\delta t}\left(\frac{\partial\{ln[\,c(\,x(t\,))]\}}{\partial x}\right)^{-1}\mathrm{d}\psi. \tag{16}$$

The symmetric form of the system (14) taking into account equations (15), (16) will have the form:

$$\mathrm{d}t = \psi dx = \left(\frac{\partial\{ln[\,c(\,x(t\,))]\}}{\partial x}\right)^{-1}\mathrm{d}\psi. \tag{17}$$

Using the separation of variables in the second differential equation (17):

$$\frac{\mathrm{d}\psi}{\psi} = \frac{\partial\{ln[\,c(\,x(t\,))]\}}{\partial x}\mathrm{d}x. \tag{18}$$

Find the general solution to the differential equation (18):

$$\psi = C_0 c(x(t)). \tag{19}$$

where C_0 is the integration constant.

The optimal control (13) taking into account (19) takes the following form:

$$u(\,t\,)^{opt} = \frac{e^{-\delta t}}{C_0 c(\,x(\,t\,))}. \tag{20}$$

Based on the obtained condition for optimal control (20), we formulate the following statement.

Statement 2.

Taking into account the discounting, the optimal production volumes for any model of the learning curve at each time point should be inversely proportional to the labor intensity of the products and directly proportional to the discount rate.

In the case of absence of discounting (discount rate $\delta = 0$), the optimal control will be written:

$$u(\,t\,)^{opt} = \frac{1}{C_0 c(\,x(\,t\,))}.$$

Based on the obtained conditions for optimal control without discounting, we formulate the following statement.

Statement 3.

In the case of no discounting, the optimal production volumes for any model of the learning curve at each time point should be inversely proportional to the labor intensity of the products.

Find the optimal control and optimal trajectory for the power model of the learning curve (2). The formula (2) can be substituted in the resulting expression for the conjugate variable (19):

$$\psi = C_1 x(\,t\,)^{-b}. \tag{21}$$

where $C_1 = C_0 a$ is the integration constant.

We substitute formula (21) into the differential equation (15):

$$\mathrm{d}t = e^{\delta t} C_1 x^{-b} dx. \tag{22}$$

The general solution to equation (22) will have the form:

$$t = -\frac{1}{\delta} ln\left[\,C_2 - C_1\delta\frac{x^{1-b}}{1-b}\right] \tag{23}$$

We define the integration constants C_1 and C_2 from the boundary conditions (7) and (8):

$$C_1 = \frac{(1-e^{-\delta T})(1-b)}{\delta[(x_0+R)^{1-b} - x_0^{1-b}]};$$ (24)

$$C_2 = 1 + \frac{(1-e^{-\delta T})x_0^{1-b}}{(x_0+R)^{1-b} - x_0^{1-b}}.$$ (25)

Substituting the constants of integration (24), (25) into formula (23), we find the equation of the optimal trajectory of the cumulative production volume:

$$x(t)^{opt} = \left(x_0^{1-b} + \frac{(1-e^{-\delta t})}{(1-e^{-\delta T})}[(x_0+R)^{1-b} - x_0^{1-b}] \right)^{\frac{1}{1-b}}.$$ (26)

We define the optimal control by substituting the formula (21) into the condition (13) with the found expression for C_1 (24):

$$u(t)^{opt} = \frac{\delta e^{-\delta t}}{1-e^{-\delta T}} \left(x_0^{1-b} + \frac{(1-e^{-\delta t})}{(1-e^{-\delta T})}[(x_0+R)^{1-b} - x_0^{1-b}] \right)^{\frac{b}{1-b}} \frac{(x_0+R)^{1-b} - x_0^{1-b}}{(1-b)}.$$ (27)

Find the labor cost function (1), taking into account formulas (26) and (27) on the optimal trajectory with optimal control:

$$C(t, x^{opt}, u^{opt}) = a \frac{\delta e^{-\delta t}}{1-e^{-\delta T}} \frac{(x_0+R)^{1-b} - x_0^{1-b}}{(1-b)}.$$ (28)

Analyzing (28) we come to the conclusion that under optimal control, the change in the instant costs function depends only on the discount factor $e^{-\delta t}$.

3. Conclusion

The paper explores the dynamic game task of executor's incentives in projects for the development of new production in continuous time.

To solve the formulated problem of incentives, the principle of cost compensation was applied. The original task is divided into the task of coordinated incentives and the task of coordinated planning. The task of coordinated incentives is as follows. The principal chooses a compensatory incentive system, which consists of compensating the agent's expenses in case of the principal chooses an optimal trajectory, or there are no material payments otherwise.

As a result of the study, a condition for the optimal production volumes determining coordination of the interests of the principal and agents was found: the optimal production volumes for any model of the learning curve at each time point should be chosen inversely to the labor intensity of the product and directly to the discount rate. In the case of absence of discounting: the optimal production volumes for any model of the learning curve at each time point should be chosen inversely to the labor intensity of the products.

As a result of analytical problem solving for power model of the learning curve, the following formula were obtained: formula for optimal production volumes at each time point, optimal trajectory for cumulative production volumes, and formula for agent labor costs at each time point for optimal trajectory with optimal control.

Appendix

Proof of the statement.

We integrate the functional (9) by parts:

$$\int_0^T e^{-\delta t} \frac{\dot{C}(t)}{C(t)} dt = e^{-\delta T} \ln C(T) - \ln C(0) + \delta \int_0^T e^{-\delta t} \ln C(t) dt.$$ (29)

We introduce the function $g(t)$:

$$g(t) = e^{-\delta t} \ln C(t).$$

Then values of the function at the initial and final moment of time are $g(0)=\ln C(0)$ and $g(T)=e^{-\delta T}\ln C(T)$. Expression (29) takes the form:

$$\int_0^T e^{-\delta t}\frac{\dot{C}(t)}{C(t)}\mathrm{d}t = g(T)-g(0)+\delta\int_0^T g(t)\mathrm{d}t. \tag{30}$$

Case A. Increasing function $g(t)$.

The geometric interpretation of the integral $S_g=\int_0^T g(t)\mathrm{d}t$ is the area of the curvilinear trapezium, bounded above by the positive function $g(t)$, below by the axis of abscissas and by the straight lines t=0 and t=T. The rectangle area bounded above by the straight line $g(t)=g(T)$, below by the axis of abscissas and by the straight lines $t=0$ and $t=T$ can be defined on the one hand through the integral and on the other hand as the multiplication of length by height:

$$S_T=\int_0^T g(T)\mathrm{d}t = Tg(T). \tag{31}$$

Similarly, the rectangle area bounded above by the line $g(t)=g(0)$, below by the axis of abscissas and by the straight lines $t=0$ and $t=T$ can be found:

$$S_0=\int_0^T g(0)\mathrm{d}t = Tg(0). \tag{32}$$

From the formulas (31) and (32) follows that:

$$g(T)=\frac{1}{T}\int_0^T g(T)\mathrm{d}t. \tag{33}$$

$$g(0)=\frac{1}{T}\int_0^T g(0)\mathrm{d}t. \tag{34}$$

Then the functional (30), taking into account formulas (33) and (34), can be written:

$$\int_0^T e^{-\delta t}\frac{\dot{C}(t)}{C(t)}\mathrm{d}t = g(T)-g(0)+\delta\int_0^T g(t)\mathrm{d}t = \frac{1}{T}\int_0^T [g(T)-g(0)]\mathrm{d}t+\delta\int_0^T g(t)\mathrm{d}t. \tag{35}$$

The integral $\int_0^T [g(T)-g(0)]\mathrm{d}t = S_{T0}$ defines the rectangle area, bounded above by a straight line $g(t)=g(T)$, below by a straight line $g(t)=g(0)$ and by straight lines $t=0$ and $t=T$.

The formula $\delta\int_0^T g(t)\mathrm{d}t$ geometrically can be interpreted as the area of a squeezed curvilinear trapezium δS_g, since $\delta<1$. In the case of an increasing function, the condition is satisfied $g(T)>g(0)$. The expression $\frac{1}{T}\int_0^T [g(T)-g(0)]\mathrm{d}t=\frac{1}{T}S_{T0}$ is a positive value and calculates the area of the squared rectangle S_{T0}.

The sum of the areas of the transformed curvilinear trapezium δS_g and the rectangle $\frac{1}{T}S_{T0}$ can be defined as the area of the curvilinear trapezium, bounded above by the positive function $\lambda_1 g(t)$ (λ_1 is the constant factor), below the axis of abscissas and the straight lines $t=0$ and $t=T$:

$$\int_0^T e^{-\delta t}\frac{\dot{C}(t)}{C(t)}\mathrm{d}t = \frac{1}{T}\int_0^T [g(T)-g(0)]\mathrm{d}t+\delta\int_0^T g(t)\mathrm{d}t = \int_0^T \lambda_1 g(t)\mathrm{d}t.$$

Since λ_1 is a constant factor, the maximization of the functional $\int_0^T \lambda_1 g(t)\mathrm{d}t$ will be equivalent to maximizing of the functional $\int_0^T g(t)\mathrm{d}t = \int_0^T e^{-\delta t} \ln C(t)\mathrm{d}t$. Thus, the statement is proved.

Case B. Decreasing function $g(t)$.

In the case of a decreasing function, the condition is satisfied $g(T) < g(0)$. The formula (35) will have the form:

$$\int_0^T e^{-\delta t} \frac{\dot{C}(t)}{C(t)}\mathrm{d}t = -\frac{1}{T}\int_0^T [g(0) - g(T)]\mathrm{d}t + \delta \int_0^T g(t)\mathrm{d}t.$$

The integral $\int_0^T [g(0) - g(T)]\mathrm{d}t = S_{0T}$ defines the rectangle area, bounded above by a straight line $g(t) = g(0)$, below by a straight line $g(t) = g(T)$ and by straight lines $t = 0$ and $t = T$.

The expression $\frac{1}{T}\int_0^T [g(0) - g(T)]\mathrm{d}t = \frac{1}{T} S_{0T}$ is a positive value and calculates the area of the squared rectangle S_{0T}.

Option 1: the conditions are met $\delta > \frac{1}{T}$, $\delta g(T) > \frac{1}{T} g(0)$.

In this case, the difference of the areas of the transformed curvilinear trapezium δS_g and the rectangle $\frac{1}{T} S_{T0}$ can be defined as the area of the curvilinear trapezium, bounded above by the positive function $\lambda_2 g(t)$ (λ_2 is the constant factor), below by the axis of abscissas and the straight lines $t = 0$ and $t = T$:

$$\int_0^T e^{-\delta t} \frac{\dot{C}(t)}{C(t)}\mathrm{d}t = -\frac{1}{T}\int_0^T [g(0) - g(T)]\mathrm{d}t + \delta \int_0^T g(t)\mathrm{d}t = \int_0^T \lambda_2 g(t)\mathrm{d}t.$$

Minimization of the functional $\int_0^T \lambda_2 g(t)\mathrm{d}t$ will be equivalent to minimizing of the functional $\int_0^T g(t)\mathrm{d}t = \int_0^T e^{-\delta t} \ln C(t)\mathrm{d}t$. The statement is proved.

Option 2: the conditions are met $\delta < \frac{1}{T}$, $\delta g(T) < \frac{1}{T} g(0)$.

In this case, the difference of the areas of the transformed curvilinear trapezium δS_g and the rectangle $\frac{1}{T} S_{0T}$ can be defined as the area of the inverted curvilinear trapezium, bounded above by the straight line $g(t) = \frac{1}{T} g(0)$, below by the function $\delta g(t)$ and the straight lines $t = 0$ and $t = T$. The negative difference of areas can be calculated $-\int_0^T [\frac{1}{T} g(0) - \delta g(t)]\mathrm{d}t = \int_0^T \delta g(t)\mathrm{d}t - g(0)$.

Since $g(0) = const$, the minimization of this expression will be equivalent to the minimization of the functional $\int_0^T g(t)\mathrm{d}t = \int_0^T e^{-\delta t} \ln C(t)\mathrm{d}t$. The statement is proved.

Option 3: the conditions are met $\delta > \frac{1}{T}$, $\delta g(T) < \frac{1}{T} g(0)$.

In this case, the difference of the areas of the transformed curvilinear trapezium δS_g and the rectangle $\frac{1}{T}S_{0T}$ can be defined as the difference of the areas of two curvilinear triangles.

The area of the first curvilinear triangle is bounded above by the function $\delta g(t)$, below by the straight line $g(t)=\frac{1}{T}g(0)$ and by the straight lines $t=0$ and $t=\tau$ (abscissa of the intersection point of the function $\delta g(t)$ and the straight line $g(t)=\frac{1}{T}g(0)$). The area of the second curvilinear triangle is bounded above by a straight line $g(t)=\frac{1}{T}g(0)$, below by the function $\delta g(t)$ and by straight lines $t=\tau$ and $t=T$.

The areas difference can be calculated: $\int_0^{\tau}[\delta g(t)-\frac{1}{T}g(0)]\mathrm{d}t-\int_{\tau}^{T}[\frac{1}{T}g(0)-\delta g(t)]\mathrm{d}t=\int_0^{T}\delta g(t)\mathrm{d}t-g(0)$. Since $g(0)=const$, the minimization of this expression will be equivalent to the minimization of the functional $\int_0^{T}g(t)\mathrm{d}t=\int_0^{T}e^{-\delta t}\ln C(t)\mathrm{d}t$. The statement is proved.

4. References

[1] Novikov D A, Smirnov M I and Shokhina T E 2002 *Mechanisms of Dynamic Active Systems Control* (Moscow: IPU RAN) p 124
[2] Ugolnitsky G A 2016 *Management of Sustainable Development of Active Systems* (Rostov on Don: Publishing House of the Southern Federal University) p 940
[3] Gorelik V A, Gorelov M A and Kononenko A F 1991 *Analysis of Conflict Situations in Control Systems* (Moscow: Radio i svyaz) p 228
[4] Gorelik V A and Kononenko A F 1982 *Game-theoretic Models of Decision Making in Ecological–economic Systems* (Moscow: Radio i svyaz) p 144
[5] Gorelov M A and Kononenko A F 2015 Dynamic conflict models III. Hierarchical games *Automation and Remote Control* **2** 89-106
[6] Basar T and Olsder G J 1999 *Dynamic Noncooperative Game Theory* (Philadelphia: SIAM) p 519
[7] Dockner E, Jorgensen S, Long N V and Sorger G 2000 *Differential Games in Economics and Management Science* (Cambridge: Cambridge University Press) p 382
[8] Li T and Sethi S P 2017 A review of dynamic Stackelberg game models *Discrete and Continuous Dyn. Syst.* B **22(1)** 125-159
[9] Olsder G J 2009 Phenomena in inverse Stackelberg games. Part 2: dynamic problems *J. Optim. Theory Appl.* **143(3)** 601-618
[10] Groot N, De Schutter B and Hellendoorn H 2012 Reverse Stackelberg games. Part I: basic framework *Proc. of the 2012 IEEE Int. Conf. on Control Applications* 421-426
[11] Groot N, De Schutter B and Hellendoorn H 2012 Reverse Stackelberg games. Part II: results and open issues *Proc. of the IEEE Int. Conf. on Control Applications* 427-432
[12] Groot N, Zaccour G and De Schutter B 2017 Hierarchical game theory for system-optimal control: applications of reverse Stackelberg games in regulating marketing channels and traffic routing *IEEE Control Systems Magazine* **37(2)** 129-152
[13] Rokhlin D B and Ougolnitsky G A 2018 Stackelberg equilibrium in a dynamic stimulation model with complete information *Automation and Remote Control* **79(4)** 701-712
[14] Wright T P 1936 Factors affecting the cost of airplanes *J. of the aeronautical sciences* **3(4)** 122-128
[15] Yelle L E 1979 The learning curve: historical review and comprehensive survey *Decision Sciences* **10(2)** 302-328

[16] Badiru A 1992 Computational survey of univariate and multivariate learning curve models *IEEE Transactions on Engineering Management* **39(2)** 176-188
[17] Mohamad Y J 2011 *Learning Curves: Theory, Models, and Applications* (Boca Raton: CRC Press) p 476
[18] Pontryagin L S, Boltyansky V G, Gamkrelidze R V and Mishchenko E F 1983 *Mathematical Theory of Optimal Processes* (Moscow: Nauka) p 392
[19] Afanasyev V N 2003 *Mathematical Theory of Control Systems Design* (Moscow: Vysshaya shkola) p 614

Text classification using convolutional neural network

L E Sapozhnikova[1], O A Gordeeva[1]

[1]Samara National Research University, Moskovskoye shosse, 34, Samara, Russia, 443086

e-mail: sapozhnikova111@gmail.com

Abstract. In this article, the method of text classification using a convolutional neural network is presented. The problem of text classification is formulated, the architecture and the parameters of a convolutional neural network for solving the problem are described, the steps of the solution and the results of classification are given. The convolutional network which was used was trained to classify the texts of the news messages of Internet information portals. The semantic preprocessing of the text and the translation of words into attribute vectors are generated using the open word2vec model. The analysis of the dependence of the classification quality on the parameters of the neural network is presented. The using of the network allowed obtaining a classification accuracy of about 84%. In the estimation of the accuracy of the classification, the texts were checked to belong to the group of semantically similar classes. This approach allowed analyzing news messages in cases where the text themes and the number of classification classes in the training and control samples do not equal.

1. Introduction

Today, volume of stored and used information continuously increases, and one of automatic text processing tasks is the problem of classifying text data, which allows separating texts into various thematic catalogs (categories, classes). Sites, documents, letters, appeals, news are classified for optimal storage and usage.

Text classifiers are used to recognize the emotional coloring of the text during reviews and comments processing. Text classification is used in antispam systems and contextual advertising via the analysis of user activity in the network and the classification of sites, which the user viewed.

Various methods and technologies can be used to classify textual information. Classification of textual information can be based on the assessment of the meaning of the text [1], on frequency analysis [2]. BigData technology is often used for solving of classification problem for text and media [3]. This article discusses the method based on the convolutional neural network. Some aspects and features of its application to solve the problem of text classification, as well as the results of applying this classification method are presented.

2. The formulation of the text classification problem

In general, the text classification problem is formulated as follows:

There is a set of objects (texts) and a beforehand defined set of classes with which objects can be compared. For some of the objects it is known which class they belong to. This subset is a training

sample. For the rest of the objects the classes are not defined. It is necessary to determine which class each object (text) from a set of objects belongs to.

The problem of text classification can be formalized as follows [4]:

There is a set of texts $D = \{d_1, ...d_n\}$. Each text $d_i \in D$ is a sequence of words $Wd = \{w_1, ..., ...\}$. A finite set of classes $C = \{c_1, ..., c_m\}$ are given. Ideal classifier which translates an object d to its class c_j can be termed as $\Phi(d)$. The task is to build another classifier $\tilde{\Phi}(d)$ which able to classify an arbitrary object d and is closest to the ideal classifier $\Phi(d)$.

The solving process includes the following main steps:

- Pre-processing of text including tokenization and vector representation of words.
- Building a classifier.
- Estimation of misclassification probability.

Text classification methods [5]:

- probabilistic (naive Bayes classifier);
- metric (k-nearest neighbours method);
- logical (decision tree classifier);
- linear (logical regression);
- methods based on neural networks

3. Text classification using convolutional neural network

3.1. General architecture of a convolutional neural network

Convolutional neural networks are very effectively used to solve the problem of text classification [6]. The result of the classification is the distribution of the probabilities that the text belongs to beforehand defined classes.

The basic architecture of the convolutional neural network consists of the following layers [7].

1. A convolutional layer, which is a set of attribute maps (matrices), each map has a convolution kernel, which is a filter (or window) that slides over the entire area of the attribute map. The set of filters determines the dimension of the new matrix. The error backpropagation algorithm for convolutional networks is also a convolution, but with spatially inverted filters.

2. Sub-sampling layer, which reduces the size of the matrix. On this layer the most frequently used method is the maximum element method (max-pooling).

3. A fully connected layer in which each neuron is connected to all neurons at the previous layer, and each connection has its own weight.

4. The output layer, which is connected with all neurons of the previous layer. The number of neurons corresponds to the number of classification classes.

3.2. The architecture of the used convolutional neural network

In this research, the specific model of the convolutional neural network was determined. The input data is words that are represented by vectors of semantic attributes. In the representation the words close in meaning are located at close distance in the vector space.

The vector $x_i \in R^k$ is k-dimensional vector corresponding to the i-word in the sentence. Then the sentence with length = n can be defined as [6]:

$$x_{1..n} = x_1 \oplus x_2 \oplus ... \oplus x_n, \quad (1)$$

where $\oplus$ is concatenation operation.

The term $x_{i..i+j}$ means the concatenation of words $x_i, x_{i+1}, ..., x_{i+j}$. Convolution uses the filter $w \in R^{hk}$ which is applied to the window containing h words to create a new attribute. For example, the attribute c_i will be generated from the window of words $x_{i..i+h-1}$ as

$$c_i = f\left(w * x_{i..i+h-1} + b\right), \quad (2)$$

where $b \in R$ is the offset step, f is nonlinear activation function.

This filter applies to every possible window of words in a sentence $\{x_{1..h}, x_{2..h+1}, ..., x_{n-h+1..n}\}$ to produce a new map of attributes

$$c = \{c_1, c_2, ...c_{n-h+1}\}, \quad (3)$$

where $c \in R^{n-h+1}$.

Then the operation of combining the set of values is applied, the maximum value of $\hat{c} = \max\{c\}$ (the most important attribute for each convolution) is selected.

In the process, the network uses several filters with different window sizes to obtain a set of attributes. These attributes from the penultimate layer are transferred to the last layer, and the output data is the probability of the distribution of attributes into classes.

As an activation function Leaky ReLU function is used [7]. The formula is:

$$f(x) = 1(x < 0) * (\alpha x) + 1(x \geq 0)(x), \quad (4)$$

where α is a constant with a small-scale value.

This function has a higher convergence rate compared to other activation functions and is also quite simple to calculate.

To regularize the neural network (to prevent overfitting), L2 regularization [7] is used in combination with the dropout [8].

L2-regularization is implemented by the penalization of the neural network by increasing the loss function. For each weight w the loss function λw^2 is added, where λ is the strength of regularization.

L2-regularization prevents a strong increase in weights of neurons and leads to a redistribution of weight values. This causes the neural network to use all neurons at least to a small extent.

Dropout is the random disconnection of neurons. At each level of training, some neurons are excluded from the network. It helps to avoid the dependence between neutrons during training.

The combination of L2-regularization and dropout allows avoiding a situation where the network shows excellent results on a training sample but is ineffective when tested on a control sample.

The architecture of the network which was used is shown in figure 1. The first layer solves the problem of the vector representation of words. Next, three convolutional layers are created (conv2d_1, conv2d_2, conv2d_3). The figure also shows the Leaky ReLU activation function for each layer, the dropout and the sub-sampling layer (max-pooling). Then the layers merge, and at the end, a fully connected layer is obtained (dense_1). The architecture is designed using the TensorBoard visualization system [9].

3.3. The input data formatting

The testing of the described classification method was carried out on the materials of the RIA Novosti news portal on the Internet. This portal contains a huge number of publications with well-defined themes. It allows to define categories (classes) for classification, as well as to generate a sufficient number of text fragments for neural network training.

Eight classes were determined - *culture*, *events*, *religion*, *society*, *economy*, *politics*, *science*, *world*. It was received 8,000 articles from the materials of the portal for each class. In total, 64,000 news articles related to one of the 8 classes were received. For data acquisition the software was developed with Node.js platform. These data were preliminarly processed before starting the training of the neural network.

3.4. Text preprocessing

The neural network input data formatting was performed in Python 3.6 using Keras and Jupyter Notebook libraries.

The maximum text size was limited to 1000 characters. The texts of a greater number of characters were divided into parts and assigned to the same class. For the training of a neural network, it is important to have the same number of examples of each class, otherwise, the neural network will ignore the semantic meaning of the text and will take into account the a priori probability of the appearance of each class articles.

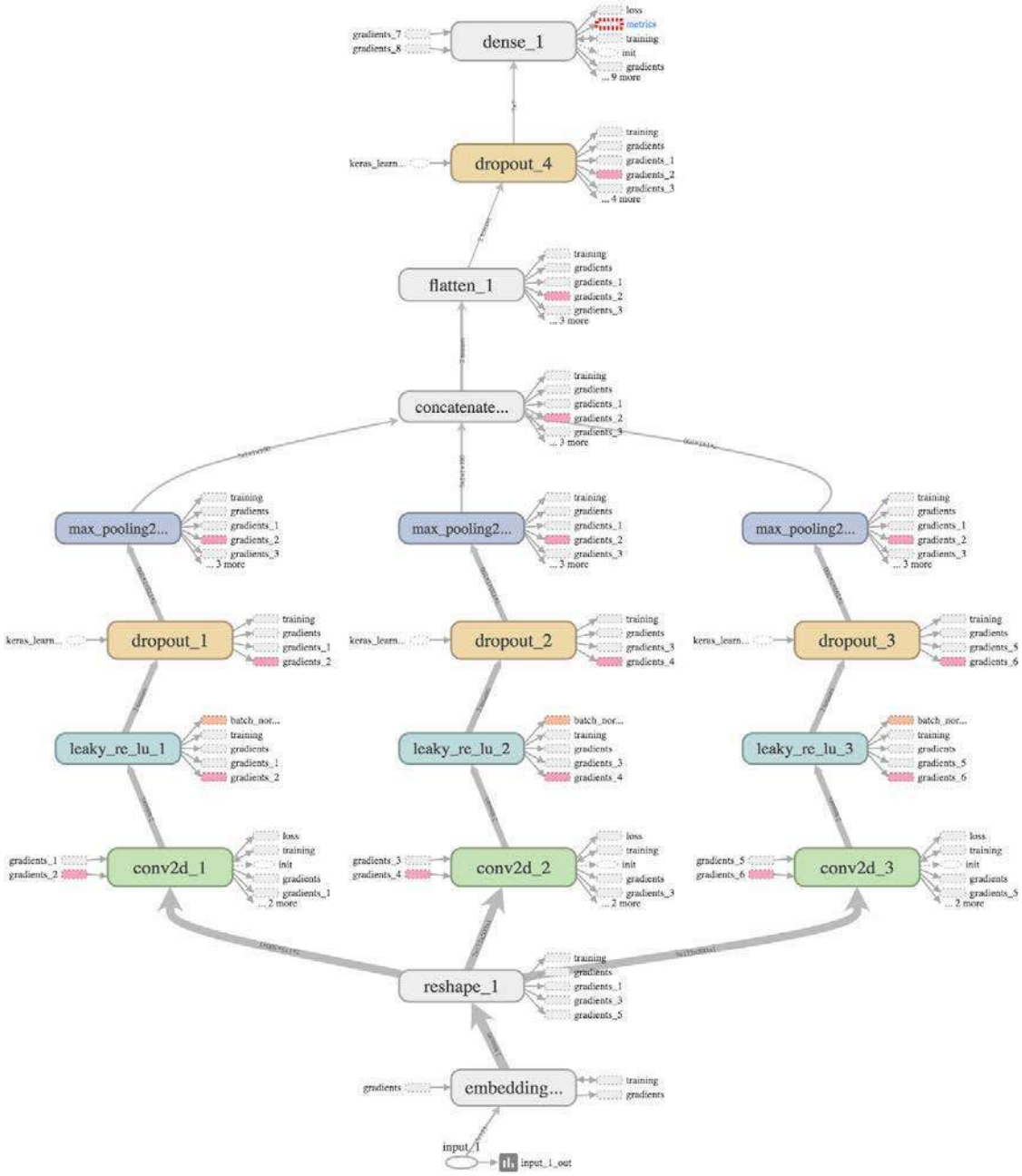

Figure 1. The architecture of the convolutional neural network.

To avoid this situation, the volumes (number of texts) of the classes were equalized with the class of the smallest volume - 11,733 texts. A total of 93,864 texts were obtained for 8 classes.

Then all texts were divided into three samples - training (60% of texts), validation (20% of texts) and control (20% of texts).

After that, the tokenization of texts in order to find unique words was carried out. As a result, 282,972 unique tokens (words) were found. The input data was formatted for the neural network with Python 3.6 programming language using the Keras and Jupyter Notebook libraries. The tokens have to be translated into vector representations of attributes for network training.

3.5. Vectors of attributes formation

Vector representation describes the dependencies between words. In vector space, similar words will have similar vectors. Research in this field was carried by Thomas Mikolov [10]. For vector

representations, he obtained important results in syntactic and semantic meaning. As a result of his research, it was determined that the resulting vector representations of words have significant syntactic and semantic patterns that are implemented in existing models and network libraries. In particular, there is a constant vector displacement between pairs of words indicating a specific relationship. Moreover, even more complex relationships were discovered. For example, you can define the relationship between words as the difference of their vectors. Also, the feminine and masculine words will have a constant vector difference.

The most popular practical way to obtain a vector of attributes is to use word2vec language models created using neural networks. These models are trained in very large volumes of natural language words in various grammatical forms, including words in different kinds, cases, inclinations, and so on. In addition, they also include stop-words. Therefore, such models do not require specific preliminary actions as removing stop-words, stemming or lemmatization, which are necessary for classification by other methods. Keeping different word forms may even increase the accuracy of the classification. As a result, semantically similar words and synonyms will have similar vectors of semantic attribute values.

In this research, the open model word2vec [11] is used. This model represents a word as a vector of 500 values of attributes. The model is pre-trained and it was designed for the Russian language. To begin with, a series of experiments of vector construction was conducted for similar words. It confirmed the ability to use the model. As a result, it was found that this vectorization model constructs similar attribute vectors for words that are close in meaning. Consequently, this trained model was found to be suitable to translate the words of the experimental sample into the vector of attributes without applying stemming or lemmatization and without removing the stop-words.

3.6. Training and use of the network

The convolutional neural network which was shown in figure 1 and described in paragraph 3.2 was trained with parameters presented in table 1. These parameters were selected based on the results of a series of experiments to investigate the dependence of classification accuracy on the parameters of the neural network.

Table 1. Neural network parameter values.

Parameter	Value
Number of learning epochs	5
Activation function	Leaky ReLU with α=0,1
Convolutional layers	3 layers with filter size = 2, 4 and 5
The number of filters	100
Regularization L2	0,1
Dropout for convolutional layers	0,5
Dropout for the fully connected layer	0,6
The speed of learning	0,001

It should be noted that with each epoch the accuracy of the classification of the training sample increases and the accuracy of the classification of the validation sample ceases to increase after the 5^{th} epoch. It indicates that the network is overfitted. Thus, after the 5^{th} epoch, the accuracy of the classification of the validation sample is 84%. All neuron weights were saved for further use in text classification tasks. The classification accuracy for the control sample, which was separated from the total set of texts at the step of text preprocessing, shows that the trained model of the neural network with the parameters specified in table 1 solves the problem of text classification with an accuracy of 84%.

One of the difficulties in text classification is that it is not always possible to determine the probability that a text belongs to a particular class if the classes are semantically related. For example, the text of the news “In country X, the president issued a decree on raising taxes” has elements of politics, economics, and, possibly, international news when it comes to a foreign country. Therefore, there is a certain subjective character of classification by both a human and automated systems of

different Internet-portals, which have different algorithms for deciding whether a text belongs to a particular class.

For the more detailed research of the classification accuracy, three control samples were compiled from various news sites to test the neural network processing on other control samples. Texts of news from portal RIA Novosti (18773 texts), Mail.ru news portal (7740 texts) and TASS news agency (16835 texts) were acquired. While the texts of the control sample from the RIA Novosti website were not used in network training.

It should be noted that the network was trained for 8 thematic classes used by RIA-Novosti: *culture*, *events*, *religion*, *society*, *economics*, *politics*, *science*, and the *world*. However, for Mail.ru news, the following classes are used: *events*, *society*, *economy*, *politics* (4 classes), and for TASS - *culture*, *events*, *society*, *economy*, *politics*, *science*, *the world* (7 classes).

The number of classes does not match, so for the sample from Mail.ru the estimated classification accuracy is slightly more than 40%, for TASS news texts the classification accuracy was 67%. As mentioned earlier, the classification accuracy for RIA Novosti data was 84% - the greatest accuracy, since the classes of the training and control samples are the same.

Next experiment the same classes in the training and classification for all three data sets was used. Four classes were chosen - *accidents*, *society*, *economics*, and *politics*. The neural network was retrained. The results of the experiments are presented in table 2.

Table2. Accuracy of control sample classification.

Sample source	RIA Novosti	Mail.ru	TASS
Training sample – 8 classes			
Number of classes for the control sample	8	4	7
Classification accuracy	84 %	46 %	65,5 %
Training sample – 4 classes			
Number of classes for the control sample	4	4	4
Classification accuracy	84 %	66 %	73 %

As can be seen from table 2, for the texts of RIA Novosti, the classification accuracy remained unchanged (84%), for Mail.ru and TASS news it increased significantly and amounted to 68% and 75%, respectively. However, these values are still lower than for the texts of RIA Novosti.

Such low values of classification accuracy are related to the fact that some of the texts of other sources can be initially attributed to semantically similar classes, and, although the classification accuracy is low, it does not indicate the poor quality of the neural network processing.

The results of the experiment show that in the presence of semantically similar classes and the classification of data from sources other than the sources of the training sample, the accuracy of the classification may be incorrectly underestimated.

To eliminate this effect, groups of semantically similar classes were identified, and the calculation of the classification accuracy was adjusted so that the classified text was checked for belonging to a group of semantically similar classes, not to a particular class.

Groups of semantically similar classes are presented in table 3.

Table 3. Groups of semantically similar classes.

Group	Classes in the group
1	the world politics
2	society events
3	culture religion
4	economy
5	science

The results of the estimation of the classification accuracy by belonging to a group of semantically similar classes are presented in Table 4.

Table 4. Comparison of the accuracy of the control sample classification without using and using groups of semantically similar classes.

Sample source	Mail.ru	TASS
Training sample – 8 classes		
Number of classes for the control sample	4	7
Classification accuracy without groups of semantically similar classes	46 %	65,5 %
Classification accuracy with groups of semantically similar classes	57,5 %	73,5 %
Training sample – 4 classes		
Number of classes for the control sample	4	4
Classification accuracy without groups of semantically similar classes	66 %	73 %
Classification accuracy with groups of semantically similar classes	73,5 %	78,5 %

As can be seen from table 4, the classification accuracy has increased significantly in all cases, both when teaching in eight classes, and when teaching in four classes (up to 12%). As a general result, an increase in the classification accuracy for control samples from other sources averaged 8–10%.

Thus, the most objective value of classification accuracy is obtained for the classification of a control sample from a source that is also a source of a training sample. However, when estimating the accuracy of the classification for control samples from other sources, the most optimal results are achievable with an equal number of classes for training and control samples and when checking to belong the control sample texts to a group of semantically similar classes.

4. Conclusion

The problem of classification is the current direction in the processing of text data. Text classification processes are implemented in various areas: classifiers for various characteristics (themes, style, the emotional coloring of the text), spam filtering, contextual advertising, and so on.

In this paper, the applicability of a convolutional neural network for solving the problem of text classification was researched. The convolutional neural network was trained using the already trained neural network for translation of words in vectors of selected attributes which represent universal semantic meanings that can be used to classify the texts of the natural Russian language.

The constructed neural network is able to classify news and other texts by themes and to provide a distribution of the probability of belonging of the text to 8 predetermined classes. The accuracy of the classification is estimated by the control sample and is 84%. For the selected number of classes, this classification result indicates the effectiveness of using a convolutional neural network for text classification.

Processing of the constructed and trained neural network is researched by control samples from various sources - RIA Novosti, TASS, Mail.ru. The highest classification accuracy was obtained on a control sample of RIA Novosti articles and amounted to 84%. To classify the data of the two other samples, using an equal number of classes of training and control samples, as well as using groups of semantically similar classes for estimation of classification accuracy, allowed to obtain a more objective and higher result. The neural network has shown its effectiveness in solving the problem of text classification. The downside of its use is the need for large amounts of data for training and validation.

5. References

[1] Mikhaylov D V, Kozlov A P and Emelyanov G M 2015 An approach based on tf-idf metrics to extract the knowledge and relevant linguistic means on subject-oriented text sets *Computer*

Optics **39(3)** 429-438 DOI: 10.18287/0134-2452-2015-39-3-429-438
[2] Mikhaylov D V, Kozlov A P and Emelyanov G M 2016 An approach based on analysis of n-grams on links of words to extract the knowledge and relevant linguistic means on subject-oriented text sets *Computer Optics* **40(4)** 572-582 DOI: 10.18287/2412-6179-2016-40-4-572-582
[3] Rytsarev I A, Kirsh D V and Kupriyanov A V 2018 Clustering of media content from social networks using bigdata technology *Computer Optics* **42(5)** 921-927 DOI: 10.18287/2412-6179-2018-42-5-921-927
[4] Eprev A S 2010 Automatic classification of text documents *Math. Struct. and modeling* **21** 65
[5] Batura T V 2017 Methods of automatic text classification *Programming products and systems* **1** 85
[6] Kim Y 2014 Convolutional Neural Networks for Sentence Classification *Proc. of EMNLP* (Doha Qatar) 1746-1751
[7] Karpathy A 2019 CS231n: Convolutional Neural Networks for Visual Recognition *Stanford CS class* URL: http://cs231n.github.io
[8] Budhiraja A 2018 *Dropout in (Deep) Machine learning* URL: https://medium.com/amarbudhiraja-learning-less-to-learn-better-dropout-in-deep-machine-learning-74334da4bfc5
[9] Tensorboard URL: https://www.tensorflow.org/programmers_guide/summaries_and_tensorboard
[10] Mikolov T, Yih W and Zweig G 2013 Linguistic Regularities in Continuous Space Word Representations *Proc. of NAACL-HLT* 746-751
[11] Model word2vec URL: http://panchenko.me/data/dsl-backup/w2v-ru

Research of parallel algorithms for solving three-diagonal systems of linear algebraic equations on a graphical computing device using various types of memory

X S Pogorelskih[1], **L V Loganova**[1]

[1]Samara National Research University, Moskovskoe Shosse, 34A, Samara, Russia, 443086

e-mail: sekih@yandex.ru, lloganova@yandex.ru

Abstract. In this paper, we research and compare different implementations of cyclic reduction and sweep algorithms on a graphics processing unit (GPU) using different types of device memory. As a result of the work, it was found that the algorithm of the run should be used to solve the set of the tridiagonal linear system. However, the best results are shown by a parallel version of the cyclic reduction algorithm with partial use of shared memory, when solving a single linear system on the GPU.

1. Introduction

The applicability of systems of linear equations of tridiagonal form is very extensive[1]. Tridiagonal matrices have an extremely important role in difference methods of solving problems of mathematical physics [2]. In addition, many linear algebra problems, such as solving equations and finding eigenvalues, are solved through transformations of matrices of general form to tridiagonal ones [3]. These matrices also play an important role in the theory of orthogonal polynomials [4].

There are many algorithms and their parallel versions for solving tridiagonal systems of linear equations. The need for parallelization naturally occurs when the size or number of systems to be solved is very large. Most methods are based on simple arithmetic operations performed many times. Therefore, the implementation of parallel versions of algorithms on the GPU is a reasonable solution [5].

GPU-clusters consume less power than the CPU [6]. In addition, the development of graphics cards allows for complex calculations on personal computers. Therefore, the ability to parallelize algorithms on the GPU is interesting for researchers.

Operations in memory take a significant time of calculations on the GPU [7]. Therefore, the optimal organization of work with memory allows to achieve a significant increase in acceleration.

Global, shared, and constant GPU memory are commonly used for calculations [8]. Constant memory is small, immutable, so not suitable for large systems [9]. Therefore, in this paper we study the global and shared memory of the GPU device.

Shared memory is much faster than global memory, but its size is very limited. These features of the types of memory must be taken into account when implementing algorithms on the GPU.

2. Problem Statement and Methodology

This article investigates parallel algorithms for solving systems of linear equations of tridiagonal form.

The traditional matrix algorithm and the cyclic reduction method are usually used to solve systems of linear algebraic equations of tridiagonal form [10].

The advantage of the cyclic reduction method is a high degree of parallelism [10]. However, it also requires a large amount of computation. When implemented on a central processing unit using MPI technology, the method requires a lot of forwarding. This significantly slows down the program [11]. However, in CUDA technology shipments are not required. Therefore, the method attracts the attention of researchers to implement on the graphics card. In addition, it allows parallelization for a single system [12].

The traditional matrix algorithm Parallels for one system worse than the parallel cyclic reduction algorithm. However, there are a large number of tasks that require the solution of a set of systems. The traditional matrix algorithm is suitable for such problems. It gives a gain in acceleration due to low computational complexity.

In this paper, we investigate which algorithm for solving tridiagonal-type systems spends less time on computation. To solve this problem, we compare the he implementation of the traditional matrix algorithm, and the serial and parallel versions of the cyclic reduction algorithm using different combinations of global and shared GPU memory. Parallelization of methods is carried out using the CUDA model. Experimental research is conducted on the supercomputer "Sergey Korolev".

3. Experimental research

This work began with the implementation and research of the traditional matrix algorithm. This method is one of the most famous and popular for solving tridiagonal systems of linear arithmetic equations.

The first version of the algorithm was implemented on the CPU for further comparison in acceleration. Then an implementation of a parallel traditional matrix algorithm on the GPU using only global memory was created. The next task was to implement this method using shared memory. Since the memory size is small, the necessary factors were loaded in portions into the shared memory immediately before use. Then, after all the necessary operations, the coefficients were replaced by the next portion. To store data in shared memory, arrays of auxiliary coefficients α and β and the sought vector x of size $2 \cdot blocksize$ and arrays of initial coefficients a, b, c and k of size $blocksize$. All calculations were performed in shared memory.

The experiments were carried out for a set of systems with matrices of size $N = 4095$. This size was chosen to compare the results with the experimental versions of the cyclic reduction algorithm implemented for the size of matrices $N = 2^q - 1$, where $q \in \mathbb{N}$.

The number of equation systems varied from 5000 to 20000. If the number of systems is less than 5000, working with memory on the GPU takes much longer than the calculations themselves.

The obtained accelerations of parallel versions of algorithms relative to the serial version on the CPU are given in table 1.

Table 1. The dependence of the acceleration of parallel versions on the serial version of the traditional matrix algorithm in solving a set of systems of linear algebraic equations, depending on the number of systems with matrices of size $N = 4095$.

Number of systems	GPU with shared memory	GPU
5000	**2.19032**	1.680011
10000	**1.705628**	1.164633
15000	**1.903806**	1.274506
20000	**1.885846**	1.027733

Average acceleration version on the GPU using only global memory is equal to 1.26. The average acceleration using shared memory is 1.86. Thus, the use of shared memory gives an increase in acceleration by 47%.

This result shows that the time it takes to copy data from global memory to shared memory and vice versa is justified by the high speed of calculations performed in shared memory.

The next step is the implementation of the sequential cyclic reduction algorithm (SERICR). This algorithm makes it impossible to carry out parallel calculations for one system, but is parallelized for a set of systems.

R. Hockney [13] considered in detail the cyclic reduction. It notes that this algorithm is suitable for any number of equations. However, for simplicity, the author gives the number of equations $N = 2^q - 1$, где q – where q is an integer. For convenience, he introduced the designation $N' = 2^q = N + 1$.

We present a routing diagram of this algorithm for $N' = 8$ in figure 1 (a). Cells that contain significant information are gray.

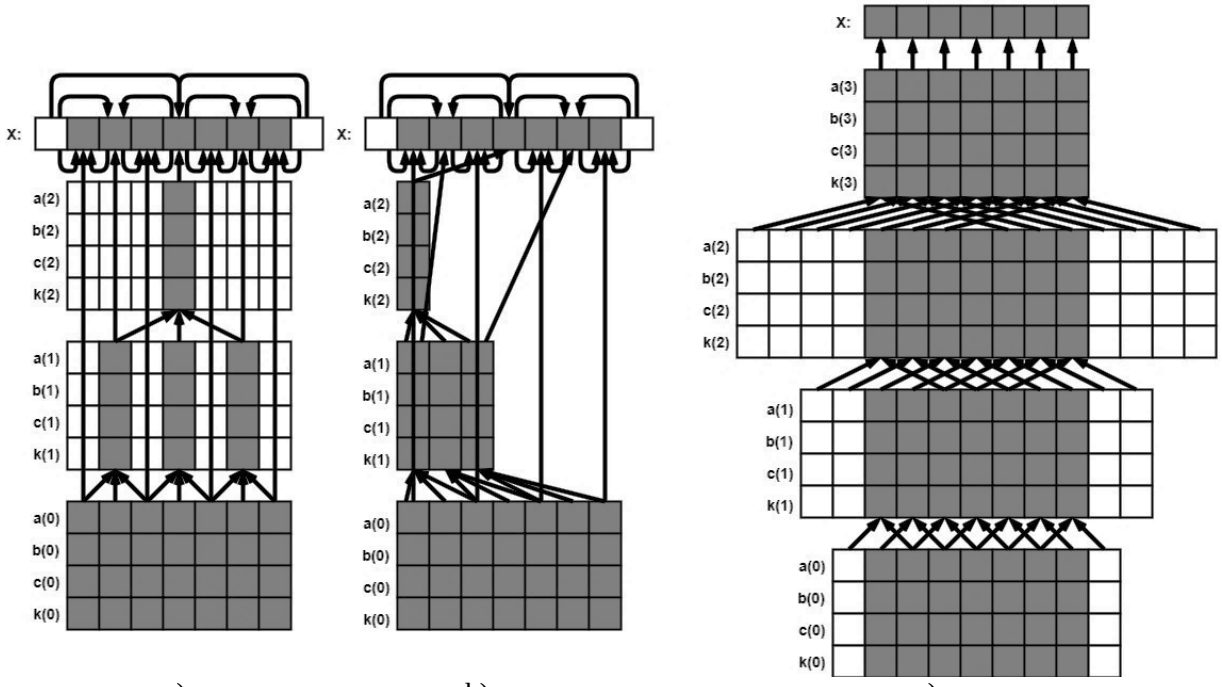

a) b) c)

Figure 1. Algorithm routing schemes for N'=8: sequential cyclic reduction SERICR (a), sequential cyclic reduction SERICR with modified indexation (b), parallel cyclic reduction PARACR (c).

In this algorithm, the coefficients of all levels of reduction are stored in memory. This requires a lot of memory. In addition, many cells do not store useful information. Therefore, the indexation of the algorithm was changed to minimize memory usage. The resulting routing scheme is shown in figure (b).

We present an algorithm with modified indexing. At the first stage new coefficients for left and right parts for reduction levels $l = \overline{1, q-1}$ with step $h = 1$ from $i = 0$ to $i = N^{(l)}$ are considered. Reduction coefficients of level $l = 0$ are assumed to be $a_i^{(0)} = a_i$, $b_i^{(0)} = b_i$, $c_i^{(0)} = c_i$ и $k_i^{(0)} = k_i$. First, we find the auxiliary coefficients:

$$\alpha_i = -\frac{a_{2i+1}^{(l-1)}}{b_{2i}^{(l-1)}};$$

$$\gamma_i = -\frac{c_{2i+1}^{(l-1)}}{b_{2i+2}^{(l-1)}};$$

Then, based on the obtained α_i and γ_i and the values of the coefficients of the left and right parts of the previous reduction level, we obtain:

$$a_i^{(l)} = \alpha_i a_{i-2^{l-1}}^{(l-1)};$$

$$c_i^{(l)} = \gamma_i c_{i+2^{l-1}}^{(l-1)};$$
$$b_i^{(l)} = b_i^{(l-1)} + \alpha_i c_{i-2^{l-1}}^{(l-1)} + \gamma_i a_{i+2^{l-1}}^{(l-1)};$$
$$k_i^{(l)} = k_i^{(l-1)} + \alpha_i k_{i-2^{l-1}}^{(l-1)} + \gamma_i k_{i+2^{l-1}}^{(l-1)}.$$

At the second stage, based on the coefficients of the left and right parts for the reduction levels $l = \overline{0, q-1}$ we find the vector of solutions x. It is assumed that $x_0 = x_{N'} = 0$. For $l = \overline{q, 1}$, for i, varying in increments $h_2 = 2^{(l-1)}$ from $i = 2^{(l-1)}$ to $i = N' - 2^{(l-1)}$, we consider:

$$x_i = \frac{k_i^{(l-1)} - a_i^{(l-1)} x_{i-2^{(l-1)}} - c_i^{(l-1)} x_{i+2^{(l-1)}}}{b_i^{(l-1)}}.$$

However, the resulting memory savings are not sufficient to use this algorithm on big data. The solution in this situation is to store only two levels of reduction and recalculate the coefficients when they are needed.

The algorithm was implemented on the central and graphics processor devices. When implementing the algorithm on the CPU, the coefficients were not recalculated, since the CPU has enough memory to store the coefficients of all levels of reduction. When implemented on the GPU recalculation was necessary. On the graphics card, the algorithm was implemented using only global memory and shared memory.

The experiments were carried out for a set of systems with matrices of size $N = 4095$. The number of systems varied from 5000 to 25000. The obtained accelerations are shown in table 2.

Table 2. The dependence of the acceleration of the sequential cyclic reduction algorithm on the GPU relative to the implementation on the CPU.

Number of systems	SERICR on a shared memory GPU	SERICR on the GPU
5000	0.316570	0.193076
10000	0.259339	0.191475
15000	0.258175	0.186748
20000	0.264068	0.190208
25000	0.253464	0.185693

GPU implementations have shown a slowdown. This is due to the need to carry out multiple recalculations of the coefficients.

The final stage of the work is the implementation of the parallel cyclic reduction algorithm. This algorithm is proposed in the work of R. Hockney [13]. Its advantage is the possibility of parallelization for one system of equations. In addition, the following reduction levels are replaced by the previous ones. This gives a noticeable gain in memory. The routing scheme of the algorithm is shown in figure 1 (c).

The algorithm was implemented on the GPU using only global memory and with full and partial loading of data into shared memory.

The experiments were carried out for a system of equations with matrices of size $N = 4095$. The number of systems varied from 5000 to 25000. The obtained accelerations are presented in table 3.

The table shows that the implementation with partial loading into shared memory shows the best results. It is 2% faster than a non-shared memory implementation and 41% faster than a fully loaded shared memory implementation. The results can be explained. Some coefficients are used only once in calculations. The time of their copying to shared memory is practically not compensated by the gain in the time of calculations. Therefore, it makes sense to load only data that is used multiple times into shared memory. In this case, the data loaded into shared memory is used twice, so the use of shared memory does not give a significant benefit.

Table 3. The dependence of the acceleration of parallel reduction algorithm implementations on the GPU relative to the sequential cyclic reduction algorithm on the CPU.

Number of systems	PARACR on the GPU with partial use of shared memory	PARACR on GPU with shared memory	PARACR on the GPU
5000	**2.006864**	1.198271	1.970711
10000	**2.021180**	1.206249	1.972713
15000	**2.008165**	1.201463	1.973943
20000	**2.007109**	1.202857	1.962254
25000	**2.017338**	1.203156	1.987762

The operating time of the traditional matrix algorithm and the cyclic reduction algorithm for solving a set of systems with matrices of size N=4095 is presented in table 4.

Table 4. The running time of the implementation of the algorithm on a GPU with a full load in the shared memory and the algorithm of parallel cyclic reduction on the GPU with a partial load in the shared memory on a set of systems with size matrices $N = 4095$.

Number of systems	Traditional matrix algorithm, c	PARACR, c
5000	**0.09**	0.59
10000	**0.19**	1.19
15000	**0.28**	1.78
20000	**0.38**	2.38
25000	**0.47**	2.96

The timeline of the algorithms when solving one system of equations is presented in Figure 2.

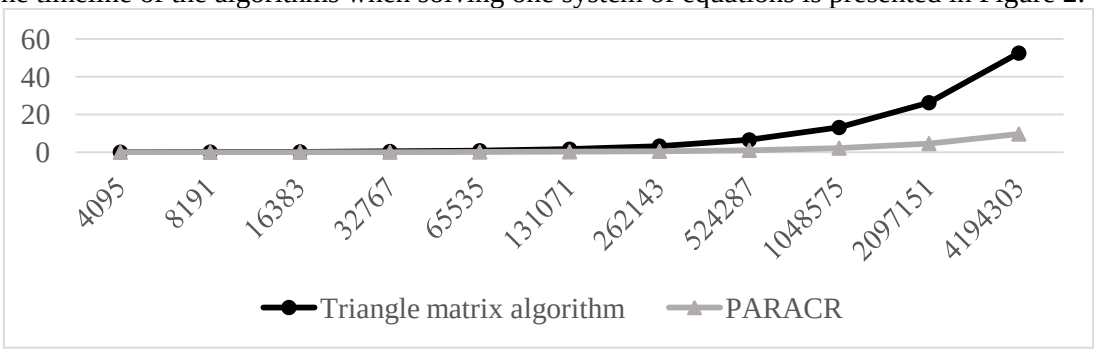

Figure 2. Schedule of implementations of traditional matrix algorithm on GPUs with full load into shared memory and parallel cyclic reduction algorithm on partial load GPUs in shared memory when solving one system (the vertical axis shows the time in seconds, the horizontal size shows the matrix size).

Thus, when solving a set of systems of linear algebraic equations, the best result is shown by the traditional matrix algorithm on a GPU with full load in the shared memory. Its running time is on average 6 times shorter than the running time of the cyclic reduction algorithm. However, when solving one system with a large matrix, it is more expedient to use a parallel cyclic reduction algorithm with partial loading into shared memory. Its implementation requires 7 times less time for calculations than the implementation of the traditional matrix algorithm.

4. Conclusion

As a result of this work, it was obtained that the use of shared memory for the traditional matrix algorithm gives an increase in acceleration by 47%. This is because data loaded into shared memory is reused.

For the cyclic reduction algorithm, it is advisable to load into the shared memory only those coefficients that are used twice in the calculations. At the same time, the acceleration is increased by 2%.

When solving a set of systems of linear algebraic equations, the best implementation of the traditional matrix algorithm is 6 times faster than the best implementation of the cyclic reduction algorithm. However, when solving a single system with a large matrix, the result is the opposite: the cyclic reduction algorithm is 7 times faster.

5. References

[1] Golovashkin D L 2002 Application of the method of counter runs for the synthesis of a parallel algorithm for solving grid equations of tridiagonal type *Computer Optics* **24** 33-39
[2] Yablokova L V, Golovashkin D L 2018 Block algorithm for the joint difference solution of the d'Alembert and maxwell's equations *CEUR Workshop Proceedings* **2212** 56-62
[3] Yablokova L V, Golovashkin D L 2018 Block algorithms of a simultaneous difference solution of D'alembert's and Maxwell's equations *Computer Optics* **42(2)** 320-327 DOI: 10.18287/ 2412-6179-2018-42-2-320-327
[4] Ilyin V P, Kuznetsov Yu I 1985 *Three-diagonal matrices and their applications* (M.: Science) p 208
[5] Yablokova L V, Golovashkin D L 2017 Application of the pyramid method in difference solution d'Alembert equations on graphic processor with the use of Matlab *CEUR Workshop Proceedings* **1902** 68-70
[6] Golovashkin D L, Loganova L V 2012 The solution to the difference equations finite difference schemes with cyclic boundary conditions on a two-dimensional grid areas using multiple graphics processing devices *Computer Optics* **36(4)** 534-540
[7] Boreskov A V 2011 *CUDA technology in the examples: an introduction to programming GPUs* (M.: DMK Press) p 232
[8] Kazennov A M 2010 Basic concepts of CUDA technology *Computer Research and Modeling* **2(3)** 295-308
[9] Boreskov A V, Kharlamov A A 2016 *Basics of CUDA technology* (Moscow: DMK Press) p 230
[10] Shinkaruk D N, Shpolyansky Yu A and Kosyakov M S 2012 Analysis of the effectiveness of the use of CUDA technology for solving systems of linear equations with three-diagonal matrices in options pricing problems *Universities. Instrument making* **10** 6
[11] Malyavko A A 2015 *Parallel programming based on OpenMP, MPI, CUDA technologies: studies. manual* (Novosibirsk: Publishing House of NSTU) p 116
[12] Yarmushkin S V, Golovashkin D L 2004 Research of parallel algorithms for solving three-diagonal systems of linear algebraic equations *Bulletin of the Samara State Technical University. Physics and Mathematics* **26** 5
[13] Hockney R, Jesshope K 1986 *Parallel computers. Architecture, programming and algorithms* (M.: Radio and communication) p 392

Security event data collection and analysis in large corporate networks

E V Chernova[1], P N Polezhaev[1], A E Shukhman[1], Yu A Ushakov[1], I P Bolodurina[1] and N F Bakhareva[2]

[1]Orenburg State University, Pobedy av., 13, Orenburg, Russia, 460018
[2]Povolzhskiy State University of Telecommunications and Informatics, L. Tolstoy str., 23, Samara, 443010

e-mail: newblackpit@mail.ru, shukhman@gmail.com

Abstract. Every year computer networks become more complex, which directly affects the provision of a high level of information security. Different commercial services, critical systems, and information resources prevailing in such networks are profitable targets for terrorists, cyber-spies, and criminals. The consequences range from the theft of strategic, highly valued intellectual property and direct financial losses to significant damages to a brand and customer trust. Attackers have the advantage in complex computer networks – it is easier to hide their tracks. The detection and identification of security incidents are the most important and difficult tasks. It is required to detect security incidents as soon as possible, to analyze and respond to them correctly, so as not to complicate the work of the enterprise computer network. The difficulty is that different event sources offer different data formats or can duplicate events. In addition, some events do not indicate any problems on their own, but their sequence may indicate the presence of a security incident. All collection processes of security events must be performed in real-time, which means streaming data processing.

1. Introduction

Recently, computer networks tend to develop rapidly. They become larger and more complex, but they still remain profitable targets for various intruders – criminals, cyber-spies, and even terrorists. Commercial services, critical systems, and information resources are at risk. The consequences can be different, ranging from the theft of strategically important information, highly estimated intellectual property, and direct financial losses to significant damages to a brand and customer trust.

The traditional approach to cybersecurity is based on the idea that it is necessary to create a special trustful environment for networks and data, that is, to organize them in such a way as to reduce access to them from the outside, but not to prevent them from performing their functions correctly. This will help to discover and eliminate vulnerabilities before the intruder will find them. Such an approach is no longer effective in modern computer networks with constantly changing threat scenarios. Attacks can be organized anytime and anywhere, and due to the complexity of networks, it is easier for the attackers to hide their tracks. In theory, the specialists should be ready for all possible variants of attacks, but, in practice, it is impossible. Thus, to protect the systems, it is necessary to collect the data from the entire network, understand how it works, detect and identify threats, and take appropriate

actions as fast as possible. Certainly, there is a huge amount of solutions to perform these tasks, but not all of them are free, able to interact with the most of available sources of security events and to work in the highly distributed networks.

A Network-wide Cyber Situational Awareness (NwCSA) has been introduced in [1] to assist a network security administrator with network security. The challenges include the overload of raw data, low speed of reaction, and a lack of context and unified view on a network. The framework leverages a distributed data stream processing system and methods for real-time big data processing. The paper describes only the concept of such system.

A cyber threat platform for real-time detection and visualization of cyber threats OwlSight is presented in [2]. The platform is composed by several building blocks and it is able to collect huge amounts of data from multiple sources, prepare and analyze the data and present the findings through a set of insightful dashboards. The platform use Cassandra for data storage and Spark for data processing. Authors describe some real usage scenarios, but do not provide results of performance testing of solutions.

In [3] authors introduce an architecture dedicated to security monitoring of network traffic in local enterprise networks. The application domain of the system is network intrusion detection and prevention. Other anomalies are not considered. This architecture integrates two systems, one dedicated to scalable distributed data storage and management and the other dedicated to data exploitation. Several well-known big data framework are compared for data processing. Spark and Shark appear to be the best performers in all tests.

The paper [4] presents a prototype of Security Information and Event Management (SIEM). The system uses a combination of three different approaches for security analysis: misuse detection, query-based analytics and anomaly detection. Authors propose to use anomaly detection in a combination with signatures and queries, applied on the same data, rather than as a full replacement for misuse detection. In this case, the majority of attacks will be captured with misuse detection, while anomaly detection will highlight previously unknown behaviour or attacks. The main drawback of the system is the use of expensive in-memory data storage (SAP HANA). Also anomaly detection methods are tested on obsolete the KDD 1999 dataset.

In [5] authors compare several methods for detecting anomalies on UNSW-NB15 dataset. They test correlation analysis, linear discriminant analysis and seven well known classification algorithms within the bigdata tool Apache Spark. Data collection methods are not covered in the paper.

In this paper, we describe the concept of a system for collection and primary analysis of security events and incidents in large corporate networks.

2. Selection and review of software tools

The main requirements for software tools are the open source, the ability to function in the distributed systems, and the support of streaming data processing. Since a large amount of heterogeneous data is formed in real-time, which is required to be converted to a general form, processed and analyzed, it should be considered that the selected tools must support the work with streaming data. Streaming data mean the data that continuously provided by a variety of sources, from which small batches are formed. The sources of such data are authentication systems, active network devices, IDS/IPS (Intrusion Detection Systems/Intrusion Prevention Systems), event logs of servers, antiviruses, vulnerability scanners, and other security and management systems.

Apache Spark [5] was selected as a framework for processing streaming data. It works much faster than *Hadoop*, supports cluster mode, and it is compatible with other Apache products. It has well-structured documentation, and it is quite popular among developers, which means there are a lot of articles, tutorials, and manuals about it. *Spark* can work in a *Hadoop* environment managed by *YARN*. *Spark* provides API for *Scala*, *Java*, *Python*, *R* languages and supports different distributed storage systems – *HDFS*, *Cassandra*, *OpenStack Swift*, *NoSQL-DBMS*, *Amazon S3*, and others. In addition, *Spark* includes the following components: *Spark SQL* for processing SQL queries, *Spark Streaming* for streaming data processing, *Spark MLib* for machine learning, and *Spark GraphX* for working with graphs.

Apache Spark has an extension to its basic API – *Spark Streaming*. It does not process entire streams, but divides them into small batches. It is called *DStream* (Discretized Stream), which is a sequence of RDDs (Resilient Distributed Datasets). They can be processed in parallel, including computations based on sliding windows. RDD supports two types of operations: transformations and actions. The result of a transformation is a new RDD; the result of an action is a specific value. Transformations are not executed immediately, that is, *Spark* remembers transformations over particular data and executes them, only when an action is called (lazy execution). Such an approach improves the efficiency of *Spark*. In addition to RDD, there is a *DataSet* in *Spark*. It differs by using the optimizer that chooses the most efficient way of computing the result. The optimizer is mainly used for SQL queries.

A *Spark* application represents a set of processes executed in a cluster and controlled by *SparkContext* object, which called a driver, created in the main program [4]. In particular, *SparkContext* can connect to cluster dispatchers of different types that distribute resources between applications. After connection, *Spark* gets available executors on the cluster nodes and sends the code to the executors, and, finally, *SparkContext* assigns tasks to the executors to perform them.

In addition, *Spark* has disadvantages. Firstly, it is the "inheritance" of batch processing – non-constant network loads during data loading and processing. Therefore, it is necessary to set up restrictions on the density of input stream, since *Spark* does not have an efficient tool for tracking it. Secondly, it cannot recover clusters after failures.

Additionally, the *Apache Kafka framework* can be used to solve these problems. It is able to create real-time data pipelines and streaming applications [6]. *Kafka* provides the designing of a distributed server for message queues. Thus, a data stream is distributed over several servers in a cluster providing high scalability. The risk of data loss is reduced due to such replicated and persistent storage.

The main abstraction of *Kafka* is a topic that is a category or feed name used to publish records to it. Topics usually have several subscribers that are consumers, which subscribe to the data written to the topics. *Kafka* provides a partitioned log for each topic. Each partition represents an ordered, immutable sequence of records, which are constantly added to a commit log. Each record in the partition has a unique sequential number that is called offset. It identifies each record in the partition.

The servers of *Kafka* clusters store the distributed commit logs of the partitions. Each server processes requests for shared access to partitions. In order to provide fault-tolerance, partitions are replicated to a configurable number of servers. A partition has a single server that is called leader and zero or more servers which function as followers. Leader processes all requests for reading and writing partitions, and followers passively replicate the leader. One of the followers will be elected as a new leader if the current leader fails. Each *Kafka* server functions as a leader for some of its own partitions, and as a follower for others, therefore, the load in the cluster is well balanced.

Kafka Streams is a client library for parallel processing and analyzing the input and output data stored in *Kafka*. It can be used for computations described as a processing topology.

3. Organization of data transfer and storage

After performing different operations, it is necessary to store the obtained results. *Apache Cassandra* [7] was selected for that as a NoSQL database management system. *Cassandra* has high scalability and throughput for reading and writing operations, and it supports replications. It does not work with SQL, but it has a similar language called CQL (*Cassandra Query Language*). A big advantage of *Cassandra* is the ability to create reliable and fault-tolerant clusters. In addition, joining new *Cassandra* instances to the cluster is very simple. Clients can access any cluster node for reading and writing because all of them are equal, and data are consistent.

Raw data enter the system from different sources like network devices, antivirus programs, firewalls, IDS/IPS. For receiving data from such sources, there is *Kafka Connect* [8], which is a tool for scalable data transfer between *Apache Kafka* and other systems. It can be used to transfer large volumes of data to or from *Kafka*. *Kafka Connect* can get the entire databases or collect data from different application servers and put them into *Kafka* partitions. In addition, the export jobs can transfer data from *Kafka* partitions to the external storages and query systems, or to the batch systems

for offline analysis. Since the sources of data are different, for each of them, the separate *Kafka* partition should be created.

Connector developed by *DataMountaineer* simplifies writing data to a *Cassandra* database [9]. It converts values from *Kafka Connect SinkRecords* to JSON, and then asynchronously inserts records into *Cassandra* tables. The connector can create secure connections over SSL. The selection of fields and partition management are handled by KCQL (*Kafka Connect Query Language*).

The *Spark Cassandra Connector* library [10] was selected to implement a connection between *Spark* and *Cassandra*. For data transferring, it is necessary to create *StreamingContext* and *DStream* that will connect to nodes. The *SparkConf* object is used to configure *StreamingContext*. It is necessary to set up the connection host, user name, and password for a *Cassandra* user. Any node of a *Cassandra* cluster can be a connection host. The driver extracts cluster topology from the connection host and can switch to the closest node in the same data center. Whenever any method is called that requires access to *Cassandra*, the options from the *SparkConf* object are used to create a new connection or to use an already opened one from the pool of connections. In addition, the *Spark Cassandra Connector* can connect to several *Cassandra* clusters.

4. Correlation analysis

Events are consumed by application based on *Spark Streaming*. They have their own place in a hierarchy, depending on the way of receiving events and their features (Figure 1). There are three large classes of events: the events from SNMP, the events from *Syslog*, and others. Classes are divided into subclasses, depending on the common features of events. Subclasses, in turn, can be divided again, etc.

The *Spark Streaming* Application takes each received *Kafka* partition, performs filtering, converts the data into classes of the hierarchy and saves them, after that a correlation analysis is performed.

At the next step, it is necessary to create rules for correlation analysis. There are many ways to organize them. In our system, we use two of them – patterns and requests. A pattern is a set of rules with some fields, which are filled in with the data from events. A request is similar to a pattern, but it works with data streams. It can join, group by, filter, deduplicate, sort data, or pass events through sliding windows. The window saves events to aggregate, join, and match them against particular patterns or subqueries. It defines which subset of events should be saved. For example, the data window saves the last *N* events, and the time window – the events during the last *N* seconds. In addition, in a pattern or a request, the reaction can be defined, that is, the action which should be performed when the data match the conditions. The simplest reaction is a notification of an administrator about suspicious activity, for example, by an e-mail message. However, there are more radical opportunities such as port closing, launching programs or running scripts (for example, to shape the traffic during DDoS attacks).

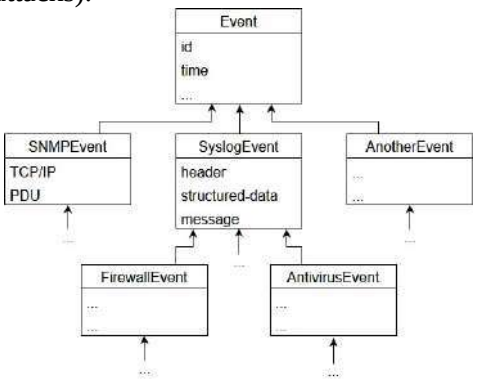

Figure 1. The hierarchy of events.

The pattern fields can be different, for example, such as the event category, the IP address of its source, the type of source device, the port number, the time thresholds, etc. The selection of the fields required for the analysis is based on available data. For example, an SNMP protocol data unit includes IP and UDP headers, protocol version, password, type of unit, request id, error status, error index, and

variable bindings. A *Syslog* message consists of a header, structured-data, and a text. The header contains information on facility, severity, protocol version of *Syslog*, timestamp, host name, application name, system process id, and message type. Knowing how the messages of these protocols are formed, it is possible to extract necessary fields using regular expressions. For each event type, a special regular expression is used, which captures the necessary data from the raw message of the event source. The following method creates a new event.

create event ExampleEvent: Event {
severity: " severitygroup",
datetime: " datetimegroup",
hostname: " hostnamegroup",
appname: " appnamegroup",
type: " typegroup",
message: " messagegroup",
}

Here double quotes indicate the names of groups from the regular expression.

In addition to the usual method of event creation, there are more intended to the events of certain types. It is for the convenience of the users.

create event SyslogEvent: Event {
facility: " facilitygroup",
severity: " severitygroup",
datetime: " datetimegroup",
hostname: " hostnamegroup",
appname: " appnamegroup",
type: " typegroup",
message: " messagegroup"
}

create event SNMPEvent: Event {
destination_address:"destination_addressgroup",
source_address: " source_addressgroup",
type_of_service: " type_of_servicegroup",
sourse_port: " sourse_portgroup",
destination_port: " destination_portgroup",
pdu-type: " pdu-typegroup",
error-status: " error-statusgroup"
}

The rules look similar to SQL queries. Firstly, the keyword "*select*" is used in the begging of the rule. Then the selection from the required group of events is specified after the keyword "*from*". According to SQL principles, "*where*" can be used to specify a condition. All logical operations ("*and*", "*or*", "*not*") should be supported. In addition, it is possible to specify the time duration within the events should happen, or the time interval between them ("*timer*"). Then, it is possible to use grouping ("*groupby*") or sorting ("*orderby*"). After that, the reaction is specified ("*then*" with "*msg*" or "*block*").

The following example is the selection of the alert time, the host IP address, the severity and the category of all incidents from the pattern, except for those which source IP address is "192.168.100" or "192.168.1.101", grouped by source IP address:

select alert_time, host_ip, severity, category from pattern
[pattern eventA=antivirus -> eventB=scanning_hosts (eventA.src_ip = eventB.host_ip)
where timer within 60]
where src_ip not "192.168.1.100" or not "192.168.1.101"
groupby src_ip.

The pattern is specified in square brackets. It starts with the keyword "*pattern*", then two events ("*eventA*" and "*eventB*") are specified with their types after the equal sign "=". The sign "->" indicates that the events are sequential. Further, the fields of these events are specified in parentheses. In this example, "*src_ip*" of "*eventA*" should be equal to "*host_ip*" of "*eventB*". This condition should be satisfied within 60 seconds, so the events will be identified as an incident. In addition, it is possible to use a previously saved pattern by specifying its name in the square brackets. The Web interface of the system should has the opportunities for editing and adding correlation rules.

5. Concept of a system for collection and primary analysis of security events and incidents in large corporate networks

Firstly, it is necessary to collect as much data as possible about the security events in computer networks. As it was already mentioned above, data are collected using the *Syslog* and SNMP

protocols. Information about other events that they do not cover can be collected using special tools, for example, IDS Suricata. All data are converted into JSON format. Tools used for data transmission support this format.

The SNMP agents collect information on devices and send it to the SNMP server (Figure 2). In addition, there are two ways for transmission of the collected information: the request-response and the trap. In the second case, the agent unilaterally sends messages to the server.

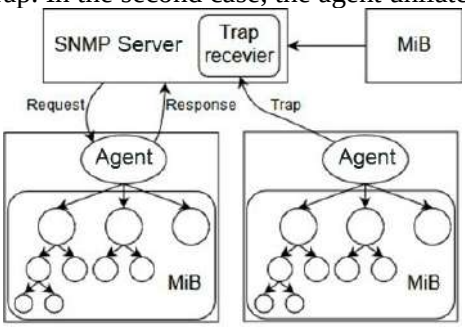

Figure 2. The interaction between the SNMP server and the agents.

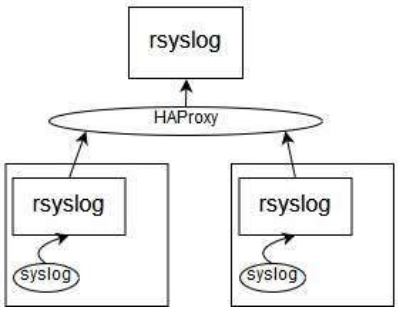

Figure 3. The *Syslog* data collection using *rsyslog* servers.

The data obtained using the *Syslog* protocol are collected by *rsyslog* servers (Figure 3). *HaProxy* is used for load balancing and availability. In order for the rsyslog server to transmit data to the *Kafka* servers, it is necessary to install the special plugin *omkafka* and to change the configuration file "*rsyslog.conf*" by adding the template for converting messages from *Syslog* to JSON format [11].

Information from the sources collected by *Suricata* is transmitted to the database using *Kafka* [12] (Figure 4). For each type of event source, *Kafka* servers should have the separate partition, which processes events of a particular source in parallel with other partitions (in this case, "*sur-topic*" for Suricata, "*rsl-topic*" for *Syslog*, and "*snmp-topic*" for SNMP). All received raw events in JSON format are stored in the database, from which they are extracted by the *Spark* application. It converts, filters, and aggregates events, after that it performs the correlation analysis. The correlation rules are loaded from separate storage. All the results are saved in a separate database. If incidents are detected, the reaction module, according to the rules, alerts the administrator or blocks the malware activity on network devices or hosts. The Web interface of the system should provide many opportunities for users including authorization, generation and viewing of reports, editing and adding correlation rules.

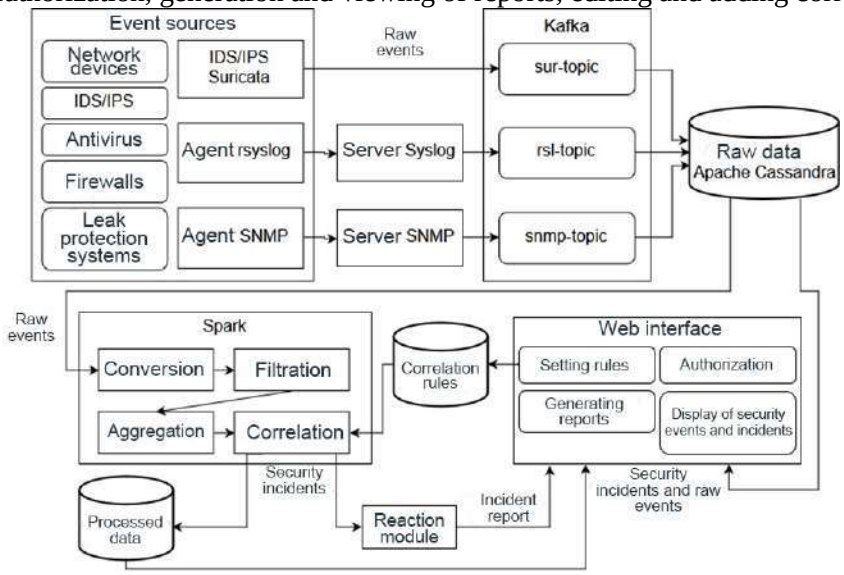

Figure 4. The architecture of the system for the collection and primary analysis of security events and incidents in the large corporate networks.

6. Experiments

The test bed was assembled to check the efficiency of the proposed approach and measure its performance parameters. Figure 5 shows the logical scheme of the test bed and reveals some details about the physical part of the infrastructure and its parameters.

The data were generated by IDS *Suricata* installed on two servers, which were attacked by malicious traffic from the system based on the *Metasploit Framework*. Thus, the accuracy of the IDS responses and the performance of storing data in *Cassandra* were simultaneously checked. For stress-testing, the logging details were chosen as the most verbosity, and the events were described in JSON format in the size of 20-22 Kb.

We used a private cloud based on *OpenNebula* 5.4.6 and 6x Intel Xeon X5670 48 Gb RAM servers for the experiments. Virtual machines were created using KVM. Their virtual disks used the write-back policy of local caching. Physical disks inside the nodes were connected via iSCSI to the SAN based on *OpenMediaVault*, where RAID-Z was configured on the ZFS system with the cache on SSDs. SAN network was 2x10GbE per node (2 nodes), the MTU was set to 9000.

The volume of generated data is 81958 poorly structured events in a mixed text/JSON format (*Syslog*) with the total size of 1703 Gb. The primary data were being saved in a single input table with which *Spark* worked later to structure them. That data were being written back to *Cassandra* to another keyspace. The structure of the data was generated in advance based on a preliminary analysis of the raw data fields.

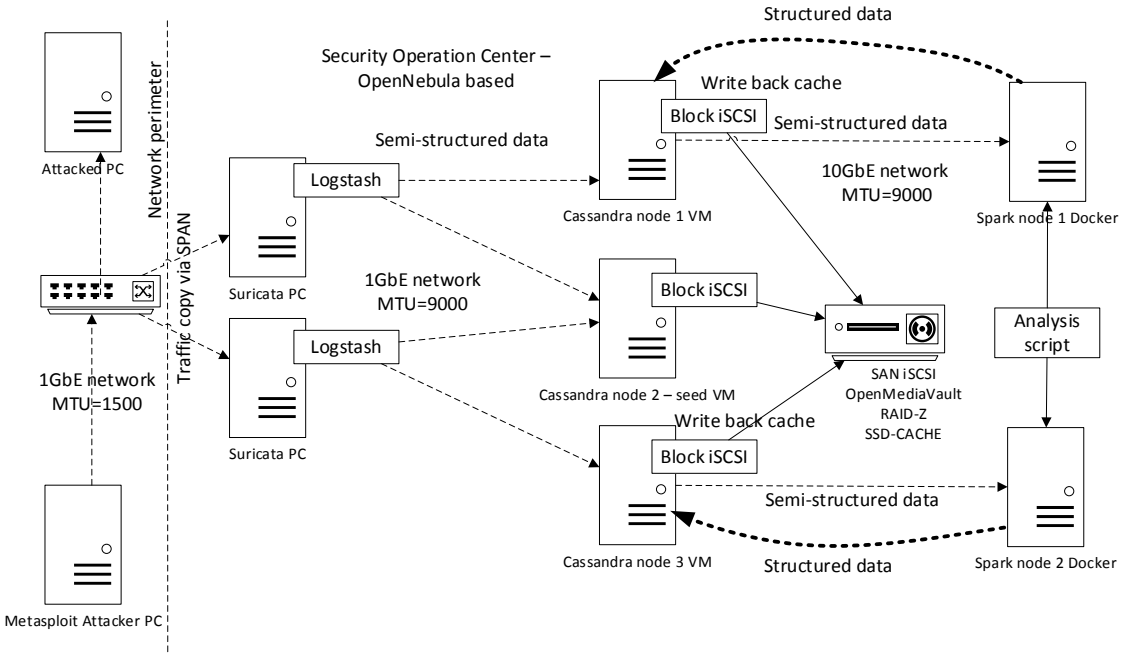

Figure 5. The architecture of the test bed.

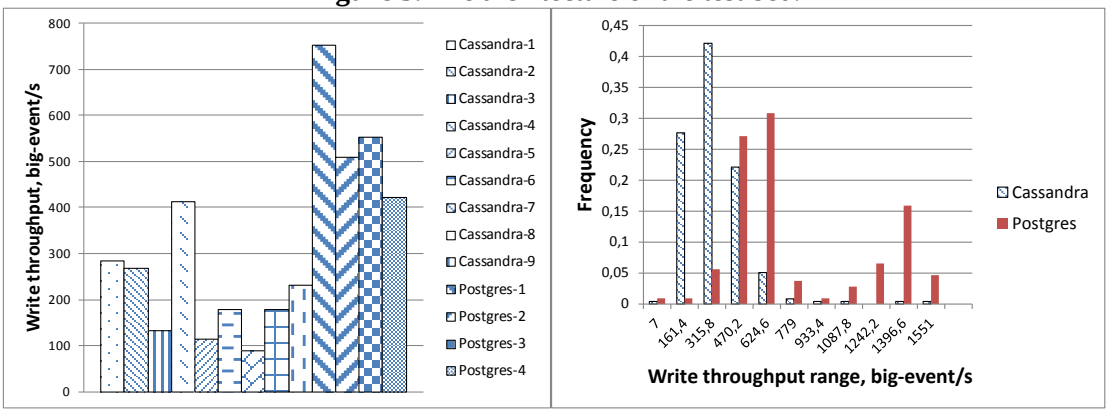

Figure 6. The write throughput for experiments.

Each experiment started with a clean system with removed data and cleared caches. We measured the performance of write throughput of the system with different values of replication factor for keyspace, partition batch size, and chunk size for *Cassandra* connector. Data were saved to volume mounted as "*/var/lib/cassandra*". It was used as a storage, but in some experiments, additionally, we used the directly mounted NFS disks to test common cases. In order to compare the performance with the traditional approach for data storage, the series of experiments were conducted on the same virtual nodes but using *PostgreSQL* as a data storage. The first series of experiments (with *Cassandra*) used the text format for all fields, the second one (with *PostgreSQL*) – JSONB for the data produced in this format. In addition, both volume and NFS disks were used as storage. The results are shown in Table 1 and in Figure 6.

The left graph of Figure 6 shows the average throughput of successful writing requests of large (>20Kb) rows for all experiments from Table 1. The right graph is the distribution histogram for 11 buckets of the write throughput aggregated over all experiments. Aggregated results are presented separately for experiments with *Cassandra* and *PostgreSQL*. According to this graph, there is a noticeable difference in distributions – *PostgreSQL* has a higher rate of requests with high throughput. In Figure 6, we use big-event/s units to distinguish the idea of a classic event for security system (several hundreds of bytes) from the full description of the security event, especially generated by IDS.

Table 1. The results of experiments.

Experiment title	Storage engine	Replication factor	Batch size	Chunk size	Number of parallel processes	Average write throughput, events/s	Average write throughput, Mbit/s
Cassandra-1	Cassandra over volume	2	5	3	2	284	50.7
Cassandra-2	Cassandra over volume	1	5	3	2	286.1	47.9
Cassandra-3	Cassandra over volume	1	5	3	1	133.9	23.9
Cassandra-4	Cassandra over volume	1	5	3	3	413.3	73.8
Cassandra-5	Cassandra over volume	2	5	4	1	115.3	20.6
Cassandra-6	Cassandra over volume	2	5	3	3	178.8	31.9
Cassandra-7	Cassandra over volume	1	3	2	2	88.4	15.8
Cassandra-8	Cassandra over volume	2	3	2	2	100.9	18
Cassandra-9	Cassandra over NFS	1	3	2	2	232	41.4
Postgres-1	PostgreSQL over volume	2	-	-	1	753.7	134.6
Postgres-2	PostgreSQL over NFS	2	-	-	1	510.1	91.1
Postgres-3	PostgreSQL over volume and JSONB fields	2	-	-	1	552.8	98.7
Postgres-4	PostgreSQL over NFS and JSONB fields	2	-	-	1	422.1	75.4

The experiments, which used a volume, showed greater performance due to more optimal caching and file system operation than the experiments with data storage based on NFS on the same server.

The number of replicas for *Cassandra* affects the write throughput less than the number of parallel writing processes. The batch and chunk sizes affect more due to the shorter transactions of the connector. At the same time, *PostgreSQL* showed significantly better performance, even when using JSONB type to store the part of data fields. However, the data integrity and consistency are guaranteed by the relational model of *PostgreSQL*, and replications are configured several times more flexible.

7. Conclusion

Thus, we proposed the concept of a distributed system for collection and primary analysis of security events and incidents in the networks. It is able to extract events from different sources in the entire network, process them, and output results in a convenient format. The system works with real-time streaming data, which is surely its main advantage. Such a solution is suitable for large corporate networks, and due to the high scalability of its components, it can work with big data.

In the future, the functions of the system can be extended by new types of analysis, optimization, and by adding as many event sources as possible.

8. References

[1] Jirsik T and Celeda P 2018 Toward real-time network-wide cyber situational awareness *Network Operations and Management Symposium*
[2] Carvalho V S, Polidoro M J and Magalhães J P 2016 OwlSight: platform for real-time detection and visualization of cyber threats *Big Data Security on Cloud (BigDataSecurity), International Conference on High Performance and Smart Computing (HPSC), and International Conference on Intelligent Data and Security (IDS)* 61-66
[3] Marchal S 2014 A big data architecture for large scale security monitoring *IEEE International Congress on Big Data* 56-63
[4] Sapegin A, Jaeger D, Cheng F and Meinel C 2017 Towards a system for complex analysis of security events in large-scale networks *Computers & Security* **67**16-34
[5] Dahiya P and Srivastava D K 2018 Network intrusion detection in big dataset using Spark *Procedia computer science* **132** 253-262
[6] Kafka 2.0 Documentation URL: http://kafka.apache.org/documentation/
[7] Apache Cassandra Documentation v4.0 URL: http://cassandra.apache.org/doc/latest/
[8] Stevenson A *Connecting to Apache Kafka. The Connect API in Kafka Cassandra Sink: The Perfect Match* URL: https://docs.confluent.io/3.0.0/connect/intro.html
[9] Kafka Connect Cassandra URL: https://www.confluent.io/connector/kafka-connect-cassandra/
[10] Kindling: An Introduction to Spark with Cassandra (Part 1) URL: https://www.datastax.com/dev/blog/kindling-an-introduction-to-spark-with-cassandra-part-1
[11] Rsyslog Documentation URL: https://www.rsyslog.com/doc/v8-stable/
[12] Suricata User Guide URL: https://suricata.readthedocs.io/en/suricata-4.1.0/

Acknowledgments

The research was supported by the Russian Foundation for Basic Research in the framework of the scientific projects No. 16-29-09639, 18-07-01446, 18-37-00460.

A multiuser web-interface for solution of systems of nonlinear equations

A N Danilenko[1], I A Zhdanov[2]

[1]Samara National Research University, Moskovskoe Shosse 34A, Samara, Russia, 443086
[2]University of Stuttgart, Keplerstraße 7, Stuttgart, Germany, 70174

e-mail: danilenko.al@gmail.com

Abstract. In this article, the idea of creating web-applications is considered by the example of developing a multiuser web-interface for the automated search for roots of non-linear equations in the Django package. The automated system is implemented in the Python programming language. It is proposed to create a web application based on a client-server technology, where the client part implements the user interface, forms queries to the server and processes the responses from it. The server part receives the request from the client, performs necessary calculations, then forms a web page and sends it to the client online. The developed application is designed for nonlinear equations systems solution. The system has the ability to save solutions on the server and the PC, and to visualize the step-by-step solution and plotting. The system efficiency was tested on real data.

1. Introduction

There are many physical systems, which are nonlinear in nature. Sometimes it is possible to describe the operation of a physical system by a linear model, but in analyzing the behavior of any physical system, one often encounters situations where the linearized model is inadequate or inaccurate; that is the time when the system of nonlinear system should be introduced and solved [1].

Indeed, systems of nonlinear equations arise in many domains of practical importance such as engineering, mechanics, medicine, chemistry, and robotics [2]. Numerous examples from all branches of the sciences are given in [3], [4], [5], [6], [7], [8], [9]. Thus, the nonlinearity in all shapes and forms is at the heart of many of the 21st century challenges to science as we try to extend the scientific framework beyond its dependency upon linear systems theory to find new ways to embrace the complex world we live in on its own irregular and imperfect terms. Contrary to linear systems, in the nonlinear systems the principle of superposition fails meaning that they are needed to be approached as a whole, since the output of the system might be greater or less than sum of its part due to synergy or interference of relationships between system elements. There are several methods to solve systems of nonlinear equations, which are covered in [10], [11]. The overview of these methods is briefly given in the Section 2 of this article.

Since the solution of nonlinear systems heavily relies on the numerical computing, the importance of the appropriate software arise. In applied science and engineering, e.g. when engineers analyze and design nonlinear dynamical systems in electrical circuits, mechanical systems, control systems, and other disciplines, there is a need to use a wide range of nonlinear analysis tools. Despite the fact that these tools have developed rapidly since the mid-1990s, the solution of nonlinear systems is still largely a tough challenge [7]. For the large-scale problems having very high computational complexity the issue of the computational power and large memory requirements arise for some numerical methods, e.g. Newton's method [2].

With the rapid development of internet and cloud services, there is a noticeable shift from desktop applications towards web and mobile applications. The journey from legacy internal servers and software to cloud-based compute, storage and memory will no happen overnight. Nor will it be without unique challenges. But as more and more the community is realizing, that these new opportunities with cloud services are just too good to ignore [12].

The big drawback of desktop native programs is their high cost and the need to be installed on each computer, which is inconvenient, for example, in large companies involved in engineering calculations. Another disadvantage is the use of outdated solution methods, which leads to a large time investment in solving resource-intensive tasks [13], [14], [15]. Currently, there is a trend to move a large amount of software into the form of web applications.

However, existing analogues have a large number of options for solving computational problems, but they have several disadvantages. For example, in the WolframAlpha system, the user can only set a limited number of non-linear equations and cannot control the minimum and maximum parameters. The developed system is able to solve as many equations as possible, even if the system as a whole is indefinite, that is, the number of equations in it is less than variables.

This paper is organized as follows in Sections 2 the current status of nonlinear methods and tools is described, in Section 3 the comparison of native and web application is highlighted, in Sections 4,5 and 6 the concept, structure and impact of the developed web application is shown, in Section 7 the conclusion is given.

2. Methods for solving of nonlinear systems

Most popular methods for solving nonlinear systems are local. A local method is an iterative scheme that converges if the initial approximation is close enough to a particular solution. Frequently, we are also able to prove rate of convergence results for the methods, which tell something about the asymptotic velocity of convergence of the process. Fortunately, in many practical cases the domain of convergence of local methods is large, so that these methods are useful. However, when the initial estimate of the solution is very poor, local methods must be modified in order to improve their global convergence properties. In general, global methods are modifications of local methods which would ensure the solution even with the poor initial conditions [11].

The local methods are:

- Newton's method [11]
- Quasi-Newton Methods [11], [16], [17], [18], [19]
- Inexact-Newton Methods [11]
- Decomposition method [11]

The main procedures currently used for globalization are:

- Optimization [11], [20], incl. multiobjective [2]
- Homotopies [11], [21]

There is no numerical method that can guarantee finding all the roots to a general system of equations in finite time. Most numerical solution techniques are based on Newton's method [3], [11]. Each iteration of Newton's method consists of computing the Jacobian matrix at a feasible point and solving a linear

system which approximates the original system at that point. The solution to the linear system is used as the starting point in the next iteration. Another class of numerical methods transforms the system into an optimization problem. In a strategy based on trust regions [2], [11], at each iteration a convex quadratic function is minimized to determine the next feasible point to step to. The convex quadratic function is the squared norm of the original system plus a linear function multiplied by the Jacobian matrix. There is also the approach of homotopy methods, sometimes referred to as continuation methods [11], [22]. This approach begins with a `starting' system of equations (not the true system). whose solution is known. This starting system is gradually transformed to the original system. At each stage, the current system is solved to find a starting solution for the next stage system. The idea is that as the system changes, the solutions trace out a path from a solution of the starting system to a solution of the original system. At each stage, the current system is normally solved by a Newton-type method, again making use of the Jacobian. Problems with this approach include not all paths converging to a finite solution. With all of the above numerical methods for solving nonlinear systems of equations, derivative information is assumed to be available.

Luckily, for the most problems where the number of equations is large, the Jacobian is structurally sparse. This means that most entries of Jacobian are zero for all x in the domain of nonlinear system. Sparsity is a particular case of the more general notion of structure. Jacobian matrices can be symmetric, antisymmetric, positive definite, combination of other matrices with some particular structure, etc. Many times we can take advantage of particular structures of Jacobian in order to obtain efficient algorithms for solving the nonlinear system [11], [23], [24], [25], [26].

3. Native, web or hybrid app

The process of choosing a development approach for a scientific, financial or engineering application (hereafter referred to as an “app”), namely native, web or hybrid, entails many parameters, such as budget, project timeframe, target audience and app functionality to name a few. Each approach carries inherent benefits and limitations, and finding the one that best addresses the organization’s needs could be a challenging task [27].

Native apps have binary executable files that are downloaded directly to the device and stored locally. The installation process can be initiated by the user or, in some cases, by the IT department of the organization. The native app is free to access all of the APIs that are made available by the OS vendor and, in many cases, has unique features and functions that are typical of that specific mobile OS. To create a native app, developers must write the source code (in human-readable form) and create additional resources, then the source code is compiled in order to create an executable in binary form that can be packaged along with the rest of the resources and made ready for distribution. These differences across platforms result in one of the most critical disadvantages of the native development approach—code written for one platform cannot be used on another, making the development and maintenance of native apps for multiple OSs a very long and expensive undertaking.

The web apps are created to be run in modern powerful browsers which support many new HTML5 capabilities, Cascading Style Sheets 3 (CSS3) and advanced JavaScript. With recent advancements on this front, HTML5 signals the transition of this technology from a “page-definition language” into a powerful development standard for rich, browser-based applications. A few examples of the potential of HTML5 include advanced UI components, access to rich media types, geolocation services and offline availability. Using these features and many more that are under development, developers are able to create advanced applications, using nothing but web technologies. One of the most prominent advantages of a web app is its multiplatform support and low cost of development [27].

The hybrid approach combines native development with web technology. Using this approach, developers write significant portions of their application in cross-platform web technologies, while maintaining direct access to native APIs when required [27].

Currently, there is a trend to move a large amount of software into the form of web and hybrid apps. This trend is widespread thanks to the following benefits:

- all program logic of the application is located on the server, in contrast to ordinary software, where the application logic is located on each user's computer. This allows to solve the problem of copyright infringement and illegal copying, since the user in reality does not receive a copy of the application, as before. All that the user receives is the program interface;
- to work with a large number of different applications, only a browser and Internet access are required;
- there is no problem accessing the web application, since it can be obtained at anytime, anywhere;
- it is possible to work with applications not only from a computer, but also from a smartphone or other gadgets with Internet access;
- when working with web applications, there is no need to download large installation files of programs and store their data on your computer;
- program update at making any introductions occurs simultaneously for all users.

Also, based on recent events related to the WannaCry virus, it was proved that it is necessary to use software that is as isolated as possible from the influence of third-party organizations and is fully controlled by the software company that uses it.

One of the main advantages of web applications is that the application is completely independent of which operating system is installed on the user's computer, that is, it can be considered cross-platform. Also, a great advantage over local applications can be considered the lack of the need to install and configure software – everything you need is already installed on the servers and configured by the developers. Due to the fact that the only copy of the application is on the server, and only the developer has access to it, there is no need to solve problems related to illegal copying of software. For developers, a positive thing is that when updates are released, they are immediately available to all users and they do not need to worry about compatibility.

The only visible disadvantage of web applications is that they cannot be used without Internet access.

4. Concept

The relevance of the paper lies in the fact that the developed web application will be used to solve engineering tasks in a company. The system may also be relevant for students and teachers of technical subjects, engineers working with large calculations.

In line with the above requirements, the web app is an online application. It has a graphical user interface and no programming capacity is required for accessing solving the systems of nonlinear equations, conducting data analysis, and building plots. The app has been optimized for low Internet bandwidths and connectivity, with a light interface that is less than 1.5 MB and that is transferred to the client when the application loads in a browser. The app has been developed following interoperability standards. To achieve smooth and fast display of information, the app architecture is composed of a stack of existing open source libraries and in-house developed functions.

In terms of user management system, the app features multiple and flexible user access levels to its tools. Each user is assigned a role of “public”, or “admin”. A role defines the access to the application’s different components.

The significance of the app is that it connects the contemporary methods of solving nonlinear equations running in background with the modern scalable and cross-platform GUI with a high level of accessibility.

5. Methods and solutions

Web application consists of client and server parts, thereby implementing the client-server technology [13]. The client part implements the user interface, forms requests to the server and processes responses from it. The server part receives a request from the client, performs calculations, then generates a web

page and sends it to the client over the network using the HTTP protocol. Figure 1 shows the architecture of a web application using a database.

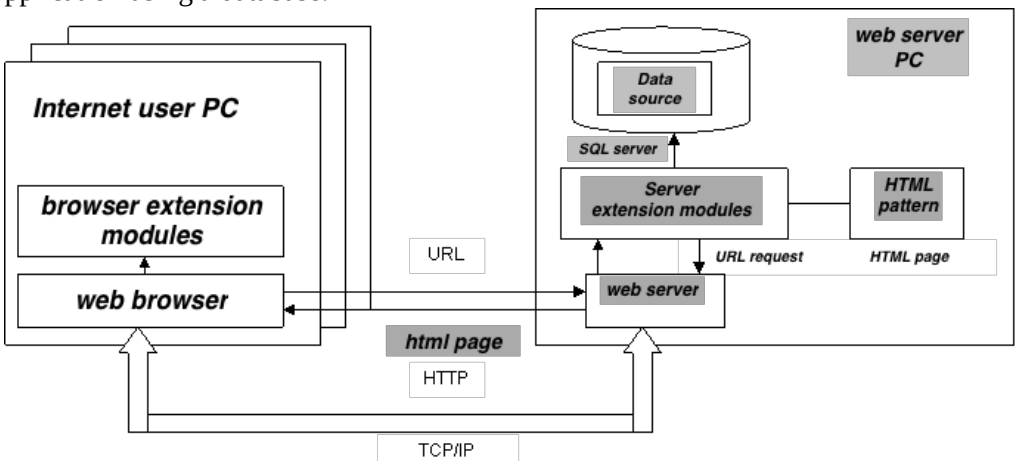

Figure 1. Architecture of a web application using a database.

The web application itself can act as a client of other services, e.g., a database or another web application located on another server. Currently a new approach is gaining popularity which is developing web applications called Ajax. While using Ajax pages, web applications do not reload entirely, but only load the necessary data from the server, which makes them more interactive and productive [14], [28].

Also of great popularity is the WebSocket technology, which does not require constant requests from the client to the server, but creates a bidirectional connection, in which the server can send data to the client without a request from the latter. Thus, it is possible to dynamically manage content in real time.

To create web applications on the server side, a variety of technologies and any programming languages that can output to a standard console are used [14], [15].

This article discusses the problems of creating a multi-user web-interface software for automated search for the roots of nonlinear equations systems [29], [30], implemented in the Python programming language.

The system for solving nonlinear equations implements a new algorithm based on matrices, which, unlike standard solvers, allows us to analyze the system of equations and find a step-by-step solution to the system. First, all the parameters that can be calculated directly are found, then subsystems are determined and solved, then the algorithm is repeated recursively. This approach makes it possible to reduce the calculation time of large systems and increase the stability of their solution, since instead of a large number of parameters at each stage, only those that are necessary and amenable to calculation are sought. The search algorithm is completed if all solutions are found or there is insufficient data to calculate the remaining variables.

The purpose of this work was to develop a web application that produces a solution of nonlinear equations systems on the server [31].

To achieve this purpose it is necessary to solve the following tasks:

1. Application integration on the server. The implemented algorithm for solving systems of nonlinear equations and associated files must be fully stored on a remote server.
2. Creating a user interface. A web application should implement a universal algorithm for solving nonlinear equation systems, have a friendly interface that allows the user to enter equations manually, load equation systems from a computer and save the results.
3. Differentiation of access rights to the system. Access to work with the web application is provided only to authorized users.

4. Visualization of the solution of the system. For clarity, the application should display the course of solving a system of nonlinear equations and build graphs.
5. Data storage and access. The system should allow saving user-defined equations in the database and provide access to them when entering the account.
6. Loading and saving systems of nonlinear equations and their solutions. The system should be able to load nonlinear equations systems from the user's computer in a text format and save the report as a pdf document.

Figure 2 shows a diagram of the simulated system objects.

The subsystem for solving systems of nonlinear equations is implemented in the Python programming language. Python is an optimal programming language for solving math problems that require large calculations. The language supports the possibility of programming within the framework of the OOP model, but does not oblige to do this if it is not necessary.

In addition to the many included in the standard set of libraries, the Python language has easy access to third-party libraries, which is another important advantage of Python. In particular, such libraries as pandas, sympy, numpy, etc. were used to solve the systems of nonlinear equations in this project.

To solve “garbage” removal problem, gc module and gc.collect () command were used, which allows to release resources.

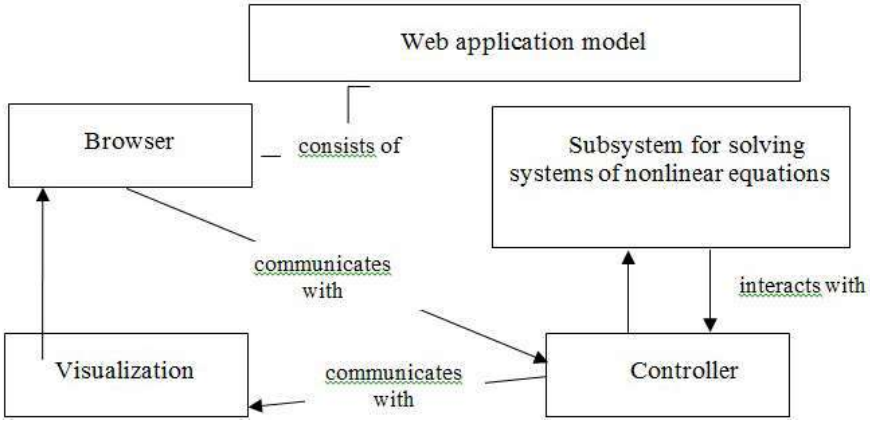

Figure 2. A diagram of the simulated system objects.

To describe the client part of the system, JavaScript was chosen, which is an object-oriented scripting language and interacts through an interface called Document Object Model (DOM) with content that can be executed on the server side (web servers) and on the client side in the web the user's browser when browsing web pages. Many web sites use client-side JavaScript technology to create powerful dynamic web.

JavaScript has several types of embedded objects, namely Object, Array, String, Number, Boolean, Function, Date and Math. Other objects belong to DOM objects (windows, forms, links, etc.).

Figure 3 shows the flow diagram of the system being developed. By defining the functions of the constructor, you can define objects. JavaScript is an object-oriented language based on prototypes. You can add additional properties and methods to individual objects after they have been created. For this, for all instances of a particular type of object, you can use a prototype – a statement.

Notepad ++ was chosen as the development environment. It is a free open source text editor for Windows with syntax highlighting for a large number of programming languages and markup. Supports opening more than 100 formats. Based on the Scintilla component, written in C ++ using STL, as well as the Windows API and distributed under the GNU General Public License. The basic functionality of the program can be extended both by plugins and third-party modules, such as compilers and preprocessors.

The environment was chosen due to the fact that it is free software that completely provides the necessary functionality to accomplish the task.

The application was developed using the Django framework, the programming language Python 3.0, in the Notepad ++ environment.

Traefik is used to manage user load. This is a balance proxy and load balancer. It creates a copy of the system calculation service, if the service load is more than the calculated one.

The application designed by the authors allows the user to:

- solve systems of nonlinear equations downloaded from the user's computer;
- solve systems of nonlinear equations manually entered into the system;
- save solutions to the server;
- download solutions in a pdf format;
- build graphs;
- describe own functions;
- show the progress of the decision

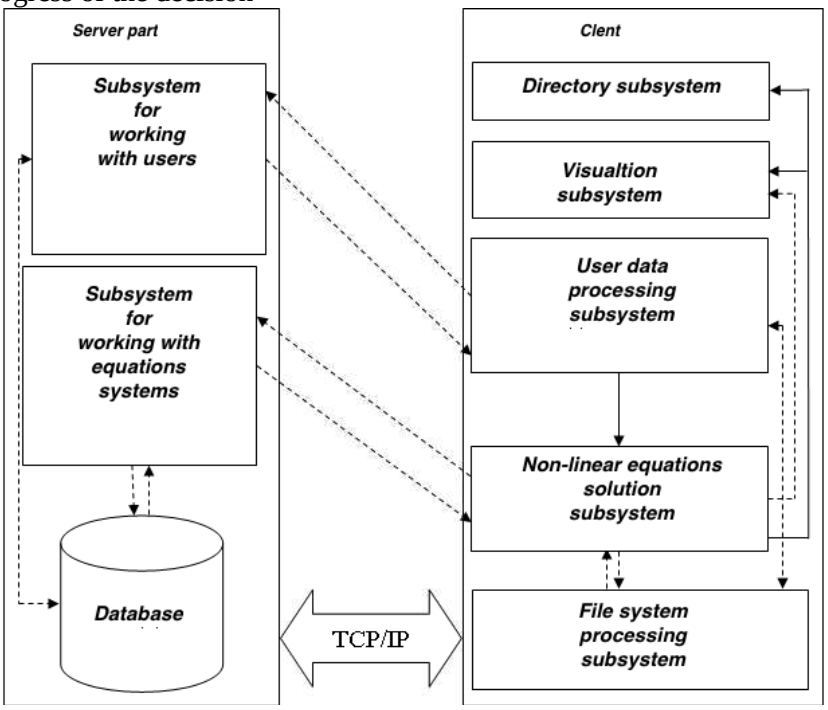

Figure 3. Flow diagram of the system being developed.

6. Results and application

A registered user has access to all functions of the system through the use of the relevant sections of the solution page, which is divided into 3 main parts: the equation input area, the solution display area, the file system operation area. The computational part of the program is based on the algorithm for solving systems of nonlinear equations, developed by a postgraduate student at the University of Stuttgart, I.A. Zhdanov. This algorithm uses the advantages of Jacobian sparsity and breaks down, if it is feasible, a whole nonlinear system into the series of independent nonlinear subsystems and explicit nonlinear equations. The system solutions are presented in a matrix form. Figure 4 shows a screen of the developed web application.

The following is an example of the developed web application. Figure 5 shows an example of an input file with a list of calculated parameters, as well as the type of system of nonlinear equations.

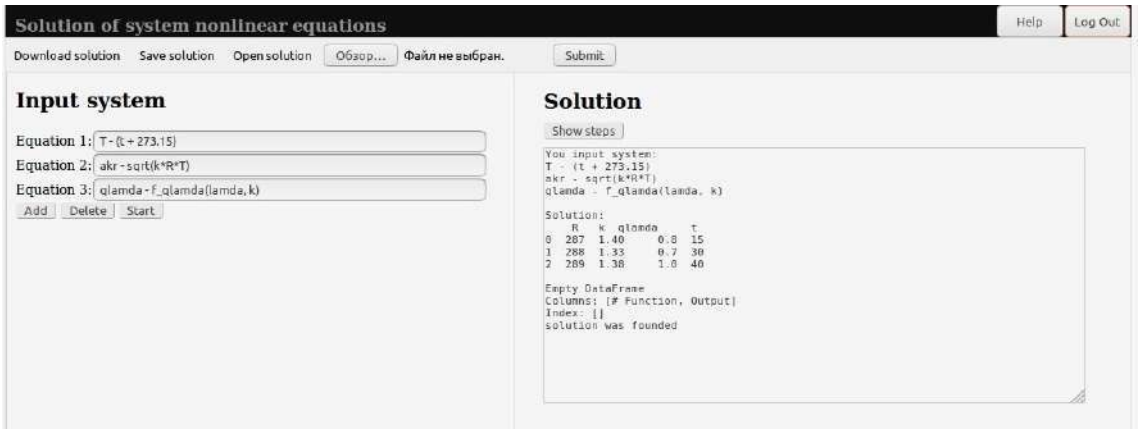

Figure 4. Screen of the web application for solving a system of nonlinear equations.

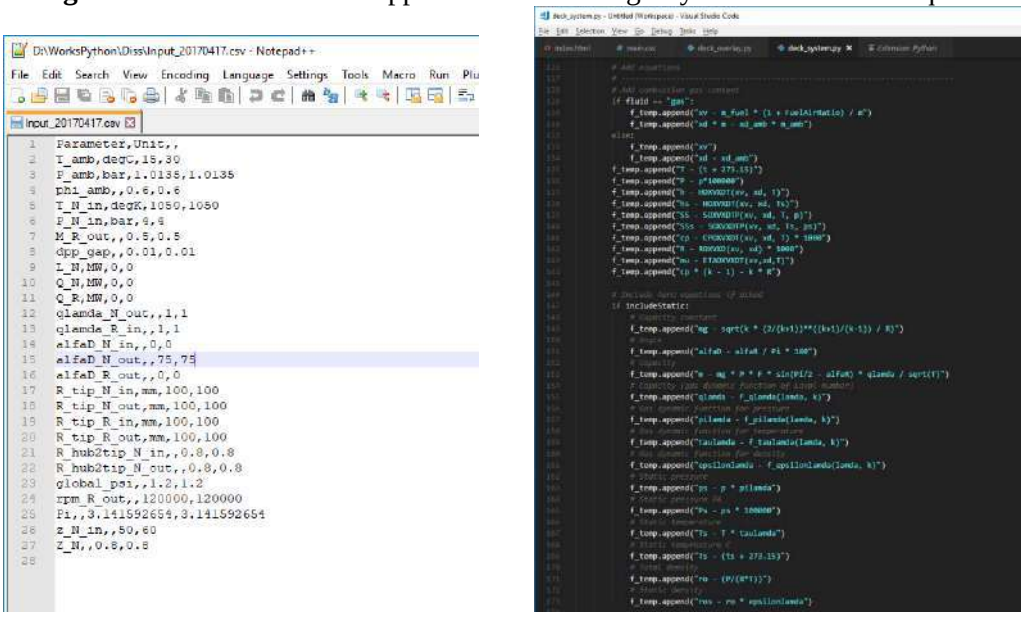

Figure 5. An example of an input file with a list of calculated parameters and the type of the nonlinear system.

Here is one of a simple example of solving a nonlinear system, where it is offered to solve the following system of equations

$$\begin{cases} x^2 + y^2 = 1 \\ (x-2)^2 + (y-1)^2 = 4 \end{cases}$$

The solution of this system of nonlinear equation are 2 points of circles intersection and it is shown in Figure 6.

There are some artificial problems which are widely used to test the solver of nonlinear equations [32]. Among them are:

— Powell's badly scaled problem
— Powell's singular function
— The 'Box- problem' etc.

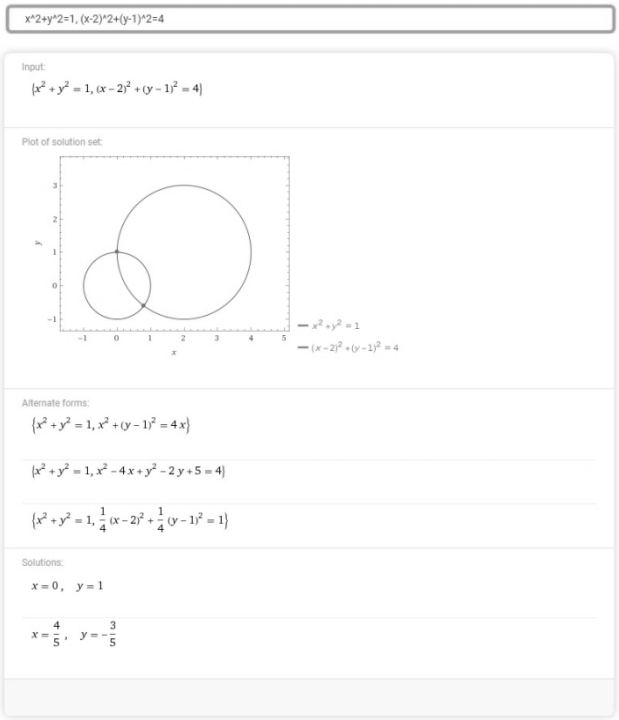

Figure 6. Example of solving a nonlinear system.

7. Conclusion

As a result, the paper shows the advantages of developing a multi-user web-interface of the system as a tool for the effective use of mathematical packages for solving engineering problems.

It is proposed to create a web application based on a client-server technology, where the client side implements the user interface, generates requests to the server and processes the responses from it, the server part receives the request from the client, performs the necessary calculations, then generates a web page and sends it to the client over the network.

The advantages of using this approach compared to common software are shown. The program logic of the application is located on the server, which allows to solve the problem of copyright infringement and illegal copying. In addition, updates to the program with the introduction of any innovations occur simultaneously for all users.

8. References

[1] Vidyasagar M 1993 *Nonlinear systems analysis, Englewood Cliffs* (New Jersey: Prentice Hall) 07632

[2] Grosan C, Abraham A 2008 A New Approach for Solving Nonlinear Equations Systems *IEEE Transactions on systems, man, and cybernetics. Part A: Systems and humans* **38(3)** 698-714

[3] Allgower E L, Georg K 1990 Computational Solution of Nonlinear Systems *American Mathematical Society*

[4] Floudas C A, Pardalos P M, Adjiman C, Esposito W, Gumus Z, Harding S, Klepeis J, Meyer C and Schweiger 1999 *Handbook of Test Problems in Local and Global Optimization* (Dordrecht: Kluwer Academic Publishers)

[5] More J J, Allgower E L and Georg K 1990 A collection of nonlinear model problems *Computational Solution of Nonlinear Systems of Equations, American Mathematical Society* 723-762

[6] Pinter J D 2001 *Computational Global Optimization in Nonlinear Systems* (Interactive Tutorial, Lionhart Publishing)
[7] Peter E G, Hokayem A 2018 *Lecture Notes on Nonlinear Systems and Control* (Zurich: ETH)
[8] Chernov V M 2018 Discrete orthogonal transforms with bases generated by self-similar sequences *Computer Optics* **42(5)** 904-911 DOI: 10.18287/2412-6179-2018-42-5-904-911
[9] Kropotov Y A, Proskuryakov A Y and Belov A A 2018 Method for forecasting changes in time series parameters in digital information management systems *Computer Optics* **42(6)** 1093-1100 DOI: 10.18287/2412-6179-2018-42-6-1093-1100
[10] Hirsch M J, Pardalos P M and Resende M G C 2006 Solving systems of nonlinear equations with continuous GRASP *AT& Labs Research Technical Report* TD-6V6JCX
[11] Martinez J M 1994 Algorithms for Solving Nonlinear Systems of Equations *Continuous Optimisation* 81-108
[12] Briggs B, Buchholz S 2019 *Deloitte Insights: Tech Trends*
[13] Shklyar L, Rozen R 2010 *Web Application Architecture* (Moskow: Eksmo) p 640
[14] Atchison L 2018 *Architecting for Scale: High Availability for Your Growing Applications* (St. Petersburg: Piter SPb) p 256
[15] Esposito D 2017 *Modern Web Development: Understanding Domains, Technologies and User Experience* (Moskow: Williams) p 464
[16] Toint P L 1977 On sparse and symmetric matrix updating subject to a linear equation *Math. Comp.* **31** 954-961
[17] Shanno D F 1980 On variable metric methods for sparse Hessians *Math. Comp.* **34** 499-514
[18] Marwil E 1978 *Exploiting Sparsity in Newton-Like Methods* (New York: Cornell University, Ithaca)
[19] Crittin F, Bierlaire M 2003 A generalization of secant methods for solving nonlinear systems of equations *Conference paper STRC: Session Model and Statistics*
[20] Taheri S, Mammadov M 2012 Solving systems of nonlinear equations using a globally convergent optimization algorithm *Global Journal of Technology & Optimisation* **3** 132-138
[21] Rahman N H A, Ibrahim A and Jayes M I 2013 Numerical solving for nonlinear using higher order homotopy Taylor-perturbation *New trends in mathematical sciences* **1(1)** 24-28
[22] Nielson B J 1999 On the kinematic analysis of robotic mechanisms *The International Journal of Robotics Research* **18(12)** 1147-1160
[23] Dennis J E and Schnabel R B 1983 *Numerical Methods for Unconstrained Optimization and Nonlinear Equations* (Prentice-Hall, Englewood Cliffx)
[24] Schubert L K 1970 Modification of a quasi-Newton method for nonlinear equations with a sparse Jacobian *Math. Comp.* **24** 27-30
[25] Griewank A, Toint P L 1984 Numerical experiments with partially separable optimization problems *Numerical Analysis* **1066** 203-220
[26] Toint P L 1986 Numerical Solution of Large Sets of Algebraic Nonlinear Equations *Mathematics of Computation* **46(173)** 175-189
[27] IBM White Paper 2012 *Native, web or hybrid mobile-app development* (IBM Corporation)
[28] Lavrischeva E P V 2018 Models of quality and reliability in software engineering URL: http://www.intuit.ru/studies/courses/ (01.07.2018)
[29] Verzhbitsky V 2000 *Numerical methods (linear algebra and nonlinear equations)* (Moskow: Higher education. shk.) p 266
[30] Research on Solving Systems of Nonlinear Equations URL: https://www.hindawi.com/journals/mpe/2015/727218/ (01.07.2018)
[31] Methodology of system analysis and system modeling URL: http://www.znannya.org/?view=summary: Methodology_analysis_system_design (26.05.2018)
[32] Hentenryck P V, McAllester D and Kapur D 1997 Solving polynomial systems using a branch and prune approach *SIAM J. Numer. Anal.* **34(2)** 797-827

Hybridization of fuzzy time series and fuzzy ontologies in the diagnosis of complex technical systems

N G Yarushkina[1], V S Moshkin[1], I A Andreev[1] and G I Ishmuratova[1]

[1]Ulyanovsk State Technical University, Severny Venetz street, 32, Ulyanovsk, Russia, 432027

e-mail: PostForVadim@yandex.ru

Abstract. The article provides a formal description of fuzzy ontologies and features of the representation of elements of fuzzy axioms in FuzzyOWL notation. An ontological model for assessing the state of helicopter units has been developed. According to the proposed approach, the summarizing of the state of a complex technical system is carried out by means of an inference based on a fuzzy ontology. As part of this work, experiments were conducted to search for anomalous situations and search for possible faulty helicopter units using the developed approach to the integration of fuzzy time series and fuzzy ontology. The proposed approach of hybridization of fuzzy time series and fuzzy ontologies made it possible to reliably recognize anomalous situations with a certain degree of truth, and to find possible faulty aggregates corresponding to each anomalous situation.

1. Introduction

The uncertainty of data and information incompleteness is an inalienable part of any complex technical system, in which the functioning quality of processes depends on a person. In the analysis, modeling, and design of such systems, a large distribution was obtained by expert systems that use experience and knowledge of the expert.

Expert assessments represent the qualitative aspect of the system element being evaluated and are presented in linguistic form.

Currently, the inference methodology of expert assessments based on the subject ontologies that play the role of a knowledge base in decision support systems (DSS) is used in various subject areas, including in the field of situational control in the energy sector [1], designing complex diagnostic systems [2], etc. Also, ontologies have been used as a knowledge base of intelligent risk prevention systems in the context of heterogeneous information for the complex technical systems critical infrastructure design phase [3].

Despite the application breadth, the classical languages of ontology and semantic networks, which are usually used to summarize and characterize the features of a subject domain, cannot be used to solve uncertainties and inaccuracies in the knowledge inherent in most real world applications in this area.

Fuzzy set theory, as well as fuzzy logic, is formalism suitable for processing incomplete knowledge, therefore ontologies based on such logic are adequate means of formalization.

One of the most effective solutions for representing a knowledge base in the context of accounting for fuzziness and uncertainty in human reasoning and evaluations in the DSS is a representation in the form of fuzzy ontologies. For example, fuzzy ontologies are used in such systems as disease diagnosis systems [4-6], fuzzy search engines [7, 8], knowledge systems based on group decision making about the importance of data [9], etc. In most cases, such systems operate with facts objects or terms that are described in natural language and contain the features of the considered domain [10, 11].

Fuzzy time series (FTS) is a way to obtain expert assessments that satisfy the conditions for completeness, consistency, and adequacy [12].

One of the main areas of application for FTS is process diagnostics. Diagnosis is the process by which a search for problems in the system occurs: defects, anomalies, faults, or lack thereof. When solving problems of diagnostics of complex technical systems, the state of which is determined by the data set in the form of FTS, it is advisable to apply methods for comparing the dynamics of processes with the expected or required dynamics.

Therefore an urgent task requiring a systemic solution is the interpretation of the results of the analysis in the form of expert assessments. To summarize the results obtained in the analysis of FTS, a system of rules is usually applied, which are stored in the knowledge base of the expert system. The knowledge base for solving this problem is ontologies and similar graph forms of knowledge representation and storage, which allow to take into account the semantic features of the object of the specified subject area, and not only their inference [13, 14].

Interpretation of the extracted comparisons in the form of expert assessments, the values of which are presented in the form of semantic units that correspond to certain classes of fuzzy ontology, taking into account the deviations between the current and the required FTS, can be obtained by solving the problem of integrating FTS and fuzzy ontology. Thus, the purpose of this work is the development of algorithms and models for the integration of fuzzy ontologies and FTS in the tasks of diagnosing complex technical systems.

2. Fuzzy time series and fuzzy ontology model

The models and algorithms for analyzing and forecasting the FTS are described in detail in [15, 16]. At present, the basic notation of the fuzzy ontology representation is the FuzzyOWL standard [17-20]. Formally FuzzyOWL-ontology is:

$$I = (If, Cf, Pf, Af, Df, Qf, Lf, Modf),$$

where *If* is an Individual that simply represents an individual of the vocabulary; *Cf* is a Concept that represents a fuzzy concept of the vocabulary:

$$C_f = \{C_f^A, C_f^C\},$$

where C_f^A are Abstract Concepts, C_f^C - Concrete Concepts; *Pf is* Property that represents a fuzzy role:

$$P_f = \{P_f^A, P_f^C\},$$

where P_f^A are Object Properties, P_f^C are Datatype Properties; *Df* is Axiom that represents the axioms:

$$D_f = \{A_f^{ABox}, A_f^{TBox}, A_f^{RBox}\},$$

where A_f^{ABox} is the Abox that contains role assertions between individuals and membership assertions, A_f^{TBox} is the Tbox that contains assertions about concepts such as subsumption and equivalence, A_f^{RBox} is the RBox that contains assertions about roles and role hierarchies. Some of the axioms are subclasses of FuzzyAxiom, which indicates that the axiom is not either true or false, but that it is true to some extent.

Of is Degree that represents a degree which can be added to an instance of FuzzyAxiom:

$$Of = \{LD_f, MD_f, ND_f, Var_f\},$$

where LD_f are Linguistic Degrees, MD_f are Modifier Degrees, ND_f are Numeric Degrees, Var_f are Variables.

Lf is Fuzzy Logic represents different families of fuzzy operators that can be used to give different semantics to the logic.

$$L_f = \{L_f^{Luk}, L_f^{Zad}, L_f^{Goed}, L_f^{Prod}\},$$

where L_f^{Luk} is the fuzzy operators logic of Lukasiewicz, L_f^{Zad} is the fuzzy operators logic of Zadeh, L_f^{Goed} is the fuzzy operators logic of Goedel, L_f^{Prod} is the fuzzy operators of produc logic.

Modf is Fuzzy Modifier that represents a fuzzy modifier, which can be used to modify the membership function of a fuzzy concept or a fuzzy role. Current subclasses are Linear Fuzzy Modifier and Triangular Fuzzy Modifier.

Table 1 shows the elements of fuzzy axioms FuzzyOWL, as well as their possible representation.

Table 1. Elements of Fuzzy Axioms in FuzzyOWL.

№	Element	Possible values	Representation in FuzzyOWL

1	LD_f – Linguistic Degrees	«high», «above average», «low»	`<AnnotationAssertion>`
			`<AnnotationProperty IRI="#fuzzyLabel"/>`
			`<IRI>#HighLoad</IRI>`
			`<Literal datatypeIRI="&rdf;PlainLiteral">fuzzyOwl2 fuzzyType="datatype";`
			`Datatype type="rightshoulder"; a="15.0";`
			`b="30.0";/fuzzyOwl2</Literal>`
			`</AnnotationAssertion>`

2	MD_f – Modifier Degrees	«very», «not very»	`type="modified" modifier="very"`
3	ND_f – Numeric Degrees	$0 \le ND \le 1$	`Degree Value=0,6`
4	Var_f – Variables	a, b,c, k1, k2	`b="30.0";`
5	L_f – Fuzzy Logic	Zadeh, Lukasiewicz Goedel and Product	`hasSemantics="Zadeh"`
6	*Modf* – Fuzzy Modifier	Linear, Triangular	`<Datatype type="triangular" a="32.0" b="41.0" c="50.0" />`

3. Subject Area

Consider the use of the integration approach of FTS and fuzzy ontologies in solving the problem of diagnosing the state of a helicopter. Diagnostics of a helicopter consists in checking its units in order to establish their exploitation and the possibility of using the helicopter.

The result of the diagnosis will be assessment values of physical quantities key indicators. The main goal is to assess the danger of values. To solve this problem, it is necessary to construct models of the behavior of the selected nodes and make conclusions about the health of the nodes by using the models. Models are built at expert base of assessment about the conduct of a particular component.

Table 2 show the parameters of the membership functions used for construct the FTS (Table 2).

Thus 5 fuzzy labels are defined for each physical quantity. The task of analyzing technical time series is reduced to the task of searching for anomalous situations in TS of main gearbox and engine propulsion system physical quantities indicators [21, 22]. The analysis is a sequence of the following steps:

1. Formation of FTS on the basis of the received information on the values of key physical quantities after the end of helicopter flight.
2. Search known abnormal situations in the resulting FTS.
3. Determination of the correct operation of the nodes. Work is incorrect if at least one abnormal situation.

The fuzzy ontology was developed for experiments. The developed FuzzyOWL ontology has a hierarchical structure and includes 55 classes, eight object properties, 40 data types.

Table 2. Parameters of the membership function.

Physical parameter	Range boundaries	Very little	Little	Good	Big	Very big
Exhaust gases temperature, °C	0-1000	a<100 b=200 c=200.5	a=100 b=275 c=350.5	a=350 b=560 c=600.5	a=600 b=700 c=720.5	a=720 b=800 c>1000
Engine oil temperature, °C	0-150	a<0 b=5 c=10.5	a=10 b=15 c=20.5	a=20 b=30 c=60.5	a=80 b=100 c=120.5	a=120 b=135 c>150
Engine oil pressure, kgf/cm^2	0-20	a<0 b=1 c=2.05	a=2.0 b=3.5 c=5.05	a=5.00 b=8 c=10.5	a=10 b=12 c=15.5	a=15.2 b=17.5 c>20
Main gearbox oil temperature, °C	0-100	a<0 b=5 c=10.5	a=10 b=15 c=20.5	a=20 b=35 c=50.5	a=50 b=70 c=80.5	a=80 b=90 c>100
Main gearbox oil pressure, kgf/cm^2	0-8	a<0 b=1 c=2.05	a=2.0 b=2.5 c=3.5	a=3.45 b=4 c=4.55	a=4.50 b=5 c=7.55	a=7.5 b=7.8 c>8

Table 3 contains objects properties of the used in the work (OP - oil pressure, EGT - exhaust gas temperature, OT - oil temperature, PP - power plant).

Table 3. Property of objects.

Property	Domain	Range
has OP main gearbox	main gearbox	OP main gearbox
has OP left engine	PP gearbox	OP PP gearbox
has OP right engine	PP gearbox	OP PP gearbox
has EGT left engine x	PP gearbox	EGT PP gearbox
has EGT right engine	PP gearbox	EGT PP gearbox
has OT main gearbox	main gearbox	OT main gearbox
has OT left engine	PP gearbox	OT PP gearbox
has OT right engine	PP gearbox	OT PP gearbox

Property declaration example for «hasOPMainGearbox»

```
<SubObjectPropertyOf>
  <ObjectProperty IRI="# hasOPMainGearbox"/>
  <ObjectProperty IRI="owl:topObjectProperty"/>
</SubObjectPropertyOf>
<ObjectPropertyDomain>
  <ObjectProperty IRI="# hasOPMainGearbox"/>
  <Class IRI="#MainGearbox"/>
</ObjectPropertyDomain>
<ObjectPropertyRange>
  <ObjectProperty IRI="# hasOPMainGearbox"/>
  <Class IRI="#OTMainGearbox"/>
</ObjectPropertyRange>
```

In addition, 40 data types were allocated: 5 fuzzy labels for 8 variants of relationships. The data type parameters correspond to the parameters of the membership function. The type of membership function in all data types was chosen triangular. Example of declaring a data type in FuzzyOWL notation:

```
<AnnotationAssertion>
  <AnnotationProperty IRI="#fuzzyLabel"/>
  <IRI>#BigOPMainGearbox </IRI>
  <Literal datatypeIRI="&rdf;PlainLiteral">
    <fuzzyOwl2 fuzzyType="datatype">
```

```
      <Datatype type="triangular" a="4.50" b="5" c="7.5" />
    </fuzzyOwl2>
  </Literal>
</AnnotationAssertion>
```

As an object of experiments, time series for the diagnostics of helicopter units and the fuzzy ontology of the helicopter units design were investigated. In the course of these experiments, the fuzzy time series and fuzzy ontologies integration algorithms were used.

4. FTS and Fuzzy ontology integration system

A software system was developed to solve the problems of forming the inference of the recommendation based on the integration of fuzzy time series and fuzzy ontologies. The software system is written in C # on the .NET 4.5 platform. The system development was carried out in the Microsoft Visual Studio 2015 environment. SQLite was used as the DBMS. The exchange protocol is a function call to the SQLite library. This method simplifies the program and shortens the response time. To store the database (definitions, tables, indexes, and the data itself), a single standard file is used on the computer on which the program runs.

The expert develops a fuzzy ontology of the domain with the help of the ontology editor Protégé. To check the adequacy and consistency of the ontology, the built-in Reasoner HermiT or FACT ++ is used. The scheme of the used software package is presented in Figure 1.

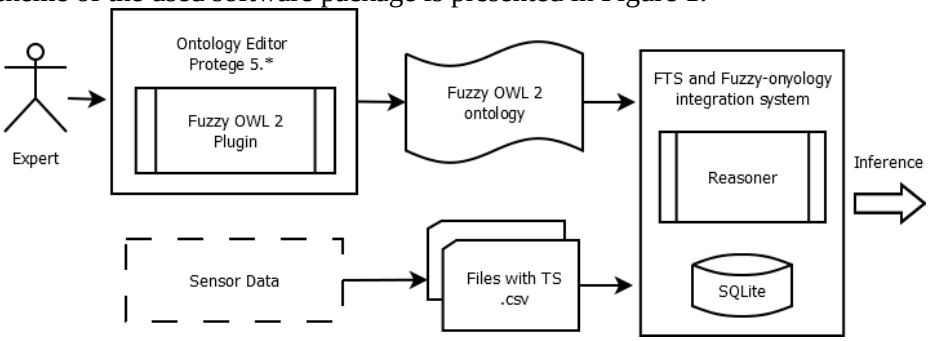

Figure 1. FTS and Fuzzy-ontology integration system.

The user has the opportunity to conduct research using the developed integration system. A prerequisite for obtaining an inference is to combine a time series with annotation properties. The result of the study is the resulting list of abnormal situations and possible faulty helicopter units.

5. Experiments

Diagnostics of a helicopter consists in checking its units in order to establish their serviceability and the possibility of operating the whole helicopter. The result of the diagnosis will be an assessment of the values of key physical quantities. The main goal is to assess the danger of values. To check the adequacy of the algorithm for integrating fuzzy time series and fuzzy ontology based on FuzzyOWL, as well as the correctness of the software that implements this algorithm, a series of experiments were conducted in which possible problem situations were performed. As part of the experiment, the following actions were carried out:

1. The expert has developed a fuzzy ontology according to the FuzzyOWL standard. To build a fuzzy ontology, the Protégé [23] editor with the connected FuzzyOWL Plugin [24] was used.
2. FuzzyOWL fuzzy ontology data types contain parameters of membership functions.
3. FuzzyOWL fuzzy ontology data types contain a binding to a specific class of ontology (Table 4).

The task of the experiments is to search for possible faulty helicopter units. The analysis represents the sequence of the following steps:

1. the formation of TS on the basis of the obtained information on the values of key physical quantities after running the machine;
2. search for defective helicopter units in the received TS;
3. determination of defective helicopter units.

Table 4. Data Type Descriptions.

Datatype	Type of membership function	Specific class	a	b	c
VeryLittleEGTLeftEngine	triangular	PP engine	100	200	200.5
Little EGTLeftEngine	triangular	PP engine	200	275	350.5
GoodEGTLeftEngine	triangular	PP engine	350	560	600.5
Big EGTLeftEngine	triangular	PP engine	600	700	720.5
VeryBigEGTLeftEngine	triangular	PP engine	720	800	1000
VeryLittleOPMainGearbox	triangular	main gearbox	0	1	2.05
LittleOPMainGearbox	triangular	main gearbox	2.0	2.5	3.5
GoodOPMainGearbox	triangular	main gearbox	3.45	4	4.55
BigOPMainGearbox	triangular	main gearbox	4.5	5	7.55
VeryBigOPMainGearbox	triangular	main gearbox	7.5	7.8	8

A helicopter unit will be considered faulty if at least one abnormal situation is detected for a physical quantity associated with a specific ontology class corresponding to the faulty unit.

The effectiveness of the diagnostic algorithm of technical systems can be evaluated when solving the problem of modeling the behavior of helicopter units. The system should correctly identify possible faulty helicopter units. To confirm the efficiency, it is necessary to analyze the data characterizing the machines, both without defects and with possible defects, and then analyze the information about the faulty units obtained by the system and received from an expert.

For the experiment, data were obtained on the run of the three machines, and data was generated that simulates certain abnormal situations. Description of the time series is given in table 5.

Table 5. Description of time series.

Series numbe	Airplane number	Period	TVG1	TVG2	Pm1	Pm2	Pmp	Tm1	Tm2	Tmp
1	210111	15.09.205	739.59	258.85	2.3	0.8	0	58.1	59.2	29.3
2	210111	16.09.205	757.29	256.93	2.4	0.8	0	57.1	59	29.3
3	210111	30.09.205	503	227.78	7.4	0.8	1.8	47.5	51.3	29
4	210111	12.04.205	536.85	520.93	7.6	6.6	4	53.9	56.5	35
5	240111	11.09.205	176.43	178	0.8	0.8	0	42.5	46	31.3
6	240111	12.09.205	176.57	178	0.8	0.8	0	42.5	46	31.3
7	240111	13.11.204	483	448.85	6.4	5.6	3.4	49.5	51.9	23.5
8	240111	11.08.204	479.13	0	6.4	5.4	3.3	51.6	55.1	29
9	250111	22.01.204	189.72	206.22	0.8	1	1.6	52.5	55.5	24.5
10	250111	23.01.204	193.3	209.22	0.8	1	1.6	52.5	55.5	24.5

The following designations are used: TVG1- left engine exhaust temperature, TVG2- right engine exhaust temperature, Pm1 - left engine oil pressure, Pm2 - right engine oil pressure, Tm1 - left engine oil temperature, Tm2 - right oil temperature engine, Pmp - oil pressure of the main gearbox, Tmp - oil temperature of the main gearbox.

Experiments were conducted with ten-time series. The results of experiments are shown in Table 6.

Table 6. Experiment results.

Period	TVG1	TVG2	Pm1	Pm2	Pmp	Tm1	Tm2	Tmp	Faulty part
15.09.2050	739.59	258.85	2.3	0.8	0	58.1	59.2	29.3	#EnginePowerPlant
16.09.2050	757.29	256.93	2.4	0.8	0	57.1	59	29.3	#EnginePowerPlan
30.09.2050	503	227.78	7.4	0.8	1.8	47.5	51.3	29	#EnginePowerPlan
12.04.2052	536.85	520.93	7.6	6.6	4	53.9	56.5	35	No broken parts
11.09.2054	176.43	178	0.8	0.8	0	42.5	46	31.3	#MainGearbox
12.09.2054	176.57	178	0.8	0.8	0	42.5	46	31.3	#MainGearbox
13.11.2046	483	448.85	6.4	5.6	3.4	49.5	51.9	23.5	No broken parts
11.08.2047	479.13	0	6.4	5.4	3.3	51.6	55.1	29	#MainGearbox
22.01.2046	189.72	206.22	0.8	1	1.6	52.5	55.5	24.5	#EnginePowerPlan
23.01.2046	193.3	209.22	0.8	1	1.6	52.5	55.5	24.5	#MainGearbox

The result of the experiment is the construction of a fuzzy time series fuzzy ontology allowed us to conclude that the helicopter unit was malfunctioning when analyzing the precise values of the aggregates.

6. Conclusion

In this paper a technique for constructing fuzzy ontologies was investigated and an ontological model of the state of helicopter units was developed. In the process of integrating fuzzy time series and fuzzy ontology, the method integrating TS and ontology was implemented, and a software product was developed that ensures the implementation of this method.

Also, experiments were conducted to search for anomalous situations and search for possible faulty units using the developed approach to the integration of fuzzy time series and fuzzy ontology.

Thus, the proposed approach of hybridization of FTS and fuzzy ontologies allows one to reliably recognize anomalous situations with some degree of truth. The algorithm also finds possible faulty units corresponding to each abnormal situation.

7. References

[1] Massel L V, Vorozhtsova T N and Pjatkova N I 2017 Ontology engineering to support strategic decision-making in the energy sector *Ontology of designing* **7(1)** 66-76 DOI: 10.18287/2223-9537-2017-7-1-66-76

[2] Grischenko M A, Dorodnykh N O, Korshunov S A and Yurin A Y 2018 Ontology-based development of diagnostic intelligent systems *Ontology of designing* **8(2)** 265-284 DOI: 10.18287/2223-9537-2018-8-2-265-284

[3] Kovalev S M, Kolodenkova A E 2017 Knowledge base design for the intelligent system for control and preventions of risk situations in the design stage of complex technical systems *Ontology of designing* **7(4)** 398-409 DOI: 10.18287/2223-9537-2017-7-4-398-409

[4] Torshizi A D, Zarandi M H F, Torshizi G D and Eghbali K 2014 A hybrid fuzzy-ontology based intelligent system to determine level of severity and treatment recommendation for Benign Prostatic Hyperplasia *Computer Methods and Programs in Biomedicine* **113(1)** 301-313

[5] Besbes G, Baazaoui-Zghal H 2016 Fuzzy ontology-based Medical Information Retrieval *IEEE International Conference on Fuzzy Systems (FUZZ-IEEE)* 178-185 DOI: 10.1109/FUZZ-IEEE.2016.7737685

[6] El-Sappagh S, Elmogy M 2017 A fuzzy ontology modeling for case base knowledge in diabetes mellitus domain *Engineering Science and Technology, an International Journal* **20(3)** 1025-1040 DOI: 10.1016/j.jestch.2017.03.009

[7] Lai L F, Wu C, Lin P and Huang L 2011 Developing a fuzzy search engine based on fuzzy ontology and semantic search *IEEE International Conference on Fuzzy Systems (FUZZ-IEEE)* 2684-2689

[8] Widyantoro D H, Yen J 2001 A fuzzy ontology-based abstract search engine and its user studies *10th IEEE International Conference on Fuzzy Systems* **2** 1291-1294 DOI: 10.1109/ FUZZ.2001.1008895
[9] Morente-Molinera J A, Pérez I J, Ureña M R and Herrera-Viedma E 2016 Creating knowledge databases for storing and sharing people knowledge automatically using group decision making and fuzzy ontologies *Information Sciences* **328** 418-434
[10] Mikhaylov D V, Kozlov A P and Emelyanov G M 2017 An approach based on analysis of *n*-grams on links of words to extract the knowledge and relevant linguistic means on subject-oriented text sets *Computer Optics* **41(3)** 461-471 DOI: 10.18287/2412-6179-2017-41-3-461-471
[11] Mikhaylov D V, Kozlov A P and Emelyanov G M 2016 Extraction of knowledge and relevant linguistic means with efficiency estimation for the formation of subject-oriented text sets *Computer Optics* **40(4)** 572-582 DOI: 10.18287/2412-6179-2016-40-4-572-582
[12] Yarushkina N G, Afanasyeva T V and Perfilyeva I G 2010 *Intellectual analysis of time series: textbook* (Ulyanovsk: UlSTU)
[13] Noy N F, McGuinness D L 2001 Ontology Development 101: A Guide to Creating Your First Ontology *Stanford Knowledge Systems Laboratory Technical Report KSL-01-05 and Stanford Medical Informatics Technical Report* SMI-2001-0880
[14] Yarushkina N G, Filippov A A, Moshkin V S and Filippova L I 2018 Application of the Fuzzy Knowledge Base in the Construction of Expert Systems *IT in industry* **6(2)** 31-36
[15] Afanaseva T V, Namestnikov A M, Perfilyeva I G, Romanov A A and Yarushkina N G 2014 *Time Series Forecasting: Fuzzy Models* (Ulyanovsk: UlSTU)
[16] Romanov A A, Egov E N, Moshkina I A and Dyakov I F 2018 *Extraction and Forecasting of the International Scientific and Practical Conference* (Ulyanovsk, Russia) 50-55
[17] Bobillo F, Straccia U 2011 Fuzzy ontology representation using OWL 2 *International Journal of Approximate Reasoning* **52** 1073-1094
[18] Lee C S, Jian Z W and Huang L K 2005 A Fuzzy Ontology *IEEE Transactions on Systems, Man and Cybernetics* **5** 859-880
[19] Straccia U 2005 Towards a Fuzzy Description: Logic for the Semantic Web *2nd Europe-an Semantic Web Conference* 167-181
[20] Yarushkina N G, Filippov A A and Moshkin V S 2018 Development of a knowledge base based on context analysis of external information resources *Proceedings of the International conference Information Technology and Nanotechnology. Session Data Science* 328-337
[21] Voronin V V 2011 Mathematical modeling of diagnostic parameters of aircraft units on the basis of granular time series: thesis for a competition scholarly step. *Cand. tech. Sciences: spec.: 05.13.18 - Mathematical modeling, numerical methods and program complexes* (Ulyan. state tech. un-t – Ulyanovsk) p 170
[22] Danilov V A, Zheleznyak I I and Mordik V V 213 *Operation and repair of the Mi-8 helicopter: [training manual for the technical staff of operational enterprises and cadets of civil aviation aviation engineering schools]* (Moscow: Mechanical Engineering) p 1980
[23] Protégé: ontology editor URL: https://protege.stanford.edu
[24] Fuzzy Ontology Representation using OWL 2 URL: http://www.umbertostraccia.it/cs/ software/FuzzyOWL/index.html

Acknowledgments
The study was supported by: The Ministry of Education and Science of the Russian Federation in the framework of the projects No. 2.1182.2017/4.6 and 2.1182.2017 and The Russian Foundation for Basic Research (Grants No. 19-07-00999 and 18-37-00450, 18-47-732007).

Comparison of the characteristics of the genetic algorithm and the method of coordinates search for optimization of temperature modes indoor areas

A P Shuravin[1], S V Vologdin[1]

[1]Kalashnikov Izhevsk State Technical University, Studencheskaya, 7, Izhevsk, Russia, 426069

e-mail: webmaster@easyprog.ru, vologdin_sv@mail.ru

Abstract. The article substantiates the relevance of optimization algorithms research for solving various applied problems and for the science of artificial intelligence. The need to solve problems of optimizing the thermal-hydraulic modes of buildings (as part of the project "Smart City") is explained. The paper presents a mathematical formulation of the problem of optimizing the temperature mode of rooms using adjustable devices. Existing work provides two methods for solving the posed problem. They are the coordinates search method and the genetic algorithm. The article contains the description of the above mentioned algorithms (including the mathematical apparatus used). The results of the computational experiment (for the considered optimization methods) are presented. These experimental results show that the genetic algorithm provides better optimization results than the coordinates search method, but it has a large computational cost. The hypothesis was confirmed that in order to increase the efficiency of solving the considered class of problems it is necessary to combine the genetic algorithm and the coordinates search method.

1. Introduction

Currently, work in the field of development and implementation of energy efficient technologies is very relevant. The main provisions defining the need for work to improve the energy efficiency of the heating system of buildings are enshrined in Federal Law No 261-F3 “On Energy Saving ...”, as well as by the decree of the Government of the Russian Federation of 13.11.09 Number 1234-p "Energy Strategy of Russia for the period until 2020". In particular, the system solution for optimization of central heating systems at different levels of the organization (district, city, individual buildings) is considered in work[1], as well as the information system IASTS, designed for automated calculation of heat networks and storing information about calculated network is presented. Energy efficiency issues are raised in the program "Smart City" [2]. The study of the joint operation of two sources of thermal energy to optimize the operation of the heating network is considered in [3]. Mathematical model of the building thermal conditions (with consideration for insolational heat input) is described in [4]. In work [5] the “Smart Home” technology is considered as the energy-saving technology of the future. The authors come to the conclusion that, at present,

the “Smart Home” technology is not widely spread in Russia, but is gradually gaining popularity. The impact of energy-saving technologies on the economy and the future is discussed in [6, 7], new advances in energy saving are discussed in [8]. The connection between energy-saving policy and environment are considered in [9]. The article discusses creating energy system with active-adaptive network in Russia.

One of the methods of energy saving is the optimization of energy consumption including the use of artificial intelligence technologies [10,11]. One of the important areas of research in the field of energy saving is the optimization of the thermo-hydraulic modes of centralized heating systems [1]. Issues of the study of problems and methods for optimizing thermal-hydraulic modes in multi-circuit thermal networks and other problems of energy saving are considered in the works of many Russian [1, 10–18] and foreign [19-22] authors.

In particular, in [10] a review of optimization problems of central heating networks is made and the need to automate the solution of these problems is justified. It is proposed to use a genetic algorithm to optimize the thermo-hydraulic modes of buildings in [11]. Multi-criteria optimization problems are considered in [12]. As a rule these problems arise before the beginning of the heating season. In [13] a mathematical model is presented for optimizing the thermal power of heat sources operating in the centralized heat supply system. A new method for solving the problem is considered, the results of test problems calculations are presented. A mathematical model for optimizing heat flows between subscribers of the heating network in order to reduce the disbalance of the heating system, including the methodology for solving such problems, is considered in [14]. There is a problem of operative regulation of heat supply depending on the outdoor temperature. This problem is solved in [15] by applying simulation. A method for optimizing the temperature of the coolant based on the use of penalty functions for indoor air temperature and the amount of heat energy consumed is considered. In [16] an issue of optimal distribution of reactive power in power supply systems and electrical networks is investigated. For these purposes, the authors proposed to apply the algorithm of swarm intelligence. In [17] a method of thermal network equivalence allows replacing a real network with a mathematical model is considered. The method is used to optimize of heating system. The ideas and dependencies that served as the basis for the creation of this model are given in the article. The adequacy of the equivalent model is substantiated. The advantages of thermal network equivalence in terms of simplifying the calculation of various modes are noted. Complex problem of schematic structural optimization of heat networks is considered in [18]. For solving this problem authors used tree search algorithm and annealing simulation method.

There are a lot of foreign papers about energy system optimization. The article [19] shows Monte Carlo method application for energy system optimization, modelling of safety, energy transfer failures at real time. The paper [20] shows optimization problems solving in electric-energy industry to decrease cost with consideration of safety. In work [21] a hierarchical optimization model for a network of charging stations for electric vehicles is considered. The authors proposed a three-layer optimization model, including optimization of gas station locations (first layer), queuing model (second layer), and optimization of battery charging process (third layer). A kriging model to reduce energy losses in distribution networks is proposed in [22]. The authors presented an algorithm for the approximation of complex distribution networks to speed up the process of finding a solution.

The development of new optimization algorithms and the study of already existing algorithms are relevant [23-25]. For example, the decentralized training algorithm is described in [23]. It is used in distributed big data application. The Constant Jacobian Gauss-Newton Optimization Algorithm is presented in [24]. Work [25] describes optimal cost almost-sure reachability in POMDPs.

Each of the optimization algorithms has certain disadvantages, for example, the lack of guarantees for achieving the global extremum of the objective function, high computational cost, etc. [26,27].

Based on the foregoing, the purpose of this work is an experimental study and comparative analysis of various approaches to optimizing the thermal-hydraulic modes of buildings. This work is supported by grant 27.06.01/18BCB of Kalashnikov ISTU.

2. The problem of optimizing the temperature of the indoor areas

Practice shows that in order to make optimal management decisions it is necessary to solve the problems of analyzing the thermo-hydraulic mode and characteristics optimization at different levels of HSS in complex with using mathematical algorithms of decreasing heat supply system disbalance, energy audit methods and computer methods of data processing for visualize and analyze heat network any elements (table 1).

Table 1. Methods of increasing energy efficiency HSS.

Methods	Goal	Brief description (task list)
Energy audit	Detecting occasions of ineffective using fuel and power resources, recommendation development	Energy inspection of energy resources production, transfer and consumption
Hydraulic modes optimization in heat networks	Decreasing disbalance of first and second level of HSS. Supporting stabilization of work	Operations management of heat network hydraulic mode while stress load reallocates between consumers of heat
Optimization of heat production and realization	Guarantee of required heat consumption mode with minimal cost	Operational reallocation heat stresses between heat sources
Thermohydraulic mode optimization of heating of buildings (HBS)	Decreasing disbalance, heat mode of HBS normalization	Resistance optimization of hydraulic adjuster. Adduction heaters power to required value
Thermohydraulic mode of HBS research	Specified temperature of indoor areas guarantee	Equilibrium temperature of indoor areas computation. Optimal design of HBS

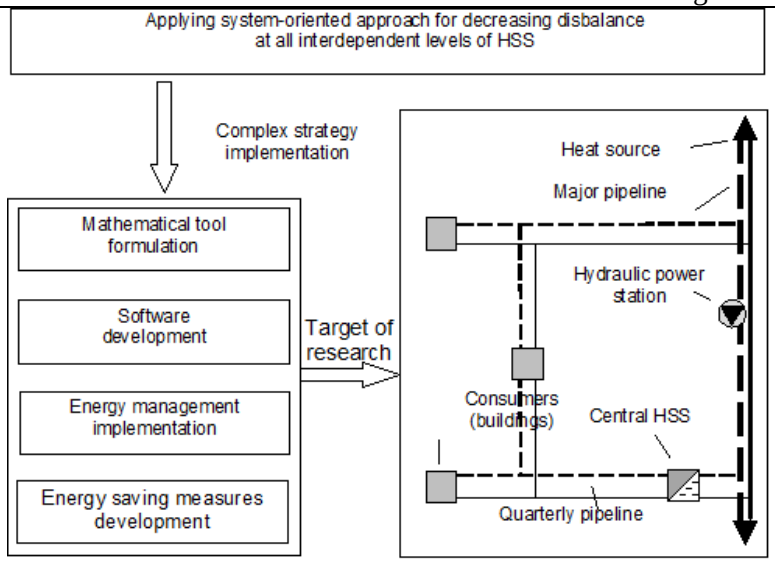

Figure 1. System-based approach applied to decreasing disbalance of central HSS (solid – cold source, dashed – hot source).

Principal elements and strategy of system-oriented approach for increasing heat efficiency of HSS through a disbalance reduction are showed at figure. 1.

Mathematical model construction methodology of decreasing disbalance of central HSS based on applying characteristics optimization methods at different levels of HSS is presented at figure 2. Methodology comprises methods: power optimization of heat sources (first level HSS), heat flows optimization between heat network subscribers (second level), resistance optimization of heater system hydraulic adjusters (third level).

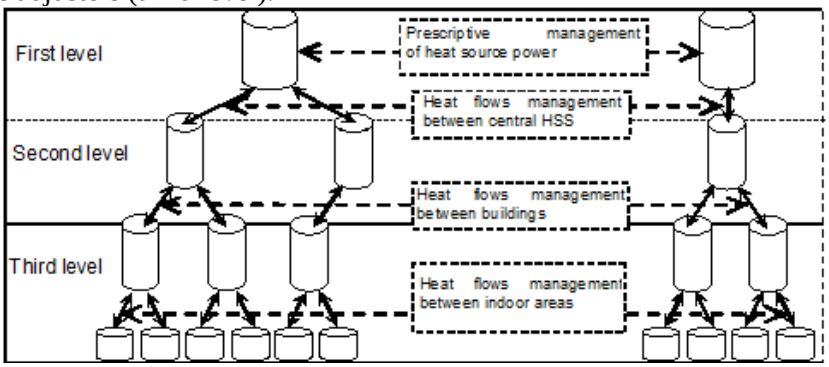

Figure 2. Generalized chart of heat flows management in centralized HSS.

In this study the energy system is optimized at the third level (heat flows management between indoor area).

Excessive energy consumption of a building heat supply system arises for the following reasons:

- ineffective thermal protection of the indoor areas;
- non-optimal scheme of heat supply of the building;
- due to the temperature disbalance of the indoor areas of heated buildings (to raise the temperature of the "cold" rooms up to the standard, it is necessary to increase the coolant temperature, while in the rooms where the temperature is normal, it becomes too hot, and consumers have to open the windows “heating the outdoor").

There are several ways to reduce the temperature disbalance of the indoor areas:

- by selection of the optimal power of the heating devices of the building indoor areas, ensuring the standard temperature in each room, taking into account the actual state of the enclosing structures (as a rule, this approach is carried out at the stage of building design or reconstruction of buildings);
- by regulating the balancing valves of the risers, this issue is considered in [11] (it is applicable to existing and projected buildings);
- by regulating the adjusting valves of the heaters (applicable to existing buildings), this issue is addressed in this article.

It is worth noting that by adjusting the balancing valves of the risers it is impossible to eliminate the disbalance of those rooms that are connected to the same riser. The working hypothesis of the study carried out under this article is that regulating the valves of the heaters, as well as the joint regulation of the valves of the heaters and the balancing valves of the risers should give the best optimization results.

The objective function of the problem of optimizing the temperature disbalance is the minimum of the standard deviation of the room temperature from the standard value:

$$\Phi(S_1,S_2,...,S_z)=\left[\frac{1}{N}\sum_{i=1}^{N}(t_{in,i}(S_1,S_2,...,S_z)-t_{opt})^2\right]^{1/2}\rightarrow min, \quad (1)$$

where z is the quantity of regulating valves of the heating devices and balancing valves of the risers, i is the number of indoor area, N is the quantity of indoor areas, $t_{in,i}$ is the design room temperature (the method of calculation it will be mentioned below), t_{opt} is the indoor area

temperature, which is planned to be reached (in the article, two optimization options are applied: relative to the standard temperature and the average temperature of the rooms in the building, will be considered below), S_j is the *j*-valve resistance.

Due to the fact that the control valves have their own range of resistance values, we introduce a restriction:

$$S_j^{min} \le S_j \le S_j^{max}, \tag{2}$$

where S_j^{min} and S_j^{max} are minimum and maximum resistance respectively [11].

The air temperature inside the heated indoor areas ($t_{in,i}$) is calculated from the heat balance equation [1], which takes into account the heat influx from the coolant in heating devices and heat losses through the enclosing structures (walls, windows, doors, floor, etc.):

$$Q_{wl}^H + Q_{fl}^H + Q_{cl}^H + Q_{dr}^H + Q_{dr}^I + Q_{win}^H + Q_{win}^I + Q_{air}^I = Q_{rd} + Q_p, \tag{3}$$

where Q_{wl}^H is heat exchange with walls, Q_{fl}^H is heat exchange with a floor, Q_{cl}^H is heat exchange with a cell, Q_{dr}^H is heat exchange with doors, Q_{dr}^I is infiltration through doors, Q_{win}^H is heat exchange with windows, Q_{win}^I is infiltration through windows, Q_{air}^I is infiltration of air, Q_{rd} is heat influx from radiators, Q_p is heat influx from pipes.

The equation (3) is written and solved separately for each room from the *N* rooms of the building. The equation is solved with iteration method at which the temperature is selected corresponding to the temperature equilibrium.

Heat transfer through the walls (similarly floor, ceiling, window and balcony structures) depends on the area of the walls, their material, thickness and temperature difference:

$$Q_{wl}^H = \frac{F_{wl}}{R_{wl}}(t_{in} - t_{out})n\beta, \tag{4}$$

where F_{wl} is area of walls, R_{wl} is reformed wall heat transfer resistance; t_{in} is indoor air temperature (in formulae (3) it is $t_{in,i}$); t_{out} is outdoor temperature; n – tabular correction factor depending on the type of fencing surface; β is correction factor taking into account the orientation of the wall relative to the cardinal points.

Heat losses due to the heating of the outside air inflowed through the windows (similar to the entrance doors) are calculated by the formula:

$$Q_{win}^I = A_{win}^I G_{win}^I F_{win} c(t_{in} - t_{out}), \tag{5}$$

where A_{win}^I is correction factor, taking into account the kind of window; F_{win} is estimated window area; G_{win}^I is the volume of infiltrated air; c is the specific mass density of air.

Heat transfer is determined on the basis of its heat flow per unit area. Heat flow depends on water flow:

$$q_{rd} = q_{nom}\left(\frac{\Delta t_{tp}}{70}\right)^{n+1}\left(\frac{x_{rd}}{360}\right)^p c_{rd}, \tag{6}$$

where x_{rd} is actual water consumption in the device, kg / h; n,p are empirical coefficients, c_{rd} is coefficient taking into account the scheme of connection of the heating device; Δt_{tp} is temperature pressure equal to the difference between the half sum of the input and output temperature and the air temperature in the room, q_{nom} is nominal heat flux density.

To determine coolant flow rates, the system of hydraulic equations is solved:

$$\begin{cases} Ax = q_\partial, \\ By = 0, \\ y + h_\partial = SXx, \end{cases} \tag{7}$$

where A is the junction matrix of ramification and node, B is the contour matrix built on the original graph, x and y are vectors of unknown variables, S is the hydraulic resistance matrix

(include resistance heaters and pipes), X is the consumption matrix, h_{∂} is the hydraulic pressures vector, q_{∂} is the vector of coolant consumption in nodes.

The heater having valve connected in parallel with the cross-connection, the hydraulic resistance of such a system is expressed by the formula [1]:

$$S_{res} = \frac{1}{\left[\left(\sqrt{S_{rd}}\right)^{-1} + \left(\sqrt{S_{jm}}\right)^{-1}\right]^2} \ . \quad (8)$$

where S_{rd} is the hydraulic resistance of the heater, S_{jm} is the hydraulic resistance of the jumper. The resistance of the heater is the sum of the resistance of the radiator and the adjusting valve:

$$S_{rd} = S_{rad} + S_{valv} \ . \quad (9)$$

where S_{rad} is it's own resistance of the heater, S_{valv} is the resistance of the heater valve.

During the optimization it is necessary to obtain the temperature of the indoor area ($t_{in,i}$) as close as possible to the desired (t_{opt}). There are two options to define the temperature:
- standard temperature, according to GOST 30494-2011 is equal to 20°[28];
- average temperature. It is calculated by formulae:

$$t_{opt} = \frac{\sum_{i}^{N} t_{in,i}}{N} \ . \quad (10)$$

3. Description of the algorithms used

Indoor area temperature cannot be analytically expressed from functional (1), therefore, only some iterative optimization methods can be used to find it. Since the functional is non-linear, we exclude methods of linear programming, such as, for example, the simplex method, from the considered methods. It is also impossible to analytically express t_{in} from equation (3), formulas (4-6) and system of equations (7), thus, it is also calculated by an iterative method. Therefore, it is also impossible to find the derivative of the functional (1), which excludes the possibility of applying gradient methods that require calculating the derivative, such as, for example, gradient descent methods. Based on these limitations, for the purposes of the study, the method of coordinate search and the genetic algorithm are chosen.

In general, the algorithm for optimizing the temperature disbalance of buildings works as follows [11]:

1. The initial values of the resistance of the valves of the raisers and the heating devices are set. Installation method is random value from the admissible range.

2. The structure of the heating network and characteristics of the indoor areas, including enclosing structures is read from the database.

3. The thermo-hydraulic balance of the heating system is calculated.

4. The air temperature in the indoor areas by calculating the equilibrium temperature of the building is calculated [1].

5. The objective function is calculated.

6. If the stop condition is reached (in this study it is the specified number of iterations), then program exits the loop.

7. The values of the valves resistance of the risers and the heaters are selected. The selection method depends on the optimization algorithm (more will be described below).

8. The program goes to step 2.

In computer science a genetic algorithm (GA) is a metaheuristic inspired by the process of natural selection that belongs to the larger class of evolutionary algorithms (EA). This is a heuristic search algorithm used to solve optimization and modeling problems by randomly selecting, combining, and varying the desired parameters using mechanisms similar to natural selection in nature. The problem is formalized in such a way that its solution can be encoded as a vector ("genotype") of genes, where each gene can be a bit, a number, or some other object. In some ways (usually random) many genotypes of the initial population are created. They are evaluated using the

objective function, as a result of which a certain value is associated with each genotype which determines how well the phenotype described by it solves the set problem. From the resulting set of solutions ("generations"), taking into account the value of objective function, solutions are selected (usually the best species are more likely to be selected), to which "genetic operators" are applied (in most crossover and mutation), resulting in new solutions. For them, the value of objective function is also calculated, and then the selection of the best decisions in the next generation is made. This set of actions is repeated iteratively, so the "evolutionary process" is modeled, which lasts several life cycles (generations) until the criterion for stopping the algorithm is fulfilled.

When using the genetic algorithm, selection performs by random mutations (random changes according to the formula) [29]:

$$\Delta S_j = \sigma\sqrt{-2ln(x_1)}\cdot cos(2\pi x_2), \tag{11}$$

where σ is the mutation step (selected empirically), x_1 and x_2 are random values in limits [0;1], having a uniform distribution (such random number generators are embedded in many programming languages). Due to formulae (11) we obtain Gaussian distribution from uniform distribution.

Also sets of valve resistance values can be crossed (mixed randomly) [11]. The probability of crossing is calculated by the formula:

$$p_{cross} = \frac{2n - k_1 - k_2}{2n - 1}, \tag{12}$$

where n is the quantity of sets in the sample («species» in the «population»), k_1 and k_2 are respectively, the number of the first and the second set of a pair, which is checked for the possibility of crossing. They take values from 0 to n-1. The removal of sets from the sample during selection also occurs randomly; the probability of deletion is the greater, the worse the objective function. This probability is expressed by the formula:

$$p_{del} = \frac{m}{n}, \tag{13}$$

where m is the number of the set to be deleted (starting from zero). For the set with the best objective function this number is 0. It means that this species will never be deleted. The deletion cycle can be repeated several times until the number of sets is less than the maximum allowable number. If the number of the set becomes less than the minimum allowable amount then at this iteration selection will not be made.

In the coordinates search method, the value of valve resistance at the next iteration is changed by increment ΔS, calculated by the formula [1]:

$$\Delta S_j^{(k)} = \frac{(s_j^{(k)} - s_j^{(k-1)})(t_{opt,j} - t_{in_j}^{(k)})}{(t_{in_j}^{(k)} - t_{in_j}^{(k-1)})}, \tag{14}$$

where $j=1,\ldots,z$ is the valve number, k is the iteration number, $t_{opt,j}$ is the required room temperature, $t_{in_j}^{(k)}$ is the indoor area temperature according to j-valve (room where set radiator with the valve or room according to ramification which adjusting by the riser valve) on the k-th iteration.

4. Experimental results

In this study, in order to compare the minima of achieving the objective function, the following experiments were conducted:

- optimization of the hydraulic resistance of the valves of the heating devices;
- optimization of the hydraulic resistances of the balancing valves of the heating risers;
- joint optimization of the hydraulic resistance of the valves of the heating devices and the balancing valves of risers.

For optimization the genetic algorithm and the coordinates search algorithm were used. In the genetic algorithm the mutation step σ [11] was taken 5 and 20 in units of Pa/(Kg/h)^2. A typical building was calculated under the average designed conditions of Izhevsk for the actual condition of enclosing structures and space heaters. Optimization was performed in two versions:

- relative to the standard temperature, which was adopted by 20°C;
- relative to the average temperature in the rooms.

The initial approximation is a random value from the range of formula (2). Comparison of results is given in tables 2-5.

Table 2. Comparison of optimization results (values of the objective function relative to the standard temperature 20°).

	Regulation of riser valves only	Regulation of battery valves only	Regulation battery valves and riser valves
Coordinates search method	3.46	3.25	2.74
Genetic algorithm with step 5	3.08	3.68	3.51
Genetic algorithm with step 20	2.85	3.68	3.40
No adjustment (all valves open)	5.14	5.14	5.14

Table 3. Comparison of optimization results (values of the objective function relative to the average temperature).

	Regulation of riser valves only	Regulation of battery valves only	Regulation battery valves and riser valves
Coordinates search method	3.21	2.91	2.67
Genetic algorithm with step 5	2.85	2.94	2.82
Genetic algorithm with step 20	3.15	2.94	3.1
No adjustment (all valves open)	3.26	3.26	3.26

Table 4. Optimization by a genetic algorithm after optimization by coordinates search (values of the objective function relative to the standard temperature 20°)).

	Regulation of riser valves only	Regulation of battery valves only	Regulation battery valves and riser valves
Coordinates search method	3.21	3.25	2.74
Genetic algorithm with step 20	2.95	2.99	1.96

Table 5. Optimization by a genetic algorithm after optimization by coordinates search (values of the objective function relative to the average temperature).

	Regulation of riser valves only	Regulation of battery valves only	Regulation battery valves and riser valves
coordinate search method	3.21	2.91	2.67
Genetic algorithm with step 20	2.93	2.6	1.94

As can be seen from Tables 1 and 2, optimization by regulating the valves of the heating devices exceeded optimization by regulating the valves of the risers only in the case of using the coordinates search. However, if after optimization by the coordinates search method, the valve resistance is again optimized by the genetic algorithm (Tables 3 and 4), this gives additional optimization. In this case joint optimization of both the balancer valves of the risers and the valves of the heaters gives the best result. This effect confirms the theoretical proposition that coordinates search method and gradient methods do not guarantee the achievement of global extremum [11,26,27].

The various advantages and disadvantages of the genetic algorithm and the coordinates search method are illustrated very well by Figure 3, which shows that coordinates search algorithm works faster, but the genetic algorithm allows achieving greater depth of optimization due to the gradual approximation, although it works slower.

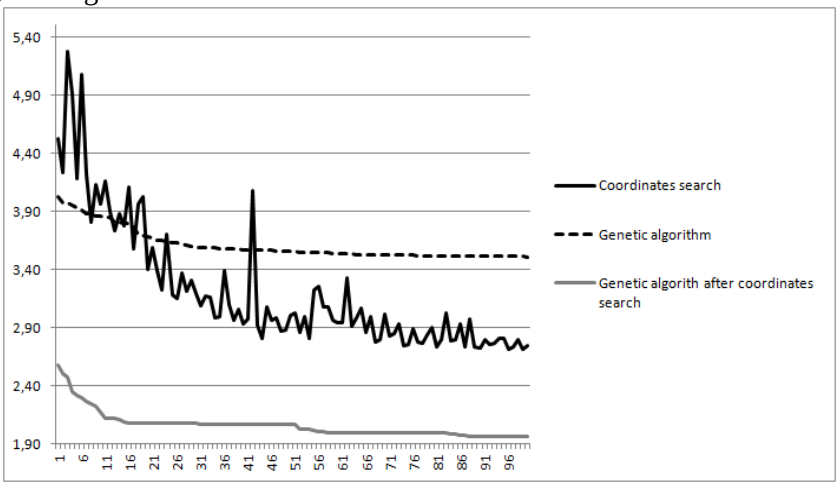

Figure 3. Comparison of optimization history using the coordinates search method and the genetic algorithm, as well as using the genetic algorithm as an additional optimization of coordinates search.

5. Conclusion

As the experimental results show, the best result of optimizing the temperature disbalance can be achieved by using joint adjusting of the risers balancing valves and heater valves, if you first apply the optimization of the coordinates search methods and then further optimize it by the genetic algorithm. This fact also confirms the hypothesis put forward in [11]: "Combining a genetic algorithm and gradient methods will allow you to create a more efficient optimization algorithm (than gradient methods) with an acceptable computation time."

6. References

[1] Vologdin S V, Jakimovich B A 2015 *Methods and algorithms for improving the energy efficiency of a multi-level district heating system: a monograph* (Izhevsk: Publishing ISTU named after M.T. Kalashnikov) p 264
[2] Smart City URL: http://city-smart.ru (18.11.2018)
[3] Zvonareva U N, Vankov U V 2015 Energy saving in heat supply systems of large municipal unions, powered from several heat sources *News of the Tomsk Polytechnic University. Georesource Engineering* **326(11)** 75-82
[4] Strizhak P A, Morozov M N 2015 Mathematical modeling of the thermal mode of a building, taking into account the insolation heat gains *Bulletin of Tomsk Polytechnic University. Engineering of Georesources* **326(8)** 36-46
[5] Zakharova A S, Orlova A K 2018 “Smart Home” technology as an energy-saving technology of the future *Economy and Entrepreneurship* **5(94)** 1166-1169

[6] Lapaeva O F 2010 Transformation of the energy sector of the economy in the transition to energy-saving technologies and renewable energy sources *Orenburg State University Bulletin* **13(119)** 50-56
[7] Shchegolikhina M S 2015 Energy saving technologies are technologies of the future *Progressive technologies and processes. Collection of scientific articles of the 2nd International Youth Scientific and Practical Conference in 3 volumes* 193-194
[8] Levinson S V 2015 What is new in energy-saving technologies *International Journal of Experimental Education* 78-80
[9] Balabanov M S, Baboshkina S V and Khamitov R N 2015 Environmental aspects in energy-saving policy at the stage of creating intelligent energy systems in Russia with an active-adaptive network *Izvestia Tomsk Polytechnic University. Engineering of Georesources* **326(11)** 141-152
[10] Shuravin A P 2018 Review of optimization problems of thermo-hydraulic modes of buildings *Collection of materials of the All-Russian scientific-practical conference with international participation* (Stavropol: Center for Scientific Knowledge "Logos") 51-55
[11] Shuravin A P, Vologdin S V 2018 The use of a genetic algorithm to optimize the temperature mode of indoor areas by adjusting the balance valves of the risers *Intellectual systems in production* **16(2)** 113-120
[12] Novitsky N N, Lutsenko A V 2016 Study of the issues and methods of multicriteria optimization of hydraulic modes of distribution heat networks *Scientific Herald of the NSTU* **3(64)** 131-145
[13] Vologdin S V, Moshkin A V 2011 Mathematical model for optimizing the cost of production and transportation of thermal energy in a centralized heating system, in the presence of a pressure and resistance regulator *The world of scientific discoveries* **8** 281-290
[14] Vologdin S V 2011 Mathematical model for optimizing heat flows between buildings of a multi-loop heat network in order to reduce the disbalance of the heat supply system by regulating the nozzles of the elevator nodes *The world of scientific discoveries* **12** 194-204
[15] Basalaev A A, SHnajder D A 2017 The method of optimizing the temperature of the coolant in the system of centralized heat supply of buildings based on simulation *Bulletin of the South Ural State University. Series: computer technology, management, electronics* **17(1)** 15-22
[16] Manusov V Z, Matrenin P V and Kirgizov A K 2017 Optimization of the distribution of compensating devices in power supply systems based on swarm intelligence *Energy Security and Energy Saving* **3** 28-32
[17] Bajbakov S A, Filatov K V 2012 Optimization of heating networks for the cost of transporting the coolant (optimization of heat transportation) *Energetic* **12** 26-33
[18] Stennikov V A, Hemerzov C A 2018 Application of tree search algorithm and annealing imitation method for circuit-structural optimization of heat networks *Software products and systems* **2** 387-395
[19] Sacaan R, Rudnick H, Lagos T, Ordóñez F, Navarro-Espinosa A and Moreno R 2017 *IEEE Manchester PowerTech* (Manchester) 1-6
[20] Dolan M J, Davidson E M, Kockar I, Ault G W and McArthur S D J 2012 *IEEE Transactions on Power Systems* **27** 790-799
[21] Kong C, Jovanovic R, Bayram I S and Devetsikiotis M 2017 A hierarchical optimization model for a network of electric vehicle charging stations *Energy* **10(5)**
[22] Wang D, Hu Q, Tang J, Lia H, Li Y, Gao S and Fan M 2017 A kriging model based optimization of active distribution networks considering loss reduction and voltage profile improvement *Energy* **10(5)**
[23] Scardapane S, Panella M and Wang D 2016 A decentralized training algorithm for Echo State Networks in distributed big data applications *Neural Networks* **78** 65-74

[24] Muñoz E, Márquez-Neila P and Baumela L 2015 Rationalizing Efficient Compositional Image Alignment: The Constant Jacobian Gauss-Newton Optimization Algorithm *International Journal of Computer Vision* **112(3)** 354-372
[25] Chatterjee K, Chmelík M, Gupta R and Kanodia A 2016 Optimal cost almost-sure reachability in POMDPs *Artificial Intelligence* **234** 26-48
[26] Akulich I L 2011 *Mathematical programming in examples and problems: Textbook. manual for students of the economy Universities* (St. Petersburg: Lan) p 352
[27] Korobeynikov A V 2013 *Programming neural networks: a teaching aid for the disciplines "Optimization Methods. Neural Networks","Neurocomputer Systems" and "Fuzzy Logic and Genetic Algorithms"* (Izhevsk: Publishing house IzhSTU) p 44
[28] GOST 30494-2011. Residential and public buildings. Indoor microclimate parameters
[29] Rabiner L, Gould B M 1978 Theory and application of digital signal processing (World) p 835

Increasing signal/acoustic interference ratio in telecommunications audio exchange by adaptive filtering methods

Y A Kropotov[1], A A Belov[1] and A Y Prockuryakov[1]

[1]Murom Institute (branch) "Vladimir State University named after Alexander and Nicholay Stoletovs", Orlovskaya street, 23, Murom, Russia, 602264

e-mail: kaf-eivt@yandex.ru

Abstract. The paper deals with the issues of increasing signal/noise ratio in telecommunication audio exchange systems. The study of characteristics of speech signals and acoustic noises, such as mathematical expectation, dispersion, relative intensity of acoustic speech signals and various types of acoustic noises and interference is carried out. It is shown that in the design of telecommunications systems, in particular loudspeaker systems operating under the influence of external acoustic noise of high intensity, it is necessary to solve the problem of developing algorithms to effectively suppress the above mentioned interference to ensure the necessary signal/noise ratio in communication systems. A mathematical model of the autocorrelation function of the speech signal by using the Lagrange interpolation polynomial of order 10, considered the creation of adaptive algorithms to suppress acoustic noise by linear filtering methods. Thus suppression of acoustic noises and hindrances is possible at the expense of operated change of area of a cutting in the interval from 0 Hz to 300-1000 Hz, depending on a hindrance conditions.

1. Introduction

The issues of increasing signal/acoustic interference in telecommunications audio exchange are relevant and widely covered in the domestic [1-4] and foreign literature [5-8]. As the main criteria for the effectiveness of telecommunications systems, to ensure a reliable exchange of information between the subscribers of the system, we can cite the signal/acoustic noise ratio and syllable intelligibility [1].

Reliable exchange of audio information in communication and telecommunication systems is possible with the provision of signal/external acoustic noise ratio in $P_s/P_n \geq 20$ dB, which, accordingly, will provide the necessary syllabic intelligibility S ≥ 93% for the effective, complete exchange of audio data and operational-command information in loudspeaker systems at multifunctional facilities of various purposes. For this reason, it is important to continue research aimed at developing new approaches and algorithms to increase signal-to-acoustic interference ratio by methods of adaptive filtration with the use of controlled change of the resection area.

2. Investigation of the characteristics of speech signals and acoustic noise

The known mathematical model of the function of probability density $P(x_i)$ of speech signals, developed in [9], allows to receive values of mathematical expectation $\bar{x}_i$ and dispersion σ^2 of speech signals according to expressions

$$\bar{x}_i = \sum_{i=-2^n+1}^{2^n-1} x_i \cdot P(x_i), \qquad \sigma^2 = \sum_{i=-(2^n-1)}^{2^n-1} x_i^2 P(x_i), \tag{1}$$

where x_i is the speech signal samples quantized at 2^n intervals and normalized relative to the maximum values in the form of $|\pm x_{max}| = 1$ V, then we obtain the values $\bar{x}_i \approx 0$ and $\sigma^2 = 0{,}126$ W/Ohm.

Accordingly, the level of sound pressure intensity I relative to the zero level of intensity $I_0=10^{-12}$ W/m^2 is defined as

$$\frac{I}{I_0}(dB) = 10 lg \frac{k\sigma^2}{S} \cdot 10^{12}, \tag{2}$$

where k is the directivity coefficient of a loudspeaker device, in case of radiation in one direction is accepted $k = 2$; $S = 4\pi R^2$ is a sphere area, R is a sphere radius in meters.

Then the relative intensity of the acoustic speech signal I_p calculated by means of expression (2) has the following value

$$\frac{I_p}{I_0}(dB) = 103dB,$$

in the case of $\sigma^2 = 0{,}126$ W, $k = 2$, R=1 m.

The relative intensities for different acoustic noises and acoustic disturbances are also calculated using the values of mathematical expectation and dispersions of different types of acoustic disturbances determined by formulas (1), in which the mathematical model of the function of probability density of acoustic disturbances is applied [10]. Values of relative intensities for different acoustic signals are presented in Table 1.

Table 1. Relative intensities for different acoustic signals.

Type of signal	P (W)	$\frac{I}{I_0}$ (dB)	$\frac{P_s}{P_n}$ (dB)
Speech signal	0.126	103	–
Quantum noise	$0.5\cdot10^{-5}$	59	44
Acoustic disturbances	$3.5\cdot10^{-4}$	85	18
The noise of the sea	0.0687	90.4	12.6
Wind noise	0.0953	91.8	11.2
The noise in the engine room	0.111	92.5	10.5

Table 1 shows that in the presence of acoustic noise such as sea noise, wind noise, noise in the engine room P_s/P_n is in the range of 10,5÷18 dB. At such signal/interference relations, the syllable intelligibility can be reduced to 65% for the case of Russian speech transmission. Reliable reception of the transmitted speech information by the subscriber under such conditions is significantly complicated.

According to the research in [10], for the correct reception of the transmitted voice message through a noisy channel, it is necessary to provide a ratio P_s/P_n of at least 20 dB. Therefore, in the design of telecommunications systems, in particular, hands free systems operating under the influence of external acoustic noise, the task is to create algorithms to effectively suppress the above mentioned interference to ensure the necessary ratio of $P_s/P_n \geq 20$ dB.

Studies of the spectral functions of speech signals and external noise interference in [9] have shown that the spectrum of the most common interference - external acoustic noise - is shifted relative to the

spectrum of speech signals in the low-frequency region, which suggests that increasing the ratio P_s/P_n can be applied linear filtering methods. Another factor allowing to apply linear filtration to suppress acoustic noise is the possibility of increasing the cutting area in the range from F=0 Hz to F_l=300-1000 Hz, according to studies in [10]. From these studies it can be seen that with the increase of the lower boundary of the reproduced frequencies up to F=1000 Hz the value of S practically does not change, it takes the value not less than 94% which is acceptable.

Thus, the above factors allow to consider the possibility of designing adaptive algorithms of speech signal processing and suppression of acoustic interference due to controlled change of the cutting area in the range from 0 Hz to (300÷1000) Hz, depending on the interference situation.

3. Development of an adaptive filtering algorithm with control of the resection area

Consider as a model of adaptive filtering a bandpass filter of rectangular shape with a floating low-frequency cut F_l in the AFC channel. Varying F_l within $0 \le F_l \le F_h$, where F_h is a fixed high-frequency section of the AFC filter. The AFC of the bandpass filter $K(f)$ is specified as

$$K(f) = \begin{cases} 1, & at \quad F_l \le f \le F_h, \\ 0, & at \quad other \quad values \quad f; \end{cases}$$

where $0 \le F_l \le F_h$, F_h=6000 Hz.

With the known spectral function of the speech signal $G(f)$, P_s at the bandpass filter output is defined as

$$P_s = \int_{F_l}^{F_h} K^2(f) G(f) df = \int_{F_l}^{F_h} G(f) df ,$$

where the second part of the P_s calculation expression is rewritten according to the $K^2(f) = 1$ integration limits of F_l to F_h.

Correspondingly changing F_l within the range of $0 \le F_l \le F_h$, we obtain the dependence of P_s on the value of low-frequency F_l AFC of the channel. Write down the spectral function of the energy spectrum of the speech signal in the form

$$G(\Delta f \cdot g) = \sum_{g=0}^{N-1} \sum_{k=0}^{k-1} R(kT) e^{-j 2\pi \Delta f \cdot g \cdot kT} ,$$

where $\Delta f = \frac{Fd}{N}$ is the sampling interval of the spectral function by frequency, N is number of speech signal samples at the final interval, g is the number of the frequency discrete component of the spectral function reference is within $0 \le g \le N-1$, $R(kT)$ is the voice signal ACF is represented as a grid function in Table 2 for one of the voice signal implementations.

Table 2. Grid function of the voice signal ACF.

k_h, k_l	$k_0=0$	$k_1=7$	$k_2=25$	$k_3=54$	$k_4=93$	$k_5=130$
$R(k_h)$	$R(k_0)=0,126$	$R(k_1)=0,115$	$R(k_2)=0,037$	$R(k_3)=-0,048$	$R(k_4)=-0,016$	$R(k_5)=-0,025$
k_h, k_l	$k_6=182$	$k_7=182$	$k_8=228$	$k_9=245$	$k_{10}=253$	
$R(k_h)$	$R(k_6)=0,026$	$R(k_7)=0,008$	$R(k_8)=-0,003$	$R(k_9)=-0,001$	$R(k_{10})=0$	

Mathematical model of speech signal ACF is represented by approximation of interpolation polynomial Lagrangian of the tenth order in the form of

$$R(k) = \sum_{k=0}^{H=10} R(k_h) \prod_{\substack{r=0 \\ r \ne q}}^{H=10} \frac{k - k_r}{k_q - k_r} ,$$

where k is the current delay multiple of the sampling period T, k_q is the delay in the node with the number q, r is current delays of other nodes at $r \ne q$.

Similarly, the power of acoustic noise P_n is calculated as

$$P_n = \int_{F_l}^{F_h} G_{\Pi}(f)df \cdot$$

The spectral function of acoustic noise $G_{\Pi}(\Delta f \cdot g)$ looks like

$$G_{\Pi}(\Delta f \cdot g) = \sum_{g=0}^{N-1}\sum_{K=0}^{K-1} R_{\Pi}(kT)l^{-j2\pi\Delta f \cdot g \cdot kT},$$

where $R_{\text{п}}(kT)$ is ACF interference is also represented by its approximation by an interpolation Lagrangian polynomial.

The process of filtration of the spectral functions of the speech signal $G(f)$ and interference $G_{\text{п}}(f)$ and, accordingly, the change in the ratio P_s/P_n depending on the change in F_l within 300 Hz $\leq F_l \leq$ 1000 Hz is experimentally simulated and the results are illustrated in Figure 1. Figure 1 clearly shows that the area of the integrative function of $G_{\text{п}}(f)$ corresponding to the P_n decreases faster with changes in F_l from 300 Hz to 1000 Hz than the area of the integrative function of $G(f)$. Figure 1 also demonstrates that the basic energy of the spectral function $G(f)$ remains in the range from 0 Hz to F_l, outside the bandwidth of the rectangular filter.

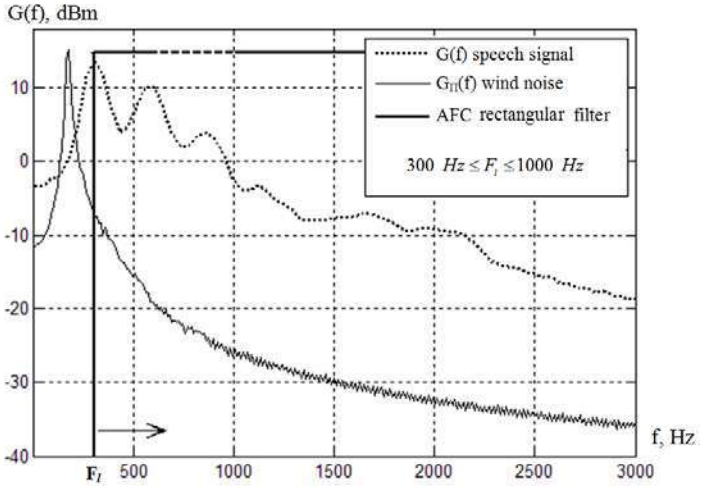

Figure 1. Illustration of the model of filtration of the spectral functions of the speech signal $G(f)$ and the interference $G_{\text{п}}(f)$ depending on the change in the value of F_l.

Thus, the ratio of the values of P_s and P_n at the output of the rectangular filter shows the dependence of the degree of suppression of acoustic noise relative to the speech signals on the value of the resection region from 0 Hz to F_l in the AFC. In the discrete case of representation of spectral functions, we obtain the ratio P_s/P_n in the form of

$$\frac{P_s}{P_n} = \frac{\sum_{g_l}^{g_h} G(g \cdot \Delta f)}{\sum_{g_l}^{g_h} G_{\Pi}(g \cdot \Delta f)},$$

where at duration of the analysis interval τ_{segm}, the number of samples in the analysis interval $N = \frac{\tau_{segm}}{T}$, $\Delta f = \frac{F_d}{N}$ of the spectral function sampling interval by frequency, $g_l = \frac{F_l}{\Delta f}$ is the number of frequency interval for low-frequency section of AFC F_l.

Thus, changing g_l in the ratio expression P_s/P_n will get a function of changing this ratio at the output of the rectangular filter depending on the width of the suppression area, which is in the range from 0 to $F_l = g_l \Delta f$.

The obtained results of studies of the effect of change in F_l on P_s/P_n a fixed F_h=6000 Hz are shown in Figure 2. In researches cases for three various realizations of speech signals concerning various external noise hindrances are considered.

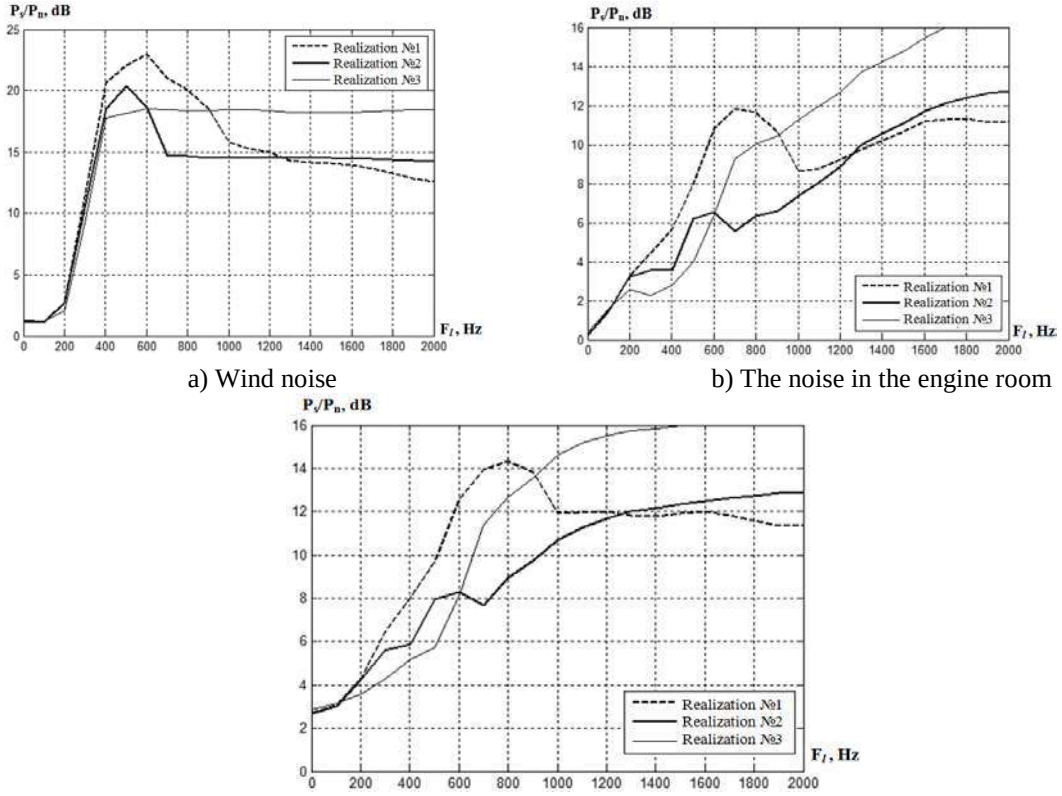

a) Wind noise

b) The noise in the engine room

c) The noise of the sea

Figure 2. Dependence of the ratio P_s/P_n at the output of a rectangular filter on the value of F_l, at a fixed value of F_h=6000 Hz.

4. Conclusion

From the diagrams in Figure 2 it can be seen that external acoustic interference of the "wind noise" type, if set to F_l=500 Hz, is suppressed by -(17÷23) dB. At the influence of acoustic noise of the type "noise in the engine room" and at F_l =700÷1000 Hz, such acoustic noise is suppressed up to -12 dB. At the influence of acoustic interference of "sea noise" type at F_l = 800÷1000 Hz, this interference is suppressed by (11÷15) dB [10]. The obtained results of acoustic noise suppression studies show that the linear filtration method can provide the necessary ratio of $P_s/P_n \geq$20 dB and, accordingly, the necessary syllabic legibility of S ≥ 93% in the telecommunications system of voice information exchange.

5. References

[1] Zheleznyak V K, Makarov Y K and Khoreev A A 2000 Some methodical approaches toevaluation of efficiency of speech information protection *Special technique* **4** 39-45

[2] Sapozhkov M A 1962 *Speech signal in cybernetics and communications* (Moscow: Svyazizdat) p 452

[3] Martin R, Heute U and Antweiler C 2008 *Advances in Digital Speech Transmission* (London: John Wiley and Son) p 572

[4] Ryabenkyi V S 2012 Mathematical model of the external noise suppression devices in the subarea of space *Mathematical modeling* **24(8)** 3-31

[5] McAulay R and Malpass M 1980 Speech enhancement using a soft-decision noise suppression filter *IEEE Trans, on Acoustics, Speech, and Signal Processing* **28(2)** 137-145

[6] Cohen I, Benesty J and Gannot S 2010 *Speech processing in modern communication* (Berlin, Heidelberg: Springer) p 342
[7] Hansler E and Schmidt G 2006 *Topics in acoustic echo and noise control: Selected methods for the cancelation of acoustic echoes, the reduction of background noise, and speech processing* (Berlin, Heidelberg: Springer) p 642
[8] Kahrs M and Brandenburg K 2002 *Applications of digital signal processing to audio and acoustics* (New York: Kluwer Academic Publisher) p 572
[9] Kropotov Y A and Belov A A 2016 Application method of barrier functions in the problem of estimating the probability density of the parameterized approximations *13th International Scientific-Technical Conference on Actual Problems of Electronic Instrument Engineering* 69-72
[10] Kolpakov A A and Kropotov Y A 2017 Advanced mixing audio streams for heterogeneous computer systems in telecommunications *CEUR Workshop Proceedings* **1902** 32-36
[11] Kropotov Y A and Proskuryakov A Y 2007 Mathematical model of probability law for the amplitudes of speech waveforms in the exponential basises *17th International Crimean Conference - Microwave and Telecommunication Technology* 364-366
[12] Breining C 1999 Acoustic echo control. An application of very-high-order adaptive filters *Signal Processing Magazine* **16(4)** 42-69
[13] Boll S 1979 Suppression of acoustic noise in speech using spectral subtraction *IEEE Transactions on Acoustics, Speech, and Signal Processing* **27(2)** 113-120
[14] Diniz P S 2008 *Adaptive filtering algoriths and practical implementation* (New York: Springer) p 627
[15] Hakansson L 2002 *Noise Reduction in Speech Applications* (Boca Raton, Florida: CRC press) p 384
[16] Kropotov Y A, Belov A A and Proskuryakov A Y 2018 Method for forecasting changes in time series parameters in digital information management systems *Computer Optics* **42(6)** 1093-1100 DOI: 10.18287/2412-6179-2018-42-6-1093-1100

The syllable intelligibility in the system of information transmission by speech signals depending on the intensity of acoustic noise

Yu A Kropotov[1], A A Belov[1], A A Kolpakov[1] and A Yu Proskuryakov[1]

[1]Murom Institute (branch) «Vladimir State University named after Alexander and Nicholay Stoletovs», Orlovskaya street, 23, Murom, Vladimir Region, Russia, 602264

e-mail: kaf-eivt@yandex.ru

Abstract. The paper investigates the effect of the signal-to-noise ratio on syllable intelligibility under the intense influence of external acoustic interference when exchanging voice messages in telecommunication systems of public address systems. The article discusses the effect on the syllable intelligibility of the signal / external acoustic noise ratio, examines the effect of the integral articulation index, the dependence of the perception coefficient of formants on the relative level of formant intensity, the dependence of the formant parameter on the geometric mean frequency of the i-th spectrum of the speech signal. In accordance with the results of studies of the integral articulation index depending on the signal-to-noise ratio, a function of syllable intelligibility depending on the signal-to-noise ratio was obtained, using which it is possible to determine the maximum value of the output signal-to-noise ratio in the audio exchange telecommunications system to obtain a given syllable intelligibility. At the same time, experimentally determined the value of the signal-to-noise ratio in the telecommunications system of audio exchange to obtain a syllable intelligibility of at least 93% for ensure full perception of the transmitted speech information.

1. Introduction

As it is known, the main criterion of efficiency of the system of telecommunication exchange of the speech information is syllabic legibility *S* % or the size of an estimation of a speech signal on scale MOS (Mean Opinion Score) [1].

Telecommunication systems of audio exchange, in particular loudspeaker systems, are considered to be effective if the transmitted speech information is perceived by the object completely and without difficulties, the syllable intelligibility in this case is not less than 93% [1,2,4] or the MOS score should be not less than 3,9 points on a five-point scale [5, 6].

2. Formulation of the problem

Dependence of syllabic intelligibility in the system of telecommunication exchange of speech information on the influence of various factors has been studied in a number of works [1,3]. However, the information in the known sources [9, 10] about the influence of the signal-to-noise ratio on the syllabic legibility on the side of receiving speech messages for the case of operational-command

telecommunication systems is insufficient, so this article considers the problem of determining the influence of the signal-to-noise ratio on the syllabic legibility in telecommunication audio exchange systems.

The known results of the studies of the assessment of syllabic legibility by the instrumental-calculation method are shown in Fig. 1 [1, 3].

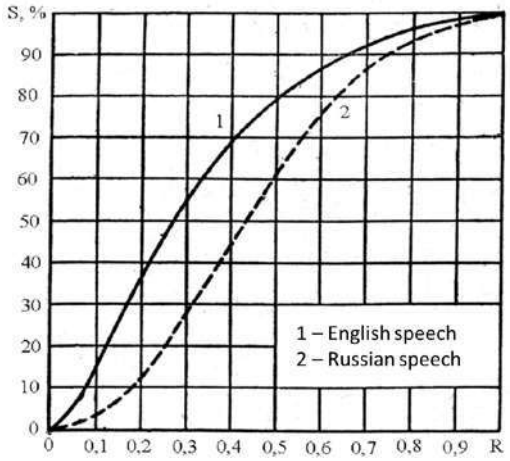

Figure 1. Dependence of syllabic legibility S on the integral articulation index *R*.

Figure 1 shows that the syllabic legibility here is represented by the dependence only on the value of the integral articulation index.

3. Instrumental-calculation method for estimating the integral articulation index and syllabic legibility

The value of the integral articulation index *R* depending on the value of the spectral articulation index R_i is determined by the expression

$$R = \sum_{i=1}^{N} R_i \ . \tag{1}$$

The articulation spectral index is calculated by the expression

$$\mathrm{R_i = p_i \cdot k_i} \ , \tag{2}$$

where p_i is formant coefficient, k_i is weighting coefficient of the presence of formant speech in the *i*-th band.

The coefficient of perception of formant p_i is calculated using the expression [3]

$$p_i = \begin{cases} \dfrac{0{,}78 + 5{,}46 \cdot \exp\left[-4{,}3 \cdot 10^{-3} \cdot \left(27{,}3 - |Q_i|\right)^2\right]}{1 + 10^{0{,}1 \cdot |Q|}}, & \text{if} \quad Q_i \le 0; \\ 1 - \dfrac{0{,}78 + 5{,}46 \cdot \exp\left[-4{,}3 \cdot 10^{-3} \cdot \left(27{,}3 - |Q_i|\right)^2\right]}{1 + 10^{0{,}1 \cdot |Q|}}, & \text{if} \quad Q_i > 0, \end{cases} \tag{3}$$

where $Q_i = q_i - \Delta A_i$ is the relative intensity level of the format.

Or the value of the perception coefficient p_i format can be determined by the graph in Figure 2.

The format parameter ΔA_i is determined by the graph in Figure 3 or by the expression

$$\Delta A(f) = \begin{cases} 200 / f^{0{,}43} - 0.37, & \text{если } f \le 1000 \text{ Гц}, \\ 1{,}37 + 1000 / f^{0{,}69}, & \text{если } f > 1000 \text{ Гц}, \end{cases} \tag{4}$$

where $f_{\text{ср}.i} = \sqrt{f_{в_i} - f_{н_i}}$ is average geometric frequency, $f_{н_i}$ is lower frequency of the *i*-th bandwidth of the speech spectrum, $f_{в_i}$ is upper frequency of the *i*-th bandwidth of the spectrum.

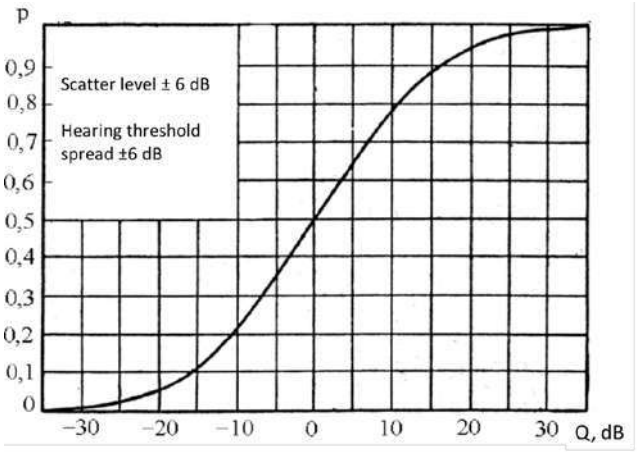

Figure 2. Dependence of the perception coefficient format p_i on the relative intensity level format Q_i.

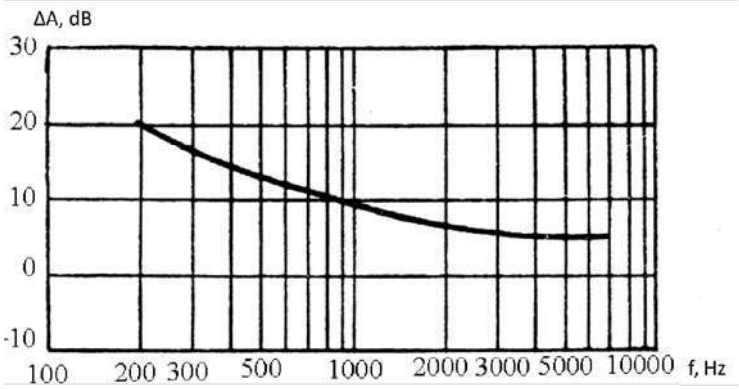

Figure 3. Dependence of the formal parameter ΔA_i on the average geometric frequency of the i-th bandwidth of the speech spectrum.

For each *i*-th (*i*=1, 2, ... *N*) frequency band at the average geometric frequency $f_{\text{cp.}i} = \sqrt{f_{в_i} - f_{н_i}}$, a formal parameter ΔA_i is determined, characterizing the energy redundancy of discrete components of the speech signal.

4. Results of experiments

Let's take the number of octave bands *N*=5. Values of the accepted limits by frequency of octave bands, values of calculated $f_{sr.i}$ and values of formal parameters ΔA_i are given in Table 1.

Table 1. Values of the accepted limits by frequency of octave bands, values of calculated $f_{cp.i}$ and values of formal parameters ΔA_i.

i	Boundary bandwidth frequency, Hz	$f_{cp.i}$, Hz	Bandwidth Δf_i	$\Delta A_i (f_{cp.i})$
1	180-355	250	175	18
2	355-710	500	355	13
3	710-1400	1000	690	9.5
4	1400-2800	2000	1400	7.5
5	2800-5600	4000	2800	5.5

With the help of expression $Q_i = q_i - \Delta A_i$, we determined the values of intensity levels of format Q_i depending on the signal to noise ratio q_i. The calculated values of Q_i are summarized in Table 2.

With the help of expression (3) or according to the diagram in Figure 2, the formatting factor p_i is determined depending on Q_i for *i*-th bands, with different values of signal-to-noise ratio, dB. The calculated p_i values for different q_i are summarized in Table 3.

Table 2. Calculated values Q_i.

$Q_i = q_i - \Delta A_i$ q_i, дБ	*Q1*	*Q2*	*Q3*	*Q4*	*Q5*
q_i = 0 дБ	-18	-13	-9.5	-7.5	-5.5
q_i = 3 дБ	-15	-10	-6.5	-4.5	-2.5
q_i = 6 дБ	-12	-7	-3.5	-1.5	+0.5
q_i = 10 дБ	-8	-3	+0.5	+2.5	+4.5
q_i = 20 дБ	+2	+7	+10.5	+12.5	+14.5
q_i = 30 дБ	+12	+17	+20.5	+22.5	+24.5

Table 3. Calculated values p_i.

q_i, dB	p_1	p_2	p_3	p_4	p_5
q_i = 0	0.07	0.18	2.2	0.29	0.34
q_i = 3	0.11	0.21	0.31	0.38	0.41
q_i = 6	0.2	0.3	0.40	0.48	0.51
q_i = 10	0.24	0.41	0.51	0.53	0.62
q_i = 20	0.47	0.6	0.79	0.81	0.88
q_i = 30	0.81	0.9	0.94	0.96	0.98

To determine the spectral articulation index R_i, the weighting coefficient of probability of presence of the format of speech in the *i*-th band k_i is determined by the formula

$$k_i = k(f_{vi}) - k(f_{ni}),$$

where $k(f_{vi})$ and $k(f_{ni})$ is weights for the upper f_{vi} and lower f_{ni} of the *i*-th bandwidth of the speech spectrum. Values $k(f_{vi})$ and $k(f_{ni})$ are determined by the formula as [3]:

$$k(f) = \begin{cases} 2{,}57 \cdot 10^{-8} \cdot f^{2,4}, & \text{если } 100 < f \le 400 \text{ Гц}; \\ 1 - 1{,}074 \cdot exp\left(-10^{-4} \cdot f^{1,18}\right), & \text{если } 400 < f \le 10000 \text{ Гц}; \end{cases} \quad (5)$$

or according to the chart in Figure 4.

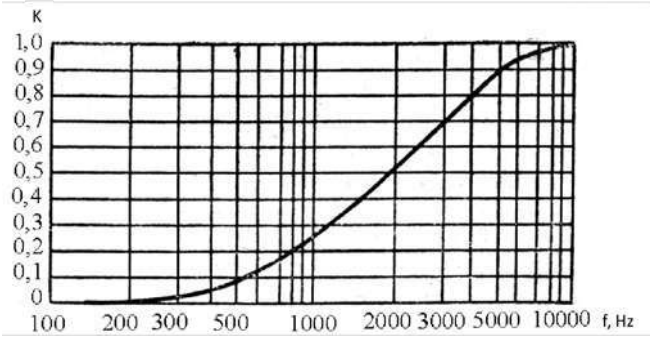

Figure 4. Weighting *k*(*f*) of the formal frequency distribution.

The results of calculations of the weighting coefficients of probability of formant speech in the *i*-th band are presented in Table 4.

Table 4. Results of calculations of the weighted probability coefficients of formal speech in the *i*-th band.

k_i	$k(f_в)$-$k(f_н)$	$k(f_{в\,i})$-$k(f_{н\,i})$	k_i
k_1	*k*(*355*)-*k*(180)	0.04-0.01	0.03
k_2	*k*(710)-*k*(355)	0.18-0.04	0.14
k_3	*k*(1400)-*k*(710)	0.36-0.18	0.18
k_4	*k*(2800)-*k*(1400)	0.63-0.36	0.37
k_5	*k*(5600)-*k*(2800)	0.92-0.63	0.29

Calculation of the R_i articulation spectral index is performed by formula (2). Calculations of R_i, at different values of signal-to-noise ratio are summarized in Table 5.

Table 5. Articulation spectral index R_i, at different signal-to-noise ratios.

$R_i = p_i \cdot k_i$	$R_1 = p_1 \cdot k_1$	$R_2 = p_2 \cdot k_2$	$R_3 = p_3 \cdot k_3$	$R_4 = p_4 \cdot k_4$	$R_5 = p_5 \cdot k_5$
q_i = 0 dB	0,07·0,03=0,0021	0,18·0,014=0,0252	0,22·0,18=0,0396	0,29·0,37=0,1073	0,34·0,29=0,0986
q_i = 3 dB	0,11·0,03=0,0033	0,021·0,14=0,0294	0,31·0,18=0,0558	0,38·0,37=0,1406	0,41·0,29=0,1189
q_i = 6 dB	0,2·0,03=0,006	0,3·0,14=0,042	0,4·0,18=0,072	0,48·0,37=0,1776	0,51·0,29=0,1479
q_i = 10 dB	0,24·0,03=0,0072	0,41·0,14=0,0574	0,51·0,18=0,0918	0,53·0,37=0,1961	0,62·0,29=0,1798
q_i = 20 dB	0,47·0,03=0,0141	0,6·0,14=0,084	0,79·0,18=0,0918	0,81·0,37=0,2997	0,88·0,29=0,2552
q_i = 30 dB	0,81·0,03=0,0243	0,9·0,14=0,126	0,94·0,18=0,1692	0,96·0,37=0,3552	0,98·0,29=0,2842

According to the results of calculations of the spectral articulation index R_i, summarized in Table 5, it became possible to calculate the integral articulation index depending on the signal-to-noise ratio. The results of the calculation of the integral articulation index made it possible to find the values of syllabic legibility depending on the signal-to-noise ratio, which are summarized in Table 6.

Table 6. Syllable intelligibility values depending on signal-to-noise ratio.

q_i signal/noise	0 dB	3 dB	6 dB	10 dB	20 dB	30 dB
R	0.273	0.348	0.4455	0.5323	0.7952	0.9589
$S_{eng.}$	48 %	61 %	73 %	82%	96%	99%
$S_{rus.}$	25%	35 %	53 %	65 %	93%	98.5%

The graph of the syllable intelligibility function S from the signal-to-noise ratio is shown in Figure 5.

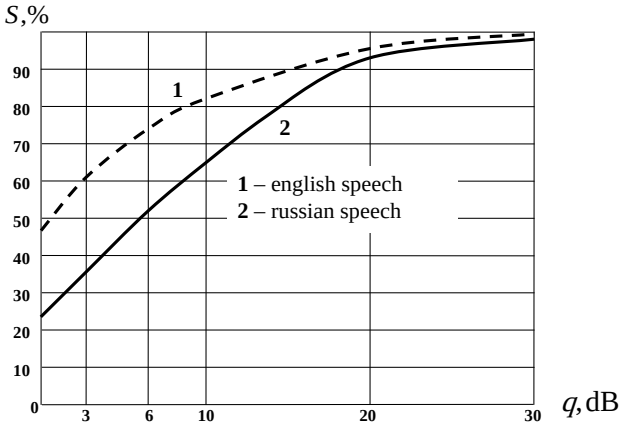

Figure 5. Graph of dependence of syllabic intelligibility on signal-to-noise ratio.

5. Conclusions

As can be seen from the graphs in Figure 5, the syllable intelligibility of the voice messaging telecommunications system is ensured by $S \geq 93\%$ for signal/noise ratio $q \geq 20$ dB [7, 8]. Thus, the dependence of syllabic intelligibility on signal-to-noise ratio, which is important for the practice of telecommunication systems, is obtained. It shows that for effective transmission of speech information by the command and control system of telecommunications, for obtaining, respectively, syllabic intelligibility of $S \geq 93\%$, in the system for transmission of speech messages, it is necessary to provide signal-to-noise ratio $q \geq 20$ dB on the receiving side of messages.

6. References

[1] Sapozhkov M A 1962 *Speech signal in cybernetics and communications* (Moscow: Svyazizdat) p 452

[2] GOST R 50840-95 *Speech transmission via communication channels. Methods to assess quality, legibility and recognizability*
[3] Zheleznyak V K, Makarov Y K and Khoreev A A 2000 Some methodical approaches toevaluation of efficiency of speech information protection *Special technique* **4** 39-45
[4] Cohen I, Benesty J and Gannot S 2010 *Speech processing in modern communication* (Berlin, Heidelberg: Springer) p 342
[5] Hansler E and Schmidt G 2006 *Topics in acoustic echo and noise control: Selected methods for the cancelation of acoustic echoes, the reduction of background noise, and speech processing* (Berlin, Heidelberg: Springer) p 642
[6] Kahrs M and Brandenburg K 2002 *Applications of digital signal processing to audio and acoustics* (New York: Kluwer Academic Publisher) p 572
[7] Kropotov Y A and Belov A A 2016 Application method of barrier functions in the problem of estimating the probability density of the parameterized approximations *13th International Scientific-Technical Conference on Actual Problems of Electronic Instrument Engineering* 69-72
[8] Kolpakov A A and Kropotov Y A 2017 Advanced mixing audio streams for heterogeneous computer systems in telecommunications *CEUR Workshop Proceedings* **1902** 32-36
[9] Ryabenkyi V S 2012 Mathematical model of the external noise suppression devices in the subarea of space *Mathematical modeling* **24(8)** 3-31
[10] McAulay R and Malpass M 1980 Speech enhancement using a soft-decision noise suppression filter *IEEE Trans, on Acoustics, Speech, and Signal Processing* **28(2)** 137-145
[11] Kropotov Y A, Belov A A and Proskuryakov A Y 2018 Method for forecasting changes in time series parameters in digital information management systems *Computer Optics* **42(6)** 1093-1100 DOI: 10.18287/2412-6179-2018-42-6-1093-1100

Analysis of the structure of the relationship between the descriptions of objects of classes and evaluation of their compactness

E N Zguralskaya[1]

[1]Ulyanovsk Technical University. Institute of Aviation Technologies and Management, Sozidateley avenue, 13A, Ulyanovsk, Russia, 432072

e-mail: iatu@inbox.ru

Abstract. The study is conducted to assess the compactness of descriptions of objects of classes on the numerical axis and in the multidimensional attribute space. The computation of compactness is possible only in the defined boundaries of areas of the attribute space. In the one-dimensional case, the boundaries are calculated by the frequency of occurrence of the values of features of objects of classes in the interval. In the multidimensional case, a subset of the boundary objects of the classes is used for a given metric. A comparative analysis is given of the values of the compactness measure by latent attributes on the numerical axis and by the sets of initial features from which they are synthesized.

1. Introduction

In the pattern recognition theory objects are structured into classes based on the compactness hypothesis. Under this hypothesis, “close” objects shall belong to the same class. It is necessary to clarify (interpret) the terms “closeness” and “compactness” of objects.

No common determination of the “compactness” term has been adopted. [1] postulates a compactness measure of disjoint groups, set of admissible values of which is determined in (0, 1] and depends on structure of relations between objects. The following factors affecting values of compactness are pointed out:

- the choice of the metric to compute distances between objects;
- the dimension of the attribute space;
- the choice of the way to scale and normalize data;
- the usage of methods to select informative collections of attributes;
- conditions to select and remove noise objects from the sample;
- the number of standard objects of the minimal coverage of the learning sample;
- linear and nonlinear transformations of the attribute space for the description of the objects.

The aim of the searching for extremal values of compactness measures on the variety of parameters listed above is to improve generalizing ability of recognition algorithms. The method to obtain a quantitative estimate for the pattern compactness, described in [2], is based on the usage of the function of competitive similarity between objects (FRiS-functions). Using the FRiS-function, one can

describe all distributions of classes by collections of standard objects. The collection of objects allows one to find the compactness measure of the whole sample or each separate object of the class and to clear the learning sample from objects adding negative contributions to the value compactness.

Implementation of machine learning algorithms becomes significantly more complicated when the dimension of the data is large. A geometric interpretation of origin of the effect of curse of dimensionality is given in [3]. The effect of curse of dimensionality arises from the fact that the number of possible sets of attributes in the description of objects significantly exceeds the number of training examples. Learning algorithm can only support correct generalization provided that the number of examples from learning sample is enough.

Compactness implies the existence of a boundary between areas of attribute space with a description of objects from different classes.

Numerical methods to obtain a quantitative estimate for compactness are differentiated as well. For one-dimensional cases the interval methods are used while for multidimensional cases – computation of measure of compactness of objects of classes and samples in a whole for a given metric. What both one-dimensional and multidimensional cases have in common is the existence of areas of attribute space on boundaries of which measure of compactness is computed.

For a one-dimensional case the objects can be compared on the numerical axis by values of its initial and latent attributes using relations “greater than”, “less than” or “equal to”.

When the measure of compactness is computed for a multidimensional case in [1] the property of connectedness of objects along the subset (spans) of boundary objects of disjoint groups is used. Based on this property the objects are decomposed into disjoint groups. Connectedness of objects S_i, S_j is treated as property of logical regularities in form of hyperballs with these objects being its centre. S_i and S_j objects are considered bound if their intersection contains spans objects. Any pair of objects (S_i,S_j) of one group can always be linked by a chain of connected objects. Ideally, all class objects shall represent one group of connected objects.

This paperwork reviews structure of relations between class objects on the numerical axis. It is suggested to use measures of compactness, computed through decomposition of either attributes values (initial and latent) or values of distance between the objects into intervals, as a research tool. Values of measure of compactness are used to detect latent patterns in data. Such patterns can be regarded as new knowledge obtained within the frames of information models of ill-structured subject areas.

2. Criteria for decomposition of attributes into intervals

Let us consider two computing algorithms put forward in [4, 5] to optimize criteria for decomposition of attributes values into intervals. For convenience let these criteria be referred to as CR1 and CR2.

When computing with respect to CR1 number of intervals on the ordered sequence of attribute values equals to number of disjoint classes. Values of interval boundaries are determined via the maximum of product of intraclass similarity and interclass difference. Ideally every interval shall be represented by all attribute values of objects of one class.

For the CR2 criterion the number of classes is 2, the number of intervals is equal to or greater than 2. When computing boundaries of disjoint intervals, number of which is initially unknown, the absolute difference in frequency of occurrence of attribute values (both initial and latent) in the description of objects of two classes is used. The values of attributes on the numerical axis form a sequence of clusters (intervals). There should not be two neighboring clusters in which representatives of one class would dominate (in terms of frequency of occurrence). Those decompositions are considered ideal in the sense of consistency, for which values of (not necessarily all) objects of only one class are contained within the boundaries of each interval.

The set of admissible values by the CR1 criterion and the consistent decomposition of attributes into intervals over CR2 are contained in the segment [0; 1] and are further considered as a measure of their compactness. The value 1 corresponds to a perfect decomposition with respect to CR1 and CR2. The degree of deviation from the ideal can be inferred by values less than 1.

Combined use of CR1 and CR2 criteria is necessary to detect latent patterns in data. The search for patterns is based on results of a computational experiment. To interpret the results of the experiment, known forms of logical regularities are used (hyperball, half-plane, parallelepiped).

Let a set of objects $E_0=\{S_1,\ldots,S_m\}$ be given, containing representatives d of disjoint classes $K_1,\ldots,K_d$. The objects are described using a set of n different types of $X(n)$ attributes, δ ($\delta<n$) of which are measured in nominal, $n-\delta$ in interval scales. Gaps and duplicate values in data are allowed.

Search for latent, that is, hidden attributes is of great interest as those can be very informative in the classification being one of the objectives of the present study. It is believed that the CR1 and CR2 criteria are used to decompose values of a quantitative attribute (both initial and latent) into disjoint intervals. Latent attributes can represent combinations of nominal and quantitative attributes [6, 7]. Required to determine:

- method to compute latent attributes;
- boundaries of intervals and CR1 criterion values on initial and latent attributes;
- number of intervals, values of their boundaries and consistency of decomposition of initial attributes by the CR2 criterion.

A variety of methods to form latent attributes and criteria for decomposition of their values into disjoint intervals is essential to detect hidden patterns in databases of subject areas. We will obtain latent attributes from a set $X(n)$ in form of combinations of x_i*x_j and x_i/x_j. If number of gradations of a nominal attribute is equal to the number of disjoint classes of objects, then they can always be associated with a set of integers $a_1,\ldots,a_d$, where $a_i\neq0$, $i=1,\ldots,d$ and $a_{j+1}-a_j=const$, where $j=1,\ldots,d-1$. Each disjoint interval in respect with CR1 will be represented by one value. For example, if number of gradations equals to 2, the choice of values from [-1, 1] would constitute a representation form convenient for calculating.

3. Selection of information attribute sets by compactness of objects

Let the metric $\rho(x, y)$ be defined on the set of attributes $X(h)\subset X(n)$, $1\leq h\leq n$. The object $S\in E_0\cap K_p$, $p=1,2$ is considered as a centre of a hyperball from which, according to the ordered set of objects $\{S,S^1,\ldots,S^{m-1}\}=E_0$, a sequence of hyperballs nested in each other is formed having radii

$$\rho(S, S)\leq\rho(S, S^1)\leq\rho(S, S^2)\leq\ldots\leq\rho(S, S^{m-1}). \quad (1)$$

Values of boundaries of intervals of each object $S\in E_0\cap K_p$, $p=1, 2$ to E_0, computed by the CR1 criterion at (1), are used as a means to select an informative set of diverse attributes from $X(n)$. The geometric interpretation of formation of the ordered set $\{S, S^1,\ldots, S^{m-1}\}$ is shown at "Figure 1".

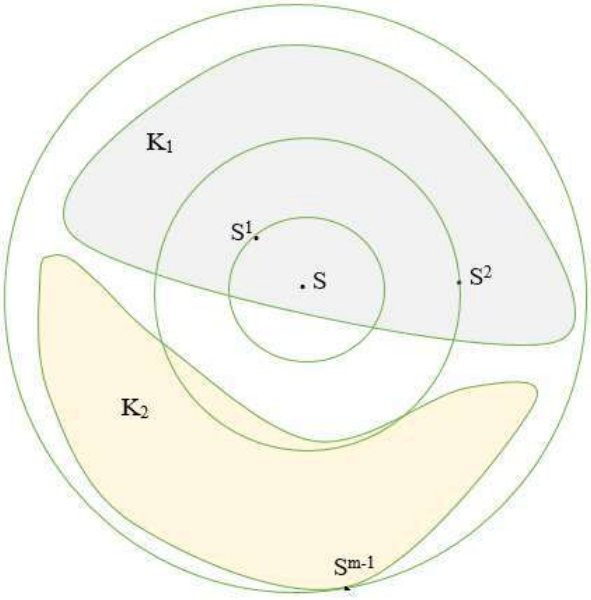

Figure 1. Sequence of nested hyperballs

Let the boundaries of the intervals $[c_1,c_2]$, $(c_2,c_3]$, $c_1=\rho(S,S)=0$ be defined at (1) in respect with CR1. Estimate of compactness of the object $S\in K_p$ by the set of attributes $X(h)\subset X(n)$ is calculated as

$$\varphi(S,X(h))=\theta_1(1-\theta_2), \tag{2}$$

where

$$\theta_1=\frac{\left|\left\{S^i\in K_p \middle| \rho\left(S,S^i\right)\in[c_1,c_2]\right\}\right|}{\left|K_p\right|}, \qquad \theta_2=\frac{\left|\left\{S^i\in K_{3-p} \middle| \rho\left(S,S^i\right)\in[c_1,c_2]\right\}\right|}{\left|K_{3-p}\right|}.$$

As a means to reduce combinatorial complexity when searching for logical regularities in [8], it is offered to use hierarchical grouping methods. It is noted how important a choice of the first step for such search for patterns is.

How these hierarchical agglomerative grouping methods are implemented depends on the rules used in them. Let $\varphi(X(h),S_i)$ be the compactness estimate (2) of the object $S_i\in E_0$ на $X(h)$. When forming the set $X(h+1)$ of $X(h)$ it is necessary to calculate

$$R\left(X\left(h+1\right)\right)=\frac{1}{m}\sum_{i=1}^{m}\begin{cases}1, \varphi\left(X\left(h+1\right),S_i\right)\geq\varphi\left(X\left(h\right),S_i\right),\\ 0, \varphi\left(X\left(h+1\right),S_i\right)<\varphi\left(X\left(h\right),S_i\right).\end{cases} \tag{3}$$

The condition (rule) for adding a attribute $x_j\in X(n)\backslash X(h)$ in $X(h+1)$ is:

$$R\left(X\left(h\right)\cup\left\{x_j\right\}\right)>\frac{1}{2} \quad u \quad R\left(X\left(h\right)\cup\left\{x_j\right\}\right)=\max_{x_i\in X(n)\backslash X(h)}R\left(X\left(h\right)\cup\left\{x_i\right\}\right). \tag{4}$$

The group (set) $X(h)$ is considered as formed if the attribute $x_j\in X(n)\backslash X(h)$, for which (4) holds true, does not exist.

One peculiarity of Bigdata methods is analysis of data samples in which the number of attributes is greater than or equal to the number of objects. The number of groups into which the set of attributes $X(n)$ is decomposed by (4) is initially unknown. It has been experimentally proved in [9] that, when majority rules in hierarchical agglomerative grouping are used, the informativeness of each subsequent group of attributes is less than that of a preceding one. Group formation sequence is determined by the principle of dynamic programming. For this reason, composition of attributes of the first group is considered as an informative set.

As the first step in selecting an informative set of attributes, it is proposed to choose a subset $Y\subset X(n)$ consisting of one or two attributes. The subset Y shall satisfy the following requirement:

$$B(Y)=\max_{\{i,j\}\in X(n)}\sum_{d=1}^{m}\left|\left\{S_j\in K_p \middle| \rho\left(S_j,S_d\right)<R, \qquad R=\min_{S_c\in K_{3-p}}\rho\left(S_c,S_d\right)\right\}\right|. \tag{5}$$

4. Computation experiment

Let us review the results of decomposition of quantitative attributes into disjoint intervals with respect of the CR1 and CR2 criteria on a data sample from [10].

The sample consists of two classes - K_1 and K_2 - and contains data on cardiovascular diseases. The description of objects is given by the following set of attributes $X(13)=(x_1,\ldots,x_{13})$. Number of objects of class K_1 is 150, ones of class $K_2$is 120. x_1, x_4, x_5, x_8, x_{10}, x_{11}, x_{12} are quantitative attributes, while x_2, x_3, x_6, x_7, x_9, x_{13} are nominal. The nominal attributes x_2, x_6, x_9 have two gradations (i.e., number of gradations of a attribute is equal to number of classes).

The compactness of the quantitative attributes from $X(13)$ and the limits of the CR1 intervals are given in Table 1.

The product of intraclass similarity and interclass difference is used to compute nominal attribute weights (as well as quantitative attributes compactness) by CR1. If the values of gradations in the description of objects of each class do not intersect each other, then the weight of the nominal attribute equals to 1. Table 2 shows the values of all six nominal attributes.

Table 1. Interval boundaries and values of compactness by CR1.

Attribute	Attribute Information	Interval boundaries	Compactness
x_1	Age	[29..54] (54..77]	0.2871
x_4	Resting blood pressure	[94..135] (135..200]	0.2548
x_5	Serum cholestoral in mg/dl	[126..252] (252..564]	0.2684
x_8	maximum heart rate achieved	[71..147] (147..202]	0.3413
x_{10}	Oldpeak = ST depression induced by exercise relative to rest	[0..1.6] (1.6..6.2]	0.3177
x_{11}	The slope of the peak exercise ST segment	(1..2] (2..3]	0.3246
x_{12}	Number of major vessels (0-3) colored by flourosopy	[0..1] (1..3]	0.3772

Table 2. Nominal attribute weights.

Attribute	Attribute Information	Weight
x_2	Sex	0.2727
x_3	Chest pain type (4 values)	0.3203
x_6	Fasting blood sugar > 120 mg/dl	0.1873
x_7	Resting electrocardiographic results	0.2762
x_9	Exercise induced angina	0.3453
x_{13}	Thal: 3 = normal; 6 = fixed defect; 7 = reversable defect	0.4193

As is seen from the Table 1 and Table 2, the compactness of quantitative (attributes) by CR1 and the values of nominal attribute weights are very different from the ideal ones. The value of quantitative attribute within the disjoint interval by CR1 can be considered as a gradation (interval number) in the nominal measurement scale. In such a description of objects the attribute weight in nominal scale will coincide with the value of compactness in respect with the CR1 criterion.

The number of disjoint intervals and the stability of the decomposition by the CR2 criterion are given in the Table 3 below.

Table 3. Attribute stability and interval boundaries by CR2.

Attribute	Interval boundaries	Stability
x_1	[29..54], [55..70], [71..76], [77..77]	0.6571
x_4	[94..122], [123..200]	0.5585
x_5	[126..160], [164..174], [175..245], [246..353], [354..394], [407..409], [417..564]	0.6309
x_8	[71..147], [148..194], [195..195], [202..202]	0.7030
x_{10}	[0..0.8], [0.9..6.2]	0.6957
x_{12}	[0.. 0], [1..3]	0.7316

As is seen from the Table 1 and Table 3, relatively high values of compactness are obtained for the attribute x_{12}.

Table 4 gives information about decomposition of latent attributes into two intervals obtained from the operations of multiplication and division of values of initial attributes.

Analysis of the results from the Table 4 and Table 1 shows that it is in fact feasible to search hidden patterns by latent attributes, the compactness of which is higher than each of the initial attributes that make up their composition.

Let a set of indices of respective quantitative and nominal attributes in the set $X(n)$ be designated by I, J . In order to unify the measurement scales, we will display the values of quantitative attributes by a linear fractional transformation in [0; 1]. The Zhuravlev metric will be used as a measure of the distance between the objects S_u, $S_v \in E_0$ ($S_c=(a_{c1},\ldots,a_{cn})$, $c=1,\ldots,m$) for selection of informative attributes

$$\rho(S_u, S_v) = \sum_{i \in I} |a_{ui} - a_{vi}| + \sum_{i \in J} \begin{cases} 1, a_{ui} \neq a_{vi}, \\ 0, a_{ui} = a_{vi}. \end{cases}$$

Table 4. Interval boundaries for latent attributes and compactness values by CR1.

Latent attribute	Interval boundaries	Compactness
x_4*x_9	[-192..105] (105..200]	0.3552
x_8*x_9	[-202..-115] (-115..186]	0.3718
x_{10}*x_{11}	[1..3.3] (3.3..21.6]	0.3684
x_2/x_8	[-0.0104..0.0067] (0.0067..0.0140]	0.3597
x_8/x_{10}	[16.8182..66.6667] (66.6667..202]	0.3726
x_8/x_{11}	[32..75] (75..202]	0.3555
x_9/x_4	[-0.0106..-0.0062] (-0.0062..0.0106]	0.3504
x_9/x_8	[-0.0140..0.0061] (0.0061..0.0113]	0.3523
x_{10}/x_8	[0.0049..0.0149] (0.0149..0.0594]	0.3726
x_{11}/x_8	[0.0049..0.0132] (0.0132..0.0312]	0.3555

The first pair of attributes added to the informative set in (5) is (x_8, x_{13}). The process of stepwise selection of attributes according to (4) is shown in the Table 5.

Table 5. Stepwise selection of informative attributes according to (4).

Number of attributes h in set	Attribute added in $X(h\text{-}1)$	Value $R(h)$ acc. to (3)
3	x_{10}	0.6926
4	x_{12}	0.6815
5	x_5	0.6852
6	x_9	0.6185
7	x_4	0.6222
8	x_3	0.6111

As a result of stepwise selection (see the Table 5) the informative set of attributes $X(8)=(x_3,x_4,x_5,x_8,x_9,x_{10},x_{12},x_{13})$ is obtained.

5. Conclusions

Two interval methods have been offered to analyze the structure of relations between objects of disjoint classes by quantitative initial and latent attributes. Numerical estimates of the structure of relations by these methods differ in that the number of disjoint intervals can be initially known or determined by the algorithm. The rule of hierarchical agglomerative grouping for the formation of an informative attribute set has been described.

The considered methods are recommended to be used to search for hidden patterns in data when developing information models based on knowledge.

6. References

[1] Ignatyev N A 2018 Structure Choice for Relations between Objects in Metric Classification Algorithms *Pattern Recognition and Image Analysis* **28** 590-597

[2] Zagoruiko N G, Kutnenko O A, Zyryanov A O and Levanov D A 2014 Learning to recognize patterns without retraining *Machine Learning and Data Analysis* **1** 891-901

[3] Goodfellow I, Bengio Y and Courville A 2016 *Deep Learning* (Cambridge: MIT Press) p 652

[4] Zguralskaya E N 2018 Stability of data partitioning into intervals in the tasks of recognition and the search for hidden patterns *Proceedings of the Samara Scientific Center of the Russian Academy of Sciences* **4** 826-829

[5] Zguralskaya E N 2012 Selection of informative features for solving classification problems using artificial neural networks *Neurocomputers: development, application* 20-27

[6] Ignatyev N A 2011 Calculation of generalized indicators and data mining *Automation and Remote Control* 183-190
[7] Saidov D Y 2017 Data visualization and its proof by compactness criterion of objects of classes *International Journal of Intelligent Systems and Applications (IJISA)* **9** 51-58
[8] Duke V A 2005 *Methodology of the search for logical laws in the subject area with fuzzy systemology: an example of clinical and experimental studies* URL: https://dlib.rsl.ru/viewer/01002930373#?page=1
[9] Madrakhimov Sh 2018 Calculation of the Generalized Estimations in Sets of Features and their Interpretation *International Journal of Software Engineering and Its Applications* **12** 29-38
[10] UCI repository of machine learning databases URL: http://archive.ics.uci.edu

Using Models of Parallel Specialized Processors to Solve the Problem of Signal Separation

V A Zasov[1]

[1]Samara State Transport University, Svobody street, 2B, Samara, Russia, 443066

e-mail: vzasov@mail.ru

Abstract. This paper considers models of highly efficient specialized processors used for parallel data processing as part of solving the problem of extracting individual signals from an additive mixture of several signals. The proposed models of recursive, nonrecursive, and regularization-based parallel specialized processors provide versatility in solving the problem of signal separation with various algorithms. An advantage of regularization-based processors is that they make the solution stable under conditions where the parameters of objects exhibit expected uncertainty when the inverse problem of signal separation is ill-posed. This paper presents the results we obtained from an asymptotic analysis of the computational complexity involved. The results identify the time it takes to solve problems by using specialized processors. The paper also identifies the conditions for the efficient use of specialized processors.

1. Introduction

The problem of signal separation consists in determining source signals unavailable for direct measurements by using source signals measured in accessible points where the signals are an additive mixture of source signals that are distorted when transmitted.

The computational complexity of algorithms involved in solving that problem is high and, for many applications, is of $O(N^3)$ order, where N is the number of signal sources [1]. This makes it difficult to use these algorithms.

Computation parallelization is the conventional approach to reducing the time it takes to solve the problem of signal separation [2,3]. Parallel algorithms for signal separation have been developed for multicore processors, multiprocessor systems with shared and distributed memory, and multicomputer systems [4]. That solution is needed in many practical fields such as monitoring and diagnosis of technical facilities [5], communications, medical diagnosis, speech [6] and image [7] processing.

This is because in complicated facilities, measured signals present an additive mixture of signals received from many components, and in most practical applications the extraction of parameters that describe the state of specific components is impossible without signal separation.

The next significant performance improvement is possible through the use of specialized processors whose architecture and computational processes correspond most to the structure of the algorithm for the class of problems in question [1,8].

Signal separation methods can be classified into two groups—deterministic and statistical [1].

The deterministic group is based on principal information about signal transmission channels (statistical, frequency, amplitude, and other channel characteristics); that is, transmission channels and

signals are known.

The statistical group is based on principal information about signal sources such as lacking source correlation and the knowledge of signal distribution laws. In this case, explicit information about transmission channels is unavailable, and only observed signals are known. For that reason, the methods within this group are often called “blind” [9].

Thus, the solution to the problem of separating of signal sources reduces to using a deterministic or statistical method to calculate the separating matrix equal or close, in terms of specific criteria, to the matrix inverse to mixing matrix.

The functionality of commercially available specialized digital signal processors and field-programmable gate arrays is insufficient for solving the complex problem of signal separation.

Reference [10] only proposes basic signal-separation functions and objectives for specialized processors used for signal separation and restoration; and for the processor models described in [11], the analysis of the computational complexity involved in parallel processing is inadequate to identify the conditions for the efficient use of the processors.

It is advisable that the structure of specialized processors should be regular and have a neural network architecture [12]. Besides, those processors do not provide stable solutions under conditions where the properties of objects exhibit expected uncertainty when the inverse problem of signal separation is ill-posed.

The purpose of this paper is to develop parallel specialized processors for signal separation under conditions where the parameters of objects exhibit expected uncertainty and to analyze asymptotically the computational complexity of parallel processing to identify the conditions for the efficient use of the processors.

2. Research Area

Since there are many algorithms for solving the problem of signal separation [1,9-13], parallel specialized processors should provide versatility in this class of problems. We will assume that the processor model consists of two units: the generic unit, which carries out the algorithm’s procedure steps; and the specialized unit, which provides structural simulation for the algorithm.

Let us assume that the model of signal formation is a linear multidimensional system with N inputs and M outputs [1,14]. The model’s input signals are $s_n(k)$, $n=1,2,...,N$; its output signals, $x_m(k)$, $m=1,2,...,M$. The input signals come from a variety of sources unavailable for direct measurement, and the output signals come from various receivers such as detectors and antennas. We will assume that each output M is linked with all the N inputs through linear signal-transmission channels.

The mathematical model of signal formation is described by discrete-convolution equations (1), where the mth observable signal is the additive mixture of channel-distorted source signals and noise [1,14] - that is,

$$x_m(k)=\sum_{n=1}^{N}\sum_{g=0}^{G-1}h_{mn}(g,\mathbf{I})s_n(k-g)+y_m(k), \tag{1}$$

where $h_{mn}(g,\mathbf{I})$ is the element $N\times M$ of the mixing matrix $\mathbf{h}(g,\mathbf{I})$ for the channels’ pulse responses; $\mathbf{y}(k)$ is the noise vector; $g=0,...,G\text{-}1$ and $k=0,...,K\text{-}1$ are the samples of the pulse responses for channels and signals, respectively.

Let us assume that the channels’ pulse responses $h_{mn}(g,\mathbf{l})$ are finite and that they depend on a certain parameter vector, $\mathbf{l}$ (time, locations of sources and receivers in relation to one another, etc.) [14].

Generally, the solution to the problem of separating source signals is (1), and it can be written as

$$\hat{s}_n(k)=\sum_{m=1}^{M}\sum_{g=0}^{G-1}w_{nm}(g,I)x_m(k-g), \tag{2}$$

where $w_{nm}(g,I)$ are the pulse responses of separating filters, and they form the separating matrix

$\mathbf{w}(g,\mathbf{I})$, which is equal or close to a matrix inverse to the matrix $\mathbf{h}(g,\mathbf{I})$.

In separating signals by source, we will split the computation into two steps.

In step 1, the elements $w_{nm}(g,I)$ of separating matrix $\mathbf{w}(g,\mathbf{I})$ are determined from the measured dynamical properties of channels or from signal parameters, and the signal-separation algorithm is adjusted. The algorithm for computing $w_{nm}(g,I)$ (the adjustment algorithm) takes into account the nuances of the given signal-separation algorithm.

In step 2, the signals are separated with the digital separating filters adjusted in step 1. This computational process is the same for different signal-separation algorithms.

With this in mind, we will look at two computational units in the model of a parallel specialized processor: the adjusting processor (AP) (the versatile unit) and the functional processor (FP) (the specialized unit).

The nonrecursive, recursive and regularization-based processor models treated below differ in the methods used to solve (1) but feature the same basic elements that the models are based on.

3. Model for a Nonrecursive Parallel Specialized Processor

The model for the nonrecursive parallel specialized processor implements the method used to solve the system of equations (1) by inversing the mixing matrix $\mathbf{h}(g,\mathbf{I})$.

The nonrecursive processor model [10,11] is best written in the form convenient for parallel stream processing in the time domain:

$$\hat{s}_1(k)=\sum_{m=1}^{M}\sum_{g=0}^{G-1}w_{1m}(g,I)x_m(k-g)$$

$$\ldots\ldots\ldots\ldots\ldots\ldots\ldots\ldots\ldots\ldots\ldots\ldots\ldots\ldots\ldots ,$$

$$\hat{s}_N(k)=\sum_{m=1}^{M}\sum_{g=0}^{G-1}w_{Nm}(g,I)x_m(k-g)$$

where $\hat{s}_1(k),\ldots,\hat{s}_N(k)$ are the calculated signals that are approximations (samples) of the true signals $s_1(k),\ldots,s_N(k)$ in the points they are formed in; and $w_{nm}(g,I)$ are the elements of separating matrix $\mathbf{w}(g,\mathbf{I})$ obtained from

$$w_{nm}(g,I)=\frac{1}{K}\sum_{k=0}^{K-1}W_{nm}(\omega_{\mathrm{g}},I)\cdot exp\left(i\frac{2\pi k\omega_g}{K}\right).$$

The frequency transmission factor $W_{nm}(\omega_g,I)$ is an element located at the crossing of the *n*th row and the *m*th column of the spectral matrix $\mathbf{W}(\omega_g,\mathbf{I})$, which is inverse of the $\mathbf{H}(\omega_g,\mathbf{I})$ matrix—that is, $\mathbf{W}(\omega_g,\mathbf{I})=\mathbf{H}^{-1}(\omega_g,\mathbf{I})$ at $M=N$ (or of the pseudo-inverse matrix $\mathbf{W}(\omega_g,\mathbf{I})=\mathbf{H}^{+}(\omega_g,\mathbf{I})$ at $M\neq N$).

The functional processor separates the source signals $x_m(k)$ according as they belong to the sources $s_n(k)$. This processor implements a model that is inverse of the signal-formation model, and the processor has the regular homogeneous structure composed of $N\times M$ adjustable filters (AF) and N adders (A).

The filters and the units compute linear convolutions simultaneously and independently of one another. The computational complexity $L_{FP}^{nonrec}(K)$ of the functional processor's operation algorithm, which determines the processing time, is characterized by the height of its parallel structure, is of $L_{FP}^{nonrec}(K)=O(K)$ order, and does not depend on the number of signal sources.

The adjustment processor calculates the coefficients $w_{nm}(g,I)$ for the AFs from the measurements of the channels' transient responses (deterministic methods) or from the characteristics of signal sources

(statistical separation methods) [9,13].

For deterministic methods, the algorithm used to compute the coefficients $w_{nm}(g,I)$ consists of the following steps: using a fast Fourier transform for the channels' transient responses to obtain the mixing spectral matrix $\mathbf{H}(\omega,\mathbf{I})$; inversing the spectral matrix $\mathbf{H}(\omega,\mathbf{I})$ to obtain the separating spectral matrix $\mathbf{W}(\omega,\mathbf{I})$; and using an inverse fast Fourier transform (IFFT) for the elements of separating matrix $\mathbf{W}(\omega,\mathbf{I})$ to obtain weight coefficients for the AFs, specified by the matrix $\mathbf{w}(g,\mathbf{I})$.

The parallel form of the adjustment algorithm's first and third steps has a width of $N \times M$ and is implemented by the $N \times M$ units of the fast Fourier transform and the inverse fast Fourier transform. The computational complexity $L_{AP1,3}^{nonrec}(G)$, which determines the time it takes to complete these steps depending on the heights of their parallel structures, is of $L_{AP1,3}^{nonrec}(G) = O(G \log_2 G)$ order.

The parallel form of the algorithm used to compute the separating matrix has a width of *G* and is implemented with *G* units for inversing *N* order matrices (assuming that *N*=*M*). Each of these units, in turn, implements the parallel form of the algorithm used to compute the inverting matrix (e.g., [3]) with a width of $O(N^4)$.

The height $L_{AP2}^{nonrec}(N) = O(\log_2^2 N)$ of the algorithm's parallel form determines the time it takes to invert the spectral matrix $\mathbf{H}(\omega,\mathbf{I})$.

The computational complexity $L_{AP1,2,3}^{nonrec}(G,N)$ of the adjustment processor's operation algorithm is significantly higher than the computational complexity $L_{FP}^{nonrec} = O(K)$ of the functional processor's operation algorithm—that is,

$$O(G \log_2 G) + O(\log_2^2 N) = O(G \log_2 G + \log_2^2 N) > O(K).$$

For instance, at $K \approx G \approx N$ the relation $\dfrac{L_{AP1,2,3}^{nonrec}(G,N)}{L_{FP}^{nonrec}(K)} \to \log_2 G$. Thus, separating signals with the proposed nonrecursive processor is acceptable if within the signal interval determined by $K \le G \log_2 G$ the parameters of the mixing matrix are assumed invariable—that is, if the signal-formation model is quasistationary.

Furthermore, given the polynomial relationship between the width $O(N^4)$ of the parallel form of the matrix-inverting algorithm and the number of signal sources, we can conclude that the model of the nonrecursive processor we discussed can be used in practice to separate the signals $s_n(k)$ when the number of signal sources is low.

4. Model for a Recursive Parallel Specialized Processor

Figure 1 shows a recursive parallel specialized processor model that implements the iteration method for solving the system of equations (1).

The model's functional processor (FP) has a regular homogeneous structure composed of *M* identical processing units (PU) [10,11]. All PUs operate parallel in time, and each implements the recursive algorithm for extracting one signal $\hat{s}_n(k)$ from an additive mixture of several signals.

The computational complexity $L_{FP}^{rec}(K\gamma)$ of the FP operation algorithm, which determines its operating time, is characterized by the height of its parallel form, is of $L_{FP}^{rec}(K\gamma) = O(K\gamma)$ order (where γ is the number of iterations), and does not depend on the number of signal sources.

The adjusting processor (AP) consists of a clock unit (CU) and *M* groups of devices comprising an adjusting unit (AU) and a memory unit (MU). The pulse responses of the filters FP_{mn}, $n = 1,...,N$, and $m = 1,...,M$ (note the exclusion of $m \ne n$) need not be calculated with the AP since the frequency characteristics of AF_{mn} filters are equal to the frequency characteristics of channels with related indexes

in the mixing matrix $\mathbf{H}(\omega,\mathbf{I})$ of the signal-formation model. These characteristics should only be stored in MU_m, $m=1,...,M$.

The transient responses $\tilde{h}_{11}(g),\tilde{h}_{22}(g),...,\tilde{h}_{MN}(g)$, $g=0,...,G-1$ of the adjustable inverse filters AIFmn (only if $m=n$) are computed in AU_m, $m=1,...,M$.

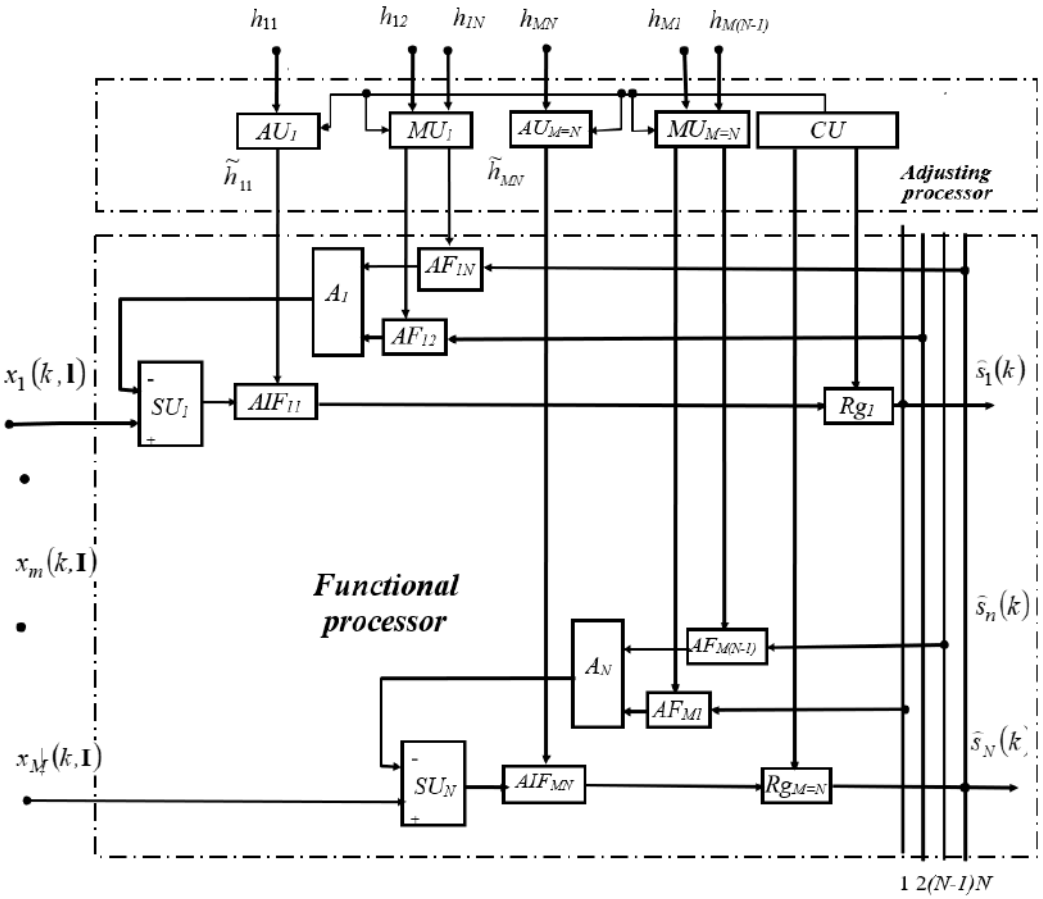

Figure 1. Model for a recursive parallel specialized processor (*N*=*M*).

The algorithm for computing $\tilde{h}_{mn(m=n)}(g,I)$ consists of the following steps: using a fast Fourier transform for the transient responses of the channels $h_{mn(m=n)}(g,I)$ to obtain the characteristics $H_{mn}(\omega_g,I)$; computing $\tilde{H}_{mn}(\omega_g,I)=\dfrac{1}{H_{mn}(\omega_g,I)}$; and using a fast Fourier transform for the characteristics $\tilde{H}_{mn}(\omega_g,I)$ to obtain the weight coefficients $\tilde{h}_{mn(m=n)}(g,I)$ for AIFs.

The parallel form of the adjustment algorithm's first and third steps has a width of N and is implemented by *N* FFT and IFFT units.

The computational complexity $L^{rec}_{AP1,3}(G)$, which determines the time it takes to complete these steps depending on the height of their parallel form, is of $L^{rec}_{AP1,3}(G)=O(G\log_2 G)$ order.

The parallel form of the algorithm used to compute the channels' inverse characteristics $\tilde{H}_{mn}(\omega_g,I)$ has a width of $O(N\times G)$ and is implemented with $N\times G$ division units, while the height

$L_{CU}^{rec}(N) = O(1)$ of the algorithm's parallel form is a constant.

The CU synchronizes the transmission of parameters from AP to FP, sets the initial conditions, and controls the output registers while completing processing iterations. This unit's operation algorithm has a constant complexity of $L_{CU}^{rec}(N) = O(1)$.

The assessment of the computational complexity of the AP and FP algorithms (e.g., at $K \approx G$),

$$\frac{L_{AP1,2,3}^{rec}(G)}{L_{FP}^{rec}(K)} = \frac{O(G\log_2 G) + O(1) + O(1)}{O(K\gamma)} \to \log_2 G,$$

for the recursive processor presents the conclusion that signal separation with the proposed recursive processor is acceptable for the quasistationary model of signal formation.

But the width of the AP algorithm's parallel form for the recursive processor is significantly lower than that of the nonrecursive one: $O(N \times G) \ll O(N^4 \times G)$.

This advantage of the recursive processor makes it possible to apply the solution to the problem of separating signals $s_n(k)$ for many more sources under conditions where computational resources are limited.

For a recursive processor to separate signals steadily, the object must allow the receivers of signals to be installed such that in the linear superposition of signals at the outputs of each of the receivers, the signal from a specific source is predominant [1].

5. Model for a Regularization-Based Parallel Specialized Processor

If the parameters of the mixing matrix $\mathbf{H}(\omega,\mathbf{I})$ or of the source signals $\mathbf{s}(k)$ make the problem of signal separation ill-posed or if those parameters show expected uncertainty, then one should at once find a regularized, stable solution to (1) or its equivalent in the frequency domain.

The proposed model for a regularization-based specialized processor is based on the Tikhonov regularization [15].

Two conditions to the Tikhonov regularization are set in the processor model: the disparity minimization $\left\|\tilde{\mathbf{H}}\mathbf{s} - \tilde{\mathbf{x}}\right\| = \min_{\mathbf{s}}$, as in the least-squares technique (LST); and the minimization of the solution norm, $\|\mathbf{s}\| = \min_{\mathbf{s}}$, as in the Moore–Penrose pseudo-inverse of a matrix [16].

The solution $\mathbf{s}_\alpha$ contained in the processor provides the absolute minimum of the smoothing functional $F^\alpha[\mathbf{s}]$ expressed as

$$F^\alpha[\mathbf{s}] = \left\|\tilde{\mathbf{H}}\mathbf{s} - \tilde{\mathbf{x}}\right\|^2 + \alpha\Omega[\mathbf{s}],$$

where $\alpha > 0$ is the regularization parameter; $\Omega[\mathbf{s}_\alpha]$ is the stabilizing functional; and $\tilde{\mathbf{H}}$ and $\tilde{\mathbf{x}}$ are approximate values of $\mathbf{H}$ and $\mathbf{x}$ for which

$$\left\|\tilde{\mathbf{H}} - \mathbf{H}\right\| \le \xi_{\mathbf{H}} \text{ and } \left\|\tilde{\mathbf{x}} - \mathbf{x}\right\| \le \delta,$$

where δ and $\xi_{\mathbf{H}}$ are the upper estimates of absolute measurement errors for the signals $\mathbf{x}$ and the mixing-matrix elements $\mathbf{H}$.

The proposed model uses $\Omega[\mathbf{s}_\alpha] = \|\mathbf{s}_\alpha\|^2$ as a stabilizing functional. For control purposes, it is more natural and convenient to present signals in time form, so we will write the smoothing functional for $M = N$ and $K = G$ as

$$F^\alpha[\mathbf{s}] = \sum_{m=1}^{M}\sum_{k=0}^{K-1}\left[\tilde{x}_m(k,\mathbf{I}) - x_m(k,\mathbf{I})\right]^2 + \alpha\sum_{n=m=1}^{N=M}\sum_{k=0}^{K-1}\left|\tilde{s}_{n,\alpha}(k)\right|^2. \quad (3)$$

The signal $\tilde{x}_m(k,\mathbf{I})$ in (3) derives from the separation results redistorted by the signal formation model; that is,

$$\tilde{x}_m(k,\mathrm{I}) = \sum_{n=1}^{N} \tilde{s}_{n,\alpha}(k) * h_{mn}(k,\mathrm{l}),$$

where $\tilde{s}_{n,\alpha}(k,\mathrm{I})$ are the regularized results of signal separation for the object's *n*th node.

Under the conditions described above, the smoothing functional can be written as

$$F^{\alpha}[\mathbf{w}] = \sum_{m=1}^{M}\sum_{k=0}^{K-1}\left[\hat{x}_m(k,\mathbf{I}) - x_m(k,\mathbf{I})\right]^2 + \alpha \sum_{n=m=1}^{N=M}\sum_{g=0}^{G-1}\left|\tilde{w}_{nm,\alpha}(g,\mathbf{I})\right|,^2$$

an expression that is more suitable for the regularized computation of the elements $\tilde{w}_{nm,\alpha}(g,\mathbf{I})$ for the separating matrix $\tilde{\mathbf{w}}_{\alpha}(g,\mathbf{I})$, which sets the weights of the functional processor's AFs.

The elements $\tilde{w}_{nm,\alpha}(g,\mathbf{I})$ for the selected regularization parameter α are determined from the minimum condition of the smoothing functional $F^{\alpha}[\mathbf{w}]$, keeping in mind that this functional's quadratic form is positively definite.

The elements $\tilde{w}_{nm,\alpha}(g,\mathbf{I})$ are calculable, for instance, by solving the system of $M \cdot N \cdot G$ equations written as $\dfrac{\partial F^{\alpha}(\tilde{w})}{\partial \tilde{w}_{nm}(g,\mathrm{l})} = 0$ relative to $\tilde{w}_{nm,\alpha}(g,\mathbf{I})$, using the parallel algorithms for solving linear algebraic equations [2,3].

For the known (specified) errors $\xi_{\mathbf{H}}$ and δ, we propose calculating the regularization parameter as the root of the equation

$$\left\|\tilde{\mathbf{H}}\mathbf{s}_{\alpha} - \tilde{\mathbf{x}}\right\|^2 = \left(\delta + \xi_{\mathbf{H}}\left\|\mathbf{s}_{\alpha}\right\|\right)^2 / \beta(r,M,N),$$

in which α is the parameter $\mathbf{s}_{\alpha}$, where $\beta(r,M,N) \geq 1$ is a scalable multiplier determined by the problem's dimension ($M \times N$) and by the measurement error of signal and channel parameters (the error depends, in particular, on the resolution r of analog-to-digital conversion).

With the regularization parameter α so obtained, the smoothness and disparity of the solution for $\mathbf{s}_{\alpha}$ are acceptable for practical purposes.

Figure 2 shows the model of a regularization-based specialized processor.

The FP is a model that is inverse of the signal-formation model and that separates measured signals. This processor has a homogeneous structure and consists of AFs and AUs.

The computation of regularization parameter α and the adjustment of AFs, whose number is equal to M^2, are run by the AP. The AP's processing unit (PU) computes AF parameters with the least-squares technique through minimizing the smoothing functional $F^{\alpha}[\mathbf{w}]$.

The elements of the mixing matrix $\mathbf{h}(g,\mathbf{I})$, which set the samples for the pulse responses of the signal-formation model's channels, enter the inputs of the AP, and the AP generates a direct signal-formation model.

Disparity evaluation units (DEUs) compute the disparity χ_m^2 for each of the processor's *m* channels. The units receive signals delayed by delay units (DUs), which serve to delay signals from the processor inputs and signals from the outputs of the direct signal-formation model.

It is advisable to use deterministic parallel optimization algorithms [17] designed for multicore processors to minimize the smoothing functional $F^{\alpha}[\mathbf{w}]$.

All the AFs operate in parallel independently of one another. This makes the proposed processor fast and reliable.

The processor model shown in figure 2 is generalized to obtain stable solutions for system (1). For that reason, the model is highly complicated. For practical applications, it can be significantly simplified by using prior information about the signal-formation model (such as the presence of reference inputs [18]) or by using simpler and parallel regularization algorithms [19].

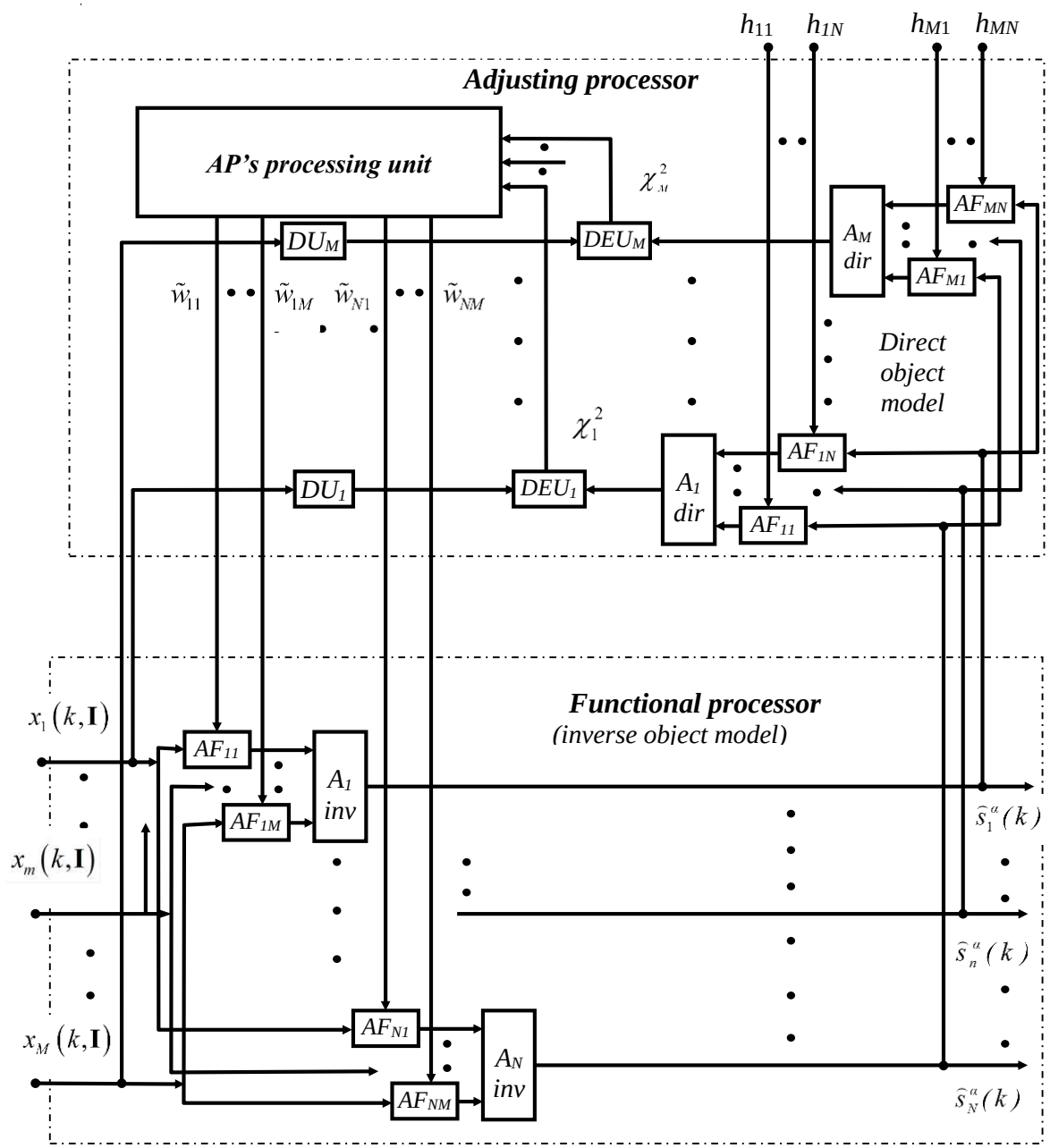

Figure 2. Model for a regularization-based parallel specialized processor.

6. Modeling Results

Figure 3 shows the modeling results for test signals separated by the nonrecursive parallel specialized processor with a multicore, GPU-based architecture.

The signal-formation model had three signal sources: the first two were triangular pulses with different frequencies and shapes while the third was a speech signal. The signal receivers used 8-bit ADCs with a sample rate of 12 kHz.

The figure 3 shows the initial signals (top), additive mixtures of signals in each of the receivers (middle), and extraction results for each signal (bottom).

The error of signal separation does not exceed 10%, a value acceptable for many engineering applications.

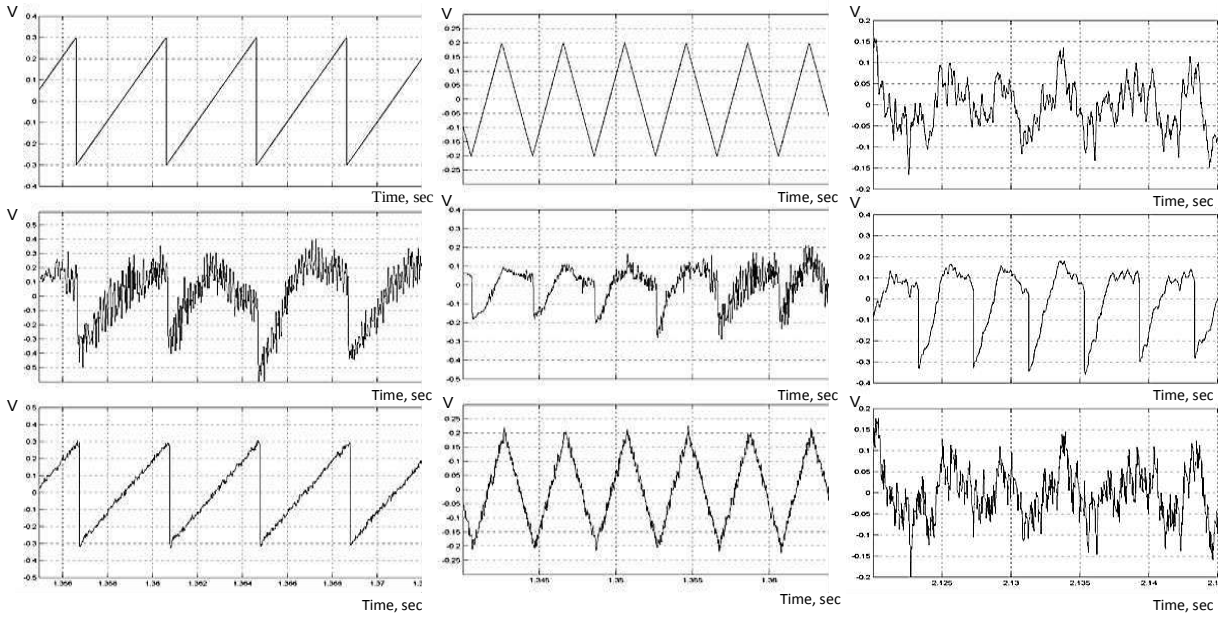

Figure 3. Modeling results for test signals separated with a nonrecursive parallel specialized processor.

The results of computational experiments shown in figure 4 for the example above show notably shorter task times (the Independent Component Analysis (ICA) [9] algorithm was used).

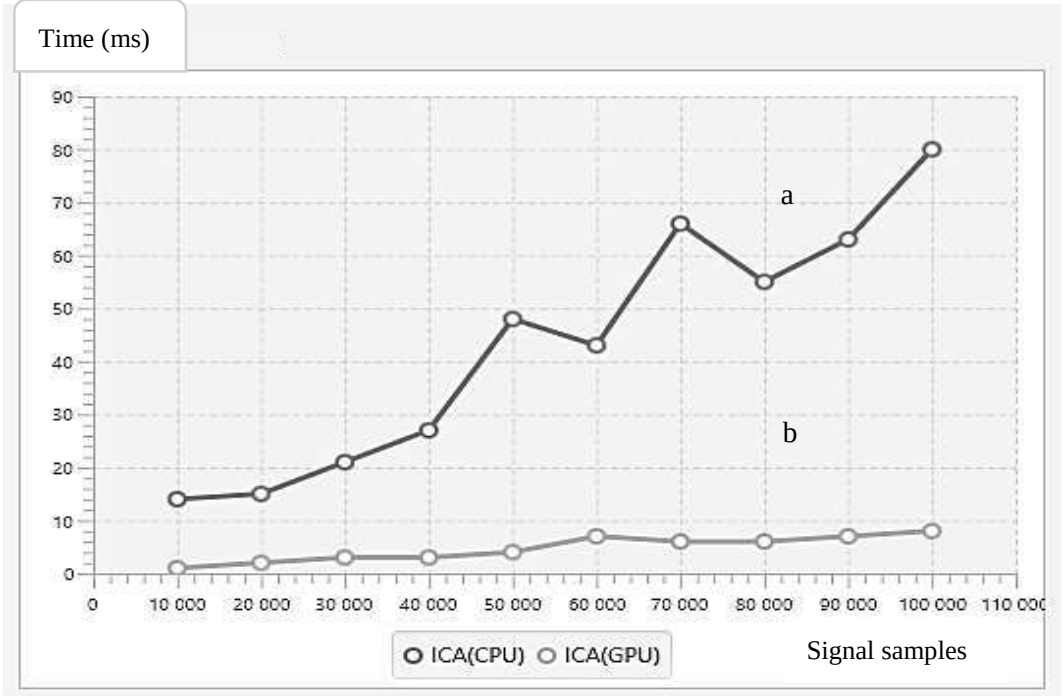

Figure 4. Experimental time–sample relationships for the problem of signal separation with a serial (a) and parallel nonrecursive specialized (b) processors.

7. Basic Conclusions

This paper proposed using models of highly efficient nonrecursive, recursive and regularization-based parallel specialized processors to solve the problem of signal separation.

Once adjusted, the processors can solve the problem within a period that does not depend on the number of signal sources—that is, the processors have a task time of $T_{FP}(N)=O(1)$ order.

These models are applicable where the parameters of the model-formation model are variable (quasistationary).

Regularization-based processors make the solution stable under conditions where the parameters of objects exhibit expected uncertainty when the inverse problem of signal separation becomes ill-posed.

The regular homogeneous structure of the functional processor can be conveniently implemented as an integrated circuit or a multicore-architecture computational system.

8. References

[1] Zasov V A 2013 *Algorithms and Computational Devices for Separating and Restoring Signals in Multivariable Dynamic Systems* (Samara: Samara State Transport University Press) p 233
[2] Gergel V P 2007 *Theories and Applications of Parallel Computations* (Moscow: IT Internet University: BINOM Knowledge Laboratory) p 423
[3] Demiyanovich Y K, Burova I G, Yevdokimova T O, Ivantsova O N and Miroshnichenko I D 2012 *Parallel Algorithms: Development and Implementation* (Moscow: IT Internet University: BINOM Knowledge Laboratory) p 344
[4] Patterson D A and Hennessy J L 2012 C*omputer Organization and Design* (Saint Petersburg: Peter) p 784
[5] Vasin N N and Diyazitdinov R R 2016 A machine vision system for inspection of railway track *Computer Optics* **40(3)** 410-415 DOI: 10.18287/2412-6179-2016-40-3-410-415
[6] Ifeachor E C and Jervis B W 2004 *Digital Signal Processing: A Practical Approach* (Moscow: Williams Publishing House) p 992
[7] Denisova A Y, Juravel Y N and Myasnikov V V 2016 Estimation of parameters of a linear spectral mixture for hyperspectral images with atmospheric distortions *Computer Optics* **40(3)** 380-387 DOI: 10.18287/2412-6179-2016-40-3-380-387
[8] Mitropolskiy Y I 1985 Problems of Versatile to Custom Tools Ratio in Computational Systems *Kibernetika i vychislitelnaya tekhnika* **1** 35-48
[9] Cichocki A and Amari Sh 2002 *Adaptive blind signal and image processing: Learning algorithms and applications* (New-York: John Wiley & Sons, Ltd) p 555
[10] Zasov V A and Romkin M V 2012 Parallel Computations for the Signal Separation Problem in Multidimensional Dynamic Systems *Parallel Computations and Management Objectives. Proc. of the 6-th Int. Conf.* (Moscow: Russian Academy of Science, Trapeznikov Institute of Control Science Press) 96-102
[11] Zasov V A and Romkin M V 2013 Parallel Computational Models for Solving the Problem of Signal Separation *Vestnik transporta Povolzhiya* **6(42)** 77-86
[12] Haykin S 2006 *Neural Networks: A Comprehensive Foundation* (Moscow: Williams Publishing House) p 1104
[13] Kravchenko V F 2007 *Digital Signal and Image Processing in Radiophysical Applications* (Moscow: Nauka, Fizmatlit) p 544
[14] Zasov V A and Nikonorov Ye N 2017 Modeling and Investigating the Stability of a Solution to the Inverse Problem of Signal Separation *CEUR Workshop Proceedings* **1904** 78-84
[15] Tikhonov A N and Arsenin V Y 1986 *Methods for Solving Ill-posed Problems: a Textbook for Universities* (Moscow: Nauka, Fizmatlit) p 288
[16] Tyrtyshnikov E E 2007 *Matrix Analysis and Linear Algebra* (Moscow: Nauka, Fizmatlit) p 480
[17] Strongin R G, Gergel V P, Grishagin V A and Barkalov K A 2013 *Parallel Computation in Global Optimization Problems* (Moscow: Moscow State University Press) p 285
[18] Dzhigan V I 2013 *Adaptive Signal Filtering: Theory and Algorithms* (Moscow: Tekhnosfera) p 528
[19] Zhdanov A I and Sidorov Y V 2015 Parallel implementation of a randomized regularized Kaczmarz's algorithm *Computer Optics* **39(4)** 536-541 DOI: 10.18287/0134-2452-2015-39-4-536-541

Orbital angular momentum acoustic modes demultiplexing by machine learning methods

D A Stankevich[1]

[1]Volgograd State University, Universitetskiy prt., 100, Volgograd, Russia, 400062

e-mail: stankevich@volsu.ru

Abstract. Orbital angular momentum (OAM) multiplexing is a promising method for MIMO multiplexing strategy. OAM multiplexing has previously been demonstrated for underwater acoustic communication, where data transmission was carried out within a single acoustic beam. Inner-product method is most often used for OAM demultiplexing, but it is sensitive to changes of signal parameters. For example, parameters changes can be associated with wave propagation through heterogeneous medium. I propose and demonstrate an approach using of machine learning methods to increase demultiplexing accuracy to 96% for non-stationary signals. In article presents experimental and numerical investigation results of proposed method.

1. Introduction

Allen [1] first showed that Laguerre-Gauss modes have an orbital angular momentum. Laser beams with an OAM are also called optical vortices. Optical vortices are used in quantum communication [2], particle manipulation [3], metrology [4], etc. A modern review of waves with OAM is given in [5].

The factor $\exp(il\varphi)$ is responsible for OAM, where φ is azimuth angle in a plane perpendicular to the beam axis, $l = 0, \pm 1, \pm 2, \ldots$ is topological charge. Thus, the energy flux vector describes a helicoidally surface in space, and beams with different l are characterized by a different distribution of the phase wave front.

Information coding using waves with different OAM consists in multiplexing several orthogonal modes in one beam [6]. This encoding method is widely used for free-space optics communication, where a record data transfer density has already been demonstrated [7]. In [8, 9], it is proposed to use waves with OAM for hydro-acoustic communication. For underwater applications increase data transmission rate due by expansion of the spectrum is made difficult by the strong attenuation of sound waves in water.

Decoding information from the spatial distribution of the wavefront is its division on orthogonal modes [6]. Usually demultiplexing is carried out by correlation methods [6, 8]. Their accuracy can be significantly reduced due to a change carrier frequency of the signal, for example, due to the Doppler effect, in case the receiver or transmitter moves. The machine learning methods could be used for synthesis of OAM demultiplexer when the carrier frequency is a priori unknown or varies. In addition, the amplitude and phase of acoustic wave depends on the temperature of the transmitters. This leads to additional phase front distortions.

2. Method of OAM wave demultiplexing

Arrange R receivers evenly around circumference with center on the beam axis. Then discrete samples of the signal from r-th receiver when registering a wave with l-th OAM can be represented as:

$$x_{rl}[n] = A_l \sin\left(2\pi f_0 n + \varphi_l + 2\pi \frac{rl}{R}\right). \quad (1)$$

Here I have introduced the following notation: n = 0, 1, 2, ..., N – 1, N is the number of samples in sample frame, f_0 is the dimensionless frequency normalized to sampling frequency f_d, φ_l is the initial phase of l-th mode. The amplitudes of the A_l signals are normalized so that the signal with several modes has same energy as the signal with a single mode.

Following [8], to encode an information symbol with a size of one byte, we will use the sum of helicoidal waves with l from –4 to 4:

$$x_r[n] = \sum_{l=-4}^{4} A_l \sin\left(2\pi f_0 n + 2\pi l \frac{r}{R} + \varphi_r\right) + \eta_r[n]. \quad (2)$$

The amplitude A_l is assumed to be zero if the corresponding bit is not set (see Figure 1). A wave with zero orbital momentum encodes a zero byte value.

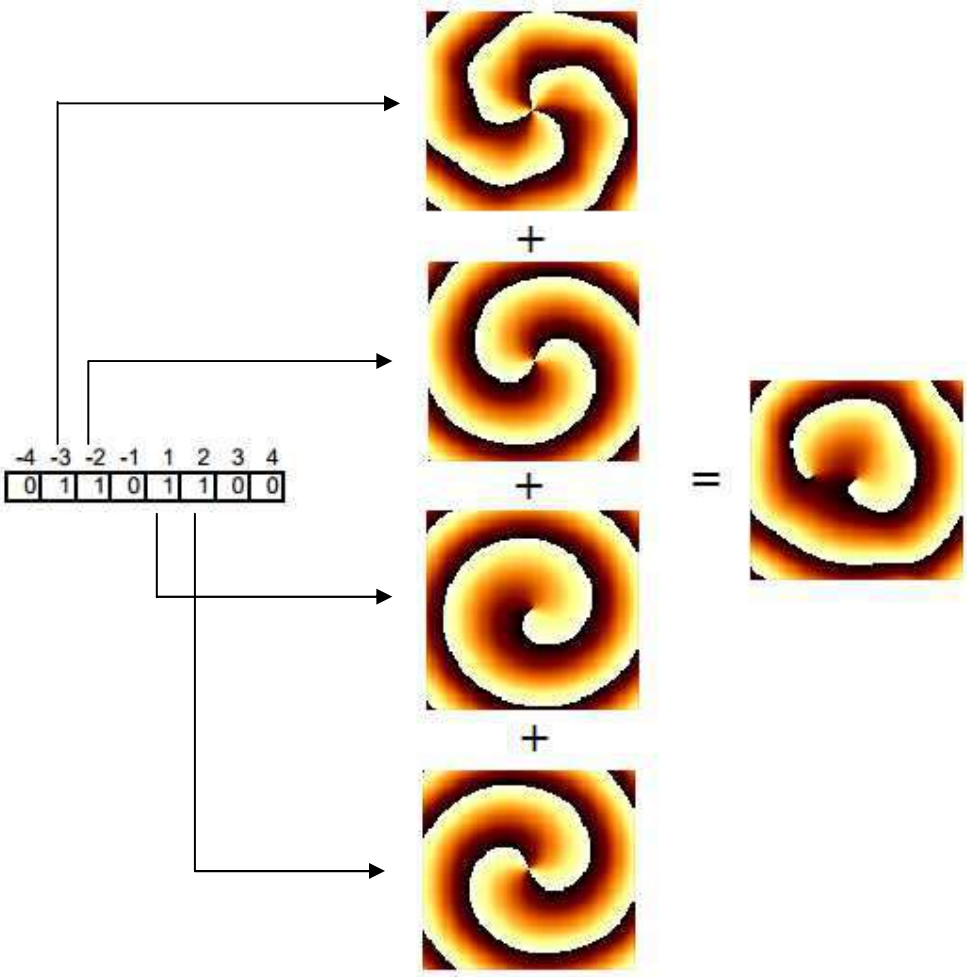

Figure 1. Multiplexing process of orthogonal modes for one byte.

A two-layer convolution network [10, 11] was used for OAM demultiplexing. A description of its architecture is given in Table 1 and shown on Figure 2. The first layer contains M = 10 convolution neurons that have R inputs:

$$y_m^{(1)}[n] = \mathrm{ReLU}\left(\sum_{r=0}^{R-1} \sum_{k=0}^{K-1} w_{mr}^{(1)}[k] x_r[k+n] + b_m^{(1)} \right),$$

Here $w_{mr}^{(1)}$, $b_m^{(1)}$ are weights and biases of first convolution layer. Input layer has nonlinear ReLU (rectified linear unit) activation function: ReLU(x) = max(0, x).

Table 1. Neural network architecture.

	Input layer	Output layer
Layer type	Conv1D	Dense
Neurons	10	8
Convolution kernel	10×1	–
Pooling	5×5 (Max)	–
Activation	ReLU	Sigmoid

Results thinning of input layer (pooling) is used to reduce the number of connections with output layer and to increase learning speed. The sequence from outputs of neuron filters is divided into disjoint intervals of 5 points, and the maximum value is selected at each interval.

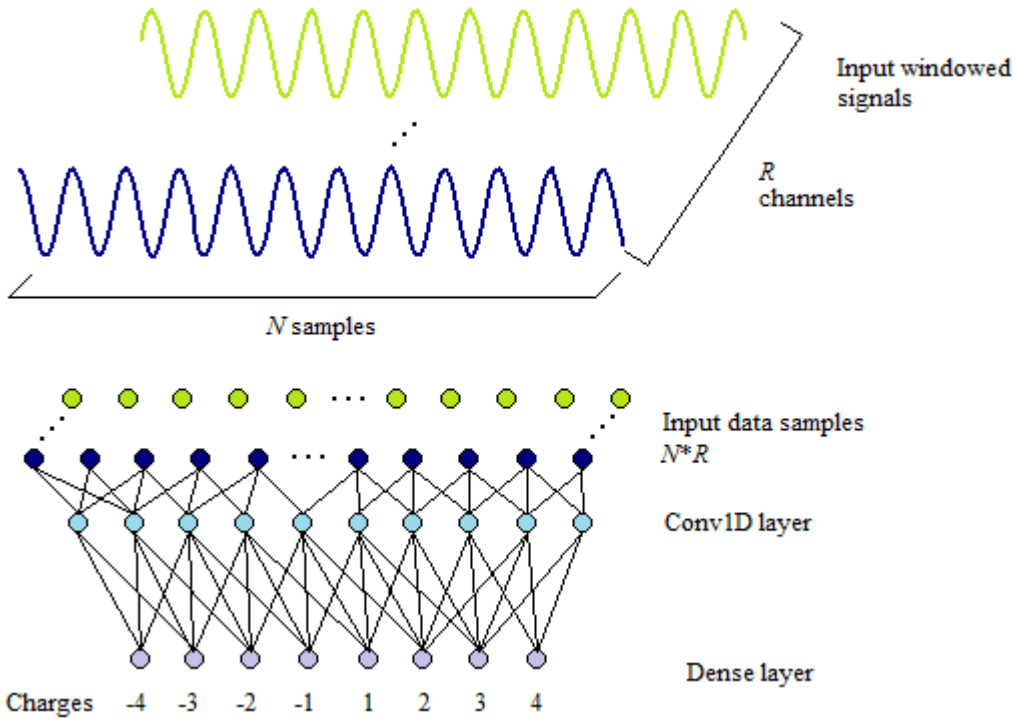

Figure 2. Architecture of the neural network.

Further, these data proceed to the output fully connected layer consisting of 8 neurons (q = 0 – 7) with a sigmoidal activation function:

$$\hat{p}_q = \left(1 + \exp\left(-b_q^{(2)} - \sum_{n=0}^{N-1}\sum_{m=0}^{M-1} w_{qnm}^{(2)} y_m^{(1)}[n]\right)\right)^{-1}$$

Thus, the activation ($\hat{p}_q > 0.5$) of output neuron q indicates the presence of a mode with given angular momentum. Note that several neurons can be activated.

The network weights are tuned in the learning process on a train set consisting of 2000 signals corresponding to different values of information symbols. Every signal consist N = 20 samples with additive normal noise with zero mean and dispersion σ^2, randomly selected from range 1.0 – 2.0. The initial phase and frequency of signals are uniformly distributed in range of 0 – 2π and 0.1 – 0.3, respectively.

Training is carried out by back-propagation error method with Keras [12] deep learning library. In the process of learning, consisting of 100 epochs, binary cross entropy was minimized with Adam [13] method. Training time on a 12-core Intel i7-3930K 3.2 GHz processor is less than 30 s.

The study of network characteristics was carried out on a different set, containing also 2000 signals. With a relatively low noise level (σ^2 = 0.1), ten receivers are enough to achieve 100% accuracy of demultiplexing (see Figure 3a). A similar result is achieved using the correlation method. Increasing noise variance by an order reduces accuracy, but it remains at level of 96%.

Accuracy of demultiplexing by the proposed method in a sufficiently wide frequency range (0.15 – 0.3) stay not lower than 91% (see Figure 3b). As opposed the correlation method loses significantly in accuracy when the signal frequency changes by 10%.

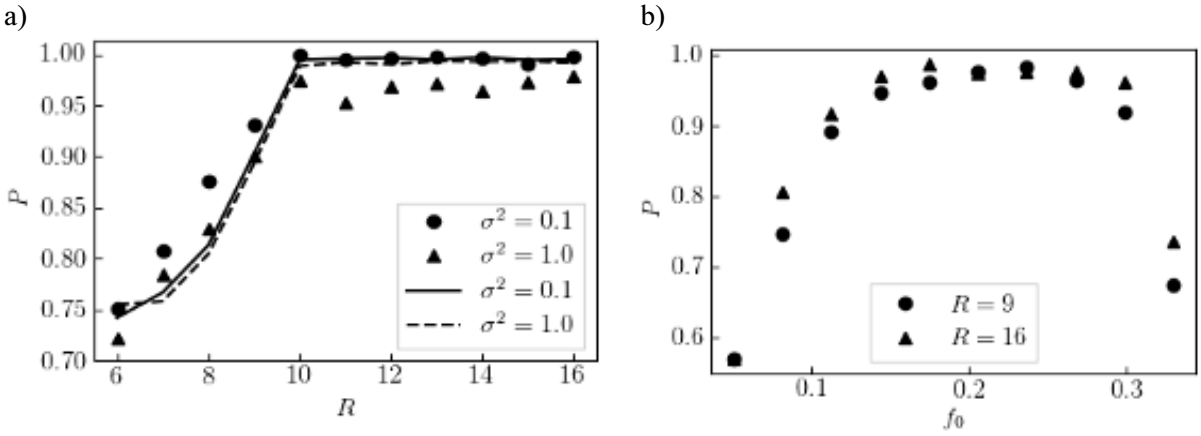

Figure 3. a) Demultiplexing accuracy dependencies P by receivers count R for neural net (circle and triangles) and for correlation method (line); b) demultiplexing accuracy dependencies P by carrier frequency f_0 of signal (σ^2 = 1.0).

3. Experimental results

An experimental setup was created to transmit information using two identical transducers array. Each array consisted of 7 piezoelectric transducers (type ZP-1) (see Figure 3). One array was connected to output of the sound card (UMC1820), and the other to its input. Transducers are placed into boxes from corrugated cardboard with a thickness of 4 mm. Noise insulation "Penolon" with a thickness of 10 mm is glued inside the boxes, and their internal volume is filled with cotton. The front panels are made of MDF and also covered with sound insulation (Figure 4). Piezo-transducers are mounted on a

round fiberglass board (1.6 mm thick and 164 mm in diameter), in which eight round holes of 36 mm in diameter are milled. Central transducer was not used in experiments.

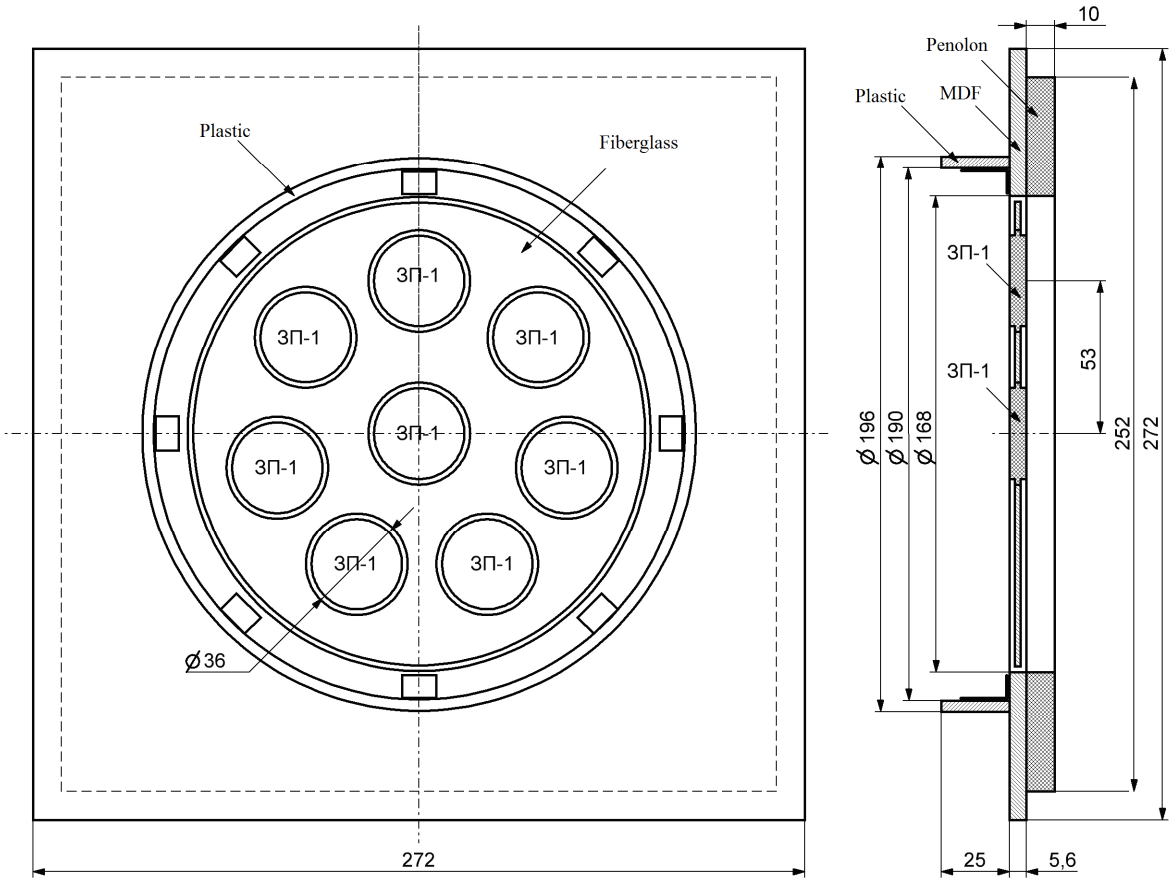

Figure 4. Transducers array front panels.

The Figure 5 shows the experimentally obtained pressure and phase distributions for waves with different topological charges. Since the amplitude-frequency response characteristic of the transducers differ, it is clear that the wave front is slightly different from the ideal helicoidal one. It is especially noticeable for higher order topological charges (see Figure 6). This circumstance required slightly different network architecture (Table 2) in order to achieve high accuracy.

Table 2. Modified neural network architecture for experiments.

	Input layer	Output layer
Layer type	Conv1D	Dense
Neurons	50	6
Convolution kernel	200×1	–
Activation	Leaky ReLU	Sigmoid

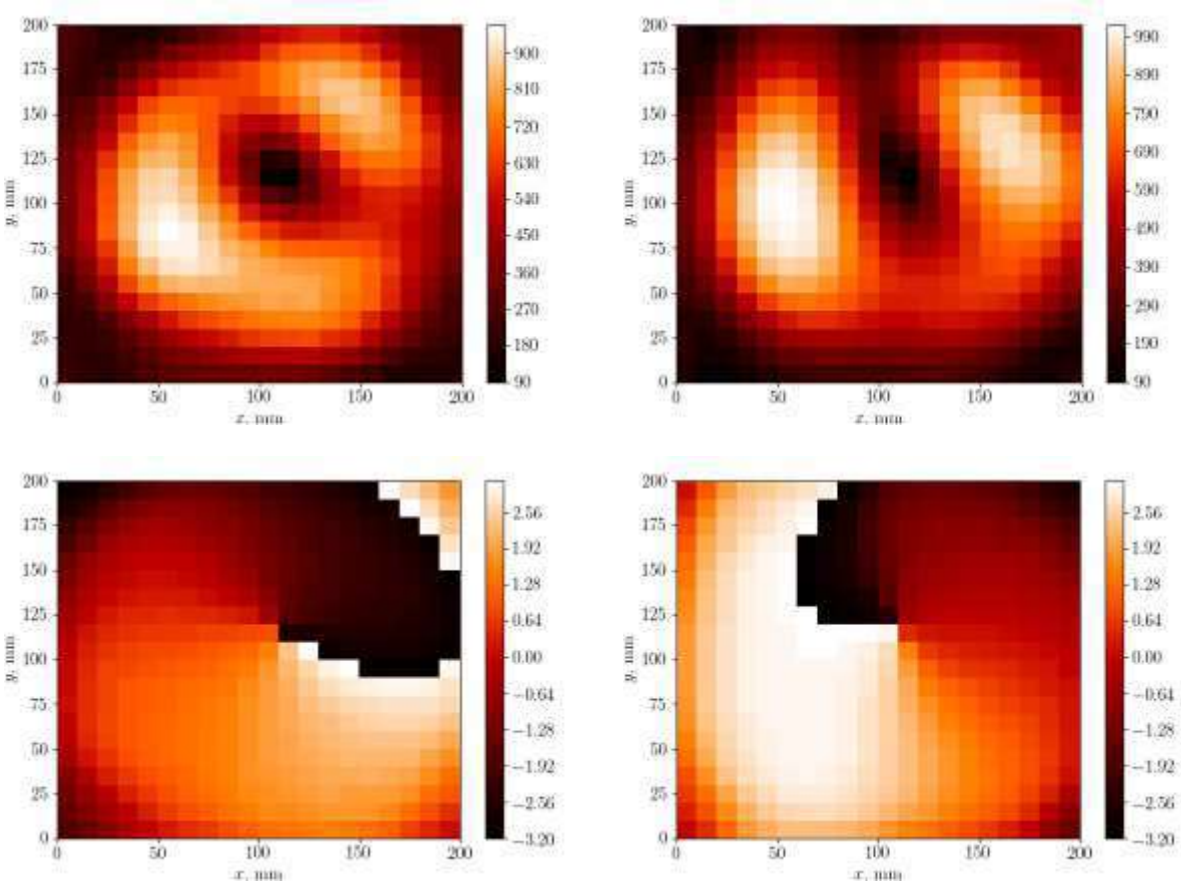

Figure 5. Experimental amplitude (top) and phase (bottom) of pressure distributions for waves with a topological charge +1 (left) and –1 (right).

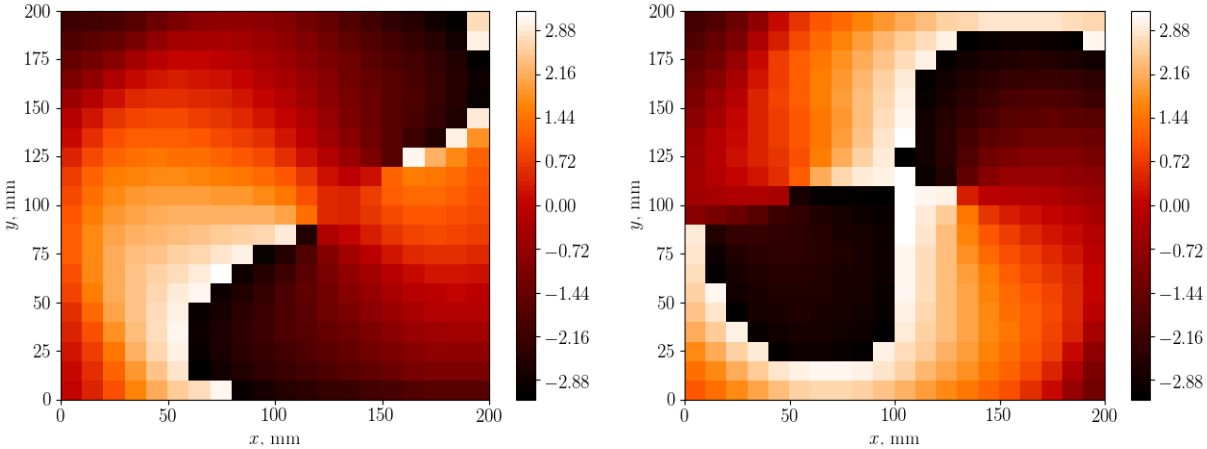

Figure 6. Experimental phase of pressure distributions for waves with a topological charge +2 (left) and –2 (right).

Real signals obtained in the experiment used for training. Each signals consisted of 400 samples. The training cycle consisted of two stages. At first, 20 signals with a random set of bits (training set) were transmitted. Then 10 signals were transmitted, according to which the accuracy of information transfer was assessed (test set).

The receiver and transmitter were located at a height of 0.5 m from the floor. Signal information (6 bits) transmits at a frequency of 2.3 kHz by topological charge coding with $l = -3...3$. The training consists of 100 cycles. At a distance of 2λ, accuracy of demultiplexing (using the developed neural network demultiplexer) was 100%, and at a distance of 17λ, it was 96%. Transmission accuracy is reduced primarily due to the presence of significant reflections from the walls and floor.

4. Conclusion

The paper presents results of numerical and experimental studies of neural network demultiplexing method for wave with orbital angular momentum. It is shown that proposed method gives a significant advantage over the classical correlation method. Usually systems using neural networks are not high performance. However, the small number of layers of the developed architecture makes it possible to solve the problem of demultiplexing on a simple signal processor.

5. References

[1] Allen L, Beijersbergen M W, Spreeuw R J C.and Woerdman J P 1992 Orbital angular momentum of light and the transformation of Laguerre-Gaussian laser modes *Phys. Rev. A* **45** 8185-8189 DOI: 10.1103/PhysRevA.45.8185

[2] Erhard M, Fickler R, Krenn M and Zeilinger A 2018 *Twisted photons: new quantum perspectives in high dimensions* (Light: Science & Applications) **7** 17146 DOI: 10.1038/lsa.2017.146

[3] Hong Z Y, Yin J F, Zhai W, Yan N, Wang W L, Zhang J and Drinkwater B W 2017 Dynamics of levitated objects in acoustic vortex fields *Scientific Reports* **7093** DOI: 10.1038/s41598-017-07477-1

[4] Yue Z, Ren H, Wei S, Lin J and Gu M 2018 Angular-momentum nanometrology in an ultrathin plasmonic topological insulator film *Nature Communications* **9** 4413 DOI: 10.1038/s41467-018-06952-1

[5] Chen R, Zhou H, Moretti M, Wang X and Li J 2019 Orbital Angular Momentum Waves: Generation, Detection and Emerging Applications *arXiv:1903.07818*

[6] Djordjevic I B 2017 Multidimensional OAM-Based Secure High-Speed Wireless Communications *IEEE Access* **17140317** 16416-16428 DOI: 10.1109/ACCESS.2017.2735994

[7] Li L, Zhang R, Zhao Z, Xie G, Liao P, Pang K, Song H, Liu C, Ren Y, Labroille G, Jian P, Starodubov D, Lynn B, Bock R, Tur M and Willner A E 2017 High-Capacity Free-Space Optical Communications Between a Ground Transmitter and a Ground Receiver via a UAV Using Multiplexing of Multiple Orbital-Angular-Momentum Beams *Scientific Reports* **7** 17427 DOI: 10.1038/s41598-017-17580-y

[8] Shi C, Dubois M, Wang Y and Zhang X 2017 High-speed acoustic communication by multiplexing orbital angular momentum *PNAS* **114(28)** 7250-7253 DOI: 10.1073/pnas.1704450114.

[9] Hefner B T, Marston P L 1999 An acoustical helicoidal wave transducer with applications for the alignment of ultrasonic and underwater systems *J. Acoust. Soc. Am.* **106(6)** 3313-3316 DOI: 10.1121/1.428184

[10] Goodfellow I, Bengio Y and Courville A 2016 *Deep learning* (MIT Press) p 775
[11] Bolotova Y A, Spitsyn V G and Osina P M 2017 A review of algorithms for text detection in images and videos *Computer Optics* **41(3)** 441-452 DOI: 10.18287/2412-6179-2017-41-3-441-452
[12] Dua R, Ghotra M S 2018 *Keras Deep Learning Cookbook: Over 30 recipes for implementing deep neural networks in Python* (Packt Publishing) p 252
[13] Kingma D, Ba J 2014 Adam: A Method for Stochastic Optimization *arXiv: 1412.6980*

Acknowledgment
This investigation was supported by the Russian Science Foundation, project no. 18-79-00080.

The implementation of "Kuznyechik" encryption algorithm using NVIDIA CUDA technology

A N Borisov[1] and E V Myasnikov[1]

[1]Samara National Research University, Moskovskoe Shosse 34A, Samara, Russia, 443086

e-mail: borisovalexey1996@gmail.com

Abstract. In this paper, we discuss various options for implementing the "Kuznyechik" block encryption algorithm using the NVIDIA CUDA technology. We use lookup tables as a basis for the implementation. In experiments, we study the influence of the size of the block of threads and the location of lookup tables on the encryption speed. We show that the best results are obtained when the lookup tables are stored in the global memory. The peak encryption speed reaches 30.83 Gbps on the NVIDIA GeForce GTX 1070 graphics processor .

1. Introduction

Cryptographic protection is an important part of a modern IT infrastructure. Nowadays, both the volume of information and computing power are continually increasing. Accordingly, there are growing demands on both the robustness and speed of cryptographic algorithms.

The idea of using graphics processors to speed up encryption algorithms appeared almost simultaneously with the idea of using them for general-purpose computing[1]. As known, the maximum profit from the use of graphics processors can be achieved only with massive parallel tasks. It is not surprising that the most noticeable results in this field were obtained for block encryption in the ECB (electronic code book) and CTR (gamming) modes, since the blocks of plain text are processed independently in this case.

At present, there is a lot of papers, which focuses on using graphics processors for encryption. Most of the papers are devoted to the AES encryption algorithm. In particular, in the paper [2], authors study the dependence of the encryption speed on the location of round keys. Experiments are carried out on NVIDIA GeForce GTX 780, NVIDIA GeForce GTX 1080 and NVIDIA GeForce Titan X graphics cards. In the paper [3], authors study popular block ciphers, namely, AES-128, CAST-128, Camelia, SEED, IDEA, Blowfish, and Threefish, using NVIDIA GeForce GTX 980. In both papers, the reported encryption speed exceeds 200 Gbit/s (25 GB/s).

The "Kuznyechik" cipher is a new symmetric encryption standard, which was introduced in Russia in 2015 [4]. By design, "Kuznyechik" is an SP-network with ten rounds of transformations, the size of a block equals to 128 bits, and the size of a key is 256 bits.

Because of a novelty and the limited use of chipher, fewer papers focus on the 'Kuznyechik" algorithm, most of them focuses on cryptoanalysis [5,6,7] rather than effective implementation of cipher. The paper [6] describes the optimization of the algorithm based on lookup tables.

The reported speed is 54 Mbps on a four-core CPU. The paper [7] is a direct continuation of the paper [6], which is devoted to the cryptanalysis of the "Magma" and "Kuznyechik" algorithms using CUDA to speed up a slide attack. The paper [8] describes the implementation of Kuznyechik cipher for FPGA using OpenCL, the reported troughput reaches 41 Gbit/s. In this paper, we study several possible implementations of the "Kuznyechik" cipher using the NVIDIA CUDA technology. The paper has the following structure. In Section 2, we givebrief theoretical foundations of the algorithm. In Section 3, we briefly discuss some features of the NVIDIA CUDA technology, which are necessary to understand this paper. Section 4 describes possible implementations of the cipher using the above technology. In Section 4, we provide the results of experiments. The paper ends up with the conclusion and reference list.

2. The description of the algorithm

As it was outlined earlier, the "Kuznyechik" algorithm is a ten-round cipher based on an SP network with the key length of 256 bits and the block length of 128 bits. An exhaustive description of the algorithm can be found in [4].

2.1. Key expansion algorithm

Before the encryption, ten 128-bit round keys $K_1, ..., K_{10}$ are generated based on the main 256-bit key K. The expansion procedure is a Feistel network. Its transformation function is analogous to the round of the main cipher with a fixed key. The first two round keys K_1, K_2 are obtained from the halves of the main one. The rest of the keys are obtained by encrypting with the Feistel network. The keys (K_{2i}, K_{2i-1}) are given to each round of the network as an input, and the output is (K_{2i+2}, K_{2i+1}).

The expansion procedure is strictly sequential. Besides, it can be executed only once to obtain the array of round keys. Thus, we do not consider this procedure in the paper.

2.2. Basic transformations

The cipher is based on two transformations:

(i) Nonlinear transformation $\pi : GF(2^8) \to GF(2^8)$ implemented through the lookup table.

(ii) Nonlinear transformation

$$\ell(a_{15}, ..., a_0) = 148 \cdot a_{15} + 32 \cdot a_{14} + 133 \cdot a_{13} + 16 \cdot a_{12} + 194 \cdot a_{11} + 192 \cdot a_{10} + 1 \cdot a_9 + \\ +251 \cdot a_8 + 1 \cdot a_7 + 192 \cdot a_6 + 194 \cdot a_5 + 16 \cdot a_4 + 133 \cdot a_3 + 32 \cdot a_2 + 148 \cdot a_1 + 1 \cdot a_0, \quad (1)$$

where $a_i \in GF(2^8)$, and operations take place in the field $GF(2^8)$. In particular, "+" is equivalent to the XOR operation).

The transformations that are used directly in the encryption are based on two previous transformations:

$$S(a) = S(a_{15}||...||a_0) = \pi(a_{15})||...||\pi(a_0), \quad (2)$$

$$R(a) = R(a15||...||a0) = \ell(a15, ..., a0)||a15||...||a1, \quad (3)$$

$$L(a) = R^{16}(a), \quad (4)$$

$$X[k](a) = k \oplus a, \quad (5)$$

where $||$ is the concatenation,
$a_i \in GF(2^8)$,
$k, a \in GF(2^{128})$,
$R^{16}(a)$ means that the R function is applied for a for 16 times.

Using the above notations, the "Kuznyechik" algorithm can be described as follows:

$$E_{K_1,...,K_{10}}(a) = X[K_{10}]LSX[K_9]...LSX[K_2]LSX[K_1](a), \quad (6)$$

where $LSX[K](a)$ is equivalent to $L(S(X[K](a)))$.

2.3. Lookup tables
It is easy to see that

$$\ell(a_{15}, ..., a_0) = \ell(a_{15}, 0, ..., 0) \oplus \ell(0, a_{14}, 0, ..., 0) \oplus ... \oplus \ell(0, 0, 0, ..., a_0), \tag{7}$$

$$\ell(a_{15} \oplus b_{15}, ..., a_0 \oplus b_0) = \ell(a_{15}, ..., a_0) \oplus \ell(b_{15}, ..., b_0). \tag{8}$$

Based on this, the LS part of the round can be predicted in advance, with the result that we get 16 lookup tables. Each of the lookup tables contains 256 entries of size 128 bit. When using lookup tables, the entire encryption process comes down to 16 lookups across tables and 16 128-bit XOR operations (15 on the search results and 1 with a round key).

3. CUDA

CUDA is a proprietary API provided by NVIDIA that facilitates the use of video cards for general purpose computing. This programming model is required since the graphics processor can process hundreds of threads simultaneously according to the so-called SIMT model. A detailed description of CUDA technology can be found in [9]. We provide only the necessary information below.

The kernel is a function intended for the execution on the GPU. The unit of execution is a thread. Threads are combined into blocks, and blocks are combined into a grid. The grid and block configuration is specified when the kernel function is started. Resources for execution are allocated per block, and not on every single thread.

From a hardware point of view, the graphics processor is divided into multiprocessors, and multiprocessors are divided into warps. The warps, in turn, consist of 32 stream processors (terminal computing units). All stream processors inside one warp are synchronized. They either execute the same instruction or idle.

The memory organization on graphics processors has a number of features. A programmer has access to a global, shared, constant, and texture memory. The global memory is equivalent to RAM. The texture memory and constant memory are the areas of global memory with special access features. The shared memory has low volume (64KB), but very high speed.

Physically, it is divided into several independent areas, called banks (banks). An attempt to simultaneously access different memory cells within one bank will lead to the subsequent execution of requests. This situation is called a bank conflict. A large number of access conflicts reduce performance significantly.

4. The implementation of "Kuznyechik" encryption algorithm using CUDA

We use lookup tables as a base for the implementation of the algorithm. At first, we execute an initialization procedure, which copies the tables to the device. Before encryption, we allocate buffers on the device. We use the allocated buffers to copy round keys and data to be transformed. We copy data back and release the buffers after the encryption. Encryption keys are best to store in the shared memory. The memory consumption is small, and the access pattern allows to avoid access conflicts (all threads of a warp always read the same key).

The issue of locating the lookup tables does not have such a straightforward solution. The size of the LS tables does not allow them to be entirely located in the shared memory since for the Pascal generation it is allowed to allocate only 48 KB per thread block. In addition, random access to the tables will result in numerous access conflicts, which significantly reduce performance. From this it follows that there are only three options for storing the tables, namely, the global, constant and texture memory. To provide an additional acceleration, we read the global memory using the $ldg()$ function.

In addition, we should also find out the optimal launch configuration of the kernel function. It does not make sense to use more than one thread per block of text. Although one XOR

operation for 128-bit values is translated into two 64-bit operations, the use of two threads to process one block of text will lead to undesirable consequences. First, an increase in the number of threads will lead to an overall decrease in simultaneously processed blocks of text, since the number of stream processors is limited. Second, since each thread needs to store its copies of local variables, the number of occupied registers will increase. This also becomes a limiting factor and reduces the amount of simultaneously processed blocks of text. However, it makes sense to study how the size of the block of threads affects the encryption speed.

In this paper, we consider the following sizes of a block: 32, 64, 128,192, 256, 384, 512, 768, and 1024 threads. There is no sense to consider less than 32 threads in a block since the minimum unit of execution on a graphics processor is a warp consisting of 32 stream processors.

5. Experimental results

We used the following configuration in our experiments:
CPU: Intel Core i5-6400
GPU: NVIDIA GeForce GTX 1070
RAM: 8 Gb DDR3

In general speed tests, the number of threads in a block was 512. The volume of encrypted data was equal to 256 MB in tests with changing block configuration. The CPU version of the "Kuznyechik" algorithm executed in 4 threads using SSE instructions. We did not take into account the time spent on copying data to the memory of the GPU and back.

The results of performance measurements are presented in Tables 1 and 2 and Figures 1 and 2 shows the results of the experiments.

Table 1. The dependence of the encryption speed on the data volume.

Data volume	Encryption speed (Gbps)			
	CPU	Global memory	Constant memory	Texture memory
1 KB	0.09	0.43	0.03	0.45
32 KB	2.46	8.55	0.34	8.36
128 KB	2.50	24.75	0.59	20.83
1 MB	3.70	24.75	0.80	16.07
16 MB	4.73	24.74	0.66	14.29
64 MB	4.74	25.09	0.65	14.01
128 MB	4.79	27.26	0.64	13.86
256 MB	4.79	30.83	0.64	13.97
512 MB	4.81	30.82	0.66	13.93

Let us consider the results in more detail.

The CUDA SDK includes a profiler, which allows getting information on the kernel execution time, resources used by the kernel, multiprocessor loading, cache efficiency, and many other parameters. The profiler data is used for a more detailed analysis of the results.

The fastest option is the global memory. The correct access pattern allows us to achieve more than 90% hits fro L2 cache and about 20% hits for L1. However, even in this case, working with memory is still an essential factor limiting performance.

Table 2. The dependence of the encryption speed on the thread block size.

Threads per block	Encryption speed (Gbps)		
	Global memory	Constant memory	Texture memory
32	30.86	0.80	16.64
64	30.94	0.66	13.59
128	30.75	0.65	13.28
192	30.66	0.67	13.85
256	30.81	0.63	13.55
384	30.70	0.66	13.81
512	30.67	0.69	14.07
768	30.81	0.77	15.03

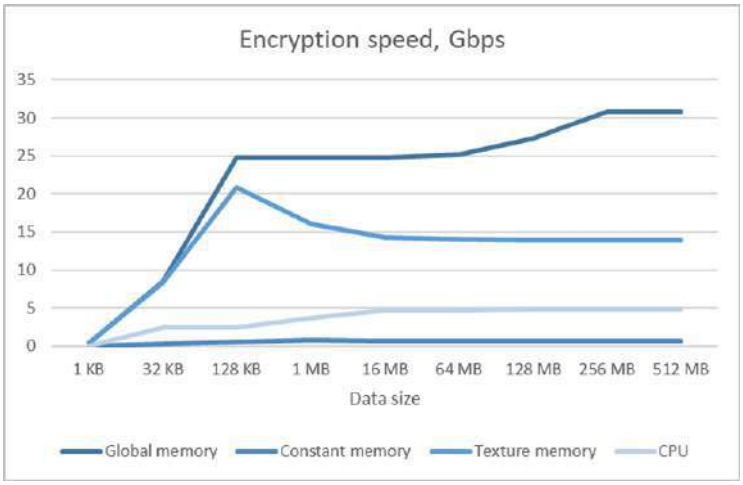

Figure 1. The dependence of the encryption speed on the data size.

The texture memory is slower due to the greater number of registers used and the greater memory load. When reading a single value, its neighbors are also loaded into the cache, so the memory subsystem has to serve the greater number of readings. So cost of each cache miss is high. In addition, in the Maxwell and Pascal architectures, the texture cache shared the memory with L1 cache and therefore does not give any gain compared to it.

For constant memory, the problem is a random access pattern, which causes frequent cache misses. Another problem is the read data size - 16 bytes per request. As a result, the performance degrades.

Let us turn to the size of the thread blocks.

No more than a certain number of threads, warps, and blocks can be executed on a multiprocessor simultaneously. In addition, there are limiting factors, namely, the total number of registers and shared memory. With small blocks, the overhead caused by the context switching is huge. At the beginning of execution, time is spent for each block to copy round keys to the shared memory. For large blocks, a multiprocessor simultaneously executes fewer blocks due to the presence of limiting factors. Besides, the location of the block cannot be taken by another one until the block is completed. In our case, the difference between thread block sizes for global memory is insignificant, since the main limiting factor is the global memory latency. Constant memory case reaches maximum troughput with 32 threads per thread block, whereas texture memory case have its maximum at 32 threads per threads block.

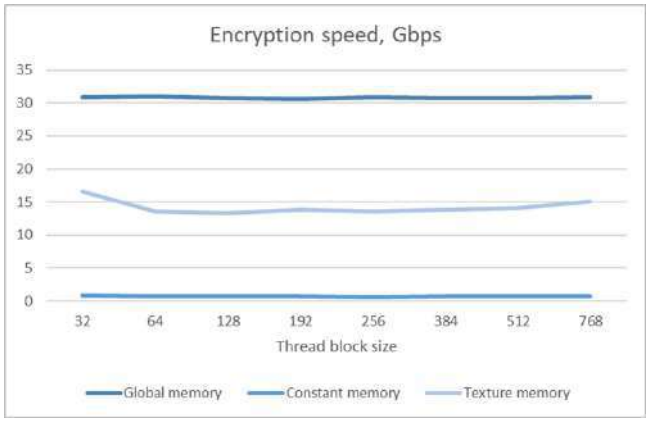

Figure 2. The dependence of the encryption speed on the thread block size.

6. Conclusion

In this paper, we considered various options for implementing the "Kuznyechik" encryption algorithm using CUDA technology. We used lookup tables as a basis for the implementation. We discussed the global, constant, and texture memory as an option for the location of the lookup tables. Besides, we considered the following sizes of thread blocks: 32, 64, 128, 192, 256, 384, 512. According to the experiments, the best results were obtained when search tables are stored in the global memory. The peak speed of the encryption was equal to 30.83 Gbps on the equipment used.

7. References

[1] Cook D L, Ioannidis J, Keromytis A D and Luck J 2005 CryptoGraphics: secret key cryptography using graphics cards CT-RSA *Lecture Notes in Computer Science* **3376** 334-350
[2] Abdelrahman A, Fouad M and Dashan H 2017 Analysis on the AES Implementation with Various Granularities on Different GPU Architectures *Advances in Electrical and Electronic Engineering* **15** 03
[3] Lee W K, Cheong H S, Phan R and Goi B M 2016 Fast implementation of block ciphers and PRNGs in Maxwell GPU architecture *Cluster Comput.* **19(01)** 335-347
[4] GOST R 34.12-2015 *Information technology. Cryptographic data security. Block ciphers* (Moskow: Standartinform) p 21
[5] Biryukov A, Perrin L and Udovenko A 2016 Reverse-engineering the S-Box of Streebog, Kuznyechik and STRIBOBr1 Advances in Cryptology *Lecture Notes in Computer Science* **3376** 372-402
[6] Ishchukova E, Babenko L and Koshucky R 2015 Implementation of high speed data encryption using "Kuznyechik" cipher *Auditorium* **04(8)**
[7] Ishchukova E, Babenko L and Anikeev M 2016 Fast Implementation and Cryptanalysis of GOST R 34.12-2015 Block Ciphers *Proc. 9th Int. Conf. on Security of Information and Networks* (New York: ACM) 104-111
[8] Korobeynikov A 2019 E˙ective Implementation of "Kuznyechik" block cipher on FPGA with OpenCL Platform *Proc. of IEEE Conf. of Russia Young Researchers in Electrical and Electronic Engineering* 1683-1686
[9] Sanders J and Kandrot E 2010 *CUDA by Example* (New York: Addison-Wesley) p 313

Acknowledgments
The work was funded by the Russian Federation Ministry of Science and Higher Education within a state contract with the "Crystallography and Photonics" Research Center of the RAS under agreement 007-GZ/Ch3363/26.

Supporting the life cycle of complex technical systems on the basis of intelligent technologies and predictive analytics

V N Blinov[1], S S Valeev[2], N V Kondratyeva[2], R R Karimov[2], A S Kovtunenko[2] and E A Kuzmina[2]

[1]Omsk State Technical University, Pr. Mira Str., 11, Omsk, Russia, 644050
[2]Ufa State Aviation Technical University, K. Marx Str., 12, Ufa, Russia, 450008

e-mail: vss2000@mail.ru

Abstract. The application of predictive analytics in the design, production and operation to achieve the efficiency of the life cycle of complex technical systems is discussed. A predictive model of information support for the life cycle of a microsatellite propulsion system based on a neural network system is proposed. The predictive model can solve the problem of estimating fuel consumption, diagnosing and detecting possible failures of a small propulsion system.

1. Introduction

The modern systems of information support of the life cycle of the large scale technical objects, such as airplanes, gas turbine engines, are widely used. But for small dynamic objects, such as drones or microsatellites, the use of life-cycle information support systems is not so obvious for many reasons. One of the main reasons why researchers and manufacturers are not ready for applying this technology is lack of the experience and rather expensive life cycle information support systems equipment and software.

The microsatellite can be considered as a subclass of the cyberphysical system functioning in autonomous mode during its mission for rather a long period of time. It is possible to control its position and payload periodically remotely from ground flight center in telecommunication sessions. An operator can send control commands through, for example, GlobalStar, and change the operation mode for the microsatellite effective use with help of special software-hardware interface [1-8].

The mission tasks of microsatellite in information sense is the data collecting, processing, and transmitting to the ground flight center the compressed information about its environment and flying conditions. Microsatellite, as a subset of a cyber physicalsystem, contains a lot of mechatronics subsystems: micro electromechanical elements and mechanisms. So, it can be considered as a complex technological product, which is designed within the enterprises cooperation on the base of information flows interchanging [9, 10]. On the stage of designing of the life cycle for autonomous technical objects, the designers have to keep in mind the possible uncertainty factors which can influence on the object operation and can cause failures of onboard equipment, energy overconsumption, noise influence and the other different factors. So, to provide the efficiency of the microsatellite mission, the information support based on predictive analytics technologies can be applied [11, 12].

2. The life cycle of the complex technical system

The small size mobile observing systems are very urgent nowadays in the most of scientific and commercial applications. One of the ways to achieve the life cycle efficiency for such a system is intelligent information support on the stages of design, production and exploitation.

A low-weight mobile autonomous system exploited without any human service during long-term periods is considered as a complex technical system. The human operator can control the complex technical system remotely in short sessions. For this purpose, the operator sends commands and sets temporal programs for complex technical system exploitation with aid of software-hardware interface. The main aims of a complex technical system are collecting, processing and transmitting objective information about its environment and also transportation, mechanical and other interactions with environmental objects.

The complex technical system contains a number of technical subsystems, microelectromechanical components and mechanisms, and software-hardware components. Therefore, a small size mobile observing system is a high technological product created within wide international cooperation.

The efficient exploitation of the complex technical system during its short active lifetime has to be assured. Increasing exploitation efficiency requires creating the integrated hardware-software system for the information support of the complex technical system life cycle.

One of the problems hard to solve is uncertainty caused by failures of onboard software-hardware subsystems, information distortion, external noise influence, energy losses, etc.

The complex technical system lifecycle includes six stages: system project, designing, manufacturing, implementation, operation and utilization. But only the operation stage assures profitable usage. For today, introductory stages duration (1-4) is approximately equal to the duration of exploitation stage (5). The introductory stages still remain rather expensive from the investor point of view. To advance overall efficiency, it is necessary to decrease duration of the stages 1-4 and increase the useful effect on the stage 5. The main stages of the complex technical system life cycle and benefits $P(t)$ and total costs $Z(t)$ functions are shown in the figure 1.

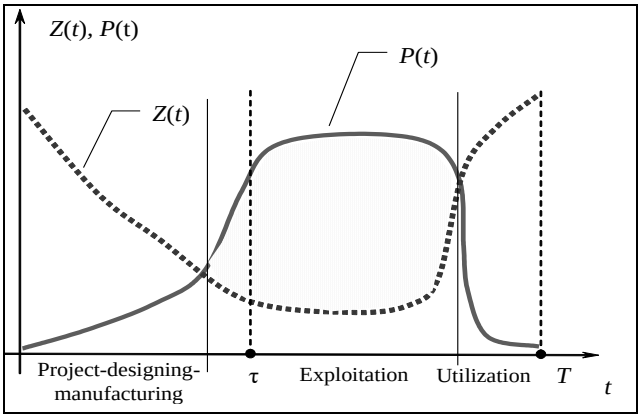

Figure 1. Benefits and total costs $Z(t)$ functions on the main stages of the complex technical system life cycle.

Target efficiency of the complex technical system life cycle could be estimated as the integral value on the base of "the through life cycle" mathematical models:

$$E(t) = \int_0^t (P(t) - Z(t))dt.$$

When planning and correcting life cycle operations and making exploitation programs, it is either required to estimate useful effects E_τ and make the forecast of probable negative or positive after-effects $E_{T-\tau}^{FC}$ – for example, the complex technical system resource degradation. This allows choosing the optimal option not for an operation at temporal time τ only, but for the entire further life cycle T:

$$E_{LC,i} = E_\tau + E_{T-\tau}^{FC} = \int_0^\tau (P(t) - Z(t))dt + \int_\tau^T (P(t) - Z(t))dt;$$

$$E_{\text{LC}} = \max_i \{E_{\text{LC},i}\}.$$

To obtain the optimal effect E_{LC}, the following tasks of the information support of the complex technical system life cycle should be solved:

- the intelligent support of complex technical system at the design stage;
- keeping the information on the complex technical system condition the actual, operational and authentic;
- estimating and forecasting the complex technical system condition;
- the decision making support using "through the life cycle" intelligent models to estimate target efficiency on the life cycle stages;
- simulation of "optimum" and "worst-case" situations while the life cycle participants interacting on the base of decision trees;
- the diagnostic and decision-making on the base of mathematical and intelligent models of the complex technical system onboard systems.

All these measures will promote total efficiency of the complex technical system life cycle due to the effective interactions between participants, high awareness of the life cycle participants and decrease wrong decision probability during the life cycle stages.

3. The life cycle of the complex technical object and predictive analytics

In sense of the life cycle paradigm of the microsatellite, the amount of data generated on prototyping and testing stages are more times bigger then data had generated on the implementation stage (figure 2).

So it is obvious, if we are trying to optimize total expenditures for the life cycle of the microsatellite:

- It is necessary to decrease the durations of the stages from prototyping to implementation.
- It is needed to increase the usefulness of information that had been generated on before the implementation stage.

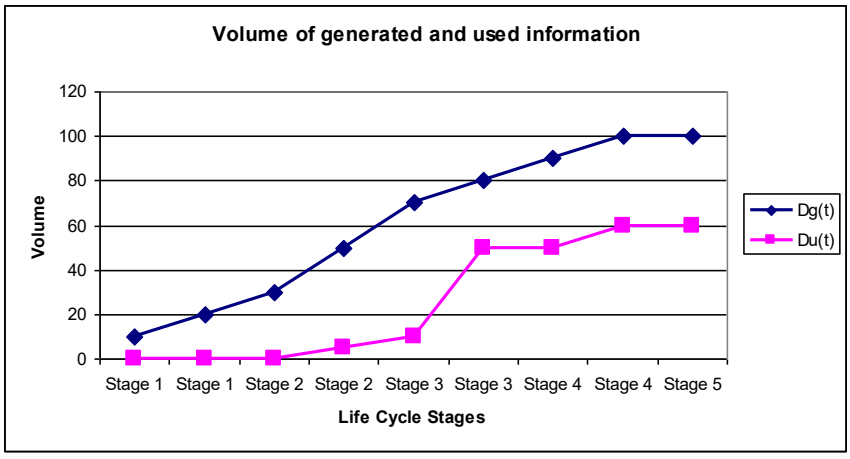

Figure 2. Volume of information generated on all stages of life cycle.

In general, the effectiveness of generated information D_E on stages of the life cycle of complex technical object can be presented as the solution of optimization task:

$$D_E(t) = \int_0^t (D_G(t) - D_U(t))dt \to \min, \quad (1)$$

where D_G is generated information, and D_U is used information.

The following tasks of the predictive analytics application have to be solved in order to obtain the positive effect in sense of (1):

- big data technologies can be applied on all stages of the life cycle. Supporting actual, operational and authentic information about the state of the complex technical object operation with help of estimating and forecasting the complex technical object state on the basis of predictive models;
- the decision making support using different predictive models to estimate the meaning of goal function on the different stages;
- simulation of different "suboptimum" and "worse" cases on the base of multi-agent real time simulation system;
- diagnostics on the base of on-line predictive models of complex technical object state with application of onboard computers.

These tasks can increase the economic efficiency of the life cycle of complex technical system due to the effective interactions of all information subsystems with application of predictive analytics on all stages of the life cycle.

4. Intelligent technologies of the life cycle information support for the complex technical system

Due to the essential uncertainty on the design, manufacturing and exploitation stages of the complex technical system life cycle, the intelligent technologies become rather actual for the life cycle information support.

First of all, on the stage of system design, developers have to solve the problem of optimal structure of the complex technical system. This problem is proposed to solve with genetic algorithms for optimizing information model of complex technical system.

The second problem is that on the exploitation stage human controller has to diagnose technical condition of the remote complex technical system, estimate internal complex technical system resources and provide process monitoring on the base of telemetry data stream.

The third problem is when planning system operations, it is necessary to build a simulation model to choose the optimal life cycle strategy and avoid worst-case situations. Last two problems are proposed to solve with help of the through-life cycle neural network model.

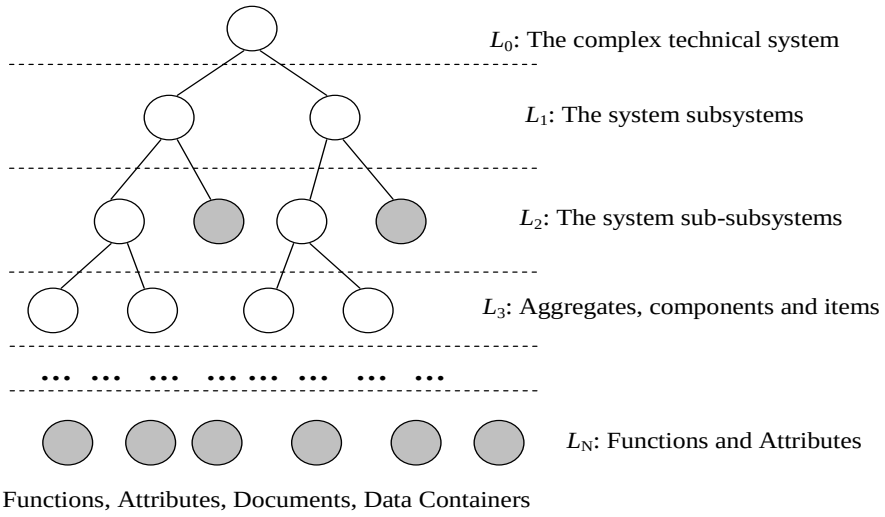

Figure 3. The information hierarchical model of the complex technical system as a genetic individual.

The information model of the complex technical system has hierarchy multilevel structure which is represented as a tree graph, the root node of which is the complex technical system itself (figure 3). On the models' second level, the complex technical system subsystems are involved, on the next levels – the complex technical system aggregates, components and items. The terminal nodes of the model are

the characteristics, attributes of the complex technical system as well as complex information objects, such as documents, data containers and others. The terminal nodes are painted hatched in figure 3.

One multilevel structure presented in figure 3 describes an individual of evolution procedures. Middle nodes as subsystems and aggregates (for example, power supply, engine, cameras, etc.) are the chromosomes of the individual, and the terminal nodes – characteristics and attributes – are the genes.

The populations, obtained by genetic algorithms within crossover and mutation, allow producing amount of the different versions of the complex technical system. Then individuals are selected with the aid of chosen criteria – fitness function.

The transitions between PDM database and the individual hierarchy could be realized via SGML (XML) transformations.

5. The Microsatellite Engine Predictive Model

The research and practical implementation work that was carried out and the results of flight and ground tests of ammonia propulsion engine with a thrust price of up to 4 W/mN for electrothermal micro engine of up to 30 mN showed their high efficiency in the small satellites “Demonstrator”, “Orbkomm” and “UgatuSat” [2].

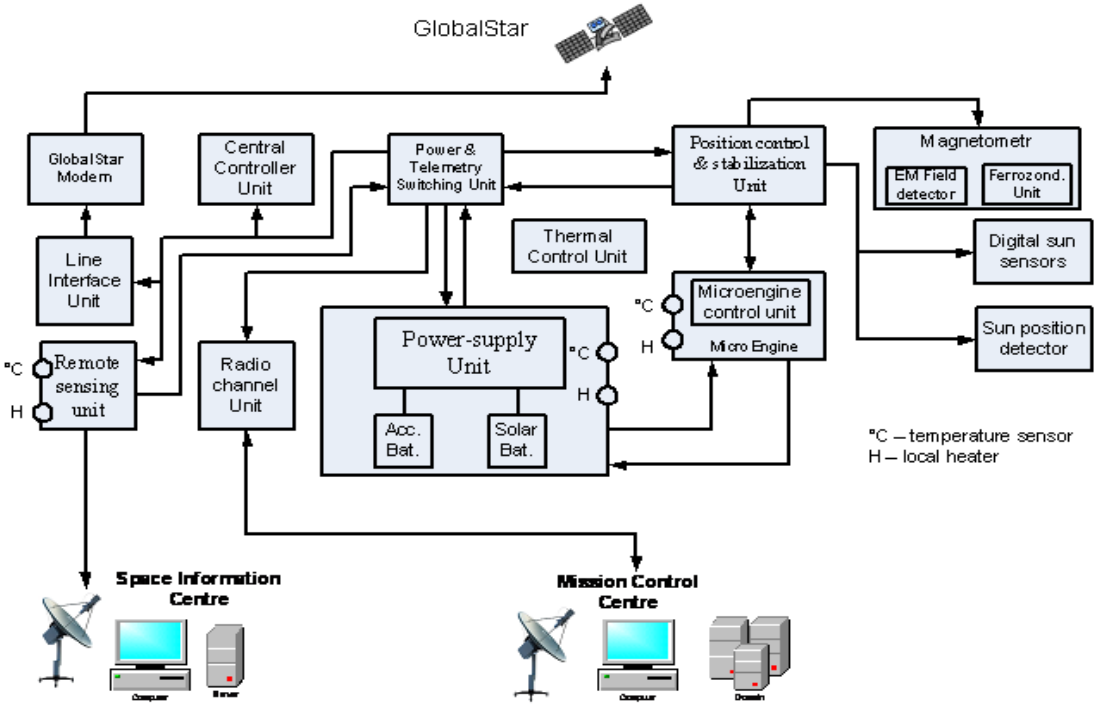

Figure 4. Predictive estimation of remaining fuel on the base of telemetry data.

Let us consider the resource and state assessment subsystem on the example of a propulsion system, which is designed to correct the orbital position of the micro satellite. The propulsion system consists of a cylindrical fuel tank, a filter, an electropneumatic valve, an evaporator for converting liquid ammonia into a gaseous state, a pressure regulator to maintain a predetermined pressure value, as well as an electrothermal engine. The considered PS is developed in the PE "Polet" (Omsk) and is used on Russian and foreign microsatellites.

The main non-renewable resource on board the microsatellite is the fuel supply. The task of determining the amount of fuel on board the spacecraft is very relevant due to the lack of a fuel sensor, extreme external conditions, the inability to refuel and other services. The factors of uncertainty include the occurrence of failures of the components of the control, loss of fuel due to leaks, chemical decomposition of fuel, etc.

The principal pneumohydraulic scheme of propulsion system is presented in figure 5, which includes an electrothermal engine, pressure sensor, pressure regulator (controller), evaporator, electropneumatic valve, filter, ammonia tank (fuel tank).

The key feature of the considered propulsion system is the formation of small impulses of thrust and operation in the "cold start" mode, as a result of which the thrust and fuel consumption are functions of time.

The principle of operation of a micro jet engine with an ammonia electro thermal engine is based on the dissociation of ammonia with its decomposition into hydrogen and nitrogen. Due to the decomposition and, accordingly, a twofold decrease in the molecular weight of the outflowing gas compared to ammonia gas, it is possible to significantly increase (up to 2600 N · s/kg) the specific thrust impulse of the electro thermal engine [3].

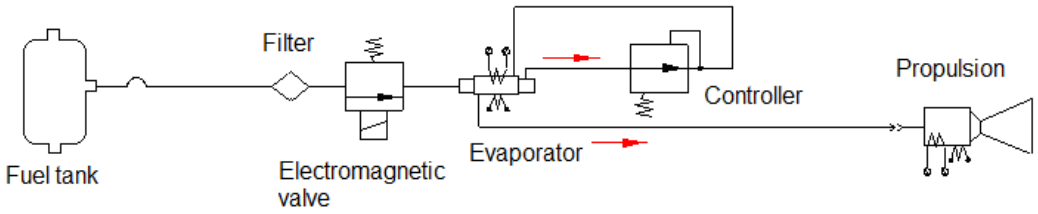

Figure 5. Schematic view of propulsion system.

For the micro-propulsion systems under consideration, there are no analytical models that allow determining the technical condition of the object, fuel consumption and its reserves with the necessary accuracy. At the same time, in the process of designing and testing, a large amount of computational and experimental information is accumulated, which can be used to create a predictive model of a micro-propulsion system based on neural networks technologies.

In the process of control the fuel consumption data received telemetric information (table 1), parameters of the control program, including the settings of the operating modes of the micro-propulsion system, data on the previous turn on of the micro-propulsion system are used (figure 6, table 2).

Table 1. Data set of the microsatellite telemetric information.

Time	I_{bs}, A	I_{ab1}, A	TxVAP	ON12	U_{bs}, V	U_{ab1}, V
13:03:04	0.59	1.33	VAP1	0	13.8	13.9
13:02:04	0.69	1.17	VAP1	0	13.6	13.8
13:01:04	0.53	1.38	VAP1	0	13.6	13.7
13:00:04	0.43	1.22	VAP1	0	13.4	13.4
12:59:04	1.17	-0.59	VAP1	0	12.1	12.2
12:58:04	0.64	-0.32	VAP1	0	12.2	12.4
12:57:04	0.85	-0.43	VAP1	0	12.2	12.3
12:56:04	0.64	-0.32	VAP1	0	12.2	12.4
12:55:04	0.85	-0.43	VAP1	0	12.2	12.3
12:54:04	0.85	-0.43	VAP1	0	12.2	12.3
12:53:04	0.69	-0.38	VAP1	0	12.2	12.4
12:52:04	1.07	-0.54	VAP1	0	12.1	12.2
12:51:04	0.64	-0.32	VAP1	0	12.2	12.4
12:50:04	0.85	-0.43	VAP1	0	12.1	12.3
12:49:04	0.75	-0.38	VAP1	0	12.2	12.4
12:48:04	0.96	-0.48	VAP1	0	12.1	12.3

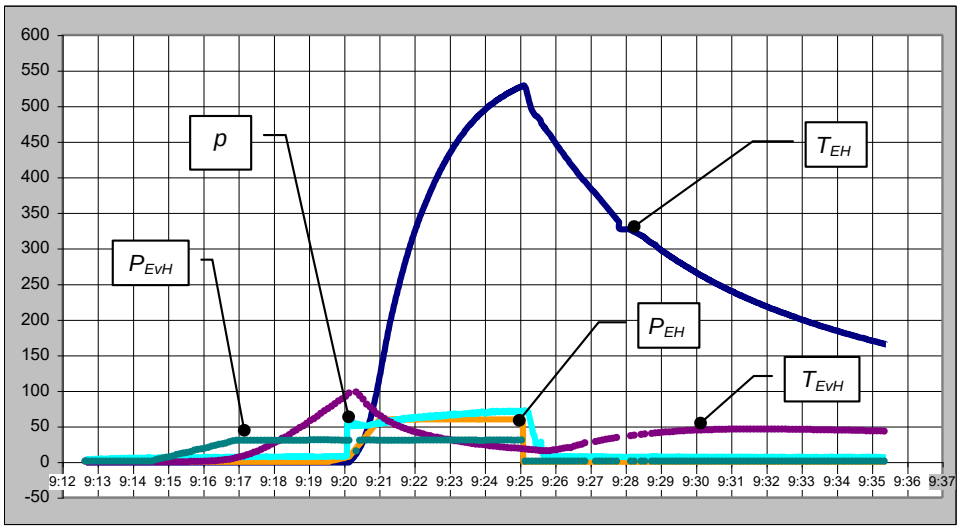

Figure 6. Data set of microsatellite parameters state.

All data that we have received on the different stages of the life cycle are stored in the information life cycle support system. This system includes the high performance computers, data warehouse subsystems, predictive analytics software and etc.

During operation, such a predictive model will allow solving the following tasks:

- evaluate the fuel reserves on board the microsatellite;
- diagnose the technical condition of the micro-propulsion system and detect its failures;
- determine the fuel consumption required to complete the orbital maneuver.

6. Predictive neural network of the fuel consumption model

In the process of modeling, telemetric information, parameters of the control program, including the settings of the operating modes of the propulsion system, data on previous inclusions of the micro jet propulsion are used. A fragment of the list of used parameters and their description are presented in table 2.

Table 2. Description of the parameters.

Parameters	Description
T_{EH}	engine heater temperature
U_{EH}	voltage on the engine heater
I_{EH}	engine heater current
T_{EvH}	evaporator heater temperature
U_{EvH}	voltage on the evaporator heater
I_{EH}	evaporator heater current
N	number of the received block with initial data (settings)
t_N	instrument time value
p	pressure in the engine chamber
T_{maxEH}	maximum engine heater temperature
T_{maxEvH}	evaporator heater maximum temperature
P_{maxEH}	maximum power of the electric current supplied to the engine heater
P_{maxEvH}	maximum power of the electric current supplied to the evaporator heater
t_{EP}	engine preparation time
t_{Σ}	engine running time

The second group is the output data group $Y = \{T_{EH}, T_{EvH}, p\}, Y \in R^{1\times 3}$. The input data are fed to the propulsion system to form a thrust impulse, while the output data allow the trust impulse to be estimated.

All developed neural networks are multilayer perceptrons trained in the backpropagation method. As a training sample, the calculated and experimental data obtained during the design and testing stages of the propulsion system were used. The structure of neural networks is given in table 3.

Table 3. Neural Network Architecture.

NN	Neural Network Architecture
NN1	12-5-3-3
NN2	3-3-5-12
NN3	15-6-4-2

The predictive neural network of the fuel consumption of the electrothermal micro propulsion engine includes three separate neural networks NN1-NN3, which are having multilayer perceptron structure trained with back propagation learning algorithm. System of neural networks NN1-NN3 and their architectures, logics block selecting simulation and monitoring modes are presented on figure 7.

The NN1 neural network is designed to determine the dependence of the output information Y on the input X and is used in the simulation mode of the propulsion system. The NN2 neural network solves the inverse problem and determines the dependence of the input information X on the output Y. The results of the NN2 neural network are used in the monitoring mode to solve the problem of diagnosing the technical condition of the engine. The NN3 neural network is used to determine the fuel consumption G_τ and assess the technical state of S_τ. In the NN3, data streams X and Y are used as input. Data on fuel consumption obtained in the process of testing the engine, can improve the accuracy and reliability of the training set. The complex of neural networks based on NN1, NN2 and NN3 is shown in figure 7.

In the simulation mode of the propulsion system, the logic unit provides interaction between the NN1 and the NN3, and in the monitoring mode, the NN2 and the NN3, which improves the accuracy of the fuel consumption estimate using additional information about the technical condition of the engine.

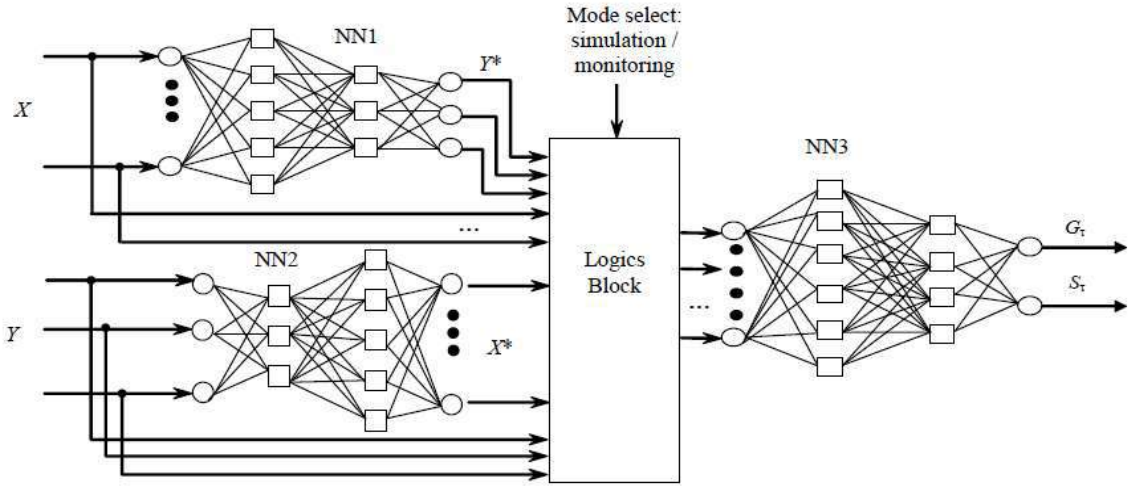

Figure 7. Predictive estimation of remaining fuel for microsatellite.

Data sets from databases of simulations results, telemetry information and control data, settings and additional information are applied for training processes for this system of neural networks.

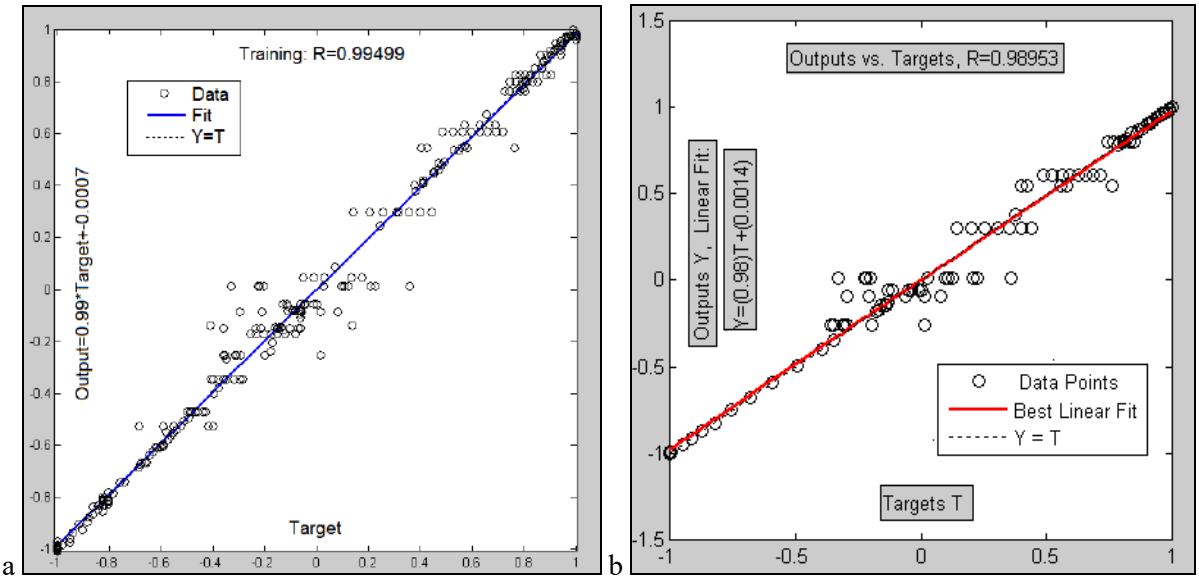

Figure 8. The predictive neural network model NN1 (a) and NN2 (b) learning results.

The telemetric information of a microsatellite with an electrothermal engine, which performs a single-pulse maneuver for orbit correction, is used as a training sample. Data sets include telemetry information on temperature of fuel thermal condition, fuel pressure, and control unit state. The learning results of the NN1 neural network are presented in figure 8. As we can see, the quality of training of the neural network is good. The architecture of NN1 neural network includes the input layer, hidden layer and output layer and has the following structure 12-5-3-3 neurons. To assess the reliability of the results of the neural network, a regression analysis was performed, obtained by comparing the reference values with the results of processing a test sample. For this, the "postreg" function is used in the MATLAB environment. The correlation coefficient between output prediction and sample data is R≈0.995 (figure 8, a). The result of the regression analysis for the neural network NN2 is presented in figure 8, b). The correlation coefficient is R ≈ 0.989. The architecture of NN2 neural network includes the input layer, hidden layer and output layer and has the following structure 3-3-5-12 neurons. The experiment on teaching the intellectual model and determining the fuel supply showed that the accuracy of solving the problem under consideration increased by 10% compared with the analytical method.

7. Conclusion

One of the modern ways to achieve efficiency of the life cycle of complex technical systems is application of predictive analytics information support in design, production and exploitation stages of the life cycle. As it known the life cycle of the complex technical objects usually contains the following stages: prototyping, designing, manufacturing, implementation, operation, utilization. The duration of stages from prototyping to implementation for microsatellite is more times longer the duration of exploitation stage. One of the modern ways to achieve efficiency of the life cycle of such systems is application of predictive analytics information support in design, production and exploitation.

Predictive models and methods for the life cycle information support on the basis of the system of neural networks are proposed. The system of neural networks that can be estimated on onboard computer is presented. This predictive model can solve the task of estimation of fuel consumption, diagnostics and possible failures detection.

The initial data for training neural networks are formed on the basis of the results of simulation modeling and telemetry data. The input values are normalized relative to the maximum values of these quantities. The initial weights of neural networks are set randomly.

The research results are expected to be used in the development of predictive analytics systems for small satellites in the future.

The proposed development technique can be used in building models for other types of engines of this class. And in the event of a change in parameters, it is necessary to develop a modified architecture of the neural network model.

8. References

[1] Kropotov Y A, Proskuryakov A Y and Belov A A 2018 Method for forecasting changes in time series parameters in digital information management systems *Computer Optics* **42(6)** 1093-1100 DOI: 10.18287/2412-6179-2018-42-6-1093-1100

[2] Mostovoi J A 2012 Simulation mathematical model of the external ambience in life cycle of on-board software of management cosmic platform *Computer Optics* **36(3)** 412-418

[3] Sweeting M N 2018 Modern Small Satellites-Changing the Economics of Space *Proceedings of the IEEE* **106(3)** 343-361

[4] Blinov V N 2015 Design features and research of Electrothermal Microthrusters with Autonomous Heating Elements for the Purposes of Small Space Vehicle Orbital Manoeuvring *Indian Journal of Science and Technology* **8(27)** IPL0581

[5] Blinov V N 2015 The studies of Small Space Vehicles Ammoniac Electrothermal Engine Units Design and Structural Layout *Modern Applied Science* **9(5)**

[6] Yan Z 2013 System Dynamic Characteristic Simulation of Spacecraft Propulsion System Based on AMESim *Advanced Materials Research* **605-607** 679-683

[7] Carroll D L, Cardin J M, Burton R L and Benavides G F 2015 Propulsion unit for CUBESATS (PUC) *62nd JANNAF Propulsion Meeting (7th Spacecraft Propulsion)* URL: http://www.cuaerospace.com/Portals/SiteContent/Publications/2015/Carroll_JANNAF_2015_PUC_4059.pdf

[8] Zelinka I, Chen G, Rössler O E, Snásel V and Abraham A 2013 Nostradamus 2013: Prediction, Modeling and Analysis of Complex Systems *Nostradamus conference Advances in Intelligent Systems and Computing* (Ostrava Czech Republic Springer)

[9] Kondratyeva N, Valeev S 2016 Fatigue test optimization for complex technical system on the basis of lifecycle modeling and big data concept *Proceedings of 10th conference on Application of Information and Communication Technologies AICT* 1-4

[10] Vasilyev V I, Valeyev S S and Shilonosov A A 2001 Design of neurocontroller for gas-turbine engine multi-mode control *Proc. 8th Int. Conf. on Neural Information Processing ICONIP*

[11] Kondratyeva N V, Valeev S S 2016 Simulation of the life cycle of a complex technical object within the concept of Big Data *CEUR Workshop Proceedings* **2004** 216-223

[12] Karimov R R, Islamgulov T V and Karpenko O Yu 2012 Application of neural network and genetic algorithms to life cycle information support of complex technical object *Proc. of 14th Int. Workshop on Computer Science and Information Technologies* **1** 228-231

Distributed stream data processing system in multi-agent safety system of infrastructure objects

S S Valeev[1], N V Kondratyeva[1], A S Kovtunenko[1], M A Timirov[2] and R R Karimov[1]

[1]Ufa State Aviation Technical University, K. Marx Str., 12, Ufa, Russia, 450008
[2]Bashkir Production Association "Progress", Kommunisticheskaya str., 23, Ufa, Russia, 450076

e-mail: vss2000@mail.ru

Abstract. The solution of the problem of resource management in distributed computing systems of processing stream data in safety systems of distributed objects is considered. The tasks of streaming data processing in a multi-level multi-agent evacuation system in an infrastructure object are considered. The features of the mathematical model of a distributed stream data processing system are discussed.

1. Introduction

An infrastructure of socio-technical systems includes various complexes of buildings that have a large area and the possible presence of a large crowd of people. The goal of risk management with the security system of an infrastructure is minimizing collective risk in the event of a critical situation in the cyber-physical system or in the context of infrastructure degradation. For the analysis of the state of these objects, various systems for collecting and processing information are used: sensors for the state of physical parameters, video surveillance systems and telecommunication systems. It should be noted that the part of the information is transmitted and processed as streaming data. In the event of a critical situation information about the state of the information field can be lost due to factors affecting the elements of the computer system. So we can lose the accuracy of measurements of the physical parameters of the internal space of the infrastructure [1-9].

So, let the observable information field be the state of the internal physical and information space of the considered infrastructure. In this case, the task of reallocating computing system resources in a technical safety system, in which information about the state of an infrastructure object is collected from various sensors in real time, becomes extremely important. This system should be considered in the class of self-learning control systems for distributed objects that have a variable structure [10-15].

The state of the information field may change depending on internal and external factors affecting the physical energy flow, which, in turn, affects the distribution of risk levels in the event that this energy goes out of control. In this case, the solution to the problem of risk management can be based on the application of self-learning elements of a multi-level management system at its planning and coordination levels. The formation of scenarios for the development of a critical situation and possible ways to minimize risks is possible with the use of a self-learning multi-agent data collection system.

The considered multi-agent system can be implemented in various ways: we can use a multi-agent software platform, such as JADE, or implement software agents based on different programming languages: Python, Java, etc. [16-18].

Although the databases can be implemented on the basis of various modern approaches, it is necessary to solve the tasks of reallocating computing power in real time in order to ensure the efficiency of solving problems of collecting and processing, including streaming data, in the safety systems of the distributed infrastructure facility [19-28].

As it is known, modern airports and other similar structures are complex socio-technical systems. For example, the system for ensuring the process of evacuating passengers in critical situations includes technical means of detecting and responding to the alarms, various sensors, computing, telecommunications and human resources of engineering services and building security systems. In addition, it is necessary to take into account the many uncertainties that affect the effectiveness of decision-making procedures in the evacuation process. Currently, the solution to the problem of reducing the risk of evacuation is still an important scientific and practical task.

Information support in critical situations based on a decision support system can serve as a risk management tool. In this regard, it is advisable to develop an intelligent decision support system (DSS) based on self-learning technologies and multi-agent modeling using streaming information processing.

2. Architecture of intelligent decision support system

It is quite difficult to ensure effective decision making in critical situations for large socio-technical systems under the conditions described above, using a centralized control scheme. One of the solutions is the use of a three-level decision support system, which allows managing the complexity of the decision-making problem and, as a result, reduce risk levels (figure 1). Upstream information from sensors I_1 from the control level of sensors and actuators is transmitted to the level of online solutions. In the opposite direction, control actions are transferred to actuators and technical equipment that support evacuation management processes I_2.

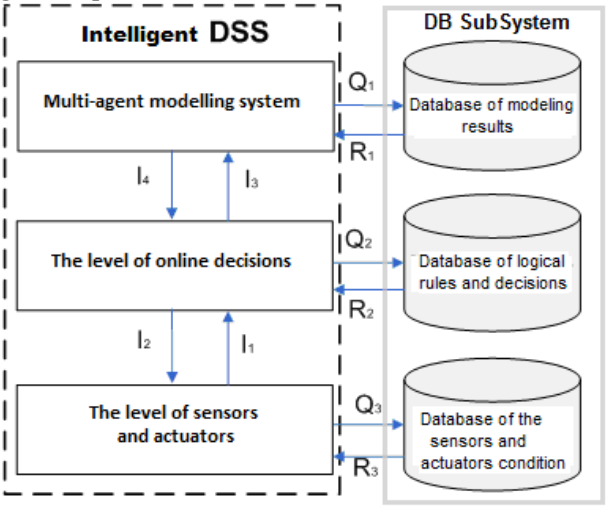

Figure 1. The information structure of intelligent decision support system.

A database storing information transmitted from sensors and actuators receives a stream of data Q_3 on the state of the information field and elements of the executive level. Information R_3 is transmitted in the opposite direction, which is necessary for the effective functioning of sensors and instruments.

Decision making at the level of online decisions in real time is based on a set of specified logical rules R_2 received in response to Q_2 requests. At the same time, the database stores information about the effectiveness of decisions made on the basis of Q_2 rules. The flow of data on the state of the critical situation I_3 is transmitted to the multiagent modeling level, which, in turn, is looking for effective solutions for transmitting information I_4 to the operational management level.

The data on the simulation results are transferred to the database of simulation results. If necessary, they can serve as input for the next stage of the simulation.

The risk of inefficient evacuation was adopted as a criterion for the effectiveness of an intelligent decision support system:

$$Q_{\mathrm{E}} = 1 - P_{\mathrm{E}}, \tag{1}$$

where P_{E} is the probability of a successful evacuation, for example, in the event of a fire.

Probability of escape P_{E} is defined in accordance with standard methods of fire risks evaluation in accordance with the requirements of GOST 12.1.004-91 “Fire safety. General Requirements” as follows:

$$P_E = \frac{0{,}8 \cdot t_{bl} - t_{est}}{0{,}8 \cdot t_{bl}},\ t_{est} < 0{,}8 \cdot t_{bl}, \tag{2}$$

where t_{bl} is the time of blocking the building exits, it depends on fire conditions, building configuration, etc. Also, as it is given in GOST 12.1.004-91 “Fire safety. General Requirements”, t_{bl} = 288 sec. in considered case; t_{est} is the estimated evacuation time determined for each of the best evacuation route. Estimated evacuation time t_{est} depends on information flows presented on figure 1 and, therefore, on the adopted solutions in an emergency evacuation. It also can be obtained on fire and evacuation integrated modeling results:

$$t_{est} = f(I_1, I_2, I_3, I_4, R_1, R_2, R_3, Q_1, Q_2, Q_3). \tag{3}$$

It should be noted that figure 1 shows only a generalized information structure of the hierarchical decision support system. In real techno-social systems, every single information flow is more powerful, all of them are transmitted in real time, and each of them by itself has a very complex information structure. With this in mind, the practical implementation of intelligent DSS requires high performance computing technologies and smart integration of hardware and software.

3. Multiagent system of infrastructure object safety

A set of agents of the coordination level use the information received by the system planner to solve the task of minimizing risks through interaction mechanisms in multi-agent systems. At the level of coordination, among other things, the problem of ensuring the integration of information on the state of the control object using multi-agent sensor systems must be solved, which makes it possible to minimize errors of the first kind and of the second kind due to the effect of self-organization of different sensors. At this level, the problem of developing control actions on the ventilation system, fire protection system, information support for evacuation must be also solved.

The architecture of multiagent system of cyber physical system safety is presented in figure 2. The structure of this system is based on hierarchical architecture.

In the sense of Big Data concept here we have different flows of information and different formats of data. We need to gather information from different types of sensors and store these data in Databases: DB_Video – Data Base of Video Sensors Data, DB_Sensor1 – Data Base of Infrastructure Sensors, DB_Sensor2 – Data Base of Dynamic Objects, DB_BD – Data Base of Mix Content, DB_M – Data Base of Simulation Results Data.

Multigent system of safety of cyber-physical system includes: Agent_Image_An – agent of Video Stream Flow Analyzer, Agent_Dy_Objects – agent of Dynamic Objects trajectory Identification, Agent_Inf_An – agent of Infrastructure State Identification, Agent_Integ_Date – agent of Integration of different flows from sensors, Agent_Mod – Agent of Simulation of the different Scenarios of Critical Situations, Agent_Integ_Dm – Agent of Analysis the state of Cyber-Physical System, Agent_R – agent of risk field identification, Agent_F – agent of integrated risk identification, Agent_U – agent of control and management of minimizing risk, Agent_U_I – agent of control signal generation for actuators, Agent_U_S – agent of management decisions realization, C&MC – implementation of control and management system.

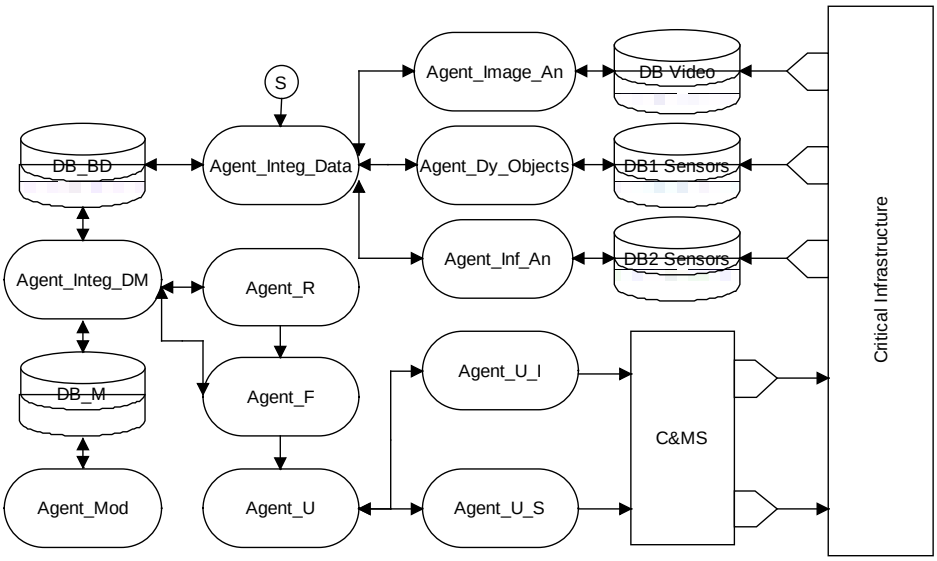

Figure 2. Multiagent system of infrastracture object safety.

So, here we have the massive application of different streaming data flows and we need to solve the resource allocation problem in case of degradation of the information system.

4. Formulation of the optimal resource allocation problem

The model of the processing and storing of streaming data (PSSD) based on the computer network includes resource model of the computer network *N*, model of data processing system (DPS) and the relation *D* describing system deployment in the network.

$$IS = \langle N, DPS, D \rangle . \tag{4}$$

Here:

- *N*– the computational network,
- *DPS* – the PSSD model,
- *D* – the deployment relation that shows $\forall p \in P$ on what node it physically deployed.

$$D = \{(w, p) : w \text{ executes } p;\ w \in W,\ p \in P\}. \tag{5}$$

Let $B : W \times R \to \mathbf{R}^+$ – function that shows $\forall w \in W$ amount of the involved resource. Values of the function can be calculated from resource capacities of data processing model and network model as follows.

$$B_{cpu}(w) = \sum_{\forall p \in D(w)} \frac{V(p)}{T(p)}. \tag{6}$$

$$B_{mem}(w) = \sum_{\forall a \in (D \circ C)(w)} M(a). \tag{7}$$

$$B_{net}^{in}(w) = \sum_{\forall p \in D(w)} \frac{\sum_{\forall a \in I(p) \cap A \setminus (D \circ C)(w)} M(a)}{T(p)}. \tag{8}$$

$$B_{net}^{out}(w) = \sum_{\forall p \in D(w)} \frac{\sum_{\forall a \in I(p) \cap (D \circ C)(w)} M(a)}{T(p)}. \tag{9}$$

The introduced notation makes it possible to formulate the problem of optimal allocation of computational resources in PSSD as the problem of combinatorial optimization. It is necessary to find such deployment relation *D**, that gives the maximum to predefined efficiency function *F*.

$$D^* = \arg \max_{D \subset W \times P} F\left(IS\langle D \rangle\right). \quad (10)$$

The following constraints apply

$$B_r(w) \le S_r(w). \quad (11)$$

Let *rem(w)* – the unitless function, that shows average free resources for every node as

$$rem(w) = \frac{1}{|R|} \sum_{\forall r \in R} \frac{S_r(w) - B_r(w)}{S_r(w)}. \quad (12)$$

and the average total of free resources as

$$\langle rem \rangle_W = \frac{1}{|W|} \sum_{\forall w \in W} rem(w). \quad (13)$$

The mathematical problem of HCNUL resource allocation can be formulated as follows. Subject to constraints (14) the optimal deployment at every point of time is

$$D(t) = \arg \min_{D \subset W \times P} \left(\max_{w \in \delta(D)} \left(\sigma_\tau^2 \left[rem(w, \tau) \right] \right) \right). \quad (14)$$

Here:

- $\sigma_\tau^2[\xi(\tau)]$ denotes the dispersion of the stochastic process ξ on the interval $\tau \in (0, t)$,
- $\delta(D)$ denotes the domain of relation D – the set of nodes where system is deployed.

5. Agent-based software architecture for PSSD systems

To create flexible, robust and scalable software that implements a multi-level security system, an agent-based approach is proposed, which involves using a software agent as a basic software object. This allows us to further talk about the software architecture based on agents and implies the presence of some additional elements in the system, such as:

- agent platform is a set of software components that support the life cycle of target agents, the interaction between them in a single namespace and the model of system events;
- agent container is a software environment that provides access to the resources of each compute node and runs software agents.

In accordance with the proposed mathematical models, security system architecture has been developed. It is assumed that the software consists of the following components of the structure:

- set of target agents, each of which is a software object that implements a procedure for processing streaming data;
- set of processing attributes implemented as an in-memory database that provides distributed storage of streaming data and access to them with low latency.

A unified storage space for streaming data is provided by a distributed cached in-memory storage that provides fast and transparent access to attribute values regardless of their physical location. The agent platform is a unified distributed execution space for data processing procedures.

The target agent is the basic software entity in the implementation of the data processing model within the proposed architecture (figure 3). It includes the following components:

- data processing procedure;
- local cache of used attributes;
- local cache of calculated attributes;
- mechanism for the management messages receiving and executing;
- mechanism for the agent initialization and self-destruction;
- agent's state.

The activity diagram of the target agent shows the process of the agent's functioning after creation. In the process of distributed data processing, the target agent can be in the following states:

- “Created” is the initial state in the agent's lifecycle.
- “Initialized” is the calculated attributes are set to the initial values.
- “Running” is the agent's operating state when the attributes are recalculating in cyclic mode.

- “Holding” is the agent's operating state when recalculating of attributes is temporary suspended.
- “Completion” is the final state in the agent's lifecycle (preparation for self-destruction, completion of all recording processes).

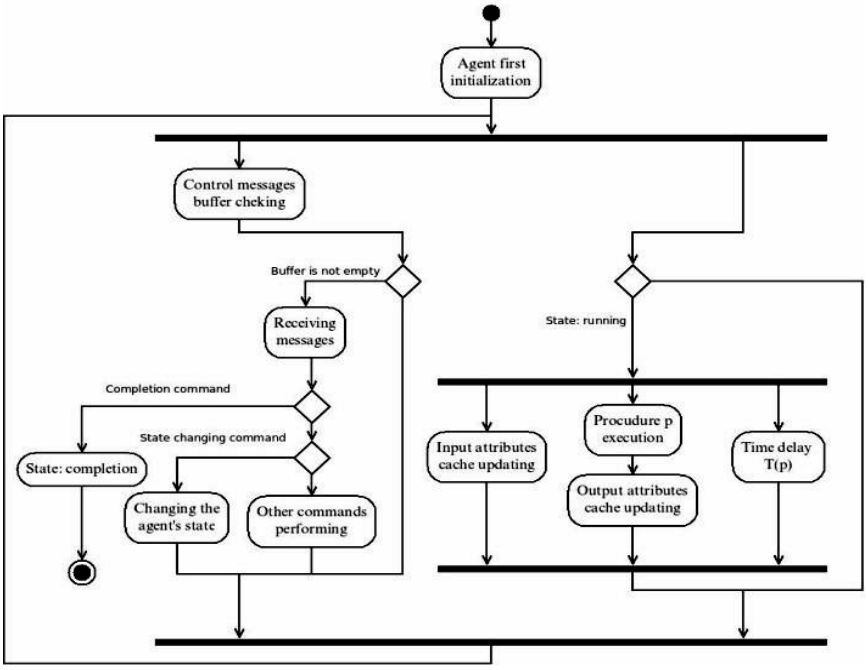

Figure 3. The part of activity diagram of the target agent.

A change of the target agent’s state occurs either according to the stage of the lifecycle, or under the influence of management commands.

6. An example of implementation of the agent-based software architecture for PSSD systems

The system is implemented as a simulation model and has a graphical user environment and allows you to use the Java language to develop models. Figure 4 shows the main interface of the program with controls that provide access to each node of the required number of CPUs and Memory for the system to work; flag "Enable/disable crashes"; a slider that sets a threshold at which tasks will be redirected to a more free node; input window required resources to perform tasks; a slider designed to select a node; a flag that allows you to switch between node selection modes; graphics processor and memory usage at each node.

For the convenience of the user, the ability to create and assign tasks has been added. The user must specify the required amount of resource that the task will request from the node on which the tasks will be performed, then you must click the “create” button. The dependence of the expenditure of CPU resource (%) on time for a computer system of two nodes (sec) is presented on figure 5.

The simulation was carried out on the capacity of the computer network, which consisted of ten nodes. The number of tasks in the system is 25 (the number of required CPUs and Memory resources is from 5-30% of the maximum). If on the node the amount of free resource is less than the threshold value (in this case, less than 20%), then the random task will be reassigned to the node with the most resources. Also, periodically, a random failure occurs, which leads to a decrease in free resources by half. After a certain time (in this case, 20 minutes), on a random node (in this example, node number 4), the amount of free resource decreased by half. Task number 13 was reassigned from the first node to the second.

7. Conclusion

The task of the risk management in cyber-physical systems on the basis of multilevel management system is considered. The principals of designing and architecture of multilevel self-learning multiagent system for risk management are discussed. Self-learning ability of the proposed multiagent

system is based on application of Big Data algorithms an machine learning algorithms.

As a result of testing software errors were not detected. To assess the quality of the developed software, failures of computing nodes were simulated. One of the handler nodes was forcibly reduced the amount of computing resources by half. At the same time, the system retained its performance; failure did not affect the functioning of other nodes.

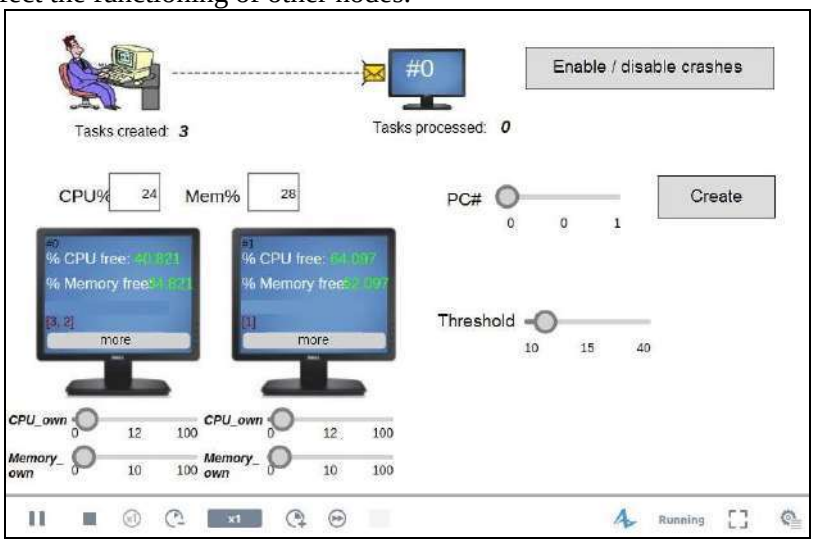

Figure 4. The main program interface.

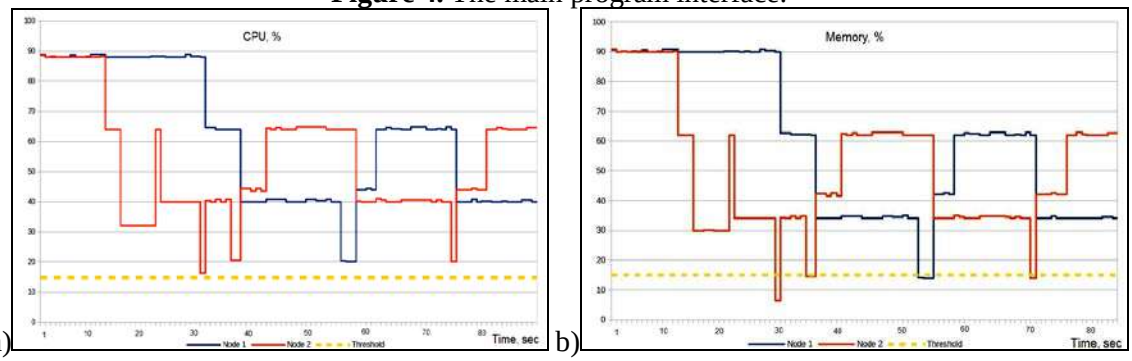

a) b)

Figure 5. The dependence of the expenditure of CPU (a) and Memory (b) (%) on time for a computer system of two nodes (sec).

8. References

[1] Jiang X, Adeli H 2008 Neuro-genetic algorithm for non-linear active control of structures *Int. J. Numer. Meth. Engng* **75** 770-786

[2] Zack M H 2007 The role of decision support systems in an indeterminate world *Decision Support Systems* **43** 1664-1674

[3] Weisenpacher P, Halada L and Glasa J 2011 Computer simulation of fire in a tunnel using parallel version of FDS *Proc. of the Mediterranean Combustion Symp., Assoc. Sezione Italiana del Combustion Inst.*

[4] Yang P, Li C and Chen D 2013 Fire emergency evacuation simulation based on integrated fire–evacuation model with discrete design method *Advances in Engineering Software* **65** 101-111

[5] Curry D M, Beaver W W and Dagli C H 2018 A system-of-systems approach to improving intelligent predictions and decisions in a time-series environment *SoSE* 98-105

[6] Gosavi A, Agarwal S and Dagli C H 2017 Predicting response of risk-seeking systems during project negotiations in a system of systems *IEEE Systems Journal* **11(3)** 1557-1566

[7] Agarwal S, Pape L E, Kilicay-Ergin N H and Dagli C H 2014 Multi-agent based architecture for acknowledged system of systems *CSER* 1-10

[8] Valeyev S, Taymurzin M and Kondratyeva N 2011 Adaptive data collection system in technical security systems *Automation in Industry* **4** 11-14

[9] Kondratyeva N, Valeev S 2016 Distributed information and control system for emergencies in critical infrastructures *Proceedings of 10th conference on Application of Information and Communication Technologies AICT* 1-4
[10] Kovtunenko A, Bilyalov A and Valeev S 2018 Distributed streaming data processing in iot systems using multi-agent software architecture *18th International Conference on Next Generation Wired/Wireless Networking (NEW2AN), and 11th Conference on Internet of Things and Smart Spaces (ruSMART) conference proceedings* 572-583
[11] Valeev S, Kondratyeva N 2015 Technical safety system with self-organizing sensor system and fuzzy decision support system *Proccedings of IEEE International Conference on Fuzzy Systems (FUZZ-IEEE)* 1-6
[12] Valeev S, Kondratyeva N 2017 Infrastructure object management in the conditions of critical situations based on situational models *Proceedings of 10th International Conference Management of Large-Scale System Development MLSD* 1-4
[13] Khakimov A, Muthanna A, Kirichek R, Koucheryavy A and Muthanna M S A 2017 Investigation of methods for remote control iot-devices based on cloud platforms and different interaction protocols *Proceedings of the IEEE Conference of Russian Young Researchers in Electrical and Electronic Engineering (EIConRus)*
[14] Ateya A A, Muthanna A, Gudkova I, Abuarqoub A, Vybornova A and Koucheryavy A 2018 Development of intelligent core network for tactile internet and future smart systems *Journal of Sensor and Actuator Networks* **7(1)**
[15] Ramakrishnan R 1998 Database Management Systems *WCB/McGraw-Hill*
[16] Valeev S S, Maslennikov V A and Kovtunenko A S 2012 Design of the middleware based on agent-oriented technologies for the automated control systems of complex technical objects *Proc. of 6th International Conference "Parallel Computing and Control Problems"* **1**
[17] Kovtunenko A S, Maslennikov V A 2014 Creation of distributed control information systems on the basis of agent-oriented approach *Proceedings of XII All-Russian Conference on Problems of Management*
[18] Soulé R, Hirzel M, Grimm R, Gedik B, Andrade H, Kumar V and Wu K L 2010 A unified semantics for stream processing languages (extended) *Technical Report* (New York University)
[19] Nikitin V S, Semyonov E I, Solostin A V, Sharov V G and Chayka S V 2016 Modeling the 'smartlink connection' performance *Computer Optics* **40(1)** 64-72 DOI: 10.18287/2412-6179-2016-40-1-64-72
[20] Agafonov A A, Myasnikov V V 2018 Numerical route reservation method in the geoinformatic task of autonomous vehicle routing *Computer Optics* **42(5)** 912-920 DOI: 10.18287/2412-6179-2018-42-5-912-920
[21] Chakravarthy S, Jiang Q 2009 Stream data processing: a quality of service perspective modeling, scheduling, load shedding, and complex event processing *Springer Publishing Company, Incorporated*
[22] Abadi D 2003 Aurora: a new model and architecture for data stream management *The VLDB Journal* **12(2)**
[23] Zdonik S B, Stonebraker M, Cherniack M, Çetintemel U, Balazinska M and Balakrishnan H 2003 The Aurora and Medusa projects *IEEE Data Eng. Bull* **26(1)**
[24] Adi A, Etzion O 2004 AMiT – the situation manager *VLDB Journal* **13(2)**
[25] FIPA ACL message structure specification 2002 *Foundation for Intelligent Physical Agents* URL: http://www.fipa.org/specs/fipa00061/SC00061G.html
[26] Zhao Y B, Sun X M, Zhang J and Shi P 2015 Networked control systems: the communication basics and control methodologies *Mathematical Problems in Engineering* **2015** 639793 DOI: 10.1155/2015/639793
[27] Lin H 2017 Estimation and control for networked systems with packet losses without acknowledgement *Studies in Systems, Decision and Control* **77**
[28] Volkov A, Khakimov A, Muthanna A, Kirichek R, Vladyko A and Koucheryavy A 2017 Interaction of the iot traffic generated by a smart city segment with SDN core network *Lecture Notes in Computer Science*

Expert system of food sensory evaluation for mobile and tablet

M A Nikitina[1], **Y A Ivashkin**[2]

[1]V.M. Gorbatov Federal Research Center for Food Systems of Russian Academy of Sciences, Talalikhina str., 26, Moscow, Russia, 109316
[2]Moscow Technical University Communication and Informatics, Aviamotornaya str., 8a, Moscow, Russia, 111024

e-mail: nikitinama@yandex.ru

Abstract. One of the main directions of statistics in sensory evaluation is an assessment of the dependence between experimental variables and measured characteristics. Statistical criteria are used to assess a degree of interaction between variables, a level of experimental effects, and allow accepting or rejecting hypothesis proposed. In sensory evaluation, people act as measurement instruments, and a variation associated with the human factor arises. This proves that the use of statistical methods is necessary. This article represents a network computer system for collection and evaluation of food sensory indicators based on the methods of rank correlation and multifactorial analysis of variance in real time. The article describes information technology of expert sensory evaluation of food quality by individual panelists and sensory panels regarding the indicators that are not measured by technical means of control, based on client-server network architecture. The software implementation of system for collecting and statistical processing of sensory data based on the principles of multifactorial analysis of variance in real-time mode makes it possible to evaluate the influence of the human factor on objectiveness and reliability of sensory evaluation results, as well as to visualize the data of expert scores by various expert panels.

1. Introduction

Sensory analysis and evaluation of food quality is the basis for commodity examination of food products and prediction of consumer demand. The usage of modern methods of sensory analysis requires from panelists not only specialized knowledge of methodology and application of, procedures for generating lexical dictionaries or scaling, but also the provision of consolidated, consistent scores that confirm the objectiveness of the results [1].

Regardless of the experience and degree of training of panelists, individual differences always arise in their scores of food quality, associated with sensory sensitivity, knowledge, and the subjectivity of the scales for sensory indicator measurement [2, 3]. Therefore, the adequate interpretation and objectification of individual panelist scores requires the development of IT technologies for factor analysis of food sensory evaluation results based on mathematical statistics methods [4-6] and computer software for processing and visualizing data from sensory evaluation of a product [7-8].

An objective assessment of food quality, taking into account a variety of parameters, alternatives and criteria, may be implement by using intelligent computer technologies for processing and formalizing knowledge with the adoption of optimal decisions based on statistical

methods of multivariate data analysis with an objective assessment of adequacy and confirmation of hypotheses.

The probabilistic spread of characteristics and properties of initial biological raw material, as well as subjectivity of individual panelist opinions determine the complexity of this problem. The samples for testing cannot be identical in nutritional and biological value (protein, fat, connective tissue, etc.). If the expert does not have enough knowledge and competencies, then even the most sophisticated software will not conduct a qualitative analysis of the data [9].

Therefore, the adequacy of the scores in each case essentially depends on the influence of the human factor with the individual psycho-physiological capabilities of sensory perception and needs correction and checking the objectivity of expert scores, considering the coherence of certain panel opinions and experience [10-13].

Information technology in a client-server network architecture is proposed based on the methods of ranking correlation and multivariate analysis of variance, for sensory evaluation of food quality by individual panelists and sensory panels regarding the indicators that are not measured by any instruments [14].

2. Rank correlation in sensory evaluation of food quality

Formal characterization of final product sensory evaluation obtained as a result of expert survey is achieved by rank correlation [8,9,11,15,16], according to which a group of quantitatively non-measurable factors is ranked by each expert independently of each other in order of decreasing or increasing their influence on the assessment of product quality. The ranking results are recorded in a rank matrix x_{ij} , $i = \overline{1, m}$, $j = \overline{1, n}$, specifying the place of j-th parameter among n other parameters by i-th expert.

Since opinions of panelists not always match each other, total ranks are determined to obtain an objective assessment.

$$R_j = \sum_{i=1}^{m} x_{i,j}; \quad j = \overline{1,n}, \tag{1}$$

and the coefficient of concordance W is calculated, which characterizes the objective relationship between the scores of m independent panelists using the equation:

$$W = \frac{12 \cdot S(d^2)}{m^2 \cdot (n^3 - n)}, \tag{2}$$

$$S(d^2) = \sum_{j=1}^{n} \left[\sum_{i=1}^{m} x_{i,j} - \frac{1}{2} m(n+1) \right]^2, \tag{3}$$

ranging from 0 in the absence of relationship between rankings by experts, to 1 with their full consent in ranking the impact on the product quality Q.

After assessing the significance showing that the indicator of consistency W of panelist opinions is not accidental, weighting factor g_j is assigned to each sensory indicator:

$$g_j = \frac{M}{\sum_{i=1}^{m} x_{ij}}; \quad j = \overline{1,n}, \tag{4}$$

where M – scale factor.

Weighting factors g_j reflect the practical experience of qualified experts and characterize comparative impact of j-th factor on total quality assessment in regression:

$$Q = Q_0 + \sum_{j=1}^{n} g_j x_j, \tag{5}$$

where Q_0 – score of reference product, and allows to objectively identify the most significant factors of deviations from the specified quality.

The vector of weight coefficients is presents as a bar chart in accordance with the index number of the indicator or in descending order of the absolute values of the coefficients. If the distribution of weights is uniform or close to it, then the level of a priori knowledge is low and further accumulation and processing of statistical data is necessary. In turn, uneven distribution with an exponential decrease in the weights corresponds to a high degree of a priori knowledge about the product quality.

3. Multifactorial analysis of variance for sensory evaluation

The data with a multi-level structure is analyzed by multifactorial statistical procedures [17], which allow determining differences between two or more data sets for all dependent variables simultaneously. This helps to reduce the level of overall mistake of the first kind and to assess the degree of relationship between dependent variables, and makes it possible to establish combinations of sensory variables, which allow distinguishing samples in the case of non-manifestation of differences in each variable separately[18-28].

The general algorithm for processing the results of sensory evaluation includes the determination of the sample size from the general population and formulation of a null (H_0) and alternative (H_1) hypotheses; choice of significance level ($\alpha = 0.01$; or $\alpha = 0.05$; or $\alpha = 0.1$) and conducting an assessment; data collection and calculation of total statistical criteria; acceptance or rejection of the null (H_0) hypothesis and result interpretation.

In the case of two-factor analysis of variance, pooling by two factors is used, and in addition to the experimental error, the variance of scores due to individual differences between panelists in the panel is taken into account [29]. In this case, the order of samples A, B and C should be individual for each panelist, and their combinations ABC, ACB, BAC, BCA, CAB, CBA are distributed in equal proportions to ensure complete randomization. The total sample variance for all experiments is equal to sum of the intergroup and intragroup variances. The value of Fisher test is calculated not only as the ratio of the intergroup and intragroup variances of panelist scores, but also as the ratio of the variance of scores between individual experts to the intragroup variance.

Analysis of variance [17, 18] is the basis for software development with a client-server architecture for collection and statistical processing of sensory data. Fisher's exact test goes through all possible options of contingency table with the same total frequencies in rows and columns, i.e. carries out all kinds of construction of null-models, which built on the assumption of no influence on the factor under study [30-32].

The general algorithm for processing the results of sensory evaluation (Figure 1) includes determining the sample size from the general population and formulating null (H_0) and alternative (H_1) hypotheses; selecting the level of significance ($\alpha = 0.01$; or $\alpha = 0.05$; or $\alpha = 0.1$) and conducting an assessment; data collection and calculation of total statistical criteria; accepting or rejecting the null (H_0) hypothesis and interpreting the results.

The influence of the factor is estimated by the Fisher-Snedecor test at the chosen level of significance, not only as the ratio of the intergroup variance of scores from the relationship of factors to the intragroup variance from the experimental error $F = \frac{MS^2_{x1x2}}{MS^2_E}$, but also as a relationships $F = \frac{MS^2_{x1}}{MS^2_E}$ and $F = \frac{MS^2_{x2}}{MS^2_E}$ of factor variances of expert scores for intragroup variance.

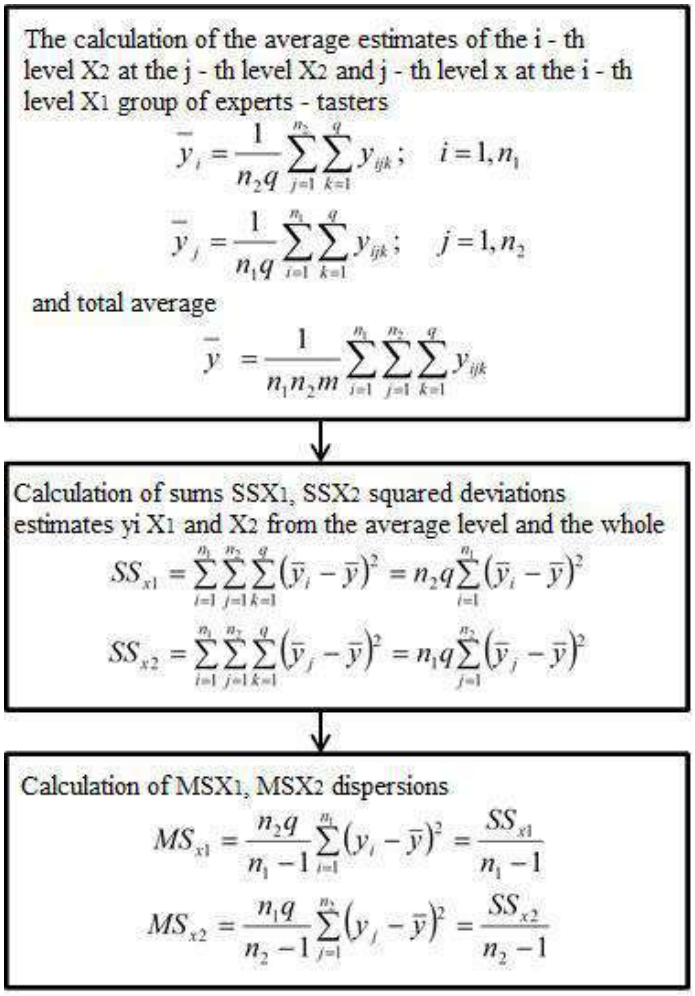

Figure 1. The integrated block diagram of two-factor analysis of variance.

4. Software implementation of expert system for food sensory evaluation with a client-server network architecture

The client-server expert software consists of two subsystems: the server software and the client software (Figure 2). The client software is installed on the user's computer and transmits requests to the server subsystem to process data and requests from clients and to return them back to user's computer.

The functional structure of the system includes six modules that enter parameters and evaluate product descriptors; creating a data set for analysis; sensory profile; comparison with reference; help (for user and administrator).

The list of parameters (Figure 3) determined by the purpose of the sensory evaluation, includes:

- the number of samples and evaluated descriptors;
- type of scale (structured or unstructured); structured five- and nine-point scales are used, according to which each indicator has 5 or 9 degrees of quality, respectively. According to a five-point scale: 5 – excellent quality; 4 – good; 3 – satisfactory; 2 – unsatisfactory, but acceptable; 1 – unsatisfactory.

Nine-point scale recommended in the V.M. Gorbatov Federal Research Center for Food Systems expands the range of sensory scores with the introduction of quantitative characteristics: 9 – optimum quality; 8 – very good; 7 – good; 6 – above average; 5 – medium; 4 or 3 – acceptable,

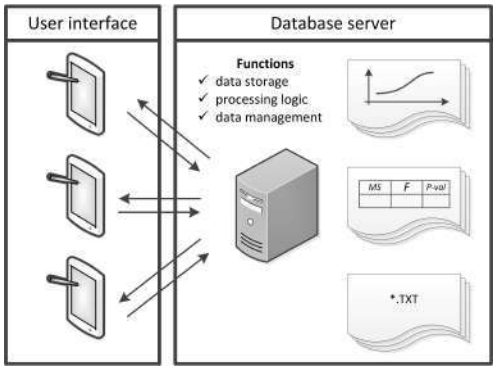

Figure 2. General scheme of the information system.

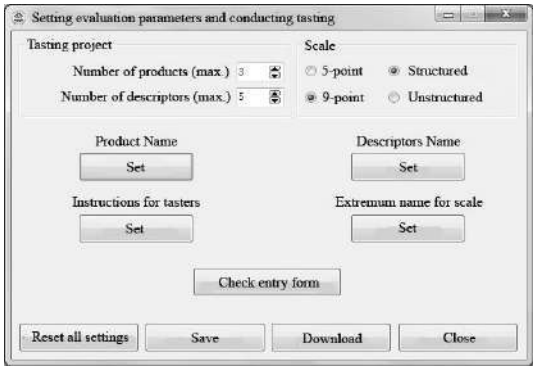

Figure 3. Start menu of the computer system.

but undesirable; 2 or 1 – unacceptable.

- name of the evaluated descriptors;
- folder for saving files with sensory evaluation results (text format *.txt);
- instruction for the sensory panel.

After setting the evaluation parameters, the panelist connects to the server software and enters his identification data (for example, full name) and further, using the intensity scale of the descriptors in the product samples, individually evaluates the intensity of the product descriptors recording the results from the beginning of the scale. After evaluating all the descriptors in the first product, the panelist proceeds with the next product or finishes the sensory evaluation.

Figure 4 represents a table with results of two-factor analysis of variance by the descriptor of "smoke odor".

As a null hypothesis (H_0), the system proposes: – tthe products do not affect the "smoke odor" tdescriptor, and the alternative hypothesis (H_1) – the products affect the "smoke odor" descriptor. To verify them, Fisher's exact test was used at a significance level of $\alpha = 0.05$.

From the data in Figure 5, the calculated value of *F-test* for x_1 factor (products) as $F \approx 19.85$, and the critical region is formed by the right-hand interval $(4.46; +\infty)$. Since F falls into the critical region, the null hypothesis (H_0) is rejected and the alternative (H_1) hhypothesis is accepted, i.e. x_1 factor (products) affects the "smoke odor".

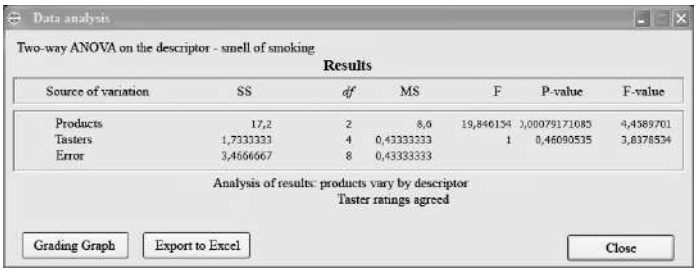

Figure 4. Result of the panelist's consistency check by the "Smoking odor": *SS* – variance; *df* – degree of freedom; *MS* – unbiased scores; *F* – calculated Fisher test; *P-value* – function of *F* distribution; *F critical value* – table value of Fisher test.

Similarly, assessment of the second factor takes place, i.e. "panelists". With a null (H_0) hypothesis, panelists do not affect the "smoke odor" descriptor and with alternative (H_1) hypothesis, panelists affect the "smoke odor" descriptor.

The values in Figure 5 show, that calculated F-test for x_2 factor (panelists) is $F = 1$, and the critical region is formed by the right-hand interval $(3.84; +\infty)$. Since F does not fall in the critical region, the null (H_0) hypothesis is accepted, i.e. influence of x_2 factor (panelists) on the "smoke odor" was not confirmed.

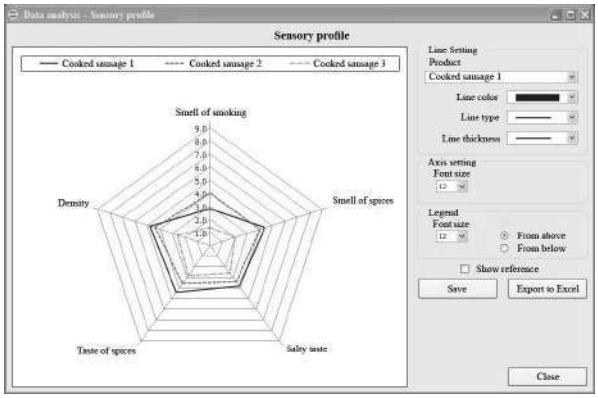

Figure 5. Sensory profile for three cooked sausage samples.

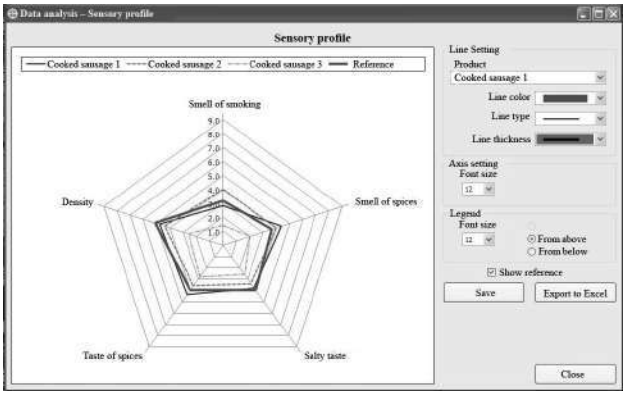

Figure 6. Sensory profile for the reference product and three cooked sausage samples.

Sample determination coefficient:

$$\overline{\rho}_{x_1^2} = \frac{SS_{x_1}}{SS_{x_1} + SS_{x_2} + SS_{x_\epsilon}} = \frac{17.2}{17.2 + 17.3 + 3.47} \approx 0.77, \tag{6}$$

shows that 77% of the total sample variation in the descriptor (smoke odor) is related to the influence of the product type on it.

In the *P-value* column P-value is determined, which corresponds to the calculated value of *F-test*.

In our example, *P-value* for x_1 factor (products) depends on the values of F; *df* and *MS* of this factor in the first row of the table, and has a value of 0.00079.

P-value for the x_2 factor (panelists) depends on the values of F; *df* and *MS* of this factor in the second row of the table, and is equal to 0.46.

According to the Fisher-Snedecor test, when *P-value* is less than 0.05 ($P < 0.05$), the data are not consistent. Based on the calculation, analysis and comparison, the system makes conclusion "Products differ in this descriptor; the scores of the panelists are consistent".

In the case of a consistent and reliable evaluation, the software allows to build a sensory profile (profilogram) of the product characteristic being evaluated (Figure 6) with a number of intensity score axes equal to the number of specific descriptors.

Figure 5 shows an example of the sensory profile for three samples of cooked sausage in the form of a polygon with vertices combining the obtained product characteristics.

Using similar procedures, the software allows to determine the position of a product among competitors based on a comparison of its profile with competitors' product profiles.

For comparison of the product profile with reference, reference product is preliminarily produced, which is the basis for comparing all the products involved in the evaluation. The characteristics of the reference sample determine the reference sensory profile, which is compared with the profile of a similar sample from another batch (Figure 6).

The computer software also allows to identify changes in the sensory characteristics of the product when replacing food ingredients, additives or spices in the formulation or using new types of packaging, etc.

5. Experimental testing of the software

The given example of the network expert system and its dialog interface along with the individual numerical scores and statistical evaluation by panelists provides the objectivized conclusion and

recommendations concerning the product quality based on processing of the subjective data from expert panels of up to 20 panelists by 15 descriptors and 6 product types with the construction of profilograms with up to 15 descriptors and a possibility of data export to MS Excel. Thus, the accuracy and reliability of the objectivized scores presented in Figure 4 is determined by the criteria values for the specific case, as well as by the degree of agreement and competence of the opinions from the qualified panelists evaluating technically uncontrollable sensory properties of food products and their influence on evaluation.

6. Conclusion

Therefore, the computer software with the client-server architecture based on the multivariate analysis of variance realizes the information technology for support of decision making in sensory food evaluation contrary to the traditional expert systems and software packages. It performs real-time collection, accumulation and statistical processing of sensory data from individual panelists and geographically distributed panels and visual presentation of the objectified results in different graphic forms.

7. References

[1] Lawless H T and Heymann H 2010 *Sensory evaluation of food: principles and practices* (New York: Springer Science & Business Media) p 596
[2] Piggott J R and Hunter E A 1999 Review: Evaluation of assessor performance in sensory analysis Italian *Journal of Food Science* **4(11)** 289-303
[3] Tomic O, Forde C, Delahunty C and Naes T 2013 Performance indices in descriptive sensory analysis Acomplimentary screening tool for assessor and panel performance *Food Quality and Preference* **28(1)** 122-133
[4] Johnson R A and Wichern D W 2007 *Applied Multivariate Statistical Analysis* (New York: Prentice-Hall) p 800
[5] Kochan A and Grimm M 1985 Die sensorische Profilmethode *Lebensmittelindustrie* **32(6)** 255-269
[6] Surmacka-Szczesniak A 1998 Sensory texture proffiling-historical and scientific perspectives F*ood Technology* **52(8)** 14-16
[7] Labbe D, Rytz A and Hugi A 2004 Training is a critical step to obtain reliable product profiles in a real food industry context *Food quality and preference* **15(4)** 341-348
[8] Savela-Huovinen U, Muukkonen H and Toom A 2018 Sensory expert assessor's learning practices at workplace: Competencies and contexts in sensory evaluation *Journal of sensory studies* **33(2)** DOI: 10.1111/joss.12315
[9] Mitchell M N 2005 Strategically using General Purpose Statistics Packages: A Look at Stata, SAS and SPS *Technical Report Series. Statistical Consulting Group: UCLA Academic Technology Services* URL: http://www.ats.ucla.edu/stat/technical-reports/umber1_editedFeb_2_2007ucla_ATSstat_trl_1.1__207.pdf (08.09.2018)
[10] Running C A and Hayes J E 2016 Individual Differences in Multisensory Flavor Perception *Multisensory flavor perception: from fundamental neuroscience through to the marketplace* (*Woodhead Publishing Series in Food Science Technology and Nutrition)* **298** 185-210 DOI: 10.1016/ B978-0-08-100350-3.00010-9.
[11] da Silva R D D N, Minim V P R, da Silva A N and Minim L A 2014 Number of judges necessary for descriptive sensory tests *Food quality and preference* **31** 21-27 DOI: 10.1016/j.foodqual.2013.07.010
[12] Turner R, Ledwith A and Kelly J 2012 Project management in small to medium-sized enterprises: Tailoring the practices to the size of company *Management Decision* **50(5)** 942-957 DOI: 10.1108/00251741211227627
[13] Yemelyanov S V, Burovoi I F and Levada F Yu 1998 Control of Indefinite Nonlinear dynamic systems. Induced internal feedback *Lecture Notes in Control and Information Sciences* **231** 196
[14] Brockhoff P B 2003 Statistical testing of individual differences in sensory profiling F*ood Quality and Preference* **14(5-6)** 425–434

[15] Naes T, Brockhoff P B andTomic O 2010 *Statistics for Sensory and Consumer Science* (John Wiley & Sons, Ltd) p 287 DOI: 10.1002/9780470669181
[16] Brand Z 2003 *Data analysis. Statistical and Computational Methods for Scientists and Engineers* (Moscow: Mir) p 686
[17] Stahle L and Wold S 1990 Multivariate analysis of variance (MANOVA) *Chemometrics and Intelligent Laboratory Systems* **9** 127-141
[18] Lee S M, Chung S J, Lee O H, Lee H S, Kim Y K and Kim K O 2008 Development of sample preparation, presentation procedure and sensory descriptive analysis of green tea *Journal of Sensory Studies* **23** 450-467 DOI: 10.1111/j.1745-459X.2008.00165.x
[19] Hoehl K, Schoenberger G U, Schwarz K and Busch-Stockfisch 2013 Is Perception of Sucrose and Caffeine Affected by Training or Experience? *Monitoring Training Effects in Female Subjects over a Half-Year Period* **28** 1–13
[20] Brockhoff P B and Sommer N A 2008 Accounting for scaling differences in sensory profile data *Proceedings of 10th European Symposium on Statistical Methods for the Food Industry* (Louvain-La-Neuve, Belgium) 283-290
[21] Smith A, Cullis B, Brockhoff P and Thompson R 2003 Multiplicative mixed models for the analysis of sensory evaluation data *Food Quality and Preference* **14(5-6)** 387-395
[22] Bi J 2003 Agreement and reliability assessments for performance of sensory descriptive panel *Journal of Sensory Studies* **18** 61-76
[23] Naima H A, Mehdi S and Morched C H 2013 Training and Control of a Tactile Sensory Panel *Journal of Applied Sciences* **13** 366-376
[24] Bi J and Kuesten C 2012 Intraclass Correlation Coefficient (ICC): A Framework for Monitoring and Assessing Performance of Trained Sensory Panels and Panelists *Journal of Sensory Studies* **27(5)** 352-364 DOI: 10.1111/j.1745-459X.2012.00399.x
[25] Grawford C M and Di Benedetto C A 2014 *New Products Management* (New York: McGraw-Hill Education) p 608
[26] Moskowitz H R, Porretta S and Silcher M 2005 *Concept research in food product design and development* (Ames: Blackwell Publishing) p 612
[27] Stone H, Bleibaum N R and Thomas A N 2012 *Sensory Evaluation Practices* (San Diego: Elsevier Academic Press) p 438
[28] Johnson R A and Wichern D W 2007 *Applied Multivariate Statistical Analysis* (New York: Prentice-Hall) p 800
[29] O'Mahony M 1986 *Sensory Evaluation of Food. Statistical Methods and Procedures* (New York: Marcel Dekker) p 488
[30] Patefield W M 1981 Algorithm AS 159. An efficient method of generating r x c tables with given row and column totals *Applied Statistics* **30(1)** 91-97
[31] Gotelli N J and Entsminger N J 2003 Swap algorithms in null model analysis *Ecology* **84** 532-535
[32] Strona G, Ulrich W and Gotelli N J 2018 Bi-dimensional null model analysis of presence-absence binary matrices *Ecology* **99(1)** 103-115 DOI: 10.1002/ecy.2043

Convolutional neural network in the images colorization problem

M V Bulygin[1], M M Gayanova[1], A M Vulfin[1], A D Kirillova[1] and R Ch Gayanov[2]

[1]Ufa State Aviation Technical University, K. Marks str. 12, Ufa, Russia, 450008
[2]Higher School of Economics, Myasnitskaya str., 20, Moscow, Russia, 101000

e-mail: vulfin.alexey@gmail.com, kirillova.andm@gmail.com

Abstract. Object of the research are modern structures and architectures of neural networks for image processing. Goal of the work is improving the existing image processing algorithms based on the extraction and compression of features using neural networks using the colorization of black and white images as an example. The subject of the work is the algorithms of neural network image processing using heterogeneous convolutional networks in the colorization problem. The analysis of image processing algorithms with the help of neural networks is carried out, the structure of the neural network processing system for image colorization is developed, colorization algorithms are developed and implemented. To analyze the proposed algorithms, a computational experiment was conducted and conclusions were drawn about the advantages and disadvantages of each of the algorithms.
Keywords: colorization, convolutional neural networks, deep neural networks, image processing, image compression, outlining of contours.

1. Introduction

Modern neural networks (NN) show good results in a wide range of image processing tasks (Figure 1), which could not be achieved earlier by other methods. Thus, the neural network ResNet50 in the classification problem on the Imagenet set showed an accuracy of 96.43%, while the average person correctly recognizes only 94.9% of the images [1-5].

The urgency of the problem is explained by the need to reduce the computational complexity of implementing neural networks for image processing.

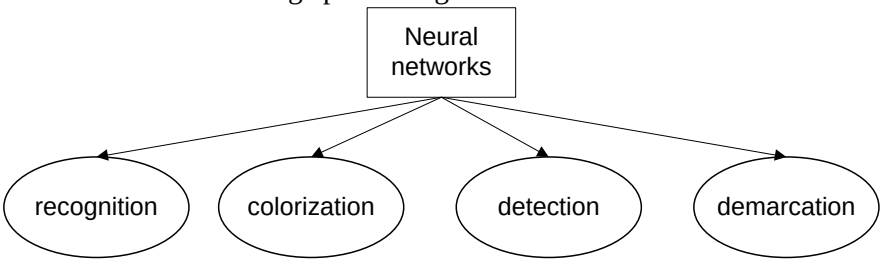

Figure 1. Tasks solved with the help of neural networks.

Goal of the work is improving the existing image processing algorithms based on the extraction and compression of features using neural networks using the colorization of black and white images as an example.

To achieve this goal it is necessary to solve the following tasks:

1. Analysis of image processing algorithms based on neural networks;
2. Development of the structure of a neural network processing system for image colorization;
3. Development of a heterogeneous neural network architecture in the problem of colorization of images;
4. Carrying out the experiment and analyzing the results.

2. Analysis of image processing algorithms based on neural networks

Image colorization is the process of adding color to a monochromatic (black and white) image or video [6]. The color space is constructed in such a way that any color is represented by a point having certain coordinates.

The problem of colorization does not have an unambiguous solution, since one gray scale corresponds to several color space points at once. For this reason, for colorization, it is necessary to use not only data about the color of the point, but also additional information. The source of such information can serve as another image (reference image), or expert opinion, or, identified in the image by a neural network an additional high-level features [7-10].

Today, colorization is in demand, for example, for color versions of black and white films. There are many methods for solving the problem of colorizing images, each of which has its own advantages and disadvantages – Table 1 [11].

Table 1. Methods of image colorization.

Method	Advantages	Disadvantages
Manual colorization	Accuracy of the colorization	Manual division into multiple zones with the color assignment; Impossibility of automatically separating the boundaries of significant areas in the presence of fuzziness or with considerable complexity
Neural network coloring based on reference points and expert data	High processing speed (5-7 s); Quite high quality of colorization due to the analysis of expert data	It is not always possible to determine the colors of the desired image points; Self-matching color for a point is a difficult task; If coloring a large number of similar images, it is necessary to specify hints points for each.
Neural network colorization based on reference points	The colorization of one image takes less than 2 minutes; The process does not require human intervention.	Low quality of colorization (photos do not turn out to be full-color, most of the pictures are painted in brown tones); The image size is limited to 1 MB.
Neural network colorization	Open source and a detailed description of the principles of its operation; It does not require large processing power and can be run in a Google Colaboratory or FloydHub environment.	Low quality of colorization of most images.

Therefore, the actuality lies in developing a neural network architecture for image colorization based on existing solutions, characterized by the organization of the input space of high-dimensional

features and the reduced number of layers and neurons in the hidden layers, which allows to increase the speed of image processing and maintain the required quality of processing.

3. Development of the structure of a neural network processing system for image colorization

When carrying out a computational experiment with a neural network based on [12], it was found that after the colorization some of the images lose their clarity. To improve the process of colorization, it is necessary to apply the image with selected contours to the inputs of the neural network as a source of additional information - meta-attributes, in addition to the image itself.

The solution proposed in this work is based on [12] and uses the allocation of image contours with the help of the neural network InceptionV3 [13] to improve the colorization of images through the use of meta-features.

In the proposed solution, a hint is a color image containing information that can help a neural network when coloring (for example, a similar color photo or a photo of a person presented in the main photo, painted by a expert).

If the neural network inputs is fed by the original image, its outlines, extracted features and the uncompressed image-hint, the neural network will have too many adjustable coefficients, which will lead to a significant increase in the requirements for computing resources for training and further work of the NN in color mode. It is suggested to compress images (original monochrome and image-hints), as well as submit selected outlines in a compressed form.

Thus, the original task is divided into the following subtasks:

1. Compress the original monochrome image;
2. Extract and compress the outlines from the original image;
3. Extract the signs from the image using one of the giant neural networks;
4. Compress the image-hint;
5. Train a neural network that takes inputs to the results of solving past subtasks and receives a color image output.

Thus, a generalized structure of a heterogeneous convolutional neural network is proposed (Figure 2).

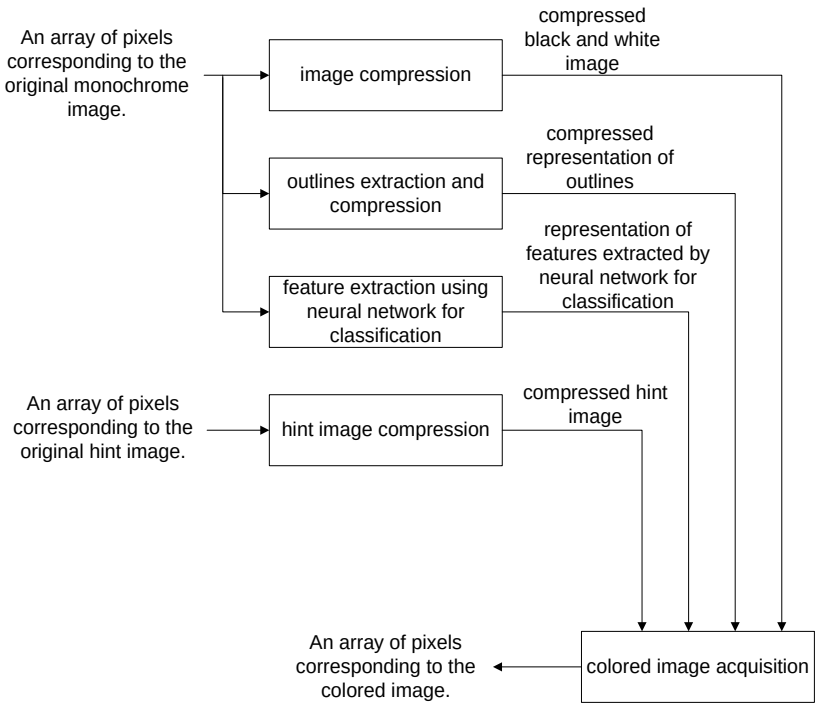

Figure 2. Generalized structure of a neural network solution.

It is important to note that the solutions obtained in solving the first four subtasks can be used to solve other problems.

3.1. Algorithms of compressing the original image

The tasks of compressing the original black-and-white image and the color hinting image are related to the tasks of information compression. It is possible to use methods that eliminate visual redundancy – information that can be deleted without compromising human perception.

A general classification and comparative analysis of image compression methods suitable for integration with subsequent neural network processing layers is shown in Figure 3 and Table 2.

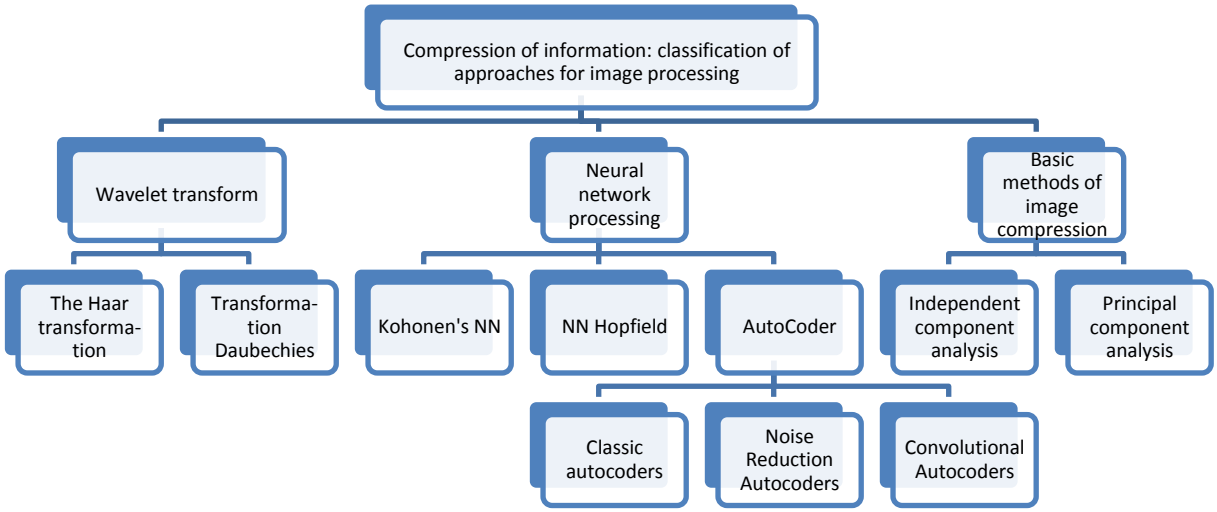

Figure 3. Classification of approaches to image compression.

When learning neural network with auto-coding, the problem of choosing the error function and optimizer arises. The most common error functions are MSE – mean squared error. Modern optimizers allow to prevent errors from reaching the local minimum, help to more evenly update the network weights and increase the speed of training. Some features can be extremely informative, but they are rare to meet. For this reason, updating the network parameters, taking into account the extent to which a typical feature represents this parameter, can make learning more effective. For this, in the Adagrad [14] Optimizer the sum of the squares of updates for each parameter is stored. The choice of the optimizer and the error function for the auto-encoder is extremely important, since this directly affects the quality and speed of the network. The empirical selection of the optimizer and the error function also seems extremely difficult, since it requires a large number of experiments that take a large amount of time. The use of the MSE error function and the optimizer Adam proved themselves in solving the colorization problem in the works of Amir Avni [9], Emil Wolner [9], Baldasar [15].

To compress the original black and white images, convolutional autocoders were used. The autocoder for image compression accepts a black and white image represented as an array. The dimensions of the original images are 512x512 pixels, so the array and the input layer of the neural network have a dimension of 512x512x1. To solve the main problem, it is necessary to compress the image up to the dimension of 128x128x1. Compression is performed using the encoder. To restore the original images in order to verify the quality of the compression, as well as the training of the encoder, it is also necessary to use a decoder.

3.2. Algorithms of selecting the image object outlines

The most popular algorithms for extracting contours are the methods of Roberts, Prewitt and Sobel, based on the use of operators. However, the resulting contour images are quite large and contain a lot of features. An autocoder could be applied to the image of contours, but data that is of value to a neural network may be lost. Also, if the filters are applied, the solution will not be homogeneous. To isolate contours and simultaneously compress them, it was decided to use an autocoder of the same structure that was used to compress the image, however, during the training of this autocoder, the outputs will be requested not for the original image but for its outlines. To extract the contours for the

training sample, we use the Sobel operator, since the contours obtained by this method are the thinnest and sharpest ones.

3.3. Neural network object recognition systems

At the moment there are many neural networks for the classification of images, but the largest of them and showing consistently high results are InceptionV3, ResNet, NasNet and VGG19. The architectures of these neural networks, as well as the weights for them after training on large image databases are freely available for download. A comparative analysis of modern neural network architectures is presented in Table 3.

Table 2. Image compression approaches.

Method	Advantages and Disadvantages	Possibility of application in the colorization problem
Wavelet compression (Haar wavelet) Wavelet compression (Daubechy wavelet)	Areas with approximately equal brightness make up a small part of the image, zeroing of the constant part is performed When processing with the help of neural networks, the high-frequency coefficients zeroed out at wavelet transform can carry a lot of information	Transformations are based on the features of human perception of images; Loss of features important for the neural network as the main core of the colorization system is possible.
Kohonen's Neural networks	If the number of network clusters is less than the number of different fragments of source images, then the recovery is not accurate.	When compressing arbitrary images that were not contained in the training sample, an image consisting of fragments that were in the training sample will be restored. In the problem of image colorization, the approach is not applicable.
Hopfield's Neural Networks	Application as an associative memory allows the exact reconstruction of a distorted image.	In the event of an arbitrary image submission, the image from the training sample closest to the image being fed will be restored.
Neural network autocoders	A feature is the ability to recreate the output of the same signal as the input (displays a larger space with complex connections in a space of smaller dimensions); Ability to represent diverse and complex varieties.	The most suitable are convolutional autocoders using the dropout algorithm of the convolution and sweep layers. The greatest effect when compressing images of one type, such as handwritten figures, aircraft or persons.
Noise-reduction neural network autocoders	Restore the input x not by itself, but from its noisy representation $\tilde{x}$. The artificial noisiness of the input data (augmentation) forces the NN to construct independent features	
Sparse neural network autocoders	Introduces a measure of dissimilarity between the distribution of attributes of input images and is added to the objective function as a regularizer	
Method	**Advantages and Disadvantages**	**Possibility of application in the colorization problem**
Conversion neural network autocoders	Built using convolutional layers in the encoder and scan layers in the decoder.	
Classical methods of dimension reduction (principal components analysis, independent components analysis)	Linear attribute systems are distinguished.	They are used when compressing images of the same type with similar characteristics.

Table 3. Features of neural networks in the task of image processing.

Neural network	Architecture	Features
VGG-19	Total number of coefficients is 144 million. Convolution with the 5x5 core is replaced by two convolutions with a 3x3 core. The saving of the number of coefficients is 22%. In case of replacing one convolutional layer 11x11 with three layers of 3x3, the savings will be 70%.	Files describing the network structure and storing its weights have a size of more than 600 MB
InceptionV3	Inception family networks are built on Inception layers and consist of layers of convolution, sweep, subsampling. Convolution layers with a 5x5 core are replaced by two 3x3 layers; The convolution layers of 3x3 are replaced by two layers of 3x1 and 1x3; The convolution architecture has been modified to avoid a sharp decrease in the dimension of the feature space.	The network achieves an accuracy of image recognition Imagenet top5 95.8%. This result is better than that shown by the person: 94.9% [13]
ResNet	ResNet is based on several initial layers with VGG-19, followed by Deep Residual Learning. ResNet uses 152 layers to predict the difference between the outputs of the last layer VGG-19 taken and the desired result.	The network contains fewer coefficients than the original VGG-19, but the ensemble of such networks set a record, the error of top5 when processing the Imagenet database was 3.57% [16].
NasNet	This neural network is created within the framework of the AutoML project for the automated creation of machine learning models. AutoML created several layers, the architecture of which has not been found before	NasNet showed results on the basis of ImageNet better than any other neural network created by man. The NasNet neural network shows classification results close to 75% accuracy, even with a small number of parameters and addition / multiplication operations, which will allow using it even in mobile devices.

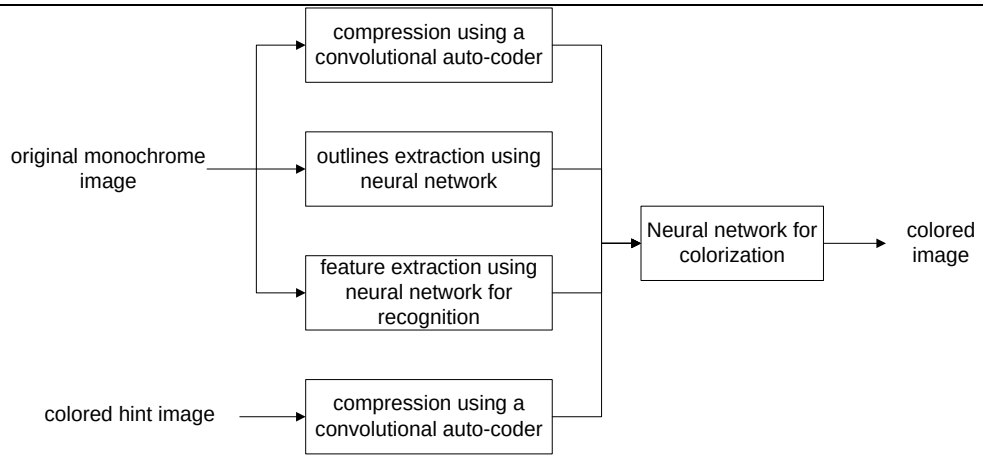

Figure 4. Neural network architecture for colorization.

To extract the features in the work, it is suggested to use the NasNet network, since it shows good classification results even with a small number of layers, and, therefore, the signs extracted with it are the most informative.

The final structure of a heterogeneous convolutional neural network for colorization is shown in Figure 4.

4. Development of algorithms for image processing using neural networks

Formation of a data set for a neural network of the selected architecture is a non-trivial task. Images from classic sets for learning neural networks, such as CIFAR-100 or STL, are too small. In Emile Wolner's decision [13], the discolored images from the Unsplash service were used to teach the neural network and its testing. These images cannot be used to learn this neural network, because the help image cannot be found. Considered the possibility of taking frames from the colorized black and white films. This idea was rejected because every film was painted by professionals in the style of the time when the film was shot and the colorization can turn unnatural. Another reason for refusing this method of obtaining data was the possible problems with copyrights. To obtain natural coloration, it was decided to search for video with a natural color transfer, and then make black and white individual frames, which will be fed as initial. As a hint, it was planned to feed frames went in the video in a few seconds. At the same time, the problem of the clarity of the original frames arose. To solve this, videos were taken that had at least 60 frames per second in the video stream. In this case, blurring when divided into frames is not so noticeable.

The number of seconds of delay between the original frame was chosen randomly in the interval from 1 to 5 to provide a different degree of similarity of frames. However, there was another problem: when training on a video containing one continuous scene, it is difficult to provide a variety of samples for training and testing. When using video collected from different scenes, there were also problems: the original frame could belong to one scene, for example, an urban landscape, and a frame-hint – another, for example, a scene shot on the sea coast. In this case, the Euclidean distance was used to select the pairs of images “original-hint” before decolorizing the original image. If it exceeded a certain threshold value, a warning was output and the frames were checked for belonging to one scene manually.

4.1. Neural network object recognition systems

Convolutional autocoders was used to compress the original black-and-white images – Table 4. The structure of the encoder is described below.

Table 4. Structure of convolutional autocoder for image compression.

Parameter	Value
Type of layers used	Convolutional, subsampling layers, layers of increasing dimension
The size of the convolution kernel	2x2
The size of the subsampling kernel	2x2
Dimension of the original image	512x512x1
Dimension of the compressed image	128x128x1
Number of learning epochs	8
Number of images in the training and validation samples	1500/500
The type of the error function (the nature of the change), Optimizer	RMS (reduction over all epochs), Adam
Activation function	ReLU - for all layers except the last one Sigmoidal - output layer
The number of weighting coefficients (total, in the autocoder)	1060356/528129

The first layer of the neural network is the input layer. The next layer is the convolution layer, this layer has 256 filters, the convolution core is 2x2 in size. Then follows the first downsampling layer, which serves to reduce the dimension. This layer has a core of dimension 2x2. At the output of this layer there are 256 signs of dimension 256x256. The next layer performs the convolution; it has a 2x2 core, as well as 128 filters. To obtain a representation of the desired dimension, a sub-sampling layer is added, having a core dimension of 2x2. The last layer of the encoder is a convolution layer with a 2x2 core, as well as a single filter. At the outputs of the last layer described, an encoded, compressed representation of the original image is removed.

The structure of the decoder has the form resembling a mirror image of the encoder structure. First, the encoded representation passes through a convolution layer, the core of which is 2x2 in size. This layer has 128 filters. Then, to increase the dimension, a layer is inserted that performs the inverse operation of the downsampling. The kernel size of this operator is 2x2. This is followed by a convolution layer, the core of which has a size of 2x2, and the number of filters is 256. Then, to obtain features of the original dimension, a dimension increase layer with a 2x2 core is used. Further, to obtain the final representation, a convolution layer with a 2x2 kernel and the number of filters equal to one is used.

Training is performed by combining the encoder and decoder into an auto-encoder. An array corresponding to the original black and white image is fed to the inputs of the auto-encoder, and the outputs require obtaining the same array. As an activation function for all layers except the last, the "ReLU" function is used. For the last layer, the sigmoidal activation function is used. The training also uses the "Adam" optimizer. The root mean square error is chosen as the error function.

The neural network was trained for eight epochs, the training sample contained 1500 images, the sample for validation had a volume of 500 images. Throughout all epochs, except the last one, a steady decrease in the error was observed, both for the training sample and during validation. The initial error value in the first epoch of learning exceeded 0.09, while by the end of the eighth epoch it was less than 0.011. The total number of coefficients for the auto-encoder is 1060356, of which 528129 are the encoder and the rest are the decoder.

The results of this neural network are shown in Figures 5 and 6.

Figure 5. Original image.

Figure 6. Image after restoration Compressing the black and white hint-image.

Convolutional autocoders was used to compress the initial color images-hints.

The results of this neural network are shown in Figures 7 and 8.

To compress the original color hint images convolutional autocoders were used. Autocoder for image compression accepts a color image as an array (RGB color space is used). The dimensions of the original images are 512x512 pixels, so the array and the input layer of the neural network have a dimension of 512x512x3. To solve the main problem, it is necessary to compress the image up to the dimension of 128x128x3. Compression is performed using the encoder. To restore the original images in order to verify the quality of the compression, as well as the training of the encoder, it is also necessary to write a decoder.

The structure of encoder is described below. The first layer of the neural network is the input layer. The next layer is the convolution layer, this layer has 768 filters, the core of the convolution is 2x2 in size. Then follows the first downsampling layer, which serves to reduce the dimension. This layer has

a core of dimension 2x2. At the output of this layer there are 768 signs of dimension 256x256. The next layer performs the convolution; it has a 2x2 core, as well as 384 filters. To obtain a representation of the desired dimension, a sub-sampling layer is added, having a core dimension of 2x2. The last layer of the encoder is a convolution layer with a 2x2 core, as well as three filters. At the outputs of the last layer described, an encoded, compressed representation of the original image is removed.

Table 5. Structure of convolutional autocoder for hint image compression.

Parameter	Value
Type of layers used	Convolutional, subsampling layers, layers of increasing dimension
The size of the convolution kernel	2x2
The size of the subsampling kernel	2x2
Dimension of the original image	512x512x1
Dimension of the compressed image	128x128x1
Number of learning epochs	8 (1500)
Error (nature of change)	RMS (reduction over all epochs)
The type of the error function (the nature of the change), Optimizer	RMS (reduction over all epochs), Adam
Activation function	ReLU - for all layers except the last one Sigmoidal - output layer
The number of weighting coefficients (total, in the autocoder)	2389254/ 1194627

Figure 7. Original image.

Figure 8. Image after restoration.

The structure of the decoder has the form resembling a mirror image of the encoder structure. First, the encoded representation passes through a convolution layer, the core of which is 2x2 in size. This layer has 384 filters. Then, to increase the dimension, a layer is inserted that performs the inverse operation of the downsampling. The kernel size of this operator is 2x2. Next comes the convolution layer, the core of which has a size of 2x2, and the number of filters is 768. Then, to obtain features of the original dimension, a layer of increasing dimension with a 2x2 core is used. Further, to obtain the final representation, a convolution layer with a 2x2 core and a number of filters equal to three is used.

Training is performed by combining the encoder and decoder into an auto-encoder. An array corresponding to the original color image is fed to the inputs of the auto-encoder, and the outputs require obtaining the same array. As an activation function for all layers except the last, the “ReLU” function is used. For the last layer, the sigmoidal activation function is used. The training also uses the Adam optimizer. The root mean square error is chosen as the error function. These decisions were made after studying neural networks created by Emil Wolner [15] and Baldasar, which showed good results.

The neural network was trained for eight epochs, the training sample contained 1500 images, the sample for validation had a volume of 500 images. Throughout all epochs, except the last one, a steady decrease in the error was observed, both for the training sample and during validation. The initial error value in the first epoch of learning exceeded 0.12, while by the end of the eighth epoch it was less than

0.02. The total number of coefficients for the autocoder is 2389254, 1194627 of which are the encoder, and the rest are the decoder.

4.2. Isolating and compressing the outlines of the original image

To isolate and compress the outlines of the original black-and-white images, convolutional autocoders were used. An array corresponding to the original black-and-white image is fed at the inputs of the autocoder, and at the outputs it is required to obtain an array corresponding to the contours of the original image extracted with the help of the Sobel operator.

Table 6. Structure of convolutional autocoder for outlines compression.

Parameter	Value
Type of layers used	Convolutional, subsampling layers, layers of increasing dimension
The size of the convolution kernel	2x2
The size of the subsampling kernel	2x2
Dimension of the original image	512x512x1
Dimension of the compressed image	128x128x1
Number of learning epochs	8
Number of images in the training and validation samples	1500/500
The type of the error function (the nature of the change), Optimizer	RMS (reduction over all epochs), Adam
Activation function	ReLU - for all layers except the last one Sigmoidal - output layer
The number of weighting coefficients (total, in the autocoder)	1060356 / 528129

The results of this neural network are shown in Figures 9 and 10.

Figure 9. The contours extracted by means of the Sobel transformation.

Figure 10. The contours restored after compression.

4.3. Features selection by the NasNet network

As a result of the analysis of the NASNet neural network architecture it was concluded that the number of features needed to build a network for coloring can be extracted from the 257-th layer, if to count from the last layer of the network. This layer has the form 32x32x16, which allows it to be transformed into a layer of dimension 128x128x1, which will be convenient for forming the final input figure for the neural network for colorization.

5. Experiments on image colorization

The implementation of all structures and architectures of neural networks described in the previous chapter was performed in the Google Colaboratory environment using the Keras library. The experiments are performed according to the Table 7:

Table 7. Experiments on image colorization.

Experiment	Input data	Features
Experiment 1	Uncompressed image	A small number of images on which a color change occurred even in the case of colorization of the image of a particular class. Long learning and getting results
Experiment 2	Image compressed with the autocoder 16 times	Realistic colorization of a large number of images of the same class. Low definition of output images in some cases
Experiment 3	An image compressed with an autocoder, as well as a compressed representation of contours	Colorization is unrealistic, but reliably colored objects (sky, water) are observed. In general, the clarity of output images is higher than without using contours
Experiment 4	The image compressed by the autocoder, as well as the compressed image hint	Most of the photos colored with low accuracy. Sharpness of images is broken, not always objects are discernible by a person. In some cases, images are obtained, painted completely reliably (there are differences from the original)
Experiment 5 (6)	Original image, outlines, hint, (NASNet features) in compressed form	Colonization is absolutely unreliable. The network is uneducable.

5.1. Colorization using a fully-connected neural network

As a result of the colorization with the help of a fully connected neural network, trained on the set of "Fruits", unrealistic images were obtained. Colorization is reduced to replacing monochrome black and white images with monochrome brown images. However, when coloring the test sample, positive results were also obtained. In particular, black-and-white photographs obtained natural dark blue shades, as well as natural shades of green when staining stems. Training neural network took a long time, this neural network of all implemented has the greatest number of coefficients, as well as addition/ multiplication operations for obtaining results – Figure 11.

Figure 11. Image from training sample "Fruits" and two output images.

5.2. Colorization with the help of convolutional autocoder

This network structure was tested on the aircraft photos of the CIFAR set. The training of this neural network was carried out in eight epochs. Training took less time than in the case of a fully connected network. The results of coloration can be characterized as good. The shades of the sky are transmitted quite accurately, realistically, the sky's coloring does not overlap planes. The color of the aircraft itself is incomplete, but distortions are not perceived by a person without viewing the original images. However, there is a part of the images, the output versions of which are very fuzzy, blurry, the detailing is much lower than the original images.

Examples of coloration using a neural network of this structure are shown in Figure 12.

Figure 12. Examples of coloration.

5.3. Colorization using a compressed representation of images and a compressed representation of contours

Colorization with the addition of a compressed representation of the contours to the original image led to improved results. This type of colorization successfully showed itself in the photographs of aircraft, as it led to an improvement in the quality of output images and was tested on a set of arbitrary images. The resulting images have become clearer than using coloring without contours, as can be seen in Figure 13, but the color component has become less significant.

Only some areas of the sky were correctly colored. Color quality is comparable to the first works by Emil Wolner.

Figure 13. Colorization without using contours and with using contours.

5.4. Coloring an arbitrary image using a color image hint

When using a color image-hint, the color component of the output image has in many cases significantly improved. Some arbitrary photographs are painted realistically and do not cause problems in human perception. However, for photos for which the hint-image is too far away, the coloration is unnatural. Objects are blurred, sometimes unrecognizable. Also typical is the situation where a neural network “does not recognize” objects and covers the entire image in blue. Also sometimes there is a situation when the network “learns” only part of the image, spends the coloration of this part, and the rest of the image turns muddy, indistinct, and also remains black and white or acquires an unnatural color. In general, this kind of colorization gives an ambiguous result. On the one hand, this method produced the best, most natural images in some cases, but in others – the images at all ceased to be recognizable, which was not observed in other types of colorization.

Examples of coloration using hinting images are presented in Figure 14.

Figure 14. A successful example of coloring using hints, an example of partially correct coloring, an example of incorrect coloring.

5.5. Colorization with the help of a complete set of selected features

When using a compressed original image, a compressed representation of the contours, and a compressed image of the hint, the learning network could not be obtained. As a result of using a neural network after one learning epoch, it was discovered that the output image for any input looks like a monotonically colored square. When analyzing activities at the outputs of a neural network, one can see that there are differences in brightness, but they are insignificant and when they are rounded up to integers they are the same.

Any noticeable changes, except for increasing the learning time and obtaining results were not observed when adding to the set of input data features extracted with the NASNet network. The results of colorization are also single-color images [16-18].

6. Conclusions

The proposed algorithms for processing images based on the extraction and compression of features using neural networks for colorization of black and white images are based on the use of deep convolutional networks of a heterogeneous architecture with pre-trained modules for solving individual subtasks.

The architecture of the neural network for image colorization is developed, based on existing solutions, characterized by the organization of the input space of high dimensionality features and the reduced number of layers and neurons in the hidden layers, which allows to increase the speed of image processing and maintain the required quality of processing.

The proposed solution uses allocation of image contours with the help of the neural network InceptionV3 to improve the colorization of images through the use of metfeatures. The hint is a color image. If the original image is used in its entirety, its outlines, extracted features, and the uncompressed image-hint, the neural network will have too many adjustable coefficients, which will lead to a significant increase in the requirements for computing resources for learning and further work of the NN in the colorization mode. It is proposed to compress images (original monochrome and image-hints), as well as submit selected outlines in a compressed form, which allowed to significantly reduce the number of customized NN coefficients and reduce the requirements for computational resources.

In the future, it is possible to develop the architecture of the colorization system, which is possible by a small increase in the depth of the network, as well as the number of filters on each layer. Perhaps, other architectures should be tested, except for convolutional ones, for example, recurrent neural networks.

7. References

[1] VGG–19 in Keras URL: https://keras.io/applications/#vgg19 (10.06.2018)
[2] ResNet50 in Keras URL: https://keras.io/applications/#resnet50 (10.06.2018)
[3] NASNet in Keras URL: https://keras.io/applications/#nasnet (10.06.2018)
[4] Convolutional Layers in Keras URL: https://keras.io/layers/convolutional/ (10.06.2018)
[5] Profile of Andrey Karpaty *Official site of Stanford University* URL: https://www.cs.stanford.edu/~karpathy/ (10.06.2018)
[6] Hand Colored Films URL: http://www.widescreenmuseum.com/old–color/handtint.htm (10.06.2018)
[7] Soldatova O P, Garshin A A 2010 The use of convolutional neural network for handwriting digit recognition *Computer Optics* **34(2)** 252-259
[8] Izotov P Yu, Kazanskiy N L, Golovashkin D L and Sukhanov S V 2011 CUDA-Enable Implementation of a Neural Network Algorithm for Handwritten Digit Recognition *Optical Memory and Neural Networks (Information Optics)* **20(2)** 98-106 DOI: 10.3103/S1060992X11020032
[9] Zoev I V, Beresnev A P, Markov N G and Malchukov A N 2017 FPGA-based device for recognizing handwritten digits in images *Computer Optics* **41(6)** 938-949 DOI: 10.18287/2412-6179-2017-41-6-938-949
[10] Vizil'ter Yu V, Gorbatsevich V S, Vorotnikov A V and Kostromov N A 2017 Real-time face identification with the use of convolutional neural network and a hashing forest *Computer Optics* **41(2)** 254-265 DOI: 10.18287/2412-6179-2017-41-2-254-265
[11] AI-Powered Software for Colorizing Black and White Photos URL: https://gizmodo.com/ai–powered–software–makes–it–incredibly–easy–to–coloriz–1795298582 (10.06.2018)
[12] Colorizing B & W photos with Neural Networks URL: https://blog.floydhub.com/colorizing–b–w–photos–with–neural–networks/ (10.06.2018)
[13] Image Recognition *InceptionV3* URL: https://www.tensorflow.org/tutorials/image_recognition/ (10.06.2018)
[14] Nikolenko S, Kadurin A and Arkhangelskaya E 2017 *Deep Learning* (Immersion in the World of Neural Networks) p 480

[15] Image Colorization using CNNs and Inception–ResNet–V2 URL: https://arxiv.org /abs/1712.03400 (10.06.2018)
[16] Gonzalez R and Woods R 2005 *Digital Image Processing* (Moscow: Tehnosfera) p 1007
[17] Rangayyan R M 2015 *Biomedical signal analysis* (John Wiley & Sons) p 720
[18] Rutkovskaya D, Pilihjskij M and Rutkovskij L 2008 *Neural Networks, Genetic Algorithms and Fuzzy Systems* (Moscow: Goryachaya Liniya – Telekom)

Acknowledgments
This work was supported by the Russian Foundation for Basic Research, research № 17-08-01569.

Using high-performance deep learning platform to accelerate object detection

S O Stepanenko[1], P Y Yakimov[1,2]

[1]Samara National Research University, Moskovskoe Shosse 34A, Samara, Russia, 443086
[2]Image Processing Systems Institute of RAS - Branch of the FSRC "Crystallography and Photonics" RAS, Molodogvardejskaya street 151, Samara, Russia, 443001

e-mail: serega.stepanenko.97@gmail.com

Abstract. Object classification with use of neural networks is extremely current today. YOLO is one of the most often used frameworks for object classification. It produces high accuracy but the processing speed is not high enough especially in conditions of limited performance of a computer. This article researches use of a framework called NVIDIA TensorRT to optimize YOLO with the aim of increasing the image processing speed. Saving efficiency and quality of the neural network work TensorRT allows us to increase the processing speed using an optimization of the architecture and an optimization of calculations on a GPU.

1. Introduction

Object detection is becoming more and more popular [1]. It has become possible with the development of new powerful computational devices and the use of neural networks, which can find objects in an image having high accuracy. A system that is based on an artificial neural network is not a big problem to be created because there is a large number of different frameworks which simplify creating of a neural network reducing the network development to functions call. The object detection problem requires high computational power, and in real tasks, for example processing of a video stream, powerful equipment is required [2]. For example, FPS of YOLO work on NVIDIA GTX Titan X is about 40 [3], FPS of SSD on NVIDIA GTX Titan X is 19 [4], FPS of FasterR-CNN on Tesla k40 is 5 [5], FPS of Fast R-CNN is 0.5 [3]. All those algorithms except for YOLO have FPS less than a common camera frame rate.

Nowadays there are many solutions for object detection [6]. All of them use different algorithms to detect, can detect with different accuracy and can have different speed of processing [7]. The most existing solutions use CUDA [8] to process data in parallel. Via CUDA, we can increase the processing speed but there are other ways to increase the processing speed as well. An optimization of the neural network architecture can be used to make the processing faster and to remain the accuracy at the same level. But it's not always easy to make especially if the network has a very complex architecture. There is a way to increase the neural network processing speed not spending much time to change the program.

There is a platform which is able to increase the neural network processing speed using algorithms to optimize an architecture and using abilities of NVIDIA GPUs to increase calculations as well. This platform is called TensorRT [9]. TensorRT provides an API for creating of neural networks and allows us to optimize models of many popular frameworks as well. It makes that convenient to use in many cases because it's possible to accelerate the program not spending many resources to change the code.

2. Convolutional neural networks inference technologies

The word inference means receiving the result of work of the neural network which was trained on some data set. This article considers a use of the platform TensorRT to accelerate an algorithm for object detection that is called YOLO [9].

2.1. YOLO

YOLO [10] – is an algorithm for object classification and detection using convolutional neural networks to do that. Pros of convolutional neural networks for tasks of this type are that convolutional neural networks can process images having more simple architecture than standard neural networks. There are many implementations of YOLO based on different frameworks and written in different programming languages. The standard implementation is based on the neural darknet which is written in the programming language C. The work of YOLO starts from changing of the input image. It becomes 448x448x3, where 448x448 is the image size, 3 is color channels amount. At first the image is passed through the modified net GoogleNet. It's the 1st 20 layers of the network. The output of this part of the network is 1024 feature maps with size of 14x14. Then the images are passed through a sequence of convolutional layers and a sequence of pooling layers. At the moment of getting into a fully connected layer there are 1024 feature maps with size of 7x7. After the images have been passed through 2 fully connected layers the network provides prediction of some class belonging and provides the position of an object in the image [11].

To define the object bounds in YOLO algorithm at first a grid with size of SxS is imposed. Then object prediction is done for each cell. A vector with size of 5*B+C is created for each grid element, where B is bound amount which are predicted by a grid element, C is class amount which the network can predict, 5 defines object amount which can be found. 1st 5*B values of the vector show coordinates of the center of the bound inside the grid cell, height and width and probability that the bound has been defined correctly. Other C values show probability that the object center is at the center of this cell. As a result, there are S*S*B bounds of objects with class probabilities. Then the vector is sorted descending and the algorithm Non maximal suppression is used. It repeats for every class. As a result, all bounds are viewed. The max probability of classes is considered for every bound and if it is positive then the bound is put on the image [3].

2.2. TensorRT

TensorRT is a platform of deep learning by NVIDIA [12]. Nowadays there are 5 versions of TensorRT. Every new version is able to interact with greater number of layer types of a neural network and mathematical operations. TensorRT enables to use implemented parsers for many popular frameworks. It contains: Tensorflow, Caffe2, PyTorch, Mxnet, Microsoft Cognitive Toolkit, Chainer. Tensorflow has built-in TensorRT 3.0 [9]. In case when the network is created on these frameworks it is very simple to use TensorRT. It is enough to use ат implemented parser. The process of the network creating with use of a TensorRT parser is shown in figure 1. If the network is not created on these frameworks, then it's possible to use the API of TensorRT to transfer the network model.

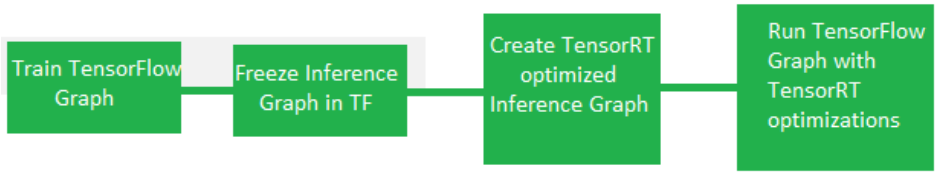

Figure 1. A flow of the network creating with use of TensorFlow on TensorRT.

The advantage of TensorRT using is that this platform is able to accelerate a neural network using an algorithm to simplify the network architecture not changing the network functionality and using abilities of NVIDIA GPUs to accelerate calculations.

To simplify the network architecture TensorRT analyzes a graph that represent the network model. If there are elements in the graph which are repeated, then TensorRT merges them. As a result the network size becomes less.

Acceleration on a GPU is possible due to an ability to use “Tensor Cores”. These cores allow to use half-precision data type float16 for calculations. It is not possible if CUDA is used. CUDA allows to use data type float32. The processing speed increases due to much more fast transfer of data and more fast calculations with this data type. This type of accelerating is possible only with use of a little amount of GPUs which can provide this technology.

3. YOLO implementation

To compare the processing speed implementations of YOLO with use TensorRT platform and without use, with use of one data set and same trained models, have been considered.

3.1. Implementation of YOLO without use of TensorRT

3.1.1. Darknet

To compare performance one of implementations of the YOLO algorithm that is based on the neural network darknet has been considered. YOLO was run on a GPU. To do that CUDA 10.0 and OpenCV were required. YOLOv2 model was used as the model. Before running it’s required to make the project. It can be done via running the command make from the project folder. After installing There will be an executable file which must be run. To type a command with required options is enough to run. The command for running the program is the follow: *./darknet detect path_to_cfg_file path_to_weights_file*. Darknet allows to process a video from a file and from a webcam.

3.1.2. Darkflow

Another implementation of the YOLO algorithm in the language python that uses Tensorflow. It is required to install CUDA 9.0, Tensorflow 1.0, Numpy, OpenCv 3.0 or above to run this program. It is required to have CUDA 10.0 and CUDA 9.0 to run darkflow and other implementations in one PC. To change the CUDA versions it is enough to update the environment variables. Darkflow has an ability to process a video stream. Before running it is required to run an installation script. After installatiom the program can be run via command: flow --model path_to_cfg_file --load path_to_weights_file --imgdir path_to_folder_with_images –gpu percent, where percent – a digit from 0 to 1 that shows the percent ofGPU usage. 0 – o% of usage. 1 – 100% of usage. The processing is on a CPU if –gpu has not been specified. Probably in this case the processing speed is significantly less than in case of processing on a GPU.

3.2. Implementation of YOLO with use of TensorRT

This article presents an implementation of YOLO with TensorRT 5.0 [13]. Before launching the program it’s required to install all dependencies. To make the program runnable CUDA 10.0, TensorRT 5.0,

OpenCV 3.4.0 are required. Files which contain trained model weights and the network configuration are required to run the program. They can be found on the official web site of the YOLO developers. A trained model YOLOv2 is used for research. This model is able to detect 80 classes of objects. At first it's required to install the project using make. Then it's required to set up the project typing paths to all dependencies and to weights and configuration files. Then the data type that will be used must be chosen. It's possible to choose Float32, Float16 and Int8. In case when the GPU doesn't support tensor cores the program can be run with use Float32 only. There is a possibility to process not only single images and batches of images. Video processing is possible when Deepstream SDK is used in addition. Deepstream SDK is developed by NVIDIA to process data in streams. It uses TensorRT, CUDA, Video Codec SDK. Today the last version of Deepstream SDK is 3.0. It's possible to process video without use of Deepstream SDK when the source code is changed to make it possible to extract frames from video streams. Such capability is provided by OpenCV. To run the program, it's required to type the following command:

trt-yolo-app

The following options are available for this command:

- Batch_size – Images amount which are processed at the moment
- Decode – Input is either True or False. It is for decoding of images. True by default.
- Seed – A parameter for the random digit generator.

After the program work has been finished files which contain processed images are saved to a folder. To process a video, it's possible to use OpenCV which extracts frames from the video stream. There is another way to process a video to use deepstream a library by NVIDIA to process streams. Deepstream uses libraries for accelerating stream processing and uses TensorRT and CUDA as well.

Also Darkflow was modified in order to be run on TensorRT.

4. Experiment researches

2 implementations of the YOLO algorithm were used with use of the one trained model YOLOv2 for experimental research. 2416 images were used as input. Output images which objects were found on were saved to a folder. Processing time of every image were written to a file for the implementation without TensorRT. Processing time of every image wasn't calculated and the average time was calculated. All experiments were done on a PC with characteristics which are presented in table 1.

Table 1. Main characteristics of the PC.

GPU	CPU	Memory
NVIDIA GeForce GT 710	AMD FX-4300	4 GB
NVIDIA GeForce GTX 950	Intel Core i5-6500	8 GB

Average FPS of the image set processing by Darkflow implementation is presented in table 2.

Table 2. FPS of Darkflow work.

GPU	FPS
NVIDIA GeForce GT 710	1.31
NVIDIA GeForce GTX 950	10.53
Tesla p100	120
NVIDIA GeForce GTX 2080 TI	170

Average FPS of the image set processing by Darknet is presented in table 3.

Table 3. FPS of Darknet work.

GPU	FPS
NVIDIA GeForce GT 710	1.2
NVIDIA GeForce GTX 950	6.25

Darknet processes the images slower than Darkflow. Average FPS of the image set processing by an implementation of YOLO in TensorRT API is presented in table 4.

Table 4. FPS of an implementation of YOLO in TensorRT.

GPU	FPS
NVIDIA GeForce GT 710	5
NVIDIA GeForce GTX 950	50

YOLO in TensorRT works faster than Darkflow and darknet. The implementation is written in C++ with use of API of TensorRT.

The time of work with different size of a batch was compared for the implementation with use of TensorRT. Batch size was from 1 to 16. It was not possible to allocate the GPU memory if the batch size was more than 16. Time of work with use of different batch size is presented in figures 2 and 3 for 2 different GPUs.

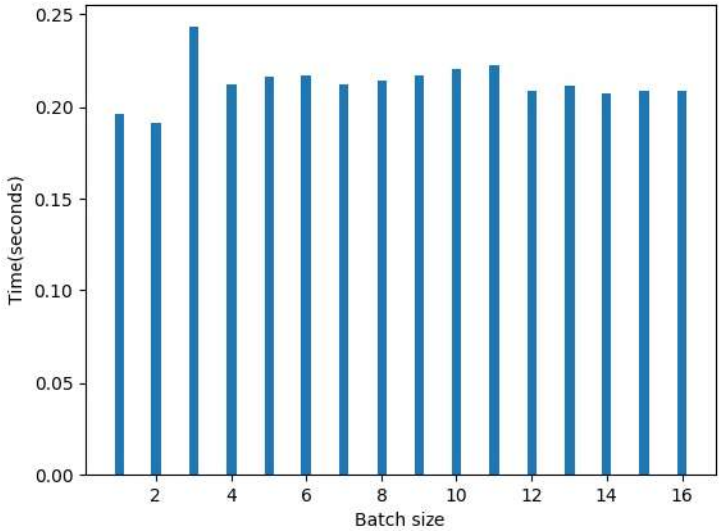

Figure 2. Time of the algorithm work with use of different batch size for NVIDIA GeForce GT 710.

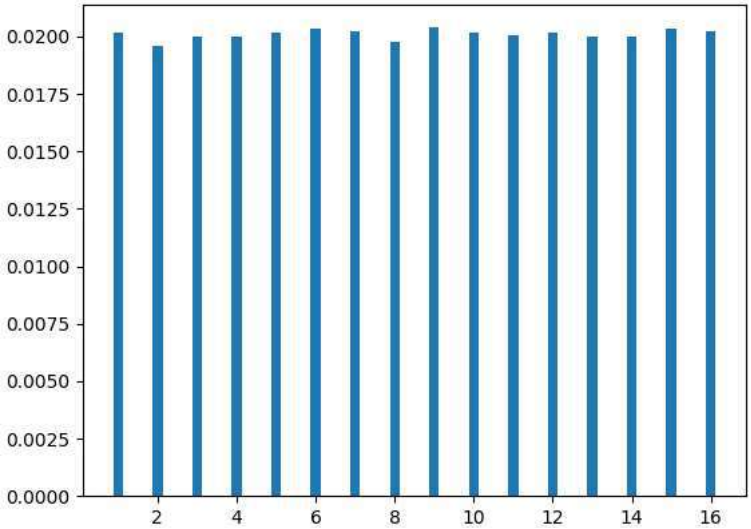

Figure 3. Time of the algorithm work with use of different batch size for NVIDIA GeForce GTX 950.

Difference between work time on 2 GPUs is not significant. The difference between the worst and the best results was about 1.27 times. This could be related to different causes and it's difficult to define the optimal size in advance. It should be done experimental.

Average FPS of Darkflow with TensorRT is presented in table 5.

Table 5. FPS of Darkflow with TensorRT.

GPU	FPS
NVIDIA GeForce GT 710	1.78
NVIDIA GeForce GTX 950	14.41
NVIDIA GeForce GTX 2080 TI	200

Darkflow with TensorRT works faster than Darkflow about in 1.36 times on NVIDIA GeForce GT 710, 1.37 times on NVIDIA GeForce GTX 950, 1.18 times on NVIDIA GeForce GTX 2080 TI. FPS of all used implementation is presented in figure 4.

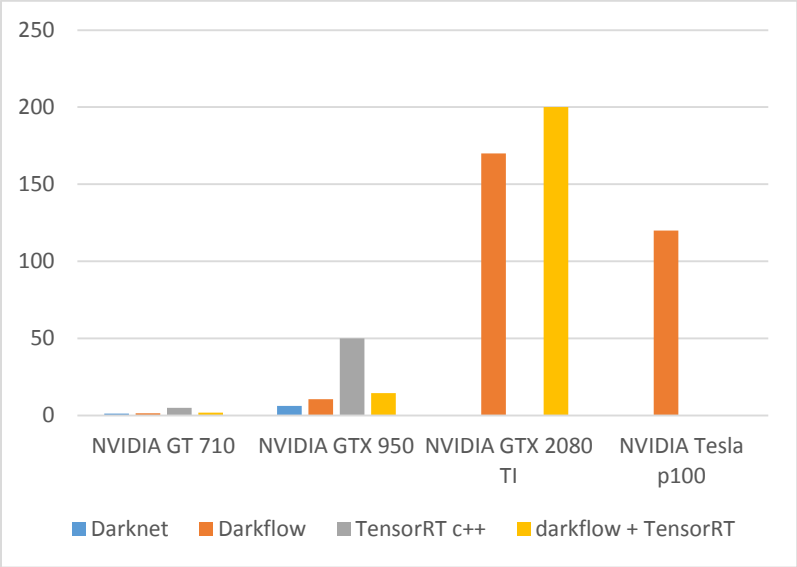

Figure 4. FPS of all used implementations.

Figure 5. A processed frame.

YOLO in TensorRT API has the best acceleration. The acceleration is about 10 times. Darkflow with TensorRT has an acceleration but it is much more less.

After using of TensorRT accuracy of YOLO work has not been reduced. An example of an image that is processed by YOLO is presented in figure 5.

5. Conclusion

The article considered 3 implementations of the YOLO algorithm to compare performance. One of these implementations uses the TensorRT platform. Another implementation was modified in order to work with TensorRT. The platform is able to accelerate the algorithm producing the same accuracy. This ability can be used on practice in video stream processing where processing speed is an important value. Using TensorRT the processing time reduced about by 4 times on NVIDIA GT 710 and about by 8 times on NVIDIA GTX 950 in comparison with the standard implementation of the algorithm if an ability of GPUs to do calculations with use of tensor cores was not used because the GPU could not do such calculations. Darkflow that was modified worked faster in 1.36 times on NVIDIA GT 710, 1.37 times on NVIDIA GeForce GT 950, 1.18 times on NVIDIA GTX 2080 TI.

6. References

[1] Bibikov S A, Kazanskiy N L and Fursov V A 2018 Vegetation type recognition in hyperspectral images using a conjugacy indicator *Computer Optics* **42(5)** 846-854 DOI: 10.18287/2412- 6179-2018-42-5-846-854
[2] Shatalin R A, Fidelman V R and Ovchinnikov P E 2017 Abnormal behavior detection method for video surveillance applications *Computer Optics* **41(1)** 37-45 DOI: 10.18287/2412- 6179-2017-41-1-37-45
[3] Redmon J, Farhadi A 2017 *YOLO9000: Better, Faster, Stronger* (University of Washington, Allen Institute for AI) p 9
[4] Wei L 2016 SSD: Single Shot MultiBox Detector *ECCV: Computer Vision* 21-37
[5] Ren Sh, He K, Girshick R and Sun J 2017 Faster R-CNN: Towards Real-Time Object Detection with Region Proposal Networks *IEEE Transactions on Pattern Analysis and Machine Intelligence* **39(6)** 1137-1149 DOI: 10.1109/TPAMI.2016.2577031
[6] Amosov O S, Ivanov Y S and Zhiganov S V 2017 Human localiztion in video frames using a growing neural gas algorithm and fuzzy inference *Computer Optics* **41(1)** 46-58 DOI: 10.18287/2412-6179-2017-41-1-46-58
[7] Shustanov A, Yakimov P 2017 CNN Design for Real-Time Traffic Sign Recognition *Procedia Engineering* **201** 718-725 DOI: 10.1016/j.proeng.2017.09.594
[8] CUDA URL: https://developer.nvidia.com/cuda-gpus (01.11.2018)
[9] Official site of TensorRT URL: https://developer.nvidia.com/tensorrt (01.11.2018)
[10] YOLO: Real-Time Object Detection URL: https://pjreddie.com/darknet/yolo/ (01.11.2018)
[11] Redmon J, Divvala S, Girshick R, Farhadi A 2015 You Only Look Once: Unified, Real-Time Object Detection *You Look Only Once* p 10
[12] TensorRT integration speeds up tensorflow inference URL: https://devblogs.nvidia.com/tensorrt-integration-speeds-tensorflow-inference/ (01.11.2018)
[13] Implementation of YOLO with TensorRT URL: https://github.com/vat-nvidia/deepstream-plugins/ (01.11.2018)

Acknowledgements

This work was partly funded by the Russian Foundation for Basic Research – Project # 17-29-03112 ofi_m and the Russian Federation Ministry of Science and Higher Education within a state contract with the "Crystallography and Photonics" Research Center of the RAS under agreement 007-ГЗ/Ч3363/26.

Selection of aggregated classifiers for the prediction of the state of technical objects

D A Zhukov[1], V N Klyachkin[1], V R Krasheninnikov[1] and Yu E Kuvayskova[1]

[1]Ulyanovsk State Technical University, Severny Venets street, 32, Ulyanovsk, Russia, 432027

e-mail: zh.dimka17@mail.ru, v_kl@mail.ru

Abstract. The basic data in the problem of the prediction of technical object's state of health based on the known indicators of its operation are the known results of the object state estimation by information about previous service. The problem may be solved using the machine learning methods, it reduces to binary classification of states of the object. The research was conducted in the Matlab environment, ten various basic methods of machine learning were used: naive Bayes classifier, neural networks, bagging of decision trees and others. In order to improve quality of healthy state identification, it has been suggested that aggregated methods combining several basic classifiers should be used. This paper addresses the issue of selection of the best aggregated classifier. The effectiveness of such approach has been confirmed by numerous tests of real-world objects.

1. Introduction

It is possible to forecast the state of the technical object using various methods. The realistic simulation using the time-series system is the most commonly used approach [1-4]. However, as often as not forecasting comes to the object state division in the target horizon in operating ones, i.e. capable of fulfilling intended functions, or faulty ones. Still and all, the diagnostics is carried out according to the object operation and the measurement of indirect values of its functioning.

For example, the engine performance is diagnosed by reference to the fuel consumption rate, the gas temperature, the noise and vibration level, the exhaust gas composition, the clearance between the cylinder and the piston, the clearance between crankshaft necks and bearings and some other indicators [5]. Therein, there is a false alarm risk (when the operating object will be considered as the faulty one) or vice versa when the faulty object is considered as the operating one will be skipped.

Basic data are a priori information about the state of the object according to the results of the previous exploitation: upon the given values of controlled indicators the technical system is operating one or the faulty one. It is assumed that there is some unknown dependence between indicators of the object functioning and its states. Based on basic data it is necessary to restore this dependence, i.e. to plot an algorithm, capable of providing a fairly valid answer about the state of the object for the given set of indicators of its functioning. It is a task for the computer-aided learning or the learning from examples (with a tutor). Binary classification, i.e. the object state division in two categories [6-8], is a special case of this task.

To assess the quality of the plotted algorithm in the context of the opportunity to forecast, the original sample is divided in two disjoint subsets. The first subset is the learning sample itself for handling the task of learning (which, usually, comes to assessing parameters of the model of the appropriate algorithm). The second subset is the control (or test) sample which is not used for learning. This part of the sample is used estimate the forecast error which characterizes the quality of learning. When using the cross-validation, the sample is divided in N parts (in practice, usually, $N = 5$ or $N = 10$). In this case, $N - 1$ parts are used for learning and the rest for control. All possible options are sorted out successively.

Methods of the computer-aided learning are actively used in all kinds of activities. Many different approaches to the classification are used. For example, classical statistical methods (Bayesian classifiers, the discriminative analysis, the logistic regression), methods specially focused on the computer-aided learning (the support vector machine, neural networks), compositional methods (bagging, boosting) and etc. The question at issue that it is impossible to determine which method from selected ones will provide the best solution of the task. That is why many different methods or their combinations are usually used. Decision to apply is made based on findings of the research of the quality functional for the control sample. In works [9-10], the aggregate approach, applying of the combination of several classification methods, is suggested to improve the forecasting quality. These results were certified by the experiment and for technical diagnostics tasks as well [11-13].

The purpose of this study is to plot selection algorithms of the best aggregated classifier.

2. Using of basic classifiers

The most widely known indicator that can be used for the quality assessment of the binary classification is the proportion of correct answers in the control sample,

$$Accuracy = \frac{Q}{N},$$

where Q is the number of correctly classified objects from the control sample and N is the overall control sample size. The opposite characteristic which is the proportion (or the percentage) of errors in the control sample is used more often.

Sometimes the error dispersion (the mean square deviations of the operating state true probability in the r-test $P(Y_r)$ from its forecasted value $\hat{P}(X_r)$) is used to assess the quality of the classification:

$$\sigma^2 = \frac{1}{N}\sum_{r=1}^{l}(P(Y_r) - \hat{P}(X_r))^2.$$

If classes are unbalanced (when there are much more operating states than faulty ones), the proportion of errors cannot be used for the reliable quality assessment of the classification [15-16]. Accuracy and completeness are far more informative

$$P = \frac{tp}{tp + fp},$$

$$R = \frac{tp}{tp + fn},$$

where tp is the number of properly classified operating states, fp is the number of misclassified operating states, fn is the number of misclassified faulty states. Based on these two indicators the uniform criterion can be formed.

$$F = \frac{2PR}{P + R},$$

– it is called the harmonic average of the accuracy and the completeness (F-measure): the closer is the value of F to one, the higher is the quality of the classification.

Area under the ROC-curve (receiver operating characteristics): AUC (area under the curve) can also be selected as the quality functional [16-20]. ROC-curve will be formed, if values $fp(c)$ are taken at the x-axis and values of $tp(c)$ are taken at the y-axis, where c is the threshold. Area under the ROC-curve gives an opportunity to assess the model in general without being related to the certain threshold. Criterion AUC-ROC is resistant to the influence of unbalanced classes. It can be interpreted

as the likelihood that the probability value of the randomly selected object from the class 1 will be closer to 1 in comparison with the randomly selected object from the class 0. Such curves are shown in Fig. 1. They are plotted in the Matlab system for the diagnostics example considered below. In this case three methods of the binary classification: the logistic regression, the support vector machine and the naïve Bayesian classifier) were used.

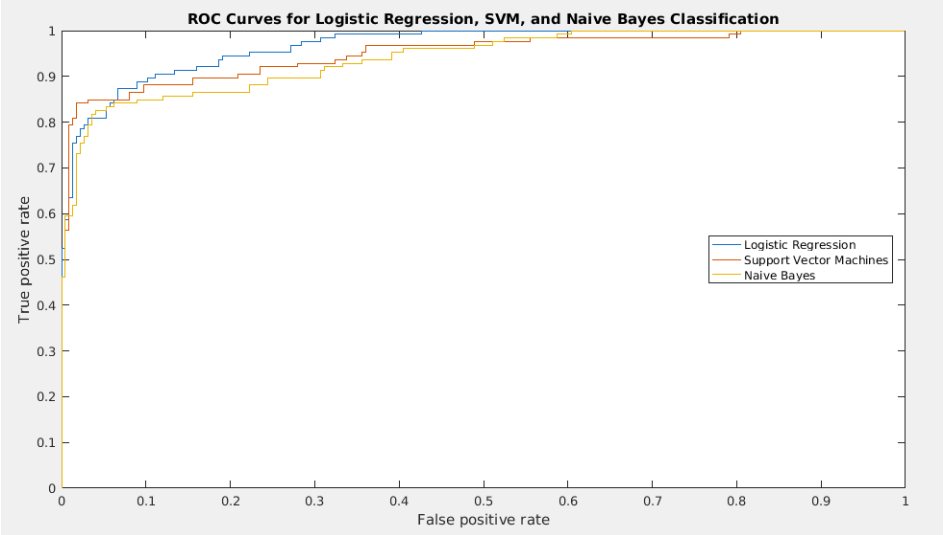

Figure 1. ROC- curves for three classification methods.

As an illustration of the numerical study we considered the water treatment system. We had the results of 348 tests upon eight quality indicators of the drinking water treatment. The system was faulty in 47 cases (when even one water quality indicator was beyond the limits). Whereas the division of basic data in the learning sample and the control sample was carried out randomly, we repeated tests 50 times.

We used the Matlab-package for tests. In Table 1 there are averaged values of the *F*-criterion and the area under the ROC-curve AUC for those five methods of the computer-aided learning where these values were maximum. Estimates suggest that the correlation between these two indicators was non-significant at the significance level 0.05. If the *F*-criterion is the same for selected classifiers, AUC values can be used for selection of the best classification method.

It is apparent that the decision tree bagging showed the best results in the considered example. *F*-criterion discrepancy between the best and the worst (0.801 for the RUSBoost method) results was 8.7%, AUC – 21.5%.

Table 1. Quality measures of various classification methods.

	F-criterion	AUC
Neural network	0.836	0.822
Decision tree bagging	0.871	0.893
Gradient boosting	0.860	0.862
AdaBoost	0.852	0.854
Logistic regression	0.844	0.870

3. Aggregated classifiers

The aggregated approach was suggested for handling tasks of the credit scoring [9-10]. Later it was used for the technical diagnostics of the system state. One and the same classification method is used for plotting of the assembly with compositional approaches (the bagging, the boosting). This method is plotted either at various sample subsets or oriented towards the error compensation of the previous iteration. Multiple use of *various* classification methods plotted with the learning sample is of interest. In this case to achieve the best result it is necessary to resolve following issues: which learning

methods shall be used? How these methods can be combined? How to make the consistent decision about the operating state of the object based on solutions of certain methods?

We will use the exhaustive enumeration of sets from *H* base methods. Then, for example, if *H* = 2, we will get three sets: two basic ones and one aggregated; if *H* = 3, there will be 7 sets: three basic ones, three aggregated ones, by two basic ones and one aggregated of all three basic methods. It is not too difficult to see that in the general case the number of sets is equal to $2^H - 1$. To make the consistent decision about the operating state of the object based on solutions from certain classification methods, we will consider the aggregation of results on the average value, on the median line and using the voting procedure.

Suppose $\hat{P}_K(X_r)$ is the probability that *r*-object is the operating one determined with the aid of the *K*-basic method, $K = 1,...,H$. In mean that when aggregating on the average value:

$$\hat{P}_{AK\,cp}(X_r) = \frac{\sum_{K=1}^{H} \hat{P}_K(X_r)}{H}$$

where $\hat{P}_{AK\,cp}(X_r)$ is the probability that *r*-object is the operating one.

When aggregating on the median line, firstly, it is necessary to range the line with the results of basic methods in the set. If the number of basic methods is odd, the probability that r-object is the operating one will be:

$$\hat{P}_{AK\,мед}(X_r) = \hat{P}_{\frac{H+1}{2}}(X_r).$$

If the number of basic methods is even, the relevant probability will be calculated as the half-sum of the median value results.

The result of the aggregated classification method on the voting procedure is the average value of of basic methods results determining the operating state of the object with the probability, for example, not lower than 0.1 ($\hat{P}_K(X_r) \geq 0{,}1$). Otherwise the probability that *r*-object is the operating one is considered as zero. $\hat{P}_K$ is the probability that *r*-object is the operating one at base values of the object X_r functioning. As can be seen from the above, values of classification probabilities lower than 0.1 are treated as 0 and the rest are treated as 1. Aggregated classification models are plotted using these very values.

In this case, as mentioned above, the division of basic data in the learning sample and the control sample is carried out randomly. That's why structures of aggregated classifiers turn out to be different. The question that has to be answered is what structure to select for making the final decision about the operating state of the object.

As before, we repeated tests 50 times. The sample volume was one and the same (25%) using all eight functioning indicators. Corresponding results of the F-criterion for five options of every aggregation type are shown in Table 2.

For example, the entry in the first line GrB+DTB+AB means that the aggregate of three basic classifiers including the gradient boosting (GrB), the decision tree bagging (DTB) and the AdaBoost boosting method was the best aggregation option on the average value when using the *F*-criterion in this experiment. The number of classifiers included in the aggregate (Table 2) fluctuates from two to six. In the general case it can include all basic classifiers.

Firstly, let us remark that any aggregated method on the *F*-criterion turned out to be better than any basic one. Secondly, values of the *F*- criterion for aggregated methods are not widely diverging. And finally, it is worth paying attention to the fact that the best of basic methods (the decision tree bagging) is included into the structure of all aggregated classifiers.

It is of interest to study the distribution pattern of the *F*-criterion values. As far as the aggregation using the voting procedure is concerned, we applied the following sequence of steps. We used the Statistica system to plot the normal probability curve. Then we transferred this curve to the value distribution histogram (Fig. 2) of this criterion. To check the normality, we used the Shapiro-Wilk criterion recommended for small samples (up to 50 tests). It is apparent that the distribution can be

considered as the normal one when the significance level is 0.05. Similar results were obtained for other classifiers (both basic and aggregated) as well.

Table 2. F-criterion when aggregating.

Aggregate structure	*F*-criterion
Aggregation on the average value	
GrB+DTB+AB	0.891
GrB+ DTB	0.889
DTB+AB	0.889
SVM+DTB+AB+LB	0,889
SVM+DTB	0.879
Aggregation on the median line	
DA+SVM+GrB+DTB+AB+GB+RB	0.892
SVM+DTB	0.881
SVM+DTB+AB+RB	0.891
SVM+DTB+LB	0.888
GrB+DTB	0.887
Aggregation using the voting procedure	
NN+SVM+DTB+AB+RB	0.887
GrB+DTB+AB	0.889
DTB+AB	0.889
GrB+DTB	0.885
SVM+GrB+DTB+LB+GB+RB	0.887

Designations:
GrB – the gradient boosting, DTB– the decision tree bagging, AB – AdaBoost, SVM – the support vector machine, LB – LogitBoost, DA – the discriminative analysis, RB – RUSBoost, NN – the neural network, GB – GentleBoost

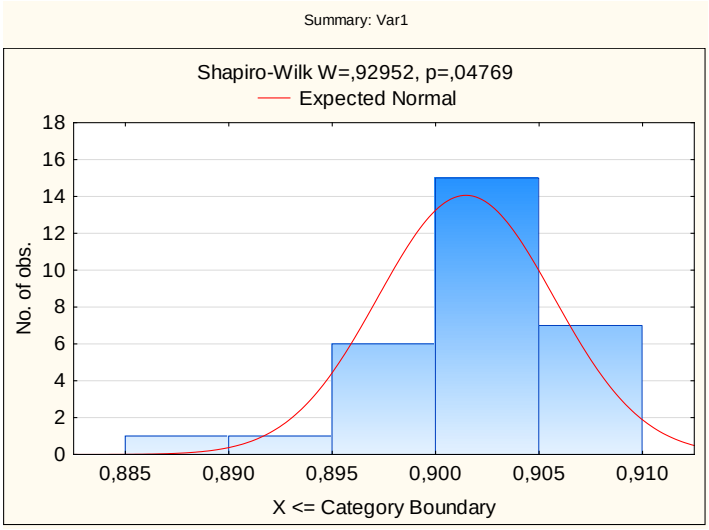

Figure 2. Distribution of *F*-criterion values.

The distribution normality gives an opportunity to use the standard approach for checking the hypothesis that in the given example the aggregation does lead to the improvement of the diagnostics quality.

We checked the null hypothesis for the equality of *F*-criterion average values when aggregating and when using basic classification methods (in comparison with data from the decision tree bagging being taken into consideration as the best basic method). As an alternative, we considered the

hypothesis for excessing of the average value when aggregating. Firstly, we compared dispersions of two samples upon the Fisher criterion (the difference turned out to be statistically non-significant). Then we tried the Student criterion with similar dispersions. It was concluded that the null hypothesis should be rejected: the average value of the *F*-criterion when aggregating is higher than when using basic classifiers.

As has already been noted, values of the *F*-criterion in Table 2 do not much differ. We checked the hypothesis that the increase in the number of basic classifiers (more than two) in the aggregate structure will non-significantly influence the value of the *F*-criterion. We divided the whole sample in two subsets. Data on aggregates consisting of only two components will be included in the first subset. All rest values will be included in the second subset.

Checking of the hypothesis for the equality of average values in these subsets shows its validity: the average value of the *F*-criterion does not change when expanding the number of basic classifiers in the aggregate structure.

A consequence of the above result is the fact that it is possible to reduce dramatically the time required for the calculation. Instead of enumerating all aggregation options when searching for the maximum value of the *F*-criterion (three aggregation methods and 11 basic classification methods used in the Matlab package, $3*(2^{11} - 1) = 6141$ options); it will be enough to enumerate only options including two basic methods ($3*11!/2!9! = 165$).

It is necessary to take into consideration one more circumstance. During all tests the aggregate included the best basic method (the decision tree bagging). Taking this fact into consideration gives an opportunity to scale back the number of options being enumerated by 30.

However, it is necessary to bear in mind that the given results are obtained in tests of only one technical object. Nevertheless, this experiment shows that the suggested approach shall be approbated for the diagnostics of any other system being studied.

4. Conclusion

To assess the operating state of the object it is recommended to select the simplest aggregated classifier with the sufficiently great value of the *F*-criterion. In the given example this classifier is the aggregation on the average value for the decision tree bagging and AdaBoost, or the decision tree bagging together with the gradient boosting (except for sufficiently great values of the *F*-criterion, these combinations can be more often found in Table 2).

The considered approach was also used (except for the water treatment system) when assessing the faulty state of the hydroelectric installation on the vibration level and the technological process of the mechanical processing when it showed similar results.

5. References

[1] Gaskarov D V, Golinkevich T A and Mozgalevskij A V 1974 *Technical condition and reliability prediction of electronic equipment* (Moscow: Soviet radio) p 224
[2] Klyachkin V N and Bubyr' D S 2014 Forecasting of technical object state based on piecewise linear regressions *Radioengineering* **7** 137-140
[3] Krasheninnikov V R, Kuvayskova Yu E, Shunina Yu S and Klyachkin V N 2017 Updating of models predicting objects' state as time series systems and multivariate classifier *Herald of Computer and Information Technologies* **6** 11-16
[4] Krasheninnikov V R, Klyachkin V N and Kuvayskova Yu. E. 2018 Models updating for technical objects state forecasting *3rd Russian-Pacific Conf. on Computer Technology and Applications (RPC). IEEE Xplore* 1-4.
[5] Birger I A 1978 *Technical Diagnostics* (Moscow: Engineering) p 240
[6] Witten I H and Frank E 2005 *Data mining: practical machine learning tools and techniques* (San Francisco: Morgan Kaufmann Publishers) p 525
[7] Merkov A B 2011 *Pattern recognition. Introduction to statistical learning methods* (Moscow: Editorial URSS) p 256
[8] Voronina V V, Miheev A V, Yarushkina N G and Svyatov K V 2017 *Machine learning: theory and practice* (Ulyanovsk: UlSTU) p 290

[9] Yumaganov A S and Myasnikov V V 2017 A method of searching for similar code sequences in executable binary files using a featureless approach *Computer Optics* **41(5)** 756-764 DOI: 10.18287/2412-6179-2017-41-5-756-764
[10] Kropotov Yu A, Proskuryakov A Yu and Belov A A 2018 Method for forecasting changes in time series parameters in digital information management systems *Computer Optics* **42(6)** 1093-1100 DOI: 10.18287/2412-6179-2018-42-6-1093-1100
[11] Klyachkin V N, Kuvayskova Yu E and Zhukov DA 2017 The use of aggregate classifiers in technical diagnostics, based on machine learning *CEUR Workshop Proc.* **1903** 32-35
[12] Maksimov A I and Gashnikov M V 2018 Adaptive interpolation of multidimensional signals for differential compression *Computer Optics* **42(4)** 679-687 DOI: 10.18287/2412-6179-2018-42-4-679-687
[13] Kuvayskova Yu E 2017 The prediction algorithm of the technical state of an object by means of fuzzy logic inference models *Procedia Engineering* **201** 767-772
[14] Voroncov K V URL: https://yadi.sk/i/FItIu6V0beBmF
[15] Sokolov E A URL: https://github.com /esokolov/ml-course-hse/blob/master/2018-fall/lecture-notes/lecture04-linclass.pdf
[16] Davis J and Goadrich M 2006 The relationship between Precision-Recall and ROC curves *Proc. of the 23rd int. conf. on Machine learning* (Pittsburgh) 233-240
[17] Klyachkin V N and Shunina Yu S 2015 System for borrowers' creditworthiness assessment and repayment of loans forecasting *Herald of Computer and Information Technologies* **11** 45-51
[18] Neykov M, Jun S Liu and Tianxi Cai 2016 On the Characterization of a Class of Fisher-Consistent Loss Functions and its Application to Boosting *J. of Machine Learning Research* **17(70)** 1-32
[19] Wyner A J, Matthew Olson, Justin Bleich and David Mease 2017 Explaining the Success of AdaBoost and Random Forests as Interpolating Classifiers *J.of Machine Learning Research* **18(48)** 1-33
[20] Chen T and Guestrin C 2016 XGBoost: A Scalable Tree Boosting System *Proc. of the 22nd ACM SIGKDD Int. Conf. on Knowledge Discovery and Data Mining* 765-794

Acknowledgments
This test was carried out with the financial support from the Russian Foundation for Basic Research (RFBR) and the Government of Ulyanovsk region, the project 18-48-730001.

Methods for finding shortest paths on graphs in organizational and economic systems and their implementation

V M Ramzaev[1], I N Khaimovich[1,2] and I V Martynov[2]

[1]Samara University of Public Administration «International Market Institute», G S Aksakova Street, 21, Samara, Russia, 443030

[2]Samara National Research University, Moskovskoe Shosse 34A, Samara, Russia, 443086

e-mail: kovalek68@mail.ru

Abstract. The article implements the functions in Postgre SQL DBMS, finding the shortest paths on graphs, using the wave algorithm method, the Dijkstra's method and the Floyd method. The authors determined models of dependencies of the running time of implementations of the shortest-path search algorithms on graphs on the number of graph vertices experimentally. A comparison of the data obtained as a result of the study was carried out to find the best applications of implementations of the shortest path search algorithms in the Postgre SQL DBMS.

1. Introduction

Modern organizational and economic systems are increasingly using technologies for collecting, analyzing and processing data [1,2], such systems in industrial enterprises include PDM - class systems. In these systems, data is arranged in undirected graphs with different weights. The main task of making decisions in PDM systems is the search for the optimal variant using graph methods [3, 4], this type of search is also actively used for analyzing social networks [5-8]. Currently, issues of the effectiveness of open source software and licenses, which practically do not impose restrictions on its use, are becoming increasingly topical. An example of such software is PostgreSQL DBMS, which by its capabilities comes close to the most common commercial Oracle database. Therefore, the study and analysis of the effectiveness of PostgreSQL DBMS is an important task [9].

In this paper, we study the theoretical foundations of constructing the shortest path search algorithms and the capabilities of the PL / PGSQL programming language built into the PostgreSQL DBMS. To implement the algorithms, databases and software have been developed for finding the shortest paths. The temporal characteristics of the algorithms on the test graphs are investigated and compared with each other.

2. Methods for finding shortest paths on graphs and analyzing the effectiveness of their implementation

Let's consider the wave algorithm, Dijkstra's algorithm, and Floyd's algorithm for finding the shortest paths on graphs. Wave algorithm (wave-tracing algorithm, Lee algorithm) is an algorithm for finding the path, the algorithm for finding the shortest path on a planar graph. It belongs to algorithms based on wide search methods. The wave algorithm in the context of finding a path through a maze was proposed by E.F. Moore. Lee independently discovered the same algorithm when formalizing the routing algorithms for printed circuit boards in 1961.

In step 1 of the algorithm, the function obtains the number of the initial vertex and calculates labels for all vertices of the graph, the resulting values are written to the nodes table.

In step 2 of the algorithm, the function obtains the number of the final vertex and calculates the shortest route to the initial vertex; the function outputs the result as an array with the vertex numbers.

To implement the search for the shortest path by the wave algorithm method on a given graph, the data are presented in the form of a table that contains the following fields: vertex number of the graph, list of adjacent vertices, path mark (No. of wave front of the wave algorithm), previous vertex number.

Here is a block diagram of the wave algorithm.

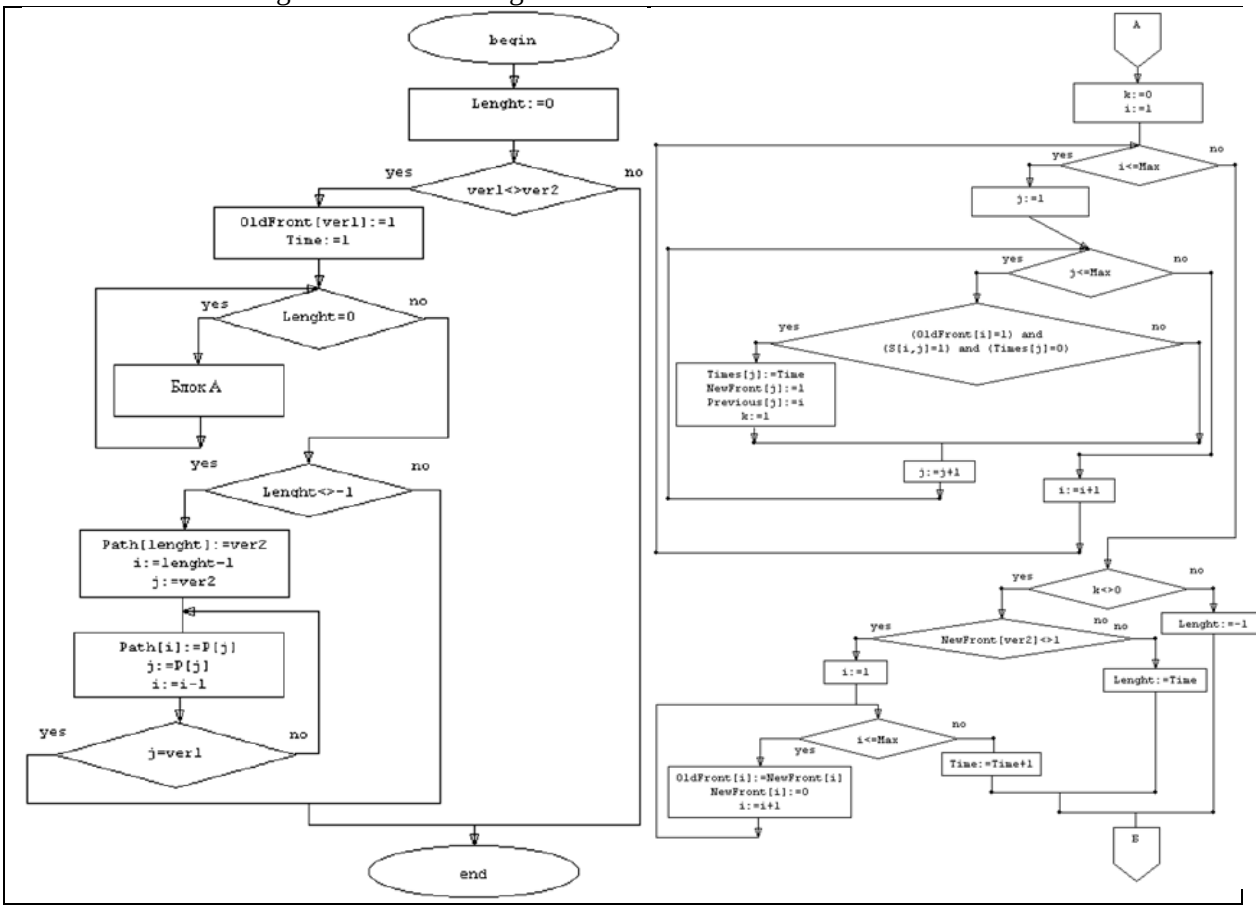

To analyze the operation time of the wave algorithm, calculations were performed on test graphs generated by the PostgreSQL DBMS using the function written by the authors. Each graph is a two-dimensional rectangular table of nodes with the size of N rows and M columns. Each node of the grid (except for the nodes of the last column and the last row) is connected by an edge with three nodes lying to the right, below and diagonally to the right-down from the current node. The lengths of all edges are 1.

To clarify, we present the data in the form of a graph (Figure 1).

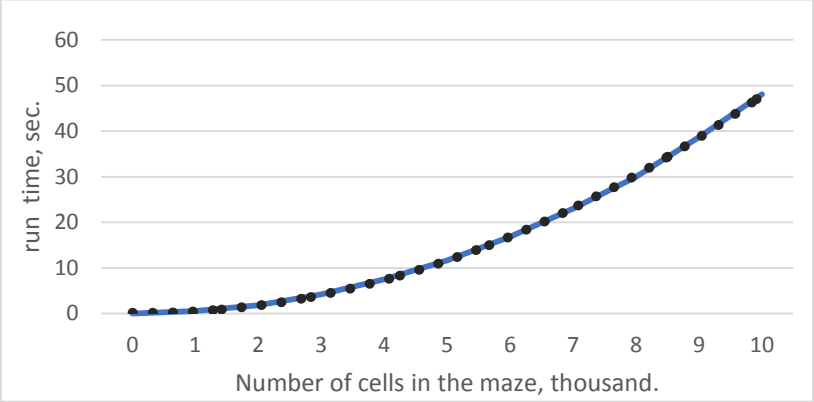

Figure 1. The dependence of the wave algorithm time on the number of vertices.

From the graph it is clear that the dependence is non-linear. We approximate, by a second-order polynomial, the obtained data, to find the function of the dependence of the algorithm time on the number of cells in the maze.

Here is the obtained function:

$$y = 0.47x2\text{-}0.19x\text{+}0.19.$$

The R-squared value (determination coefficient) of the current model is 0.9472, which corresponds to a model of good quality. The next shortest path search algorithm is Dijkstra's. This algorithm was proposed by the Dutch scientist Dijkstra in 1959. The algorithm is described in many sources [9].

Dijkstra's algorithm is applicable to an oriented weighted graph with non-negative weights [10].
In step 1 of the algorithm, the initial node S is assigned the status of a permanent label with zero value d (S). This vertex is called basic and denoted by V.

In step 2, the vertices directly reachable from the base vertex V are assigned temporary label values equal to d (V) + w (V → U), where w (V → U) is the edge weight from the vertex V to the vertex U.

In step 3, among the vertices marked with temporal values, the vertex U is selected with the minimum mark and assigned the status of a permanent mark. The value of the constant label will be equal to the length of the shortest path from the initial vertex S to the vertex U.

In step 4, the vertex U is taken as the base vertex V and the transition to step 2 takes place.
The algorithm ends when all reachable vertices are marked with permanent labels.

To implement the algorithm in the PostgreSQL DBMS, it is necessary to create an Edge table in which the number of the initial vertex for each edge is stored, as well as the number of the final vertex, and the weight of the edge. To restore the path, add the Node table in which everything will be stored.

To implement the algorithm, we use the PL / pgSQL [10] programming language built into the DBMS, in which besides executing SQL queries, we can use standard high-level control instructions for languages.

To analyze the operation time of the Dijkstra algorithm, calculations were made on test graphs. The lengths of all the edges were chosen randomly in the range from 1 to 1,000,000.

For clarity, we present the data in the form of a graph (Figure 2).

The graph shows clearly that the dependence is non-linear. We approximate, by a second-order polynomial, obtained from the data, to find the function of the dependence of the running time of the algorithm on the number of cells in the maze.

Here is the obtained function:

$$y = 1.64x2\text{-}0.06x\text{+}0.05.$$

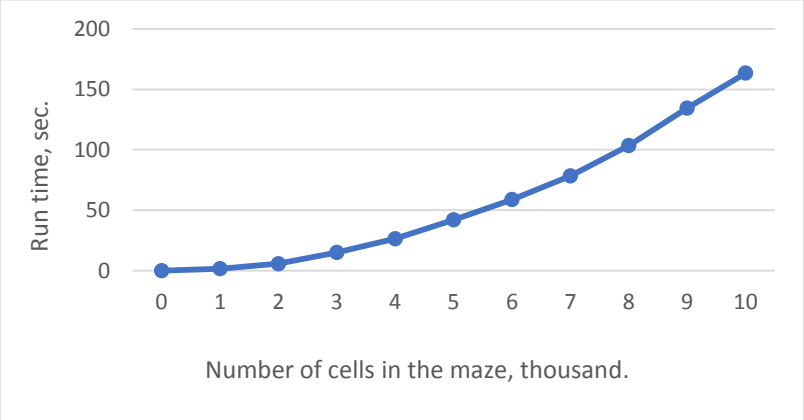

Figure 2. The dependence of the time of the Dijkstra's algorithm on the number of vertices.

The R-squared value (determination coefficient) of the current model is 0.9141, which corresponds to a model of good quality. The next algorithm for finding the shortest paths on graphs is the Floyd's algorithm. This algorithm is a dynamic algorithm for finding the shortest distances between all vertices of a weighted oriented graph. It was developed in 1962 by Robert Floyd and Stephen Worshall.

In step 1, the algorithm calculates and writes into the ADS table of the mD matrix which is the shortest path length matrix; mS is the auxiliary matrix to restore the path.

In step 2, the algorithm will calculate the optimal route from the vertex u to the vertex v of the graph.

To implement the algorithm in PostgreSQL DBMS, create an Edge table in which for each edge we will store the record number, and in fact the task number; the number of vertices of the graph; adjacency matrix; shortest path length matrix; auxiliary matrix to restore the path.

To implement the algorithm, we use the PL / pgSQL [10] programming language built into the DBMS, in which besides executing SQL queries, we can use standard high-level control instructions for languages.

To analyze the Floyd's algorithm time, calculations were made on test graphs. The lengths of all the edges were chosen randomly in the range from 1 to 1,000,000.

To clarify, we present the data in the form of a graph (Figure 3).

From the graph it is clear that the dependence is non-linear. We approximate, by a second-order polynomial, obtained from the data, to find the function of the dependence of the running time of the algorithm on the number of cells in the maze.

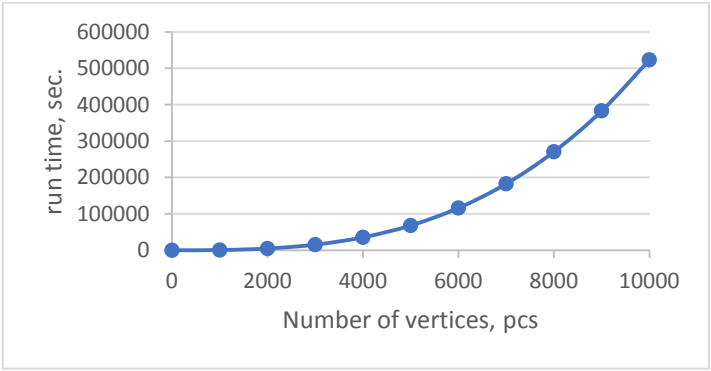

Figure 3. The dependence of the Floyd algorithm time on the number of vertices.

Here is the obtained function:

$$y=5*10^{-7}*x^3+0.0003x^2-0.0735x+2.8405.$$

The R-squared value (determination coefficient) of the current model is 0.9462, which corresponds to a model of good quality. Let us analyze the time of the wave algorithm and the Dijkstra's algorithm on graphs with unit weights containing from one thousand to ten thousand vertices.

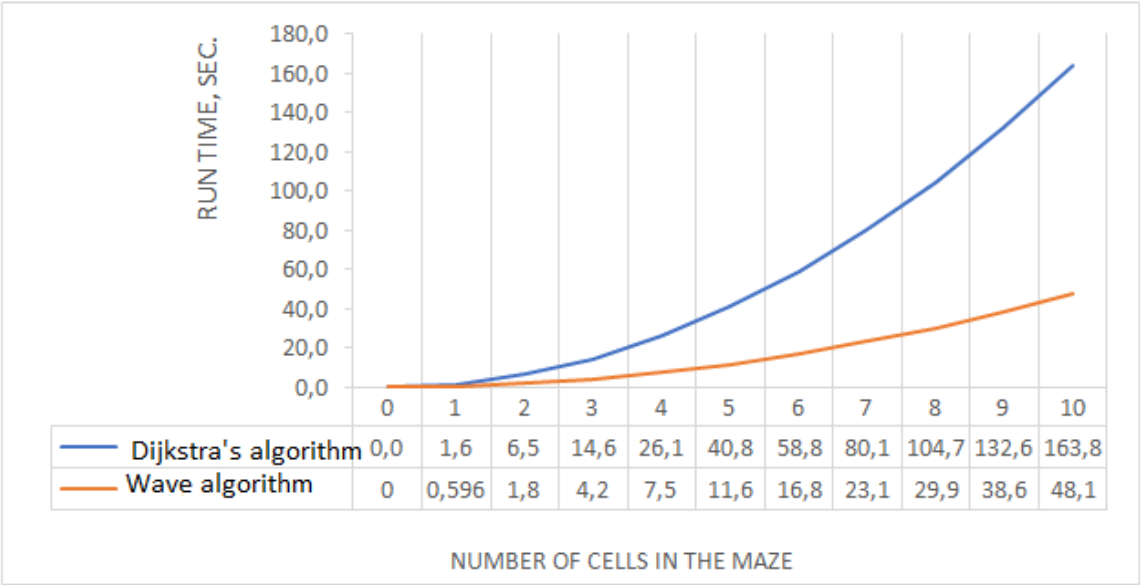

	0	1	2	3	4	5	6	7	8	9	10
Dijkstra's algorithm	0,0	1,6	6,5	14,6	26,1	40,8	58,8	80,1	104,7	132,6	163,8
Wave algorithm	0	0,596	1,8	4,2	7,5	11,6	16,8	23,1	29,9	38,6	48,1

Figure 4. Comparison of the running time of the wave algorithm and the Dijkstra's algorithm.

Let us write the equation of the dependence of the operating time of the proposed implementation of the wave algorithm on the number of vertices in the graph:

$$y=0.47x^2-0.19x+0.19.$$

The R-squared value (determination coefficient) of the current model is 0.8534, which corresponds to a model of good quality. Let us write the equation of the dependence of the operating time of the proposed implementation of the Dijkstra's algorithm on the number of vertices in the graph:

$$y=1.64x^2-0.06x+0.05.$$

The R-squared value (determination coefficient) of the current model is 0.9472, which corresponds to a model of good quality. To calculate the time difference of the proposed implementations of these algorithms, we compare the coefficients at the highest powers in the obtained equations:

$$a= 1.64/0.47=3.48$$

It turns out that the proposed implementation of the wave algorithm copes with the task by 3.5 times faster than the proposed implementation of the Dijkstra's algorithm. From which it can be concluded that in not oriented graphs with unit weights it is best of all to use the wave algorithm.

Let us consider a comparison of the running time of the of Floyd's and Dijkstra's algorithm on test graphs.

Due to the fact that Floyd's algorithm is based on finding the shortest distances between all the graph vertices, and Dijkstra's algorithm for finding the shortest distance from one of the graph vertices

to all others, we will use the following method to compare their operation time. We will compare the time of the Floyd's algorithm and the time of the Dijkstra's algorithm multiplied by *n*, where *n* is the number of vertices of the graph.

Let us present data in the form of a Figure 5.

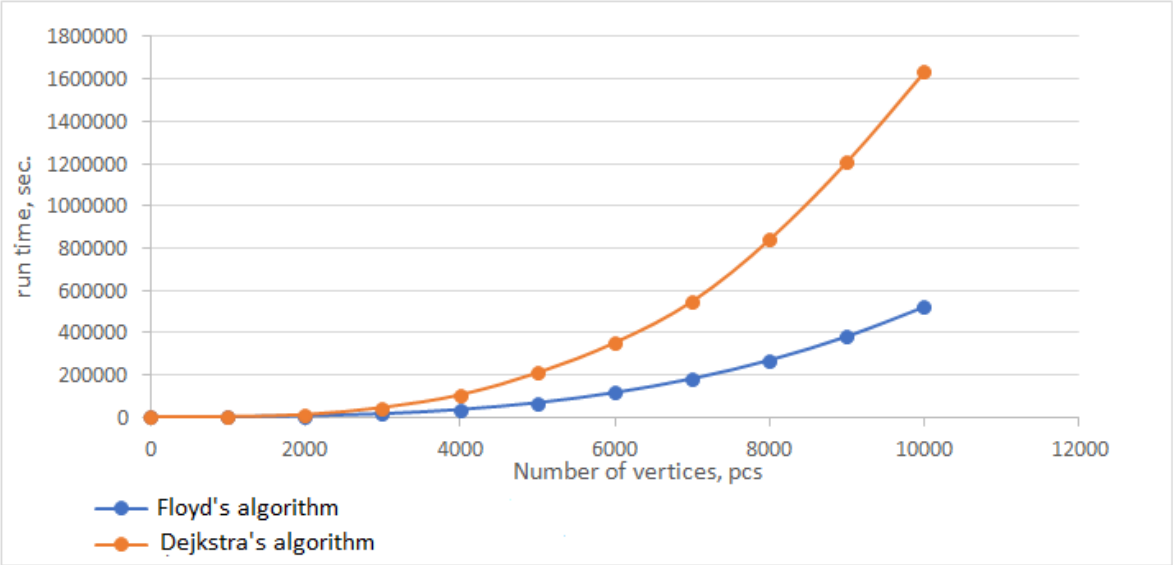

Figure 5. Comparison of the Floyd's algorithm time and the Dijkstra's algorithm time.

Let us write the equation of the dependence of time of the proposed implementation of the Floyd's algorithm on the number of vertices in the graph:

$$y=5*10^{-7}x^3+0.0002x^2-0.0684x+0.5874.$$

The R-squared value (determination coefficient) of the current model is 0.9235, which corresponds to a model of good quality. Let us write the equation of the dependence of time of the proposed implementation of the Dijkstra's algorithm on the number of vertices in the graph:

$$y=2*10^{-6}x^3-2*10^{-5}x^2-0.0247x+47.552.$$

The R-squared value (determination coefficient) of the current model is 0.9242, which corresponds to a model of good quality. To calculate the difference in the operation time of the proposed implementations of these algorithms, compare the coefficients at the highest powers in the obtained equations:

$$a= 2*10^{-6}/5*10^{-7}=4$$

It turns out that the proposed implementation of the Floyd's algorithm copes with the task of finding the shortest path from all the vertices at 4 times faster than the proposed implementation of the Dijkstra's algorithm. From which we can conclude that in such problems it is better to use the Floyd's algorithm. Let us compare the runtime of the Dijkstra's algorithm implementations on the example of implementations in PostgreSQL and C ++.

The result of the analysis of the running time of the implementation of the Dijkstra's algorithm in PostgreSQL and C ++ is shown in table 1.

For clarity, the test results are illustrated in the Figure. 6.

Table 1. The dependence of processing time on the number of vertices on the graph.

Number of vertices/pcs.	Processing time/sec.	
	PostgreSQL	C++
0	0	0
100	0.3	0
200	0.6	0
500	1.1	0
1000	1.8	0.04
2000	5.7	0.13
5000	42.1	0.75
10000	163.5	40
10500	180.23	73
11000	197.78	115.2
12000	235.49	182.3
14000	320.65	549.9
15000	368.15	809

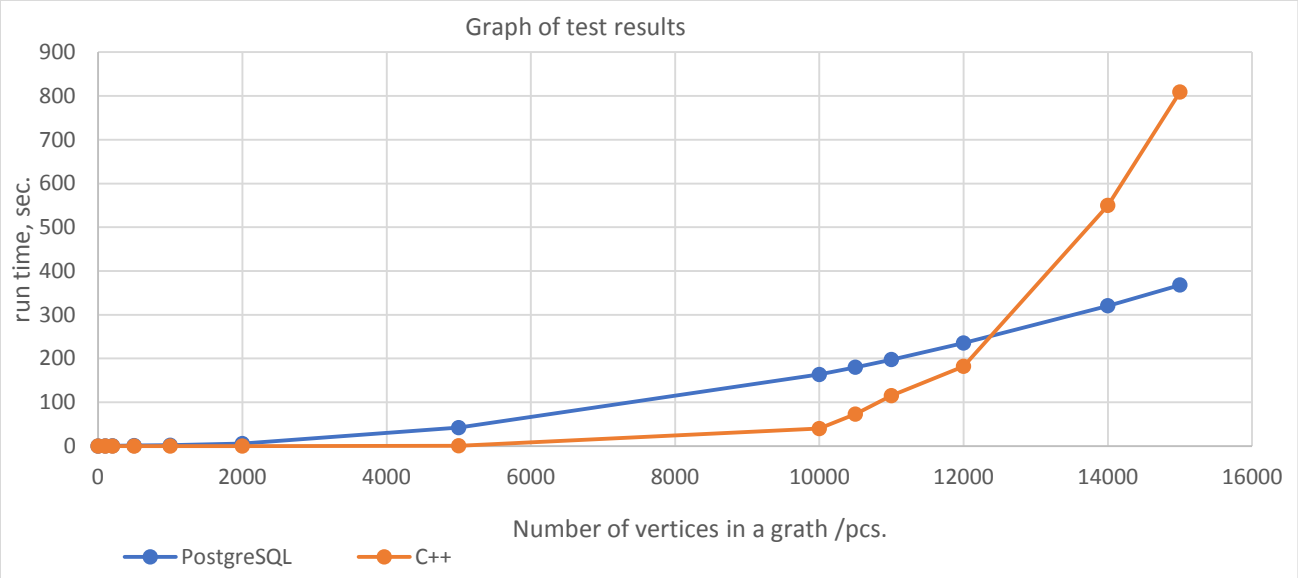

Figure 6. Comparison of the operating time of the implementation of the Dijkstra's algorithm in C ++ and PostgreSQL .

3. Analysis of obtained results

From the research results we can draw the following conclusions:

- the proposed implementation of the wave algorithm is best suited for solving the problems of finding the shortest path in not oriented graphs with unit weights;
- the proposed implementation of the Dijkstra's algorithm is best suited for solving problems of finding the shortest path in not oriented graphs with different weights;
- the proposed implementation of the Floyd's algorithm is best suited for solving problems of finding the shortest path in not oriented graphs with any weights, where the graph remains unchanged for a long time, for example, a graph of roads or a metro system.

Of the algorithmic advantages of solving the problem using the database tools, two points are most significant: specification of the distances to unvisited adjacent vertices within a single UPDATE query and accelerated search for vertices using the indexing tools built into the database engine.

The main disadvantage of this implementation is the relatively low execution speed of single queries to the database, which is noticeable when solving organizational and economic problems of

small and medium dimensions [11 - 14]. The application of data of graph search acceleration algorithms is particularly important in life cycle management systems of industrial products, such as PDM systems. In these systems, new modules have emerged related to the analysis of big data, as in industrial enterprises there are opportunities to integrate design and technological data on all parts and assembly elements of complex innovative products, such as aircraft products and products of the rocket-space complex (about 10 million parts and assembly elements in one product). For complex technological products, we create certifications for parts and working operations associated with loading photographs and measurements into the databases for quality control and destruction during the operation of these products. Such modules in PDM - systems include modules: Siemens TeamCenter 4G Big DATA, Enovia SmarTeam 4G Big Data.

4. References

[1] Chemodanov D A, Esposito F, Calyam P and Sukhov A 2018 Constrained Shortest Path Scheme for Virtual Network Service Management I*EEE Transactions on Network and Service Management* p 17
[2] Chemodanov D A, Calyam P, Esposito F and Sukhov A 2016 General Constrained Shortest Path Approach for Virtual Path Embedding T*he 22nd IEEE international symposium on local and metropolitan area networks* (Rome, Italy) 1-7
[3] Khaimovich I N, Ramzaev V M and Chumak V G 2016 Use of big data technology in public and municipal management *CEUR Workshop Proceedings* **1638** 864-872
[4] Khaimovich I N, Ramzaev V M and Chumak V G 2015 Challenges of data access in economic research based on Big Data technology *CEUR Workshop Proceedings* **1490** 327-337
[5] Wang Y 2016 A branch-and-price framework for optimal virtual network embedding *Computers Networks* **94** 318-326
[6] Chowdhury M, Rahman M and Boutaba R 2012 Vineyard: Virtual network embedding algorithms with coordinated node and link mapping *IEEE ACM Trans. Netw.* **20(1)** 206-219
[7] Esposito F, Paola D and Matta I 2014 On Distributed Virtual Network Embedding with Guarantees *IEEE ACM Trans. Netw.* **24(1)** 569-582
[8] Danna E, Mandal S and Singh A 2012 A practical algorithm for balancing the max-min fairness and throughput objectives in traffic engineering *Proc. of IEEE INFOCOM* 846-854
[9] Cormen T, Leiserson C and Rivest R 1990 *Introduction to Algorithms* (Cambridge) p 1091
[10] Worsley J, Drake J 2003 *Practical PostgreSQL* (O'Relly Media Inc.) p 640
[11] Chumak P V, Ramzaev V M and Khaimovich I N 2015 Models for forecasting the competitive growth of enterprises due to energy modernization *Studies on Russian Economic Development* **26(1)** 49-54
[12] Khaimovich A I, Grechnikov F V 2015 Development of the requirements template for the information support system in the context of developing new materials involving Big Data *CEUR Workshop Proceedings* **1490** 364-375
[13] Geras'kin M I, Chkhartishvili A G 2017 Analysis of Game-Theoretic Models of an Oligopoly Market under Constrains on the Capacity and Competitiveness of Agents *Automation and Remote Control* **78(11)** 2025-2038
[14] Kazanskiy N L, Stepanenko I S, Khaimovich A I, Kravchenko S V, Byzov E V and Moiseev M A 2016 Injectional multilens molding parameters optimization *Computer Optics* **40(2)** 203-214 DOI: 10.18287/ 2412-6179-2016-40-2-203-214

Multimodel clustering of social networks in social dampening applying BIG DATA (acquiring knowledge from data)

I N Khaimovich[1,2], V M Ramzaev[1] and V G Chumak[1]

[1]Samara University of Public Administration "International Market Institute", 21, G.S.Aksakova Street, Samara, Russia 443030
[2] Samara National Research University, Moskovskoe Shosse 34A, Samara, Russia, 443086

e-mail: kovalek68@mail.ru

Abstract. The developed methodology provides a solution to two essential tasks, thereby revealing the gnoseological potential of Big Data technology: social forecasting in the three most significant areas of the information society based on a model which identifies conditions for social resonance; successful implementation of the social dampening procedure based on the use of appropriate management options using multimodal clusterization of social networks based on Big Data technology. The article suggests the tool that helps to increase work efficiency in the sphere of social dampening in the region. The proposed method of regulation may be efficient when it comes to the control of the regional social dampening processes which have variety of forms and broad range of elements and factors, as well as growth dynamics and active transformation of life activities. At the same time using modern products make it possible to evaluate and show changes on a real-time basis which can be useful for local government authorities.

1. Introduction

Let us consider the analysis of the gnoseological potential of Big Data from the standpoint of synergetics, which focuses mainly on unbalanced, disordered systems, which are formed both in natural and social environments, which acquire balance only at certain moments, often extremely fleeting, but no less important and requiring comprehensive thinking.

Certainly, the destabilization of the system, and above all the social system, is extremely interesting from the dialectical positions both as awareness of the reasons, and in terms of exploring the possibility of providing the system with a steady state. However, the pragmatic reality convinces us that numerous ordinary people who are the direct elements of various systems, as well as the political elite, who seek to hold the position of a leading social force possessing certain levers of influence on social dynamics, are still primarily interested in the stability of the system structures. Deviation from the average values of social indicators is clearly perceived as deviance. Under these conditions, the technical capabilities of Big Data allow us to consider them as a tool for indicating the level of deviation of the most diverse social processes from the optimal model for a given society, contributing

to the development of a mechanism for returning to the averaged, balanced form of both a single process and their complex.

In our opinion, in order to conduct a scientific analysis of social processes, it is necessary to reveal the essence of the many-sided deviations that arise in certain situations in society. The analysis carried out in this direction shows the possibility of identifying two main types of changes in social processes. The first type is characterized by a rather slow deviation of social processes from the norms and principles established in society, described by an additive function. In this case, social smoothing, response can be considered as a cognitive impact on each social subject in particular, regardless of its nature: individual or collective. Here, the dominance of the elementary approach to the description of reality manifests itself, in which the quality of a system is determined by the quality of its constituent elements, which are quite accessible for comprehensive analysis using Big Data.

The essence of the second type of changes in social processes is determined by the explosive changes inherent in it and, first of all, by social cataclysms that bring society out of balance. The second type in its essence reveals deviations of the multiplicative type, which are intensified due to the extremely low efficiency of the interaction processes of social subjects. Here, in contrast to the first type, a social explosion occurs in a sharper form, much more concentrated in time and determined in many respects by the disadvantages of intergroup interaction, similar to social resonance. This situation is an example of the manifestation of a systematic approach to reality in social practice, based on the principles of which the quality and, therefore, the sustainability of a social system depends on the links of its constituent elements.

In order to analyze social processes classified in the above manner, ensure their management and bring social deviations to an acceptable standard, the authors propose to introduce into the conceptual apparatus the term “social dampening”, fundamentally new to social and humanitarian knowledge. This concept is intended to denote the desire of society to average in terms of the manifestation of its activity, therefore, in stability. It is expedient to characterize such stable existence of a society as a social equilibrium, a special state of a social system that has developed due to historical continuity, which manifests itself in a whole set of factors of economic, social, ethnic, etc. character.

Deviation from the criteria of social stability is the essence of social balance and leads to a “lifting” of the social equilibrium curve, which necessitates social dampening as a significant manifestation of management processes that can, among other things, solve the problem of cognitive control of consciousness, differing in its mental manifestations.

“Leveling” of quantitative (digital) characteristics should be carried out in indicators acceptable for a given society. Using Big Data as the most sensitive tool for measuring and detailing biogeosocial processes allows for the necessary iterations that cannot be performed using conventional scientific tools, identifying the “dominant that directs the vector of development of a specific phenomenon or process” [1] and the trend of their changes.

The formulation of the problems presented by the authors of the study is also aimed at clarifying the issue related to the need to determine the vector of the social management algorithm itself, namely: if we set a completely obvious goal for us to ensure proper management of social systems, then the following question arises: what (as a social goal) should we control in this way. The use of Big Data technologies provides new opportunities for solving such problems. This, in turn, means the need to determine the factors and criteria for the stable state of structures, and more precisely, the control objects, in the system of social coordinates. The frequency of deviations from these indicators, as well as the ability of their leveling, according to the authors, will be a fundamental point in understanding the quality of social management, which actualizes the need to develop a methodology for assessing the degree of deviation of social processes and the qualitative state of the systems involved in them from their equilibrium states. This method should necessarily include the possibility of both direct and indirect impact on social systems, which, in fact, additionally reveals the above concept of “social dampening” as a fundamentally significant theoretical basis for the formation and subsequent implementation of managerial influences on society, allowing for reduce, by using Big Data, the peak values of social indicators that go beyond the social acceptability. If we ignore them it can not only

partially unbalance the social system, but make it fully socially uncontrollable and prone to social explosions.

At the same time, in addition to social processes leading to a deviation of the environment from the social "normal", which can be regulated by social dampening, it is necessary to consider in greater detail identifying the essence of the process of social resonance. Social resonance is such a state of interacting factors and criteria that characterize the social environment, which leads to an explosive deviation from the "normal". The "removal" of such social aggravations can be interpreted as a process of returning from social resonance to the norm, which seems to the authors an extremely important task of social management, the successful solution of which is determined by the need to take into account the effect of passionate interaction, understood as a kind of "activity manifested in the individual's striving for the goal (often - illusory) and in the capacity for superstressing and sacrifice in order to achieve this goal", at the same time "sacrifice is understood ... as refusal to satisfy immediate needs, sometimes essential to life, for the sake of the dominant social or ideal needs, perceived as a goal "with a predominance of "development needs"[1].

Thus according to the authors, Big Data makes it possible to form a model of "removing" of social deviations, including social resonance, arising from a combination of a wide range of factors, the interaction of which is very difficult to analyze and often invisible to the researcher through the prism of traditional cognitive tools. In its turn, the implementation in practice of this kind of social dampening model let us create a comprehensive understanding of social processes as a neurobiological manifestation of human activity and forms the necessary opportunities to overcome its negative consequences.

Hiding the analysis of additive and multiplicative effects behind the facade of large-scale computer calculations, Big Data makes it possible to ensure that objective decisions are made, especially significant in the management of multifactorial social and natural systems [2,3], which, thanks to the implementation of social dampening procedures, makes it possible to guarantee stability, manageability and predictability of biogeosocial processes.

The carried out research clearly convince that the methodology of this kind must consist of two semantic blocks: the methodological, structuring algorithm for the study of social systems and processes with Big Data technology and management, which determines the possible methods of management influence based on the carried out analysis.

The first methodological block supposes, first of all, isolation, accompanied by analysis and evaluation, in the sphere of the information space of multimodal clusters, the most explosive in terms of their potential to destabilize the social system, taking it out of relative equilibrium. Here, as global clusters, attention is drawn to the three classical spheres of society: political, economic and social. The undeniable scale of these spheres makes it possible to isolate subclusters in each of them with the possibility of further detailing them into groups (including interests) and IP addresses.

This specification is quite possible to carry out on the basis of keywords that are set in accordance with the research task and are used by the Big Data technology to isolate subclusters and elements of their internal structure. Further, the practical implementation of this stage of the proposed methodology will require the parallel development of the "system learning" algorithm, allowing the program to isolate words, terms, concepts, etc. for the subsequent clustering and identification of significant communications.

The next step of the first methodological block is the construction of an algebraic lattice of the number of links of multimodal clustering, which represents a peculiar coordinate system of the specific carried out analysis. It will allow modeling the system of links within the cluster. The increase in the number of links within the cluster (or its subsystem) is the main indicator of the subsequent system out of equilibrium - social resonance.

The greatest interest for the subsequent management impact should present connections that demonstrate sustainable growth. When they are identified, you should:

- precise the topics that ensure the applicability of these links;
- carry out an analysis of the frequency dynamics;

- identify danger zones for social resonance.

The completion of the first methodological block is the differentiation of the resonance rate. This involves the identification of areas of social, informational interactions on which there has been a steady growth; subsequent finding of stable relationships to identify the topic of interaction. At the same time, a sharp increase in the number of links per unit of time by an order of magnitude should be interpreted, within the framework of this methodology, as the main condition for the soonest occurrence of social resonance.

The second methodological block identifies possible options for a practical transition from gnoseological reasoning to direct management impact on the social situation. A management decision point as a manifestation of social dampening can be represented on the graph at the point of transition from a smoothly increasing curve, indicating an increase in the number of social connections (within the identified cluster, subcluster, etc.) to a vertical straight line, representing the ordinal increase in social connections.

In this case, the second methodological block admits the possibility of two management impacts:

- Management of the number of socially significant connections, which primarily involves minimizing them in order to prevent or level social resonance;

- Management of the social environment dissipativity, which provides for an instrumental, informational impact (including through informational attack or subject readdressing of links) on the identified cluster, an impact that does not allow the formation of social relations that could in the long run lead to social resonance.

Otherwise, the coincidence of the “resonance frequencies” in the process of intersubject interaction can cause a global, uncontrolled social resonance.

2. Application of the formal concepts analysis method for social networks

The methodology of social dampening consists of the social resonance definition in social networks groups and the search for control actions to reduce tensions. The methodology of social dampening is based on multimodal clustering of social networks. Clustering is based on the formal concept analysis method (Formal Concept Analysis, FCA) [4–9]. A large amount of structured and unstructured data generates trivial data.

According to the method of formal concepts, we introduce the following definitions:

G is a set of objects, M is a set of attributes, relation $I \subseteq G \times M$ such that $(g,m) \in I$ if and only if, the object *g* has attribute *m*. $K := (G,M,I)$ is called a formal context.

Let us define Galois operators in the following manner for $A \subseteq G, B \subseteq M$:

$$A' \overset{def}{=} \{ m \in M \,|\, g / m \forall g \in A \}, B' \overset{def}{=} \{ g \in G \,|\, g / m \forall m \in B \}.$$

A formal concept is the pair $(A,B): A \subseteq G, B \subseteq M, A' = B$ and $B' = A$, where A is a formal extent, B is a formal intent.

The concepts, ordered by the dependency $(A_1,B_1) \geq (A_2,B_2) \Leftrightarrow A_1 \supseteq A_2 (B_2 \supseteq B_1)$, form a complete lattice, which is called context lattice $\underline{\beta}(G,M,I)$.

The example of social networks context and their context hashtags is shown in Figure 1.

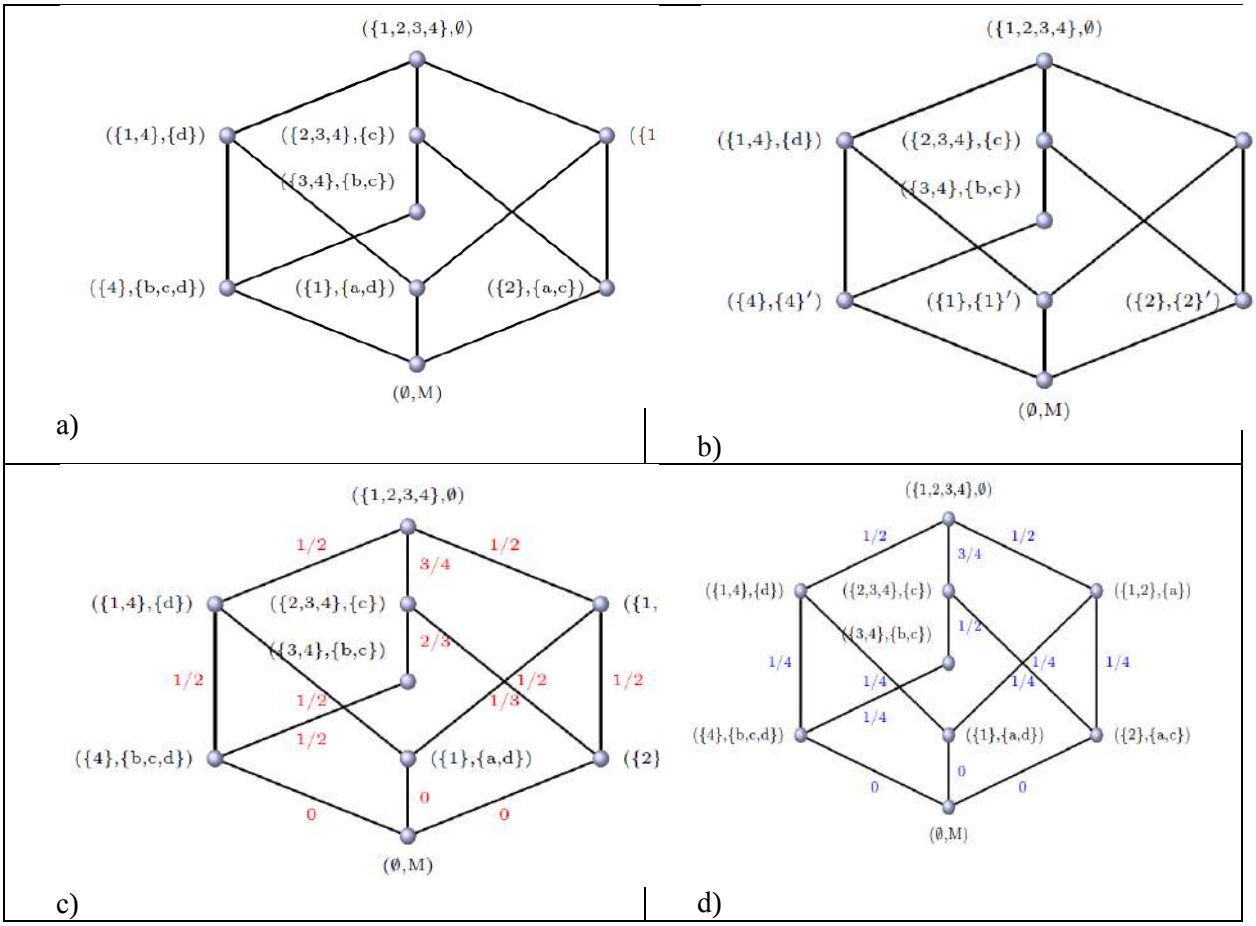

Figure 1. Social networks with context hashtags: A) context hashtags for social networks; B) social hashtags for social networks with implications; C) hashtags with reliability of associative links; D) the example of hashtags with support of association rules.

Let us consider implications in the lattice and define the operation "implication" in the following manner: implication $A \to B$, where $A,B \subseteq M$ exists if $A' \subseteq B'$, i.e. every object that has all attributes from A set also has all attributes from B set. Implications correspond to Armstrong's axioms: reflexivity $(A \to B / A \cup C \to B)$;augmentation$(A \to B / A \cup C \to B)$; pseudo-transitivity $(A \to B, D \cup B \to C / A \to C)$.

Among implications there is the Duquenne-Guigues basis of implications i.e. a minimal number of implications which can help to derive other implications using the Armstrong rules. The basis is sought through methods of machine learning: "object-by-object" algorithm of implication basis construction or through interactive learning procedure. As a result we have a hashtag with implications (Figure 2б).

Implications: $abc \to d, b \to c, cd \to b$ allow to redefine the nodes of hashtags.

Let us consider partial implications or association rules.

Definition 1. $A \xrightarrow[m,n]{} B$ is partial implication (association rule) of context (G,M,I), if $A,B \in M$; has a support of $sup\ p(A \to B) = |(A \cup B)'| / |G|$ has a confidence $conf\ (A \to B) = |(A \cup B)'| / |A'|$.

Further we consider the algorithm identifying association rules:

1) to find all frequent sets of attributes (with support which is not below the assigned);
2) it is enough to find all the frequent closed sets of attributes of the context.

The example of hashtags with reliability of associative links (Figure 1c).

The example of hashtags with support of association rules (Figure 1d).

Good rules with $sup\ p \geq 1/2$ and $min\ \ conf \geq 3/4$ are defined according to the following algorithm:

1. $0 \to c, sup\ p(0 \to c) = conf\,(0 \to c) = 3/4;$
2. $c \to b, sup\ p(c \to b) = 1/2, conf\,(c \to b) = 2/3.$

The use of this clustering method will allow determining the interest groups, with an increase in connections it will be necessary to make management decisions. In terms of information, it will be necessary to combine messages from groups with an increased number of links with calm "stable" groups in which the number of links does not undergo a drastic change.

3. Method of Using Data Mining in Social Dampening Methodology

Formal Concept Analysis (FCA) allows to establish stable links and cluster data (create new knowledge) using Armstrong rules in context lattices. To create a portrait and information model of resonant groups, it is necessary to use BIG DATA technologies [10, 11, 12]. The method of using data mining is as follows:

1. Forming a big data set in hadoop from twitter using the "Samara region" filter which reveals hit counts;
2. Separation of the formed set by various filters associated with the basic factors of resonance deviations;
3. Monitoring of streaming content analysis on filters;
4. Adoption of operational activities in cases of sustained "hits" in hit counts;
5. Development of a program in the Scala language for working with filtering in Big Data field;
6. Debugging and testing the program with a set of practical data;
7. Analysis of the calculation results.

The social network twitter is used to obtain data, since it is an "open" product, its use does not require additional investments, and 50% of Internet users have profiles in this program. Twitter is the second most popular network among users worldwide, second only to Facebook. However, unlike Facebook, which does not provide open access to its data, Twitter provides such access, there are no restrictions on access to server data sets. Users of this social network exchange mostly text information, which is an undoubted advantage in processing. Twitter is not a subject network and most widely reflects public opinion on many issues of interest, so for the formation of groups for analyzing the social resonance in the region, the processing of data from this social network was optimal.

To work with BIG DATA in social networks, it is necessary to use methods of collecting, processing and analyzing data. Data collection is carried out in real time, within a certain geolocation, or within the entire network, using certain patterns. Information of interest for the analysis in this area is: location, date and time, content, content "author" (user), communication between users. Data collection in social networks can be performed using the following tools: Apache Hadoop, Biglnsights (IBM), Cloudera, Hortonworks, Storm. Hortonworks was chosen to carry out research in the field of social dampening. The Twitter Application (apps.twitter.com) was used for work, in which key parameters were defined and refined: API key, API secret, Access token, Access token secret.

To collect data using the Hortonworks, Twitter App, the flume service configuration file was used in the Hortonworks Sandbox virtual machine. After installing the Hortonworks_ Sandbox version 2.3 virtual machine and setting up the flume service, the system is ready to download data from twitter. To view and download the downloaded files, go to the HDFS folder, where we process the data. View of the HDFS file structure in the Hortonworks virtual machine when solving a problem in the sphere of social dampening is shown in Figure 2.

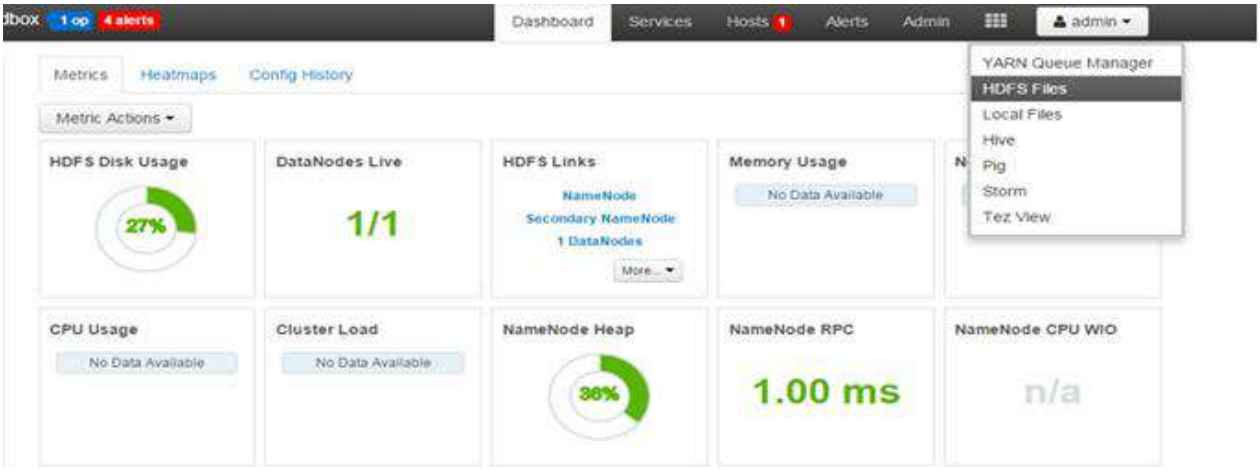

Figure 2. HDFS visualization in Hortoworks when file download to solve social dampening.

The collected data must be structured (i.e., processed) in accordance with the MapReduce paradigm. MapReduce is a framework for performing distributed tasks using a large number of computers forming a cluster.

Using MapReduce allowed us to structure the flow of data from social networks by criteria: fonts, text size, color, link to user profile, location, time, and so on.

To determine the portrait of the respondent, the following types of data are needed: location, text, language, and time. In order to extract only this information, you can use the MapReduce technology built into the Hortonworks Sandbox tool. For data processing, we use the Hive DBMS in the Hadoop environment, which allows performing operations on data and their analysis using SQL-like queries. To do this, create a file for processing and creating the necessary hivedll.sql tables.

Run this file using command: Hive_f hiveddl.sql. Structured data will be presented in the Table 1.

Table 1. Headings to analyze structured XML data in tasks for social dampening.

A	B	C	D	E	F
Data/Time	Time/Zona	language	Text	location	Sentiments

For data analysis the following variables are used. Total amount of twitts (Kol_i) for every location (R) is defined by:

$$Kol_R = \sum_{i=1}^{N} k_i, k_i \in R,$$

where k_i is every next twitt in the considered stream.

Frequency of unique word usage ch(m) is defined from the general variety of L text data:

$$ch(m) = \sum_{i=1}^{N} m_i, m_i \in L.$$

The attitude of every twitt otn (m,rez) may be defined from the thesaurus tez, where the attitude to this word is written up:

$$otn(m, rez) = \begin{cases} 0, m - negative\_meaning \\ 1, m - neural\_meaning \\ 2, m - positive\_meaning \end{cases}.$$

For further work, a dictionary was compiled, consisting of domain filters, to further determine the number of tweets for placement ch (m) and the number of tweets for placement taking into account the relation otn (m, rez). We define a thesaurus taking into account filters by basic factors: salary, unemployment, political developments and housing and utility infrastructure. As a result, we obtain 4 basic factors of resonance deviations.

«Salary» factor P_1 gives the number of twitts in general quantity of text data L:

$$Kol_{otnP_1} = \sum_{i=1}^{N} S_i(S_i \in P_1)/L = 10\%.$$

«Unemployment» factor P_2 gives the number of twitts in general quantity of text data L:

$$Kol_{otnP_2} = \sum_{i=1}^{N} S_i(S_i \in P_2)/L = 9\%.$$

«Political» factor P_3 gives the number of twitts in general quantity of text data L:

$$Kol_{otnP_3} = \sum_{i=1}^{N} S_i(S_i \in P_3)/L = 7\%.$$

«Infrastructure» factor P_4 gives the number of twitts in general quantity of text data L:

$$Kol_{otnP_4} = \sum_{i=1}^{N} S_i(S_i \in P_4)/L = 13\%.$$

4. Results and discussion

As a result, it can be concluded that what factors of deviations are associated with the Samara region. According to Figure 3 it can be seen that the main factor of discontent is the housing sector.

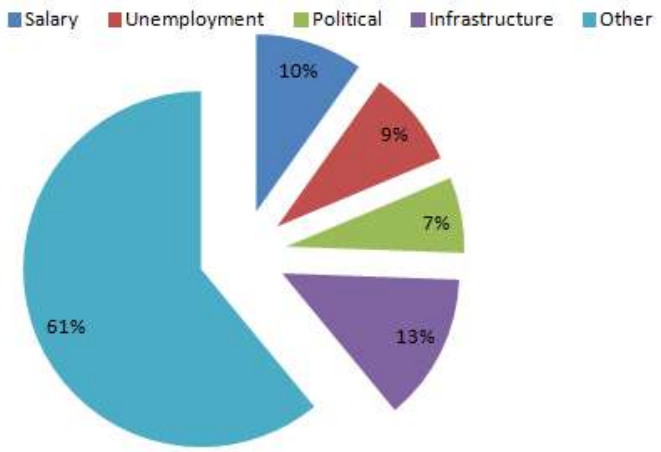

Figure 3. Factors of social dampening in Samara Oblast.

Due to BIG DATA technology, it is possible to store and update data in the “hadoop” file system using the “Samara Oblast” filter (filter1 = {Samara Oblast}). Then, it is necessary to filter this area by the basic factors of social dampening, by installing, for example, the following filters: Filter2 (salary) = {money, ruble *, dollars *, currencies *, crypt *}; Filter3 (unemployment) = {job search, engineer *, worker *, build *}; Filter4 (political developments) = {elections, deputy *, penny *, administrator *}; Filter5 (housing and utility infrastructure) = {garbage collection, pipes *, water *, gas *}.

The set of descriptors by which the Internet discourse will be filtered is determined by the lexical representatives of the concept formed in the world picture by the average Russian-speaking consumer.

To make decisions in the field of social resonance in the region, multimodal clustering of social networks was carried out. A large number of structured and unstructured data of social sites in the considered area can be represented as the next triple (user, group, interest) (Figure 4).

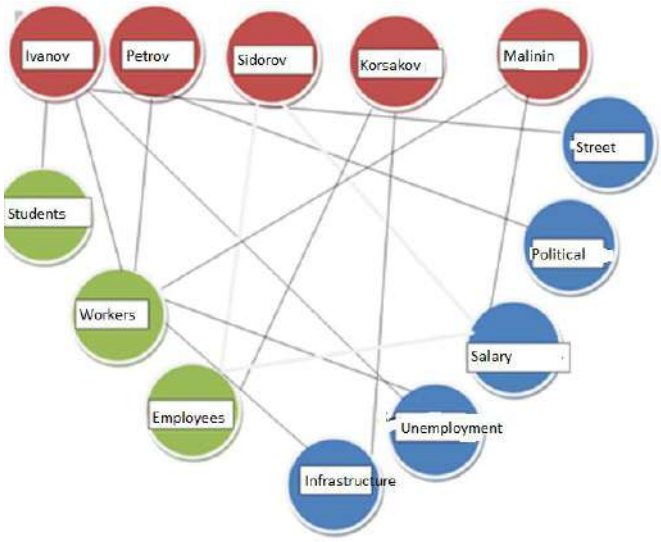

Figure 4. Data for social resonance analysis from Twitter social network as a graph

Using the method of formal concepts, we form a complete lattice, called the context lattice $\underline{\beta}(G,M,I)$. An example of the context of social networks in the field of social dampening and their context hashtags are shown in Table 2 and Figure 5.

Table 2. The example of Social network context and its context hashtags (a - attributes on «salary» filter, b - attributes on «unemployment» filter, c - attributes on «political developments» filter, d - attributes on «housing and utility infrastructure» filter).

	G/M	a	b	c	d
1	pensioners	x			x
2	employees	x		x	
3	workers		x	x	
4	students		x	x	x

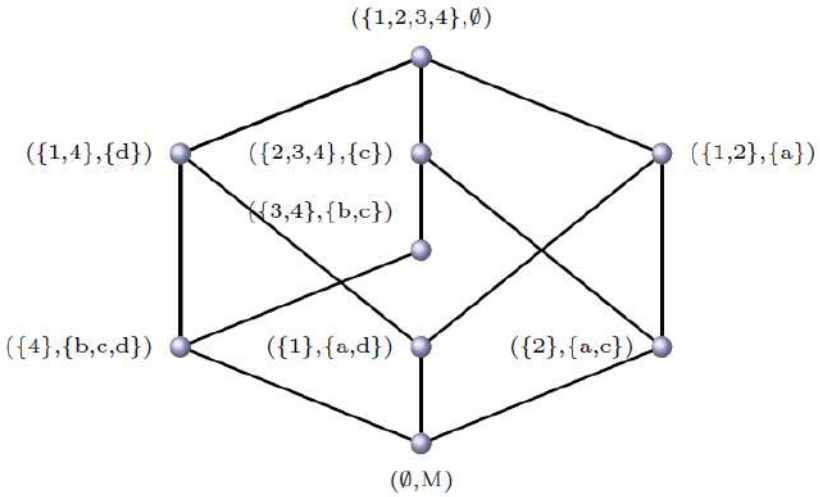

Figure 5. Context hashtags for social network.

The use of this clustering method will give the opportunity to determine interest groups, with an increase in links in which management decisions will be required. But this tool has limitations on use. Users who work with the social network "Twitter" are in the "students" group and partly in the "employees", "workers" groups and only slightly affect the "retirees" group, so for complete management decision making it is necessary to add new groups.

You can get graphs of the user hit counts by filters on data collection time (Figure 6). The data collection time from the Internet is unlimited in BIG DATA technology.

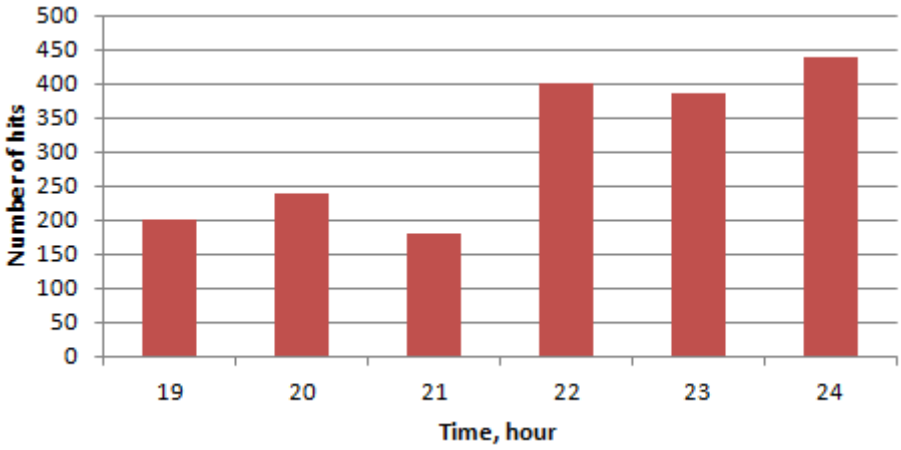

Figure 6. Dependency graph of hit counts using filters from data collection time.

As a result, we obtain a dynamic change of information in real-time from the Internet, which allows monitoring the streaming analysis of unstructured information (In-Memory Data Processing and Stream technology) with minimal investment by filters. To implement this method, a program in the Scala language was written.

After the work of the program, we obtain a dynamic change of parameters in the BIG DATA environment, which allow us to determine social resonance zones in the region, taking into account unstructured information. If steady "bursts" of data on hits counts are detected on charts in accordance with the forms of resonance, management regulation for this type of activity in the region should be implemented.

Thus, a tool has been proposed to increase the effectiveness of work in the field of social dampening in the region. This is the most important task under modern economic conditions, the basis of which is the possibility to make optimal management decisions. The proposed method of regulation can be effective in managing the processes of social dampening of a region, which are characterized

by a variety of forms and a wide range of components and factors, as well as an inherent dynamics of development and active transformation of life activity.

At the same time, the use of modern software and hardware gives the opportunity to make the assessment and visualization of changes in fact in real time, which can be useful for local authorities. It is important to note that social dampening is not a strict limiter of social actions "in amplitude". It only softens social actions, allowing them to manifest themselves in other areas, it does not "break" the social system, but allows it to transform, creating the visibility of smooth compliance with the requirements of the social interaction subjects.

5. References

[1] Bodrov A A, Ramzaev V M 2015 Philosophic aspects of developing new knowledge under data intellectual analysis (BIGDATA) *CEUR Workshop Proceedings* **1490** 338-345
[2] Khaimovich I N, Ramzaev V M and Chumak V G 2016 Use of big data technology in public and municipal management *CEUR Workshop Proceedings* **1638** 864-872
[3] Khaimovich I N, Ramzaev V M and Chumak V G 2015 Challenges of data access in economic research based on Big Data technology *CEUR Workshop Proceedings* **1490** 327-337
[4] Wille R 1982 Restructuring lattice theory: An approach based on hierarchies of concepts *Ordered Sets. NATO Advanced Study Institutes Series (Series C – Mathematical and Physical Sciences)* **83** p 470
[5] Ganter B, Whille R 1996 *Formale Begriffsanalyse* (Springer, Heidelberg) p 540
[6] Ganter B, Whille R 1999 F*ormale Consept Analysis* (Springer) p269
[7] Davey B, Priestly H 1990 *Introduction to Order and Lattices* (Cambridge University Press, Cambridge) p 460
[8] Denecke K, Erne M and Wismath S L 2004 *Galois Connections and Applications* (SpringerScience and Business Media) **565** p 498
[9] Bonacich P 2007 Power and Centrality: A Family of Measures *American Journal of Sociology* **92(5)** 1170-1182
[10] Chumak P V, Ramzaev V M and Khaimovich I N 2015 Models for forecasting the competitive growth of enterprises due to energymodernization *Studies on Russian Economic Development* **26(1)** 49-54
[11] Khaimovich A I, Grechnikov F V 2015 Development of the requirements template for the information support system inthe context of developing new materials involving Big Data *CEUR Workshop Proceedings* **1490** 364-375
[12] Kazanskiy N L, Stepanenko I S, Khaimovich A I, Kravchenko S V, Byzov E V and Moiseev M A 2016 Injectional multilens molding parameters optimization *Computer Optics* **40(2)** 203-214 DOI: 10.18287/ 2412-6179-2016-40-2-203-214

Modelling and forecasting of quasi-periodic processes in technical objects based on cylindrical image models

V R Krasheninnikov[1], Yu E Kuvayskova[1]

[1]Ulyanovsk State Technical University, Severny Venets street, 32, Ulyanovsk, Russia, 432027

e-mail: kvrulstu@mail.ru, u.kuvaiskova@mail.ru

Abstract. Accurate forecasting of the state of technical objects is necessary for effective management. The technical condition of the object is characterized by a system of time series of monitored indicators. The time series often have difficultly predictable irregular periodicity (quasi-periodicity). In this paper, to improve the accuracy of such series forecasting, models of quasi-periodic processes in the form of samples of a cylindrical image are used. The application of these models is demonstrated by forecasting of a hydraulic unit vibrations. It is shown that the use of these models provides a higher accuracy of prediction compared with the classical approaches.

1. Introduction

In order to improve the management of a technical object an accurate forecast of its technical condition is required, which is characterized by a variety of controlled indicators. These indicators are recorded by sensors at certain time intervals in the form of signals with discrete time. These signals can be used to predict state of an object in order to make effective management decisions.

The set of registered values of the object's indicators can be represented as a system of time series. To represent the time series, a large number of models have been developed: autoregressive, spectral, wave, wavelets, and so on, for example, [1–4]. A very important task is the prediction of time series, which is associated with the management of objects. To solve this problem, the methods of mathematical statistics, artificial neural networks, fuzzy logic, machine learning and so on are used, for example, in [5-14].

Often time series have irregular periodicity, that is, quasi-periodicity. Quasi-periodic behavior is a repetition with a component of unpredictability. For example, the vibration of various engines, turbines, units and so on.

Different models can be used to describe and predict such processes, for example, autoregressive models with complex roots of the characteristic equation or harmonic models. However, these models do not always allow to predict a quasi-periodic process with high accuracy. In this paper, to improve the accuracy of predicting the state of technical objects, it is proposed to use models of quasi-periodic processes based on cylindrical images [15-18].

2. Quasi-periodic process as a scan of an image

Double correlation is a characteristic property of a quasi-periodic process, that is, there is a strong correlation both between adjacent values and between values separated by several periods.

There are a number of approaches to describe quasi-periodicity: the imposition of noise or higher frequencies on the main harmonic, periodic nonstationarity (fluctuation of moments and other characteristics), and so on. A common manifestation of such representations is the high correlation of process values at distances that are multiples of a period. In this paper,this property is

taken as a basis, that is, as the main property of a quasiperiodic process.

As quasi-periods of the process, we could take the lines of a certain rectangular image: the required correlation will be ensured by the vertical correlation of the image. Consider, for example, an image on a rectangle, given by the Habibi model [19]:

$$x_{k,l} = a\, x_{k,l-1} + b\, x_{k-1,l} - ab\, x_{k-1,l-1} + \beta\sqrt{(1-a^2)\,(1-b^2)}\;\xi_{k,l}\,, \qquad (1)$$

where k is the line number, l is the column number, $\xi_{k,l}$ is a set of independent standard random variables. The generated image has a covariance function (CF)

$$V(m,n) = M[x_{k,l}\; x_{k+m,l+n}] = \beta^2 a^{|m|} b^{|n|}\,.$$

Parameters a and b affect the vertical and horizontal image correlation, respectively; β affects the variance of the image. Figure 1 shows an example of simulated image.

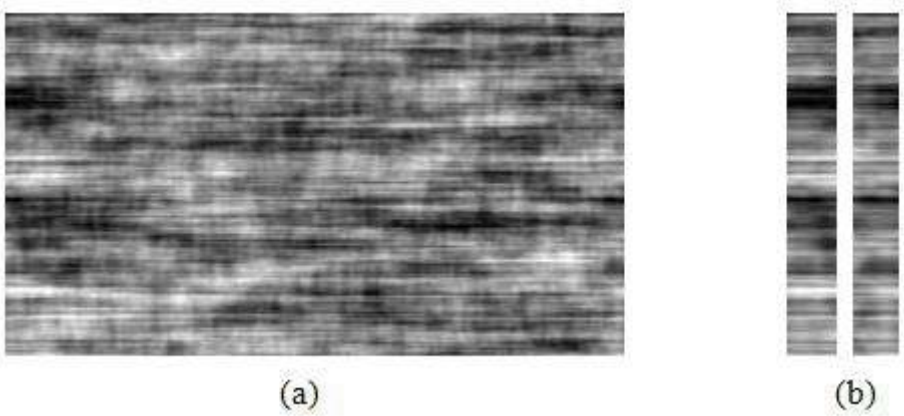

Figure 1. Image simulated by model (1): (a) full image, (b) the first and last five columns.

Image rows are highly correlated if $b \approx 1$. Therefore, by combining the rows into a sequence, we can get a model of a quasi-periodic process. Figure 2 shows an example of such process. The boundaries of the periods are indicated by vertical lines, where sharp jumps are noticeable. In fact, this figure shows the brightness graphs of successive rows of the image.

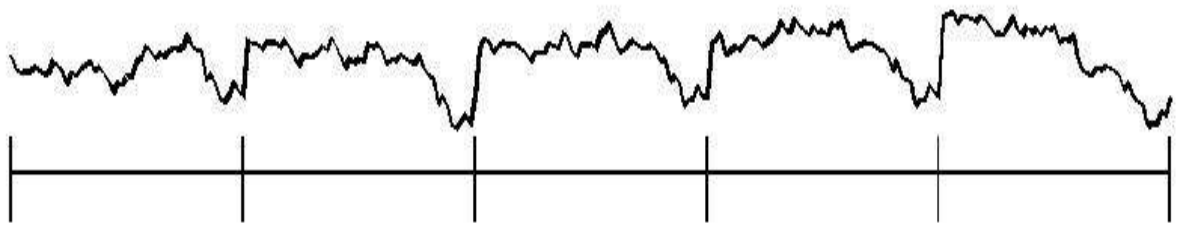

Figure 2. Process simulated using model (1).

The CF of the process is shown in Figure 3. Correlations between elements of the image decrease along the rows. Therefore, the CF of the process decreases along the period, but increases sharply at the junction of the periods. This property of the CF just ensures the quasi-periodicity of the process.

However, the beginning and end of each row, being at a considerable distance, are practically independent of each other, which is noticeable in Figure 1, b. Therefore, at the junctions of the quasi-periods of the process obtained by joining the rows, there will be a weak correlation of neighboring values, leading to sharp jumps that are not typical of relatively continuous processes. Similar discontinuity is obtained by combining rows from other rectangular images. Thus, rectangular images

do not provide acceptable representations of quasi-periodic processes. In this paper, modeling processes using images on a cylinder is considered.

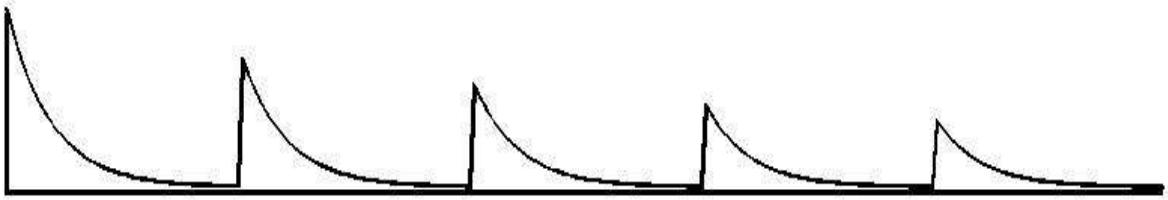

Figure 3. The correlation function of the model (1).

Let's consider a cylindrical image, which is scanned along a spiral on this cylinder (figure 4 (a)). In [15], the following model was used to represent images on a cylindrical grid similar to Habibi autoregression model (1):

$$x_{k,l} = a\,x_{k,l-1} + b\,x_{k-1,l} - a\,b\,x_{k-1,l-1} + c\,\xi_{k,l} \quad (2)$$

where k is a spiral turn number; l is a node number $l = 0,...,T$; $x_{k,l} = x_{k+1,l-T}$ when $l \geq T$; T is the period, i.e. the number of points in one turn; $\xi_{k,l}$ are independent standard random variables.

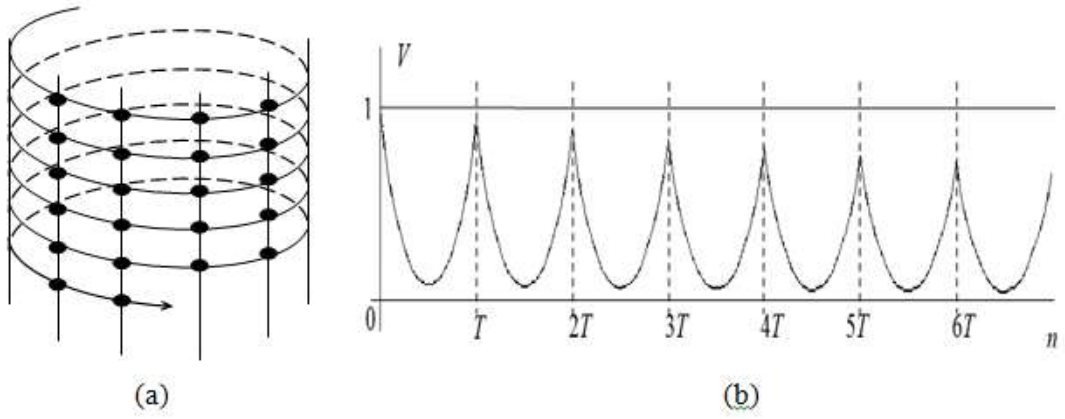

Figure 4. Cylindrical image: (a) cylindrical spiral, (b) normalized correlation function.

An example of an image simulated using this model is shown in Figure 5 (a). Its first 5 columns are shown in Figure 5 (b). It is noticeable that the first and last columns are strongly correlated.

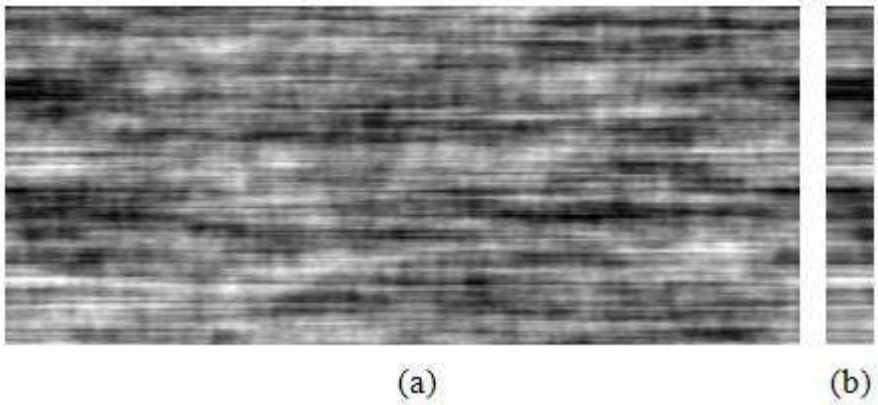

Figure 5. Simulated cylindrical image (a) and its first columns (b).

For convenience of analyzing this model, assume that the pixels are numbered and located on a cylindrical spiral (figure 4 (a)). Then model (2) can be represented in an equivalent form as a model of a random process, which is a scan of the image along the spiral:

$$x_n = a\,x_{n-1} + b\,x_{n-T} - a\,b\,x_{n-T-1} + c\,\xi_n\,, \tag{3}$$

where $n = kT + l$. Applying the z-transform, we obtain the CF

$$V(n) = M[x_m x_{m\pm n}] = c^2\left(\frac{1}{(1-b^2)T}\sum_{k=0}^{T-1}\frac{z_k}{(1-a\,z_k)(z_k-a)}z_k^n + \frac{s}{(1-a^2)(1-bs)(s-b)}\rho^n\right), \tag{4}$$

where $z_k = \sqrt[T]{b}\exp(i2\pi k/T)$ and $s = a^T$.

In particular, when $n = mT$ we obtain

$$V(mT) = \frac{c^2}{(1-a^2)(1-b^2)(1-sb)(b-s)}\left((1-s^2)b^{m+1} - (1-b^2)s^{m+1}\right)$$

and the variance, when *m=0*:

$$\sigma^2 = \frac{c^2(1+bs)}{(1-a^2)(1-b^2)(1-bs)}\,.$$

To reduce the calculations, it is possible to calculate only *V(0), V(1),..., V(T)* by formula (4), and for the rest of values, use recurrent formula

$$V(n) = a\,V(n-1) + b\,V(n-T) - a\,b\,V(n-T-1)\,.$$

This CF (3) decreases with increasing distance *n*, but at distances divisible by period *T*, CF is high (figure 4 (b)), which is typical for quasi-periodic processes.

The parameter *a* affects the correlation along the rows, that is, the smoothness of the process. The parameter *b* affects the correlation of values over a period distance. For values of *b* close to 1, the adjacent rows of the image (spiral turns) will be strongly correlated. In this case the process is closed to periodic one (figure 6(a)). The periodicity property weakens as *b* decreases (figure 6(b)).

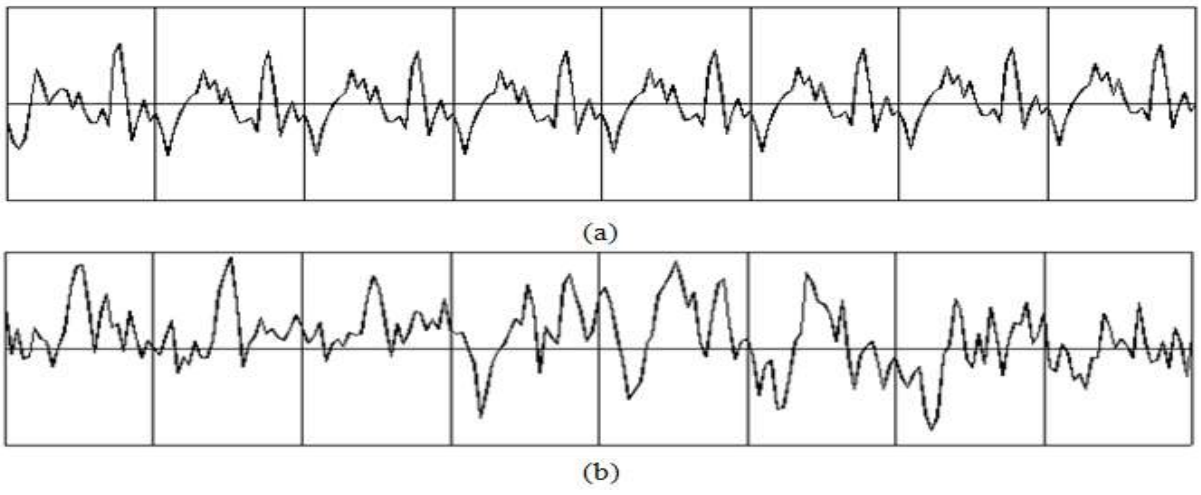

Figure 6. Simulated processes: (a) *b*=0.99; (b) *b*=0.9.

We note in particular that these graphs of simulated processes are continuous, in contrast to Figure 2. This is a consequence of the continuity of the CF (4), shown in Figure 4 (b). Thus, model (3) is suitable for describing continuous quasi-periodic processes. By varying the parameters of this model, it is possible to represent processes with a given correlation within quasi-periods and between them.

3. Prediction of the state of a technical object

As an object of study, we consider data on a hydraulic unit (one of the turbines of the Krasnaya Polyana Hydroelectric Power Plant, Russia). Figures 7-9 show vibration plots obtained from three sensors located on different parts of the unit. The task was to predict the next process value using its previous values. Visually, the presence of quasi-periodicity in these processes is observed. This makes it possible to apply the model of quasiperiodic processes described above to these data. The volume of each sample was 96 observations.

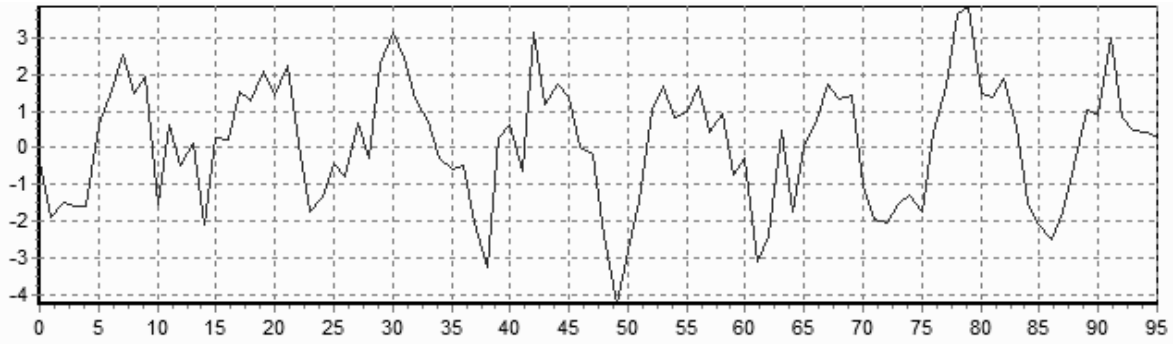

Figure 7. The first process of vibration of the hydraulic unit.

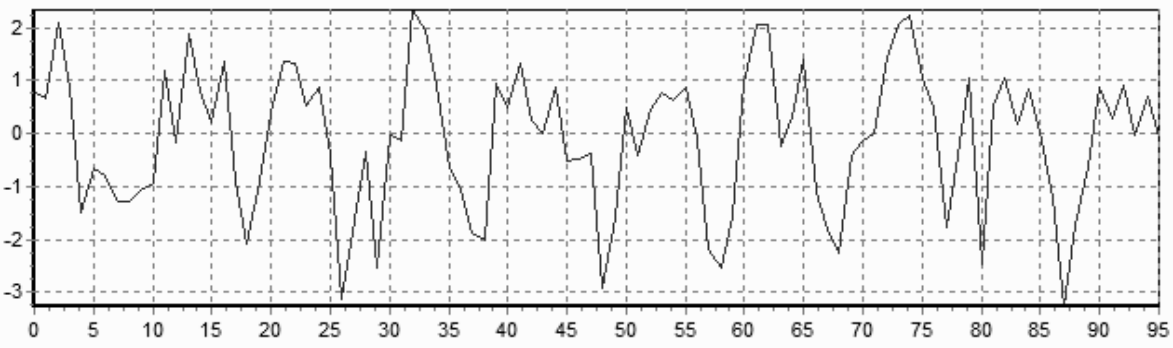

Figure 8. The second process of vibration of the hydraulic unit.

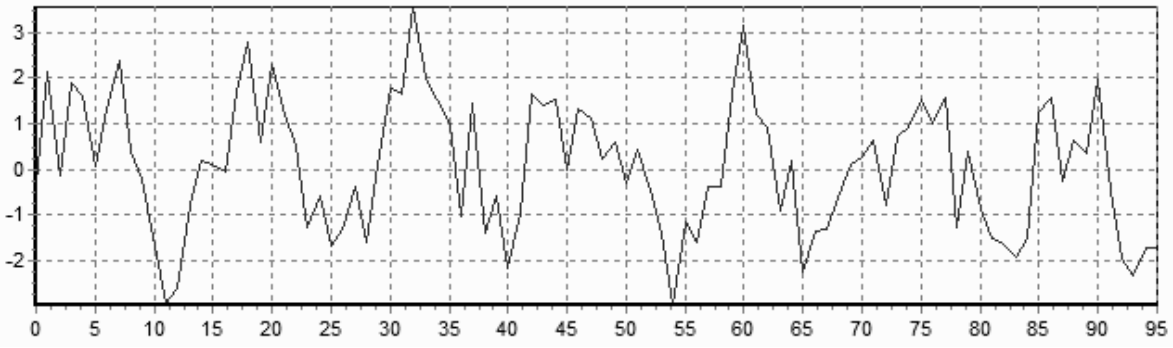

Figure 9. The third process of vibration of the hydraulic unit.

To assess the quality of forecasting of these processes, the sampling of values is divided into two parts: a training sample (90% of the volume of initial observations) and a control sample (10% of the volume of initial observations). According to the training sample, we construct by the least squares method three models of the studied processes: an autoregressive model of a cylindrical image (3), a usual autoregressive model of the second order with complex roots of the characteristic equation and a harmonic model. For the control sample, we estimate the prediction accuracy of the constructed models as $\sigma_{\Delta} = \sqrt{\frac{1}{k}\sum_{n=1}^{k}(x_n - \hat{x}_n)^2}$, where k is the volume of the control sample; x_i are the values of the observation; $\hat{x}_i$ are the predicted value of the process according to the constructed model. In the case of a cylindrical model, the equation

$$\hat{x}_n = a\, x_{n-1} + b\, x_{n-T} - a\, b\, x_{n-T-1}$$

was used to predict the next process value from its previous values. The results of the comparison of models for prediction accuracy are presented in Table 1.

Table 1. Prediction errors with different models.

Process model	Prediction error (σ_{Δ})		
	Process 1	Process 2	Process 3
Autoregressive cylindrical image model (2)	0,6401	0,6561	0,6676
Second order autoregressive model	0,7950	0,7606	0,7756
Harmonic model	0,9698	0,9316	0,9532

It follows from this table that the prediction error of the vibrations processes is decreased up to 1.5 times with the use of cylindrical models of images, as compared with the autoregressive and harmonic models.

4. Conclusions

It is proposed to use models of quasi-periodic processes in the form of a spiral on a cylindrical image to predict the state of technical objects. The results of numerical experiments show that the use of these models provides a higher prediction accuracy in comparison with the classical time series models.

5. References

[1] Anderson T W 1971 *The statistical analysis of time series* (John Wiley & Sons Inc. N-Y London Sydney Toronto)
[2] Hannan E J 1970 *Multiple time series* (John Wiley & Sons Inc. N-Y London Sydney Toronto)
[3] Jenkins G M and Watts D G 1968 *Spectral Analysis and Its Application* (San Francisco: Golden-Day) p 525
[4] Daubechies I 1992 *Ten lectures on wavelets* (Soc Ind Appl Math Philadelphia)
[5] Montgomery D C 2009 *Introduction to statistical quality control* (New York: John Wiley and Sons) p 754
[6] Montgomery D C, Johnson L A and Gardiner J S 1990 *Forecasting and Time Series Analysis* (New York: Mc Graw-Hill) p 394
[7] Bahiraee E and Raissi S 2014 Economic design of Hotelling's T2 control chart on the presence of fixed sampling rate and exponentially assignable causes *Journal of Industrial Engineering International* **10** 229-238
[8] Chou C Y and Chen C H 2006 Economic design of variable sampling intervals T2 control charts using genetic algorithms *Expert Systems Appl* **30** 233-242

[9] Witten I H and Frank E 2005 *Data mining: practical machine learning tools and techniques* (San Francisco: Morgan Kaufmann Publishers)
[10] Klyachkin V N 2011 *Models and methods of statistical control of a multi-parametric process* (Moscow: Fizmatlit)
[11] Kuvayskova Y E 2017 The prediction algorithm of the technical state of an object by means of fuzzy logic inference models *Procedia Engineering* **201** 767-772
[12] Yumaganov A S and Myasnikov V V 2017 The method of searching for similar code sequences in executable binary files using the unmarked approach *Computer Optics* **41(5)** 756-784 DOI: 10.18287/2412-6179-2017-41-5-756-764
[13] Kropotov Yu A, Proskuryakov A Yu and Belov A A 2018 A method for predicting changes in the parameters of time series in digital information control systems *Computer Optics* **42(6)** 1083-100 DOI: 10.18287/2412-6179-2018-42-6-1083-1092
[14] Maksimov A I and Gashnikov M V 2018 Adaptive interpolation of multidimensional signals in differential compression *Computer Optics* **42(4)** 679-687 DOI: 10.18287/2412-6179-2018-42-4-679-687
[15] Krasheninnikov V R, Kalinov D V and Pankratov Yu G 2001 Autoregressive Model of a Quasiperiodic Signal *Pat Rec and Im An* **11(1)** 211-213
[16] Krasheninnikov V R and Kuvayskova Y E 2016 Prediction of object dynamics using autoregressive models on a cylinder *Radio engineering* **2016(9)** 36-39
[17] Krasheninnikov V R and Subbotin A Yu 2018 Doubly stochastic model of a quasi-periodic process as an image on a cylinder *Proceedings of the International Scientific and Technical Conference "Advanced Information Technologies"* (Samara: Samara Scientific Center of the Russian Academy of Sciences) 1017-1021
[18] Krasheninnikov V R and Vasil'ev K K 2018 Multidimensional image models and processing *Computer Vision in Control Systems-3 ISRL* **135** 11-64
[19] Habibi A 1972 Two-dimensional Bayesian estimate of images *Proc IEEE* **60(7)** 878-883
[20]Polyak B T and Tsypkin Ya Z 1973 Pseudogradient adaptation and training algorithms *Automation and Remote Control* **1973(3)** 45-68

A combined method of similar code sequences search in executable files

A S Yumaganov[1]

[1]Samara National Research University, Moskovskoye shosse, 34, Samara, Russia, 443086

e-mail: yumagan@gmail.com

Abstract. The article is devoted to the development of a method of similar code sequences search in executable files, which is based on both syntax analysis of the code and function's control flow graphs analysis. The syntax analysis method used in this paper is based on a comparison of the spatial distribution of processor instructions in the function body. The analysis of function control flow graph is used a structural description of fixed-order subgraphs of the function control flow graph. The results of experimental studies, including the comparison of the proposed method and previously known methods of searching for similar code sequences, are presented.

1. Introduction

The problem of finding similar code sequences in executable files is very relevant today. According to the studies presented in [1, 2], developers often use previously created program code during the process of the new software development. This approach to software development is called code reuse. Despite the obvious advantages of this approach, it can also cause errors and vulnerabilities in the software being developed. In addition, third-party code reuse may be illegal. This approach is also used in the development of various malicious programs [3]. Thus, solving the problem of finding similar code sequences in executable files allows us to solve several problems: finding known vulnerabilities, finding plagiarism in software, and searching for malware.

Currently, there are a large number of methods of similar code sequences search in executable files. All known algorithms and methods for solving the above problem are usually based either on the syntactic analysis of the assembler program code or on the analysis of the structure of control flow graphs of the executable file functions.

Let us consider the methods based on the syntax analysis of the code. In [4, 5], similar methods of similar code sequences search was presented. These methods are based on comparing sequences or permutations of processor instructions of a fixed length (k-grams or n-perms) in functions. The IDA disassembler uses the IDA FLIRT algorithm [6] to identify library functions, which is based on a comparison of function's patterns. The author of [7] presented a method for detecting malware, based on the analysis of the frequency of processor instructions occurrence inside the examined file. Significant impact on the quality of the similar code sequences search for this group of methods is made by syntactic code changes: replacing processor instructions with equivalent ones, rearranging instructions, inserting new ones, and deleting old instructions. The methods based on the analysis of the functions control flow graph allow to overcome this

drawback. The authors of the method presented in [8] used the information of basic blocks (the vertices of the control flow graph) to detect and classify malware. The authors of [9] used a method based on determining the isomorphism of control flow graphs to identify malware. A similar approach was described in [10], where the detection of malware was based on determining the isomorphism of fixed length function's subgraphs and comparing the signatures (fingerprints) of their basic blocks. However, this group of methods also has several disadvantages: low search accuracy for functions with a small number of basic blocks, high sensitivity to structural changes in functions.

In this paper, a combined method for searching functions of an executable file, which are similar to the known functions from some software "archive" is proposed. The basis of the proposed method is to use of both the syntactic analysis of the code and the analysis of functions control flow graph. The description of the function in the presented method is formed by its similarity with the functions of the basis library.

The paper is structured as follows. The first section presents the basic definitions and a brief description of the proposed method. The second section discusses the process of getting a syntactic description; the third one describes the process of getting the structural description of functions. The fourth section is devoted to the description of the similar functions search algorithm. The fifth section provides the effectiveness evaluation technique of the proposed method and the results of the experiments. In the final part of the paper, the conclusions and a list of references are presented.

2. Basic concepts and principle of operation

The following definitions are used in this paper:

- current library - the set of the investigated executable file functions;
- archival data - the set of the known functions;
- basis library - an auxiliary set of functions used to compare the functions of archived data and the current library.

Taking into account the above definitions, the problem solved by the proposed method is formulated as follows: for a given (or each) function of the current library, find the most similar function from the archive data. In this paper, we use two definitions of the functions similarity measure. The first one is based on the position of the functional groups of processor instructions in the body of functions. The second one is based on the analysis of the structure of the functions control flow graph. In the previously published works of the author [11, 12], two methods of similar code sequences search were presented, each of which is based on one of the above definitions of the function similarity measure, respectively. This paper presents a combined method of similar code sequences search. In this method, the description of function is formed through its similarity with the functions of the basis library, using two different definitions of the functions similarity measure described in [11, 12].

The proposed method of similar code sequences search includes several stages. At the first stage, the description of the archive data functions is formed through the library of basis functions. In addition, for each function, two descriptions are obtained (syntactic and structural) corresponding to different measures of functions similarity. At the second stage, the description of the current library functions is formed similarly. At the final stage, the search for similar functions is performed. The algorithm of search is described in detail in the fifth section.

3. The syntactic description of the function

Using the IDA [13] disassembler, we can obtain a partition of the assembler code of the analysed executable file into functions. The assembler code consists of a sequence of processor instructions and associated operands. All processor instructions can be divided into K functional groups

according to the type of operations they perform. Examples of such groups are: a group of arithmetic instructions, a group of logical instructions, a group of data transfer instructions. For each of the K functional groups for a given function, we obtain a list of offsets relative to the beginning of the function, on which the instructions of this group are located.

Let us determine the spatial distribution of the k instruction type as the absolute frequency of the instructions of this type entering in a relative normalized i-th interval ($I = 100$):

$$\tilde{f}_i^k = \sum_{j=0}^{N_k-1} I\left(\frac{n_j^k}{N} \cdot 100 \in (i-1, i]\right), \quad i = \overline{1, I}, \tag{1}$$

where $n_0^k, ..., n_{N_k-1}^k$ are absolute offsets relative to the beginning of the function of instructions of group k, N_k is a total number of instructions of this group in this function, N is the length of the function, $I(.)$ is the event indicator, which takes the values "0" or "1" depending on the truth of the corresponding argument.

To obtain the spatial distribution of instructions in the integral form, we use the following formula:

$$\hat{f}_i^k = \frac{\sum_{y=0}^{i} \tilde{f}_y^k}{\sum_{j=0}^{I} \tilde{f}_j^k}, i = \overline{1, I}. \tag{2}$$

Then, the spatial position of the k-th group of processor instructions in the body of the function is described by the vector:

$$\bar{a}_k = \left(\hat{f}_1^k, \hat{f}_2^k, \ldots, \hat{f}_I^k\right)^T, k = \overline{0, K-1}. \tag{3}$$

As a result, the description of the considered function has the following form:

$$A = \left(\bar{a}_0, \bar{a}_1, \ldots, \bar{a}_{K-1}\right). \tag{4}$$

The matrix B, which represents the description of the basis library functions, is formed in a similar way. The measure of functions similarity, which description is given by the matrices A and B, has the following form:

$$\mu\left(A, B\right) = \sum_{k=0}^{K-1} \alpha_k \mu_{\cos}(\bar{a}_k, \bar{b}_k), \quad \sum_{k=0}^{K-1} \alpha_k = 1, \tag{5}$$

where

$$\mu_{\cos}$$

is the cosine distance. If two functions are identical, the measure of similarity takes the value "1", otherwise "0".

Let a library of basis functions contains J functions, each of which has a description in the form of a matrix B_j. Then the description of the considered function through the library of basis functions will have the following form:

$$\bar{x}_A = \left(\mu\left(A, {}_0\right), \mu\left(A, {}_1\right), \ldots, \mu\left(A, {}_{J-1}\right)\right)^T. \tag{6}$$

Further, using the obtained intermediate description of the function, its final description is formed using the PCA (principal component analysis) method for reducing the dimensionality of the data. The process of forming the final description is described in detail in [11]. The resulting description of the function is stored in the corresponding database (archive or current).

4. The structural description of the function

IDA disassembler allows to obtain a control flow graph of the analysed executable file functions. The control flow graph of a function is a directed graph which vertices are the basic blocks of function. The basic block of function is a sequence of processor instructions. The first instruction of the basic block receives the control from some processor instruction, and the last one is an instruction, which passes the control to another basic block. The edges of the control flow graph determine the order of the basic blocks in the control flow of the function.

The control flow graph of the analysed function is divided into subgraphs of fixed order k (k-subgraphs) as follows: each basic block is chosen as a starting node and all edges beginning from that node are traversed until k nodes are encountered. In this paper, $k = 3$ is used.

The description of each of the k-subgraphs of the function consists of a pair of vectors: $\bar{a}$ and $\bar{b}$. The $\bar{a}$ vector is a binary vector obtained by combining the rows of the adjacency matrix of a given k-subgraph. The $\bar{b}$ vector characterizes the presence or absence of reading or writing operations in operands of various types in this k-subgraph. A detailed description of the vector $\bar{b}$ is presented in [12]. Thus, the initial description of a function consists of a set of pairs of vectors $\bar{a}$ and $\bar{b}$ describing each k-subgraph of the function.

The intermediate description of the function is formed on the basis of its similarity with the functions of the basis library. As a measure of similarity, we use the generalized Jaccard index [14]:

$$J(x, y) = \frac{\sum\limits_i \min(x_i, y_i)}{\sum\limits_i \max(x_i, y_i)}, \tag{7}$$

where x is a set of vector pairs which described the first function, y is a set of vector pairs which described the second function,x_i is a number of pairs i in set x,y_i is a number of pairs i in set y, i passed through all unique pairs of vectors in the combined set $x \bigcup y$. In the case of complete similarity between functions the value of similarity measure is "1", in case of complete dissimilarity it is "0".

Let x be a set of vector pairs described the analysed function, y_i is a set of vector pairs described the i-th function of the basis library, I is a number of functions in the basis library, then the intermediate description of the function under investigation has the following form:

$$\bar{z} = (J(x, y_0), J(x, y_1), ..., J(x, y_{I-1}))^T. \tag{8}$$

The final description of the function is obtained after applying the PCA dimension reduction method and is stored in the appropriate database (archive or current).

5. Search for similar functions

The final stage of the proposed method is the search for similar functions based on the previously obtained function description vectors.

In the previous works of the author, a search algorithm with the following assumption was used: the size of the changed functions differs from the original by no more than 30% [11]. This assumption was used to increase the quality of the search. Thus, at the first stage of the search, the archive functions were filtered by their size, then the Euclidean distance to each function was calculated from the filtered list of archive functions, and the result was sorted by increasing the Euclidean distance.

This paper presents a combined method of similar functions search, which uses a syntactic and structural description of functions. However, if the number of basic blocks of the function being studied is small ($bb_{\min} \leq 5$), only the syntactic description of the function and the search algorithm described above are used. This condition allows to increase the search accuracy since

the structural description of small functions can be very similar to the structural description of the similar size functions due to their small size.

The search method presented in this paper uses the following algorithm for similar functions search (if $bb_{\min} > 5$):

- At the first stage, preliminary filtering of archive functions is performed. For the function under study and all the functions of the archival data, the Euclidean distance between the vectors of the syntactic (or structural) description of the functions is calculated and sorted by ascending distance. The first $top_{th} = 30$ elements of the list of the most similar archive functions are used in the second stage of the search.
- At the second stage of the search, the Euclidean distance from the function under investigation to the list of functions obtained above is calculated. However, in this case, we use another type of vectors as the description vectors. In other words, if at the first stage the functions were compared by the vectors corresponding to their syntactic description, then at the second stage functions will be compared by the vectors corresponding to their structural description and vice versa. Then, the obtained result is sorted by increasing the Euclidean distance.

As a result, for the analysed function, a list of archive data functions is obtained, sorted by similarity in descending order.

6. Experiments

To evaluate the efficiency of the proposed method of similar code sequences search in executable files, the functions of one dynamic library are used as archive data, and the functions of the same library, but of a different version, are used as the current library. It was considered that in the process of switching from one version of the dynamic library to another, the names of the functions did not change and there are no functions with the same name among the functions of the archive data.

Using the search algorithm described in the fifth section, for a given function of the current library, we obtain an ordered list of archive data functions. Let us assign a binary sequence $\beta = (\beta_1, \beta_2, ..., \beta_L)$ to this list, the i-th element of which is equal to one, if the name of the function at the i-th position of the list is identical to the name of the function being checked, and the i-th element of which is equal to zero otherwise. The following criteria to evaluate the quality of information retrieval [15, 16] are used:

- Precision for the k-th position of the list: $P_k = \frac{\sum\limits_{l=1}^{k} \beta_l}{k}$
- Recall for the k-th position of the list: $R_k = \frac{\sum\limits_{l=1}^{k} \beta_l}{K}$
- The average precision of the list: $AveP = \sum\limits_{k=1}^{L} P_k(R_k - R_{k-1}), R_0 = 0$

The average precision for all functions included in the current library is calculated by the formula:

$$P = \frac{1}{S} \sum_{s=0}^{S-1} AveP_s, \tag{9}$$

where S is a number of functions in the current library.

Several versions of the libtiff library [17] were used for experiments. The functions of the library libtiff 4.0.8 were used as functions of the archived data. These libraries were compiled with the optimization flag /Od (optimization disabled).

The results of comparing two methods of preliminary filtering of the archival data functions are presented in table 1.

Table 1. Comparing preliminary filtering methods of the archival data functions.

Current library	Average precision of search P, filtering by syntactic description	Average precision of search P, filtering by structural description
libtiff 3.9.2	0.7424	0.7592
libtiff 3.9.7	0.7551	0.7707
libtiff 4.0.3	0.7835	0.8290
libtiff 4.0.5	0.7943	0.8432

The average precision of the search for the considered libraries is higher when preliminary filtering of the archival data functions by structural description is used. Therefore, in further experiments, this method of preliminary filtering of archive functions will be used.

In next experiment, the average precision of search of the proposed method was compared with some previously known methods: a method based on the analysis of the spatial position of processor functional groups [11] and a method based on k-gram comparison [4].As a comparison object for the first method, the comparison object recommended by the authors was used (the spatial distribution of instructions in the function body in integral form). For the second method, the value of the parameter $k = 5$ was also chosen based on the recommendations of the authors. The results are presented in table 2.

Table 2. Comparison of similar functions search methods.

Current library	Average precision of search P,using proposed method	Average precision of search P,using k-gramm based method	Average precision of search P,using method presented in [11]
libtiff 3.9.2	0.7592	0.7528	0.7370
libtiff 3.9.7	0.7707	0.7681	0.7524
libtiff 4.0.3	0.8290	0.7970	0.8257
libtiff 4.0.5	0.8432	0.8119	0.8427

The analysis of the obtained results shows that the method of similar code sequences search presented in this paper is superior to the previously known methods in each of the used current libraries. Moreover, the "closer" the version of the current library to the version of the archive data library, the less advantage the presented method has over the method [11]. This is explained by the fact that for libraries used in experimental studies, some functions of older versions of the current library have significant syntactic changes with respect to archive functions. And preliminary filtering of archival data by structural description can significantly improve the precision of the search.

7. Conclusion

The paper presents a combined method of similar code sequences search in executable files using both syntactic and structural descriptions of functions. The results of experiments demonstrating the superiority of the developed method over some previously known methods have been presented. Further studies will be carried out in improving the accuracy of similar functions search and studying the efficiency of the proposed method using executable files compiled with different compilation settings.

8. References

[1] Abdalkareem R, Shihab E and Rilling J 2017 On code reuse from StackOverow: An exploratory study on Android apps *Information and Software Technology* **88** 148-158
[2] Gharehyazie M, Ray B and Filkov V 2017 Some from here, some from there: cross-project code reuse in GitHub *Proc. of the 14th International Conference on Mining Software Repositories* **1** 291-301
[3] Examining Code Reuse Reveals Undiscovered Links Among North Koreas Malware Families URL:https://securingtomorrow.mcafee.com/mcafee-labs/examining-code-reuse-reveals-undiscovered-links-among-north-koreas-malware-families/ (05.11.2018)
[4] Myles G and Collberg C 2005 K-gram based software birthmarks *Proc. of the ACM symposium on Applied computing* 1 314-318
[5] Karim M, Walenstein A, Lakhotia A and Parida L 2005 Malware phylogeny generation using permutations of code *Journal in Computer Virology* **1** 13-23
[6] IDA F.L.I.R.T Technology: In-Depth URL: https://www.hex-rays.com/products/ida/tech/irt/indepth.shtml (05.11.2018)
[7] Bilar D 2007 Opcodes as predictor for malware *International Journal of Electronic Security and Digital Forensics* **1** 156-168
[8] Gheorghescu M 2005 An automated virus classi_cation system *Virus Bulletin Conference* **1** 294-300
[9] Bruschi D, Martignoni L and Monga M 2006 Detecting selfmutating malware using control-ow graph matching *Proc. of the Third international conference on Detection of Intrusions and Malware & Vulnerability Assessment* **1** 129-143
[10] Kruegel C, Kirda E, Mutz D, Robertson W and Vigna G 2005 Polymorphic worm detection using structural information of executables *Recent Advances in Intrusion Detection* **1** 207-226
[11] Yumaganov A and Myasnikov V 2017 A method of searching for similar code sequences in executable binary files using a featureless approach *Computer Optics* **41(5)** 756-764 DOI: 10.18287/2412-6179-2017-41-5-756-764
[12] Yumaganov A and Myasnikov V 2018 Searching for similar code sequences in executable files based on the structural analysis of functions *J. Phys.: Conf. Ser.* **1096** 012093
[13] Hex-Rays IDA: About URL: http://hex-rays.com/products/ida/ (05.11.2018)
[14] Spath H 1981 The minisum location problem for the Jaccard metric *Operations-Research-Spektrum* **3** 91-94
[15] Buckland M and Gey F 1994 The relationship between recall and precision *JASIS* **45** 12-19
[16] Powers D 2011 Evaluation: From Precision, Recall and F-Measure to ROC, Informedness, Markedness & Correlation *Journal of Machine Learning Technologies* **2** 37-63
[17] TIFF Library and Utilities URL: http://www.libti_.org/ (05.11.2018)

Using ontology merging for the integration of information systems and the production capacity planning system

N Yarushkina[1], A Romanov[1], A Filippov[1], A Dolganovskaya[1] and M Grigoricheva[1]

[1]Ulyanovsk State Technical University, Severny Venets street, 32, Ulyanovsk, Russia, 432027

e-mail: jng@ulstu.ru, romanov73@gmail.com, al.filippov@ulstu.ru, gms4295@mail.ru

Abstract. This article describes the method of integrating information systems of an aircraft factory with the production capacity planning system based on the ontology merging. The ontological representation is formed for each relational database (RDB) of integrated information systems. The ontological representation is formed in the process of analyzing the structure of the relational database of the information system (IS). Based on the ontological representations merging the integrating data model is formed. The integrating data model is a mechanism for semantic integration of data sources.

1. Introduction

As part of the work on automating the process of production capacity of the aircraft factory, it is necessary to take into account the presence of heterogeneous information systems in the aircraft factory that automates various business processes [1]. Data consistency can be realized by integrating the production capacity planning system with existing information systems of the aircraft factory. Data integration means the integration of data from different sources and the providing of data to users in a unified way. The main difficulties of data integration are:

(i) Data models heterogeneity.
(ii) Independence of information systems of the aircraft factory from each other.
(iii) Data can be located in different segments of the local network of the aircraft factory and (or) on the Internet.
(iv) Different data formats.
(v) Different value representations.
(vi) Loss of data relevance by one of the data sources.

Thus, the organization of the information interaction between the production capacity planning system and the existing information systems of the aircraft factory raises the need to solve the following methodological problems [2, 3, 4, 5, 6, 7, 8, 9]:

(i) Creating an integrating data model. Integrating data model is the basis of a single user interface in the integration system.
(ii) Development of methods for building onological representations for specific models of various data sources.
(iii) Development of methods for building integrating data model for specific models of various data sources.
(iv) Solving the problem of data sources heterogeneity.
(v) Development of mechanisms for semantic integration of data sources.

2. Ontological representation of data source

The proposed information interaction algorithm consists of the following steps:

(i) Extracting metadata from the RDB schema for automatic generation of ontologies for the source and target RBDs.
(ii) Ontology merging to configure correspondence between objects, attributes, and relationships of integrated ISs. Creation of metaontology.
(iii) Using the metaontology to perform the interaction procedure on a schedule or event.

The metaontology is the settings contains correspondences between data models (tables and columns) of integrated ISs.

Ontology is a model knowledge representation of a specific problem area [10]. An ontology contains a set of classes, individuals, properties, and relations between them. An ontology is based on the dictionary of terms which reflecting the concepts of a problem area. Also, the dictionary contains a set of rules (axioms). Terms can be combined to construct a set of statements about the state of the problem area based on a set of axioms.

At the moment, a lot of researchers use the ontological approach for extracting metadata from the RDB schema:

(i) The Relational.OWL [11] currently supporting only MySQL and DB2 database management systems (DBMS). The generated ontology contains classes: Database, Table, Column, and PrimaryKey, and properties: has, hasTable, hasColumn, isIndentifiedBy, references, scale, length. The main disadvantage of ontology generated by Relational.OWL is the presence of limited coverage of the domain, not considering, for instance, data type, foreign keys, and constraints.
(ii) The OWL-RDBO [12, 13] currently supporting only MySQL, PostegreSQL and DB2 DBMSs. The generated ontology contains classes: DatabaseName, RelationList, Relation, AttributeList, Attribute, and properties: hasRelations, hasType, referenceAttribute, referenceRelation. ,The main disadvantage of ontology generated by OWL-RDBO is the presence of concepts external to the domain, such as RelationList to group a set of Relation, and AttributeList to group a set of attributes.
(iii) Other approaches, such as [14, 15] extract the real world relations from the RDB structure, and unable to reconstruct the original schema of the RDB.

The relational data model can be represented as the following expression:

$$RDM = \langle E, H, R \rangle, \tag{1}$$

where $E = \{E_1, E_2, \ldots, E_p\}$ is a set of RDB entities (tables);
$E_i = (name, Row, Col)$ is the i-th RDB entity that contains the name, set of rows Row and columns Col;
$Col_j = (name, type, constraints)$ is the j-th column of the i-th RDB entity that contains

properties: the name, the type and set of constraints;
$H = \{H_1, H_2, \ldots, H_q\}$ is a hierarchy of RDB entities in the case of using the table inheritance function:

$$H_j = E_i D\,(x)\, E_k, \tag{2}$$

where E_i and E_k are RDB entities;
$D\,(x)$ is a 'parent-child' relation between E_i and E_k;
$R = \{R_1, R_2, \ldots, R_r\}$ is a set of RDB relations:

$$R_l = E_i \frac{F\,(x)}{G\,(x)} E_k, \tag{3}$$

where $F\,(x)$ is an RDB relation between E_i and E_k;
$G\,(x)$ is an RDB relation between E_k and E_i.

Functions $F\,(x)$ and $G\,(x)$ can take values: U is a single relation and N is multiple relations.

The ontological representation of the RDB data model is:

$$O = \langle C, P, L, R \rangle, \tag{4}$$

where $C = \{C_1, C_2, \ldots, C_n\}$ – is a set of data model ontology classes;
$P = \{P_1, P_2, \ldots, P_m\}$ – is a set of properties of data model ontology classes;
$L = \{L_1, L_2, \ldots, L_o\}$ – is a set of data model ontology constraints;
R is a set of data model ontology relations:

$$R = \{R_C, R_P, R_L\}, \tag{5}$$

where R_C is a set of relations defining the hierarchy of data model ontology classes;
R_P is a set of relations defining the 'class-property' data model ontology ties;
R_L is a set of relations defining the 'property-constraint' data model ontology ties.

The following function is used to map the RDB structure (ex. 1) to the ontological representation (ex. 4):

$$F\,(RDM, O) : \{E^{RDM}, H^{RDM}, R^{RDM}\} \rightarrow\ \rightarrow \{C^O, P^O, L^O, R^O\}, \tag{6}$$

where $\{E^{RDM}, H^{RDM}, R^{RDM}\}$ is a set of RDB entities and relations between them (eq. 1);
$\{C^O, P^O, L^O, R^O\}$ is a set of ontology entities (eq. 4).

The process of mapping the RDB structure into an ontological representation contains several steps:

(i) *Formation of ontological representation classes.*
A set of ontological representation classes C is formed based on the set of RDB entities $C\ E_i \rightarrow C_i$. The number of classes of the ontological representation must be equal to the number of RDB entities.

(ii) *Formation of properties of ontological representation classes.*
A set of properties P of the i-th ontological representation class C_i is formed based on the set of columns Col of the i-th RDB entity E_i $Col_j \rightarrow P_j$. The number of properties of the i-th ontological representation class C_i must be equal to the number of columns of the i-th RDB entity E_i. The name of the j-th property P_j is the name of the j-th column Col_j of the RDB entity.

(iii) *Formation of ontological representation constraints.*
A set of constraints L of the properties of the i-th ontological representation class C_i is formed based on the set of columns Col of the i-th RDB entity E_i $Col_k \rightarrow \hat{L}$. The number of constraints of the i-th ontological representation class C_i must be equal to the number of constraints of the i-th RDB entity E_i. However, there are limitations to this approach due to the difficulty of mapping constraints if their presents as triggers or stored procedures.

(iv) *Forming hierarchy of ontological representation classes.*
It is necessary to form a set of ontology relationships R_C between all the child and parent classes corresponding to the hierarchy of RDB entities if table inheritance uses in RDB $H \rightarrow R_C$. The domain of the j-th ontological representation relationship R_{Cj} is indicated by the reference to the parent class C_{parent}. The range of the j-th ontological representation relationship R_{Cj} is indicated by the reference to the child (or a set) class C_{child}.

(v) *Formation of relations between classes and properties of classes of ontological representation.*
A set of ontological representation relationships R_P is formed based on the set of columns Col of the i-th RDB entity E_i and the set of RDB relations R. Two types of relationships are formed for each j-th ontological representation property P_j:
   (a) The relationship 'class-property'. The domain of the ontological representation relationship is indicated by the reference to the i-th class C_i to which the j-th property belongs, and the range to the j-th property reference P_j.
   (b) The relationship 'property-data type class'. The domain of the k-th ontological representation relationship is indicated by the reference to the j-th property P_j. The range is indicated by the reference to the l-th class C_l corresponding to the l-th RBD entity E_l, or the reference to the m-th ontology class C_m corresponding to the data type of the j-th RBD column Col_j.

(vi) *Formation of relations between properties of classes and constraints of properties of classes of ontological representation.*
A set of relations R_L of ontological representation is formed based on the set of columns Col of the i-th RDB entity.The domain of the j-th ontological representation relationship R_{Lj} is indicated by the reference to the k-th property P_k. The range of the j-th ontological representation relationship R_{LJ} id indicated by the reference to the k-th constraint $Col \rightarrow R_L$.

3. Integrating data model

It is necessary to form an integrating data model based on the ontological representations that obtained after mapping the RDB structure of each of the integrated information systems into the ontological representation. The definition of an ontological system is used as a formal representation of an integrating data model:

$$\sum^{O} = \langle O^{META}, O^{IS}, M \rangle, \tag{7}$$

where O^{META} is the integrating data model ontology (metaontology);
$O^{IS} = \{O_1^{IS}, O_2^{IS}, \ldots, O_g^{IS}\}$ is a set of ontological representations of information systems that must be integrated;
M is a model of reasoner.

The following steps are necessary to form an integrating data model based on the set of ontological representations of the information systems that must be integrated:

(i) *Formation of the universal concept dictionary for the current domain.*
The process of forming an integrating data model O^{META} is based on the presence of common terminology. Ontological representations of all information systems that must be integrated O^{IS} should be built from a single concept dictionary. The concept dictionary is formed by the expert based on the analysis of the obtained ontological representations.

(ii) *Formation an integrating data model O^{META}.*
At this step, the set of top-level classes C^{META} are added to the integrating data model O^{META}. The set of top-level classes C^{META} describes systems that must be integrated and is used as the basis for ontology merging.

(iii) *Formation of class hierarchy of integrating data model* O^{META}.
At this step, the integrating data model establishes a correspondence between the class hierarchies $C^{O_i^{IS}}$ of ontological representations O^{IS} of information systems that must be integrated.

(iv) *Formation of class properties of the integrating data model* O^{META}.
At this step, the integrating data model establishes a correspondence between the properties $P^{O_i^{IS}}$ of ontological representations O^{IS} of information systems that must be integrated. The expert decides which class properties of ontological representations O^{IS} should be included in the integrating data model O^{META}.

(v) *Formation of axioms of classes and properties, checking the integrating data model* O^{META} *for consistency.*
At this step, constraints $L^{O^{IS}}$ are applied to the properties $P^{O^{IS}}$ and classes $C^{O^{IS}}$ of the integrating data model O^{META} based on the constraints presents in the ontological representations O^{IS}. After that, the resulting integrating data model O^{META} should be checked for internal consistency using the reasoner M. However, the development of methods for checking the conditions of constraints is required, since the existing reasoners do not support working with such objects.

The proposed method is allowed to configure the correspondence between tables and fields of two RDBs. The main problem is the need for ontology merging. However, that problem can be solved due to the use of specialized tools to automate the ontology merging process. Also, specialized tools allow dividing the developer and domain expert roles. The main advantage of the proposed method is the ability to dynamically generate the necessary SQL queries for select and insert data from/to the RBD based on metaontology.

4. Example of creation the ontological representation of data source

Let see the following example of the ontological representation formation.

Table 1 shows the structure of the "Equipment and Tools" table of the aircraft factory IS.

Thus, the ontological representation of the "Equipment and Tools" entity (tab. 1) can be represented as:

$O = \langle$
$C = \{$ Equipment and Tools (E&T), CHAR, NUMBER, BLOB, DATE $\}$,
$P = \{$ t2_ob, t2_ng , t2_nn, t2_r1, t2_r2, t2_r3, t2_p1, t2_z1, t2_p2, t2_z2, t2_p3, t2_z3, t2_gm, t2_p3, t2_z3, t2_gm, up_dt, up_us, t2_dc, t2_vid, t2_doc, t2_prim, t2_yyyy $\}$
$L = \{$ nullable, $\langle$ length, 2 $\rangle$, $\langle$ length, 4 $\rangle$, $\langle$ length, 8 $\rangle$, $\langle$ length, 32 $\rangle$, $\langle$ length, 100 $\rangle$, $\langle$ length, 200 $\rangle$, $\langle$ length, 255 $\rangle$, $\langle$ precision, 5 $\rangle$, $\langle$ precision, 6 $\rangle$ $\}$
$R_P = \{$ $\langle$ E&T, t2_ob, CHAR $\rangle$, $\langle$ E&T, t2_ng, NUMBER $\rangle$, $\langle$ E&T, t2_nn, NUMBER $\rangle$, $\langle$ E&T, t2_r1, CHAR $\rangle$, $\langle$ E&T, t2_r2, CHAR $\rangle$, $\langle$ E&T, t2_r3, CHAR $\rangle$, $\langle$ E&T, t2_p1, CHAR $\rangle$, $\langle$ E&T, t2_z1, CHAR $\rangle$, $\langle$ E&T, t2_p2, CHAR $\rangle$, $\langle$ E&T, t2_z2, CHAR $\rangle$, $\langle$ E&T, t2_p3, CHAR $\rangle$, $\langle$ E&T, t2_z3, CHAR $\rangle$, $\langle$ E&T, t2_gm, CHAR $\rangle$, $\langle$ E&T, up_dt, DATE $\rangle$, $\langle$ E&T, up_us, CHAR $\rangle$, $\langle$ E&T, t2_dc, BLOB $\rangle$, $\langle$ E&T, t2_vid, CHAR $\rangle$, $\langle$ E&T, t2_doc, CHAR $\rangle$, $\langle$ E&T, t2_prim, CHAR $\rangle$, $\langle$ E&T, t2_yyyy, CHAR $\rangle$ $\}$
$R_L = \{$ $\langle$ E&T, t2_ob, $\langle$ length, 200 $\rangle$ $\rangle$, $\langle$ E&T, t2_ng, $\langle$ precision, 5 $\rangle$ $\rangle$, $\langle$ E&T, t2_nn, $\langle$ precision, 6 $\rangle$ $\rangle$, $\langle$ E&T, t2_p1, $\langle$ length, 2 $\rangle$ $\rangle$,

⟨ E&T, t2_p1, nullable ⟩, ⟨ E&T, t2_z1, ⟨ length, 8 ⟩ ⟩,
⟨ E&T, t2_z1, nullable ⟩, ⟨ E&T, t2_p2, ⟨ length, 2 ⟩ ⟩,
⟨ E&T, t2_p2, nullable ⟩, ⟨ E&T, t2_z2, ⟨ length, 8 ⟩ ⟩,
⟨ E&T, t2_z2, nullable ⟩, ⟨ E&T, t2_p3, ⟨ length, 2 ⟩ ⟩,
⟨ E&T, t2_p3, nullable ⟩, ⟨ E&T, t2_z3, ⟨ length, 8 ⟩ ⟩,
⟨ E&T, t2_z3, nullable ⟩, ⟨ E&T, up_us, ⟨ length, 32 ⟩ ⟩,
⟨ E&T, t2_vid, ⟨ length, 4 ⟩ ⟩, ⟨ E&T, t2_doc, ⟨ length, 100 ⟩ ⟩,
⟨ E&T, t2_prim, ⟨ length, 100 ⟩ ⟩, ⟨ E&T, t2_doc, nullable ⟩,
⟨ E&T, t2_yyyy, ⟨ length, 4 ⟩ ⟩ }
⟩.

Table 1. The "Equipment and Tools" table of the aircraft factory IS.

Column	Data type	Description
t2_ob	CHAR(200)	Name
t2_ng	NUMBER(5)	Group
t2_nn	NUMBER(6)	Position
t2_r1	CHAR	Type #1: 0 — equipment; 1 — tool; 2 — material; 6 — special tool.
t2_r2	CHAR	Type #2: 0 — standard; 1 — special.
t2_r3	CHAR	Type #3: 20 — no; 21 — design; 30 — model; 31 — design and model.
t2_p1	CHAR(2) nullable	Parameter #1
t2_z1	CHAR(8) nullable	Parameter #1 value
t2_p2	CHAR(2) nullable	Parameter #2
t2_z2	CHAR(8) nullable	Parameter #2 value
t2_p3	CHAR(2) nullable	Parameter #3
t2_z3	CHAR(8) nullable	Parameter #3 value
t2_gm	BLOB	Geometric model
up_dt	DATE	Date of last update
up_us	CHAR(32)	User
t2_dc	BLOB	Attachment
t2_vid	CHAR(4)	Tooling type
t2_doc	CHAR(100)	Document name
t2_prim	CHAR(100) nullable	Notes
t2_yyyy	CHAR(4)	Production date

As you can see from this example, the resulting ontology representation O has some sets of

objects:

(i) A set of classes C contains the "Equipment and Tools" table and some data types: CHAR, NUMBER, BLOB, DATE. The OWL representation of ontology O uses Class signature to represent the table.

(ii) A set of properties P contains all columns of the "Equipment and Tools" table. The OWL representation of ontology O uses built-in data types to represent RDB data types (*xsd:string, xsd:double, xsd:dateTime, xsd:base64Binary*), and Class signature to represent RDB relationships.

(iii) A set of constraints L contains all variants of restrictions for columns of the "Equipment and Tools" table. This set is not translated to OWL representation directly.

(iv) A set of relations between classes and properties R_P contains ties between table and columns that belong to this table. The OWL representation of ontology O uses ObjectProperties and DataProperties signatures to represent a set of relations R_P. ObjectProperties signatures are used to represent foreign keys. DataProperties signatures are used to represent columns that contain a value.

(v) A set of relations between properties and constraints R_L contains a tie between column and constraints of this column. OWL datatype restrictions are used for constraints specification. For example:
DatatypeRestriction(
xsd:integer xsd:minInclusive "5"^^xsd:integer xsd:maxExclusive "10"^^xsd:integer
) .

Thus, the ontological approach is commonly used to solve the methodological problem of building an integrating data model of information systems.

5. Conclusion

This article presents the implementation of the method of integrating the information systems of the aircraft factory with the production capacity planning system. The principles of ontological engineering allows mapping database structure of each information system that must be integrated into ontological representation. From the proposed methodology, an integrated data model is formed based on the obtained ontological representations for each information systems that must be integrated.

The proposed method allows organizing information interaction without the participation of developers in contrast to the traditional approach of consolidation, based on the method of direct data exchange. The only requirement of the proposed method is the presence of metaontology. The disadvantages of the proposed method implementation currently are:

(i) The need for implementation of the data type casting algorithms in case of their mismatch for each DBMS.

(ii) The need for adapting the proposed method implementation to the SQL dialect of DBMS involved in the exchange process. Random DBMS cannot be supported by this implementation.

6. References

[1] Yarushkina N, Romanov A, Filippov A, Guskov G, Grigoricheva M and Dolganovskaya A 2019 The building of the production capacity planning system for the aircraft factory *Research Papers Collection OpenSemantic Technologies for Intelligent Systems* **3** 123-128

[2] Clark T, Barn B S and Oussena S 2012 A method for enterprise architecture alignment *Practice-Driven Research on Enterprise Transformation* 48-76

[3] Rouhani D B 2015 A systematic literature review on Enterprise Arquitecture Implementation Methhodologies *Information and Software Technology* 1-20
[4] Medini K and Bourey J P 2012 SCOR-based enterprise architecture methodology *Int. J. Comput. Integrat. Manuf.*
[5] Poduval A 2011 *Do more with SOA Integration: Best of Packt*
[6] Caselli V, Binildas C and Barai M 2008 *The Mantra of SOA. Service Oriented Architecture with Java* (Birmingham. UK)
[7] Berna-Martinez V J, Zamora C, Ivette C, Perez M, Paz F, Paz L and Ramon C 2018 *Method for the Integration of Applications Based on Enterprise Service Bus Technologies*
[8] Evsutin O O, Kokurina A S and Meshcheryakov R V 2019 A review of the methods of embedding information in digital objects for security in the Internet of things *Computer Optics* **43(1)** 137-154 DOI: 10.18287/2412-6179-2019-43-1-137-154
[9] Rycarev I A, Kirsh D V and Kupriyanov A V 2018 Clustering of media content from social networks using bigdata technology *Computer Optics* **42(5)** 921-927 DOI: 10.18287/ 2412-6179-2018-42-5-921-927
[10] Gruber T 2019 *Ontology* URL: http://tomgruber.org/writing/ontology-in-encyclopedia-of-dbs.pdf
[11] de Laborda C P and Conrad S 2005 Relational. owl: a data and schema representation format based on owl *Proceedings of the 2nd Asia-Pacific conference on Conceptual modeling* 43 89-96
[12] Trinh Q, Barker K and Alhajj R 2006 Rdb2ont: A tool for generating owl ontologies from relational database systems Telecommunications *International Conference on Internet and Web Applications and Services/Advanced* 170
[13] Trinh Q, Barker K and Alhajj R 2007 Semantic interoperability between relational database systems *Database Engineering and Applications Symposium* 208-215
[14] Barrett T, Jones D, Yuan J, Sawaya J, Uschold M, Adams T and Folger D 2002 Rdf representation of metadata for semantic integration of corporate information resources *International Workshop Real World and Semantic Web Applications*
[15] Bizer C 2003 D2R MAP – A Database to RDF Mapping Language *Proc. of the 12th International World Wide Web Conference – Posters*

Acknowledgments
The study was supported by:
- the Ministry of Education and Science of the Russian Federation in the framework of the project No. 2.1182.2017/4.6. Development of methods and means for automation of production and technological preparation of aggregate-assembly aircraft production in the conditions of a multi-product production program;
- the Russian Foundation for Basic Research (Projects No. 18-47-732016, 18-47-730022, 17-07-00973, No. 18-47-730019).

Industrial application of big data services in digital economy

O L Surnin[1], P V Sitnikov[2], A A Khorina[2], A V Ivaschenko[3], A A Stolbova[4] and N Yu Ilyasova[4,5]

[1]SEC "Open Code", Yarmarochnaya Str., 55, Samara, Russia, 443001
[2]ITMO University, Birzhevaya liniya, 14, lit. A, Saint-Petersburg, Russia, 199034
[3]Samara State Technical University, Molodogvardejskaya street, 244, Samara, Russia, 443100
[4]Samara National Research University, Moskovskoe Shosse, 34, Samara, Russia, 443086
[5]Image Processing Systems Institute of RAS - Branch of the FSRC "Crystallography and Photonics" RAS, Molodogvardejskaya street 151, Samara, Russia, 443001

e-mail: surnin@o-code.ru, sitnikov@o-code.ru. anastasiakhorina@mail.ru, anton.ivashenko@gmail.com, stolbova@o-code.ru

Abstract. Nowadays, the world is moving to automation. Appropriate programs for the implementation of industrial applications are developed by many companies. But is it so easy to implement systems capable of processing large amounts of information in production? Despite multiple positive results in research and development of Big Data technologies, their practical implementation and use remain challenging. At the same time most prominent trends of digital economy require Big Data analysis in various problem domains. We carried out the analysis of existing data processing works. Based on generalization of theoretical research and a number of real economy projects in this area there is proposed in this paper an architecture of a software development kit that can be used as a solid platform to build industrial applications. Was formed a basic algorithm for processing data from various sources (sensors, corporate systems, etc.). Examples are given for automobile industry with a reference of Industry 4.0 paradigm implementation in practice. The given examples are illustrated by trends graphs and by subject area ontology of the automotive industry.

1. Introduction

Big data processing remains one of the key technological directions of digitalization of the economy in Russia. According to the National Program for the Development of the Digital Economy, one of the most important areas of application of the information technology (IT) infrastructure is a smart factory, implemented in accordance with the concept of Industry 4.0. This concept is based on the development of cyber-physical systems capable of controlling industrial processes, providing contextual and decentralized decision support. Solving these problems requires analyzing big data in real time.

Therefore, modern industrial enterprises are considered as a source of big data that describe the process of various information exchanges. Information obtained from various sources allows to draw conclusions about the processes of production and manufacturing. The use of methods and software solutions for working with big data in the course of solving this problem allows us to build efficient production at all levels.

Despite the positive results in research and development of big data technologies, their practical application in industrial applications remains a challenge. The challenges are related to the requirement to use unified and integrated software services based on a reliable platform, instead of developing individual algorithms and software solutions. To cover this gap in this article, it is proposed to summarize existing experience in this area [1, 2] and develop an architectural solution for a software development kit that can be used as a reliable platform for building industrial applications.

2. Technology review

Big data technologies include a range of approaches, tools, and methods for processing structured and unstructured data of vast amounts and considerable diversity. These technologies are used to obtain the obtained results that are effective in the conditions of constant growth, spreading information over numerous nodes of a computer network.

Big data processing services are usually implemented as part of research in developing research institutes, but in modern conditions organizations create a large amount of unstructured data, such as text documents, images, video tapes, computer codes, tables, etc. All this information is stored in many repositories, sometimes even outside the organization. Companies may have access to a vast array of their own data and may not have the necessary tools that could establish relationships between these data and draw important conclusions based on them. Big data processing technologies can make a big contribution to the industrial world.

The modern level of automation of modern industrial enterprises allows the introduction of intelligent technologies for analyzing production and business processes, focusing on the concept of a smart factory [3,4]. In accordance with this concept, human resources and robotic production equipment are integrated into a single information space and form a virtual community of participants with autonomous behavior and self-organization. The concept of Industry 4.0 is intensively and massively investigated in [5, 6]. The concept of an integrated solution based on the introduction of modern IT technologies for the development of cyber-physical systems for intelligent factories is described.

The process of user interaction in a single information space in modern manufacturing enterprises and in supply chains generates a sequence of events exchanging documents, messages and other information objects. The number of events is large (large physical volume of data); they vary and require high-speed processing. In this regard, the task of managing the collection and processing of information data in a system for collecting and processing data with a multi-layered architecture can be attributed to the problem of big data [7, 8].

One of the solutions may be close to a subject-oriented approach to business process management (S-BPM), which presents the process as a joint work of several actors organized through structured communication [9]. A model of interaction of subjects (subjects) in a single information space, which can be implemented using multi-agent software, can be proposed. The ideas of indirect and conditional project management, creating a soft influence on highly motivated autonomous actors, are successfully implemented in online communities and social networks [10-14].

During the development, a significant increase in key performance indicators is expected, according to the McKinsey Digital Economy Report [1]:

- Optimization of production and logistics operations
- Reduced equipment downtime and repair costs, due to increased equipment loading and equipment performance
- Rapid prototyping and quality control, due to the analysis of large data arrays in the development and improvement of products
- Decrease in an n expense of the electric power and fuel, due to reduction of production losses of raw materials

All these characteristics, one way or another, are related to data and the use of Big Data technologies in processing information about processes in production contributes to the efficiency of operations.

3. Big data industrial sources

Data sources for personnel monitoring and control can be very diverse and include: workflow, work time tracking system, equipment sensors, personal computer (PC) monitoring programs, motion detection sensors in video cameras, information about calls from an employee's work phone, mailbox activity analysis, etc.

When analyzing the workflow systems, conclusions can be drawn about the time spent working with each of the documents and the effectiveness of the tasks in working with documents. Viewing and analyzing the movement of documentation can help identify bottlenecks in working with each of the documents, displaying up-to-date information about the employee, which slows down the chain of work on the document.

The system of accounting of working time and time allows you to analyze the work of the employee, as well as track the periods when the employee is absent from the office, at inappropriate times.

Equipment sensors will evaluate the effectiveness of equipment use, with the ability to determine periods of downtime. This information allows you to build recommendations for the maintenance of equipment.

Analyzing information from a PC monitoring program and determining the working periods of a user's activity on a specific computer will allow evaluating the effectiveness of using a PC and the effectiveness of an employee's work on a PC. PC data will help to analyze the statistics of the location of an employee outside the workplace, when analyzing PC activity in combination with motion detection sensors.

Motion detection sensors in video cameras will allow you to evaluate the performance of certain algorithms by tracking the movement of a person in production and analyze employee location statistics outside the workplace.

Information from all possible data sources forms a single information space. The common information space contains information about events occurring at the enterprise, and some characteristics of streaming.

Events that will be monitored in the system include the following events: the fact and time of staff in the enterprise and at the workplace, the performance of official duties, the operation of equipment and their changes. An event that we call a change in the state of production facilities or an employee over time. Events are characterized by the objects to which they relate, the time when the event occurred, the type of event and the type of data source. An event of the same type can relate to different objects. Events are discrete values.

Flow characteristics are a continuous quantity that describes the trajectory of a person's movement. Critical changes in the trajectory, namely a sharp change in the trajectory, will be considered an event.

Events and characteristics form an array of source data. There are positive and negative behaviors in this input array. Positive behavior is the user's behavior without visible deviations, his work patterns, the algorithm works. Negative behavior will be considered as behavior that does not correspond to the standard behavior of the user in a particular situation.

Analysis of data taken from various sources allows you to track the work of staff, track downtime, identify the causes of reduced productivity and production efficiency, as well as personalize personal development plans and recommendations for a specific employee.

4. Solution architecture

Let us consider what properties the universal information system for processing Big Data should have:

- Flexibility. A system that has been subjected to a specific regulatory or adaptive effect can change its state and behaviour within the limits determined by the critical values of its parameters.
- Scalability. The system should be expanded depending on the purpose of the customer.
- Configurability. The system should be able to customize the features of a particular enterprise and the class of tasks to be solved.

- Interpretability of results. The system should be able to apply measurement results for various purposes.

To respect all conditions, the system should provide the following basic levels of services (Figure 1).

- System services are located on the lower level of the service distribution scheme and include::
- Geo-platform for working with maps and location data;
- Enterprise Service Bus for interfacing with external systems;
- Data Lake, which is a data warehouse from various external data providers, on the basis of which the necessary databases, knowledge bases and directories are formed.

Basic services are mandatory services and components that define the main functionality of the system, including:

- Analytical tools for data processing;
- Business Process Support Tools;
- Data storage facilities;
- Platform management subsystem that provides logging of system processes.
- Specialized services for working with Big Data, including services such as:
- Apache Spark;
- Apache Hadoop;
- TensorFlow;
- Apache Kafka;
- MongoDB;
- Celery;
- Block of Big Data analysis methods (simulation modelling, machine learning, evolutionary algorithms, neural networks, etc.).

Specialized domain services are narrowly focused tools aimed at solving specific problems. The example shows the services of the system for analyzing user behavior in social networks:

- Tag knowledge base containing a list of tags that classify deviant users;
- Behaviour patterns knowledge base, which reflects scenarios of possible user behaviour, both deviant and reference;
- Description of ontology for a specific subject area;
- Model of deviant behaviour, which is the construction of deviant behaviour.

User Interface is the top level of the service distribution system and contains the following components:

- User interface designer with the ability to select the available functionality depending on the goals of the system;
- Visualization tools for graphical presentation of information;
- Access rights separation subsystem.

Consider one of the data processing algorithms that allows you to analyze data obtained from various production systems. In this scheme (Figure 2), information is presented in the form of events characterizing a particular user action (sending a message, passing through sensors, entering production, etc.). The data is sorted in accordance with the algorithm in relation to the user, after which the resulting graphs are constructed allowing to draw conclusions about the patterns of user behavior in production, which makes it possible to organize the workflow more efficiently. Not only data inside the production process can be analyzed, but also external data sources, for example, news sources, for analyzing the reputation on the market, the next paragraph considers the possibility of analyzing information from open sources, largely built using the same algorithm

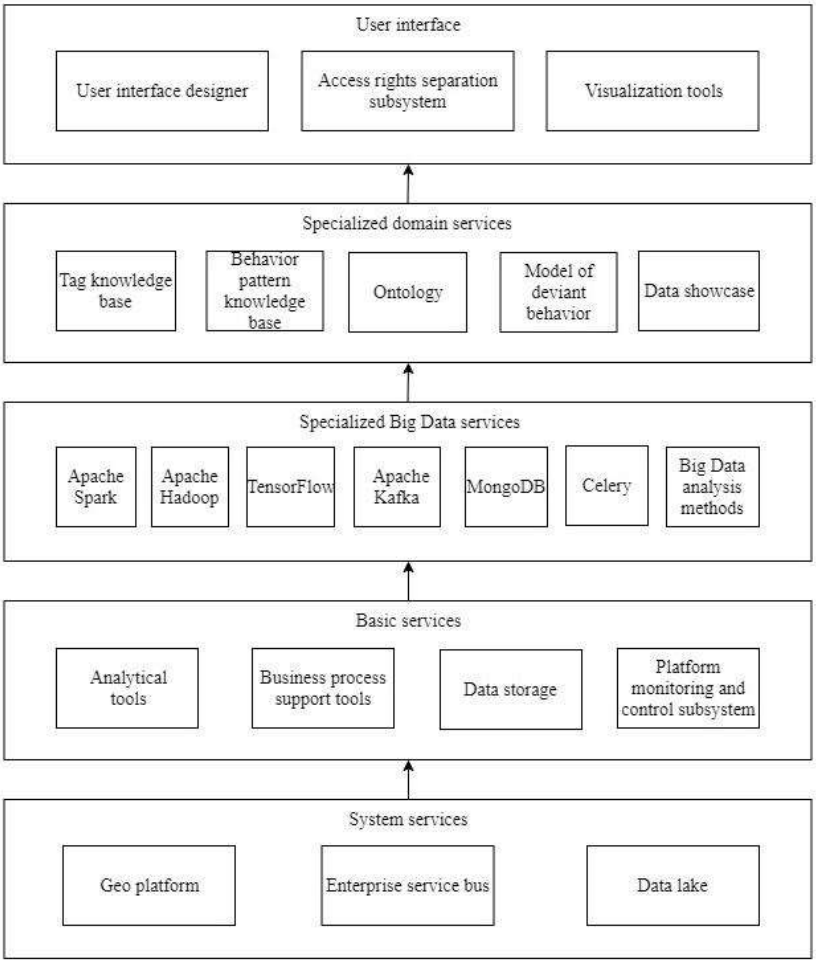

Figure 1. The distribution scheme of services in the system for detecting deviant behaviour.

5. Implementation and practical use

Let's see how information is analyzed for an open source enterprise. Consider an example of improving the marketing effectiveness of a car company.

Take information from open sources and analyze the data on the mention of a specific part of the production to determine the main trends and reviews about the production, to identify the weak points of production or marketing.

Within this example, two groups of consumer interests were identified: “Construction” (which includes tags related to the details of the car’s construction: doors, engines, etc.) and “Production” (including tags related to corporate culture and Team Management) . Deviations were found in both groups that corresponded to various aspects of the commodity market at a given point in time.

The figure 3 describes the ontology of these groups, tags and limitations of each tag.

Below is an analysis of information about several production machines for the most popular tags of a particular production.

As an example (Figure 4-6) illustrated strategic description of industrial companies for the automotive industry. The main Wikipedia articles on popular car trademarks and their changes have been analysed..

The dynamics of such updates turned out to be surprisingly high, despite the fact that these articles contain high-level descriptions that also include historical aspects of this area, additional information about trademarks that are updated, added and edited in real time by various types of users.

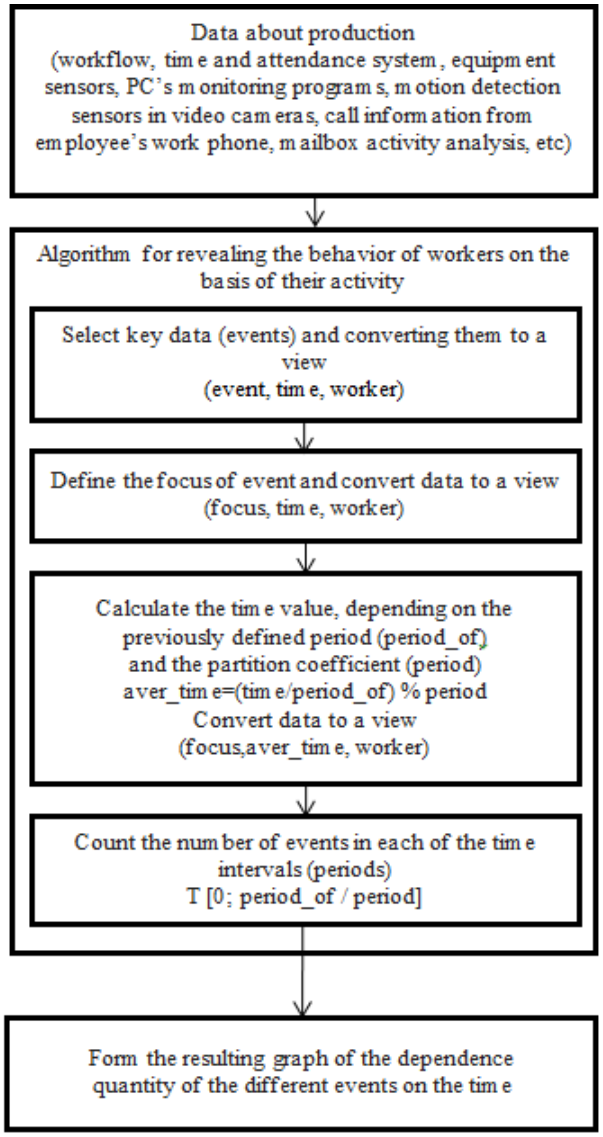

Figure 2. Analysis algorithm of production data.

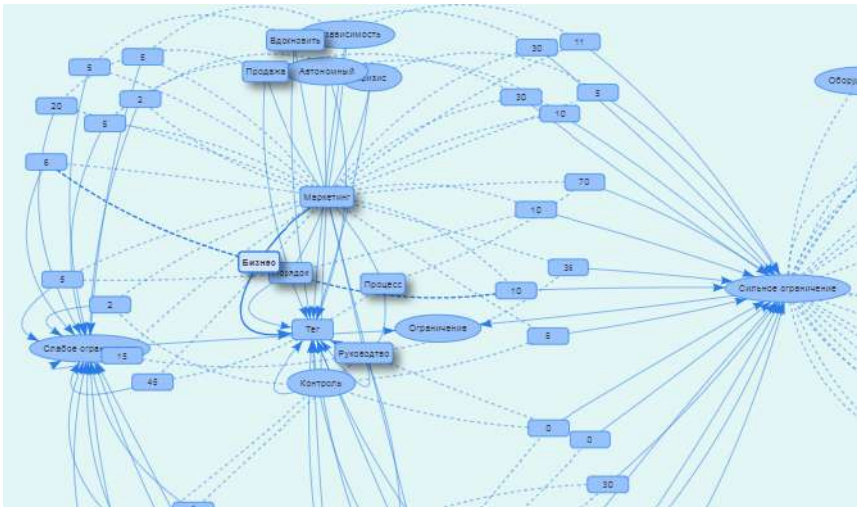

Figure 3. Ontology of groups "Construction" and "Production".

In the framework of this example, the consumer group “Production” was identified (including tags of corporate culture and team management).

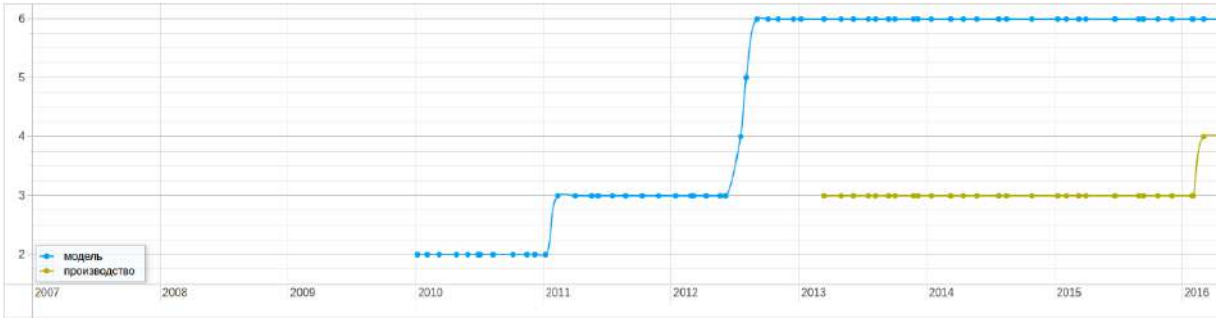

Figure 4. Dynamics of content change for the Lada trademark on the topic “Production”.

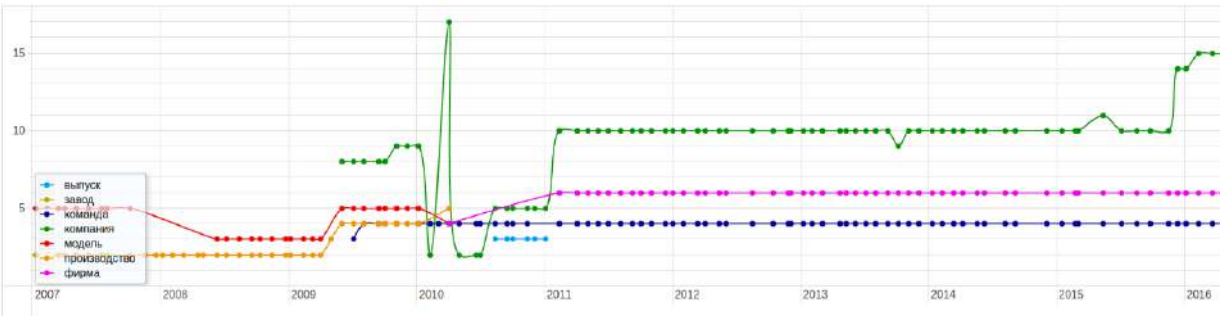

Figure 5. Dynamics of content change for the Audi brand in the theme“Production”.

Figure 6. Dynamics of content change for the BMW brand under the theme “Production”.

So, Lada, a popular Russian car manufacturer, is not paying more attention to the production segment due to the emergence of new trademarks. Other popular car manufacturers such as: Audi, BMW were also considered. In the graphs above for other manufacturers, you can also see statistics based on a study showing a surge in interest in a particular market segment.

Analysis of data from several open sources will allow to monitor the work of the marketing department, the work of production, to monitor the trends of bursts of interest among potential customers.

6. Conclusion

Based on the foregoing, it can be concluded that it is advisable to use systems based on Big Data technology in production. The capabilities of these systems allow you to optimize production processe.

7. References

[1] Surnin O L, Sitnikov P V, Ivaschenko A V, Ilyasova N Yu and Popov S B 2017 Big Dataincorporation based on open services provider for distributed enterprises *CEUR Workshop Proceedings* **1904** 42-47
[2] Ivaschenko A V, Ilyasova N Yu, Khorina A A, Isayko V A, Krupin D N, Bolotsky V A and Sitnikov P V 2018 Integration issues of Big Data analysis on social networks *CEUR Workshop Proceedings* **2212** 248-254
[3] Digital Russia 2017 *New Reality Electronic resource* (Digital McKinsey)
[4] Internet of things - Electronic resource
[5] Lasi H, Kemper H-G, Fettke P, Feld T and Hoffmann M 2014 Industry 4.0 *Business & Information Systems Engineering* 239-242
[6] Kagermann H, Wahlster W and Helbig J 2013 Recommendations for implementing the strategic initiative Industrie 4.0 Final report of the Industrie 4.0 *Working Group* p 82
[7] Baesens B 2014 *Analytics in a Big Data world: The essential guide to data science and its applications* (Hoboken: Wiley) p 232
[8] One Internet 2018 *Global commission on Internet Governance* (Electronic resource)
[9] Fleischmann A, Schmidt W and Stary C 2014 *S-BPM in the wild* (Springer) p 282
[10] Balakrishnan H, Deo N 2006 Discovering communities in complex networks *Proceedings of the 44th annual Southeast regional conference* 280-285
[11] Bessis N, Dobre C 2014 *Big Data and Internet of Things: A roadmap for smart environments* (Berlin: Springer) p 450
[12] Gubbi J, Buyya R, Marusic S and Palaniswami M 2013 Internet of Things (IoT): A vision, architectural elements, and future directions *Future generation computer systems* 1645-1660
[13] Mikhaylov D V, Kozlov A P and Emelyanov G M 2016 Extraction of knowledge and relevant linguistic means with efficiency estimation for the formation of subject-oriented text sets *Computer Optics* **40(4)** 572-582 DOI: 10.18287/2412-6179-2016-40-4-572-582
[14] Rycarev I A, Kirsh D V and Kupriyanov A V 2018 Clustering of media content from social networks using bigdata technology *Computer Optics* **42(5)** 921-927 DOI: 10.18287/2412-6179 -2018-42-5-921-927

Acknowledgments

This work was financially supported by the Russian Foundation for Basic Research under grant # 19-29-01135, # 17-01-00972 and by the Ministry of Science and Higher Education within the State assignment to the FSRC “Crystallography and Photonics” RAS.

Investigation of optimal configurations of a convolutional neural network for the identification of objects in real-time

M A Isayev[1], D A Savelyev[1,2]

[1]Samara National Research University, Moskovskoe Shosse 34A, Samara, Russia, 443086
[2]Image Processing Systems Institute of RAS - Branch of the FSRC "Crystallography and Photonics" RAS, Molodogvardejskaya street 151, Samara, Russia, 443001

e-mail : michailisaev.home@gmail.com

Abstract. The comparison of different convolutional neural networks which are the core of the most actual solutions in the computer vision area is considers in hhe paper. The study includes benchmarks of this state-of-the-art solutions by some criteria, such as mAP (mean average precision), FPS (frames per seconds), for the possibility of real-time usability. It is concluded on the best convolutional neural network model and deep learning methods that were used at particular solution.

1. Introduction

At present, the field of computer vision is actively developing, especially at the time of emergence of convolutional neural networks (CNN) [1, 2] and unmanned devices [3]. Another integral part of computer vision field is the detection of objects and classifying based on special object features [4]. Object detection is successfully used in vehicle tracking, positioning, surveillance [5-7]. The difference between the classification and detection algorithms is that the detection algorithms contain the boundaries of the region of interest (object) and are defined in the image. It is also worth noting the big difference between the concepts of classification and clustering - the main difference between classification and clustering is that when solving the classification problem, groups of objects are already known, while clusters are already determined at the moment of solving the clustering problem. Obviously, for object detection tasks, you should not use a regular neural network with a fully connected layer at the end. This is due to the fact that, as a rule, the length of the output layer is dynamic, which is associated with a non-fixed number of appearing objects.

One approach to solve this problem is to obtain different areas from an image (Region of Interests) and use convolutional neural networks to determine the presence of an object within this area. This solution does not take into account the possibility of a different location of the object and different proportions of the side. Consequently, it will be necessary to process a huge number of such areas, which is so expensive in terms of computational power. Another solution is special algorithms that were developed for the problem of detecting objects in real time. [8].

Solutions in the field of image recognition in real time are divided into two main families: Region Proposes (the frame regions are alternately proposed and classified) and Single Shot (all objects are immediately detected on the resulting image). The first family includes neural networks such as R-

CNN, Fast R-CNN, Faster R-CNN [9-11]. The second family includes YOLO, SSD [5, 12]. Neural networks that use recognition by region have a rather slow recognition time in the qualitative determination of objects.

In this paper, we study the determination of the optimal solution for the problem of detecting objects in real time based on testing solutions of R-CNN, R-FCN, SSD (VGG-16), YOLOv3 (Darknet-53), based on metrics such as mAP and FPS.

2. A convolutional neural network used to identify objects

The following parameters were used for the study: dataset - PASCAL VOC 2012 [8]. Faster R-CNN, R-FCN, SSD (VGG-16), YOLOv3 (Darknet-53) solutions were tested. Faster R-CNN uses RPN (Region Proposal Network) instead of the slow selective search algorithm. RPN is a complete replacement for the selective algorithm, and works as follows: at the last level of the original CNN, a 3x3 sliding window bypasses the feature map and reduces its dimension and for each sliding window position, RPN generates many possible areas based on the k boundaries of a possible object. R-FCN, or Region-based Fully Convolutional Net is a fully connected network and raises one of the main problems in the design of neural networks. On the one hand, when performing a classification of an object, it is necessary to train the model on the property of the invariance of the object's location: despite where the object appears in the image, the object must be uniquely determined. On the other hand, it is necessary that the trained model selects the boundaries of the object in the place of the image where it appears (local variation). The compromise between variance and location invariance is to use positional scorecards. The input image is processed by CNN, adding a fully connected layer to create a storage of position-sensitive rating maps that RoI generates. Next, for each region, the assessment storage is checked for the fact whether this region is the corresponding position of some object.

SSD, in contrast to Faster R-CNN, which uses algorithms for the regional classification and generation of prediction domains, simultaneously determines the frame of the object, as well as its class at the time of image processing. The SSD sends the image for processing through a series of convolutional layers, receiving several sets of feature maps, for each position in each of these feature maps, a 3x3 convolutional filter is used to obtain a set of reference coordinates of the image boundaries, where for each set of coordinates, the offset and the probability of being within the boundaries of these object coordinates.

YOLOv3, like SSD, belongs to the Single Shot family, and also uses softmax with independent logistic classifiers to calculate the similarity of the input data with a particular class. Instead of using MSE (mean squared error) to compute a classification error, YOLOv3 uses binary cross-entropy for each class label. To determine the coordinates of the boundaries of the object, YOLOv3 uses the k-means clustering algorithm.

3. An anthropometric model-based method for extracting facial specified features to improve classification

Detection of objects in images and videos using neural networks, including the identification of [13] real-time faces [14] is an important task today. In particular, V.S. Gorbatsevich and al. propose original iterative proposal clustering (IPC) algorithm for aggregation of output face proposals formed by CNN and the 2-level “weak pyramid” providing better detection quality on the testing sets containing both small and huge images [15].

To extract important features from person`s face at the first stage, it is necessary to mark the key points on the person’s face, which will determine the relative position of the main elements of the person’s face and take the necessary measurements, which in the next stage are fed to the classifier. figure 1 shows the 68 face landmarks on the left and the main anthropometric parameters on the right.
The key points of a person’s face are used to mark the image of protruding regions of a person’s face, such as: eyes, eyebrows, nose, mouth, jaw line. At the moment, they are actively used in applications for aligning faces in an image, presenting a model of a pose of a human head, detecting flicker, etc.

The detection of such points is a subtask of determining the shape and shape of the input object. Obtaining an image as an input, the predictor tries to localize the key points, taking into account the shape and shape of the object [16].

At the stage when the necessary key points are known and their coordinates relative to the whole image, the necessary proportions are calculated based on the anthropometric model [17]. Facial measurements are presented at the figure 2.

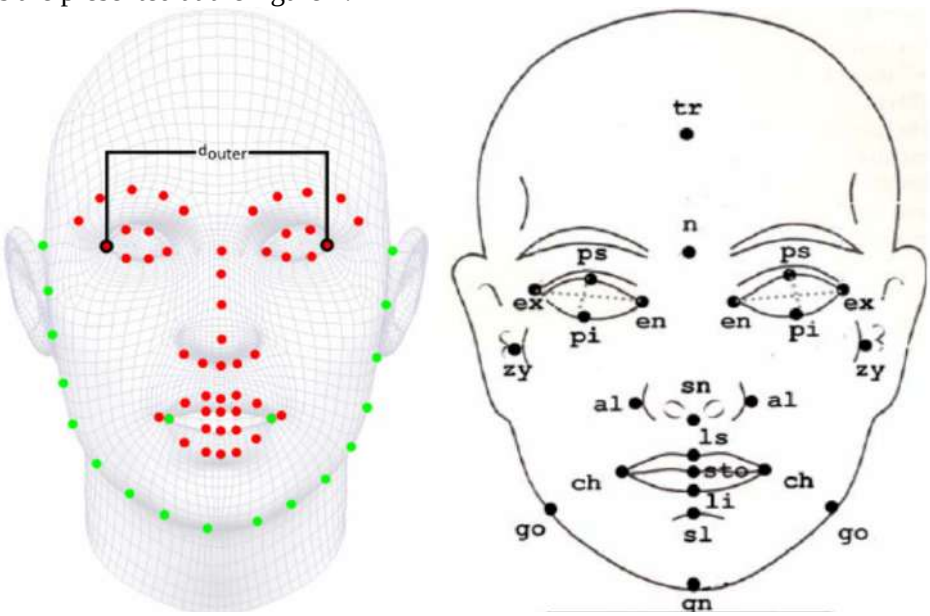

Figure 1. The important facial measurements as a main feature for signs extraction.

$$FI = \frac{n-gn}{zy-zy};\ MI = \frac{sto-gn}{go-go};\ II = \frac{en-en}{ex-ex};\ OWI = \frac{ex-en}{en-en};$$
$$EFI = \frac{ps-pi}{ex-en};\ NI = \frac{al-al}{n-sn};\ VHI = \frac{ls-sto}{sto-li};\ MFWI = \frac{ch-ch}{zy-zy}.$$

Figure 2. Facial indexes for anthropometric model.

4. The method based on hybrid Hesse filter for extracting facial specified features to improve classification

The Hesse filter is a tool for detecting wrinkles in the input image. After all, it is no secret that the appearance of wrinkles on a person's face is the most expected changes in a person's face and skin as his age increases.

The algorithm is based on the use of the Hesse matrix and directional gradient [17]. The Hessian hybrid filter detects wrinkles by computing the Hessian matrix for each pixel of the input image. The maximum eigenvalues of the Hessian matrix indicate that a particular pixel of the image belongs to the outline of the wrinkle, regardless of its position. The eigenvalues in this context are independent vector measurements for the components of the second derivatives at each point. A small value of the eigenvalue indicates a weak rate of change of the surface of the face in the corresponding direction of the vector of eigenvalues, and vice versa.

First of all, a two-dimensional image is converted into an image with only one shade. We denote the image as I (x, y). The gradient (Gx, Gy) is calculated from the single-channel image as: $\Delta I(x, y) = (\partial I / \partial x, \partial I / \partial y)$, where $\partial I / \partial x$, $\partial I / \partial y$ are directional gradients, that is, $\partial I / \partial x = Gx$, and $\partial I / \partial y = Gy$. The directional gradient significantly smoothes the image, but retains the data that are of interest in the original task. Gy is used as the input image for the Hessian hybrid filter, that is, as input to calculate the Hessian matrix H, which is used to extract horizontal lines. To modify the algorithm for detecting vertical wrinkles, Gx is used as input to the modified Hessian hybrid filter.

In this case, Hessian matrix determines as follows:

$$H(x,y,\sigma)=\begin{bmatrix}\frac{\partial^2 I(x,y)}{\partial I(y)\partial I(y)} & \frac{\partial^2 I(x,y)}{\partial I(x)\partial I(y)}\\ \frac{\partial^2 I(x,y)}{\partial I(x)\partial I(y)} & \frac{\partial^2 I(x,y)}{\partial I(x)\partial I(x)}\end{bmatrix}=\begin{bmatrix}H_a & H_b\\ H_b & H_c\end{bmatrix}. \quad (1)$$

Figure 3 shows the result of the work of the Hesse hybrid filter. This method is a reliable tool for extracting age characteristics from the input image, but with all the reliability of this method, it should be understood that wrinkles may appear at all at different times, depending on race, lifestyle and genes [17].

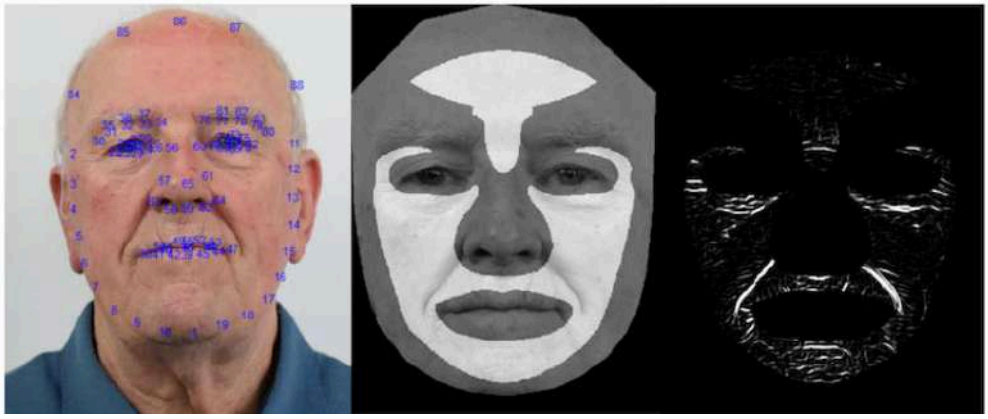

Figure 3. Visualization of the Hesse hybrid filter (HHF) work.

At the stage when arrays of features are received, these age signs are fed to the input of the classifier, for its subsequent training. In the framework of this work, classifiers were used based on the random forest algorithm.

Random forest is an ensemble decision tree algorithm because the final prediction, in the case of a regression problem, is an average of the predictions of each individual decision tree, in classification; it's the average of the most frequent prediction [18]. So, the algorithm takes the average of many decision trees to arrive at a final prediction, as shown on figure 4.

As part of this work, the following architectures of convolutional neural networks were used, which were trained to solve the problem to the identification of objects: InceptionV3, ResNet50.

It is quite obvious that convolutional neural network models, their configuration and training is very resource-intensive, even on modern computers. In view of this, many researchers have proposed and developed modifications of convolutional neural networks (such as residual networks and inception blocks), the task of which was to simplify the initial problem with resources [19].

Comparison of the results of age estimation task by the considered methods showed: accuracy of RF + HHF method is 81.1%, accuracy of Inception v3 is 80.8%, and accuracy of ResNet50 is 85.7%.

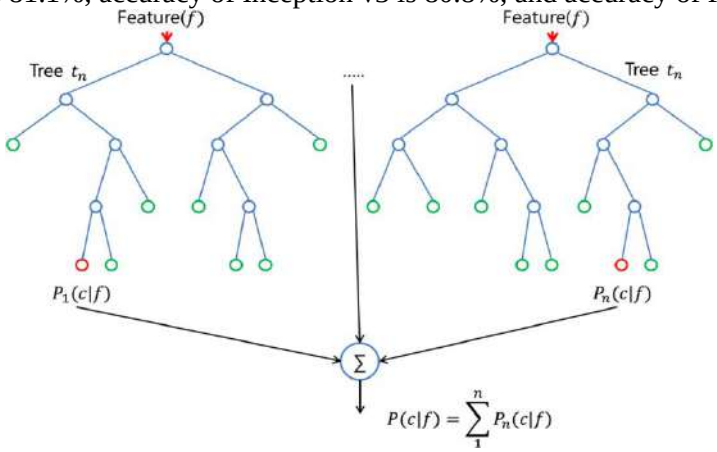

Figure 4. Visualization of the Random forest (RF) method.

The generalized result of the objects identification research is given in table 1.

Table 1. Comparison of the results of objects identification by the considered neural networks in p. 2.

Solution	Dataset	mAP, %
R-FCN	COCO + VOC 12	59.8
Faster R-CNN	COCO + VOC 12	60.15
SSD	PASCAL VOC 12	64.00
YOLOv3	COCO	63.35

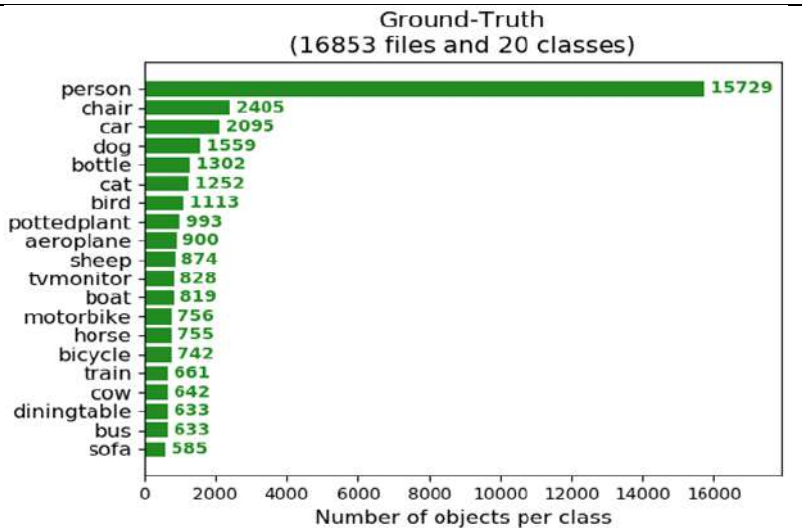

Figure 5. The number of ground-truth labels per class.

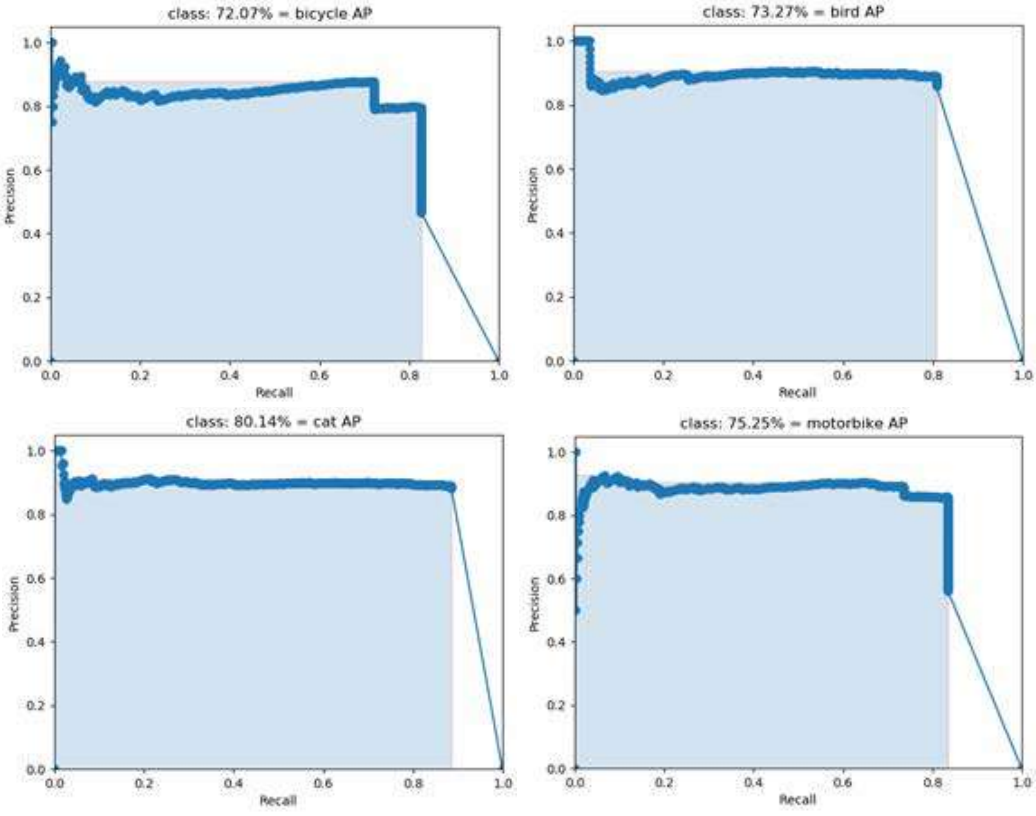

Figure 6. The results of AP estimations for some class of objects.

Figure 5 shows the number of labeled data by class, and figure 6 shows the results of the average detection accuracy for some classes of objects when using the YOLOv3 solution.

5. Conclusion

We compared various convolutional neural networks in this paper. The study includes comparing data on computer vision solutions for such criteria as mAP, FPS, i.e. the possibility of using them in real time. Based on the study, it was shown that the most suitable solution for real-time object identification task is YOLOv3. Despite not the highest mAP rating, YOLOv3 has a high processing speed of the video stream. Therefore, YOLOv3 has great prospects as a tool for tracking and detecting objects in a video stream.

As a result of the study, it is shown that convolutional neural networks successfully cope with the task of automatically determining a person's biological age on his face: : accuracy of RF + HHF method is 81.1%, accuracy of Inception v3 is 80.8%, and accuracy of ResNet50 is 85.7%.

6. References

[1] Shi, W, Caballero J, Huszar F, Totz J, Aitken A P, Bishop R, Rueckert D and Wang Z 2016 Real-time single image and video super-resolution using an efficient sub-pixel convolutional neural network *Proceedings of the IEEE Conference on Computer Vision and Pattern Recognition* 1874-1883

[2] Szegedy C, Vanhoucke V, Ioffe S, Shlens J and Wojna Z 2016 Rethinking the inception architecture for computer vision *Proceedings of the IEEE conference on computer vision and pattern recognition* 2818-2826

[3] Pestana J, Sanchez-Lopez J L, Saripalli S and Campoy P 2014 Computer vision based general object following for gps-denied multirotor unmanned vehicles *American Control Conference (ACC)* 1886-1891

[4] Magdeev, R, Tashlinskii A G 2019 Efficiency of object identification for binary images *Computer Optics* **43(2)** 277-281 DOI: 10.18287/2412-6179-2019-43-2-277-281

[5] Redmon J, Divvala S, Girshick R and Farhadi A 2016 You only look once: Unified, real-time object detection *Proceedings of the IEEE conference on computer vision and pattern recognition* 779-788

[6] Protsenko V I, Kazanskiy N L and Serafimovich P G 2015 Real-time analysis of parameters of multiple object detection systems *Computer Optics* **39(4)** 582-591 DOI: 10.18287/0134-2452-2015-39-4-582-591

[7] Kazanskiy N L, Protsenko V I and Serafimovich P G 2017 Perfomance analisys of real-time face detection system baced on stream data mining frameworks *Procedia Engineering* **201** 806-816 DOI: 10.1016/j.proeng.2017.09.602

[8] Girshick R, Donahue J, Darrell T and Malik J 2014 Rich feature hierarchies for accurate object detection and semantic segmentation *Proceedings of the IEEE conference on computer vision and pattern recognition* 580-587

[9] Dai J, Li Y, He K, Sun J 2016 R-fcn: Object detection via region-based fully convolutional networks *Advances in neural information processing systems* 379-387

[10] Girshick R 2015 Fast r-cnn *Proceedings of the IEEE international conference on computer vision* 1440-1448

[11] Ren S, He K, Girshick R and Sun J 2015 Faster r-cnn: Towards real-time object detection with region proposal networks *Advances in neural information processing systems* 91-99

[12] Liu W, Anguelov D, Erhan D, Szegedy C, Reed S, Fu C Y and Berg A C 2016 Ssd: Single shot multibox detector *European conference on computer vision* (Springer, Cham) 21-37

[13] Nemirovskiy V B, Stoyanov A K 2017 Clustering face images *Computer Optics* **41(1)** 59-66 DOI: 10.18287/2412-6179-2017-41-1-59-66

[14] Vizilter Yu V, Gorbatsevich V S, Vorotnikov A V and Kostromov N A 2017 Real-time face identification via CNN and boosted hashing forest *Computer Optics* **41(2)** 254-265 DOI: 10.18287/2412-6179-2017-41-2-254-265

[15] Gorbatsevich V S, Moiseenko A S and Vizilter Y V 2019 FaceDetectNet: Face detection via

fully-convolutional network *Computer Optics* **43(1)** 63-71 DOI: 10.18287/2412-6179-2019-43-1-63-71

[16] Krizhevsky A, Hinton G andSutskever I 2012 ImageNet Classification with Deep Convolutional Neural Networks *NIPS'12 Proceedings of the 25th International Conference on Neural Information Processing Systems* **1(1)** 1097-1105

[17] Karthikeyan D, Balakrishnan G 2018 A comprehensive age estimation on face images using hybrid filter-based feature extraction *Biomedical Research Medical Diagnosis and Study of Biomedical Imaging Systems and Applications* 472-480

[18] Bosch A, Zisserman A and Munoz X 2007 Image Classification using Random Forests and Ferns *11th International Conference on Computer Vision* 1-8

[19] Szegedy C, Ioffe S, Vanhoucke V and Alemi A 2017 Inception - v4, Inception-ResNet and the Impact of Residual Connections on Learning *Thirty-First AAAI Conference on Artificial Intelligence* 4278-4284

Acknowledgments

This work was financially supported by the Ministry of Science and Higher Education of the Russian Federation.

Using the cluster "Sergey Korolev" for modelling computer networks

D Y Polukarov[1], A P Bogdan[1]

[1]Samara National Research University, Moskovskoe Shosse, 34A, Samara, Russia, 443086

e-mail: plkw@mail.ru

Abstract. Modelling large-scale networks requires significant computational resources on a computer that produces a simulation. Moreover, the complexity of the calculations increases nonlinearly with increasing volume of the simulated network. On the other hand, cluster computing has gained considerable popularity recently. The idea of using cluster computing structures for modelling computer networks arises naturally. This paper describes the creation of software which combines an interactive mode of operation, including a graphical user interface for the OMNeT++ environment, with a batch mode of operation more natural to the high-performance cluster, "Sergey Korolev". The architecture of such a solution is developed. An example of using this approach is also given.

1. Introduction

Modeling large-scale networks requires significant computational resources on a computer that produces a simulation. Many universities have at their disposal computational cluster architectures of various sizes. The aim of this current work is to improve the quality of network simulation by using cluster "Sergey Korolev" of Samara National Research University. OMNeT++ is used in this work to model computer networks. OMNeT++ is a discrete event simulation environment [1]. The primary application area of OMNeT++ is the simulation of communication networks. OMNeT++ has a number of examples in its composition. This simplifies the process of deploying and verifying the system on a cluster.

The use of the high performance cluster "Sergey Korolev" often dictates a batch (and not interactive) mode of operation [2], without no graphical interface being available. And although there are nevertheless some opportunities for interactive work using the cluster, and some graphical output [2] can be made available in relation to this, these possibilities are severely limited.

For simulation of computer networks, it is more convenient to use an interactive mode of operation alongside a graphical user interface. For these purposes, software should be created which is capable of interacting with the user via graphical tools. In such a case, the OMNeT++ system [1] can serve as a convenient shell. The user can use the OMNeT++ system models but make the necessary calculations using the cluster in batch mode. Subsequently, the results of the calculations are transmitted to the user's local computer.

2. Related works

In [3], the authors analyzed a set of INET models [4], in terms of the ability of such model networks, in OMNeT++, to run in parallel. The authors found several issues which prevented the parallel execution of INET models. They analyzed these problems and developed solutions to them – to allow parallel launching of INET models. A situational analysis (using the case-study method) showed the feasibility of this approach. Although there are some elements of the model range that have not yet been investigated, and the performance attained still leaves some room for improvement, the results show an acceleration due to parallelization across most configurations.

A number of papers are devoted to the use of clusters in scientific applications.

In [5], the authors implemented a fast installation of a virtual cluster in heterogeneous environments. To do this, they created a performance model that predicted the installation time of a virtual cluster. They proposed a resource selection policy based on the model made as well. They divided the entire installation of the virtual cluster into five logical steps and created a model for each step. Each step is represented as a linear combination of software and hardware parameters, including processor speed, disk I/O performance, and installation package size. An advanced virtual cluster installer was also made. Experiments using the advanced installer have shown the effectiveness of the selection policy based on the models created.

The work [6] is the result of efforts to support a data analysis cluster (DAC) with minimal effort from the local system administrator. The authors tried to enable the scientist to focus on analyzing the data and not on managing the cluster. They developed a tool that allows a scientist to deploy and restore entire clusters with minimal effort. Puppet CMS was used to implement the deployment algorithm. This allowed system administrators to spend less time deploying a cluster. The ATLAS Tier 3 Cluster is given as an example. Reducing the time spent deploying and maintaining the cluster will result in more scientific results being produced from the DACs.

There are works that offer novel algorithms for storing and processing data on clusters.

Article [7] contains an approach to distributed image storage. This is done to improve the efficiency of parallel image processing algorithms. The distributed image was defined as a set of overlapping fragments. This made it possible to avoid bottlenecks of parallel processing and overlapping associated with reading/writing image data. Since the efficiency of a distributed system for processing large-sized images is largely determined by data access methods in image processing software and the convenience of visualizing processing results. The authors analyzed the advantages and bottlenecks of popular parallel image processing systems. A novel approach to data organization in distributed systems for image processing and storage is proposed. This approach is based on the concept of a distributed image. The concept of the organization of distributed image data is proposed, which solves most of the current problems. Achieved the required level of fault tolerance of the distributed storage of image fragments.

A number of papers are devoted to the use of the OMNeT++ simulator on cluster architectures.

The article [8] describes the parallelization of OMNeT++ simulations with Xgrid. The necessary changes in OMNeT++ for the automatic creation of job description files for Xgrid are developed. This allows the user to easily set up a simulation for Xgrid. By processing the job specification file, the Xgrid controller then distributes the individual simulation runs to all available parallel computing machines. Smaller files, such as configuration files, may be included in the job description file. Large files should be read or written to network shares for increased performance. The actions developed accelerated simulation modeling, almost linear with respect to additional computing power, compared to conventional single-process computing.

The article [9] presents a scheme for cluster modeling of distributed systems based on Ethernet (RTEthernet) in real time. It relies on the OMNeT++ discrete event simulation environment associated with the ARM-based coprocessor. The presented approach allows us to associate the real RTEthernet subsystem with virtual components operating in discrete modeling that implement the required behavior for the subsystem. The authors estimated the performance limits of this approach with respect to latency and jitter when running a simulation on a Linux system with a real-time kernel fix. The results showed that synchronization requirements for cluster modeling of small RTEthernet networks can be achieved.

This paper demonstrates the concept of cluster modeling of RTEthernet systems. The computing platform is based on a standard PC with an RT-Linux kernel, on which RTEthernet models work in the OMNeT++ simulation environment and the ARM9 microcontroller as a coprocessor.

The evaluation showed that the platform provides sufficient performance for the latency requirements of distributed real-time systems in the 230μs range, which is limited and has a linear dependence on frame size. The observed jitter is below 40μs.

The article [10] reports on the novel parallel and distributed modeling architecture for OMNeT++, an open source discrete-event modeling environment. The main application area of OMNeT++ is network communication modeling. Support for the conservative PDES protocol (zero message algorithm) and relatively new simulation protocol has been implemented. The OMNeT++ PDES implementation has a modular and extensible architecture that makes it easy to add new synchronization protocols and new communication mechanisms, which also makes it an attractive platform for PDES research. The advantage of the implementation is that it has the principle of "separation of experiments from models" and, thus, allows simulation models to run in parallel without any changes. It is based on a new placeholder approach for instantiating the model on different logical processes (LPs).

So, to summarize, the above article describes an analysis of the parallelization problems inherent in the INET set of OMNeT++ models and demonstrates the possibility of INET parallelization, using a number of modifications to the models; this parallelization was primarily aimed at distributed initialization of the INET models.

The concept of distributed multistage initialization allows for the creation of a simulation model which supports distributed simulation execution. The tests showed that there is an acceleration of execution, due to parallelization, for the given example in most configurations, although there is still potential for further optimization. The implementation covers the most commonly used protocols, such as Ethernet, IPv4, TCP, and UDP, as well as the related models such as ICMPv4 or the application of UDP.

3. Deploy and run a project on a cluster

3.1 Deploying

According to the official documentation [2], the cluster is accessed via SSH-2, and SFTP is used to transfer files. Programs are run as part of batch processing tasks.

To deploy a network simulator on a cluster, the steps presented in Table 1 are necessary.

Table 1. Steps for deploying a network.

Deploying steps
• access the cluster; • upload the necessary files to the cluster; • create a task which build the OMNeT++ network simulator and wait for its completion (there is a version of OMNeT++ without an IDE, this is what was used here); • create a task which build the INET Framework; • create a test simulation model; • create a task which runs the simulation and wait for its completion; • download the result of the work.

However, interactive task execution is possible on the cluster - given access to a free node in the cluster. The simulation will be run as follows (in Figure 2).

It is worth noting that the main difficulties encountered when deploying a simulator on a cluster are to do with recreating the necessary environment and also there are the problems relating to the limited access available (all work is done in the console mode).

After initial testing, it was found that the INET Framework does not support parallel simulation work. To solve this problem, the proposals in "Parallel INET for OMNeT++" [11] were used.

However, this work has the disadvantage that it is based on the old versions of OMNeT++ and the INET Framework (from 2014), and so dictates a slightly different structure for the modules (changes in the algorithm are necessary).

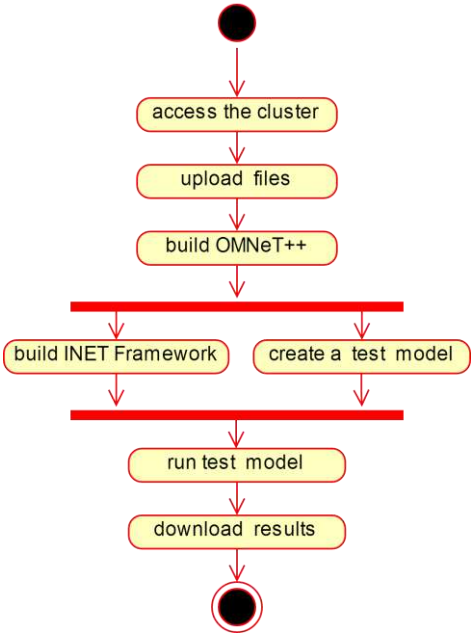

Figure 1. Deploying diagram.

```
OMNeT++ Discrete Event Simulation  (C) 1992-2018 Andras Varga, OpenSim Ltd.
Version: 5.4.1, build: 180629-5e28390, edition: Academic Public License -- NOT F
OR COMMERCIAL USE
See the license for distribution terms and warranty disclaimer

Setting up Cmdenv...

Loading NED files from ../simulations:  1
Loading NED files from .:  3
Loading NED files from ../../inet4/src:  703
Loading NED files from ../../inet4/examples:  163
Loading NED files from ../../inet4/tutorials:  20
Loading NED files from ../../inet4/showcases:  37

Preparing for running configuration General, run #0...
Assigned runID=General-0-20190607-09:05:04-9643
Setting up network "mymodel.TestNetwork"...
Initializing...

Running simulation...
** Event #0   t=0   Elapsed: 2e-05s (0m 00s)
     Speed:     ev/sec=0   simsec/sec=0   ev/simsec=0
     Messages:  created: 86   present: 86   in FES: 4
** Event #218880   t=948.40025311   Elapsed: 2.00164s (0m 02s)
     Speed:     ev/sec=109351   simsec/sec=473.813   ev/simsec=230.79
     Messages:  created: 57410   present: 90   in FES: 9
** Event #230713   t=1000   Elapsed: 2.10892s (0m 02s)
     Speed:     ev/sec=110299   simsec/sec=481.018   ev/simsec=229.303
     Messages:  created: 60521   present: 86   in FES: 0

<!> No more events, simulation completed -- at t=1000s, event #230713
```

Figure 2. Running the simulation in interactive mode.

3.2 Run on cluster

To work with MPI, the Tictoc1 system was selected; this consists of two modules. These modules should be assigned to different MPI nodes, as shown in Figure3.

```
[General]
parallel-simulation = true
parsim-communications-class = "cMPICommunications"
parsim-synchronization-class = "cNullMessageProtocol"
# nothing here

[Config Tictoc1]
network = Tictoc1
*.tic.partition-id = 0
*.toc.partition-id = 1
```

Figure 3. Configuring an MPI project.

Then the project in OMNeT++ is built on the local machine.

```
$ make MODE=release
MSGC: tictoc14.msg
MSGC: tictoc17.msg
MSGC: tictoc18.msg
txc1.cc
txc10.cc
txc11.cc
txc12.cc
txc17.cc
txc18.cc
txc2.cc
txc8.cc
txc9.cc
tictoc14_m.cc
tictoc17_m.cc
tictoc18_m.cc
Creating executable: out/gcc-release//tictoc
```

Figure 4. Building the project on a local machine.

To check the functionality from the project directory via mpirun, the following command is issued:

`$ mpirun -np 2 ./tictoc -m -u Cmdenv -c Tictoc1 omnetpp.ini.`

The result of such a command should look like this:

```
OMNeT++ Discrete Event Simulation  (C) 1992-2018 Andras Varga, OpenSim Ltd.
Version: 5.4.1, build: 180629-5e28390, edition: Academic Public License -- NOT FOR COMMERCIAL USE
See the license for distribution terms and warranty disclaimer

OMNeT++ Discrete Event Simulation  (C) 1992-2018 Andras Varga, OpenSim Ltd.
Version: 5.4.1, build: 180629-5e28390, edition: Academic Public License -- NOT FOR COMMERCIAL USE
See the license for distribution terms and warranty disclaimer

Setting up Cmdenv...

Setting up Cmdenv...

cMPICommunications: started as process 0 out of 2.
cMPICommunications: started as process 1 out of 2.
Loading NED files from .:  19
Loading NED files from .:  19

Preparing for running configuration Tictoc1, run #0...

Preparing for running configuration Tictoc1, run #0...
Assigned runID=Tictoc1-0-20190122-11:31:28-3629
Assigned runID=Tictoc1-0-20190122-11:31:28-3630
Setting up network "Tictoc1"...
Setting up network "Tictoc1"...
Initializing...
Initializing...

Running simulation...

Running simulation...
** Event #0   t=0   Elapsed: 1.4e-05s (0m 00s)
** Event #0   t=0   Elapsed: 1.5e-05s (0m 00s)
     Speed:     ev/sec=0   simsec/sec=0   ev/simsec=0
     Messages:  created: 2   present: 2   in FES: 2
     Speed:     ev/sec=0   simsec/sec=0   ev/simsec=0
     Messages:  created: 3   present: 2   in FES: 2
** Event #154880   t=30975.9   Elapsed: 2.00195s (0m 02s)
     Speed:     ev/sec=77365.5   simsec/sec=15472.9   ev/simsec=5.00005
     Messages:  created: 154883   present: 3   in FES: 2
** Event #154880   t=30976   Elapsed: 2.00199s (0m 02s)
     Speed:     ev/sec=77363.8   simsec/sec=15472.7   ev/simsec=5.00003
     Messages:  created: 154884   present: 3   in FES: 2
```

Figure 5. Test result.

In order to execute the simulation on the supercomputer, three files must be copied from the project folder to the working folder (the latter on the supercomputer).

Table 2. Files of test model.

Testing model structure
• omnet.ini; • tictoc; • tictic1.ned.

Next, the folder containing the project itself and the folder containing the source files must be copied over in order that the necessary libraries can be collected together into a working folder on the

supercomputer, so that all can then be compiled (the libraries, and the project itself). The list of required libraries can be viewed using `ldd %executable_file_name%`, usually the necessary libraries will be only those that are in the OMNeT++ folder.

```
linux-vdso.so.1 (0x00007ffe7d1d6000)
liboppcmdenv.so => /home/anoneth/Документы/omnetpp-5.4.1/lib/liboppcmdenv.so (0x00007fa59aa9e000)
liboppenvir.so => /home/anoneth/Документы/omnetpp-5.4.1/lib/liboppenvir.so (0x00007fa59a7e1000)
liboppsim.so => /home/anoneth/Документы/omnetpp-5.4.1/lib/liboppsim.so (0x00007fa59a22a000)
libdl.so.2 => /lib/x86_64-linux-gnu/libdl.so.2 (0x00007fa59a026000)
libstdc++.so.6 => /usr/lib/x86_64-linux-gnu/libstdc++.so.6 (0x00007fa599ca4000)
libm.so.6 => /lib/x86_64-linux-gnu/libm.so.6 (0x00007fa5999a0000)
libgcc_s.so.1 => /lib/x86_64-linux-gnu/libgcc_s.so.1 (0x00007fa599789000)
libc.so.6 => /lib/x86_64-linux-gnu/libc.so.6 (0x00007fa5993ea000)
liboppcommon.so => /home/anoneth/Документы/omnetpp-5.4.1/lib/liboppcommon.so (0x00007fa5990ae000)
liboppnedxml.so => /home/anoneth/Документы/omnetpp-5.4.1/lib/liboppnedxml.so (0x00007fa598d7e000)
libxml2.so.2 => /usr/lib/x86_64-linux-gnu/libxml2.so.2 (0x00007fa5989c3000)
libmpi_cxx.so.20 => /usr/lib/x86_64-linux-gnu/libmpi_cxx.so.20 (0x00007fa5987a8000)
libmpi.so.20 => /usr/lib/x86_64-linux-gnu/libmpi.so.20 (0x00007fa5984b5000)
libpthread.so.0 => /lib/x86_64-linux-gnu/libpthread.so.0 (0x00007fa598298000)
/lib64/ld-linux-x86-64.so.2 (0x00007fa59af07000)
libicui18n.so.57 => /usr/lib/x86_64-linux-gnu/libicui18n.so.57 (0x00007fa597e1e000)
libicuuc.so.57 => /usr/lib/x86_64-linux-gnu/libicuuc.so.57 (0x00007fa597a76000)
libicudata.so.57 => /usr/lib/x86_64-linux-gnu/libicudata.so.57 (0x00007fa595ff9000)
libz.so.1 => /lib/x86_64-linux-gnu/libz.so.1 (0x00007fa595ddf000)
liblzma.so.5 => /lib/x86_64-linux-gnu/liblzma.so.5 (0x00007fa595bb9000)
librt.so.1 => /lib/x86_64-linux-gnu/librt.so.1 (0x00007fa5959b1000)
libutil.so.1 => /lib/x86_64-linux-gnu/libutil.so.1 (0x00007fa5957ae000)
libhwloc.so.5 => /usr/lib/x86_64-linux-gnu/libhwloc.so.5 (0x00007fa595572000)
libopen-rte.so.20 => /usr/lib/x86_64-linux-gnu/libopen-rte.so.20 (0x00007fa5952e7000)
libopen-pal.so.20 => /usr/lib/x86_64-linux-gnu/libopen-pal.so.20 (0x00007fa595035000)
libnuma.so.1 => /usr/lib/x86_64-linux-gnu/libnuma.so.1 (0x00007fa594e2a000)
libltdl.so.7 => /usr/lib/x86_64-linux-gnu/libltdl.so.7 (0x00007fa594c20000)
```

Figure 6. Required dependencies.

Next, it necessary to build the project on the cluster.

```
checking build system type... x86_64-unknown-linux-gnu
checking host system type... x86_64-unknown-linux-gnu
checking target system type... x86_64-unknown-linux-gnu
checking for a BSD-compatible install... /usr/bin/install -c
checking whether ln works... yes
checking whether ln -s works... yes
checking for a sed that does not truncate output... /bin/sed
checking for gawk... gawk
checking for libatomic support... yes
checking for libcilkrts support... yes
checking for libitm support... yes
checking for libsanitizer support... yes
checking for libvtv support... yes
checking for gcc... gcc
checking for C compiler default output file name... a.out
checking whether the C compiler works... yes
checking whether we are cross compiling... no
checking for suffix of executables...
checking for suffix of object files... o
checking whether we are using the GNU C compiler... yes
checking whether gcc accepts -g... yes
checking for gcc option to accept ISO C89... none needed
checking for g++... g++
checking whether we are using the GNU C++ compiler... yes
checking whether g++ accepts -g... yes
checking whether g++ accepts -static-libstdc++ -static-libgcc... no
checking for gnatbind... no
checking for gnatmake... no
checking whether compiler driver understands Ada... no
checking how to compare bootstrapped objects... cmp --ignore-initial=16 $$f1 $$f2
checking for objdir... .libs
checking for the correct version of gmp.h... buggy but acceptable
checking for the correct version of mpfr.h... buggy but acceptable
checking for the correct version of mpc.h... buggy but acceptable
```

Figure 7. Building project on a cluster.

Then you need to create, in the working folder on the supercomputer, the task file *.pbs. Sample file content is as follows:

```
#!/bin/bash
#PBS -N helloOMNeT                //name of task
#PBS -A  helloOMNeT
#PBS -l walltime=00:01:00         //required time
```

```
#PBS -l nodes=1:ppn=2            //number of nodes and processes
#PBS -j oe                       //error stream to standard output
cd $PBS_O_WORKDIR
export PATH=$PBS_O_PATH
# Loading Intel MPI v4 environment
module load impi/4
export I_MPI_DEVICE=rdma
export I_MPI_DEBUG=0
export I_MPI_FALLBACK_DEVICE=disable
# command run task taking into account the features of the environment
mpirun -r ssh -machinefile $PBS_NODEFILE -np $PBS_NP ./tictoc -m -u
Cmdenv -c Tictoc1 omnetpp.ini.
```

4. Future work

We plan to test the work of OMNeT++ on the cluster "Sergey Korolev" using the project INET Framework. It is also planned to organize the possibility of full interactive work in the graphical interface of the modeling environment. To illustrate the effectiveness of the method used, it is planned to measure the performance of applications running on a cluster.

5. Conclusion

In this paper, we showed the development of software which allows us to combine an interactive mode of operation of the OMNeT++ modeling system and the batch mode of the cluster “Sergey Korolev”. in Via initial testing, it was discovered that the way by which networks are created in the course of simulation does not work in Parallel INET for OMNeT++. As a result, it was decided to create a network for parallel simulation using a Python script, and for ordinary simulation using a module created for OMNeT++. These results can be used to solve the other, related, problems [12].

6. References

[1] OMNeT++ Discrete Event Simulator URL: https://omnetpp.org/ (23.01.2019)
[2] Instructions for working with computer systems at SCC of Samara University *Supercomputer center of Samara University* URL: http://hpc.ssau.ru/node/19/ accessed 23.01.2019
[3] Enabling Distributed Simulation of OMNeT++ INET Models URL: https://arxiv.org /pdf/1409.0994.pdf (23.01.2019)
[4] INET Framework URL: https://inet.omnetpp.org/ (23.01.2019)
[5] Yamasaki S, Maruyama N and Matsuoka S 2007 Model-based resource selection for efficient virtual cluster deployment *Proceedings of the 2nd international workshop on Virtualization technology in distributed computing* p 6
[6] Hendrix V, Benjamin D and Yao Y 2012 Scientific Cluster Deployment and Recovery–Using puppet to simplify cluster management *Journal of Physics: Conference Series* **396(4)** 042027
[7] Kazanskiy N L, Popov S B 2011 Distributed storage and parallel processing for large-size optical images *Proceedings of SPIE* (*Optical Technologies for Telecommunications)* **8410** 84100I DOI: 10.1117/12.928441
[8] Seggelmann R, Rüngeler I, Tüxen M and Rathgeb E P 2009 Parallelizing OMNeT++ simulations using xgrid *Proceedings of the 2nd International Conference on Simulation Tools and Techniques* (Institute for Computer Sciences, Social-Informatics and Telecommunications Engineering) p 69
[9] Karfich O, Bartols F, Steinbach T, Korf F and Schmidt T C 2013 A hardware/software platform for real-time ethernet cluster simulation in OMNeT++ *Proceedings of the 6th International ICST Conference on Simulation Tools and Techniques* (Institute for Computer Sciences, Social-Informatics and Telecommunications Engineering) 334-337
[10] Varga A, Sekercioglu A Y 2003 Parallel simulation made easy with OMNeT++ *15th European Simulation Symposium*
[11] Parallel INET for OMNeT++ URL: https://redmine.comsys.rwth-aachen.de/redmine/ projects/parallel-inet/ (01.05.2019)

[12] Nikitin V S, Semenov E I, Solostin A V, Sharov V G and Chayka S V 2016 Modeling the" smartlink connection" performance *Computer Optics* **40(1)** 64-73 DOI:10.18287/2412-6179-2016-40-1-64-73

Acknowledgments
This work was undertaken as a component of the project part of the state task of the Ministry of Science and Higher Education of the Russian Federation No. 2.974.2017/4.6.

Big Data, Internet of Things, Augmented Reality: technology convergence in visualization issues

D A Smuseva[1], A Y Rolich[1], L S Voskov[1] and I Y Malakhov[1]

[1]National Research University "Higher School of Economics", Myasnitskaya str., 20, Moscow, Russia, 101000

e-mail: dasmuseva@gmail.com, arolich@hse.ru, lvoskov@hse.ru

Abstract. The paper reviews the current situation of the Augmented Reality and Internet of Things markets. The implementing possibilities of AR for Big Data visualization from IoT devices are considered in this paper. The review and the analysis of methods, tools, products and data system of the visualization are presented. The paper provides an overview of the programs and devices of Augmented Reality, and an overview of development environments. The paper presents the existing classifications of computerized data visualization tools and proposes new classification, which takes into account interactive visualization, the purpose of the tool, the type of software product, the availability of ready-made templates, and other characteristics. The article proposes the architecture of the system for collecting data from IoT endpoint devices based on the Heltec modules. Experiments based on the developed experimental stand were carried out with Heltec devices of both versions to determine the number of losses with increasing distance between the sending device and the receiving device. The results of measuring the power consumption of these devices are presented in two modes: in standby mode and when sending a message to the Heltec endpoint device and in standby mode and when receiving a message for the base station. These studies were conducted using various data transfer protocols (LoRa, Wi-Fi and Bluetooth). The paper presents the result of the development of a digital twin of a university building and the development of augmented reality software for receiving data from real-time data collection devices.

1. Introduction

The introduction of new technologies is often focused on simplifying the routine actions of a person in everyday life. An example is the introduction of the Internet of Things technology, which requires an integrated approach to development that combines new technologies, skills and capabilities supported by effective management and organization. Such technology requires the support of user interaction and the digital ecosystem to enable the management of connected equipment. For this, it is necessary that the program can analyze and visualize the data obtained from the sensors. The relevance of this work lies in the fact that the two-dimensional visualization of data obtained from the sensors of the Internet of things, is not enough.

In this regard, there is a big growth in services for analyzing and visualizing the data received from the sensors. The novelty of the work lies in the fact that for the most part, such services represent information in a two-dimensional form. The problem is that programs of this format cannot ensure the full assimilation of information. With a large amount of data, the user may miss key points and, for example, in production, do not notice breakages due to clutter of the interface.

Fortunately, nowadays modern technologies allow solving this problem with the help of augmented reality [1]. Consideration of the use of this technology in the field of IoT, it is possible to present its use in enterprises for timely identification of problems, in the home for remote control of equipment, in large production facilities for personnel training through the visualization of processes and instructions. In this regard, the purpose of this work is to identify methods, approaches and technologies for visualizing big data on the Internet of things using augmented reality.

2. Big Data

Over the past two decades, technological advances have led to a huge increase in data volumes. The term Big Data was coined for working with such data streams. This type of data is not only characterized by a large volume, but also demonstrates other unique characteristics compared to traditional data. For example, Big data is usually unstructured and may require real-time analysis. That is why for working with big data many new systems were created for collecting, transmitting, storing and processing large-scale data.

Due to the great popularity and diversity of Big Data technology, today there is no generally accepted definition for this term. In essence, big data means not only a large amount of data, but other functions that distinguish it from the concepts of "massive data" and "very large data". In the literature, you can find many definitions for Big data, consider three of them, which well explain the essence of the term Big data.

One of the currently popular definitions appeared back in 2001, in the report of META Group analyst (now Gartner) Dag Lani [2], who noted the equivalence of data management issues in three aspects (3Vs):

- Volume. Big data is very large, often in petabytes or more. Examples include user data on Facebook, the flow of people on the subway or transactions using credit cards;
- Velocity. Big data is often generated continuously, often even in real time. For example, Twitter messages, cell phone locations, weather and air quality sensors;
- Variety. Big data can be of any type consisting of numbers, text, photos, video, audio and other data. Therefore, Big Data analysis must be flexible enough to deal with any type of data and be able to combine them.

Big data has three varieties: structured, semi-structured, and unstructured. Traditional data is usually structured and therefore easy to use and can be easily stored. However, the vast majority of today's data from sources such as Facebook, Twitter, YouTube and other user-generated content is unstructured. The high rate of receipt of large data means that data sets should be analyzed at a rate corresponding to the speed of data production.

Today, Big data can be found in many areas [3, 4]. One of the most common ways to get big data is to collect data from sensors and devices. The popular branch of the development of this technology is the Internet of Things (IoT). It implies a global collection of all indicators from several sensors simultaneously (often in real time), the compilation of these data and their analysis.

3. Internet of Things

The Internet of Things (IoT) provides a network for connecting people, things, programs and data over the Internet to provide remote control and interactive implementation of services. Today, the amount of mobile devices with Internet connection exceeds the number of people on Earth. Moreover, in 2015, Gartner predicted [5] that by 2020 about 20.8 billion smart devices will be connected to the IoT. In order to support the work of devices connected to the IoT, it is necessary to have a special Internet of Things support service. Such IoT services need to collect, analyze and process information about sensors, they must have an interface for the operational management of information. The data collected from IoT devices can be impressive in size, since the number of sensors on the Internet of Things is very large. Therefore, a platform that can collect and store a huge amount of information from sensors is needed to

control IoT. Such a platform should include IoT databases where cloud computing support is needed. Moreover, IoT data analysis and Big Data support is required.
The economic effect can be seen where the connection between the machines (hereinafter - M2M) is becoming increasingly important. However, person-to-person (hereinafter - P2P), person-to-machine (hereinafter - P2M) and machine to person (hereinafter - M2P) connections still remain the majority of the economic value of IoT. In the table below you can see the comparison of M2M with M2P or P2M, as well as with P2P technology.
IoT is used in various fields, consider some of them:

- Security. In this area, IoT is used to monitor alarms, monitor and control surveillance systems in real time and track people [6];
- Transport sphere. Intelligent applications for transportation systems are used for fleet management, road safety, emissions control, toll payments, real-time traffic monitoring, etc;
- Health. In this area, IoT is used for e-health, which includes individual health systems based on sensors for the human body;
- Utility management. The Internet of Things allows you to measure, prepare, and bill for gas, water, electricity, and more;
- Production. Production control is carried out through the monitoring and automation of the product chain;
- The scope of services. Control of supply and distribution, vending machines can also be monitored, and support can be provided in managing and providing services;
- Management of funds. Campus, building and home automation can be reached using IoT technology.

4. Augmented Reality

Augmented Reality (AR) is a technology that allows a user to real-time overlay virtual text or computer-generated images onto objects in the real world. Recognition occurs, usually with the help of a camera, and the output of augmented reality through the user's screen, telephone, monitor, helmet or Augmented Reality glasses, window or windshield of the car. Virtual text or image can be superimposed on the selected objects in the environment surrounding the user, to display additional information about the selected object.

It is customary to use two basic definitions of augmented reality. In 1994, Paul Milgram described the continuum "virtuality-reality" [7], i.e. the space between reality and virtuality, between which are Augmented Reality and augmented virtuality (figure 1). The real environment and the virtual environment unite in a mixed reality, where, in turn, augmented reality is based more on reality, and augmented virtuality on virtuality. Thus, Augmented Reality is the result of adding virtual objects to the number of objects perceived by man as elements of the real world.

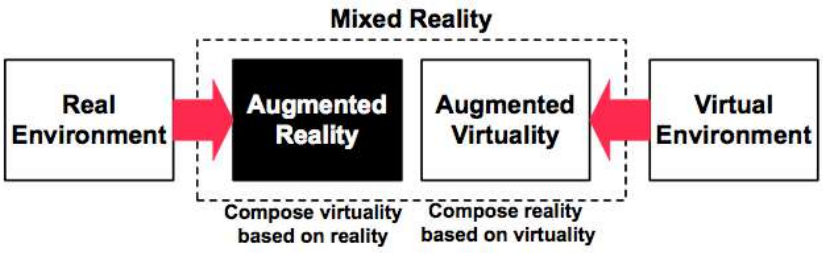

Figure 1. Milgram definition.

Augmented reality is based on context-sensitive computations. Thanks to this technology for the user, the real world and virtual objects coexist on the same view. For example, this technology can be applied to museums. If you point the camera of a smartphone with a special application of augmented reality on any exhibit, information about it will be displayed next to the exhibit. The user of augmented reality can

receive useful information about a location or objects and can interact with virtual content in the real world.

5. Data visuialization methods

5.1. Classification

There are many computer visualization tools that allow you to convert large amounts of abstract data into formats that are effective for perception, cognition and communication. For example, in the work [8] the following classification of computer visualization tools is given:

1) Tool functionality: user (professional or beginner), teamwork support (how many people can simultaneously develop a model), extensibility (possibility of making changes), scalability.
2) Methods (characteristics of the methods used): number of methods, method type.
3) Task (characteristics of the problem to be solved): type of information (quantitative, qualitative), subject area (science, business, education)
4) Manufacturer (characteristics of the product): manufacturing-firm: (domestic, foreign), type of product (commercial, training and demonstration, conditionally free)

This classification considers the functionality of the tool from the point of view of user experience: the level of user skills, support for teamwork, extensibility and scalability. The availability of ready-made templates, interactive visualization and other important characteristics are not taken into account in this work. The division of instrument manufacturers into domestic and foreign ones can be replaced by the multi-lingual nature of the proposed interfaces.

Consider the following classification of visualization and data analysis tools [9], the following classification of visualization and data analysis tools is proposed:

1) Category: analysis and charting, PC application, geographic information systems (GIS), library, network analysis, statistical analysis, time data analysis, data retrieval, data cleansing, data conversion, application/service for visualization and analysis, word clouds.
2) Multiple user support: true or false.
3) Data display on the map: true or false.
4) Platform.
5) User skill level: users who can work with spreadsheets, partially advanced users who are not afraid to spend two hours learning a new application, advanced users, users with programming experience or specialized knowledge in the field of GIS or network analysis.
6) Storage and processing location: user device, external server, public external server.
7) Posting results to the web: yes, with plugin, as a picture, no.

The considered classification summarizes such phenomena as a PC application, library, network analysis, statistical analysis and a word cloud. However, a PC application and a library are types of software, network analysis and statistical analysis are the purpose of the tool, and the word cloud is a data visualization method.

We have developed a new improved classification of computer visualization tools that expands and improves the previously proposed options:

1) Purpose: general purpose; specialized (GIS, business intelligence tools, network analysis); auxiliary (designed to prepare data for visualization).
2) User skill level: beginer; intermediate; advanced; user with programming experience or special knowledge.
3) Software: programming language (R, Python); library (D3, ChartJS, Highcharts JS, Raphaël и др.); application/service.
4) Platform.
5) Distribution: commercial; conditionally free; free.
6) Multilingual interface: yes; no.
7) Need to register: yes; no.
8) Multiplayer mode: yes; no.
9) Types of visualized data: qualitative; qualitative and quantitative; quantitative.

10) Supported Databases and file formats.
11) Availability of ready-made templates: yes; no.
12) Interactive visualization: yes; no.
13) Storage and processing location: user device; external server; public external server.
14) Formats of export results.

This classification takes into account interactive visualization, the purpose of the tool, the type of software product, the availability of ready-made templates, and other characteristics.

4.2. Analysis of Big Data visualization methods

The aggregated data from all devices connected to the IoT network must be correctly reproduced for the decision maker. For these purposes, visualization is a suitable tool. Data visualization represents data in some systematic form, including attributes and variables for a unit of information. Visualization approaches are used to create tables, charts, images, and other intuitive ways to display data. Big data visualization is not as simple as traditional small data sets [10]. The expansion of traditional approaches to visualization has already appeared, but far from enough. With large-scale data visualization, many researchers use feature extraction and geometric modeling to significantly reduce the size of the data before actually rendering the data. Choosing the right data representation is also very important when visualizing big data [11].

Often, standard methods of data visualization are used, which include such methods as a table, histogram, scatter plot, line diagram, pie chart, block diagram, bubble chart, combination of charts, time line, entity relationship diagram, etc. In addition, the standard methods of data visualization include additional methods: parallel coordinates, treemap, cone-shaped tree, semantic network, etc [10]. Parallel coordinates (figure 2) are used to construct individual data elements in many dimensions. This method of data visualization is very useful when displaying multidimensional data [12].

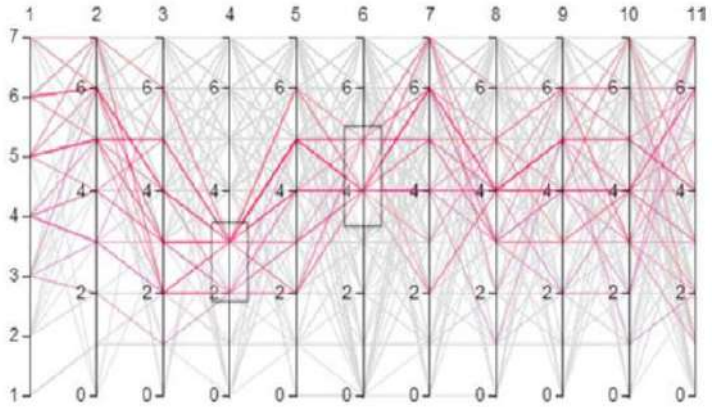

Figure 2. Parallel coordinates.

Treemap (figure 3) - an effective method of visualizing the hierarchy, which is a map, divided into sections. The smallest rectangles represent one measure, while color is often used to represent another measure of data. Figure 3 shows an example of a treemap collection set for streaming music and video tracks in a social networking community [13].

A cone-shaped tree is another method that displays hierarchical data, such as an organizational body in three dimensions. Branches grow in the form of a cone. The semantic network is a graphical representation of the logical connection between different concepts. It generates a directed graph, a combination of nodes or vertices, edges or arcs, and an inscription above each edge [10]. Visualization is not only static, but also interactive, thanks to such approaches as scaling (zooming in and out); review and detail; pan; as well as focus and context or fisheye [10]. Below are the steps for interactive visualization:

- Choice. This implies an interactive selection of data objects, a subset, parts of whole data, or the entire data set in accordance with the interests of the user;

- Linking: useful for linking information between several types of graphs. An example is shown in figure 4;
- Filtering: helps users adjust the amount of information to display. It reduces the amount of data and focuses on information of interest;
- Regrouping or reuse: since spatial layout is the most important visual display, rebuilding the spatial layout of information is very effective for creating different ideas;

Figure 3. Analysis of musical compositions using a treemap.

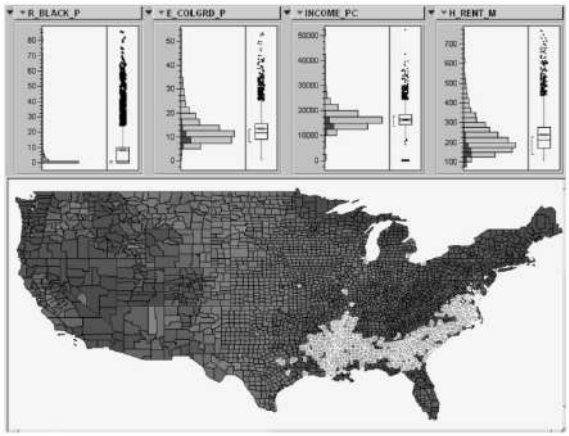

Figure 4. Interactive linking between histogram graphs and a geographic map.

The scalability and dynamics inherent in big data are the main problems in visual analytics. Big data visualization with diversity and heterogeneity (structured, semi-structured, and unstructured) is a big problem. As described above, speed (Velocity) is one of the important factors for analyzing Big Data. Cloud computing and an advanced graphical user interface can be combined with big data to better manage the scalability of big data [14].

Big data often has an unstructured data format, so due to bandwidth limitations and power requirements, the visualization must fit the data in order to efficiently get up-to-date information. Because of the large size of the data, there is a need for parallel computations, the task of which is to distribute computations for independent tasks that can be performed simultaneously [15].

The following problems exist in Big Data visualization [16]:

- Visual noise. Most of the objects in the dataset are too relative to each other. Users cannot separate them as separate objects on the screen;

- Loss of information. To simplify the calculations, it is often necessary to reduce the data sets, which leads to loss of information;
- Complicated image perception. Data visualization methods are limited not only by the aspect ratio and resolution of the device from which the visualization is viewed, but also by the physical limitations of perception;
- High speed image change. Users observe the data and cannot respond to the amount of data changes or their intensity on the display;
- High performance requirements.

Visualizing each data point can overwhelm the schedule and can suppress users' perceptions and cognitive abilities, and reducing data by sampling or filtering can lead to a loss of interesting emissions and deviations. Requesting large data warehouses can lead to high latency, disrupting real-time interaction [17].

Ways of solving problems of Big Data visualization [18]:

1. Satisfying the need for speed. This implies improved hardware with increased memory and powerful parallel processing,
2. Understanding the data. One solution is for people who receive data to have relevant experience and knowledge for quick understanding,
3. Solving the problem of data quality. It is necessary to control that the data arriving at the visualization were cleared from unnecessary information,
4. Synthesis of information. One way is to combine the data into a higher-level view, where smaller groups of data are visible and the data can be effectively visualized,
5. Create exceptions for emissions. A possible solution is to remove outliers from the data or create a separate chart for outliers.

Big data can be visualized using a number of approaches and methods that were analyzed and classified (table 1) according to the following data criteria: large data support, support for different types of data, and the capacity to dynamically display data changes [7].

- Treemap: based on the visualization of spatial images of hierarchical data;
- Circle Packing: A direct alternative to treemap. However, it uses circles as a primitive form, which can also be included in circles from a higher level of hierarchy;
- Sunburst: uses a treemap visualization and converts it into a polar coordinate system. The main difference is that the variable parameters are not the width and height, but the radius and length of the arc;
- Parallel coordinates: extends visual analysis using a variety of data factors for different objects;
- Streamgraph: this is a type of graph of a stack region that is offset around a central axis, which results in a smooth and organic form;
- Circular Network Diagram: The data object is placed around the circle and connected by curves based on the level of their interconnections. Different line widths or color saturation are commonly used to measure the coherence of an object.

Table 1. Analysis of big data visualization methods.

	Large amount of data	Variety of data	Data dynamics
Treemap	+	-	-
Circle Packing	+	-	-
Sunburst	+	-	+

Many data visualization tools work on the Hadoop platform. Such modules in Hadoop are: Hadoop Common, Hadoop Distributed File System (HDFS), Hadoop YARN, and Hadoop MapReduce. There

are also separate softwares, but they all represent a two-dimensional visualization of data, which is a difficulty for the user to understand the information. The solution to this problem is to use augmented reality as a visualization tool, which will facilitate the work of the user and allow you to visualize the data in a convenient form.

6. Big Data, IoT and AR: technology convergence in visualization issues

In 1979, a major accident at a nuclear power plant occurred in the United States, the cause of the accident was erroneous actions by personnel who did not understand the incoming data and did not identify the problem in time [12]. The introduction of Augmented Reality in the visualization of data collected from IoT-sensors, will make work in many areas more secure and effective. The use of this technology will allow real-time monitoring of the indicators of the sensors, output the data in a visual form, it is also possible remote user interaction with the equipment. Thus, not only the working personnel who are in close proximity to the equipment can make an inspection, but also the manager will be able to more accurately control the production situation with the help of installed smart sensors in all rooms. If something goes wrong, workers can instantly fix the problem, or transmit the data to engineers outside the building.

Also, this technology can be used for training and staff training. Companies can develop interactive manuals in augmented reality, filling them with interactive 3D equipment models and visual step-by-step instructions. For example, global manufacturer Caterpillar Inc. makes good use of AR to train its engineers and makes them more efficient. Engineers can use AR glasses or a smartphone to get virtual, step-by-step live instructions on how to efficiently perform machine repairs and other maintenance tasks. Many examples can also be seen in the areas of health, education, aviation and space, travel, real estate and other sectors.

The interaction of AR and IoT requires a large number of calculations; in addition, the volume of processing of augmented reality directly affects the power consumption of the device and its lifespan. That is why to work with AR on smartphones an additional cloud database is needed to reduce the load, save energy and overcome the limitations of the phone's memory. It is worth noting that the use of cloud technologies should be controlled by adaptive management, since the transfer of all computational processes to the cloud platform can lead to large delays in the operation of the program. To use cloud resources efficiently, you need to monitor the cloud server load and network congestion status so that they are balanced. It is necessary to monitor the state of the network, the status of the cloud server, the energy status of the device and the quality of perception (QoE, Quality of Experiance).

Using an AR application on smartphones, tablets, or corporate AR headsets, workers can monitor connected equipment to identify problems and perform maintenance. AR headsets, such as Google Glass Enterprise and Microsoft HoloLens, can also be useful in enterprises, displaying step-by-step online training and tutorials for assembling and operating equipment that would otherwise require reading thick technical manuals and instructions.

To create an Augmented Reality program with the ability to visualize data from the IoT sensors, you can use the existing augmented reality SDKs: ARToolkit [19], EasyAR [20], OpenCV [21], Maxst [22], Kudan [23], Catchoom On-Device Image Recognition SDK [24] and Vuforia SDK [25]. With the help of such SDKs, only a part with augmented reality can be developed, but additional programs will be needed to connect IoT devices and collect data.
For the productive implementation of programs, there are ready-made solutions that combine all stages of program development, including connecting sensors and visualizing data. The main leaders among the platforms for creating programs with AR for the Internet of Things are PTC, Augmenta, Bosh, Reflect.

Currently, the main area of convergence of the listed technologies is the visualization of big data coming from IoT-devices in real time on mobile devices with augmented reality function. Conventionally, we can distinguish the following types of convergence:

1. Visualization of sensor data and object management.
2. Monitoring equipment performance and decision support systems. The information presented in a visual form will allow timely troubleshooting equipment problems and improving the quality of

manufactured products. Ideally, this technology should be implemented at every stage of production.

3. People will be able to interact with electronics using 3D interfaces, which raises new questions about the energy efficiency of mobile devices, which are displays for data visualization (smartphones, tablets, smart watches or AR helmets).

The current trends in the field of the Internet of Things are the creation of new hardware platforms, the development of specialized operating systems, the development and optimization of application layer protocols, and the development of models and methods for data visualization aimed at improving the energy efficiency of the Internet of Things, including mobile devices, to increase battery life. The lack of mathematical models, methods and tools for organizing dynamic reconfiguration of graphical interfaces of IoT devices (including using the AR) is a serious obstacle for further research, as well as for increasing the time for effective functioning of mobile devices and networks of software systems with limited resources. In this regard, the task of research and development of an integrated model that makes it possible to assess the efficiency of energy consumption and other limited resources of mobile devices, methods that make it possible to optimize the consumption of resources of a mobile device according to the criterion of maximizing residual energy taking into account the limitations and requirements of users for final applications and graphic interfaces, and means of organizing reconfiguration of graphic interfaces of devices.

7. Experimet and technology convergence example

To demonstrate the process of convergence of technologies we used software for iOS. This software allows you to visualize data from sensors of various devices, combined in a data collection system, using augmented reality. The experimental data acquisition system (figure 5) consists of endpoint devices that can collect temperature, humidity, light, noise and the presence of movement data. Each end device sends data using one of the LoRa, Wi-Fi or Bluetooth protocols to the base station, which generates data messages and sends them to the ThingWorx cloud platform. Heltec LoRa 32 (V2) [26] microcontrollers were used as the main components for receiving and transmitting data from various sensors. Most of them served as endpoint devices that processed and prepared for sending messages containing indicators from the sensors. While the other part was used as a basic device for receiving messages from all end sensors. For the base station organization, the Raspberry PI 3 single board computer was used. This computer is a ready-made solution for working with low-resource programs. The approach that was chosen to work with this computer allows you to use it as a full-fledged server without using external interfaces and communicating and sending commands to the Raspberry only over an SSL connection. With the help of this computer, it became possible to store data coming from devices with sensors on the Raspberry, thus turning it into a machine with the ability to send data for services, including applications, using a special network broker.

Mosquitto is used as an MQTT broker. It allows you to send mqtt messages to both cloud platforms and directly to applications. This is done because MQTT is an inter-computer connection (M2M) protocol, in other words, for the Internet of things. It was designed as an extremely easy way to publish publish (subscribe) and subscribe. This is useful for connections to remote locations where a small amount of code and high bandwidth are required. For example, it is widely used in sensors that communicate with a broker through satellite communications, through dial-up connections with health care providers, and in a number of home automation scenarios. It is also ideal for mobile applications because of its small size, low power consumption, minimized data packets and efficient distribution of information to one or several recipients. MQTT broker is used as follows: we form a request in Unity MQTT, which is needed in order to get data from the cloud platform. When the data on the platform changes, the broker sends the data with changes. MQTT broker and Unity are connected in publisher-subscriber mode. The software subscribes to receive data from the broker's MQTT and polls it with a given frequency.

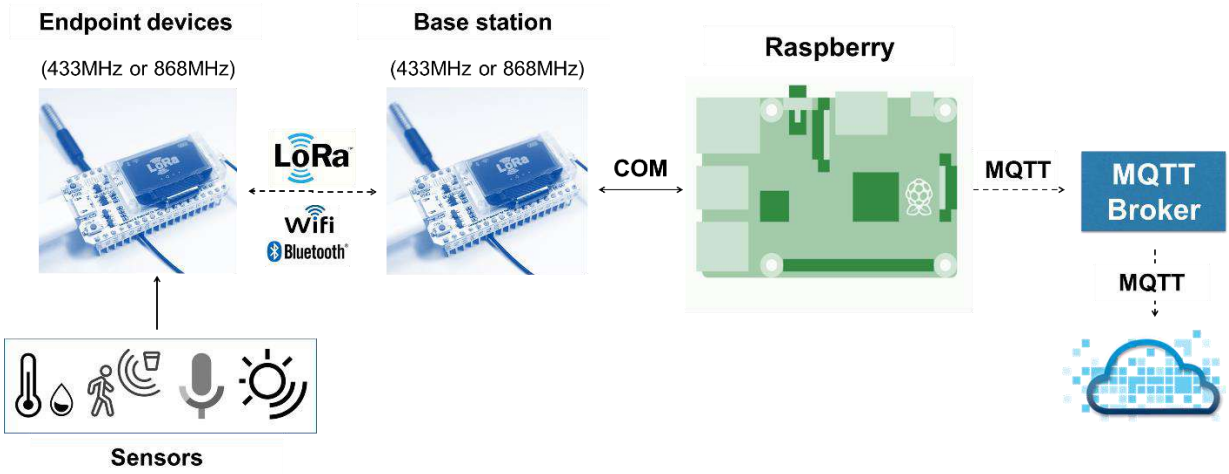

Figure 5. Data acquisition system architecture.

The developed experimental stand allowed us to analyze both versions of Heltec devices for the number of losses when the distance between the sender device and the receiver device was increased, to measure the power consumption of these devices in two modes: during standby and while sending a message for the final Heltec, but also during waiting time and while receiving a message for the base station. These studies were conducted using LoRa, Wi-Fi and Bluetooth, for each type of device, the average operating time per battery charge will be calculated.

The first test involves the use of two devices, one receiver, it is in a stationary position, and one transmitter, and it must be transferred, thereby increasing the distance between these devices. The results of the experiment are presented in table 2. As can be seen from the information received, regardless of the version and the Heltec clock frequency, up to 40 meters from each other, all devices work with 100% packet delivery, which means that no packet was lost for the tested period. After increasing the distance between devices by 10 meters more, the number of undelivered packages in all cases began to grow, but the percentage of packets received is still very high, not a single value has dropped below 95%. After the next 2 iterations of the increase in the distance between the Heltec modules, the number of lost packets increases by about 3 and 4 times, respectively. At the same time, it becomes obvious that devices of the second version have a preponderance of losses in the direction of the lower frequency, 9 packets against 5 at 60 meters and 16 against 10 at 70 meters. With a slight advance, the best packet delivery percentage is at Heltec LoRa v2, operating at a frequency of 868 MHz. Thus, it was revealed that, at long distances, priority is given to using the device second versions with a clock frequency of 868 MHz.

In the second experiment, an analysis of the current consumption of the endpoint devices was carried out using various data transfer protocols. This experiment allows you to check the actual current consumption by the Heltec endpoint devices with the payload on the microcontroller in the form of sending packets using various data transfer interfaces. There is no intentional distinction here between the versions of the Heltec modules, since both versions consume almost the same amount of current, so the separation of tests by versions has no scientific basis [27]. Table 3 presents data from tests of current consumption by devices in two modes: waiting for polling and sending a packet. As you can see from the data, as expected, the highest energy efficiency was achieved using the LoRa interface. The second place in terms of efficiency of current consumption was taken by the protocol for Bluetooth communication, while Wi-Fi was in last place in terms of current consumption both in data transfer mode and in standby mode. In this case, the relationship between the readings of the end device and the base station is traced, so the base station consumes on average about 35% more current than the end device in standby mode (polling). In this case, the difference between the energy indices for the transmission (reception) modes is about one tenth of the consumption of the Heltec end device.

Table 2. Dependence of the number of delivered Heltec packages on the distance.

	Heltec LoRa v1	Heltec LoRa v2	Heltec LoRa v2
Distance / Frequency	MHz	MHz	MHz
>40 meters	100%	100%	100%
50 meters	96,6%	95%	96,6%
60 meters	90%	85%	91,6%
70 meters	81,6%	73,3%	83,3%

To demonstrate the convergence process of the technology IoT and AR was used Vuforia. The key factor in choosing was the maximum distance to capture and hold the marker. The most important thing is that Vuforia has integration with the Thingworx cloud platform, in which the data collection system is connected. The software has two modes of operation: identification of endppont devices and data output in augmented reality (figure 6) or the output of a virtual digital twin of the building in which the data acquisition system is located (figure 7), and data output in different parts of this digital twin. All data that comes from the endpoint devices in the form of text comes to the 3D rendering unit along with 3D models, in which information about the properties of the models, textures, materials and illumination is processed. In the first mode of operation, the camera compares the received frames with the base of markers. As soon as the similarity is found, a request for a cloud platform is formed, a response from the broker's MQTT comes and then digital content is output. In the second case, using the camera, it is necessary to scan the surrounding space to create a mesh grid to which the virtual digital twin of the building can be attached.

Table 3. Dependence of power consumption of the endpoint data collection device and the base station on the operating mode used.

	Endpoint data collection device		Base station	
Protocol / Operating mode	Standby			
LoRa	80 mA	170 mA	130 mA	180 mA
Wi-Fi	170 mA	300 mA	240 mA	330 mA
Bluetooth	130 mA	230 mA	200 mA	270 mA

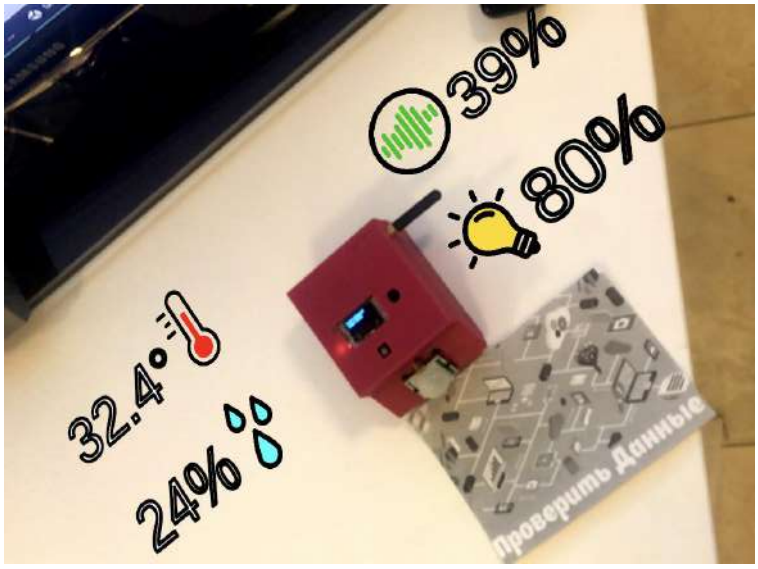

Figure 6. Endpoint device and data vusualization using AR.

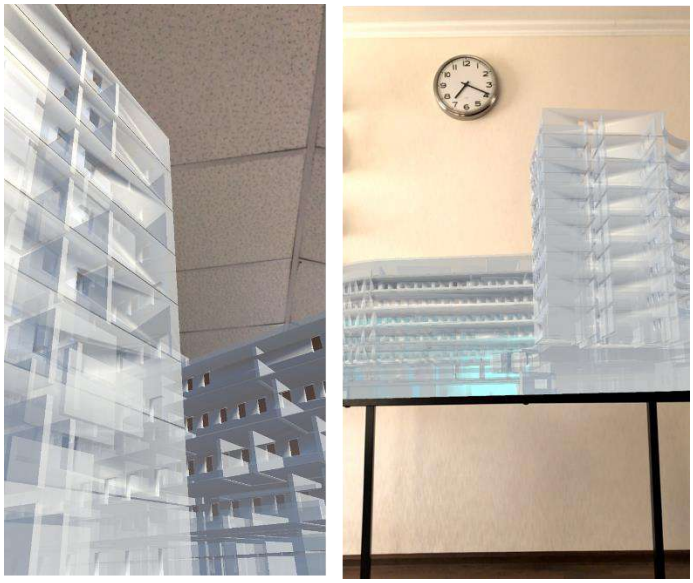

Figure 7. Digital twin of the building in which the data acquisition system is located.

8. Conclusion

The connenction of AR with the IoT ecosystem presents tremendous opportunities for various industries. Using this approach can make machines smarter by integrating sensors and intelligent systems that can monitor and produce data to solve problems in a timely manner and prevent downtime and breakdowns. IoT platforms provide a scalable, flexible, and secure way to cost-effectively extend AR applications. The use of such programs will allow companies to remotely diagnose and fix problems, preventing equipment and system system failures before they occur. This predictive service not only eliminates system downtime, but also optimizes energy use, which saves money. This paper proposes a classification of computer-based data visualization tools that can be used in developing a decision support system in the data visualization field.

To demonstrate the potential convergence of technology, an experimental data collection system stand was developed. The proposed data collection system allowed us to conduct experiments to determine the dependence of the data transmission distance in the building of the university on the use of specific models of Heltec modules of various versions and at different frequencies. Experiments were carried out to measure the energy consumption of data collection endpoint devices based on Heltec modules. To visualize data coming in real time from elements of the data collection system, software was developed using the Vuforia library, which allows visualizing the digital twinof the university building and all the information from the data collection system.

9. References

[1] Agogi E 2011 Augmented Reality in Education *Athens, Greece: EDEN-2011 Open Classroom Conference* 1-88

[2] Laney D 2001 *3d data management: Controlling data volume, velocity and variety* (Gartner, Stamford, CT, USA, White Paper)

[3] Rytsarev I A, Kirsh D V and Kupriyanov A V 2018 Clustering of media content from social networksusing bigdata technology *Computer Optics* **42(5)** 921-927 DOI: 10.18287/2412-6179-2018-42-5-921-927

[4] Agafonov A A, Yumaganov A S and Myasnikov V V 2018 Big data analysis in a geoinformaticproblem of short-term traffic flow forecasting based on a k nearest neighbors method *Computer Optics* **42(6)** 1101-1111 DOI: 10.18287/2412-6179-2018-42-6-1101-1111

[5] van der Meulen R *Gartner* URL: https://www.gartner.com/newsroom/id/3165317 (14.04.2018)

[6] Evsutin O O, Kokurina A S and Meshcheryakov R V 2019 A review of methods of embedding information in digital objects for security in the internet of things *Computer Optics* **43(1)** 137-154 DOI: 10.18287/2412-6179-2019-43-1-137-154

[7] Milgram P, Kishino A F 1994 Taxonomy of Mixed Reality Visual Displays *IEICE Transactionson Information Systems* 1321-1329
[8] Gavrilova T A, Gulyakina N A 2008 Visual methods of working with knowledge: an attempt to review *Iskusstvennyj intellekt i prinyatie reshenij* **1** 15-21
[9] Machlis Sh *Chart and image gallery: 30+ free tools for data visualization and analysis* URL: https://www.computerworld.com/article/2506820/business-intelligence/business-intelligence-chart-and-image-gallery-30-free-tools-for-data-visualization-and-analysis.html (18.04.2018)
[10] Khan M, Khan S S 2011 Data and Information Visualization Methods and Interactive Mechanisms: a Survey *International Journal of Computer Applications* 1-14
[11] Chen C L P, Zhang C Y 2014 Data-intensive applications *Challenges, Techniques and Technologies* 314-347
[12] Porter B 2012 Visualizing Big Data in Drupal: Using Data Visualizations to Drive Knowledge Discovery *Report, University of Washington* 1-38
[13] Keahey T A 2013 Using Big Data *Technical Report* 1-16
[14] Sucharitha V, Subash S R and Prakash P 2014 Visualization of Big Data: Its Tools and Challenges *International Journal of Applied Engineering Research* 5277-5290
[15] Childs H, Geveci B, Meredith J, Moreland K, Sewell C, Bethel E W, Kuhlen T and Schroeder W 2013 Berkeley National Laboratory Joint Research Report, Oak Ridge National Laboratory Sandy National Laboratories, *Los Alamos National Laboratory, RWTH Aachen University* 1-11
[16] Gorodov E Y, Gubarev V V 2013 Analytical Review of Data Visualization Methods in Big Data *Journal of Electrical and Computer Engineering* 4 1-7
[17] Liu Z, Jiangz B and Heer J 2013 imMens: Real-time Visual Querying of Big Data *Eurographics Conference on Visualization (EuroVis)* 421-430
[18] SAS Institute Inc 2013 Survey data analyzers *Report* 1-2
[19] Azuma R T 1997 A survey of augmented reality *Presence: Teleoperators and virtual environments* **6(4)** 355-385
[20] Open Source Augmented Reality SDK *ARToolKit.org* URL: https://artoolkit.org/ (22.04.2018)
[21] Easy AR SDK URL: http://www.easyar.com/ (12.05.2018)
[22] OpenCV library URL: http://opencv.org/ (15.05.2018)
[23] Maxst URL: http://maxst.com/image_ar/?_Lang=en (22.05.2018)
[24] Kudan Computer Vision *Kudan limited* URL: https://www.kudan.eu/ (22.04.2018)
[25] Catchoom - Image Recognition and Augmented Reality URL: https://catchoom.com (22.04.2018)
[26] Vuforia *Augmented Reality* URL: https://www.vuforia.com (22.04.2019)
[27] WiFi LoRa 32 (V2) URL: https://heltec.org/project/wifi-lora-32/ (22.04.2019)
[28] Fernández-Ahumada L M 2019 Proposal for the Design of Monitoring and Operating Irrigation Networks Based on IoT, Cloud Computing and Free Hardware Technologies *Sensors* **19(10)** 2318

Acknowledgments
The publication was prepared within the framework of the Academic Fund Program at the National Research University Higher School of Economics (HSE) in 2019– 2020 (grant № 19-04-022) and by the Russian Academic Excellence Project "5-100".

Network traffic analyzing algorithms on the basis of machine learning methods

R I Battalov[1], A V Nikonov[1], M M Gayanova[1], V V Berkholts[1] and R Ch Gayanov[2]

[1]Ufa State Aviation Technical University, K. Marks str., 12, Ufa, Russia, 4500082
[2]Higher School of Economics, Myasnitskaya str., 20, Moscow, Russia, 101000

e-mail: nikonovandrey1994@gmail.com, torina4@yandex.ru

Abstract. Traffic analysis systems are widely used in monitoring the network activity of users or a specific user and restricting client access to certain types of services (VPN, HTTPS) which makes content analysis impossible. Algorithms for classifying encrypted traffic and detecting VPN traffic are proposed. Three algorithms for constructing classifiers are considered - MLP, RFT and KNN. The proposed classifier demonstrates recognition accuracy on a test sample up to 80%. The MLP, RFT and KNN algorithms had almost identical performance in all experiments. It was also found that the proposed classifiers work better when the network traffic flows are generated using short values of the time parameter (timeout). The novelty lies in the development of network traffic analysis algorithms based on a neural network, differing in the method of selection, generation and selection of features, which allows to classify the existing traffic of protected connections of selected users according to a predetermined set of categories.

1. Introduction

The term “deep package inspection” (DPI) [1] refers to the analysis of the network packet at the upper levels (application and presentation level) of the open systems interaction model (OSI) [2].

In addition to analyzing network packets [3] using standard patterns by certain standard patterns that can be used to unambiguously determine whether a package belongs to a specific application, for example, by the format of headers, port numbers, etc., the DPI system performs behavioural analysis of traffic. This allows to recognize applications that do not use known data headers and data structures for data exchange.

For identification, an analysis of the sequence of packets with the same characteristics is carried out. Analyzed characteristics are Source_IP: port - Destination_IP: port; packet size; frequency of opening new sessions per unit of time, etc. The analysis based on behavioral (heuristic) models corresponding to such applications.

The main component of the DPI solution [4] is the classification module. It is responsible for the classification of network flows. The classification can be performed with different accuracy depending on the purposes of the DPI application:

- the type of protocol or application (for example, Web, P2P, VoIP);
- a specific application-layer protocol (HTTP BitTorrent, SIP);

- applications using the protocol (Google Chrome, uTorrent, Skype).

Traffic analysis using traditional tools becomes impossible without selecting a key for streaming data with encryption (for example, TLS / SSL protocols). It takes a lot of resources to find the key. The relevance of hacking remains only at the governmental or military level [5].

In the [6] the classification of network encrypted traffic from Skype, Tor, PuTTY (SSHv2), CyberGhost (VPN) is discussed by application types for detecting security threats using such machine learning methods as the Naive Bayes, C4.5, AdaBoost and Random Forest algorithms. For the analysis, more than two million network packets from four applications that transmit encrypted traffic were collected: Skype, Tor, PuTTY (SSHv2), CyberGhost (VPN). Two different classification approaches were considered: the formation and analysis of flows for network packets whose IP addresses of the sender / recipient and the network protocol are the same, as well as the interception and analysis of each network packet [7]. When using each approach, the various attributes were identified and with the use of which the classification was made. Obtained results can be used to build traffic classifiers and intrusion detection systems, effectively processing the encrypted traffic used by various network applications.

In [8] it is shown that comparison of various algorithms for classifying network traffic is significantly difficult due to the lack of a generally accessible base of fully-fledged network routes on which it would be possible to make comparisons. One of the most actively developing areas at the moment is the use of various machine learning algorithms, graph and statistical analysis, because of their applicability to encrypted traffic (as opposed to the DPI approaches), whose share is growing rapidly. Another emerging focus is the development of combined approaches and classification systems. One of the reasons for development is an attempt to overcome the shortcomings of individual approaches (for example, low accuracy or processing speed) and use their advantages [9, 10].

Therefore, the development of algorithms that allow classifying the traffic of secure connections with the required level of detail by protocol is relevant [11].

Objective: improving the algorithms for analyzing the network traffic of secure connections.

The main tasks of the study:

1. Analysis of algorithms for network traffic classification;
2. Development of the network traffic analysis system structure;
3. Development of the algorithm for analyzing the network traffic of secure connections on the basis of algorithms of feature generation and selection for construction a neural network classifier;
4. Software implementation of algorithms for analyzing network traffic and evaluating the effectiveness of the proposed solution on the basis of full-scale data.

2. Analysis of algorithms and systems of network traffic treatment

Traffic classification [12] allows to identify various applications and protocols transmitted over the network. Also, the classification function is the management of this traffic, its optimization and prioritization. All packets become marked by belonging to a specific protocol or application after classification. This allows network devices to apply quality of service policies (QoS) based on these labels and flags.

There are two main methods of traffic classification (Figure 1):

- Classification based on data blocks (Payload-Based Classification). It is based on the analysis of data packet fields. This method is the most common but does not work with encrypted and tunneled traffic.
- Classification based on statistical analysis (time between packets, session time, etc.).

A universal approach to traffic classification based on information in the header of the IP packet. This is usually IP address (Layer 3), MAC address (Layer 2) and the protocol used. This approach has its limitations [13].

Deep package inspection (DPI) allows to implement more advanced classification . The main mechanism for identifying applications in DPI is signature analysis [14]. Each application has its own unique characteristics, which are entered in the database of signatures. Comparing the sample from the database with the analyzed traffic allows to determine the application or protocol. However, new

applications periodically appear, the signature database also needs to be updated to ensure high identification accuracy.

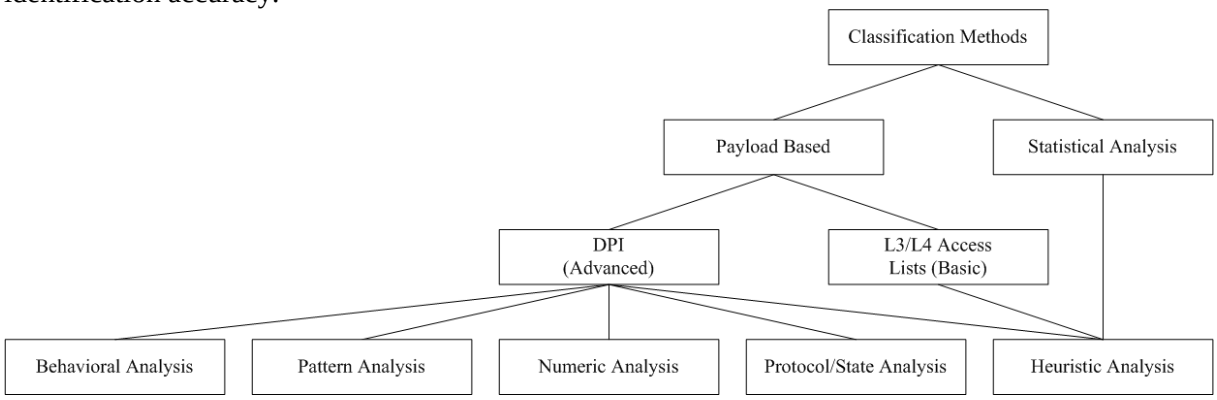

Figure 1. Methods for classifying network traffic.

There are several methods of signature analysis:

Pattern analysis

The applications contain certain sample sequences in the package data block. They can be used for identification and classification. Not every package contains a sample application data, so the method does not always work.

Numerical analysis

Numerical analysis uses the quantitative characteristics of the sequence of packets, such as: size of the data block, response time, interval between packets. Simultaneous analysis of multiple packets is time consuming, which reduces the effectiveness of this method.

Behavioral analysis, Heuristic analysis

Method is based on the analysis of traffic dynamics of the running application. While the application is running, it creates traffic that can also be identified and labeled [15].

Protocol/state analysis

Protocols of some applications are a sequence of certain actions. Analysis of such sequences allows to accurately identify the application. reduces the effectiveness of this method.

Behavioral and heuristic analysis are used when working with encrypted traffic. For more accurate identification, cluster analysis is used, which combines the methods of heuristic and behavioral analysis [16, 17].

3. Development of the network traffic system analysis based on machine-learning training

The development of analysis algorithm for classifying network traffic of secure connections of dedicated users according to a pre-defined set of categories is actual [18-20].

Two scenarios of network traffic analysis are considered:

- analysis of encrypted traffic;
- analysis of encrypted traffic passing through a virtual private network (VPN).

The figure 2 shows the organization's LAN structure with an analysis module for network traffic of encrypted connections.

Traffic arrives from the edge router. There is a seizure and preprocessing of traffic using the libpcap library. The primary features of the data flow are extracted from the received pcap files. Vector of primary features and sessions with a duration of 15, 30, 60 and 120 seconds is formed. The generation and selection of features for the neural network classifier training is performed. The prepared vector of features is fed to the neural network analysis module of user sessions. The settings for training and work are set by the administrator.

This process is shown in the figure 3.

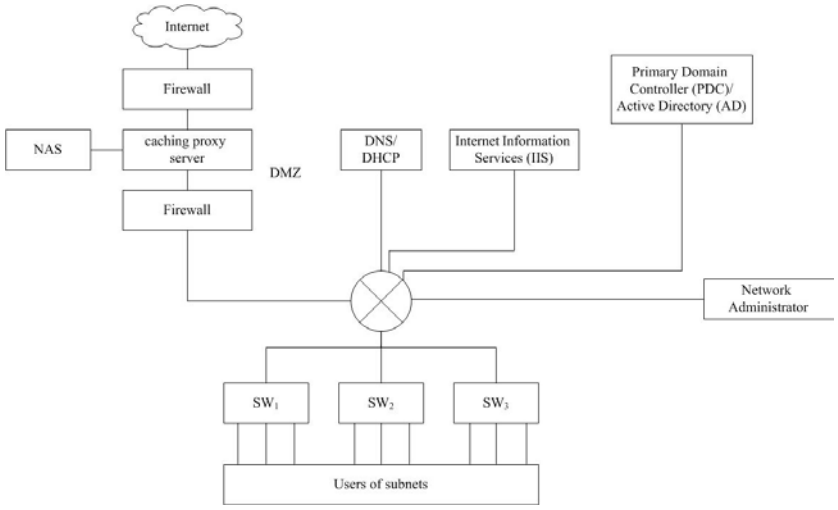

Figure 2. The structure of the LAN with an expanded system for analyzing network traffic.

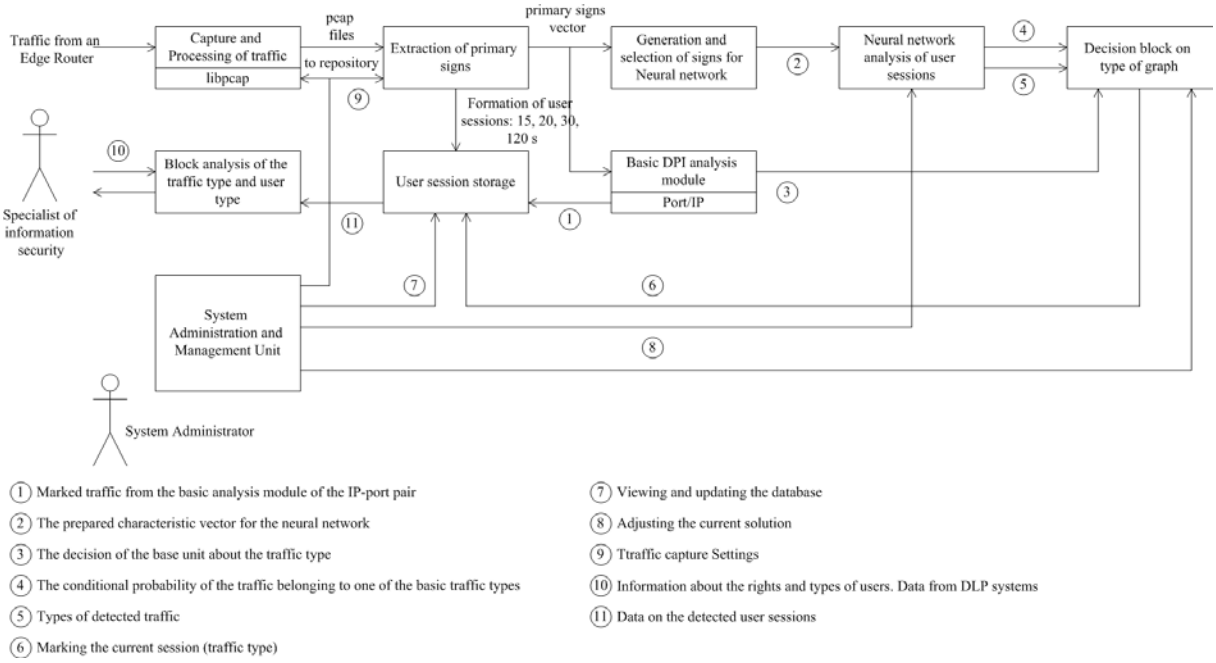

Figure 3. Structure of the network traffic analysis system.

Further, the following information comes to the decision block: the decision of the base block on the type of traffic, the probability of the traffic belonging to one of the basic types and the types of recognized traffic from the NA block analyzing user sessions. Administrator can perform the adjustment of the current solution on the decision block on the type of traffic.

Then, the current traffic from the decision block and marked traffic from the basic traffic analysis module (sender's IP, recipient's IP, port, sender, port of the recipient) are sent to the user sessions store.

Further, data on recognized user sessions is sent to the traffic type analysis module and the user type. An information security specialist receives information about the types of users and their rights. The administrator interacts with the repository to view and replenish the database and sets the parameters for capturing traffic.

Development of an algorithm for analyzing network traffic

At the first step, the fragment of the intercepted traffic is downloaded, then the classifier scenario is selected. Based on the features indicated in the scenario, a training sample is formed to build the initial

knowledge base. After analyzing the given features on the test sample, the accuracy of the classifier is determined. If the accuracy satisfies the requirements, the current state is saved, otherwise the cycle returns to the definition of the type of the script. The block diagram of the network traffic classifier is shown in Figure 4.

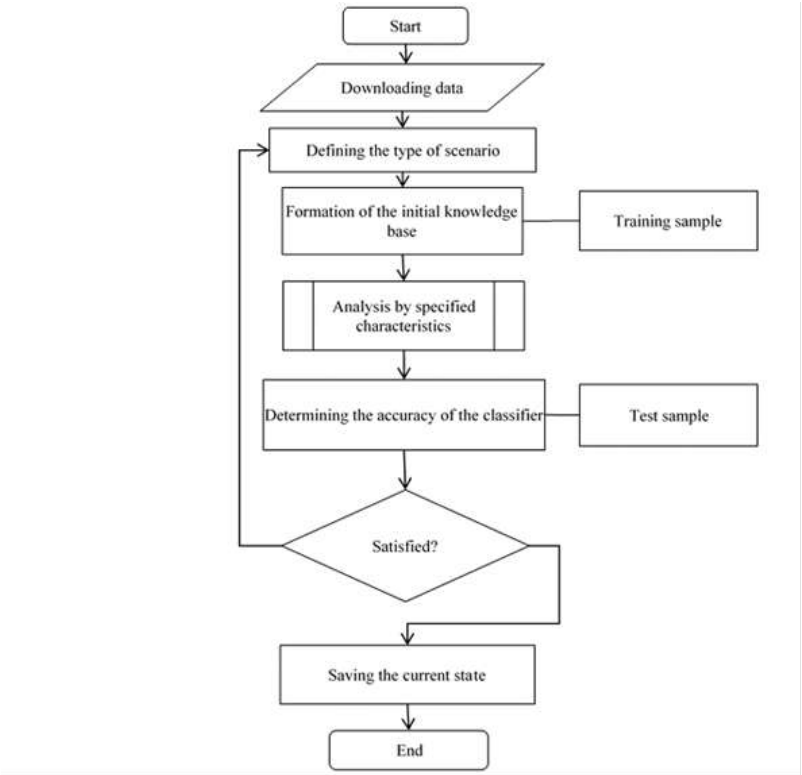

Figure 4. Block diagram of the network traffic classifier.

4. Realization of network traffic analysis algorithms and experiment on natural data

Traffic classification is based on the analysis of the temporal characteristics of the intercepted network packets stream for the formation of encrypted and VPN-traffic features (time-related features). The temporal characteristics of the flow make it possible to reduce the computational cost of building a set of features extracted from the encrypted network traffic by reducing the set of fixed parameters.

The experiment uses a dump of network traffic [21-29] with 14 different traffic type tags generated by different applications (7 for conventional encrypted traffic and 7 for VPN traffic).

Table 1. Fixed time-dependent network traffic parameters.

Function	Description
duration	Flow duration
fiat	The interval between 2 packets sent from the network client (average, min, Max).
biat	The interval between the two packets sent to the network client (average, min, Max).
flowiat	The interval between two packets sent in any direction (average, min, Max).
active	The interval during which the network exchange was active, before switching to the standby mode (average, min, Max).
idle	The interval during which the network exchange was in the standby mode (average, minimum, maximum).
fb psec	Intensity of the flow, bytes per second
fp psec	Intensity of flow, packets per second

The quality criterion for traffic classification is the accuracy of classifying samples. Assessment of the classification accuracy can be carried out by cross-validation [30]. The separation into the training and test sets is performed by dividing the sample in a certain pro-portion – the training set is two-thirds of the data and the test set is one-third of the data.

To solve the classification problem, the following algorithms are considered:

- Random Forest algorithm (RFT);
- K-Nearest Neighbor method (KNN);
- Multilayer Perceptron (MLP) [31].

As the source data, the real traffic generated by such applications and services as Skype, Facebook, etc. is used. Table 1 provides a complete list of the different types of traffic and applications included in the source dataset.

For each type of traffic (VoIP, P2P, etc.), open sessions and sessions are used in the created VPN tunnel, therefore there are in total 14 categories of traffic: VoIP, VPN-VoIP, P2P, VPN-P2P, etc.

Table 2. List of captured protocols and applications.

Traffic	Content	Method of generation
Web-browsing	Firefox, Chrome	HTTPS traffic generated by users while viewing or executing any task that involves using the browser.
Email	SMPTS, POP3S, IMAPS	Samples of traffic generated by the Thunderbird client and Gmal accounts. Clients are configured to deliver mail through SMTP / S, receive and use it using POP3 / SSL in one client and IMAP / SSL in another
Chat	ICQ, AIM, Skype, Face-book, Hangouts	The chat label defines applications for instant messaging (Face-book and Hangouts via web browser, Skype, and IAM and ICQ).
Streaming video	Vimeo, YouTube	The streaming label defines multimedia applications that require a continuous and stable data flow. For example, the services of YouTube (HTML5 and Flash version) and Vimeo, using Chrome and Firefox.
File Transfer	Skype, FTPS and SFTP using FileZilla and external service	The label identifies the application traffic for sending or receiving files and documents. The files were transferred to Skype, FTP through SSH (SFTP) and FTP through SSL (FTPS).
VoIP	Voice calls on Facebook, Skype	The IP Telephony Label groups all traffic generated in voice ap-plications (Facebook, Hangouts and Skype)
P2P	uTorrent and transfer (BitTorrent)	A label is used to identify file sharing protocols, such as Bit-Torrent

Traffic was captured using the Wireshark sniffer. For VPN-traffic, the external service of the VPN provider was used, the connection was made using OpenVPN. To generate SFTP and FTPS traffic, use an external service provider and FileZilla as the client.

Let's define two different scenarios A and B (Figure 5). Four different time duration values were used to generate the data sets.

Scenario A: The purpose is to select the features of encrypted traffic with VPN identification, for example, distinguishing between voice calls (VoIP) and voice calls passing through VPN (VPN-VoIP). As a result, there are 14 different types of traffic: 7 regular types of encrypted traffic and 7 types of traffic passing through the VPN. The first classifier uses VPN and non-VPN traffic separation, and then each traffic type classified separately (VPN and non-VPN).

Scenario B: in this case we use a mixed data set. The classifier's input is regular encrypted traffic and VPN traffic, and the output is allocated the same 14 different categories.

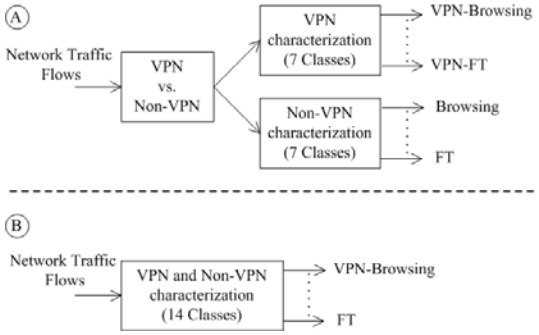

Figure 5. Scenarios for handling captured traffic.

Using general definition of traffic, it is determined by the sequence of packets with the same values for: destination IP address, sender's IP address, sender's port, sender's port, and protocols (TCP or UDP).

Streams are considered bidirectional. Together with the generation of traffic, the features associated with each type of traffic are determined. TCP stream are usually terminated when the connection is broken (by the FIN packet), and the UDP stream are terminated by a thread interruption. The value of the thread interrupt can be assigned arbitrarily. In particular, we set the duration of the streams to 15, 30, 60 and 120 seconds [32-34].

Scenario A analysis

MLP is a neural network of direct propagation. It consists of two hidden layers. In the first hidden layer there are 30 neurons, and in the second there are 15 neurons. Size of input vector of features is 23. The activation function of neurons is a hyperbolic tangent [35]. As a numerical metric, the root-mean-square error is used to estimate the network error. As a learning algorithm, the method of conjugate gradients is used. The number of learning epochs is 5000.

When testing the KNN algorithm, the neighbor number parameter is 50.

When testing the random tree method, the classifier type “Bag” is used. The number of ensemble training cycles is 150.

Table 3. Obtained data for scenario A1.

Session Length and Type	Classifier	Training sample			Test sample		
		Sensitivity	Specificity	Accuracy	Sensitivity	Specificity	Accuracy
120s-VPN	MLP	0.799	0.851	0.826	0.748	0.822	0.787
120s-VPN	KNN	0.786	0.715	0.749	0.763	0.712	0.736
120s-VPN	RFT	0.957	0.998	0.978	0.805	0.848	0.828
15s-VPN	MLP	0.820	0.831	0.826	0.796	0.783	0.789
15s-VPN	KNN	0.798	0.776	0.786	0.784	0.764	0.773
15s-VPN	RFT	0.975	0.999	0.988	0.848	0.866	0.857
30s-VPN	MLP	0.826	0.847	0.837	0.774	0.819	0.798
30s-VPN	KNN	0.753	0.773	0.764	0.764	0.774	0.770
30s-VPN	RFT	0.969	0.998	0.984	0.831	0.880	0.857
60s-VPN	MLP	0.831	0.791	0.813	0.787	0.729	0.761
60s-VPN	KNN	0.826	0.687	0.764	0.826	0.659	0.750
60s-VPN	RFT	0.964	0.996	0.978	0.838	0.808	0.824

The cross validation (Tables 4, 5) was performed in order to assess how classifiers are able to work with real data, while producing a result whose accuracy is correlated to accuracy in the test sample [36].

Table 4. Cross-validation results for scenario A1.

Session Length and Type	Classifier	Average accuracy	Deviation
120s-VPN	KNN-crossval	0.730	0.015
120s-VPN	RFT-crossval	0.826	0.007
15s-VPN	KNN-crossval	0.770	0.010
15s-VPN	RFT-crossval	0.858	0.009
30s-VPN	KNN-crossval	0.747	0.013
30s-VPN	RFT-crossval	0.840	0.008
60s-VPN	KNN-crossval	0.751	0.013
60s-VPN	RFT-crossval	0.815	0.007

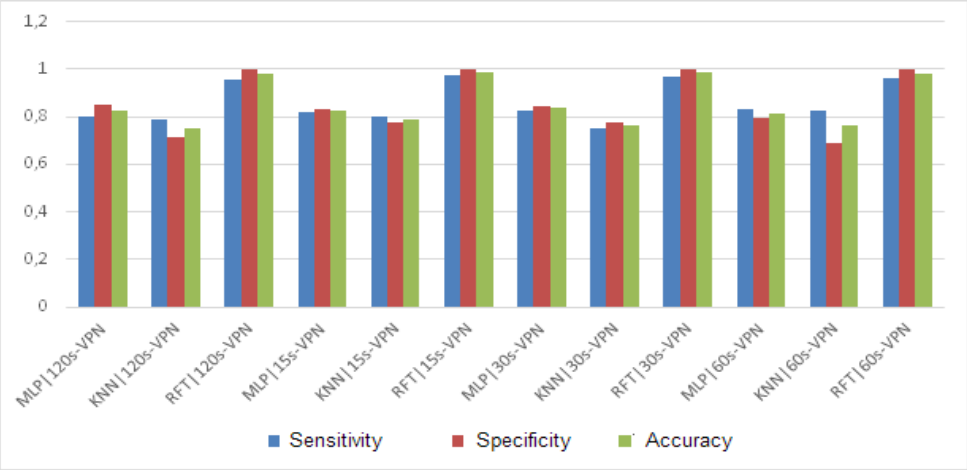

Figure 5. Classification results on the training sample for scenario A.

There is a direct relationship between the length of the captured session of the thread and the performance of the classifiers. When using the RFT classifier, the accuracy on the test sample decreases from 0.857 with a flow time of 15 seconds to 0.828 using a 120 second flow. Similar behavior is observed for the KNN and MLP algorithms. The best results are achieved using the RFT algorithm, with the time required to create the stream equal to 15. These results show that, using shorter time-out values for the traffic classifier, you can in-crease the accuracy value.

The second part of scenario A focuses on the separation of VPN and non-VPN traffic. The input is classified according to traffic categories. The results for shorter duration values are better than the results for larger values, albeit with some exceptions. In the case of VPN classifier, as VPN-mail, where the best result is obtained with the value of ftm equal to 30 seconds. In the case of a non-VPN classifier, the same thing happens.

Analysis of scenario B

All encrypted streams and VPN traffic are mixed in one set of data. The goal is to classify traffic without prior VPN separation from non-VPN traffic. There are 14 types of traffic: 7 encrypted and 7 VPN traffic types.

The short duration of the session of the captured stream does not provide the greatest accuracy. For example, for the MLP algorithm, the test accuracy is 0.795 and 0.51 for 15 seconds, and for a session time of 30 seconds, the accuracy on the test sample for the same algorithm is 0.798 and 0.637. The highest accuracy on the test sample for different interrupt values is 0.847 (RFT algorithm with a flow time of 120 seconds).

Table 5. Cross-validation results for scenario A2.

Session Length and Type	Classifier	Average accuracy	Deviation
120s-NO-VPN	KNN-crossval	0.776	0.012
	RFT-crossval	0.882	0.007
120s-VPN	KNN-crossval	0.679	0.020
	RFT-crossval	0.838	0.009
15s-NO-VPN	KNN-crossval	0.807	0.012
	RFT-crossval	0.889	0.006
15s-VPN	KNN-crossval	0.721	0.019
	RFT-crossval	0.830	0.009
30s-NO-VPN	KNN-crossval	0.798	0.008
	RFT-crossval	0.875	0.006
30s-VPN	KNN-crossval	0.710	0.017
	RFT-crossval	0.846	0.008
60s-NO-VPN	KNN-crossval	0.744	0.013
	RFT-crossval	0.854	0.006
60s-VPN	KNN-crossval	0.670	0.016
	RFT-crossval	0.817	0.009

Table 6. Obtained data for scenario B.

Session Length and Type	Classifier	Training sample			Test sample		
		Sensitivity	Specificity	Accuracy	Sensitivity	Specificity	Accuracy
120s-AllinOne	MLP	0.922	0.872	0.802	0.909	0.859	0.787
120s-AllinOne	KNN	0.911	0.772	0.739	0.915	0.762	0.735
120s-AllinOne	RFT	0.913	0.999	0.965	0.507	0.984	0.847
120s	MLP	0.853	0.895	0.629	0.829	0.886	0.607
120s	KNN	0.816	0.832	0.604	0.818	0.835	0.618
120s	RFT	0.972	1	0.964	0.457	0.993	0.767
15s-AllinOne	MLP	0.896	0.945	0.834	0.860	0.929	0.795
15s-AllinOne	KNN	0.8782	0.8802	0.769	0.878	0.873	0.752
15s-AllinOne	RFT	0.979	0.999	0.984	0.622	0.968	0.846
15s	MLP	0.870	0.839	0.521	0.879	0.841	0.510
15s	KNN	0.656	0.904	0.662	0.615	0.905	0.653
15s	RFT	0.996	1	0.982	0.565	0.984	0.776
30s-AllinOne	MLP	0.915	0.941	0.830	0.882	0.930	0.798
30s-AllinOne	KNN	0.892	0.858	0.744	0.889	0.844	0.737
30s-AllinOne	RFT	0.967	0.999	0.979	0.605	0.970	0.844
30s	MLP	0.811	0.922	0.661	0.780	0.916	0.637
30s	KNN	0.727	0.892	0.634	0.722	0.892	0.629
30s	RFT	0.986	1	0.980	0.537	0.983	0.767
60s-AllinOne	MLP	0.911	0.930	0.795	0.889	0.913	0.754

60s-AllinOne	KNN	0.902	0.842	0.734	0.882	0.840	0.717
60s-AllinOne	RFT	0.952	0.999	0.973	0.576	0.970	0.810
60s	MLP	0.799	0.922	0.622	0.750	0.911	0.602
60s	KNN	0.757	0.891	0.615	0.763	0.883	0.606
60s	RFT	0.973	0.999	0.971	0.544	0.985	0.737

Table 7. Inaccuracy matrix of all traffic with a flow duration of 60 seconds.

Inaccuracy matrix		**Actual data of the session**						
		Web-browsing	Chat	File Transfer	Email	P2P	Streaming video	VoIP
The result of the classifier's work	Web-browsing	189	18	10	1	7	15	53
	Chat	19	373	27	7	13	21	24
	File Transfer	15	30	234	3	0	4	14
	Email	0	3	6	74	1	3	1
	P2P	7	9	1	3	803	41	9
	Streaming video	29	54	16	18	28	340	8
	VoIP	69	66	19	16	19	28	1131

The cross-validation (Table 8) was performed to assess the effectiveness of the KNN method and the RFT method.

Table 8. Cross-validation results for scenario B.

Session Length and Type	**Classifier**	**Average accuracy**	**Deviation**
120s-AllinOne	KNN-crossval	0.722	0.014
	RFT-crossval	0.829	0.009
120s	KNN-crossval	0.582	0.013
	RFT-crossval	0.733	0.011
15s-AllinOne	KNN-crossval	0.757	0.008
	RFT-crossval	0.845	0.009
15s	KNN-crossval	0.643	0.014
	RFT-crossval	0.768	0.012
30s-AllinOne	KNN-crossval	0.733	0.018
	RFT-crossval	0.835	0.008
30s	KNN-crossval	0.616	0.017
	RFT-crossval	0.757	0.013
60s-AllinOne	KNN-crossval	0.721	0.011
	RFT-crossval	0.819	0.009
60s	KNN-crossval	0.594	0.014
	RFT-crossval	0.724	0.011

5. Conclusion

Traffic analysis systems are widely used in monitoring the network activity of users or a specific user and restrict the client's access to certain types of services (VPN, HTTPS). This makes analysis of content impossible. Algorithms for classification of encrypted traffic and detection of VPN traffic are proposed. Three algorithms for constructing classifiers: MLP, RFT and KNN, are considered.

The effect of the session length of the captured data stream on the accuracy of the classification is established. The developed classifier demonstrates the accuracy of recognition on the test sample to 80%. Algorithms MLP, RFT and KNN had almost identical indicators in all experiments.

It is also established that the proposed classifiers work better when network traffic flows are generated using short time-out values.

The novelty lies in the development of algorithms for analyzing network traffic on the basis of a neural network. This method differs in the way of features generation and selection, which allows classifying the existing traffic of protected connections of selected users according to a predefined set of categories.

The developed algorithms can improve the security of the data transmission network by improving the algorithms for analyzing network traffic as part of a data leak prevention system.

6. References

[1] DPI Technology Overview – Deep Packet Inspection URL: https://habr.com/post/111054/
[2] Olifer V G, Olifer N A 2011 *Computer networks. Principles, technologies, protocols: Textbook for high schools* (SPb.: Peter) p 944
[3] Analyzers of network packets URL: https://compress.ru/article.aspx?id=16244
[4] Smith R 2008 Deflating the big bang: fast and scalable deep packet inspection with extended finite automata *ACM SIGCOMM Computer Communication Review* **38(4)** 207-218
[5] Traffic security URL: https://habr.com/post/46321/
[6] Kostin D V, Sheluhin O I 2016 Comparison of machine learning algorithms for encrypted traffic classification *T-Comm.* **10(9)** 43-52
[7] Get'man A I 2017 Overview of tasks and methods for solving them in the field of classification of network traffic *Proc. of the Institute for Syst. Prog. of the Russian Academy of Sciences* **29(3)**
[8] Lim Y 2010 Internet traffic classification demystified: on the sources of the discriminative power *Proc. of the 6th Int. Conf. (ACM)* p 9
[9] Moore A W, Zuev D 2005 Internet traffic classification using bayesian analysis techniques *ACM SIGMETRICS Performance Evaluation Review* **33(1)** 50-60
[10] Federal Law № 149-FZ "On Information, Information Technologies and Information Protection" URL: www.internet-law.en/law/inflaw/inf.htm
[11] Traffic classification and Deep Packet Inspection URL: https:// vasexperts.ru/blog/klassifikatsiya-trafika-i-deep-packet-inspection/
[12] Sukhov A M, Sagatov E S, Baskakov A V 2014 Analysis of Internet service user audiences for network security problems *2nd Int. Symp. on Telecommunication Technologies (ISTT)* 214-219
[13] The composition of the DPI system URL: https://vasexperts.ru/blog/sostav-sistemy-dpi/
[14] Moore A W, Zuev D 2005 Internet traffic classification using bayesian analysis techniques *Int. Conf. Measurement and Modeling of Comp. Syst.* URL: http://www.cl.cam.ac.uk/~awm22/ publications/moore2005internet.pdf
[15] Russian manufacturers of DPI and their platforms URL: https://vasexperts.ru/blog/rossijskie-proizvoditeli-dpi-i-ih-platfo/
[16] Foreign DPI manufacturers and their platforms URL: https://vasexperts.ru/blog/inostrannye-proizvoditeli-dpi-i-ih-platf/
[17] Sherry J, Lan C, Popa R A and Ratnasamy S *Blindbox: Deep packet inspection over encrypted traffic* URL: http://iot.stanford.edu/pubs/sherry-blindbox- sigcomm15.pdf
[18] Shen F, Pan C and Ren X 2007 Research of P2P traffic identification based on BP neural network *3rd Int. Conf. on Intelligent Information Hiding and Multimedia Signal Processing* **2** 75-78
[19] Raahemi B 2008 Classification of Peer-to-Peer traffic using incremental neural networks (Fuzzy ARTMAP) *Canadian Conf. on Electrical and Comp. Eng.* 719-724
[20] The UNSW-NB15 Dataset Description URL: https://www.unsw.adfa.edu.au/australian-centre-for-cyber-security/cybersecurity/ADFA- NB15-Datasets/
[21] Tor-non Tor dataset (ISCXTor2016) URL: http://www.unb.ca/cic/datasets/tor.html

[22] Lotfollahi M et al 2017 Deep Packet: A Novel Approach For Encrypted Traffic Classification Using Deep Learning *arXiv preprint arXiv:1709.02656*
[23] Lopez-Martin M et al 2017 Network traffic classifier with convolutional and recurrent neural networks for Internet of Things *IEEE Access* **5** 18042-50
[24] Miller B 2014 I know why you went to the clinic: Risks and realization of https traffic analysis *Int Symp. on Privacy Enhancing Technologies* (Springer, Cham) 143-163
[25] Foremski P 2013 On different ways to classify Internet traffic: a short review of selected publications *Theoretical and Applied Informatics* **25(2)** 119-136
[26] Smit D 2017 Looking deeper: Using deep learning to identify internet communications traffic *Macquarie Matrix: Special edition, ACUR* **1** 1318-1323
[27] Michael A K J *Network traffic classification via neural networks* Technical Report (University of Cambridge, Computer Laboratory) p 25
[28] Belov S D 2008 Detection of patterns and recognition of abnormal events in the data stream of network traffic *Vestnik NGU: Information Technologies* **6(2)** 57-68
[29] Haykin S 2006 *Neural networks. Neural networks: a full course* (Moscow: Publishing house "Williams") p 1104
[30] Data science. What is cross-validation? URL: http://datascientist.one/cross-validation/
[31] Sukhov A M, Sagatov E S and Baskakov A V 2017 Rank distribution for determining the threshold values of network variables and the analysis of DDoS attacks *Procedia Engineering* **201** 417-27
[32] Galtsev A A, Sukhov A M 2011 Network attack detection at flow level *11th Int. Conf., NEW2AN: Lecture Notes in Computer Science* **6869** 326-334
[33] Salimov A S 2018 Application of SDN Technologies to Protect Against Network Intrusions *Int. Scien. and Techn. Conf. Modern Comp. Network Technologies (MoNeTeC)* 1-9
[34] Multilayer perceptron URL: http://www.aiportal.ru/articles/neural-networks/multi-perceptron.html
[35] Mastering fuzzy modeling methods and developing an algorithm to optimize the fuzzy classifier rules base based on observable data using a genetic algorithm URL: http:// refleader.ru/jgernayfsyfs.html

Acknowledgments
This work is partially supported by the Russian Science Foundation under grants № 17-07-00351.

SoC opportunities for boosting SDR GNSS performance

A A Kumarin[1], I A Kudryavtsev[1]

[1]Samara National Research University, Moskovskoe Shosse, 34A, Samara, Russia, 443086

e-mail: alky_samara@mail.ru

Abstract. Software-defined-radio (SDR) becomes an attractive technique for the development of GNSS receivers due to universal hardware and high flexibility. However, the performance of signal processing can be a challenging task. Real-time mode implementation requires fast floating point calculations in several threads, not available for most part of embedded systems. This paper describes the system-on-chip based device drastically increasing computational performance. A summary of computational complexity of each stage of GNSS receiver is provided and several particular solutions are proposed.

1. Introduction

Modern global navigation satellite systems (GNSS) such as GPS, GLONASS and Galileo allow users to obtain positioning accuracy of about several meters using relatively simple receiver. However, there are many areas, where either better accuracy or special measurements are required [1]. In addition, GNSS signal structure is being modified permanently. A software defined radio (SDR) based receiver may be a solution, providing flexibility and advantages of combined usage of several systems. SDR usually has a universal RF-front-end capable of handling different types of signals in different bands, however, this simplicity requires complex software signal processing. One of the problems is the necessity to execute all the computations in real time mode.

In a typical SDR-based GNSS receiver signal acquisition and tracking are performed independently for each available satellite and each processed signal type e.g. C/A code, L2C, L5 etc. It implies significant computational burden, motivating engineers to seek efficient methods of hardware and/ or software implementations.

Maintaining real-time computations in software is a challenging task. Using general-purpose microprocessor is a relatively expensive and power consuming solution. A less power consuming option is using digital signal processor (DSP). However, both aforementioned solutions are limited by the number of parallel threads. Field programmable Gate Arrays (FPGA) allow boosting computational performance and implementation of many parallel channels. Thus, this paper presents an attempt of using system-on-chip (SoC) to build a GNSS receiver. It becomes an attractive platform nowadays [2]. A typical SoC is a combination of FPGA and a hardware processor system (HPS), allowing parallel acquisition and/or tracking and sequential computation of coordinates. The analysis if recent publications [3-7] shows, that SoC is considered to be used for SDR-based GNSS receivers, however most of the authors use FPGA parts of their SoCs to synthesize additional cores rather than to design their own implementation of computational modules. Another problem is that SoC's FPGA part is not as large as of FPGA-only solutions. Therefore, most of the researches use high-end devices such as Intel Arria-10 or implement just a fraction of the acquisition module. Other authors consider only using FPGA [8-9]. It is our belief that only combining FPGA and HPS opportunities an effective solution can be achieved.

2. Algorithm overview

NSS signal acquisition usually involves search of a correlation peak in a 2D array, containing time delay and Doppler frequency. The frequency dimension is usually about 40 cells for rough acquisition. In every frequency cell it is necessary to perform several FFT and IFFT calculations of several thousand points length. Is is a heavy computational load and we need a powerful floating point computational unit to execute it in an appropriate time period [10-11].

Signal tracking algorithm includes scalar product calculation for more than 20 thousand complex elements-long arrays. It can take over 80% of operational time and it is important to note that we have to repeat it for every period of PRN sequence in order to maintain continuous tracking. Position calculation usually uses least squares method to assess position vector. It also involves some data corrections and auxiliary conversions.

3. Serial algorithm performance

Finding the best way to reduce computation time, is to optimize the part of the algorithm consuming the most amount of processor time. For that purpose, a performance profiler tool of Visual Studio has been used on C++ GNSS receiver implementation, designed in this study based on [12]. The acquisition stage and the tracking stage have been assessed. Assuming the "worst case scenario" with minimum of tracking of four satellites performed every 1ms and acquisition performed once per second on 32 channels, with position computed 10 times per second, tracking stage takes about 87% of processing time. In other cases, it would take even more time. Thus, boosting and parallelizing tracking is the primary task.

The tracking algorithm consists of preparation and the main loop. In the main loop there is trigonometric function (SINCOS) computation, value scaling and correlation computation. Finally, after the loop processing there is the frequency correction procedure based on the correlation value. Performance profiling indicates that computations outside the loop take negligible CPU time. The load distribution is shown in the diagram (figure 1). The correlation computation and the scaling are relatively simple and takes that much processor time probably due to cache issues. Sine and cosine computation on the other hand is a complex task and is discussed further in this paper.

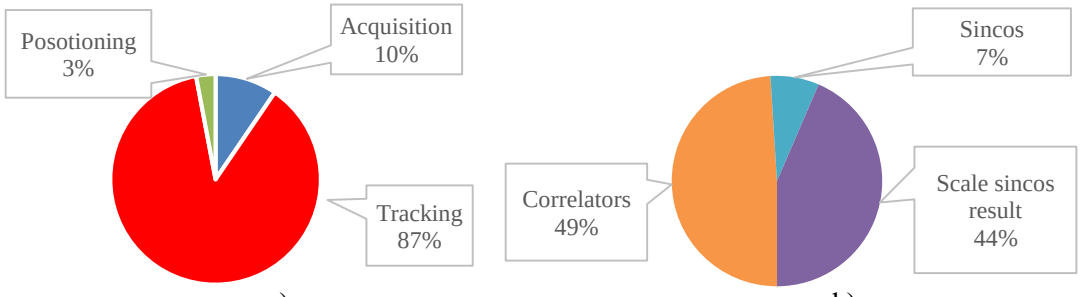

Figure 1. Serial algorithm processing time distribution: a) the whole algorithm, b) tracking only.

4. Possible architectures and details of implementation

There are several possible architectures in this study. Using only FPGA or only HPS is not considered. The simplest solution is creating custom FPGA-based operation modules to expand the main assembler instruction set (figure 2a). For example, matrix operations can be implemented. As mentioned, position calculation uses least squares method which involves linearized equation system solving. It's described by the formula:

$$A^T Ax = A^T b \quad (1)$$

This task requires LU, QR or similar algorithms requiring much CPU time. Executing such algorithm using FPGA frees the HPS for performing other tasks.

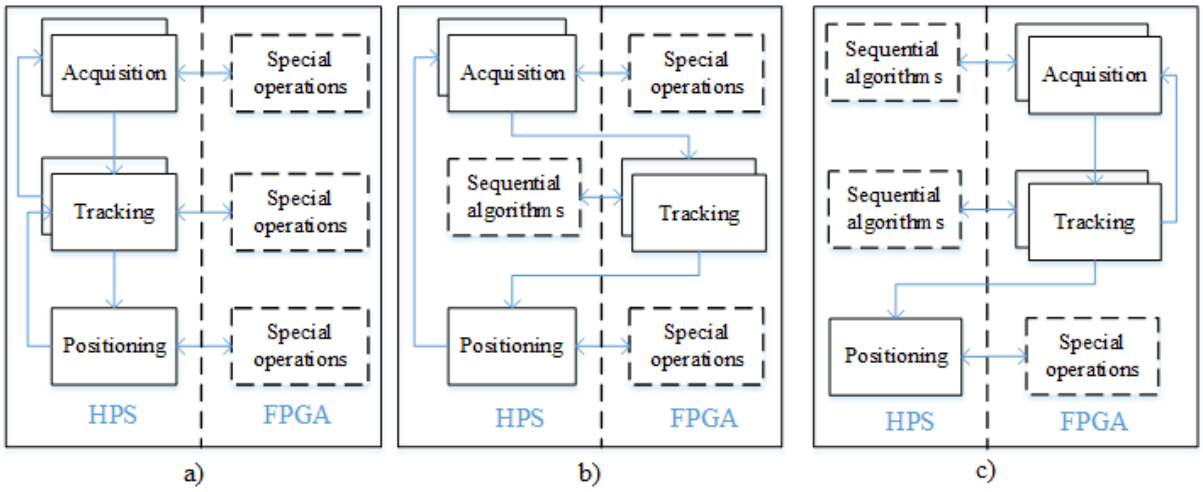

Figure 2. Possible SoC GNSS receiver architecture.

In the second architecture (figure 2b) the entire tracking stage is implemented in an FPGA. In this case HPS executes signal acquisition and position computation. After the signal is acquired, its parameters are transferred into a tracking module following signal changes as long as it is available. If the signal is lost, the module sets a flag making the HPS to try reacquisition. As soon as enough navigation data is available, the HPS starts position calculating. It may be assisted by FPGA-executed instructions.

The third architecture (figure 2c) performs both acquisition and tracking in FPGA. The acquisition module constantly tries to acquire all available signals, which are not found yet. Acquired signals are automatically tracked by the tracking modules. These modules may use assistance of the HPS to perform serial algorithms, though this may slow down the process. When there is enough data, the position calculation algorithm is performed by the HPS. It can be assisted by FPGA-based operations.

5. Possible tracking solutions

Since the tracking stage is the heaviest computational load, this paper proposes using the second architecture (figure 2b). Tracking has the structure shown on schematic diagram (figure 3).

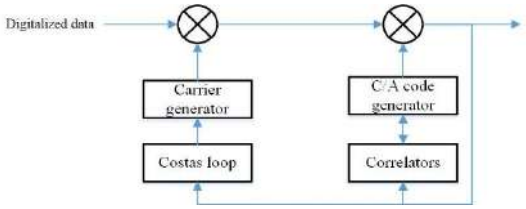

Figure 3. Tracking stage.

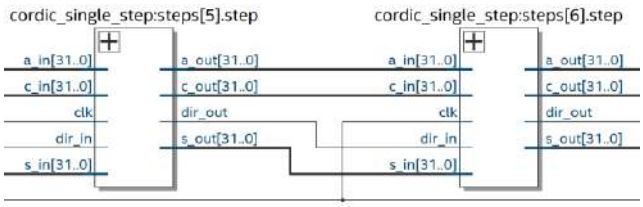

Figure 4. CORDIC rotators connected in series.

The most challenging task is the implementation of trigonometric functions computing in the carrier generator. In this paper a modified CORDIC algorithm has been developed for that purpose. It computes new values based on previous ones. Considering the arguments are supplied in arithmetic progression, with the small difference between adjacent steps. Thus, there is no need to rotate vector by big angles and number of iterations can be reduced. For example, for the difference of 1° number of iterations can be reduced by 6. The computation module is built as a combination of rotator modules as shown in figure 4. The rotator internal structure, generated by Quartus Prime RTL Viewer tool from developed Verilog code is shown in figure 5.

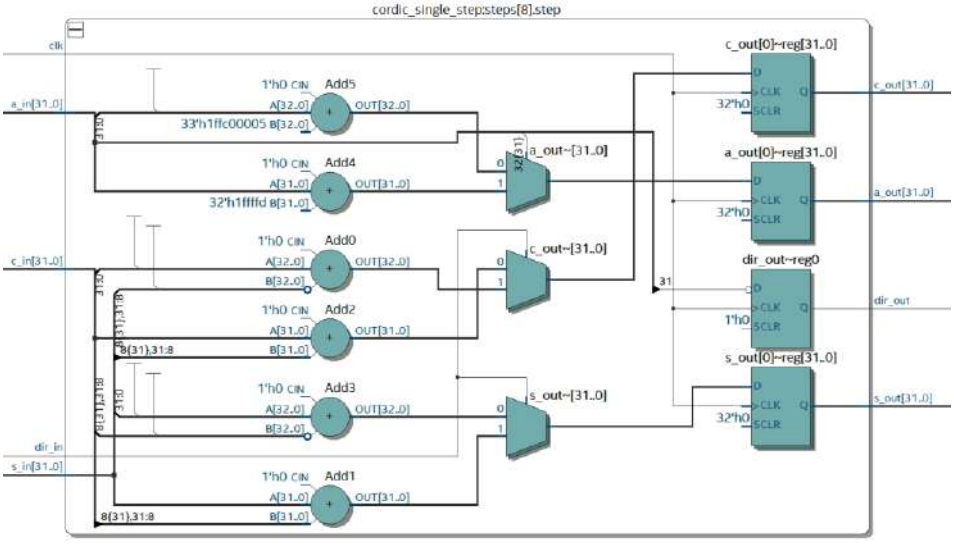

Figure 5. CORDIC rotator internal structure.

6. Discussion

The first architecture is the simplest to implement by a software engineer. It can be as close as needed to processor-only version and has the same logic. It does not require a very sophisticated SoC. The performance gain of this architecture depends on FPGA-based operations set and their implementation. For example, calculating the sum of more than 20 thousand complex numbers elements for each signal in every 1ms period of the signal is a heavy computational load and takes about 80% of time. This task could be executed in parallel by FPGA, drastically reducing operational time. The number of adders, that can be synthesized is limited only by the quantity of available logic cells. However, the HPS is still heavily loaded by signal gathering which have to be done with relatively low latency due to the limited input data buffers' capacity.

The second architecture allows much more freedom for HPS because tracking is executed without involving processor core. It allows the HPS to perform other important tasks, not necessarily navigational. The position calculation routine is typically called once per second. Reacquisition and search of new signals are not frequent tasks either. Thus, this architecture allows using HPS as a system CPU, not just for positioning.

The third architecture allows executing heavy computational loads other than navigation. Moreover, the HPS can postpone its navigational tasks in favor of more urgent tasks without substantial loss of performance. However, such architecture requires much more logic cells, which implies using high-consuming FPGAs, which could be inacceptable sometimes.

In each architecture it should be taken into account, that FPGA is limited in using floating point arithmetic. Some FPGA provide DSP latches, which contain hardware adders and multipliers. However, the number of such latches is limited. In addition, operations like root, sine, cosine etc. should be implemented in logic cell usage-efficient way. For example, CORDIC can be used. Thus, the developer should choose the architecture based on the amount of available logic cells, channel number and latency requirements.

Since the choice of the most appropriate architecture depends on the number of channels, complexity of the signal processing algorithms and the power of used HPS and programmable logic, it looks reasonable to compare software and hardware implementations of the critical computational blocks. The most time-consuming part, which has to be executed cyclically to avoid data loss, is tracking. In fact, the main task of tracking is to monitor Doppler frequency and code delay changes with subsequent determination of bit boundaries. In most cases, position calculation is usually performed in the moments when a new data word is received and decoded. The idea of the algorithm, used for GPS, is the following:

1. Calculation of IP/QP, IL/QL, IE/QE for a chunk of data, equal at least to one signal period (1ms);
2. Correction of the phase and frequency of local code and carrier generators;
3. Determination of a phase change on the bit boundary (if any) on every 20th signal period;

4. Collection of the received bits with grouping them into words with parity check;
5. Collection of the words in data blocks with subsequent data extraction;
6. Preparing data for a pseudorange calculation.

These steps are performed every signal period, however, steps 3-6 are performed relatively rare, thus the main computational burden is confined in the steps 1 and 2. To demonstrate C++ implementation, used by the authors it is reasonable to look only at the most "heavy" loop, shown in Fig. 7.

```
for (unsigned int i = 0; i < Size; i++)
{
        Tm += Mult;                     // Elementary phase
        cosT = cos(Tm);
        sinT = sin(Tm);
        V = Datt[i].I;                  // Data[] is an array of data samples
        W = -Datt[i].Q;                 // I and Q are real and imaginary parts
        ICON = cosT*V - W*sinT;
        QCON = sinT*V + W*cosT;
        TauCode += CodeTau;
        Tx = TauCode - Spacing;         // Data spacing for the code dicriminator
        if (Tx < 0) Tx = 1023.0 + Tx;
        if (C_A[(unsigned int)Tx] == 1){
                IE += ICON;
                QE += QCON;
        }else{
                IE -= ICON;
                QE -= QCON;
        }
        … To save space here, similar operations with IP/QP and IL/QL are omitted
}
```

Figure 7. Code fragment of the main part of tracking implementation.

It could be seen that the main computational load here is concentrated in sine and cosine calculation. It is worth to notice that we use floating-point variables of the double size. Intel did not modify the implementation of sine and cosine computation for a long time and the only acceleration, which we can achieve here, is a combined cosine/sine computation, using *fsincos* instruction [13]. This instruction takes about 100-200 CPU cycles depending on an architecture and argument type. Variable `Size` in the experiment varies in the range from 30000 to 50000 depending on sampling frequency of RF Front-End. Intel CPU implementation of the code above could involve some low-level improvements of the code, for example, using SIMD extensions allows parallel execution of arithmetic operations for `IP/QP` and other variables. We do not discuss here cash memory issues, like false sharing and other similar ones. Using debugging tools, one can see that these sine/cosine computations takes about 70-80% of the whole time, thus it is reasonable to select this operation and accelerate it using hardware implementation. This paper considers using coordinate rotation digital computer (CORDIC) algorithm [14]. It allows simultaneous sine and cosine computation without explicit multiplication operations. Since the angle changing step remains constant during cycle (figure 5), an optimized algorithm can be used: the microrotation directions can be calculated once before executing main loop. Thus, proposed FPGA implementation scheme is shown in figure 3 and 4.

Each iteration increases the accuracy. The result is provided on the adder/subtractor output. The number of iterations usually equals to the desired result size *s*. Therefore, serial computation requires about *s* times *Size* cycles.

It has to be noted that FPGA allows pipeline implementation of this algorithm. The latency of the CORDIC would be about s + 2 due to the necessity of scaling the output data. The overall cycle iteration duration is estimated as 5 cycles in pipeline implementation. Serial computation uses about 20 macro operations or about 230 cycles. This makes the operational time of 50MHz FPGA execution comparable to 2.3 GHz CPU serial execution in a single thread. A CPU implementation typically uses sequential tracking channel-after-channel or using several processor cores in parallel. The number of available cores is usually less than required number of tracking channels, that reduces overall performance. FPGA, on the contrary, relatively easily provides any required number of processing modules even for multisystem GNSS receivers. This boosts computation performance drastically, allowing the HPS to perform other tasks.

Thus, FPGA implementation and partial execution of certain GNSS receiver algorithms assists HPS, allowing reducing computational load in comparison with a CPU-only solution. Multichannel pipeline architecture allows fast execution of the heaviest parts of the algorithm.

7. References

[1] Shafran S V, Gizatulova E A, Kudryavtsev I A 2018 Snapshot technology in GNSS receivers *25th Saint Petersburg International Conference on Integrated Navigation Systems* 1-3
[2] Guruprasad S 2016 Feature Article: Design and Implementation of a Low-Cost SoC-Based *Software GNSS Receiver* **10** 14-19
[3] Wang B S 2011 A new solution to GNSS receiver baseband signal processing SoC platform based on OpenRISC processor *7th International Conference on Wireless Communications, Networking and Mobile Computing, WiCOM* 1-4
[4] Wang E 2008 Implementation of an Embedded GPS Receiver Based on FPGA and Micro Blaze *Wireless Communications, Networking and Mobile Computing. Dalian, China* 2008-2011
[5] Fridman A, Semenov S 2013 System-on-Chip FPGA-based GNSS receiver *Proceedings of IEEE East-West Design and Test Symposium, EWDTS* 1-7
[6] Kappen G, Noll T G 2006 Application Specific Instruction Processor Based Implementation of a GNSS Receiver on an FPGA *Proceedings of the Design Automation & Test in Europe Conference* 2-7
[7] Namassivaya N, Pal S and Ratnam D V 2018 Design of Software-based Global Navigation Satellite System Receiver for Satellite Applications *IETE J. Res.* (Taylor & Francis) 1-10
[8] Engel F 2004 An Open GNSS Receiver Platform Architecture *J. Glob. Position. Syst.* **3(1-2)** 63-69
[9] Rodriguez S 2017 Design of a dual-antenna and dual-band GPS receiver for CubeSats *IEEE URUCON* (Montevideo, Uruguay) 1-4
[10] Psiaki M L 2001 Block Acquisition of Weak GPS Signals in a Software Receiver *Proceedings of ION GPS* 1-13
[11] Guruprasad S 2016 Design and Implementation of a Low-Cost SoC-Based Software GNSS Receiver *IEEE Aerospace and Electronic Systems Magazine* **31(4)** 14-19
[12] Borre K *Easy Suite* URL: https://ssau.ru/english/easysuite/ (27.06.2019)
[13] Agner Fog *Lists of instruction latencies, throughputs and micro-operation breakdowns for Intel, AMD and VIA CPUs* URL: www.agner.org/optimize/ (01.02.2019)
[14] Meher P K, Member S and Park S Y 2013 CORDIC Designs for Fixed Angle of Rotation *IEEE transactions on very large scale integration systems* **21(2)** 217-228

Data mining algorithms in the task of diagnosing the welded joints quality

R R Akhmedyanov[1], K F Tagirova[1], A M Vulfin[1], V V Berkholts[1] and R Ch Gayanov[2]

[1]Ufa State Aviation Technical University, K. Marks st., 12, Ufa, Russia, 450077
[2]Higher School of Economics, Myasnitskaya str., 20, Moscow, Russia, 101000

e-mail: vulfin.alexey@gmail.com

Abstract. The paper discusses the issue of creating an intelligent diagnostic system for welded joints based on the radiographic method. This will speed up the process of decoding radiographic images and reduce the number of errors associated with human factors, since at this time most of the work on decoding images is done manually.
The goal of the work is to develop an intelligent system for finding defects in a welded joint in a radiographic image using neural networks. The obtained results are the algorithm of operation of the intelligent diagnostic system for welded joints based on the radiographic method, a trained neural network for detecting defects of welded joints.

1. Introduction

When performing welding work, it is obligatory according to the current regulatory documents to conduct radiographic inspection of welded joints. The most common type of radiographic inspection is to obtain X-rays of the welds. The conclusion about the quality of the test compound is made by a flaw detector technologist based on the results of X-ray image decoding. Most of the mistakes made during such control are due to the fatigue of people employed in repeated visual checks.

The object of the study are welded joints made by melting the metals being welded. The subject of research is the quality control of welded joints using an intelligent system.

The goal of the work is the development, research and implementation of digital image processing algorithms in the system for diagnostics of welded joints based on the radiographic method.

To achieve the goal, the following tasks were set:

- Development of the structure of the defects recognition system in welded joints based on the analysis of images of radiographic images of welded joints using a neural network;
- Development of an algorithmic and software implementation of the localization of defects in welded joints using a neural network.

2. Development of the structure of the system for detecting defects of welded joints based on image analysis

Radiographic control (Radio-graphic method of NDT) is a method of radiation non-destructive testing (NTD), based on the transformation of the image of the monitored object into a radiographic image or recording of this image on a memory device and subsequent conversion to a light image [1, 18].

Radiographic control is carried out in order to identify surfacing and welded joints (seam and heat-affected zone):

- cracks;
- lack of fusion;
- pores;
- metal and non-metallic inclusions, the density of which differs from the density of the welded joint metal (tungsten, slag, oxide, etc.);
- inaccessible for external inspection of undercuts, burn-throughs, etc. [2].

The process of radiographic inspection of a welded joint is shown in Figure 1.

- analysis of signals characterized by a high degree of uncertainty, e.g., "non-stochastic" type, which includes most biomedical signals, including ECS;
- increasing the level of intelligent assistance of medical specialists;
- revealing hidden regularities and extracting new knowledge from the accumulated data, which will allow to build production systems of explaining the diagnostic solutions.

The process of radiographic inspection of a welded joint is shown in Figure 1.

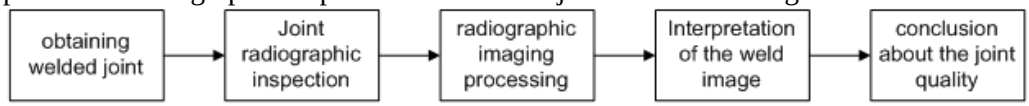

Figure 1. Block diagram of the process of radiographic control.

Interpretation of X-rays of welded joints is carried out in a visual way. This leads to the fact that subjective factors affect the results of the monitoring and, as a result, the quality of the decoding of images and the reliability of the results of the monitoring are significantly reduced. A large amount of work performed by a person leads to the fact that the process of flaw detection takes a long time and lags far behind the performance of the main process - welding of the product.

According to the standard "GOST 30242-97 Defects of compounds during fusion welding. Classification, designations and definitions" [3] defects are classified into six groups. In this research, such defects as "pores", "inclusions" and "lack of fusion" are considered.

Interpretation a radiographic image can be extremely difficult if it is too light or dark. In such a picture it is impossible to detect fine details, which may affect the detectability of the defect. To increase the probability of detecting a defect in a welded joint, it is necessary that the dark and light areas of the image of the welded joint do not exceed the working density range. According to the standards "GOST 7512-82" [4] and the unified methodology for radiographic control "PNAE G-7-017-89" optical density of the image should not be less than 1.5 B and not more than 3.5 B.

In case of deviation from specifications and regulatory documents, violations of the welding process, as well as lack of qualifications of the welder, defects in welded joints occur.

According to the standard "GOST 30242-97 Defects of compounds during fusion welding. Classification, designations and definitions" defects in welding metals by fusion are formed due to violation of the requirements of regulatory documents for welding materials, preparation, assembly and welding of the elements being joined, thermal and mechanical processing of welded joints and the design as a whole [11].

In this standard, defects are classified into six groups, as shown in Figure 2.

Cracks are the most dangerous defects of a welded joint; their appearance is not permissible (Figure 3). Cracks are divided into external and internal.

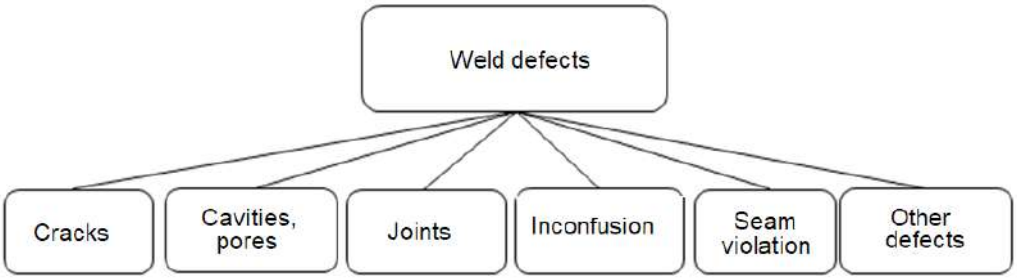

Figure 2. Classification of defects in welded joints.

The formation of cracks occurs as a result of uneven heating, cooling and shrinkage in the metal when welding a welded joint. Also in high carbon and alloy steels, cracks may form as a result of the hardening of the metal after welding [8]. Cracks are divided by size into macro and microscopic ones, and, depending on the origin, into cold and hot. By location: transverse and longitudinal.

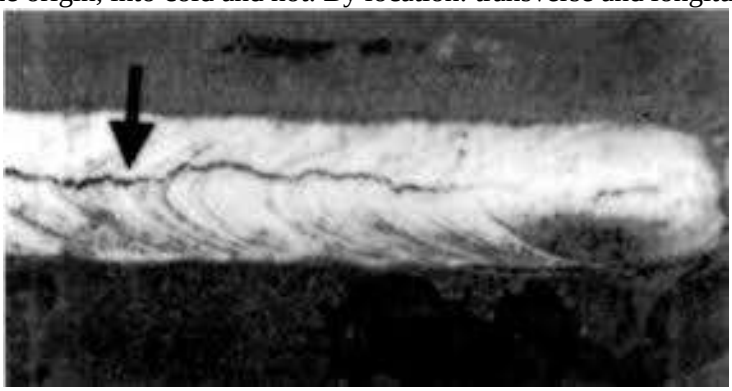

Figure 3. Crack in welded joint.

The formation of internal and surface pores is associated with the ingress of gases, nitrogen, hydrogen, carbon dioxide, etc.) into the weld metal during welding (Figure 4). Pores with nitrogen are formed due to the ingress of atmospheric air into the weld metal with poor-quality protection. Hydrogen is formed due to the ingress of moisture, oils and electrode coating components. Carbon dioxide is formed in the process of welding a welded joint when carbon burns in the metal of the product being welded. The main reason for the appearance of pores is the poor preparation of welded edges, the presence of dirt, rust, moisture, oils, the use of raw electrodes [8].

Pores can be distributed in a welded joint as follows:

- uniformly over the entire length of the welded joint;
- congestion in a separate area;
- chained.

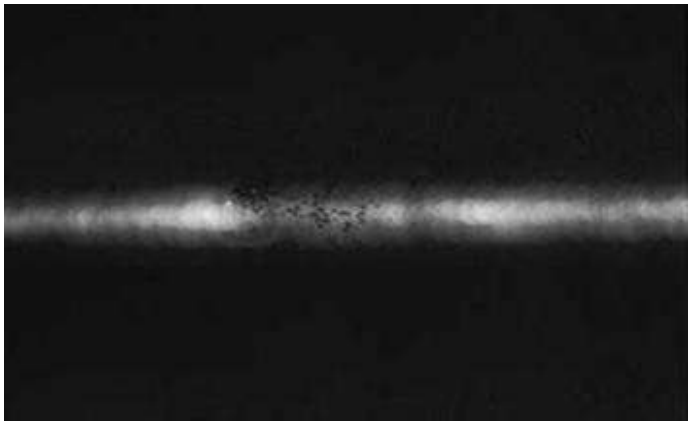

Figure 4. Gas pores accumulation.

The formation of nonmetallic inclusions is characterized by the use of small welding currents, low quality electrodes, welding wire, flux, as well as when the edges are contaminated and the slag is poorly cleaned from welding during multi-layer welding (Figure 5) [5]. There are the following types of inclusions:

- slag inclusions;
- flux inclusions;
- oxide inclusions;
- metal inclusions.

Negative factors of inclusions are the weakening of the cross section of the seam and the decrease in strength and ductility of the welded joint.

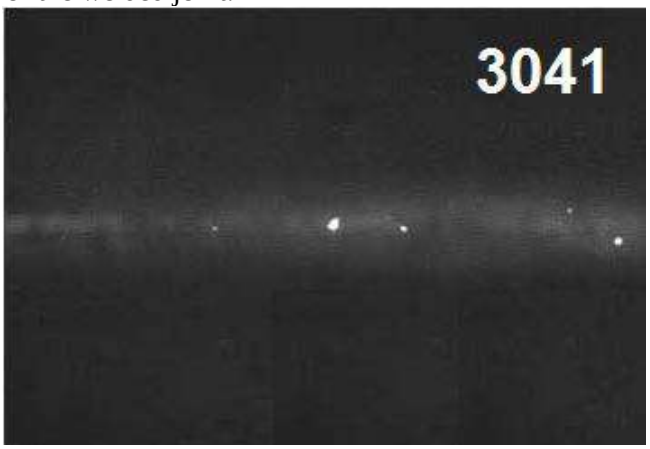

Figure 5. Slag inclusions.

Leakage is a defect in the form of non-fusion in a welded joint (Figure 6) due to incomplete melting of the edges of the base metal or surfaces of previously made weld beads [1].

The sagging is the result of the deposition of the deposited metal on the unheated surface of the base metal or the roller previously made without fusing with it. Such defects can be with low qualification of the welder, poor-quality electrodes and mismatch of the welding speed and welding current to weld seam [8].

Figure 6. Inconfusion of welted joint.

Violation of the seam shape is expressed in the discrepancy between the height and width of the seam and abrupt transition from the base metal to the weld metal (Figure 7). These defects are the result of poor preparation of welded edges, poor build quality for welding.

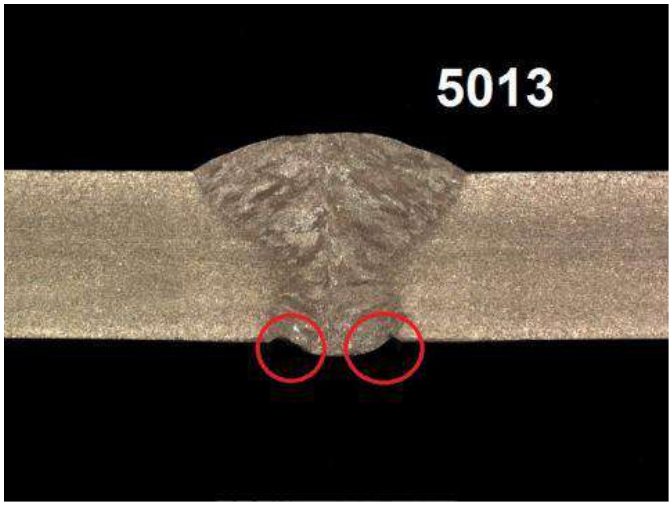

Figure 7. Shrinkage groove.

Violations of the seam shape include the following defects:

- undercuts;
- shrinkage grooves;
- Excess convexity butt and fillet welds;
- excess of the fusion;
- wrong seam profile
- linear and angular displacements of welded elements;
- leaking;
- burnout;
- not completely filled cutting edges;
- excessive asymmetry of the corner seam;
- uneven joint width;
- uneven surface;
- concavity of the root of the weld.

3. Radiographic image quality analysis

The quality of the radiographic image is determined by the following parameters:

- optical density of blackening;
- contrast;
- image sharpness.

Decoding a radiographic image can be extremely difficult if it is too light or dark. In such a picture it is impossible to detect fine details, which may affect the detectability of the defect. To improve the quality of detection of a defect in a welded joint, it is necessary that the dark and light areas of the image of the welded joint should not exceed the working density range. According to the standards, GOST 7512-82 and the unified methodology for radiographic monitoring of the PNAE G-7-017-89, the optical density of the image should not be less than 1.5 B and not more than 3.5 B.

The actual sensitivity of the control depends on the degree of detection of small defects. The defining parameters of the real sensitivity control are the contrast and sharpness of the image.

The contrast of the image in the picture is determined by the formula 1:

$$\Delta D_o = D_{o2} - D_{o1}, \quad (1)$$

where D_{o2} and D_{o1} are the optical density of the image parts.

The visual assessment of the contrast of the image depends largely on the human factor, and specifically on the physiological and psychological characteristics. The contrast of the image or the minimum difference between the two areas in the image that the human eye is able to distinguish is 0.02 - 0.04.

The sharpness of the image is determined by sharp transitions between the blackening density of the image areas. The greatest sharpness is characterized by a narrow transition from light to dark areas of the image, which gives a significant distinctiveness of the contours of the object. An image with high sharpness has clear contours of the object of translucence and the desired defects of the welded joint, which ensures their detectability.

With a wide transition between the areas, a blur of the contours of the object is formed, which greatly affects the detectability.

For registration of closely spaced defects, the resolution of the radiographic film is not unimportant. The fine-grained films have the highest resolution, their use ensures a good detectability of defects.

The following factors influence the sensitivity of radiographic monitoring (Table 1):

- geometric conditions of scanning;
- the shape of the defect and its location relative to the direction of transmission;
- X-ray stiffness, thickness and density of the translucent material;
- characteristics of the film and the correctness of its photo processing after exposure;
- The use of reinforcing screens.

The amount of unsharpness is determined by:

- geometric blur;
- internal detector blurriness.

According to PNAE G-7-010-89, images allowed for decoding should meet the following requirements:

- on the image of the seam and the controlled heat-affected zone there should be no spots, stripes, dirt and damage to the emulsion layer;
- the pictures should be visible clear images of restrictive labels, marks and standards of sensitivity (except for cases provided by this method, when the control is carried out without the installation of restrictive marks or marks, or standards of sensitivity, or both);
- the optical density of the images of the controlled areas of the weld and the heat-affected zone, as well as the sensitivity standards, should not be less than 1.5 and more than 3.5 (when monitoring welded joints with a variable cross-section, it is possible to increase the optical density of images of the welded joint sections with a minimum thickness of 4.0);
- reduction of the optical density of the image of the seam and the controlled heat-affected zone on any part of this image with respect to the optical density of the image of the sensitivity standard (or the area on which the sensitivity standard is installed) must not exceed 1.0;
- control sensitivity determined from the image of the sensitivity standard (minimum depth of the groove of the groove pattern or minimum wire diameter of the wire standard visible in the picture) must meet the requirements of ПНАЭ Г-7-010-89 [2].

Table 1. Factors affecting the quality of the radiographic image.

Radiographic contrast		**Resolution**	
Contrast due to transmission	**Film contrast**	**Geometric blur**	**Film grain**
Affect: - product parameters (density, chemical composition, thickness); - radiation rigidity; - - diffuse	Affect: - type of film; - technology of photo processing; - optical density, the presence and type of screens (fluorescent,	Affect: - the size of the focal spot; - distance source - film: - distance product - film,	Affect: - type of film; - type of screens; - radiation rigidity; - photo processing technology.

radiation	lead); - charging circuit cassette.	- differential thickness of the product; - the quality of the contact between the screens and the film, - clean screens; - - object displacement relative to film	

Weld seams, images that are not approved for decoding, must be re-examined.

4. Automation of the process of diagnosing the quality of a welded joint based on the radiographic method

4.1. Description of the algorithm of the process of diagnosing the quality of a welded joint based on radiographic monitoring

The block diagram of the system of diagnostics of welded joints is shown in Figure 3, the algorithm of the system is shown in Figure 8.

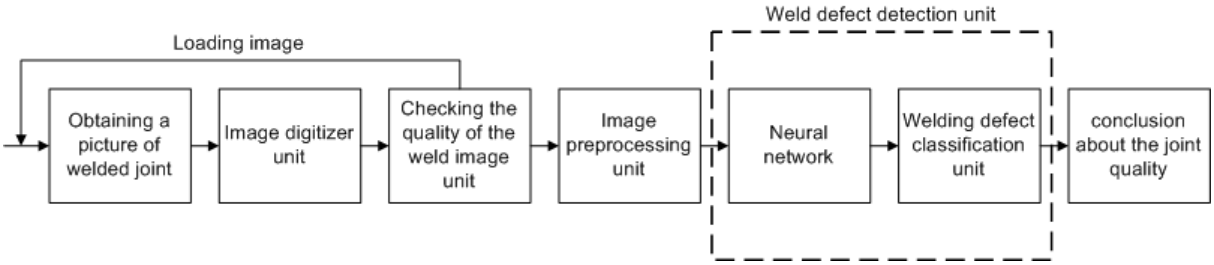

Figure 8. Block diagram of the system diagnostics of welded joints.

The image obtained during digitization must be transferred from color to halftone, noise must be removed and the contrast of the image must be increased for further work.

Images entered into a computer are often low-contrast. Often, low contrast is caused by a large range of reproducible brightness with non-linearity of the level transfer characteristic. The dependence of the brightness of pixels on the minimum value to the maximum also affects the image quality. The optimal is the linear form of the function of changing the intensity of the brightness of pixels. With a convex characteristic, the image will be brighter, and with a more concave dark. In both cases, the attributes of objects can be distorted and their recognition can be difficult. Correcting the brightness of the image significantly improves its quality.

4.2. Algorithm of the process of determining the weld image quality

In radiographic control, one of the stages preceding the decoding of the image is the determination of the quality of the image and its compliance with all the necessary requirements. One of the requirements is the compliance of the optical density of the images of the controlled areas of the weld and the heat-affected zone, as well as the standards of sensitivity (Figure 10).

The ratio of the amount of incoming light to the amount of light passing through a certain area is called the optical density of the film and is determined by the formula (2):

$$D = log\frac{I_0}{I_1} \qquad (2)$$

where D – optical density; I_0 – intensity of light falling on the film; I_1 – intensity of light emanating from this part of the film.

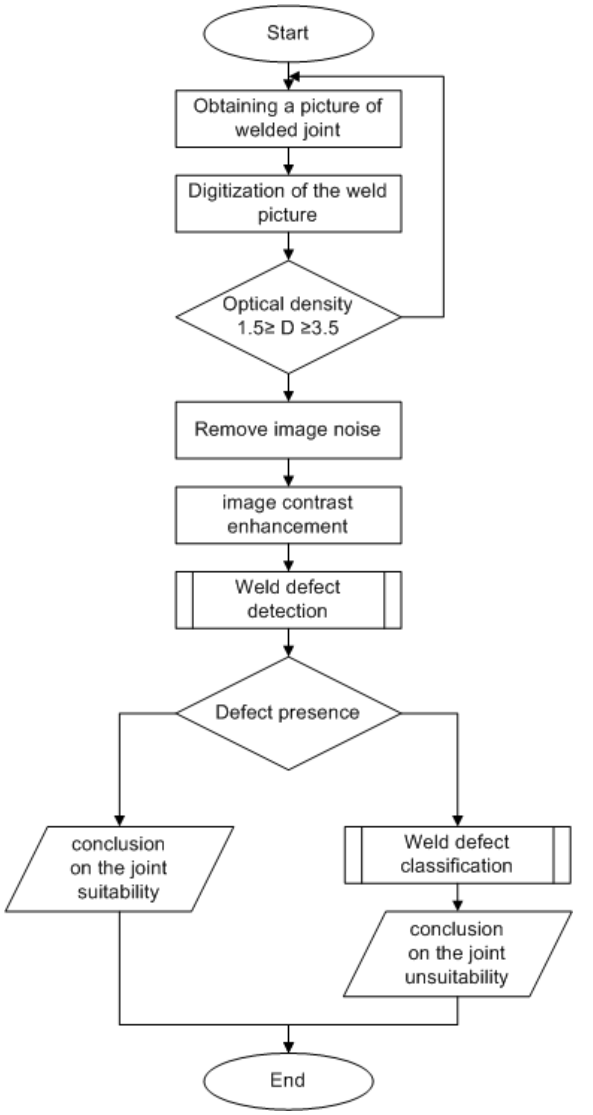

Figure 9. Graphic diagram of the algorithm for diagnosing a welded joint based on the radiographic method.

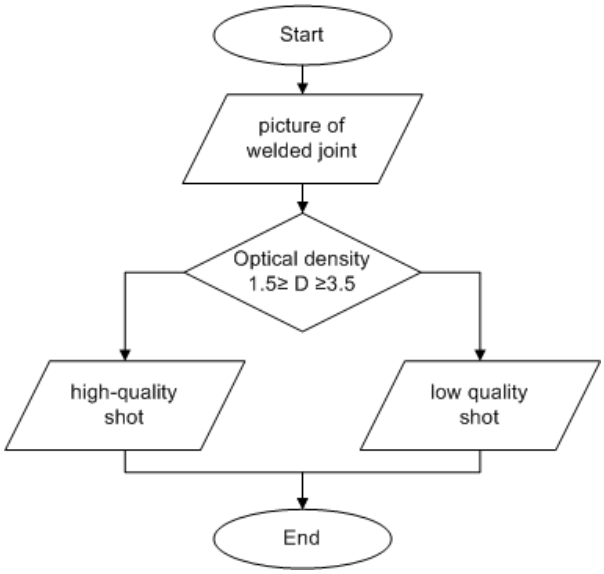

Figure 10. Algorithm for assessing the quality of a radiographic image.

The dependence of optical density and exposure is represented as a graphical characteristic. The curve reflects the ratio of the logarithms of the relative exposures to the resulting optical densities of the blackening of the film (Figure 11).

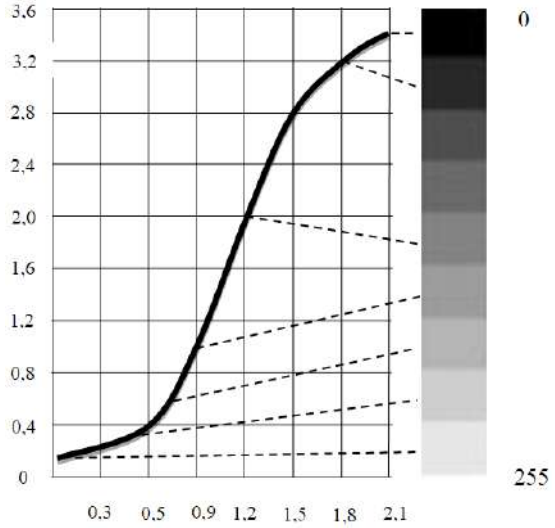

Figure 11. The characteristic curve of the x-ray film.

To automate the process of identifying compliance with the requirements of X-ray films, digitization of the image is necessary. After digitization, it is necessary to convert color (RGB) images to halftone. In a grayscale image, pixel brightness has a uniform scale from 0 to 255. Accordingly, optical density can be represented in arbitrary brightness units, where the value 0 corresponds to the darkest part of the image (black) and 255 the brightest part of the image (white).

According to "PNAE G-7-010-89" [5], the optical density of images of monitored sections of the weld and heat affected zone, as well as sensitivity standards, should not be less than 1.5 and more than 3.5. Accordingly, it is possible to distinguish the working range of optical densities and the corresponding pixel brightness in the zones of monitored areas (Figure 12).

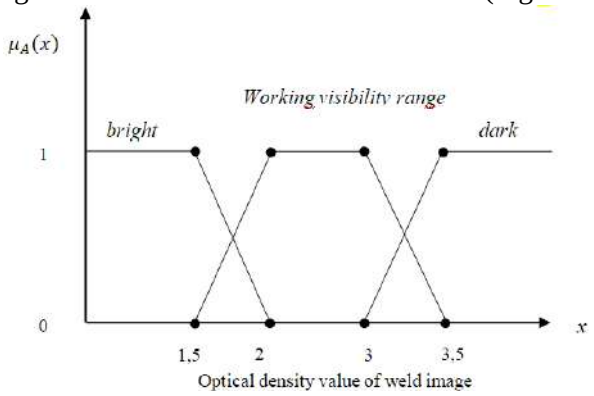

Figure 12. Fuzzy definition of the quality of the weld image.

The graph shows that the useful density range is in the range from 2 to 3 Bell, which corresponds to a pixel brightness of 40 units to 130. The working brightness range provides maximum visibility of defects in welded joints, which significantly affects the control results. Images whose control areas are beyond the allowable values according to "PNAE G-7-010-89" less than 1.5 and more than 3.5 Bell, which is in the pixel brightness range above 155 units and below 20, are considered non-compliant. Control areas of welds whose images did not pass quality control are subject to repeated radiographic control.

5. Experimental studies of the automated system for diagnosing the quality of welded joints

To test the developed recognition algorithms, a compiled database of images of radiographic images of welded joints was used, containing images of defects, as well as corresponding tags. For the training of classifiers 900 images were used, each image in the area of the defect is marked with labels of the area of interest (ROI label).

Three types of markers of areas of interest (ROI) were created corresponding to defects on the image array of welded joints:

- lack of fusion;
- pores;
- inclusions;

Marks of interest were placed on each image with the intended location of the corresponding defect (Figure 13-15).

A defect in the form of a “pore” is characterized by a small area of darkening of a spherical shape on the image of a welded joint, in most cases in this sample of images of welded joints, the pores are in a group.

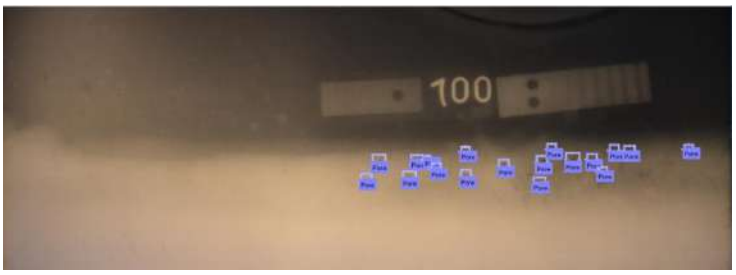

Figure 13. Selection of areas of interest in the form of defects “Pore”.

A defect in the form of “Inclusion” is characterized by a darkening area of a fairly large, irregularly shaped. An example of the selection of the area of interest with a defect in the form of inclusion (Inclusion) is presented in Figure 14.

Figure 14. Selection of areas of interest in the form of defects “Inclusion”.

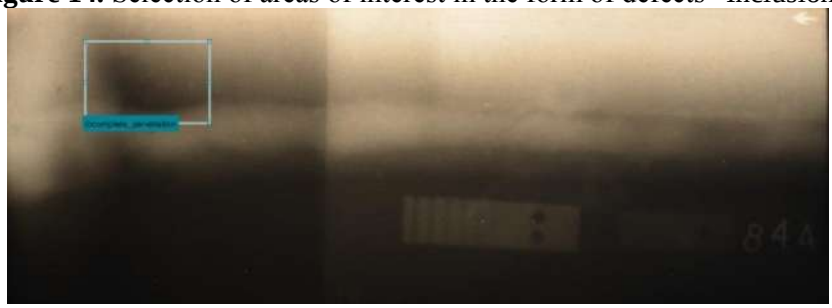

Figure 15. Selection of areas of interest in the form of defects “lack of fusion”.

The defect in the form of “lack of fusion” is characterized by a darkening area of sufficiently large size and length, in some cases along the entire length of the weld. An example of the selection of the region of interest with a defect in the form of “lack of fusion” is presented in Figure 15.

After applying labels of areas of interest to the entire array of images, it is necessary to export the label base using the 'Export Labels' function for further use in training the AlexNet neural network.

5.1. Pre-processing of images when learning neural network

Pre-processing includes the following:

- transferring the image to grayscale, smoothing the image using a median filter and noise removing;
- improving image contrast: adaptive histogram equalization.

The obtained image is color for effective detection of defects in the welded joint is necessary to convert the color image into a halftone.

A median filter was used to smooth the image. A 4x4 matrix is used as a filter mask. Pixels of the original grayscale image corresponding to all elements of the filter mask form an ordered sequence A. Pixel D (r, s), where r and c are the coordinates of the current position of the center element of the mask, is assigned the value of the median of sequence A. The operation is applied non-recursively for all mask positions [6, 7, 21].

To improve the image quality, an equalization of the image histogram was used (Figures 16-17).

a) b)

Figure 16. Image of the radiographic image (a) Original; b) improved contrast with gamma correction).

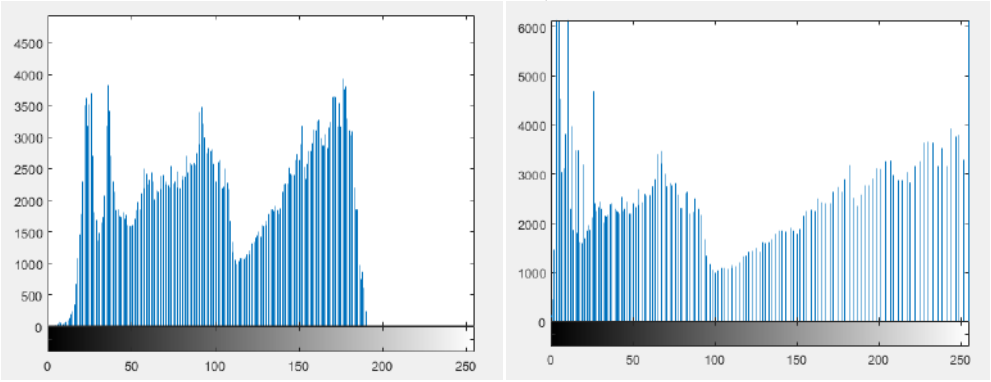

a) b)

Figure 17. Histogram of the brightness of pixels of the image of the radiographic image (a) of the original; b) improved).

Luminance values $0 \leq i \leq 255$ are plotted on the abscissa axis, and $0 \leq f(x) \leq 1$ along the ordinate axis. If the histogram uses a narrow range of brightness, the equalization method allows you to increase the range of brightness of the image. After equalization of the image, its contrast will increase and the image will contain a greater number of semitones.

5.2. Defect recognition results

In this work, the AlexNet convolutional neural network model was implemented and used with the following architecture [7, 19, 20].

In the photographs (Figures 18-22) after the neural network processing, the recognition result is visible, where the area with the recognized defect of the welded joint is highlighted, indicating the degree of confidence in the pattern.

To determine the accuracy of recognition, it is necessary to find out the number of correct recognition of the neural network for each type of defect (Table 2).

For the convenience of calculating the share of correct recognition in the image, the labels of the region of interest are highlighted (ROI Label). Let's consider several examples of images from a test sample with identified defects to determine the accuracy of the diagnostic system [8-14].

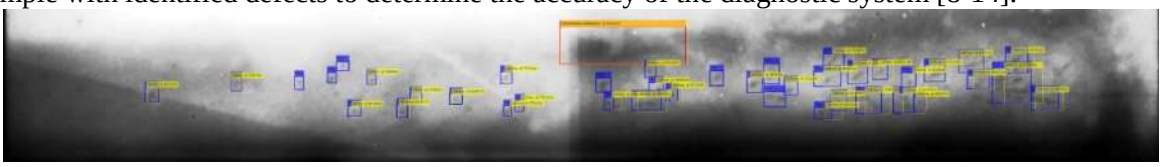

Figure 18. Image No. 1 of a radiographic image with recognized defects like "pore" and "lack of fusion".

For defects found, it is necessary to issue a report and recommendations for repairing the welded joint. An important point is the indication of the possible causes of the defect to enhance the control of the engineering and technical structure of the enterprise over compliance with the welding process and compliance with all technological requirements, which will help avoid the occurrence of defects in welds in the future [15-17].

Conclusion for this snapshot: according to the results, the welded joint is not suitable. It has a large number of defects in the form of "pore" located close enough to each other, just as in the picture there is a defect "lack of fusion".

The cause of the defect in the form of "pore" is the poor quality preparation of the welded edges of the product, the presence of dirt, oil and rust on the surface. Also a possible cause may be poor preparation of the welding material.

The cause of the defect in the form of "lack of fusion" is the incomplete melting of the edges of the base metal due to poor welding material, low quality of the welder, or mismatch of the welding speed and welding current.

Figure 19. Image No. 2 of the radiographic image with the recognized defect "lack of fusion".

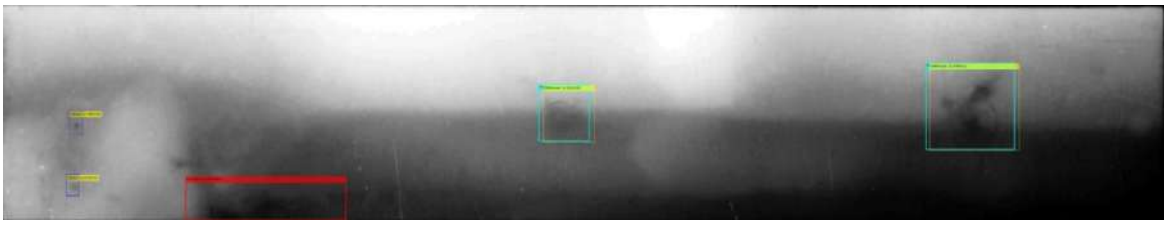

Figure 20. Image No. 3 of a radiographic image with recognized defects of the type "pore", "inclusion" and "lack of fusion".

Figure 21. Image No. 4 of a radiographic image with recognized defects of the type "pore", "inclusion" and "lack of fusion".

In this picture, in addition to defects “pore” and “lack of fusion”, there is a defect “inclusion”. A possible cause of the occurrence of this defect is poor-quality welding materials, contamination of edges, failure to comply with the welding mode.

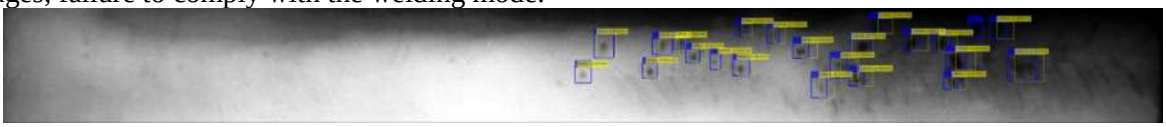

Figure 22. Image No. 5 of a radiographic image with recognized defects of the “Pore” type.

Table 2. Determining the authenticity of recognition for the images.

Picture number	Defect name	Amount	Detected
1	Pore	39	32
	Lack of fusion	1	1
2	Lack of fusion	1	1
3	Pore	2	2
	Inclusion	2	2
	Lack of fusion	1	1
4	Pore	1	1
	Inclusion	1	1
	Lack of fusion	1	1
5	Pore	23	22

Let’s calculate the total accuracy of the test sample of thirty images of defects in welded joints (Table 3).

Table 3. Determination of the reliability of recognition of defects on the test sample of images [11-17].

Defect name	Amount	Detected	Accuracy
Pore	162	143	0,8827
Inclusion	15	14	0,9333
Lack of fusion	22	21	0,9545

According to the data obtained (Table 3), it can be concluded that 88.27% of defects of the first type of pore were correctly classified as pores, 93.33% of defects of the second type of inclusion (Inclusion) were correctly classified as inclusions, 95.45% defects of the third type of incomplete (Incomplete_penetration) were correctly classified as incomplete. Overall, 92.35% of the predictions made by the neural network are correct and 7.65% are erroneous.

6. Conclusions

The paper presents an overview of modern methods of digital image processing and image recognition methods, implemented algorithmic and software, presents the results of modeling a system for detecting defects in welded joints using a neural network.

- The analysis of the methods of obtaining digital images of extended welded joints based on the radiographic method was carried out;
- The typical structures of diagnostic systems and digital image processing algorithms were investigated;
- The structure and principles of functioning of the system for detecting defects in welded joints based on images of radiographic images of welded joints using a neural network have been developed;
- Developed algorithmic and software implementation of the localization of defects in welded joints using a neural network;

- A simulation of the welded joint defect detection system using a neural network was made.

The proposed methods and software system allow you to automate the process of technical diagnostics of welded joints according to the results of radiographic monitoring. The developed algorithm using the neural network allows recognition of defects in welded joints.

7. References

[1] Gorbachev V I, Semenov A P 2007 *Radiographic control of welded joints* (Moscow: Sputnik) p 486
[2] PNAE G-7-017-89 1990 *Unified control methodology of base metals (semi-finished products), welded joints and surfacing of equipment and pipelines. Radiographic control* (Moscow)
[3] GOST 30242-97 1997 *Defects of joints during fusion welding. Classification, notation and definitions* (Moscow)
[4] GOST 7512-82 1982 *Non-destructive control. Welded joints. Radiographic method* (Moscow)
[5] PNAE G-7-010-89 2000 *Equipment and pipelines of nuclear power plants. Welded joints and cladding. Rules of control* (Moscow)
[6] Zapata J 2010 An adaptive network based fuzzy inference system for classification of welding defects *NDT&E International* **43** 191-199
[7] Kozhenkov E V, Lyasin D N 2016 *Research of automated analysis methods of welded joints X-rays* (Volzhskiy)
[8] Valavanis I, Kosmopoulos D 2010 Multiclass defect detection and classification in weld radiographic images using geometric and texture features *Expert Systems with Applications* **37** 7606-7614
[9] Thiruganam M 2010 Automatic Defect Detection and Counting In Radiographic Weldment Images *Int. J. of Comp. Applications* **2(10)** 1-5
[10] Vilar R, Zapata J and Ruiz R 2009 An automatic system of classification of weld defects in radiographic images *NDT&E International* **42** 467-476
[11] Wang X, Wong B S and Tan C S 2010 Recognition of Welding Defects in Radiographic Images by Using Support Vector Machine Classifier *Research Journal of Applied Sciences, Engineering and Technology* **2(3)** 295-301
[12] Mahmoudi A, Regragui F 2009 Welding Defect Detection by Segmentation of Radiographic Images *IEEE Conf. on World Congress on Comp. Science and Inf. Engineering* 111-115
[13] Ghazvini M 2009 Defect Detection of Tiles Using 2D-Wavelet Transform and Statistical Features *World Academy of Science, Engineering and Technology* **49** 901-904
[14] Xiaomeng W 2009 Detection of Weld Line Defect for Oil-gas Pipeline Based on X-rays Image Processing *Proc. Int. Symp. on Web Information Systems and Applications* 273-275
[15] Bishop C M 2006 *Pattern Recognition and Machine Learning* (NY.: Springer) p 738
[16] Gonzalez R, Woods R 2008 Digital Image Processing 3rd edition (Prentice Hall) p 976
[17] Phung S L, Bouzerdoum A 2009 *MATLAB Library for Convolutional Neural Networks. Technical report* (Wollongong) p 20
[18] Gaydel A V, Pervushkin S S 2013 The study of textural signs for the diagnosis of diseases of the bone tissue on X-ray images *Computer Optics* **37(1)** 113-119
[19] Soldatova O P, Garshin A A 2010 Application of convolutional neural network for handwriting recognition *Computer Optics* **34(2)** 252-259
[20] Izotov P Yu, Kazanskiy N L, Golovashkin D L and Sukhanov S V 2011 CUDA-Enable Implementation of a Neural Network Algorithm for Handwritten Digit Recognition *Optical Memory and Neural Networks (Information Optics)* **20(2)** 98-106 DOI: 10.3103/S1060992X11020032
[21] Kalinovskii I A, Spitsyn V G 2016 Review and testing of frontal face detectors *Computer Optics* **40(1)** 99-111

Acknowledgements
This work was supported by the Russian Foundation for Basic Research, research № 17-08-01569.

Decision support system in the task of ensuring information security of automated process control systems

A D Kirillova[1], V I Vasilyev[1], A V Nikonov[1] and V V Berkholts[1]

[1]Ufa State Aviation Technical University, K. Marx str., 12, Ufa, Russia, 450008

e-mail: kirillova.andm@gmail.com

Abstract. The problem of ensuring the information security of an automated process control system (APCS) is considered. An overview of the main regulatory documents on ensuring the safety of automated process control systems is given. For the operative solution of the tasks of ensuring information security of the automated control system of technological processes it is proposed to use an intelligent decision support system (DSS). An example of the construction and implementation of decision rules in the composition of the DSS based on the use of neuro-fuzzy models is considered.

1. Introduction

In recent years, the object of targeted attacks is increasingly becoming industrial enterprises and automated process control systems (APCS). According to the report of Kaspersky Lab, in the first half of 2018, the share of attacks on APCS in the world increased by 3.5% and amounted to 41.2%. For the current year, this figure has increased by 4.6%. According to the research [1, 2], Russia ranks 19th in the list of countries in terms of the percentage of attacks on computers for APCS. The increase in the percentage of attacks on the APCS is mainly associated with a general increase in malicious activity, while any incident of information security violations can lead to serious consequences. Until recently, the main regulatory requirements in the field of safety of APCS in the Russian Federation were:

- requirements of the guidance documents of Russia Federal Service on Technical and Export Control (FSTEC) on key systems of information infrastructure;
- Federal Law No. 256-FZ dated by 21.07.2011 “On safety of fuel and energy complex facilities” [3];
- The Order of Russia FSTEC No. 31 dated by 14.03.2014 “On approving the Requirements to protection in automated production and technological processes control systems at the critically important objects, representing the enhanced danger for the people life and health and for the environment” [4].

Since the beginning of 2018, the Federal Law “On the security of critical information infrastructure of the Russian Federation” № 187-FZ dated by 26.07.2017 came into force [5]. The notion of critical information infrastructure (CII) objects covers such groups of objects as information systems, information-telecommunication networks, automated control and management systems of the Russian Federation subjects, functioning of which is critically important for the state. In accordance with 187-FZ, the information systems of organizations operating in the fields of health, science, transport,

communications, energy, banking and other areas of the financial market, fuel and energy complex, in the field of atomic energy, defense, rocket and space, mining, metallurgical and chemical industries, or organizations that provide the interaction of these systems are subject to mandatory protection, in order to ensure their sustainable functioning when conducting against their computer attacks.

According to the law should be a categorization of CII objects, compiled a national register of significant CII objects, provides for the implementation of mandatory requirements to ensure the safety of significant CII objects, controlled by the state.

In order to concretize the requirements provided by the Federal law 187-FZ, and the conditions for their use, the FSTEC of Russia issued a sub-legal regulatory base:

- The Order of Russia FSTEC No. 235 dated by 21.12.2017 “On approval of requirements for the creation of security systems for significant objects of the critical information infrastructure of the Russian Federation and for ensuring their functioning” [6], containing requirements to structure and functioning of security systems, and also organizational and administrative documents on safety of significant CII objects;
- The Order of Russia FSTEC No. 239 dated by 25.12.2017 “On approval of requirements to providing security of significant objects of the critical information infrastructure of the Russian Federation” [7], which recommendations on safety of significant objects at various stages of their life cycle, and also lists the composition of the basic set of safety measures for significant objects of the CII of various categories of significance.

However, these changes in the legal base, currently there are no formal methods and techniques of qualitative and quantitative assessment of the level of protection and choice of effective countermeasures to ensure full compliance with regulatory requirements to ensure comprehensive information security APCS. This doesn't allow one to fully counteract the influence of a wide range of possible cyber threats on the information resources of organizations and enterprises.

Therefore, it is urgent to develop decision support algorithms, the use of which would improve the efficiency of information security APCS of a particular enterprise.

The purpose of the study in this article is to develop the structure of the decision support system (DSS), implementing the risk assessment of information security APCS.

To achieve this goal should be solved by the following tasks:

1. Development of the DSS structure applicable to the construction of a secure APCS;
2. Development of decision support algorithm in the task of assessing the requirements to ensure the protection of information in the APCS based on artificial intelligence technologies;
3. Evaluation of the possibility of using DSS by an example illustrating the features of the application of the proposed algorithm to the construction of the APCS.

2. Analysis of existing approaches to assessing the level of security of APCS

The solution of the tasks of ensuring information security of the APCS has its own characteristics. This is primarily:

- high uncertainty of initial information and complexity of its receipt;
- the need to consider many of the requirements for information security when evaluating and choosing the best options.

The article [8] deals with the implementation of the system of requirements for ensuring the protection of information of the automated process control system, provided for by Order of Russia FSTEC No. 31. The goal is to develop a formalized methodology for the integrated assessment of compliance with the requirements for ensuring information security in an automated system using the fuzzy inference method and expert assessments. A procedure is proposed for determining the level of significance (criticality) of the information being processed based on a system of fuzzy rules (products), considering the degree of possible damage from the violation of the integrity, availability or confidentiality of information. The use of fuzzy models requires time-consuming configuration of model parameters with the participation of subject matter experts and information security specialists.

When forming the requirements for information security in the APCS by the Order of the Russia FSTEC, it is implied that it is necessary to develop a model of information security threats. It should contain a description of the APCS and current threats to information security.

As a result of analyzing the processes of ensuring information security of an APCS, the following main tasks can be identified, solved with the help of DSS:

- accumulation and systematization of information on information security of APCS;
- assistance in developing recommendations for minimizing the possible information security risks of APCS.

Under the risk refers to the expected potential damage from the impact of an actual threat through vulnerability to a specific information (material) asset.

At the first stage of risk analysis, the level of security of the APCS [2, 7]. In the case of non-compliance with any requirements, for threats that are not subject to the necessary protection measures, a risk assessment is made from the impact of these threats.

Fuzzy neural networks ANFIS are used for quantitative risk assessment.

The process of analyzing the security of automated systems is different in that when assessing information risks, fuzzy values in the form of expert assessments are often used as input data. This necessitates the use of fuzzy models, the main advantage of which is associated with the possibility of using for their development much smaller amounts of information about the simulated system, compared with traditional mathematical models. In this case, the information may be approximate, fuzzy in nature.

To implement a comprehensive risk assessment, it is necessary to build a system of fuzzy production rules. At the same time, the three-factor risk formula is used as a base: Risk (damage) = Threat * Vulnerability * Information (material) resource, where Threat * Vulnerability = Degree of realization of the threat (threat).

3. Development of the DSS structure for assessing the level of information security risk in APCS

The indicators used in the development of DSS for ensuring information security of the APCS can be both quantitative and qualitative. Therefore, there is always uncertainty in making decisions on assessing the risks of information security of the APCS. In this case, to determine the level of information security risk of the APCS, it is proposed to use data mining technologies using a modular (ensemble) neural network [9], which allows you to take into account accumulated experience in assessing the level of protection of the APCS and adjust the parameters of a fuzzy system based on specific expert assessments.

The general architecture of the DSS to ensure information security of the APCS is shown in Figure 1.

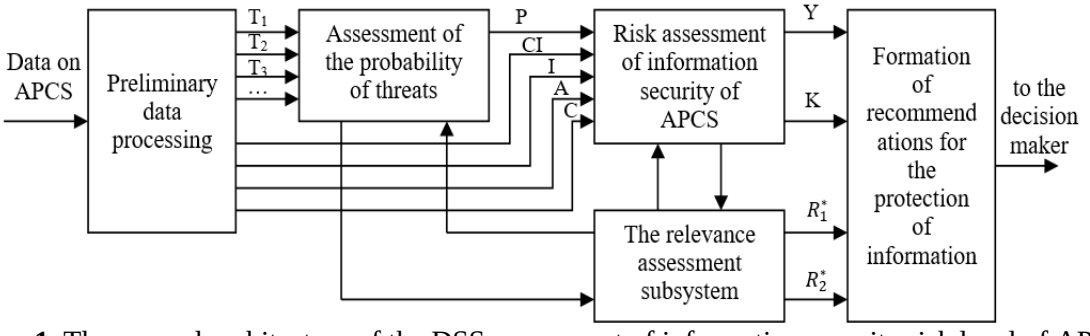

Figure 1. The general architecture of the DSS assessment of information security risk level of APCS.

The module of preliminary data processing on the APCS leads the input values of the modular neural network to a single scale. The inputs of a fuzzy neural network are given indicators of identified information security vulnerabilities of the APCS ($T_1 \div T_4$), indicators of the value of information contained in the system (*CI*), as well as the degree of possible damage in case of breach of confidentiality (*C*), integrity (*I*) or availability (*A*). The neural network determines the probability of realization of the threat P, after which, based on a set of rules, it assesses the risk Y and determines the

security class (*K*) of the APCS. The output data of the rule relevance assessment subsystem are R_1^* – vector of assessments of the contribution of rules to the formation of an assessment of the probability of threats, R_2^* – vector of assessments of the contribution of rules to the formation of an information security risk assessment.

It is assumed that all rules work to some extent, i.e. have a different level of activity. However, exceeding a certain threshold value indicates a significant contribution of certain rules to the result. The selected rules can show which of the parcels are the most suitable and therefore lead to the result.

Based on the obtained security class and risk assessment Y, taking into account the contribution of decision rules to the definition of this assessment, recommendations are made in determining the composition of information protection measures.

The adoption of the correct and timely decision to ensure information security of APCS directly depends on the completeness and correctness of the established rules base. It contains solutions to one or another problem on information security of the APCS, based on the analysis of the subject area and the knowledge of experts. Therefore, the creation of a rules base in the design of DSS is a primary task.

Decision rules can be represented in a fuzzy rules base in the Mamdani fuzzy inference system and have the following form:

R_j: If X_1 is A_1^j and X_2 is A_2^j and … and X_n is A_n^j, then Y_j is B^j, where R_j – *j*-th rule (j = 1,2,…,m); X_i – input variable, (i = 1,2,…,n); Y_j – the result of applying the *j*-th rule A_i^j and B^j – terms (fuzzy subsets).

An important task of the study is to map the set of decision-making tasks to ensure the information security of an APCS on a set of decision-making rules.

The impact of vulnerability on the implementation of a specific threat is reflected in the rules that have the following scheme:

IF Vulnerability – HIGH, THEN the probability of threats – HIGH, etc.

According to this principle, the number of rules of the module for assessing the probability of threats implementation will depend on the number of vulnerabilities, differentiated according to the degree of danger and determining the impact of this threat.

To determine the security class, three input indicators of confidentiality (*C*), integrity (*I*) and availability (*A*) were introduced; at the output of the neural network, we obtain the security class of the APCS.

Input indicators of confidentiality (*C*), integrity (*I*) and availability (*A*) are determined by three linguistic terms, which are evaluated by an expert on a scale from 0 to 1:

L – (0; 0,3) – “Low damage”;

M – [0,3; 0,7] – “Middle damage”;

H – (0,7; 1] – “High damage”.

The security class of the APCS (*K*), which depends on confidentiality, integrity and availability indicators, is also determined by three linguistic terms, the values of which are determined using a neural network based on the rules established by an expert:

L – [0; 0,3] – “First security class”;

M – (0,3; 0,7) – “Second security class”;

H – [0,7; 1] – “Third security class”.

Rules that determine the security class of the APCS listed in Table 1. Since at the input we have three variables *I*, *A* and *C*, defined by three linguistic terms L, M and H, the rule table contains 3^3 =27 rules.

Similar to the definition of the class of security APCS, Figures 2 and 3 show the membership functions and rules that are used to determine the likelihood of realization of threats of information security of APCS.

In the course of the work, the compiled system of rules was implemented in the FuzzyToboxbox package of mathematical modeling in Matlab based on the ensemble of neuro-fuzzy networks ANFIS.

Table 1. The system of rules for determining the security class.

No.	Input indicators			Security class, *K*
	I	*A*	*C*	
1.	L	L	L	L
2.	L	L	M	M
3.	L	L	H	H
4.	L	M	L	M
5.	L	H	L	H
…	…	…	…	…
27.	H	H	H	H

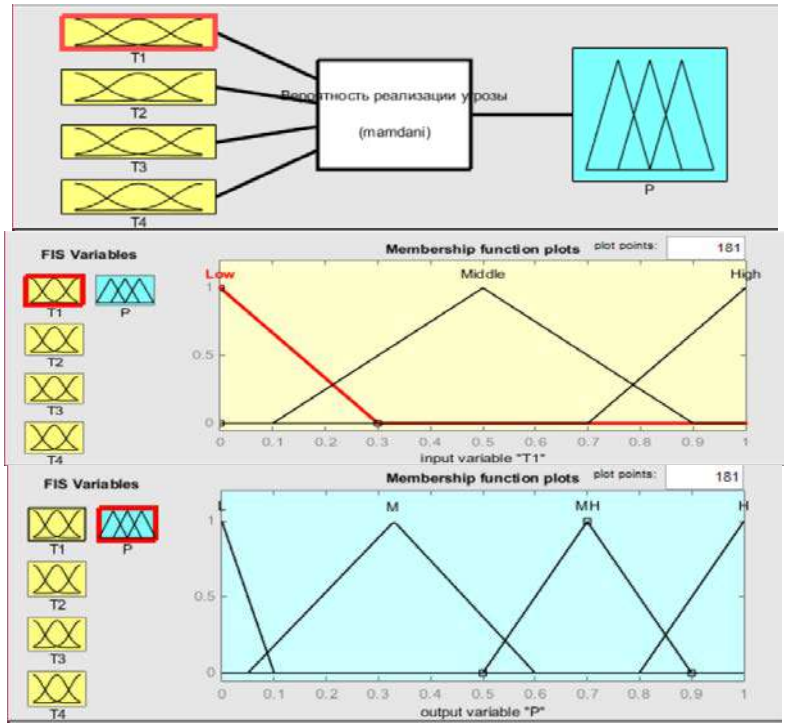

Figure 2. Membership functions in determining the likelihood of a threat.

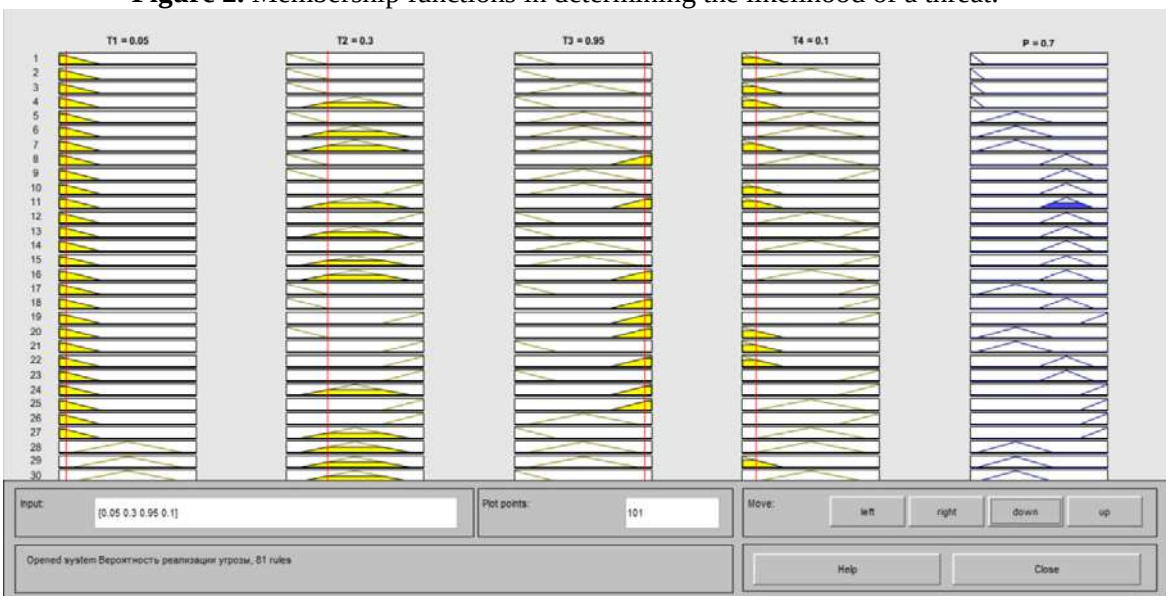

Figure 3. The rules used to determine the likelihood of threats to the information security of APCS.

Table 2. The system of rules for determining the likelihood of a threat.

No.	Input indicators				Probability of the threat, P
	T_1	T_2	T_3	T_4	
1.	L	L	L	L	L
2.	L	L	L	M	L
3.	L	L	M	L	L
4.	L	M	L	L	L
5.	L	L	M	M	M
6.	L	M	M	M	M
…	…	…	…	…	…
81.	H	M	L	M	M

Table 3. The system of rules for assessing the threat of information security of APCS.

No.	Input indicators		Risk assessment, Y
	CI	P	
1.	L	L	L
2.	L	M	L
…	…	…	…
16.	H	H	H

The structure of the ensemble of neuro-fuzzy networks, proposed for solving the problem of information security risk assessment of APCS, is presented in Table 4 and Figure 4:

Table 4. Parameters of the ensemble of neuro-fuzzy networks in the DSS.

Parameter	NFN assessment of security class	NFN assessment of the probability of threats	NFN risk assessment of information security
Number of inputs (input linguistic variables)	4	4	5
Number of terms of each linguistic variable	1	3	2
Number of generated rules	27	81	16
Fuzzy Inference algorithm	Sugeno	Sugeno	Sugeno
Learning iterations	1000	1000	1000
Training sample size	75	75	75
Test sample size	25	25	25
Error on test sample	1e-3	1e-3	1e-3

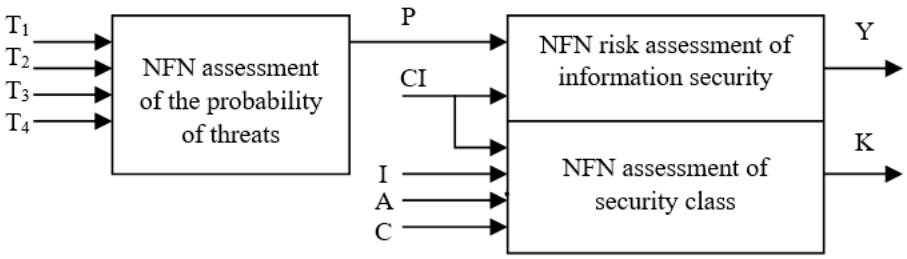

Figure 4. The structure of the ensemble of neuro-fuzzy networks in the DSS.

The training and test samples are based on the basis of expert assessments and contain options for solving the set tasks based on the analysis of the subject area. For the construction of training, sets can also be used data from systems included in the system of information security APCS.

The detailed structure of the network that determines the probability of threats is shown in Figure 5.

The first layer is the terms of the input variables T1÷T4. Input data in this layer is converted to fuzzy. At the output of the layer, we obtain the degree of belonging to the input variable value to a certain term.

The second layer is the antecedents of fuzzy rules. Each node of this layer corresponds to one fuzzy rule. In this case, to determine the probability of threats to be realized, the inference system has 81 rules. The output node of the layer is the degree of execution of the rule $\mu_i(T)$.

The third layer is the conclusion of the rules. The nodes calculate the contribution of the corresponding rule to the network output.

The fourth layer is the combination of the result obtained according to different rules. The node of this layer summarizes the contributions of all the rules.

One of the drawbacks of fuzzy models is the effect of "retraining". The model gives a minimal error on the elements of the training set with a large error on the elements of the testing set. To overcome this drawback, the initial sample is divided into two subsets: training and test.

Increasing the dimension of the input vector of linguistic variables exponentially increases the number of elements of layer 2 of the ANFIS model, as well as the number of adjustable weight coefficients. This makes it difficult to train the model and increases the requirements for the training sample [10].

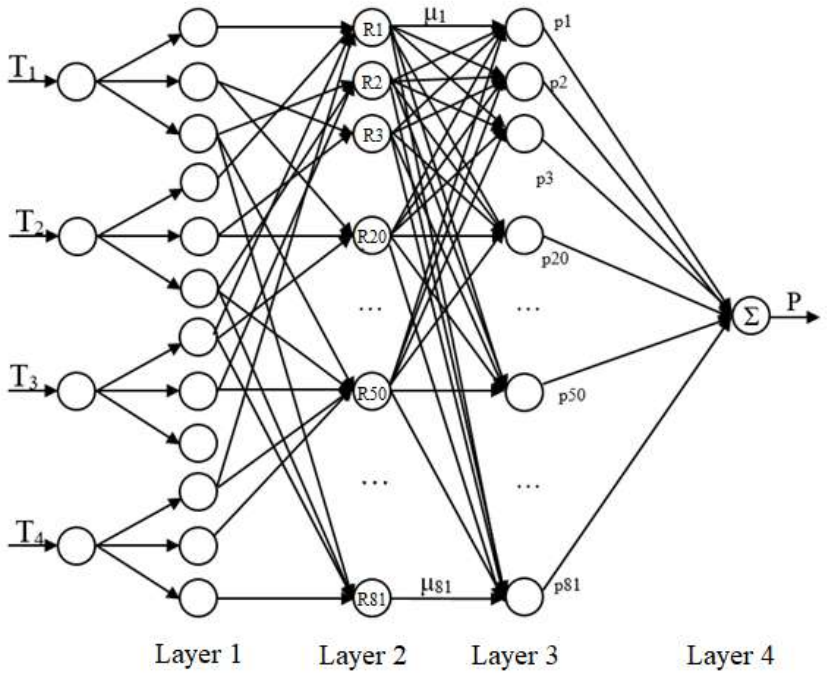

Figure 5. The structure of fuzzy neural network for threat probability assessment.

This paper uses the generation of a fuzzy model using fuzzy clustering (FCM) to reduce the dimension of the second layer of the neuro-fuzzy model ANFIS. When using FCM clustering, it is possible to control the sample size (the number of observations in the sample, the number of input variables) used to build the model, and the type of model (Sugano / Mamdani) [10, 11, 12].

The implementation of the rule system in the Fuzzy Toolbox mathematical modeling package is shown in Figure 6.

In order to formulate recommendations for reducing the level of information security risk in an APCS, all the rules in this case work to varying degrees. But exceeding the threshold value allows you

to select the rules with the most significant contribution to the result. An analysis of the parts of the antecedents of the ranked list of rules makes it possible to identify linguistic variables and their meanings that lead to the current result.

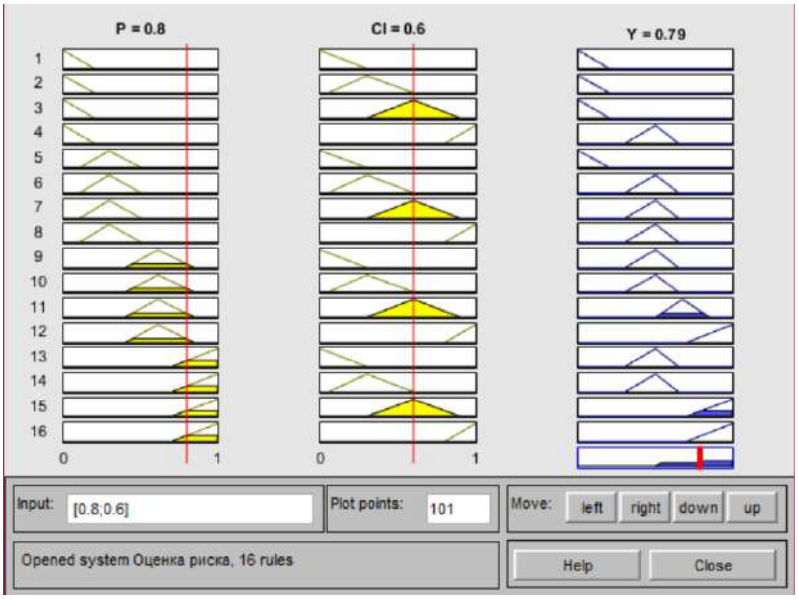

Figure 6. The rules for determining the risk assessment.

As a result of the research, a DSS was built, which allows to assess the level of information security risk of the APCS and issue recommendations for its minimization.

4. Evaluation of the possibility of using DSS

The example of using the developed DSS is illustrated by the example of the APCS, the physical architecture of which is shown in Figure 7. DSS helps to assess the practical implementation of the requirements of information security standards and to ensure the necessary level of security for APCS.

The input data for the DSS are the results of the information security audit conducted at the security facility, which includes security analysis to search for vulnerabilities, analysis of the documentation, structure and configuration of the system. The initial data for the audit are including the results of using network security scanners and the accumulated data of intrusion detection systems [13].

Suppose that according to the results of the audit, the APCS has the following vulnerabilities:

T_1 – Lack of identification and authentication of subjects and objects of access;

T_2 – Incorrect Default Permissions;

T_3 – No perimeter protection of APCS, connection with corporate networks and the Internet;

T_4 – Lack of protection against denial of service attacks. The input parameters of the neural network are defined as follows: $T_1 = 0.3$ (M); $T_2 = 0.1$ (L); $T_3 = 0.6$ (M); $T_4 = 0.95$ (H).

At the same time, the value of information processed and circulated in data transmission networks of the APCS is defined as $CI = 0.6$.

At the output of the neural network, we obtain the values of the probability of the threat realization (P), the information security risk assessment of the APCS (Y), and the vector of assessments of the contribution of rules to the formation of the probability of the threat (R_1^*) and the risk estimate (R_2^*).

As the calculations showed, the probability value of the threat realization is 0.727. This suggests that the probability of a threat acting through these vulnerabilities is above average. In turn, the inputs of a fuzzy neural network to determine the level of information security risk of the APCS are given the values $P = 0.727$ and $CI = 0.6$. With such input indicators at the output of the network, we obtain the value of the risk level equal to 0.537, that is, the risk level is also above average.

Formation of recommendations for reducing the level of information security risk of the APCS is as follows. All the rules in this case work in various degrees but exceeding the threshold value (in this

case it is equal to 0.95) allows you to select the rules with the most significant contribution to the final result. These selected rules allow us to show why such an assessment of probability and risk was obtained, and to identify weak points. Based on knowledge of weak points, appropriate measures are taken to protect information from the APCS.

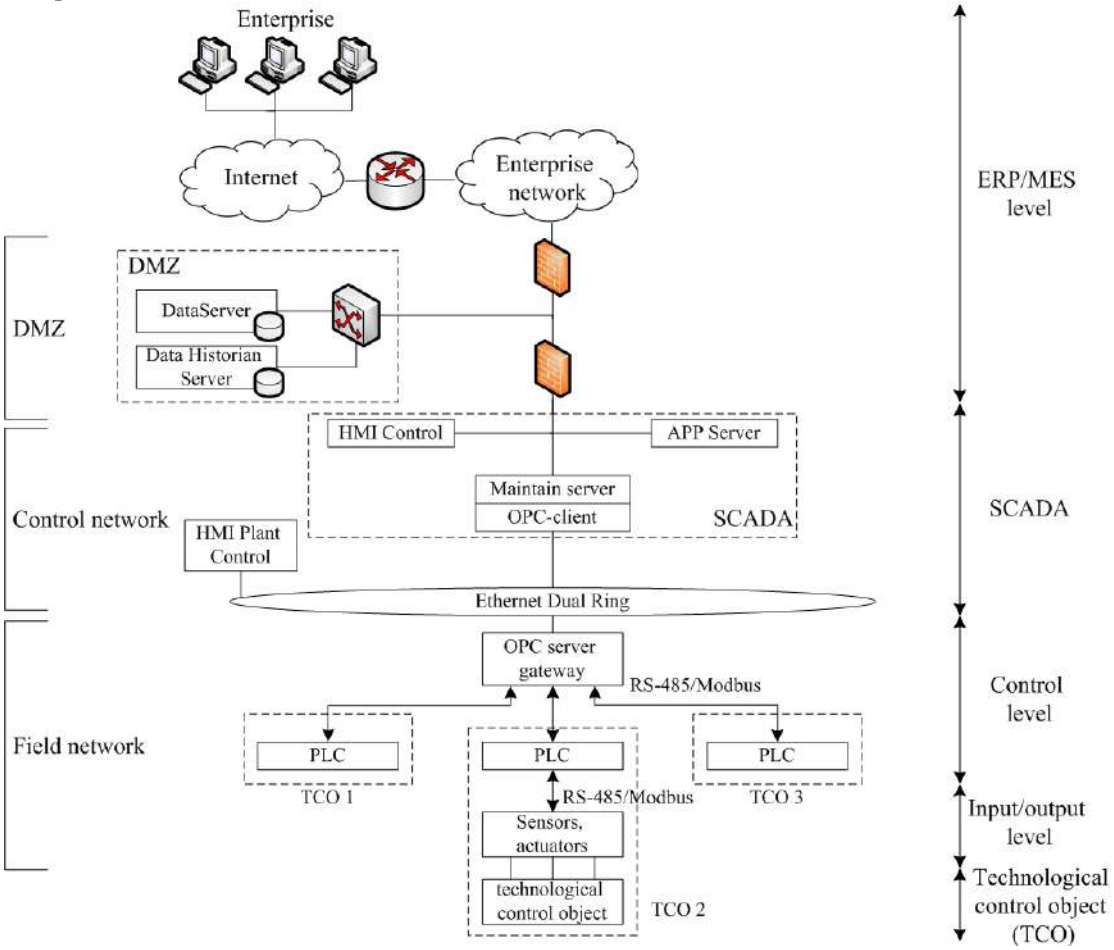

Figure 7. Physical architecture of APCS.

The DSS ultimately issues an information security risk assessment for the APCS, and recommendations for ensuring a given level of information security with instructions on what should be paid priority attention.

5. Conclusion

The proposed structure of the DSS to ensure information security of automated process control systems.

The algorithm for decision support based on data mining technology using a modular (ensemble) neural network has been developed, which allows solving the problem of risk assessment and compliance of requirements for ensuring information security of an APCS and identifying current threats to a specific protection object.

Risk assessment of information security of APCS is necessary to develop recommendations for reducing the risk level and choice of effective countermeasures that ensure full compliance with the regulatory requirements for ensuring comprehensive information security of the APCS.

The use of the proposed fuzzy neural network in assessment information risks of the APCS makes it possible to adequately use the qualitative and quantitative evaluations obtained from the experts as input data and will also improve the level of enterprise security by maintaining the information protection system of the APCS up to date.

6. References

[1] Cybersecurity of industrial automation systems in 2018 URL: https://ics.kaspersky.ru /media/2018-Kaspersky-ICS-Whitepaper-ru.pdf (13.11.2018)
[2] Threat landscape for industrial automation systems: H1 2018 URL: https://ics-cert.kaspersky.com/reports/2018/09/06/threat-landscape-for-industrial-automation-systems-h1-2018/ (13.11.2018)
[3] On safety of fuel and energy complex facilities *Federal Law No. 256-FZ dated by 21.07.2011*
[4] On approval of requirements to provision of information security in automated systems of production and technological processes control at critically important objects, potentially dangerous objects, and the objects representing higher danger to the human life and health and environment *Order of FSTEC of Russia No. 31 dated of 14.03.2014*
[5] On the security of critical information infrastructure of the Russian Federation *Federal Law No. 187-FZ dated of 26.07.2017*
[6] On approval of requirements for the creation of security systems for significant objects of the critical information infrastructure of the Russian Federation and for ensuring their functioning *Order of Russia FSTEC No. 235 dated by 21.12.2017*
[7] On approval of Requirements to providing security of significant objects of critical information infrastructure of the Russian Federation *Order of FSTEC of Russia No. 239 dated of 23.12.2017*
[8] Vasilyev V I, Gvozdev V E, Guzairov M B and Kirillova A D 2017 Integrated assessment of information security requirements implementation in automated control systems intended for production and technological processes *Information and security* **20** 618-623
[9] Vasilyev V I, Vulfin A M, Guzairov M B and Kirillova A D 2017 System of decision making support on information security maintenance of automated technologic processes systems *Infokommunikacionnye tehnologii* **15(4)** 319-325
[10] Jang J R 1993 ANFIS: adaptive-network-based fuzzy inference system Jang J-S R 1993 ANFIS: adaptive-network-based fuzzy inference system *IEEE Transactions on Systems, Man and Cybernetics* **23(3)** 665-685
[11] Takagi T and Sugeno M 1985 Fuzzy Identification of Systems and its Applications in Modeling and Control *IEEE Transactions System, Man, Cybernetics SMC* **15(1)** 116-132
[12] Takagi T and Sugeno M 1992 Stability Analysis and Design of Fuzzy Control Systems *Fuzzy Sets and Systems* **45(2)** 135-156
[13] Shanmugavadivu R and Nagarajan N 2011 Network intrusion detection system using fuzzy logic *Indian Journal of Computer Science and Engineering* **2(1)** 101-111

Acknowledgments
This work is partially supported by the Russian Science Foundation under grants №17-48-020095.

Integrity control algorithms in the system for telemetry data collecting, storing and processings

V V Berkholts[1], A I Frid[1], M B Guzairov[1] and A D Kirillova[1]

[1]Ufa State Aviation Technical University, K. Marks st., 12, Ufa, Russia, 450008

e-mail: torina4@yandex.ru, kirillova.andm@gmail.com

Abstract. The issues of improving the security of the modular system for collecting, storing and processing telemetric information on the state of the onboard subsystems of the aircraft in automatic mode are considered. It is based on an analysis of the use of modern technologies for the protection and processing of telemetric information to ensure certain aspects of the guaranteeability of the system as a whole.

1. Introduction

Emerging malfunctions and pre-failure states of the onboard equipment of the aircraft can be diagnosed based on telemetric information (TMI). This allows the specialists of ground technical services to plan repair and preventive measures based on an assessment of the current state of the equipment. Accumulated and processed TMI will allow specialists of the manufacturer to provide reasonable support to engineers of ground services in making decisions in case of technical failure of the blocks and modules of the aircraft. TMI analysis will improve the operational efficiency of the aircraft in case of any malfunctions and attacks by intruders.

The aim of the study is to increase the security of the system for collecting, storing and processing TMI on the state of the onboard aircraft subsystems in automatic mode. It is based on an analysis of the use of modern (including intellectual) technologies for the protection and processing of TMI.

To achieve this goal, a structural diagram of a protected system for collecting, storing and processing telemetric information on the state of the aircraft subsystems on the basis of a modular principle has been developed.

2. Analysis of the problem of secure collection, storage and processing of TMI in a geographically distributed information system

The proposed automated information system (AIS) of ground maintenance services is a set of software and hardware. They are necessary for the reception, storage and processing of information about the parameters of the state of complex technical products (CTP) on the aircraft. AIS is a geographically distributed system that combines the infrastructure of the information systems of ground-based maintenance stations and the information system of the manufacturer through secure communication channels. Preparation TMI realized by reading a status log for CTP aircraft during inspection and maintenance at ground stations via wireless and / or wired sensor networks.

The dependability of the TMI transmission systems with an aircraft allows for a comprehensive solution of the tasks of ensuring reliability, fault tolerance, availability, security, maintainability, and observability. An urgent task is to build a hierarchy of models that allow a comprehensive assessment of various aspects of the TMI transmission system and the development of a methodology for assessing the integral indicator of the system's guaranteed performance.

Ensuring the availability of TMI transmission systems is the primary task of ensuring the effective functioning of the aircraft (A/C). The volume of TMI collected is significant. It is an incentive for the development of the concept of the industrial Internet of things (IIoT). It is a promising platform for use in solving such problems [1]. For example, a jet airliner demonstrated at the Bombardier Paris Air Show, whose engine is equipped with more than 5,000 sensors that generate up to 10 GB of data per second. One twin-engine aircraft can generate up to 844 TB of data average in 12-hour flight [2].

The ability to transfer TMI about the actual state of individual modules during operation and the entire A/C equipment complex in real time to the manufacturer of aeronautical engineering components will improve the operational efficiency of the aircraft in its normal state and in the event of malfunctions and attacks by intruders when investigating incidents. Thus, a study of ground-to-air communication systems showed that ACARS, despite its versatility and widespread use, is vulnerable, and if hacked in conjunction with ADS-B, an attacker can gain access to the flight control system, download flight plans and detailed commands [3].

Ensuring the availability of telemetry information on the state of the aircraft

An automated information system (AIS) of ground maintenance services is a set of software and hardware. They are necessary for receiving, storing and processing information on the technological parameters of complex technical products (CTP) on board the aircraft.

A review of the main approaches to the relevance of the problem of ensuring the reliability of such systems is considered in the works of the authors [4, 5, 6]. AIS solves the main problems associated with the reception of TMI on the state of the onboard aircraft systems. The main methods of obtaining data are presented in the figure (Figure 1):

1. Directly from the CTP
2. By means of reading devices of the event log from the sensors of modules CTP. When carrying out technical inspection and maintenance, devices of this type read and store data on the state of the modules throughout the entire previous period of operation [5].
3. Entering events into the database manually. The operator processes the information and enters the information through the WEB application [4].

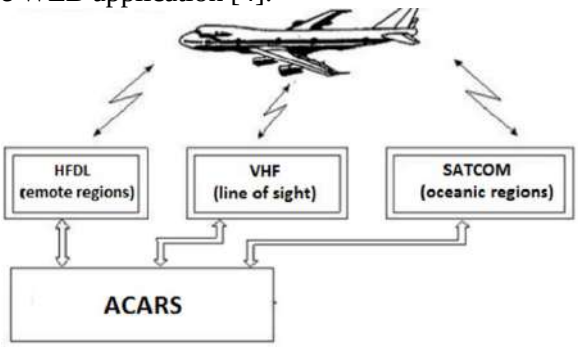

Figure 1. Methods for obtaining TMI.

In the first case, telemetry information is transmitted from the aircraft through a radio channel. To create a transmission channel, the following approaches can be used:

- Communication satellites (IRIDIUM, SATCOM).

Existing telemetry data transmission technologies use satellite communications. For example, the GE Aviation concern, producing aircraft engines, transmits telemetry from the aircraft in this way.

The obvious disadvantage of such way of transfer is its high cost. Streaming telemetry information involves the transfer of significant amounts (gigabytes) of data sent. The second disadvantage is the low noise immunity of the satellite communication channel. Incorrectly transmitted data can serve as a signal for a false alarm, or there is a chance to miss a system failure.

- Channel of wireless high-speed data transmission LTE and LTE-a

Air to ground (A2G) LTE is capable of providing data rates of up to 75 Mbps for ground-to-air communications and up to 25 Mbps for air-to-ground communications at distances of 100 kilometers and speeds of 1,200 kilometers per hour using licenses. FDD 2x15 MHz. The standard 4G LTE can be used for continental flights, developed by Nokia.

Despite the currently available satellite and hybrid A2G systems, there is still no low-cost, high-throughput solution for broadband in-flight.

Thus, none of these technologies has no set of properties that allow for continuous broadcast telemetry data. ACARS does not allow to transfer a large amount of accumulated data, satellite communication is too expensive, and LTE-A is still at the development and implementation stage, and in the future it will cover only the continental part of flights.

Moreover, the current TMI transmission and processing systems demonstrate vulnerabilities that allow an attacker to gain access not only to passenger and airline data, but also to significantly affect flight parameters.

In the second and third cases, the information enters the database through a WEB application, which is an insulating layer between external networks and the internal structure of the AIS, since access from the external network is one of the most vulnerable points of the system. Improving the security of access to the database (DB) containing critical information about the product in use is based on the development of the architecture of a secure WEB application that acts as an insulating layer for external AIS clients, which allows for the possibility of transferring and analyzing ground-based service points from the aircraft and provide the ability to remotely access the necessary data. The architecture of this solution is presented in [5].

Preventing the appearance of vulnerabilities in the WEB application was carried out by implementing measures to develop secure software established by GOST R ISO / IEC 12207. Modeling security threats and identified vectors of possible attacks, as well as analyzing them, made it possible to formulate countermeasures for each of the vectors at different architectural levels WEB-applications. However, the analysis of the security of the entire TMI transmission system requires advanced modeling and the construction of a detailed model of interaction between the onboard information system of the aircraft and the ground-based AIS.

The growth of telemetry information forces the aviation industry to consider new approaches to the collection and analysis of a large amount of data on the state of individual components and elements of the aircraft. The concept of the industrial Internet of Things is being actively developed - an expanded network consisting of a large number of devices equipped with a set of sensors that communicate with each other through low-power and short-term wireless connections. The first step is to collect data from the sensors. One of the most promising solutions is a protocol with low power consumption and small radius of IEEE 802.15.4 IEEE 802.15.4e transmission. Short range is sufficient for data transmission within the ground service station. The IEEE 802.15.4 and IEEE 802.15.4e protocols and their architecture layers comply with IETF standards.

The question of analyzing the security of the system for collecting, transmitting and receiving telemetry information about the state of individual elements of the onboard aircraft systems during data transmission over the first two channels remains open.

The decomposition of the TMI transfer in the form of a hierarchical model of interacting levels of collecting, transmitting and analyzing information with the corresponding protocol stack is the basis for analyzing and building a system for analyzing the transmission system security (Figure 2).

In recent years, satellite communication systems in accordance with the Regulations of the International Telecommunication Union (ITU) are switching to a higher-frequency Ka-band (15.40-26.50 and 27.00-30.20 GHz).

The grouping of satellites in geostationary orbit and ground control centers make it possible to form a network infrastructure with high reliability indicators and the possibility of building distributed state networks. Channels of transmission of such networks provide a fairly high level of encryption and data protection.

Transmission of information in such networks is characterized by a low level of errors - no more than one per 10 million transmitted information bits and reliable operation - up to 100 thousand hours.

The speed of work on the satellite channel is from 16 Kbps to 10 Mbps and more, which is comparable with the data transfer rate in the terrestrial channel.

The main methods for ensuring the security of telemetry information transmission in a wireless satellite channel is the use of software and hardware means of information protection. Widely used standards for secure protocols IPsec.

IPsec protocol (set of protocols) provides:

- integrity of the virtual connection, authentication of the source of information using the AH protocol (Authentication Header);
- encryption of information transmitted via the ESP (Encapsulating Security Payload) protocol;
- initial connection setup, mutual authentication and confidential key exchange.

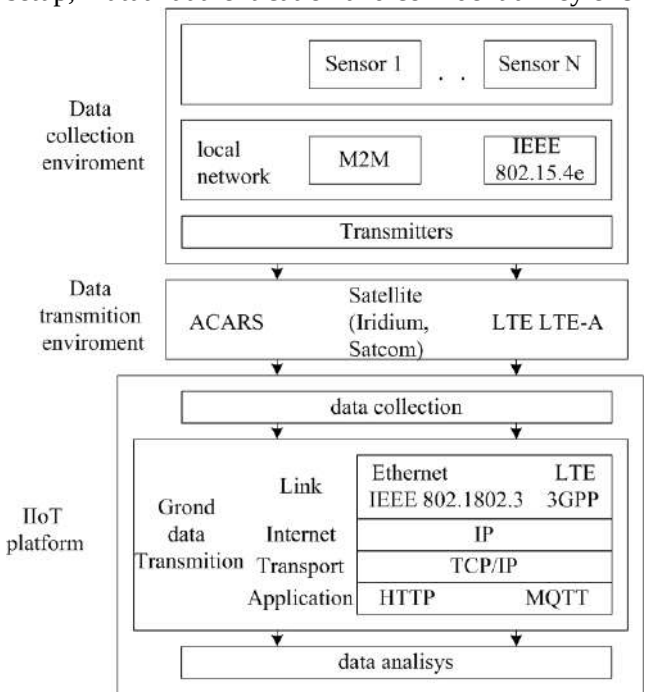

Figure 2. Extended scheme of data transmission from the aircraft.

At present, modern bilateral satellite communication networks use coding systems at the software and hardware level, which makes the interception and decoding of information over the radio channel almost impossible.

All data transmitted via satellite channel pass through a multi-stage system of transformation and encryption. The result of this:

- application of proprietary data encryption algorithms;
- terminal authentication when it is registered on the operator's network (hardware key);
- encryption of both the entire session (software key) and each session separately (session keys);
- application of proprietary algorithms for converting source data into internal data formats (structures), which are then transmitted via satellite channel; thus, the tasks of additional protection of information, delivery of service information and error correction are solved;
- in the created virtual channels, source data in TCP sessions are grouped, compressed, and prioritized.

Satellite channels in the direction from A/C to TMI processing centers are reverse satellite channels. Currently, the most common ways of functioning of transmitters in such channels are the principles of access with time-frequency division of TDMA / FDMA channels. Each reverse channel is located in a certain frequency range or has a carrier with frequency modulation and with a given coding algorithm for detecting and correcting errors of transmitted data - Turbo Coding.

To transmit TMI from the aircraft, it is necessary to provide a mechanism for changing the frequencies of the carrier reverse channels, which makes it much more difficult to intercept the transmitted data.

Data encryption in the satellite channel is carried out with the participation of both satellite terminals on board the aircraft and specialized high-performance servers at the TMI ground collection station. The server of the ground station for collection and processing of TMI hosts a secure database of encryption keys and session keys of all satellite terminals. In order for the aircraft board to operate in the transmission network, the information in the key database must match the hardware onboard key.

Telecommunications systems using the UMTS (Universal Mobile Telecommunications System) standards are third-generation mobile communication systems - 3G. For mobile communication of the third generation, the decimeter frequency band is used (about 2 GHz), and data transmission is provided at a speed of 2 Mbit / s.

All information security threats in the UMTS network can be distributed depending on the location of the impact of their respective attacks:

- on the radio access area (radio interface);
- on other parts of the network.

The radio section between the aircraft and the service network is one of the most vulnerable points of attack in UMTS. The threats related to this site and described below are divided into the following categories:

- unauthorized access to data;
- threats to data integrity;
- “denial of service”;
- unauthorized access to services.

Table1. Describes some of the threats to unauthorized access to data on the radio site.

Threat designation	Threat name	Threat description
T1a	Interception of user traffic	Violators can intercept user traffic
T1b	Interception of alarm and control data	Violators can intercept alarm data and control data
T1c	Masking as a participant	Violators can be disguised as a network element
T1d	Passive traffic analysis	Violators can monitor the characteristics of messages
T1e	Active traffic analysis	Violators can actively initiate a connection and then access information

Table 2. Threats to the integrity of information.

Threat designation	Threat name	Threat description
T2a	User traffic manipulation	Violators can modify, insert, repeat or destroy user traffic. This manipulation may be accidental or intentional.
T2b	Alarm data manipulation	The intruder can modify, insert, repeat, or destroy alarm or control data.

Table 3. Denial of service threats.

Threat designation	Threat name	Threat description
T3a	Physical intervention	Violators can physically interfere with the transmission of user traffic, signaling data and control data.
T3b	Protocol Intervention	Violators may introduce special protocol failures.
T3c	Denial of service due to masking as a participant in communication	Violators may refuse to serve a legitimate user.

Below are tables with descriptions of information security threats. The accepted designations of the threat TAn correspond to: T - the first letter of the English word "threat" (threat): A - the number corresponds to the number of the threat group (table number); n - the letter corresponds to the ordinal number of the threat in the threat group (in accordance with the list of threats in the ETSI document.

Table 4. Threat of unauthorized access to services.

Threat designation	Threat name	Threat description
T4a	Masking as another user	The intruder is disguised as another network user. First, the intruder is disguised as a base station with respect to the user.

3. Threats related to attacks on other parts of the system

Although attacks on a radio channel represent the most serious threats, attacks on other parts of the system also require analysis from the point of view of information security.

Table 5. Threats to unauthorized access to data.

Threat designation	Threat name	Threat description
T5e	Unauthorized access to data on the system object	Violators (by physical influence or logical control) can gain access to local or remote data.
T5f	Compromising information about the location	A legitimate user of a UMTS service may obtain information about the location of other users of the system
T6c	Manipulation of masking as a communication partner	Violators can be disguised as a network element in order to modify, insert, repeat or destroy traffic
T6f	Manipulation of data on the objects of the system	Violators can modify, insert, destroy data that is contained in the objects of the system.
T7a	Physical intervention	Violators may interfere with transmission on any system interface (wired or wireless). For example, the physical method of an obstacle on a wired interface could be a broken wire.
T7b	Protocol intervention	Violators can interfere with the transmission of user traffic or signaling data on any interface of the system (wired or wireless) or by signaling the protocol to fail.
T7c	Denial of service by masking communication partners	Violators can deny service to users by impeding the transmission of user traffic and signaling data, controlling them by blocking as a result of masking as a network element.
T7d	Incorrect use of emergency services	Violators can interfere with access to the services of other users and at the same time cause disruption of the equipment to perform functions in emergency situations.
T8a	Disagreement with the submitted invoice	Disagreement with the submitted invoice. This may be expressed in the refusal of the service or in the refusal that the service was actually provided.
T8b	Failure of user traffic source	The user can refuse to send traffic.
T9a	Custom masking	Violators can introduce themselves as a user in order to use the authorized services of this user. The intruder was able to get this opportunity from other objects such as the serving network, home environment and even the user himself.

T9b	Masking under the serving network	Violators can introduce themselves as a service network or part of a service network infrastructure.
T9c	Home environment masking	Violators can introduce themselves as a home environment in order to obtain information that enables them to disguise themselves as users.
T9d	Misuse of user priorities	Users may misuse their assigned priorities in order to gain unauthorized access to services or simply use their subscription intensively for free.
T9e	Incorrect use of serving network priorities	Service networks may misuse their priorities to gain unauthorized access to services.

Table 6. Threats related to attacks on the terminal and UICC / USIM.

Threat designation	Threat name	Threat description
T10h	Masking to receive data on the UICC interface - terminal.	Violators can be disguised as USIM or a terminal in order to intercept data on the interface of a UICC terminal.
T10j	Confidentiality of certain user data in the terminal and UICC / USIM	Violators may wish to gain access to personal user data stored in the terminal or UICC, for example, the telephone book of interacting subscribers.
T4a, T9a, T9c	It must be possible to prevent unauthorized access to 3G services by disguising themselves as legitimate users.	Requirements for security access to service.
T4a, T8a, T9d, T9e	An alarm should be provided to the provider informing him of the security event. Provide service providers with the ability to authenticate users upon request and during the provision of the service.	Security Requirements
T7b, T7c	Protection against unauthorized modification of user traffic should be provided.	System integrity requirements
T7a, T7b, T7c	Protection against unauthorized modification of certain signaling and control data must be provided.	System integrity requirements
T1a, T1b	The user should be provided with the ability to verify that his traffic and information about his calls are confidential.	Personal data protection requirement
T10h, T10k	It should not be possible to access USIM data that is intended for use only within USIM, such as authentication keys and algorithms	USIM security requirement

4. Development of a block diagram of a secure system for collecting, storing and processing telemetric information on the state of the aircraft subsystem

The generalized structure of a geographically distributed hierarchical system for the collection, storage and processing of TMIs arriving from airplanes based on ground maintenance stations is presented in Figure 4.

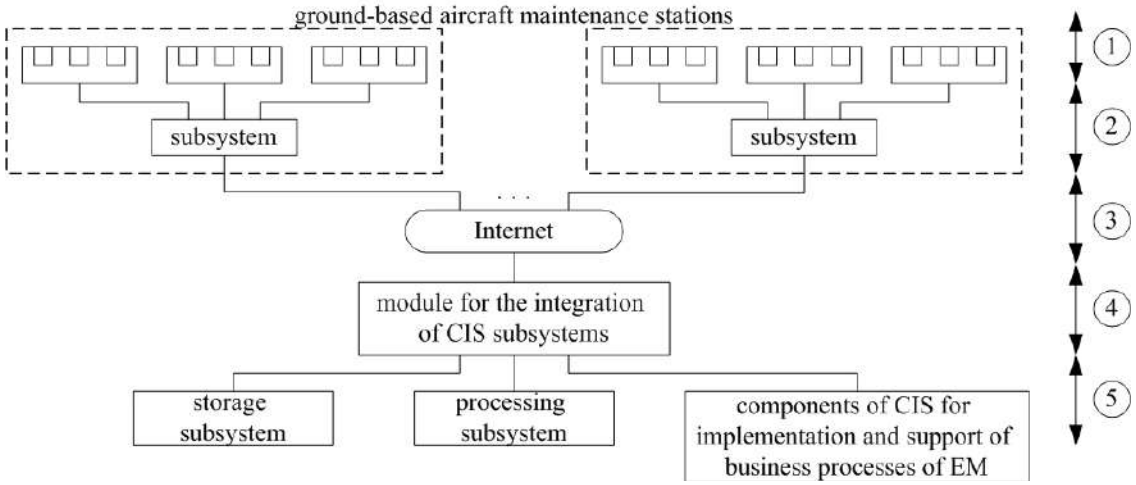

Figure 4. Generalized structural diagram of a protected system for collecting, storing and processing TMI (1 – level of TMI collection from wired and wireless sensors of ground-based aircraft servicing systems; 2 – level of primary surveillance and preparation of TMI for transmission to the AIS of the manufacturer's enterprise (AIS EM); 3 – level of data transmission over secure channels through global data networks in the AISEM; 4 – level of organization of reception and distribution of TMI on EM; 5 – level of storage and processing of TMI in the CIS).

The creation of a secure channel through global communication networks and the transfer of TMI to a part of the AIS EM is realized at the transmission level of accumulated data. Organization levels of reception and distribution of information at the enterprise are realized according to the three-layer CISCO model. There is a level in the corporate information network of EM. It includes subsystems for storage and processing of TMI. Also, there is a segment designed to support and implement the business processes of the enterprise.

5. Development of the structure of the collection and storage subsystem TMI at the ground stations of aircraft maintenance

The vast majority of Industrial Ethernet protocols do not have built-in security mechanisms. Consequently, the actual problem is the security of industrial networks.

To ensure the security of subsystems that implement the first two levels of the proposed structure, it is necessary to be guided by the normative documents of the international and federal standards. When designing the wireless sensor network collection subsystem of the TMI, take into account the requirements of GOST R ISO / IEC 27033-1-2011 and GOST R ISO / IEC 27033-3-2014.

The physical architecture of the TMI collection and storage subsystem at the ground is presented in Figure 5.

Mechanisms for collecting and storing a large amount of TMI on the state of individual components and elements of aircraft should take into account the actively developing concepts of the industrial Internet of things (IIoT). It is proposed to use heterogeneous wired (physical RS-485 interface) and wireless sensor networks (IEEE 802.15.4, IEEE 802.15.4e) to collect protocol-based TMI using embedded Modbus over TCP mechanisms to ensure the protection of transmitted data (streaming encryption). The IEEE 802.15.4 and IEEE 802.15.4e protocols and their architecture levels follow the IETF standards.

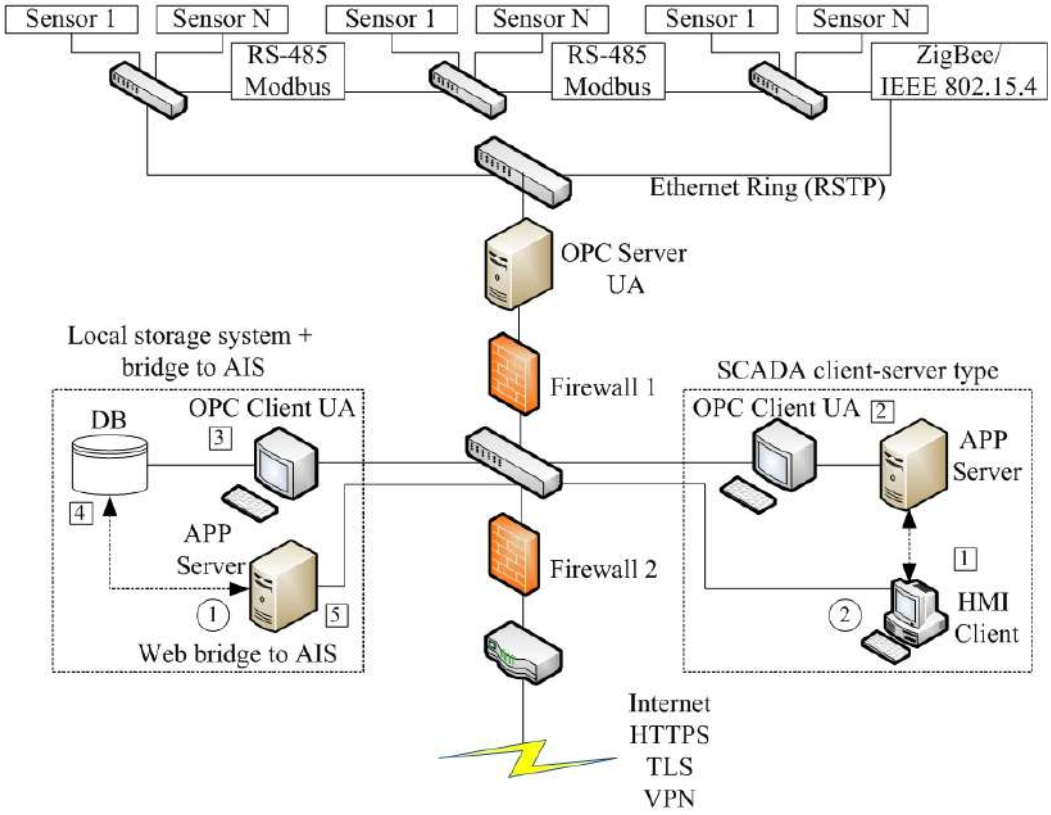

Figure 5. The subsystem of data collection and storage at aircraft service stations.

6. Development of the structure of the subsystem for receiving, storing and processing TMI in AIS

The organizations for receiving and distributing TMIs on PIs are implemented according to the three-tier CISCO model and Security Architecture for Enterprise (SAFE) design methodology, which allows to take into account modern experience in deploying secure networks based on the deep-echelon defense against external and internal attacks.

The main element of the TMI distributed processing system is the distributed file system HDFS. Additional measures to ensure the confidentiality of stored data is encryption at the level of individual database columns. To audit access to big data, you need to apply Database Activity Monitoring class solutions.

7. The concept of data integrity and verification of data sources

The actual problem is the security of industrial networks, which is not solved by existing approaches, since the attacker's intervention is possible not only at the network level from outside or inside, but also at the level of the data sources themselves. The main hardware and software part of the CTP is free from possible "bookmarks", which is guaranteed by the manufacturer, but it is necessary to comprehensively analyze the progress of the object, identifying abnormal situations not related to equipment breakdowns or failure of individual components and assemblies, but potentially caused by the intervention of an attacker. It is necessary to improve the monitoring system of CTP as an element of the intrusion detection system, considering the complexity of the control object, the nonlinearity of the processes and the possible conditions of the equipment that lead to emergency or catastrophic situations. The system of monitoring the condition of CTP, implemented as a component of the intrusion detection system, involves continuous monitoring of the parameters of CTP to identify significant deviations from the" normal behavior", which in turn will indicate possible malicious intentions. This approach is a development of the concept of Data Centric Security [7], which implies the security of the data itself. To determine deviations from the" normal behavior " it is proposed to use the system model of the object – the CTP, which is the development of the concept of Fault

Detection and Identification [8]. The process of monitoring the state of the CTP is a sequential operation of collection, processing and analysis of technological information, the main of which is to detect the impact of an attacker on the course of the CTP and the components of the information system by comparing the mathematical model of the CTP and the current performance of the real object will improve the security of the object. Using the proposed concept of monitoring the CTP comparing the fixed state of the object with the real model is a tool that allows you to control the presence of hardware and software interventions in the infrastructure of the information system.

The algorithm is based on a comparison of the characteristics of time series arriving from the aircraft, and time series generated by the gas turbine engine (GTE) model which is simulating the same mode and the same flight conditions in which the GTE operates in real time. Information receiving from A/C is the result of GTE and its ACS operation.

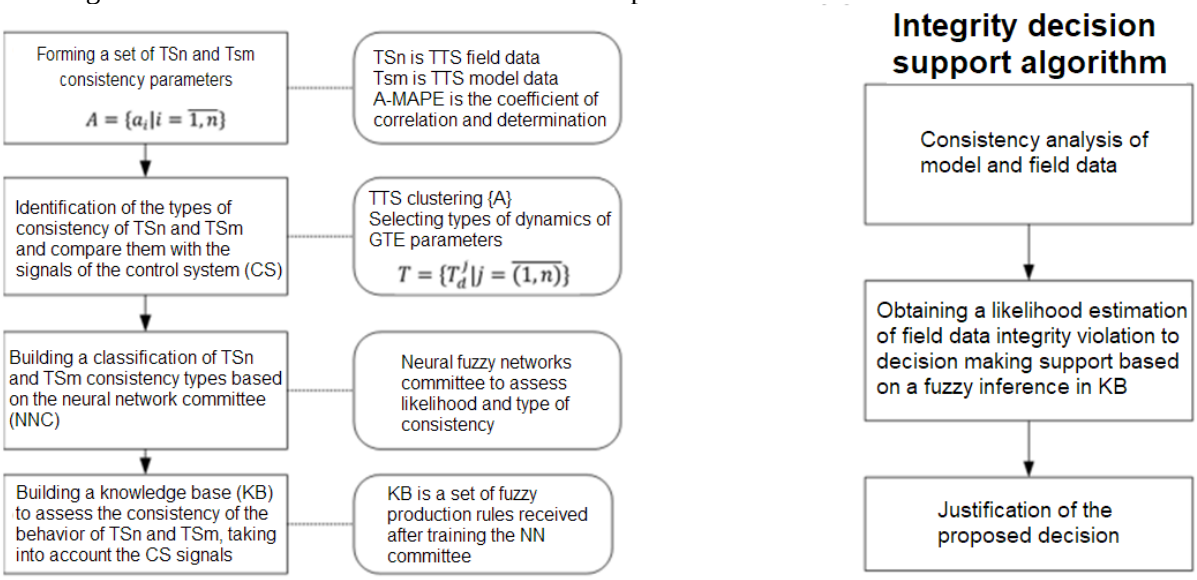

Figure 6. Method of analyzing the consistency parameter of model and field data.

Figure 7 shows the block diagram of the monitoring system of GTE A/C TMI parameters. The AIS of the manufacturer receives the vector of specified values of the controlled coordinates of the object Y0, the vector of perturbing factors F and the vector of measured perturbing factors F'. The control object receives the vector of control actions U generated by the control system. Data from the monitoring system via a communication channel is sent to the manufacturer. The communication channel can be exposed both to an attacker (the Z vector) and to the external environment that generates noise (the N vector). Similar control signals are received in a model that simulates signals from A/C sensors.

A set of GTE parameters was selected to analyze the data discrepancies obtained from the model and data obtained from the aircraft. The k-means clustering method was performed on the training sample, during which nine types of GTE behavior dynamics were identified.

For carrying out preliminary experiments and learning the decision block for each type of dynamics, its own neural network NARX model was built.

For real-time integrity monitoring, a multidimensional time series (TS) of the mismatch parameters of model data and TMI indicators for a sliding window is constructed [9].

To make a final decision on the state of the data transmission system from the aircraft and the presence or absence of intruder interventions into the data channel, a decision block was built that takes into account not only the type of data mismatch from the aircraft and the data generated by the model, but also the signal control systems about the state of the GTE, obtained from the aircraft in real time, as well as the type of dynamics of the GTE at a given time. All these three parameters are taken into account for the block to make a decision on the state of the data transmission channel ("break", "normal operation", "integrity violation", etc.). The second output signal of the decision block is an

estimation of the degree of confidence about the decision made, namely the estimate of the probability of such a state, calculated from the three input parameters [10].

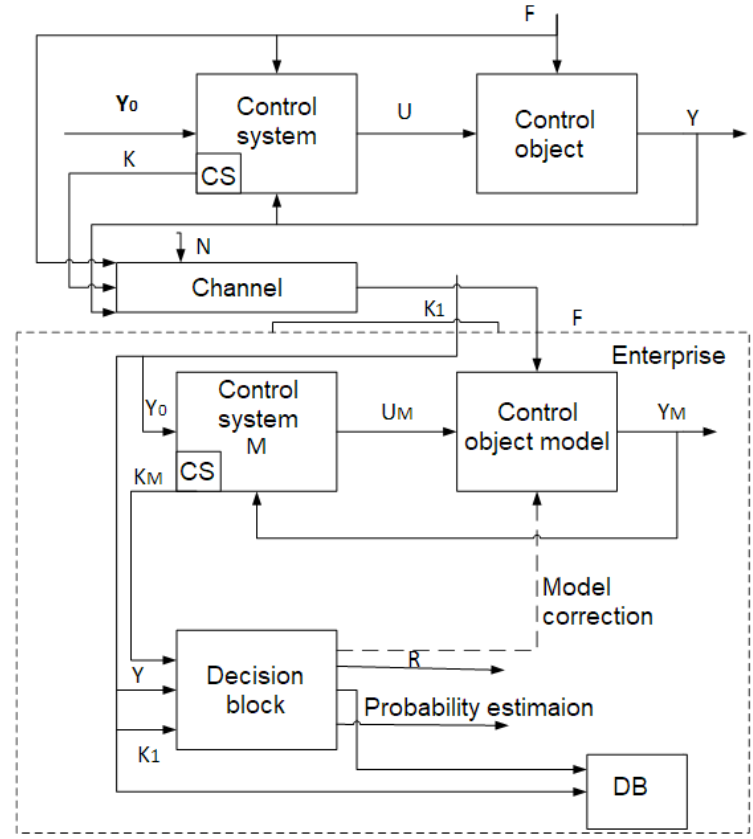

Y0- Vector of specified values of the object's controlled coordinates
F1- Vector of measurable perturbing factors
K- Vector of transmitted information about the object state
R- Decision vector
Y- Vector of managed object coordinates Z-Intruder Impacts
CS - Control system

Figure 7. Block diagram of the integrity monitoring system of GTE A/C TMI parameters.

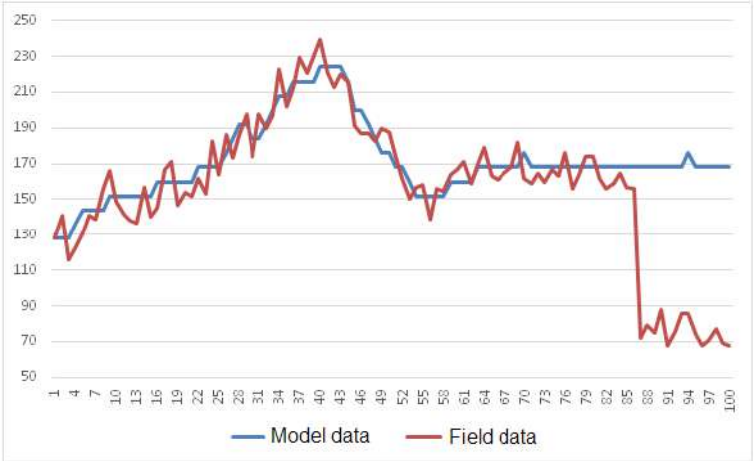

Figure 8. Simulation experiment №1 of hardware failure.

8. Simulation of possible situations arising during the A/C operation

Experiment 1.

In this example, a hardware failure or interruption in signal transmission occurs. From the figure it is clear that, starting with iteration 85, the values of the data received from the object have changed

dramatically and the value of their average value has decreased relative to the average value of the previous values obtained from the sensor of the technological process. The changes in the values are shown in Fig. 8. The fall of the amplitude of the received signal occurred almost at the last iterations in the current time window.

When calculating the correlation and determination coefficients, the following results were obtained:

$$r_{xy} = 0.56$$
$$R = 0.34$$

The average value of the coefficients indicates possible problems with the data obtained from the process.

For an additional test of this data, the MAP coefficient was calculated:

$$MAPE = 11{,}88\%$$

Check the value of the MAPE coefficient before the jump:

$$MAPE = 4.6\%$$

As can be seen, the MAPE coefficient has changed, but not critically. Such a small change in the level of MAPE error and the average value of the correlation and determination coefficients is due to the late signal jump in the time window.

Experiment 2.

In this example, the signal transmission is also interrupted. At about 77 iterations, the average value of the transmitted signal has changed dramatically in comparison with previous data. As in the previous example, in the current time series, signal distortion occurs at late iterations, which will reduce the sensitivity of the coefficients of determination and correlation.

Figure 9. Simulation experiment №2 of hardware failure.

When calculating the correlation and determination coefficients, the following results were obtained:

$$r_{xy} = 0.19$$
$$R = 0.08$$

The values of both coefficients are too low, which indicates a serious problem with the received data. Calculate the coefficient MAPE:

$$\text{MAPE}=16{,}31\%$$

The MAPE error rate is high, which confirms the hypothesis that there are problems in the data transmission channel.

Calculate the MAPE coefficient before the start of problems with the signal:

$$\text{MAPE} = 4.11\%$$

In this example, the signal drop occurred earlier than in the previous one. This explains the lower values of the correlation coefficients and determination, and the percentage of errors, on the contrary,

is higher. It is also worth noting that the percentage of errors before the start of the signal jumps is approximately the same in both examples.

Experiment 3.

This experiment also illustrates problems with signal transmission or equipment failure. The fall in the average value occurs in the time window fairly early, at about 37 iterations.

When calculating the correlation and determination coefficients, the following results were obtained:

$$r_{xy} = 0{,}36$$
$$R = 0.11$$

The values of both coefficients are too low, which indicates a serious problem with the received data. Calculate the coefficient MAPE:

MAPE=41.81%

The MAPE error rate is high, which confirms the hypothesis that there are problems in the data transmission channel.

Calculate the MAPE coefficient before the start of problems with the signal:

MAPE = 4.61%

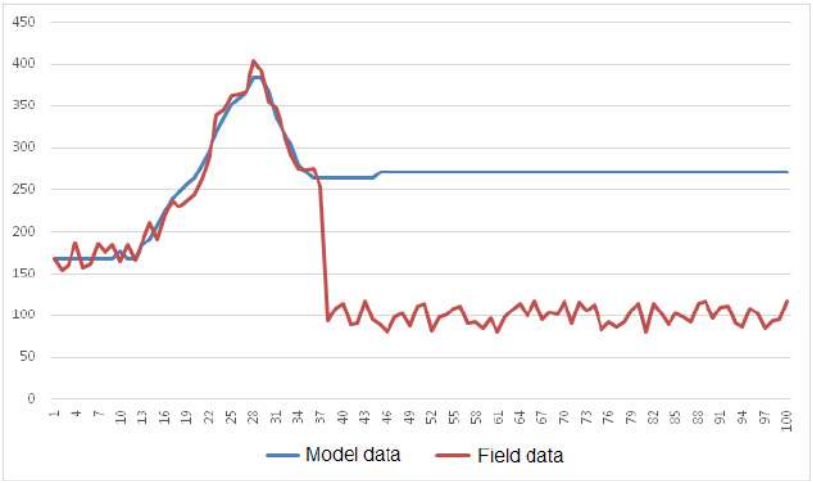

Figure 10. Simulation experiment №3 of hardware failure.

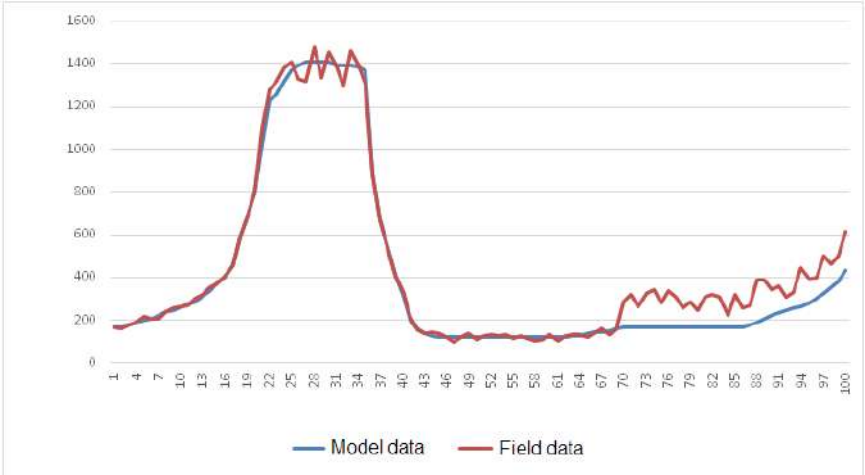

Figure 11. Simulation experiment №4 of hardware failure.

The correlation coefficient is not too different from the previous example, but the MAPE error rate is very high. Such a large value is due to the early appearance of signal distortion in the time window.

Experiment 4.

This experiment is different from previous ones. Here, starting from the 69th iteration, there is a smooth growth of data values obtained from the technological process in parallel with the growth of

model values; however, the average value of the received signal is significantly higher than the reference data. Such data behavior may have a weak effect on the values of the correlation coefficient and determination.

When calculating the correlation and determination coefficients, the following results were obtained:

$$r_{xy} = 0.98$$
$$R = 0.97$$

The values of both coefficients are too low, which indicates a serious problem with the received data. Calculate the coefficient MAPE:

$$\text{MAPE}=23.11\%$$

The MAPE error rate is high, which confirms the hypothesis that there are problems in the data transmission channel.

Calculate the MAPE coefficient before the start of problems with the signal:

$$\text{MAPE} = 5.01\%$$

As shown by calculations, the coefficients of determination and correlation take a very high value. However, when paired with a high MAPE, the values obtained should raise suspicions. There may be problems with the equipment, as well as falsification of the transmitted data.

Experiment 5.

This experiment is a case where nothing happened to the data and it is transmitted normally.

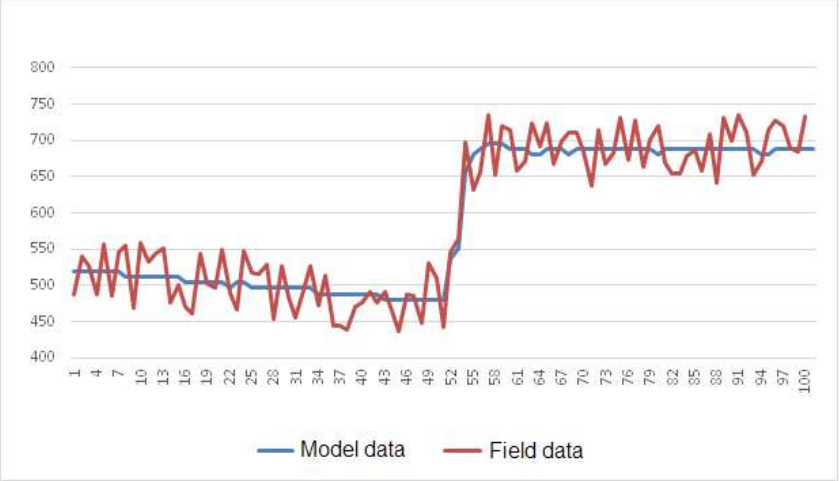

Figure 12. Simulation experiment №5 of hardware failure.

When calculating the correlation and determination coefficients, the following results were obtained:

$$r_{xy} = 0.94$$
$$R = 0.90$$

Calculate the coefficient MAPE:

$$\text{MAPE}=4.72\%$$

The combination of these three factors indicates that there are no problems with the signal. The resulting data can be trusted.

Experiment 6.

This example is similar to the previous one. Here the data obtained from the aircraft is just noisy and not distorted in any way.

When calculating the correlation and determination coefficients, the following results were obtained:

$$r_{xy} = 0.76$$
$$R = 0.58$$

Calculate the coefficient MAPE:

$$\text{MAPE}=2.38\%$$

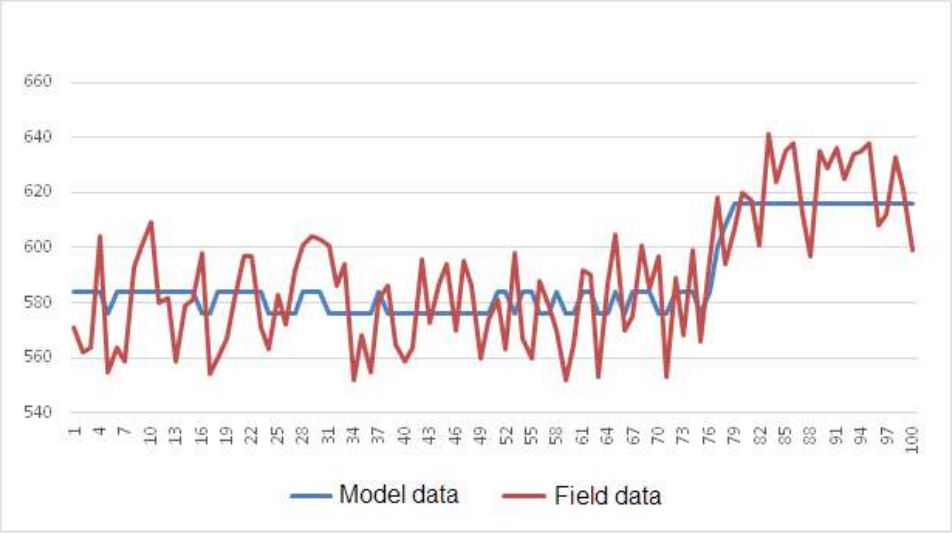

Figure 13. Simulation experiment №6 of hardware failure.

The correlation and determination coefficients show the average value of the relationship between the data obtained from the model and the data obtained from the object of the technological process. However, the MAPE value is low. This combination of the three coefficients allows us to say that everything is in order with the obtained data and that they can be trusted.

Experiment 7.

This experiment explains the low correlation coefficient from example two. Here, as well as in the two previous experiments, data is presented that has not been changed by the attacker.

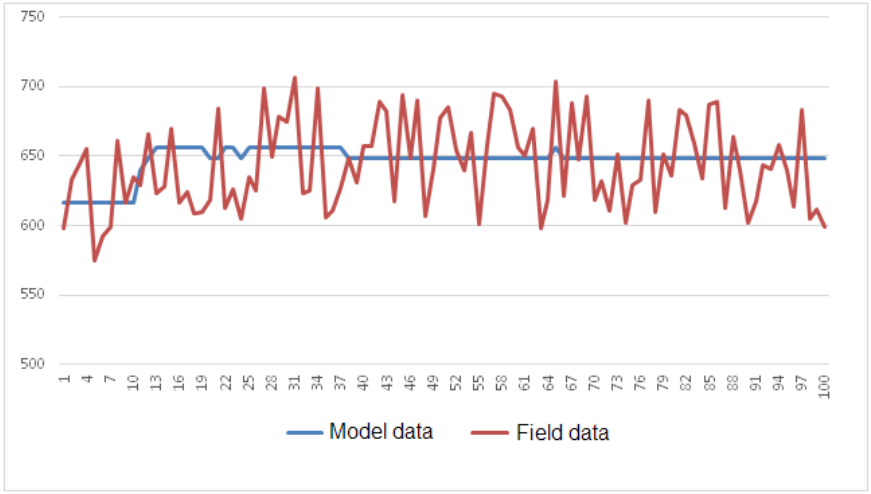

Figure 13. Simulation experiment №6 of hardware failure.

When calculating the correlation and determination coefficients, the following results were obtained:

$$r_{xy} = 0.21$$
$$R = 0.04$$

Calculate the coefficient MAPE:

MAPE=4.25%

Such a low correlation coefficient and determination may appear not only in case of equipment failure or fake messages. In the case when the model readings are close to a constant, and the data from the technological object undergo analog-digital transformations and undergo slight distortions during transmission, the correlation coefficient takes very low values. However, the MAPE coefficient

shows a small percentage of errors, which means that the deviations of the model and TP object values are insignificant. Data can be trusted.

9. The rule base for decision making

For the decision block, the following set of rules was developed, on the basis of which the decision on the integrity of the transmitted TMI was made.

CMS is the channel monitoring system. In case if CMS = 1, everything is normal with the channel, otherwise - CMS = 0;

Rule 1. $(r_{xy} =' \text{middle}')AND(R =' \text{middle}')AND\ (MAPE =' \text{middle}')$ *AND*(CMS=0) THEN signal breakage occurred;

Rule 2. $(r_{xy} =' \text{low}')AND(R =' \text{low}')AND(MAPE =' \text{high}')AND$ (CMS=0) THEN signal breakage occurred;

Rule 3. $(r_{xy} =' \text{low}')AND(R =' \text{low}')AND(MAPE =' \text{high}')AND$ (CMS=0) THEN signal breakage occurred;

Rule 4. $(r_{xy} =' \text{high}')AND\ (R =' \text{high}')AND(MAPE = '\text{high}')\ AND$ (CMS=1) THEN data fraud is possible;

Rule 5. $(r_{xy} =' \text{high}')AND(\ R =' \text{high}')AND\ (MAPE = '\text{high}')\ AND$ (CMS=1) THEN normal operation;

Rule 6. $(r_{xy} =' \text{средний}')$И$(R =' \text{средний}')$И$(MAPE = '\text{низкий}')$ И (CMS=1) THEN normal operation;

Rule 7. $(r_{xy} =' \text{low}')\ AND(R =' \text{low}')AND\ (MAPE = '\text{low}')\ AND$ (CMS=1) THEN normal operation.

10. Conclusion

A block diagram of a protected system for collecting, storing and processing telemetric information on the state of aircraft subsystems based on the modular principle is proposed. The difference of the proposed solution is that it contains rather large subsystems with a high degree of connectivity of the components inside and a sufficient degree of autonomy at the level of interaction of the subsystems themselves. Each subsystem is built on the basis of organizational principles specific to the specifics of the problem being solved, and is governed by existing regulatory documents to ensure specific aspects of the system's reliability.

An algorithm for monitoring the integrity of the TMI on the state of the GTE in service has been developed, which determines the type of TS dynamics coming not only from the aircraft, but also the type of the TS model and GTE mismatch dynamics, which allows evaluating the actual state of the GTE ACS and detecting intrusion interference.

11. References

[1] Internet of Things Volume G4: Security Framework URL: http://www.iiconsortium.org/pdf/IIC_PUB_G4_V1.00_PB-3.pdf (10.11.2018)

[2] Rapolu B 2016 Internet of Aircraft Things: An Industry Set to be Transformed *AVIATION WEEK NETWORK* URL: http://aviationweek.com/connected-aerospace/internet aircraft-things-industry-set-be-transformed (10.11.2018)

[3] Aircraft Hacking Practical Aero Series *n.runs Professionals Stations* URL: http://www.sita.aero/file/3744/Aircom (10.11.2018)

[4] Frid A I, Vulfin A M, Zakharov D Ju, Berkholts V V and Mironov K V 2017 Architecture of the security access system for information on the state of automatic control systems of aircraft *Proc. of the 19th Int. Workshop on Computer Science and Information Technologies* **2** 21-27

[5] Frid A I, Vulfin A M and Berkholts V V 2018 Analysis of the methods of constructing information attack models for the system of telemetric information transmission *Proc. of the Information Technology Intelligent Decision Support* (Russia: Ufa) 226-229

[6] Rapolu B 2016 Internet of aircraft things: an industry set to be transformed *AVIATION WEEK NETWORK* URL: http://aviationweek.com/connected-aerospace/internet-aircraft-things-industry-set-be-transformed (13.11.2018)
[7] Zhang L, Afanasyev A, Burke J, Jacobson V, Crowley P, Papadopoulos C, Wang L and Zhang B 2014 Named Data Networking *ACM SIGCOMM Computer Communication Review* **44(3)** 66-73
[8] Choi S W, Lee C, Lee J M, Park J H and Lee I B 2005 Fault detection and identification of nonlinear processes based on kernel PCA *Chemometrics and Intelligent Laboratory Systems* **75(1)** 55-67
[9] Kropotov Yu A, Proskuryakov A Yu and Belov A A 2018 A method for predicting changes in the parameters of time series in digital information control systems *Computer Optics* **42(6)** 1093-1100 DOI: 10.18287/2412-6179-2018-42-6-1093-1100
[10] Plotnikov D E, Kolbudaev P A and Bartalev S A 2018 Identification of dynamically homogeneous areas with time series segmentation of remote sensing data *Computer Optics* **42(3)** 447-56 DOI: 10.18287/2412-6179-2018-42-3-447-456

Acknowledgments
This work is partially supported by the Russian Science Foundation under grants № 17-07-00351.

Research and analysis of messages of users of social networks using BigData technology

I A Rytsarev[1,2], A V Kupriyanov[1,2], D V Kirsh[1,2] and R A Paringer[1,2]

[1]Samara National Research University, Moskovskoe Shosse 34A, Samara, Russia, 443086
[2]Image Processing Systems Institute of RAS - Branch of the FSRC "Crystallography and Photonics" RAS, Molodogvardejskaya street 151, Samara, Russia, 443001

e-mail: rycarev@gmail.com

Abstract. In this paper is dedicated to the World Cup held in the city of Samara from June 15 to July 15, 2018. As part of the work, a multithreaded collection in real time was organized, filtering and processing messages from users of the social network Twitter within the host city and its surroundings from May 15 to August 15, 2018. Then, a study was conducted of the texts of user messages on the subject of the popularity of topics and the construction of a "word cloud". The second study was the construction of a diagram of the dynamics of the number of messages in different languages. As part of the work, modules for collecting, filtering and processing data using BigData technology were implemented.

1. Introduction

Currently, social networks are booming: every day their users generate hundreds of terabytes of media content: images and video. The analysis of such content is of great importance for many areas of business. For example, it is impossible to overestimate the impact of Internet marketing on the promotion of goods and services. However, clear understanding of user requests is essential to use these mechanisms effectively. The source of such information can be the materials published by users of social networks, as well as the shares and reposts by users and the entire communities. But in the period of any major events the population of online communities can vary greatly. In this paper, a comparison is made between the flow of messages before the World Cup, during and after it.

The task considered in the framework of this work is undoubtedly an urgent task, the solution of which is also of great scientific importance in the field of data analysis. In the article [1], a large dataset of geotagged tweets containing certain keywords relating to climate change is analyzed using volume analysis and text mining techniques such as topic modeling and sentiment analysis. In the article [2], the local and global term frequencies are computed through a bag-of-words (BOW) model. To remove the negative impact of high dimensionality on the global term weighting, the principal component analysis is adopted; thereafter the fuzzy c-means algorithm is employed to retrieve the semantically relevant topics from the documents. In the article [3], examine the long-term relationship between signals derived from nine years of unstructured social media microblog text data and financial market developments in five major economic regions. Employing statistical language modeling techniques we construct directional sentiment metrics. In the article [4], the authors propose a

background clustering technology for discussion. Compared with the traditional methods, background future clustering keeps the constrains caused by data sparseness and spatio-temporal dependence off, and can be used for unpredictable activities discovery.In the article [5], the method of applying cross-references was considered to improve the accuracy of providing dictionaries in the task of calculating distributions between social communities based on text messages. In the article [6], the technology of processing large-scale text data on data collected from a social network was tested. The article [7] proposed a mathematical model for calculating the activity of users of social networks. Article [8] proposed a technology for normalizing text data. To capture the contextual meaning of tokens, authors create a neural word embeddings using word2vec trained on over a million social media messages representing a mix of domains and degrees of linguistic deviations.

2. Social network data collection

The Twitter social network was selected as a data source for this study. The reasons for this choice are as follows:

- the network provides open access to its data (no restrictions on accessing the server data);
- Twitter is the second most popular social network (after Facebook, which does not provide open access to its data) among users all over the world;
- Twitter is not a specialized network, which means it reflects the public opinion of a wider range of users [9].

The data collection from the Twitter social network can be carried out using the software products Apache Ambari and Flume, this method is described in more detail in [10]. However, it is often more convenient to develop a dedicated software product using standard libraries (twitter4j, tweepy, etc.) to collect the data using a number of filters [11, 12].

As part of this study, a Python software package was developed, containing an authorization module, a data collection module, and a filtration module. This software package allows to collect data by geolocation, by keywords, by user. The Twitter social network has a restriction in the form of a message limit that a client can receive during real-time monitoring. According to the documentation, this limit is 60 messages per second (this is about 1% of the average rate of tweets). A network of computers located in different cities was set up and cloud services were involved in order to avoid interruptions in the operation of the software complex, and to minimize message loss. Multiple unique authorization keys have been implemented in each copy. The designed software complex operates in real-time monitoring mode, and can make requests to receive information located on servers.

The geolocation filtering parameters were the coordinates of the city of Samara (the host city of the World Cup) in the form of an extended geobox (48.9700523344,52.7652295668, 50.7251182524,53.6648329274), which includes not only the city of Samara, but also the city of Togliatti (the training base of football players and the city where the tourists lived), airport Kurumoch and the settlements nearby the city of Samara.

More than 1,200,000 user messages were collected during the operation of the distributed network of the software complex nodes.

3. Analysis of the collected data using the BigData technology

The merging of the collected data, data processing and analysis using traditional approaches requires huge computational resources and takes a long time. For this reason, it was decided to use the BigData technology and the computing cluster for processing extra-large data available at the Samara University.

First of all, the data collected had to be merged. For this purpose, a data merging module was implemented using MapReduce technology. As a result of the module operation, we received more than 170,000 unique user messages.

The second task was the primary data processing. Streaming data obtained from social networks contains a lot of service information. Only the relevant data is important for further analysis; therefore, it is necessary to separate the service information from the relevant data. For this purpose, a json-response processing module has been implemented. This module uses the MapReduce technology for data structuring by way of arranging the data and excluding non-relevant and service data.

The third task was to analyze the data collected. The first study was the construction of a “tag cloud” for each of the three months separately. The results of the study are provided in Fig. 1, 2 and 3 respectively.

Figure 1. “Tag Cloud” for the period 15.05-14.06, 2018.

Figure 2. “Tag Cloud” for the period 15.06-14.07, 2018

Figure 3. “Tag Cloud” for the period 15.07-14.08, 2018.

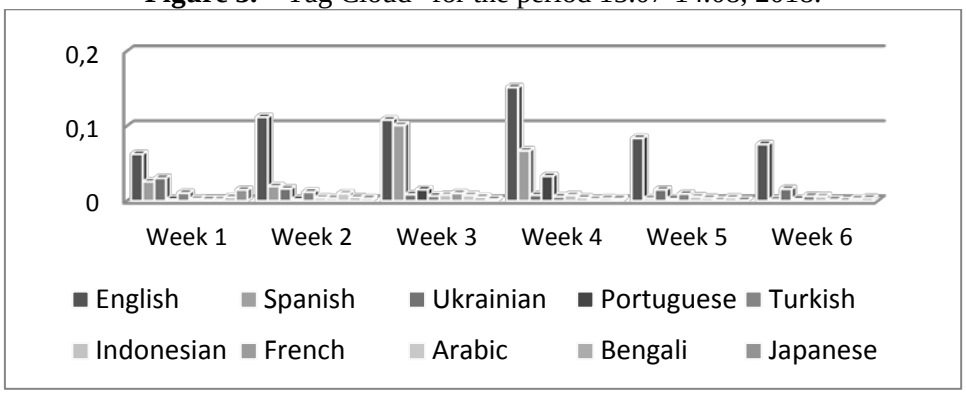

Figure 4. Distribution of messages by language for the period 11.06-22.07.2018.

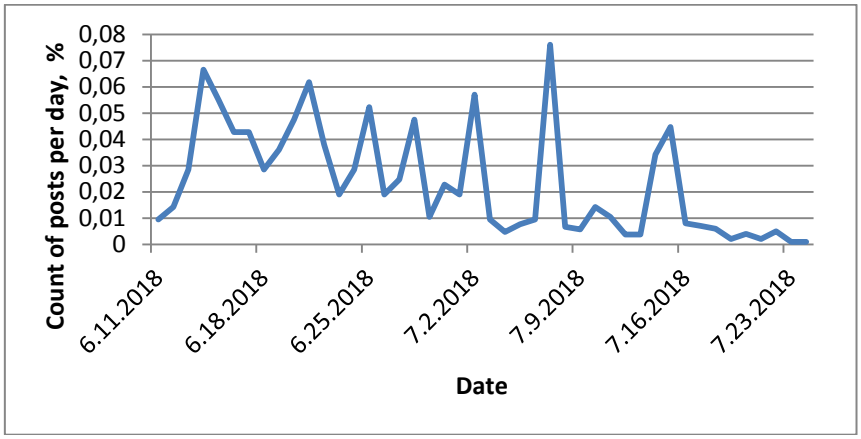

Figure 5. The distribution of the count of messages by day for the period 11.06-24.07 2018.

Thu 14 Jun 16:00	Russia	-	Saudi Arabia	Moscow
Fri 15 Jun 13:00	Egypt	-	Uruguay	Yekaterinburg
Fri 15 Jun 16:00	Morocco	-	Iran	Saint Petersburg
Fri 15 Jun 19:00	Portugal	-	Spain	Sochi
Sat 16 Jun 11:00	France	-	Australia	Kazan
Sat 16 Jun 14:00	Argentina	-	Iceland	Moscow
Sat 16 Jun 17:00	Peru	-	Denmark	Saransk
Sat 16 Jun 20:00	Croatia	-	Nigeria	Kaliningrad
Sun 17 Jun 13:00	Costa Rica	-	Serbia	Samara
Sun 17 Jun 16:00	Germany	-	Mexico	Moscow
Sun 17 Jun 19:00	Brazil	-	Switzerland	Rostov-on-Don
Mon 18 Jun 13:00	Sweden	-	South Korea	Nizhny Novgorod
Mon 18 Jun 16:00	Belgium	-	Panama	Sochi
Mon 18 Jun 19:00	Tunisia	-	England	Volgograd
Tue 19 Jun 13:00	Colombia	-	Japan	Saransk
Tue 19 Jun 16:00	Poland	-	Senegal	Moscow
Tue 19 Jun 19:00	Russia	-	Egypt	Saint Petersburg
Wed 20 Jun 13:00	Portugal	-	Morocco	Moscow
Wed 20 Jun 16:00	Uruguay	-	Saudi Arabia	Rostov-on-Don
Wed 20 Jun 19:00	Iran	-	Spain	Kazan
Thu 21 Jun 13:00	Denmark	-	Australia	Samara
Thu 21 Jun 16:00	France	-	Peru	Yekaterinburg
Thu 21 Jun 19:00	Argentina	-	Croatia	Nizhny Novgorod
Fri 22 Jun 13:00	Brazil	-	Costa Rica	Saint Petersburg
Fri 22 Jun 16:00	Nigeria	-	Iceland	Volgograd
Fri 22 Jun 19:00	Serbia	-	Switzerland	Kaliningrad
Sat 23 Jun 13:00	Belgium	-	Tunisia	Moscow
Sat 23 Jun 16:00	South Korea	-	Mexico	Rostov-on-Don
Sat 23 Jun 19:00	Germany	-	Sweden	Sochi
Sun 24 Jun 13:00	England	-	Panama	Nizhny Novgorod
Sun 24 Jun 16:00	Japan	-	Senegal	Yekaterinburg
Sun 24 Jun 19:00	Poland	-	Colombia	Kazan
Mon 25 Jun 15:00	Uruguay	-	Russia	Samara
Mon 25 Jun 15:00	Saudi Arabia	-	Egypt	Volgograd
Mon 25 Jun 19:00	Iran	-	Portugal	Saransk
Mon 25 Jun 19:00	Spain	-	Morocco	Kaliningrad
Tue 26 Jun 15:00	Denmark	-	France	Moscow
Tue 26 Jun 15:00	Australia	-	Peru	Sochi
Tue 26 Jun 19:00	Nigeria	-	Argentina	Saint Petersburg
Tue 26 Jun 19:00	Iceland	-	Croatia	Rostov-on-Don
Wed 27 Jun 15:00	South Korea	-	Germany	Kazan
Wed 27 Jun 15:00	Mexico	-	Sweden	Yekaterinburg
Wed 27 Jun 19:00	Serbia	-	Brazil	Moscow
Wed 27 Jun 19:00	Switzerland	-	Costa Rica	Nizhny Novgorod
Thu 28 Jun 15:00	Japan	-	Poland	Volgograd
Thu 28 Jun 15:00	Senegal	-	Colombia	Samara
Thu 28 Jun 19:00	England	-	Belgium	Kaliningrad
Thu 28 Jun 19:00	Panama	-	Tunisia	Saransk
Fri 29 Jun				
Sat 30 Jun 15:00	C1	-	D2	Kazan
Sat 30 Jun 19:00	A1	-	B2	Sochi
Sun 01 Jul 15:00	B1	-	A2	Moscow
Sun 01 Jul 19:00	D1	-	C2	Nizhny Novgorod
Mon 02 Jul 15:00	E1	-	F2	Samara
Mon 02 Jul 19:00	G1	-	H2	Rostov-on-Don
Tue 03 Jul 15:00	F1	-	E2	Saint Petersburg
Tue 03 Jul 19:00	H1	-	G2	Moscow
Wed 04 Jul				
Thu 05 Jul				
Fri 06 Jul 15:00	W49	-	W50	Nizhny Novgorod
Fri 06 Jul 19:00	W53	-	W54	Kazan
Sat 07 Jul 15:00	W55	-	W56	Samara
Sat 07 Jul 19:00	W51	-	W52	Sochi
Sun 08 Jul				
Mon 09 Jul				
Tue 10 Jul 19:00	W57	-	W58	Saint Petersburg
Wed 11 Jul 19:00	W59	-	W60	Moscow
Thu 12 Jul				
Fri 13 Jul				
Sat 14 Jul 15:00	L61	-	L62	Saint Petersburg
Sun 15 Jul 16:00	W62	-	W61	Moscow

Figure 6. World Cup World Cup schedule 2018.

It can be seen in Figures 1, 2 and 3, that the filling of the “clouds” changed dramatically with the beginning of the World Cup in the Samara Region. Taking into account the results of the previous study, the decision was taken to look at the dynamics of changes in the number of messages in different languages in the next study. The analysis of the language of writing a message was carried out on the basis of data provided by the Twitter social network in json-response. A 7-day period was selected as an analysis period. The results are provided in Fig. 4.

As it can be seen from Fig. 4, the number of messages in the languages other than Russian varied in accordance with the football games held in the city of Samara. It started to increase a week before the beginning of the tournament, then the number of messages remained at the same level throughout the tournament and then dropped to the values close to zero due to the departure of delegations.

Additionally, we construct a graph of user activity by day (Figure 5) and relate it to the schedule of games (Figure 6).

As can be seen on the graph, the peak of user activity fell on the days of the games at the Samara Arena stadium. On the days of the games at other stadiums, user activity was lower than on the days of matches in Samara. On the other days, the activity did not exceed 0.01 percent (the exception was the match days for the third place and the final). The peak of activity came on 07.07.18 when the matches at the Samara Arena and Russia - Croatia took place. After the end of the World Cup, user activity has declined sharply.

4. Conclusion

In this paper, a study was conducted of the activity of the users of the social network Twitter of the Samara region, as well as the activity of the guests of the 2018 World Cup who came to support the national teams in the city of Samara. The study showed that a major event can drastically change the main subjects of messages and dictionaries of frequently used words in social networks. From this it follows that when analyzing social network data in the period of any major events, it is necessary to apply methods of reactive data analysis, as well as take into account user profile information for correct data processing (collect separate statistics, since it will be completely different from statistical data which was collected before the event).

5. References

[1] Dahal B, Kumar S A P and Li Z 2019 Topic modeling and sentiment analysis of global climate change tweets *Social Network Analysis and Mining* **9(1)** 24

[2] Rashid J, Shah S M A and Irtaza A 2019 Fuzzy topic modeling approach for text mining over short text *Information Processing & Management* **56(6)** 102060

[3] Groß-Klußmann A, König S and Ebner M 2019 Buzzwords build Momentum: Global Financial Twitter Sentiment and the Aggregate Stock Market *Expert Systems with Applications*

[4] Zhu C, Du J 2018 Background feature clustering and its application to social text *Information Processing Letters* **136** 44-48

[5] Rytsarev I A, Kupriyanov A V, Kirsh D V and Liseckiy K S 2018 Clustering of social media content with the use of BigData technology *Journal of Physics: Conference Series* **1096(1)** 012085.

[6] Blagov A, Rytcarev I, Strelkov K and Khotilin M 2015 Big Data Instruments for Social Media Analysis *Proceedings of the 5th International Workshop on Computer Science and Engineering* 179-184

[7] Rytsarev I, Blagov A 2017 Creating the Model of the Activity of Social Network Twitter Users *Journal of Telecommunication, Electronic and Computer Engineering (JTEC)* **9(1-3)** 27-30

[8] Kusumawardani R P, Priansya S and Atletiko F J 2018 Context-sensitive normalization of social media text in bahasa Indonesia based on neural word embeddings *Procedia computer science* **144** 105-117

[9] Rytsarev I A, Blagov A V 2017 Development and research of algorithms for clustering data of super-large volume *CEUR Workshop Proceedings* **1903** 80-83

[10] Mikhaylov D V, Kozlov A P and Emelyanov G M 2016 Extraction of knowledge and relevant linguistic means with efficiency estimation for the formation of subject-oriented text sets *Computer Optics* **40(4)** 572-582 DOI: 10.18287/2412-6179-2016-40-4-572-582
[11] Rytsarev I A, Kirsh D V and Kupriyanov A V 2018 Clustering of media content from social networks using BigData technology *Computer Optics* **42(5)** 921-927 DOI: 10.18287/2412-6179-2018-42-5-921-927.
[12] Kropotov Y A, Proskuryakov A Y and Belov A A 2018 Method for forecasting changes in time series parameters in digital information management systems *Computer Optics* **42(6)** 1093-1100 DOI: 10.18287/2412-6179-2018-42-6-1093-1100

Acknowledgments
This work was financially supported by the Russian Foundation for Basic Research under grant # 19-29-01135, # 18-37-00418, # 17-01-00972 and by the Ministry of Science and Higher Education within the State assignment to the FSRC “Crystallography and Photonics” RAS No. 007-GZ/Ch3363/26 (theoretical results).

Forecast of water-cut at wells under design by machine learning methods

M R Enikeev[1], M F Fazlytdinov[1], L V Enikeeva[2] and I M Gubaidullin[2,3]

[1]Gazpromneft STC, Moika River emb., 75-79, liter D, St. Petersburg, Russia, 190000
[2]Ufa State Petroleum Technological University, Kosmonavtov St., 1, Ufa, Russia, 450062
[3]Institute Petrochemistry and Catalysis - Subdivision of the Ufa Federal Research Centre of RAS, Oktyabria pr., 141, Ufa, Russia, 450075

e-mail: mat-83@mail.ru, leniza.enikeeva@gmail.com

Abstract. A large amount of data is generated during the operation of oil fields. Such data can be both data already interpreted by a specialist, or "raw" data obtained directly from the devices, both structured and not structured, or locally structured (that is, allowing for local analysis, but in such form not allowing analyzing in conjunction with other types of data). To obtain from such a set of more informative data that will allow making decisions in the course of field operation, it is necessary to involve specialists from different areas of the oil industry. Therefore, it is possible and necessary to use non-deterministic methods for analyzing the data obtained. The article discusses the use of machine learning methods in the task of determining the initial water-cut based on well logging data.

1. Introduction

Initial water content (or water cut) of the well is the relative water content in the produced liquid, expressed as a percentage, at the beginning of the well operation. It allows assessing the feasibility of commissioning an oil well. One of the necessary tasks is the forecast of water cut in new wells and the allocation of the share of unproductive production/injection during the operation of wells that open water-saturated horizon in addition to the target horizon. Dynamics of water-flooding of oil wells is determined by the nature of oil reservoirs water-cut. The nature of the reservoir water-cut can significantly differ and depends on the properties of the productive layers, the initial conditions of oil occurrence in the reservoir. In addition, the nature of water-flooding and the water-flooding dynamics is influenced by layered and zonal heterogeneity. The intensity of watering depends on the permeability of the layer. The uneven watering of the layers by their thickness and strike increases with a high ratio of oil and water viscosity. Many of these factors are embedded in the methods of well logging.

Well logging is a set of exploration geophysics methods used to study the properties of rocks in the near-well and inter-well spaces and to control the technical condition of wells. Well logging is composed of two groups of methods — geophysical logging and geological logging.

Normally, well logging data represent strongly and randomly fluctuating functions (Figure 1).

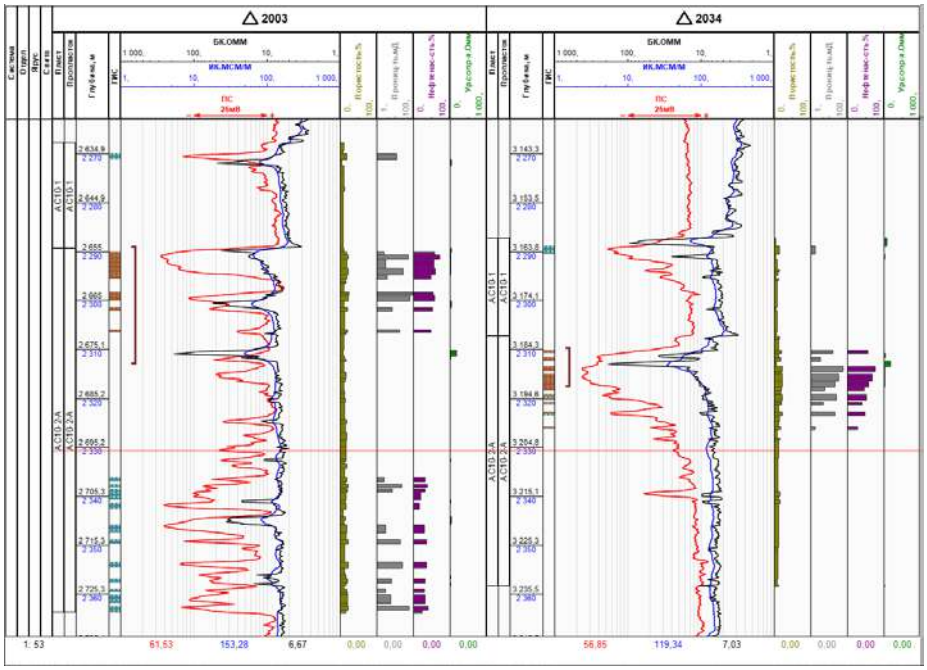

Figure 1. Example of logging data: the y-axis is usually the depth, the x-axis is the logging value.

In work [1] considers the possibility of applying analog-statistical methods in the forecast of the water-cut of production wells with the consideration of the influence of geological and technological indicators. One of the key elements of the methodology is building the modified dependences of wells water content on the degree of production of recoverable oil reserves for analog models. The conclusion about the adequacy of the forecast to the real geological object can be made by comparing the actual and forecast productivity. The use of such techniques can significantly reduce errors in the forecast of flow rates and water cut of new wells and increase the reliability of the operational production forecast. Deshenenkov [2] proposed a method for predicting the productivity and initial water content of oil deposits using: relative permeability to oil and water, field geophysical data and effective porosity. To predict water cut based on well logging data, the paper [3] uses the formulas of the Corey model, which determine the permeability for oil and water. Then, in the perforated intervals, accumulated permeabilities for water and oil are calculated. After that, taking into account the viscosities of both phases, the water-cut ratio is estimated. In these works, pre-defined model formulas are used to compare the values of water cut and logging data, but no in-depth analysis of the impact of different types of logging on the values of water cut has been made.

2. Problem statement

As mentioned earlier, well logging data are the main source of information about the reservoir at the stage of building of the geological model and the creation of the concept for oil field development. The aim of this work is to develop a method for forecasting water cut on new wells based on logging data.

Modern development of machine learning methods can effectively solve a wide range of problems in various fields. For example, when predicting the occurrence of a stroke [4], predicting the state of electromechanical systems of rolling production [5], predicting red shifts of galaxies [6], as well as in the oil industry, for example, to interpret seismic data [7] and to predict the development of corrosion of pipe steel [8]. The oil industry is a source of large amounts of structured and unstructured data. A large number of engineering (analytical / empirical) methods for studying the subject area have been developed. Machine learning methods well complement the existing set of tools for working with studied and developed oil fields.

In terms of machine learning, the problem of water cut prediction refers to the classification problem — it is necessary to divide the set of objects X (the set of logging data from the field) into M

disjoint classes Y (different water cut values). Thus, the concepts of object space and class space are defined. As it is known, there are two stages in machine learning tasks — the learning stage and the application stage. In this case, the training sample is a set of logging curves interpreted by the geophysicist, where for each element it is known what value of water cut it belongs to. An integral preparatory stage for the classification algorithm is also the selection of objects features, which will be discussed later.

3. Implementation of the approach

The problem is reduced to the feature classification problem. First, the data were pre-processed: filtering by values was carried out ('nan' values were removed from the data, obviously incorrect values were also removed (for example, values > 1 for 'aps', values < 0 for 'kint', and so on)). Then, for each parameter, its feature description was built. Features were generated based on different approaches:

- Data approximation
- Statistics
- Fourier analysis (not included in the final solution)

Further, in the report each approach is described in detail and justified. The classification was performed with regression algorithms that estimated the water-cut value from the logging data.

The capabilities of the following algorithms were studied in detail:

- Random forest
- Gradient boosting
- Neural networks

Technically, the problem was solved as follows. Using the lasio library and a python script, the data was unloaded from the LAS format into CSV (with depth parameter values). Then these data were loaded in another script, the data were filtered, the roof and floor values were determined, and the features for the training task were generated. The set of LAS features was matched with the water cut values (Matlab was used to generate features by Fourier method). The data were separated for training and control, in ratio of 70/30. These features were used to configure regressors from the skit-learn library and on tensorflow and keras neural networks.

3.1. Data loading and analysis

For the initial data analysis, it was decided to check whether there is an explicit dependence of the water cut (wc) value on the logging data. During the data analysis, it was observed that it is better to analyze the area lying between the roof and the floor. For the evaluation, it was decided to compare scaled data with the averaging values in this area for each parameter, to establish a relationship between them (Figure 2). From Figure 2 it can be concluded that the allocation of meaningful information is not possible. Dependency analysis on a logarithmic scale also gave no results. Therefore, it was decided to check how effective the various feature generation algorithms are.

3.2. Feature generation

The problem of feature classification was reduced to the classical feature classification, when each object (in this case, a curve or a set of curves) was described by a fixed set of real features. The simplest example of a feature is the average value on the curve. However, the features should be selected to describe the signal as accurately as possible, and to take into account the physics of the described processes. In addition, various heuristics can be used to generate the features.

Several approaches were used to generate features. All of them are described below. The result of such generation is a set of features, from tens to hundreds of values, depending on the method.

In order to determine more effective methods of feature generation, experiments were conducted with the setting up classifiers on different feature spaces and evaluating the classification quality on the control sample (30% of the total).

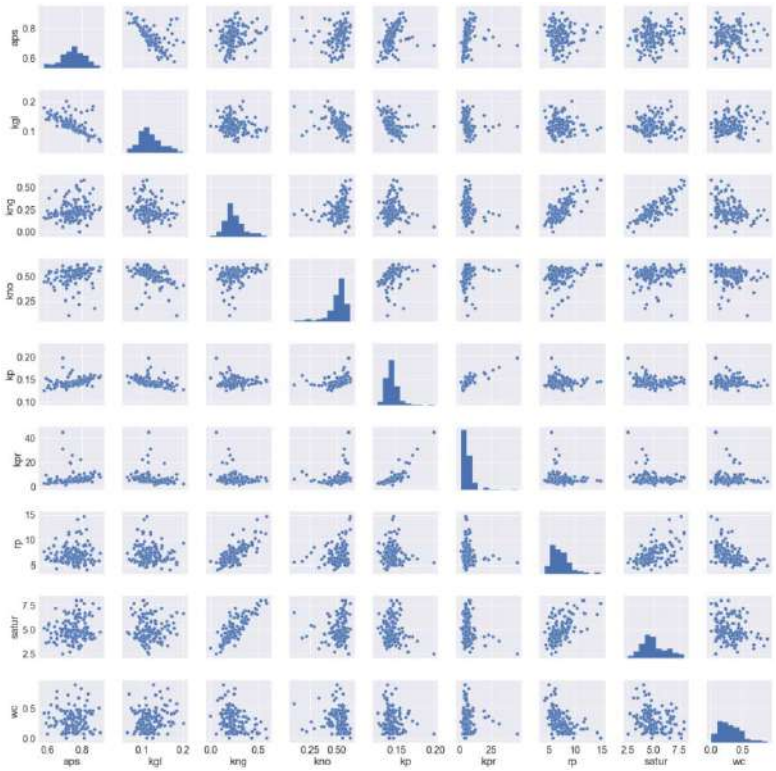

Figure 2. Correlation between various well parameters for which water cut values averaged over depth.

3.2.1. Feature evaluation

MAE (Mean absolute error) method was used to assess feature quality:

$$\text{MAE} = \frac{\sum_{i=0}^{N-1} |wc_{cor} - wc_{predict}|}{N}$$

where wc_{cor} – expected water cut value, $wc_{predict}$ – water cut value predicted by the classifier, N – number of wells in the control sample.

3.2.2. Features based on piecewise linear interpolation

The method based on piecewise linear interpolation was tested first. The data on the selected parameter (curve), after removing the incorrect values, were considered in the interval between the roof and the floor (this operation will be further denoted as preprocessing), after which the value was generated at k points, with the same depth step. Next, the values at these k points are submitted to the classifier.

3.2.3. Statistical features

First, each curve was preprocessed, then the statistical features for both the signal and its derivatives were calculated. The generation at this stage is carried out in the following order:

- Preprocessing
- For the signal $(x_1, \dots, x_n)$, derivative $(x_2 - x_1, x_n - x_{n-1})$ and modulus of the derivative $(|x_2 - x_1|, |x_n - x_{n-1}|)$ the following feature values are calculated: mean value, standard deviation, proportion of intersections with level a (a = 0, a = mean, a = mean + std)

An variant was also considered using features of percentile values (p10, p50, p90, etc.), mean value and deviation.

3.2.4. Features based on Fourier decomposition (transform)

When analyzing signals, one of the most successful methods is the use of the Fourier transform (in our case, the one-dimensional discrete Fourier transform (DFT)).

Using the DFT coefficients, it was not possible to achieve good results in the classification, so it was decided to lay out not the entire curve, but its sections. Then, these decompositions should be averaged (with logic to obtain stable features). For this, matlab was used, that has a spectrogram function, for dividing the signal into segments and calculating the DFT at each of them. Unfortunately, this method proved to be worse than the first two.

3.2.5. Selection of the optimal features and the parameter by which to conduct training

To select the optimal method of feature generation, it was decided to classify the ensemble of trees, with the search for the optimal settings for the method (changing the maximum depth of a tree, the number of trees in the ensemble of solutions, the number of selected features).

For a complete analysis of the optimal well logging curve for classification, the following curves were analyzed: 'kint', 'r05', 'r20', 'r14', 'r10', 'f07', 'f10', 'f14', 'r07', 'f20', 'f05', 'phit', 'mres', 'sg', 'kgl', 'sxwb', 'gz3', 'nphi', 'gz2', 'gz4', 'gz1', 'cild', 'prox', 'lld', 'gz7', 'aps', 'kps', 'gz5', since these curves are most densely filled with data.

The results of the comparison of the feature generation algorithms for most curves are shown in Figure 3. As a result of this test, it was decided to use an algorithm based on statistical features.

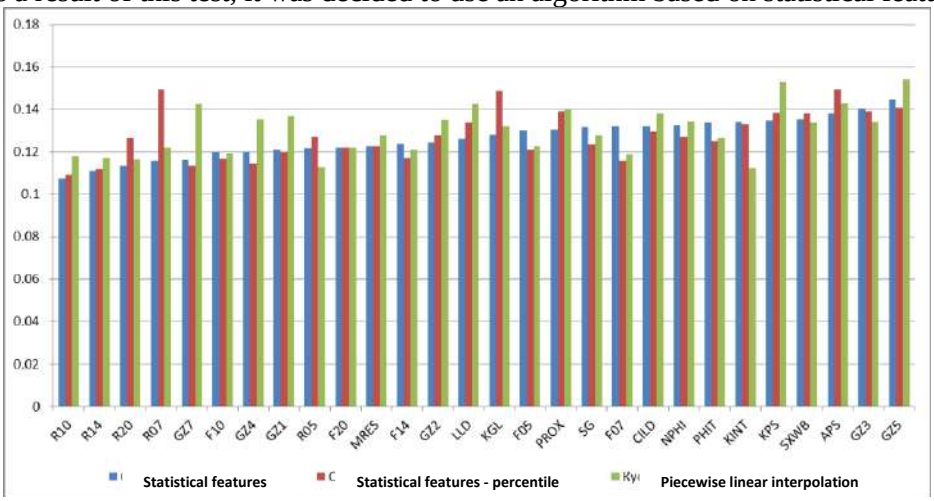

Figure 3. Comparison of feature generation methods for training.

The average MAE values for different methods are [0.127, 0.128, 0.130], and as we can see, the result is almost independent of the method of generating parameters and on the choice of the curve from the logging data.

The result on the control sample (30% of the test) on the gz5 curve is shown in Figure 4. Features were calculated by a statistical method. The real water cut values are shown in red, the predicted values are in blue.

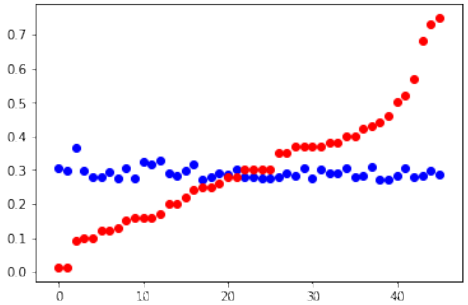

Figure 4. The result of the classifier by gz5 (red – real water cut values, blue - predicted values).

A similar pattern is observed for other logging curves. Tests were conducted on the combination of some logging curves in the generation of training parameters. There was no significant change in the prediction results.

It can be assumed that the result is a consequence of the uneven distribution of water cut values in the training sample and the classifier seeks to predict the average water cut value in the input data (Figure 5).

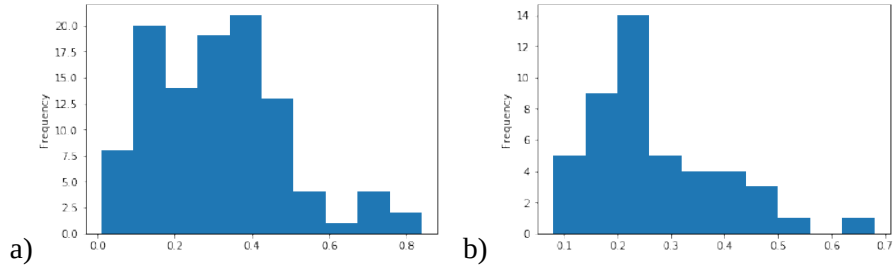

a) b)

Figure 5. Histograms of water-cut values: for the training sample a) and for the control sample b).

It was decided to check how the classifier would behave on a more extensive training sample.

4. Modeling/simulation of the logging data by the spectral method

One of the main requirements for the application of machine methods task is a large set of training samples. Possible solutions to the problem of expanding the training sample:

- Modeling of logging data by spectral method and interpolation (approximation) of the water cut map. Articles [9 – 11] describe the approach used to generate logging data of a field.
- Use of logging data and water cut for several "similar" fields (for example, all fields of Western Siberia).

In this paper, the first solution was used.

To generate target water cut values, a water cut map is required. It was obtained by logarithmic approximation of the initial water cut data provided.

The described scheme for obtaining logging curves data and the water-cut map is shown in Figure 6.

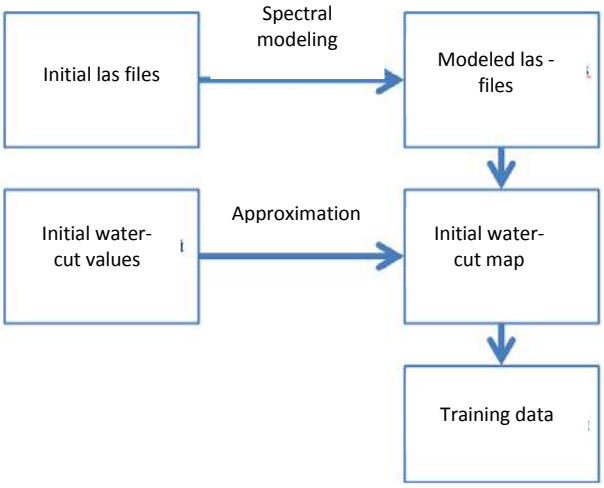

Figure 6. The generation of the extended training sample.

The results of the logging data obtained by spectral modeling are shown in Figure 7 (the original logging is shown in blue, modeled logging is shown in red) the well 105 did not participate in the modeling, and as a result was correctly predicted.

As a result of the simulation, the training sample was expanded to 5349 wells. That is, extended data were obtained for training the classifier.

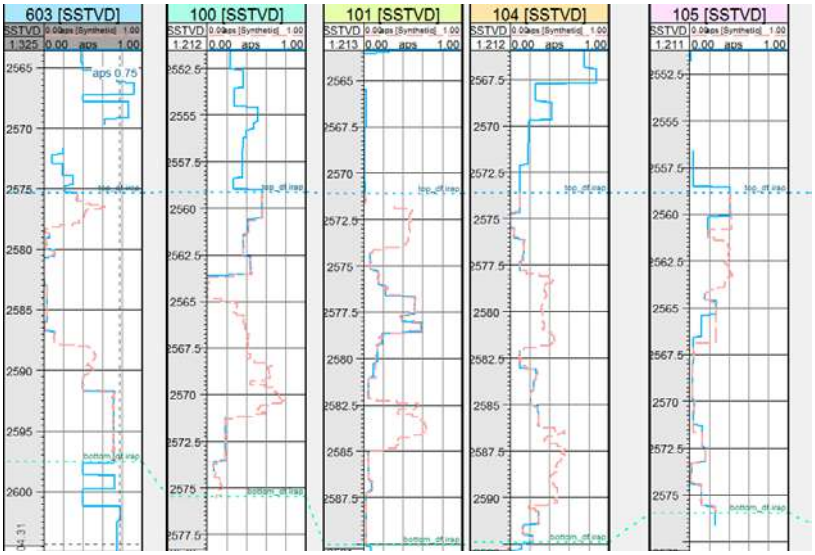

Figure 7. Results of spectral modeling on the aps curve.

4.1.1. Training on an extended training sample

In this sample, piecewise linear interpolation was used to generate features. The aps and kgl curves from well log interpretation data were considered as initial data, since it was not possible to analyze and expand the sample from well logging data within the framework of the task.

The ensemble of trees with search of optimal settings for the method and multilayer neural network were considered as a classification tool.

The structure of the considered multilayer neural network is as follows

```
_________________________________________________________________
Layer (type)                 Output Shape              Param #
=================================================================
dense_1 (Dense)              (None, 250)               25250
_________________________________________________________________
dense_2 (Dense)              (None, 200)               50200
_________________________________________________________________
dense_3 (Dense)              (None, 100)               20100
_________________________________________________________________
dropout_1 (Dropout)          (None, 100)               0
_________________________________________________________________
dense_4 (Dense)              (None, 100)               10100
_________________________________________________________________
dense_5 (Dense)              (None, 49)                4949
_________________________________________________________________
dense_6 (Dense)              (None, 1)                 50
=================================================================
Total params: 110,649
Trainable params: 110,649
Non-trainable params: 0
```

The trained model was tested on three types of data: control sample (selected from the extended training set), *wc* values on the approximated map (for initial wells) and real *wc* values (for initial wells).

Below are the results of the analysis of the classifiers. Red colour indicates expected values, blue colour indicates predicted values. To clarify the result, the following values are additionally attached to each chart: ‘MSE’, ‘MAE’, ‘R2 score’, ‘Explained variance score’:

- MSE – mean square error.

$$\mathrm{MSE} = \frac{\sum_{i=0}^{N-1}\left(wc_{cor} - wc_{predict}\right)^2}{N}$$

- MAE - mean absolute error, described in 3.2.1.
- R2 score – coefficient of determination, is an indicator of the quality of the regression model. A value of 1 represents the ideal predictive ability, and a value of 0 represents the constant of the model that predicts the average of the responses.

$$R^2 = 1 - \frac{\sum_{i=0}^{N-1}\left(wc_{cor} - wc_{predict}\right)^2}{\sum_{i=0}^{N-1}(wc_{cor} - wc_{mean})^2}$$

- *Explained variance score* – explained variation.

$$\text{explained}_{\text{variance}} = 1 - \frac{Var\{wc_{cor} - wc_{predict}\}}{Var\{wc_{cor}\}}$$

In the above formulas: where wc_{cor} – expected water cut value, $wc_{predict}$ – water cut value predicted by the classifier, N – number of wells in the control sample, $Var\{\}$ – dispersion.

The results of classification on the aps data (ensemble of trees) are shown in Figure 8.

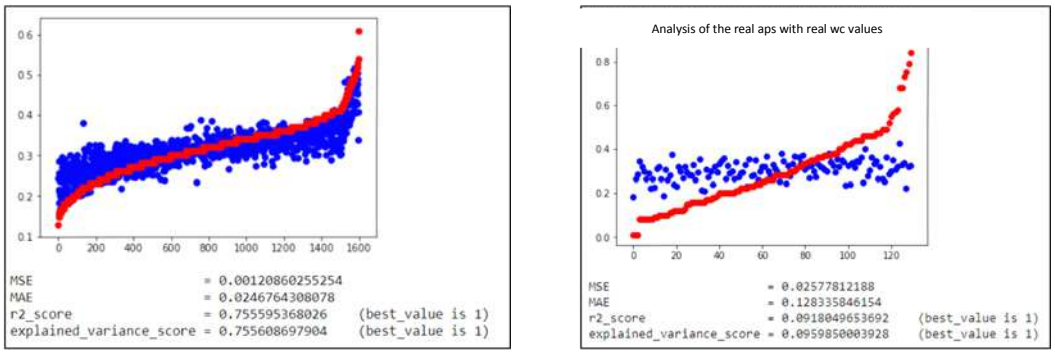

Figure 8. Results of the classification by the ensemble of trees with feature generation by piecewise interpolation method based on aps data.

The results of classification on the aps data using a neural network are shown in Figure 9.

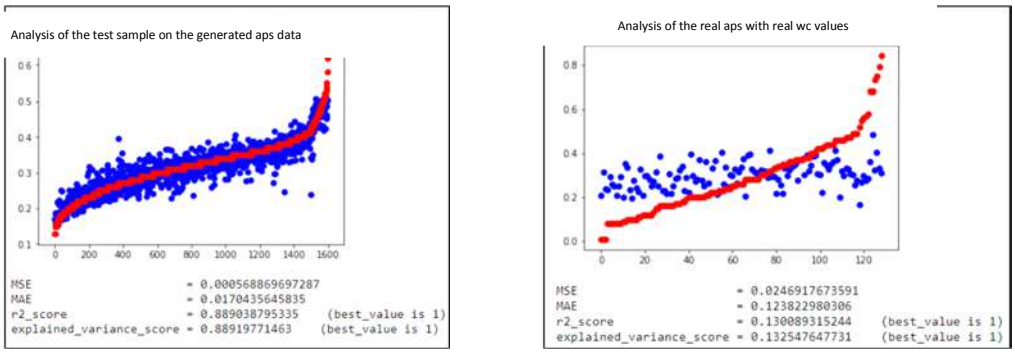

Figure 9. Results of the classification by neural network with feature generation by piecewise linear interpolation method based on aps data.

Since the results of the classifiers' work by the ensemble of trees and by neural networks differ slightly, on the example of aps, it was decided to carry out further checks by any of the classifiers. The results of classification on kgl data using a neural network are shown in Figure 10.

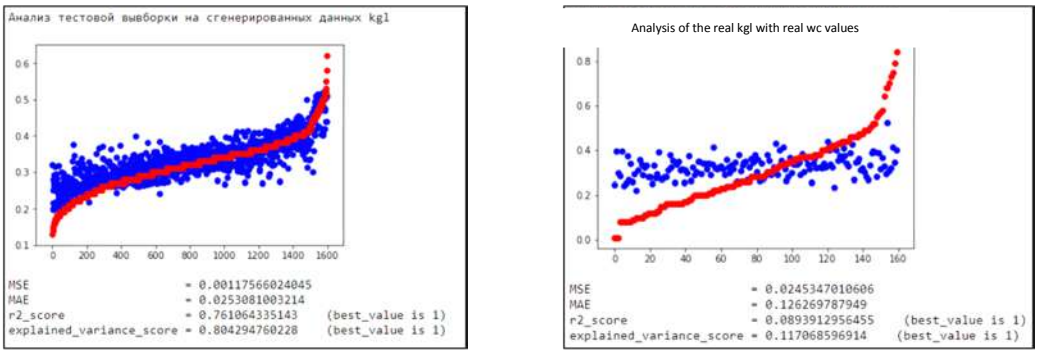

Figure 10. Results of the classification by neural network with the feature generation by piecewise linear interpolation method based on kgl data.

The results of classification on a combination of aps and kgl data were analyzed (Figure 11):

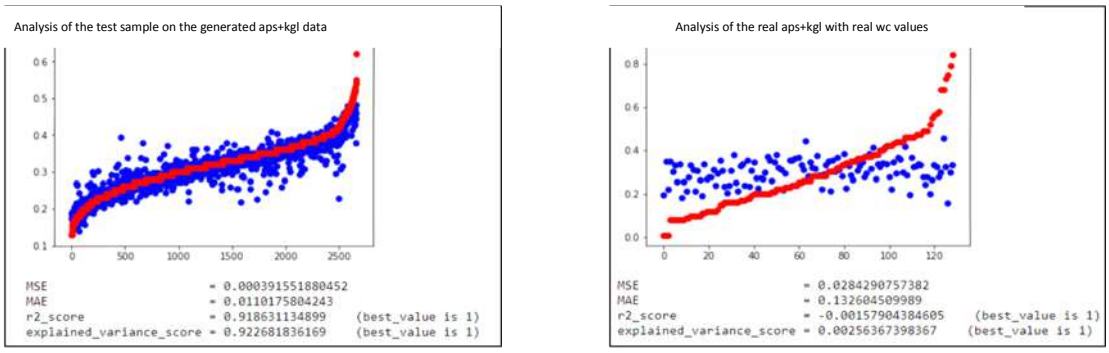

Figure 11. Results of the classification by neural network with the feature generation by piecewise linear interpolation method on combined kgl and aps data.

As we can see, on the real data, all models showed the result of the same order (on the extended data, the combination of kgl and aps showed the best prediction, r2_score = 0.92 on the control sample). High accuracy on the control sample, and much worse prediction on real wells. For example, r2_score = 0.92 and r2_score = -0.07, respectively. Therefore, it was decided to check how the classifier trained on extended data works for the data obtained from a different spectral experiment, but with the same initial data (Figure 12). From Figure 12 and Figures 7 – 8, it follows that on the data of the same type (modeled by the spectral method), the classifier shows similar results.

For the neural network r2_score = 0.89 and r2_score = 0.75, on the first and second spectral experiments, respectively.

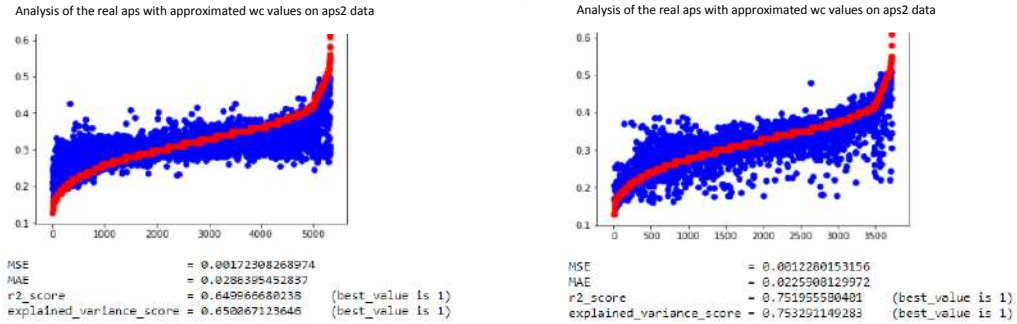

a) b)

Figure 12. Results of classification (a) by an ensemble of trees, (b) by a neural network with feature generation by piecewise linear interpolation method from aps data on part of the data of the second set of spectral modeling.

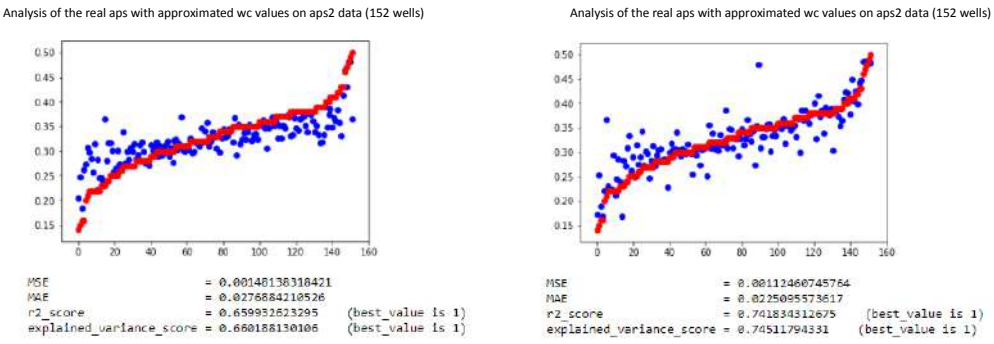

a) b)

Figure 13. Results of classification (a) by an ensemble of trees, (b) by a neural network with feature generation by piecewise linear interpolation method from aps data on part of the data of the second set of spectral modeling (152 wells).

The accuracy of the r2_score prediction is determined by the amount or quality of the data, so it was decided to test the classifiers on a small amount of test data generated for the aps2 experiment. Random 152 wells were selected. As follows from Figure 13 and Figure 12, the amount of data does not affect the estimate of the forecast accuracy (the values of the accuracy metrics coincide). It is possible that the outliers lie in a small vicinity of real wells, and if they are not submitted to the classifier, the accuracy of the prediction on the extended data will be higher.

The reasons that the classifier shows high accuracy on extended data and low accuracy on real data may be:

- Incorrect or incomplete selection of curves for features generation.
- Data pre-processing practically did not take into account the physical patterns of well log interpretation data.
- Method of features generation. Perhaps, the chosen method is sensitive to the shape of the curve, and therefore it reveals patterns of data generation by the spectral modeling method.

5. Conclusions

The paper deals with the main aspects of image processing and analysis in the study of the mechanism of corrosion damage:

- The analysis and pre-processing of well logging data. Rapid analysis of the correlation between the well log interpretation data and water cut did not reveal any visible patterns. The amount of data and the distribution of water cut values (see Fig. 4) is insufficient to configure the regression and multi-class classifier.
- Four methods of features generation were studied. piecewise linear interpolation, 2 methods of generating statistical features and DFT analysis. DFT analysis turned out to be poorly applicable (perhaps, the authors could not find the optimal coefficients that should be used for training). The method based on piecewise linear interpolation and methods based on statistical features showed almost identical results.
- Four methods of classification were considered: trees, random forest, gradient boosting and multi-layer neural networks. On the generated features all methods showed close results (except for a single tree), the ensemble of trees and neural networks had a slight advantage in training time.
- The classifiers are set up on the well log interpretation data and well logging data and it is concluded that they tend to predict the average water-cut value. Therefore, in order to increase the variety of data for training, the training sample was extended to well log interpretation data, using spectral modeling for logging data and water cut approximation.
- Classifiers were trained on the well log interpretation data extended sample, which showed high prediction accuracy on the control extended sample (one set for training and one set for establishing accuracy, about 5000 in each set, and training was done on 3500). However, the accuracy of these classifiers on the source data was low.

6. References

[1] Ilyushin P I, Galkin S 2011 Forecast of production watering in producing wells of the Perm region using analog-statistical methods *Bulletin of the Perm National Research Polytechnic University. Geology, oil and gas and mining* **10(1)** 76-84

[2] Deshenenkov I S 2013 Forecast of productivity and initial water cut of oil wells of one of the fields of western Siberia according to field geophysics data *Drilling and oil* **7(8)** 32-35

[3] Alekseev A D, Aniskin A A, Volokitin Ya E, Zhitnyy M S and Khabarov A V 2011 Experience and Prospects for the Use of Modern GIS and Gdis Complexes in the Salym Group Deposits *Production engineering and technical oil and gas magazine "Engineering practice"* **11-12** 62-75

[4] Karp V P, Sayapina Yu A, Khetagurova L G and Botoeva N K 2012 Building decision rules in the study of the dynamics of cosmophysical indicators in order to predict situations that provoke the occurrence of stroke episodes *Health and education in the XXI century* **14(1)** 221-222

[5] Kozhevnikov A V, Ilatovsky I S and Solov'eva O I 2017 The use of machine learning methods in predicting the state of electromechanical systems of rolling production *Bulletin of Cherepovets State University* **1** 33-39
[6] Gerasimov S V, Meshcheryakov A V 2017 Application of the Microsoft Azure HDInsight platform for processing and analyzing large astronomical data arrays *International Journal of Open Information Technologies* **5(1)** 81-87
[7] Krasnov F V, Butorin A V and Sitnikov A N 2018 Automated detection of geological objects in seismic field images using deep learning neural networks *Business Informatics* **2** 7-16
[8] Enikeev M R, Gubaidullin I M and Maleeva M 2017 A Information-computational analytical system for the assessment and prediction of corrosion processes on the surface of steel and aluminum *Informatics systems and tools* **27(3)** 155-170
[9] Baikov V A, Bakirov N K and Yakovlev A A 2010 New approaches in the theory of geostatistical modeling *Bulletin of Ufa State Aviation Technical University* **14(2)** 209-215
[10] Baikov V A, Bochkov A S and Yakovlev A A 2011 Accounting for heterogeneity in geological and hydrodynamic modeling of the Priobskoye field *Oil industry* **5** 50-54
[11] Khasanov M M, Belozerov B V, Bochkov A S, Ushmaev O S and Fuks O M 2014 Application of spectral theory for the analysis and modeling of reservoir properties of a reservoir *Oil industry* **12** 60-64

Determining the proximity of groups in social networks based on text analysis using big data

A S Mukhin[1], I A Rytsarev[1,2], R A Paringer[1,2], A V Kupriyanov[1,2], D V Kirsh[1,2]

[1]Samara National Research University, Moskovskoe Shosse 34A, Samara, Russia, 443086
[2]Image Processing Systems Institute of RAS - Branch of the FSRC "Crystallography and Photonics" RAS, Molodogvardejskaya street 151, Samara, Russia, 443001

e-mail: andrey63ru@mail.ru

Abstract. The article is devoted to the definition of such groups in social networks. The object of the study was selected data social network Vk. Text data was collected, processed and analyzed. To solve the problem of obtaining the necessary information, research was conducted in the field of optimization of data collection of the social network Vk. A software tool that provides the collection and subsequent processing of the necessary data from the specified resources has been developed. The existing algorithms of text analysis, mainly of large volume, were investigated and applied.

1. Introduction

Currently, social networks are booming: every day their users send billions of messages and leave millions of comments under the relevant posts. The analysis of such content is of great importance for many areas of business. For example, it is impossible to overestimate the impact of Internet marketing on the promotion of goods and services. However, clear understanding of user requests is essential to use these mechanisms effectively. The source of such information can be the materials published by users of social networks, as well as the shares and reposts by users and the entire communities. Thus, the issue of determining the proximity of groups in the social network Vkontakte using the BigData technology, considered in this paper, is certainly a relevant objective and a task of great scientific importance in the field of data analysis.

Data processing from social networks is very popular now. For example, in the article [1] proposes a text normalization with deep convolutional character level embedding (Conv-char-Emb) neural network model for SA of unstructured data. This model can tackle the problems: (1) processing the noisy sentence for sentiment detection (2) handling small memory space in word level embedded learning (3) accurate sentiment analysis of the unstructured data. In the article [2], authors introduce SS3, a novel supervised learning model for text classification that naturally supports these aspects. SS3 was designed to be used as a general framework to deal with ERD problems. In the article [3], authors propose a nonparametric model (NPMM) which exploits auxiliary word embeddings to infer the topic number and employs a “spike and slab” function to alleviate the sparsity problem of topic-word distributions in online short text analyses. NPMM can automatically

decide whether a given document belongs to existing topics, measured by the squared Mahalanobis distance. In the article [4], examine the long-term relationship between signals derived from nine years of unstructured social media microblog text data and financial market developments in five major economic regions. Employing statistical language modeling techniques we construct directional sentiment metrics. In the article [5], the authors propose a background clustering technology for discussion. Compared with the traditional methods, background future clustering keeps the constrains caused by data sparseness and spatio-temporal dependence off, and can be used for unpredictable activities discovery

2. Social network data collection

The social network Vkontakte was selected as a data source for this study [6]. The reasons for this choice are as follows:

- the network provides open access to its data (no restrictions on accessing the server data);
- Vkontakte is the most popular social network in Russia and the fifth most popular social network in the world;
- Vkontakte is a full-fledged social network (unlike Twitter and Instagram, which are microblogs) allowing to create thematic communities, which are particularly interesting for this study.

As part of this study, a Python software package was developed, containing an authorization module, a data collection module, and a filtration module. This software package allows to collect data and filter them to take the relevant information only.

Within this study, the developed software package was used to collect more than 8,000 posts and over 280,000 comments on them from the two most popular communities of the city of Samara ("Podslushano Samara" and "Uslyshano Samara") and from the community of the Samara University students ("Podslushano Samarsky Universitet").

Streaming data obtained from social networks contains a lot of service information. Only the relevant data is important for further analysis; therefore, it is necessary to separate the service information from the relevant data. The software package pre-processing module structures the collected data and filters the relevant and the service fields.

3. Determination of the proximity of groups using BigData technology

To determine the proximity of groups, several metrics for the comparison of word indexes were considered: Euclidean distance, city-block distance and Mahalanobis distance [7, 8]. The Euclidean distance was chosen, since it is most suitable for this experiment according to the following criteria:

1) It is the most widely used and universal metric;
2) The Euclidean distance is calculated based on the original, not the standardized data.

To calculate this metric, attribute vectors were formed between the groups by combining two word indexes or more into a common one [9]. Weight was assigned to each word in the word index, thus each group took the form of a vector of attributes (words) with own weights. In this paper, it was decided to use the word frequency count as the weight [10, 11].

Such an approach for calculating the weights of words in word indexes using traditional methods and technologies requires huge computational resources and takes a long time when the volume and the number of analyzed word indexes increases, so it was decided to use BigData technology and computational clusters for this purpose [12]. At this stage, an algorithm involving MapReduce technology was developed, that rejected non-informative parts of the word index (words consisting of less than three or more than fifteen characters) and also counted the frequency of words in the text. As a result, three word indexes were developed, the elements of which had their own weights, one of them is presented in Fig. 1.

At the next step, it was decided to use two word indexes (of the groups "Podslushano Samara" and "Uslyshano Samara") to get a common word index, and to use the other word index (of the

group “Podslushano Samarsky Universitet”) for test counting. The common word index consisted of overlapping words with the weights recalculated according to formula 2.

```
('что', 1780)
('пожалуйст', 1078)
('анон', 881)
('карт', 625)
('помог', 584)
('ребят', 570)
('сказал', 568)
('можн', 489)
('есл', 401)
('был', 368)
('только', 303)
('андрей', 294)
('скажит', 291)
('город', 234)
('наход', 231)
('самар', 228)
('потер', 217)
('спасиб', 213)
('марат', 207)
('человек', 207)
('подскаж', 199)
('когда', 197)
('сказал', 195)
('говорил', 191)
('теперь', 184)
('очень', 183)
```

Figure 1. Part of the word index developed for the group “Podslushano Samara”.

$$g(g_1, g_2) = \left(\frac{g_1 + g_2}{n}\right) \quad (1)$$

where: $g(g_1, g_2)$ is the weight of the word in the common word index; g_1 is the weight of the word in the first word index; g_2 is the weight of the word in the second word index.

The last step was to calculate first the distances between the resulting word index and the groups it was based on, and then the distance between the resulting word index and the test group. The Euclidean formula of distance between the two groups was used to measure this value.

$$d(x, y) = \sqrt{\sum_{i=1}^{n} (x_i - y_i)^2} \quad (2)$$

The results are provided in the Table 1.

Table 1. The results of calculating the distances between the groups.

Title	Euclidean distance
“Podslushano Samara”	188.32
“Uslyshano Samara”	173.11
“Podslushano Samarsky Universitet”	165.98

Based on the results, we can conclude that the distances between the first two groups are very close. This implies that the common word index is compiled quite accurately and reflects the context of the messages in the said groups well. After analyzing the distance to the test group, one can notice the proximity of all three values, but it is also clear that this distance has doubled as compared to the other two. It can be assumed that this group is slightly different from the other two.

4. Conduct research for five groups

In the next step, it was decided to add two more communities to the already analyzed groups and conduct additional research. The distribution of groups with their number, the number of subscribers, the number of posts and the number of comments below them is presented in Table 2.

Table 2. Analyzed communities and their quantitative indicators.

Group number	№1	№2	№3	№4	№5
Count of subscribers at the time of receiving data	217 679	92 024	150 587	60 225	10 465
Count of posts	32 485	10 957	20 783	8 572	1 034
Count of comments	3 898 212	1 949 106	133 188	171 444	22 748
Count of words	40 167 816	17 541 954	14 650 780	1 371 552	107 650

In order to show the applicability of the proposed method for calculating distances between groups using a common dictionary, we calculated the distances between groups without using a common dictionary and with its use. Table 3 presents the results of calculations without a common dictionary. Table 4 presents the results of calculating the Euclidean distances between all pairs of groups and the templates of common dictionaries built on their basis.

Table 3. Euclidean distance calculation results for all five groups without using a common dictionary.

	№1	№2	№3	№4	№5
№1	-	-	-	-	-
№2	513.363	-	-	-	-
№3	571.324	603.66	-	-	-
№4	644.413	863.041	867.504	-	-
№5	701.423	727.723	689.51	974.583	-

Table 4. The results of the calculation of the Euclidean distances between groups and their common vocabulary.

	№1	№2	№3	№4	№5
№1	-	-	-	-	-
№2	188.32 173.11	-	-	-	-
№3	195.55 365.98	219.66 386.85	-	-	-
№4	296.01 542.91	288.95 589.46	272.03 541.34	-	-
№5	193.5 390.71	201.74 402.43	225.43 453.11	167.21 467.21	-

Comparing the obtained results, we can notice that the distances for calculations using a common dictionary are less than calculations without it. From this we can assume that the use of the method of finding a common dictionary for calculating Euclidean distances is justified and applicable for solving the problem posed.

5. The study of the dependence of the volume of the general dictionary used to calculate the Euclidean distance between groups

We investigate at what volume of a general dictionary the results of determining the degree of similarity of groups among themselves give the most informative readings. To do this, we carry out an experimental calculation of the Euclidean distances for groups numbered 1 and 2 between them

and their common vocabulary by changing the dimensions of the common vocabulary. For the study, we will choose the size of the dictionary equal to the greatest number of unique words for the second group (18.948 words), the small size of the general dictionary (300 words) and several intermediate values. Table 5 shows the results of calculations of this experiment.

After analyzing the results obtained, it can be noted that for the anomalously large and, on the contrary, anomalously small size of the general dictionary, the results turned out to be as non-informative as possible. Most likely this is explained by the fact that with a small dictionary, for the most part, only the most common words that do not carry more information and are approximately equally found in the texts of both groups, for the maximum size of a common dictionary, the situation is fundamentally opposite, tk. Many rare words come into account that are found only in one of the groups, and therefore the results show such an abnormally large scatter. When analyzing the results produced for the intermediate sizes of the general dictionary, it is seen that the values of the distances cease to have strong leaps relative to each other when using a common dictionary of about 3/5 of the amount of unique words for the group with the highest number. Such a result is due to the fact that with such a volume the most non-informative words and words are cut off.

Table 5. The results of the calculation of the Euclidean distances between groups and their common vocabulary.

Dictionary size	Distance to group number 1	Distance to group number 2
18948	349.92	306.92
14000	278.21	249.96
11000	188.32	173.11
9000	195.44	181.06
2000	161.32	155.78
300	60.66	61.05

6. Conclusion

Within the framework of this study, a set of software modules was developed allowing to determine the distance between the communities of the social network Vkontakte. As a result of the work, a common word index was compiled, on the basis of which the degrees of proximity between 3 communities were determined. In the future, the results of the work can be used to develop algorithms for determining the proximity of larger groups and communities using the BigData technology.

7. References

[1] Arora M, Kansal V 2019 Character level embedding with deep convolutional neural network for text normalization of unstructured data for Twitter sentiment analysis *Social Network Analysis and Mining* **9(1)** 12

[2] Burdisso S G, Errecalde M and Montes-y-Gómez M 2019 A text classification framework for simple and effective early depression detection over social media streams *Expert Systems with Applications* **133** 182-197

[3] Chen J, Gong Z and Liu W 2019 A Nonparametric Model for Online Topic Discovery with Word Embeddings *Information Sciences*

[4] Groß-Klußmann A, König S and Ebner M 2019 Buzzwords build Momentum: Global Financial Twitter Sentiment and the Aggregate Stock Market *Expert Systems with Applications*

[5] Zhu C, Du J 2018 Background feature clustering and its application to social text *Information Processing Letters* **136** 44-48

[6] Xu X 2007 Scan: a structural clustering algorithm for networks *Proceedings of the 13th ACM SIGKDD international conference on Knowledge discovery and data mining* 824-833

[7] Rytsarev I A, Kozlov D D, Kravtsova N S, Kupriyanov A V, Liseckiy K S, Liseckiy S K, Paringer R A and Samykina N Yu 2018 Application of the principal component analysis to detect semantic differences during the content analysis of social networks *CEUR Workshop Proceedings* **2212** 262-269
[8] Rytsarev I A, Kupriyanov A V, Kirsh D V and Liseckiy K S 2018 Clustering of social media content with the use of BigData technology *Journal of Physics: Conference Series* **1096(1)**
[9] Rytsarev I A, Kirsh D V and Kupriyanov A V 2018 Clustering of media content from social networks using BigData technology *Computer Optics* **42(5)** 921-927 DOI: 10.18287/2412-6179-. –2018-42-5-921-927
[10] Mikhaylov D V, Kozlov A P and Emelyanov G M 2016Extraction of knowledge and relevant linguistic means with efficiency estimation for the formation of subject-oriented text sets *Computer Optics* **40(4)** 572-582 DOI: 10.18287/2412-6179-2016-40-4-572-582
[11] Rytsarev I A, Kupriyanov A V, Kirsh D V and Liseckiy K S 2018 Clustering of social media content with the use of BigData technology *Journal of Physics: Conference Series* **1096(1)** DOI: 10.1088/1742-6596/1096/1/01208
[12] Kropotov Y A, Proskuryakov A Y and Belov A A 2018 Method for forecasting changes in time series parameters in digital information management systems *Computer Optics* **42(6)** 1093-1100 DOI: 10.18287/2412-6179-2018-42-6-1093-1100

Acknowledgments
This work was financially supported by the Russian Foundation for Basic Research under grant # 19-29-01135, # 18-37-00418, # 17-01-00972 and by the Ministry of Science and Higher Education within the State assignment to the FSRC “Crystallography and Photonics” RAS No. 007-GZ/Ch3363/26 (theoretical results).

Development of the documents comparison module for an electronic document management system

M A Mikheev[1], P Y Yakimov[1,2]

[1]Samara National Research University, Moskovskoe Shosse 34A, Samara, Russia, 443086
[2]Image Processing Systems Institute of RAS - Branch of the FSRC "Crystallography and Photonics" RAS, Molodogvardejskaya street 151, Samara, Russia, 443001

e-mail: mmasyz@mail.ru, Pavel.y.yakimov@gmail.com

Abstract. The article is devoted to solving the problem of document versions comparison in electronic document management systems. Systems-analogues were considered, the process of comparing text documents was studied. In order to recognize the text on the scanned image, the technology of optical character recognition and its implementation — Tesseract library were chosen. The Myers algorithm is applied to compare received texts. The software implementation of the text document comparison module was implemented using the solutions described above.

1. Introduction

Document management is an important part of any business today. Negotiations, contracts, protocols, agreements must be documented. Documents go through several stages of preparation in most cases, and there is a possibility of replacing or correcting of files by one member without notifying other members. EDMSs with built-in checking mechanisms guarantees the identity of two documents versions in this case.

A variety of data formats as well as a low degree of automation or its complete absence significantly complicates the process of finding differences between documents. As a result, some companies ignore such important process without considering how risky this approach to organization of workflow in a company can be [1].

All the above suggests that the topic chosen by the authors is relevant. Automation of documents and, in particular, the process of comparing versions of documents requires attention and detailed study.

There are a lot of web services and software products for document comparison now. The most common are ABBYY Comparator and Compare Suite. They provide a lot of features for customers. Also, there are software products embedded in enterprise applications and extending its functionality, such as ABBYY ScanDifFinder SDK. But the main drawback all these products is the high coast (up to 40% of the license value).

This paper considers a product that can be used as a component in main application, based on open source libraries and process documents without sending them to the third party.

2. Studying of documents comparison process

The task of text documents comparison is quite extensive. The case of PDF documents comparison is considered in this work. A simplified diagram of this process is presented in Figure 1.

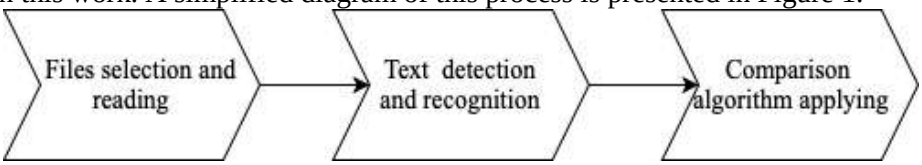

Figure 1. Document comparison process.

The comparison task is complicated by the fact that the PDF files involved in the process can contain both plain text and scanned copies of documents. Thus, first of all, the text in the image should be detected and recognized, and then the comparison algorithms should be applied.

2.1. Text recognition

Optical Character Recognition (OCR) is a mechanism that converts printed text or handwriting images into digital form for the purpose of further editing, searching, analysis.

OCR has a number of significant problems, including a variety of languages and fonts, distortion of images of characters, size and scale variations of characters. Methods from various computer science disciplines (image processing, pattern classification, natural language processing) are used to solve these problems [2].

The OCR process is a complex activity consisting of several phases performed sequentially.

Image retrieval is the initial stage of OCR, which involves extracting a digital image and transforming it into a suitable form that can be easily processed by a computer. This can involve quantization as well as compression of image [3, 4].

Various preprocessing methods are used to improve the image quality after its receiving: noise removal, thresholding, min and max filters.

At the segmentation stage, the characters in the image are separated for further transmission to the classification. The simplest methods are analysis of related components and projection profiles. However, in situations where characters are overlapped or broken, advanced character segmentation methods are used.

In the next step, the segmented characters are processed for extracting various features that uniquely identify these characters. Then characters are recognized on basis this features. The extracted features should be efficiently computed, minimize intraclass variations and maximize interclass variations.

At the classification stage features of a segmented image are associated with various categories or classes. Some of the approaches of statistical classification are the Bayes classifier, the classifier of the decision tree, the neural network classifier [5], the classifiers of the nearest neighborhoods, etc. [6].

After a character has been classified, various approaches can be used to improve the accuracy of recognition results. One approach is to use several classifiers, the results of which can then be combined. To improve recognition results, you can also perform context analysis [6].

The most popular OCR implementation is the Tesseract engine. Tesseract is an open source library currently maintained by Google. The principle of its work is described in article [7].

Document processing goes according to the traditional step-by-step scheme. At the first, page layouts are defined. After that, text strings are grouped into Blob objects. Strings are selected in the resulting objects, and then they are broken into words by analyzing the length of the spaces between the characters.

The recognition process is carried out in two stages. At the first, the algorithm tries to recognize each word in turn, and passes each successful attempt to the classifier as a training set. The classifier further uses this data when moving through the page at the second stage of recognition, when the algorithm re-works with those words that could not be recognized for the first time.

A distinctive feature of the latest versions of Tesseract is using LSTM (long short-term memory) networks to define page layouts, select lines and individual words. Long short-term memory networks

are a type of recurrent network (RNN). However, unlike conventional RNN that contain one layer with the tanh activation function, the LSTM contains 4 layers that interact in a certain way (Figure 2).

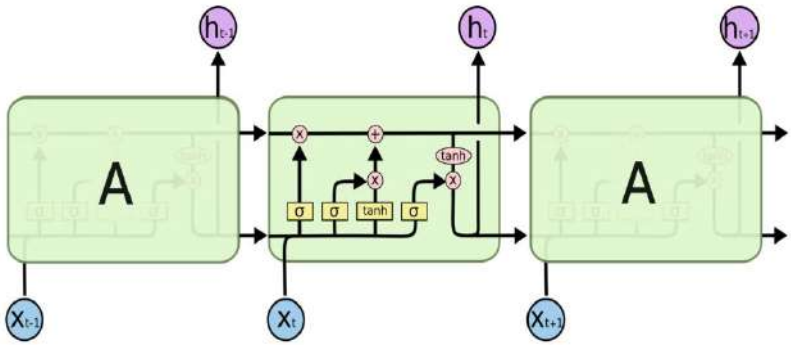

Figure 2. LSTM model.

So, LSTM solves the problem of long-term dependence (loss of ability to bind information due to the large distance between the actual information and the point of its application).

The introduction of LSTM networks in Tesseract has led to a significant improvement in recognition results. The number of errors decreased on 15% [8].

There are other open source software products designed for text recognition. The best results show Tesseract, CuneiForm and OCRopus (table 1). However, with the release of Tesseract 4, which supports LSTM, this library gets preference.

Table 1. The average percent recognition errors.

Library	Errors, %
Tesseract	14,04
Ocropus	31,42
CuneiForm	37,68
Ocrad	50,25
GOCR	64,46

2.2. Simple texts comparison

Detecting differences between words is a fundamental part of text comparison. Formally, the task of determining the differences between two sequences of characters is to find the longest common subsequence or, equivalently, find the minimum script for deleting and inserting characters that transform one sequence into another.

The most popular algorithms for finding the largest common sub-sequence are the Wagner-Fischer algorithm, the Hirschberg's algorithm, and the Hunt-Szymanski algorithm.

The idea of Wagner and Fischer is to consistently estimate the distance between all the longer line prefixes — until the final result is obtained. Intermediate results are calculated iteratively and stored in an array of length $(m + 1) \times (n + 1)$. Thus, the calculation required $O(m \times n)$ time using memory of the same order.

The Hirschberg's algorithm computes LCS in $O(n_1 \times n_2)$ time, but uses memory of $O(n)$, where $n = \min \{n_1, n_2\}$. Saving memory is due to the fact that at any given point in time, only two rows of the array required by dynamic programming are stored in memory. However, this leads to a more sophisticated method of allocating two lines of LCS.

The Hunt-Szymanski algorithm computes LCS in a $O(n \times \log (n))$ time, using memory of $O(n)$, where $n = \max \{n_1, n_2\}$. The time complexity of this algorithm exceeds $O(n \times \log (n))$ only when the rows x_1 and x_2 have the number of matching letters greater than a value of the order of $O(n)$ (for example, when the size of the alphabet is small relative to the length of the rows).

In practice, the calculation of the distance between the lines is of interest only when this distance d is relatively small compared to the length of the lines. In this case the Ukkonen-Myers algorithm, considered in article [9], is preferable. The complexity of the Myers algorithm is approximately proportional to the sum of the lengths of the sequences, and not to the product, as in the Wagner-Fischer algorithm. The same can be said about the memory used by the algorithm $O(n_1 \times n_2)$, where $n = \min\{n_1, n_2\}$. Thus, this is the best-known algorithm for solving our problem [10, 11, 12].

3. Development of the document versions comparison module

The development of any system begins with the design stage. Design includes the development of a system model at the logical and physical levels, as well as the choice of software.

3.1. Choice and justification of the software

CUBA Studio 2018.3, developed on the basis of IntelliJ IDEA was chosen as the development environment and Java was chosen as a programming language. There are a lot of open source projects, libraries, frameworks written in Java, which in terms of the task will greatly simplify the work. Java is the foundation for all types of network applications and the universal standard for developing enterprise software.

3.2. Choice of frameworks

The application is based on the CUBA platform. This platform is a high-level Java framework for quickly building enterprise applications with a full-fledged web interface. It abstracts the developer from heterogeneous technologies, allowing him to focus on solving business problems.

The text document processing module is based on the Apache PDFBox library, an open source tool that supports the development of Java applications that create, convert and process PDF documents [13].

For pixel-by-pixel document comparison, the PdfCompare library, built on the basis of Apache PDFBox, is used. It provides the ability to graphically highlight different areas of documents. Apache PDFBox contains many methods designed to manage certain aspects of the system, in particular, memory consumption [14].

Text comparison uses the high-performance Google Diff Match Patch library, which implements the Myers algorithm, which is generally considered the best general-purpose difference algorithm. some optimizations should be made to improve the runtime before such computationally expensive process as a comparison. After that, the remaining text is compared by a difference algorithm, the result is processed, taking into account the semantic features of the text [15].

3.3. Logical database model

It is necessary to develop an application that briefly reflects the subject area we need to demonstrate the work of the document comparison module. In our case, it is a document management flow.

Figure 3 shows the logical model of the database system. The main entities of the system are: “Document type”, “Attachment”, “Document category”. "Document". Entities are connected to each other by one-to-one and many-to-one relationships and are reflected in the object model of the system.

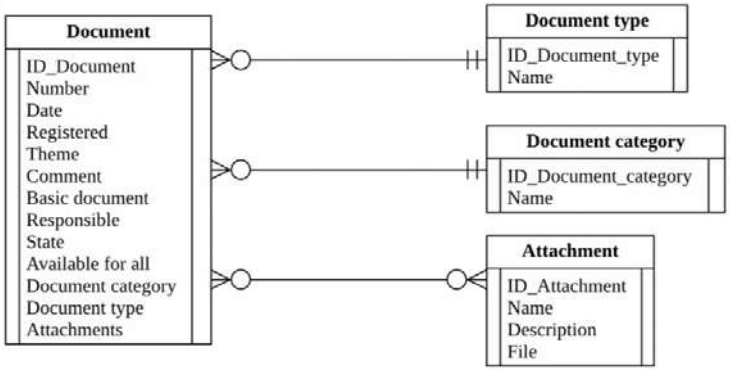

Figure 3. Logical database model.

3.4. Class diagram

The class diagram serves to represent the static structure of the system model in the terminology of the classes of object-oriented programming [16]. Figure 4 shows the class diagram of the system.

DocumentCategory, DocumentKind, DocumentAttachment and Document are entities stored in the database. Work with them is performed using a universal user interface and already implemented operations of creation, deletion and modification.

Special attention should be given to the DocumentEdit document editing screen controller. Its main compareFiles method is called by clicking on the “Compare” button and starts the document comparison mechanism by calling the compareFilesPixelToPixel and CompareFilesText methods of the DocComparisonService service. Services form a component layer that defines a variety of Middleware operations available to the client level of the application. The service interface is located in the global module and is available at the client level and at the Middleware.

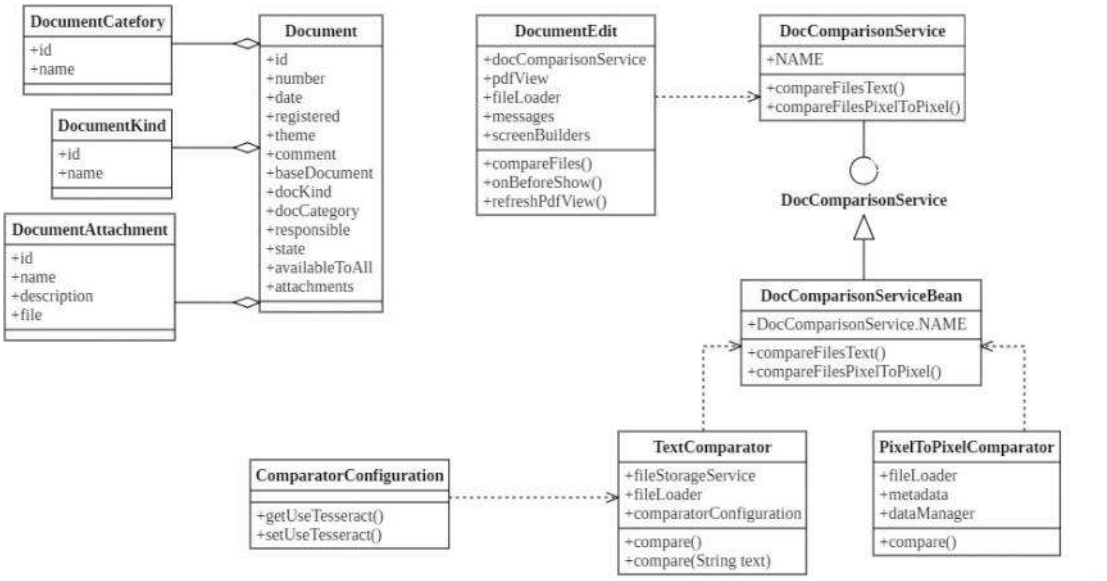

Figure 4. Class diagram of the system.

4. The results of experimental studies of the module

In order to demonstrate the work of the module, an information system that partially implements the functions of electronic document management was developed.

After launching of application and entering personal data, the main system form with the items “Documents”, “Reference books”, “Administration” and “Help” is shown.

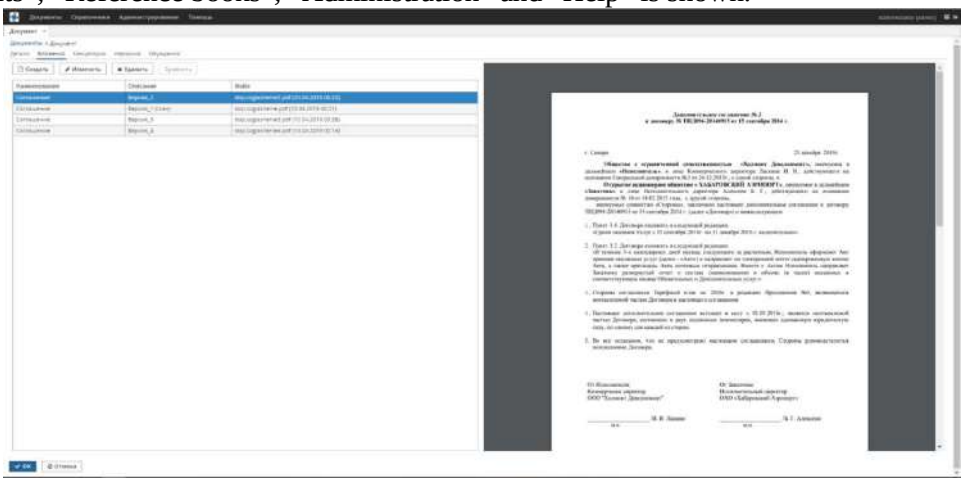

Figure 5. Documents editing form.

The document editing form is a set of tabs “Details”, “Attachments”, “Office”, etc.

The Attachments tab (Figure 5) presents a form containing a table of document versions, the main attributes of which are “Name”, “Description” and “File” — a PDF document attached in the attachment editing screen. A form of a preview document is shown on the right side of the screen.

Pressing the button "Compare" causes the main logic — the comparison of documents. Upon completion of the comparison, the form opens, with the results of pixel-by-pixel and textual comparison (Figure 6).

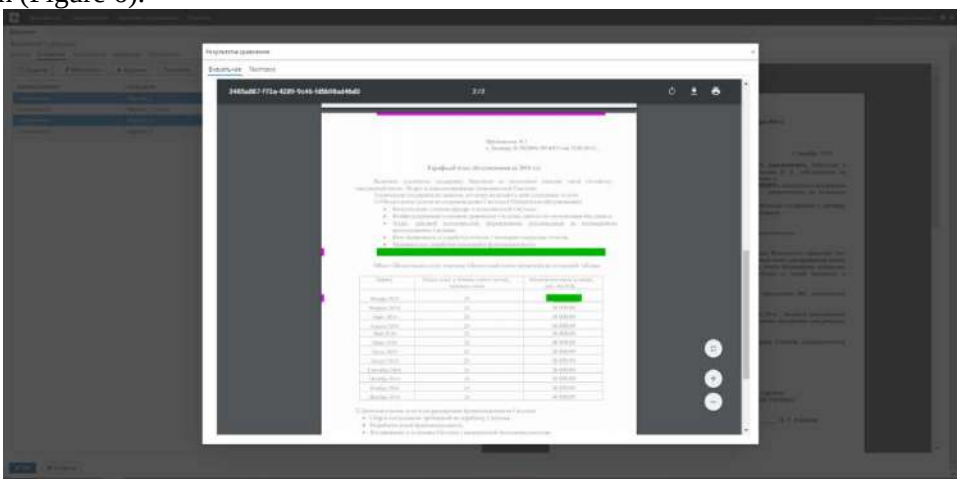

Figure 6. Visual comparison result form.

Differing pixels are marked in red and green. Ignored areas are marked with a yellow background. Deleted pages are highlighted with a red frame and added pages highlighted with a green frame (Figure 7).

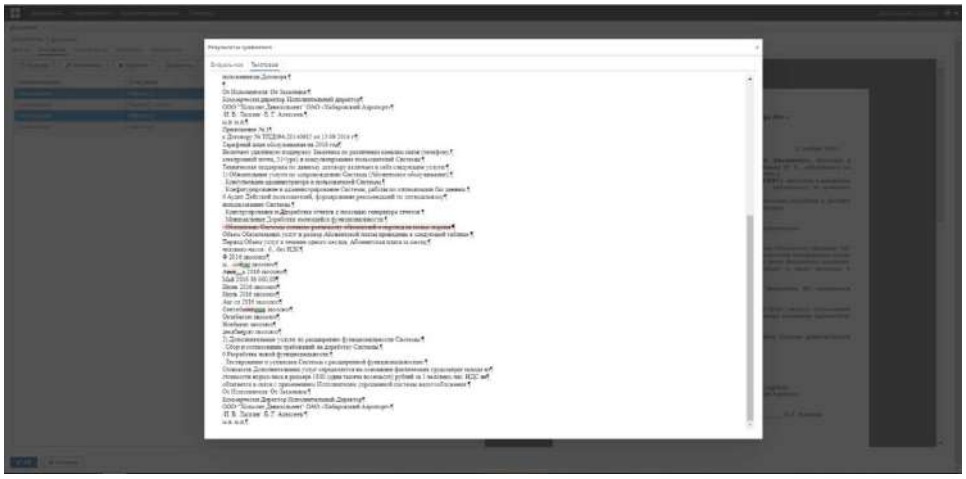

Figure 7. Textual comparison result form.

Added characters are highlighted in green and underlined, deleted characters are highlighted in red and strikethrough.

Several experiments were conducted in order to explore recognition accuracy. 3 pdf-files containing scanned copies of text documents participated in the test. Recognition results are presented in table 2.

Table 2. The result of recognitions.

Experiment’s number	Number of recognized characters / Total number
Experiment 1	1127 / 1148
Experiment 2	1502 / 1531
Experiment 3	964 / 1021

The percentage of correctly recognized characters is more than 98%, which confirms the data declared by the Tesseract's developer. Most of the mistakes are in recognizing punctuation marks and some pairs of similar characters.

The main drawback detected during the experiments process is the incorrect recognition of multi-column text, as well as recognition errors in the presence of pictures and in areas with stamps and signatures. These features should be fixed on the pre-processing stage.

5. Conclusion

As a result of the work done, the task of text documents comparison in the electronic document management system was solved.

The mechanism of optical character recognition on the image for obtaining texts from the scanned image was studied. The most popular libraries that implement OCR were considered, a comparative analysis of the effectiveness of character recognition was conducted. The main approaches to the comparison of texts are investigated, in particular, the Myers algorithm, which is the most suitable in our case, is considered.

The result of the work is the results of researches that substantiate the choice of technologies used, as well as a software product available for use by third-party developers. Currently, the developed module allows to compare text documents in PDF format and returns the result in a form that is easy to read.

6. References

[1] Algorithms and document comparison software analysis URL: http://cad.kpi.ua/attachments/093_2017p_Ishchenko.pdf (16.01.2019)
[2] Islam N, Islam Z and Noor N 2016 A Survey on Optical Character Recognition System *Journal of Information and Communication Technology* **10** 1-4
[3] Lazaro J, Martin J L, and Arias J 2010 Neuro semantic thresholding using OCR software for high precision OCR applications *Image and Vision Computing* **28** 571-578
[4] Lund W B, Kennard D J and Ringger E K 2013 Combining Multiple Thresholding Binarization Values to Improve OCR *Output Document Recognition and Retrieval XX Conf.* **8658** 11
[5] Amosov O S, Ivanov Y S and Zhiganov S V 2017 Human localiztion in video frames using a growing neural gas algorithm and fuzzy inference *Computer Optics* **41(1)** 46-58 DOI: 10.18287/2412-6179-2017-41-1-46-58
[6] Ciresan D C, Ciresan D C, Meier U and Gambardella U 2011 Convolutional neural network committees for handwritten character classification *Int. Conf. on Document Analysis and Recognition* **2** 1135-1139
[7] Smith R 2007 An overview of the Tesseract-OCR engine *Int. Conf. on. IEEE* **2** 629-633
[8] Understanding LSTM Networks URL: http://colah.github.io/posts/2015-08-Understanding-LSTMs/ (17.04.2019)
[9] The Myers diff algorithm url: https://blog.jcoglan.com/2017/02/12/the-myers-diff-algorithm-part-1/ (16.04.2019)
[10] Myers E W 1986 An O(ND) Difference Algorithm and its Variations *Algorithmica* **1** 251
[11] Common subsequences URL: http://algolist.manual.ru/search/lcs/ (16.04.2019)
[12] Smith B 2006 *Methods and algorithms of calculation on strings* (Moscow: Williams publisher) p 485
[13] Apache PDFBox librart URL: https://pdfbox.apache.org (16.04.2019)
[14] PdfCompare library URL: https://github.com/red6/pdfcompare (22.04.2019)
[15] Diff Strategies URL: https://neil.fraser.name/writing/diff (22.04.2019)
[16] Leonenkov A V 2007 *UML 2 Tutorial* (Saint Petersburg: BHV-Petersburg) p 558

Acknowledgements

This work was partly funded by the Russian Federation Ministry of Science and Higher Education within a state contract with the "Crystallography and Photonics" Research Center of the RAS under agreement 007-ГЗ/Ч3363/26.

Optimization of the process of 3D visualization of the model of urban environment objects generated on the basis of the attributive information from a digital map

M P Osipov[1], O A Chekodaev[1]

e-mail: osipovmp@mail.ru

[1]National Research Lobachevsky State University of Nizhny Novgorod, Prospekt Gagarina, 23, Nizhny Novgorod, Russia, 603950

Abstract. The paper presents methods for optimizing the process of visualization of the urban environment model based on the characteristics of its presentation. Various approaches are described which provide a reduction in computational complexity in visualizing three-dimensional models that can optimize the display of their geometry and the amount of video memory used. Methods are considered that allow optimizing both the scene as a whole and its individual components.

1. Introduction

The visualization of the urban environment model is widely used to solve various problems in such areas as construction, urban management, education, culture, etc. [1-3]. Three-dimensional visualization allows users to perceive information in a spatial form that is familiar to them. Its analysis does not require any special technical knowledge, so decision-making on the basis of the information thus provided is much faster and easier. The most complete information about the object, which allows the immersion into the model space, is provided by real-time visualization that imposes significant time constraints on the process of scene rendering.

2. Problem statement

The process of urban environment model visualization is a computationally complex task. In [4], a method for automatic generation of three-dimensional models of objects in the urban environment using attributive information from a digital map is described. To render the surface of extended areas of terrain with highly detailed objects, an enormous number of polygons is required. Therefore, the need arises to use special algorithms that optimize the 3D representation of the urban environment model.

The aim of this paper is to analyze the existing methods for optimizing the process of 3D visualization, to choose some more efficient approaches and to adapt them to the specifics of the rendering of a three-dimensional urban environment model.

3. Methods for optimizing the process of 3D visualization of the urban environment model

The urban environment model (Figure 1) includes a digital terrain model and models of urban environment objects.

Figure 1. 3D visualization of the urban environment model.

3.1 Visualization of the digital terrain model

3.1.1 Geometry optimization

The process of displaying a terrain model, which is a highly detailed description of an extended terrain surface, is a computationally complex element in visualizing an urban environment model. Displaying on the screen the entire terrain model at once will result in a noticeable loss of performance. At the same time, when forming a frame, most of the model will be out of sight. Therefore, it is necessary to develop algorithms that will cut off the data that in any case will not be displayed on the screen, thereby optimizing the visualization process. The surface in the background, due to its remoteness, does not require high detail. Therefore, the visualization algorithm should dynamically change the level of the model detail, depending on the distance from the observer.

The digital model of the urban environment is built on the basis of the elevation information (horizontals, elevation marks, etc.) contained in the digital map. Since the elevation information is an irregular point cloud, the surface is approximated by means of irregular triangulation (TIN).

The process of visualization of an irregular network of triangles is difficult to optimize, because, unlike in the case of the regular representation, it is difficult to parallelize this process on multiprocessor architectures. Therefore, conversion from an irregular to a regular structure is envisaged.

Optimizing the process of a terrain model visualization often consists in producing a tree structure from surface areas that have varying degrees of detail. Each link in the tree approximates a certain part of the surface. The descendants of this link break the area into parts and approximate them with greater accuracy. The process continues up to a given limit of approximation accuracy. All hierarchical algorithms are similar in terms of their principle of operation and differ mainly by the types of entities chosen as links. In particular, the ROAM algorithm [5] implies a binary tree of triangles, the QuadTree [6], a quad-tree of squares, the Chunked LOD [7], a quad-tree of rectangular patches, which are separate triangular grids, etc. [5]. When visualizing, such structures can be used to quite effectively cut off the areas invisible to the observer and to remove unnecessary details in the distant parts of the terrain model. The main disadvantage of such hierarchies is the presence of recursiveness and complexity of their transfer to the GPU. Besides, considerable time is required to form the structure of the hierarchical algorithms.

The Displacement Mapping technique [8] allows transferring the model optimization problem to a graphics processor. Unlike hierarchical methods, Displacement Mapping, when using hardware

tessellation, performs all calculations on the GPU, with a minimal load on the central processor. The time required to prepare data is also significantly reduced. Therefore, the process of visualization of extended urban terrain models was optimized using Displacement Mapping methods with hardware tessellation (Figure 2).

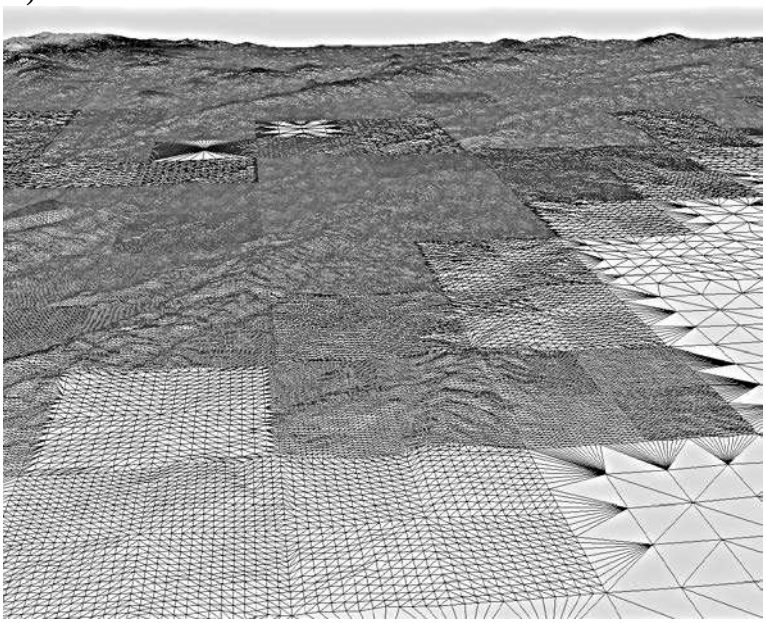

Figure 2. Visualization of a digital terrain model using Displacement Mapping methods.

3.1.2 Material optimization

The underlying surface characterizes the features of the upper part of the earth crust. In the urban environment, objects that denote paved areas, green areas, squares, courtyards, etc., can act as the underlying surface. These objects completely repeat the geometric features of the terrain, so it is reasonable to represent them as part of the digital terrain model rather than as a separate object and to designate them using an appropriate texture.

a) 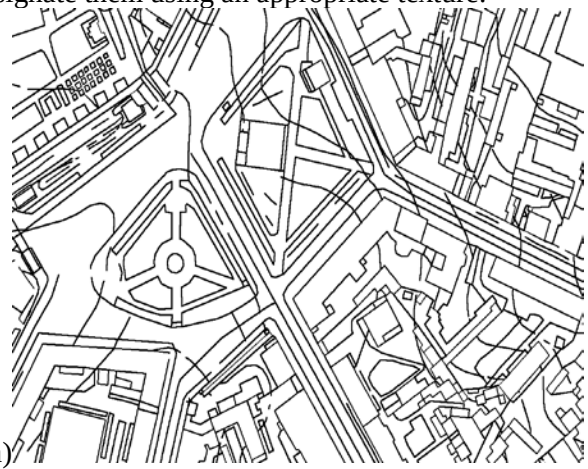 b) 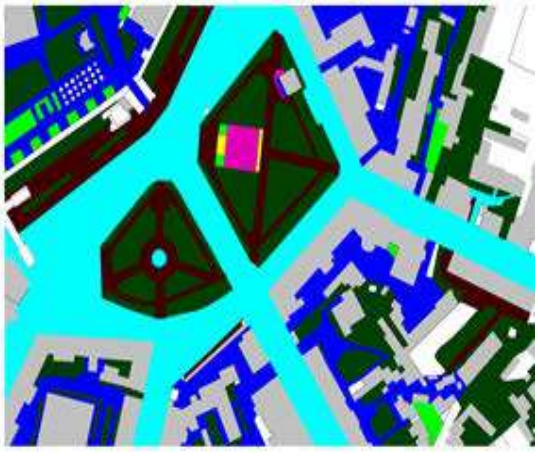

Figure 3. A fragment of a digital map (a) and a mask (b) compiled from its data.

To render highly detailed information about the underlying surface of an extended terrain, a super-large texture are required. The information about the elements of the underlying surface is stored in the digital map as a set of characteristics describing these elements. All elements of the underlying surface are categorized into types and their color at each point of the surface can be formed at the moment of visualization. For this purpose, an algorithm was developed that forms a mask in advance, based on the information of the digital map. The mask is in the form of a graphic file with dimensions multiple to the size of the digital map (Figure 3).

Figure 4. A 3D scene of the urban environment with the underlying surface formed using the mask from Figure 3.

Each pixel of the mask covers a specific area of the terrain and contains information about the type of coating of the underlying surface in the corresponding area. The information about the texture of a certain type of the underlying surface is stored in the texture atlas as a set of tiles. Thus, the color at each point of the underlying surface can be calculated at the stage of visualization in the fragment shader based on the information of the mask map and texture atlas (Figure 4). Based on this principle, an algorithm was developed for texturing the underlying surface, which makes it possible to avoid producing the texture of the entire underlying surface in advance and to achieve significant memory saving.

3.2 Visualization of urban environment objects

3.2.1 Geometry optimization

When rendering a model of the urban environment, the visualization of buildings, vegetation, small architectural forms, etc., accounts for the greatest computational load. Optimizing the process of visualization of such objects consists in cutting off the data that are outside the field of vision (Figure 5). By means of tree-like segmentation of the scene, it is possible to cut off such data more efficiently. As part of our research, segmentation algorithms based on octrees, R-trees and Priority R-tree (a hybrid between a k-dimensional tree and an R-tree) have been implemented [9]. It was established experimentally that segmentation of a scene based on an Priority R-tree is most suitable for urban objects. Based on the nature of the location of objects in the urban environment, optimal segmentation parameters were selected.

Figure 5. Cutting off 3D scene objects out of the field of vision by using scene segmentation based on an R-tree.

When rendering the urban environment, a significant part of the objects will fall within the field of the camera vision (viewing frustum), but will not be seen during visualization, since it will be completely obscured by other objects. The technology based on coherent hierarchical culling [10], by analyzing the previous frame, efficiently cuts off the "obscured" objects that will not be processed in the course of visualization. In combination with scene trees, this provides a very effective way of clipping - the scene is traversed hierarchically. Internal nodes contain objects and other nodes, which makes it possible to check for visibility and cut off a large number of objects at once.

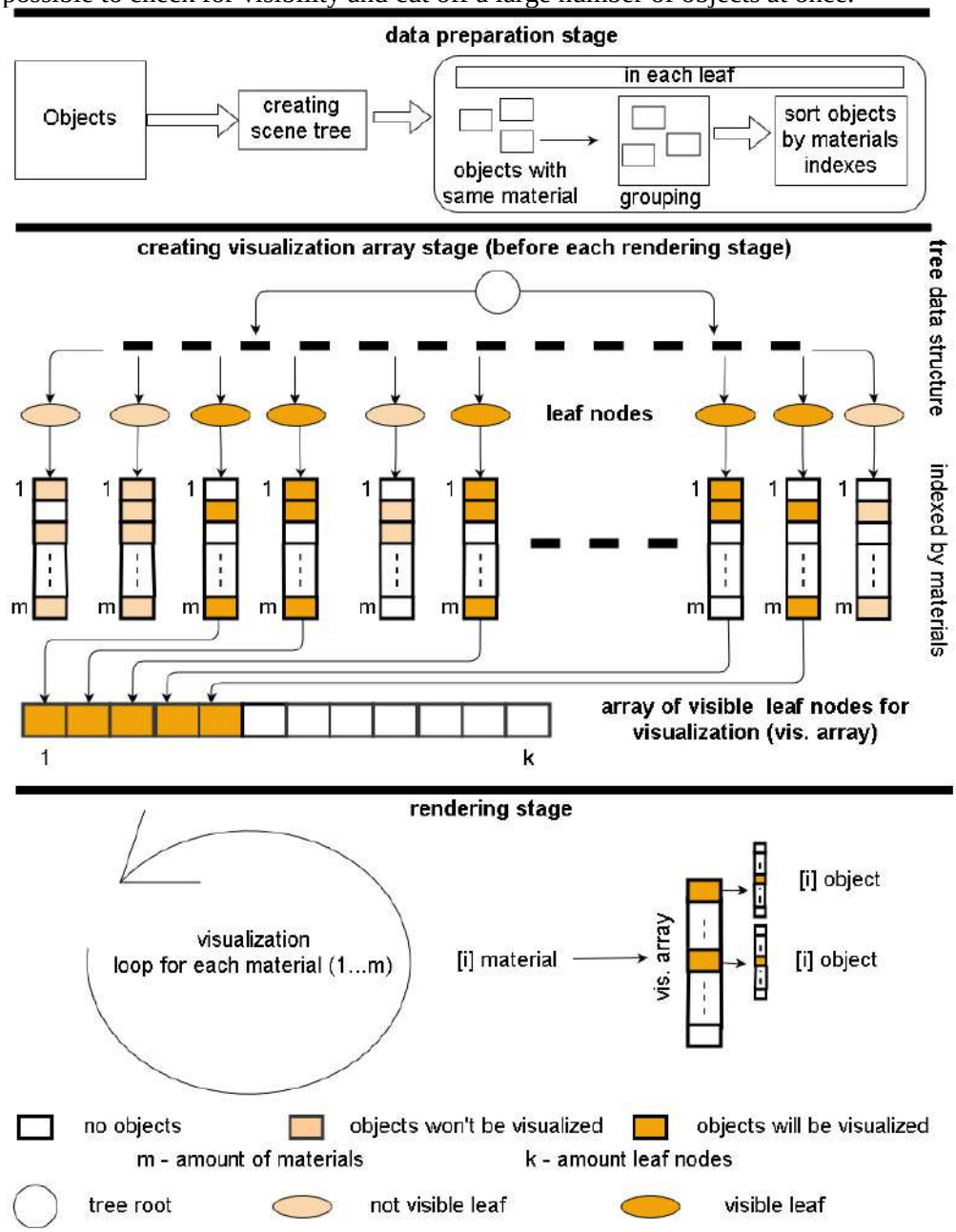

Figure 6. The process of grouping objects using the same material.

Objects in the background, due to their remoteness, do not require high detail [11]. The possibility of associating various levels of model detail with one object was implemented. Thus, if there are several models of one object with different degrees of detail, the level of detail of the group of objects being visualized in the scene node will depend on the distance between the observer and this node.

The generated model of the urban environment is characterized by a large number of identical objects. Such objects may include vegetation (trees, bushes) and objects of small architectural forms (kiosks, stalls, benches, street lights, etc.). To visualize a large number of such repeating objects in leaf nodes, the Geometry Instancing [10] technology was used, which allowed visualizing multiple copies of the object in one drawing cycle. This approach reduces the exchange of information between the CPU and the GPU, thereby significantly increasing the speed of visualization of a large number of identical objects without loss of quality.

3.2.2 Materials optimization

The principle of generating a model of the urban environment based on the attributive information from a digital map implies the creation of objects of the same type that have different geometric representations, but are characterized by the same type of surface material. An example of such objects are buildings and structures. In order to reduce the number of accesses to the graphics processor, an algorithm is implemented that grouping objects using the same material. The process is divided into three stages. First, at the data preparation stage, it is monitored to ensure that materials and textures are not duplicated in memory. Then a scene tree is formed. At the end of this process, the leaf nodes of the tree will contain scene objects. After the formation of a scene tree, in each of its leaf, objects with the same material are merged. Thus, in each leaf of a tree, one material corresponds to a maximum of one object. Next, the objects contained in the leaf are sorted by materials, so that the i object of the leaf corresponds to the i material. Before the formation of each frame in the process of visualization, a walk through the scene tree is performed. During this process, a list of leaf nodes that fall into scope is formed. Thus, using established correspondences, for each material, a set of objects ready for drawing in the current frame is established. The resulting structure allows direct access to objects using the current material. The general scheme of grouping by materials is presented in the figure 6.

The process of combining involves the objects that have common material. Models of urban environment objects often have a common type of surface material. The only difference is the color map (for example, the texture of the building facades). Therefore, the textures of objects with the same type of material are combined into one texture atlas [12]. Thus, when visualizing an urban environment model containing tens of thousands of buildings, the use of the proposed three-stage material optimization algorithm reduces the number of unique materials to just several dozen.

4. Low-level optimization

At the moment, GPU has overtaken CPU in terms of performance, and the performance growth rate continues to increase. Therefore, it is reasonable to move the computational load of the visualization process to the GPU and to minimize the amount of data transferred between the CPU and the GPU, since this data transfer is a real bottleneck in the system performance. In the framework of the OpenGL (DirectX) specification, manufacturers of video adapters provide ample opportunities for the effective use of the equipment's potential for 3D visualization.

In particular, in the process of visualization of the urban environment model, VertexBufferObjects (VBO), IndexBufferObject (IBO), VertexArrayObject (VAO) technologies were used to upload the geometry of the urban environment model to the video device; hardware texture compression was used to speed up the loading of textures to video memory; triple buffering, for avoiding excessive synchronization of the CPU and GPU; MultiDrawIndirect, for reducing the number of accesses from CPU to GPU; programmable pipeline, Uniform Buffer (UBO), Shader Storage Buffer (SSBO) were used to generate the underlying surface, etc. [13]. The use of low-level optimization in the proposed optimization algorithms is presented in the figure 7.

5. Conclusions

The paper presents some methods and algorithms for optimizing the process of visualization that have been modified, taking into account the specific features of the urban environment model. These methods and algorithms have been implemented in software. This approach has significantly optimized the process of visualization of the urban environment model. Experimental studies have

shown that the use of the proposed optimization algorithms provides on the average a tenfold increase in the performance of the visualization model of urban environment objects. The tests were conducted on a scene containing 10000 objects with a total of 7000000 triangles.. The performance was 4-6 frames per second **(**fps) before applying all optimizations, 56-64 fps - after. Technical characteristics of the test bench: AMD fx-6300 processor 3.5GHz, Nvidia GeForce GTX 1050 Ti video card 4 GB, 12 Gb DDR3 RAM.

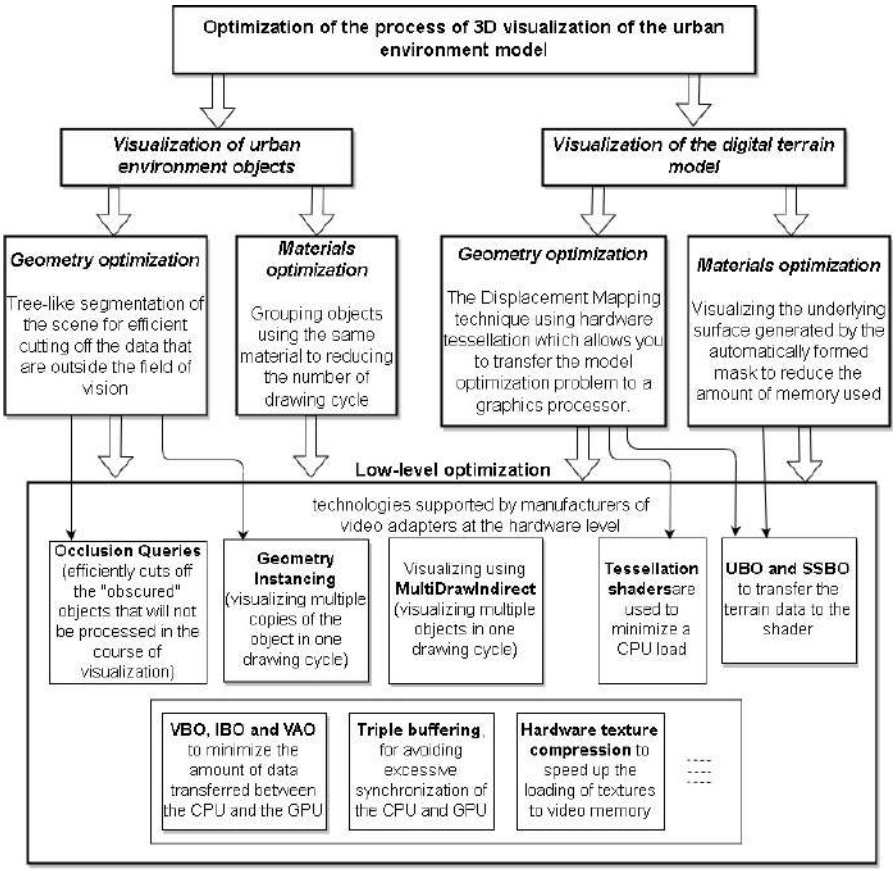

Figure 7. Methods for optimizing the process of 3D visualization of the urban environment model.

6. References

[1] Vasin Yu G, Osipov M P and Tomchinskaya T N 2011 Development of Interactive Virtual Models of the Urban Landscape of the Historical Center of Nizhni Novgorod *Pattern Recognition and Image Analysis* **21(2)** 351-353

[2] Pechenkin V V and Korolev M S 2017 Optimal placement of surveillance devices in a three-dimensional environment for blind zone minimization *Computer Optics* **41(2)** 245-253 DOI: 10.18287/2412-6179-2017-41-2-245-253

[3] Choudhary K, Boori M S and Kupriyanov A 2017 Mapping and evaluating urban density patterns in Moscow *Computer Optics* **41(4)** 528-534 DOI: 10.18287/2412-6179-2017-41-4-528-534

[4] Osipov M P and Chekodaev O A 2018 Algorithms of automation of 3D modeling of urban environment objects using attributive information from a digital map *CEUR Workshop Proceedings* **2212** 359-365

[5] Barton R 2010 Modern Algorithms for Real-Time Terrain Visualization on Commodity Hardware *Geinformatics FCE CTU* **5** 5-22

[6] Samet R and Ozsavas E 2007 Optimization of Quadtree Triangulation for Terrain Models *Advanced Concepts for Intelligent Vision Systems. Lecture Notes in Computer Science* (Springer, Berlin, Heidelberg) **4678** 48-59

[7] Ulrich T 2002 Rendering massive terrains using chunked level of detail control *SIGGRAPH Course Notes* **3(5)** 14
[8] González C, Pérez M and Orduña J M 2017 Combining displacement mapping methods on the GPU for real-time terrain visualization *The Journal of Supercomputing* **73(1)** 402-413
[9] Suhaibah A, Uznir U, Francois A, Darka M and Alias A R 2013 Review of Spatial Indexing Techniques for Large Urban Data Management *Workshop Conference: International Symposium & Exhibition on Geoinformation* 23
[10] Pharr M and Fernando R 2005 *GPU Gems 2: Programming Techniques for High-Performance Graphics and General-purpose Computation* (Addison-Wesley Professional First Edition edition) p 814
[11] Gong J, Zhu Q, Zhang H, Li X and Zhou D 2011 An adaptive control method of lods for 3D scene based on r-tree index *Acta Geodaetica et Cartographica Sinica* **4** 531-534
[12] Dai X, Xiong H and Gong J 2015 A multi-texture automatic merging approach for the 3D city models *Wuhan Daxue Xuebao (Xinxi Kexue Ban)* **40(3)** 347-352
[13] OpenGL Wiki URLt: https://www.khronos.org/opengl/wiki/Main_Page

Acknowledgements
This research was supported by the Russian Science Foundation, grant No. 16-11-00068.

Methods for emotions, mood, gender and age recognition

D D Pribavkin[1], P Y Yakimov[1,2]

[1]Samara National Research University, Moskovskoe Shosse 34A, Samara, Russia, 443086
[2]Image Processing Systems Institute of RAS - Branch of the FSRC "Crystallography and Photonics" RAS, Molodogvardejskaya street 151, Samara, Russia, 443001

e-mail: pribavkindenis@gmail.com

Abstract. Recognition on images not only of shapes, but also of metadata is becoming increasingly popular among researchers in the field of convolutional neural networks and deep learning. This article provides an analytical overview of modern software solutions that recognize the images of emotions, mood, gender and age of a person. Enthusiasts invent all new and new architectures of convolutional neural networks, allowing to solve the tasks with considerable recognition accuracy.

1. Introduction

In recent years, there has been a rapid development of parallel data processing technologies, in particular due to the development of graphics processors, which are no longer intended only for computer graphics. This made it possible to train even the most complex neural networks in their architectures and opened up a whole horizon of unsolvable tasks [1], [2], [3]. Modern intellectual systems focus not only on pattern recognition from the input image, but also learn to isolate metadata from recognized objects, such as emotions, mood, gender, or a person's age.

Many researchers and enthusiasts in the field of machine learning and convolutional neural networks develop and offer their own, unique solutions that are different both ideologically and technically.

This article offers an analytical review of the following software solutions in the field of recognition of emotions, mood, sex and age of a person:

- Emotion recognition using Deep Convolutional Neural Network [4].
- A Compact Soft Stagewise Regression Network [5].
- Real-time Convolutional Neural Networks for Emotion and Gender Classification [6].
- Age Recognition using CNNs [7].

2. Review of existing solutions

2.1. Emotion recognition using Deep Convolutional Neural Networks

A solution that is a trained neural network that recognizes real-time emotions on a human face recognized from the input video stream.

It was built using the TFLearn programming library for the python programming language, based on the well-known TensorFlow machine learning framework developed by Google in 2015 [8]. This framework simplifies the development of the network, as it requires describing only the layers themselves instead of describing each neuron separately, and also simplifies network training by providing real-time process feedback and learning accuracy. Moreover, the library allows you to save the result of a trained model to use it later.

The resulting neural network model is shown in Figure 1.

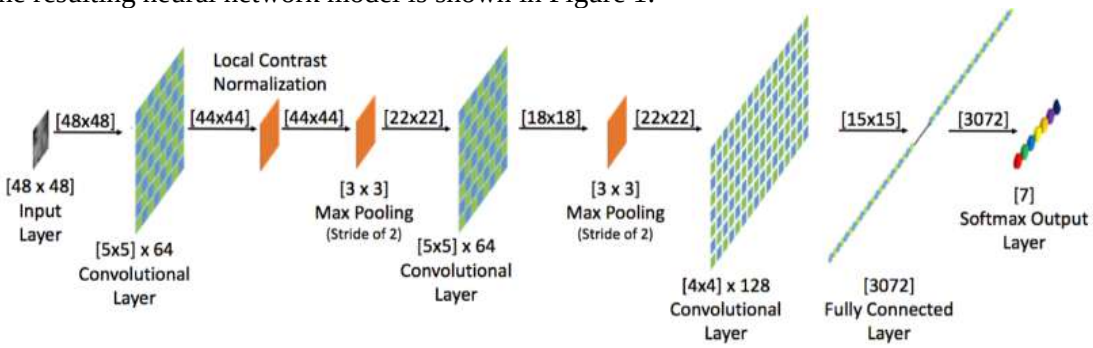

Figure 1. Neural network model.

In each frame of the video stream, an attempt is made to recognize a human face (s). This is achieved using the OpenCV open library recognition method [9]. Then, if a face was recognized in the image, that face is cut out and scaled to a size of 48x48 pixels. Only after that it is fed to the input of the neural network. Thus, we get optimized software that affects neural network resources only if there is at least one human face in the frame.

The model was trained with the help of dataset FERC-2013, which has about 20,000 images containing examples of the following emotions: anger, fear, happiness, sadness, surprise, indifference and disgust. The density of the distribution of emotions in this data is reflected in Figure 2.

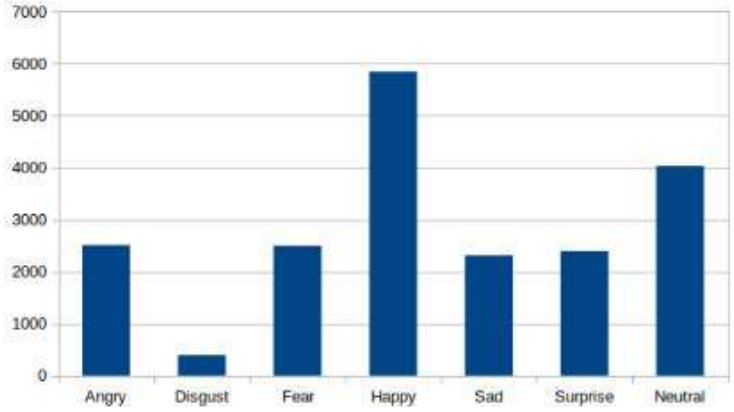

Figure 2. Density of distribution of emotions in dataset FERC-2013.

According to the results of training, the accuracy of recognition of emotions was achieved in 67%.

2.2. SSR-Net

This solution is an original neural network with soft stepwise regression (soft stagewise regression network) for recognizing age and sex. The network recognizes age and gender according to the following principle: images of 64x64 pixels are fed to the input of the network, a multi-level classification is made from several classes, where each level serves to refine the previous result, and then the result of the classification is processed using a regression.

The model itself is very compact and takes only 0.32 MB. But in spite of its compact dimensions, the performance of SSR-Net is close to the characteristics of the most modern methods, the sizes of models of which are 1500 times larger.

A model of this neural network with three levels and a pool size of 2 is shown in Figure 3.

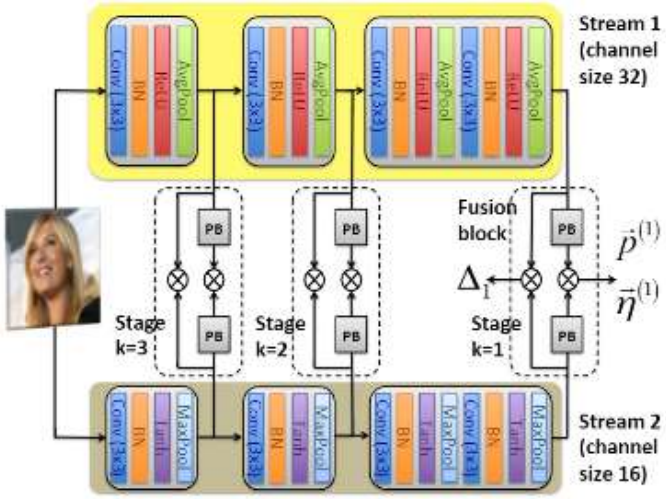

Figure 3. Neural network model SSR-Net.

For training this model, such datasets as IMDB, WIKI and Morph2 [11] were used. About 80% of randomly selected images from datasets were used to train the network, and the remaining 20% were used for testing.

An example of dependence of the number of SSR-Net, MobileNet and DenseNet network recognition errors trained in Morph2 data on the number of epochs is presented in Figure 4.

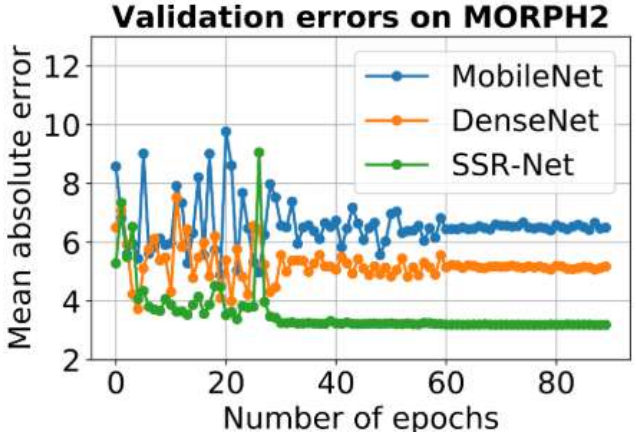

Figure 4. Graph of recognition errors versus the number of epochs.

2.3. Face classification and detection from the B-IT-BOTS robotics team

It is a real-time classifier of emotions and gender of a person, based on the convolutional neural network and the open image processing library openCV [9]. The model of this neural network is shown in Figure 5 and contains 600,000 parameters.

This model was trained in IMDB dataset, which has about 460,723 RGB images, each of which belongs to one of the classes: male or female [10]. At this dataset, recognition accuracy of 96% was achieved. Also, this model was validated on dataset FER-2013, which includes 35,887 images in gray tones, each of which belongs to one of the classes of emotions: anger, disgust, fear, joy, sadness, surprise and indifference. At this dataset, 66% accuracy was achieved.

2.4. Age and gender estimation

This solution is the implementation of a convolutional neural network for recognizing the sex and age of a person from the input image. The basis for the VGG-16 network architecture was taken due to its depth and controllability. This network accepts 256x256 pixel images as input.

The training was carried out on IMDB-WIKI datasets, and recognition accuracy of 64% was achieved [10].

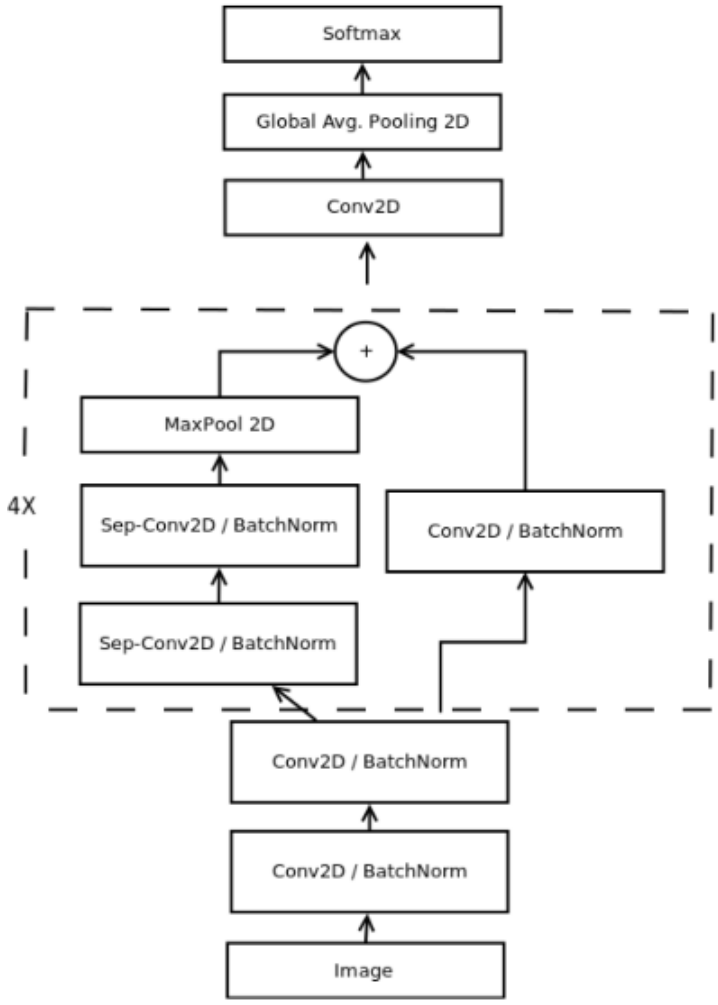

Figure 5. Neural network model.

2.5. General comparison of implementations

As a result of the analytical review, the decisions contained in the publications [6, 7] were selected:

1. A solution that recognizes a person's age, trained in dataset IMDB-WIKI with a recognition accuracy of 64%.
2. A solution that recognizes the sex of a person, trained in dataset IMDB with a recognition accuracy of 96%.
3. A solution that recognizes a person's emotions, trained in dataset FER-2013 with a recognition accuracy of 66%.

The source code of each solution was carefully analyzed and revised so that the digital image was provided as input to the software, and the result of the prediction of a convolutional neural network was obtained.

3. Conducting experimental studies

At the end of the previous section, software solutions were obtained, the main task of which is to recognize the age, gender and emotions of a person from a digital face image.

These solutions were chosen as objects for conducting an experimental study of their performance on 10 random images of the faces of people from the IMDB-WIKI dataset.

The following equipment and software were used during the pilot study:

1. Processor: intel Core i5-4570 3.2 GHz.
2. RAM: 8 Gb.
3. Operation system: Manjaro 18.0.4 «Illyria».

4. Programming language: Python 3.6.5.

Below (Figures 6–15)are the images used in the pilot study:

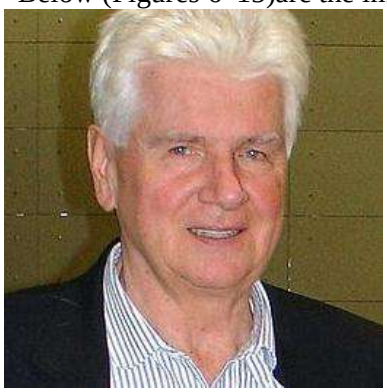

Figure 6. Image number 1.

Figure 7. Image number 2.

Figure 8. Image number 3.

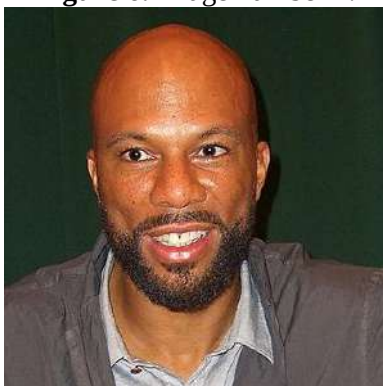

Figure 9. Image number 4.

Figure 10. Image number 5.

Figure 11. Image number 6.

Figure 12. Image number 7.

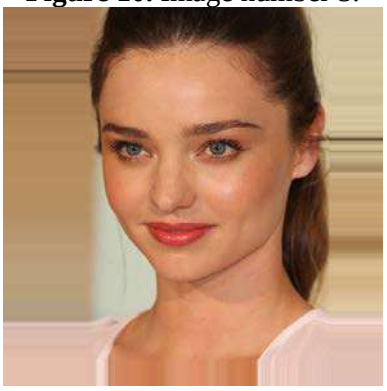

Figure 13. Image number 8.

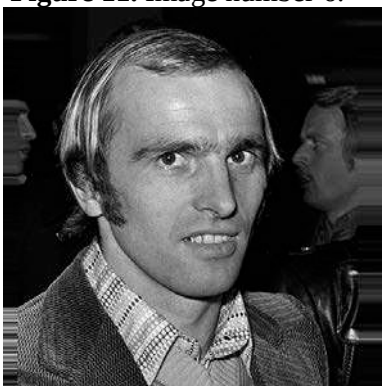

Figure 14. Image number 9.

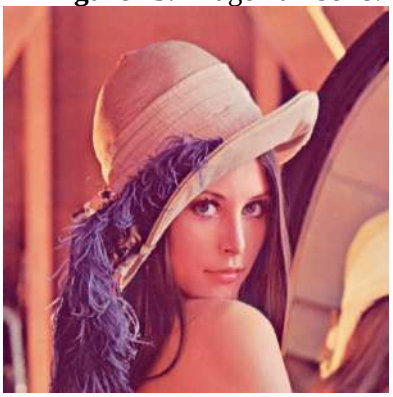

Figure 15. Image number 10.

Since the neural network with the same input data always produces the same result, performing multiple independent attempts at recognition in a row does not have much value, however, to measure a more accurate execution time of a convolutional neural network in a single digital image.

Tables 1, 2 and 3 present the results of recognizing age, gender and emotions, respectively, as well as the average execution time for 5 runs of a convolutional neural network in the next digital image.

Table 1. Final Age Recognition.

Image, №	Age	Average time, ms
1	64	523
2	31	642
3	39	627
4	34	510
5	47	481
6	17	524
7	56	537
8	25	450
9	34	583
10	25	592

Table 2. Final Gender Recognition.

Image, №	Gender	Average time, ms
1	Man	324
2	Woman	451
3	Man	430
4	Man	318
5	Man	293
6	Woman	305
7	Man	421
8	Man	326
9	Man	432
10	Woman	476

Table 3. Final Emotion Recognition.

Image, №	Emotion	Average time, ms
1	Happiness	389
2	Happiness	513
3	Surprise	527
4	Happiness	408
5	Fear	362
6	Happiness	385
7	Happiness	503
8	Happiness	476
9	Sadness	513
10	Neutral	563

As we can see from tables 1, 2 and 3, although the accuracy of recognition stated by the authors still requires some refinements (for example, a neural network that recognizes the sex of a person is clearly mistaken in image No. 8), these pre-trained convolutional neural networks are capable of producing meaningful results, reflecting reality.

4. Conclusion

As a result, we can conclude that such tasks as the recognition of emotions, mood, gender and age are very popular among researchers all over the world. Enthusiasts use different approaches to the

implementation of intelligent systems that can solve such problems and achieve good results in accuracy of recognition, even with limited resources. The main means of the implementation of the tasks are convolutional neural networks of various architectures, trained in well-known in the network dataset images.

5. References

[1] Bibikov S A, Kazanskiy N L and Fursov V A 2018 Vegetation type recognition in hyperspectral images using a conjugacy indicator *Computer Optics* **42(5)** 846-854 DOI: 10.18287/2412-6179-2018-42-5-846-854
[2] Shatalin R A, Fidelman V R and Ovchinnikov P E 2017 Abnormal behavior detection method for video surveillance applications *Computer Optics* **41(1)** 37-45 DOI: 10.18287/2412- 6179-2017-41-1-37-45
[3] Shustanov A, Yakimov P 2017 CNN Design for Real-Time Traffic Sign Recognition *Procedia Engineering* **201** 718-725 DOI: 10.1016/j.proeng.2017.09.594
[4] Correa E, Jonker A, Ozo M, Stolk R *Emotion Recognition using Deep Convolutional Neural Network* URL: https://github.com/isseu/emotion-recognition-neural-networks/blob/master/paper/Report_NN.pdf (1.11.2018)
[5] Tsun-Yi Y, Yi-Hsuan H, Yen-Yu L, Pi-Cheng Hu, Yung-Yu Ch *SSR-Net: A Compact Soft Stagewise Regression Network for Age Estimation* URL: https://github.com/shamangary/SSR-Net/blob/master/ijcai18_ssrnet_pdfa_2b.pdf (14.11.2018)
[6] Arriaga O, Plöger P G, Valdenegro M *Real-time Convolutional Neural Networks for Emotion and Gender Classification* URL: https://github.com/oarriaga/face_classification/blob/master/report.pdf (8.10.2018)
[7] Pakulich D, Alyamkin S, Yakimov S 2019 Age estimation using face recognition with convolutional neural networks *Avtometriya* **55(3)** 52-61 (in Russian) DOI: 10.15372/AUT20190307
[8] TFLearn library URL: http://tflearn.org/ (04.10.2018)
[9] OpenCV library URL: http://opencv.org (04.10.2018)
[10] IMDB-wiki dataset URL: https://data.vision.ee.ethz.ch/cvl/rrothe/imdb-wiki/ (04.10.2018)

Acknowledgements
This work was partly funded by the Russian Foundation for Basic Research – Project # 17-29-03112 ofi_m and the Russian Federation Ministry of Science and Higher Education within a state contract with the "Crystallography and Photonics" Research Center of the RAS under agreement 007-ГЗ/Ч3363/26.

High performance radar images modelling and recognition of real objects

D A Zherdev[1,2]**, V V Prokudin**[1]

[1]Samara National Research University, Moskovskoe Shosse 34A, Samara, Russia, 443086
[2]Image Processing Systems Institute of RAS - Branch of the FSRC "Crystallography and Photonics" RAS, Molodogvardejskaya street 151, Samara, Russia, 443001

e-mail: t_treasure@mail.ru

Abstract. In the work there is a modernization of the parallel algorithm for the radar images formation of 3D models with the synthesis of the antenna aperture. In the formation of the scene description, the various structures are used in which it is possible to use more efficient and derived calculations. In addition, it is the topical task to recognize objects on radar images. Thus, on the basis of the implemented parallel program for modelling, the high performance required for simulating multiple radar images can be achieved.

1. Introduction

This research is a continuation of ideas and methods used in [1], where high-performance radar images modeling approach was considered. The goal of this work is to obtain a greater acceleration of the parallel program for synthetic aperture radar modeling by building a kd tree describing a three-dimensional scene [2-4]. We used CUDA to perform a high-performance computing on a graphic card and achieve this goal. It is the main difficulty to form a trajectory signal along with the radar travel and then compute a radar image. In this study, an algorithm for obtaining radar characteristics was implemented with the construction of the kd tree structure, that allow to describe any three-dimensional scene.

2. Modelling and recognition

The main computationally expensive part of the radar images modelling algorithm is in the processing of radiated and reflected radar signals. In this work, a modification of the CUDA algorithm was implemented, which difference at the stage of the trajectory signal constructing is in a previously calculated kd-tree for any three-dimensional scene. The subsequent execution of the synthesis of the radar aperture was performed the same way as discussed in [1]. This approach of computable operations reducing allowed us to achieve a three-fold acceleration compared with the previous algorithm implementation.

In addition, during the research, we carried out the experiments of object recognition in radar images. There are many methods and approaches of object recognition, among which the popular methods are convolutional neural networks [5], support vectors, nearest neighbours, etc. [6]. In this work, the object recognition was performed using the method of support subspaces [7]. We used three-

dimensional models of the tank, BMP, BTR to construct the radar images. All sizes of the models were matched to the corresponding sizes of their real prototypes at the three-dimensional coordinate system. We used the modelling parameters presented in Table 1 when generated the training set. The bearing angle was 17°, which corresponds to the conditions of the real obtained SAR images training dataset. We modelled 100 images for each object. The step of rotation was equal the 3.6° in the observation plane. Figure 3 shows the real and modeled SAR images of BTR.

There are the results of research shown below which related to the construction of a training model sample and the subsequent recognition of real images using model images at the training stage. Figure 1, a), b) shows the real radar images of a tank from the widely known MSTAR database, and figure 2, a), b) shows radar images obtained by modelling using the synthetic aperture radar method, with angles the bearing angle of 17° and 15° and the aspect angles are 17 ° and 100 °, respectively.

Table 1. Modelling parameters.

#	Parameter	Value
1	Radar start point (x,y,z), m	(-4335.5,1325.5,-50)
2	Radar observation mode	spotlight
3	Synthesis lenght, m	100
4	Wave length (chirp), m	0.029 – 0.033
5	Azimuth resolution, m	0.3
6	Range resolution, m	0.3
7	Impulse duration, mcs	0.5
8	Min range, m	4510
9	Max range, m	4630
10	Azimuth step, m	0.25
11	Range step, ns	0.5

a) 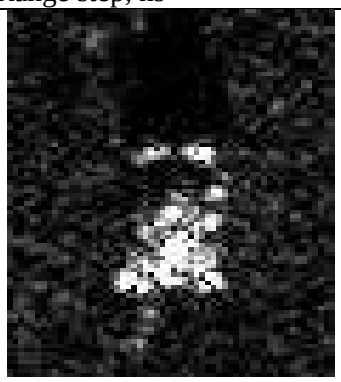 b) 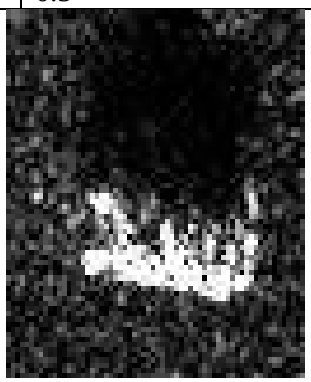

Figure 1. MSTAR dataset SAR images: a) bearing angle 17°, elevation angle 15°; b) bearing angle 17°, elevation angle 100°.

a) 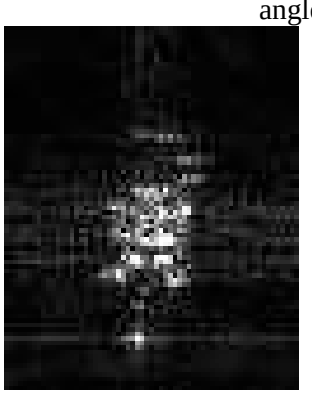 b) 

Figure 2. Modelled SAR images: a) bearing angle 17°, elevation angle 15°; b) bearing angle 17°, elevation angle 100°.

The recognition results for three classes obtained using the recognition contingency index based algorithm [7] (without subclassing) are listed in Table 2. Note that the result of 62.78% correct recognition of the three classes was obtained on a relatively small training set (300 images). The MSTAR training sample contains 587 of image samples.

a) 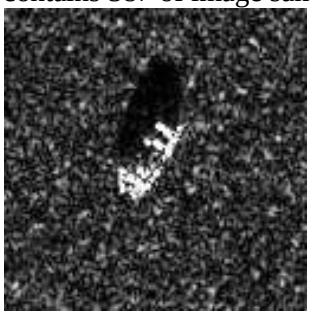 b) 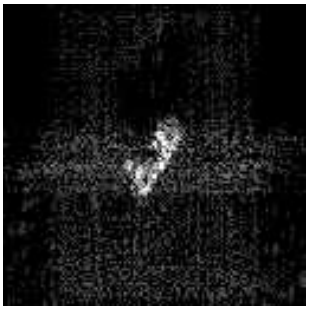

Figure 3. SAR images: a) model and b) real BTR target.

Table 2. Recognition results with modelled dataset training.

	Evaluated class			
	BMP2	BTR70	T72	
BMP2	402	124	61	68.48%
BTR70	134	43	19	21.93%
T72	119	51	412	70.79%

At the binary classification: the BMP and tank using the same algorithm, the result of 80.24% was achieved. The recognition results of the two classes without division into subclasses are shown in Table 3.

Table 3. Results of two objects recognition.

	Evaluated class		
	BMP2	T72	
BMP2	496	91	84.50%
T72	140	442	75.94%

In addition, we carried out the experiment of the real images recognition by training on model images, which obtained using the ray tracing approach [8]. Table 4 shows the recognition results. The total percentage of correct recognition was 27.6%. These results show that images modelled via raytracing is not quite suitable for recognition real images. Perhaps they can be used to create a simplified model of a three-dimensional scene.

Table 3. Results of objects recognition (dataset modelled via raytracing).

	Evaluated class			
	BMP2	BTR70	T72	
BMP2	207	270	221	29.66%
BTR70	78	67	51	34.18%
T72	331	146	105	18.04%

It should be noted that in the MSTAR database, the training sample has 587 images. In contrast to presented model images dataset, the rotation of an object in the MSTAR images was performed with an irregular step and with rather large positioning errors.

3. Conclusion

The paper shows that the results of objects recognition using real images has the ability of the effective usage at the developed software. The images were obtained by modeling can form the training dataset at the proposed algorithm. In addition, the parallel algorithm acceleration is obtained

by kd-tree construction let us help to perform high-computing and effective scattering calculation on the various object surfaces.

4. References

[1] Zherdev D A, Prokudin V V and Minaev E Y 2018 HPC implementation of radar images modelling method using CUDA *Journal of Physics: Conference Series* **1096** 012083
[2] Horn D R, Sugerman J, Houston M and Hanrahan P 2007 Interactive kd tree GPU raytracing *Proceedings of the symposium on Interactive 3D graphics and games* 167-174
[3] Wehr D, Radkowski R 2018 Parallel kd-tree construction on the gpu with an adaptive split and sort strategy *International Journal of Parallel Programming* **46(6)** 1139-1156
[4] Vinkler M, Havran V and Bittner J 2016 Performance Comparison of Bounding Volume Hierarchies and Kd-Trees for GPU Ray Tracing *Computer Graphics Forum* **35(8)** 68-79
[5] Savchenko A V 2018 Trigonometric series in orthogonal expansions for density estimates of deep image features *Computer Optics* **42(1)** 149-158 DOI: 10.18287/2412-6179-2018-42-1-149-158
[6] Borodinov A A, Myasnikov V V 2018 Classification of radar images with different methods of image preprocessing *CEUR Proceedings* **2210** 6-13
[7] Fursov V, Zherdev D and Kazanskiy N 2016 Support subspaces method for synthetic aperture radar automatic target recognition *International Journal of Advanced Robotic Systems* **13(5)** DOI: 10.1177/1729881416664848
[8] Zherdev D A, Fursov V A 2015 Support plane method applied to ground objects recognition using modelled SAR images *Applications of Digital Image Processing XXXVIII International Society for Optics and Photonics* **9599**

Acknowledgments

The work was funded by the Russian Federation Ministry of Education and Science (agreement 007-GZ/Ch3363/26) and RFBR (project # 17-29-03112 ofi_m).

Intrusion detection system on the basis of data mining algorithms in the industrial network

M A Gurin[1], A M Vulfin[1], V I Vasilyev[1] and A V Nikonov[1]

[1]Ufa State Aviation Technical University, K. Marks st., 12, Ufa, Russia, 450008

e-mail: vulfin.alexey@gmail.com, nikonovandrey1994@gmail.com

Abstract. The purpose of the work is to increase the security of the industrial network of an automated process control system based on intelligent network traffic analysis algorithms. The analysis of the problem of detecting and recording actions of violators on the implementation of a network attack on an automated process control system in the industrial network of an enterprise has been performed. A structural and functional model of the monitoring system of the industrial network of industrial control systems is proposed. An algorithm is developed for the intellectual analysis of network traffic of industrial protocols and a software package that implements the proposed algorithms as part of a monitoring system to evaluate the effectiveness of the proposed solution on field data.

1. Introduction

Security of the critical infrastructure of automated process control system (APCS) [1] under the conditions of the automation level of modern production in the Russian Federation and around the world is becoming an increasingly priority task. The imperfection of the protection and vulnerability of modern SCADA-systems (Supervisory Control and Data Acquisition systems) is due to a number of features of the organization of such systems [2]. Special viruses and target attacks, sponsored by terrorist groups or governments of competing countries, increasingly began to target at the industrial production facilities [3, 4, 5]. The Internet of things gradually comes to the enterprises networks, expanding the already extensive list of industrial protocols and forming the concept of an industrial Internet of things (IIoT) [4, 5]. The means to ensure the information security of process control systems at this stage of their development are not able to withstand such threats [6, 7].

Today, there is a transition to automated digital production, controlled by intelligent systems in real time, in constant interaction with the external environment, going beyond the boundaries of one enterprise, with the prospect of combining into a global industrial network of things and services. This approach is developed in the concept of “Industry 4.0” and describes the current trend in the development of automation and data exchange, which includes cyber-physical systems, the Internet of things and cloud computing [8, 9, 10]. There are many advantages of using wireless sensor networks (WSN, Wireless sensor network) as an environment for wireless interaction of digital objects within the industrial Internet of things network in various automated systems [11].

Network security is becoming one of the main directions in the development of information security through the use of a set of technical means [3]. Since any computer process control system

can be attacked, which usually results in serious technical, reputation and economic losses, it is necessary to timely detect both known and previously unknown attacks in industrial networks. Attacks of malicious persons are constantly improving, becoming combined and spread almost instantly. Intrusion detection systems (IDS) implement monitoring functions and detect attacks that have bypassed the firewall. IDS informs the administrator, who, in turn, takes a further decision on the response to the attack [12].

Thus, it can be concluded that the network attacks detection systems based on the use of artificial intelligence methods as a key element of ensuring cybersecurity of the critical infrastructure [13, 14, 15] of the APCS in the concept of the development of the digital economy are of relevance and need to be improved.

The research goal is to increase the effectiveness of network attack detection system by using a neural network analysis module as part of the IDS. To achieve this goal, it is necessary to solve the following tasks:

- Analysis of the problem of detecting network attacks in industrial networks APCS.
- Development of the structure of the system for monitoring the industrial network of APCS;
- Development of algorithms for intellectual analysis of network traffic of industrial networks;

Development of a software package that implements the proposed algorithms as part of a monitoring system, and an assessment of the effectiveness of the proposed solution on full-scale data.

2. Analysis of the problem of detecting network attacks in industrial networks

The process of automation of industrial production continues to evolve: the number of “intelligent” terminal devices is increasing, the number of microcontroller-based computing systems involved in the process control and process control is growing. Under these conditions, the role of data collected at all levels of the process control system significantly increases. Requirements imposed by consumers of this information are increasingly being tightened in terms of the volume, speed and reliability of data acquisition, as well as information security of the entire system [5]. In turn, increasing degree of automation of the enterprise functioning promoted the mutual integration of information (IT) and so-called operational (OT) technologies [7].

An industrial network is a data transmission environment that must meet a variety of diverse, often contradictory requirements; a set of standard data exchange protocols that allow to link equipment together (often from different manufacturers), and also to ensure interaction between the lower and upper levels of the enterprise management system.

In IIoT, the main types of “things” that need to be connected to the network are various types of sensors and actuators. These devices, on the one hand, have an interface with a communication network, and on the other hand, an interface that provides physical interaction with the process to be monitored (Ethernet, Wi-Fi, cellular networks, Sigfox, LoRa, ZigBee, etc.).

Not so long ago, the hierarchy of the APCS had a clear boundary between the levels. The trends of recent years have made this structure much more complex and diffuse. The automated process control system is more and more integrated with the automated control system, and through it inevitably enters the sphere of Internet technologies. Unification of the corporate and industrial network of an enterprise inevitably poses a serious problem of information security of the industrial network of industrial control systems.

The traditional process control system is a real-time system. To ensure error-free process control, continuous process operation monitoring is necessary [16]. If IT security methods are applied in the process control system, in the event of possible data comprometation, the security system may limit access to this data. This, in turn, can lead to loss of control over the TP and man-made or environmental catastrophe (in critical infrastructure, petrochemical industry and other industries). Therefore, in relation to industrial control systems, the inverse distribution of the significance of safety aspects is widely used [16, 17]:

- availability;
- integrity;
- confidentiality.

The following main threats to the security of an industrial network can be identified [16, 17]:

- Traditional virus software (malware);
- Targeted attacks;
- Unintentional staff errors;
- Suppliers of equipment and software, partners, contractors;
- extortion programs;
- Internal and external sabotage;
- Errors of specialized industrial control systems;
- Failure of hardware.

Summary information of the information security systems of automated process control systems shown in Table 1.

Table 1. Information security support systems in APCS.

Product name	**Kaspersky Industrial CyberSecurity** [17,18]	**Security Matters SilentDefense** [20,21]	**Positive Technologies Industrial Security Incident Manager (PT ISIM)** [19]	**Honeywell Risk Manager**
Meeting the requirements of regulators (FSTEC №31)	+	-	+	-
Security audit	+	-	+	+
Creating rules for the operation of technological processes	+	+	+	-
Intgration with Human-Machine Interface (HMI)	+	-	-	-
System distribution	KICS for Nodes, KICS for Networks, Security Center	Sensors + Command Center	Full distribution	A single control center that collects information from external monitoring and security systems
Recommendations for elimination	-	-	+	+
Intervention in technological process	Uses a copy of network traffic (SPAN / TAP), but contains an intrusion prevention system	Uses copy of network traffic (SPAN-ports)	Uses copy of network traffic (unidirectional gateway)	Data collection without intervention, integration with intrusion prevention system is possible
Software developer certification for APCS	Siemens (WinCC, WinCC OA), Emerson	-	-	Honeywell Experion

An example of the use of wireless sensor networks is the use of wireless sensor networks in electrical substations [22]. The compactness and autonomy of the sensor nodes make it possible to install them in hard-to-reach places without solving the tasks of organizing wired communication

channels for transmitting telemetric information such as: power flows in the power system, control of active and reactive power, frequency and voltage in certain areas to the control room. Due to the transition from wired to wireless network technologies to collect telemetry data, network security is determined not only by hardware and software solutions for industrial controllers and sensor nodes, but also by the chosen principles of their information interaction during the synthesis of network topology, determination of routing parameters and data transmission.

A wireless sensor network [11] consists of many autonomous sensor nodes distributed in areas of the industrial system that are of interest for the collection of operational data and the joint transmission of collected data over wireless channels to a central node that is a node or base station (BS).

Most information security threats in wireless networks are similar to threats and attacks on wired networks, except that wireless networks are harder to protect due to the use of an open medium as a data transmission channel and the broadcast nature of wireless connections. Network protection is complicated due to limited resources: the energy of an autonomous power source and computing resources. Such limiting characteristics make traditional security measures, for example, the use of complex encryption algorithms, multifactor authentication, firewalls, etc. [23] – not always sufficient. A significant factor is the time delay requirements for data transmission in the transport environment and closed protocols for the operation of the software and hardware of the APCS, which do not always allow the implementation of protection technologies using IPSec, SSL, VPN.

The current trend in the development of the transport environment of industrial networks is the use of self-organizing wireless networks with equal rights of nodes, a dynamically changing topology, the possibility of reconfiguration, self-healing, dynamic routing, etc.

The classification of attacks on wireless sensor networks in the direction of impact is given in [24, 25, 26].

Active attacks are various modifications of data during communication by unauthorized persons. Of most interest are routing attacks implemented at the network level. The most common attacks are presented in [11].

Wireless Intrusion Detection System – WIDS [27, 28, 29] is a software and hardware solution that includes software agents that perform the function of collecting, processing and analyzing network traffic packets. Agents interact with the server, transmit intercepted packets to it. The server processes the received data to detect attack signatures and detect abnormal behavior of network nodes, and also responds to events.

3. Network attack detection methods

There are two groups of methods: learning with a teacher (supervised) showed in Table 2, and uncontrolled learning (without a teacher) showed in Table 3 [30, 35, 36]. The essential difference between them is the fact that learning with a teacher uses a fixed sequence of assessment parameters and some data on the meaning of assessment parameters. In learning without a teacher, the set of assessment parameters changes and the process of further training is continuous. Table 4 describes supervised learning methods for intrusion detections.

Table 2. Network attack detection: supervised learning [30].

Method	Description
Rule modeling	Intrusion detection system during training determines a set of rules for normal network behavior. During the operation process, an IDS applies this set of rules and, if it does not match, generates an intrusion detection signal.
Descriptive statistics	The system determines the “distance” between the actual vectors of indicators and vectors collected during the training stage. If the distance between the vectors exceeds a certain threshold, the behavior is considered abnormal.
Neural networks	The neural network is trained on data describing the normal functioning of the system.

Table 3. Network attack detection: learning without a teacher [30].

Method	Description
Simulation of multiple states	Network behavior is described by a set of states and transitions between them. States are described by feature vectors.
Descriptive statistics	The system determines the “distance” between the actual vectors of indicators and vectors collected during the training stage. If the distance between the vectors exceeds a certain threshold, the behavior is considered abnormal.

Table 4. Abuse detection: supervised learning [30].

Method	Description
States modelling	An intrusion is represented as a set of states and transitions between them. States are described by feature vectors. Such systems use Petri nets tools or ordinary chains of events.
Expert systems	Intrusions are represented as a set of rules.
Rules modelling	Simplified expert systems.
Parsing	The intrusion detection system performs parsing to detect a specific combination of characters.

4. Development of the structure of the system for monitoring the industrial network of APCS

Figure 1 shows network structure of an enterprise with tools for collecting and analyzing network traffic of a network intrusion detection system (IDS).

The structure of the network attack detection system based on data mining is shown in the Figure 2. At the first stage, network traffic is captured. In Figure 1, the numbers indicate the following components: 1 is a router as a means of collecting incoming / outgoing network traffic, 2 is a router as a means of collecting traffic within the enterprise network. The collection of necessary data is performed using the package sniffer.

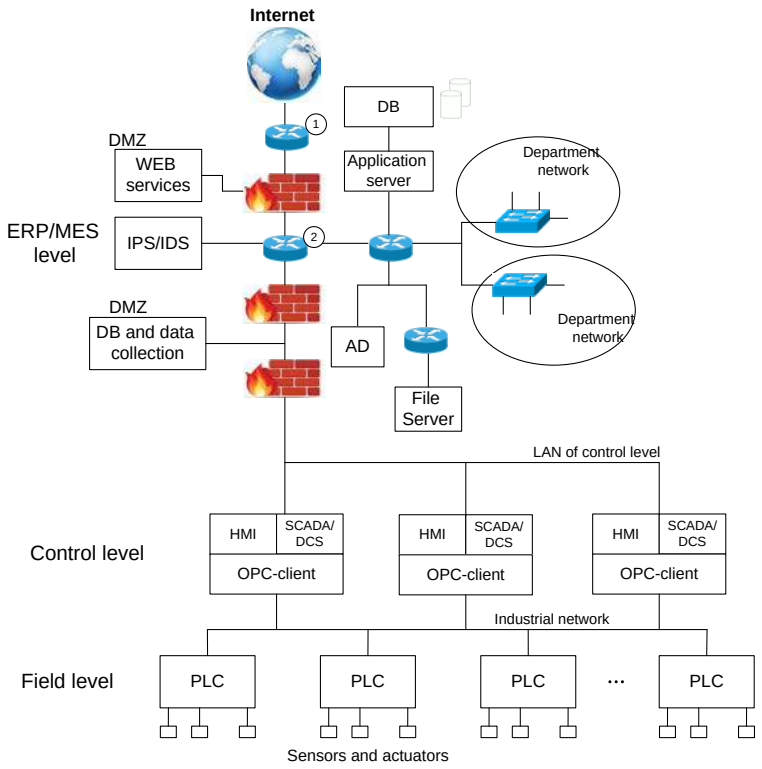

Figure 1. The structure of the enterprise network in which information is collected.

The second stage identifies the most significant parameters that characterize network activity.

At the third stage, detection and classification of attacks is carried out. The results of this recognition are transmitted to related systems for reporting and visualization, depending on the capabilities and specifics of adjacent systems. In addition, information about the attack on the APCS is added to a special archive designed to investigate cybersecurity incidents by authorized specialists and managers.

5. Development of algorithms for intellectual analysis of network traffic of industrial networks

An effective network attack detection system based on artificial intelligence methods can be built only with a high-quality dataset of training and test samples that simulates various intrusions.

KDDCUP99 – intrusion detection dataset based on the data set DARPA 98, is one of the only publicly available labeled data set [31]. Dataset NSL-KDD proposed to improve KDD dataset. This dataset has the following advantages over the KDD dataset:

- it does not include redundant entries in the training set, therefore classifiers will not be retrained due to the frequency of such entries;
- there are no duplicate entries in the proposed test suites;
- number of records in the training and test sets is optimal, which makes it possible to conduct experiments on the full set.

Each entry has 41 attributes describing the various functions of the connection, and the label assigned to each of them: attack or normal connection.

Dataset UNSW-NB15 [32] contains data of normal traffic in modern networks and network traffic of synthesized networks.

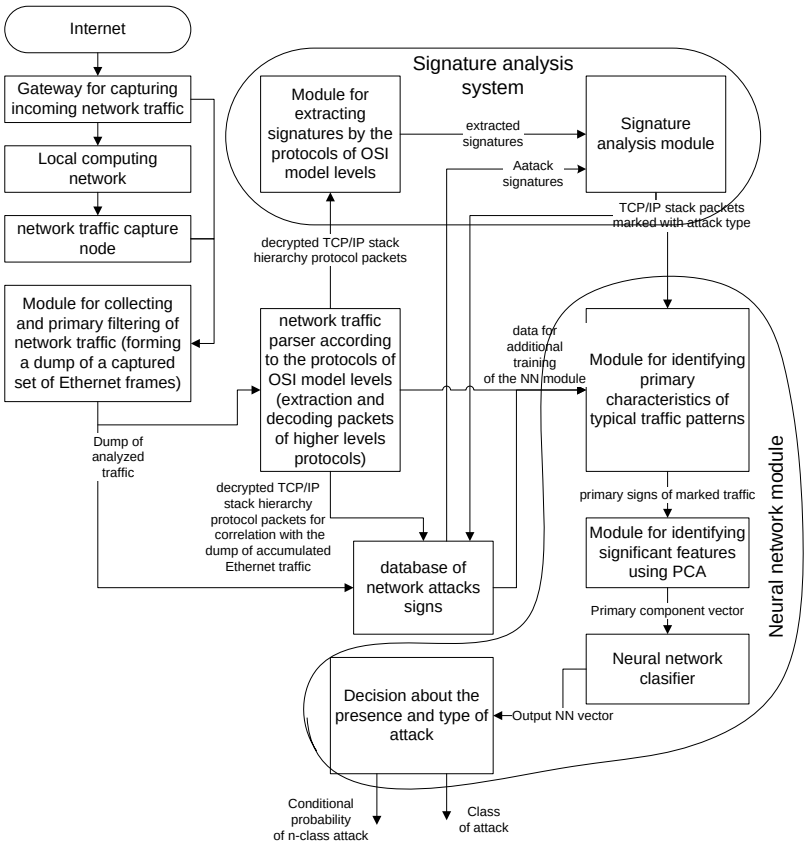

Figure 2. Structural scheme of the network attack detection system.

Each entry in this set contains attributes that describe the various functions of the connection, and the label assigned to each of them: attack or normal connection [32].

The comparative table (Table 5) of the NSL-KDD and UNSW-NB15 methods is shown below:

Table 5. Comparative table of the NSL-KDD and UNSW-NB15 methods.

№	Parameters	NSL-KDD	UNSW-NB15
1	Number of networks	2	33
2	Number of different IP addresses	11	45
3	Traffic simulation	Yes	Yes
4	Duration of data collection	5 weeks	16 days 15 hours
5	Format of data collected	3 types (tcpdump, BSM and dump-files)	PCAP-files
6	Attack classes	4	9
7	Feature Extraction Tools	Bro-IDS	Argus, Bro-IDS and etc.
8	Number of attributes in the record	42	49

Table 6. Network attack methods comparison.

Attack Type	Description	Implementation Features	Method of combating
Buffer overflows	Search for vulnerabilities that can violate the memory boundaries, execute an arbitrary binary code on behalf of an authorized user	1. Preparation of code to be executed in the context of a privileged program. 2. Changing the sequence of program execution with transfer of control to the prepared code.	• Adjustment of the source code of the program. • The use of non-executable buffers. • The use of checks overstep the border. • Conduct integrity checks.
Specialized programs	Viruses, Trojan horse, sniffer, rootkit	The hidden nature of the functioning in the system, data collection, avalanche dissemination	• Anti-virus tools and regular updating of their signatures; • Encryption; • Antisniffera; • Firewalls; • Anti-rootkits [4].
Network intelligence	Collect network information using publicly available data and attack planning applications.	Network intelligence is conducted in the form of DNS queries, ping sweep, and port scanning	• Disable ICMP echo and echo reply on peripheral routers. • The use of intrusion detection systems (IDS).
IP- spoofing	The attacker impersonating an authorized user of the system	Insert false information or malicious commands into the normal data stream	• Access control • The use of cryptographic authentication.
Injections	SQL injection, crossite scripting (XSS attack), XPath injection.	Changing the query parameters to the database, embedding arbitrary code in the web page.	• Rules for building SQL queries; • Encoding data and control characters; • Regular update.
Denial of Service (DoS)	Creating conditions under which legitimate users cannot access the system.	Keeping all connections in busy state. During DoS attacks, normal Internet protocols (TCP and ICMP) can be used.	• Anti-spoofing functions. • Anti-DoS features. • The use of network attack detection systems.
Phishing-attacks	Cheating or social development of enterprise employees to steal their identity and transfer them for criminal use.	Using spam-mailing via e-mail or instant messengers, the use of computer-bots, methods of social engineering.	• The use of proven resources; • Antivirus tools and signature database updates; • Education and training of staff.

Dataset UNSW-NB15 is selected for use in the system:

- number of classes of attacks is more than 2 times;
- test stand contained 33 subnets (NSL-KDD – 2 subnets);

- when collecting traffic on the network, 45 IP addresses participated in the exchange of information against 11 in NSL-KDD;
- traffic was collected by several means (in NSL-KDD - Bro-IDS);
- UNSW-NB15 set contains more attributes for the record (49 vs. 42 in NSL-KDD).

At the moment, in relation to industrial networks the following types of network attacks can be distinguished (Table 6).

Of all types of attacks implemented in the industrial network, network attack detection systems are able to most effectively cope with network intelligence, DoS attacks, as well as various types of injections and buffer overflow attacks. IDS is a practically universal tool capable of detecting most types of attacks implemented on an industrial network.

Main steps of the network traffic analysis algorithm in the industrial network are presented in the Table 7.

Table 7. Characteristics and tools for analysis.

Analysis stage	Characteristics and tools used
Extract traffic	To solve the problem of capturing traffic, it is proposed to use switches with port mirroring and connecting devices with the sniffer and packet analyzer installed.
Feature selection	When analyzing the main parameters of network traffic, one has to deal with an interconnected system of input parameters (factors). Not all of the factors studied are essentially interconnected, but separate groups of input parameters. A transition is needed to a set of independent parameters containing the necessary information about the variation or dispersion of the initial set of factors of the process under study [15]. It is proposed to use: • Principal Component Analysis, PCA; • Neural network autoencoder; • Neural network autoencoder on the basis of convolutional neural network.
Classification	In relation to the problem of classification of network traffic and network discovery it is proposed to use: • Artificial neural networks (multilayer perceptrons); • Decision Tree Ensemble; • Classifier k nearest neighbors (KNN).

6. Development of a software package that implements the proposed algorithms as part of a monitoring system

Table 8 presents the parameters of two common data sets used to build and test network attack detection systems. The choice is made in favor of the UNSW-NB15 data set.

Table 8. Dataset statistics.

Analysis stage		NSL-KDD	UNSW-NB15
Duration of data collection		16 hours	15 hours
Amount of threads		987,627	976,882
Number of bytes of packet sender		4,860,168,866	5,940,523,728
Number of bytes of packet recipient		44,743,560,943	44,303,195,509
Number of sender packets		41,168,425	41,129,810
Number of recipient packets		53,402,915	52,585,462
Protocol	TCP	720,665	720,665
	UDP	301,528	688,616
	ICMP	150	374
	Other	150	374
Label	Normal	1,064,987	1,153,774
	Attack	22,215	299,068
Unique adresses	Sender	40	41
	Recipient	44	45

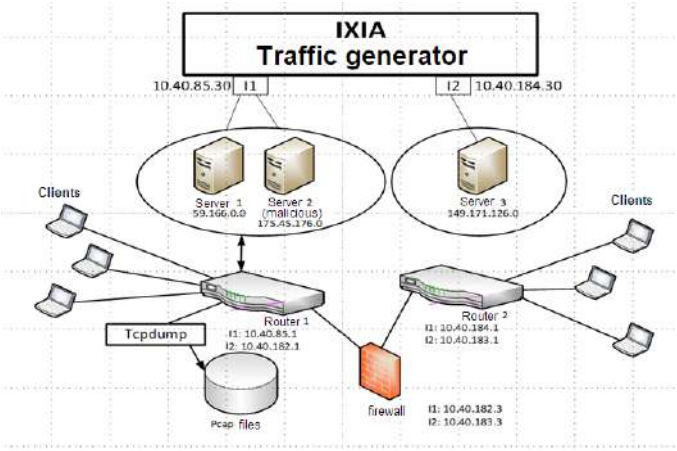

Figure 3. The structure of the experimental stand.

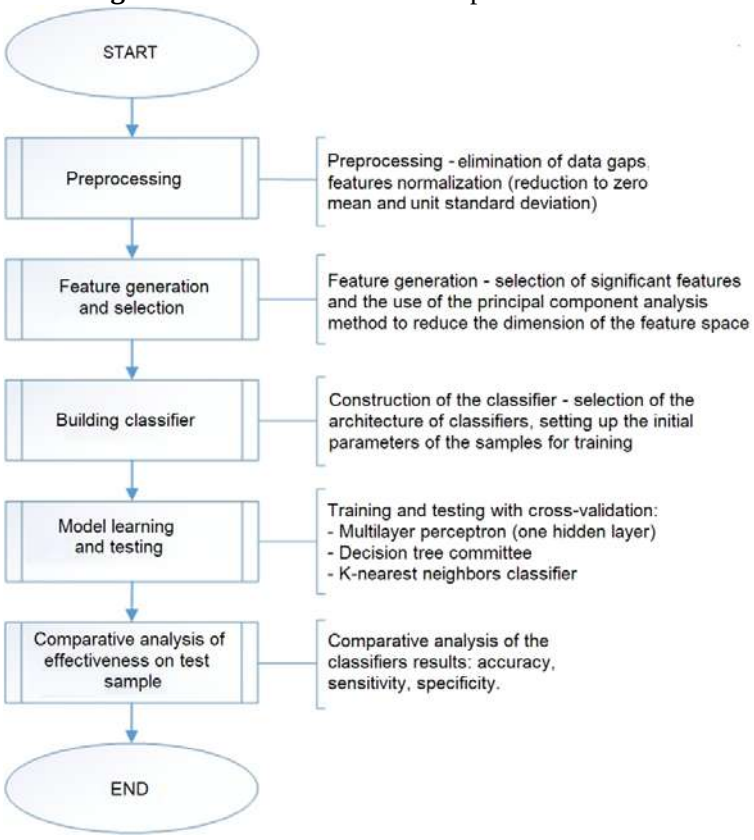

Figure 4. Flow chart of network traffic analysis.

When pre-processing the parameters of the selected data set UNSW-NB15, the attack classes containing less than 5000 examples are excluded from the training set (Table 9).

Table 9. The attack classes.

id	Class name	Number of records
1	DoS	16353
2	Exploits	44525
3	Fuzzers	24246
4	Generic	58871
5	Normal	93000
6	Reconnaissance	13987

Categorical variables are coded into numeric ones. The entire data set is divided into a training and test sample in the ratio of 75% to 25%.

In order to compare the effectiveness of the use the classifier for a specific task, it is necessary to compare the learning results of these classifiers on real data sets. To quantify the classifiers, the following coefficients are applied [34]:

1) False Positive Rate – FPR;
2) True Positive Rate – TPR;
3) Sensitivity;
4) Specificity;
5) Proportion of correctly recognized examples – Correct Rate.

The sensitivity of the algorithm is equal to the proportion of false positive classifications FPR (a, X).

$$Sen = FPR(a, X)$$

A sensitive diagnostic test is called overdiagnosis – the maximum prevention of missing malicious code.

Table 10. Classifier Parameters.

Classifier	Basic Parameters
Decision Trees Committee (RFT)	The maximum number of nodes in the decision tree is assumed to be 250.
Multilayer perceptron (MLP)	The number of neurons in the hidden layer was selected during training to achieve the minimum error on the test sample, the activation function of the hidden layer neurons is the hyperbolic tangent; The number of 5000 epochs of learning, the learning algorithm is conjugate gradients.
Decision Trees Committee (RFT) + main component method for feature selection	Before the classification, features are selected by the method of principal components. The maximum number of nodes of the decision tree is assumed to be 100. The results of the work of the "decision trees" method using feature selection by the principal component method on the test sample are presented in Table 12. The maximum number of nodes in the decision tree is assumed to be 250. The results of the "decision trees" method are presented in table 11.
Classifier based on k-nearest neighbors	Parameter k was hit to achieve optimal error on the test sample. $k \in [5; 100]$
Multilayer perceptron + Autoencoder	Before making a classification, features are selected using a two-layer neural network autoencoder

Table 11. Inaccuracy matrix for decision trees.

	C_1	C_2	C_3	C_4	C_5	C_6
C_1	**23317** **100%**	0 0%	0 0%	0 0%	0 0%	0 0%
C_2	0 0%	**2677** **76.55%**	172 1.52%	5 0.08%	28 0.68%	1 0.01%
C_3	0 0%	711 20.33%	**10156** **90.31%**	689 11.43%	3410 82.25%	239 1.65%
C_4	0 0%	15 0.43%	252 2.24%	**5256** **87.21%**	68 1.64%	23 0.16%
C_5	0 0%	94 2.69%	649 5.77%	73 1.21%	**632** **15.24%**	24 0.17%
C_6	0 0%	0 0%	17 0.15%	4 0.07%	8 0.19%	**14226** **98.02%**
Total	**23317** 100%	**3497** 100%	**11246** 100%	**6027** 100%	**4146** 100%	**14513** 100%

The specificity of the algorithm is calculated as follows:

$$Spe = 1 - TPR(a, X)$$

A specific diagnostic test only diagnoses for certain traffic related to network attacks.

In the course of the research, a series of experiments were carried out, the essence of which consists in determining the presence of an attack and attributing it to a specific class (Table 10).

Table 12. Indicators of detection efficiency of the “decision trees” method depending on the number of components on the test sample.

Number of components	2	4	6	8	10	12	14	16
Average proportion of correctly recognized examples (correct rate)	0.695	0.725	0.755	0.764	0.771	0.776	0.805	0.811
Scatter	0.001	0.001	0.001	0.001	0.002	0	0.001	0

Dependence of the Correct Rate indicator on the number of main components is presented in Figure 5.

A comparison of all methods is presented in table 13. The results given in the table are indicated with an accuracy of 0.01%.

As can be seen from the summary table, in the course of the experiments, the best indicators of correctly recognized images were shown by the algorithms “decision trees” (89.67%) and the multilayer perceptron (89.06%). Sensitivity indicators for FitKNN, MLP and autocoder methods do not exceed 20%.

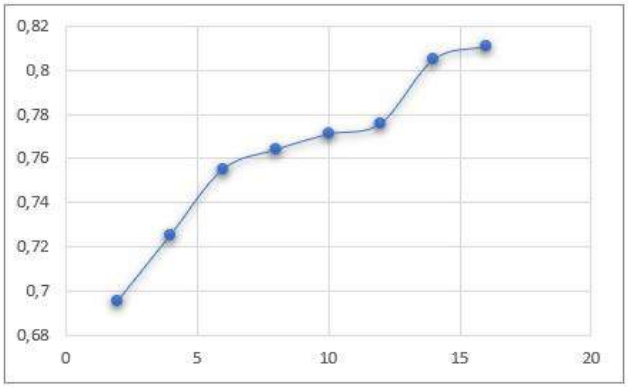

Figure 5. Dependence of the Correct Rate indicator on the number of main components.

Table 13. Comparative experimental results.

Name of the indicator	FitKNN	RFT	MLP	Autocoder	RFT+PCA
Sensitivity	0.1746	0.9877	0.1356	0.0842	0.9168
Specificity	0.9776	0.9897	0.9888	0.9917	0.9335
Correct rate,%	86.24%	89.67%	89.06%	88.58%	81.10%

When using the “decision trees” method together with the principal component method for decreasing the dimension, the indicators decrease (sensitivity - by 8%, specificity - by 6.6%, the proportion of correctly recognized examples - by 8.5%), and require more time and computational resources.

7. Conclusion

During the research the following tasks were solved:

1) The main security threats and the types of intruders in the industrial network of the enterprise are considered. A comparative analysis of software systems to ensure the safety of automated

process control systems was conducted: Kaspersky Industrial CyberSecurity, Silent Defense, PT Industrial Security Incidents Manager, Honeywell Risk Manager.

2) A structural scheme of a network attack detection system based on data mining techniques has been developed.
3) Analyzed the data sets of network traffic, suitable for modeling the traffic of the industrial network of enterprises: KDD99 CUP, NSL-KDD, UNSW-NB15 for the task of detecting network attacks. The UNSW-NB15 set is selected for use in the system, since the number of attack classes is twice as large; test stand contained 33 subnets (NSL-KDD – 2 subnets); in collecting traffic on the network, 45 IP addresses participated in the exchange of information against 11 in NSL-KDD; traffic collection was carried out by several means (in NSL-KDD – Bro-IDS); the UNSW-NB15 set contains more attributes in the record (49 vs. 42 in NSL-KDD).
4) A software package has been developed that implements a comparative analysis of network attack detection algorithms. The most effective is the "decision trees" method with sensitivity indicators Sen = 1, specificity Spe = 0.9877, and the mean correct rate MCR = 89.67%.

8. References

[1] Knapp E D, Langill J T 2014 Industrial Network Security: Securing critical infrastructure networks for smart grid, SCADA, and other Industrial Control Systems *Syngress*
[2] Ralston P A, Graham J H and Hieb J L 2007 Cyber security risk assessment for SCADA and DCS networks *ISA transactions* **46(4)** 583-594
[3] Montgomery G *SCADA: Threat landscape* URL: https://energy.gov/sites/prod/files/cioprod/documents/Cracking_Down_SCADA_Security_-_Garrett_Montgomery.pdf
[4] Langner R *To kill a centrifuge – a technical analysis of what Stuxnet's creators tried to achieve* URL: http://www.langner.com/en/wp-content/uploads/2013/11/To-kill-a-centrifuge.pdf
[5] Alert IR-ALERT-H-16-056-01 Cyber-Attack Against Ukrainian Critical Infrastructure URL: https://ics-cert.us-cert.gov/alerts/IR-ALERT-H-16-056-01
[6] Ginter A 2016 *SCADA Security. What's broken and how to fix it* (Abterra Technologies) p 165
[7] Steenstrup K IT and Operational Technology Alignment Innovation Key Initiative Overview URL: https://www.gartner.com/doc/2691517/it-operational-technology-alignment-innovation #a-98481934
[8] Greengard S 2015 *The internet of things* (MIT Press) p 232
[9] Zaramenskih E, Artemev I 2017 *Internet of Things. Research and scope* (Infra-M Publisher) p 188
[10] Roth A 2016 *Einführung und Umsetzung von Industrie 4.0. Grundlagen, Vorgehensmodell und Use Cases aus der Praxis* (Springer Gabler Verlag, Wiesbaden) p 272
[11] Almomani I, Al-Kasasbeh B and Al-Akhras M 2016 WSN-DS: a dataset for intrusion detection systems in wireless sensor networks *Journal of Sensors* **2016**
[12] Karnouskos S 2012 A SOA-based architecture for empowering future collaborative cloud-based industrial automation *38th Annual Conference on IEEE Industrial Electronics Society* 5766-5772
[13] Yan Y, Qian Y, Sharif H, and Tipper D 2012 A survey on smart grid communication infrastructures: Motivations, requirements and challenges *IEEE communications surveys & tutorials* **15(1)** 5-20
[14] Maglaras L A 2018 Cyber security of critical infrastructures *ICT Express* **4(1)** 42-45
[15] Sun C C, Hahn A and Liu C C 2018 Cyber security of a power grid: State-of-the-art *International Journal of Electrical Power & Energy Systems* **99** 45-56
[16] Meltzer D, Lund J *Industrial Cyber Security for dummies* URL: http://www.vectorinfotech.com/assets/files/Industrial-Cyber-Security-for-dummies.pdf
[17] Kaspersky Industrial CyberSecurity URL: https://ics.kaspersky.ru/
[18] Kaspersky Industrial Cybersecurity URL: https://softprom.com/sites/default/files/materials/KICS_rus_0816.pdf

[19] Positive Technologies Industrial Security Incident Manager URL: https://www.ptsecurity.com /ru-ru/products/isim/
[20] Security Matters SilentDefense URL: https://www.secmatters.com/product
[21] SilentDefense datasheet URL: https://www.secmatters.com/hubfs/Security_Matters-March 2017/PDF/SilentDefense-Datasheet.pdf
[22] Yick J, Mukherjee B and Ghosal D 2008 Wireless sensor network survey *Computer networks* **12(52)** 2292-2330
[23] Pathan A S K, Lee H W and Hong C S 2006 Security in wireless sensor networks: issues and challenges *8th International Conference Advanced Communication Technology (ICACT)* **2** 1043- 1048
[24] Chelli K 2015 Security issues in wireless sensor networks: Attacks and countermeasures *Proceedings of the World Congress on Engineering* (London, UK) 1-3
[25] Loo J, Mauri J L and Ortiz J H 2016 *Mobile ad hoc networks: current status and future trends* (CRC Press) p 538
[26] Sinha P 2017 Security vulnerabilities, attacks and countermeasures in wireless sensor networks at various layers of OSI reference model: A survey *IEEE International Conference on Signal Processing and Communication (ICSPC)* (Coimbatore, Tamil Nadu, India) 288-293
[27] Can O, Sahingoz O K 2015 A survey of intrusion detection systems in wireless sensor networks *6th International Conference on Modeling, Simulation, and Applied Optimization (ICMSAO)* (Istanbul, Turkey) 1-6
[28] Al-Dabbagh A W, Li Y and Chen T 2018 An intrusion detection system for cyber attacks in wireless networked control systems *IEEE Transactions on Circuits and Systems II: Express Briefs* **8(65)** 1049-1053
[29] Almomani and Al-Kasasbeh B 2015 Performance analysis of LEACH protocol under Denial of Service attacks *Proceedings of the 6th IEEE International Conference on Information and Communication Systems (ICICS)* (Amman, Jordan) 292-297
[30] Kornienko A A, Slyusarenko I M *Intrusion Detection Systems and Methods: Current State and Areas for Improvement* URL: http://citforum.ru/security/internet/ids_overview/
[31] Kashyap S, Agrawal P, Pandey V S and Keshri S P 2013 Soft Computing Based Classification Technique Using KDD 99 Data Set for Intrusion Detection System *Int. J. Advanced Research in Electrical, Electronics and Instrumentation Engineering* **2(2)** 1398-1405
[32] Moustafa N, Slay J 2015 UNSW-NB15: a comprehensive data set for network intrusion detection system (UNSW-NB15 network data set) *Military Communications and Information Systems Conference (MilCIS)* (Canberra, Australia)
[33] Perrin C *The CIA Triad* URL: https://www.techrepublic.com/blog/it- security/the-cia-triad/
[34] Easton V J, McColl J H *Hypothesis testing* URL: http://www.stats.gla.ac.uk/steps/ glossary/hypothesis_testing.html
[35] Branitskiy A A, Kotenko I V 2016 Analysis and classification of network attack detection methods *Proc. SPIIRAN* **2(45)** 207-44
[36] Katasev A S, Kataseva D V and Kirpichnikov A P 2015 Neural network diagnostics of abnormal network activity *Bulletin of Kazan Technological University* **18(6)** 163-167

Acknowledgments
This work was supported by the Russian Foundation for Basic Research, research №17-48-020095.

Restoration of images of social networks that have undergone processing, on the example of the social network Instagram

M I Khotilin[1], N S Kravtsova[1], A V Kupriyanov[1,2] and R A Paringer[1,2]

[1]Samara National Research University, Moskovskoe Shosse 34A, Samara, Russia, 443086
[2]Image Processing Systems Institute of RAS - Branch of the FSRC "Crystallography and Photonics" RAS, Molodogvardejskaya street 151, Samara, Russia, 443001

e-mail: turbomax.94@yandex.ru, natalyroom483@gmail.com, rusparinger@gmail.com

Abstract. This paper is devoted to finding the source images for the processed images of social networks. Existing methods and approaches that take place in the performance of this task are considered. The algorithms of image recovery is investigated and planned for finalization.

1. Introduction

In the modern world it is continuously generated a huge amount of data, whether the data received from the satellite, or sensors in the aircraft, bank transactions, patient diagnostic data, etc. A special place is occupied by social networks. The significance of social networks is due to the fact that, on the one hand they are the subject of socialization of people, and on the other - the most powerful and affordable political, ideological and economic instrument. A number of papers are dedicated to researches of social networks as systems, which contain large volumes of dat.

Images have always occupied an important place in the life of people: whether it be cave paintings in primitive society, paintings by great artists, and especially photographs. With the advent of social networks, photos began to move from the category of personal to the category of public domain and became not only a new way of self-presentation, but also gave rise to other ways of thinking and vision [1]. People literally convey their individuality through photos: express their opinions, upload so-called “selfies”, arrange discussions, share impressions and emotions in comments to photos or by color processing photos using various editors or filters.Social network “Instagram” began to play a huge role in the life of modern society. Data and images from it helps in various areas of life, for example, the police can solve crimes through photo data, psychologists can study various trends in the lives of modern people.

The color characteristic is one of the most significant characteristics describing the image. With it, you can extract various data that can be useful in many areas of human activity, such as psychology and sociology. In 2015, the Laboratory for the Study of Big Data, under the leadership of Lev Manovich, collected and analyzed 2.3 million photographs from the Instagram social network of large cities such as New York, Tokyo, Bangkok, San Francisco and eleven other global cities. With the help of the analysis conducted by the laboratory, it was possible to see the “biological rhythms” for which

the metropolis lives, as well as the life of a resident of one city differs from that of another, as the time frame and much more differ [2].

Also, the extracted data can be useful for example in medicine, in object selection and recognition of objects and in many other areas.

Image restoration is one of the most important tasks of computer vision and image processing. It finds its solution, for example, when detecting various kinds of tumors in medicine, when tracking objects in security systems, when restoring images, and in many others. For image restoration, various methods are used, both classical and modern, using work with neural networks and big data processing tools, or BigData.

In the future it is planned to transfer the implementation to such services as Apache Flume for data collection and Apache Spark for data processing as well as use Apache Cassandra for data storage.

This paper describes a method for finding the original image by determining the filter characteristic with which it was processed.

2. Getting the source data for image recovery

During the work, it was decided to use the social network Instagram, for analysis. Users of this social network often post photos and images that have been previously processed by various filters.

To obtain the original data, as a first step it was decided to write software that allows access to the social network through special API and obtain the necessary data from it, namely the image itself and additional service information containing the description and so-called tags indicating the filters used.
To gain access to the images, it is necessary to authenticate, which requires special access keys. Authentication occurs through OAuth protocol version 2.0. This protocol is an open authorization protocol that allows limited access to protected resources to a third party (our software system), without the need to transfer a username and password to a third party (complex). After passing authorization and authentication, it becomes possible to access images and their descriptions and service information, and to download it to the computer as files.

3. Restoration of original images

Each image is a set of pixels characterized by its color brightness values and the whole image can be viewed as a three-layer table, each layer of which is a table consisting of pixels with specific brightness values of red, green, and blue. Images processed using special filters have a color-brightness distribution different from the original image.

In the course of the work, an educational sample of images was prepared, containing 100 pairs of images - the original and processed by a certain type of filter, as well as its name. An example of image data is shown in figure 1.

Figure 1. Used images sample.

Next, using the written analysis software, color analysis of the images was carried out: the distribution of colors by brightness was calculated and histograms were constructed for each of the used filters. An example of the initial histogram of color distribution by layers of a single image is presented in figure 2.

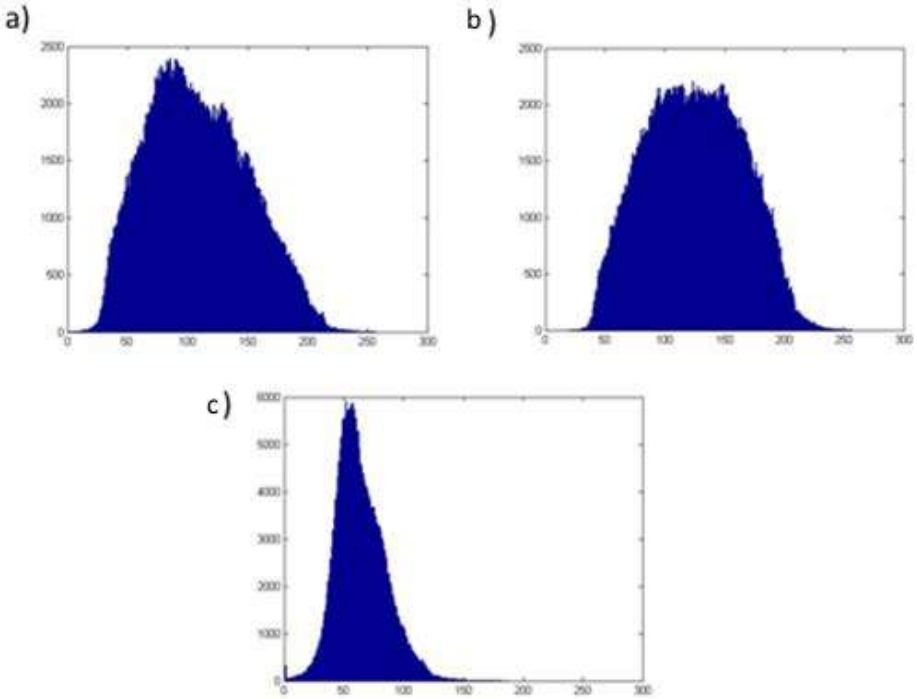

Figure 2. Example of color distribution of one image (a) - red, b) - green, c) - blue).

The distribution for the whole class of images processed by a certain filter is similarly constructed.

Further, since the filter uses the same brightness transformations, then by subtracting the image processed by the filter from the matrix of the original image from the matrix, the filter matrix can be obtained. By adding all the results of calculating the matrices of filters for pairs of images processed by the same filters, and also by normalizing, we obtain a common matrix for a filter of a certain type.

Hence, since the service information obtained from the social network in the previous step contains data on the applied filter, it is not difficult to restore the original image using the filter matrix.

To test this hypothesis, a test sample was organized, containing about 1000 images received from the Instagram network, and analysis and restoration of the original images was carried out. An example of the result of the work can be seen in figure 3.

Figure 3. Example of processed and original reconstructed image (a) - processed, b) - original reconstructed).

4. Conclusion

Definition of source images is one of the most significant tasks of computer vision and image processing. It finds its solution in various fields of human activity. Often, existing image processing

methods work fine with relatively small amounts of raw data. Processing of large arrays of source images takes considerable time, which is absolutely unacceptable in a number of tasks.

Currently, work is underway to adapt the above methods to work with large volumes of data or BigData, and software is being developed that allows for the proper processing of image arrays and the recognition of objects on them.

5. References

[1] Manovich L Z 2015 Instagram is a window in the mind and imagination of a person Instagram is a window in the mind and imagination of a person Instagram is a window in the mind and imagination of a person *MediaProfi*
[2] Khaykin S 2008 *Neural networks: full course* (Williams Publishing House) p 1131
[3] Sergeev V V 1998 Application of the methodology of pattern recognition in digital image processing tasks *Autometry* **2** 63-76
[4] Verhagen K, Doyne R and Groon F 1985 *Pattern Recognition: Status and Prospects* (M.: R&S) p 104
[5] Samal D I 2002 Algorithms for human identification from a photo portrait based on geometric transformations *Thesis for the degree of Candidate of Science. Institute of Technical Sciences. Cybern* (NAS of Belarus, Minsk) p 170
[6] Graphic filters based on the torsion matrix URL: https://habrahabr.ru/post/43895 (01.05.2019)
[7] Kravtsova N S, Paringer R A and Kupriyanov A V 2017 Parallel implementation of the informative areas generation method in the spatial spectrum domain *Computer Optics* **41(4)** 585-587 DOI: 10.18287/2412-6179-2017-41-4-585-587
[8] Khotilin M, Blagov A 2016 Visualisation and cluster analysis of social networks *CEUR Workshop Proceedings* **1638** 843-850
[9] Reece A, Danforth C 2019 Instagram photos reveal predictive markers of depression *EPJ Data Science* URL: https://epjdatascience.springeropen.com/articles/10.1140/epjds/s13688-017-0110-z (07.05.2019)
[10] *Image Pre-processing – Towards Data Science* URL: https://towardsdatascience.com/image-pre-processing-c1aec0be3edf (17.05.2019)
[11] Krishnaveni C, Udhayakumar U 2018 Big Data Analytics: Challenges and Applications for Social Media Data *International Journal of Engineering and Techniques - National Conference On Emerging Trends in Computing Technologies* **107** 1-6

Acknowledgments

This work was financially supported by the Russian Foundation for Basic Research under grant # 19-29-01135, # 18-37-00418, # 17-01-00972 and by the Ministry of Science and Higher Education within the State assignment to the FSRC “Crystallography and Photonics” RAS No. 007-GZ/Ch3363/26 (theoretical results).

САМАРСКИЙ УНИВЕРСИТЕТ
SAMARA UNIVERSITY

ИСОИ IPSI

NVIDIA.

HUAWEI

intel

CERN openlab

Locus